

Chang Q Sun

Relaxation of the Chemical Bond

Skin Chemisorption Size Matter
ZTP Mechanics H₂O Myths



Springer Series in Chemical Physics

Volume 108

Series editors

Albert W. Castleman, University Park, USA

Jan Peter Toennies, Göttingen, Germany

Kaoru Yamanouchi, Tokyo, Japan

Wolfgang Zinth, München, Germany

For further volumes:

<http://www.springer.com/series/676>

The purpose of this series is to provide comprehensive up-to-date monographs in both well established disciplines and emerging research areas within the broad fields of chemical physics and physical chemistry. The books deal with both fundamental science and applications, and may have either a theoretical or an experimental emphasis. They are aimed primarily at researchers and graduate students in chemical physics and related fields.

Chang Q Sun

Relaxation of the Chemical Bond

Skin Chemisorption Size Matter
ZTP Mechanics H₂O Myths

 Springer

Chang Q Sun
Electrical and Electronic Engineering
Nanyang Technological University
Singapore
Singapore

Additional material to this book can be downloaded from <http://extras.springer.com>

ISSN 0172-6218

ISBN 978-981-4585-20-0

ISBN 978-981-4585-21-7 (eBook)

DOI 10.1007/978-981-4585-21-7

Springer Singapore Heidelberg New York Dordrecht London

Library of Congress Control Number: 2014933535

© Springer Science+Business Media Singapore 2014

This work is subject to copyright. All rights are reserved by the Publisher, whether the whole or part of the material is concerned, specifically the rights of translation, reprinting, reuse of illustrations, recitation, broadcasting, reproduction on microfilms or in any other physical way, and transmission or information storage and retrieval, electronic adaptation, computer software, or by similar or dissimilar methodology now known or hereafter developed. Exempted from this legal reservation are brief excerpts in connection with reviews or scholarly analysis or material supplied specifically for the purpose of being entered and executed on a computer system, for exclusive use by the purchaser of the work. Duplication of this publication or parts thereof is permitted only under the provisions of the Copyright Law of the Publisher's location, in its current version, and permission for use must always be obtained from Springer. Permissions for use may be obtained through RightsLink at the Copyright Clearance Center. Violations are liable to prosecution under the respective Copyright Law. The use of general descriptive names, registered names, trademarks, service marks, etc. in this publication does not imply, even in the absence of a specific statement, that such names are exempt from the relevant protective laws and regulations and therefore free for general use.

While the advice and information in this book are believed to be true and accurate at the date of publication, neither the authors nor the editors nor the publisher can accept any legal responsibility for any errors or omissions that may be made. The publisher makes no warranty, express or implied, with respect to the material contained herein.

Printed on acid-free paper

Springer is part of Springer Science+Business Media (www.springer.com)

In memory of and dedicated to my parents

Bond formation and relaxation and the associated energetics, localization, entrapment, and polarization of electrons mediate the macroscopic performance of substance accordingly

Preface

Phenomena due to chemical bond reformation and relaxation are ubiquitous and important. A consistent and systematic understanding of such matters is yet urgently needed, which is the driving force behind the author's efforts in the past two decades.

Pauling indicated in 1939 that the nature of the chemical bond bridges the structures and properties of crystals and molecules. In order to change the physical properties of a substance, one has to control the processes of formation, dissociation, relaxation, and vibration of the chemical bond. The foremost task for accomplishing such goals is to correlate the detectable properties of a material to the parameters of all bonds and nonbonds involved, and to ascertain the interdependence of various properties. Consistent insight into the nature, length, and the energy of the chemical bonds and the associated energetics and dynamics of densification, localization, polarization, and redistribution of electrons during the process of bond reformation and relaxation are essential. Hence, identifying and subsequently controlling the factors and efficient means in engineering bonds and electrons are the ultimate objectives of the community of condensed matter physics and chemistry. The aim of this book is to explore these perspectives.

This book is composed of four parts:

Part I deals with the formation and relaxation dynamics of bonds and nonbonds during chemisorption of O, N, and C to the skins of solid specimens from the perspectives of chemical bond, energy band, surface potential barrier (3B), and their correlation. This part demonstrates that: (i) sp^3 -orbit hybridization is necessary for O, N, and C interacting with atoms in the solid phase to form H_2O , NH_3 , and CH_4 -like tetrahedral structures, which determines the crystallography, morphology, potential barrier, band structure, and the chemical physical properties of the chemisorbed skins; (ii) chemisorption modifies the valence band of the host with four additional energy states, i.e., bonding electron pairs, nonbonding lone pairs, antibonding dipoles, and electronic holes. Such a practice formulates the valence evolution dynamics of atoms on oriented and reconstructed surfaces in different phases of Ag, Cu, Co, Ni, V, Pd, Pt, Ru, diamond, and N and C reacting with Ni surfaces as well; (iii) numerical analysis of measurements results in the quantification of the Cu_3O_2 bond geometry and its four-stage formation and relaxation dynamics as well as the N–Ni and C–Ni bonding dynamics and bond stress; (iv) the 3B premise unifies and empowers the experimental techniques for

crystal geometry (LEED, XRD), surface morphology (STM), electron binding energy (STS, UPS, XPS), lattice vibration frequency (Raman, EELS), and thermal desorption (TDS) in terms of bonding and electronic dynamics. It is emphasized that the concept of solid skin up to three atomic layers thick describes better the properties and processes at the solid/vacuum interface than the conventional concept of surface without invoking thickness.

Part II is focused on the relaxation of bonds between atoms with fewer neighbors than the ideal in bulk with unraveling of the bond order-length-strength (BOLS) correlation, which clarifies the difference in nature between nanostructures and bulk of the same substance. This part proves that: (i) bonds between undercoordinated atoms become shorter and stronger; (ii) bond contraction increases the local density of bonding electrons and binding energy while bond strengthening deepens the interatomic potential wells and results in quantum entrapment; (iii) the densely and locally entrapped bonding electrons in turn polarize the weakly bound nonbonding electrons (NEP) to form Dirac-Fermi polarons with emergence of properties that bulk parents do not demonstrate; (iv) interaction between undercoordinated atoms in the skin and the fraction of such undercoordinated atoms determine the unusual behavior of nanostructures. The BOLS correlation clarifies the common origin for the unusual performance of defects, surfaces, grain boundaries, and nanostructures of various shapes in chemistry, dielectrics, electronics, magnetism, mechanics, thermodynamics, phononics, and photonics. Based on the core-shell configuration and the local bond average (LBA) approach, the BOLS-NEP notation reconciles the size and shape dependence of known bulk properties and the emerging anomalies of materials at the nanoscale such as catalytic, magnetic, conductor-insulator transition, topologic insulation, etc. The new degree-of-freedom of crystal size results in determination of the energy levels of an isolated atom, the specific heat per bond, etc. It is emphasized that the size-induced emergence of properties are equally important to the size-induced change of known bulk properties at the nanoscale.

Part III deals with the relaxation dynamics of bonds under heating and compressing and describes the rules governing the temperature- and pressure-resolved elastic and plastic properties of under- and hetero-coordinated systems. This part shows that: (i) binding energy density determines the elasticity and the yield strength; the atomic cohesive energy determines the thermal stability of materials; and the applied forces in measurements create defects and heat the specimen; (ii) undercoordination-induced energetics determines the unusual mechanical performance of atomic chains, atomic sheets, nanotubes, nanowires, point defects, nanograins, liquid and solid skins, and hetero-junction interfaces; (iii) the enhancement of elasticity and polarization of the skin dictates the superhydrophobicity, superfluidity, superlubricity, and supersolidity at the contacting interfaces; (iv) competition between the energy density and atomic cohesive energy determines intrinsically while competition among the dislocation creation and accumulation, and heat softening determines extrinsically the superelasticity, superplasticity, superrigidity, and the extreme strength in the

inverse Hall–Petch relationship of solid at the nanoscale. It is emphasized that the concepts of local binding energy density and atomic cohesive energy are more efficient than the conventional concept of free energy in describing attributes of a solid at the skin and the interface regions.

Efforts of the above have led to systematic understanding of the unusual behavior of graphene, nanostructured Silicon, ZnO, water ice, etc., and measures and techniques for practical applications.

Part IV is focused on the geometric structure, local potentials, relaxation dynamics of the hydrogen bond (O:H–O), and the associated anomalies of water and ice under cooling, compressing, and clustering. An extension of Pauling’s Ice Rule results in not only the correlation between the size, separation, structure order, and mass density of molecules packing in water and ice but also the O:H–O bond as a pair of asymmetric and coupled oscillators with ultra-short-range interactions. Hydrogen proton undergoes no “frustration” in the O:H–O bond because of the asymmetric local potentials. This part verifies that: (i) Coulomb repulsion between the electron pairs on adjacent oxygen atoms and the disparity within the O:H–O bond determine the difference in nature between water and other common materials; (ii) when the environment changes, the O:H van der Waals bond and the H–O polar-covalent bond relax in the same direction but by different amounts; (iii) compression shortens and stiffens the O:H bond significantly but lengthens and softens the H–O bond via Coulomb repulsion; coordination number reduction (clusters, surface skins, and ultrathin films) causes H–O bond contraction and results in the opposite trends of O:H–O bond relaxation to that happening under compression; the bonding part with a relatively lower specific-heat contracts upon cooling, meanwhile, this part forces the other to elongate by different amounts via the repulsion. This process leads to the thermally driven density and phonon-stiffness oscillations of water and ice in four temperature regions. In the liquid and solid phases, the softer O:H bond contracts more than the stiffer H–O elongates, hence, an O:H–O cooling contraction and the seemingly regular process of cooling densification take place. In the water–ice transition phase, the H–O contracts less than the O:H elongates, leading to an O:H–O elongation and volume expansion during freezing. At temperature below 80 K, density increases slightly due to O:H–O bond angle stretching as the length and energy of the H–O and the O:H bond conserve. In ice, the O–O distance is longer than it is in water, resulting in a lower density, so that ice floats; (iv) liquid water is comprised of a high-density body of tetrahedrally coordinated structures with O:H–O bond angle and intermolecular distance fluctuations and a supersolid skin that is elastic, hydrophobic, polarized, ice-like, with two molecular layers of ultra-low density. The supersolid skin not only slipperizes ice but also enhances the surface tension of water. Modulation of the intermolecular Coulomb repulsion by replacing O with other ions results in Hofmeister series. It is emphasized that focusing on the statistical mean of all the cooperative parameters is more reliably revealing than on the instantaneous accuracy of one parameter at a time for the strongly correlated and fluctuating system of liquid water.

Apart from the perspective in each part, this work ends with a solution to the Mpemba paradox—hotter water freezes quicker than colder water does. O:H-O bond exhibits memory to emit heat at a rate depending on the initial storage. The skin supersolidity creates gradient of heat diffusion coefficient to ensure thermal current flowing outwardly. Being sensitive to the liquid volume and the drain temperature, the paradox happens only in the non-adiabatic “source-path-drain” cycling system.

It is a great pleasure to share these personal thoughts and learnings though some formulations need further refinement and improvement. Critiques from readers are cordially welcome and much appreciated.

I hope that this book will inspire fresh ways of thinking and stimulate more interest and activities toward coordination bond and electronic engineering. Directing effort to the areas of nonbonding electronics, water and soft matter electronics, quantitative phonon and electron spectroscopy, and materials gene engineering could be even more challenging, fascinating, promising, and rewarding.

I would like to express my sincere thanks to colleagues, friends, peers, and seniors for their encouragement, invaluable input, and support, to my students and collaborators for their contribution, and to my family, my wife Meng Chen and daughter Yi, for their assistance, patience, support, and understanding throughout this adventurous journey.

February 2014

Chang Q Sun

Contents

Part I O, N, and C Chemisorption

| | | |
|----------|---|----|
| 1 | Introduction | 3 |
| 1.1 | Scope | 3 |
| 1.2 | Overview | 4 |
| 1.3 | Issues to Be Addressed | 6 |
| 1.3.1 | Bond Nature and Bonding Kinetics | 6 |
| 1.3.2 | Alternation of Atomic Valencies | 7 |
| 1.3.3 | Spectroscopic Correspondences | 8 |
| 1.3.4 | Driving Forces Behind Reconstruction | 9 |
| 1.3.5 | Work Function and Inner Potential Change | 10 |
| 1.3.6 | Factors Controlling Bond Formation | 10 |
| 1.4 | Objectives | 11 |
| | References | 12 |
| 2 | Theory: Bond–Band–Barrier (3B) Correlation | 17 |
| 2.1 | Basics | 17 |
| 2.1.1 | Regular Bonds: Interatomic Potential and Electron Configuration | 17 |
| 2.1.2 | Chemisorption Bonding Environment | 18 |
| 2.1.3 | Bonding Effects | 20 |
| 2.1.4 | Surface Bond Contraction | 24 |
| 2.2 | Chemical Bond: Tetrahedron Geometry | 24 |
| 2.3 | Energy Band: Valence Density of States | 26 |
| 2.4 | Surface Potential Barrier: Morphology | 29 |
| 2.5 | Summary | 31 |
| | References | 31 |
| 3 | STM and LEED: Atomic Valences and Bond Geometry | 33 |
| 3.1 | Phase Ordering | 33 |
| 3.2 | O–Cu(001), (110), (111) | 35 |
| 3.2.1 | O–Cu(001) | 35 |
| 3.2.2 | O–Cu(110) | 39 |
| 3.2.3 | O–Cu(111) | 47 |

| | | |
|----------|---|------------|
| 3.2.4 | VLEED from O–Cu(001) | 48 |
| 3.2.5 | XRD from O–Cu(110) | 66 |
| 3.2.6 | Summary | 68 |
| 3.3 | O–(Rh, Pd)(110) | 69 |
| 3.3.1 | STM Morphology and Crystallography | 69 |
| 3.3.2 | Formulation: Bond and Atomic Valence | 72 |
| 3.4 | O–(Co, Ru)(10 $\bar{1}$ 0) Surface Tri-Phase Ordering | 76 |
| 3.4.1 | STM Morphology and Crystallography | 76 |
| 3.4.2 | Formulation: Atomic Valence and Bond Geometry | 78 |
| 3.5 | O–Rh(111) and O–Ru(0001) | 83 |
| 3.5.1 | Crystallography and Morphology | 83 |
| 3.5.2 | Formulation: Bond Geometry and Atomic Valence | 84 |
| 3.6 | O–(Ag, V)(001) | 90 |
| 3.6.1 | O–Ag(001) | 90 |
| 3.6.2 | O–V(001) | 91 |
| 3.7 | O–Rh(001) and (N, C)–Ni(001) | 95 |
| 3.7.1 | Observations | 95 |
| 3.7.2 | Formulation: Rhombi Chain along the $\langle 11 \rangle$ Direction | 99 |
| 3.7.3 | Quantification: Driving Force and Bond Stress | 102 |
| 3.8 | Cu ₃ C ₂ H ₂ Molecules | 104 |
| 3.9 | Summary | 105 |
| | References | 106 |
| 4 | STS and PES: Valence DOS | 115 |
| 4.1 | Signature Generality | 115 |
| 4.1.1 | STS | 115 |
| 4.1.2 | PES, IPES, and XPS | 118 |
| 4.1.3 | Indication | 124 |
| 4.2 | Specification | 125 |
| 4.3 | Valence DOS of Nitrides | 126 |
| 4.4 | Summary | 127 |
| | References | 128 |
| 5 | TDS: Bond Nature and Bond Strength | 133 |
| 5.1 | TDS and Work Function Correspondence | 133 |
| 5.2 | Specification | 137 |
| 5.3 | Summary | 138 |
| | References | 138 |
| 6 | EELS and Raman: Nonbond Interactions | 141 |
| 6.1 | EELS: Dipole Vibration | 141 |
| 6.2 | Raman: Lone Pair in Oxides, Nitrides, and Bio-Molecules | 143 |
| 6.3 | Summary | 144 |
| | References | 144 |

| | | |
|----------|--|-----|
| 7 | Kinetics of Bond Forming and Bond Switching | 147 |
| 7.1 | Four-Stage Oxide-Bond-Forming Kinetics | 147 |
| 7.2 | Bond Switching: O-Floating and O-Diffusing | 149 |
| 7.3 | Summary | 150 |
| | References | 151 |
| 8 | Design Materials and Processes | 153 |
| 8.1 | Nitrogen-Induced Anomalies | 153 |
| 8.2 | Group Symmetry: Corrosion and Anti-Corrosion | 154 |
| 8.3 | Lone-Pair Interaction: Excessive Elasticity and Mechanical Strength | 156 |
| 8.4 | Magnetic Modulation: Polarization | 158 |
| 8.5 | Bandgap Modulation: Photoluminescence | 160 |
| 8.5.1 | Nitrogen Acceptor: Electron–Hole Pair Production | 160 |
| 8.5.2 | Oxide Blue Light Emission | 161 |
| 8.6 | Work Function Reduction for Field Emission | 162 |
| 8.7 | Geometric Selectivity: Diamond Oxidation | 165 |
| 8.8 | Diamond–Metal Adhesion Enhancement | 168 |
| 8.9 | Perspectives: Molecular Functional Groups | 169 |
| 8.9.1 | B-, C-, N-, O-, and F-induced High- T_c Superconductivity | 169 |
| 8.9.2 | CF ₄ Anticoagulation in Synthetic Blood | 170 |
| 8.9.3 | NO Signaling and Living Cells | 170 |
| 8.10 | Summary | 171 |
| | References | 172 |
| 9 | Concluding Remarks | 177 |
| 9.1 | General Understanding | 177 |
| 9.1.1 | Essential Events on a Surface | 177 |
| 9.1.2 | Bond Nature and Bond-Forming Kinetics | 178 |
| 9.1.3 | Orientation Specificity of the Tetrahedron | 179 |
| 9.1.4 | Consequences of Bond Forming | 181 |
| 9.1.5 | Driving Forces Behind Reconstruction | 182 |
| 9.1.6 | Factors Controlling Bond Formation | 183 |
| 9.2 | Capability Enhancement of Probing Techniques | 183 |
| 9.2.1 | STM and STS | 183 |
| 9.2.2 | PES, TDS, EELS, and VLEED | 184 |
| 9.3 | Advancement in Applications | 185 |
| 9.4 | Recommendations | 185 |
| | References | 188 |

Part II Size Matter

| | |
|--|-----|
| 10 Introduction | 193 |
| 10.1 Scope | 193 |
| 10.2 Overview: Size Fascinations | 194 |
| 10.3 Challenge | 197 |
| 10.4 Objectives | 198 |
| References | 198 |
| 11 Theory: BOLS and NEP | 203 |
| 11.1 Broken Bond | 203 |
| 11.1.1 Barrier Confinement | 203 |
| 11.1.2 Atomic CN Reduction | 204 |
| 11.2 Bond Relaxation in Length and Energy | 205 |
| 11.2.1 Atomic CN-Radius Correlation | 205 |
| 11.2.2 BOLS Notation | 205 |
| 11.2.3 Pauling's Notation | 207 |
| 11.2.4 Physical BOLS | 208 |
| 11.2.5 Chemical BOLS | 210 |
| 11.3 Non-Bonding Electron Polarization | 210 |
| 11.3.1 Attributes of Non-Bonding Electrons | 210 |
| 11.3.2 Non-Bonding Electron Polarization | 211 |
| 11.4 Shape and Size Dependency | 212 |
| 11.4.1 Core-Shell Configuration: Skin Volume Fraction | 212 |
| 11.4.2 Local Bond Average | 213 |
| 11.5 Scaling Relations | 214 |
| 11.5.1 LBA Scaling Relation | 214 |
| 11.5.2 Surface-to-Volume Ratio | 216 |
| 11.6 Summary | 217 |
| References | 220 |
| 12 Skin Bond Relaxation and Nanosolid Densification | 223 |
| 12.1 Skin Bond Relaxation | 223 |
| 12.1.1 Monolayer Relaxation | 223 |
| 12.1.2 Multilayer Relaxation | 226 |
| 12.2 Liquid Skin, Gas Phase, and Interface | 226 |
| 12.3 Nanosolid Densification | 227 |
| 12.3.1 Known Facts | 227 |
| 12.3.2 Possible Mechanisms | 229 |
| 12.3.3 BOLS Formulation | 229 |
| 12.3.4 Strain-Induced Stiffness | 232 |
| 12.4 Energy Entrapment | 233 |
| 12.5 Summary | 234 |
| References | 234 |

| | | |
|-----------|---|-----|
| 13 | End and Edge States: Entrapment and Polarization | 239 |
| 13.1 | Atomic Chains, Nanowires, and Clusters | 239 |
| 13.1.1 | Quantum Entrapment with Polarization | 239 |
| 13.1.2 | Entrapment Without Polarization | 244 |
| 13.2 | Graphite Monolayer Skin and GNR Edges | 245 |
| 13.2.1 | Defect and Edge: Entrapment with Polarization | 245 |
| 13.2.2 | Monolayer Skin: Entrapment Without Polarization | 247 |
| 13.2.3 | CN-Resolved Bond Energy | 247 |
| 13.2.4 | DFT-TB Derivatives: Dirac–Fermi Polarons | 248 |
| 13.3 | Summary | 248 |
| | References | 249 |
| 14 | Thermal Stability: Atomic Cohesive Energy | 253 |
| 14.1 | Cohesive Energy | 253 |
| 14.1.1 | Definition | 253 |
| 14.1.2 | Known Mechanisms | 254 |
| 14.1.3 | BOLS Formulation | 255 |
| 14.1.4 | Atomic Vacancy Formation | 256 |
| 14.2 | Liquid–Solid Phase Transition | 259 |
| 14.2.1 | Undercooling: Skin Pre-Melting | 259 |
| 14.2.2 | Overheating: Interface Effect | 262 |
| 14.2.3 | BOLS Formulation | 262 |
| 14.2.4 | Verification: Liquidation and Evaporation | 265 |
| 14.2.5 | T_m Oscillation | 268 |
| 14.2.6 | Remarks | 271 |
| 14.3 | Solid Phase Transition | 271 |
| 14.3.1 | Observations | 271 |
| 14.3.2 | BOLS Formulation | 275 |
| 14.3.3 | Verification: Critical Size | 277 |
| 14.4 | Diffusion and Crystal Growth | 280 |
| 14.4.1 | Diffusivity | 280 |
| 14.4.2 | Crystal Growth | 283 |
| 14.4.3 | Thermally Control of Crystal Size and Bandgap | 286 |
| 14.5 | Summary | 288 |
| | References | 288 |
| 15 | Lattice Dynamics: Phonon Relaxation | 299 |
| 15.1 | Background | 299 |
| 15.1.1 | Acoustic Phonon Stiffening | 300 |
| 15.1.2 | Optical Phonon Softening | 302 |
| 15.2 | BOLS Formulation | 304 |
| 15.2.1 | Scattering by Vibrations | 304 |
| 15.2.2 | Frequency of Lattice Vibration | 304 |
| 15.2.3 | Size Dependence | 306 |

| | | |
|-----------|--|------------|
| 15.3 | Verification and Quantification | 306 |
| 15.3.1 | CN-Resolved Optical Phonon Softening | 306 |
| 15.3.2 | LFR: Intercluster Interaction | 307 |
| 15.3.3 | Amplitude and Frequency of Skin Atom Vibration | 308 |
| 15.4 | Summary | 310 |
| | References | 310 |
| 16 | Electrons: Entrapment and Polarization | 313 |
| 16.1 | Known Facts | 313 |
| 16.1.1 | Core-Level Shift | 313 |
| 16.1.2 | Known Mechanisms | 317 |
| 16.2 | BOLS-TB Formulation | 318 |
| 16.2.1 | Hamiltonian and Energy Dispersion | 318 |
| 16.2.2 | BOLS: Coordination Resolution | 320 |
| 16.3 | Coordination-Resolved Electronic Binding Energy | 322 |
| 16.3.1 | Surface: Skin-Resolved Quantum Entrapment | 322 |
| 16.3.2 | Surface Energetics | 322 |
| 16.4 | Nanosolid CLS | 324 |
| 16.4.1 | Skin, Size, and Edge Entrapment | 324 |
| 16.4.2 | Core-Shell Discriminative Entrapment | 330 |
| 16.4.3 | Number-of-Layer Dependence of Graphene | 330 |
| 16.4.4 | Size-Induced Polarization | 333 |
| 16.5 | Electroaffinity and Work Function | 334 |
| 16.5.1 | Electroaffinity Modulation: Valance Entrapment | 334 |
| 16.5.2 | Workfunction: Polarization or Entrapment | 335 |
| 16.6 | Summary | 338 |
| | References | 339 |
| 17 | Bandgap Expansion: Photon Emission and Absorption | 345 |
| 17.1 | Observations | 345 |
| 17.2 | Known Mechanisms | 348 |
| 17.3 | BOLS Formulation | 349 |
| 17.3.1 | Energy Band Formation | 349 |
| 17.3.2 | Hamiltonian Perturbation | 351 |
| 17.4 | Process of Photon Emission and Absorption | 352 |
| 17.4.1 | Electron-Phonon Coupling | 352 |
| 17.4.2 | E_G Expansion | 354 |
| 17.4.3 | PL Blueshift | 354 |
| 17.5 | Bandwidth and Band Tails | 356 |
| 17.5.1 | Bandwidth: Charge Densification | 356 |
| 17.5.2 | Surface States and Band Tails | 358 |
| 17.6 | E_G Expansion of GNRs | 359 |

| | | |
|-----------|--|------------|
| 17.6.1 | Experimental and Numerical Inconsistency | 359 |
| 17.6.2 | Impurity States | 360 |
| 17.6.3 | BOLS-TB: Edge Quantum Entrapment | 361 |
| 17.6.4 | Dispersion Linearization | 363 |
| 17.7 | Summary | 364 |
| | References | 365 |
| 18 | Dielectric Suppression: Electron Polarization | 371 |
| 18.1 | Background | 371 |
| 18.2 | BOLS Formulation | 373 |
| 18.2.1 | Electron Polarization | 373 |
| 18.2.2 | Complex Dielectrics | 374 |
| 18.3 | Numerical Verification | 376 |
| 18.3.1 | Dielectric Suppression | 376 |
| 18.3.2 | Blueshift of Photoabsorption Coefficient | 379 |
| 18.4 | Summary | 380 |
| | References | 381 |
| 19 | Magnetic Modulation: Atomic CN and Thermal Coupling | 383 |
| 19.1 | Background | 383 |
| 19.1.1 | Observations | 383 |
| 19.1.2 | Known Mechanisms | 386 |
| 19.2 | BOLS Formulation | 388 |
| 19.2.1 | Charge Localization | 388 |
| 19.2.2 | Brillouin Function | 389 |
| 19.3 | Experimental and Numerical Verification | 390 |
| 19.3.1 | Ni Films at the Ambient Temperature | 390 |
| 19.3.2 | Monte Carlo Computation | 391 |
| 19.4 | Summary | 396 |
| | References | 397 |
| 20 | Functionalities of Non-Bonding Electrons: Size Emergence | 401 |
| 20.1 | Significance of Non-Bonding Electrons | 401 |
| 20.2 | Diluted Magnetism: Defect Locked Dipoles | 402 |
| 20.2.1 | Nonmagnetic Metals at the Nanoscale | 402 |
| 20.2.2 | Graphite Vacancy and GNR Edges | 403 |
| 20.2.3 | Oxides and Nitrides | 403 |
| 20.2.4 | Edge States Versus Dilute Magnetism | 404 |
| 20.3 | Conductor-Insulator Transition: E_G Opening and Surface Plasmonics | 405 |
| 20.4 | Catalytic Conversion and Enhancement | 406 |
| 20.5 | Superhydrophobicity, Superfluidity, Superlubricity, and Supersolidity | 410 |

| | | |
|---|--|------------|
| 20.5.1 | Observations | 411 |
| 20.5.2 | Known Mechanisms | 415 |
| 20.5.3 | BOLS-NEP Formulation | 416 |
| 20.5.4 | Electrolevitation | 417 |
| 20.6 | Electric Energy Harvesting | 420 |
| 20.7 | Summary | 421 |
| | References | 422 |
| 21 | Concluding Remarks | 427 |
| 21.1 | Attainment. | 427 |
| 21.2 | Limitations | 429 |
| 21.3 | Prospects | 431 |
| | References | 432 |
| | | |
| Part III Atomistic Solid Mechanics | | |
| 22 | Introduction | 439 |
| 22.1 | Scope | 439 |
| 22.2 | Overview. | 440 |
| 22.2.1 | Basic concepts | 440 |
| 22.2.2 | Challenges | 443 |
| 22.3 | Objectives | 449 |
| | References | 450 |
| 23 | Theory: Multiple-Field Coupling | 457 |
| 23.1 | Pressure-, Strain-, and Temperature-Resolved BOLS. | 457 |
| 23.1.1 | BOLS Formulation | 457 |
| 23.1.2 | Thermal Expansion | 459 |
| 23.1.3 | High-Temperature and Low-Stress Approximation | 462 |
| 23.2 | Multi-Field Coupling | 463 |
| 23.3 | Factors Dominating Mechanical Strength. | 464 |
| 23.4 | Summary | 465 |
| | References | 465 |
| 24 | Liquid and Solid Skins | 469 |
| 24.1 | Observations | 470 |
| 24.1.1 | Surface Energetics: Classical Concepts | 470 |
| 24.1.2 | Solid Skin Rectification. | 473 |
| 24.1.3 | Liquid Skin Elasticity: Adsorption and Thermal Excitation | 477 |
| 24.2 | Atomistics of Surface Energetics | 480 |
| 24.2.1 | Motivation | 480 |
| 24.2.2 | Atomistic Definition | 481 |

| | | |
|-----------|--|------------|
| 24.3 | Analytical Expressions | 483 |
| 24.3.1 | Surface Energetics | 483 |
| 24.3.2 | Elasticity and Yield Strength | 483 |
| 24.4 | Strain-Induced Skin Elasticity and Stress. | 484 |
| 24.4.1 | Bond Nature and Surface Curvature | 484 |
| 24.4.2 | T-Dependent Liquid Skin Tension | 486 |
| 24.4.3 | Strain-Induced Skin Elasticity and Strength. | 489 |
| 24.5 | Adsorbate-Induced Skin Stress: Bonding Effect | 489 |
| 24.5.1 | Observations | 489 |
| 24.5.2 | Electronic Origin: Charge Entrapment and Polarization | 492 |
| 24.6 | Nitrogen-Enhanced Elasticity and Hardness. | 494 |
| 24.6.1 | Observations | 494 |
| 24.6.2 | Atomistic Mechanism | 494 |
| 24.7 | Summary | 496 |
| | References | 497 |
| 25 | Monatomic Chains: Strength and Extensibility | 503 |
| 25.1 | Observations | 503 |
| 25.1.1 | Temperature-Dependent Strain Limit | 503 |
| 25.1.2 | Known Mechanisms | 505 |
| 25.2 | T-BOLS Formulation | 507 |
| 25.2.1 | Chain Melting Energetics | 507 |
| 25.2.2 | Elasticity and Extensibility | 508 |
| 25.2.3 | Strain Limit | 508 |
| 25.3 | Bonding Identities | 510 |
| 25.3.1 | MC Bonding Identities | 510 |
| 25.3.2 | Specific Heat and Breaking Limit. | 510 |
| 25.3.3 | Criteria for MC Formation. | 511 |
| 25.4 | Summary | 512 |
| | References | 513 |
| 26 | Atomic Sheets, Nanotubes, and Nanowires. | 517 |
| 26.1 | Observations | 517 |
| 26.1.1 | Stiffness and Elasticity | 517 |
| 26.1.2 | Thermal and Chemical Stability. | 518 |
| 26.2 | BOLS Formulation | 520 |
| 26.3 | Verification | 520 |
| 26.3.1 | CN-Resolved C–C Bond Length. | 520 |
| 26.3.2 | C–C Bond Energy and Elasticity | 521 |
| 26.3.3 | Elasticity: Wall Thickness Dependence. | 522 |
| 26.3.4 | Superplasticity of CNT | 523 |

| | | |
|-----------|--|------------|
| 26.4 | Nanowires | 524 |
| 26.4.1 | Elasticity and Strength | 524 |
| 26.4.2 | Nanowire Superplasticity: Bond Unfolding | 526 |
| 26.4.3 | Breaking Modes of Nanowires | 528 |
| 26.5 | Summary | 529 |
| | References | 530 |
| 27 | Nanograins: I. Elasticity and Compressibility | 535 |
| 27.1 | Known Mechanisms | 535 |
| 27.1.1 | Size Dependence | 535 |
| 27.1.2 | Temperature Dependence | 536 |
| 27.1.3 | Pressure Dependence | 537 |
| 27.2 | TP-BOLS Formulation | 537 |
| 27.2.1 | Size, Pressure, and Temperature Dependence. | 537 |
| 27.2.2 | Debye Temperature and Specific Heat | 540 |
| 27.2.3 | Raman Shift Versus Young's Modulus | 542 |
| 27.3 | TP-BOLS Expectations | 543 |
| 27.3.1 | Elasticity and Extensibility | 543 |
| 27.3.2 | Debye Temperature and Specific Heat | 545 |
| 27.4 | <i>K</i> , <i>P</i> , and <i>T</i> Dependence of Elasticity and Vibration Frequency | 547 |
| 27.4.1 | Au and Ag Metals | 547 |
| 27.4.2 | Group IV Elements | 548 |
| 27.4.3 | II–VI Semiconductors | 553 |
| 27.4.4 | III–V Semiconductors | 554 |
| 27.4.5 | Other Compounds. | 555 |
| 27.5 | Summary | 561 |
| | References | 562 |
| 28 | Nanograins: II. Plasticity and Yield Stress. | 571 |
| 28.1 | Hall–Petch Relationship | 571 |
| 28.2 | Mesoscopic Models | 573 |
| 28.2.1 | HPR-I: Linear Hardening. | 574 |
| 28.2.2 | IHPR-II: HPR Deviation | 575 |
| 28.2.3 | IHPR-III: Softening | 575 |
| 28.2.4 | HPR-IHPR Transition | 576 |
| 28.2.5 | Strongest Grain Size | 577 |
| 28.2.6 | $T_m(K)$ Dependent IHPR | 578 |
| 28.3 | T-BOLS Formulation: Dual Competition. | 578 |
| 28.4 | Verification | 581 |
| 28.4.1 | Strongest Sizes in the IHPR. | 581 |
| 28.4.2 | T_C for Phase Transition. | 581 |
| 28.4.3 | Strongest Grain Size | 581 |
| 28.4.4 | The Strongest Size | 585 |

| | | |
|-----------|--|------------|
| 28.4.5 | Size Effect on $T_C(x)$ and $T_m(x)$ | 586 |
| 28.4.6 | Quasi-Molten State and Superplasticity | 587 |
| 28.5 | Elasticity Versus Hardness. | 588 |
| 28.6 | Size and Pressure Compensation on T_C | 590 |
| 28.6.1 | Known Identities | 590 |
| 28.6.2 | Known Mechanisms | 591 |
| 28.6.3 | BOLS Formulation | 591 |
| 28.6.4 | Verification | 592 |
| 28.7 | Summary | 594 |
| | References | 595 |
| 29 | Atomic Vacancy, Nanocavity, and Porous Foams. | 603 |
| 29.1 | Observations | 603 |
| 29.1.1 | Atomic Vacancies and Point Defects | 603 |
| 29.1.2 | Nanocavity | 604 |
| 29.1.3 | Metallic Foams | 606 |
| 29.2 | Known Mechanism | 609 |
| 29.3 | BOLS Formulation: Defect Mechanics | 611 |
| 29.4 | Verification | 612 |
| 29.4.1 | Critical Size: Total Energy Storage. | 612 |
| 29.4.2 | Defect-Mediated Strength of Graphene | 613 |
| 29.4.3 | Elasticity and Thermal Stability | 614 |
| 29.4.4 | Plasticity and IHPR | 615 |
| 29.5 | Summary | 616 |
| | References | 617 |
| 30 | Compounds and Nanocomposites: Hetero-Coordination | 621 |
| 30.1 | Known Facts | 621 |
| 30.1.1 | Hetero-Junction Interfaces | 621 |
| 30.1.2 | Intergrain Twin Boundaries | 622 |
| 30.1.3 | Filler–Matrix Interaction in Nanocomposites | 624 |
| 30.1.4 | High-Entropy Alloys. | 625 |
| 30.2 | Known Mechanisms | 625 |
| 30.2.1 | Interface Interaction | 625 |
| 30.2.2 | Ionicity, Bond Length, and Bandgap Dominance | 626 |
| 30.2.3 | Bond Length and Charge Transfer Dominance. | 627 |
| 30.3 | BOLS: Hetero-Coordination Entrapment or Polarization | 628 |
| 30.4 | Verification | 628 |
| 30.4.1 | Interface Bond Contraction | 628 |
| 30.4.2 | Bond Nature Alteration | 630 |
| 30.4.3 | Tian Series: Covalency and Bond Length | 631 |

| | | |
|--------------------------------|--|------------|
| 30.5 | Interface Energy Determination: XPS | 635 |
| 30.5.1 | Atomistic Definition of Interface Energy. | 635 |
| 30.5.2 | Interface Core-Level Shift | 635 |
| 30.5.3 | Interface Bond Energy | 638 |
| 30.5.4 | Binding Energy Density and Atomic Cohesive Energy | 640 |
| 30.6 | Summary | 641 |
| | References | 641 |
| 31 | Concluding Remarks | 647 |
| 31.1 | Attainment. | 647 |
| 31.2 | Limitations | 651 |
| 31.3 | Prospects | 653 |
| | References | 655 |
| Part IV Water Myths | | |
| 32 | Introduction | 661 |
| 32.1 | Scope | 661 |
| 32.2 | Overview. | 662 |
| 32.2.1 | Significance. | 662 |
| 32.2.2 | Known Mechanisms | 663 |
| 32.3 | Challenges and Objectives. | 665 |
| | References | 665 |
| 33 | Theory: Hydrogen Bond Cooperativity | 671 |
| 33.1 | H-Bond: Asymmetric, Coupled, H-Bridged Oscillators | 671 |
| 33.1.1 | Extended Ice Rule | 671 |
| 33.1.2 | Hydrogen Bond Segmentation | 672 |
| 33.1.3 | Asymmetric Short-Range Interactions | 674 |
| 33.1.4 | Forces Driving Asymmetric Relaxation. | 675 |
| 33.1.5 | Segmental Asymmetric Relaxation | 677 |
| 33.1.6 | Electron Pair Localization and Polarization | 678 |
| 33.1.7 | Vibrational Features and Orbital Image. | 679 |
| 33.2 | Segmental Disparity | 682 |
| 33.2.1 | Mechanical Disparity | 682 |
| 33.2.2 | Thermodynamic Disparity | 682 |
| 33.2.3 | Molecular Undercoordination: Extended BOLS | 684 |
| 33.3 | Correlation of Detectable Quantities | 685 |
| 33.3.1 | Non-Bonding Electron Polarization. | 685 |
| 33.3.2 | Binding Energy Entrapment. | 685 |

| | | |
|-----------|--|------------|
| 33.3.3 | Elastic Modulus and Transition Temperature | 686 |
| 33.3.4 | Phonon Frequency and Segmental Stiffness | 686 |
| 33.4 | Summary | 687 |
| | References | 687 |
| 34 | Compressed Ice: Inter Electron-Pair Repulsion | 691 |
| 34.1 | Observations | 691 |
| 34.2 | Density Profile Decomposition | 692 |
| 34.3 | Phonon Stiffness Relaxation Dynamics | 694 |
| 34.4 | T_C Depression and H-O Bond Energy E_H | 694 |
| 34.5 | Bandgap Expansion | 696 |
| 34.6 | Summary | 696 |
| | References | 697 |
| 35 | Molecular Clusters, Skins, and Ultrathin Films | 701 |
| 35.1 | Observations | 701 |
| 35.2 | O:H and H-O Length Cooperativity | 703 |
| 35.3 | Phonon Cooperative Relaxation | 705 |
| 35.4 | Volume Expansion and Viscosity Elevation | 706 |
| 35.5 | Entrapment and Polarization | 707 |
| 35.6 | Summary | 708 |
| | References | 709 |
| 36 | Thermally Driven Density and Phonon-Stiffness Oscillation | 713 |
| 36.1 | Observations: Why Does Ice Float? | 713 |
| 36.2 | Bond Angle-Length and Density Oscillation | 717 |
| 36.3 | Cooperative Phonon Relaxation | 719 |
| 36.4 | Phonon Relaxation of Light and Heavy Water | 721 |
| 36.5 | Binding Energy Entrapment | 723 |
| 36.6 | Summary | 724 |
| | References | 725 |
| 37 | H-Bond Asymmetric Local Potentials | 729 |
| 37.1 | Lagrangian Mechanics | 729 |
| 37.1.1 | Asymmetric Short-Range Interactions | 729 |
| 37.1.2 | Lagrangian Oscillator Dynamics | 730 |
| 37.2 | General Solutions | 732 |
| 37.3 | Specific Solutions | 732 |
| 37.3.1 | Short-Range Interactions | 732 |
| 37.3.2 | Force Constants and Vibration Frequencies | 733 |
| 37.3.3 | Pressure-Dependent d_x , ω_x , k_x , and E_x | 735 |

| | | |
|-----------|---|------------|
| 37.3.4 | Potential Paths for H-Bond Length Symmetrization . . . | 735 |
| 37.3.5 | Potential Paths for Undercoordinated H-Bond | 737 |
| 37.4 | Summary | 738 |
| | References | 738 |
| 38 | Molecular Size, Separation, Packing Order, and Density | 741 |
| 38.1 | Geometric Uncertainties | 741 |
| 38.2 | Bond Length Cooperativity | 742 |
| 38.3 | Solution Uniqueness | 742 |
| 38.4 | Summary | 744 |
| | References | 745 |
| 39 | Skin Supersolidity of Water and Ice | 747 |
| 39.1 | Ultra-Low Density Yet High Elasticity | 747 |
| 39.2 | Charge Polarization and Entrapment | 748 |
| 39.3 | Skin Phonon | 749 |
| 39.4 | Thermal Stability | 750 |
| 39.5 | Slippery of Ice | 751 |
| 39.6 | Further Evidence | 752 |
| 39.7 | Summary | 753 |
| | References | 754 |
| 40 | <i>P</i>, <i>T</i>, and <i>z</i> Coupling Effect | 757 |
| 40.1 | Size and T Effect on Phonon Frequencies | 757 |
| 40.2 | Size and Pressure Effect on O1s Energy | 758 |
| 40.3 | P and T Effect on Phase Stability | 759 |
| 40.4 | Water Surface Tension and O:H Bond Energy | 759 |
| 40.5 | Summary | 761 |
| | References | 761 |
| 41 | Mpemba Paradox: H-Bond Memory and Skin Supersolidity | 763 |
| 41.1 | Hotter Water Freezes Faster | 763 |
| 41.2 | O:H–O Bond Relaxation | 764 |
| 41.3 | Numerical Solution: Skin Supersolidity | 766 |
| 41.4 | Experimental Verification: O:H-O Bond Memory | 768 |
| 41.5 | Summary | 771 |
| | References | 772 |
| 42 | Prospects | 775 |
| 42.1 | Negative Thermal Expansion and Spin Ices | 775 |
| 42.2 | Electro-, Mechano-, and Magneto-Freezing | 777 |
| 42.3 | Hofmeister Series, De-Icing, and Anti-Icing | 781 |
| 42.4 | Dielectric Relaxation | 783 |
| 42.5 | H ₂ O-Cancer Cells and DNA Interaction | 785 |

| | | |
|-----------|---|------------|
| 42.6 | H-Bond Likes in Organic Materials | 787 |
| 42.7 | Dynamic Wetting: Droplet Tap Dance and Leidenfrost Effect. | 788 |
| 42.8 | Summary | 790 |
| | References | 790 |
| 43 | Conclusion | 795 |
| | Appendices | 799 |
| | Author Biography | 807 |

Nomenclature

| | |
|----------------|---|
| ω | The angular frequency/Raman frequency |
| μ | Atomic magnetic momentum |
| β | Compressibility/extensibility |
| χ | Dielectric susceptibility |
| η | Electronegativity |
| σ | Surface stress/conductivity |
| Φ | Work function |
| Θ (ML) | Oxygen coverage (unit in Monolayer) |
| ϵ'_r | Imaginary part of dielectric constant |
| ϵ_0 | Dielectric permittivity of vacuum |
| η_1 | Specific heat per coordinate |
| η_2 | Thermal energy per coordinate for evaporating a molten atom |
| μ_B | Bohr magneton |
| θ_D | Debye temperature |
| γ_d | Energy density gain |
| γ_f | Atomic residual cohesive energy |
| γ_i | Atomic portion in the i th atomic shell over the entire solid of size D |
| α_i (T) | Temperature-dependent thermal expansion coefficient (TEC) |
| δ_K | Kobo gap |
| γ_{qj} | Grüneisen mode parameter |
| ϵ_r | Real part of dielectric constant |
| γ_s | Surface tension or surface energy |
| 3B | Bond-band-barrier |
| a.u. | Atomic unit ($e = m = \hbar = 1$; 1 a.u. = 1 Bohr radii = 0.529 Å; $E = 27.21$ eV) |
| AES | Auger electron spectroscopy |
| AFAM | Atomic force acoustic microscopy |
| AFM | Atomic force microscopy |
| APECS | Auger photoelectron coincidence spectroscopy |
| AR | Added-row |
| ARIPES | Angular-resolved inverse photoemission spectroscopy |
| BA | Bond angle |
| BL | Bond length |

| | |
|-------------------|--|
| BOLS | Bond order-length-strength |
| BR | Buckled-row |
| BZ | Brillouin zone |
| C_i | Bond contracting factors |
| CN(z) | Coordination number |
| CNT | Carbon nanotube |
| $C_v(T/\theta_D)$ | Debye specific heat |
| CVD | Chemical vapor deposition |
| D | Diameter of a spherical nanosolid |
| d_0 | Atomic diameter or bond length |
| DFT | Density function theory |
| DLC | Diamond like carbon |
| DOS | Density-of-state |
| DSIC | Deep submicron integrated circuit |
| $E_v(0)$ | v th energy level of an isolated atom |
| E/LDS | Electron/laser stimulated desorption spectroscopy |
| E_B | Atomic cohesive energy/vacancy formation energy |
| E_b | Cohesive energy per bond |
| EELS | Electron energy loss spectroscopy |
| E_F | Fermi energy |
| E_G | Band gap |
| e-h | Electron-hole |
| EMT | Effective-medium theory |
| e-p | Electron-phonon |
| EXAFS | Extended X-ray absorption fine structure spectroscopy |
| FWHM | Full width at half maximum |
| GB | Grain boundary |
| GGA | Generalized gradient approximation |
| GIXR | Grazing incidence X-ray reflectivity |
| H-/M-/ | High-, medium-, and low-energy ion scattering |
| LEIS | |
| HOPG | Highly oriented pyrolytic graphite |
| HREELS | High-resolution electron-energy-loss spectroscopy |
| ICISS | Impact-collision ion-scattering spectrometry |
| IHPR | Inverse Hall–Petch relationship |
| K | Dimensionless form of the radius of a sphere or the thickness of a plate |
| k_B | Boltzmann constant |
| L | Langmuir (10^{-6} torr•s) |
| ϕ_L | Local work function |
| LBA | Local bond average |
| LDOS | Local DOS |
| LEISS | Low-energy-ion scattering spectroscopy |
| MC | Monatomic chain |
| MD | Molecular dynamics |

| | |
|-----------------|---|
| MR | Missing row |
| M_s | Saturation magnetization |
| MWCNT | Multi-walled carbon nanotube |
| NW | Nanowire |
| PDF | Pair distribution function |
| PED | Photoelectron diffraction |
| PEEM | Photoelectron emission microscopy |
| PES | Photoelectron spectroscopy |
| PL | Photoluminescence |
| p-Si | Porous silicon |
| PZT | PbZrTi oxide |
| Q(K) | Measurable quantity of a nanosolid |
| QC | Quantum confinement |
| R | Radius/Resistance |
| RCL | Resistance–capacitance–inductance |
| RSGF | Real-space Green's function method |
| RT | Room temperature |
| SAW | Surface acoustic wave |
| SBC | Surface-bond contraction |
| SEM | Scanning electron microscopy |
| SEXAFS | Surface extended X-ray absorption fine-structure spectroscopy |
| SIB | Saturated image barrier |
| SIMS | Secondary ion mass spectroscopy |
| SMAT | Surface mechanical attrition treatment |
| SPA-LEED | Spot analysis LEED |
| SPB | Surface potential barrier |
| STE | Self-trapping exciton |
| STM/S | Scanning tunneling microscopy/spectroscopy |
| SWCNT | Single-walled carbon nanotube |
| T-BOLS | Temperature-dependent Bond-order-length-strength correlation |
| T_c | Critical/Curie temperature |
| TDS | Thermal desorption spectroscopy |
| TEM | Transition electronic spectroscopy |
| T_m | Melting point |
| TOF | Time-of-flight |
| $U(T/\theta_D)$ | Atomic vibration/internal energy |
| UHV | Ultra-high-vacuum |
| UPS | Ultraviolet photoelectron spectroscopy |
| V/LEED | Very/low-energy electron diffraction |
| W | Stokes shift |
| XAFS | X-ray absorption fine structure spectroscopy |
| XANES | X-ray absorption near edge spectroscopy |
| XPD/S | X-ray photoelectron diffraction/spectroscopy |

| | |
|-----|--|
| XPS | X-ray photoelectron spectroscopy |
| XRD | X-ray diffraction |
| Y | Young's modulus |
| ZPS | Zone-resolved photoelectron spectroscopy |

Part I

O, N, and C Chemisorption

Abstract O, N, and C hybridize their *sp* orbitals and form bonds in four discrete stages, which create four valence DOS features upon reacting with a solid skin; the valence states of the acceptor, the electronegativity, the scale, and geometrical orientation of the host specify bond-forming dynamics.

Part I is focused on the formation and relaxation dynamics of bond and nonbond in the process of chemisorption and its consequences on the valence electrons and the surface potential barrier (SPB, a description of surface morphology). This framework leads to a bond-band-barrier (3B) correlation for chemical reaction. In the process of chemisorption, O, N, and C atoms hybridize their *sp* orbitals to form tetrahedrally bonded structures upon reacting with atoms in a solid surface. Electronic holes and anti-bonding dipoles of the host, bonding electron pairs and nonbonding lone pairs on the electronegative acceptors, and hydrogen-like bonds are formed, which add the corresponding features of density of states (DOS) to the valence band of the host. Bond formation also alters the sizes and valences of the involved atoms and causes a collective dislocation of these atoms, which not only corrugates the morphology or the potential barrier of the surface but also creates vacancies in occasions where atoms become excessive for bonding. This premise has reconciled the oxidation 3B dynamics of the low-index surfaces of transition metals, such as Cu, Co, Ni, and V, noble metals, such as Ag, Rh, Ru, and Pd, non-metallic diamond, as well as N and C reacting with Ni surfaces. The 3B premise also defined the identities probed using instrument such as STM/S, LEED, XRD, PES, TDS, EELS, and Raman in terms of atomic valences, bond geometry, valence DOS, bond strength, bond vibration, and bond formation kinetics. Formation of the basic tetrahedron, and consequently, the four discrete stages of bond formation kinetics, and the emerging DOS features, are intrinsically common for all the analyzed systems though the morphologic and crystallographic patterns of observations may vary from situation to situation. What differs one chemisorbed surface from another in observations are: (i) the site selectivity of the adsorbate, (ii) the order of the ionic bond formation, and (iii) the orientation of the tetrahedron in the outermost two layers of the host. The valence states of the acceptor, the scale and geometrical orientation of the host lattice, and the

electronegativity of the host elements determine these specific differences extrinsically. Extending the premise of sp-orbital hybridization to the reactions of (C, N)-Ni(001) surfaces has led to an approach neutralizing the diamond-metal interfacial stress and hence strengthening the diamond-metal adhesion substantially. The 3B correlation has also led to means in designing and fabricating materials for photoluminescence, electron emission and ultrahigh elasticity, etc. In dealing with chemisorption, undercoordination-induced surface bond contraction and bond energy gain play a significant role. Such a bond order-length-strength (BOLS) correlation is essential for determining the physical behavior of low-dimensional systems such as defects, surfaces, and nanostructures, which will be the focus of Part II.

Chapter 1

Introduction

- *Surface chemisorption is a process of bond breaking and bond making, which is beyond the description in terms of potential landscape or dislocation of atoms individually.*
- *Charge transportation, polarization, and localization take places associated with potential barrier and work function change.*
- *Interplay of crystallography, microscopy, and energetic and vibronic spectroscopies with theoretical computations and proper modeling guidelines would derive comprehensive quantitative information of the reaction dynamics.*
- *Grasping with factors and efficient means controlling the process of bond breaking and making, at will, would be the foremost task of the community.*

1.1 Scope

The part will start, in this chapter, with a brief overview on puzzles in oxygen chemisorption, for instance, what are the challenges in generalizing knowledge from various species observed with different techniques. [Chapter 2](#) will describe the O, N, and C (extend to F) tetrahedron bonding and its effect on the valence density of states (DOS) and the surface potential barrier (SPB). Basic conditions for possible tetrahedron bond formation and the effects of bond forming on the charges are classified. Emphasis will be given on crucial yet often overlooked events, such as non-bonding lone pairs, antibonding dipoles, and the formation of hydrogen-like bonds during reaction. [Chapters 3, 4, 5, 6](#) and [7](#) present systematic analysis of observations using STM, LEED/XRD, STS, UPS/XPS, TDS, EELS, and Raman of typical samples for generalized information. On the framework of the chemical bond–valence band–potential barrier (3B) correlation, the analysis aims to derive the following:

1. the formulae of reaction with specific valence value of individual atom,
2. kinetics of charge transportation and polarization,
3. bond geometry and atomic dislocation,

4. the driving forces and bond strength for surfaces with chemisorption, and
5. correspondence between the 3B mechanism and the signatures of observations.

Two concepts are essential. One is the bond contraction at surfaces or sites surrounding defects where the atomic coordination number (CN) is reduced, and the other is the essentiality of *sp*-orbital hybridization for O, N, and C (extend to *F*) atoms upon interacting with a solid surface, which widens the bandgap by charge transportation and polarization. [Chapters 8](#) introduce findings in practical applications driven by the developed 3B correlation knowledge. [Chapter 9](#) features main conclusions in response to the challenges addressed in this chapter with recommendations on further extension of the current approaches in materials design.

1.2 Overview

The atomic and electronic process of chemical reaction with electronegative acceptors plays an essential role in many fields such as environmental chemistry (CO and NO oxidation, radiation protection, and ozone layer protection), bio-electronics (DNA folding and protein signaling), and pharmacology (NO regulating and messaging). Oxygen interaction with solid surfaces of metals and nonmetals relates to the technical processes of corrosion, bulk oxidation, and heterogeneous catalysis. Studies of these processes laid the foundations for applications in microelectronics (MOSFET gate devices and deep submicron integrated circuit (DSIC) technologies), photoelectronics (photoluminescence, photoconductance, and field emission), magnetoelectronics (superconductivity and colossal magnetoresistance), and dielectrics (ferro-, piezo-, pyro-electrics). For both scientific and technological reasons, oxygen interaction with solid surfaces has formed the subject of extensive study over decades [1, 2].

Chemisorption has been a historically great battlefield for scientists to fight with the small atoms or molecules involved in the reaction with solid surfaces. For instance, solid surfaces with chemisorbed oxygen have been extensively examined from a macroscopic to an atomistic point of view and both experimentally and theoretically. Various techniques have been used to characterize the atomic and electronic properties:

- Crystallography includes low-energy-electron diffraction (LEED), surface X-ray diffraction (XRD), X-ray photoelectron diffraction (XPD), high-, medium-, and low-energy ion scattering (HEIS, MEIS, LEIS).
- Microscopy contains scanning tunneling microscopy (STM) and photoelectron emission microscopy (PEEM).
- Spectroscopy includes scanning tunneling spectroscopy (STS) for the on-site DOS cross-Fermi energy (E_F), inverse photoelectron spectroscopy (IPES) for surface image states, angular-resolved ultraviolet photoelectron spectroscopy

(ARUPS) for the valence DOS features, and X-ray photoelectron spectroscopy (XPS) for the energy shift of a core band. Surface extended X-ray absorption fine-structure spectroscopy (SEXAFS) and impact-collision ion-scattering spectroscopy (ICISS) are also commonly used in the chemisorption studies.

- Techniques for bond activation and lattice vibration include the thermal, electron, and laser-stimulated desorption spectroscopy (TDS, EDS, and LDS), the electron-energy-loss spectroscopy (EELS), Raman scattering, and Fourier transform infrared spectroscopy (FTIR) spectroscopies.

Numerous theoretical approaches have been employed to investigate the details of oxygen chemisorption including the semiempirical effective medium theory (EMT) [3], the tight binding theory [4–6], the first-principle method [7, 8], and the density function theory (DFT) [9–14].

Usually, the process in which an electronegative atom exchanges electrons with the solid surface is defined as chemisorption; otherwise, it is physisorption. The kinetics of surface chemisorption generally consists of dissociating the initial guest molecules at the surface and trapping of the guest atoms into the corrugated well of potential. Chemisorption breaks the host–host surface bonds and then creates new kinds of guest–host bonds [15]. In the oxidation of metals, for example, oxygen in the atmosphere is adsorbed onto the metal surface and reacts with the metallic atoms to form an ionic or polar covalent type of compound. To a certain extent, the degree of adsorption and reaction is the function of the orientation of the crystal facet exposed to the gas and the partial pressure or activity of the adsorbate in the atmosphere. The actual mechanism for the oxidation of each surface was thought to be quite different and very complicated [16, 17].

The invention of STM and STS has led to revolutionary impact on studying the chemisorption of metal surfaces on an atomic scale and in real time. In spite of the difficulties in interpreting the STM images, valuable, direct, yet qualitative information for systems with adsorbate has been gained from such observations [18, 19]. It is possible to investigate the kinetic and the static features of the chemisorbed systems using STM and STS and hence to [15]:

- (a) distinguish between the different reconstruction models and thus optimize the proper ones and
- (b) elucidate the driving force behind such surface phase transitions.

Models, derived from STM observations or from the fitting of diffraction (such as LEED and XRD), provide information about static atomic structures of the surface. These structural models succeed in describing specific situations in terms of the static positions of the adsorbates that are often assumed rigid spheres. The general characteristics of electronic structures and atomic arrangement on a variety of chemisorbed metal surfaces have been now fairly determined [20, 21] with many landmark reviews on the progress in this field [15, 17, 20, 22–32].

1.3 Issues to Be Addressed

The key concerns in chemisorption are the correlation between the chemical bonds, valence DOS, surface morphology, and the corresponding properties of the chemisorbed surfaces and their relaxation dynamics. Understanding the nature and kinetics of bond breaking and bond making and their consequences on the behavior of atoms and valence electrons at surfaces is essential [15–31]. This part will address the following issues.

1.3.1 Bond Nature and Bonding Kinetics

Long-range ordered O–M–O chains (M for metal) are generally created on the oxygen-chemisorbed surfaces, which provide the major forces that stabilize the reconstructed surface. Oxygen is suggested to bond more covalently to a Cu atom than to a Ni atom, and with very small 3d-electron participation in the O–Cu bonding [33]. An alternative opinion [34] suggests that the O–Cu bond is an ionic one with a significant Cu–3d-electron contribution. The colinear O–Cu–O chain is suggested to be formed through the $O(2p_{xy})$ – $Cu(3d_{x^2-y^2})$ interaction [35, 36] or connected by the delocalized O–Cu antibonding states [37]. The O–M bond is suggested to have a mixture of ionic–covalent character and that the O–M bond transforms from ionic/covalent to covalent/ionic in nature when the $Cu(001)$ – $c(2 \times 2)$ –2O phase transforms into the $Cu(001)$ – $(\sqrt{2} \times \sqrt{2})R45^\circ$ –2O structure [38–41]. The covalent bond character becomes weaker in the case of $Cu(001)$ – $c(2 \times 2)$ –2O than in the case of $Ni(001)$ – $c(2 \times 2)$ –2O [40, 41]. Through a study of dc resistance and infrared reflectance of the epitaxial Cu(100) films with adsorbed oxygen, McCullen et al. [42] found that the standard surface resistivity models based on free electrons and point scatters are inadequate, even if the adsorbate-induced changes in conduction electron density are considered. They found that to interpret their findings within a free electron framework would require that each adsorbate localizes an unreasonably large number of conduction electrons. Therefore, knowing how the electron transports among the bonding constituent atoms and how the adsorbate localizes the electrons is essential. Oxidation is actually a kinetic process of bond breaking and forming, and it is difficult to detect accurately the static position of the moving surface atoms, particularly the light oxygen, with alternated valences and sizes. Therefore, the nature and kinetics of oxide bonding and its consequences on the behavior of host atoms and the valence electrons at the host surface are of key importance.

1.3.2 Alternation of Atomic Valencies

The common features of the STM images of metal surfaces with chemisorbed oxygen are the pronounced dimensions and contrasts of protrusions compared with those of clean metal surfaces. STM studies have confirmed the presence or absence of the O–M–O chains. The oxygen adsorbates could ‘squeeze out’ atoms at a certain number of surfaces so that metal rows are missing from these surfaces. Furthermore, the shapes of the protrusions and the orientations of the O–M–O chains vary considerably with the substance and the crystal orientation. For instance, O–Cu pairing chains form on the Cu(001)–($\sqrt{2} \times 2\sqrt{2}$)R45°–2O surface and the ‘dumbbell’ protrusions are as high as 0.45 Å [37] at 0.5 ML (monolayer) adsorbate coverage while “check board” protrusions present on the Cu(001)–c(2 × 2)–2O phase at coverage below 0.5 ML. In contrast, zigzagged O–O chains form between two Co rows along the close-packed direction on the Co(10 $\bar{1}$ 0)–c(4 × 2)–4O surface [43]. The ‘honeycomb’ protrusions on the O–Co(10 $\bar{1}$ 0) surface are up to 1.0 Å [44]. The resulting reconstructed phases of (Ag, Ni, Cu, Pt)(110)–(2 × 1)–O surfaces [9, 45–47] possess ‘a high degree of similarity in the sense that they all are stabilized by single O–M–O strings perpendicular to the close-packed direction.’ The ‘spherical’ protrusion on the Cu(110)–(2 × 1)–O surface is about 0.8 Å in height contrasting to that of 0.15 Å for the clean Cu(110) surface [48]. The ‘oval’ protrusions are observed in the Cu(110)–c(6 × 2)–8O phase [49], and the ‘honeycomb’ protrusions composed of the ‘dumbbells’ are observed from the Cu(111)–O surface at higher temperature [50]. All the (Ag, Cu, Ni, Pt)(110)–(2 × 1)–O and the Cu(001)–($\sqrt{2} \times 2\sqrt{2}$)R45°–2O phases have missing rows. However, some others have no atoms that are missing during the reaction such as Ni(001)–O [51], Pd(001)–O [52], (Co, Ru)(10 $\bar{1}$ 0)–O [43, 44], Cu(111)–O [50], Rh(001)–O [53], Rh(111)–O [54, 55], and Ru(0001)–O surfaces [56, 57].

STM is able to reveal inherently common features caused by hetero-coordinated adsorption from all the specific forms. Determination of the behavior of surface electrons is beyond the scope of the structural models in terms of rigid spheres. STM features for metal surfaces with adsorbate can hardly be explained in terms of crystallographic alone [19]. Correct correspondence between the STM/S signatures and the valences of surface atoms is critical. The atomic valences may alter from metallic to ionic, dipole, or missing-row vacancies upon reaction. The definition of surface atomic valence may then enable the reaction of a specific surface to be formulated. The patterns of morphology and crystallography may vary from situation to situation; the guest–host bond configuration and the valence DOS distribution modified by electronegative acceptors should be naturally common. This would eventually lead to deeper and consistent insight into the observations of different atomically adsorbed systems for generalized information.

1.3.3 Spectroscopic Correspondences

Spectroscopic methods such as UPS, XPS, STS, TDS, and EELS are important tools commonly used in chemisorption studies. UPS with $E < 50$ eV (He-I and He-II excitation) is often used to obtain direct information about the distribution of valence electrons below E_F of a specimen. XPS at higher energy (10^2 eV) reveals the energy shift of the core bands of the surface. The core-level shift fingerprints the crystal field experienced by the core electrons. Shortened bond and alternatively charged ions will enhance the binding energy and hence the crystal field. Charge transportation alters the nature of atomic interaction and also weakens the effect of valence screening on the particular core-level states [58]. Therefore, the chemical shift in XPS reflects the occurrence of electron transport and atomic dislocation due to the bond reformation and relaxation. STS provides on-site DOS information around the E_F of atoms at the surface. UPS and STS also provide information about any work function change caused by dipole layer formation at the surface [59]. For example, STS profiles from the O–Cu–O chain region on the O–Cu(110) surface have revealed two DOS features around E_F [48]. One is the empty energy states (peaks) located at 0.8–1.8 eV above E_F , and the other is the newly occupied state that is 1.4–2.1 eV below E_F . The STS DOS features below E_F are substantially the same as those detected using UPS from the Cu(110)–O [60], Cu(001)–O [36], and Pd(110)–O [61] surfaces. Oxygen does not add simply its 2s and 2p states to the valence bands of the host metals but exchanges and polarizes electrons of the host atoms.

On the other hand, TDS could resolve the individual process of bond breaking, i.e., the opposite process of bond forming by thermal activation [62]. TDS profiles possess peaks of which the intensities oscillate with increasing oxygen exposure. For example, TDS from O–Pd [63] and O–Rh [64] surfaces shows a similar number of peaks (4–5) with slight difference in the characteristic peak temperatures. The TDS peaks correspond to different bond strengths and the peak intensity oscillation to the bond forming kinetics.

High-resolution EELS from O–Ru [65, 66] and O–Rh surfaces revealed that the stretching modes of dipole vibration are at energy around ~ 0.05 eV, being equivalent of 600 K. The peak shifts toward higher binding energy when oxygen coverage increases. The blueshift of vibration energy reflects the strength variation of the weak interaction of the dipoles. The value of 0.05 eV is at the same energy level as that for the hydrogen bond vibration detected from protein, H_2O , and DNA molecules.

Therefore, the variation in the spectral features of STS, UPS, TDS, and EELS corresponds to the dynamics of bond formation and relaxation, bond strength, and the adsorbate-derived valence DOS relaxation.

1.3.4 Driving Forces Behind Reconstruction

Oxygen adsorbates could ‘push’ or ‘pull’ the entire first atomic layer of a surface outward by 8–30 % and squeeze the spacing between the second and the third atomic layers closer by ~ 5 %. For a pure metal surface, the first interlayer spacing often contracts by 3–30 %, instead [67–74]. It is hard to imagine that the oxygen adsorbates resting above the surface are able to ‘pull out’ the entire first atomic layer without external forces ‘pulling’ the adsorbates. It is not certain yet how the oxygen adsorbates enhance the interaction between the second and the third atomic layer. Furthermore, adsorbates can remove atoms from the surface to form the missing-row vacancies without applying any external stimulus. Based on the effective medium theory, Jacobsen and Nørskov [3] assumed that oxygen atoms penetrate into the Cu(001) and the Cu(110) surfaces and push the top Cu layer outward. Such a subsurface-oxygen structural configuration on the Cu(110) surface agrees with the conclusion drawn by Feidenhansl et al. [75] from their surface XRD studies.

A first-principles study of the O–Al(111) surface by Kiejna and Lundqvist [76, 77] revealed that the oxygen adsorbate prefers the hcp tetrahedral site, 1.92 Å below the topmost Al layer, that has relaxed by 25–37 %. For the simultaneous subsurface and on-surface adsorption at a coverage of $\Theta = 1.0$, the binding energy of adsorbates in the hcp hollow subsurface site is 0.2 eV/atom lower than that in the on-surface fcc hollow sites. The hcp hollow subsurface oxygen is favorable in the Al(111) surface because of the lower binding energy. Hypotheses of subsurface oxygen are reasonably true, as the oxygen adsorbate needs to move into the surface to form bonds with its surrounding atoms in both the top first and the underneath second atomic layers and then penetrate into the bulk, proceeding the oxygen-attacked corrosion. The oxygen adsorbates push up the entire top layer and squeeze some metal atoms away from their original sites, as a result of bond formation. The interaction between metal ions in the second layer with neutral metal atoms in the third layer should be stronger than the original pure metallic interaction, which shall drive the second and the third atomic planes to come closer.

The driving forces for reconstruction were attributed to the formation of the O–M–O chains and the formation of the missing rows at the surface. However, neither missing rows nor O–M–O chains could be formed on the (Co, Ru)(10 $\bar{1}$ 0)–O, Rh–(111)–O, Ru(0001)–O, and Rh(001)–O surfaces. Therefore, formation of the missing row and the O–M–O chain may not be an essential mechanism driving the reconstruction but a consequence of reaction. Jacobsen and Nørskov [3] related the driving force to a ‘stronger O-metal bond’ formation on the reconstructed surface, because they noticed that the oxygen 2p states hybridize (bond) more strongly with the *d* states of metal atoms. Further, they noted that the O–M bond becomes stronger if the oxygen bonds to metal atoms with fewer neighbors [78] according to their EMT results.

1.3.5 Work Function and Inner Potential Change

The work function of a surface is the separation in energy between E_F and the vacuum level. The work function often changes when dipoles form at the surface. If the negative end of the dipole is toward the vacuum, the work function reduces, and vice versa. The muffin-tin inner potential constant corresponds to the net quantity of electrons around the atom [79]. For metal surfaces with chemisorbed oxygen, the work function often reduced by about 1.2 eV, and such a reduction depends on the phases and adsorbate exposures [24, 80].

Zhang et al. [81] detected that the work function of a Gd(0001) surface reduces from 3.3 to 2.5 eV upon oxygen chemisorption. Moreover, they noted that the work function decreases quickly upon exposure to oxygen and the reduction rate slows down when the oxygen coverage is over 0.5 ML. Occasionally, work function of a surface increases at higher oxygen exposures.

The inner potential constants for the Cu [82] and the Ru [83] surfaces reduce upon oxygen adsorption. Pfnür et al. [84] found it necessary to assume such a reduction in analyzing the very low-energy electron diffraction (VLEED) spectra from the O–Ru system. The VLEED calculations with rigid sphere models by Thurgate and Sun [82] showed a 1.2 eV or more reduction in the inner potential for the top layer of the O–Cu(001) surface. The inner potential reduction also varies for different phases due to the possible crystal structures [85]. VLEED optimization revealed that the inner potential for the top Cu atomic layer reduced by 9.5 % (from 11.56 to 10.5 eV) upon oxygen chemisorption [79]. Besides the strong localization of surface charge due to the missing-row formation and charge transportation, the residual ion cores provide an additional likely mechanism for reducing the inner potential.

1.3.6 Factors Controlling Bond Formation

Models of rigid spheres for a specific reconstructed system can illustrate the static atomic positions at a certain moment of snapshot. However, such models reveal little information about the kinetics and dynamics of bonds and electrons at the surface. During reaction, atomic position and atomic size change; atomic valences and the form of atomic interaction change; electrons, strongly localized, transport from one constituent atom to the other and from one energy level to another. Some occupied energy states in the valence band are emptied, and some empty ones are filled up. It seems impractical to locate accurately the static positions of the individual atoms at a surface at a time. It is also not realistic to base all observations on atomic dislocation or crystal structure change [23].

Understanding the process of bond forming kinetics and dynamics is beyond the scope of any instrumentation and theoretical approximation alone. For example, results of numerical optimizations are subject to the assumptions made or to the

initial conditions taken [56, 86, 87]. Fitting diffraction data often involves a huge number of strongly correlated parameters [88]. The independent treatment of the correlated parameters often leads to an infinite number of numerical solutions [89–91]. In addition, theoretical calculations often consider the electrostatic interaction between the adsorbates and host atoms, being treated as rigid spheres, rather than the true process of bond formation [92], with essential contraction of bonds at the surface. Therefore, physical constraints on all the observations and their interdependence are necessary. It is quite often that some undetectable factors play the dominant roles behind the observations. It would be interesting and rewarding to cope with the above-mentioned challenges and thus perhaps to discover methods to control the processes of bond making or breaking.

1.4 Objectives

Decoding the kinetic VLEED data from the O–Cu(001) surface has resulted in a compact model for the oxide tetrahedron bonding [93, 94] and its effects on the valence DOS [95, 96] and the SPB with chemisorbed oxygen [89]. The developed *3B* correlation has enabled in turn the capacity and reliability of VLEED to be fully explored [97] and the STM images to be explained in terms of bond geometry and atomic valences. The decoding technique and the *3B* models have enabled the kinetic VLEED from the O–Cu(001) surface to be quantified and consistently understood in terms of four-stage Cu_3O_2 bonding kinetics and its effects on the valence DOS [98].

The objective of this part is to share with the community what the practitioner experienced and learnt in the past decades with focus on extending the *3B* correlation mechanism to the electronic process of O, N, and C chemisorption and enhancing the capacity of STM, STS, PES, TDS, and EELS for general understanding.

1. Surface chemisorption is a kinetic process in which charge transportation/polarization dominates and atomic dislocation and even evaporation happen consequently. The events of O–M bonding, lone pair non-bonding, metal dipole antibonding, and H-like bonding are crucial to the processes of O, N, and C reacting with solid surfaces. Meanwhile, atomic sizes and atomic valences change, and the bonds at the surface contract. These events dislocate surface atoms collectively and modify the valence DOS of the host. These events also roughen the surface (or SPB) and change the physical properties of a chemisorbed surface.
2. The electronegativity, the scale of lattice constant, and the geometrical orientation of the host surface determine the specific details of the adsorbate facilitation, bond ordering, and the orientation of the tetrahedron. This process gives rise to the versatile modes of crystal reconstruction and surface morphologies. For the analyzed representatives of transition metals, noble metals, and a

nonmetallic diamond, it is consistently concluded that the phase ordering, crystallography, and surface morphology vary from situation to situation. However, formation of the basic H_2O -, NH_3 -, and CH_4 -like tetrahedron, with sp -orbital hybridization and lone pair production, corresponding valence DOS features and the kinetic processes of bond formation are substantially the same by nature.

3. The combination of STM, LEED/VLEED, PES/STS, TDS, and EEELS/Raman are essential for a comprehensive insight into the bonding and electronic process occurring at a surface. Furnished with the $3B$ correlation premise, these techniques allow one to extract information about the surface atomic valences, bond geometry, valence DOS, bond strength, and bond forming kinetics.

References

1. F.W. Young, J.V. Cathcart, A.T. Gwathmey, The rates of oxidation of several faces of a single crystal of copper as determined with elliptically polarized light. *Acta Metall.* **4**(2), 145–152 (1956)
2. G. Ertl, Untersuchung von oberflächenreaktionen mittels beugung langsamer elctronen (LEED).I. wechselwirkung von o_2 und n_2o mit (110)-(111)-und (100)-kupfer-oberflächen. *Surf. Sci.* **6**(2), 208–232 (1967)
3. K.W. Jacobsen, J.K. Norskov, Theory of the oxygen-induced restructuring of Cu(110) and Cu(100) surfaces. *Phys. Rev. Lett.* **65**(14), 1788–1791 (1990)
4. P. Liu, Y. Wang, A tight-binding molecular dynamic simulation of the Cu(110) surface covered with oxygen. *Surf. Sci.* **440**(1–2), 81–86 (1999)
5. P. Liu, Y. Wang, Theoretical study on the structure of Cu(110)- $p2X1$ -O reconstruction. *J. Phys. Condens. Matter* **12**(17), 3955–3966 (2000)
6. L.H. Tjeng, M.B.J. Meinders, G.A. Sawatzky, Relationship between atomic and electronic-structure of clean and oxygen covered copper (110) surface. *Surf. Sci.* **233**(1–2), 163–183 (1990)
7. J.M. Ricart, J. Torras, F. Illas, J. Rubio, Bonding of atomic oxygen to Cu(100) and Ag(100) surfaces—a study of the nature of the interaction. *Surf. Sci.* **307**, 107–112 (1994)
8. J.M. Ricart, J. Torras, A. Clotet, J.E. Sueiras, Atomic oxygen-chemisorption on Cu(110) and Ag(110)—an ab-initio study. *Surf. Sci.* **301**(1–3), 89–96 (1994)
9. T. Shimizu, M. Tsukada, Origin of the different formation modes of the oxygen added row overlayer on Ag(110) and Cu(110) surfaces. *Surf. Sci.* **295**(1–2), L1017–L1022 (1993)
10. M. Lynch, P. Hu, A density functional theory study of CO and atomic oxygen chemisorption on Pt(111). *Surf. Sci.* **458**(1–3), 1–14 (2000)
11. N.D. McClenaghan, P.J. Hu, C. Hardacre, A density functional theory study of the surface relaxation and reactivity of Cu_2O (100). *Surf. Sci.* **464**(2–3), 223–232 (2000)
12. C.J. Zhang, P. Hu, Why must oxygen atoms be activated from hollow sites to bridge sites in catalytic CO oxidation? *J. Am. Chem. Soc.* **122**(9), 2134–2135 (2000)
13. C. Noguera, Insulating oxides in low dimensionality: A theoretical review. *Surf. Rev. Lett.* **8**(1–2), 121–167 (2001)
14. F.E. Olsson, N. Lorente, M. Persson, STM images of molecularly and atomically chemisorbed oxygen on silver. *Surf. Sci.* **522**(1–3), L27–L35 (2003)
15. F. Besenbacher, Scanning tunnelling microscopy studies of metal surfaces. *Rep. Prog. Phys.* **59**(12), 1737–1802 (1996)
16. M.J. Sinnott, *The solid state for engineers*, (ed. by J. Wiley and S. Inc., New York, 1963)

17. J. Winterlin, R.J. Behm, *In the Scanning Tunneling Microscopy I*, ed. by H.J. Güntherth and R. Wiesendanger, (Springer, Berlin, 1992)
18. D.A. Bonnell, Scanning tunneling microscopy and spectroscopy of oxide surfaces. *Prog. Surf. Sci.* **57**(3), 187–252 (1998)
19. M.A. VanHove, J. Cerda, P. Sautet, M.L. Bocquet, M. Salmeron, Surface structure determination by STM vs. LEED. *Prog. Surf. Sci.* **54**(3–4), 315–329 (1997)
20. M. Kittel, M. Polcik, R. Terborg, J.T. Hoeft, P. Baumgartel, A.M. Bradshaw, R.L. Toomes, J.H. Kang, D.P. Woodruff, M. Pascal, C.L.A. Lamont, E. Rotenberg, The structure of oxygen on Cu(100) at low and high coverages. *Surf. Sci.* **470**(3), 311–324 (2001)
21. V.E. Henrich, Metal-oxide surfaces. *Prog. Surf. Sci.* **50**(1–4), 77–90 (1995)
22. F. Besenbacher, J.K. Nørskov, Oxygen-chemisorption on metal-surfaces—general trends for Cu, Ni and Ag. *Prog. Surf. Sci.* **44**(1), 5–66 (1993)
23. D.A. King, Chemisorption on metals—a personal review. *Surf. Sci.* **299**(1–3), 678–689 (1994)
24. G. Ertl, Reactions at well-defined surfaces. *Surf. Sci.* **299**(1–3), 742–754 (1994)
25. M.A. Vanhove, G.A. Somorjai, Adsorption and adsorbate-induced restructuring—A LEED perspective. *Surf. Sci.* **299**(1–3), 487–501 (1994)
26. W. Liu, K.C. Wong, H.C. Zeng, K.A.R. Mitchell, What determines the structures formed by oxygen at low index surfaces of copper? *Prog. Surf. Sci.* **50**(1–4), 247–257 (1995)
27. F.M. Leibsle, P.W. Murray, N.G. Condon, G. Thornton, Scanning tunnelling microscopy studies of reactions on metal surfaces and model oxide supports. *J. Phys. D Appl. Phys.* **30**(5), 741–756 (1997)
28. G. Comelli, V.R. Dhanak, M. Kiskinova, K.C. Prince, R. Rosei, Oxygen and nitrogen interaction with rhodium single crystal surfaces. *Surf. Sci. Rep.* **32**(5), 167–231 (1998)
29. H. Over, Crystallographic study of interaction between adspecies on metal surfaces. *Prog. Surf. Sci.* **58**(4), 249–376 (1998)
30. H.J. Freund, H. Kühlenbeck, V. Staemmler, Oxide surfaces. *Rep. Prog. Phys.* **59**(3), 283–347 (1996)
31. C. Noguera, Polar oxide surfaces. *J. Phys. Condens. Matter* **12**(31), R367–R410 (2000)
32. G. Renaud, *Oxide surfaces and metal/oxide interfaces studied by grazing incidence X-ray scattering*. *Surf. Sci. Rep.* **32**(1–2), 1–90 (1998)
33. A. Mattsson, I. Panas, P. Siegbahn, U. Wahlgren, H. Åkeby, Model studies of the chemisorption of hydrogen and oxygen on Cu(100). *Phys. Rev. B* **36**(14), 7389–7401 (1987)
34. P.S. Bagus, F. Illas, Theoretical-analysis of the bonding of oxygen to Cu(100). *Phys. Rev. B* **42**(17), 10852–10857 (1990)
35. L. Fritsche, B. Weimert, H. Kranefeld, J. Noffke, Bonding in the $o(p2 \times 1)/Cu(110)$ system analyzed in terms of Cu–O–Cu chain properties. *Surf. Sci.* **291**(3), 309–316 (1993)
36. R.A. Didio, D.M. Zehner, E.W. Plummer, An angle-resolved UPS study of the oxygen-induced reconstruction of Cu(110). *J. Vac. Sci. Technol. Vac. Surf. Films* **2**(2), 852–855 (1984)
37. F. Jensen, F. Besenbacher, E. Laegsgaard, I. Stensgaard, Dynamics of oxygen-induced reconstruction of Cu(100) studied by scanning tunneling microscopy. *Phys. Rev. B* **42**(14), 9206–9209 (1990)
38. D. Arvanitis, G. Comelli, T. Lederer, H. Rabus, K. Baberschke, Characterization of 2 different adsorption states for O on Cu(100)—ionic versus covalent bonding. *Chem. Phys. Lett.* **211**(1), 53–59 (1993)
39. T. Lederer, D. Arvanitis, G. Comelli, L. Troger, K. Baberschke, Adsorption of oxygen on Cu(100). I. Local-structure and dynamics for 2 atomic chemisorption states. *Phys. Rev. B* **48**(20), 15390–15404 (1993)
40. S. Stolbov, A. Kara, T.S. Rahman, Electronic structure of the $c(2 \times 2)O/Cu(001)$ system. *Phys. Rev. B* **66**(24), 245405 (2002)
41. S. Stolbov, T.S. Rahman, Role of long range interaction in oxygen superstructure formation on Cu(001) and Ni(001). *Phys. Rev. Lett.* **89**(11), 116101 (2002)

42. E.F. McCullen, C.L. Hsu, R.G. Tobin, Electron density changes and the surface resistivity of thin metal films: Oxygen on Cu(100). *Surf. Sci.* **481**(1–3), 198–204 (2001)
43. R. Koch, E. Schwarz, K. Schmidt, B. Burg, K. Christmann, K.H. Rieder, Oxygen-adsorption on Co(10(1)bar-0)—different reconstruction behavior of hcp (10(1)bar-0) and fcc (110). *Phys. Rev. Lett.* **71**(7), 1047–1050 (1993)
44. R. Koch, B. Burg, K. Schmidt, K.H. Rieder, E. Schwarz, K. Christmann, Oxygen-adsorption on Co(10(1)O)—the structure of p(2 × 1)2O. *Chem. Phys. Lett.* **220**(3–5), 172–176 (1994)
45. M. Taniguchi, K. Tanaka, T. Hashizume, T. Sakurai, Ordering of Ag–O chains on the Ag(110) surface. *Surf. Sci.* **262**(3), L123–L128 (1992)
46. L. Eierdal, F. Besenbacher, E. Laegsgaard, I. Stensgaard, Interaction of oxygen with Ni(110) studied by scanning-tunneling-microscopy. *Surf. Sci.* **312**(1–2), 31–53 (1994)
47. M. Pascal, C.L.A. Lamont, P. Baumgartel, R. Terborg, J.T. Hoeft, O. Schaff, M. Polcik, A.M. Bradshaw, R.L. Toomes, D.P. Woodruff, Photoelectron diffraction study of the Ag(110)–(2 × 1)–O reconstruction. *Surf. Sci.* **464**(2–3), 83–90 (2000)
48. F.M. Chua, Y. Kuk, P.J. Silverman, Oxygen-chemisorption on cu(110)—an atomic view by scanning tunneling microscopy. *Phys. Rev. Lett.* **63**(4), 386–389 (1989)
49. R. Feidenhansl, F. Grey, M. Nielsen, F. Besenbacher, F. Jensen, E. Laegsgaard, I. Stensgaard, K.W. Jacobsen, J.K. Norskov, R.L. Johnson, Oxygen-chemisorption on Cu(110)—a model for the c(6 × 2) structure. *Phys. Rev. Lett.* **65**(16), 2027–2030 (1990)
50. F. Jensen, F. Besenbacher, E. Laegsgaard, I. Stensgaard, Oxidation of Cu(111)—2 new oxygen induced reconstructions. *Surf. Sci.* **259**(3), L774–L780 (1991)
51. I.P. Batra, J.A. Barker, Helium diffraction from adsorbate-covered surfaces—a study of the O–Ni(001) system. *Phys. Rev. B* **29**(10), 5286–5291 (1984)
52. D.T. Vu, K.A.R. Mitchell, O.L. Warren, P.A. Thiel, Tenser LEED analysis of the Pd(100)–($\sqrt{5} \times \sqrt{5}$)R27°–o surface-structure. *Surf. Sci.* **318**(1–2), 129–138 (1994)
53. J.R. Mercer, P. Finetti, F.M. Leibsle, R. McGrath, V.R. Dhanak, A. Baraldi, K.C. Prince, R. Rosei, STM and SPA-LEED studies of O-induced structures on Rh(100) surfaces. *Surf. Sci.* **352**, 173–178 (1996)
54. K.D. Gibson, M. Viste, E.C. Sanchez, S.J. Sibener, High density adsorbed oxygen on Rh(111) and enhanced routes to metallic oxidation using atomic oxygen. *J. Chem. Phys.* **110**(6), 2757–2760 (1999)
55. S. Schwegmann, H. Over, V. DeRenzi, G. Ertl, The atomic geometry of the O and CO+O phases on Rh(111). *Surf. Sci.* **375**(1), 91–106 (1997)
56. C. Stampfl, S. Schwegmann, H. Over, M. Scheffler, G. Ertl, Structure and stability of a high-coverage (1 × 1) oxygen phase on Ru(0001). *Phys. Rev. Lett.* **77**(16), 3371–3374 (1996)
57. K. Meinel, H. Wolter, C. Ammer, A. Beckmann, H. Neddermeyer, Adsorption stages of O on Ru(0001) studied by means of scanning tunnelling microscopy. *J. Phys. Condens. Matter* **9**(22), 4611–4619 (1997)
58. D. Briggs, J.C. Rivière, *Practical Surface Analysis*, vol. 1 (Wiley, New York, 1990)
59. G. Ertl, T.N. Rhodin, *The Nature of Surface Chemical Bond* (North-Holl Press, Amsterdam, 1979)
60. S. Hüfner, *Photoelectron spectroscopy: Principles and applications* (Springer, New York, 1995)
61. K. Yagi, K. Higashiyama, H. Fukutani, Angle-resolved photoemission-study of oxygen-induced c(2 × 4) structure on Pd(110). *Surf. Sci.* **295**(1–2), 230–240 (1993)
62. P.A. Redhead, The first 50 years of electron stimulated desorption (1918–1968). *Vacuum* **48**(6), 585–596 (1997)
63. V.A. Bondzie, P. Kleban, D.J. Dwyer, XPS identification of the chemical state of subsurface oxygen in the O/Pd(110) system. *Surf. Sci.* **347**(3), 319–328 (1996)
64. E. Schwarz, J. Lenz, H. Wohlgemuth, K. Christmann, The interaction of oxygen with a rhodium (110) surface. *Vacuum* **41**(1–3), 167–170 (1990)
65. S. Schwegmann, A.P. Seitsonen, V. De Renzi, H. Dietrich, H. Bludau, M. Gierer, H. Over, K. Jacobi, M. Scheffler, G. Ertl, Oxygen adsorption on the Ru(10(1)over-bar0) surface: Anomalous coverage dependence. *Phys. Rev. B* **57**(24), 15487–15495 (1998)

66. P. He, K. Jacobi, Vibrational analysis of the 1×1 -O overlayer on Ru(0001). *Phys. Rev. B* **55**(7), 4751–4754 (1997)
67. P.J. Jennings, C.Q. Sun, *In the Surface Analysis Methods in Materials Science*, ed. by D.J. O'Connor, B.A. Sexton, R.C. Smart (Springer, New York, 2002)
68. D.L. Adams, H.B. Nielsen, J.N. Andersen, I. Stensgaard, R. Feidenhansl, J.E. Sorensen, Oscillatory relaxation of the Cu(110) surface. *Phys. Rev. Lett.* **49**(9), 669–672 (1982)
69. J.W.M. Frenken, J.F. Vanderveen, G. Allan, Relation between surface relaxation and surface force-constants in clean and oxygen-covered Ni(001). *Phys. Rev. Lett.* **51**(20), 1876–1879 (1983)
70. I.P. Batra, Lattice-relaxation in aluminum monolayers. *J. Vac. Sci. Technol. Vac. Surf. Films* **3**(3), 1603–1606 (1985)
71. R.P. Gupta, Lattice-relaxation at a metal-surface. *Phys. Rev. B* **23**(12), 6265–6270 (1981)
72. Y.N. Hwang, S.H. Park, D. Kim, Size-dependent surface phonon mode of CdSe quantum dots. *Phys. Rev. B* **59**(11), 7285–7288 (1999)
73. Y.S. Li, F. Jona, P.M. Marcus, Low-energy-electron-diffraction study of multilayer relaxation on a Pb(311) surface. *Phys. Rev. B* **44**(15), 8267–8273 (1991)
74. P.J. Feibelman, Relaxation of hcp(0001) surfaces: A chemical view. *Phys. Rev. B* **53**(20), 13740–13746 (1996)
75. R. Feidenhansl, F. Grey, R.L. Johnson, S.G.J. Mochrie, J. Bohr, M. Nielsen, Oxygen-chemisorption on Cu(110)—a structural determination by x-ray-diffraction. *Phys. Rev. B* **41**(8), 5420–5423 (1990)
76. A. Kiejna, B.I. Lundqvist, First-principles study of surface and subsurface O structures at Al(111). *Phys. Rev. B* **63**(8), 085405 (2001)
77. A. Kiejna, B.I. Lundqvist, Stability of oxygen adsorption sites and ultrathin aluminum oxide films on Al(111). *Surf. Sci.* **504**(1–3), 1–10 (2002)
78. L.B. Hansen, P. Stoltze, J.K. Norskov, B.S. Clausen, W. Niemann, Is there a contraction of the interatomic distance in small metal particles. *Phys. Rev. Lett.* **64**(26), 3155–3158 (1990)
79. C.Q. Sun, Oxygen-reduced inner potential and work function in VLEED. *Vacuum* **48**(10), 865–869 (1997)
80. H.H. Rotermund, Investigation of dynamic processes in adsorbed layers by photoemission electron-microscopy (PEEM). *Surf. Sci.* **283**(1–3), 87–100 (1993)
81. J.D. Zhang, P.A. Dowben, D.Q. Li, M. Onellion, Angle-resolved photoemission-study of oxygen-chemisorption on Gd(0001). *Surf. Sci.* **329**(3), 177–183 (1995)
82. S.M. Thurgate, C. Sun, Very-low-energy electron-diffraction analysis of oxygen on Cu(001). *Phys. Rev. B* **51**(4), 2410–2417 (1995)
83. M. Lindroos, H. Pfnur, G. Held, D. Menzel, Adsorbate induced reconstruction by strong chemisorption—Ru(001)p(2×2)-O. *Surf. Sci.* **222**(2–3), 451–463 (1989)
84. H. Pfnur, M. Lindroos, D. Menzel, Investigation of adsorbates with low-energy electron-diffraction at very low energies (VLEED). *Surf. Sci.* **248**(1–2), 1–10 (1991)
85. S.M. Thurgate, G. Hitchen, C.Q. Sun, *Surface structural determination by VLEED analysis*. *Surface Science: Principles and Applications*, ed. by R.J. MacDonald, E.C. Taglauer, K.R. Wandelt. vol. 29 (Springer, Berlin, 1996)
86. C. Stampfl, M. Scheffler, Theoretical study of O adlayers on Ru(0001). *Phys. Rev. B* **54**(4), 2868–2872 (1996)
87. N. Materer, U. Starke, A. Barbieri, R. Doll, K. Heinz, M.A. Vanhove, G.A. Somorjai, Reliability of detailed LEED structural-analyses—Pt(111) and Pt(111)-p(2×2)-O. *Surf. Sci.* **325**(3), 207–222 (1995)
88. Y.M. Wang, Y.S. Li, K.A.R. Mitchell, A LEED crystallographic analysis for the half monolayer structure formed by O at the Zr(0001) surface. *Surf. Sci.* **342**(1–3), 272–280 (1995)
89. C.Q. Sun, S. Li, B.K. Tay, X.W. Sun, S.P. Lau, Solution certainty in the Cu(110)-(2×1)-2O($2-$) surface crystallography. *Int. J. Mod. Phys. B* **16**(1–2), 71–78 (2002)
90. C.Q. Sun, C.L. Bai, Modelling of non-uniform electrical potential barriers for metal surfaces with chemisorbed oxygen. *J. Phys.: Condens. Matter* **9**(27), 5823–5836 (1997)

91. C.Q. Sun, C.L. Bai, Oxygen-induced nonuniformity in surface electrical-potential barrier. *Mod. Phys. Lett. B* **11**(5), 201–208 (1997)
92. J.T. Hoeft, M. Kittel, M. Polcik, S. Bao, R.L. Toomes, J.H. Kang, D.P. Woodruff, M. Pascal, C.L.A. Lamont, Molecular adsorption bond lengths at metal oxide surfaces: Failure of current theoretical methods. *Phys. Rev. Lett.* **87**(8), 086101 (2001)
93. C.Q. Sun, A model of bonding and band-forming for oxides and nitrides. *Appl. Phys. Lett.* **72**(14), 1706–1708 (1998)
94. C.Q. Sun, C.L. Bai, A model of bonding between oxygen and metal surfaces. *J. Phys. Chem. Solids* **58**(6), 903–912 (1997)
95. C.Q. Sun, What effects in nature the two-phase on the O-Cu(001)? *Mod. Phys. Lett. B* **11**(2–3), 81–86 (1997)
96. C.Q. Sun, Origin and processes of O-Cu(001) and the O-Cu(110) biphas ordering. *Int. J. Mod. Phys. B* **12**(9), 951–964 (1998)
97. C.Q. Sun, Spectral sensitivity of the VLEED to the bonding geometry and the potential barrier of the O-Cu(001) surface. *Vacuum* **48**(5), 491–498 (1997)
98. C.Q. Sun, Exposure-resolved VLEED from the O-Cu(001): Bonding dynamics. *Vacuum* **48**(6), 535–541 (1997)

Chapter 2

Theory: Bond–Band–Barrier (3B)

Correlation

- *Chemical bond, energy band, and surface potential are closely correlated.*
- *O, N, and C hybridize their sp orbit upon reacting with atoms in any phase to create tetrahedral bonding orbits.*
- *Non-bonding lone electron pairs and bonding shares electron pairs occupy the orbits. The number of lone pairs follows the $(4-n)$ rule with n being valance value.*
- *The lone pair polarizes its neighboring atoms to form dipoles.*
- *Bond and non-bond formation creates four DOS features in the valence band, i.e., bonding pairs, non-bonding lone pairs, holes, and antibonding dipole states.*
- *Bond formation corrugates the surfaces with subjective production of missing-row vacancies.*

2.1 Basics

2.1.1 Regular Bonds: Interatomic Potential and Electron Configuration

The covalent, ionic, and metallic bonds are the most popular kinds of interatomic interaction [1]. These regular bonds are realized through valence charge sharing, either locally by neighboring atoms in the ionic and covalently bonded systems or delocally by all atoms of the entire body of a metal [1, 2]. The energies of the regular bonds are several electron volts (eV) in magnitude at equilibrium. The nearest distance between atoms and ions at equilibrium corresponds to the bond length. For example, Na is interacted with metallic bond and a cohesive energy of 1.1 eV per atom, which determines the Na to be ductile and electrically and thermally conductive. NaCl is an ideal specimen of ionic bond with a cohesive energy of 3.28 eV/atom, which makes NaCl harder, having high melting point and soluble in polar liquids such as water. Diamond being an ideal example of covalent

bond with cohesive energy of 7.4 eV per atom is so far the hardest natural material with high melting point of 3,800 K; diamond is insoluble in nearly all solvents. The polar covalent bond, in the form between the covalent and the ionic, exists in most alloys or compounds. The electronegativity difference between the constituent elements of the specimen dictates the nature of the bond or the way of charge sharing.

The interatomic potentials for these stronger interactions dominate the atomic cohesive energy, the Hamiltonian and the band structure, dispersion relations, the allowed density of states (DOS) of the valence band and below, and the effective mass and group velocity of charges in various bands as well. At equilibrium, the coordinates of a pairing potential correspond to the bond length and bond energy (d , E_b) that determine the binding energy density, E_b/d^3 . The product of the number of bonds (z) of an atom and the cohesive energy per bond is the atomic cohesive energy ($z_b E_b$). All the detectable quantities of the bulk materials, such as the critical temperature for crystal structural phase transition, electronic and optical properties, hardness, elasticity, and melting point, are all closely related to the bond nature, order, length, and energy represented by m , z , d , and E_b , or their combinations such as the cohesive energy, energy density, and lattice vibration frequency. The cohesive energy determines the thermal stability; the binding energy density determines the elasticity and mechanical strength. Quantum approximations could describe these regular bonds and their functionalities because of their periodically ordered homogeneity and uniformity.

2.1.2 Chemisorption Bonding Environment

Patterns of crystallographic and morphologic observations of the chemisorbed surfaces depend on the scale and geometry of the surface lattice and the difference in electronegativity between the guest and the host.

Figure 2.1 illustrates the typical coordination environment of the low-index fcc and hcp surfaces. Host atoms are arranged at sites between the first two planes of the fcc(001), (110), (111), and the hcp($10\bar{1}0$), (0001) surfaces regularly. The C_{4v} , C_{3v} , and C_{2v} point-group symmetries apply to the unit cells. The shortest atomic separation (atomic diameter) is a . These structures represent the majority of coordination environments so far documented. Table 2.1 compares the lattice geometry of the unit cells.

In the fcc(001) surface unit cell (see Fig. 2.1a), five atoms surrounding the C_{4v} hollow site form an upside-down pyramid. The atomic structures of the fcc(111) and the hcp(0001) surfaces in Fig. 2.1b are the same in the top two atomic planes where atoms arrange in the same AB order. Atoms surrounding the hcp(0001) hollow (indicated I) site form a tetrahedron, while atoms surrounding the fcc(111) hollow (indicated II) site cannot because there is no atom in the second layer underneath.

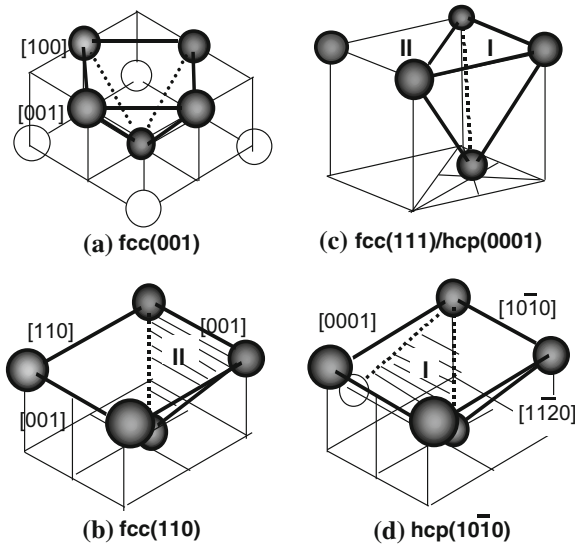


Fig. 2.1 Possible coordination environment for atomic chemisorption. **a** Atoms surrounding the fcc(001) fourfold (C_{4v}) hollow site form an upside-down pyramid. **b** On the fcc(111) and hcp(0001) surfaces, there are two types of threefold (C_{3v}) hollow sites. Atoms surrounding the hcp(0001) hollow (*I*) form a tetrahedron. No atom exists in the substrate second layer below the fcc(111) hollow site (*II*). **c** The fcc(110) and its analog. **d** hcp($10\bar{1}0$) surfaces possess alternate hcp(0001) (*I*) and fcc(111) (*II*) facet sites along the close-packed direction (reprinted with permission from [3])

Table 2.1 Comparison of the lattice geometry of the unit cells of various surfaces (unit in atomic diameter, a) (reprinted with permission from [3])

| | a_1 | a_2 | a_3 (layer spacing) |
|---------------------|-------|------------|-----------------------|
| fcc(001) | 1 | 1 | $1/\sqrt{2}$ |
| fcc(110) | 1 | $\sqrt{2}$ | $1/2$ |
| fcc(111) | 1 | 1 | 0.6934 |
| hcp($10\bar{1}0$) | 1 | 1.747 | 0.2887 |
| hcp(0001) | 1 | 1 | 0.8735 |

Atoms surrounding the fcc(110) and the hcp($10\bar{1}0$) hollow sites, in Fig. 2.1c, d, form a rectangular pyramid of C_{2v} symmetry. Besides the long-bridge hollow site, there are two facet sites along the close-packed direction in the fcc(110) and the hcp($10\bar{1}0$) surfaces. One is the hcp(0001) facet hollow site (*I*) that contains one atom in the top layer and two atoms in the second layer; the other is the fcc(111) facet (labeled *II*) that contains two atoms in the top layer and one in the second layer along the close-packed direction. The fcc(110) and (111) surfaces are analogous to the hcp($10\bar{1}0$) and (0001) surfaces with a slight difference in the interatomic spacing.

Table 2.2 lists the values of electronegativity (η), possible valences, and the atomic radius of representative elements of different electronic structures. The difference in electronegativity between atoms of two elements determines the nature of the bond between them. If the $\Delta\eta$ is sufficiently high (around 2), the bond is ionic; otherwise, it is covalent or polar covalent [1]. Normally, the atomic size of a noble ($4d$) metal is greater than that of a transition ($3d$) metal and the electronegativity of the noble metals is higher than that of transition metals. An atomic radius is not a constant but varies with the coordination number (CN) of this atom. Importantly, atomic radii change with alternation of valences. These basics play important roles in specifying the site of the adsorbate and the orientation of the tetrahedron bonds involving C, N, and O and therefore the patterns of observations for the chemisorbed surfaces.

2.1.3 Bonding Effects

Bond formation is a process in which valence electrons transport. This should have enormous effects on the surroundings by polarization and mass transportation. Alternation of atomic sizes will change the atomic distances and modify the surface morphology. Besides the well-known bonding states of metallic, covalent, ionic, and Van der Waals bonds in nature, polar covalent bonds, non-bonding lone pairs, antibonding dipoles, H-like bonds, and hydrocarbon-like bonds also exist.

Despite the well-known bonding events illustrated in Fig. 2.2a–h describes the formation of an ionic bond, non-bonding lone pairs, and their consequences on the wave functions of their atomic neighbors. The electronegative adsorbate or additive (smaller broken circle labeled *A*) interacts with the heavier host atoms (bigger broken circle labeled *B*) by either capturing electrons from the host *B* atom or polarizing the electrons of *B*. The polarization will raise the binding energy of the polarized electrons to the higher energy levels. Electron transport alters the atomic valences and atomic sizes of both the adsorbate *A* and the host *B*. For example, an oxygen atom changes its radius from 0.66 to 1.32 Å when the oxygen atom evolves into an O^{-2} ion. A copper atom alters its radius from 1.278 to 0.53 Å when the Cu atom becomes a Cu^{+} ion.

All the ions, whether positive or negative, and the non-bonding lone pairs are apt to polarize their neighbors, giving rise to the host dipoles with localized nature. Dipoles are formed with the expansion of atomic sizes and elevation of the DOS in energy. The production of the dipoles and the dipole–dipole interaction in the opposite direction will raise the system energy. It is therefore reasonable to term such an event as antibonding dipole formation—an extreme case of the Van der Waals bond interaction. Antibonding is a by-product of reaction, and it never forms between atoms of different electronegativities [4].

Non-bonding lone pairs meant that a pair of electrons of a specific atom occupies a directional bonding orbital of this atom. Lone-pair formation happens only to electronegative elements in the upper right part of the periodic table, such as

Table 2.2 Electronegativity, possible valences, and the CN-related atomic radius of typical elements (after Goldschmidt [2] and Pauling [1])

| Element | C | N | O | Si | Co | Cu | Ag | Ru | Rh | Pd | V |
|----------------------------|-----------|-----------|-----------|-----------|------------|---------------|---------------|------------|------------|---------------|------------|
| Electronic structure | $2s^2p^2$ | $2s^2p^3$ | $2s^2p^4$ | $3s^2p^2$ | $3d^74s^2$ | $3d^{10}4s^1$ | $4d^{10}5s^1$ | $4d^75s^1$ | $4d^85s^1$ | $4d^{10}5s^0$ | $3d^34s^2$ |
| η | 2.5 | 3.0 | 3.5 | 1.9 | 1.9 | 1.9 | 1.9 | 2.2 | 2.2 | 2.2 | 1.6 |
| R_{ion} (valence) | 2.6 (-4) | 1.71 (-3) | 1.32 (-2) | 0.41 (4) | 0.82 (2) | 0.53 (1) | 1.00 (1) | - | - | - | - |
| R_{m} (CN = 1) | 0.771 | 0.70/0.74 | 0.66/0.74 | 1.173 | 1.157 | 1.173 | 1.339 | 1.241 | 1.252 | 1.283 | 1.224 |
| R_{m} (CN = 12) | 0.914 | 0.88/0.92 | - | 1.316 | 1.252 | 1.276 | 1.442 | 1.336 | 1.342 | 1.373 | 1.338 |

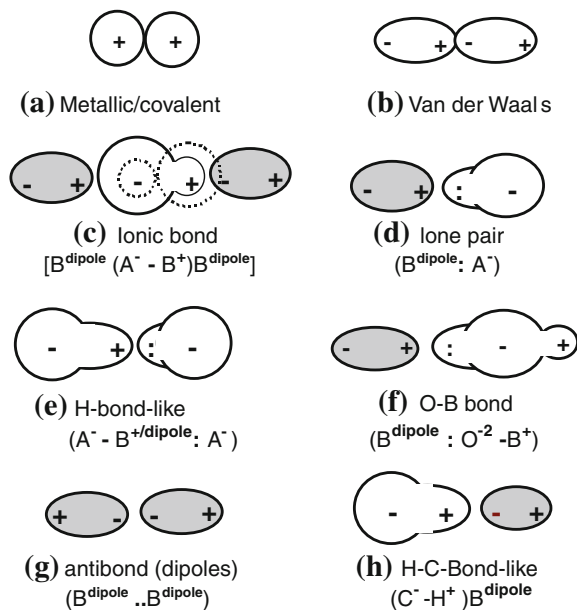


Fig. 2.2 The possible bond configurations and their consequences on the electron clouds of surrounding atoms (*shaded areas* stand for dipoles). **a** and **b** are the well-known bonding events. **c** Ionic bond formation alters atomic sizes (*broken circles*) and valences. **d** Non-bonding lone-pair formation (represented by ‘:’) induces B^P. **e** H-like bond forms if B^{+*p*} replaces the H^{+*p*}. **f** O–M bonds involve non-bonding lone pairs and bonding electron pairs. **g** Antibonding dipoles. **h** Hydrocarbon-like bonds can form by replacing H⁺ with B⁺, which also induces antibonding dipoles (reprinted with permission from [3])

nitrogen, oxygen, and fluorine when the $2s$, $2p_x$, $2p_y$, $2p_z$ orbitals of these elements are hybridized [5]. It is often the case that a fraction of the hybridized orbitals is occupied by shared electron pairs (bonding) and the remaining orbitals by the lone electron pairs (non-bonding) of the electronegative additives. The number of lone pairs of an adsorbate follows a ‘ $4-n$ ’ rule, and the n is the valence value of the adsorbate. For oxygen ($n = 2$), two lone pairs are present, while for nitrogen ($n = 3$), only one lone pair forms during the sp -orbital hybridization. The ‘ $4-n$ ’ rule holds for any elements in which the sp orbits hybridize. The lone pair requires an interaction with a B atom through polarization without any charge transport. The lone pair is actually not a bond but the weaker part of the hydrogen bond.

The classical hydrogen bond ($O^{-2} - H^{+p}; O^{-2}$), known for over 50 years, plays an essential role in the structure and function of biologic molecules. The ‘-’ and ‘:’ represent the bonding pair and the non-bonding lone pair, respectively. Hydrogen bonds are responsible for the strength and elasticity of materials such as wood or a spider’s web, molecular binding, as well as base pairing and folding in DNA. Hydrogen bonds are also responsible for the synthesis and transferring of protein signaling [6, 7].

The formation of the hydrogen bond is not due to the existence of hydrogen or oxygen but a consequence of the non-bonding lone pairs. If the lone-pair-induced B^p bonds further to an electronegative element A , then an H-like bond ($O^{-2}-B^{+p}; O^{-2}$) forms. H-like bonding differs from the classical hydrogen bond simply in that the B^{+p} replaces the H^{+p} in the hydrogen bond (see Fig. 2.2e). If an atom of another electronegative element, such as C, replaces one of the oxygen ions, then the ($C^{-4}-B^{+p}; O^{-2}$) configuration forms, which was specified as the anti-hydrogen bond [8]. This is also an H-like bond. Formation of such an H-like bond depends merely on the existence of the lone pair rather than the particular B elements involved. Hence, the H-like bond is more generally applicable though it is not often referred to as such. The same is true for the hydrocarbon-like bonds. The hydrocarbon bond is polar covalent in nature. The naked H^+ also polarizes and attracts electrons of its neighboring atoms. Hydrocarbon-like bond can form by replacing the H^+ with B^+ . The B^+ is less electronegative than the carbon.

The production of non-bonding lone pairs, antibonding dipoles, H-like bonds, and the hydrocarbon-like bonds is often overlooked. However, these events indeed play crucial roles in determining the physical properties of a system that involves electronegative additives. Quite often, a system contains several kinds of chemical bonds, such as in graphite and in an oxide. Because of the sp^2 -orbital hybridization of carbon, the Van der Waals bond dominates in the [0001] direction, while the stronger covalent bond dominates in the (0001) plane of the graphite. As is shown in Fig. 2.2f, g, O–B bond formation involves sharing pairs of electrons (bond), non-bonding lone pairs, and antibonding dipoles. The electronic environment surrounding an oxygen atom or a nitrogen atom is anisotropic.

From an energy point of view, bond formation lowers the system energy and stabilizes the system. Antibond dipole formation requires additional energy. Although it is energetically less favorable, the antibond can still form as a by-product of the events of bonding and non-bonding. Occupation of the orbitals by non-bonding electron lone pairs of an electronegative element, in principle, neither raises nor lowers the system energy with respect to the initially specific energy level of the isolated atoms of the electronegative element [4, 9, 10]. From the band structure point of view, the antibond-derived DOS (or polaron) should locate at energy above E_F or near to it due to the energy rise of the polarized electrons. The DOS features for bonding are located below the originally occupied levels of the electronegative element, while the DOS features of non-bonding lone pairs are located between those of the bond and those of the antibond. Hydrogen-like bond formation will stabilize the system as electrons transport from the high-energy antibonding states to the lower bonding states. Bond and antibond formations will produce holes below the E_F of the host material [11], which should be responsible for the transition from metal to semiconductor when a compound forms.

2.1.4 Surface Bond Contraction

Besides the well-known fact that an atom changes its radius when its valence alternates, both the ionic and metallic radii of an atom contract with reducing the CN of this atom. Goldschmidt [2] suggested that if an atom changes its CN from 12 to 8, 6, and 4, then the ionic radius would be reduced by 3, 4, and 12 % correspondingly. Pauling [1] also noted that the metallic radius contracts considerably with the reduction in the CN of the metal atom. One may extend the CN -imperfection-induced radius contraction to atoms at a solid surface or sites surrounding defects (such as point defects and stacking errors). It is understandable that the surface provides an ideal environment for CN reduction. Termination of the lattice periodicity in the surface normal direction reduces the CN of an atom at the surface. Such a CN reduction shortens the remaining bonds of the surface atom. It is essential to consider the CN effect on the Goldschmidt contraction for an ionic bond or a Pauling contraction for a metallic bond.

2.2 Chemical Bond: Tetrahedron Geometry

Extending the FH , H_2O , NH_3 , and CH_4 molecular structures to a chemisorbed surface by replacing the H atom with the host atom of an arbitrary element B , one can construct the tetrahedron bond configuration, as illustrated in Fig. 2.3a for oxide instance. During the modeling, two factors are taken into consideration. Firstly, the atomic radius is not constant but varies with the changes in not only its atomic valence, but also its CN . Secondly, the sp orbitals of oxygen hybridize and a quasi-tetrahedron forms. The bond angles and the bond lengths are not constant but vary within limits. Therefore, an oxygen atom can react with atoms, in any gaseous, liquid, or solid states of an arbitrary element B through two bonding electron pairs and two non-bonding lone pairs.

Oxygen atom has initially six electrons in the $2s$ and $2p$ orbitals and then captures two more electrons from each of its B neighbors. The eight electrons fully occupy the $2s$ and $2p$ levels of an oxygen atom that hybridizes its sp orbitals then to form four directional orbitals. The eight electrons repopulate in the four directional orbitals with two electron pairs shared between O and B . The remaining two orbitals are occupied by the lone electron pairs of oxygen.

In a bonding orbital, the extent of electron sharing, or the nature of the bond, depends on the difference in electronegativity (η) between the oxygen and element B . Due to the high η value (see Table 2.2), oxygen catches an electron from B (labeled 1 and 2 in Fig. 2.3a) to form the ionic bond with Goldschmidt contraction at the surface. Formation of the non-bonding lone pairs, however, is independent of the nature of element B . The lone pairs polarize atom B (labeled 3 in Fig. 2.3a), and the B atom becomes a B^p dipole with associated expansion of size and elevation of energy of the polarized electrons that occupy the antibonding energy levels.

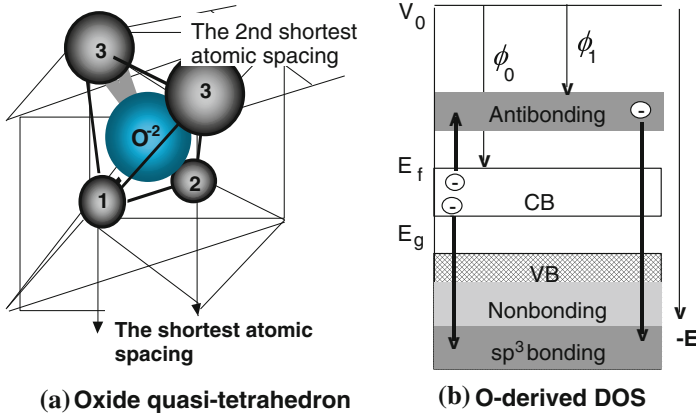


Fig. 2.3 **a** the primary oxide quasi-tetrahedron and, **b** the corresponding DOS features of bonding, non-bonding, antibonding, and electronic holes [12]. Each of the two ions, 1 and 2, donates one electron to the central oxygen to form ionic bonds with Goldschmidt contraction. Atoms labeled 3 are the lone-pair-induced metal dipoles with expansion of sizes and elevation of energy states. Due to the repulsion between the electron pairs, the angle BA33 is greater than 109.5° and the angle BA12 is smaller than 104.5° . Arrows in (b) represent the process of charge transportation. The arrow from the antibonding sub-band to the bond states corresponds to the process of H-like bond formation (reprinted with permission from [3])

In an oxide tetrahedron, the plane (3O3) composed of the lone pairs and the oxygen nucleus should be ideally perpendicular to the plane (1O2) that consists of two bonding orbits. The distance (1–2) between the two B^+ ions and the spacing (3–3) between the B^P and B^P match closely the first and second shortest atomic spacings at a surface, which involves two atomic layers. The B^P tends to locate at the open end of a surface due to the strong repulsion between the dipoles. The B_2O primary tetrahedron is not a standard one, but it is distorted due to the following effects: (1) the difference in repulsion between the occupied orbits varies the bond angles [BA_{ij} (angle $\angle iOj$), where $i, j = 1, 2, 3$ correspond to the atoms as labeled; $BA_{12} \leq 104.5^\circ$, $BA_{33} > 109.5^\circ$] and (2) the difference in CN of atoms at different sites adjusts the bond length [$BL_i = (R_M^+ + R_O^{2-}) \times (1 - C_i)$, where $i = 1, 2$; C_i are the effective bond contracting factors]. The length of BL3 and the angle BA33 vary with the coordination circumstances in a real system. The bonding environment for an oxygen atom is anisotropic at the atomic scale.

The formation of tetrahedrons dislocates the B atoms collectively in the otherwise regular lattice sites. Moreover, an oxygen atom always seeks four neighbors to form a stable quasi-tetrahedron. The expansion of atomic radius and the energy rise of the dipole electrons are responsible for the protrusions in the STM images and the reduction in the local work function. The localized dipole electrons are also responsible for the non-Ohmic rectification at the surface, even though the local work function reduces significantly. The strong localization of dipole electrons at the surface increases the surface contact resistance because

these electrons cannot move easily. The oxygen adsorption affects the STM current predominantly by polarizing metal electrons, because of antibonding dipole formation [13–15].

At the initial stage of oxidation, the oxygen molecule dissociates and the oxygen atom interacts with the host atoms through a single bond. The O^{-1} chooses a specific site where the O^{-1} bonds directly to one of its neighbors and polarizes the rest. For the transition metals, such as Cu and Co, of lower electronegativity ($\eta < 2$) and smaller atomic radius ($< 1.3 \text{ \AA}$), the oxygen atom often bonds to an atom at the surface first. For noble metals, such as Ru and Rh, of higher electronegativity ($\eta > 2$) and larger atomic radius ($> 1.3 \text{ \AA}$), the oxygen atom tends to sink into the hollow site and bonds to the atom underneath the first atomic layer. The ordering of bond formation leads to different patterns of reconstruction. The O^{-1} also polarizes other neighbors and pushes the B^P at the surface radially outward from the adsorbate. Because of oxide tetrahedron formation with lone-pair non-bonding and dipole antibonding, the electronic structure surrounding a certain atom varies from site to site.

2.3 Energy Band: Valence Density of States

The formation of bonds, non-bonding lone pairs, and antibonding dipoles as well as the H-like bonds generates corresponding features adding to the DOS of the valence band and above of the host, as illustrated in Fig. 2.3b. Arrows represent the kinetic processes of electron transportation. Initially, energy states below the E_F of a metal are fully occupied in the ideal case at $T = 0$. The work function, ϕ_0 , Fermi energy, E_F , and the vacuum level, E_0 , follow the simple relation: $E_0 = \phi_0 + E_F$. For Cu, as an example, $E_0 = 12.04 \text{ eV}$, $\phi_0 = 5.0 \text{ eV}$, and $E_F = 7.04 \text{ eV}$. The Cu-3*d* band locates at energies range over from -2.0 to -5.0 eV below E_F . The oxygen 2*p* states are around -5.5 eV with respect to E_F for Cu. At the initial stage of reaction, an electron from a metal is transported from its outermost shell to the unoccupied 2*p* orbit of the oxygen, which produces a hole in the outermost shell of the metal. The O^{-1} polarizes its rest neighbors to form a polaron, as a result. This first stage creates additional DOS features of bonding ($\ll E_F$), holes ($\leq E_F$), and antibonding dipoles ($\geq E_F$).

With the full occupancy of the *p*-orbit of oxygen, the *sp* orbits of the O^{-2} hybridize, which brings about four additional DOS features, as illustrated in Fig. 2.3b:

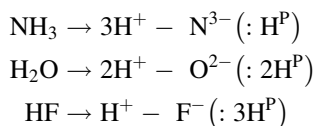
- Electronic vacancies pertaining to the host are produced right below E_F , generating a gap between the conduction band and the valence band of a metal. The electron transportation can also expand the original bandgap of a semiconductor from E_{G0} to E_{G1} .
- The non-bonding states of O^{-2} locate below E_F without apparent energy change, in principle, compared with the 2*p* level of an isolated atom of oxygen [9].

- The bonding states are close to the originally occupied $2p$ level of the isolated oxygen.
- The antibonding (lone-pair-induced dipole) states are located above E_F or near to it. The oxygen-induced dipole reduces the work function from ϕ_0 to ϕ_1 .
- Upon being overdosed with oxygen, H-like bonds form at the surface. The overdosed oxygen gets electrons from the dipoles, and the B^P becomes B^{+P} . The arrow from the antibonding states above E_F to the deeper bonding sub-band represents the process of H-like bond formation. Apparently, this process lowers the system energy and increases the work function.

The hole production and the lone-pair production are independent but simultaneous, which result in the joint DOS features below E_F . If the products of both processes are compatible in quantity, the joint DOS features derived by the two processes may not be easily identified. The hole production is due to two mechanisms: bonding and antibonding. For the Cu example, the $4s$ electrons (in the conduction band, CB) either contribute to oxygen for the bonding or jump up to the outer empty shell (Cu $4p$, for example) for the antibonding dipole. Such bonding and antibonding processes empty the states just below E_F , which result in the Cu oxide being a semiconductor with a known bandgap ranging from 1.2 to 1.5 eV [16, 17].

STS and VLEED revealed that the states of antibonding of the O–Cu system range over 1.3 ± 0.5 eV above the E_F and the non-bonding states -2.1 ± 0.7 eV below. Angular resolved inverse PES [18] detected that the features of empty states at +2.0 eV decrease with increasing oxygen coverage on the Cu(110) surface. The PEEM studies of O–Pt surfaces [19–22] have detected the conversion of the dark islands, in the scale of 10^2 μm , into very bright ones with work functions ~ 1.2 eV lower than that of the clean Pt surface. The bonding states are around -5.5 eV below E_F , which is shifted slightly toward an energy level lower than the $2p$ level of the oxygen because the hybrid bond lowers the system energy. Most strikingly, all the oxygen-derived DOS features are strongly localized in real space.

Non-bonding lone pairs and antibonding dipoles are generated in a reaction with sp^3 -orbit hybridization being involved, such as in the processes of



Usually, the parts in the brackets are omitted in formulating reactions because they share no charges with the electron acceptors. Under UV irradiation or thermal excitation, the hybrid sp^3 -orbit can be dehybridized, and the lone pairs and dipoles are removed accordingly.

Figure 2.4 illustrates the residual DOS of N- and O-chemisorbed metals and semiconductors. Likewise, a nitrogen atom needs three electrons for sharing and

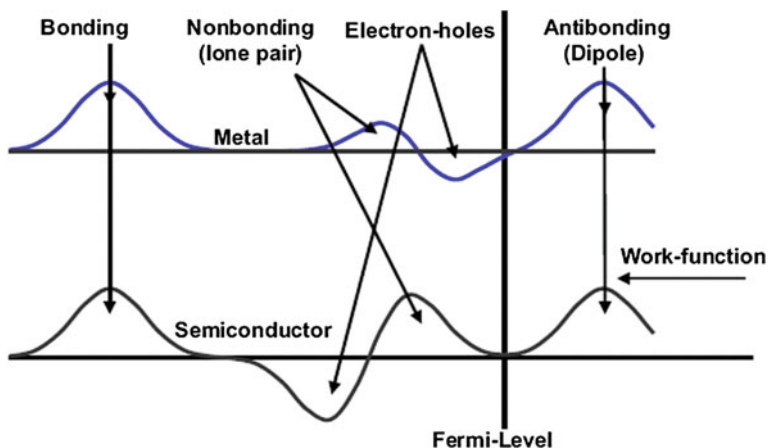


Fig. 2.4 N, O, and F chemisorption modified valence DOS for a metal and a semiconductor with four excessive DOS features: bonding ($\ll E_F$), lone pairs ($< E_F$), electron holes ($< E_F$), and dipoles ($> E_F$). The three DOS features close to the E_F are often overlooked, yet they are crucial to the performance of a compound (reprinted with permission from [3])

generates one lone pair. Similarly, an F atom forms a tetrahedron with three lone pairs. In addition to the weak interactions with energies of ~ 50 meV [3], these lone pairs polarize the neighboring atoms instead causing their change to dipoles. Strikingly, the manner of electronic distribution, bond type, bond length, and bond energy surrounding the central O or N atom in the tetrahedron is anisotropic.

In semiconductor compounds, the holes form at the upper edge of the valence band, which expand the semiconductor's bandgap further and turn a semiconductor into an insulator. In metallic compounds, the holes are produced at the Fermi surface and hence causing the formation of a bandgap. This is the reason for the metallic compound's loss of conductivity to become either a semiconductor or an insulator. Non-bonding states are situated in the bandgap to form impurity states close to Fermi surface, while antibonding states are situated above the Fermi energy. The production of dipoles will shift the surface potential barrier outwardly with high saturation [23], opposing to the effect of the charged ions. The former can be observed using STM as protrusions, while the latter depressions. The orientation of such a tetrahedron in a bulk is also subject to its coordination environment [24]. The difference between N, O, and F is in the structural symmetry and the number of lone pairs in one tetrahedron.

The weak interactions contribute insignificantly to the Hamiltonian or the atomic cohesive energy. These electrons add, however, impurity states near Fermi energy, which neither follow the regular dispersion relations nor occupy the allowed states of the valence band and below. They are located right in the energy scope of STM/S. The lone-pair and dipole interactions not only act as the most important function groups in the biologic and organic molecules but also play an important role in the inorganic compounds.

2.4 Surface Potential Barrier: Morphology

The SPB experienced by LEED incident electrons traversing the surface region contains two parts [25]:

$$\begin{aligned} V(r, E) &= \text{Re}V(r) + i\text{Im}V(r, E) \\ &= \text{Re}V(r) + i\text{Im}[V(r) \times V(E)] \end{aligned} \quad (2.1)$$

The shape and the saturation degree of the SPB depend on the surface atomic valence states [26], but the height of the SPB approaches to the muffin-tin inner potential constant of atoms inside the solid, V_0 [27]. The real (elastic) and imaginary (inelastic) parts of the SPB take the following forms [27, 28]:

$$\begin{aligned} \text{Re}V(z) &= \begin{cases} \frac{-V_0}{1 + A \exp[-B(z - z_0)]}, & z \geq z_0 \text{ (a pseudo-Fermi-}z \text{ function)} \\ \frac{1 - \exp[\lambda(z - z_0)]}{4(z - z_0)}, & z < z_0 \text{ (the classical image potential)} \end{cases} \\ \text{Im}V(z, E) &= \text{Im}[V(z) \times V(E)] \\ &= \gamma \times \rho(z) \times \exp\left[\frac{E - \phi(E)}{\delta}\right] \\ &= \frac{\gamma \times \exp\left[\frac{E - \phi(E)}{\delta}\right]}{1 + \exp\left[-\frac{z - z_1}{\alpha}\right]} \end{aligned}$$

where A , B , γ , and δ are constants. α and λ describe the degree of saturation. z_0 is the origin of the image plane inside which electron is located. $\phi(E) = E_0 - E_F$, the energy-dependent local $\phi(E)$ depends on the density of states $\rho(E)$. The $\nabla^2[\text{Re}V(z)] = -\rho(z) \propto \text{Im}V(z)$ describes the spatial distribution of charges. The terms $z_1(z_0)$ ($\rho(z_1) = 0.5\rho_{\text{bulk}}$) and $\alpha(z_0)$ (saturation degree) involved in the Fermi z function describe the spatial distribution of electrons contributing to the damping of incident beams. The spatial integration of $\rho(z)$ from a position inside the crystal to infinitely far away from the surface gives the local DOS ($n(x, y)$). Therefore, $\phi_L(E)$ can extend to cover situations that are E dependent and to large surface areas over which the LEED method integrates (Fig. 2.5).

The real part, $\text{Re}V(r)$, describes the elastic scattering of the incident electron beam. Integration of the $\text{Re}V(r)$ along the moving path of the electron beam determines the phase shift of the electron beam in diffraction. The imaginary part, $\text{Im}V(r)$, describes the spatial decay of the incident beam. $\text{Im}V(E)$ represents the joint effects of all the dissipative processes including excitation of phonons, photons, and single electron as well as plasmon excitation. Plasmon excitation occurs at energy much higher than E_F (normally ~ 15 eV above E_F). Excitation of phonon and photon requires energy smaller than the work function. Single-electron excitation occurs at any beam energy that is greater than the work function and in the space occupied by electrons. The spatial distribution of electrons is described by $\rho(r)$ (charge density) that is related to the inelastic damping potential, $\text{Im}V(r)$. An $\text{Im}V(z, E)$ can be defined

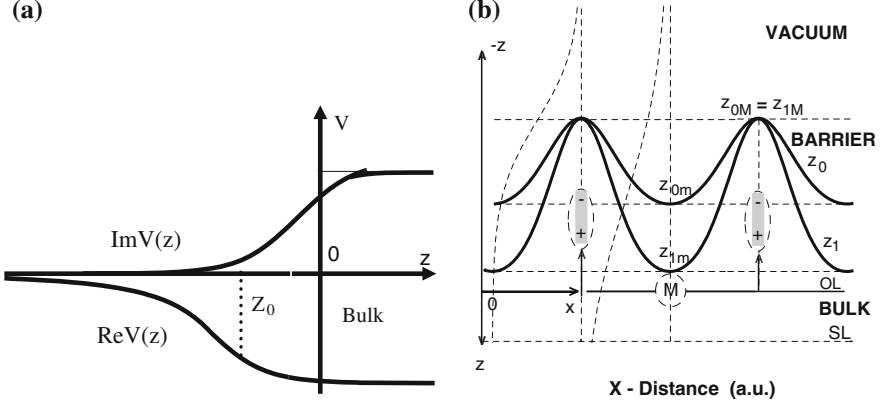


Fig. 2.5 **a** The real (elastic) and imaginary (damping) parts of the SPB with z -axis directed into the crystal, and z_0 is the origin for the image plane. The imaginary part describes surface charge distribution and saturation, which correspond to the surface morphology. The elastic part is related to the path and phase shift of diffracted electron beams in LEED measurements. **b** The SPB correlates STM surface morphology. At dipole site, the SPB origin shifts out of the surface with high saturation, while at vacancy or the ionic site, the SPB shifts inward and less saturated (reprinted with permission from [3])

to include the damping effects that occurs in the electron-occupied space (Fermi z decay) and that takes place at incident beam energy being greater than the work function, which depends on the occupied DOS [29].

The $\text{Re}V(r)$ correlates with the $\text{Im}V(r)$ through the Poisson equation:

$$\nabla^2[\text{Re}V(r)] = -\rho(r); \text{ and, } \text{Im}V(r) \propto \rho(r)$$

The gradient of the $\text{Re}V(r)$ relates to the intensity of the electric field $\varepsilon(r)$: $\nabla[\text{Re}V(r)] = -\varepsilon(r)$. If $\rho(r) = 0$, then the $\text{Re}V(r)$ corresponds to a conservative field in which the moving electrons will suffer no energy loss and the spatial variation in the inelastic potential $\text{Im}V(r) \propto \rho(r) = 0$. The $\text{Re}V(z)$ transforms at $z = z_0$ from the pseudo-Fermi z function to the $1/(z-z_0)$ -dominated classical image potential. Therefore,

$$\nabla^2[\text{Re}V(z_0)] = -\rho(z_0) = 0.$$

The origin of the image plane, z_0 , acts as the boundary of the surface region occupied by electrons. If z_0 varies with the surface coordinates, then the $z_0(x, y)$ provides a contour of the spatial electron distribution, which should be similar to that plotted using STM imaging [29].

At the dipole site, $z_{1M} \approx z_{0M} = -3.425$, $\alpha \approx \lambda^{-1}$, while in the atomic vacancy or ion positions, $z_{1m} \ll z_{0m} = 1.75$ Bohr radii due to the strong localization of electrons at the surface. The SPB increases its degree of saturation with the outward shift of the image plane z_0 . This means that formation of metal dipoles shifts the electron clouds outwardly and enhances the density of the shifted electronic clouds.

2.5 Summary

The H_2O -, NH_3 -, and FH-like molecular structures and the concept of *CN*-imperfection-induced bond contraction can be extended to the chemisorption of a solid surface. This leads to the framework of tetrahedral bond formation and its effects on the valence DOS and the surface potential barrier, as well as their interdependence:

- O, N, C, and F can interact with atoms of an arbitrary element B to form a tetrahedron with bonding and non-bonding states, as well as antibonding dipoles due to polarization.
- Chemisorption of electronegative additives derives four additional DOS features that add to the valence band and above of the host. These features of bonding, non-bonding, antibonding, and electron holes are strongly localized.
- The SPB parameters are correlated with the image plane (z_0) corresponding to the boundary of the surface region occupied by electrons, which describe the STM imaging features.
- The bond geometry, atomic valence values, valence DOS, and the SPB are interdependent. One may need to pay equal attention to these categories in dealing with surface chemisorption. This way of thinking will amplify immensely the physics behind observations and enhance the capacity of available instrumentation.
- Some important yet often overlooked events, such as non-bonding lone pairs, antibonding dipoles, H-like bond, and surface bond contraction, are crucial to practical applications.

References

1. L. Pauling, Atomic radii and interatomic distances in metals. *J. Am. Chem. Soc.* **69**(3), 542–553 (1947)
2. V.M. Goldschmidt, Crystal structure and chemical correlation. *Ber. Deut. Chem. Ges.* **60**, 1263–1296 (1927)
3. C.Q. Sun, Oxidation electronics: bond-band-barrier correlation and its applications. *Prog. Mater. Sci.* **48**(6), 521–685 (2003)
4. S.R. Morrison, *The Chemical Physics of Surfaces* (Plenum press, NY and London, 1977)
5. C.W. Keenan, D.C. Kleinfelter, J.H. Wood, *General College Chemistry* (Harper and Row Publishers, New York, 1979)
6. W.G. Han, C.T. Zhang, A theory of nonlinear stretch vibrations of hydrogen-bonds. *J. Phys.: Condens. Matter* **3**(1), 27–35 (1991)
7. R.H. Crabtree, Chemistry—A new type of hydrogen bond. *Science* **282**(5396), 2000–2001 (1998)
8. P. Hobza, Z. Havlas, The fluoroform center dot center dot center dot ethylene oxide complex exhibits a C–H center dot center dot center dot O anti-hydrogen bond. *Chem. Phys. Lett.* **303**(3–4), 447–452 (1999)
9. J.M.D. Coey, H. Sun, Improved magnetic-properties by treatment of iron-based rare-earth intermetallic compounds in ammonia. *J. Magn. Magn. Mater.* **87**(3), L251–L254 (1990)

10. P.W. Atkins, *Physical Chemistry* (Oxford University Press, Oxford, 1990)
11. C.Q. Sun, C.L. Bai, A model of bonding between oxygen and metal surfaces. *J. Phys. Chem. Solids* **58**(6), 903–912 (1997)
12. C.Q. Sun, What effects in nature the two-phase on the O–Cu(001)? *Mod. Phys. Lett. B* **11**(2–3), 81–86 (1997)
13. N.D. Lang, Apparent barrier height in scanning tunneling microscopy. *Phys. Rev. B* **37**(17), 10395–10398 (1988)
14. N.D. Lang, Small adsorbate dipole-moments need not imply small charge transfers. *Surf. Sci.* **127**(2), L118–L122 (1983)
15. N.D. Lang, in *Scanning Tunneling Microscopy III*. Springer Series in Surf. Sci., Vol. 29, ed. by R. Wiesendanger, H.J. Güntherodt (Springer, Berlin, 1993)
16. J. Ghijsen, L.H. Tjeng, J. Vanelp, H. Eskes, J. Westerink, G.A. Sawatzky, M.T. Czyzyk, Electronic-structure of Cu₂O and CuO. *Phys. Rev. B* **38**(16), 11322–11330 (1988)
17. F. Marabelli, G.B. Parravicini, F. Salghetti-drioli, Optical gap of CuO. *Phys. Rev. B* **52**(3), 1433–1436 (1995)
18. A. Goldmann, M. Donath, W. Altmann, V. Dose, Momentum-resolved inverse photoemission-study of nickel surfaces. *Phys. Rev. B* **32**(2), 837–850 (1985)
19. H.H. Rotermund, Investigation of dynamic processes in adsorbed layers by photoemission electron-microscopy (PEEM). *Surf. Sci.* **283**(1–3), 87–100 (1993)
20. H.H. Rotermund, J. Lauterbach, G. Haas, The formation of subsurface oxygen on Pt(100). *Appl. Phys. A-Mater. Sci. Process.* **57**(6), 507–511 (1993)
21. J. Lauterbach, H.H. Rotermund, Spatiotemporal pattern-formation during the catalytic CO-oxidation on Pt (100). *Surf. Sci.* **311**(1–2), 231–246 (1994)
22. J. Lauterbach, K. Asakura, H.H. Rotermund, Subsurface oxygen on Pt (100): kinetics of the transition from chemisorbed to subsurface state and its reaction with CO, H₂ and O₂. *Surf. Sci.* **313**(1–2), 52–63 (1994)
23. C.Q. Sun, O-Cu (001): I. Binding the signatures of LEED, STM and PES in a bond-forming way. *Surf. Rev. Lett.* **8**(3–4), 367–402 (2001)
24. C.Q. Sun, Electronic process of Cu (Ag, V, Rh)(001) surface oxidation: atomic valence evolution and bonding kinetics. *Appl. Surf. Sci.* **246**(1–3), 6–13 (2005)
25. J.B. Pendry, *Low Energy Electron Diffraction: The Theory and its Application to the Determination of Surface Structure* (Academic Press, London, 1974)
26. C.Q. Sun, Spectral sensitivity of the VLEED to the bonding geometry and the potential barrier of the O-Cu (001) surface. *Vacuum* **48**(5), 491–498 (1997)
27. C.Q. Sun, C.L. Bai, Modelling of non-uniform electrical potential barriers for metal surfaces with chemisorbed oxygen. *J. Phys.: Condens. Matter* **9**(27), 5823–5836 (1997)
28. R.O. Jones, P.J. Jennings, O. Jepsen, Surface-barrier in metals: a new model with application to W(001). *Phys. Rev. B* **29**(12), 6474–6480 (1984)
29. C.Q. Sun, S. Li, B.K. Tay, X.W. Sun, S.P. Lau, Solution certainty in the Cu (110)-(2×1)-2O(2-) surface crystallography. *Int. J. Mod. Phys. B* **16**(1–2), 71–78 (2002)

Chapter 3

STM and LEED: Atomic Valences and Bond Geometry

- *A combination of LEED crystallography and STM microscopy enables quantification of CuO bond geometry and formulation of reaction dynamics with specification of evolution of atomic valence values in each phase.*
- *O, N, and C chemisorption involves at least the outermost two atomic layers with the adsorbates buckling in between in four discrete stages.*
- *Adsorbate valence evolves from -1 to $-n$ ($n = 2, 3, 4$ for O, N, and C, respectively), which results in the attributes of crystallography, valence DOS, and surface morphology.*
- *The adsorbate of -1 valence may locate at any site, i.e., atop, bridge, hollow to form single bond with the host atom, and polarize the rest neighbors. The adsorbate of $-n$ valence tends to form a tetrahedron with n bonds to neighbors and $4 - n$ lone pairs to polarize the rest.*
- *Host atoms may miss or electron cloud of dipoles may serve as donor for tetrahedron formation.*
- *Atomic sizes, crystal orientation, and electronegativity difference between the guest and host determine the bond ordering, tetrahedron orientation, and phase structures in reaction.*

3.1 Phase Ordering

Table 3.1 features the phase ordering occurred at the low-index O-(Cu, Rh)(110), (111) surfaces and their analogs of O-(Co, Ru)($10\bar{1}0$), (0001) surfaces. The O-Pd(110) surface performs in the same way as the O-Rh(110) surface. The O-(V, Ag)(100) surfaces perform differently from the O-(Cu, Rh)(001) surfaces despite the same geometrical configuration. Incorporating the primary tetrahedral bond to these structures led to formulation of reaction, which specifies the valence relaxation of atoms in the outermost two atomic layers of the chemisorbed surface. The phase transition results from nothing more than the alternation of the oxygen valence under a certain geometrical configuration at different oxygen coverage.

Table 3.1 Oxygen-induced phase ordering on the typical metal surfaces. The hcp(0001) and hcp($10\bar{1}.0$) faces are analogs to the fcc(111) and fcc(110) faces, respectively

| | Cu(fcc) | Rh(fcc) | Co(hcp) | Ru(hcp) |
|---------------------------------|---|---|---|---|
| fcc(001) | c(2×2)- $2O^{-1}$ off-centered pyramid ($\sqrt{2} \times 2\sqrt{2}$)R45°- $2O^{-2}$ missing row | c(2×2)- $2O^{-1}$ radial and inverse pyramid c(2×2)p4g- $2O^{-2}$ or c($4\sqrt{2} \times 4\sqrt{2}$)- $16O^{-2}$ | | |
| fcc(110) or hcp($10\bar{1}0$) | (2×1)- O^{-2} (Ni, Ag, Pt) c(6×2)- $8O^{-2}$ | Disordered (1×1)- O^{-1} (hollow) | Disordered (2×1)- $2O^{-1}$ (atop) | c(2×4)- $4O^{-2}$ (2×1)p2mg- $2O^{-2}$ Radial (2×2)- O^{-1} (hcp-hollow) |
| fcc(111) or hcp(0001) | '29' and '44' structures | Radial (2×2)- $2O^{-2}$ pairing-row (1×1)- O^{-2} | | c(2×2)- $2O^{-2}$ pairing-row (1×1)- O^{-2} |

Reprinted with permission from [1]

3.2 O–Cu(001), (110), (111)

3.2.1 O–Cu(001)

3.2.1.1 STM Morphology and Crystallography

Since 1956, when Young et al. [2] found that the Cu(001) surface is more easily oxidized than other faces of the single crystal of Cu, there have been many conflicting opinions regarding the oxygen-induced Cu(001) surface reconstruction. Different atomic superstructures have been derived with various experimental techniques [3] and theoretical approaches [4, 5]. Oxygen chemisorption results in a short-ordered nanometric Cu(001)- $c(2 \times 2)$ -O⁻¹ precursor phase at 25 L (Langmuir = 10⁻⁶ torr second) exposure or lower, followed by the ordered missing-row (MR)-type ($\sqrt{2} \times 2\sqrt{2}$)R45°-2O⁻² structure, see Fig. 3.1 [6–11]. (The valences of oxygen are denoted based on the development of this work for readers' convenience).

STM images in Fig. 3.1a, b resolved that oxygen prefers the next-nearest-neighboring hollow site throughout the course of reaction, showing strong site specificity of the adsorbate [9, 12]. At the initial stage of reaction (Fig. 3.1a), nanometric $c(2 \times 2)$ -2O⁻¹ domains dominate with zigzag and U-type protruding boundaries of 'checkerboard'-like patterns. Upon increasing exposure to oxygen, the short-ordered $c(2 \times 2)$ -O⁻¹ phase evolves into the ordered ($\sqrt{2} \times 2\sqrt{2}$)R45°-2O⁻² structure by every fourth row of Cu atoms becoming missing. In the second phase, the 'dumbbell'-shaped protrusions in Fig. 3.1b bridge over the missing rows. The separation between the paired rows was estimated to be 2.9 ± 0.3 Å. The length of the bright spot was about 5.1 Å. The height of the bright spot was 0.45 Å compared to 0.3 Å protrusions on the pure Cu(001) surface [13]. (001)R45° is equivalent of (110) with row separation of $2.55 \times \sin(45^\circ) = 1.80$ Å. In the precursor, the atomic valences of the Cu atoms sitting inside the domain of 'depression' differ completely from that of the Cu atoms composing the protruding boundaries. The atomic valences of the paired protrusions also differ from the depressions in the second phase.

The creation of the 'dumbbell' protrusions was corresponded to: 'the pairing of Cu–O–Cu chains by displacing the Cu *and/or* O atoms next to the missing row by about 0.35 Å toward the missing row' and 'the O–Cu–O chain is formed by the delocalized antibonding states' [13].

The two sequential phases on the O–Cu(001) surface are reversible. The ($\sqrt{2} \times 2\sqrt{2}$)R45°-2O⁻² phase reverses into the initial precursor state after sputtering by an energetic Ar⁺ beam and followed by flashing the sample up to 520 K [14]. When annealing the ($\sqrt{2} \times 2\sqrt{2}$)R45°-2O⁻² surface at a temperature corresponding to the 'dull red' color of the Cu surface for half an hour [15], *sp*-orbital de-hybridization occurs to the oxygen [16].

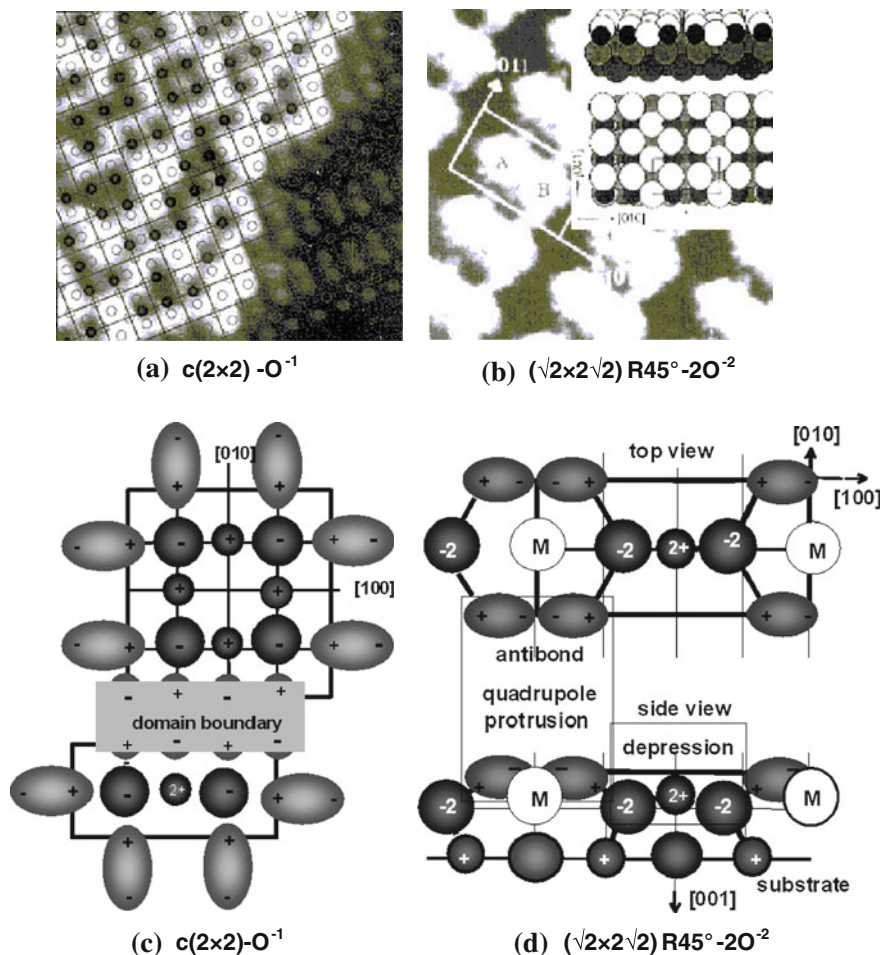


Fig. 3.1 STM images and the corresponding description [8] for the O-Cu(001) bi-phase structures: **a** and **c** correspond to the nanometric $c(2 \times 2) - O^{-1}$ domains with zigzag- and U-shaped protruding boundaries [9], **b** and **d** are the fully developed $(\sqrt{2} \times \sqrt{2}) R45^\circ - 2O^{-2}$ structure [13]. The O-Cu-O pairing-chains (dumbbell-shaped bright spots cross the missing-row vacancies) lie along the (010) direction. Inset of **b** shows the missing-row-type rigid sphere reconstruction model [1] (reprinted with permission from [1])

Extensive research on the crystallography of O-Cu(001) surface has been conducted with derivative of debated crystal structures in terms of atom dislocations in the x (perpendicular to the MR) and z (vertical) directions. Table 3.2 features the atomic geometry of the O-Cu(001) surface probed using various techniques.

Table 3.2 Structural discrepancies for O–Cu(001) surface (unit in Å)^a

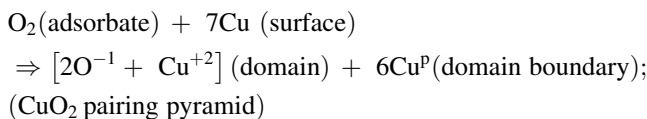
| References | Method | DCu _x | DO _x | DO _z | DCu _z | D ₁₂ | Bond length |
|------------|----------------------|---|-----------------|-----------------|------------------|-----------------|--------------------|
| [17] | VLEED | | | –0.8 | | 1.90 | c(2 × 2) |
| | | 0.3 | 0.0 | –0.2 | –0.1 | 1.90 | |
| [7] | SEXAFS | 0.25 | 0.03 | 0.2 | 0.1 | | 1.86, 2.07 |
| | | –0.15 to –0.3 | –0.1 | 0.8 | 0–0.25 | | c(2 × 2) |
| [18] | STM, LEED | 0.3 | 0.0 | 0.1 | 0.1 | 1.94 | 1.91 |
| [11] | LEED | 0.3 | 0.0 | 0.1 | 0.1 | 1.94 | 1.81, 2.04 1.84(2) |
| [19] | LEED, PED, NEXAFS | 0.1 ± 0.2 | 0–0.25 | 0.25 | 0.1 ± 0.2 | 2.05 | 1.94 |
| [9] | LEED | 0.10 | 0.0 | 0.10 | –0.05 | 2.06 | |
| [20] | EMT | >0.0 | | <0.0 | 0.3–0.5 | | |
| [13] | STM | ~0.35 | ~0.35 | | | | |
| [21, 22] | VLEED | Bond length: 1.63(1); 1.77(1); 1.94(2) Å; Ionic bond angle: 102.5°, lone-pair angle: 140.0° | | | | | |

Reprinted with permission from [1]

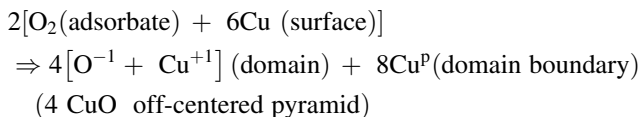
^a All are missing-row structures unless otherwise denoted c(2 × 2). Parameters are the first interlayer spacing, D₁₂, the shift of the atom near the missing row (DCu_x, DCu_z) and the displacement of the adsorbate (DO_x, DO_z)

3.2.1.2 Cu(001)–c(2 × 2)–2O^{–1}: Off-centered CuO₂ Pairing Pyramid

Oxygen bonding to surface atoms follows a certain constraints. It is forbidden for an oxygen adsorbate to form identical bonds with four neighboring atoms which are located in the same plane because oxygen possesses at most four *directional* orbits [23, 24]. It is impossible for an O to capture two electrons from any single-host atom. Initially, O₂ molecule dissociates and then the oxygen atom immediately bonds to one atom at the surface. The model in Fig. 3.1c indicates that the O^{–1} forms a bond with one of its four neighbors at the surface and the O^{–1} polarizes the rest. This gives rise to two typical domains in a (√2 × 2√2)R45° cell, which can be described as (Fig. 3.1c):



or a 2√2(1 × 1)R45° complex unit cell:



The [2O^{–1} + Cu⁺²] or the 4[O^{–1} + Cu⁺¹] domains form the depressed domains in the STM image. The O^{–1}-induced Cu^P builds up the ‘engaged cog-wheels’ domain boundary that is detected as the U- or the zigzag-shaped patches of protrusions in STM imaging (Fig. 3.1a). Larger domains consisting of c(2 × 2)–2O^{–1} unit cells can be constructed by adding more oxygen adsorbates to the

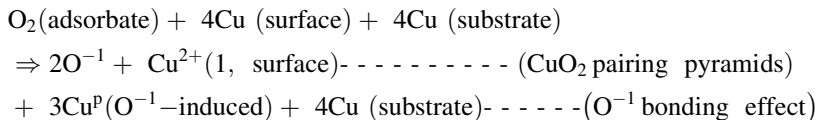
surface. The additional oxygen catches one electron from a dipole and polarizes its rest neighbors in the top layer.

The surface matrix in Fig. 3.1c shows the alternative sign of charge distribution both within the domains and in the domain boundaries. Therefore, the surface is fully covered with dipoles in a way that stabilizes not only the domains but also the domain boundaries. Hence, the surface undergoes the tensile stress due to electrostatic attraction among the charged bodies. The atomic valences of the copper atoms within the domain (O^{-1} , Cu^{+1} or Cu^{+2}) differ from that at the domain boundary (Cu^p). The surface reaction in the O^{-1} -derived phase takes place without involvement of the second atomic layer at the precursor O^{-1} stage. There are no atoms missing in the short-ordered $c(2 \times 2)-2O^{-1}$ surface but only electron repopulation and polarization. VLEED optimization revealed an off-centered O^{-1} pyramid with a position of the adsorbate ($DO_z \sim 0.40 \text{ \AA}$. $DO_x \sim 0.18 \text{ \AA}$ is about 5 % of the fourfold hollow dimension) with respect to the fourfold hollow [1].

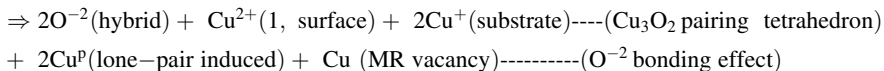
3.2.1.3 $Cu(001)-(\sqrt{2} \times 2\sqrt{2})R45^\circ-2O^{-2}$: Cu_3O_2 Pairing Tetrahedron

Upon increasing oxygen exposure, the short-ordered nanometric $Cu(001)-c(2 \times 2)-2O^{-1}$ domain develops into the long-ordered $(\sqrt{2} \times 2\sqrt{2})R45^\circ-2O^{-2}$ phase in which every fourth row of Cu atoms is missing. As an intermediate and quasi-stable state, the O^{-1} tends to catch another electron from its neighbors underneath. Once its two bonding orbits are fully occupied, the *sp*-orbital hybridization follows [22]. Consequently, a quasi-tetrahedron forms with two additional orbits that are occupied by lone electron pairs of the oxygen. The $Cu(001)$ surface geometry facilitates the intriguing Cu_3O_2 pairing-tetrahedron to form in such a way that the substrate is involved, as shown in Fig. 3.1d.

The $O-Cu(001)$ bi-phase ordering is formulated as the effect of the O^{-1} and subsequently the hybridized O^{-2} formation. The complete process of reaction is described as follows:



then, upon increasing oxygen exposure,



In the first phase, the Cu^{2+} pairs the off-centered pyramids on the surface to form a CuO_2 (see lower side in Fig. 3.1c). In the second phase, the Cu^{2+} couples the Cu_2O tetrahedra, giving rise to the Cu_3O_2 structure. The top layer of the $Cu(001)-(\sqrt{2} \times 2\sqrt{2})R45^\circ-2O^{-2}$ surface contains rows of Cu^{2+} , a pairing [O^{-2} : Cu^p : O^{-2}]-row and the MR vacancy; the second layer is composed of

alternate rows of Cu and Cu⁺. In the second phase, the surface stress seems to be compressive due to the repulsion among the surface dipoles. The adsorbate–adsorbate interaction is always repulsive throughout the course of phase transformation because of their identical valences. As the origin of the observations, the bond-forming processes are hardly detectable but one can observe the consequence of bonding—dipole protrusions and missing-row vacancies formation.

3.2.2 O–Cu(110)

3.2.2.1 Geometrical Uncertainty

LEED study of the O–Cu(110) surface crystallography was firstly conducted by Ertl in 1967 [25]. A MR type reconstruction was derived using LEIS [26, 27] and SEXAFS [28–30]. In comparison, HEIS [31] and STM [32, 33] investigations support a buckled-row (BR) model in which the every other row of Cu atoms is not missing but is shifted outwardly. Moreover, XRD [34], LEED [35], and ICISS [36, 37] measurements preferred an added-row (AR)-type reconstruction. The AR, the BR, and the MR type are actually the same in geometry, but the mass-transportation mechanisms are different [38]. The MR model requires removal of alternate [010] Cu rows, while the AR model requires addition of the same [010] Cu rows by Cu surface diffusion. The BR model requires no mass transportation. Step edges presumably serve as sinks or sources for Cu atoms missing or adding. STM imaging [39–41] could finally settle the discrepancy in favor of the MR reconstruction, which can be viewed as an ‘added-row’ phase.

Table 3.3 features the crystallography structural parameters pertaining to the O–Cu(110) surface. Results vary considerably depending on the data sources. XRD [34] gives a considerably large first-layer expansion $D_{12} = 1.65 \text{ \AA}$ (+30 %) and a second-layer contraction $D_{23} = 1.15 \text{ \AA}$ (–11 %), and the oxygen is located, $D_{\text{O}} = 0.34 \text{ \AA}$, beneath the MR layer. In contrast, a theoretical optimization [42] suggested a smaller first-layer expansion $D_{12} = 1.331 \text{ \AA}$ (+4 %) with oxygen located $\sim 0.5 \text{ \AA}$ above the top. For the clean Cu(110) surface, $D_{12} = 1.17 \text{ \AA}$ (–8.5 %) and $D_{23} = 1.307 \text{ \AA}$ (+2 %) [43, 44], as compared to the bulk-interlayer distance $D_{\text{bulk}} = 1.278 \text{ \AA}$. The lateral displacements (parallel to the surface) of the Cu atoms remain very small. The measured vertical position of the oxygen is quite uncertain and it varies considerably from positions above to below the expanded first layer of Cu atoms.

Pouthier et al. [45] examined the reported data and found that the positions of oxygen and the AR Cu, D_{O} and D_{12} , are strongly correlated. This correlation could generate numerical uncertainty of the relative position of the Cu and the O. Figure 3.2 shows that the correlation between the D_{O} and the D_{12} can be accounted for by a simple linear expression [46]:

$$D_{\text{O}} = -1.982 \times D_{12} + 2.973 \pm 0.136 \text{ \AA}.$$

Table 3.3 The geometrical details of the Cu(110)-(2 × 1)-O surface (unit in Å) derived from diffraction^a

| | D ₁₂ | D ₂₃ | Δ | D _O | D _{Cu(1)-O} | D _{Cu(2)-O} |
|--------------------------------------|-----------------|-----------------|---------------|----------------|----------------------|----------------------|
| ICISS[44] | 1.60 ± 0.13 | 1.15 ± 0.06 | | | | |
| ICISS [26] | 1.51 ± 0.04 | | | -0.10 ± 0.10 | 1.81 ± 0.01 | 1.90 ± 0.10 |
| ICISS [36, 37] | 1.51 ± 0.04 | 1.28 ± 0.20 | 0.12 ± 0.07 | -0.08 ± 0.15 | 1.81 ± 0.01 | 2.00 ± 0.14 |
| LEED [35] | 1.49 ± 0.03 | 1.21 ± 0.03 | 0.03 ± 0.03 | 0.04 ± 0.03 | 1.81 ± 0.01 | 2.01 ± 0.05 |
| SEXAFS [30] | | | | ~0.35 | 1.82 ± 0.02 | 1.99 ± 0.02 |
| SEXAFS [28] | ~1.31 | | | ~0.2 | 1.84 ± 0.02 | 2.00 ± 0.05 |
| XRD [34] | 1.65 ± 0.05 | 1.28 ± 0.01 | 0.031 ± 0.005 | -0.34 ± 0.17 | 1.84 ± 0.06 | 1.85 ± 0.16 |
| Theory [42] | ~1.331 | | | ~0.48 | | |
| Theory [45] | 1.60 ± 0.05 | | | -0.21 ± 0.1 | | |
| Model [8, 16, 22, 71, 72] +data [34] | 1.655 | | 0.031 ± 0.005 | -0.60 | 1.675 | 1.92 |
| Theory [148] | 1.877 ± 0.2 | | | -0.1 ± 0.2 | | |

^a Listed are layer spacing D of the corresponding layers, the lateral shift Δ of the second-layer atoms toward the missing first-layer rows, the vertical O position D_O relates to the first layer, and the bond length to the nearest and the next-nearest Cu neighbors of the O adsorbate [54]

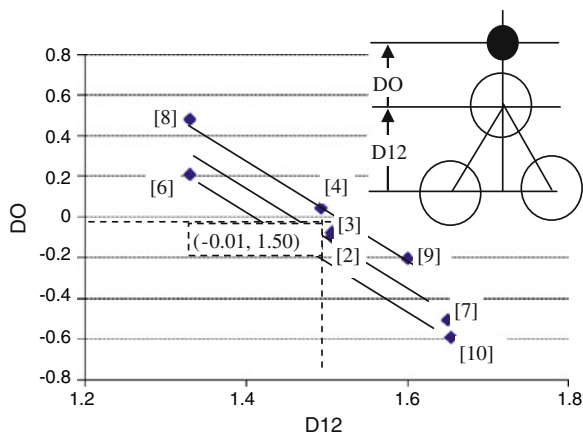


Fig. 3.2 Correlation between the interlayer spacing D_{12} and the oxygen position D_O with respect to the topmost Cu plane (see inset) [46]. The data and references are given in Table 3.3. The symmetry points for O and Cu are -0.01 ± 0.59 and 1.50 ± 0.16 Å. The operation of rotating the O–Cu–O chain around its axis by 180° and shifting the axis from 1.166 (O above) to 1.540 Å (O below), transforms point [8] into point [10]. This inverse symmetry of O and Cu position indicates the uncertainty of atomic positions derived from diffraction (reprinted with permission from [76])

All the solutions covered by the correlation region (Fig. 3.2) could be correct from a numerical point of view as the diffraction peak intensity depends on the arrangement of the scatters with various cross sections. The cross section of diffraction should vary with the effective number of electrons of the scattering atom. The arrangement of scatters determines the phase shift of the diffracted beams. The cross section of the scatter determines the amplitude of the diffracted waves. Therefore, the diffraction meter can identify nothing about the nature of the scattering centers but only show the resultant effect of scattering from the geometrical arrangement of the scattering centers. Using XRD and DFT calculations, Vlieg et al. [47] determined the Cu(410)–O surface with two structural solutions, which give equally acceptable fits to the XRD data.

Figure 3.2 shows that the vertical position of the adsorbate ranges from $D_O = -0.01 \pm 0.59$ Å relative to the buckled Cu layer [76]. The spacing between the top and the second Cu layer D_{12} is 1.50 ± 0.16 Å. If the top Cu layer buckles up, the adsorbate will buckle-in, and vice versa. For each pair of values of (D_{12}, D_O) that fit the diffraction data, there must be a counterpart that also fit. For example, the value at point [8] couples with the value at point [10]. Both are the numerical solutions to the same system. An inverse operation by rotating the O–Cu–O chain 180° around its axis and followed by offsetting the O–Cu–O chain in the vertical direction switches between the two cases [8–10]. The exchange in the vertical position of O and Cu ($0.59/0.16 = 3.68$) seems to approach the ratio of atomic numbers $Z_{Cu}/Z_O = 58/16 = 3.63$. This relation infers indeed, to a certain extent, that the cross section depends on the charge of the specific scattering center.

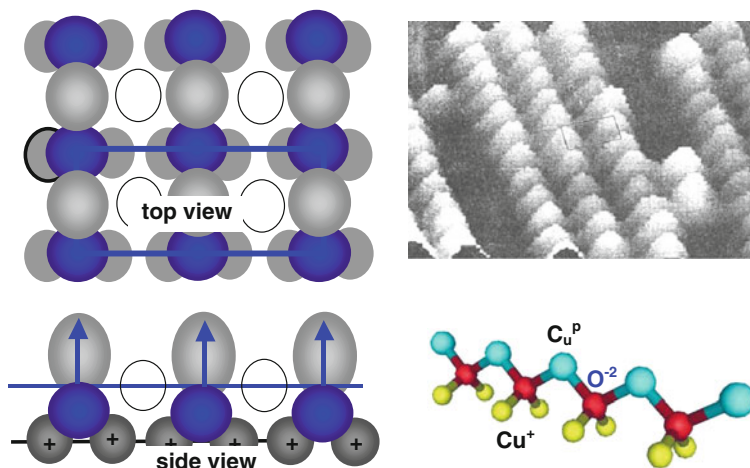


Fig. 3.3 STM image (reprinted with permission from [32]) and the corresponding models [21] for the $\text{Cu}(110)-(2 \times 1)\text{-O}^{-2}$ surface [39]. The STM gray scale is 0.85 \AA , much higher than that of metallic Cu on a clean (110) surface (0.15 \AA). The ‘ O^{-2} : Cu^{P} : O^{-2} ’ chain is zigzagged by the nonbonding lone pairs with Cu^+ seeded in the second layer. The basic structure unit is the H_2O like tetrahedron with $\text{Cu}^{\text{P}}\text{-Cu}^{\text{P}}$ in the [010] direction of 3.60 \AA separation on top and $\text{Cu}^+\text{-Cu}^+$ in the [110] direction of 2.55 \AA in the second layer

Therefore, all the solutions along the line from [8] to [10] can find a counterpart that could fit the diffraction data.

The vertical change of positions for both the partners should satisfy the numerical relation between D_0 and D_{12} . However, the simple operation on the Cu:O:Cu chain provides entirely different physical meanings. Therefore, physical constraints should be necessary for the numerical solutions. For instance, the on-surface oxygen should be ruled out for the fully developed surface oxidation. The on-surface oxygen neither produces protrusions in the STM images nor expands the first interlayer spacing.

3.2.2.2 $\text{Cu}(110)-(2 \times 1)\text{-O}^{-2}$: Missing-row-type Reconstruction

Figure 3.3 shows a typical STM image and the corresponding model for the $(2 \times 1)\text{-O}$ phase [32, 33, 36, 37, 40, 48]. In the STM image, the round bright spots of $0.8 \pm 0.2 \text{ \AA}$ in height are separated by 5.1 \AA in the [110] direction and 3.6 \AA in the [010] direction. Single O-Cu-O strings are formed along the [010] direction, or perpendicular to the close-packed Cu row. In contrast, the protrusion for the clean $\text{Cu}(110)$ surface is about 0.15 \AA [32].

3.2.2.3 Cu(110)–c(6 × 2)–8O⁻²: Pairing-row-type Reconstruction

Exposing the Cu(110)–(2 × 1)–O⁻² surface to higher amounts of oxygen at *T* > 300 K initiates a second structural phase of c(6 × 2)–8O⁻². STM images show a corrugation pattern consisting of a quasi-hexagonal arrangement of ‘ellipsoid’ protrusions [48–51]. Figure 3.4 shows the c(6 × 2) domains adjacent to the (2 × 1) phase. High-resolution image of the c(6 × 2) structure in the right-hand panel displays additional weaker features between the large ‘bumps.’ The height of the bright spots was reported to be 0.6 ± 0.1 Å, slightly lower than the round spot in the (2 × 1)–O⁻² surface, 0.85 Å, but much higher than that of the clean Cu(110) surface.

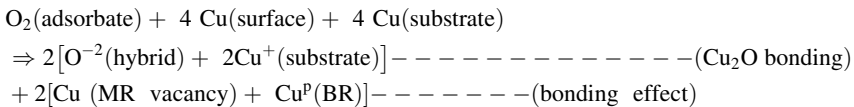
Based on their observations using the combination of STM, XRD, and EMT computations, Feidenhans’l et al. [49, 51] derived a model. This model suggests that in the second phase of the O–Cu(110) surface, there are two kinds of oxygen atoms with different vertical positions; every third row of Cu atoms is missed and additional Cu atoms are buckled up, crossing over the missing rows (see Fig. 3.4). Tensor-LEED [52] and LEISS (low-energy ion-scattering spectroscopy) [53] studies confirmed this model. As shown in Fig. 3.4, the sublayers (labeled 1 and 3) are composed of Cu and the layers 2 and 4 are oxygen. Table 3.4 features the vertical positions of the atoms.

3.2.2.4 Formulation of O–Cu(110) Reaction

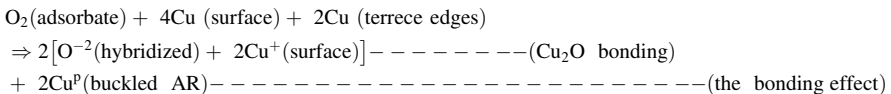
(a) Cu(110)–(2 × 1)–O⁻²: the O⁻²:Cu^p:O⁻² chain

Comparatively, the Cu(110)–(2 × 1)–O⁻² surface reaction, as shown in Fig. 3.3, can also be expressed as an effect of the hybridized O⁻² formation. The characteristics of this phase is the combination of the alternate MR of Cu and the BR of the ‘O⁻²: Cu^p: O⁻²’ chain. The lone electron pair of oxygen zigzags the buckled string.

The following formulates the first phase of the MR + BR reconstruction for a c(2 × 2) unit cell:



or even the added-row (AR) model:



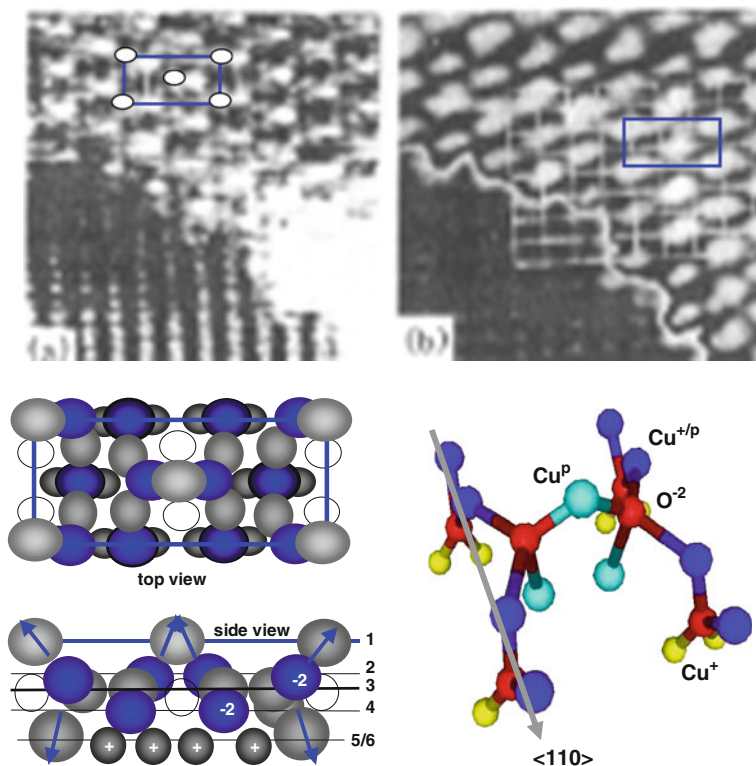


Fig. 3.4 STM image [49] and the corresponding models [21] for the Cu(110)-c(6 × 2)-8O⁻² phase. The STM gray scale is 0.66 Å. The ‘O⁻²: Cu^p: O⁻²’ chains are paired by the rotation of every other tetrahedron that produce the dipole bridge over the missing row. The pairing-chains interlock the Cu^{+p} at the surface with regularly protruding dipoles

Table 3.4 Summary of the vertical positions of ion cores for the Cu(110)-c(6 × 2)-8O surface

| | D ₁₃ | D ₂₃ | D ₃₄ |
|---|-----------------|-----------------|-----------------|
| STM, XRD, EMT [49, 51] Tensor-LEED [52] | 1.2 | 0.4 | 0.2 |
| LEIS [53] | 0.45 ± 0.12 | 0.40 ± 0.12 | 0.12 ± 0.12 |

From the mass-transport point of view, the Cu(110)-(2 × 1)-O⁻² phase is made simply by every other O⁻²: Cu^p: O⁻² making, which isolates and squeezes the neighboring row of Cu atom missing.

This mechanism can also be applied to the MR reconstruction of the fcc(110)-c(n × 1)-O⁻² surface of Ni, Ag [54], Pt [55], and Cu(112) surfaces, as well as the bcc(112) surface of Mo and Fe with chemisorbed oxygen. The O-Mo(112) surface shares the same STM patterns as that of the O-Cu(110) [56, 57]. The O-Cu(112) surfaces share the same STM and LEED patterns with one-dimensional Cu-O-Cu

strings addition [58, 59]. LEED study [60] revealed an MR type reconstruction happens at the Fe(112)–p(2 × 1)–O phase, where the O–M–O chain runs perpendicular to the close-packed rows of the substrate.

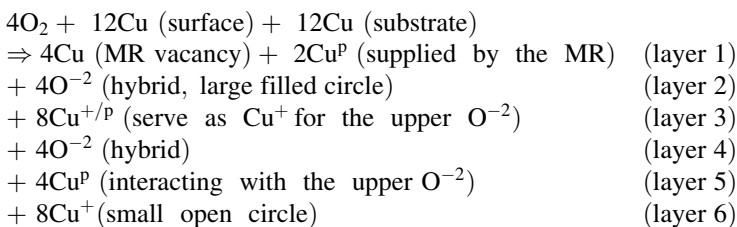
From the bond-forming point of view, the bi-phase and related phenomena on the O–Cu(001), (110) surfaces are due to valence alteration from the O⁻¹ to the hybridized O⁻². The O⁻¹-derived phase has not yet been resolved because of the geometric difference. Oxygen catches electrons one by one from its two nearest neighbors. As the effect of hybridized O⁻² on both the Cu(001) and the Cu(110) surfaces, the lone-pair-induced dipoles are responsible for the protrusions in the STM images.

Clearly, the O⁻²: Cu^p: O⁻² chain is ‘zigzagged’ by the lone pairs (Fig. 3.3) rather than it is co-lined by states of antibonding, covalent bonding, or even ionic bonding. The removal of the MR atom from both surfaces results from the isolation and repulsion of the specific Cu atom as its neighbors have already bonded to the oxygen. The Cu(110)–(2 × 1)–O⁻² phase, whether AR or MR, differs in origin from the Cu(001)–(√2 × 2√2)R45°–2O⁻² surface by nothing more than that the [O⁻²: Cu^p: O⁻²:] chain rotates around its axis by 45° in the surface plane to fit the coordination surroundings along the [110] direction. The difference in the coordination geometry between the (001) and the (110) surfaces determines the complexity of oxidation of these two surfaces.

Instead of an intermediate O⁻¹ state like that on the Cu(001) surface, O⁻² forms directly at the Cu(110) surface. The oxygen adsorbate may catch two electrons from its nearest neighbors (shortest spacing, 2.552 Å) in sequence. This process may be too quick to catch. Meanwhile, the adsorbate also requires extra atoms for the Cu^p to complete the tetrahedron. Due to the expansion of dipole dimension and the repulsion between the nonbonding lone pairs, dipoles tend to expose to the open end of the surface.

(b) Cu(110)–c(6 × 2)–8O⁻²: Tetrahedron re-orientation

The Cu(110)–c(6 × 2)–8O⁻² phase can be formulated with specification of the atomic valences in six sublayers (unit cell in Fig. 3.3d):



Instead of varying the valences of the oxygen adsorbate, further exposure at raised temperature increases the oxygen coverage from 1/2 to 2/3 ML. The process of oxygen bond switching, which reorganizes the tetrahedron and the Cu atoms at the surface, changes the structural pattern. Self-organization of the Cu₂O tetrahedron yields two kinds of oxygen positions (layer 2 and 4), as can be seen from

the side view of Fig. 3.4. The lower O^{-2} , the Cu^+ at layer 6, and the Cu^P at layer 3 build up the first Cu_2O tetrahedron, which orientates the same as the Cu_2O in the $(110)(2 \times 1)-O^{-2}$ phase.

Acting as a donor for further bonding, the Cu^P at layer 3 provides an electron to the upper O^{-2} and the Cu^P becomes Cu^{+P} . The nonbonding lone pairs of the upper O^{-2} then induce the Cu^P at layer 1 and 5 to form another Cu_2O tetrahedron with altered orientation, which interlocks the O^{-2} : Cu^P : O^{-2} chains near to the missing row. Different from the $(2 \times 1)-O^{-2}$ configuration, the substrate (sublayers 5 and 6) is composed of Cu^+ and Cu^P alternatively along the original O^{-2} : Cu^P : O^{-2} chain. They are arranged in a much more complicated array than even that of the second layer of the $Cu(001)-(\sqrt{2} \times 2\sqrt{2})R45^\circ-2O^{-2}$ phase.

Two of the four missing vacancies are filled up by Cu atoms and then they become Cu^P that bridges over the missing row, which are responsible for the recorded STM ‘ellipsoid’ protrusions. The atomic arrangement defined by the tetrahedron agrees with results shown in Table 3.4. One oxygen adsorbate locates below the Cu layer labeled 3 and the other oxygen above. The possible mechanism causing such a more complicated phase is that thermal energy relaxes the Cu_2O bonding and further exposure enhances the self-organization. The reversibility of the bond forming and a suitable ambient produces a phase with more close-packed Cu_2O and H-like bond involvement, which is even stable. Figure 3.4 also shows the molecule structure of the pairing $O-Cu-O$ chain bridges over the missing row.

The lone-pair-induced Cu^P (layer 3) interacts further with the upper O^{-2} . Such a set of interactions (O^{-2} : Cu^{+P} : O^{-2}) forms an identical system to the hydrogen bond by definition. Such a configuration forms the H-like bond to discriminate the Cu^{+P} from the H^{+P} in the hydrogen bond. According to the bond theory of Atkins [61], one may further infer that the H-like bond forms if the lone-pair-induced dipole combines further with other electronegative specimen through bonding orbitals. Otherwise, an antibonding dipole retains. The major contribution to an antibonding state is made by the dipoles of the less electronegative element [61]. Therefore, antibonding dipole-dipole interaction hardly ever forms between specimens with large differences in electronegativity.

A typical example of the antibonding configuration is the quadruples in Fig. 3.1d, or the ‘dumbbell’ protrusions in the $Cu(001)-(\sqrt{2} \times 2\sqrt{2})R45^\circ-2O^{-2}$ STM image. This inference may be necessary in understanding the heterogeneous catalysis. For example, the formation of H-like bonds may provide a more feasible mechanism for forming isocyanate (N, C, O) on the $Ru(0001)$ surface. As found by Kostov et al. [12], the isocyanate could only be formed on the $Ru(0001)$ surface in the presence of pre-adsorbed oxygen. It is expected that the antibonding electrons of the dipoles readily combine with new adsorbates (nitrogen or carbon), lowering the system energy.

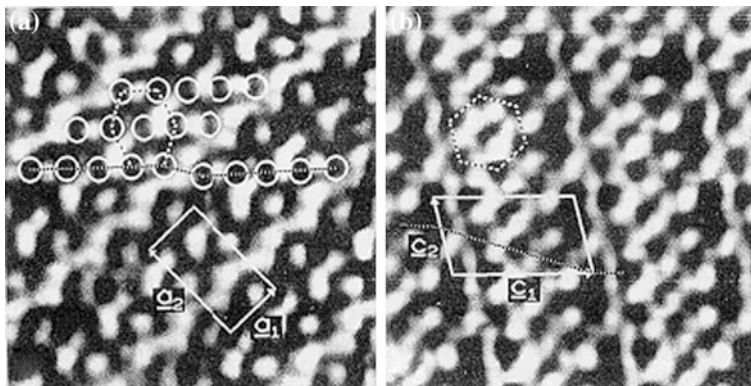


Fig. 3.5 STM images of **a** ($I_t = 2.9$ nA, $V_s = 55$ mV) a $60 \times 60 \text{ \AA}^2$ region of O–Cu(111) surface showing the ‘29’ structure. Gray scale is 0.27 \AA and of **b** ($I_t = 4.9$ nA, $V_s = 7$ mV) a $60 \times 60 \text{ \AA}^2$ region showing the ‘44’ structure. The gray scale from *black* to *white* is 0.55 \AA (reprinted with permission from [67])

3.2.3 O–Cu(111)

The adsorption of oxygen on the Cu(111) surface roughens the surface in short-range order [25, 62]. Oxygen prefers the threefold hollow site, either in, or below, the outermost plane of Cu atoms, resulting in a small change in work function [63]. The O–Cu bond of $1.83 \pm 0.02 \text{ \AA}$ approaches the corresponding bulk value for Cu_2O [64]. Oxygen addition induces a restructuring that involves a 0.3 \AA displacement of Cu atoms [65]. The Cu–Cu distance is considerably relaxed ($3.15 \pm 0.1 \text{ \AA}$) with respect to the Cu–Cu separation in the bulk (2.555 \AA). An extra band around 3.0 eV is produced above $-E_F$ at Γ point, the center of the first Brillouin zone [66]. The rearrangement of Cu atoms indicates that the impinging oxygen adsorbate ‘pushes out’ the Cu atoms that roughen the surface of the disordered oxide precursor [54] by dipole and atomic vacancy formation.

With a combination of STM, HEISS, and LEED, Jensen et al. [67] found two ordered, O-induced commensurate reconstructions with extremely large unit cells, 29 and 44 times the (1×1) surface lattice, after an exposure of 300-L oxygen at 673 K followed by post-annealing at 723 and 773 K, respectively. Matsumoto et al. [68] confirmed these structural phases in an LEED and STM study. As shown in Fig. 3.5, there is a series of ‘double-holes’ and distorted ‘honeycomb’ frames composed of the ‘dumbbell’-shaped bright spots as observed in the O–Cu(001) surface.

Reconstruction phases on the Cu(111)–O surface are most complicated and the corresponding reaction formulae need to be defined. The Cu–Cu lattice distortion ($3.15 \pm 0.10 \text{ \AA}$ being the scale of dipole–dipole separation) is indicative of oxide tetrahedron formation. The STM protrusions (Fig. 3.5) and the oxygen-derived DOS ($\sim 3.0 \text{ eV}$) above the E_F imply the presence of antibonding dipoles in the Cu(111)–O surface. The tetrahedron is the basic and stable building block in oxidation.

3.2.4 VLEED from O–Cu(001)

3.2.4.1 Kinetic VLEED from O–Cu(001)

VLEED (with $E < 16$ eV, or lower than the plasma excitation energy) spectral collects simultaneously comprehensive yet nondestructive information from the outermost two atomic layers about the bond geometry, surface potential barrier (SPB), valence electrons (DOS features), Brillouin zones, and work function, reaction dynamics [69, 70]. VLEED is very insensitive to dislocations of atoms in the third layer and below [69, 70]. In the VLEED, electron beams interact with the valence electrons of atoms in the outermost two layers and resonant within the barrier of surface potential.

The LEED package of Thurgate enables the factors to be classified being responsible for the shape ($\text{Re}V(z)$), the absolute intensity ($\text{Im}V(z, E)$) and the partial features (bond geometry) of the VLEED I – E curves, which is beyond the conventional wisdom by treating all the bonding and SPB parameters independently. Besides the adequacy of the calculation code, the reliability of VLEED depends largely on the modeling approaches and decoding skills that must represent reasonably well not only the correlation among the crystal geometry and the SPB but also the real process occurred. Justification for the capacity and reliability of VLEED leads to new knowledge summarized below:

- The VLEED spectra are highly more sensitive to the bond geometry than to the individual atomic dislocations. Individually varying atomic position is not practical in simulating the process of surface bond forming. Agreement of the trends between the measurements and calculations by adjusting the bond variables challenges further efforts toward quantifying the O–Cu(001) bonding kinetics.
- The shape of the I – E curve is sensitive to the elastic potential $\text{Re}V(z)$ of which the integration determines the phase change of the diffracted electron beams.
- The inelastic damping predominates only in the topmost layer in the VLEED. Therefore, LEED at very low energies is the unique technique that collects nondestructive information from monolayer skin of a substance and its energy covers the valence band.

Figure 3.6 illustrates the off-centered O^{-1} pyramid and the O^{-2} -induced Cu_3O_2 structure for VLEED optimization. The input parameters include the first inter-layer spacing, D_{12} , the shift of the Cu^{P} (DCu_x, DCu_z), and the displacement of the adsorbate (DO_x, DO_z). The tetrahedron bond geometry defines these parameters uniquely and collectively. The bond variables vary within a range that is subject to physical constraints. The bonds contract by C_1 (or Q) = 0.12, $C_2 = 0.04 \pm 0.04$, the Cu^{P} shifts within $DCu_x = 0.25 \pm 0.25$ Å, and the bond angle BA12 varies within 104.5° . The VLEED code optimizes the SPB constants such as the inner potential constant, V_0 , the amplitude of the inelastic potential, γ , and the slope of the energy dependence, δ , of the imaginary part of the SPB.

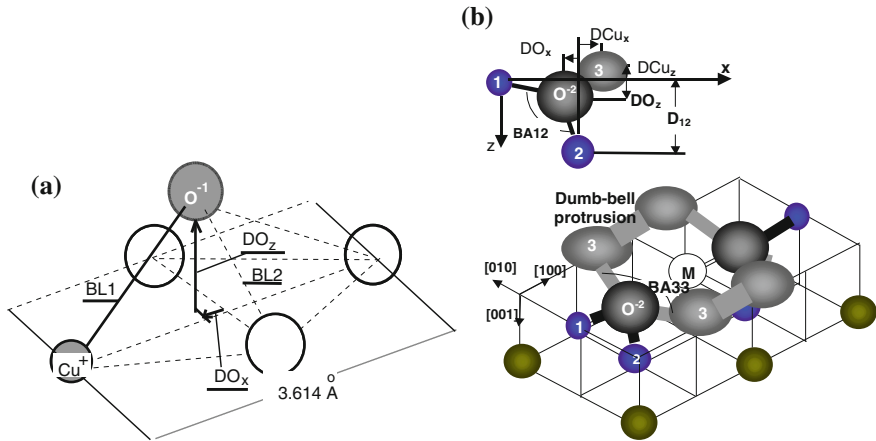
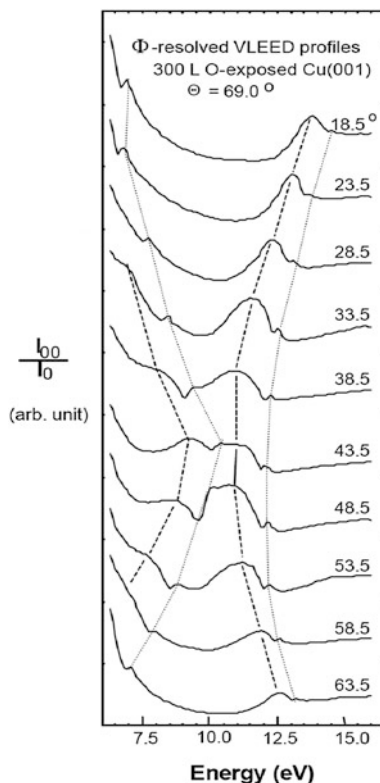


Fig. 3.6 Perspectives of (a) the off-centered O^{-1} pyramid and (b) the Cu_3O_2 pairing-tetrahedron in the $Cu(001)-(\sqrt{2} \times 2\sqrt{2})R45^\circ-2O^{-2}$ unit cell [22]. O^{-1} forms one contracted bond with a surface Cu atom and polarizes the rest nearest neighbors without bothering atoms in the second layer. O^{-2} prefers the center of a quasi-tetrahedron. Atoms 1 and 2 are Cu^{+2} and Cu^+ . Atom 3 is Cu^p , and M is the vacancy of the missing Cu. Atoms in yellow are metallic. The pairing-dipole forms 'dumbbell'-like protrusion cross the missing-row vacancy (Reprinted with permission from [1])

With respect to the clean $Cu(001)$ surface, the SPB is parameterized by varying z_0 over -2.5 ± 1.25 [for pure $Cu(001)$] in a step of 0.25 (atomic unit). A contour plot of z_0 versus E is then drawn with a matching between the calculated intensity and the measured data, $I_c(z_{0i}, E)/I_m(E) = 1.0 \pm 0.05$. The $z_0(E)$ contour plot is the unique yield of the calculation of this method. The plot shows the shape of the $z_0(E)$ curve that gives the desired best fit of the measurement and shows all the possible solutions within the limits of parameter variation. This z_0 -scanning method is also a convenient way to compare different models and to refine the parameters of the SPB and the bond geometry.

Once the refinement of the $z_0(E)$ plot is completed, the program automatically fits the value of the $z_0(E_i)$ to give a desired level of agreement (for example 3 % error bar). In contrast to the z_0 -scanning method, the step of Δz_0 automatically varies from 0.25 to 0.0005 depending on the ratio of $\kappa = I_c(E_i)/I_m(E_i)$. If κ reaches the required precision, calculation will automatically turn to the next energy step E_{i+1} of measurement. This method yields simply the geometry-dependent $z_0(E)$ profile and reproduces the measured VLEED spectrum. Quantities such as the bond geometry, work function, barrier shapes, and energy band structure are the outcome of the VLEED analysis.

Fig. 3.7 Azimuth-angular-resolved VLEED profiles collected from a Cu(001) surface exposed to 300-L oxygen at 69.0° incidence. There is a ‘cross-point’ at about 45° azimuth. Two small sharp peaks (indicated by dotted lines) appear on each curve. The broaden fine-structure feature (dashed lines) splits when the azimuth moves away from the $\langle 11 \rangle$ direction



3.2.4.2 Angular-resolved VLEED: Brillouin Zones, Band Structure, and Bond Geometry

Decoding the angular-resolved VLEED profiles from the O–Cu(001) surface has yielded static information about the Brillouin zones, band structure, and bond geometry (Fig. 3.7 [71, 72]). Calculations also reveal the nonuniformity and anisotropy of the SPB, and the distribution of the DOS in the upper part of the valence band. Oxygen adsorption has reduced the inner potential constant (V_0) by 9.6 % (from 11.56 to 10.5 a.u.) and the work function by 1.2 eV from 5.0 to 3.8 eV. The oxygen-induced reduction in V_0 is due to the transportation of atoms and valence electrons at the surface. The lowered work function arises from surface dipole formation that increases the local charge density.

VLEED profiles. The VLEED I – E profiles were collected from a Cu(001) surface exposed to 300-L oxygen. For the symmetry consideration, angles from 18.5° to 63.5° with 5° increment are sufficient to represent the full azimuth of the surface. The following features the VLEED fine-structure in Fig. 3.7:

1. Two sharp, solitary troughs or violent peaks (indicated by dotted lines) appear on each curve. These two troughs move away from each other as the azimuth moves away from the $\langle 11 \rangle$ direction. The angular-resolved sharp features divide the VLEED energies (6.0–16.0 eV) into three regions with variation in energy of the boundaries. Calibration of these critical positions gave the reduction in work function of ~ 1.1 eV [15].
2. The fine-structure feature (indicated by the dashed lines) splits into its separate components as the azimuth moves away from the symmetric point 45.0° . The first component vanishes outside the region of 33.5° – 58.5° . The second one becomes narrower while moving away from the symmetric point. Further, the intensity of the second peak tends to be weaker when the azimuth is greater than 45.0° .
3. The peak positions and intensities of the curves show a reduction in symmetry relative to the symmetric center. The reduction in the intensities at higher azimuth angles may come from the development of the reaction, as the long-term aging leads to a general attenuation of the spectral intensity. The deviation of the symmetry means the original C_{4v} group symmetry has been destroyed upon reaction.

Brillion zones, effective mass, and energy bands. The primary unit cell in the Cu(001)- $(\sqrt{2} \times 2\sqrt{2})R45^\circ$ structure is the concern of the community of solid-state physics. The presence of defects and impurities, such as the MR vacancy and the oxygen adsorbate, has no effect on constructing either the real lattice or the reciprocal lattice. Displacements of lattice atoms, such as the DCu_x for the atoms closing to the MR, or at $\langle 11 \rangle$ direction, however, deform both the real and the reciprocal lattice.

The emergence of new diffraction beam is independent of the inner potential and the barrier shapes. It depends only on the incident and diffraction conditions, and the two-dimensional geometry of the surface lattice. Emergence happens when the lateral components of the diffracted wave, with vector $k'_{//}$, and the incident wave $k_{//}$ satisfy the Bragg diffraction condition,

$$k'_{//} - k_{//} = g,$$

where g is the vector of a reciprocal lattice. It is the right Bragg condition that yields the bandgap reflection at the boundary of a Brillouin zone. Therefore, the sharp features closing to the emergence of new beam on the VLEED spectra arise from the bandgap reflections at the boundaries of Brillouin zones.

Accordingly, two-dimensional Brillouin zones can be constructed from the sharp-peak positions in the angular-resolved VLEED data, as summarized in Table 3.5. The location of a peak E_p can be decomposed in k -space as (in atomic units: $m = e = \hbar = 1$, 1 a.u. = 0.529 Å and 27.21 eV):

Table 3.5 Positions of the sharp peaks, E_{p1} and E_{p2} , in the angular-resolved VLEED profiles of the O–Cu(001) surface. The incident angle keeps constant at 69.0°

| Azimuth | E_{p1} (eV) | E_{p2} (eV) |
|--------------|---------------|---------------|
| 18.5° | 5.00 | 14.50 |
| 23.5° | 5.20 | 14.00 |
| 28.5° | 5.60 | 13.30 |
| 33.5° | 8.30 | 12.50 |
| 38.5° | 9.50 | 12.20 |
| 43.5° | 10.40 | 12.00 |
| 48.5° | 10.00 | 12.20 |
| 53.5° | 8.80 | 12.30 |
| 58.5° | 5.80 | 12.60 |
| 63.5° | 5.00 | 13.20 |

$$E_p = \frac{\left[k_{\langle 01 \rangle}^2 + k_{\langle 10 \rangle}^2 + k_z^2 \right]}{2m^*} \quad (3.1)$$

$$\text{with } k_{\langle 10 \rangle} = \sqrt{2m^*E_p} \sin \theta \cos \phi, \quad \text{and } k_{\langle 01 \rangle} = \sqrt{2m^*E_p} \sin \theta \sin \phi,$$

where m^* , the effective mass of electron populated near the boundary of Brillouin zone, is introduced such that it compensates for the reduction in the diffracted k' due to its energy loss. θ represents the incident angle and ϕ the azimuth angle of the incident beam. The resultant wave vectors, $k_{\langle 10 \rangle}$ and $k_{\langle 01 \rangle}$, extend from the center to the boundary of the first Brillouin zone. The first two experimental Brillouin zones then can be drawn by optimizing m^* to match the theoretical calibrations, ($k_{\langle 10 \rangle} = k_{\langle 01 \rangle} = n\pi/a$, $n = 1, 2$) as represented by solid lines in Fig. 3.8. The effective masses of electrons surrounding the Brillouin zone boundaries are the adjustable that makes the match between theoretical and measurement BZ. The optimal values are: $m^*_1 = 1.10$ and $m^*_2 = 1.14$. The increase in m^* with energy coincides with the trend that the energy loss of the diffracted beam ($k' = k/\sqrt{m^*}$) increases with the incident beam kinetic energy. On the other hand, the first Brillouin zone contracts at Y but expands near X. The contraction at Y correlates to the atomic shift of Cu^p along the $\langle 11 \rangle$ direction in the real lattice, DCu_x , while the expansion near X needs to be identified.

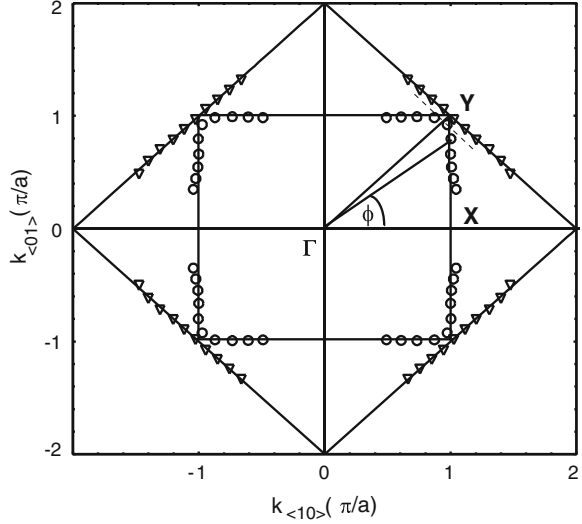
In-plane lattice distortion. The mutual reciprocal relationship between the k -space with basic vector k_i and the r -space with basic vector a_i :

$$a_i \cdot k_i = 2\pi\delta_{ij}; \quad \delta_{ij} = \begin{cases} 1, & i = j \\ 0, & i \neq j \end{cases} \quad (3.2)$$

which implies that the deviation of the experimental Brillouin zone from the theoretical form originates from the deformation of the primary unit cell. Therefore, one can trace inversely the DCu_x from the contraction of the Brillouin zone at Y.

The distance in k -space, $\overline{F\bar{Y}} (= \frac{1}{2}|k_i + k_j| = \sqrt{2}\pi/a)$, correlates to a quantity $a_{\langle 11 \rangle}$ through the mutual reciprocal relation:

Fig. 3.8 The first two Brillouin zones (indicated by open circles and triangles) derived from the critical positions on the angular-resolved VLEED profiles, compared with the theoretical ones in solid lines, which results in the effective electron masses as an adjustable. Deformation of the first Brillouin zone near Y point corresponds to the DCu_x in real lattice



$$a_{\langle 11 \rangle} \cdot (k_i + k_j) = a_{\langle 11 \rangle} \cdot 2\overline{\Gamma Y} = 2\pi, \quad (3.3)$$

yields,

$$a_{\langle 11 \rangle} = \pi / \overline{\Gamma Y} = a / \sqrt{2},$$

which corresponds to the shortest row spacing on the (001) surface. Taking the logarithm and derivative from both sides of Eq. (3.3) results in,

$$\frac{da_{\langle 11 \rangle}}{a_{\langle 11 \rangle}} + \frac{d\overline{\Gamma Y}}{\overline{\Gamma Y}} = 0.$$

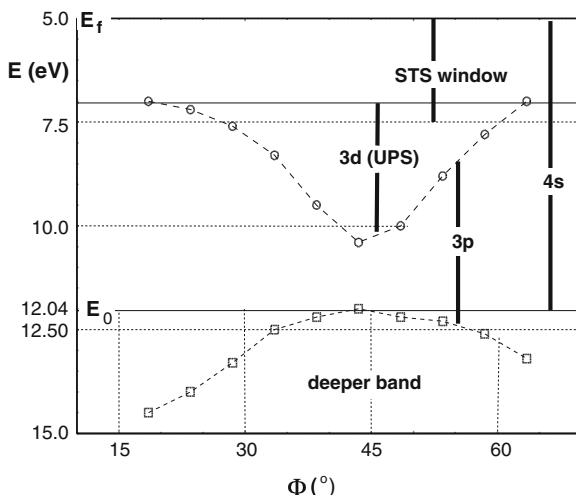
Thus, the atom shifts laterally by:

$$DCu_x = da_{\langle 11 \rangle} = -\frac{a_{\langle 11 \rangle}}{\overline{\Gamma Y}} d\overline{\Gamma Y} = -\frac{a^2}{2\pi} d\overline{\Gamma Y} \quad (3.4)$$

Substituting $m_1^* = 1.10$, $\theta = 69.0^\circ$ and $E_{p1} = 10.4 \text{ eV} = 0.3804 \text{ a.u.}$ (at 43.5° close to the $\langle 11 \rangle$ direction) into Eq. (3.4) yields $\overline{\Gamma Y}' = \sqrt{2m_1^* E_{p1}} \sin \theta = 0.8104 \text{ (1/a.u.)}$. On the other hand, by adopting $a = 2.555/0.529 = 4.8308 \text{ (a.u.)}$, one can have the theory value $\overline{\Gamma Y} = \sqrt{2}\pi/a = 0.9217 \text{ (1/a.u.)}$. Therefore,

$$\begin{aligned} DCu_x &= -\frac{a^2}{2\pi} (\overline{\Gamma Y}' - \overline{\Gamma Y}) \\ &= 0.4133 \text{ a.u.} \\ &\cong 0.22 \text{ \AA}, \end{aligned}$$

Fig. 3.9 Band structure extracted from the angular-resolved VLEED profiles [75]. The boundary lines divide the VLEED energies into various bands as indicated. The VLEED window covers that of both STS and UPS in the valence band and above



which coincides with the values (0.2–0.3 Å) optimized with LEED, XRD, and VLEED (~ 0.25 Å) [70].

Valence bands. As identified, the critical positions correspond to the boundaries of Brillouin zones, which are edges of the energy bands. Therefore, the zone boundaries divide the current VLEED energies into three regions, as shown in Fig. 3.9. These regions correspond to the valence bands of copper. The first sharp-peak positions varying from 7.0 to 10.4 eV can be ascribed as the bottom of Cu–3*d* band, which agrees with the known 3*d* band structure, 2.0–5.0 eV below- E_F (5.0 eV), as detected by ARUPS [73, 74]. Accordingly, the region between the two sharp peaks corresponds to the Cu–3*p* band. The 3*p* band overlaps partially the 3*d* band due to the azimuth effect. The more delocalized 4*s* band between E_F and vacuum level E_0 (12.04 eV) fully covers both 3*p* and 3*d* band. Energies higher than the second Brillouin zone correspond to deeper bands that are not of immediate concern in valence-electron transportation between oxygen and copper.

Angular-resolved VLEED analysis yields the change in energy states that contribute to the damping. Notable regions exhibiting DOS features:

- (a) Features below 7.5 eV are independent of azimuth angles. These humps coincide with the STS and PES signatures O–Cu(110) signatures around 7.1 eV, which have been specified as the contribution of nonbonding states of O^{-2} . The anti-resonance of this feature (intensity independence of azimuth and incident energy) on O–Cu(001) surface has been confirmed with PES by Warren et al. [76], indicating a strong one-dimensional localization of the [O:Cu:O] chain. Coincidence of the VLEED (reduction in work function) with the STS (polarization states) in the above- E_F (antibonding) and the below- E_F (nonbonding) features can be convincing evidence that the oxygen adsorbate hybridizes itself and polarizes electrons of its neighboring metal atoms.

- (b) Bandgap reflection along the boundary of the second Brillouin zone is apparent, while such reflection at the boundary of the first Brillouin zone is invisible near the symmetry point (45°). The invisible features are obviously due to the strong overlap of the Cu $4s3d3p$ bands near the $\langle 11 \rangle$ direction, as illustrated in Fig. 3.9.
- (c) The damping surrounding the second Brillouin zone can be featured as electron excitation at the edges of different bands. The excitation of electrons from the bottom of a band seems to be harder than that from the top edge of a band where the electrons is denser.

3.2.4.3 Inner Potential and Work Function

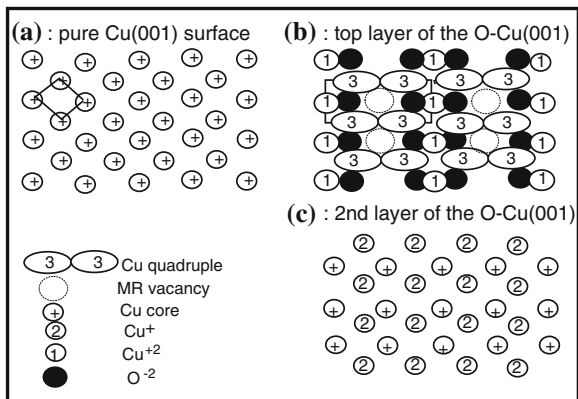
The inner potential relates to the charge quantity and the work function depends on the density of the polarized electrons at the surface. The 3B model explains consistently the reduction both in the inner potential constant and the work function. With expansion of sizes and elevation of energy states, metal dipoles are responsible for the reduction in the local work function. Electron transportation due to reaction dominates the change of the inner potential constant. Besides, at very low incident beam energies, the exchange interaction between the energetic incident beams and the surface is insignificant, and hence, the VLEED is such a technique that collects nondestructive information from the skin of two-atomic-layer thick.

(A) Observations

Beam-energy-reduced V_0 . The inner potential V_0 decreases exponentially with the increase in the incident energy (so-called E -reduced V_0), as the surface dipole formation due to electron ejection or plasma generation affects by the V_0 . However, the V_0 changes insignificantly at energies lower than 40 eV for the Cu surfaces. The V_0 decreases as energetic incident beams bombard the surface and drag out the surface ion cores to neutralize the surface negative charge. The sputtering of the surface by the incident beams reduces the quantity of net charge. If one electron was sputtered away from the surface the residual ion core will also reduce the net negative charge. Therefore, the quantity of surface charge dominates the V_0 .

Oxygen reduced V_0 . Chemisorbed oxygen changes the V_0 in a way that is much more complicated. The amount of the reduction varies with crystal structure. For a Cu(001)– $c(2 \times 2)$ –2O and a $(2\sqrt{2} \times \sqrt{2})R45^\circ$ –2O structure, the reduction was found 1.21 and 2.15 eV, respectively [17]. Calculations of VLEED I – E curves with the Cu_3O_2 bond configuration require a 1.06 eV (9.2 %) reduction in the V_0 from the bulk value of Cu(001), 11.56 eV[70]. Pfnür et al. [77] used a step function to describe the reduction in the V_0 of the O–Ru top layer. It is certain that oxygen chemisorption results in a pronounced reduction in the V_0 .

Fig. 3.10 Surface-charge distribution in both clean and O-chemisorbed Cu(001) surfaces. **a** Pure Cu(001) surface with Cu-ion cores regularly arranged in the Fermi sea, **b** and **c** are the top and the second layer of the Cu(001)-(2√2 × √2)R45°-2O⁻² surface. Panels (a) and (b) match closely to the STM images (Fig. 2.1)



Oxygen induced and localized dipole states lowers the $\phi_L(E)$. Another striking feature of oxygen chemisorption is the reduction in the work function, $\phi_L(E)$. Characterization of the $\Delta\phi$ has hence been developed as one standard means used to determine the surface electronic properties. The ϕ decreases when oxygen incorporates into the Cu(001) surface [78, 79]. Oxygen chemisorbs threefold hollow sites on the Cu(111) surface, either in or below the outmost plane of Cu atoms, resulting in a work-function change [63]. Formation of the surface dipole layer reduces $\Delta\phi$ [80] with an inverted dipole moment of oxygen atom when it goes beneath the surface [81, 82]. However, analytical correspondence between the work function and the dipole layer was hardly to be established.

(B) 3B mechanisms

Surface-charge density. The $c(2 \times 2)-2O^{-1}$ domains, or the off-centered CuO_2 pairing-pyramid, evolves into the Cu_3O_2 pairing-tetrahedron that gives rise to the Cu(001)-(2√2 × √2)R45°-2O⁻² phase. Figure 3.10 illustrates the variation in the surface charge caused by the reaction. Comparing with the clean Cu(001) surface with ion cores arranged regularly in the Fermi sea, as shown in panel (a), panels (b), and (c) correspond to the top and the second layer of the Cu(001)-(2√2 × √2)R45°-2O⁻² surface. Cu_3O_2 bonding results in two hybridized O⁻² ions, one Cu⁺², two Cu^p, and a MR vacancy in a complex unit cell at the top layer. In the second layer, each Cu atom in the every other row along the [010] direction contributes one electron to the oxygen atom. Two Cu⁺ ions are produced in a unit cell. Panels (a) and (b) illustrate satisfactorily the corresponding STM signatures. In particular, panel (b) can account for the depressions and the ‘dumbbell’ protrusions that bridge over the missing rows.

Oxygen- and beam-energy-reduced V_0 . The Cu_3O_2 structure accounts for the reduction in V_0 caused by the process of bond reformation. Initially, there are four Cu atoms in a Cu(001)-(2√2 × √2)R45°-2O⁻² unit cell at the top layer. The chemisorption of O₂ leads to one Cu atom missing. The oxygen atom catches one electron from each of the top and second substrate layer. The total number of

electrons at each layer contributing to the V_0 is reduced by the adsorption of oxygen (with 8 electrons for each O atom) and the removal of one Cu (with each Cu atom there are 29 electrons). The transportation of the two electrons from the second layer to the oxygen adsorbate also varies the V_0 of both the top and the second layers. Hence, the relativistic charge quantity in the top layer is:

$$\begin{aligned} & \left([29e \times 2(\text{Cu dipole}) + (29 - 2)e \times 1(\text{Cu}^{+2}) + 29e \times 0(\text{MR})] \right. \\ & \quad \left. + [(8 + 2)e \times 2(\text{O}^{-2})] \right) / (29e \times 4(\text{Cu})) \\ & = 105/116 = 90.5\% \\ & \cong 10.50/11.56 = 90.8\% \text{ (VLEED optimization)} \end{aligned}$$

In the second layer, each Cu atom in every other row along the [100] direction donates one electron to the oxygen adsorbate. In the case of a Cu atom that has lost one electron, the residual ion core will also reduce the V_0 due to its residual positive charge. Every loss of an electron equals taking two electrons away from the sum of the negative charge, so that the relativistic variation in the V_0 of the second layer is:

$$[29e \times 2(\text{Cu}) + (29 - 2)e \times 2(\text{Cu}^+)] / 29e \times 4(\text{Cu}) = 112/116 = 96.5\%$$

Thus, the net charges of the top and the second layer are reduced by 9.5 and 3.5 %, respectively. The net charge finally approaches to the bulk value in the third metallic layer or below, the V_0 of which is less affected by the reaction according to the current model. The V_0 gradually approaches to the bulk value of the clean Cu(001) when getting inside into the crystal, but the deeper layers are beyond the scope of VLEED. Agreement between the analysis and the numerical optimization of the V_0 for the top layer further evidences the reality and integrity of the Cu_3O_2 bond model for the $\text{Cu}(001) - (\sqrt{2} \times 2\sqrt{2})\text{R}45^\circ - 2\text{O}^{-2}$ surface reaction.

Although the analysis is simply based on a classical viewpoint for the particular $\text{Cu}(001) - (2\sqrt{2} \times \sqrt{2})\text{R}45^\circ - 2\text{O}^{-2}$ phase, result reveals the correlation between the bond forming and the reduction in V_0 and work function. It is clear that the V_0 relates to the charge quantity of the corresponding layer and that at very low energies the exchange interaction between the incident beams and the surface is weak enough to be neglected. The plasma excitation energy is often ~ 15 eV below the E_F , and the incident energy is not sufficient to generate plasma at the surface. This adds another advantage to the VLEED for nondestructive detection.

Oxygen-reduced $\phi_L(\mathbf{E})$. The $\phi_L(\mathbf{E})$ is related to the valence DOS density $n(\mathbf{E})$. As justified, the z -directional integration of the $\rho(x, y, z)$, from the second layer to infinitely far away of the surface, yields the local DOS $n(x, y)$ that contributes to the SPB as well. Since the VLEED integrates over large surface areas, all the quantities depending on coordinate (x, y) become E dependent. Therefore, at a certain energy, the VLEED integration results the $n(x, y)$ into $n(E)$ that relates to the occupied DOS and the local work function.

The work function depends uniquely on the electron density at surface. However, the concept ϕ_L holds for large surface areas over which the VLEED

integrates for the DOS, and the ϕ_L is also extended to being energy dependent. The work function depends uniquely on the $n(E)$, a z -dimensional integration of the $\rho(x, y, z)$ at energy E . The z_0 is the boundary of the $\rho(x, y, z)$ ($\rho(z_0) = 0$). Clearly, the work function is uniquely determined by the z_0 , and the $\Delta\phi$ originates from the formation of the antibonding dipoles. $\Delta z_0 \cong 1.0$ a.u. (from -2.3 to -3.3 a.u., closing to the gray scale of the STM image) corresponds to a $\Delta\phi \cong -1.2$ eV reduction. This quantity coincides with the PEEM results of the O–Pt system though the two systems seemed irrelevant. The antibonding sub-band is induced by either the O^{-1} or the nonbonding lone pairs of the O^{-2} . In real space, the dipoles buckle up with expansion of sizes and elevation of energy states. The buckling dipole changes nothing about the net charge of the surface layer but shifts the critical position z_0 outward of the surface. The SPB is more saturated due to the dipole formation. Therefore, the dipoles have no apparent influence on the V_0 but occupy the empty DOS above- E_F . Because VLEED integrates over large area of surface, it is impractical to try to discriminate the V_0 from site to site on the surface.

It is clear now that the oxygen-reduced V_0 and work function originates from the surface dipole formation. The V_0 relates to the quantity of net charges while the ϕ depends on the z -dimensional distribution of polarized electrons. It is clarified that the buckling dipoles reduce the ϕ by increasing the occupied DOS at surface while the dipoles affect little the V_0 . At very low energies the exchange interaction between the incident beams and the surface is too weak to affect either the quantity or the distribution of the surface charges. Therefore, VLEED is an ideal means to collect nondestructive information about the behavior of surface electrons.

3.2.4.4 Thermal sp^3 -Orbital De-hybridization

Annealing at a temperature of ‘dull red’ supplies energy for oxygen de-hybridization with the absence of the 7.1 eV DOS feature rather than providing driving force to enhance bond formation. Both the off-centered-pyramid structure with oxygen higher than 0.4 Å above the top layer and the centered-pyramid structure with four identical O–Cu bonds for the precursor $c(2 \times 2)\text{-O}^{-1}$ phase were ruled out by VLEED analysis [16].

(A) Aging and annealing VLEED

Figure 3.11a shows the effect of annealing and aging on the VLEED I – E curves of a 300 L oxygen-exposed Cu(001) surface. The time-resolved spectra to be decoded were collected at 72.0° incidence and 42.0° azimuth angle. The following features the fine-structure features with the change of experimental conditions:

- There are two broad peaks at 9.0, 11.0 eV and two sharp peaks at 10.5 and 12.0 eV in scan A that was taken immediately after the clean Cu(001) surface exposed to 300 L oxygen.
- Scan B was taken after 25-min aging and produced the same result, apart from a change in slope (goes up) below 9.5 eV.

- Scan C was taken after 5 min of mild heating, to a dull red color (estimated 670 K) and showed a change in structure. Besides the slope below 9.5 eV, the whole spectrum increases in intensity.
- Scan D was taken after a further three-hour aging. No change in structure from scan C is noted apart from a general attenuation in intensity of the spectrum and intensity decreases significantly below 9.5 eV. The changes between scan C and D are similar in effect to the result of oxygen exposure greater than 200 L.

The spectral shape and intensity below 9.5 eV (lone-pair feature dominance) are more sensitive to the aging and annealing, which indicates that reaction modifies energy states in the upper part of the valence band.

(B) Thermal de-hybridization of the *sp*-orbital

Figure 3.11 shows (b) the optimized $z_0(E)$ profiles and (c) the bulk damping $\text{Im}V(E)$ for scans A–D. Table 3.6 lists the structural parameters. Calculated spectra indicate that the aging, and annealing effect is not readily, as did the exposure effect, quantified by varying individual bond parameter except for the long-duration aging (from scan C to D). Spectra under long-duration aging can be simulated simply by changing the DCu_x alone. However, features below 9.5 eV in Fig. 3.11a can be modulated by the combination of BA_{12} and Q_2 . Features in scan C, after five-minute annealing, can be produced by reducing DCu_x . The adjustment of DCu_z produces no apparent variation of the spectrum that could match observed trends. The structure sensitivity examination revealed that the time-resolved VLEED data reflect the bonding kinetics appears not as explicit as that happened in the processes of increasing oxygen exposure [70].

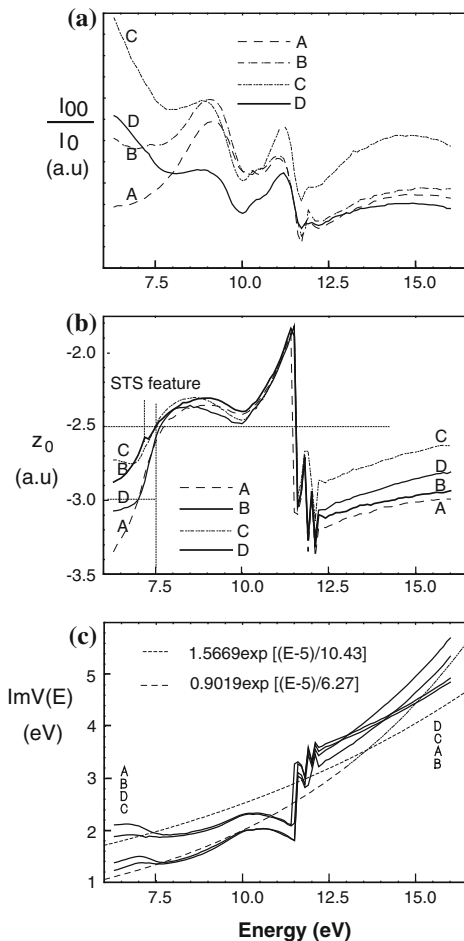
The $z_0(E)$ and $\text{Im}V(E)$ profiles in Fig. 3.11b, c vary their shapes apparently at energies outside 7.5–12.5 eV. Features below 7.5 eV correspond to the non-bonding states of O^{-2} . The $z_0(E)$ features above 12.5 eV are dominated by inelastic damping. Apart from profile B, the small feature at 7.1 eV, the *sp* hybridization of oxygen, is absent from the $z_0(E)$ profiles. This fact suggests that the *sp* hybridization be not fully developed yet immediately after the specimen being exposed (scan A) to oxygen and that the de-hybridization occurs due to annealing (scan C). The absence of the small feature from curve D is similar to that happened to the oxygen exposure greater than 600 L, due to the annihilation of the lone-pair features by the fully developed metal dipoles. The intensity of the hybridization states (<7.5 eV) in curve C is obviously weakened. On the other hand, annealing treatment (for scan C and D) changes the slope of damping as indicated in Fig. 3.11c.

At lower energies, the $\text{Im}V(E)$ becomes relatively lower while at higher energies, the $\text{Im}V(E)$ are higher. Features below 7.5 eV imply that the energy states in the upper valence bands are more readily affected by annealing than states in the bottom of the valence band. The change of upper states corresponds to the formation of nonbonding lone pairs, namely, the hybridization of O^{-2} . The lower states correspond to the O–Cu bonding. Weakening the $z_0(E)$ and $\text{Im}V(E)$ features at lower energy due to annealing indicates that oxygen de-hybridization takes place.

Fig. 3.11 Annealing and aging effect on the **a** VLEED spectra and the corresponding, **b** energy dependence of $z_0(E)$ profiles, and **c** the damping $\text{Im}V(E)$, which provide duplication of the VLEED spectra.

Annealing increases the slope of the inelastic damping.

Except for the $z_0(E)$ plot B, the hybridization feature at 7.1 eV is invisible for all the $z_0(E)$ curves. The lowering of the $z_0(E)$ below 7.5 eV (lone-pair features) for scan C indicates the de-hybridization of oxygen due to annealing



Therefore, annealing supplies energy for oxygen to be de-hybridized, which forms also the basis of thermal desorption and bond switching of oxide tetrahedron.

(C) Precursor confirmation

As far as the structure of the precursor phase (scan A in Fig. 3.11a) is concerned, eight different structures were compared by z_0 -scanning calculations [70]. In the z_0 -scanning method, determination of the structure models was carried out by comparing the shapes of the contour plots of $z_0(E)$. The interdependence between crystal structure and the corresponding $z_0(E)$ profile allows for judging a reasonable structure from the infinite number of mathematical solutions by properly setting up criteria to the shape of the $z_0(E)$ profile. Optimal results revealed that pyramid with $DO_z \leq 0.4 \text{ \AA}$ with a lateral off set along the $\langle 11 \rangle$ direction is the preference of the precursor stage (see Fig. 3.6).

Table 3.6 Cu₃O₂ structure varies with aging and annealing of the O–Cu(001) surface [Ref. 83]

| VLEED scans | | A* | B* | C | D |
|--------------------|------------------|---------|---------|---------|---------|
| Bond length (Å) | BL1 | 1.628 | 1.628 | 1.628 | 1.628 |
| | BL2 | 1.776 | 1.776 | 1.776 | 1.776 |
| | BL3 | 1.9053 | 1.9112 | 1.9202 | 1.9297 |
| Bond | BA12 | 101.00 | 101.25 | 101.50 | 102.00 |
| | BA31 | 105.42 | 105.48 | 105.40 | 105.17 |
| Angle (°) | BA32 | 96.83 | 95.52 | 98.77 | 100.03 |
| | BA33 | 143.02 | 141.98 | 140.46 | 138.92 |
| | DCu _x | 0.150 | 0.175 | 0.225 | 0.275 |
| Atomic | DCu _z | –0.0844 | –0.1015 | –0.1375 | –0.1679 |
| Shift (Å) | DO _x | –0.1852 | –0.1858 | –0.1864 | –0.1877 |
| | DO _z | 0.1442 | 0.1488 | 0.1553 | 0.1682 |
| Layer spacing | D ₁₂ | 1.9086 | 1.9150 | 1.9215 | 1.9343 |
| Damping | γ | 1.5669 | | 0.9019 | |
| Potential | δ | 10.427 | | 6.2736 | |

*Adjustable variables are BA12 and DCu_x. V₀ = 10.56 eV

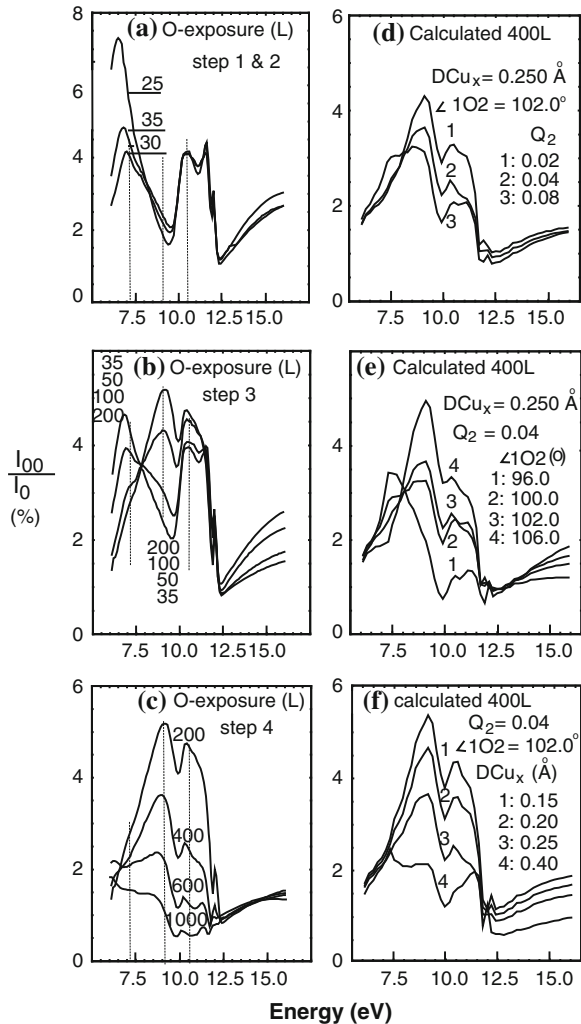
It should be emphasized that oxygen possesses no more than two bonding orbitals. It is unrealistic for oxygen to bond identically with the four neighbors in a surface plane. On the other hand, the difference in electronegativity ($\Delta\chi = 1.8$) between oxygen and Cu determines the nature of O–Cu bonding mainly ionic. No covalent, metallic, or even antibond between oxygen and copper are permitted as they are subject to the $\Delta\chi$ criterion ($\ll 2$). Forming the antibond requires extra energy higher than that for the nonbonding lone pairs. Therefore, the acceptable solution for the precursor state is the off-centered pyramid with an O^{–1} located 0.4 Å above the Cu(001) surface, as justified with the z_0 -scanning calculations. Oxygen forms one contracting ionic bond in the precursor phase with one Cu atom, rather than four identical bonds with its surface neighbors in the same plane.

Briefly, the effect of aging and annealing on the O–Cu(001) system is slightly complex, and therefore, it is less explicit than the effect of increasing oxygen exposure. However, it is certain that long-term aging affects the same as higher oxygen exposure on the spectral features that can be understood as the development of interaction between the nonbonding lone pairs and the lone-pair-induced Cu^p. The annealing provides a force to de-hybridize the oxygen, reducing the DCu_x and the DOS features of lone pairs rather than enhancing the bond formation. The preferred precursor is the off-centered pyramid as confirmed with STM.

3.2.4.5 Four-stage Cu₃O₂ Bonding Dynamics

Figure 3.12 a–c shows the VLEED (00) beam reflectance I_{00}/I_0 versus the incident beam energy measured at 70° incidence and 42° azimuth angles [15]. The VLEED spectral features are very sensitive to the oxygen exposure. The variations in the typical peaks at 7.1, 9.1, and 10.3 eV show that the reaction progresses in four discrete stages:

Fig. 3.12 Exposure-resolved VLEED spectra (a–c) measured at 70.0° incidence and 42.0° azimuth from the O–Cu(001) surface [15] and the calculated results (d–f) from varying the individual bond variables of $Q_2(C_2)$, BA12, and DCu_x with fixed $C_1 = 0.88$. Variations in intensities in panel (a–c) at 7.1, 9.1, and 10.3 eV show four reaction stages. Calculations (d–f) for 400-L oxygen exposure using bond variables can reproduce the trends of measurement at different stages (reprinted with permission from [1])



- $\Theta_O \leq 30$ L: The peak at 7.1 eV decreases in magnitude with increasing oxygen exposure until it reaches 30 L, while other peaks remain almost unchanged.
- $30 \text{ L} < \Theta_O \leq 35$ L: The decreased peak intensity at 7.1 eV recovers a little.
- $35 \text{ L} < \Theta_O \leq 200$ L: The first peak attenuates while one new peak at 9.1 eV emerges, and then, both the peaks at 9.1 eV and at 10.3 eV increase to maximum values up to 200 L.
- $\Theta_O > 200$ L: A general attenuation of the entire spectrum occurs.

The calculations for the 400-L oxygen exposure by individually varying the bond variables BA12, Q_2 , and BL2 can reproduce the measured trends, as summarized in Fig. 3.12d–f and Table 3.7.

Table 3.7 Four-stage O-Cu(001) surface bonding kinetics^a

| Reaction stages | 1 (<30 L; BL1 formation); 2 (30–35 L; BL2 and \angle 102 change); 3 (35–200 L; \angle 102 expansion) 4 (>200 L; DCu _x increase) | | | | | | | | | |
|-----------------------|---|--------|--------|--------|--------|--------|--------|--------|--------|------------|
| | Exposure (L) | 25 | 30 | 35 | 50 | 100 | 200 | 400 | 600 | \geq 800 |
| Bond geometry | | | | | | | | | | |
| Q ₁ = 0.12 | Q ₂ | 0 | 0 | 0.04 | 0.04 | | | | | |
| | BA12 | 92.5 | 94.0 | 98.0 | 100.0 | 101.0 | 102.0 | | | |
| | DCu _x | 0.125 | 0.150 | 0.150 | 0.150 | 0.150 | 0.150 | 0.250 | 0.355 | 0.450 |
| Atomic shift (Å) | -DCu _z | 0.1460 | 0.1440 | 0.1268 | 0.0938 | 0.0844 | 0.0709 | 0.1495 | 0.2239 | 0.2849 |
| | -DO _x | 0.1814 | 0.1796 | 0.1802 | 0.1831 | 0.1852 | 0.1877 | | | |
| | DO _z | — | 0.0889 | — | | | | | | |
| D ₁₂ | | | | 0.0447 | | | | | | |
| | 1.7522 | 1.7966 | 1.8287 | 1.8824 | 1.9086 | 1.9343 | 0.1682 | | | |
| Bond length (Å) | BL1 | 1.628 | | | | | | | | |
| | BL2 | 1.850 | | | | | | | | |
| | BL3 | 1.8172 | 1.8326 | 1.776 | 1.8983 | 1.9053 | 1.9121 | 1.9262 | 1.9396 | 1.9505 |
| Bond angle (°) | BA13 | 95.70 | 98.82 | 104.24 | 105.12 | 105.64 | 105.33 | 105.30 | 104.01 | 103.83 |
| | BA23 | 91.80 | 93.11 | 95.75 | 96.46 | 96.83 | 95.18 | 99.52 | 101.67 | 103.43 |
| | BA33 | 165.87 | 160.83 | 145.26 | 144.32 | 143.02 | 141.82 | 139.43 | 135.38 | 135.71 |

Reprinted with permission from [1]

^a Empty space is identical in value to that in the previous cell. All information is provided by the controlling variables (BA12, Q₂, DCu_x). Error bars for bond variables are 0.010 Å and 0.2°The SPB constants: V₀ = 10.50 eV, γ = -0.9703, δ = 6.4478

Results indicate the following:

- The oxygen coverage stabilizes at 0.5-ML throughout the course of reaction.
- The results, especially, in panels (e) and (f), agree remarkably well with the measured trends given in panels (b) and (c), respectively. This indicates that the process of Cu_2O bond forming dominates in the reaction while the SPB is relatively insensitive to the oxygen exposures.
- The four discrete stages of reaction correspond to the variation in the bond variables individually. For instance, the increase in $\angle\text{1O2}$ or the BL2 dominate the features appearing in the range from 35 to 200 L. However, $\angle\text{1O2}$ expansion and BL2 contraction are physically reasonable process. The spectral features for samples with oxygen exposure greater than 200 L result from the increase in DCu_x alone. From 30 to 35 L, the recovery of the peak at 7.1 eV can be realized by increasing the Q_2 with smaller $\angle\text{1O2}$ and smaller DCu_x .
- Variation in DCu_z gives a little change of the spectral intensity between 9.5 eV and 11.5 eV. Varying the DCu_z produces no features that could match measurements. Therefore, the individual shift of an atom at a time does not occur in the real process of bond formation.

Figure 3.13 shows the offset of the oxygen-exposure-resolved $z_0(E)$ profiles, which reproduce the measured spectra in Fig. 3.12a–c. It is seen that the $z_0(E)$ profiles, in general, are relatively insensitive to the variation in the exposure. The $z_0(E)$ profiles are similar in shape, except for the slight difference below 7.5 eV for 25 L exposure. This further confirms the assumption that the SPB is much less sensitive to the exposure than the bond geometry. The slight outward shift ($-z$ -direction, relative to -2.5 a.u. as indicated by broken lines) of the $z_0(E)$ curves at higher exposures increases the $n(E)$, which reduces the work function in the area over which VLEED integrates (μm level).

The shape of the $z_0(E)$ profile is a joint contribution of the occupied DOS, $n(E)$, and the surface corrugation [local spatial DOS $n(x, y)$]. The nonconstant form of the $z_0(E)$ can be attributed to the O-induced ‘rather local’ properties as revealed by STM and the nonuniform DOS in the valence band as well. The $\Delta z_0(E)$ in the z -direction is about $(-2.3) - (-3.3)$ (atomic unit) = 0.53 \AA which coincides with the $\sim 0.45 \text{ \AA}$ STM gray scale [13]. Vacating, ionizing, and polarizing of atoms at the surface result in the strong corrugation of the surface, as described in the counter plots of Fig. 3.13.

The small features at 7.1 eV which appeared in the $z_0(E)$ curves of 30–600 L coincide with the sharp peak at 2.1 eV below $-E_F$ (with respect to work function of 5.0 eV) probed with STS from the O–Cu–O chain region [32]. The new occupied states below 7.5 eV are identified as the contribution from nonbonding lone pairs. Hence, the absence of the lone-pair features below 7.5 eV at 25-L oxygen exposure implies the absence of the sp -orbit hybridization in the O^{-1} -derived precursor phase. It is thus clear that the sp orbitals of oxygen can only hybridize upon the two bonding orbitals of the oxygen that are fully occupied. The absence of the 7.1 eV sharp features above 600-L oxygen exposure is the annihilation of the lone-pair information by the antibonding dipoles that are shifted outward and are highly saturated, as specified in the SPB model [69].

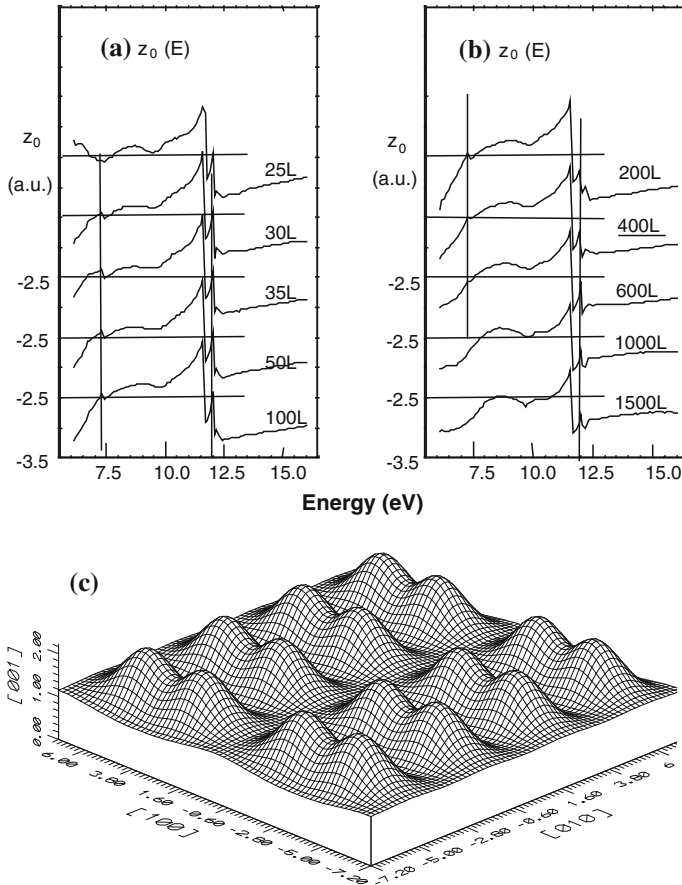


Fig. 3.13 a, b The exposure-resolved $z_0(E)$ profiles duplicate the spectra in Fig. 3.12a–c. The z -axis directs into the bulk. The 7.1 eV features on the $z_0(E)$ curves (≤ 600 L) correspond to the nonbonding lone-pair states, which agree with those appearing in STS from O–Cu–O chain [32]. Absence of the feature below 7.1 eV for 25 L indicates that the O^{-1} dominates at this coverage. Broken lines indicate the z_0 value (-2.5 a.u.) for a pure Cu(001) surface. The general outward shift of the $z_0(E)$ profiles corresponds to a reduction in the work function [22]. c O^{-2} -derived surface morphology of the surface, which matches the corresponding STM image (reprinted with permission from [1])

The violent features at 11.8–12.5 eV come from the bandgap reflection. Features surrounding the bandgap come from electron excitation near band edges and the formation of standing waves at the boundaries of Brillouin zones. It is noted that the shapes of all the $z_0(E)$ profiles are quite similar at energies higher than 7.5 eV. The DOS at the bottom of the valence band of Cu, and even the deeper p -band, are less affected by oxidation. The DOS features for the bonding (-5 eV below $-E_F$) are not detectable with VLEED because these features are annihilated by the standing waves at the boundary of the Brillouin zone. Therefore, exercises focusing on the variation in the valence DOS are on the right track [22].

The four-stage Cu_3O_2 bond-forming kinetics is quantified as follows (refer to Table 3.7, also a multimedia as supplementary information in Appendix A1):

- $\Theta_{\text{O}} \leq 30 \text{ L}$: The dissociated oxygen atom forms one contracting ($Q_1 = 12 \%$) ionic bond with a Cu atom (labeled 1) on the surface. Meanwhile, metallic bonds break up and the missing-row forms. The DCu_x reaches 0.18 \AA and $\angle 1\text{O}2$ reaches 94.0° . The O^{-1} locates $<0.1 \text{ \AA}$ above the surface and forms an off-centered pyramid with its surface dipole neighbors. The dipoles squeeze the atoms that are eventually evaporated.
- $30 \text{ L} < \Theta_{\text{O}} \leq 35 \text{ L}$: The O^{-1} forms the second contracting (increase Q_2 from 0 to 4 %) ionic bond with a Cu atom (labeled 2) in the substrate second layer, the sp orbitals of the O^{-2} start to hybridize. The O^{-2} penetrates into the bulk; meanwhile, the angle $\angle 1\text{O}2$ expands from 94.0° to 98.0° .
- $35 \text{ L} < \Theta_{\text{O}} \leq 200 \text{ L}$: The angle $\angle 1\text{O}2$ increases from 98.0° to a saturation value of 102.0° , which causes the first interlayer spacing D_{12} to expand by about 10 %, while other parameters have little change.
- $\Theta_{\text{O}} > 200 \text{ L}$: The interaction between the O^{-2} and the lone-pair-induced Cu^{P} develops. Lone pairs push the Cu^{P} outward, and consequently, pairing-dipoles form and bridge over the missing row. The DCu_x increases from 0.15 to a maximum 0.45 \AA at 800 L and above.

Representing the joint spatial and energy DOS, the variations in the structural-dependent $z_0(E)$ profiles (Fig. 3.13) agree with the bonding kinetics:

- The slight outward shift of the $z_0(E)$ profile at higher exposures reduces the work function, which corresponds to the development of the antibonding Cu^{P} .
- Features below 7.5 eV, particularly the small sharp peak at 7.1 eV, are derivatives of the nonbonding lone pairs of the O^{-2} . The absence of these features at 25 L originates from the O^{-1} precursor, in which no lone pair has formed; while at higher oxygen exposures, the lone-pair information is annihilated by the protruding Cu^{P} characteristics.
- Similarity of the fine-structure shapes at energies higher than 7.5 eV of all the profiles implies that electrons in the lower part of the valence band barely participate in the process of charge transportation. In contrast, electrons in the upper part of the valence band dominate in oxidation: holes and lone pairs form simultaneously. The DOS features of bonding (around 12 eV) are not detectable with VLEED due to the standing wave formation at the boundaries of Brillouin zones.

3.2.5 XRD from O–Cu(110)

Both XRD [34] and EMT [20] measurements confirmed that the oxygen adsorbates are located underneath the MR top layer to form the zigzag O–Cu–O chains (refer to Fig. 3.3) along the [110] direction. Referring to the inset in Fig. 3.2, in which the vertical displacement of the dipole (labeled 3) is denoted as $D3_z$. The

Table 3.8 Comparison of the tetrahedron bond geometries derived from the XRD of the Cu(110)–(2 × 1)–O^{−2} and the VLEED of the Cu(001)–(√2 × 2√2)R45°–2O^{−2} surfaces [21]

| Variable | Cu(110) (2 × 1)–O ^{−2} | | | Cu(001) (√2 × 2√2)R45°–2O ^{−2} | Conclusion |
|--------------------------------|---------------------------------|-------|-------|---|------------|
| | I | II | III | | |
| DO _z (below dipole) | ≤0.34 | 0.51 | 0.60 | 0.18 | – |
| BL1 (Å) | ≥1.85 | 1.73 | 1.675 | 1.628 | <1.85 |
| BL2 (Å) | ≥1.85 | 1.73 | 1.675 | 1.776 | <1.85 |
| BL3(2)(Å) | ≤1.84 | 1.88 | 1.921 | 1.926 | ~1.92 |
| BA12 (°) | ≤90.0 | 96.0 | 102.5 | 102.0 | <104.5 |
| BA33 (°) | ≥156.7 | 146.5 | 140.3 | 139.4 | ~140.0 |
| BA13/23(°) | ≤97.4 | 100.2 | 102.3 | 99.5/105.3 | ~102.5 |

Column III is preferred for tetrahedron bond formation, which is the same happened in the (001) surface (reprinted with permission from [1])

distance from oxygen to the buckled Cu top layer is DO_z . The lateral displacement of the Cu⁺ row in the second layer is $D1_x$. The z -axis is directed into the bulk. Thus, the bond parameters are [34]:

$$(D1_x, DO_z, D3_z) = (0.031 \pm 0.005, 0.34 \pm 0.17, -0.37 \pm 0.05) \text{ \AA}.$$

Table 3.8 shows that a slight change of the DO_z varies the bond geometry. The different values of bond lengths represent quite different meanings in the physics. The value of $DO_z = 0.34 \text{ \AA}$ gives a tetrahedron with four O–Cu bonds that are nearly identical in length (Column I). The value of $BL3 \leq 1.85 \text{ \AA}$ implies that the atom labeled 3 is an ionic one. The Cu⁺ ion is hardly detectable by STM due to the partially emptied d-states and the reduced atomic radius (from 1.27 to 0.53 Å). This is apparently conflicting with the STM images that show the Cu atom buckling up the surface.

Lowering the oxygen adsorbate within the error bar (0.17 Å) to $DO_z = 0.51 \text{ \AA}$ gives results in Column II. BL1 has a 6.5 % contraction, and BL3 extends slightly compared with the standard ionic bond length, 1.85 Å. The bond geometry is now acceptable as the shorter bond corresponds to the ionic state of the Cu. Structural parameters in Column II are acceptable, while those in Column I are strictly forbidden in line with physical constraints and STM observations. The ideally suggested case, assuming the CN of the O^{−2} and the Cu⁺ as 4 ($C = 0.12$) and 8 ($C = 0.03$), is shown in Column III. By adopting the value $D3_z = 0.37 + 0.05 \text{ \AA}$, one can then insert into this frame a tetrahedron [$BL1 = BL2 = 1.32 \times (1 - 0.12) + 0.53 \times (1 - 0.03) = 1.675 \text{ \AA}$], in which the O^{−2} ion is located 0.6 Å beneath the dipole layer. The geometry of this tetrahedron is nearly identical to that determined for the Cu(001)–(√2 × 2√2)R45°–2O^{−2} phase. Although the patterns of reconstruction and morphology are different, the basic tetrahedron is the same in both the Cu(001)–O^{−2} and the Cu(110)–O^{−2} surfaces.

3.2.6 Summary

The 3B premise formulates the O–Cu(001), (110), (111) surface reconstruction in terms of reaction dynamics with specification of the atomic valences. The evolution of the adsorbate from O^{-1} to the subsequent O^{-2} with sp -orbital hybridization results in the phase ordering and the crystallographic and morphologic patterns. Difference appearances of the Cu(001), (110), (111) surfaces upon oxygen chemisorption result from nothing more than the geometrical orientations for bond forming as the atomic size and electronegativity are all the same.

The Cu_3O_2 pairing-tetrahedron evolves from the O^{-1} -induced pyramid on the Cu(001) surface. In the precursor phase, the O^{-1} locates eccentrically above the fourfold hollow site of the $c(2 \times 2)-2O^{-1}$ domain to form an off-centered pyramid. The off-center shift of the O^{-1} is $DO_x \approx 1.807 - [1.85 \times (1 - 0.12)] \approx 0.18 \text{ \AA}$, which is comparable to the values of 0.10–0.13 \AA [7, 19]. The vertical distance of the O^{-1} to the surface is $<0.1 \text{ \AA}$ above the surface. The absence of the lone-pair DOS features implies that no sp -orbital hybridization occurs of oxygen in the O^{-1} -induced precursor phase.

Except for the Cu(001)– $c(2 \times 2)-2O^{-1}$, all the available phases on the O–Cu(001) and the O–Cu(110) surfaces are composed of the primary Cu_2O tetrahedron. The parameters for the Cu_2O tetrahedron are nearly the same, as summarized in Table 3.8. The work function is reduced by $\sim 1.2 \text{ eV}$ and the inner potential constant decreases from 11.56 eV for the clean Cu(001) surface to 10.50 eV upon being oxidized. The SPB parameters vary from site to site on the surface [46]. At the dipole site, $z_1 \cong z_0$, $\alpha \cong \lambda^{-1}$. The metal dipoles enhance the SPB through the outward shift of the wave function. Dipole formation also strengthens the degree of saturation of both the real and the imaginary part of the SPB at the dipole site.

The SPB of the Cu(001)– O^{-2} surface varies considerably from that of the clean Cu(001) surface. The z_{0M} at dipole site is ($z_{0M}/z_0(\text{Cu}) = 3.37/2.50 \approx 1.35$ times) and the λ_M is ($\lambda_M/\lambda(\text{Cu}) = 1.27/0.9 \approx \sqrt{2}$ times) that of the pure Cu(001) surface. The values of z_{0M} and λ_M quantify the protrusions in the STM image to a certain extent as the higher the electronic islands are, the denser the electrons will be there. In the MR site, $z_1 \ll z_0$, $\alpha \gg \lambda^{-1}$, i.e., the MR vacancy is not occupied by ‘free electrons’ of the solid. This quantifies to a certain accuracy of the depression in the STM imaging. On the Cu(001)– O^{-2} surface, the lowest saturation degree and the smallest z -scale of the SPB is ($z_{0m}/z(\text{Cu}) = 1.75/2.5 \cong \lambda_m/\lambda(\text{Cu}) = 0.65/0.9 \approx 1/\sqrt{2}$ times) that of the clean Cu(001) surface. Therefore, electrons at the surfaces with chemisorbed oxygen are rather local. It is reasonable to describe metal surfaces with chemisorbed oxygen at higher coverage as a non-Fermi system. This is because of the lack of freely moving electrons at the surface. This mechanism should cause the nonohmic rectifying and higher contact resistance even though the local work function is much lower than that of the clean Cu(001) surface. It is understandable now why a standard free-electron resistance mechanism could not work in such a strongly localized system [84].

Only three bond parameters dominate the four-stage Cu_3O_2 bonding kinetics. In the process of oxidation, the oxygen adsorbate first forms one Goldschmidt-contraction ionic bond to a Cu atom on the surface, followed by another contracting ionic bond between the oxygen atom and a Cu atom in the substrate. As a result, the oxygen adsorbate buckles into the bulk. Then, the ionic bond angle increases, leading to the relaxation of layer spacing. Finally, interaction develops between the lone pairs of oxygen and the lone-pair-induced metal dipoles. The sp -orbital hybridization takes place only when the sp orbitals of the oxygen are fully occupied. During the process of oxidation, the change of the SPB is not apparent except for the DOS features of the nonbonding lone pairs.

The bi-phase ordering on both the O–Cu(001) and the O–Cu(110) surfaces results from the evolution of the adsorbate from O^{-1} to O^{-2} valence. The formation of the O^{-1} and subsequently the hybridized O^{-2} gives in nature the Cu(001)– $c(2 \times 2)$ – 2O^{-1} and then the Cu(001)– $(\sqrt{2} \times 2\sqrt{2})\text{R}45^\circ$ – 2O^{-2} phases. Reassembling of the primary Cu_2O tetrahedron transforms the Cu(110)– (2×1) – O^{-2} into the Cu(110)– $c(6 \times 2)$ – 8O^{-2} phase at elevated temperatures and higher exposures. As consequences of O^{-2} -hybridization, the Cu(001)– $(\sqrt{2} \times 2\sqrt{2})\text{R}45^\circ$ – 2O^{-2} differs from the Cu(110)– (2×1) – O^{-2} in origin by nothing more than the fact that the $[\text{O}^{-2}; \text{Cu}^{\text{P}}; \text{O}^{-2}]$ string rotates itself by $\pm 45^\circ$ in-plane to match the specific coordination environment. Such a chain operation yields entirely different reconstruction patterns and surface morphologies of the two surfaces. Therefore, the phase ordering on the Cu(001)–O and the Cu(110)–O surface is simply the consequence of the Cu_2O formation at different stages and under various bonding circumstances. The mechanism for the O–Cu(111) surface reconstruction should be the same because the Cu(001), (110), (111) surfaces differ one from another by nothing more than the crystal orientation.

3.3 O–(Rh, Pd)(110)

3.3.1 STM Morphology and Crystallography

Oxygen adsorbate occupies the long-bridge hollow site on the fcc(110) surfaces of Cu, Ni, Ag, and Pt to form a tetrahedron with its four surrounding atoms. Such a manner of occupation yields the alternative ‘ $\text{O}^{-2}; \text{M}^{\text{P}}; \text{O}^{-2}$ ’ string and the parallel ‘missing-row’ vacancies. In contrast, oxygen adsorbate prefers the alternate hcp(0001) or fcc(111) facet site and form rope-like strings *along* the close-packed direction of the fcc(110) surface of Rh [85–96] and Pd [97–100]. Adsorbates tend to locate at the troughs crossing a row of Rh or Pd atoms to form the zigzag O–M–O chains, instead. The preference of the hcp or the fcc site of the oxygen is still under debate. LEED studies [101–105] revealed five patterns of (1×2) , (1×3) , $c(2 \times 4)$, $c(2 \times 6)$, and a ‘complex’ structure. A series of the ‘complex’ superstructures of (2×3) and $c(2 \times 4)$ present at 100 K and under 3-L oxygen exposure. The reconstruction occurs in the (2×3) and $c(2 \times 4)$ modes [106]. This

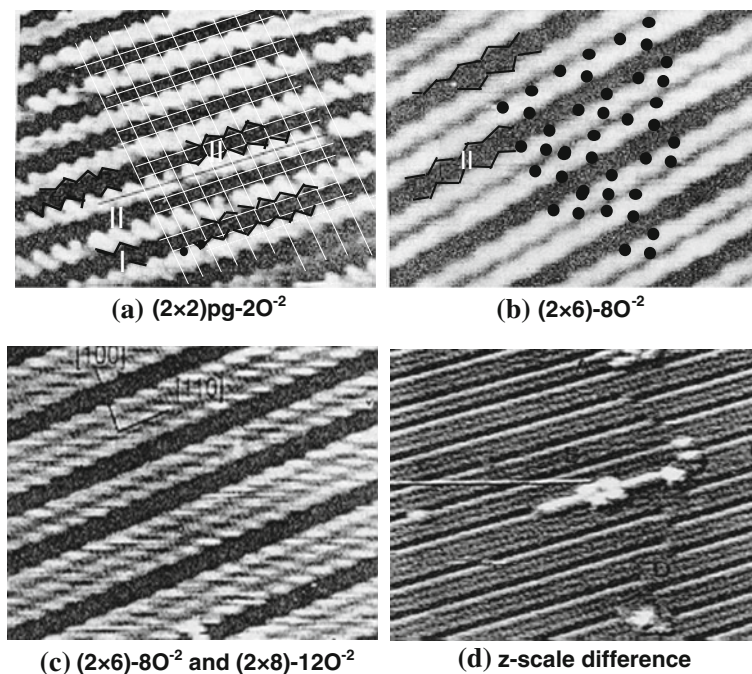


Fig. 3.14 STM images of the O–Rh(110) surfaces (reprinted with permission from [88, 91]). The bright protrusions correspond to the buckled metal atoms with lateral displacement, while the dark stripes to missing-row vacancies. Grids help to locate the positions of oxygen adsorbates as the dark spots. Images were recorded at the following conditions: (a) and (b) (2.0 V, 1 nA), (c) (0.4 V, 0.25 nA), and (d) (0.35 V, 0.25 nA). Panel (d) distinguishes the z-scale difference of the edge protrusions next to the missing rows

arrangement gives rise to the corresponding (1×3) and (1×2) periodicity at the Pd(110) surface. At low temperature (170 K) and low coverage, the oxygen adsorbate prefers short-bridge or nearly short-bridge sites on the Rh(110) surface rather than the threefold sites [107, 108].

Figure 3.14 shows the STM images of the O–Rh(110) surface obtained for various values of oxygen coverage [88, 91, 93]. These images are essentially the same as those probed from the O–Pd(110) surface [97]. Grids on the STM photographs help to specify the locations of the adsorbates as represented by the small dark spots. Zigzag or sawtooth-like protrusions form along the close-packed directions. Oxygen adsorbates rest beside the protrusion spot. The following features the distinct features of the STM images and interpretations:

- Two kinds of zigzag strips of depressions were present, which were assumed as rows of metals that have been missed out upon reconstruction. One strip of depression corresponds to the $(2 \times 2)pmg-2O$ (a mirror and a glide symmetry) arrangement and the other to the $(2 \times 2)p2mg-2O$ phase (twofold mirror and a glide symmetry).

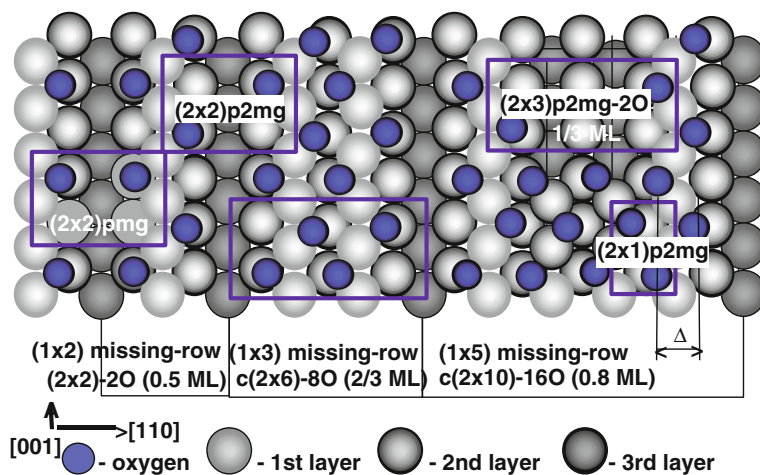


Fig. 3.15 Missing-row-type hard-sphere models for the Rh(110) and Pd(110) surfaces with chemisorbed oxygen (Reprinted with permission from [93]). Oxygen coverage determines the phases change. Oxygen occupies the apical site of a tetrahedron and forms O-metal bonds to two atoms at the surface and one atom in the second substrate layer. The number of missing rows decreases with increasing oxygen coverage. Unit cells for typical phases and the corresponding coverage are indicated. The Δ represents the distance between the O-O zigzagged chains across the protrusions

- The strips of bright protrusions were referred to as buckled Rh or Pd atoms of the first layer with lateral displacements in a zigzag fashion.
- The scale difference crossing the MR is $\sim 0.7 \text{ \AA}$, while it is 0.16 \AA along the row of protrusions.
- Strikingly, Fig. 3.14d shows that protrusions of the rows next to the ‘missing rows’ are relatively higher than that of other protruding rows.

The O-induced reconstruction, in both the O-Rh(110) and O-Pd(110) surfaces, is usually assumed as the MR type. One out of a certain number of the Rh(Pd) rows is removed from the surface. Common to other oxygen-metal systems, the first-layer spacing expands and the second contracts.

Figure 3.15 illustrates the hard-sphere models for the O-(Pd, Rh)(110) surfaces at different values of oxygen coverage. Indicated by the blue boxes are the $(2 \times 1)p2mg-2O$ (1.0 ML), $(2 \times 2)p2mg-2O$, and $(2 \times 2)p2mg-2O$ (0.5 ML) unit cells. These unit cells compose the complex $c(2 \times 2n)$ ($n = 3, 4, 5$) structures. Indicated by the black lines are phases corresponding to $1/3$, $2/3$, and $4/5$ -ML oxygen coverage. The atomic structural model suggested that:

- At very low coverage, oxygen occupies a fourfold hollow site of C_{2v} symmetry.
- At $\Theta_O < 0.5 \text{ ML}$, the adsorbate starts to induce a (1×2) MR reconstruction of the surface. Oxygen atoms occupy every other fcc(111) facet site along both sides of a metal row in the close-packed direction. Each adsorbate interacts with two atoms at the surface and one atom in the second substrate layer.

Table 3.9 O–Rh(110) surface atomic geometry ($D_{\text{bulk}} = 1.34 \text{ \AA}$)

| | DO_z | Δ | D_{12} | D_{23} | Bond length |
|---|--------|----------|----------|----------|-------------|
| $(2 \times 1)\text{p}2\text{mg}-2\text{O}$ [96] | 0.60 | 1.13 | 1.33 | 1.39 | 1.86, 2.07 |
| $(2 \times 1)\text{pg}-2\text{O}$ | 0.6 | 1.16 | 1.36 | 1.38 | 1.97; 2.04 |
| $(2 \times 2)\text{pg}-\text{O}$ [90] | 0.54 | 6.99 | 1.34 | 1.27 | |
| $(2 \times 2)\text{p}2\text{mg}-2\text{O}$ | 0.71 | 1.13 | –3 % | | 2.00; 2.05 |
| $(2 \times 1)\text{p}2\text{mg}-2\text{O}$ [87] | 0.66 | 0.70 | –3 % | | 1.99; 2.06 |
| Subsurface O [93] | 0.50 | 1.10 | –3 % | | 2.00, 1.88 |

Reprinted with permission from [1]

- At $\Theta_{\text{O}} = 0.5 \text{ ML}$, the (1×2) MR reconstruction is fully developed.
- At $\Theta_{\text{O}} > 0.5 \text{ ML}$, the (1×2) MR reconstruction starts to degrade. The missing rows are gradually replaced by the protruding metal rows until all the missing rows are fully recovered.
- At $\Theta_{\text{O}} = 1$, the O–fcc(110) surface is again unreconstructed and the oxygen adsorbates form a $(2 \times 1)-2\text{O}$ LEED pattern.

It is surprising that, as the oxygen coverage increases, the number of missing rows reduces from every other ($1/2$) to every n th ($1/n$) and, finally, to zero. It remains a puzzle how the adsorbates can turn the atomic vacancies into real atoms that are then buckled up.

Table 3.9 features the crystal geometry of O–Rh(110) surfaces. LEED [85, 90, 93, 95, 96] and DFT [87, 89] optimizations suggested that oxygen adsorbate prefers the hcp(0001)-facet site in the Rh(110)– $(2 \times 1)\text{p}2\text{mg}-2\text{O}$ phase. Oxygen atom sits $0.5\text{--}0.6 \text{ \AA}$ above the top layer and bonds to one atom in the first layer and to two in the second. The O–Rh bond lengths are $1.86\text{--}1.97 \text{ \AA}$ to the Rh atom in the top layer and $2.04\text{--}2.07 \text{ \AA}$ to the Rh atom in the second layer. The Δ in Fig. 3.15, labeling the distance between the oxygen rows, is $2.26\text{--}2.80 \text{ \AA}$. Under the influence of oxygen chemisorption, the $[100]$ row in the second layer is distorted in a zigzag fashion by $\sim 0.1 \text{ \AA}$ with the Rh atomic positions shifted toward the nearest oxygen positions. However, agreement needs to be reached on the preferential site of oxygen. Whether the fcc(111) or the hcp(0001) facet is preferable and what the vertical distance of the oxygen atom is.

3.3.2 Formulation: Bond and Atomic Valence

In order to examine the effects of electronegativity and the scale of the lattice constant on the observations, one may compare the patterns of reconstruction of the O–(Rh, Pd)(110) surfaces with those of the O–Cu(110) surface.

It is easy to understand that, reacting with the more open (Pd, Rh)(110) surfaces, oxygen adsorbates move from the C_{2v} hollow sites to the tilted threefold fcc(111)-facet sites rather than the hcp(0001) facet sites of the fcc(110) surface (Fig. 2.1). Bonding to two atoms in the second layer will create the same pattern of

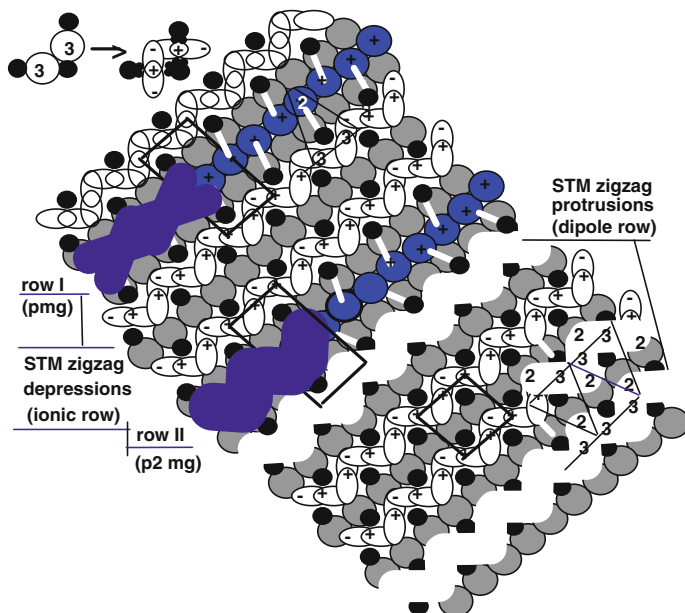
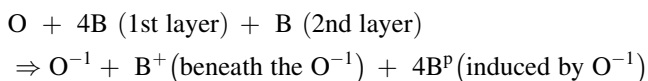


Fig. 3.16 Bond model for the pmg and p2mg reconstructions of the O-(Pd, Rh)(110) surface [86] specifies the STM protrusions to be the metal dipoles. Depressions arise from the B^+ ions rather than missing-row vacancies. O^{-2} locates always in the center of a quasi-tetrahedron represented by the unit 1233. Surface bond network with involvement of H-like bond interlocks all the surface atoms and hence there are no atoms are missing during the reaction. The top-left inset illustrates how the lone pairs of the oxygen adsorbates polarize and deform the metal dipoles. Two kinds of depression rows correspond to the pmg and p2mg glide symmetry of adsorbate distribution. The number of depressed rows decreases with increasing oxygen exposure because the B^+ converts to B^p with increasing oxygen coverage. The triangle show the tetrahedron formation with surface atoms labeled 2 (electron cloud for bonding) and 3 (dipoles) and another bond to the B atom underneath (reprinted with permission from [1])

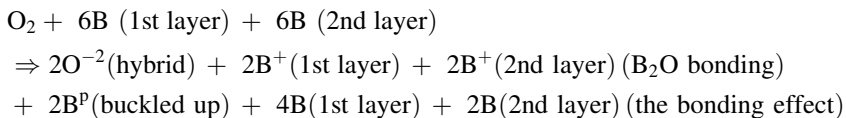
reconstruction occurring on the O-Cu(110) surface: a protruding row perpendicular to the close-packed direction. The fcc(111)-facet-sited oxygen must find a fourth atom to form the tetrahedron inside which the oxygen adsorbate locates. As illustrated in Fig. 3.16, the triangles indicate the primary tetrahedron (1233) in the corresponding $(2 \times 1)p2mg-2O$, $(2 \times 2)p2mg-2O$, and the $(2 \times 2)pmg-2O$ phases. The nature of the bond and the kinetics of the bonding, as well as the individual valences of surface atoms can be formulated as below.

In the precursor phase, or at very low oxygen coverage, oxygen deposits randomly into the C_{2v} hollow site to form a B_5O cluster. This cluster can be expressed as:



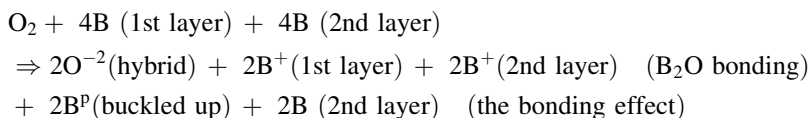
B₅O forms by bonding to the B atom underneath and the O⁻¹ polarizes its four surface neighbors.

At $\Theta_{\text{O}} = 1/3$ ML, O⁻² develops and the (2 × 3)-2O⁻² unit cell forms. The (2 × 3) unit cell contains two quasi-tetrahedron, which can be expressed as:

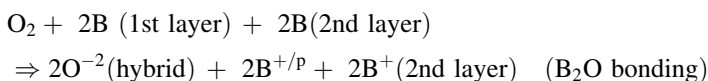


Oxygen retains the bond to the B atom underneath and gets another electron from the B atom in the surface row near the protrusions. Lone-pair formation induces B^P dipoles that form the row of protrusions. The protrusions are zigzagged because the atomic coordination determines that the tetrahedron has to rotate slightly (imagine a triangle consisting of three apexes of a tetrahedron). On the other hand, the tetrahedron rotation releases the compression between the lone pairs of an adsorbate as the atomic distance along the close-packed direction may be too short for the B^P-B^P spacing (see model in Fig. 3.3a). Except for the dipole in the BR, every other B atom in the top and the second layers near the oxygen becomes B⁺. Therefore, interaction between the B⁺ and B along the B-B⁺-B row (which used to be assumed as a MR) becomes stronger than the interaction between pure metal atoms. The density of the nearly free electrons along the B-B⁺-B row becomes lower. The B atoms and B⁺ ions are hardly detectable using an STM, being similar to the images of a missing row. Therefore, the invisible rows are often assumed as 'missing rows.' If the adsorbate locates at the hcp(0001) facet site, the B-B⁺-B row should be composed of a B^P, which is the case for the O-Cu(110) surface.

At $\Theta_{\text{O}} = 0.5$ ML oxygen coverage, the hybridized O⁻² gives rise to the (2 × 2)pmg-2O⁻² or the (2 × 2)p2mg-2O⁻² phase. The unit cell contains a pair of quasi-tetrahedron, and it can be formulated as:



At $\Theta_{\text{O}} = 1.0$ ML oxygen coverage, the (2 × 1)p2mg-2O⁻² phase forms:



At this stage, an H-like bond forms, which lower the STM protrusions and stabilize the surface. As the surface atomic ratio O:B = 1, each adsorbate must interact with three B atoms at the surface. Therefore, each B atom becomes B^{+/p} as two lone pairs are acting on it. The adsorbate drags the electron cloud of the dipoles to compensate for the lack of one atom for the tetrahedron formation.

The formulae for all the possible phases on the O-(Rh, Pd)(110) surfaces represent the kinetics of bond formation with specification of atomic valences. The oxide tetrahedron forms by evolving a B_5O cluster into a B_4O and then a B_3O cluster. During the transition of the B_5O into the B_4O , the fifth B atom at the surface is released and then is involved in the formation of a new B_4O cluster. The lack of one atom in the B_3O cluster at even higher coverage is compensated by the formation of the H-like bond, as illustrated in Fig. 3.16. Dipoles provide electrons to the oxygen to form the second ionic bond. In the $(2 \times 2)\text{-}2O^{-2}$ phase (0.5 ML), the entire second layer is half composed of B^+ ions and the other half of B atoms; in the $(2 \times 1)\text{p}2\text{mg-}2O^{-2}$ phase (1.0 ML), the second layer is fully composed of B^+ ions. The displacement of B and B^+ in the second layer is not avoidable subjecting to the bond geometry.

The reaction formulae indicate that the B^p or B^{+p} gradually replaces the B^+ that used to be assumed as the ‘missing-row’ vacancy. Hence, the number of the invisible rows decreases with increasing oxygen coverage, which elaborates well-experimental observations. It is unlikely that the oxygen adsorbate is able to turn the atomic vacancies into metal atoms that then turned to be the buckled dipoles. The tetrahedron model, however, defines a feasible mechanism for the mass transport. The B^+ row evolves into the B^p or the B^{+p} row with increasing adsorbates. Therefore, the zigzag depressions in the STM image correspond to B^+ ions (Row I and Row II in Fig. 3.16) rather than to MR vacancies.

The difference in the shape between the depressed Row I and Row II is due to the different glide symmetries of the oxygen adsorbates as can be seen from Fig. 3.16. Row I corresponds to the $(2 \times 2)\text{p}2\text{mg-}2O^{-2}$ symmetry, while Row II to the $(2 \times 2)\text{p}2\text{mg-}2O^{-2}$. It was noted earlier that the H-like bond forms by dragging the electron cloud of the protruding dipoles to the bonding orbitals of the oxygen, and hence, the H-like bond formation lowers the protrusions. Therefore, the slightly higher STM protrusions near the invisible row results from the absence of the H-like bond near the edge B^+ rows.

The B_4O tetrahedron bonding requires that oxygen is located inside a tetrahedron rather than at the apical site. Therefore, the bond geometry determines the relaxation of the first interlayer distance. Due to the reduced atomic sizes of metal ions in the second layer and the strong interaction between the B^+ in the second layer and the B in the third layer, the second interlayer distance contracts. In this sense, the observed layer spacing relaxation and mass transportation as well as the surface morphologies of various phases become clear. Apparently, the difference in the host atomic size and host electronegativity determines the site specificity of the oxygen and the orientation of the tetrahedron. This delineates the (Rh, Pd)(110)-O surface from the Cu(110)-O surface in terms of reconstruction patterns, although the basic oxide tetrahedron is commonly the same.

3.4 O–(Co, Ru)(10 $\bar{1}$ 0) Surface Tri-Phase Ordering

3.4.1 STM Morphology and Crystallography

The hcp(10 $\bar{1}$ 0) plane with close-packed rows separated by the c -axis distance is an analog to the fcc(110) surface with slight difference in layer spacing. In contrast to the (2×1) MR reconstruction patterns on the O–(Cu, Ni, Ag, Pt)(110) surfaces, three intriguing superstructures show in sequence on the O–Co(10 $\bar{1}$ 0) surface [109–113] and two on the O–Ru(10 $\bar{1}$ 0) surface [114–116]. From the standpoint of microscopy and crystallography, O–(Co, Ru)(10 $\bar{1}$ 0) multiphase ordering has been well identified. In an earlier LEED study, Schwarz et al. [112] found that the Co(10 $\bar{1}$ 0)– (2×1) p2mg–2O phase is developed from the p (2×1) –O or the c (2×4) –4O phase by increasing the oxygen coverage at higher temperatures. Based on STM observations, Koch et al. [109, 110] proposed models for the reconstructed O–Co(10 $\bar{1}$ 0) phases. LEED calculations [113] suggested that in the final (2×1) p2mg–2O phase, oxygen occupies the threefold-coordinated fcc(111) facet site and bonds to two Co or Ru atoms in the first atomic layer and one Co or Ru atom in the second, this being the same as that occurring on the O–(Rh, Pd)(110) surface.

Oxygen adsorbate rests above the top layer of the otherwise-unreconstructed surface. The oxygen adsorbates prefer locations between two neighboring metal rows and form a zigzag O–O chain along the close-packed direction. Contrastively, oxygen adsorbates prefer the same fcc(111) facet sites but locate beside one specific (Rh, Pd) metal row to form the zigzag O–M–O row at lower coverage. This is the major difference between the O–(Rh, Pd)(110) and the O–(Co, Ru)(10 $\bar{1}$ 0) in observation.

Furthermore, chemisorption of oxygen causes a significant expansion ($\sim 25\%$) of the first Co interlayer spacing and a slight contraction ($\sim 5\%$) of the second Co interlayer spacing with respect to that of the bulk. LEED, DFT, and HREELS studies conducted by Schwegmann et al. [117] revealed that the O–Ru(10 $\bar{1}$ 0) surface shares the same reconstruction patterns as the last two phases of O–Co(10 $\bar{1}$ 0) despite the trivial details concerning atomic positions and interlayer spacing.

The following features O–Co(10 $\bar{1}$ 0) tri-phase ordering and the structural models:

- The disordered p (2×1) –O forms upon flashing the c (2×4) –4O phase to 450 K. The STM image in Fig. 3.17a exhibits a checkered pattern of black and white rectangles. The dimensions of the rectangles are 5.0 Å ($\sim 2a_{\text{Co}}$) by 4.0 Å ($\sim c_{\text{Co}}$) along the $[1\bar{2}10]$ and the $[0001]$ directions, respectively. The gray scale is about 1.1 Å. This less-ordered p (2×1) –O phase corresponds to the precursor state.

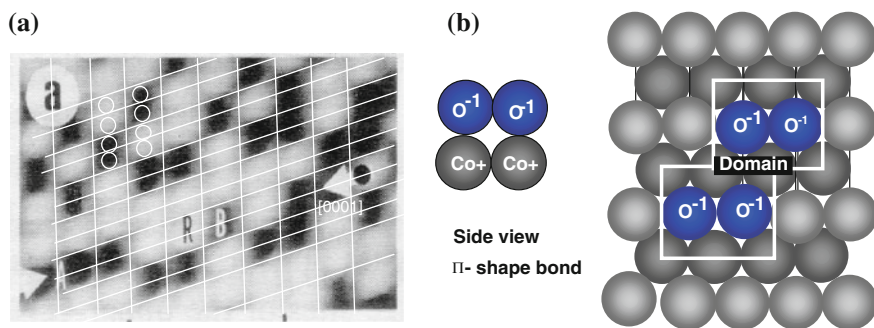


Fig. 3.17 **a** STM image (reprinted with permission from [110]), and **b** the corresponding bond configuration [111] for the Co(10 $\bar{1}$ 0)-p(2 × 1)-2O⁻¹ precursor phase with randomly filled checkerboard domains. The pairing O⁻¹-O⁻¹ dimer rests on the top of surface atoms forming a 'Π-shape' dimer bond along the close-packed direction (reprinted with permission from [1])

- The c(2 × 4)-4O phase forms when the clean Co(10 $\bar{1}$ 0) surface is exposed to 2.5-L oxygen at 300 K. STM imaging revealed that the ordered c(2 × 4)-4O phase forms uniformly over large areas (see Fig. 3.18a). Rows of white oval bumps with double Co periodicity ($2a_{\text{Co}} \sim 5.0 \text{ \AA}$) are present in the direction of the close-packed Co rows. Separation between rows of bumps is 8.0 \AA ($\sim 2c_{\text{Co}}$). The bright bumps, $\sim 1.1 \text{ \AA}$ in height, are resolved as a honeycomb-like pattern separated by the zigzag depressions. Based on the STM image, Koch et al. suggested that oxygen occupies the hcp(0001) facet site and bonds with one Co atom in the top layer.
- The (2 × 1)p2mg-2O phase was obtained by dosing oxygen (5–10 L) at room temperature to either the c(2 × 4)-4O or the (2 × 1)-O phase. STM revealed a regular array of protrusions, being similar to that of clean metal surfaces in the scale of $\leq 0.3 \text{ \AA}$. All the Co atoms of the topmost plane are at nearly the same levels of height. The model proposed for this phase interlocks the model for the c(2 × 4)-4O phase with oxygen preferring the hcp(0001) facet site. However, LEED studies by Gierer et al. [113] have ruled out the hcp(0001) facet site preference of the adsorbate. The adsorbate atoms are located above the fcc(111) facet site instead, agreeing with the model proposed by Comelli et al. [94] for the O-(Rh, Pd)(110) surfaces. The optimal atomic geometry is that oxygen atoms reside in the fcc(111) facet sites $0.74 \pm 0.05 \text{ \AA}$ above the first Co layer. The lateral distance between oxygen and the densely packed Co rows is $1.13 \pm 0.10 \text{ \AA}$ ($\Delta/2$ in Fig. 3.15). The O-Co bond lengths are estimated to be $1.83 \pm 0.10 \text{ \AA}$ (1) (to the Co atom in the first layer) and $1.99 \pm 0.10 \text{ \AA}$ (2) (to the Co atoms underneath the oxygen). The oxygen-derived structure of the Co(10 $\bar{1}$ 0) surface is one where the first Co interlayer expands from 0.62 to 0.90 \AA , which amounts to 25 % with respect to the bulk value, 0.72 \AA .

Comparatively, the O-Ru(10 $\bar{1}$ 0) bi-phase ordering and the structural models are nearly the same:

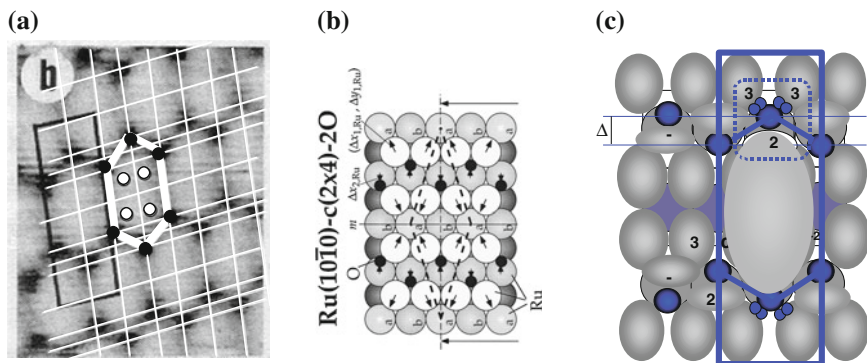


Fig. 3.18 **a** STM image of the $\text{Co}(10\bar{1}0)-(2 \times 4)-4\text{O}^{-2}$ surface (Reprinted with permission from [110]), **b** the hard-sphere model for the $\text{Ru}(10\bar{1}0)-(2 \times 4)-4\text{O}^{-2}$ structure [117], and **c** the bond configuration [111] with the dotted square framing the tetrahedron. The lack of one (Co, Ru) atom for the tetrahedron is compensated by a virtual bond between O^{-2} and the electron cloud labeled 2, which sharpens the tip of the honeycomb-like bumps in the STM images (Reprinted with permission from [1])

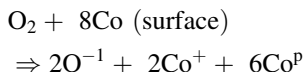
- The $c(2 \times 4)-4\text{O}$ and the $(2 \times 1)p2mg-2\text{O}$ phases form in sequence on the $\text{O}-\text{Ru}(10\bar{1}0)$ surface at room temperature by oxygen exposure of 0.7 and 2.5 L, respectively. This is easier to achieve than the formation of these phases on the $\text{O}-\text{Co}(10\bar{1}0)$ surface.
- According to the LEED and DFT measurements [117], oxygen adsorbate locates at the apical site of a tetrahedron and interacts with two Ru atoms in the top layer and one in the second layer. Oxygen atoms reside in the threefold hollow sites 1.02 (LEED)– 1.05 (DFT) Å above the first Ru layer in the first phase, with a lateral distance to the densely packed Ru rows of 1.18 – 1.19 Å ($\Delta/2$). The $\text{O}-\text{Ru}$ bond lengths are $2.09(1)$ and $2.10(2)$ Å. In the second phase, oxygen sites 0.96 (LEED)– 1.06 (DFT) Å above the first layer. All the three $\text{O}-\text{Ru}$ bonds are identical in length, 2.03 Å. The $\text{O}-\text{Ru}$ distance ($\Delta/2$) becomes 1.13 (LEED)– 1.19 (DFT) Å. Oxygen adsorption expands slightly the $\text{Ru}(10\bar{1}0)$ first interlayer spacing by $\sim 4\%$.

3.4.2 Formulation: Atomic Valence and Bond Geometry

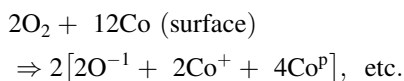
3.4.2.1 $\text{Co}(10\bar{1}0)-p(2 \times 1)-\text{O}^{-1}$: Pairing $\text{O}^{-1}-\text{O}^{-1}$ (≤ 0.5 ML)

Figure 3.17 models the STM image of the $\text{Co}(10\bar{1}0)-p(2 \times 1)-\text{O}$ precursor phase. STM images the oxygen adsorbates as depressions, even though the oxygen atoms are located above the surface, because the $\text{O}-2p$ state is lower than the E_F of a metal. Hence, the rectangular STM depressions correspond to the pairing $\text{O}^{-1}-\text{O}^{-1}$ dimers. The $\text{O}^{-1}-\text{O}^{-1}$ dimer rests atop of two Co atoms forming the $\text{O}^{-1}-\text{O}^{-1}$ bond along the close-packed direction. The O^{-1} catches one electron from the Co atom underneath and shares one electron with the other O^{-1} .

The O⁻¹ polarizes its rest neighbors, which produce the STM protrusions of this precursor phase. Reaction at this stage involves no charge transport between the oxygen adsorbate and Co atom in the second layer. The dark or bright rectangular domains (5.0 × 4.0 Å in two dimensions) are in the scale of the regular lattice. The reaction at this stage follows:



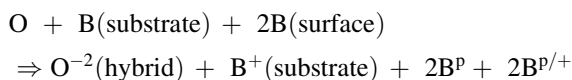
or



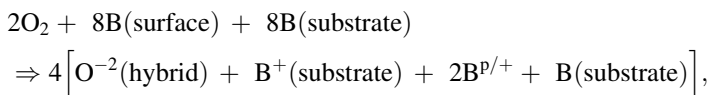
Unlike the nanometric Cu(001)-c(2 × 2)-O⁻¹ precursor state, in which oxygen forms an off-centered pyramid (4(O⁻¹ + Cu⁺¹) or 2O⁻¹ + Cu⁺²) with its surface neighbors, the oxygen adsorbates in the Co(10 $\bar{1}$ 0)-p(2 × 1)-O⁻¹ phase prefer the atop atomic positions. In contrast, in the O-(Rh, Pd)(110) precursor states, O⁻¹ occupies the C_{2v}-hollow site and bonds to the atom underneath first. Obviously, the O⁻¹ performs quite differently at these surfaces because of the difference in the scale and geometry of the host lattice and the electronegativity between the host surfaces.

3.4.2.2 (Co, Ru)(10 $\bar{1}$ 0)-c(2 × 4)-4O⁻²: Hybridized O⁻² (0.5 ML)

With increasing oxygen exposure, the O⁻¹ evolves into O⁻² and the oxide tetrahedron forms through a process of rebonding, as shown in Fig. 3.18. The basic quasi-tetrahedron denoted as (1233) is expressed as (B = Ru, Co):



In a c(2 × 4)-4O⁻² unit cell,



where the 2B^{P/+} represents the fact that a virtual bond forms between the O⁻² and the electron cloud of the dipoles. The virtual bond is not a real one, but it compensates for the lack of one atom in the oxide tetrahedron formation.

The honeycomb-like or oval-shaped protrusions in the STM image are composed of four Co^P that head toward the center of the ‘oval.’ In the Co₂O tetrahedron, the lack of one Co atom for the bond is compensated by the polarized electron cloud (as denoted 2) as do the (Rh, Pd)(110)-c(2n × 2)pmg-2O⁻²

phases. This process leads to a ‘virtual bond’ between the O^{-2} and the pairing-dipoles, which sharpen the ‘tips’ of the ‘honeycomb’ protrusions, see Fig. 3.18. As all the surface atoms are interlocked by the bond network, no atoms are missing there, being the same as that occurred in the $O-(Pd, Rh)(110)-(2n \times 2)-2O^{-2}$ surfaces. In addition, every other close-packed row in the second layer is composed of Co^+ . Although the STM images for the $Ru(10\bar{1}0)-c(2 \times 4)-4O^{-2}$ phase are lacking, the reconstruction pattern determined using LEED and DFT is the same as the $Co(10\bar{1}0)-c(2 \times 4)-4O^{-2}$ surface, as can be compared with models in Figs. 3.17 and 3.18. Therefore, the specification here should hold for both surfaces.

The contribution from the electron clouds of the dipoles to the oxide tetrahedron formation in the $(Co, Ru)(10\bar{1}0)-(2 \times 4)-4O^{-2}$, the $(Co, Ru)(10\bar{1}0)-(2 \times 1)p2mg-2O^{-2}$, and the $Cu(110)-c(6 \times 2)-8O^{-2}$ phases evidences that the *sp*-orbit hybridization of an O^{-2} is independent of its bonding constituents. Oxygen can bond to any component whether it is an atom or electron cloud of a single or a cluster of dipoles, which is able to supply electrons to fill the hybridized orbital of the oxide tetrahedron.

The minor geometrical difference among the $(Pd, Rh)(110)$, the $(Cu, Ni, Ag, Pt)(110)$, and the $(Co, Ru)(10\bar{1}0)$ causes entirely different orientations of the ‘ O^{-2} : B^P : O^{-2} ’ chains. Contrary to the single $O-Cu-O$ chain perpendicular to the close-packed direction of the $(Cu, Ni, Ag, Pt)(110)$ surfaces, the pairing $O-O$ zigzag chains in Figure 3.18 runs along the close-packed direction of Ru and Co . The fact is that the *c*-axis lattice $4.06/4.33 \text{ \AA}$ of Co/Ru is too long for the distance of B^P-B^P and the *a*-axis lattice $2.51/2.68 \text{ \AA}$ may be too short for the B^+-B^+ distance forces the oxygen to create a new environment for the Co_2O or Ru_2O tetrahedron. This leads to the entirely different orientation of the $O-(Co, Ru)-O$ chain and the shapes of the protrusions. As discussed previously, in the $(Pd, Rh)(110)-c(2 \times 2)-2O^{-2}$ surface, oxygen adsorbates prefer to locating in the troughs beside a specific metal row, which yields the alternating ionic row and buckled dipole row observed as the zigzag $O-M-O$ chain. However, oxygen atoms prefer positions, located in the $(Co, Ru)(10\bar{1}0)-c(2 \times 4)-4O^{-2}$ phase, between two nearest metal rows. The latter leads to the ‘honeycomb’ pairing-dipole rows on the $(Co, Ru)(10\bar{1}0)$ surface rather than the ‘sawtooth’-like single protruding rows on the $(Rh, Pd)(110)$ surface, instead. Therefore, the lattice geometry determines the site specificity of the adsorbate, which results in different reconstruction patterns.

3.4.2.3 $(Co, Ru)(10\bar{1}0)-(2 \times 1)p2mg-2O^{-2}$: H-like Bond (1.0 ML)

The $(Co, Ru)(10\bar{1}0)-(2 \times 1)p2 \text{ mg}-2O^{-2}$ phase, as shown in Fig. 3.19, interlocks with the $c(2 \times 4)-2O^{-2}$ phase by adding the zigzagged $O-O$ chains at positions between the pairing-dipole rows. The chemical reaction follows the relationship in the unit cell:

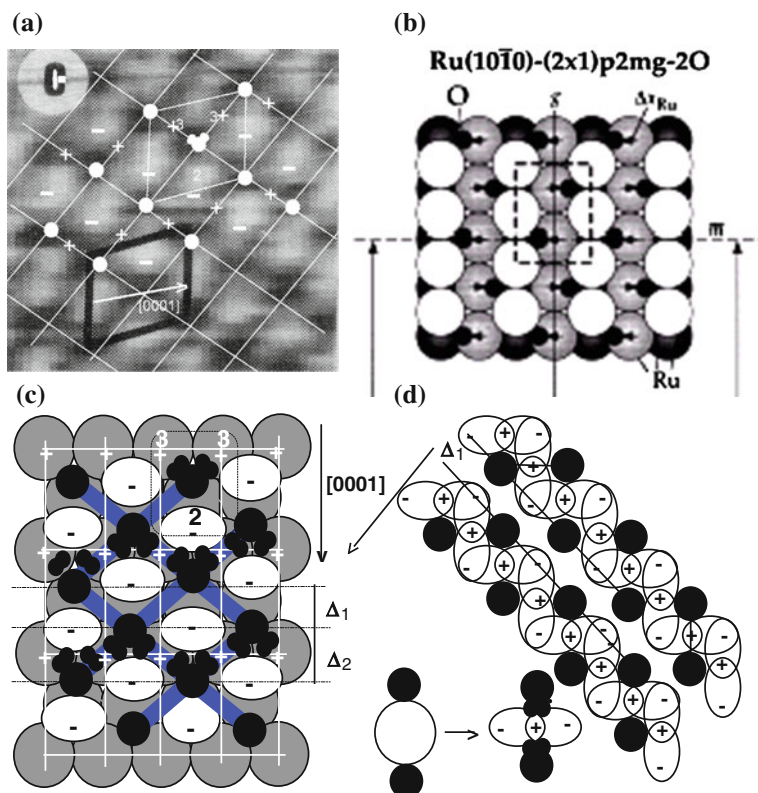
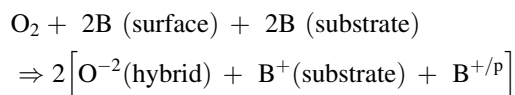


Fig. 3.19 **a** STM image of the Co(10 $\bar{1}$ 0)-(2 \times 1)p2mg-2O $^{-2}$ surface (reprinted with permission from [110]), **b** the hard-sphere model for the Ru(10 $\bar{1}$ 0)-(2 \times 1)p2mg-2O $^{-2}$ surface [117], **c** and **d** the bond configuration [111] showing the lone pairs (small dots) of the oxygen adsorbates that squeeze the electron cloud of a Co or Ru atom, which corrugate the surface morphology. The STM protrusions in this case correspond to dense polarized electrons (–) rather than ion core (+) positions. As the bond network interlocks all the surface atoms with atom missing, the H-like bond formation restores significantly the decreased work function and protects the surface from further reaction (reprinted with permission from [1])



In the present phase, each Co and Ru atom at the surface has three O $^{-2}$ neighbors due to the 1.0-ML coverage. Every Co or Ru atom at the surface becomes the B $^{+/p}$. Therefore, H-like bonds dominate at the surface, which lowers the STM protrusions and narrows the antibonding band of the surface substantially. This restores the oxygen-reduced work function of the Ru(10 $\bar{1}$ 0)-O surface by an amount of 0.49 and 1.12 eV, respectively, as the surface turns to be the c(2 \times 4)-4O $^{-2}$ and the (2 \times 1)p2mg-2O $^{-2}$ phase [117]. The effect of H-like

bonds becomes more apparent on the STM protrusions and the work-function recovery when the oxygen coverage increases from 0.5 to 1.0 ML. The scale of the image in the latter reduces to a level similar to that for clean metals (0.15–0.3 Å). It is expected that the (Co, Ru) (10 $\bar{1}$ 0) surfaces are readily oxidized but quickly saturated, protecting the substance from further corrosion.

All the Co atoms in the second layer become Co⁺ ions with reduced radii and lowered energy states. The interaction between the second layer (Co⁺ ions) and the third layer (metallic Co atoms) is stronger than that between two metallic layers. Therefore, the first interlayer distance expands by an amount that depends on the bond geometry and the second interlayer spacing contracts driven by the enhanced Co⁺–Co interlayer interaction. This mechanism should hold for the Ru(10 $\bar{1}$ 0)–O surface though LEED and DFT revealed a different amount of relaxation for the Co(10 $\bar{1}$ 0)–O surface.

Figure 3.19 also shows how the nonbonding lone pairs of the two O²⁻ ions squeeze and deform the electron cloud of one Co or Ru atom. This configuration accounts for the STM protrusions not only of the current Co(10 $\bar{1}$ 0)–O²⁻ phases but also of the (Rh, Pd)(110)–O²⁻. At these surfaces, STM protrusions correspond to the dense electron cloud (labeled ‘-’) rather than the ion core positions as labeled with ‘+.’ As indicated, the slight protrusion in Fig. 3.19 locates between two ion cores. Therefore, it is not always true to derive atomic structural information simply from the locations of the protrusions without considering the atomic valence alteration.

Comparing the reconstruction which has occurred to the (Co, Ru)(10 $\bar{1}$ 0)–(2 × 1)p2mg–2O²⁻ surfaces with that to the (Rh, Pd)(110)–(2 × 1)p2mg–2O²⁻ surfaces, it can be found that both systems have the same adsorbate arrangement. However, they yield entirely different patterns in the STM imaging. The former presents zigzag strips, while the latter gives a regular array of depressions and protrusions. One may attribute such a difference to the Δ values in Figs. 3.15 and 3.19:

- For the Rh(110)–(2 × 1) p2mg–2O²⁻: $\Delta_1 = 3.81$ – $\Delta_2 = 3.81 - 2 \times 1.13 = \sim 1.55$ Å and $\Delta_2 = \sim 2.26$ Å.
- For the Co(10 $\bar{1}$ 0)–(2 × 1)p2mg–2O²⁻: $\Delta_1 = \sim 2.26$ Å and $\Delta_2 = 4.06$ – $\Delta_1 = \sim 1.80$ Å.

An alternation of the Δ_1 and Δ_2 values and a small geometrical difference (0.25 Å) determine the site specificity of oxygen and gives quite a remarkable difference in the form of the STM images.

Knowledge about the O–(Co, Ru)(10 $\bar{1}$ 0) surface reaction has thus been described in terms of bond forming. The disordered Co(10 $\bar{1}$ 0)–p(2 × 1)–O precursor is identified as the derivative of the O⁻¹. The Π -shaped O⁻¹–O⁻¹ dimer rests atop of the surface Co atoms along the close-packed direction. Meanwhile, O⁻¹ polarizes its rest neighbors leading to the protruding domain boundaries. At higher oxygen coverage of the (Ru, Co)(10 $\bar{1}$ 0) surface, oxygen performs quite the same as that of the (Rh, Pd)(110) surfaces. O²⁻ locates at the fcc(111) facet site and forms a tetrahedron with two Co or Ru atoms at the surface and one Co or Ru

atom underneath. The O drags the electron cloud of the dipoles to compensate for the lacking of one atom in the tetrahedron formation. For both the Ru and Co, a $c(2 \times 4)\text{-}4\text{O}^{-2}$ phase forms and then a $(2 \times 1)\text{p}2\text{mg}\text{-}2\text{O}^{-2}$ phase follows. The H-like bond lowers substantially the STM protrusions and narrows the antibonding sub-band, which recovers the reduced work function significantly and protects the surface from being oxidized further.

3.5 O-Rh(111) and O-Ru(0001)

3.5.1 Crystallography and Morphology

Both the O-Rh(111) and the O-Ru(0001) surfaces share considerable similarities in the patterns of O-induced reconstruction [118]. For instance, three phases of $p(2 \times 2)\text{-O}$, $c(2 \times 2)\text{-}2\text{O}$, and $p(1 \times 1)\text{-O}$ form sequentially on these two surfaces. The Ru(0001)- $p(1 \times 1)\text{-O}$ phase can form under N_2O pretreatment [119, 120] while the Rh(111)- $p(1 \times 1)\text{-O}$ phase can be obtained by low-energy oxygen-ion-beam irradiation [121]. Common to all other O-chemisorbed systems, the first-layer spacing expands and the second contracts.

In the $p(2 \times 2)\text{-O}$ precursor phase ($\Theta \approx 0.25$ ML), the R (= Ru, Rh) atoms buckle up radially away from (or toward, as disputed) the adsorbate and the original C_{3v} symmetry of the unit cell remains. In the $c(2 \times 2)\text{-}2\text{O}$ phase ($\Theta \approx 0.5$ ML), pairing-row forms at the surface. In the $p(1 \times 1)\text{-O}$ phase ($\Theta = 1.0$ ML), the surface becomes unreconstructed.

However, discrepancies yet remain regarding the vertical position and the site specificity of the adsorbate. DFT [118, 120, 121] and LEED optimizations [122–126] suggested that oxygen adsorbates are located ~ 1.2 Å above the top layer of the surface and the oxygen site specificity follows the rules of homoepitaxial growth of the regular fcc(111) or hcp(0001) crystal lattices. The adsorbate prefers the apical site of a tetrahedron and remains identical bond length to the surface atoms throughout the course of reaction. The bond length, 2.00–2.10 Å, equals approximately to the sum of the atomic radii of oxygen and R atoms. In contrast, a DFT calculation [127] of the incorporation of oxygen into the basal plane of the late $4d$ noble metals of Ru, Rh, Pd, and Ag suggested that the occupation of subsurface sites is always connected with a significant distortion of the host lattice. O always favors adsorption in the hollow sites, which represent a continuation of the bulk stacking sequence, i.e., hcp sites on Ru(0001) and fcc sites on Rh(111), Pd(111), and Ag(111).

The combination of on-surface O in fcc sites and subsurface O in tetra-I sites is to be either most stable or energetically very close to the most stable geometry. The tetra-I site for Ru would only allow an O-metal bond length of 1.65 Å. This situation gradually becomes favorable for other elements, yet for Ag that has the largest lattice constant. In that case, the value of 1.80 Å is still significantly too short. Thus, subsurface O incorporation always induces a substantial local

expansion of the metallic lattice. With increasing coverage, the repulsive interaction among the more densely packed adsorbates decreases the preference for on-surface adsorption; eventually O penetration may then become more favorable than a continued filling of the on-surface sites. Therefore, O incorporation into the subsurface region commences at progressively lower coverage for the late 4d transition metal sequencing from Ru to Ag.

STM studies of the O–Ru(0001) surface [128, 129] implied that a subsurface oxygen layer is preferred, and the bond nature of the different phases is entirely different. In a velocity-distribution spectroscopic study, Gibson et al. [130] suggested that both the subsurface and the on-surface oxygen coexist and they share common kinetics. Ganduglia and Scheffler [118] proposed that at higher coverage, oxygen might occupy either the fcc(111) or the hcp(0001) hollow site of the Rh(111) surface due to the small difference in binding energy between these two sites in computation. Table 3.10 gives information about the O–Ru(0001) and the O–Rh(111) surface reconstruction determined using LEED and DFT.

In the DFT studies, Stampfl et al. [120] found that an oscillation takes place of both the work-function change ($\Delta\phi$) and the dipole moment with increasing oxygen coverage on the Ru(0001) surface. The dipole moment reaches its maximum at 0.5-ML oxygen coverage and then drops down swiftly. Madey et al. [131] observed that $\Delta\phi$ decreases from its maximal 1.2 eV at 0.75 ML with increasing oxygen coverage. In observing oxygen motion on the Ru(0001) surface with STM, Renisch et al. [132] found it is essential to include the lateral interaction in modeling the collective phenomena such as surface diffusion or reaction.

Figure 3.20 presents the STM images for the $p(2 \times 2)$ -O and $c(2 \times 2)$ -2O phases at the Ru(0001) surface [128, 136]. Figure 3.21 shows models for the O–Rh(111) [133, 137] and O–Ru(0001) surfaces [119, 120] determined by LEED and DFT. The on-surface oxygen adsorbate derives the ‘radial’ and ‘pairing-row’ structure patterns at the surfaces. Similar STM patterns have been observed from O–Au(111) [138] and Ag(111)[139] surface after prolonged annealing in oxygen (1 bar) at 800 °C.

3.5.2 Formulation: Bond Geometry and Atomic Valence

The electronic configuration is $4d^75s^1$ and $4d^85s^1$ for Ru and Rh, respectively. The electronegativity of both Ru and Rh is of the same value of 2.2. Their atomic radii [$a = 2.672(\text{Ru})$ and $2.684(\text{Rh})$ Å] are comparable. The top two layers of both hcp(0001) and fcc(111) surfaces share the same lattice geometry, packing in an AB order. The tetrahedral hcp(0001) site is more favorable than the fcc(111) hollow site to facilitate an R_4O tetrahedron. The nature and kinetics of the R_4O cluster bonding and its consequences on the atomic valence and surface morphology for the two systems can be formulated as follows.

Table 3.10 Structural information of O–Rh(111) ($D_{\text{bulk}} = 2.20 \text{ \AA}$) and O–Ru(0001) surface reconstruction (units in \AA)

| O position | $-\text{DO}_z$ | DO_s | D_{12} | D_{23} | Bond length | $D_{//}$ |
|-------------------------------|----------------|---------------|--------------|--------------|-------------|------------------|
| Rh(111)-fcc | | | | | | |
| (2 × 1) (LEED) [122] | 1.22 | 0.05 | 2.23 | 2.21 | 1.92; 2.01 | 0.03 radial |
| (2 × 2) | 1.24 | 0.03 | 2.11 | 2.21 | 2.00 | −0.07; −0.01 |
| (2 × 1) | 1.18 | | 2.19 | 2.19 | 1.95 | Pairing-row |
| (1 × 1) (DFT) [118] | 1.16 | | 2.37 | 2.25 | 2.00 | 0.02 radial |
| (2 × 2) | 1.24 | 0.03 | 2.25 | 2.19 | 1.95 | −0.06; −0.01 |
| (2 × 1) | 1.23 | | 2.24 | 2.19 | | Pairing-chain |
| (1 × 1) (LEED) [133] | 1.16 | | 2.37 | 2.25 | | |
| Ru(0001)-hcp | | | | | | |
| (2 × 1) (LEED) [124] | 1.25 | | | | ~2.02 | Pairing-row 0.12 |
| (2 × 2) (LEED) [134] | 1.22 ± 0.02 | | 2.26 | 2.25 | 2.03 ± 0.06 | 0.09 |
| (2 × 2) | 1.3 | | 2.10 | 2.16 | 2.03 | Radial |
| (2 × 1) | 1.26 | | 2.14 | 2.18 | | Pairing |
| (1 × 1) (DFT/LEED) [119, 120] | 1.25 | | 2.22(+2.7 %) | 2.13(−0.9 %) | | Buckle-in |
| (2 × 1) (0.6 ML) | 1.23 | | 2.14 | 2.15 | | |
| (1 × 1) (0.9 ML) | 1.19 | | 2.17 | 2.11 | | |
| (1 × 1) (1.6 ML) MEIS [135] | 1.16 | | 2.22 | 2.10 | | |

Reprinted with permission from [1]

*Z-axis is directed into the bulk. DO_s stands for the lateral dislocation of oxygen. $D_{//}$ is the lateral dislocation of R atoms

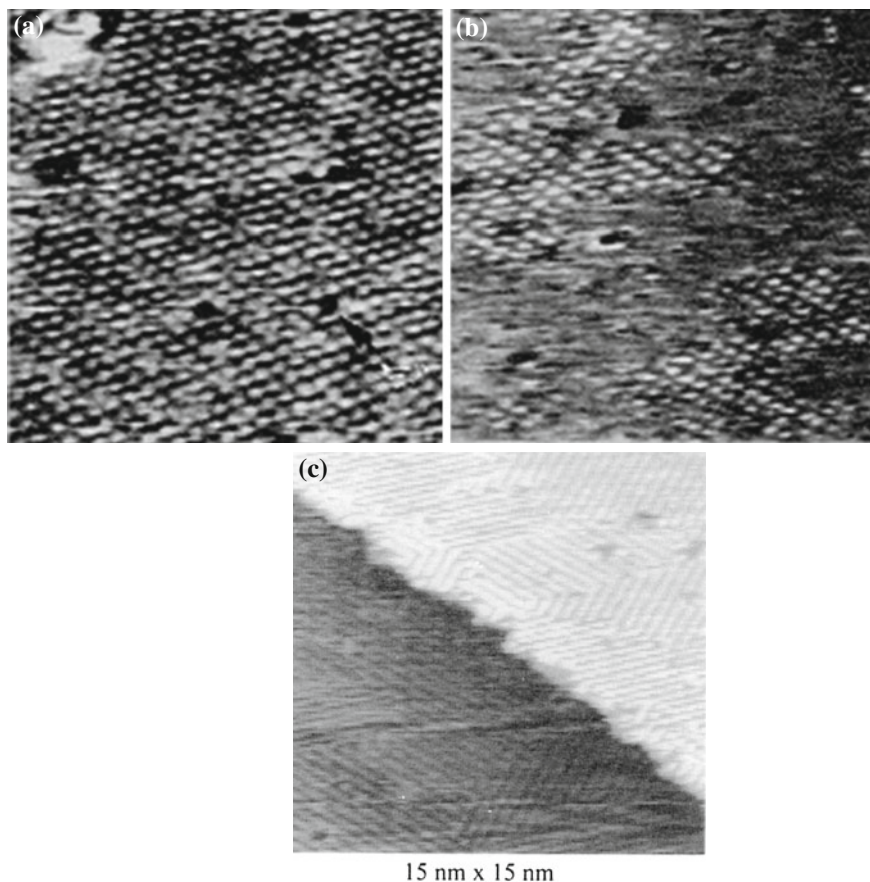
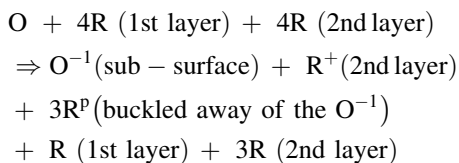


Fig. 3.20 STM images of Ru(0001) surface with chemisorbed oxygen at 400 K. The images correspond to **a** 0.20 ML, **b** 0.25 ML, and **c** 0.5 ML exposures, respectively. The $p(2 \times 2)$ -O (radial) and the $p(2 \times 1)$ -O (pairing-row) structures are fully developed at 0.25 and 0.5 ML (reprinted with permission from [1, 128, 136])

3.5.2.1 O^{-1} Effect ($\Theta_O = 0.25$ ML): Radial Reconstruction with C_{3v} Symmetry

For the $p(2 \times 2)$ - O^{-1} precursor phase, the reaction can be expressed as:



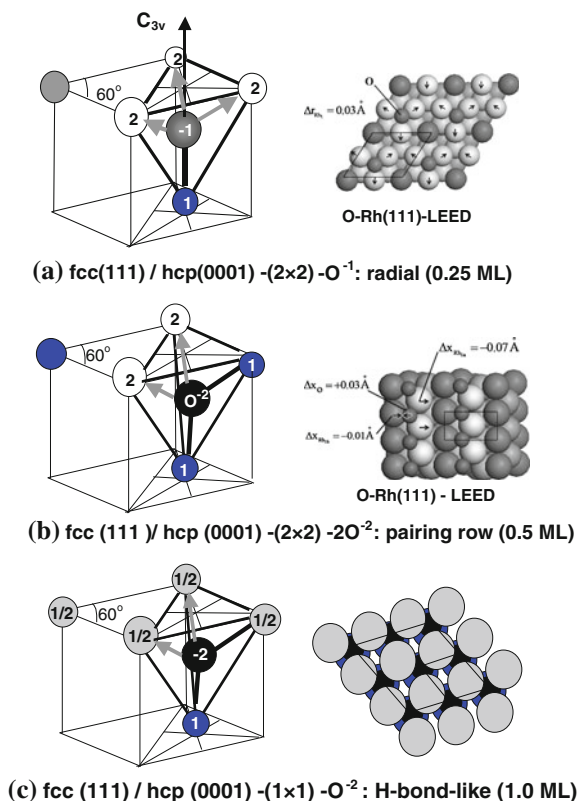
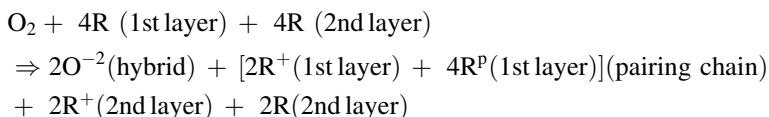


Fig. 3.21 R₄O cluster bonding (reprinted with permission from [137, 140]) and the reconstruction models for the O–Rh(111) [118, 133] and the O–Ru(0001) surfaces of C_{3v} symmetry [119, 120]. **a** At $\Theta_{\text{O}} \leq 1/4$ ML coverage, O⁻¹ locates in the center of one of the four tetrahedral sites to form one bond with the atom labeled 1. The O⁻¹ induces and pushes the dipoles labeled 2 radially away and the C_{3v} symmetry remains, producing the clusters of STM protrusion. **b** At $\Theta_{\text{O}} \leq 1/2$ ML, O⁻¹ evolves into O⁻² by forming another bond with a surface R atom labeled 1. The lone pairs sustain the dipoles (labeled 2). The dipole and ionic row move closer toward the sites without adsorbates, which generates the pairing-STM protrusion-depression patterns. **c** At $\Theta_{\text{O}} \leq 1.0$ ML, H-like bonds dominate at the surface. Two lone pairs polarize each surface R atom (1/2) which donates meanwhile one electron to other adsorbate. Formation of the H-like bonds restores the reduced work function and lowers the STM protrusions. The entire surface network is stabilized and becomes unreconstructed and restores the C_{3v} crystallographic symmetry (reprinted with permission from [1])

Instead of locating above the top layer, oxygen atom tends to sink into the center of one of the four C_{3v} tetrahedral sites to form an R₄O cluster (Fig. 3.21a). Oxygen forms one bond with the R (labeled 1) underneath. The O⁻¹ then polarizes and pushes its three surface neighbors (labeled 2) radially outwards. Therefore, the C_{3v} symmetry remains. The clustered dipoles are responsible for the STM protrusions. At the surface, there is still a metal atom in a unit cell.

3.5.2.2 O^{-2} Effect ($\Theta_O = 0.5$ ML): Paring-row Reconstruction

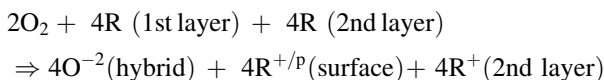
The $p(2 \times 1)-O^{-2}$ or $c(2 \times 2)-2O^{-2}$ phase can be decomposed as:



At this stage, oxygen forms the second bond with one (labeled 1) of its three surface neighbors and then the *sp* orbitals of oxygen start to hybridize (Fig. 3.21b). The number of dipoles of the same R_4O tetrahedron reduces from three to two. The lone pairs of oxygen replace the role of O^{-1} in sustaining the R^P (labeled 2). On the surface, the atoms with altered valences form the alternative rows of protrusion (R^P) and depression (R^+), and the original C_{3v} symmetry of the tetrahedron breaks, as predicted by the DFT and LEED optimizations and detected with STM imaging. The valence of the R^+ underneath the O^{-2} remains. The mechanism for the surface relaxation is common to the situations addressed in previous sections, that is, the bond geometry determines the first-layer expansion and the altered atomic valence in the second layer shortens the second interlayer spacing.

3.5.2.3 O^{-2} Effect ($\Theta_O = 1.0$ ML): H-like Bond Dominant

The $p(1 \times 1)-O^{-2}$ phase on the C_{3v} surface can be formulated as:



As shown in Fig. 3.21c, oxygen adsorbates have occupied all the tetrahedral sites on the surface. Each adsorbate needs one R atom for the bond and two to be polarized at the surface. Because the atomic ratio $O:R = 1$, each of the surface R atoms has to interact with three oxygen neighbors through one ionic bond and two lone pairs. Therefore, all the R^+ and R^P at the surface turn to be $R^{+/P}$ (labeled 1/2), and hence, H-like bonds dominate at the surface. In such a way, the surface dipole moment and the dipole-related $\Delta\phi$ are weakened substantially, and the surface becomes unreconstructed in crystallography, agreeing with the DFT calculations and work-function measurements, as mentioned above. This trend is the same as that occurred to the (Co, Ru)(10 $\bar{1}$ 0)- O^{-2} surfaces and the (Rh, Pd)(110)- O^{-2} surfaces at higher oxygen coverage.

The analysis strongly supports the model of subsurface oxygen formation though most of the numerical optimizations favor an on-surface oxygen mechanism (see Table 3.10) for oxygen chemisorption on these C_{3v} surfaces. One cannot, however, exclude the possibility of multiple numerical solutions due to the correlation among the parameters and the initial conditions used in optimization, as discussed earlier. Nevertheless, existing grounds rule out the possibility that three identical bonds

form and remain unchanged throughout the course of reaction. If the oxygen is located above the top layer and bonds to its three surface neighbors identically, one could explain neither the interlayer relaxation nor the STM protrusions. The on-surface oxygen mechanism should shrink the D_{12} instead, as the R^+ reduces its size considerably and the R^+ produces STM depressions under normal tip conditions.

Actually, the adsorbate, whether it is O^{-1} or O^{-2} , retains always at the nearly central position of the oxide tetrahedron throughout the course of reaction with the C_{3v} surfaces. What happens is that the O valance and coverage change to alter the surface symmetry and surface atomic valence. The striking significance of the precursor is that the O^{-1} polarizes all of its surface neighbors that maintain the original C_{3v} symmetry. O^{-2} forms two ionic bonds with the host atom in the $p(2 \times 1)-O^{-2}$ phase or electron clouds in the $p(1 \times 1)-O^{-2}$ phase, which breaks the C_{3v} symmetry. The O^{-2} polarizes its two atomic neighbors through the lone-pair interaction. The O^{-2} should be slightly off-centered inside the tetrahedron by an amount that might be too small to be detectable. The oxidation alters the valences of O into the O^{-1} and the O^{-2} , and the R atoms into the R^+ , the R^p and eventually the R^{+p} with the measurable variation in $\Delta\phi$ and the surface dipole moment. The real process of oxidation is that electron transport dominates and oxygen adsorbates reside inside the bulk rather than float atop the surface of larger atomic size.

In summary, oxygen adsorbates sink into and remain at the hcp(0001) hollow sites throughout the course of reaction with the C_{3v} surfaces of large atomic size. During the process of reaction, the R_4O cluster configuration remains the same but the valences of atoms at the surface change continually and substantially. The O^{-1} reconstructs the surface in a radial mode, and then, the O^{-2} produces the pairing-row pattern. Further exposure to oxygen ($\Theta \geq 0.5$ ML) yields the $p(1 \times 1)-O^{-2}$ phase in which H-like bonds are dominant, which stabilize the surface by annihilating the R^p into R^{+p} . The H-like bond formation interlocks all the surface atoms, which shall form a barrier protecting the substance from being attacked by further diffusion of the adsorbate [141]. This conclusion should be valid for other fcc(111) and hcp(0001) surfaces of larger lattice size with chemisorbed oxygen. A DFT calculation of Ganduglia et al. [142] suggests that oxygen switches from the on-surface fcc site to the subsurface hcp sites of the Rh(111) plane and indicates that at even higher coverage oxygen incorporation is followed by oxygen agglomeration in two-dimensional subsurface islands directly below the first metal layer. Inside these islands, the metastable hcp/octahedral (on-surface/subsurface) site combination will undergo a barrier less displacement, introducing a stacking fault of the first metal layer with respect to the underlying substrate and leading to a stable fcc/tetrahedral site occupation. The subsurface oxygen atoms in tetrahedral sites are fourfold coordinated to metal atoms. These elementary steps, namely, oxygen incorporation, aggregation into subsurface islands, and destabilization of the metal surface are more general and precede the formation of a surface oxide at close-packed transition metal surfaces. A DFT calculation by Reuter et al. [143] predicted that the oxidation of the Ru(0001) surface proceeds via the accumulation of subsurface oxygen in two-dimensional islands between the first and second substrate layers. This leads locally to decoupling of an O–Ru–O tri-layer from the

underlying metal. Continued oxidation results in forming and stacking of these trilayers, which unfold into the $\text{RuO}_2(110)$ rutile structure once a critical film thickness is exceeded. Along this oxidation pathway, they identified various metastable configurations in which oxygen occupies the octahedral and tetrahedral sites, respectively. These configurations are rather close in energy, indicating a likely lively dynamics between them at elevated temperatures.

3.6 O-(Ag, V)(001)

3.6.1 O-Ag(001)

3.6.1.1 Crystallography and Morphology

Oxygen chemisorption could induce two different phases on the Ag(001) surface [144], which is the same to those happened to the Cu(001) but in an opposite order. At low temperatures, the system displays a $c(2 \times 2)$ LEED pattern with an EELS peak at 37 meV. By increasing the temperature from 180 to 300 K, a transition to a (1×1) LEED pattern happens at 247 K, and the EELS peak shifts from 37 meV to a lower value of 30 meV. The EELS shift indicates the softening of the stretching vibration of the oxygen adsorbate through nonbond interaction. This phase transition is reversible. It is interpreted that the high-temperature (1×1) structure correspond to full oxygen coverage ($\Theta = 1$ ML), while the low-temperature $c(2 \times 2)$ structure arise from a lower coverage ($\Theta = 0.5$ ML), with a substantial amount of oxygen adsorbed on the subsurface. A combination of LEED, HREELS, XPS, and XPD [145] confirmed the existence of this reversible phase transition but led to a different structural model. The estimated oxygen coverage is never greater than 0.4 ML. Atomic oxygen would sit in the fourfold hollow site at low temperature to result in the same to the O-Cu(001) second phase with the Cu_3O_2 pairing-tetrahedron configuration. In the second phase, oxygen atoms sit in the hollow sites near the Ag missing rows of the substrate and thus gives rise to a $c(2 \times 2)$ LEED pattern. A first principle DFT calculation [146] suggested that the MR reconstruction degenerates in energy with the non-reconstructed $c(2 \times 2)$ structure, both of which share the same LEED pattern.

DFT-derived geometrical details differ slightly from those inferred from XPD measurements [144]. The surface fourfold-coordinated hollow sites and the subsurface fivefold-coordinated hollow sites are most stable, practically degenerated, and separated by an energy barrier of ~ 25 meV or less. The first Ag interlayer spacing expands by up to 30 % upon oxygen adsorption [146]. According to the XPD [145], oxygen adsorbates displace laterally by 0.36 \AA toward the missing row and shift down vertically by 0.15 \AA below the top Ag atoms. The Ag atoms close to the missing row shift up by 0.3 \AA and laterally by a negligible amount.

The overall missing-row structure coincides with the $\text{Cu}(001)-(\sqrt{2} \times 2\sqrt{2})\text{R}45^\circ-2\text{O}^{-2}$ phase which is dominated by the Cu_3O_2 structure where oxygen atoms

move away from the missing row and go below the Cu atoms by ~ 0.16 Å near the missing row for the tetrahedron formation. The Cu^p shifts up and relaxes laterally toward the missing row by ~ 0.25 Å to form the ‘dumbbell’ protrusion cross over the missing row.

The significant difference between the O-Cu(001) and the O-Ag(001) is the critical temperature for phase transition. Missing row forms at ~ 700 K on the O-Cu(001) surface while it forms at 246 K on the O-Ag(001) surface. XPS profiles [145] from O-Ag(001) show that the lower binding energy component of the O 1s (528.3 eV) increases its intensity with temperature at an expenses of decreasing the high binding energy (530.9 eV) peak that dominates at $T \leq 300$ K. This binding energy weakening is also in line with the $37 \rightarrow 30$ meV EELS peak transition. The transition of both the XPS binding energy and the EELS stretching energy indicates that the O-Ag(001) surface undergoes a phase transition from stable to less stable when aging at ~ 246 K for 3,200 s.

With oxygen adsorption, an additional DOS feature at -2.0 to -3.0 eV emerges [145, 147], which agrees with those observed from the O-Ag(110) (-1.5 to -3.3 eV)[148] and O-Ag(111) (-2.0 eV)[149] surfaces. These features arise from the nonbonding lone pairs of O⁻² instead of the O 2p-states alone [145].

3.6.1.2 Lattice Scale Effect

Ag and Cu share the same electronegativity (1.9), the same lattice geometry, but different atomic sizes (1.276/1.442). The O-Ag(001) bi-phase structures are partly analogies of the O-Rh(001) and the O-Cu(001) surfaces. The fivefold-coordinated oxygen is the same as that in the Rh(001)- $c(2 \times 2)$ - $2O^{-1}$ phase. The low-temperature MR structure is the same as that of the Cu(001)- $(\sqrt{2} \times 2\sqrt{2})R45^\circ$ - $2O^{-2}$ phase. Like neither the transition from CuO₂ pairing-pyramid to the Cu₃O₂ pairing-tetrahedron on the Cu(001) surface nor the transition from the Rh₅O to the rotated Rh₄O on the Rh(001) surface, the O-Ag(001) surface transits from the Ag₅O to the Ag₃O₂ at much lower critical temperature. This intriguing inverse order of phase transition results from nothing more than the large atomic size ($r_{Ag} = 1.442$ Å) of Ag atom. At low temperature, O⁻² is more stable than the O⁻¹ according to the XPS and EELS spectral features. The O⁻² de-hybridizes at a temperature of 246 K that is lower than ~ 700 K for the Cu(001) surface [16].

3.6.2 O-V(001)

3.6.2.1 Observations

STM images in Fig. 3.22 show apparently the bi-phase structures beside the visible dark lines arranged regularly on the surface along the $\langle 10 \rangle$ directions [150]. The distance between the dark lines is usually 4–6 vanadium $\langle 10 \rangle$ lattice constants,

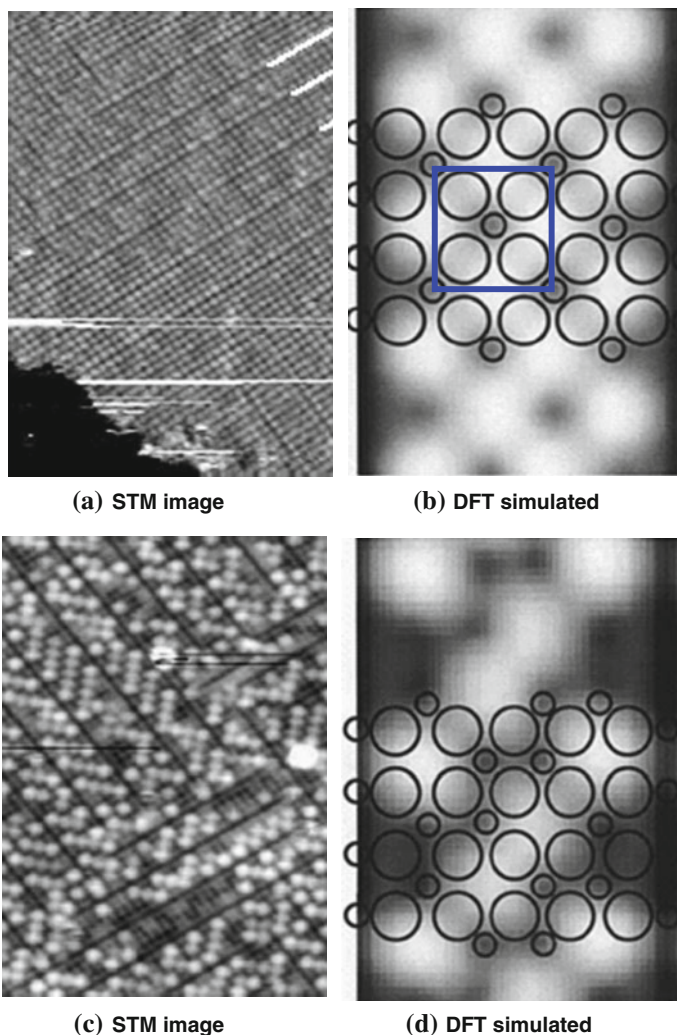


Fig. 3.22 STM images of the O-V(001) bi-phase structures (reprinted with permission from [150]) and the hard-sphere models for (a, b) the $V(001)-c(2 \times 2)-2O^{-1}$ and (c, d) the $(\sqrt{2} \times 3\sqrt{2})R45^\circ-4O^{-2}$ phases. The first phase (a) is composed of V_5O . The second phase consists of the V_4O tetrahedron. In the second, the zigzagged O-O chain forms along the $\langle 11 \rangle$ direction (Reprinted with permission from [1])

and, therefore, a (1×5) reconstruction mode presents. In the simulated STM images, the fourfold hollow sites occupied by oxygen atoms appeared as dark spots, while the unoccupied hollow sites remain bright. The first phase within the domain is the same as the $Rh(001)-c(2 \times 2)-2O^{-1}$ phase (R_5O pyramid). Oxygen occupies the next-nearest fourfold hollow site and induces the radial reconstruction, as indicated in the STM image (b), at oxygen coverage of $2/3$ ML.

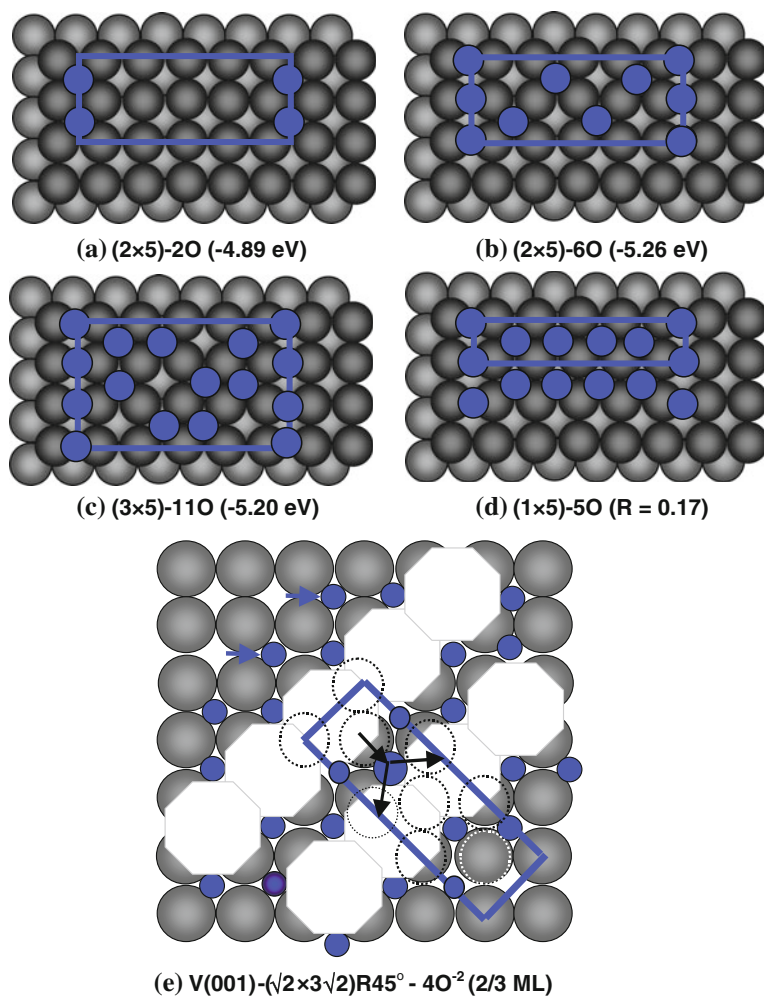


Fig. 3.23 Comparison of the structural models. Ab initio optimization of **a** the C_{4v} -hollow-sited oxygen in the dark lines and the arrangement of oxygen for **b** the first and the **c** second phase as observed with STM. Panel **d** shows the LEED optimal structure for the reconstructed surface at higher oxygen coverage. Panel **e** is a short-ordered $\text{V}(001)\text{-}(\sqrt{2} \times 3\sqrt{2})\text{R}45^\circ\text{-}4\text{O}^2$ ($2/3$ ML) reconstruction with O^{2-} -centered tetrahedron (reprinted with permission from [1])

With increasing oxygen coverage to ~ 0.73 ML, the second phase appears, in which the dark lines remain. The short-ordered, zigzagged O–O chains form along the $\langle 11 \rangle$ direction. The bright spot is composed of four atoms.

Figure 3.23b, c shows the optimal structures at higher oxygen coverage with binding energies of -5.26 and -5.20 eV, respectively. The oxygen atoms in the dark lines now prefer the bridge sites in the two phases involving the reconstructed domains compared with the initial phase of oxidation.

LEED optimization [150] with a total number of 26 independent parameters leads to a structural model for the second phase (Fig. 3.23d). The oxygen atoms in the bridge sites reside 0.12–0.18 Å above the top vanadium layer, while oxygen atoms in the C_{4v} hollow sites are ~ 0.5 Å above the top layer. The structural discrepancy determined by different methods corresponded to: (1) the ab initio data are for $T = 0$ K, whereas the LEED was taken at room temperature; (2) the involvement of the (1×4) and (1×6) superstructures may influence the LEED measurements. Nevertheless, both the LEED and DFT optimization revealed an expansion of the first-layer spacing (+4.2 %) and a contraction (−3.2 %) of the second with respect to the clean V(001) surface that contracts by −7 to −8.5 % (LEED) or −15 % (DFT).

3.6.2.2 Formulation

Disregarding the accuracy in the vertical positions of the adsorbates in the dark lines, the bi-phase structure for the O–V(001) surface can be formulated. The formula for the first O^{-1} -derived phase may refer to that for the Rh(001)– $c(2 \times 2)$ – $2O^{-1}$ ($\Theta = 1/2$ ML) surface which showed the radial reconstruction. The oxygen forms a bond with a Vanadium atom underneath and then polarizes the surface neighbors, which form the V_5O structure. With the increase in oxygen coverage, the O^{-1} evolves into the O^{-2} that gives rise to the short-ordered $(\sqrt{2} \times 3\sqrt{2})R45^\circ$ – $4O^{-2}$ phase at $\Theta = 2/3$ ML:

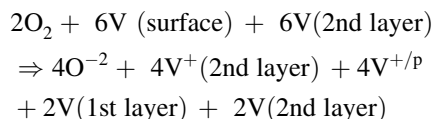


Figure 3.23e shows the V(001)– $(\sqrt{2} \times 3\sqrt{2})R45^\circ$ – $4O^{-2}$ complex unit cell. The bright protrusions correspond to $V^{+/p}$. Compared with the patterns of reconstructions on the fcc(001) surface of Cu and Rh, the V(001)–O surface exhibits a quite different pattern of reconstruction.

Two outstanding issues need to be clarified. One is the inconsistency between structures determined by LEED and DFT/STM observations; the other is the oxygen coverage. AES detected higher oxygen coverage (0.67 and ~ 0.73 ML for the two phases, respectively), but the models give only 1/2 and 2/3 ML ideally for the two corresponding phases. The structural discrepancy arises from the huge LEED parameter space that warrants nonunique solutions [70]. Agreement between the STM and the DFT results supports each other, which may indicate the essentiality of searching for other possible numerical solutions in LEED optimization, such as subsurface oxygen.

Modeling analysis conducted here insofar indicates that the oxygen adsorbate always tends to be located inside the tetrahedron. On the other hand, the V atoms in the center of the bright protrusions are expected to be missing as these V atoms

interact with no oxygen atoms, but they experience strong repulsion from the neighboring V^{+P} . The expected V missing reduces the number of V atoms at the surface layers. In addition, the density of oxygen in the dark lines is higher than the oxygen atoms inside the reconstructed domains. This configuration further increases the surface atomic ratio of O:V. These two factors could account for the difference in the oxygen coverage between the AES measurement and the model specification.

A comparison of the O-(Cu, Rh, Ag, V)-(001) surface reconstruction suggests that difference in atomic size and in electronegativity give rise to the entirely different patterns of reconstruction on the four surfaces of the same lattice geometry. The process of tetrahedron bond formation is the same despite the transition temperatures and the corresponding patterns of observations.

3.7 O-Rh(001) and (N, C)-Ni(001)

3.7.1 Observations

With increasing oxygen exposure of the Rh(001) surface, three outstanding phases form sequentially, as identified using LEED [151–153], STM, SPA-LEED and PES [154, 155]. The disordered $p(2 \times 2)$ -O phase ($\Theta = 1/4$ ML) forms first, then the $c(2 \times 2)$ -2O ($\Theta = 1/2$ ML) radial reconstruction, and, finally, the $c(2 \times 2)p4g$ -2O ($\Theta = 1/2$ ML) clockwise and anticlockwise rotation of the unit cells. These reconstruction patterns are the same as those occurring on the Ni(001) surfaces with chemisorbed carbon and nitrogen.

Figure 3.24 shows the STM images of the two ordered phases for the O-Rh(001) surface. Oxygen adsorbate fills in the next-nearest fourfold hollow site of the Rh(001) surface, in the same way as that of oxygen on the Cu(001) surface. It can be seen that both the $c(2 \times 2)$ -2O and the $c(2 \times 2)p4g$ -2O phases require the same local oxygen coverage of $1/2$ ML. Formation of these two ordered phases depends not on the local oxygen coverage but rather on the overall oxygen exposure [154].

Direct LEED studies revealed, however, that oxygen resides in hollow sites of the Ni(001) surface [156, 157] to form bond between oxygen and the nickel atom underneath without any rotation [158]. The first interlayer spacing expands and the second contracts.

Figure 3.24c shows a centered-pyramid model for the ‘p4g’ clock reconstruction [156, 160, 161]. The model indicates that a ‘stress release’ provides forces driving the ‘radial’ reconstruction phase to transit into the ‘clock’ rotation. The oxygen adsorbate was determined to locate $DO_z > 0.6$ Å above the C_{4v} hollow site and form a centered pyramid with the four Rh atoms at the surface [162]. The compressive stress of the pyramid in the Rh(001)- $c(2 \times 2)$ -2O surface is released through the rotation of the Rh_4O pyramid. The release of stress provides the forces that drive the reconstruction while the basic R_4O pyramid remains during the process of reconstruction despite a slight change of the vertical position of the oxygen.

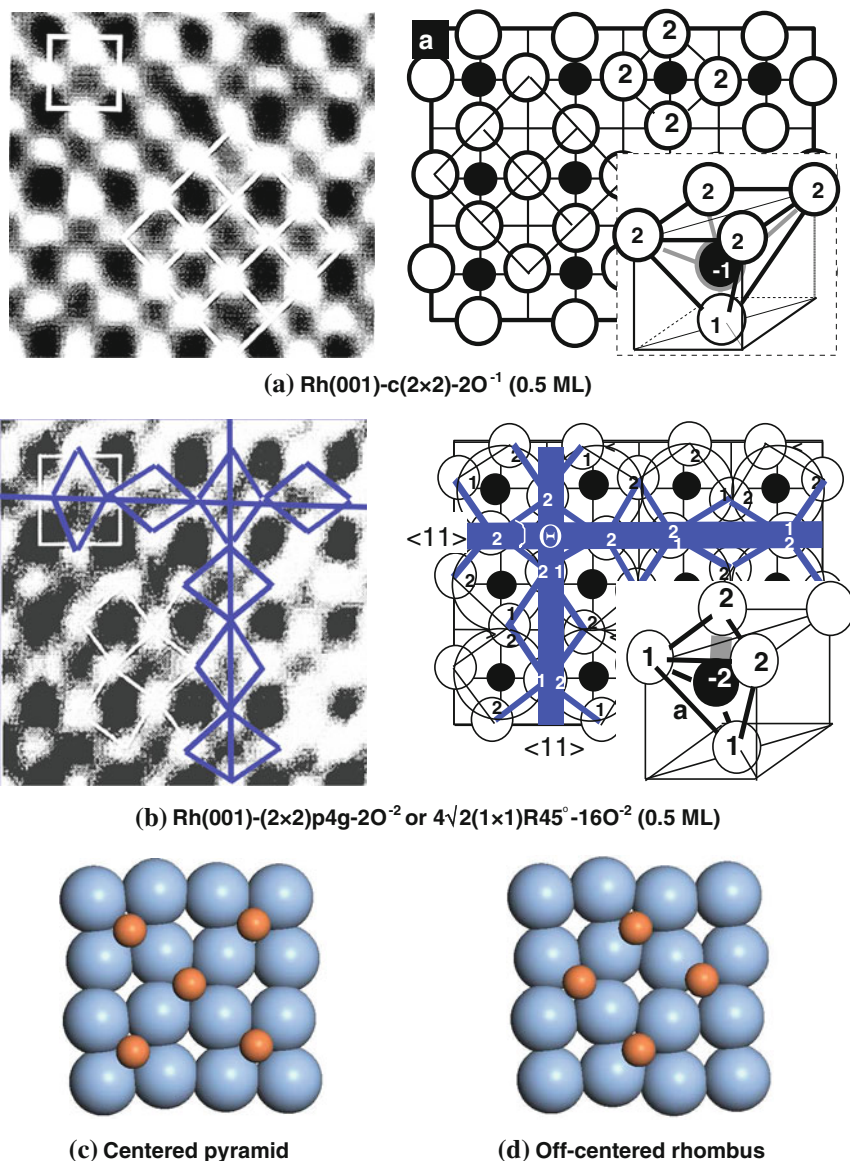


Fig. 3.24 STM images (reprinted with permission from [154]) and models [159] for **a** the Rh(001)-c(2 × 2)-2O⁻¹ radical, and **b** the 4√2(1 × 1)R45°-16O⁻² phases. O⁻¹ results in a Rh₅O pyramid (inset) with 4Rh^p at the surface, which evolves into the O⁻²-centered Rh₄O tetrahedron (inset) turning half of the surface atoms to be Rh^p (labeled 2) and another half Rh^{+p} (labeled 1/2). The equilibrium of the electrostatic forces and bond stress create rhombi chains along the <11> directions. **c** the ‘centered pyramid’ [156] and **d** the ‘off-centered rhombus’ [105] hard-sphere models (reprinted with permission from [1])

Figure 3.24d shows an alternative for the Rh(001)– $c(2 \times 2)p4g-2O$ second phase [108, 163, 164]. The adsorbate prefers the site eccentrically above the ‘rhombus’ and jumps back and forth along the longer axis of the rhombus. XRD measurement suggested that in the second ‘p4g’ phase, the Rh atom is displaced eccentrically by $0.19 \pm 0.05 \text{ \AA}$ in the plane along the $\langle 11 \rangle$ direction [165]. The oxygen atom is situated in the rhombus sites with an in-plane shift of $0.20 \pm 0.05 \text{ \AA}$ on either side of the center.

The ‘off-centered-rhombus’ model leads to a conclusion [108] that for all the Rh(001), (110), (111) surfaces at medium–high oxygen coverage, oxygen adsorbate tends to locate at an apical site of a tetrahedron and to form three identical bonds with the Rh atoms. So Rh_3O tetrahedron displays a C_{3v} point-group symmetry and the lengths of all the three O–Rh bonds in the Rh(001), (110), (111) surfaces to be in the range of 2.00–2.06 \AA with the Rh–O–Rh bond angle of around 90° . Table 3.11 features the geometrical information for the ‘p4g’ reconstruction for the Rh(001)– $4\sqrt{2}(1 \times 1)R45^\circ-16O^{-2}$ and the Ni(001)– $4\sqrt{2}(1 \times 1)R45^\circ-16(N^{-3}, C^{-4})$ surfaces. This $4\sqrt{2}(1 \times 1)R45^\circ$ notion is preferred as it represents the complex unit cell with full periodicity containing 16 adsorbates.

STM images in Fig. 3.25a, b for the ordered Ni(001)– $4\sqrt{2}(1 \times 1)R45^\circ-16C^{-4}$ [174] and Ni(001)– $4\sqrt{2}(1 \times 1)R45^\circ-16N^{-3}$ [173] surfaces exhibit the same type of ‘clock’ reconstruction occurring on the O–Rh(001) surface albeit the slight difference in the rotation angles. However, the calculated STM image shows the C atoms as depressions while in the experiment, a small protrusion is resolved [175]. The Ni(100)– $4\sqrt{2}(1 \times 1)R45^\circ-16N^{-3}$ STM image exhibits two orientations of the depressions. With slight deviation, one is along the [10] direction and the other closes to the [01] direction. This provides the opportunity for one to identify the atomic valences of N at the surface.

Kirsch and Harris [176] calculated Ni(001) surface reconstructions induced by C, N, and O adsorption and suggested that C and N atoms prefer the nearly coplanar sites with the top Ni surface, which induce the ‘clock’ reconstruction of the surface. However, O atoms prefer sites slightly above the Ni(100) surface plane and have little effect on the overall surface structure. The local environments of the C, N, and O atoms on these surfaces are similar to their environments in a series of late transition metal carbonyl clusters, suggesting that some of the same electronic factors may play a role in favouring different structures. Results of the calculations suggest that adsorbates occupy coplanar sites on Ni(100) surface disrupt the Ni–Ni bonding within the surface layer and bonds between the surface and second layers.

On the C- and N-covered surfaces, the disruption is overcompensated by the formation of strong adsorbate–Ni bonds and by new Ni–Ni surface bonds resulting from the clock reconstruction. When O is forced into a coplanar site, however, both the higher electron count and increased electronegativity of the O atoms lead to severe disruption of the surface bonding and the formation of weak Ni–O bonds. When O atoms sit above the surface, they form more polar Ni–O bonds, contribute less electron density to the Ni surface bands, and cause less disruption to the Ni–Ni surface bonds. These results suggest that similar to the organometallic clusters, the

Table 3.11 Atomic geometry of the Rh(001)- $4\sqrt{2}(1 \times 1)R45^\circ-16O^{-2}$ surface ($D_{12} = 1.902 \text{ \AA}$; z is directed into the bulk) and the Ni(001)- $4\sqrt{2}(1 \times 1)R45^\circ-16(N^{-3}, C^{-4})$ surfaces (reprinted with permission from [1])

| Model (references) | DO_z | DO_s | $D_{(11)}$ | D_{12} | D_{23} |
|---|---|------------------|-----------------|------------------|-----------------|
| Off-centered rhombus model [105] For O-Rh(001) | O-Rh(001) (LEED) [108] (DFT) [163] | 0.29 ± 0.15 | 0.2 ± 0.07 | 1.94 ± 0.05 | 1.87 ± 0.03 |
| | DFT [164] | 0.21 | 0.35 | 1.922 | |
| | SXRD [165] | 0.20 ± 0.05 | 0.19 ± 0.02 | 1.96 ± 0.05 | |
| Centered-pyramid model [160] for all the 'p4g' | N-Ni(001) (IES) [162] SEAFS [166, 167] | 0.2 ± 0.1 | 0.77 ± 0.10 | | |
| | PED [168] | -0.25 ± 0.05 | 0.55 ± 0.20 | $+0.15 \pm 0.10$ | |
| | SXRD [169] | -0.20 ± 0.10 | 0.30 ± 0.01 | $+0.17 \pm 0.01$ | |
| | C-Ni(001), PED [168] | -0.30 ± 0.05 | 0.55 ± 0.20 | $+0.15 \pm 0.10$ | |
| | LEED [160] | -0.30 ± 0.12 | 0.35 ± 0.05 | $+0.20 \pm 0.05$ | |
| | SEXAFS [170] | -0.2 ± 0.2 | | | |
| | LEED [171] | -0.31 ± 0.05 | 0.45 ± 0.07 | $+0.19 \pm 0.04$ | |
| Rhombus-chain model [172] for all the 'p4g' | Rh ₂ O [172] + STM [154] | >0 | 0.3 | | |
| | Ni ₃ N [172] + STM [173] | >0 | 0.37 | | |
| | Ni ₄ C [172] + STM [174] | >0 | 0.64 | | |

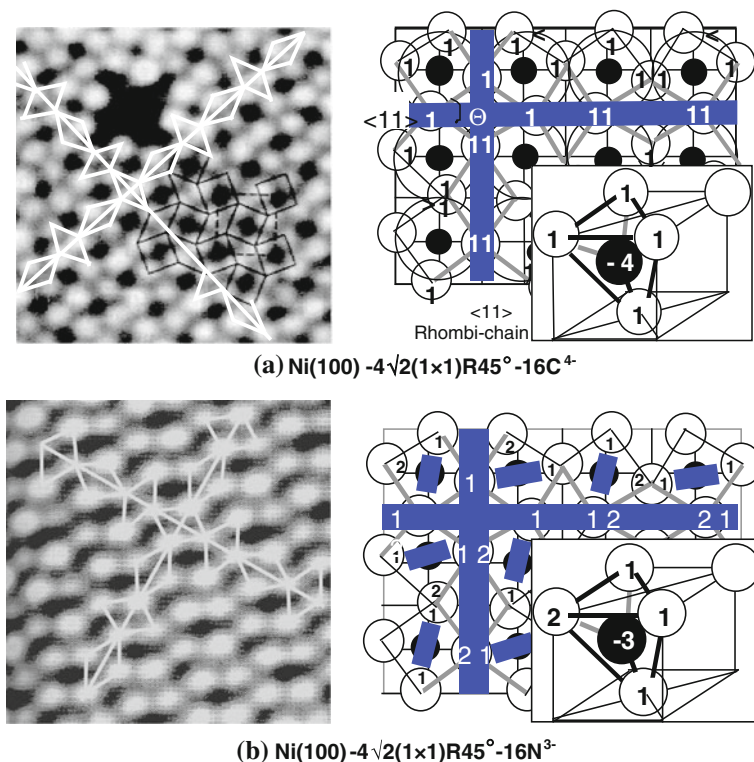


Fig. 3.25 STM images (reprinted with permission from [173, 174]) and models (insertions) for (a, b) the $\text{Ni}(001)\text{-}4\sqrt{2}(1 \times 1)\text{R}45^\circ\text{-}16(\text{C}^{4-}, \text{N}^{3-})$ clock reconstruction. Indicated are individual atomic valences. Although they appeared the same to that of the $\text{Rh}(001)\text{-}4\sqrt{2}(1 \times 1)\text{R}45^\circ\text{-}16\text{O}^{2-}$ phase, the surface atomic valences and the driving forces are different (reprinted with permission from [1])

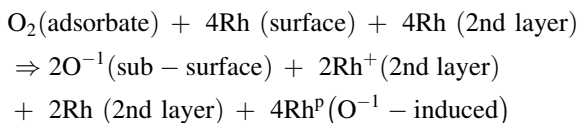
site preferences of C, N, and O atoms are directly related to their electron count, and in turn to the relative occupation of both the Ni–Ni and the X–Ni (X = C, N, O) antibonding bands.

3.7.2 Formulation: Rhombi Chain along the $\langle 11 \rangle$ Direction

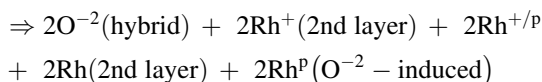
The 3B premise provides an alternative view on the reconstruction suggesting that O, N, and C tend to find their own environment to form the tetrahedron with bond and nonbond creation. Tetrahedron bond formation drives the radial and the subsequent ‘clock’ reconstruction on the O–Rh(001) surface. Meanwhile, the O^{-1} transits into an O^{-2} with sp -orbital hybridization. The sp -orbital hybridization also holds for the C and N when they react with the Ni(001) surface. The electrostatic

force due to charge redistribution drives the p4g reconstruction [172, 177, 178]. The balance of bond tension against the electrostatic force along the $\langle 11 \rangle$ direction stabilizes the clock rotation on the O–Rh(001) and N–Ni(001) surfaces. However, equilibrium of electrostatic repulsion along the $\langle 11 \rangle$ direction and a response of bond compression stabilize the C–Ni(001) clock rotation. Although the patterns of reconstruction and morphologies for the O–Rh(001) and the (C, N)–Ni(001) surfaces are the same, the surface atomic valences and the driving forces are completely different due to different valences of C^{-4} , N^{-3} , and O^{-2} .

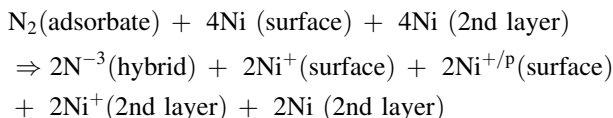
The Rh(001)– $c(2 \times 2)$ – $2O^{-1}$ radial and the subsequent Rh(001)– (2×2) p4g– $2O^{-2}$ clock reconstruction can be formulated as follows (Fig. 3.24a, b):



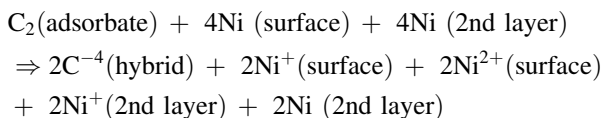
This O^{-1} -induced phase transits into the Rh(001)– $4\sqrt{2}(1 \times 1)R45^\circ$ – $16O^{-2}$ phase (see the corresponding deformed unit cell in Fig. 3.24b):



Similarly, the Ni(001)– $4\sqrt{2}(1 \times 1)R45^\circ$ – $16(N^{-3}, C^{-4})$ surfaces can be formulated as (Fig. 3.25) [172]:



and,



The p4g STM images induced by C^{-4} , N^{-3} and O^{-2} exhibit the same rhombi chain despite the rotation angle. Linking the Ni^+ ions labeled 1 in N–Ni(001) surface (see Fig. 3.25b) matches ideally the orientations of the STM depressions. This configuration verifies that the radius of an Ni^+ ion is much smaller than that of an $Ni^{+/p}$. Therefore, using a proper bonding scheme, one is able to identify individual atomic valence and the bond relaxation dynamics from the STM images.

Table 3.12 features information for the C^{-4} , N^{-3} , and O^{-2} -derived ‘p4g’ phases on the Ni(001) and Rh(001) surfaces. For instance, oxygen sinks into the C_{4v} hollow site in the Rh(001) surface and bonds to the Rh atom underneath. An Rh_5O cluster forms in the $c(2 \times 2)$ – $2O^{-1}$ precursor phase. The O^{-1} polarizes and

Table 3.12 Summary of the geometrical change, driving force F_i , and bond tension T , of the ‘p4g’ clock rotation (Φ) derived from the STM images with the current model [172]

| (2×2) p4g | Rh(100)–O ^{−2} | Ni(100)–N ^{−3} | Ni(100)–C ^{−4} |
|------------------------------|-------------------------|-------------------------|-------------------------|
| Rotation angle Φ (°) | 0.0; 9.0 | 0.0; 12.0 | 0.0; 20.0 |
| $S_{\langle 11 \rangle}$ (Å) | 0.00; 0.30 | 0.00; 0.37 | 0.00; 0.64 |
| Bond strain $\Delta L/L$ (%) | 1.2 | 2.2 | 6.4 |
| Electrostatic forces F_i | 7.99; 11.09 | 8.21; 14.59 | −3.11; −91.17 |
| Bond stress F_b (dyn) | 35.16 | 35.95 | −133.00 |
| Surface atomic states | p; +/p | +; +/p | +; 2+ |

Reprinted with permission from [1]

pushes the electron cloud of the surface atoms radially away from the central adsorbate. In the second phase, the $c(2 \times 2)$ cell deforms into two rhombi (without adsorbate) and two squares with adsorbates inside. The Rh₅O pyramid will evolve into an Rh₄O tetrahedron with an off-centered shift of the adsorbate in the hollow, and one Rh atom at surface will be released from the original Rh₅O pyramid.

As the O^{−2} has already bonded to one Rh atom underneath, the tetrahedron defines one Rh⁺ (labeled 1) and two lone-pair-induced Rh^p dipoles (labeled 2) of the four nearest surface neighbors. The Rh₅O → Rh₄O transition gives rise to the overall ‘p4g’ reconstruction. As can be seen from the primary unit cell containing the adsorbate (Fig. 3.24b), three of the four surface neighbors are labeled with 1, 2, and 2, respectively. Because the surface atomic ratio O:Rh = 1:2 and each oxygen bonds to one atom at surface and needs two atoms to be polarized, half of the overall surface atoms are thus defined as Rh^p and another half as Rh^{+/p}. The Rh^{+/p} contributes to the H-like bond.

One can find that atoms labeled 1 change their positions in a clockwise fashion if one counts the O-occupied hollows along the $\langle 11 \rangle$ direction (gray thick lines). The adsorbate dislocates eccentrically in the $\langle 11 \rangle$ direction in a periodic way. From this point of view, it would be essential and complete to consider a $c(4\sqrt{2} \times 4\sqrt{2})\text{R}45^\circ\text{--}16\text{O}^{-2}$ complex unit cell in practice due to the periodicity of the off-centered adsorbate positions. Strikingly, the ‘rhombi’ hollows without adsorbates form chains along the $\langle 11 \rangle$ direction. The above argument is also applicable to the (N^{−3}, C^{−4})–Ni(001) surfaces.

From the atomic structure point of view, the current tetrahedron description favors the existing hard-sphere models to a considerable extent. Oxygen prefers the site inside (subsurface) the C_{4v} hollow and eccentrically in a periodic way. Most importantly, specification of the valences of the adsorbates gives great detail about the electronic structures, driving forces, and bond stresses of the Rh(001)–O and the Ni(001)–(C, N) surfaces [172].

Although the STM and LEED show similar signatures for these three ‘p4g’ reconstructed surfaces derived by C, N, and O, the underlying mechanisms are quite different. Therefore, the reaction is a process in which charge transportation, and bond switching and relaxation dominate, which give rise to the corresponding features observed by STM and LEED [172].

3.7.3 Quantification: Driving Force and Bond Stress

One can estimate the lateral displacements of the Rh atoms by measuring the sharp angle θ of a rhombus in the STM image. The average value of measured θ is 72° . The unit cell containing the O^{-2} adsorbate rotates by $\Phi = (90^\circ - \theta)/2 = 9^\circ$. This process displaces the Rh atom along the $\langle 11 \rangle$ direction by $S_{\langle 11 \rangle} = \sqrt{2}R \times \text{tg}\Phi = 0.30 \text{ \AA}$, where $R = 1.342 \text{ \AA}$ is the atomic radius of Rh. Table 3.12 features the geometrical change, driving force F_i , and bond stress T of the ‘p4g’ clock rotation (Φ) derived from the C^{-4} , N^{-3} , and O^{-2} -induced ‘p4g’ reconstruction on the fcc(001) surface of Rh and Ni [172].

Inspecting Figs. 3.24b and 3.25, one can find that the surface network is composed of one-dimensional ‘ $-2-(1/2)-(1/2)-2-2-(1/2)-(1/2)$ ’ rhombi chains along the $\langle 11 \rangle$ directions. Labels 1 and 2 represents the valences of ‘+’ and ‘dipole,’ respectively. The electrostatic charges of the Rh^{+p} ($1/2$) and the Rh^p (2) are not equal and the Rh^{+p} is slightly positive compared with the Rh^p that has a negative nature.

The strength of interaction is in the order: $2-2 \approx (1/2)-(1/2) > 0 > 2-(1/2)$. The repulsion between the $2-2$ or $(1/2)-(1/2)$, and the slight attraction between the $2-(1/2)$ determines that the distance of $2-2$ or $(1/2)-(1/2)$ is longer than the distance of $(1/2)-2$. Rhombus formation displaces the Rh atoms along the $\langle 11 \rangle$ direction, and consequently, leads to the overall rhombi-chain network at the surface. The alternate attraction and repulsion along the chain will squeeze the $2-(1/2)$ closer without otherwise a response of bond tension to equilibrate the electrostatic force along the chain.

From Fig. 3.26a, b, it is seen that the bond expands by an amount $\Delta L/L = 1/\cos\Phi - 1 = 1.2 \%$, which is negligible and, therefore, the mechanism of bond-tension-increase rather than the mechanism of bond-compression-release dominates in the $Rh(001)-(4\sqrt{2} \times 4\sqrt{2})R45^\circ-16O^{-2}$ phase transition.

Without knowing the exact dipole moment, one may assume that Coulomb interaction dominates along the rhombi chain that contains infinite number of atoms ($n \geq \pm 100$ is sufficient for calculation). The Coulomb potential V_i and the electrostatic force F_i acting on the i th atom in the rhombi chain are:

$$V_i = \frac{1}{4\pi\epsilon_0} \sum_{i \neq j} \frac{q_j}{r_{ij}} = \frac{1}{4\pi\epsilon_0} \sum_{i \neq j} (-1)^j \left[\frac{1}{(2j-1)a-2s} - \frac{1}{(2j-1)a+2s} \right]$$

$$F_i = -q_i \frac{\partial V_i}{\partial r}$$

The relative charges for Rh^p and Rh^{+p} are defined as $q_i = -\epsilon e$ and ϵe , respectively, by introducing an effective charge factor $\epsilon = \epsilon_c + \Delta\eta(\epsilon_i - \epsilon_c)/2$, which considers the valence screening effect. $\epsilon_c = 0.5$ ($\Delta\eta = 0$) and $\epsilon_i = 1.0$ ($\Delta\eta = 2$) correspond to covalent and ionic states, respectively. For the current O-Rh system, $\Delta\eta = 3.5 - 2.2 = 1.3$, $\epsilon = 0.825$.

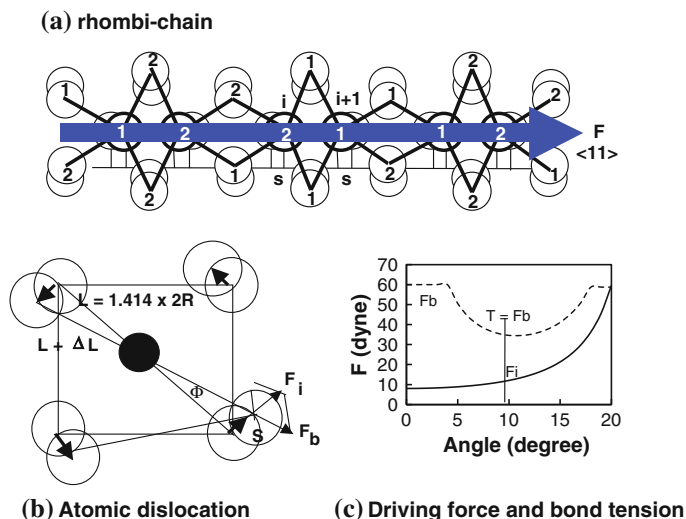


Fig. 3.26 **a** The nonuniform ‘–2–1/2–1/2–2’ rhombi chain along the $\langle 11 \rangle$ direction of the STM images enables the estimation of **b** atomic dislocation, **c** driving force, and bond stress. Labels 2 and 1/2 stand for different valences (refer to Table 3.12) for O^{-2} , N^{-3} , and C^{-4} induced chains. The clock rotation angle Φ is derived from the STM rhombus angle Θ . $\Phi = (90^\circ - \Theta)/2$; $S = \sqrt{2}R \times \text{tg}\Phi$; $\Delta L/L = 1/\cos\Phi - 1$; F_i is decomposed as F_b . **c** Shows the rotation angle dependence of the driving force F_i . Rotation is stabilized at 9° by $T = F_b$. If $\Phi > 9^\circ$, $T > F_b$; otherwise, $T < F_b$ (reprint with permission from [172])

As a component of the electrostatic force F_i , the F_b in Fig. 3.26b balances the bond tension T and hence the clock rotation of the unit cell:

$$F_b = \frac{F_i}{\sqrt{2\{1 + \cos[2(90^\circ - \Phi)]\}}}$$

When the Rh_4O tetrahedron rotates from 0° to 9° (see Table 3.12), $S_{\langle 11 \rangle}$ shifts from 0 to 0.3 \AA and the electrostatic force F_i increases from 8 to 11 dyn. The tensile bond stress T increases to 35 dyn at $\Phi = 9^\circ$. It is easy to understand that, at $\Phi < 9^\circ$, $T < F_b$, while at $\Phi > 9^\circ$, $T > F_b$. Therefore, the coupling of the alternative electrostatic attraction and repulsion along the rhombus chain with the response of the bond tension stabilizes the rotation.

The bond tension might be over-estimated because the dipole potential should take the r_{ij}^{-6} form rather than the simple Coulomb potential. However, this can be precisely determined provided a known dipole moment. Nevertheless, the force driving the $\text{Rh}(001)\text{--}O^{-2}$ clock rotation comes from the electrostatic interaction along the rhombi chain and further rotation of the tetrahedron is constrained by the response of a bond tension. This bond-tension-increase mechanism also holds for the $\text{Ni}(001)\text{--}N^{-3}$ surface. The $\text{Ni}(001)\text{--}C^{-4}$ rotation is driven by the nonequivalent electrostatic repulsion in the $\langle 11 \rangle$ direction and the rotation is balanced by the bond-compression-increase, instead [172].

The following features the understanding of C, N, and O interaction with the low-index (100) surface of Ni and Rh:

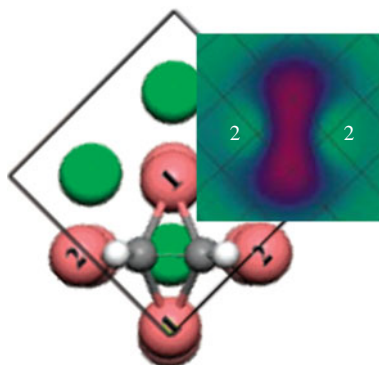
- The C/N–Ni(001) and O–Rh(001) surface reaction is a dynamic process in which C^{-1} , N^{-1} , or O^{-1} centered-pyramid forms first and then C^{-4} , N^{-3} , or O^{-2} -centered quasi-tetrahedron follows. The adsorbate sinks initially into the fourfold hollow site and forms an AB_5 cluster. The B atoms underneath the adsorbate become B^+ . The full surface layer is composed of the A^{-1} -induced B dipoles. With the development of adsorbate hybridization, the AB_5 cluster evolves into an AB_4 tetrahedron that yields the rhombi-chain network in the $\langle 11 \rangle$ direction.
- The clock reconstruction is driven by the electrostatic force along the $\langle 11 \rangle$ direction arising from charge transportation. During the bond forming, surface-charge redistribution leads to the one-dimensional inhomogeneous charge strings along the $\langle 11 \rangle$ directions. The electric interaction along the rhombi chain provides tangential force driving the clock rotation and the corresponding bond tension or compression that stabilize the clock rotation. The O–Rh and N–Ni bonds suffer slight tension while the C–Ni bond suffers strong compression.
- O–Rh(001) surface is covered by B^{+p} and B^p that are weakly bonded to the oxygen and the bulk. N–Ni(001) surface is composed of B^+ and B^{+p} , while the C–Ni(001) surface consists of B^+ and B^{2+} with high compression of the bond. Therefore, the surface atomic states, surface stress, and the mechanism for reconstruction are different though the morphology and crystallography are nearly the same for the p4g-reconstructed systems.

3.8 $Cu_3C_2H_2$ Molecules

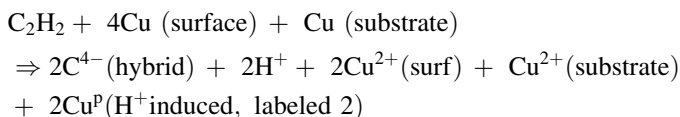
Acetylene (C_2H_2) adsorption on Cu surfaces has initiated much scientific interest as it involves notable elementary catalytic reactions, such as the trimerization reaction of C_2H_2 to form benzene on Cu substrates [179, 180]. In general, C_2H_2 always decomposes on transition metal surfaces (such as Pd, Pt, Ni, and Rh) at low temperature, and the adsorption behaviors of C_2H_2 on these surfaces are different. In particular, the trimerization reaction of C_2H_2/Cu is unique due to the formation of complex molecules on Cu surfaces. Cu is a much more versatile C_2H_2 coupling catalyst than Pd because C_2H_2 trimerization on Cu surface is far less structurally sensitive than on the Pd surface [3]. In addition, unlike ethylene (C_2H_4) and ethane (C_2H_6) molecules, the C_2H_2 rearranges its geometry and changes its intramolecular binding significantly, which provides insight into the fundamental chemistry of triple C–C bonds on the metallic surfaces.

Figure 3.27 shows the STM images and the corresponding bond configurations for the C_2H_2 molecule chemisorption on Cu(001)– (1×1) surface [179]. The $Cu_3C_2H_2$ molecular configuration was optimized using DFT calculations [181]. This chemical reaction is formulated with identification of individual atomic valences as follows:

Fig. 3.27 STM images and the bond configurations for $\text{Cu}_3\text{C}_2\text{H}_2$ on the Cu(001) surface (reprinted with permission from [179]. The bright protrusions (labeled 2) are dipoles induced by H^+ , while the depressions are ions (reprinted with permission from [1])



For the $\text{C}_2\text{H}_2\text{-Cu}(100)\text{--}(1 \times 1)$ surface reaction:



Each C atom bonds to one H atom, two Cu atoms, and the other C atom to form a distorted tetrahedron. The slight protrusions (2) in the STM images correspond to the Cu^{P} dipole induced by H^+ . The ‘dumbbell’-shaped depression is the Cu^{2+} (1) and C^{4-} , lined along the $\langle 11 \rangle$ direction in the same plane. This reaction also happens to the (110) and the (111) surfaces with the involvement of the surface atoms at different geometries.

3.9 Summary

Analysis of the STM and LEED observations based on 3B notations revealed the following:

1. The sp-orbit hybridization is essential for O, N, and C chemisorption, which gives rise to the morphology and reconstruction of surface.
2. The 3B formation in four discrete stages evolving the adsorbate valence states.
3. A numerical analysis of VLEED and STM results in clear four stage of Cu_3O_2 forming dynamics on Cu(001) SURFACE.
4. Rhombi chains form along the $\langle 11 \rangle$ direction of O-Rh(001) and N-, C-Ni(001) surfaces with different valence states and bond stresses.
5. The difference in atomic size, electronegativity and the crystal orientation determines the manner of tetrahedron orientation and the patterns of reconstruction.
6. H-bond like formation may prevent further oxidation and recovers the work function of chemisorbed surfaces.

References

1. C.Q. Sun, Oxidation electronics: bond-band-barrier correlation and its applications. *Prog. Mater. Sci.* **48**(6), 521–685 (2003)
2. F.W. Young, J.V. Cathcart, A.T. Gwathmey, The rates of oxidation of several faces of a single crystal of copper as determined with elliptically polarized light. *Acta Metall.* **4**(2), 145–152 (1956)
3. D.P. Woodruff, T.A. Delchar, *Modern Techniques of Surface Science* (Cambridge University Press, Cambridge, 1986)
4. P.S. Bagus, F. Illas, Theoretical-analysis of the bonding of oxygen to Cu(100). *Phys. Rev. B* **42**(17), 10852–10857 (1990)
5. J.K. Norskov, Theory of adsorption and adsorbate-induced reconstruction. *Surf. Sci.* **299**(1–3), 690–705 (1994)
6. M. Kittel, M. Polcik, R. Terborg, J.T. Hoeft, P. Baumgartel, A.M. Bradshaw, R.L. Toomes, J.H. Kang, D.P. Woodruff, M. Pascal, C.L.A. Lamont, E. Rotenberg, The structure of oxygen on Cu(100) at low and high coverages. *Surf. Sci.* **470**(3), 311–324 (2001)
7. T. Lederer, D. Arvanitis, G. Comelli, L. Troger, K. Baberschke, Adsorption of oxygen on Cu(100). 1. Local-structure and dynamics for 2 atomic chemisorption states. *Phys. Rev. B* **48**(20), 15390–15404 (1993)
8. C.Q. Sun, What effects in nature the two-phase on the O-Cu(001)? *Mod. Phys. Lett. B* **11**(2–3), 81–86 (1997)
9. T. Fujita, Y. Okawa, Y. Matsumoto, K. Tanaka, Phase boundaries of nanometer scale $c(2 \times 2)$ -O domains on the Cu(100) surface. *Phys. Rev. B* **54**(3), 2167–2174 (1996)
10. H.C. Zeng, R.A. McFarlane, R.N.S. Sodhi, K.A.R. Mitchell, LEED crystallographic studies for the chemisorption of oxygen on the (100) surface of copper. *Can. J. Chem. Rev. Can. Chim.* **66**(8), 2054–2062 (1988)
11. H.C. Zeng, K.A.R. Mitchell, Further LEED investigations of missing-row models for the Cu(100)-(2-square-root-2xsquare-root-2)r45-degrees-O surface-structure. *Surf. Sci.* **239**(3), L571–L578 (1990)
12. K.L. Kostov, H. Rauscher, D. Menzel, The role of coadsorbed oxygen in NCO formation on Ru(001). *Surf. Sci.* **287**, 283–287 (1993)
13. F. Jensen, F. Besenbacher, E. Laegsgaard, I. Stensgaard, Dynamics of oxygen-induced reconstruction of Cu(100) studied by scanning tunneling microscopy. *Phys. Rev. B* **42**(14), 9206–9209 (1990)
14. K. Tanaka, T. Fujita, Y. Okawa, Oxygen induced order-disorder restructuring of a Cu(100) surface. *Surf. Sci.* **401**(2), L407–L412 (1998)
15. G. Hitchen, S. Thurgate, P. Jennings, A LEED fine-structure study of oxygen-adsorption of Cu(001) and Cu(111). *Aust. J. Phys.* **43**(4–5), 519–534 (1990)
16. C.Q. Sun, Time-resolved VLEED from the O-Cu(001): Atomic processes of oxidation. *Vacuum* **48**(6), 525–530 (1997)
17. S.M. Thurgate, C. Sun, Very-low-energy electron-diffraction analysis of oxygen on Cu(001). *Phys. Rev. B* **51**(4), 2410–2417 (1995)
18. C. Woll, R.J. Wilson, S. Chiang, H.C. Zeng, K.A.R. Mitchell, Oxygen on Cu(100) surface-structure studied by scanning tunneling microscopy and by LEED multiple-scattering calculations. *Phys. Rev. B* **42**(18), 11926–11929 (1990)
19. M.C. Asensio, M.J. Ashwin, A.L.D. Kilcoyne, D.P. Woodruff, A.W. Robinson, T. Lindner, J.S. Somers, D.E. Ricken, A.M. Bradshaw, The structure of oxygen-adsorption phases on Cu(100). *Surf. Sci.* **236**(1–2), 1–14 (1990)
20. K.W. Jacobsen, J.K. Norskov, Theory of the oxygen-induced restructuring of Cu(110) and Cu(100) surfaces. *Phys. Rev. Lett.* **65**(14), 1788–1791 (1990)
21. C.Q. Sun, C.L. Bai, A model of bonding between oxygen and metal surfaces. *J. Phys. Chem. Solids* **58**(6), 903–912 (1997)

22. C.Q. Sun, Exposure-resolved VLEED from the O–Cu(001): Bonding dynamics. *Vacuum* **48**(6), 535–541 (1997)
23. C.W. Keenan, D.C. Kleinfelter, J.H. Wood, *General College Chemistry* (Harper and Row Publishers, New York, 1979)
24. L. Pauling, *The Nature of the Chemical Bond*, 3rd edn. (Cornell University Press, Ithaca, NY, 1960)
25. G. Ertl, Untersuchung von oberflächenreaktionen mittels beugung langsamer elctronen (LEED).I. wechselwirkung von o2 und n2o mit (110)-(111)-und (100)-kupfer-oberflächen. *Surf. Sci.* **6**(2), 208–232 (1967)
26. E. Vanderiet, J.B.J. Smeets, J.M. Fluit, A. Niehaus, The structure of a clean and oxygen covered copper surface studied by low-energy ion-scattering. *Surf. Sci.* **214**(1–2), 111–140 (1989)
27. R.P.N. Bronckers, A.G.J. Dewit, Reconstruction of the oxygen-covered Cu(110) surface identified with low-energy Ne⁺ and H₂O⁺ ion-scattering. *Surf. Sci.* **112**(1–2), 133–152 (1981)
28. M. Bader, A. Puschmann, C. Ocal, J. Haase, Surface extended x-ray-absorption fine-structure study of the O(2 × 1)/Cu(110) system—missing-row reconstruction, and anisotropy in the surface mean free-path and in the surface debye-waller factor. *Phys. Rev. Lett.* **57**(26), 3273–3276 (1986)
29. U. Dobler, K. Baberschke, J. Haase, A. Puschmann, Azimuthal-angle-dependent and polar-angle-dependent surface extended x-ray absorption fine-structure study—(2 × 1)O on Cu(110). *Phys. Rev. Lett.* **52**(16), 1437–1440 (1984)
30. U. Dobler, K. Baberschke, D.D. Vvedensky, J.B. Pendry, X-ray absorption near-edge structure of adsorbate-induced reconstruction—(2 × 1)O on Cu(110). *Surf. Sci.* **178**(1–3), 679–685 (1986)
31. R. Feidenhansl, I. Stensgaard, Oxygen-adsorption induced reconstruction of Cu(110) studied by high-energy ion-scattering. *Surf. Sci.* **133**(2–3), 453–468 (1983)
32. F.M. Chua, Y. Kuk, P.J. Silverman, Oxygen-chemisorption on cu(110)—an atomic view by scanning tunneling microscopy. *Phys. Rev. Lett.* **63**(4), 386–389 (1989)
33. Y. Kuk, F.M. Chua, P.J. Silverman, J.A. Meyer, O chemisorption on Cu(110) by scanning tunneling microscopy. *Phys. Rev. B* **41**(18), 12393–12402 (1990)
34. R. Feidenhansl, F. Grey, R.L. Johnson, S.G.J. Mochrie, J. Bohr, M. Nielsen, Oxygen-chemisorption on Cu(110)—a structural determination by x-ray-diffraction. *Phys. Rev. B* **41**(8), 5420–5423 (1990)
35. S.R. Parkin, H.C. Zeng, M.Y. Zhou, K.A.R. Mitchell, Low-energy electron-diffraction crystallographic determination for the Cu(110)2 × 1-O surface-structure. *Phys. Rev. B* **41**(8), 5432–5435 (1990)
36. H. Durr, R. Schneider, T. Fauster, Added-row growth of the (2 × 1)O–Cu(110) reconstruction. *Phys. Rev. B* **43**(2), 1802–1804 (1991)
37. H. Durr, T. Fauster, R. Schneider, Surface-structure determination of the (2 × 1)O–Cu(110) reconstruction by low-energy ion-scattering. *Surf. Sci.* **244**(3), 237–246 (1991)
38. J. Haase, B. Hillert, A.M. Bradshaw, Oxygen-chemisorption on Cu(110)—an atomic view by scanning tunneling microscopy—comment. *Phys. Rev. Lett.* **64**(25), 3098 (1990)
39. F. Jensen, F. Besenbacher, E. Laegsgaard, I. Stensgaard, Surface reconstruction of Cu(110) induced by oxygen-chemisorption. *Phys. Rev. B* **41**(14), 10233–10236 (1990)
40. D.J. Coulman, J. Wintterlin, R.J. Behm, G. Ertl, Novel mechanism for the formation of chemisorption phases—the (2 × 1)O–Cu(110) added-row reconstruction. *Phys. Rev. Lett.* **64**(15), 1761–1764 (1990)
41. K. Kern, H. Niehus, A. Schatz, P. Zeppenfeld, J. George, G. Comsa, Long-range spatial self-organization in the adsorbate-induced restructuring of surfaces—Cu(110)-(2 × 1)O. *Phys. Rev. Lett.* **67**(7), 855–858 (1991)
42. T. Shimizu, M. Tsukada, Origin of the different formation modes of the oxygen added row overlayer on Ag(110) and Cu(110) surfaces. *Surf. Sci.* **295**(1–2), L1017–L1022 (1993)

43. D.L. Adams, H.B. Nielsen, J.N. Andersen, I. Stensgaard, R. Feidenhansl, J.E. Sorensen, Oscillatory relaxation of the Cu(110) surface. *Phys. Rev. Lett.* **49**(9), 669–672 (1982)
44. J.A. Yarmoff, D.M. Cyr, J.H. Huang, S. Kim, R.S. Williams, Impact-collision ion-scattering spectroscopy of Cu(110) and Cu(110)-(2 × 1)-O using 5-keV⁶ Li⁺. *Phys. Rev. B* **33**(6), 3856–3868 (1986)
45. V. Pouthier, C. Ramseyer, C. Girardet, P. Zeppenfeld, V. Diercks, R. Halmer, Characterization of the Cu(110)-(2 × 1)O reconstruction by means of molecular adsorption. *Phys. Rev. B* **58**(15), 9998–10002 (1998)
46. C.Q. Sun, S. Li, B.K. Tay, X.W. Sun, S.P. Lau, Solution certainty in the Cu(110)-(2 × 1)-2O₂-surface crystallography. *Int. J. Mod. Phys. B* **16**(1–2), 71–78 (2002)
47. E. Vlieg, S.M. Driver, P. Goettkindt, P.J. Knight, W. Liu, J. Ludecke, K.A.R. Mitchell, V. Murashov, I.K. Robinson, S.A. de Vries, D.P. Woodruff, Structure determination of Cu(410)-O using X-ray diffraction and DFT calculations. *Surf. Sci.* **516**(1–2), 16–32 (2002)
48. J. Wintterlin, R. Schuster, D.J. Coulman, G. Ertl, R.J. Behm, Atomic motion and mass-transport in the oxygen induced reconstructions of Cu(110). *J. Vac. Sci. Technol., B* **9**(2), 902–908 (1991)
49. R. Feidenhansl, F. Grey, M. Nielsen, F. Besenbacher, F. Jensen, E. Laegsgaard, I. Stensgaard, K.W. Jacobsen, J.K. Norskov, R.L. Johnson, Oxygen-chemisorption on Cu(110)—a model for the c(6 × 2) structure. *Phys. Rev. Lett.* **65**(16), 2027–2030 (1990)
50. D. Coulman, J. Wintterlin, J.V. Barth, G. Ertl, R.J. Behm, An STM investigation of the Cu(110)-c(6 × 2)O system. *Surf. Sci.* **240**(1–3), 151–162 (1990)
51. R. Feidenhansl, F. Grey, R.L. Johnson, M. Nielsen, Determination of the Cu(110)-c(6 × 2)-O structure by x-ray-diffraction. *Phys. Rev. B* **44**(4), 1875–1879 (1991)
52. W. Liu, K.C. Wong, K.A.R. Mitchell, Structural details for the Cu(110)-c(6 × 2)-o surface determined by tensor LEED. *Surf. Sci.* **339**(1–2), 151–158 (1995)
53. G. Dorenbos, M. Breeman, D.O. Boerma, Low-energy ion-scattering study of the oxygen-induced reconstructed p(2 × 1) and c(6 × 2) surfaces of Cu(110). *Phys. Rev. B* **47**(3), 1580–1588 (1993)
54. F. Besenbacher, J.K. Norskov, Oxygen-chemisorption on metal-surfaces—general trends for Cu. *Ni Ag Prog. Surf. Sci.* **44**(1), 5–66 (1993)
55. E. Janin, H. von Schenck, M. Gothelid, U.O. Karlsson, M. Svensson, Bridge-bonded atomic oxygen on Pt(110). *Phys. Rev. B* **61**(19), 13144–13149 (2000)
56. T. Schroeder, J.B. Giorgi, A. Hammoudeh, N. Magg, M. Baumer, H.J. Freund, Oxygen-induced p(2 × 3) reconstruction on Mo(112) studied by LEED and STM. *Phys. Rev. B* **65**(11), 115411 (2002)
57. A.K. Santra, B.K. Min, D.W. Goodman, Oxygen-induced p(1 × 3)-O reconstruction on Mo(112): a precursor to the epitaxial formation of MoO₂(100). *Surf. Sci.* **513**(3), L441–L444 (2002)
58. K.C. Tan, Y.P. Guo, A.T.S. Wee, C.H.A. Huan, (2 × 1) oxygen superstructure on Cu(210) surface studied by quantitative LEED analysis and STM. *Surf. Rev. Lett.* **6**(5), 859–863 (1999)
59. Y.P. Guo, K.C. Tan, H.Q. Wang, C.H.A. Huan, A.T.S. Wee, Low-energy electron diffraction study of oxygen-induced reconstructions on Cu(210). *Phys. Rev. B* **66**(16), 165410 (2002)
60. J. Sokolov, F. Jona, P.M. Marcus, Missing-row surface-structure on body-centered-cubic (211)-Fe(211)₂ × 1-O. *Europhys. Lett.* **1**(8), 401–408 (1986)
61. J.M.D. Coey, H. Sun, Improved magnetic-properties by treatment of iron-based rare-earth intermetallic compounds in ammonia. *J. Magn. Mater.* **87**(3), L251–L254 (1990)
62. S.M. Thurgate, P.J. Jennings, Effects of oxygen-adsorption on the LEED fine-structure features of Cu(001), Cu(110), Cu(111) and Ni(001). *Surf. Sci.* **131**(2–3), 309–320 (1983)
63. L.H. Dubois, Oxygen-chemisorption and cuprous-oxide formation on Cu(111)—a high-resolution EELS study. *Surf. Sci.* **119**(2–3), 399–410 (1982)
64. J. Haase, H.J. Kuhr, Reconstruction and relaxation of the oxygen-covered Cu(111) surface—a SEXAFS study. *Surf. Sci.* **203**(3), L695–L699 (1988)

65. H. Niehus, Surface reconstruction of Cu(111) upon oxygen-adsorption. *Surf. Sci.* **130**(1), 41–49 (1983)
66. W. Jacob, V. Dose, A. Goldmann, Atomic adsorption of oxygen on Cu(111) and Cu(110). *Appl. Phys. A: Mater. Sci. Process.* **41**(2), 145–150 (1986)
67. F. Jensen, F. Besenbacher, I. Stensgaard, 2 new oxygen induced reconstructions on Cu(111). *Surf. Sci.* **270**, 400–404 (1992)
68. T. Matsumoto, R.A. Bennett, P. Stone, T. Yamada, K. Domen, M. Bowker, Scanning tunneling microscopy studies of oxygen adsorption on Cu(111). *Surf. Sci.* **471**(1–3), 225–245 (2001)
69. C.Q. Sun, O–Cu(001): I. Binding the signatures of LEED, STM and PES in a bond-forming way. *Surf. Rev. Lett.* **8**(3–4), 367–402 (2001)
70. C.Q. Sun, O–Cu(001): II. VLEED quantification of the four-stage Cu₃O₂ bonding kinetics. *Surf. Rev. Lett.* **8**(6), 703–734 (2001)
71. C.Q. Sun, Coincidence in angular-resolved VLEED spectra: Brillouin zones, atomic shifts and energy bands. *Vacuum* **48**(6), 543–546 (1997)
72. C.Q. Sun, Angular-resolved VLEED from O–Cu(001): Valence bands, chemical bonds, potential barrier, and energy states. *Int. J. Mod. Phys. B* **11**(25), 3073–3091 (1997)
73. R.A. Didio, D.M. Zehner, E.W. Plummer, An angle-resolved UPS study of the oxygen-induced reconstruction of Cu(110). *J. Vac. Sci. Technol. A: Vac. Surf. Films* **2**(2), 852–855 (1984)
74. U. Dobler, K. Baberschke, J. Stohr, D.A. Outka, Structure of c(2×2) oxygen on Cu(100)—a surface extended x-ray absorption fine-structure study. *Phys. Rev. B* **31**(4), 2532–2534 (1985)
75. P. Liu, Y. Wang, Theoretical study on the structure of Cu(110)-p2 × 1-O reconstruction. *J. Phys.: Condens. Matter* **12**(17), 3955–3966 (2000)
76. S. Warren, W.R. Flavell, A.G. Thomas, J. Hollingworth, P.L. Wincott, A.F. Prime, S. Downes, C.K. Chen, Photoemission studies of single crystal CuO(100). *J. Phys.: Condens. Matter* **11**(26), 5021–5043 (1999)
77. H. Pfnur, M. Lindroos, D. Menzel, Investigation of adsorbates with low-energy electron-diffraction at very low energies (VLEED). *Surf. Sci.* **248**(1–2), 1–10 (1991)
78. C. Benndorf, B. Egert, G. Keller, H. Seidel, F. Thieme, Oxygen interaction with Cu(100) studied by AES, ELS, LEED and work function changes. *J. Phys. Chem. Solids* **40**(12), 877–886 (1979)
79. P. Hofmann, R. Unwin, W. Wyrobisch, A.M. Bradshaw, Adsorption and incorporation of oxygen on Cu(100) at t greater than or equal to 300 K. *Surf. Sci.* **72**(4), 635–644 (1978)
80. G. Ertl, T.N. Rhodin, *The Nature of Surface Chemical Bond* (North-Holl press, Amsterdam, 1979)
81. H.H. Rotermund, Investigation of dynamic processes in adsorbed layers by photoemission electron-microscopy (PEEM). *Surf. Sci.* **283**(1–3), 87–100 (1993)
82. J. Lauterbach, H.H. Rotermund, Spatiotemporal pattern-formation during the catalytic cooxidation on Pt(100). *Surf. Sci.* **311**(1–2), 231–246 (1994)
83. N.D. McClenaghan, P.J. Hu, C. Hardacre, A density functional theory study of the surface relaxation and reactivity of Cu₂O(100). *Surf. Sci.* **464**(2–3), 223–232 (2000)
84. E.F. McCullen, C.L. Hsu, R.G. Tobin, Electron density changes and the surface resistivity of thin metal films: oxygen on Cu(100). *Surf. Sci.* **481**(1–3), 198–204 (2001)
85. E. Schwarz, J. Lenz, H. Wohlgemuth, K. Christmann, The interaction of oxygen with a rhodium (110) surface. *Vacuum* **41**(1–3), 167–170 (1990)
86. C.Q. Sun, On the nature of the O-Rh(110) multiphase ordering. *Surf. Sci.* **398**(3), L320–L326 (1998)
87. K. Stokbro, S. Baroni, The surface chemistry of metal-oxygen interactions: a first-principles study of O:Rh(110). *Surf. Sci.* **370**(2–3), 166–178 (1997)
88. P.W. Murray, F.M. Leibsle, Y. Li, Q. Guo, M. Bowker, G. Thornton, V.R. Dhanak, K.C. Prince, R. Rosei, Scanning-tunneling-microscopy study of the oxygen-induced reconstruction of Rh(110). *Phys. Rev. B* **47**(19), 12976–12979 (1993)

89. P.J. Kundrotas, S. Lapinskas, A. Rosengren, Theoretical study of the oxygen-induced missing-row reconstruction on the Rh(110) surface. *Surf. Sci.* **377**(1–3), 7–10 (1997)
90. M. Gierer, H. Over, G. Ertl, H. Wohlgemuth, E. Schwarz, K. Christmann, Low-energy electron-diffraction analysis of the Rh(110)-(2 × 1)-O phase. *Surf. Sci.* **297**(1), L73–L78 (1993)
91. V.R. Dhanak, K.C. Prince, R. Rosei, P.W. Murray, F.M. Leibsle, M. Bowker, G. Thornton, STM study of oxygen on Rh(110). *Phys. Rev. B* **49**(8), 5585–5590 (1994)
92. V.R. Dhanak, G. Comelli, G. Cautero, G. Paolucci, K.C. Prince, M. Kiskinova, R. Rosei, (1XN) reconstruction of the Rh(110) surface with N = 2, 3, 4, 5. *Chem. Phys. Lett.* **188**(3–4), 237–240 (1992)
93. C. Comicioli, V.R. Dhanak, G. Comelli, C. Astaldi, K.C. Prince, R. Rosei, A. Atrei, E. Zanazzi, Structure of Rh(110)(1 × 2) and Rh(110) (2 × 2)p2mg-O surfaces. *Chem. Phys. Lett.* **214**(5), 438–442 (1993)
94. G. Comelli, V.R. Dhanak, M. Kiskinova, G. Paolucci, K.C. Prince, R. Rosei, Adsorption of oxygen on Rh(110) and reactivity of different overlayer structures. *Surf. Sci.* **270**, 360–364 (1992)
95. G. Comelli, V.R. Dhanak, M. Kiskinova, N. Pangher, G. Paolucci, K.C. Prince, R. Rosei, Adsorption of oxygen on Rh(110)—a LEED, Auger-electron spectroscopy and thermal-desorption study. *Surf. Sci.* **260**(1–3), 7–13 (1992)
96. J.D. Batteas, A. Barbieri, E.K. Starkey, M.A. Vanhove, G.A. Somorjai, The Rh(110)-P2 Mg(2X1)-2O surface-structure determined by automated tensor LEED—structure changes with oxygen coverage. *Surf. Sci.* **339**(1–2), 142–150 (1995)
97. H. Tanaka, J. Yoshinobu, M. Kawai, Oxygen-induced reconstruction of the Pd(110) surface—an STM study. *Surf. Sci.* **327**(1–2), L505–L509 (1995)
98. S. Ladas, R. Imbihl, G. Ertl, Kinetic oscillations during the catalytic Co oxidation on Pd(110)—the role of subsurface oxygen. *Surf. Sci.* **219**(1–2), 88–106 (1989)
99. M. Nishijima, M. Jo, Y. Kuwahara, M. Onchi, Electron-energy loss spectra of a Pd(110) clean surface. *Solid State Commun.* **58**(1), 75–77 (1986)
100. C.Q. Sun, Nature and dynamics of the O-Pd(110) surface bonding. *Vacuum* **49**(3), 227–232 (1998)
101. J.W. He, U. Memmert, K. Griffiths, P.R. Norton, Interaction of oxygen with a Pd(110) surface. 1. Structures and coverages. *J. Chem. Phys.* **90**(9), 5082–5087 (1989)
102. J.W. He, U. Memmert, P.R. Norton, Interaction of oxygen with a Pd(110) surface. 2. Kinetics and energetics. *J. Chem. Phys.* **90**(9), 5088–5093 (1989)
103. M. Jo, Y. Kuwahara, M. Onchi, M. Nishijima, Oxygen-adsorption on Pd (110) at 300-k-low-energy electron-diffraction and electron-energy loss spectroscopy studies. *Chem. Phys. Lett.* **131**(1–2), 106–111 (1986)
104. C.W. Tucker, Chemisorbed oxygen structures on rhodium (110) surface. *J. Appl. Phys.* **37**(11), 4147–4155 (1966)
105. D. Alfe, P. Rudolf, M. Kiskinova, R. Rosei, HREEL spectra of various oxygen structures on Rh(110). *Chem. Phys. Lett.* **211**(2–3), 220–226 (1993)
106. B. Brena, G. Comelli, L. Ursella, G. Paolucci, Oxygen on Pd(110): Substrate reconstruction and adsorbate geometry by tensor LEED. *Surf. Sci.* **375**(2–3), 150–160 (1997)
107. F. Bondino, G. Comelli, A. Baraldi, R. Rosei, S. Lizzit, A. Goldoni, R. Larciprete, G. Paolucci, Photoelectron diffraction study of the low-temperature low-coverage oxygen layer on Rh(110). *Phys. Rev. B* **66**(7), 075402 (2002)
108. A. Baraldi, J. Cerda, J.A. Martin-Gago, G. Comelli, S. Lizzit, G. Paolucci, R. Rosei, Oxygen induced reconstruction of the Rh(100) surface: General tendency towards threefold oxygen adsorption site on Rh surfaces. *Phys. Rev. Lett.* **82**(24), 4874–4877 (1999)
109. R. Koch, E. Schwarz, K. Schmidt, B. Burg, K. Christmann, K.H. Rieder, Oxygen-adsorption on Co(10 $\bar{1}$ 0)—different reconstruction behavior of hcp (10 $\bar{1}$ 0) and fcc (110). *Phys. Rev. Lett.* **71**(7), 1047–1050 (1993)

110. R. Koch, B. Burg, K. Schmidt, K.H. Rieder, E. Schwarz, K. Christmann, Oxygen-adsorption on Co(10(1)over-bar-0)—the structure of $p(2 \times 1)2O$. *Chem. Phys. Lett.* **220**(3–5), 172–176 (1994)
111. C.Q. Sun, On the nature of the O-Co(1010) triphase ordering. *Surf. Rev. Lett.* **5**(5), 1023–1028 (1998)
112. E. Schwarz, K.H. Ernst, C. Gonserbuntrock, M. Neuber, K. Christmann, Ordered oxygen phases on a Co(1010) surface. *Vacuum* **41**(1–3), 180–184 (1990)
113. M. Gierer, H. Over, P. Rech, E. Schwarz, K. Christmann, The adsorption geometry of the (2×1) -20 oxygen phase formed on the Co(10(1)over-bar-0) surface. *Surf. Sci.* **370**(2–3), L201–L206 (1997)
114. H. Over, G. Kleinle, G. Ertl, W. Moritz, K.H. Ernst, H. Wohlgemuth, K. Christmann, E. Schwarz, A LEED structural-analysis of the Co(1010) surface. *Surf. Sci.* **254**(1–3), L469–L474 (1991)
115. S. Poulston, M. Tikhov, R.M. Lambert, Structure and properties of au overlayers on Ru(100). *Surf. Sci.* **331**, 818–823 (1995)
116. T.W. Orent, R.S. Hansen, Interactions of nitric-oxide and oxygen with Ru(1010). *Surf. Sci.* **67**(1), 325–350 (1977)
117. S. Schwegmann, A.P. Seitsonen, V. De Renzi, H. Dietrich, H. Bludau, M. Gierer, H. Over, K. Jacobi, M. Scheffler, G. Ertl, Oxygen adsorption on the Ru(10(1)over-bar0) surface: Anomalous coverage dependence. *Phys. Rev. B* **57**(24), 15487–15495 (1998)
118. M.V. Ganduglia-Pirovano, M. Scheffler, Structural and electronic properties of chemisorbed oxygen on Rh(111). *Phys. Rev. B* **59**(23), 15533–15543 (1999)
119. C. Stampfl, S. Schwegmann, H. Over, M. Scheffler, G. Ertl, Structure and stability of a high-coverage (1×1) oxygen phase on Ru(0001). *Phys. Rev. Lett.* **77**(16), 3371–3374 (1996)
120. C. Stampfl, M. Scheffler, Theoretical study of O adlayers on Ru(0001). *Phys. Rev. B* **54**(4), 2868–2872 (1996)
121. K.D. Gibson, M. Viste, E.C. Sanchez, S.J. Sibener, High density adsorbed oxygen on Rh(111) and enhanced routes to metallic oxidation using atomic oxygen. *J. Chem. Phys.* **110**(6), 2757–2760 (1999)
122. K.C. Wong, W. Liu, K.A.R. Mitchell, LEED crystallographic analysis for the Rh(111)- (2×1) -O surface structure. *Surf. Sci.* **360**(1–3), 137–143 (1996)
123. B. Narloch, G. Held, D. Menzel, Structural rearrangement by coadsorption—a LEED-IV determination of the Ru(001)- $p(2 \times 2)$ (2O+CO) structure. *Surf. Sci.* **317**(1–2), 131–142 (1994)
124. H. Pfnur, G. Held, M. Lindroos, D. Menzel, Oxygen induced reconstruction of a close-packed surface—a LEED-iv study on Ru(001)- $p(2 \times 1)$ O. *Surf. Sci.* **220**(1), 43–58 (1989)
125. D.G. Castner, G.A. Somorjai, LEED, AES and thermal-desorption studies of the oxidation of the rhodium(111) surface. *Appl. Surf. Sci.* **6**(1), 29–38 (1980)
126. U. Starke, M.A. Vanhove, G.A. Somorjai, Adsorbate-induced relaxations of close-packed fcc and hcp metal-surfaces. *Prog. Surf. Sci.* **46**(2–3), 305–319 (1994)
127. M. Todorova, W.X. Li, M.V. Ganduglia-Pirovano, C. Stampfl, K. Reuter, M. Scheffler, Role of subsurface oxygen in oxide formation at transition metal surfaces. *Phys. Rev. Lett.* **89**(9), 096103 (2002)
128. K. Meinel, H. Wolter, C. Ammer, A. Beckmann, H. Neddermeyer, Adsorption stages of O on Ru(0001) studied by means of scanning tunnelling microscopy. *J. Phys.: Condens. Matter* **9**(22), 4611–4619 (1997)
129. H. Over, Y.D. Kim, A.P. Seitsonen, S. Wendt, E. Lundgren, M. Schmid, P. Varga, A. Morgante, G. Ertl, Atomic-scale structure and catalytic reactivity of the RuO₂(110) surface. *Science* **287**(5457), 1474–1476 (2000)
130. K.D. Gibson, J.I. Colonell, S.J. Sibener, Velocity distributions of recombinatively desorbed O₂ originating from surface and subsurface oxygen Rh(111). *Surf. Sci.* **343**(1–2), L1151–L1155 (1995)
131. T.E. Madey, H.A. Engelhardt, D. Menzel, Adsorption of oxygen and oxidation of CO on ruthenium (001) surface. *Surf. Sci.* **48**(2), 304–328 (1975)

132. S. Renisch, R. Schuster, J. Winterlin, G. Ertl, Dynamics of adatom motion under the influence of mutual interactions: O/Ru(0001). *Phys. Rev. Lett.* **82**(19), 3839–3842 (1999)
133. S. Schwegmann, H. Over, V. DeRenzi, G. Ertl, The atomic geometry of the O and CO+O phases on Rh(111). *Surf. Sci.* **375**(1), 91–106 (1997)
134. M. Lindroos, H. Pfnur, G. Held, D. Menzel, Adsorbate induced reconstruction by strong chemisorption—Ru(001) $p(2 \times 2)$ -O. *Surf. Sci.* **222**(2–3), 451–463 (1989)
135. P. Quinn, D. Brown, D.P. Woodruff, T.C.Q. Noakes, P. Bailey, Structural analysis of the Ru(0001)(1×1)-O and Ru(0001)(2×1)-O structures by medium energy in scattering. *Surf. Sci.* **491**(1–2), 208–218 (2001)
136. A.K. Schmid, R.Q. Hwang, N.C. Bartelt, Predicting the future of a complicated surface structure: Grain coarsening of $p(2 \times 2)$ O/Ru(0001). *Phys. Rev. Lett.* **80**(10), 2153–2156 (1998)
137. C.Q. Sun, O-Ru(0001) surface bond and band formation. *Surf. Rev. Lett.* **5**(2), 465–471 (1998)
138. L. Huang, J. Chevrier, P. Zeppenfeld, G. Cosma, Observation by scanning-tunneling-microscopy of a hexagonal Au(111) surface reconstruction induced by oxygen. *Appl. Phys. Lett.* **66**(8), 935–940 (1995)
139. C.I. Carlisle, T. Fujimoto, W.S. Sim, D.A. King, Atomic imaging of the transition between oxygen chemisorption and oxide film growth on Ag{111}. *Surf. Sci.* **470**(1–2), 15–31 (2000)
140. C.Q. Sun, Oxygen interaction with Rh(111) and Ru(0001) surfaces: bond-forming dynamics. *Mod. Phys. Lett. B* **14**(6), 219–227 (2000)
141. W.F. Egelhoff, P.J. Chen, R.D. McMichael, C.J. Powell, R.D. Deslattes, F.G. Serpa, R.D. Gomez, Surface oxidation as a diffusion barrier for Al deposited on ferromagnetic metals. *J. Appl. Phys.* **89**(9), 5209–5214 (2001)
142. M.V. Ganduglia-Pirovano, K. Reuter, M. Scheffler, Stability of subsurface oxygen at Rh(111). *Phys. Rev. B* **65**(24), 245426 (2002)
143. K. Reuter, M.V. Ganduglia-Pirovano, C. Stampfl, M. Scheffler, Metastable precursors during the oxidation of the Ru(0001) surface. *Phys. Rev. B* **65**(16), 165403 (2002)
144. C.S.A. Fang, Surface structural transition of adsorption of oxygen on Ag(100). *Surf. Sci.* **235**(1), L291–L294 (1990)
145. M. Rocca, L. Savio, L. Vattuone, U. Burghaus, V. Palomba, N. Novelli, F.B. de Mongeot, U. Valbusa, R. Gunnella, G. Comelli, A. Baraldi, S. Lizzit, G. Paolucci, Phase transition of dissociatively adsorbed oxygen on Ag(001). *Phys. Rev. B* **61**(1), 213–227 (2000)
146. G. Cipriani, D. Loffreda, A. Dal Corso, S. de Gironcoli, S. Baroni, Adsorption of atomic oxygen on Ag(001): a study based on density-functional theory. *Surf. Sci.* **501**(3), 182–190 (2002)
147. L. Savio, L. Vattuone, M. Rocca, V. De Renzi, S. Gardonio, C. Mariani, U. del Pennino, G. Cipriani, A. Dal, Corso, and S. Baroni, Substrate reconstruction and electronic surface states: Ag(001). *Surf. Sci.* **486**(1–2), 65–72 (2001)
148. L.H. Tjeng, M.B.J. Meinders, G.A. Sawatzky, Electronic-structure of clean and oxygen covered silver (110) surface. *Surf. Sci.* **236**(3), 341–368 (1990)
149. T.E. Felter, W.H. Weinberg, G.Y. Lastushkina, A.I. Boronin, P.A. Zhdan, G.K. Borekov, J. Hrbek, An XPS and UPS study of the kinetics of carbon-monoxide oxidation over Ag(111). *Surf. Sci.* **118**(3), 369–386 (1982)
150. R. Koller, W. Bergermayer, G. Kresse, E.L.D. Hebenstreit, C. Konvicka, M. Schmid, R. Podloucky, P. Varga, The structure of the oxygen induced (1×5) reconstruction of V(100). *Surf. Sci.* **480**(1–2), 11–24 (2001)
151. C.W. Tucker, Oxygen faceting of rhodium (210) and (100) surfaces. *Acta Metall.* **15**(9), 1465–1474 (1967)
152. L.H. Dubois, Vibrational-spectra of atomic adsorbates—carbon, oxygen, and sulfur on Rh(100). *J. Chem. Phys.* **77**(10), 5228–5233 (1982)
153. W.M. Daniel, Y. Kim, H.C. Peebles, J.M. White, Adsorption of Ag, O₂ and N₂O on Ag-Rh(100). *Surf. Sci.* **111**(2), 189–204 (1981)

154. J.R. Mercer, P. Finetti, F.M. Leibsle, R. McGrath, V.R. Dhanak, A. Baraldi, K.C. Prince, R. Rosei, STM and SPA-LEED studies of O-induced structures on Rh(100) surfaces. *Surf. Sci.* **352**, 173–178 (1996)
155. J.R. Mercer, P. Finetti, M.J. Scantlebury, U. Beierlein, V.R. Dhanak, R. McGrath, Angle-resolved photoemission study of half-monolayer O and S structures on the Rh(100) surface. *Phys. Rev. B* **55**(15), 10014–10021 (1997)
156. K. Heinz, W. Oed, J.B. Pendry, Direct low-energy electron-diffraction analysis of $c(2 \times 2)O/Ni(100)$ including substrate reconstruction. *Phys. Rev. B* **41**(14), 10179–10181 (1990)
157. S.R. Chubb, P.M. Marcus, K. Heinz, K. Muller, Adsorption-induced relaxation of $Ni(001)-c(2 \times 2)-O$. *Phys. Rev. B* **41**(8), 5417–5419 (1990)
158. D. Norman, J. Stohr, R. Jaeger, P.J. Durham, J.B. Pendry, Determination of local atomic arrangements at surfaces from near-edge x-ray-absorption fine-structure studies—O on Ni(100). *Phys. Rev. Lett.* **51**(22), 2052–2055 (1983)
159. C.Q. Sun, Driving force behind the O-Rh(001) clock reconstruction. *Mod. Phys. Lett. B* **12**(20), 849–857 (1998)
160. J.H. Onuferko, D.P. Woodruff, B.W. Holland, LEED structure-analysis of the $Ni(100)(2 \times 2)c(p4g)$ structure—case of adsorbate-induced substrate distortion. *Surf. Sci.* **87**(2), 357–374 (1979)
161. S. Stolbov, S.Y. Hong, A. Kara, T.S. Rahman, Origin of the C-induced $p4g$ reconstruction of Ni(001). *Phys. Rev. B* **72**(15), 155423 (2005)
162. Y.G. Shen, A. Qayyum, D.J. O'Connor, B.V. King, Oxygen-induced surface $(2 \times 2)p4g$ reconstruction of Rh(001). *Phys. Rev. B* **58**(15), 10025–10030 (1998)
163. D. Alfe, S. de Gironcoli, S. Baroni, The reconstruction of Rh(001) upon oxygen adsorption. *Surf. Sci.* **410**(2–3), 151–157 (1998)
164. D. Alfe, S. de Gironcoli, S. Baroni, The reconstruction of nickel and rhodium (001) surfaces upon carbon, nitrogen or oxygen adsorptions. *Surf. Sci.* **437**(1–2), 18–28 (1999)
165. A.G. Norris, F. Schedin, G. Thornton, V.R. Dhanak, T.S. Turner, R. McGrath, Surface x-ray diffraction study of the $Rh(100)(2 \times 2)-O$ reconstruction. *Phys. Rev. B* **62**(3), 2113–2117 (2000)
166. L. Wenzel, D. Arvanitis, W. Daum, H.H. Rotermund, J. Stohr, K. Baberschke, H. Ibach, Structural determination of an adsorbate-induced surface reconstruction— $p4g(2 \times 2)n$ versus $c(2 \times 2)O$ on Ni(100). *Phys. Rev. B* **36**(14), 7689–7692 (1987)
167. D. Arvanitis, K. Baberschke, L. Wenzel, Multiple-scattering effects in surface extended x-ray absorption fine-structure. *Phys. Rev. B* **37**(12), 7143–7146 (1988)
168. A.L.D. Kilcoyne, D.P. Woodruff, A.W. Robinson, T. Lindner, J.S. Somers, A.M. Bradshaw, A photoelectron diffraction study of the $Ni(100)(2 \times 2)-c(p4g)$ and $Ni(100)(2 \times 2)-n(p4g)$ structures. *Surf. Sci.* **253**(1–3), 107–115 (1991)
169. E. Dudzik, A.G. Norris, R. McGrath, G. Charlton, G. Thornton, B. Murphy, T.S. Turner, D. Norman, The $Ni(100)(2 \times 2)p4g-N$ reconstruction determined by surface X-ray diffraction. *Surf. Sci.* **433**, 317–321 (1999)
170. M. Bader, C. Ocal, B. Hillert, J. Haase, A.M. Bradshaw, Surface extended-x-ray-absorption fine-structure study at the carbon k-edge—the $p4g(2 \times 2)-C/Ni(100)$ system. *Phys. Rev. B* **35**(11), 5900–5902 (1987)
171. Y. Gauthier, R. Baudouingsavois, K. Heinz, H. Landskron, Structure determination of $p4g Ni(100)-(2 \times 2)c$ by LEED. *Surf. Sci.* **251**, 493–497 (1991)
172. C.Q. Sun, The sp hybrid bonding of C, N and O to the fcc(001) surface of nickel and rhodium. *Surf. Rev. Lett.* **7**(3), 347–363 (2000)
173. F.M. Leibsle, A scanning-tunneling-microscopy study of the $(2 \times 2) p4g$ nitrogen-induced surface reconstruction on Ni(100). *Surf. Sci.* **297**(1), 98–105 (1993)
174. C. Klink, L. Olesen, F. Besenbacher, I. Stensgaard, E. Laegsgaard, N.D. Lang, Interaction of c with Ni(100)—atom-resolved studies of the clock reconstruction. *Phys. Rev. Lett.* **71**(26), 4350–4353 (1993)

175. G. Hormandinger, J.B. Pendry, F.M. Leibsle, P.W. Murray, R.W. Joyner, G. Thornton, Scanning-tunneling-microscopy investigation of the Ni(100)-p(2 × 2)_c surface. *Phys. Rev. B* **48**(11), 8356–8364 (1993)
176. J.E. Kirsch, S. Harris, Electronic structure studies of Ni(100) surface reconstructions resulting from carbon, nitrogen, or oxygen atom adsorption. *Surf. Sci.* **522**(1–3), 125–142 (2003)
177. C.Q. Sun, Mechanism for the N-Ni(100) clock reconstruction. *Vacuum* **52**(3), 347–351 (1999)
178. C.Q. Sun, P. Hing, Driving force and bond strain for the C-Ni(100) surface reaction. *Surf. Rev. Lett.* **6**(1), 109–114 (1999)
179. B.C. Stipe, M.A. Rezaei, W. Ho, Single-molecule vibrational spectroscopy and microscopy. *Science* **280**(5370), 1732–1735 (1998)
180. G. Kyriakou, J. Kim, M.S. Tikhov, N. Macleod, R.M. Lambert, Acetylene coupling on Cu(111): formation of Butadiene, Benzene, and Cyclooctatetraene. *J Phys Chem B* **109**(21), 10952–10956 (2005)
181. W. Liu, J.S. Lian, Q. Jiang, Theoretical study of C₂H₂ adsorbed on low-index Cu surfaces. *J. Chem. Phys. C* **111**(49), 18189–18194 (2007)

Chapter 4

STS and PES: Valence DOS

- *O and N adsorbates create commonly four DOS features in the valence band, corresponding to the host antibonding dipoles ($>E_f$), adsorbate non-bonding lone pairs ($<E_f$), electron holes of host (E_f), and the adsorbate–host bonding states.*
- *Electron holes and lone pair states may overlap and cancel each other.*
- *Dipole formation lowers the work function of the surfaces. Overdosing of adsorbates restores the work function as the dipoles serve as donor for further bond formation, which provide mechanism for surface antioxidation.*
- *Electronegativity, lattice size, dosage, and temperature are factors controlling bond and band formation and relaxation dynamics.*

4.1 Signature Generality

Chemisorption is a process in which chemical bond forms and the valence electrons transport among the bonding constituent atoms. Processes of charge transport modify the valence band structure and introduce additional DOS features. The derived DOS features are detectable using STS (around E_F), PES ($E < E_F$), and IPES (inverse PES, $E > E_F$).

4.1.1 STS

STS measurements record the $dI_t/dV_t - V_t$ or the $d(\ln I_t)/d(\ln V_t) - V_t$ curves, at a constant tip current, I_t , and various tip voltages, V_t . The features of an STS spectrum are associated with the on-site DOS of a few atoms at a surface [1, 2]. Features below E_F (tip negative bias) correspond to the occupied DOS at the surface, while features above E_F (tip positive) represent the allowed, yet unoccupied, DOS of the sample surface [3].

Figure 4.1 shows the STS spectra of a Cu(110) surface [4] and an Nb(110) surface [5] with and without chemisorbed oxygen. In the first panel, spectrum A was taken from the clean Cu(110) surface, while B and C were taken from, respectively, the site above the bright spot (dipole) and the site between two bright spots along the ‘ $\text{O}^{-2} : \text{Cu}^{\text{p}} : \text{O}^{-2}$ ’ chain at the Cu(110)-(2 × 1)- O^{-2} surface. On the clean surface, empty DOS of 0.8–1.8 eV above E_{F} are resolved and no extra DOS structures are found below E_{F} . The STS spectra recorded from the Cu(110)-(2 × 1)- O^{-2} islands reveal that the original empty DOS above E_{F} are partially occupied by electrons upon chemisorption, which result in a slight shift of the empty DOS to higher energy. Additional DOS features are generated around –2.1 eV below the E_{F} . The sharp features around –1.4 eV have been detected with ARPES [6] and with the de-excitation spectroscopy of metastable atoms [7]. The Cu-3d DOS are between –2 and –5 eV [6, 8, 9], and the O–Cu bonding derivatives are around the 2p level of oxygen, from –5.6 to –7.8 eV below E_{F} [10]. Both Cu-3d and O–Cu bond DOS features are outside the energy range of the STS ($E_{\text{F}} \pm 2.5$ eV).

The STS features of spectrum C (taken from between the bright spots) are more pronounced than that of spectrum B. Taking the tip-size effect of an STS (with ~ 2.5 Å lateral uncertainty) and the constant current mode into account, the origin of the intensity difference between spectra B and C can be easily understood. Spectrum C corresponds to the depression (inward curvature) that is atop an oxygen adsorbate. The above- E_{F} feature is dominated by the two neighboring dipole protrusions, while the below- E_{F} information comes from the lone pair of the O^{-2} underneath. Therefore, the above- E_{F} features of profile C should be stronger than those of profile B as profile C is collected mainly from a dipole (from outward curvature) site. The tip above the dipole collects information of both the lone pair and the dipole, but the signal is relatively weaker because of the positive curvature at the dipole site. So the intensity of an STS spectrum is determined by (1) the tip size, (2) the on-site curvature, and (3) the energy states of O^{-2} adsorbate ($<E_{\text{F}}$, lone pair electrons) and Cu^{p} ($>E_{\text{F}}$, polarized electron). Therefore, the new peaks at –2.1 eV represent the lone pair, and the peak at 0.8–1.8 eV corresponds to the antibonding dipoles [11].

STS spectra in the energy range from –8 to 8 eV from the O–Nd(110) surface (Fig. 4.1) show DOS features near the E_{F} of O–Nb(110) is not that apparent as that from the O–Cu–O chain [5]. They are rather weak compared with the intense resonant features. The resonant peaks at positive bias (unoccupied states) arise from a tunneling via quantized states in a potential well induced by the combination of image states and the applied electrical field [12, 13]. Since the lowest image state is energetically tied to the vacuum level, the position of the first resonance can be used for the estimation of the work function [13]. The successive higher resonance at 6.4 and 7.7 eV are in accordance with resonance found for other transition metals such as Cu/Mo(110) [12] and Ni(001) surfaces [13, 14]. These resonances shift to lower energies on the O–Nb surfaces, independent of the tip positions, i.e., on or away from the O–Nb chains. The resonance shift was related to the variation in work function upon oxidation [5].

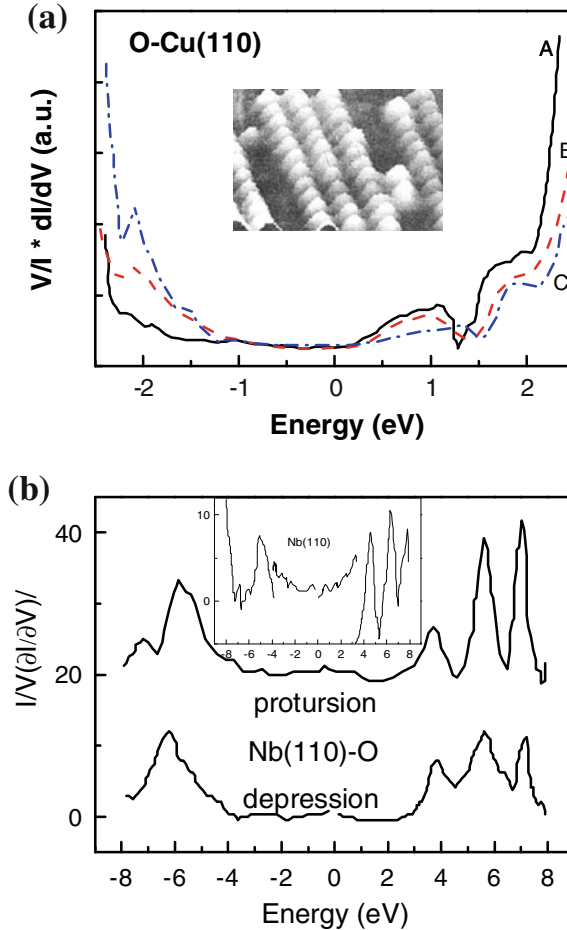


Fig. 4.1 STS profiles of **a** Cu(110) surface (reprinted with permission from [4]) and **b** Nb(110) surface (reprinted with permission from [5]) with and without chemisorbed oxygen. Spectra in panel **a** were obtained (*A*) at a metallic region, (*B*) on top of, and (*C*) between protrusions of the ‘ $\text{O}^{-2} : \text{Cu}^{\text{p}} : \text{O}^{-2} :$ ’ chain [11] on the Cu(110)- (2×1) - O^{-2} surface.

During oxygen chemisorption at room temperature, an initial decrease by $\Delta\phi = -0.45$ eV for less-than-monolayer coverage was observed and then is followed by an increase of 0.8 eV at higher oxygen coverage. The latter is higher than that of the clean surface [15]. The shift of the second peak at 5.6 eV coincides well with the work function increase and the rest two peaks correspond to satellites of resonance. The occupied DOS features of the O–Nb chain are at -5.8 eV and at -6.2 eV at the STM triangular vacancy positions compared to the DOS at -5.0 eV for clean Nb(110) surface. The energy shift of the occupied states results from the overlap of O-2p and Nb-4d states with convolution of the reconstruction effect [5].

4.1.2 PES, IPES, and XPS

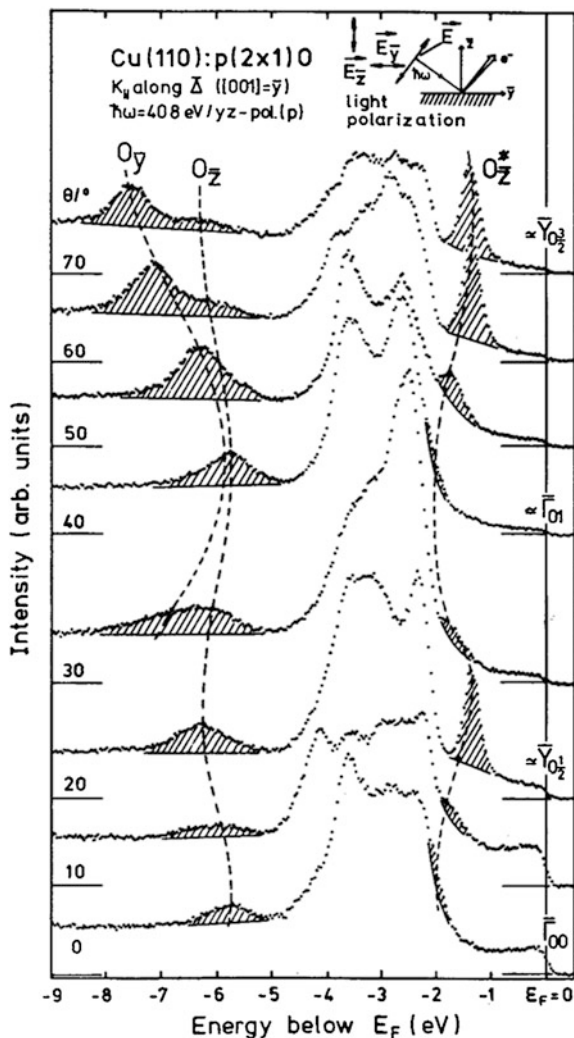
Figure 4.2 shows the ARPES spectra from the O–Cu(110) surface. Three apparent features were recognized, and they are interpreted as follows [16]. The assignment of $p_{\bar{y}}$ and $p_{\bar{z}}$ comes from two sources. Based on the geometrical structure, it was assumed that the *strongest* Cu–O interaction is along the O–Cu–O chains, and thus, one will make the assignment $p_{\bar{y}}$ to the structure with the largest dispersion. Secondly, this feature is only observed at large incident angles ϑ (angle between the incident beam and the surface normal), which suggests that one is observing an orbital in the plane, and this could only be the $p_{\bar{y}}$ orbital (along the O–Cu–O chain) because of the polarization dependence. The assignment of the $p_{\bar{z}}^*$ structure (the asterisk indicates an antibonding level) stems from the observed polarization dependence and the comparison with the dispersion of the $p_{\bar{z}}$ orbital. Hüfner [16] explained that the O–p bands located below the Cu–d band correspond to the O–Cu bonding band, and those above the Cu–d bands are the occupied O–Cu ‘antibonding’ bands. The oxygen 2 $p_{\bar{y}}$ band shows the largest dispersion, as expected from the geometrical arrangement, which was suggested as indicative of strong bonding along the O–Cu–O strings. UPS observation of the O–Cu/Ag(110)(2×2)p2mg phase reveals three additional DOS features surrounding -1 , -3 , and -6 eV, and some of the features were ascribed as Cu-3d (-3 eV) and O-2p (-1 to -2 eV) states [17].

A set of PES profiles from an O–Cu(001) [18] surface shows three new DOS features around -1.45 , -3.25 , and -5.35 eV within the valence band (above -7.04 eV) compared to that of a clean Cu(001) surface. The states around -1.45 eV (which coincide with the -1.4 eV STS feature in Fig. 4.1a) are anti-resonant, i.e., the intensity has no apparent change with varying incident beam energy. The anti-resonant DOS feature is the character of electrons that are strongly confined in one dimension such as molecular chains [19]. Thus, the anti-resonant DOS features around -1.45 eV can be related to the electron lone pairs that zigzag the ‘O⁻² : Cu^p : O⁻²’ strings at the Cu(001)-O⁻² surface.

He-II (21.22 eV) PES revealed that with increasing the number of oxygen atoms on a polycrystalline Cu surface, oxidation takes place in three steps [9]:

- In the first step (the lowest, 12 L, exposures), oxidation begins, which immediately leads to the rise of a shoulder at -1.5 eV and a small peak at -6.0 eV in the PES spectra. The emergence of the new DOS features is at the expense of a sharp fall of the DOS features between -3.0 eV and E_F .
- At the second step (12–1,000 L), a further increase in the oxygen exposure leads to the increase of both the -6.0 eV DOS feature and the sharp fall at $E_F > E > -3.0$ eV. The DOS at E_F fall to zero and produce a bandgap of ~ 1.0 eV width.
- At the third step with an oxygen exposure of 5×10^3 L, a surface compound forms, which displays semiconductive properties. Its electronic structure is quite the same as that of the bulk Cu₂O.

Fig. 4.2 ARPES spectra for O-Cu(110) surfaces (reprinted with permission from [16]). Additional (shaded) features around -1.2 and -6 eV are the nonbonding and bonding states



These reaction steps agree well with the Cu_3O_2 bonding kinetics of O-Cu(001) surface as determined with VLEED.

A set of ARPES spectra, as shown in Fig. 4.3a, b, from the O-Pd(110) surface [20] displays that two adjacent clusters of DOS populate below the E_F of the Pd(110) surface. One is around -2.0 eV, and the other is around -5.0 eV. These signatures arise at the expense of the weakening of the DOS close to the E_F . PES investigations on the O-Rh(001) surface [21–23] showed that oxygen induces significant change in the energy states around -2 to -6 eV below E_F . Figure 4.3c, d [22] compares the ARPES spectra from the $c(2 \times 2)\text{-O}^{-1}$ (radial reconstruction) and $(2 \times 2)\text{p}4\text{g-O}^{-2}$ phase on the Rh(001) surface. DOS for holes below the E_F

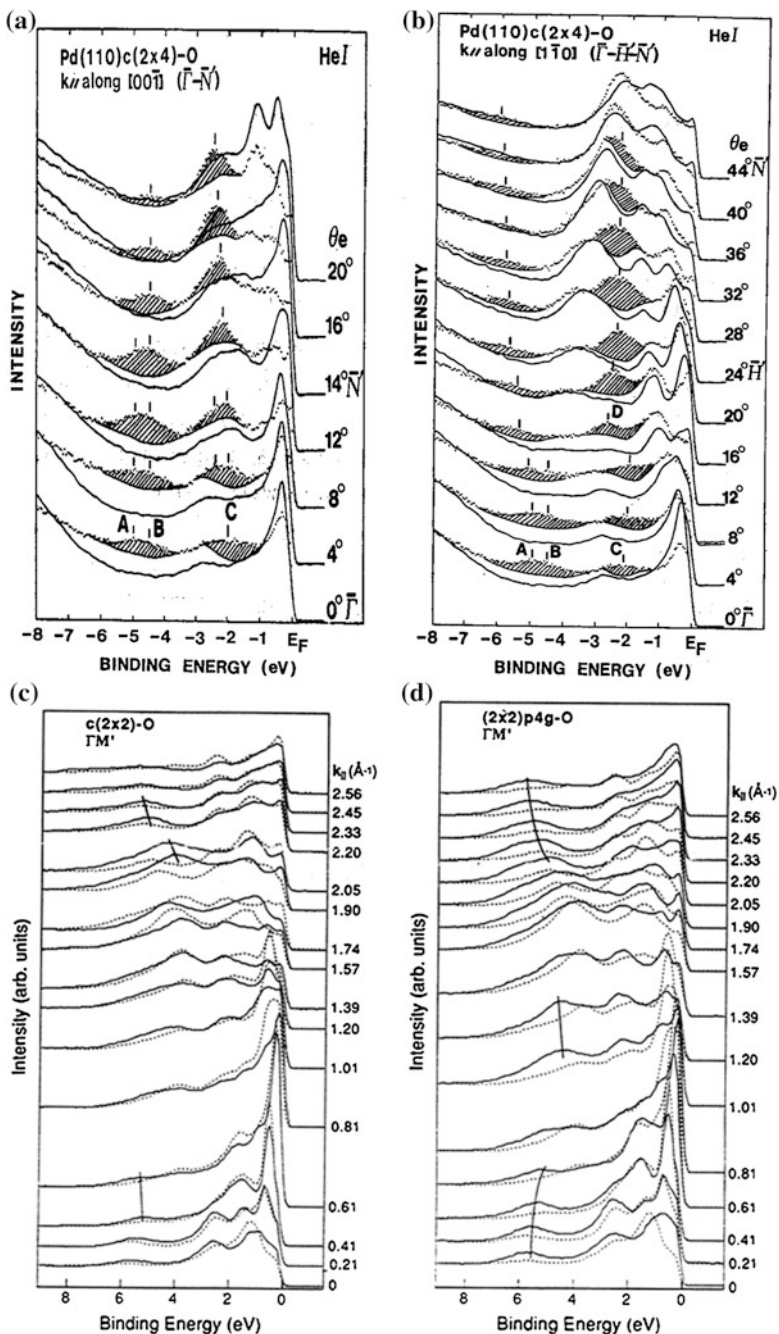


Fig. 4.3 ARPES profiles for **a**, **b** O-Pd(110) (reprinted with permission from [20]) and **c**, **d** O-Rh(001) (Reprinted with permission from [53]) surfaces. *Shaded* areas are features derived by oxygen adsorption. A notable aspect upon the reconstruction is the two new humps around -2 and -5 eV. The ARPES intensity near E_F at some angles such as 0° and 44° is reduced. For O-Rh(001), O derives additional features at around -5 eV for the (2×2) -2O phase. The feature at -5.0 eV shifts to -6.0 eV with an additional feature at about -2.0 eV at some azimuth angles when the $(2 \times 2)p4g$ -2O phase is developed

can be resolved from the PES profiles of both phases. Additional O-derivatives can be identified at around -5 eV for the first $(2 \times 2)\text{-O}^{-1}$ phase. The feature around -5 eV shifts down a little with an additional peak at about -2.0 eV at the some azimuth angles for the O^{-2} -induced ‘p4g’ phase. The PES features of the O–Pd(110) and O–Rh(001) surfaces are substantially the same as those observed from the O–Rh(110) [24] and the O–Cu(001) and (110) [18] surfaces as well, despite the slight difference in peak positions. The DOS evolution kinetics of the O–Rh(001) surface in the phase transition agrees with the trend for the O–Cu(001) phase transition as determined with VLEED [25] and PES [9].

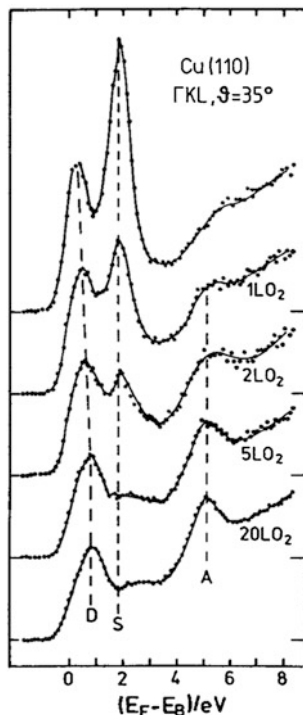
Figure 4.4 shows the exposure dependence of the unoccupied bands of the O–Cu(110) surface measured using ARIPES (9.7 eV) [26] of which the resonant features are quite similar to the STS from O–Nb(110) surface (Fig. 4.1b). It was explained in Ref. [26] that the state centered at 4 eV above E_F corresponds to a Cu-3d¹⁰ state, in keeping with the Cu-3d⁹ interpretation for the ground state, because with the IPES technique an additional electron is added to the copper–oxygen system. The obviously symmetric dispersion of this state with respect to the occupied oxygen $2p_{\bar{y}}$ states is in agreement with a two-level approximation for the O–Cu σ -bond. The band above E_F is an empty surface state, which means that the agreement of its dispersion with that of the O-2 $p_{\bar{y}}$ state below E_F is accidental [27]. There appears to be no definite interpretation to this phenomenon up to now. One might, however, take a very pragmatic view of that problem. Any state in a monatomic surface layer can be viewed as a surface state. In this sense, the two different interpretations given for the unoccupied state of the O–Cu(110) surface may not be all that different as commented by Hüfner [16]. Nevertheless, it should be noted that the feature at +2 eV coincides with those probed using STS on the same O–Cu(001) surface. This empty feature decreases with increasing oxygen exposure.

PES, IPES, and XPS data are available for systems of PdO [28, 29], O–Cu(110) [30], O–Nb(110) [31], AgO [32], and Bi₂Sr₂CaCu₂O₈ [33]. These spectra share considerable DOS similarities in the valence band and above. Au nanoclusters deposited on TiO₂(110) substrate also exhibits a weak feature at -1.0 eV due to the interfacial oxidation [34].

XPS study [35] revealed that oxygen adsorption shifts the Pd(3d_{5/2}) core level by ~ 0.6 eV toward lower (deeper) binding energy, which coincides with the O–1s core-level shift detected from the O–Cu(001) surface [36]. The O–1s level (-529.5 eV) shifts 0.6 to -530.1 eV when the oxygen reacts with the Cu(001) surface. The Rh-3d binding energy increases about 0.3 eV per bond given an oxygen adsorbate at the Rh(111) surface [37]. Two distinct components in the Ru-3d_{5/2} core-level spectra have been detected from the clean Ru(0001) surface [38]. With increasing oxygen coverage on the Ru(0001) surface, the Ru-3d_{5/2} core-level peaks shift by up to -1.0 eV.

The core-level shift detected with an XPS shows that (1) the O adsorbate does capture electrons from metal atoms, and (2) the core-level shift of the clean Ru(0001) surface is indicative of the bond relaxation at the surface, which

Fig. 4.4 IPES (inverse photoemission) spectra of Cu(110)-O (9.7 eV) (Reprinted with permission from [26]) show the similar STS resonant features to that from the O-Nb(110) surface [5]. Feature *D* is a direct transition in the bulk band structure, while *S* a surface state. Feature *A* is an oxygen-induced orbital. Oxygen attenuated peak at 2.0 eV represents the occupancy of the empty surface states by antibonding dipoles



modifies the crystal field upon which core-level shift depends. Therefore, chemisorption is indeed a kinetic process in which electron transport dominates. Unfortunately, an XPS is unable to reveal direct information about the process of valence charge transport. In this sense, STS and UPS are more favorable than XPS, but mechanism for charge transportation must be clear.

Figure 4.5 shows that oxidation of a polycrystal Cu surface proceeds in three steps with the increase in the number of oxygen atoms on [9]. In the first step (the lowest exposures), chemical adsorption begins, which immediately leads to the rise of the shoulder *K* (−1.5 eV) and the small peak *D* (−6.0 eV) in the He-I spectra in Fig. 3. In the second step, further increase in oxygen leads to the intensity increase in the *D* feature and the disappearance of the maxima *A*, *A'* and *C*. In the third step at oxygen exposure of 5×10^3 L, a surface compound is formed, which exhibits semiconductive properties, and its electronic structure is very similar to that of the bulk copper protoxide Cu_2O . Emerging of the new features is at the expenses of a sharp fall of the feature at −3.0 eV and above. The DOS at E_F fall to zero and produce a gap of ~ 1.0 eV. PES study of a cleaved single Cu-O(001) crystal [18] as shown in Fig. 4.5, revealed three features centered at −1.45, −3.25, and −6.35 eV below the E_F .

Figure 4.6 shows the DFT optimal O-Ti(0001) surface structures and the TB-derived valence DOS. The four DOS features are the same to those 3B

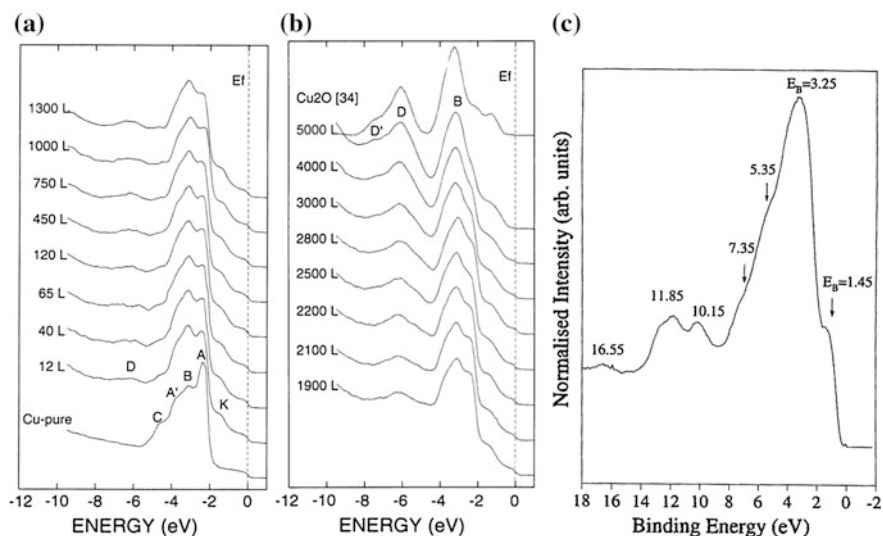


Fig. 4.5 **a, b** Oxygen exposure dependence of the He-I photoelectron spectra at the successive stages of oxygen adsorption on polycrystal Cu surface (reprinted with permission from [9]). Two apparent features *K* (-1.5 eV) and *D* (-6 eV) are similar to those appeared in other oxide surfaces. **c** PES of cleaved crystal of O-Cu(001) valence band spectral features recorded at 70 eV energy. Labeled energies indicate the DOS features (reprinted with permission from [18])

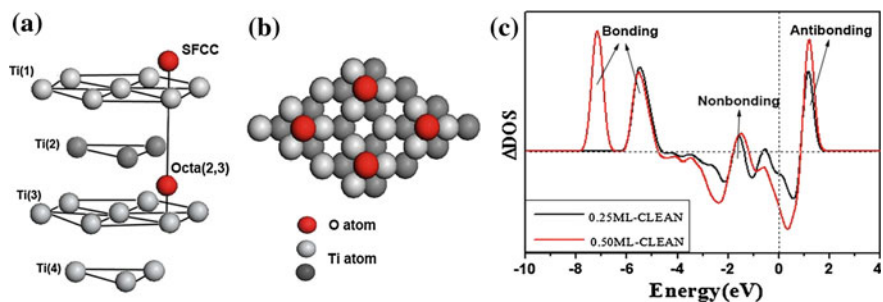


Fig. 4.6 DFT derivatives of the **a** side and **b** top views of oxygen reaction with Ti(0001)- $p(2 \times 2)$ surface and **c** tight-binding approximation of the residual energy states, $n(\text{Ti} + \text{O}) - n(\text{Ti})$. Oxygen atoms occupy the surface face-centered cubic (SFCC) sites at 0.25 ML and then occupy both the SFCC and the octahedral sites between the second and the third Ti layers [Octa(2, 3)] sites at 0.50 ML. Four DOS features correspond to the antibonding ($+1.2$ eV), nonbonding (-1.6 eV), holes (-2.3 eV), and bonding (-6.0 eV) states, agreeing with the 3B prediction

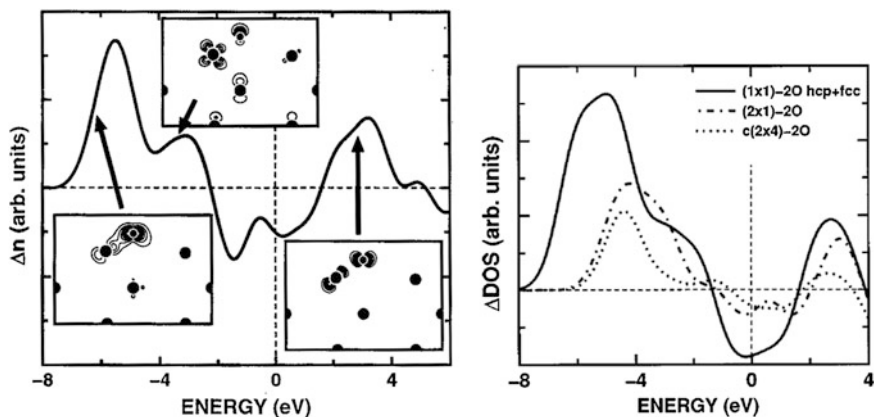


Fig. 4.7 Tight-binding approximation of the residual DOS, $n(\text{Ru} + \text{N/O}) - n(\text{Ru})$, among the Ru(0001)- $c(2 \times 2)$ -N, Ru(10 $\bar{1}$ 0)- $c(2 \times 1)$ -O, and Ru(0001) surfaces (reprinted with permission from [39]). Four DOS features correspond to the antibonding (~ 3.0 eV), hole (-1.0 eV), non-bonding (-3.0 eV), and bonding (-6.0 eV) states as specified by the 3B prediction on O and N addition

expects. The DOS definition also applies to reactions involving other electro-negative elements such as N and S. Figure 4.7 compares residual DOS for both the N-Ru(0001) [39] and the O-Ru(10 $\bar{1}$ 0) [40] surfaces, which are the same and the identities agree with those specified by the current 3B correlation premise. The features correspond to bonding (-6.0 eV), non-bonding (-3.0), holes (-1.0), and antibonding ($+3.0$) states. N-induced lone pair states of nitrogen have been widely observed [41–44]. STS [45] also revealed strong DOS features in the conduction band of CN_x nanotubes close to the Fermi level (0.18 eV).

4.1.3 Indication

Comparing the DOS features detected using STS, PES, and IPES, one may conclude immediately that the oxygen-derived valence DOS features are very common for all the analyzed systems. All the DOS features appeared in the valence band or above of oxide surfaces, such as O-Cu(110), O-Cu(111), and O-Pd(110), are actually the same despite their surface crystal geometries and morphologies. The patterns of morphology and crystallography vary indeed from situation to situation, as discussed in Sect. 4.3, but the DOS spectral features detected are commonly the same.

4.2 Specification

Opinions regarding the O-induced valence DOS features are controversial. For instance, the additional DOS features around -1.4 to -2.0 eV of the copper oxide were argued as (1) O–Cu antibonding states [6, 18, 46], (2) O-2p antibonding states [6, 16, 46], (3) oxygen 2s states [47, 48], and (4) the O-2p electrons with the *spd* hybridized electrons of Cu [9]. The additional DOS features around -5.5 eV were interpreted as O-2p states adding to the valence band of the host surface [6, 8, 16]. The sharp fall of the DOS features at $E_F > E > -3.0$ eV corresponds to the disappearance of the clean Cu surface states.

Chemisorption is a kinetic process in which the valences of the bonding constituents change and hence the sizes and positions of surface atoms change. Electrons transport from the valence band of the host to the empty *p*-orbital of oxygen for the bonding, and then, the oxygen hybridizes with the production of lone pairs. The lone pairs polarize in turn their surrounding neighbors, and the electrons of the host dipoles move from the original energy level to the higher energy levels. These sequential processes will redistribute electrons at the valence band and above of the host with four additional DOS features.

Table 4.1 features the adsorbate-derived DOS features in the valence band of metals. The 3B modeling premise defines the O-derived DOS features consistently:

- The DOS features above E_F (~ 2.0 eV for Cu) correspond to the occupation of the empty surface states by the antibonding dipoles, which lower the work function. Resonant peaks come from the surface image states.
- The shift of the resonances for O–Nb(110) to lower energy corresponds to the increase in work function due to H-like bond formation at the surface.
- Lone pair production generates the DOS feature between -1.5 and -2.0 eV below E_F .
- Features around -5.5 eV are derivatives of the O–metal bonding.
- The sharp fall of the DOS features near the E_F results from the hole production in the process of bond and antibonding dipole formation.

Electronic hole production and lone pair production have opposite effects on the DOS distribution between -3.0 eV and E_F . The former weakens the DOS intensity, while the latter enhances it. What one can detect is the resultant of these two effects. The DOS change detected in this region may be insignificant if these two opposite processes are comparable in quantity.

Therefore, the D feature in Fig. 4.5 corresponds to the O–Cu hybrid bonding and the K feature to the oxygen nonbonding states. The fall of the upper part of *d* band corresponds to the process of electron transportation from the outer shell of Cu to the deeper empty *sp* hybrid orbitals of oxygen, or to the even higher empty levels of Cu to form dipoles. The rise of the K feature in energy space is independent of the fall of the intensity near the E_F . The exposure dependence of the valence DOS change should provide valuable information about the dynamics of

Table 4.1 Adsorbate-derived DOS features adding to the valence band of hosts (unit in eV) (reprinted with permission from [11])

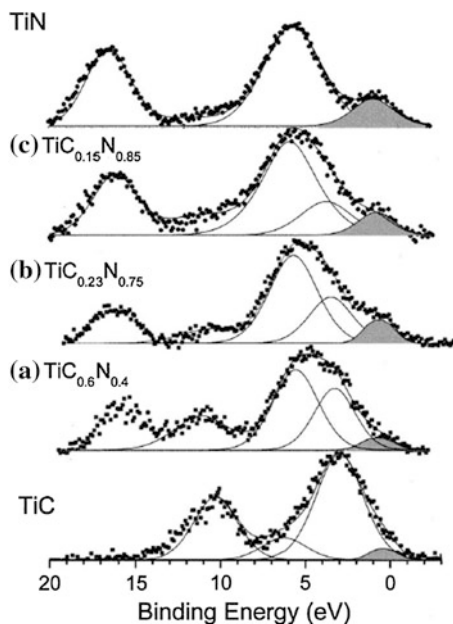
| Other methods | Antibond dipole, $>E_F$ | Lone pair $<E_F$ | M (hole) $<E_F$ | O–M bond $<E_F$ |
|---------------------------------|-----------------------------|----------------------------------|-------------------|-----------------|
| O–Cu(001) [18, 55] | | -1.5 ± 0.5 | -3.0 ± 1.0 | -6.5 ± 1.5 |
| | 1.2 | -2.1 | | |
| O–Cu(001) [46] | | $-1.37; -1.16$ | | |
| O–Ni(001) [56] | | | | $E_F \sim -6.0$ |
| O–Cu(110) [4, 6, 8, 26, 57, 58] | ~ 2.0 1.3 ± 0.5 | -1.5 ± 0.5 -2.1 ± 0.5 | -3.0 ± 1.0 | -6.5 ± 1.5 |
| O–Cu(poly) [9] | | -1.5 | -3.0 ± 1.0 | -6.5 ± 1.5 |
| O–Cu/Ag(110) [17] | | -1.5 | | $-3.0; -6.0$ |
| O–Rh(001) [59] | 1.0 | -3.1 | | -5.8 |
| O–Pd(110) [35] | | -2.0 ± 0.5 | $-0.5, 3.0$ | -4.5 ± 1.5 |
| O–Al(poly) [60] | 1.0 | | | |
| O–Gd(0001) [61] | | -3.0 | $-1.0, -8.0$ | -6.0 |
| O–Ru(0001) [62] | | -1.0 ± 1.0 | | -5.5 ± 1.5 |
| O–Ru(0001) [63] | | -0.8 | | -4.4 |
| O–Ru(0001) [64] | 1.5 | -4 | | $-5.5, -7.8$ |
| O–Ru(0001) [65] | 1.7 | -3.0 | | -5.8 |
| O–Ru(10 $\bar{1}$ 0) [40] | 2.5 | -2 to -3.0 | | -5.0 |
| MgO/Ag(001) [66] | | -3.0 ± 1.0 | | |
| O–Co(Poly) [67] | | -2.0 | -0.7 | -5.0 |
| O–diamond (001) [68] | | -3.0 | | |
| O–C(nanotube) [69] | 0.8 | | | |
| (O, S)–Cu(001) [70] | | -1.3 | | -6.0 |
| (O, S, N)–Ag(111) [71] | | -3.4 | | -8.0 |
| N–Cu(001) [56, 70] | 3.0 | -1.2 | | -5.6 |
| | | -1.0 | -4.0 | -5.5 |
| N–Ru(0001) [39] | 3.0 | -3.0 | | -6.0 |
| N–Ag(111) [70] | | -3.4 | | -8.0 |
| TiCN [54] | | 0.0 ± 1.0 | | -5.7 |
| a–CN [72] | | -4.5 | | -7.1 |
| CN [73] | | -2.3 | | |

electron transportation. Slight difference in the peak positions may result from the difference in electronegativity that determines the ease of charge transport.

4.3 Valence DOS of Nitrides

Compared with the nanometric SiC, nanostructured SiN shows two additional DOS features located at ~ 3.3 eV below E_F and 1–3.8 eV above E_F [49]. The below- E_F feature corresponds to the N lone pair states and the above to the lone-pair-induced dipoles. A first-principle calculation [50] predicted that the N–N lone pair repulsion in the carbon nitride leads to a ~ 2.2 eV elevation in antibonding energy. Figure 4.8

Fig. 4.8 Evolution of the valence DOS from TiC to TiN showing the additional shaded lone pair features around E_F (reprinted with permission from [54])



shows the evolution of the valence DOS features upon C being gradually replaced by N in a TiC compound. The shaded broad peak around E_F corresponds to the lone pair, whereas the energy of the antibonding DOS is beyond the scope of XPS [51]. STS measurement [45] has revealed strong DOS features in the conduction band of CN_x nanotubes near the Fermi level (-0.18 eV), evidencing the existence of the lone pairs. For carbide, neither lone pair nor antibonding dipole could form upon reaction. However, nitrogenation adds a ~ 2.31 eV antibonding DOS [50]. An XPS, UPS, NEXAFS, and XES revealed the lone pair (~ -3.8 eV), σ (~ -8.8 eV) and π (~ -6.4 eV) bond configurations from carbon nitride films [52].

4.4 Summary

Electron spectroscopic observations confirm the creation and evolution dynamics of the valence states during chemisorption. In addition to the bonding states, the nonbonding lone pair of the adsorbate, the antibonding dipole states of the host, and the electron hole of the host atom can never be neglected, which modify the physical properties of a chemisorbed surface.

References

1. Y. Kuk, P.J. Silverman, Scanning tunneling microscope instrumentation. *Rev. Sci. Instrum.* **60**(2), 165–180 (1989)
2. J.B. Pendry, A.B. Pretre, B.C.H. Krutzen, Theory of the scanning tunneling microscope. *J. Phys.: Condens. Matter* **3**(24), 4313–4321 (1991)
3. J. Wintterlin, R.J. Behm, in *The Scanning Tunnelling Microscopy I*, ed. by H.J. Günthert, R. Wiesendanger (Springer, Berlin, 1992)
4. F.M. Chua, Y. Kuk, P.J. Silverman, Oxygen-chemisorption on cu(110): an atomic view by scanning tunneling microscopy. *Phys. Rev. Lett.* **63**(4), 386–389 (1989)
5. C. Surgers, M. Schock, H. von Lohneysen, Oxygen-induced surface structure of Nb(110). *Surf. Sci.* **471**(1–3), 209–218 (2001)
6. W. Jacob, V. Dose, A. Goldmann, Atomic adsorption of oxygen on Cu(111) and Cu(110). *Appl. Phys. A-Mater. Sci. Process.* **41**(2), 145–150 (1986)
7. W. Sesselmann, H. Conrad, G. Ertl, J. Kupperts, B. Woratschek, Probing the local density of states of metal-surfaces by deexcitation of metastable noble-gas atoms. *Phys. Rev. Lett.* **50**(6), 446–450 (1983)
8. R.A. Didio, D.M. Zehner, E.W. Plummer, An angle-resolved ups study of the oxygen-induced reconstruction of Cu(110). *J. Vac. Sci. Technol. Vac. Surf. Films* **2**(2), 852–855 (1984)
9. V.P. Belash, I.N. Klimova, V.I. Kormilets, V.Y. Trubitsin, L.D. Finkelstein, Transformation of the electronic structure of Cu into Cu₂O in the adsorption of oxygen. *Surf. Rev. Lett.* **6**(3–4), 383–388 (1999)
10. R. Courths, B. Cord, H. Wern, H. Saalfeld, S. Hufner, Dispersion of the oxygen-induced bands on Cu (110): an angle-resolved UPS study of the system p(2 × 1)O/Cu(110). *Solid State Commun.* **63**(7), 619–623 (1987)
11. C.Q. Sun, S. Li, Oxygen-derived DOS features in the valence band of metals. *Surf. Rev. Lett.* **7**(3), 213–217 (2000)
12. G. Binnig, K.H. Frank, H. Fuchs, N. Garcia, B. Reihl, H. Rohrer, F. Salvan, A.R. Williams, Tunneling spectroscopy and inverse photoemission: image and field states. *Phys. Rev. Lett.* **55**(9), 991–994 (1985)
13. T. Jung, Y.W. Mo, F.J. Himpsel, Identification of metals in scanning-tunneling-microscopy via image states. *Phys. Rev. Lett.* **74**(9), 1641–1644 (1995)
14. M. Portalupi, L. Duo, G. Isella, R. Bertacco, M. Marcon, F. Ciccacci, Electronic structure of epitaxial thin NiO(100) films grown on Ag(100): towards a firm experimental basis. *Phys. Rev. B* **64**(16), 165402 (2001)
15. R. Pantel, M. Bujor, J. Bardolle, Continuous measurement of surface-potential variations during oxygen-adsorption on (100), (110) and (111) faces of niobium using mirror electron-microscope. *Surf. Sci.* **62**(2), 589–609 (1977)
16. S. Hüfner, *Photoelectron Spectroscopy: Principles and Applications* (Springer, New York, 1995)
17. D. Sekiba, D. Ogarane, S. Tawara, K. Yagi-Watanabe, Electronic structure of the Cu-O/Ag(110)(2 × 2)p2 mg surface. *Phys. Rev. B* **67**(3), 035411 (2003)
18. S. Warren, W.R. Flavell, A.G. Thomas, J. Hollingworth, P.L. Wincott, A.F. Prime, S. Downes, C.K. Chen, Photoemission studies of single crystal CuO(100). *J. Phys. Condens. Matter* **11**(26), 5021–5043 (1999)
19. E.G. Emberly, G. Kirzenow, Antiresonances in molecular wires. *J. Phys. Condens. Matter* **11**(36), 6911–6926 (1999)
20. K. Yagi, K. Higashiyama, H. Fukutani, Angle-resolved photoemission-study of oxygen-induced c(2 × 4) structure on Pd(110). *Surf. Sci.* **295**(1–2), 230–240 (1993)
21. C.W. Tucker, Oxygen faceting of rhodium (210) and (100) surfaces. *Acta Metall.* **15**(9), 1465–1474 (1967)

22. J.R. Mercer, P. Finetti, M.J. Scantlebury, U. Beierlein, V.R. Dhanak, R. McGrath, Angle-resolved photoemission study of half-monolayer O and S structures on the Rh(100) surface. *Phys. Rev. B* **55**(15), 10014–10021 (1997)
23. M. Zacchigna, C. Astaldi, K.C. Prince, M. Sastry, C. Comicioli, R. Rosei, C. Quaresima, C. Ottaviani, C. Crotti, A. Antonini, M. Matteucci, P. Perfetti, Photoemission from atomic and molecular adsorbates on Rh(100). *Surf. Sci.* **347**(1–2), 53–62 (1996)
24. E. Schwarz, J. Lenz, H. Wohlgenuth, K. Christmann, The interaction of oxygen with a rhodium (110) surface. *Vacuum* **41**(1–3), 167–170 (1990)
25. C.Q. Sun, Exposure-resolved VLEED from the O–Cu(001): bonding dynamics. *Vacuum* **48**(6), 535–541 (1997)
26. V. Dose, Momentum-resolved inverse photoemission. *Surf. Sci. Rep.* **5**, 337–378 (1986)
27. C.T. Chen, N.V. Smith, Unoccupied surface-states on clean and oxygen-covered Cu(110) and Cu(111). *Phys. Rev. B* **40**(11), 7487–7490 (1989)
28. T. Pillo, R. Zimmermann, P. Steiner, S. Hufner, The electronic structure of PdO found by photoemission (UPS and XPS) and inverse photoemission (BIS). *J. Phys. Condens. Matter* **9**(19), 3987–3999 (1997)
29. K. Yagi, H. Fukutani, Oxygen adsorption site of Pd(110)c(2 × 4)–O: analysis of ARUPS compared with STM image. *Surf. Sci.* **412–13**, 489–494 (1998)
30. R. Ozawa, A. Yamane, K. Morikawa, M. Ohwada, K. Suzuki, H. Fukutani, Angle-resolved UPS study of the oxygen-induced 2 × 1 surface of Cu(110). *Surf. Sci.* **346**(1–3), 237–242 (1996)
31. Y.S. Wang, X.M. Wei, Z.J. Tian, Y.M. Cao, R.S. Zhai, T. Ushikubo, K. Sato, S.X. Zhuang, An AES, UPS and HREELS study of the oxidation and reaction of Nb(110). *Surf. Sci.* **372**(1–3), L285–L290 (1997)
32. A.I. Boronin, S.V. Koscheev, G.M. Zhidomirov, XPS and UPS study of oxygen states on silver. *J. Electron Spectrosc. Relat. Phenom.* **96**(1–3), 43–51 (1998)
33. A.M. Aprelev, V.A. Grazhulis, A.M. Ionov, A.A. Lisachenko, UPS (8.43-eV and 21.2-eV) data on the evolution of DOS spectra near E(f) of Bi₂Sr₂CaCu₂O₈ under thermal and light treatments. *Physica C* **235**, 1015–1016 (1994)
34. A. Howard, D.N.S. Clark, C.E.J. Mitchell, R.G. Egdell, V.R. Dhanak, Initial and final state effects in photoemission from Au nanoclusters on TiO₂(110). *Surf. Sci.* **518**(3), 210–224 (2002)
35. V.A. Bondzie, P. Kleban, D.J. Dwyer, XPS identification of the chemical state of subsurface oxygen in the O/Pd(110) system. *Surf. Sci.* **347**(3), 319–328 (1996)
36. H. Tillborg, A. Nilsson, B. Hernnas, N. Martensson, O/Cu(100) studied by core level spectroscopy. *Surf. Sci.* **270**, 300–304 (1992)
37. M.V. Ganduglia-Pirovano, M. Scheffler, Structural and electronic properties of chemisorbed oxygen on Rh(111). *Phys. Rev. B* **59**(23), 15533–15543 (1999)
38. S. Lizzit, A. Baraldi, A. Groso, K. Reuter, M.V. Ganduglia-Pirovano, C. Stampf, M. Scheffler, M. Stihler, C. Keller, W. Wurth, D. Menzel, Surface core-level shifts of clean and oxygen-covered Ru(0001). *Phys. Rev. B* **63**(20), 205419 (2001)
39. S. Schwegmann, A.P. Seitsonen, H. Dietrich, H. Bludau, H. Over, K. Jacobi, G. Ertl, The adsorption of atomic nitrogen on Ru(0001): geometry and energetics. *Chem. Phys. Lett.* **264**(6), 680–686 (1997)
40. S. Schwegmann, A.P. Seitsonen, V. De Renzi, H. Dietrich, H. Bludau, M. Gierer, H. Over, K. Jacobi, M. Scheffler, G. Ertl, Oxygen adsorption on the Ru(10 $\bar{1}$ 0) surface: anomalous coverage dependence. *Phys. Rev. B* **57**(24), 15487–15495 (1998)
41. C.Q. Sun, A model of bonding and band-forming for oxides and nitrides. *Appl. Phys. Lett.* **72**(14), 1706–1708 (1998)
42. C.Q. Sun, A model of bond-and-band for the behavior of nitrides. *Mod. Phys. Lett. B* **11**(23), 1021–1029 (1997)
43. Y.Q. Fu, C.Q. Sun, H.J. Du, B.B. Yan, Crystalline carbonitride forms harder than the hexagonal Si-carbonitride crystallite. *J. Phys. D-Appl. Phys.* **34**(9), 1430–1435 (2001)

44. C.Q. Sun, B.K. Tay, S.P. Lau, X.W. Sun, X.T. Zeng, S. Li, H.L. Bai, H. Liu, Z.H. Liu, E.Y. Jiang, Bond contraction and lone pair interaction at nitride surfaces. *J. Appl. Phys.* **90**(5), 2615–2617 (2001)
45. M. Terrones, P.M. Ajayan, F. Banhart, X. Blase, D.L. Carroll, J.C. Charlier, R. Czerw, B. Foley, N. Grobert, R. Kamalakaran, P. Kohler-Redlich, M. Ruhle, T. Seeger, H. Terrones, N-doping and coalescence of carbon nanotubes: synthesis and electronic properties. *Appl. Phys. Mater. Sci. Process.* **74**(3), 355–361 (2002)
46. F. Pforte, A. Gerlach, A. Goldmann, R. Matzdorf, J. Braun, A. Postnikov, Wave-vector-dependent symmetry analysis of a photoemission matrix element: the quasi-one-dimensional model system Cu(110)(2 × 1)O. *Phys. Rev. B* **63**(16), 165405 (2001)
47. C. Benndorf, B. Egert, G. Keller, H. Seidel, F. Thieme, Oxygen interaction with Cu(100) studied by AES, ELS, LEED and work function changes. *J. Phys. Chem. Solids* **40**(12), 877–886 (1979)
48. C. Benndorf, B. Egert, G. Keller, F. Thieme, Initial oxidation of Cu(100) single-crystal surfaces: electron spectroscopic investigation. *Surf. Sci.* **74**(1), 216–228 (1978)
49. M. DrissKhodja, A. Gheorghiu, G. Dufour, H. Roulet, C. Senemaud, M. Cauchetier, Electronic structure of nanometric Si/C, Si/N, and Si/C/N powders studied by both x-ray-photoelectron and soft-x-ray spectroscopies. *Phys. Rev. B* **53**(8), 4287–4293 (1996)
50. T. Hughbanks, Y.C. Tian, On the structure and composition of carbon nitride. *Solid State Commun.* **96**(5), 321–325 (1995)
51. C.Q. Sun, Oxidation electronics: bond-band-barrier correlation and its applications. *Prog. Mater. Sci.* **48**(6), 521–685 (2003)
52. N. Hellgren, J.H. Guo, Y. Luo, C. Sathe, A. Agui, S. Kashtanov, J. Nordgren, H. Agren, J.E. Sundgren, Electronic structure of carbon nitride thin films studied by X-ray spectroscopy techniques. *Thin Solid Films* **471**(1–2), 19–34 (2005)
53. J. Wintterlin, R. Schuster, D.J. Coulman, G. Ertl, R.J. Behm, Atomic motion and mass-transport in the oxygen induced reconstructions of Cu(110). *J. Vac. Sci. Technol. B* **9**(2), 902–908 (1991)
54. G.G. Fuentes, E. Elizalde, J.M. Sanz, Optical and electronic properties of TiC_xNy films. *J. Appl. Phys.* **90**(6), 2737–2743 (2001)
55. C.Q. Sun, S. Li, B.K. Tay, X.W. Sun, S.P. Lau, Solution certainty in the Cu(110)-(2 × 1)-2O(2-) surface crystallography. *Int. J. Mod. Phys. B* **16**(1–2), 71–78 (2002)
56. H. Tillborg, A. Nilsson, T. Wiell, N. Wassdahl, N. Martensson, J. Nordgren, Electronic-structure of atomic oxygen adsorbed on Ni(100) and Cu(100) studied by soft-x-ray emission and photoelectron spectroscopies. *Phys. Rev. B* **47**(24), 16464–16470 (1993)
57. A. Spitzer, H. Luth, The adsorption of oxygen on copper surfaces.1. Cu(100) and Cu(110). *Surf. Sci.* **118**(1–2), 121–135 (1982)
58. A. Spitzer, H. Luth, The adsorption of oxygen on copper surfaces. 2. Cu(111). *Surf. Sci.* **118**(1–2), 136–144 (1982)
59. D. Alfe, S. de Gironcoli, S. Baroni, The reconstruction of Rh(001) upon oxygen adsorption. *Surf. Sci.* **410**(2–3), 151–157 (1998)
60. A.C. Perrella, W.H. Rippard, P.G. Mather, M.J. Plisch, R.A. Buhrman, Scanning tunneling spectroscopy and ballistic electron emission microscopy studies of aluminum-oxide surfaces. *Phys. Rev. B* **65**(20), 201403 (2002)
61. J.D. Zhang, P.A. Dowben, D.Q. Li, M. Onellion, Angle-resolved photoemission-study of oxygen-chemisorption on Gd(0001). *Surf. Sci.* **329**(3), 177–183 (1995)
62. A. Bottcher, H. Niehus, Oxygen adsorbed on oxidized Ru(0001). *Phys. Rev. B* **60**(20), 14396–14404 (1999)
63. A. Bottcher, H. Conrad, H. Niehus, Reactivity of oxygen phases created by the high temperature oxidation of Ru(0001). *Surf. Sci.* **452**(1–3), 125–132 (2000)

64. G. Bester, M. Fahnle, On the electronic structure of the pure and oxygen covered Ru(0001) surface. *Surf. Sci.* **497**(1–3), 305–310 (2002)
65. C. Stampfl, M.V. Ganduglia-Pirovano, K. Reuter, M. Scheffler, Catalysis and corrosion: the theoretical surface-science context. *Surf. Sci.* **500**(1–3), 368–394 (2002)
66. S. Altieri, L.H. Tjeng, G.A. Sawatzky, Electronic structure and chemical reactivity of oxide-metal interfaces: MgO(100)/Ag(100). *Phys. Rev. B* **61**(24), 16948–16955 (2000)
67. R. Mamy, Spectroscopic study of the surface oxidation of a thin epitaxial Co layer. *Appl. Surf. Sci.* **158**(3–4), 353–356 (2000)
68. J.C. Zheng, X.N. Xie, A.T.S. Wee, K.P. Loh, Oxygen-induced surface state on diamond (100). *Diam. Relat. Mat.* **10**(3–7), 500–505 (2001)
69. L.W. Lin, The role of oxygen and fluorine in the electron-emission of some kinds of cathodes. *J. Vac. Sci. Technol. Vac. Surf. Films* **6**(3), 1053–1057 (1988)
70. G.G. Tibbetts, J.M. Burkstrand, J.C. Tracy, Electronic properties of adsorbed layers of nitrogen, oxygen, and sulfur on copper (100). *Phys. Rev. B* **15**(8), 3652–3660 (1977)
71. G.G. Tibbetts, J.M. Burkstrand, Electronic properties of adsorbed layers of nitrogen, oxygen, and sulfur on silver (111). *Phys. Rev. B* **16**(4), 1536–1541 (1977)
72. S. Souto, M. Pickholz, M.C. dos Santos, F. Alvarez, Electronic structure of nitrogen-carbon alloys (a-CN_x) determined by photoelectron spectroscopy. *Phys. Rev. B* **57**(4), 2536–2540 (1998)
73. Z.Y. Chen, J.P. Zhao, T. Yano, T. Ooie, Valence band electronic structure of carbon nitride from x-ray photoelectron spectroscopy. *J. Appl. Phys.* **92**(1), 281–287 (2002)

Chapter 5

TDS: Bond Nature and Bond Strength

- TDS resolves bond breaking dynamics.
- TDS features and work function change coincidentally demonstrate four-stage bond forming kinetics and associated valence charge relaxation.
- The four stages include the following: (1) O^{1-} formation, (2) O^{1-} turns to O^{2-} with *sp*-orbit hybridization, (3) tetrahedron relaxation, and (4) dipole annihilation upon oxygen overdosing.

5.1 TDS and Work Function Correspondence

One of the striking TDS features of the O–Pd(110) surface is the coincidence of the exposure-resolved TDS with the work function change ($\Delta\phi$) [1]. Figures 5.1 and 5.2 show coincidence as follows:

(1) The four TDS peaks assigned as β_1 , β_2 , γ_1 , and γ_2 oscillate with increasing oxygen exposure to the Pd(110) surface. The changes in the TDS peak intensities show clearly the discrete stages of reaction:

- β_2 emerges first upon introduction of oxygen to the surface and the β_2 peak saturates at 2.5 L exposure, and then keeps constant until 240 L;
- β_1 emerges at 1.5 L and increases gradually in intensity until 240 L;
- after an extremely high oxygen exposure (22,800 L), a reversal, or oscillation, in the spectral intensities of β_1 and β_2 occurs. β_1 is substantially more intense than β_2 , which differs significantly from the trends at lower oxygen exposures, where β_1 is always weaker than β_2 . At the extremely high exposure, two troughs, γ_1 (600 K) and γ_2 (705 K), emerge at the expense of slowing the increase in intensity of β_2 .

TDS from an O–Pd(001) surface exhibits the same trend [2]. The Pd(001) surfaces exposed to oxygen at 350 K temperature results in a single TDS peak at 850 K. The peak shifts from 850 K at lower coverage to 800 K after a 10 L exposure at which the highest temperature peak saturates. After the 800 K peak saturates, a new TDS peak appears at 700 K that saturates at an exposure of 20 L.

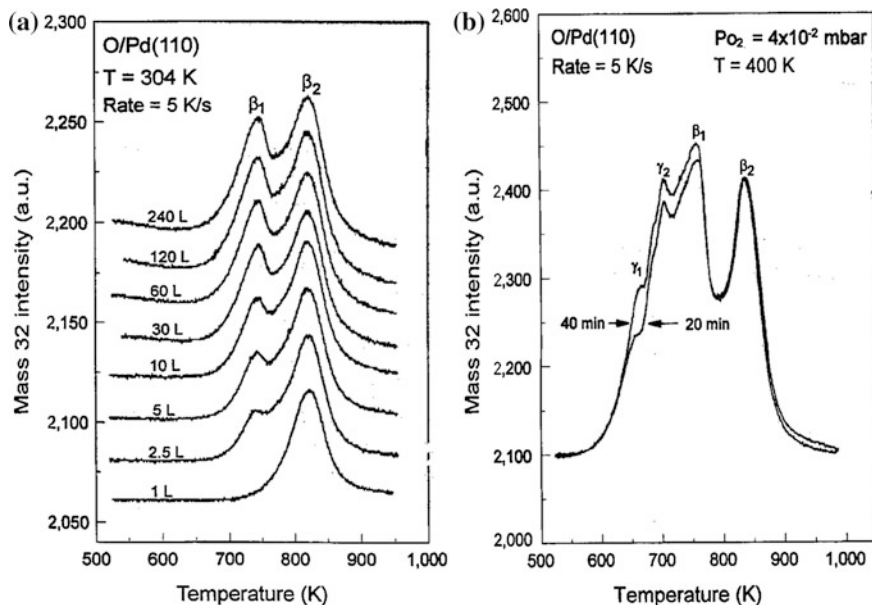


Fig. 5.1 a TDS profiles from Pd(110) surface exposed to oxygen at 304 and 400 K show the oscillation of the β_1 (730 K), β_2 (830 K), γ_1 (660 K), and γ_2 (700 K) TDS peaks with increasing oxygen exposure (reprinted with permission from [1])

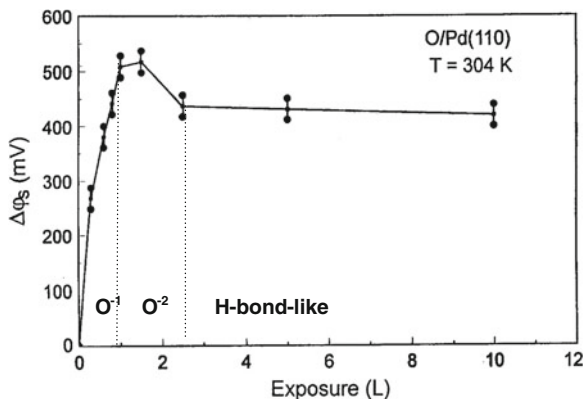


Fig. 5.2 The oxygen exposure dependence of the work function change $\Delta\phi$ derived from the UPS spectra of the O-Pd(110) surface. The separated regions correspond to the O^{-1} -induced polarization, O^{-2} -hybrid-induced polarization, and H-like bond formation annihilated polarization (reprinted with permission from [1])

Meanwhile, another peak shows up at 650 K, which shifts toward 700 K with further increase in exposure. Above 1,000 L, the oxygen uptake slows and an additional peak shoulder at 600 K presents.

The exposure-derived $\Delta\phi$ of the O–Pd(110) surface agrees with that of the O–Ru(0001) surface [3, 4] and the O–Gd(0001) surface as well [5]. The $\Delta\phi$ for the O–Pd(110) surface changes in the following ways [1]:

- the $\Delta\phi$ reaches 500 meV at 1.0 L oxygen exposure and then to a maximum 520 meV at 1.5 L;
- from 1.5 to 2.5 L, the $\Delta\phi$ decreases from 520 to 430 meV;
- the $\Delta\phi$ reduces from 430 meV at 2.5 L and below significantly to 400 meV at 10 L.

Figure 5.3 shows the exposure-resolved TDS profiles recorded from the O–Rh(110) surface [6–8]. The TDS profiles exhibit five desorption maxima around 797, 835, 909, 1,095, and 1,150–1,190 K. Besides the addition of the fifth peak, the emerging trend and the oscillation of these peaks are substantially the same as the set for the O–Pd(001) and (110) surfaces though the peak positions differ slightly. The peak temperatures for the O–Rh(110) surface are slightly higher than that of the O–Pd(001) and the O–Pd(110) surfaces. The broadened peak β_5 which shifts to lower temperature with increasing population of desorption states indicates the second-order desorption kinetics. All other TDS maxima are invariant with coverage according to the first-order kinetics.

Combining the TDS profiles and LEED crystallography of the O–Rh(110) surface, Schwarz et al. [7] correlated the TDS peaks to the LEED patterns of various reconstructed phases. Comelli et al. [6] reinterpreted the TDS data of the O–Rh(110) surface based on the known adsorbate's locations. The most stable structure corresponds to the p2mg phase and so the adsorbate binds to the surface more strongly. Due to the repulsive interactions, the adsorbate in the unreconstructed troughs binds to the surface weakly.

Similarly, TDS studies [9–12] revealed that the O–Rh(001) surface reaction involves three phases. The first phase gives no desorption feature up to 350 K because of physisorption. For temperatures above 500 K, chemisorption takes place. The latter two states yield oxygen ions of different kinetic energies. Three peaks (820, 920, and 1,325–1,200 K with the corresponding enthalpy of 210, 260, and 360 kJ/mol) are present in the TDS spectrum of the same O–Rh(001) surface [13]. A kinetic Monte Carlo simulation supports this measurement with derivative of desorption peaks at 820, 925, and 1,250 K [14].

The state of desorption of O–Rh(110) at $T > 1,200$ K was related to the $p(2 \times 2)\text{-O}^{-1}$ structure (at oxygen coverage less than 0.5 ML) and it is a second order. The 920 K state showed first-order kinetics, which was related to the $c(2 \times 2)\text{-2O}^{-1}$ phase (at 0.5 ML coverage). The 820 K peak was associated with desorption from the $c(2 \times 2)\text{p4g-2O}^{-2}$ structure (O^{-2} dominates with H-like bond involvement at 0.5 ML coverage). This TDS spectrum entirely indicates that the adsorption enthalpy of oxygen *decreases* with the evolution of oxygen valence from the O^{-1} to the O^{-2} . The initial precursor O^{-1} states are more stable than the fully developed O^{-2} phase [14], which is different from descriptions of the O–Rh(110) surface [6, 7].

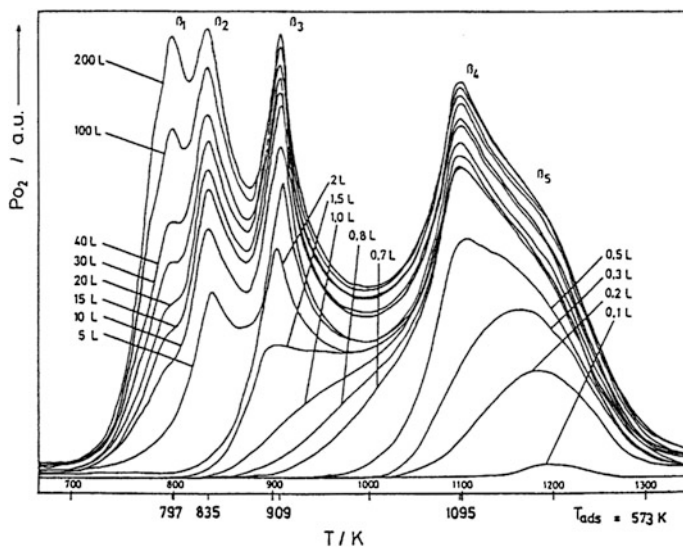


Fig. 5.3 TDS profiles for the Rh(110) surface exposed to oxygen at 573 K (reprinted with permission from [7]). Features oscillate with a similar trend to those for the O–Pd(110) surface upon increase in oxygen exposure

Based on their TDS profiles from the O–Rh(111) surface, Peterlinz and Sibener [15] suggested that (1) subsurface oxygen forms first on the Rh(111) surface at a temperature below 375 K; (2) the subsurface oxygen starts to segregate to the surface at 375 K, and (3) the desorption occurs at above 650 K. The velocity distribution of the desorbed oxygen is the same as that of the adsorbed oxygen. This velocity identity can be indicative that oxygen desorbing from the surface is in the same state as the original state of oxygen before desorbing from the surface. Using the time-of-flight spectroscopy, Gibson et al. [16, 17] found that the velocity distribution of the desorbed oxygen follows approximately the Maxwell–Boltzmann description. Such a characteristic is related to a ‘hot’ desorption, that is, the temperature of the desorbing gas is higher than the surface temperature. The gas temperature of 1,175 K is higher than the sample temperature in TDS (700–1,100 K), which implies that the TDS value of the heat of adsorption should be corrected slightly.

Böttcher et al. [18] detected two TDS peaks at 400 and 1,100 K from O–Ru(0001) surface at oxygen coverage below 0.25 ML. This result differs somewhat from the phase diagram showing two peaks at 754 and 555 K [19]. Despite the difference in the number of the TDS peaks and the binding strengths that vary with the surface orientation and with materials, the TDS features of oxide surfaces share considerable similarities as compared in Fig. 5.4.

The origins of the TDS identities remain controversial. A good example is the TDS spectrum of O–Pd(110) surface. It is suggested that the β_1 peak and the more strongly bound β_2 peak are related to subsurface oxygen and surface oxygen, respectively [1, 22, 23]. However, another commonly accepted explanation [24] is

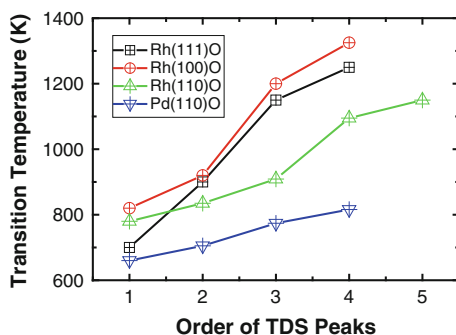


Fig. 5.4 Comparison of the desorption temperatures and the number of TDS peaks for the O–Pd(110) [1], O–Rh(001) [13], O–Rh(110) [7], and O–Rh(111) [20] surfaces. The number of the TDS peaks is nearly the same although the binding strengths vary from situation to situation with the surface orientations and with materials (reprinted with permission from [21])

that these two peaks come from the O [25] and the O isotopes [26]. The reason for the β_1 and β_2 oscillation for O–Pd(110) corresponds to a process of oxidation–reduction [1] or to the filling and depletion of subsurface oxygen [22, 23]. The detailed nature of the subsurface states of oxygen is to be defined precisely though the subsurface oxygen was widely reported on the Rh surfaces [6].

TDS revealed four TD peaks at 415, 545, 620, and 750–950 K for O–Au(110) surface [27]. These peaks are associated with chemisorbed atomic oxygen, oxygen atoms chemically dissolved in the bulk, and gold oxide. The peak positions depend strongly on the oxygen ion beam energy bombarding the surface (penetration depth) and the substrate temperature. Increasing the ion energy from 1.0 to 5.0 keV, the 750 K peak shifts to 850 K with attenuation of peak intensity of the lower temperatures, indicating the bulk site occupation. With constant ion energy at 2.0 keV, the 750 K peak shifts to 800 K and announced low temperature peaks present when the sputtering time is prolonged from 1 to 20 min. Raising the heating rate has the similar effect as prolonging the sputtering duration on oxide formation on Au surface.

5.2 Specification

Thermal desorption, known as bond breaking, is actually a reverse process of bond formation. As noted by Redhead [28], TDS can clearly separate the multiple binding states of the adsorbate atoms. Therefore, the peaks in the TDS profiles are associated with the individual process in which a specific bond forms. The similarity of the TDS signatures and the generality of the DOS features for all the analyzed systems exhibit the inherent correlation between bond formation and charge transportation. Encouragingly, the process of electronic transportation and the nature and relaxation of the chemical bonds involved are intrinsically common

Table 5.1 Correlation between the bond nature and the TDS and the valence DOS features for the O–Pd(110) and O–Pd(001) surfaces (reprinted with permission from [21])

| Bond nature | TDS features (K) | | DOS features (eV) |
|-------------|------------------|-----------------------|-----------------------|
| | O–Pd(110) [1] | O–Pd(001) [2] | O–Pd(110) |
| Ionic bond | $\beta_2(816)$ | 850 \rightarrow 800 | –5 |
| Lone pair | $\beta_1(774)$ | 800 | –2 |
| H-like bond | $\gamma_2(705)$ | 700 | $\Delta\phi$ recovery |
| H-like bond | $\gamma_1(660)$ | 600–650 | $\Delta\phi$ recovery |
| Dipole | $\Delta\phi$ | | +2 |

for all the analyzed systems, despite different patterns of observations by other means. This enables one to relate the TDS signatures to the bonds of different nature and to the DOS features in the valence band, for the O–Pd(110) and O–Pd(001) examples, as listed in Table 5.1.

This specification also applies to the TDS signatures in Fig. 5.3 correspondingly. These peaks correspond to the activation energies for the individual bond breaking. It should be a helpful practice for interested readers to interpret the TDS of the O–Rh(110) surface. The fifth peak may relate to the contracting ionic bond at the initial stage of reaction and the bond length relaxes with the development of the tetrahedron, which lowers the activation energy. The two peaks at 754 and 555 K appearing in the O–Ru(0001) phase diagram [19] are also related to the ionic bond and the non-bonding lone pair interactions, which has been confirmed to exist in the DFT outcomes [29, 30]. The low coverage TDS features [18] may correspond to the on-surface oxygen (400 K) and the first contracting bond (1,100 K) between the O^{–1} and the Ru atom underneath.

As will be shown in Chap. 7, such specification allows the TDS oscillation for O–Pd(001), (110) to be related to the bond forming kinetics, agreeing with observations using other means, such as PES and VLEED, for other systems with chemisorbed oxygen.

5.3 Summary

TDS features the strength and breaking kinetics of individual bond and nonbond. Incorporation of TDS and work function confirmed the generality of four stage boning kinetics upon oxygen chemisorption.

References

1. V.A. Bondzie, P. Kleban, D.J. Dwyer, XPS Identification of the chemical state of subsurface oxygen in the O/Pd(110) system. *Surf. Sci.* **347**(3), 319–328 (1996)
2. G. Zheng, E.I. Altman, The oxidation mechanism of Pd(100). *Surf. Sci.* **504**(1–3), 253–270 (2002)

3. N. Materer, U. Starke, A. Barbieri, R. Doll, K. Heinz, M.A. Vanhove, G.A. Somorjai, Reliability of detailed LEED structural-analyses—Pt(111) and Pt(111)—p(2 × 2)—O. *Surf. Sci.* **325**(3), 207–222 (1995)
4. T.E. Madey, H.A. Engelhardt, D. Menzel, Adsorption of oxygen and oxidation of CO on ruthenium (001) surface. *Surf. Sci.* **48**(2), 304–328 (1975)
5. J.D. Zhang, P.A. Dowben, D.Q. Li, M. Onellion, Angle-resolved photoemission-study of oxygen-chemisorption on Gd(0001). *Surf. Sci.* **329**(3), 177–183 (1995)
6. G. Comelli, V.R. Dhanak, M. Kiskinova, K.C. Prince, R. Rosei, Oxygen and nitrogen interaction with rhodium single crystal surfaces. *Surf. Sci. Rep.* **32**(5), 167–231 (1998)
7. E. Schwarz, J. Lenz, H. Wohlgenuth, K. Christmann, The interaction of oxygen with a rhodium (110) surface. *Vacuum* **41**(1–3), 167–170 (1990)
8. M. Bowker, Q.M. Guo, R.W. Joyner, Oxidation of carbon-monoxide catalyzed by rhodium (110). *Surf. Sci.* **280**(1–2), 50–62 (1993)
9. K. Ueda, A. Takano, K. Tanaka, Oxygen-adsorption study on Rh(100) surface by electron-stimulated desorption spectroscopy. *Jpn. J. Appl. Phys. Part 1-Regul. Pap. Short Notes Rev. Pap.* **34**(7A), 3662–3665 (1995)
10. J.H. Craig, Characteristic energies of electronically desorbed ions from Rh(100). *Appl. Surf. Sci.* **35**(4), 520–526 (1989)
11. V.V. Gorodetskii, W.M.H. Sachtler, G.K. Boreskov, B.E. Nieuwenhuys, Adsorption of oxygen and its reactions with carbon-monoxide and hydrogen on rhodium surfaces—comparison with platinum and iridium. *Appl. Surf. Sci.* **7**(4), 355–371 (1981)
12. A.N. Salanov, V.I. Savchenko, Oxygen interaction with rhodium at low-pressures. *Surf. Sci.* **296**(3), 393–399 (1993)
13. G.B. Fisher, S.J. Schmieg, The molecular and atomic states of oxygen adsorbed on Rh(100)—adsorption. *J. Vacuum Sci. Technol. a-Vacuum Surf. Films* **1**(2), 1064–1069 (1983)
14. E.W. Hansen, M. Neurock, First-principles-based Monte Carlo methodology applied to O/Rh(100). *Surf. Sci.* **464**(2–3), 91–107 (2000)
15. K.A. Peterlinz, S.J. Sibener, Absorption, adsorption, and desorption studies of the oxygen/RH(111) system using O⁻², NO, and NO₂. *J. Phys. Chem.* **99**(9), 2817–2825 (1995)
16. K.D. Gibson, M. Viste, E.C. Sanchez, S.J. Sibener, High density adsorbed oxygen on Rh(111) and enhanced routes to metallic oxidation using atomic oxygen. *J. Chem. Phys.* **110**(6), 2757–2760 (1999)
17. K.D. Gibson, J.I. Colonell, S.J. Sibener, Velocity distributions of recombinatively desorbed O⁻² originating from surface and subsurface oxygen Rh(111). *Surf. Sci.* **343**(1–2), L1151–L1155 (1995)
18. H. Böttcher, H. Conrad, H. Niehus, Thermal rearrangement of oxygen adsorbed on oxygen-rich Ru(0001). *Surf. Sci.* **478**(3), 229–239 (2001)
19. P. Piercy, M. Maier, H. Pfnür, *The Structure of Surface II*, 11th edn. (Springer, Berlin, 1986)
20. A.D. Logan, A.K. Datye, J.E. Houston, The nature of the oxide phases formed during progressive oxidation of the rhodium(111) surface. *Surf. Sci.* **245**(3), 280–288 (1991)
21. C.Q. Sun, Oxidation electronics: bond-band-barrier correlation and its applications. *Prog. Mater. Sci.* **48**(6), 521–685 (2003)
22. S. Ladas, R. Imbihl, G. Ertl, Kinetic oscillations during the catalytic Co oxidation on Pd(110)—the role of subsurface oxygen. *Surf. Sci.* **219**(1–2), 88–106 (1989)
23. M.R. Bassett, R. Imbihl, Mathematical-modeling of kinetic oscillations in the catalytic co oxidation on Pd(110)—the subsurface oxygen model. *J. Chem. Phys.* **93**(1), 811–821 (1990)
24. A. Rar, T. Matsushima, Desorption and dissociation of oxygen admolecules on a stepped platinum(533) surface. *Surf. Sci.* **318**(1–2), 89–96 (1994)
25. M.A. VanHove, J. Cerda, P. Sautet, M.L. Bocquet, M. Salmeron, Surface structure determination by STM versus LEED. *Prog. Surf. Sci.* **54**(3–4), 315–329 (1997)
26. J. Winterlin, R.J. Behm, *In the Scanning Tunnelling Microscopy I*, ed. by H.J. Güntherth, R. Wiesendanger (Springer, Berlin, 1992)

27. J.M. Gottfried, N. Elghobashi, S.L.M. Schroeder, K. Christmann, Oxidation of gold by oxygen-ion sputtering. *Surf. Sci.* **523**(1–2), 89–102 (2003)
28. P.A. Redhead, The first 50 years of electron stimulated desorption (1918–1968). *Vacuum* **48**(6), 585–596 (1997)
29. S. Schwegmann, A.P. Seitsonen, V. De Renzi, H. Dietrich, H. Bludau, M. Gierer, H. Over, K. Jacobi, M. Scheffler, G. Ertl, Oxygen adsorption on the Ru(10 $\bar{1}$ 0) surface: anomalous coverage dependence. *Phys. Rev. B* **57**(24), 15487–15495 (1998)
30. S. Schwegmann, A.P. Seitsonen, H. Dietrich, H. Bludau, H. Over, K. Jacobi, G. Ertl, The adsorption of atomic nitrogen on Ru(0001): geometry and energetics. *Chem. Phys. Lett.* **264**(6), 680–686 (1997)

Chapter 6

EELS and Raman: Nonbond Interactions

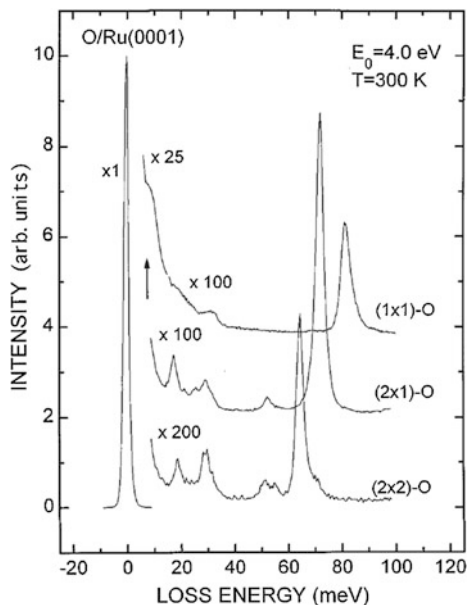
- *Raman and EELS are able to discriminate vibrations due to nonbond interaction at terahertz frequencies.*
- *Transition of vibration frequencies at the 10^1 meV indicates the conversion of dipole formation due to O^{1-} , O^{2-} , and the weakened interaction by H-bond like formation.*
- *The events of O^{-1} formation, O^{-2} sp-hybrid bonding, non-bonding lone pair, anti-bonding dipole and the H-like bonding are essential in the electronic process of oxidation, and in the reactions involving other electronegative additives as well.*

6.1 EELS: Dipole Vibration

He and Jacobi [1] observed an EELS dipole-active stretch vibration mode, $v_{\perp}(\text{Ru}-\text{O})$, of transition from O–Ru(0001) surface. Figure 6.1 shows the energy evolution of the $v_{\perp}(\text{Ru}-\text{O})$ mode from 62 to 66 and then to 81 meV when the (2×2) -O phase (O^{-1} dominates at 0.25 ML) transits to the (2×1) -O (O^{-2} dominate at 0.5 ML) and then to the $p(1 \times 1)$ -O phase (O^{-2} and H-like bonds dominate at 1.0 ML coverage).

The low-frequency EELS and infrared peaks have also been observed from other oxide surfaces [2, 3]. The characteristic losses for the O–Rh(111) surface increase from 62 to 68 meV with increasing oxygen coverage [4]. On the O–Rh(001) surface [5], peak at 48 meV at lower oxygen coverage (O^{-1} dominates) shifts to 54 meV at higher oxygen coverage (O^{-2} dominates). Upon the Rh(110)- $(2 \times 1)p2mg$ -O structure formation, two peaks at 46 ± 1 and 64 ± 1 meV are observed simultaneously under dipole-scattering conditions. The EELS peak transits at low temperature from 36 to a lower value of 30 meV [6] when the O–Ag(001) surface changes from the O^{-2} -derived phase to the O^{-1} -derived one. The transition from lower energy to slightly higher energy indicates a higher binding energy since the $(2 \times 2)p2mg$ structure is more stable. Upon oxygen adsorption to

Fig. 6.1 EEL spectra revealed the ordered Ru(0001)-(2 × 2)-O⁻¹ (0.25 ML), (2 × 1)-O⁻² (0.5 ML), and (1 × 1)-O⁻² (1.0 ML with H-bond-like creation) phases with characteristic peaks shifting from 62 to 66 and to 81 meV (reprinted with permission from [1])



the Cu(110) surface, an EELS peak appears at ~ 50 meV [7]. The origin and the energy shift of the detected modes need to be defined, as this observed energy difference has usually been thought but never fortuitous [8, 9].

A nuclear inelastic scattering of synchrotron radiation measurement [10] of the vibrational DOS of nanocrystalline (6–13 nm) α -Fe with oxide covered surface revealed: (1) Enhanced population of low-energy vibrational modes around 18 meV attributed to vibrational modes of interface atoms, arising from the high fraction of interfacial sites connected with the small crystallite size. (2) A broadening of the DOS peaks at 30–35 meV due to phonon confinement and the stiffening mode. (3) An additional intensity at 40–50 meV presents due to oxidation. Experiments and computer simulations indicate that the DOS contains low- and high-energy modes, which are not observed from coarse-grained counterparts. These modes seem to originate from vibrations of atoms with reduced atomic coordination and modified local environment, i.e., at surface/interface sites. Oxidation contributes similarly to the low-energy DOS but additionally brings about stiff modes above the high-frequency cutoff of bulk α -Fe.

The energy of the O–M stretch vibration around 50 meV coincides with the typical energy of the hydrogen bond detected using infrared and Raman spectroscopy from H₂O, protein, and DNA [11]. The energy for an ionic bond is normally around 3.0 eV and the energy for a Van der Waals bond is about 0.1 eV. Therefore, the vibrations detected using EELS from the Ru, Rh, and Ag oxide surfaces correspond to the weak non-bonding interaction between the host dipole and the adsorbate.

For the O–Ru and O–Rh surfaces, it has been clear that, in the precursor states at low oxygen coverage, the weak interaction between oxygen and the O^{-1} -induced dipoles. A lone pair replaces the O^{-1} when the O^{-1} evolves into the O^{-2} with increasing oxygen coverage. The lone pair dominates the weak part of a hydrogen bond. Finally, an H-like bond forms with further increasing oxygen coverage, which stabilizes the bond network at the surface by reducing the dipole moment. Therefore, the interaction between oxygen adsorbate and the metal dipoles increases with the evolution from O^{-1} , O^{-2} to O^{-2} with H-like bond formation.

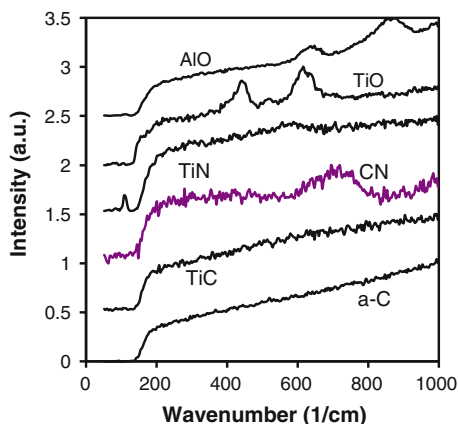
Dipole-oxygen interaction through a lone pair seems to be stronger than that through the O^{-1} . The H-like bond formation stabilizes the surface-bond network, and hence raises the frequencies of vibration. Therefore, the detected EELS and vibration DOS features correspond to the non-bonding interaction and their energy shifts agree with the transition of the non-bonding components from O^{-1} induction to lone-pair interaction and then to the H-like bond contribution in the process of oxidation. The soften mode of 18 meV in the vibration DOS of oxide embedded α -Fe should arise from interparticle interaction, which is even weaker than the non-bonding interaction. The transition from 36 to 30 meV [6] with the alteration from O^{-2} to O^{-1} on the O–Ag(001) surface further evidences that the lone-pair interaction is stronger than the electrostatic force between O^{-1} and the O^{-1} -induced dipoles.

6.2 Raman: Lone Pair in Oxides, Nitrides, and Bio-Molecules

The lone pair is produced intrinsically by the *sp*-orbit hybridization of O and N. The number of lone pairs in a tetrahedron follows the rule of ‘4-*n*’, where ‘*n*’ is the valence value of the electronegative additive. Vibration of the dipole induced by the lone pairs should be detectable by Raman spectroscopy in the frequency range below $1,000\text{ cm}^{-1}$. A Raman experimental survey (HeNe laser, normal incidence) from the following specimens confirmed this expectation [12]. Figure 6.2 shows Raman spectra of (1) Al_2O_3 and TiO_2 powders; (2) thin films of Ti nitride (TiN) and amorphous carbon nitride; and, (3) films of amorphous carbon (α -C) and Ti carbide (TiC). As anticipated, the lone-pair features of the oxides ($n = 2$) are stronger than those of the nitrides ($n = 3$) while no such features can be resolved from carbides ($n = 4$). The appearance and the relative intensity of these low-frequency Raman features support the prediction and the rules of ‘4-*n*’ for lone-pair formation as well.

The detected Raman features are quite similar to that of H_2O , protein, and DNA [11]. The peak positions depend on the reduced atomic mass, $\mu = m_1 m_2 / (m_1 + m_2)$, of the components, and the force constant, k , of the weak interaction ($\omega \propto (k/\mu)^{1/2} = (Yd/\mu)^{1/2}$). The k equals the second derivative of the interatomic potential in a Taylor series and approximates Ed^{-2} from the dimensional consideration. Therefore, the frequency shift corresponds to the square root of the

Fig. 6.2 Low-frequency Raman shifts indicate that non-bonding lone-pair interaction exists in oxides and nitrides but carbides. Peak intensities of oxides are stronger than that of nitrides because of the number of the lone pairs that follow the 4-n rule (reprinted with permission from [12])



stiffness of the particular non-bond interaction. The stiffness is the product of the elastic modulus Y (energy density) and the bond length d [13].

The multi-peak of Raman shift corresponds to different orders of the Fourier coefficients in the numerical solutions of the Schrödinger equation of the vibronic systems. In bio-molecules, the characteristic vibration frequency of the hydrogen bond is about $\sim 200 \text{ cm}^{-1}$. It is known that the hydrogen bond is actually composed of a lone pair (:) on one side and a covalent bond (-) on the other in the $B^{+l/p} (A^{-n}-B^{+l/p}; A^{-n})$. The B is less electronegative than A of which the sp orbits hybridize upon reaction. The covalent bond vibration contributes to the spectra at much higher energy for H_2O instance ($3,000 \text{ cm}^{-1}$). Therefore, low-frequency features of Raman come from the vibration of the lone-pair-induced dipoles that are common to oxides, nitrides, and bio-molecules.

6.3 Summary

EELS and Raman provide detailed information about the weak nonbonding interactions evolved from Coulomb to lone pair and to the H-bond likes at oxygen chemisorbed surfaces and presence of the lone pair in oxide and nitride with characteristic frequencies at low frequencies.

References

1. K. Miyake, N. Satomi, S. Sasaki, Elastic modulus of polystyrene film from near surface to bulk measured by nanoindentation using atomic force microscopy. *Appl. Phys. Lett.* **89**(3), 031925 (2006)
2. P.M. Ajayan, M. Terrones, A. de la Guardia, V. Huc, N. Grobert, B.Q. Wei, H. Lezec, G. Ramanath, T.W. Ebbesen, Nanotubes in a flash—ignition and reconstruction. *Science* **296**(5568), 705 (2002)

3. C. Lee, X.D. Wei, J.W. Kysar, J. Hone, Measurement of the elastic properties and intrinsic strength of monolayer graphene. *Science* **321**(5887), 385–388 (2008)
4. E. Cadelano, P.L. Palla, S. Giordano, L. Colombo, Nonlinear elasticity of monolayer graphene. *Phys. Rev. Lett.* **102**(23), 235502 (2009)
5. Z.C. Tu, Z. Ou-Yang, Single-walled and multiwalled carbon nanotubes viewed as elastic tubes with the effective Young's moduli dependent on layer number. *Phys. Rev. B* **65**(23), 233407 (2002)
6. K.K. Nanda, Bulk cohesive energy and surface tension from the size-dependent evaporation study of nanoparticles. *Appl. Phys. Lett.* **87**(2), 021909 (2005)
7. C.O. Girit, J.C. Meyer, R. Erni, M.D. Rossell, C. Kisielowski, L. Yang, C.H. Park, M.F. Crommie, M.L. Cohen, S.G. Louie, A. Zettl, Graphene at the edge: stability and dynamics. *Science* **323**(5922), 1705–1708 (2009)
8. T.A. Parthasarathy, S.I. Rao, D.M. Dimiduk, M.D. Uchic, D.R. Trinkle, Contribution to size effect of yield strength from the stochasticity of dislocation source lengths in finite samples. *Scr. Mater.* **56**(4), 313–316 (2007)
9. M.X. Gu, C.Q. Sun, Z. Chen, T.C.A. Yeung, S. Li, C.M. Tan, V. Nosik, Size, temperature, and bond nature dependence of elasticity and its derivatives on extensibility, Debye temperature, and heat capacity of nanostructures. *Phys Rev B* **75**(12), 125403 (2007)
10. F. Scarpa, S. Adhikari, R. Chowdhury, The transverse elasticity of bilayer graphene. *Phys. Lett. A* **374**(19–20), 2053–2057 (2010)
11. H. Hakkinen, R.N. Barnett, A.G. Scherbakov, U. Landman, Nanowire gold chains: formation mechanisms and conductance. *J. Phys. Chem. B* **104**(39), 9063–9066 (2000)
12. R.F. Egerton, P. Li, M. Malac, Radiation damage in the TEM and SEM. *Micron* **35**(6), 399–409 (2004)
13. F. Scarpa, S. Adhikari, A.J. Gil, C. Remillat, The bending of single layer graphene sheets: the lattice versus continuum approach. *Nanotechnology* **21**(12), 125702 (2010)

Chapter 7

Kinetics of Bond Forming and Bond Switching

- *Oxygen diffuses into the bulk interior under the ambient conditions causing O-attacked corrosion.*
- *Oxygen floats up the surface at proper temperatures once the oxygen layer is covered with a monolayer of metals.*
- *A ‘quantum laddering’ mechanism dominates the floating/diffusing because of the inhomogeneous bond nature, length, angle, and the repulsive forces.*

7.1 Four-Stage Oxide-Bond-Forming Kinetics

Combining the LEED, STM, PES/STS, EELS/Raman, and TDS spectral signatures in terms of the chemical bond, surface morphology, valence DOS, low-frequency vibration, and bond strength makes it possible to clarify the chemisorption 3B dynamics. As an additional example, one may look at the particular O–Pd(110) surface based on the kinetic TDS and UPS profiles (please refer to Fig. 5.1 for the profiles and Sect. 3.3 for structural details) obtained during the increase in oxygen exposure:

1. Stage 1 ($\Theta < 1.5$ L): O^{-1} dominates giving a Pd_5O cluster with one ionic bond to the Pd atom underneath and four surface-metal dipoles. In TDS, the ionic-bond feature β_2 emerges prior to the presence of the lone-pair feature β_1 that does not appear yet until the turning point at 1.5 L. The O^{-1} -induced dipoles reduce $\Delta\phi$ considerably. O^{-1} at 1.5 ML dominates the highest $\Delta\phi$ value. This agrees with data derived with VLEED from the O–Cu(001) surface at an oxygen-coverage lower than 25 L. No lone-pair features can be detected at the O^{-1} -dominated stage.
2. Stage 2 ($1.5 \leq \Theta \leq 2.5$ L): O^{-2} *sp*-orbital hybridization occurs and completes, giving rise to a tetrahedron with two ionic bonds and two non-bonding lone pairs. The lone-pair feature β_1 emerges upon the *sp*-orbit of the O^{-2} being hybridized. The lone-pair feature β_1 becomes apparent at 2.5 L. The bond

feature β_2 increases its intensity until the number of the ionic bonds saturates at 2.5 L. $\Delta\phi$ drops from 520 meV at 1.5 L down to 430 meV at 2.5 L because the number of dipoles decreases. Two of the four surface dipoles are retained, and the remaining two become Pd^+ or metallic Pd when the Pd_5O evolves into the Pd_4O tetrahedron.

3. Stage 3 ($2.5 < \Theta \leq 240$ L): Interaction develops between the adsorbate and dipoles. The non-bonding feature β_1 increases its intensity gradually indicating that more lone pairs are produced and the lone-pair interaction develops. The constant intensity of β_2 implies that the oxygen coverage saturates gradually with the exposure. In fact, there is no direct correspondence between the oxygen coverage and the exposure. The slight decrease in $\Delta\phi$ from 430 meV at 2.5 L to 400 meV at 10 L implies that the H-like bonds start to form. The H-like bonds reduce the width of the antibond sub-band and restore the work function, consequently.
4. Stage 4 ($\Theta \sim 22,800$ L): The number of H-like bonds increases with increase in the O:M ratio at the surface. O^{-2} bonds to one neighbor atom on the surface and polarize the rest two. Therefore, the increased number of H-like bonds replaces some of the original ionic bonds at the surface. The development of H-like bond create TDS features of γ_1 (600 K) and γ_2 (705 K). H-like bonds replace the ionic bonds at the surface, which lowers the ionic-bond peak β_2 relative to the lone-pair peak β_1 . The considerable increase in β_1 intensity indicates that more lone pairs have been produced, and, thereby, oxygen coverage is increased.

The TDS oscillation of the O–Pd(001) and (110) corresponds to the sequence of bond formation: (1) an ionic bond forms first, (2) a lone pair follows upon second bond formation, and then, (3) an H-like bond replaces the ionic bond at the surface with increase in the number of oxygen atoms adsorbed. These processes are the same as the processes for the O–Cu(001) surface, and this has been quantified with VLEED. The trend also agrees with the reaction kinetics of the polycrystalline O–Cu surface revealed by PES [1]. In general, the identities of the kinetic UPS and VLEED correspond to the oxygen-derived DOS features. The exposure-resolved TDS signatures can be related to the processes of bond forming. Therefore, it is easy to view the oxide bond and band-forming kinetics from any complete kinetic spectra database, using the 3B notation.

All the analyzed samples show consistently that oxidation proceeds in four discrete stages:

1. O^{-1} forms one bond initially with its neighbor at very low oxygen coverage and polarizes the rest neighbors;
2. O^{-2} forms another bond to hybridize its *sp*-orbitals. This process creates lone pairs that polarize another two neighbors;
3. Interaction develops between lone pairs and dipoles; and finally,

4. H-like bonds form at higher exposure and the H-like bonds replace the surface ionic bonds. These processes give rise to the corresponding DOS features in the valence band and modify the surface morphology and crystallography, accordingly.

Therefore, the events of O^{-1} formation, O^{-2} *sp*-hybrid bonding, non-bonding lone pair, antibonding dipole, and the H-like bonding are essential in the electronic process of oxidation, and in the reactions involving other electronegative additives as well.

7.2 Bond Switching: O-Floating and O-Diffusing

In the process of oxidation and corrosion of metals, oxygen breaks the adsorption barrier and the metal–metal bond to move into the bulk. One can observe the bulk oxidation with the naked eye as the oxide powders peeling off the metals, known as rusting. However, in epitaxial growth of metals onto oxygen pre-covered metal surfaces, oxygen atoms always float up to the surfaces. These two opposite processes seem to be very complicated and involve the kinetics and dynamics of oxide-bond switching. Understanding the driving forces and the kinetic process of oxide-bond switching is particularly important to both fundamental science and technological applications.

SIMS and secondary electron-emission examination revealed that the Cu layers deposited on the $c(2 \times 2)$ -O/Ni(100) substrate are always covered by an adsorbed layer of oxygen [2]. AES [3], ICISS [4], work function measurements [5, 6], and STM observations [7, 8] revealed that oxygen atom is always present on the surface of the grown Cu films deposited on an oxygen pre-covered Ru(0001) surface. Under certain conditions ($\theta_O = 0.2$ – 0.4 ML, $T \sim 400$ K), the work function, monitored during film deposition, oscillates with a period of one monolayer of copper epitaxial growth.

The oxygen serves as a surfactant for a layer-by-layer mode of Cu growth on the O–Ru(0001) surface, periodically inducing a high density of islands. Densely packed triangular islands of O/Cu surfactant cover the surface at lower θ_O . The O–Cu structure is locally ordered in a distorted hexagonal lattice, namely, with the hcp(0001) or fcc(111) features. The structure also consists of O–Cu–O strings inducing the observed corrugation. The epitaxial growth of Cu on the O–Cu(111) surface exhibits the same O-floating phenomena [9]. The oxygen-induced He-scattering features oscillate at ~ 400 K. Oxygen atoms segregate back to the surface during the epitaxial growth of Cu on the Cu(001)– $(\sqrt{2} \times \sqrt{2})R45^\circ$ - $2O^{-2}$ surface, while the $(\sqrt{2} \times \sqrt{2})R45^\circ$ - $2O^{-2}$ structure retains at the grown surface [10]. One possible mechanism for the floating of oxygen is that the strain of the first Cu layer promotes the formation of the Cu₂O-like $(3 \times 2\sqrt{3})$ structure [7]. Once the structure is formed, elements of it float onto the top of the growing film and act as a surfactant layer for further Cu film growth.

Similarly, co-adsorption of Ni and O on the W(110) surface and subsequent annealing to 500–1,000 K leads to segregation of Ni and O, with the formation of Ni crystallites largely $\langle 111 \rangle$ oriented along the surface normal. The heights of these Ni ‘towers’ can be adjusted by varying the amounts of co-adsorbed oxygen and Ni [11].

Therefore, oxygen floating in the process of Cu/O/Ru(0001), Cu/O/Cu(111), and Cu/O/Cu(001) growth and Ni cluster on the O–W(110) surface is driven by a common, yet poorly known, mechanism [7].

The reversible four-stage 3B dynamics shall provide a possible mechanism for the kinetics and dynamics of oxide-bond switching. As oxidation takes place in four discrete stages in which O^{-1} forms first and then O^{-2} follows with *sp*-orbital hybridization and lone-pair production, or inversely like that happened to the Ag(001) surface. Annealing the O–Cu(001) surface at a ‘dull red’ temperature could remove the lone-pair DOS features from the $z_0(E)$ profile, which means that the hybridized *sp*-orbitals of the O^{-2} has de-hybridized [12, 13]. Hence, annealing at a certain temperature provides forces that reverse the reaction by oxide-bond breaking and reforming.

Oxygen floating occurs in general at ~ 400 K, at which O^{-2} de-hybridizing and oxygen re-bonding tend to occur because annealing activates the bond breaking. At the thermally activated state, oxygen can adjust itself toward a stable tetrahedron or the inverse. It is worth to mention that the lone-pair-induced dipoles tend to direct into the open end of a surface. The dipole forms periodically with the epitaxial layer growth observed experimentally as the periodic change of the work function. Therefore, the strong repulsion between the dipoles and the repulsion between the lone pairs provide the driving force for oxygen to float up under a thermal activation in the process of homo- or hetero-epitaxial growth of metals.

The interaction between the dipoles and oxygen is rather weak (~ 50 meV). With an external stimulus or under certain circumstances, the dipoles may escape from the bound by the lone pairs, and then oxygen reactants have to re-bond to other atoms to form the stable tetrahedron, which is the case of bulk oxidation or rusting. Although O-diffusing and O-floating are inverse processes, they share the same mechanism of bond switching. The mechanism for the oxide-bond switching may be extended to bioelectronics such as the folding, signaling, and regulating of DNA, proteins, and NO, in which the lone pair, dipole, and H-bond like may dominate.

7.3 Summary

Oxygen attacked corrosion proceeds in a way of “quantum laddering” by bond and nonbond formation and reformation, which is much more complicated than atomic diffusion. Oxygen can float up of the surface or penetrate in the bulk under proper thermal conditions.

References

1. V.P. Belash, I.N. Klimova, V.I. Kormilets, V.Y. Trubitsin, L.D. Finkelstein, Transformation of the electronic structure of Cu into Cu²O in the adsorption of oxygen. *Surf. Rev. Lett.* **6**(3–4), 383–388 (1999)
2. M.A. Karolewski, Determination of growth modes of Cu on O/Ni(100) and NiO(100) surfaces by SIMS and secondary electron emission measurements. *Surf. Sci.* **517**(1–3), 138–150 (2002)
3. K. Kalki, M. Schick, G. Ceballos, K. Wandelt, Thin-film growth on an O-precovered Ru(0001) surface. *Thin Solid Films* **228**(1–2), 36–39 (1993)
4. Y.G. Shen, D.J. Oconnor, H. Vanzee, K. Wandelt, R.J. Macdonald, The growth of thin Cu films on an O-precovered Ru(0001) surface studied by low-energy ion-beams. *Thin Solid Films* **263**(1), 72–78 (1995)
5. M. Schmidt, H. Wolter, M. Schick, K. Kalki, K. Wandelt, Compression phases in copper-oxygen co-adsorption layers on a Ru(0001) surface. *Surf. Sci.* **287**, 983–987 (1993)
6. M. Schmidt, H. Wolter, K. Wandelt, Work-function oscillations during the surfactant-induced layer-by-layer growth of copper on oxygen precovered Ru(0001). *Surf. Sci.* **307**, 507–513 (1994)
7. H. Wolter, K. Meinel, C. Ammer, K. Wandelt, H. Neddermeyer, O-mediated layer growth of Cu on Ru(0001). *J. Phys. Condens. Matter* **11**(1), 19–37 (1999)
8. K. Meinel, C. Ammer, M. Mitte, H. Wolter, H. Neddermeyer, Effects and structures of the O/Cu surfactant layer in O-mediated film growth of Cu on Ru(0001). *Prog. Surf. Sci.* **67**(1–8), 183–203 (2001)
9. W. Wulfhekel, N.N. Lipkin, J. Kliewer, G. Rosenfeld, L.C. Jorritsma, B. Poelsema, G. Comsa, Conventional and manipulated growth of Cu/Cu(111). *Surf. Sci.* **348**(3), 227–242 (1996)
10. M. Yata, H. Rouch, K. Nakamura, Kinetics of oxygen surfactant in Cu(001) homoepitaxial growth. *Phys. Rev. B* **56**(16), 10579–10584 (1997)
11. J.E. Whitten, R. Gomer, Reactivity of Ni on oxygen-covered W(110) surfaces. *J. Vac. Sci. Technol. A: Vac.Surf. Films* **13**(5), 2540–2546 (1995)
12. C.Q. Sun, Time-resolved VLEED from the O–Cu(001): Atomic processes of oxidation. *Vacuum* **48**(6), 525–530 (1997)
13. C.Q. Sun, O–Cu(001): II. VLEED quantification of the four-stage Cu₃O₂ bonding kinetics. *Surf. Rev. Lett.* **8**(6), 703–734 (2001)

Chapter 8

Design Materials and Processes

- *One electron (lone pair) difference differentiates a nitride from an oxide substantially.*
- *Both O and N can create a bandgap and enlarge existing bandgaps; both modulate the ferromagnetism and work function by charge exchange and polarization.*
- *A nitride demonstrates generally high elasticity, self-lubricity, and corrosion resistance.*
- *N creates tensile but C compressive stress at a surface. A combination of both enhances diamond–metal adhesion.*
- *The non-bonding interaction associated with O, N, C, B, and F forms important gradient in organic and inorganic substances.*

This part has verified up two concepts that should be of immediate application. One is the *sp*-orbit hybridization of the electronegative adsorbate as a charge acceptor and the other is the bond contraction of the host surface. Table 8.1 features functionalities and potential applications of the bonding events. The bond contraction is not limited to an oxide surface, but it happens at any site, where the atomic *CN* is lower than the bulk standard.

The nature of the chemical bond bridges the structures and properties of crystals and molecules [1]. Interatomic interaction and electronic distribution in the valence band are the keys to engineering materials. The spontaneous bond contraction enhances the binding energy of the remaining bonds of the lower coordinated atom. Chemical reaction modifies directly the occupied valence DOS by charge transportation or polarization. Bond relaxation and valence band modulation change the properties of a solid.

8.1 Nitrogen-Induced Anomalies

Nitrides have formed a class of materials with fascinating properties that have been widely used for mechanical and elastic enhancement, wear and corrosion resistance, photon and electron emission, as well as magnetic modulation [2, 3].

Table 8.1 Predictions of functionalities and potential applications of electronegative additives reacting with solid materials

| Events | Characterization techniques | Functions | Potential applications |
|---------------------------------|-----------------------------|---|---|
| Antibonding (dipole) $> E_F$ | STM/S, IPES UPS | Work function reduction ($\Delta\phi$) | Cold-cathode field emission |
| Holes $< E_F$ | Photoemission | Bandgap expansion | PL Blueshift UV detection |
| Non-bonding (Lone pair) $< E_F$ | Raman/FTIR, STS, VLEED | Polarization of metal electrons | High elasticity Far-IR activity |
| H- or CH-like bond | STM/S, UPS, EELS | $\Delta\phi$ -Recovery | Surface bond network stabilization |
| Bonding | XRD, LEED, UPS, XPS | Mass transport atomic shift Phase change | Compound formation |
| Surface bond contraction | XRD/XPS | Crystal field Cohesive energy Hamiltonian | Origin for the tunability of nanosolids |

For instance, nitrogenation modulates the crystal structures, saturation magnetization (M_S), and Curie temperature (T_C) of Fe films [4, 5], substantially. An addition of a small amount of N raises the M_S value of the α'' -Fe₁₆N₂ phase by $\sim 25\%$ of that of pure Fe ($2.22 \mu_B$). Further doping of N lowers the M_S value associated with crystal structure transition from ϵ , γ , ζ , to the paramagnetic phase of amorphous FeN [6]. Nitrogenation also raises the M_S value and the T_C of rare earth I-ferromagnet (Co and Fe) considerably [7]. The M_S of the R(Fe, Co) alloys is increased by 30–40 % relative to their parent alloys [7].

Inclusion of N in the synthetic diamond films could significantly reduce the threshold of cold cathode emission of the films [8]. The work function of carbon nitride films could be reduced to ~ 0.1 eV [9]. Nitrogenation creates and widens a bandgap and turns a conductor into a semiconductor or even an insulator, such as AlN [10], GaN [11], and InN [12]. N-based group-III and group-IV semiconductors are prosperous materials for blue and green light emitting [13], which have been commercially available for applications in flat-panel displays and blue-ultraviolet laser diodes that promise high-density optical data storage, optic communication, and high-resolution laser printing. Nitride films show surprisingly high elasticity ($\sim 100\%$) and high mechanical strength at relatively low indentation load (< 1 mN) [14].

8.2 Group Symmetry: Corrosion and Anti-Corrosion

What differentiating an N atom from an O or a C atom is only one electron gain or loss. The fifth valence electron makes a nitride to perform differently from either an oxide or carbide. N prefers the NH₃-like configuration with a lone-pair

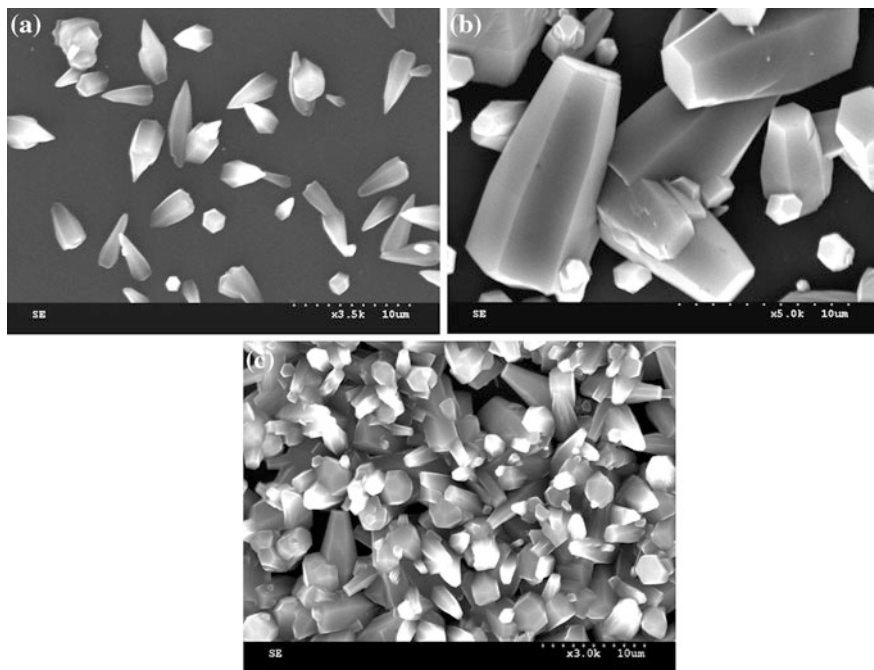


Fig. 8.1 SEM images of the SiCN crystals formed on Si substrate with a 10/4 sccm N_2/CH_4 gas mixture for **a** 4 h and **b** 10 h, and **c** 50/1 sccm in CVD for 10 h. SiCN crystallites prefer the hcp structures (reprinted with permission from [15])

production when it reacts with other atoms that are less electronegative. Nitride tetrahedron follows the C_{3v} symmetry of a NB_4 cluster as most of the nitrides prefer the hcp(0001) or the fcc(111) orientation, such as AlN, GaN, TiN, etc.

Figure 8.1 shows the scanning electron microscopy of the hcp-structured SiCN crystals grown on Si substrate with a gas mixture of $N_2 + CH_4$ in chemical vapor deposition [15].

Cu_3N patches form on the Cu(001) and Cu(h11) surfaces whose image is of $\sim 0.8 \text{ \AA}$ below the clean surface [16], without signatures of polarization being resolved. STM images show that the N atom sinks deeply into the threefold hollow site of the top Ru(0001) layer with a radially away reconstruction of the N-Ru(0001) surface [17]. These observations indicate central position of the N in the NB_4 cluster of C_{3v} symmetry with lone pair pointing from the N to the bulk interior other than direct into the surface. AES, EELS, and UPS investigations of GaN(0001)-(1 \times 1) surface revealed that nitride formation proceeds in the same way as that of the ammonia and aniline formation: The N atom is located in a fourfold-coordinated configuration, bridging two surface Ga atoms [18]. The lone pair is directed sideways into the open end of the Ni(001) surface, and the electrostatic interaction between the alternative Ni^+ and Ni^P drives the Ni(001) surface to be reconstructed with rhombi chain forming along the $\langle 11 \rangle$ directions.

Nitrogenation of a surface prevents a metal surface from being rusted by oxygen-attached corrosion. Ideally, an N atom prefers a location between the top two layers of the skin and the lone pair directs into the bulk interior. The surface layer is hence networked with the smaller B^+ bonding to the N^{3-} ions with densely packed electrons. The B atom donates electrons in the outermost shells from the upper DOS states to the lower empty DOS states of nitrogen upon bond formation. The reaction not only lowers but also causes densification of the valence DOS due to the B^+ and N^{3-} formation. Therefore, the top surface layer should be chemically inert as it is harder for one additional acceptor to catch electrons from the lowered valence DOS. Electrons in the saturated bond should be more stable compared with the otherwise electrons in the neutral host atoms. This configuration explains why a nitride surface is corrosion resistant and why it exhibits STM depressions [16, 17].

8.3 Lone-Pair Interaction: Excessive Elasticity and Mechanical Strength

The high strength of the intra-surface $N^{3-} - B^+$ ionic bonding network could be responsible for the hardness and corrosion resistance of the skin. The $N^{3-} - B^+$ network at the surface interacts with the substrate mainly through the non-bonding interaction. The non-bonding interaction is rather weak (~ 0.05 eV/bond) compared with the original metallic bonds (~ 1.0 eV/bond) or the intra-surface ionic bond (2–3 eV per bond). The weak interaction due to lone-pair formation should be highly elastic within a critical load, which makes the two adjacent surface layers more elastic under a compressive load lower than the critical value at which the weak interaction breaks. Therefore, the enhanced intra-layer strength makes a nitride usually harder (~ 20 GPa), and the weakened interlayer bonding makes the nitride highly elastic and self-lubricate at a relatively low load.

Nanoindentation profiles from TiCrN surface and sliding friction measurements from CN and TiN surfaces confirmed the predicted high elasticity, high hardness, and the existence of the critical scratching load [14]. As compared in Fig. 8.2a, under 0.7 mN load of indentation, the elastic recovery and hardness for a GaAlN film (100 % recovery) [19] are higher than that of an amorphous carbon film. The GaAlN surface is also harder than the amorphous-C film under the lower indentation load. TiCrN skin is twice harder than the bulk because of the ionic bond network and the surface bond contraction [14]. The abrupt increase in the friction coefficient of nitride films under higher load in Fig. 8.2c and d indicates the presence of critical load beyond which the lone pair breaks [14]. Under higher pressing load (>5 mN) of indentation, the elastic recovery reaches the values of 65 and 85 %, for CN and TiN, respectively [20]. The absence of lone pairs in a-C film makes the film less elastic than a nitride film under the same pressing load.

The hardness and the elastic modulus of β - C_3N_4 are expected to be comparable to or exceeding those of diamond [21, 22]. Only a few were successful in preparing α - C_3N_4 and β - C_3N_4 powders using the liquid–solid reaction between anhydrous

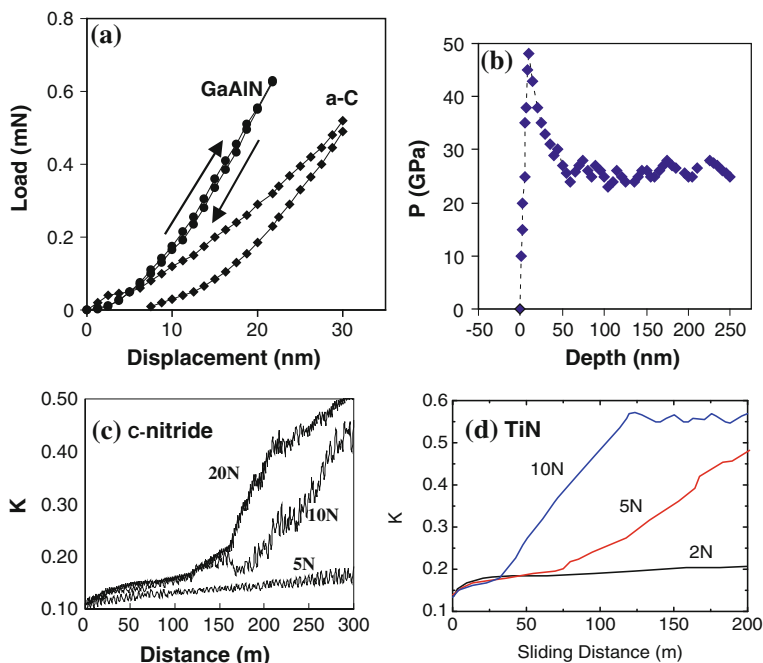


Fig. 8.2 Elasticity and mechanical strength of nitride films. **a** GaAlN/ Al_2O_3 exhibits 100 % elastic recovery under 0.7 mN indentation load, while amorphous carbon shows 65 % elastic recovery under the same scale of load. **b** TiCrN skin is twice harder than the bulk because of surface bond contraction. The abrupt increase of the friction coefficient for **c** C nitride and **d** Ti nitride in the pin-on-disk test of sliding friction [14] exhibits the critical load that breaks the surface bond. Diamond thin films show no abruptness of the coefficient at even higher loads (reprint with permission from [14])

$\text{C}_3\text{N}_3\text{Cl}_3$ and Li_3N in benzene at 355 °C and 5–6 MPa for 12 h [23]. The N/C atomic ratio reaches 2/3, being lower than the predicted stoichiometry of 4/3. Theoreticians [24–27] suggested that the C_3N_4 phase can only be produced at higher pressure (68 GPa). Considering the non-bonded N–N repulsion, the N concentration should be no more than 50 % [25] as both C and N undergo *sp*-orbit hybridization and each of them tends to find four nearest neighbors. The ideally allowed N/C ratio is unity.

In fact, the hardness of CN films decreases with increasing N content, instead. The excess electrons on N lower the hardness but enhance the elasticity [28]. The elasticity of the CN varies with substrate temperature and N content. Increasing the substrate temperature from 100 to 350 °C at 2.5 mTorr N_2 pressure, the elastic recovery increases from ~60 to ~90 % [14]. This value can be reduced to 68 % by increasing N_2 pressure from 2.5 to 10 mTorr at a substrate temperature of 350 °C [29]. Although the highest hardness of CN available to date [20] (~60 GPa) is below that of a diamond (~100 GPa), the elasticity has been

confirmed rather high under a critical load for plastic deformation. These observations indicate the presence of the lone pair, or the fifth electron in nitrogen, which prohibits carbon nitride from being harder than a diamond.

One way to obtain the expected hardness is to remove the fifth electron of N atom under abnormally high pressure and high temperature or by forming layered structures to make use of the interface effect [25–27, 30]. The hardness of nanocrystalline/amorphous composites such as nc-TiN/a-Si₃N₄, nc-TiN/a-Si₃N₄, nc-TiSi₂, nc-(Ti_{1-x}Al_x)N/a-Si₃N₄, nc-TiN/TiB₂, and nc-TiN/BN could approach that of diamond because of the interfacial mixing effect [31, 32]. The hardness and elasticity of nanometric TiN/CrN and TiN/NbN multi-layered thin films increase with reduction in the structural wavelength (optimal at 7.0 nm) [33, 34]. The hardness of a sophisticatedly processed nanotwinned BN surpasses that of a diamond [35].

8.4 Magnetic Modulation: Polarization

Nitrogen addition could tune the magnetic properties of ferromagnetic materials. The α' -Fe₁₆N₂ phase [5, 36] with an N concentration of 5–7 at.% shows soft magnetic properties [37] with various magnetization depending the preparation conditions. Single-crystal α' films have a magnetization of 3.2 μ_B per Fe atom—higher than any other binary alloys. A comparison of the magnetic behavior of equivalent α' -Fe₈N in chemical composition with that of α' -Fe₁₆N₂ suggested that the magnetic variability is due to different degrees of structural order–disorder because the latter is with a higher N-atom ordering. Figure 8.3 shows the N content dependence of the M_S of Fe films [6, 38].

According to the Ising approximation, the overall M_S under zero external field follows

$$H_{\text{ex}} = \sum_{\langle i,j \rangle} J_{ij} S_i \cdot S_j \propto \frac{S_i S_j}{r_{ij}} \cos \theta_{ij} \quad (8.1)$$

S_i and S_j is the magnetic momentum of individual atom i and j , respectively, and the J_{ij} is the coefficient of exchange interaction between momentum i and j . θ_{ij} represents the angle between the S_i and S_j moment. There are several factors controlling the H_{ex} and hence determine the overall magnetization. θ_{ij} varies with the applied magnetic field; the J_{ij} varies with atomic distance; and S_i and S_j vary with atomic valences. Chemical reaction not only changes the separation between the atoms and the structure ordering but also varies the electron distribution in orbitals that modifies the atomic valence and the S_i and S_j values. If the atomic separation is too large, the system will be paramagnetic disregarding the S_i and S_j values.

Table 8.2 lists the possible variation of the total angular momentum when the Fe alters its atomic valence to Feⁿ⁺ (n is an integer) or Fe^p dipoles. In the former,

Fig. 8.3 Nitrogen content dependence of saturation magnetization $4\pi M_s$ of the Fe–N films (reprinted with permission from [6])

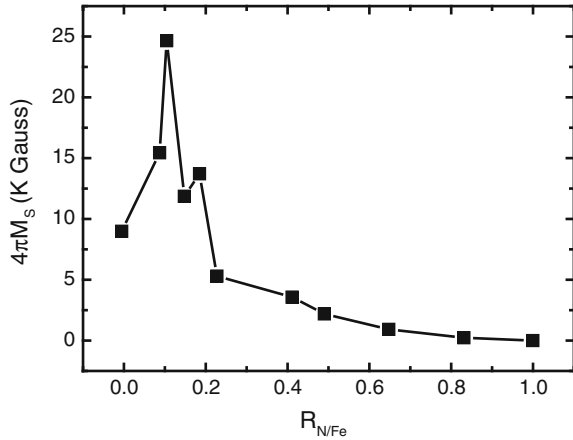


Table 8.2 Variations of angular momentum (unit in μ_B) of Fe with its atomic states [3]

| Valence state | Configuration | $S = \sum Si$ | $L = \sum Li$ | $J^a = \sum(L \pm S)i$ |
|---------------|------------------|---------------|---------------|------------------------|
| Fe | $3d^6 4s^2$ | 2 | 0 (L-frozen) | 2 (2.22) |
| Fe^+ | $3d^5 4s^2$ | 2.5 | 0 | 2.5 |
| Fe^{2+} | $3d^5 4s^1$ | $2.5 + 0.5$ | 0 | 3.0 |
| Fe^{3+} | $3d^4 4s^1$ | $2.0 + 0.5$ | 0 | 2.5 |
| Fe^{4+} | $3d^3 4s^1$ | $1.5 + 0.5$ | 0 | 2.0 |
| Fe^{p-1} | $3d^5 4s^2 4p^1$ | $2.5 + 0.5$ | $0 + 1$ | 4.0 |
| Fe^{p-2} | $3d^5 4s^2 4d^1$ | $2.5 + 0.5$ | $0 + 2$ | 5.0 |

^a The total angular momentum follows Hund’s rule. Fe^{p-2} corresponds to the antibonding states being well above the E_F

the Fe atom donates 3d electrons to the N acceptor; in the latter, the lone pair of N^{3-} ions polarizes Fe 3d electrons and shifts the electrons to an outer shell orbital of the Fe atom, 4p or 4d of higher binding energy. The N^{3-} and its electrons do not contribute to the magnetization. The momentum of the Fe^{n+} varies from 2.0 to 3.0 μ_B and then drops to 2.0 μ_B when the valence is changed from 1 to 4.

The momentum for Fe^p ($3d^5 4s^2 4p^1$) is 4.0 or even 5.0 μ_B ($3d^5 4s^2 4d^1$). The average momentum of an isolated tetrahedron ($N^{3-} + 3Fe^+ + Fe^p$) is then 2.875 or 3.125 μ_B , being 25–40 % higher than that of a pure Fe atom (2.22 μ_B). H-like bond formation will annihilate the Fe^p , resulting in the Fe^{+p} with substantially lowered magnetization. This configuration explains why the $Fe_{16}N_2$ possesses the highest magnetization order than the Fe_4N phase in which the Fe^{+p} is not avoidable. For amorphous FeN, every Fe atom has four N neighbors and the Fe becomes $Fe^{3+/p}$ ideally. The low angular momentum of the $Fe^{3+/p}$ and the expanded lattice should take the responsibility for ferromagnetic–paramagnetic transition upon amorphous FeN being formed [36].

The magnetization of a system varies with not only the angular momentum of individual atoms but also their exchange interaction that depends inversely on the atomic separation [4–7, 36, 39–41]. For rare earth, the $4f$ electrons combine more weakly than the $3d$ electrons of transition metal to their ion cores. The $4f$ electrons readily jump to higher energy shells and thus raise the momentum for the increase in M_S [39]. This lone-pair polarization and annihilation instead of the donor effect dictate the magnetic modulation of nitrogenated systems [6]. The less electronegative Fe atom can never capture electrons from the highly electronegative nitrogen “donor” except for the polarization. Mechanisms of modification on atomic valence, structure order, and atomic separation are complementary, and these effects may exist simultaneously determining the magnetic properties of the nitride compounds.

8.5 Bandgap Modulation: Photoluminescence

8.5.1 Nitrogen Acceptor: Electron–Hole Pair Production

N inclusion widens significantly the bandgap of an intrinsic semiconductor. For instance, the bandgap of Si increases from 1.1 to 3.5 eV when SiN is formed [42]. Nitrogen expands the bandgap of α -Ge and amorphous-Si from ~ 1.1 to ~ 4.0 eV [43]. Nitrogen also widens the bandgap of amorphous carbon (a -CN_x:H) [44]. Figure 8.4 shows the bandgap enlargement of (a) III-nitrides and (b) amorphous Ge- and Si-nitrides.

The width of the bandgap depends on the bond length [13] and energy and the electronegativity of the corresponding element ($\eta_{Al} = 1.5$, $\eta_{Ga} = 1.6$, and $\eta_{In} = 1.7$). Reynolds et al. [45] suggested that the yellow band of GaN and the green band of ZnO share some common yet unclear mechanisms. Chambouleyron and Zanatta [43] related the bandgap expansion of α -Ge:N and α -Si:N compounds to the substitution of Si–Si or Ge–Ge bonds by the stronger Si–N or Ge–N bonds.

For amorphous semiconductors, the transition of carriers happens between the conduction band and the valence band tail states. Luminescence spectra [42] of the α -Si:H showed that the n -type (phosphorous) doping shifts the luminescence peak of the α -Si:H from 1.1 to 0.81 eV, and the p -type (boron) doping shifts the peak from 1.1 to 0.91 eV. The shallow n -donor levels and the deeper p -acceptor levels are located within the initial bandgap (1.1 eV) near to the band tails. Co-doping of B and P narrows the bandgap even further because of the simultaneous creation of the co-doped impurity levels. However, the luminescence peak of the α -Si:N:H compound moves to higher energy with increasing nitrogen concentration [46]. The broadened bandgap through nitrogenation is beyond the traditional thought of donor scheme, though the nitrogen is always thought as n -type donor.

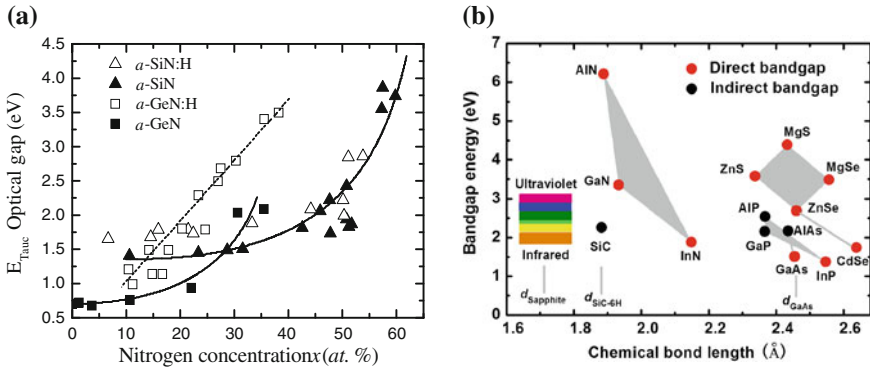


Fig. 8.4 **a** Optical bandgap expansion of the group III-nitride [13] and **b** the N-concentration dependence of the optical bandgap (E_{Tauc}) of α -Ge:N:H [47, 48] and α -Si:N:H [49] thin films [43]. Nitrogen generates a bandgap to the metallic group III materials, and the width of the bandgap depends on the bond energy or the electronegativity (reprinted with permission from [50])

8.5.2 Oxide Blue Light Emission

Chemical reaction-induced bandgap expansion provides guidelines for discovering or inventing sources for light emission with an expected wavelength. Oxides are much cheaper and easier to make compared with the group-III nitrides [51]. Figure 8.5 shows intense blue light emission from the $\text{Pb}(\text{Zr}_x\text{Ti}_{1-x})\text{O}_3$ pellets under Ar^+ ultraviolet (UV) irradiation (inset) [52]. Only one broad band located at 475 ± 50 nm with an excitation band centered at 305 ± 45 nm. Changing the x value causes a negligible shift of both the PL and PE peaks. The fluorescence decay curves of the PZT samples show that the lifetime of the photons varies markedly from 0.03 ms (at $x = 0.5$) to 0.6 ms (at $x = 1.0$). The 0.6-ms lifetime is much longer than that for other reported defect-related luminescence. Visible light emission of other oxides has been reported [53] such as SrCu_2O_2 [54], Sr_2CeO_4 [55], SiON [56], and ITO/SiO [57]. ZrO_2 and TiO_2 or their mixtures without Pb presence give no light though the samples were prepared under the same conditions. This means that the Pb plays an important yet unclear role in determining the PL features. Figure 8.6 shows the PL spectra of $\text{GaAs-Al}_{0.3}\text{Ga}_{0.7}\text{As}$ with and without anodic SiO_2 , SiO_2 films containing Si nanocrystals, and $\text{ZnO-Ga}_2\text{O}_3$ nanofibres. Controllable oxidation could modulate the band gap, which is within the 3B expectation.

The quantum efficiency (Y_{PL}) of photoluminescence follows the relation [42]: $Y_{PL} = P_r / (P_r + P_{nr})$, where P_r and P_{nr} are the probability of radiative and non-radiative combination of electron-hole pairs. Electron transiting from the conduction band tail to the valence band tail is responsible for the radiative combination, while electron transiting from the conduction band tail to the defect states that are located within the bandgap is responsible for the non-radiative combination [61]. The decrease in the PL intensity of Si in SiO_2 indicates that

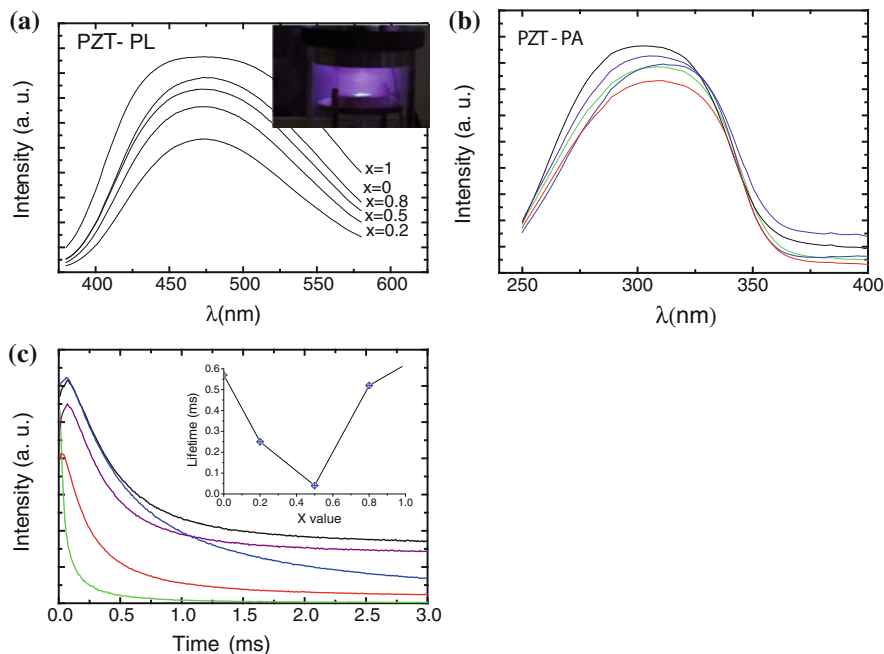


Fig. 8.5 Spectra of **a** photoluminescence (*PL*) and **b** photoexcitation (*PE*) for the PZT at room temperature. The peak corresponds to 2.65 eV (467 nm) and the FWHM is 0.5 eV. The lifetime **c** varies from 0.03 to 0.6 ms. Inset shows the visible light under Ar^+ excitation (reprinted with permission from [52])

oxidation creates defects in this particular system due to the non-bonding lone-pair production.

The 3B mechanism unifies the bandgap expansion of both nitrides and oxides with the same electron–hole pair production scheme in the valence band. Physically, the bandgap is twice the first coefficient of the Fourier series of the crystal field. The change of bond nature and bond energy modulate the crystal field, and consequently, change the width of the bandgap. Chemically, hole production empties the top edge of the valence band of the host and thus widens the bandgap. This bandgap expansion mechanism also explains the increase in resistivity and activation energy of the CN films with nitrogen incorporation [62].

8.6 Work Function Reduction for Field Emission

Doping proper amount of properly selected elements lowers the work function (Φ) or the threshold (V_T) in cold-cathode field emitters such as diamond, diamond-like carbon (a-C), or carbon nanotubes (CNTs) [4, 9, 63–65]. The V_T of the N-doped

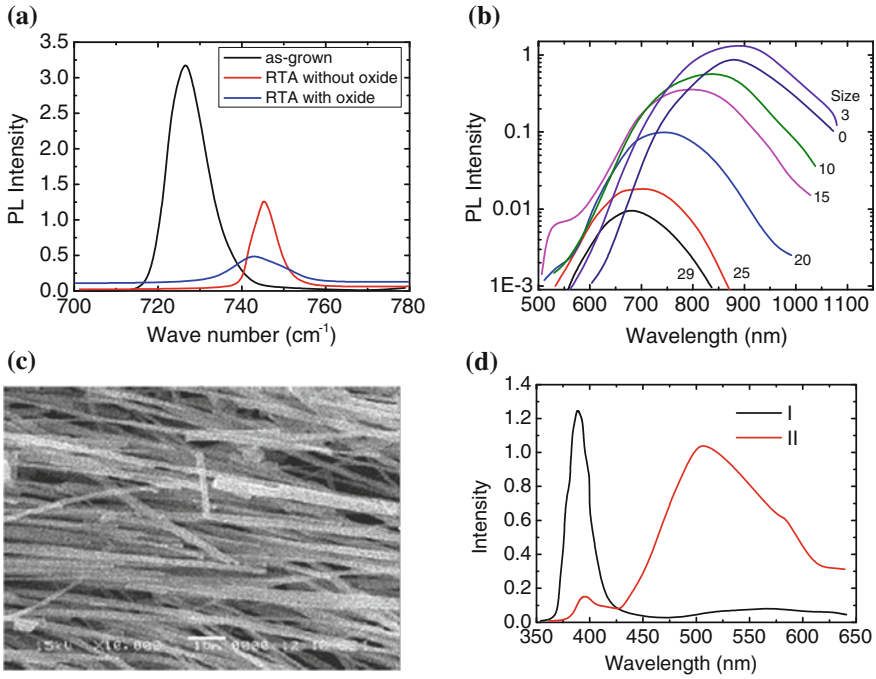
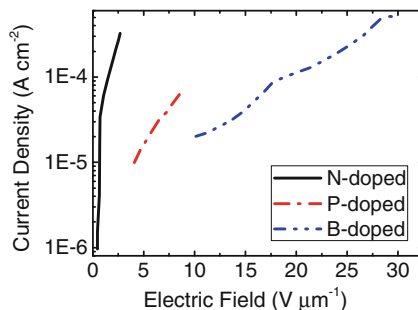


Fig. 8.6 Room temperature PL spectra of **a** the GaAs-Al_{0.3}Ga_{0.7}As ‘quantum-well’ laser with and without anodic SiO₂ annealed at 920 °C for 120 s [58]. **b** 100-nm-thick SiO₂ films containing Si nanocrystals oxidized for 0, 3, 10, 15, 20, 25, and 29 min at 1,000 °C. **c** ZnO-Ga₂O₃ nanofibres (150 nm in diameter) synthesized at 850 °C in tube furnace using graphite powder as catalysis [59], by heating the mixture of ZnO + Ga₂O₃ + C (Curve I) and ZnO + C (Curve II). An arrow indicates the bandgap wavelength of bulk Si. The inset shows schematically the change in the nanocrystal size distribution upon oxidation [60]. Thermal annealing of the oxidized laser causes a blue shift and an enhancement of the PL spectrum (reprinted with permission from [50])

diamond is even lower than the V_T of the diamond doped with boron and phosphor [8, 66–69], see Fig. 8.7.

Mechanisms such as negative affinity [70–72], antenna effect of conducting channels [73], impurity gap states [8, 66, 74], band bending at depletion layers [75], and surface dipole formation [9] explain the work function reduction due to N addition. Dipole formation creates the expected sub-band above E_F . According to the impurity gap state argument, N locates at a distorted substitutional site in the host matrix with one long but weak C–N bond, which forms a deep singly occupied donor level, ~ 1.7 eV below the conduction band edge E_C . On the other hand, two neighboring nitrogen atoms relax away from each other due to the weak lone-pair interaction, which form doubly filled states located ~ 1.5 eV above the valence band E_V . These two mid-gap impurity levels might play dominant roles in lowering the V_T . Furthermore, N may create a depletion layer that causes band bending at the back contact. At sufficiently high donor concentrations, this band bending narrows the tunneling distance and allows emission into the diamond conduction band.

Fig. 8.7 N, P, and B doping effect on the threshold of cold field electron emission of diamond (reprinted with permission from [8])



If the N-induced mid-gap impurity levels ($1.7 \text{ eV} < E_C$ and $1.5 \text{ eV} > E_V$) are dominant, the carbon co-doped with P and B should perform better than the carbon doped with N, as the P- and B-derived states ($0.46 \text{ eV} < E_C$ and $0.38 \text{ eV} > E_V$) are more beneficial to the band structure. Boron is a shallow substitutional acceptor in diamond with a level at 0.38 eV above the valence band edge E_V , and phosphorus can act as a shallow donor with a level 0.46 eV below the conduction band edge E_C [76].

The 3B correlation mechanism resolves the discrepancy regarding chemical effect on the work function. The weakly bounded $3sp$ orbitals of a P atom are hard to be hybridized compared with the $2sp$ orbitals of O and N because the $3sp$ electrons are more mobile than the $2sp$ electrons of N and O. The delocalized $3sp$ electrons determine that the P atom acts as a n -type donor that adds simply a DOS feature to a position 0.46 eV below the E_C of a diamond [76]. The fact that P doping gives little reduction in the work function compared to O or N doping [66] means that the impurity gap levels narrow the bandgap but barely reduce the work function.

Unlike P and B, O and N could expand the bandgap of a semiconductor instead, through compound formation. Therefore, N and O act not as impurity donors or acceptors traditionally in semiconductors, as charge transportation and polarization occur during the process of reaction.

The work function of Cs and Li ($\sim 3.5 \text{ eV}$) is much lower than that of other metals ($\sim 5.0 \text{ eV}$). However, adding Cs and Li to the diamond surface is ineffective in improving the emission properties. In fact, one is unable to prevent carbide formation in the mixture of metal and carbon. In the process of carbide formation, the conducting electrons of the metal will ‘flow’ from the upper edge of the conduction band to the empty p orbital of carbon, which lowers the occupied DOS of the doping metals instead. However, co-doping with both low- Φ metals, such as Li, Cs, and Ga, and electronegative element of N and O could form metal dipoles at the surface, which should reduce the work function of the low- Φ metals even further by $\sim 1.25 < 3.5 \text{ eV}$. Therefore, co-doping low- Φ metals with O or N could be promising measures in lowering the work function of carbon. However, overdosing of N and O produces the H-like bond that annihilates the dipoles. Appropriate doping would be necessary to avoid H-like bond formation that enlarges the work function [77].

Similarly, ceramic oxides, such as PZT, also emit electrons [78, 79]. Formation of the Cs–O–C surface bonds reduces the work function of diamond surface to 1.25 eV to promote electron emission of the surface [80]. Lowering the work function of a cathode by adsorbing both oxygen and electropositive metallic elements on its surface is more effective than by adsorbing simply the metallic element [81]. An appropriate amount of oxygen atoms adsorbed on the cathode surface results in a better dispenser cathode. Fluorine adsorption improves electron emission stability. The emission currents of CNTs are significantly enhanced when oxygen is adsorbed at the tip [82]. O₂ and O₃ treatment increases the emission current of the carbon nanotube array by ~800 % along with a decrease in the onset field emission voltage from 0.8 to 0.6 V/μm [83]. However, excessive amount of oxygen [84] causes adverse effect on the field emission.

With the 3B correlation as origin, the impurity gap levels (lone pair) [66, 74] and the surface dipole [9] models would be correct and complete. The lone-pair impurities below E_F contribute indirectly to the work function reduction as they induce the antibonding dipoles with the states above E_F . According to the impurity gap state argument, N locates at a distorted substitutional site with one long but weak C–N bond, which forms a deep singly occupied donor level, ~1.7 eV below the E_c . On the other hand, two neighboring nitrogen atoms relax away from each other due to the weak lone-pair interaction, which form doubly filled states located ~1.5 eV above the E_v . These impurity levels play dominant roles in lowering the V_T . Furthermore, N may create a depletion layer that causes band bending at the back contact. At sufficiently high donor concentrations, this band bending narrows the tunneling distance there and allows emission into the diamond conduction band.

8.7 Geometric Selectivity: Diamond Oxidation

Oxidation and graphitization of synthetic diamond is an important issue for practical applications. Oxidation limits the performance of diamond used in cutting tools, optical windows, and electronic devices when the diamond exposed to air or other gaseous ambient at high temperatures. The infrared transmittance of diamond windows drops by 6–12 % after being heated in air at 1,070 K for 255 s [85].

Diamond oxidation occurs at ~1,070 K preferentially at grain boundaries, local defects, and in the diamond-like carbon phase [86, 87]. Molecular oxygen adsorption happens to the clean (111) and (110) surfaces of diamond at room temperature [88]. Thermal desorption produces CO from both surfaces. Apart from a low-temperature desorption peak, TDS shows two CO desorption peaks at 1,060 and 1,300 K for the C(111)–(2 × 1) surface, whereas only one desorption peak presents in the 1,030–1,160 K range for the C(110) surface.

According to the ‘periodic bond chain’ theory [89–92] and the ‘defect density’ mechanism, diamond (111) surface is most stable in resisting oxidation than other faces [92]. However, dry oxygen roughens the (111) surface very fast, while the (100) surface is largely inert to oxygen below 1,220 K [93].

One needs to understand why the densely packed diamond (111) planes are oxidized easier than the (001) or the (220) planes and how the oxygen penetrates into the (111) face during the course of reaction. The geometrical selectivity of oxide tetrahedron formation and the mechanism of oxide bond switching could resolve the discrepancy.

SEM images in Fig. 8.8 show that annealing up to 1,400 K in vacuum graphitizes the diamond surface without any preference of crystal orientation. Annealing in air at 1,070 K rusts the (111) surface significantly without any roughening of the (110) surface except for defects [94]. Diamond erosion occurs preferentially in the planes possessing C_{3v} symmetry. The (110) rectangular planes experience no change apart from the defect sites.

Generally, the (111) planes grow in CVD synthesis at a relatively higher temperature than the (220) planes [95]. The synthetic diamond changes at $1,100 \pm 50$ K from (220) plane dominance to a (111)-dominated phase. The (111) planes form hexagonal platelets, truncated hexagonal platelets, decahedrons (pseudo fivefold symmetry), icosahedral (20 faces), and triangular shapes, depending on stacking errors [6]. The (111) never forms platelet of C_4 symmetry. Therefore, the square or rectangle platelets in Fig. 8.8a correspond to the (220) faces, or equivalent planes.

It is important to note that the lone pairs of oxygen possess the special ability of inducing dipoles. Interaction between the dipole and the oxygen ion, and hence the dipole to the bulk, is rather weak (~ 50 meV, Chap. 6) as there is no electron sharing between the dipole and the oxygen. Due to the strong repulsion of the non-bonding lone pairs, the dipoles tend to locate at the open end of a surface. The loosely bounded dipoles therefore tend to be eroded away from the surface in the process of corrosion.

The atomic density ratio of the (111) plane to that of the (220) plane is given as (refer to Fig. 8.8b, d being the lattice parameter):

$$\frac{n\{111\}}{n\{220\}} = \frac{\frac{1}{(\sqrt{2}d)^2 \sin(60^\circ)/2}}{\frac{1.5}{\sqrt{2}d^2}} = \sqrt{\frac{32}{27}} > 1$$

The (111) interplane distance is $(\sqrt{3}-1)d/2$ (from the plane comprising atoms labeled 123 to atom 0). The (220) plane separation is $\sqrt{3}d/2$ (from atom 0 to atom 4). Each of the two planes cuts through three C atoms, but the geometrical arrangement of these atoms in the planes is entirely different. Atoms labeled 1, 2, and 3 in the (111) plane form a C_{3v} hollow with identical edges of $a = \sqrt{2}d$, and of $(\sqrt{3} - 1)d/2$ in depth. The diamond bond length is $\sqrt{3}d/2$ or 1.54 \AA . However, atoms labeled 0, 1, and 2 in the (220) plane are packed in such a way that the triangle edges are d , d , and $\sqrt{2}d$ in length. Therefore, it is easier for an oxygen adsorbate to find the fourth C atom (labeled 0) underneath the C_{3v} hollow site in the (111) plane to form a quasi-tetrahedron.

However, atom labeled 3 or 4 underneath the (220) plane composed of atoms labeled 0, 1, and 2 could hardly form a frame in which an oxide tetrahedron could

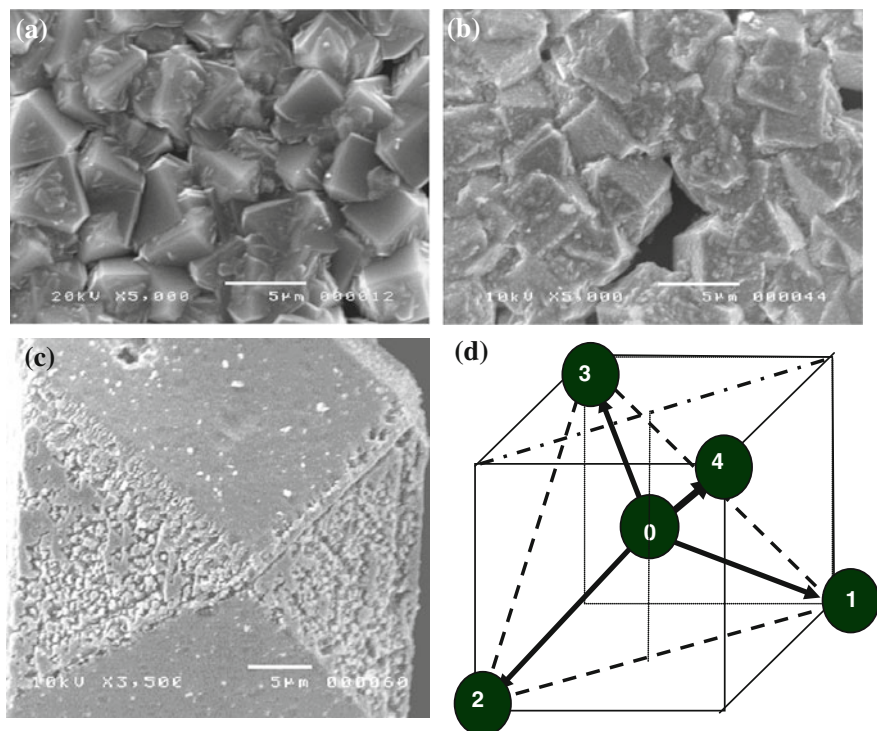


Fig. 8.8 SEM images of **a** CVD diamond, **b** vacuum thermal graphitization, **c** preferential oxidation of the (111) plane throughout the course of reaction, and **d** schematic illustration of the geometrical environment of the (111) and the (220) planes. The (111) plane facilitates more easily an oxide tetrahedron than the (220) plane (Reprinted with permission from [96])

fit in. Therefore, it is harder to facilitate the oxide tetrahedron in the (220) plane than in the (111) plane. This explains why the densely packed (111) plane oxidizes easier than the (220) plane.

Although the atomic sizes and the geometrical arrangement of the considered metals (Chaps. 3–6) are different, the oxide tetrahedron formation is essentially the same. During the process of oxidation of the diamond, oxygen atoms penetrate easily into the (111) planes and loosen the C atoms at the surface by forming the weakly bound dipoles. The dipoles are readily eroded away at elevated temperatures and then the oxygen seeks new partners for the formation of a new tetrahedron. Oxygen can always survive by fitting itself into a suitable bonding environment to build up the tetrahedron through bond switching.

It appears that diamond is not essentially the same to metals in the process of reaction. In fact, factors dominating the oxidation of a solid surface are as follows: (1) the difference in electronegativity, (2) the scale and geometry of the lattice, and (3) the temperature and oxygen pressure, disregarding the host atom. Electronegativity determines the nature of the bond or the easiness and amount of charge

transportation between the bonding constituents. The atomic geometry and lattice constant determine the way of facilitating the oxide tetrahedron. The temperature and the ambient oxygen pressure determine the rate of reaction. Therefore, the mechanism of oxidation is valid for a solid surface whether it is a metal or not. No specification of element or its phase is necessary for oxide tetrahedron formation.

Diamond erosion starting at 750 K in air shows strong geometric selectivity for oxide tetrahedron formation, which is the same to metal surface oxidation. Diamond (111) planes provide a more suitable bonding environment than the loosely packed (220) planes. Oxygen penetrates into the bulk by bond switching and leaves behind the weakly bound dipoles that are eroded away during the process of corrosion. The presence of the lone-pair features (around -3.0 eV below E_F) for the diamond (111) planes with chemisorbed oxygen justifies the discussion.

8.8 Diamond–Metal Adhesion Enhancement

The poor adhesion of diamond films to metal substrates has been a long-standing issue that prevents practical applications of the excellent properties of synthetic diamond. Analysis [97] of Ni surface chemisorption indicated that the C–Ni(001) bond experiences strong compression and the surface is covered with Ni^+ and Ni^{2+} , while the N–Ni(001) bond undergoes slight tension and the surface comprises Ni^+ and $\text{Ni}^{+/p}$ alternatives. XRD measurement [15] has confirmed the prediction that carbon turns the tensile stress of Ti surface to be compressive. Comparison of the surface morphology of TiC with that of TiN indicates that the surface stresses are different in nature [98].

Inserting a graded TiCN interlayer between the metal substrate and the synthetic diamond neutralizes the interface stress, which improved the adhesion between diamond and the Ti substrate substantially [98]. Figure 8.9 compares the cross section of the diamond/Ti system with and without the graded TiCN interlayer. The graded TiCN interlayer removes cracks and improves the adhesion of the diamond film significantly. Adhere diamond to the Ti substrate strongly. The critical scratch load for the adherent diamond is as high as 135 N in comparison with the adhesion strength of 55 N for nanostructured diamond on the tungsten carbide substrate. These exercises provide a prototype for joining metals with nonmetals in composite materials.

The success of this approach evidences that the extension of the *sp* hybrid bonding of oxygen to carbon and nitrogen is on an essentially correct track. The *sp* hybrid bonding of nitrogen helps to understand why it is more difficult to form the crystalline carbon nitride than the hexagonal SiCN crystallite [99] and that overdose (>75 % partial pressure) of nitrogen in diamond deposition could turn the diamond to SiCN [100].

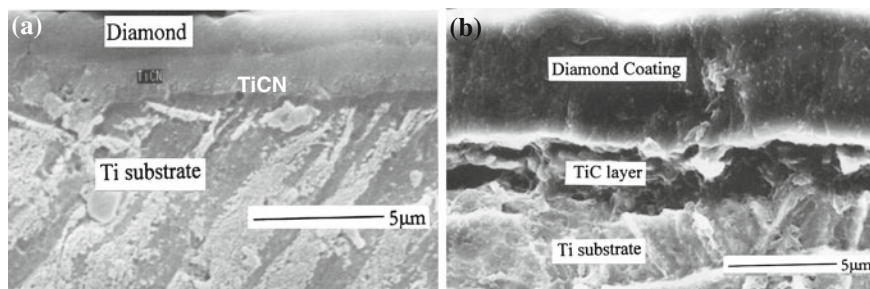


Fig. 8.9 SEM cross section observation of diamond **a** with and **b** without the designed graded TiCN buffer layer. The porous carbide with strong bond repulsion prohibits the adhesion, while the buffer layer allows the diamond and Ti substrate to bond strongly (reprinted with permission from [98])

8.9 Perspectives: Molecular Functional Groups

8.9.1 *B-, C-, N-, O-, and F-induced High- T_c Superconductivity*

The original Bardeen-Cooper-Schrieffer (BCS) theory of superconductivity adequately describes the origination and behavior of conventional superconducting metals and alloys, whose critical temperatures of transition to superconductivity are extremely low, never higher than 30 K. According to the BCS theory, a large Bose–Einstein condensation resulting from the coupling of electron pairs near the Fermi surface, which are known as Cooper pairs, at low temperatures governs the superconductivity. However, in 1986 and subsequent years, copper oxides were discovered to become superconducting at temperatures up to 136 K and even 160 K when this new type of materials were subject to pressure. The emergence of the new ‘high- T_c superconductor’ also marked the start of a revolution in its applications as well as scientific hypotheses regarding it, because the BCS theory was evidently inadequate.

The fact that some compounds of B, C, N, O, F, and other elements exhibit high- T_c superconductivity, albeit different critical temperatures, implies an underlying similarity in these inducing elements. Fortunately, it has been certain, as discussed, that in N, O, and F, the sp^3 hybridization generates the non-bonding and antibonding states near the Fermi surface. In turn, these localized lone-pair electrons and highly energetic antibonding electrons may have a high chance of forming Cooper pairs that dominate the character of the high- T_c superconductors. When an external electric field is applied, these localized pairs of electrons are easily excited and hence become highly conducting given suitable channels of transportation. Compared with the findings of graphene edge states, the effective mass of these electrons is very small and their group velocity is very high. An important characteristic is that these high- T_c superconductors all assume a two-

dimensional layered structure, such as Cu–O chains or planes, on which superconductivity occurs. Most strikingly, the unique ‘Cu^P: O⁻²: Cu^P:’ chains on the copper surfaces generate dipoles and lone pairs associated with missing rows of atoms. Bound energy states locating at energies near the Fermi surface in oxide superconductors [101] further corroborate the importance of antibonding and non-bonding states in effecting superconductivity.

As a plausible mechanism governing the high- T_C superconductivity, the strong correlation of electrons with spins has attracted much attention. The presence of the non-bonding and the antibonding states near Fermi surface should play at least a role of competence. If the 1s electrons of B and C are excited to occupy the hybridized $2sp^3$ orbits, B and C would likely form valence band structures similar to those of N and O and hence result in the superconductivity. The exposition of the mechanism of high- T_C superconductivity from the perspective of antibond and non-bond formation and the corresponding electronics and energetics would be a revolutionary approach culminating a breakthrough.

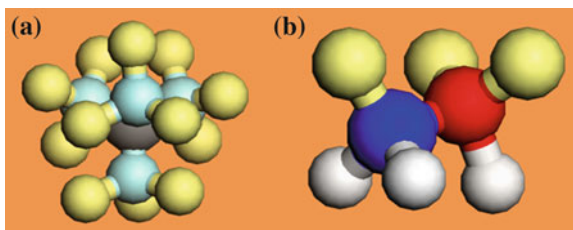
8.9.2 CF_4 Anticoagulation in Synthetic Blood

A key unresolved challenge in creating artificial blood is anticoagulation. CF_4 is an excellent artificial blood anticoagulant although the microscopic mechanism is yet unknown. The sp -orbit hybridization of C and F and the presence of non-bonding states may apply to this instance. As illustrated in Fig. 8.10, the sp orbits of C and F undergo hybridization to form tetrahedron. A central C^{4+} ion is surrounded by 12 pairs of non-bonding electrons provided by the four surrounding F^- ions with each of them carrying three pairs of non-bonding electrons. These lone-pair electrons form a function group that attracts and polarizes nearby atoms weakly, making them mobile in fluids, which translates to an anticoagulating function. Since NF_5 and SF_6 also possess 15 and 18 lone pairs of electrons with structure being similar to CF_4 , respectively, they are expected to perform in the same way as CF_4 in synthetic blood anticoagulation.

8.9.3 NO Signaling and Living Cells

All organic and living cells are composed primarily of H, C, N, and O. Similarly, most pharmaceutical products are also composed of these elements, apart from tiny amounts of dopant and their molecular configurations. For example, Nitric Oxide, NO, is a short-lived, endogenously produced gas that acts as a signaling molecule in the body. This is an entirely new principal of signaling in the human organism, in which signal is transmitted by the gas, which is produced by one cell and then penetrates membranes and regulates the function of other cells. NO not only combats many arterial-related diseases but also plays an important role in molecule signaling

Fig. 8.10 Hypothetic **a** CF_4 ($\text{C}^{4+} + 4\text{F}^- + 4 \times (-)$) and **b** NO ($\text{N}^{3-} + \text{O}^{2-} + 3(-) + 3(-)$) molecules. $(-)$ represents the dangling bond and $(:)$ the non-bonding lone pair (Reprint with permission from [102])



outside the cardiovascular system and has become a useful tool in the practice of medication. However, the bonding mechanism of the NO is yet to be clear.

If the N and O atoms are linked by a single bond to form an NO molecule with hybridized sp^3 orbitals (Fig. 8.10) of both, one side of the molecule has three lone pairs, while the other has three dangling bonds. Such a structure enables the NO molecule to locate in a certain place by forming bonds via the dangling bonds and polarize its surroundings via the lone pairs, producing regulation channels required in meditation. Under certain chemical conditions, the molecular orbitals of NO can hybridize or dehybridize to alter their functionalities. In addition, in the body, the lone-pair electrons and antibonding dipoles produced by O, N, and C are mainly responsible for the synthesis, folding, and unfolding mechanisms of cells, protein, DNA, and RNA as well.

8.10 Summary

The 3B correlation could unify the anomalous properties of C, N, O, and F involved compounds. For instance, the N -enhanced magnetization, bandgap expansion for light emission, N -lowered threshold of cold cathode emission, wear and corrosion resistance, and super elasticity of nitrides all arise from the nitride tetrahedron formation with involvement of bonding, non-bonding, hole, and antibond dipole production. Therefore, the extent and type of nitrogen lone-pair interactions are the most important functional groups present not only in the organic molecules [103] but also in inorganic compounds. A combination of density functional calculation and UPS measurement would be most effective in revealing the dynamics of bond and band formation. Besides, the 3B correlation theory could provide complementary mechanism to correlate the electronic configuration in the bonding process and its derivatives on the valence DOS and physical properties. The 3B correlation and the concept of lone-pair non-bonding, antibonding dipoles, and hole states may provide guidelines for controllable modification of existing materials and in the pursuit of new functional properties of compounds or molecules with C, N, O, and F involvement.

References

1. L. Pauling, *The Nature of the Chemical Bond*, 3rd edn. (Cornell University Press, Ithaca, NY, 1960)
2. P. Schaaf, Laser nitriding of metals. *Prog. Mater. Sci.* **47**(1), 1–161 (2002)
3. W.T. Zheng, C.Q. Sun, Electronic process of nitriding: mechanism and applications. *Prog. Solid State Chem.* **34**(1), 1–20 (2006)
4. X. Wang, W.T. Zheng, H.W. Tian, S.S. Yu, W. Xu, S.H. Meng, X.D. He, J.C. Han, C.Q. Sun, B.K. Tay, Growth, structural, and magnetic properties of iron nitride thin films deposited by dc magnetron sputtering. *Appl. Surf. Sci.* **220**(1–4), 30–39 (2003)
5. K.H. Jack, α'' Fe₁₆N₂: a giant magnetic moment material?, in *Nitrides and Oxynitrides*, ed. by S. Hampshire, M.J. Pomeroy (Trans Tech Publications Ltd, Zurich-Uetikon, 2000), pp. 91–97
6. E.Y. Jiang, C.Q. Sun, J.E. Li, Y.G. Liu, The structures and magnetic-properties of Fe films prepared by the facing targets sputtering method. *J. Appl. Phys.* **65**(4), 1659–1663 (1989)
7. J.M.D. Coey, H. Sun, Improved magnetic-properties by treatment of iron-based rare-earth intermetallic compounds in ammonia. *J. Magn. Magn. Mater.* **87**(3), L251–L254 (1990)
8. K. Okano, S. Koizumi, S.R.P. Silva, G.A.J. Amaratunga, Low-threshold cold cathodes made of nitrogen-doped chemical-vapour-deposited diamond. *Nature* **381**(6578), 140–141 (1996)
9. W.T. Zheng, J.J. Li, X. Wang, X.T. Li, Z.S. Jin, B.K. Tay, C.Q. Sun, Electron emission of carbon nitride films and mechanism for the nitrogen-lowered threshold in cold cathode. *J. Appl. Phys.* **94**(4), 2741–2745 (2003)
10. B.K. Agrawal, S. Agrawal, P.S. Yadav, S. Kumar, Ab initio calculation of electronic properties of Ga_{1-x}Al_xN alloys. *J. Phys. Condens. Matter* **9**(8), 1763–1775 (1997)
11. Z.Q. Yang, Z.Z. Xu, A theoretical study of electronic and optical properties in wurtzite GaN. *J. Phys. Condens. Matter* **8**(43), 8303–8308 (1996)
12. C.L. Bai, *Scanning Tunneling Microscopy and its Applications*, vol. 32. Springer Series in Surface Science (Springer, Berlin, 1995)
13. F.A. Ponce, D.P. Bour, Nitride-based semiconductors for blue and green light-emitting devices. *Nature* **386**(6623), 351–359 (1997)
14. C.Q. Sun, B.K. Tay, S.P. Lau, X.W. Sun, X.T. Zeng, S. Li, H.L. Bai, H. Liu, Z.H. Liu, E.Y. Jiang, Bond contraction and lone pair interaction at nitride surfaces. *J. Appl. Phys.* **90**(5), 2615–2617 (2001)
15. Y.Q. Fu, C.Q. Sun, B.B. Yan, H.J. Du, Carbon turns the tensile surface stress of Ti to be compressive. *J. Phys. D-Appl. Phys.* **34**(24), L129–L132 (2001)
16. M. Sotto, S. Gauthier, F. Pourmir, S. Rousset, J. Klein, LEED study of activated nitrogen adsorption on (100) and (h11) faces of copper. *Surf. Sci.* **371**(1), 36–44 (1997)
17. S. Schwegmann, A.P. Seitsonen, H. Dietrich, H. Bludau, H. Over, K. Jacobi, G. Ertl, The adsorption of atomic nitrogen on Ru(0001): geometry and energetics. *Chem. Phys. Lett.* **264**(6), 680–686 (1997)
18. V.M. Bermudez, Functionalizing the GaN(0001)-(1x1) surface II. Chemisorption of 3-pyrroline. *Surf. Sci.* **499**(2–3), 124–134 (2002)
19. D. Caceres, I. Vergara, R. Gonzalez, E. Monroy, F. Calle, E. Munoz, F. Omnes, Nanoindentation on AlGa_n thin films. *J. Appl. Phys.* **86**(12), 6773–6778 (1999)
20. H. Kamimura, E.M. Matsuno, H. Ushio, *Com. Cond. Matt. Phys.* **15** (1992)
21. S. Veprek, The search for novel, superhard materials. *J. Vac. Sci. Technol. A-Vac. Surf. Films* **17**(5), 2401–2420 (1999)
22. T. Malkow, Critical observations in the research of carbon nitride. *Mater. Sci. Eng. Struct. Mater. Prop. Microstruct. Process.* **292**(1), 112–124 (2000)
23. Q. Lv, C.B. Cao, C. Li, J.T. Zhang, H.X. Zhu, X. Kong, X.F. Duan, Formation of crystalline carbon nitride powder by a mild solvothermal method. *J. Mater. Chem.* **13**(6), 1241–1243 (2003)

24. P.J. Jennings, C.Q. Sun, in *The Surface Analysis Methods in Materials Science*, ed. by D.J. O'Connor, B.A. Sexton, R.C. Smart, (Springer, Berlin, New York, 2002)
25. T. Hughbanks, Y.C. Tian, On the structure and composition of carbon nitride. *Solid State Commun.* **96**(5), 321–325 (1995)
26. D.M. Teter, R.J. Hemley, Low-compressibility carbon nitrides. *Science* **271**(5245), 53–55 (1996)
27. C.M. Niu, Y.Z. Lu, C.M. Lieber, Experimental realization of the covalent solid carbon nitride. *Science* **261**(5119), 334–337 (1993)
28. Y. Zhang, H. Sun, C.F. Chen, Strain dependent bonding in solid C₃N₄: high elastic moduli but low strength. *Phys. Rev. B* **73**(6), 064109 (2006)
29. E. Broitman, W.T. Zheng, H. Sjoström, I. Ivanov, J.E. Greene, J.E. Sundgren, Stress development during deposition of CN_x thin films. *Appl. Phys. Lett.* **72**(20), 2532–2534 (1998)
30. P.J. Jennings, in *The Surface Analysis Methods in Materials Science*, ed. by D.J. O'Connor, B.A. Sexton, R.C. Smart (Springer, Berlin, 1992)
31. S. Veprek, Electronic and mechanical properties of nanocrystalline composites when approaching molecular size. *Thin Solid Films* **297**(1–2), 145–153 (1997)
32. C. Ossadnik, S. Veprek, I. Gregora, Applicability of Raman scattering for the characterization of nanocrystalline silicon. *Thin Solid Films* **337**(1–2), 148–151 (1999)
33. X.T. Zeng, S. Zhang, C.Q. Sun, Y.C. Liu, Nanometric-layered CrN/TiN thin films: mechanical strength and thermal stability. *Thin Solid Films* **424**(1), 99–102 (2003)
34. X.T. Zeng, TiN/NbN superlattice hard coatings deposited by unbalanced magnetron sputtering. *Surf. Coat. Technol.* **113**(1–2), 75–79 (1999)
35. Y.J. Tian, B. Xu, D.L. Yu, Y.M. Ma, Y.B. Wang, Y.B. Jiang, W.T. Hu, C.C. Tang, Y.F. Gao, K. Luo, Z.S. Zhao, L.M. Wang, B. Wen, J.L. He, Z.Y. Liu, Ultrahard nanotwinned cubic boron nitride. *Nature* **493**(7432), 385–388 (2013)
36. K.H. Jack, The occurrence and the crystal structure of α' -iron nitride: a new type of interstitial alloy formed during the tempering of nitrogen-martensite. *Proc. Royal Soc. Lond. Ser. Math. Phys. Sci.* **208**(1093), 216–224 (1951)
37. J.P. Zhou, D. Li, Y.S. Gu, X.R. Chang, C.H. Zhao, F.H. Li, L.J. Qiao, Z.H. Tian, G.D. Fang, Q.H. Song, The structure and magnetic properties of Fe-N thin films. *Sci. China Ser. A-Math. Phys. Astron.* **45**(2), 255–263 (2002)
38. W.H. Zhong, C.Q. Sun, S. Li, Size effect on the magnetism of nanocrystalline Ni films at ambient temperature. *Solid State Commun.* **130**(9), 603–606 (2004)
39. H.G. Pan, F.M. Yang, Y. Chen, X.F. Han, N. Tang, C.P. Chen, Q.D. Wang, Magnetic properties of a new series of rare-earth iron nitrides R₃(Fe, Mo)₂₉N-x (R = Ce, Nd, Sm, Gd, Tb, Dy or Y). *J. Phys. Condens. Matter* **9**(11), 2499–2505 (1997)
40. D.C. Sun, C. Lin, E.Y. Jiang, Epitaxially grown Fe₁₆N₂ single-crystal films with high saturation magnetization-prepared by facing targets sputtering. *J. Phys. Condens. Matter* **7**(18), 3667–3674 (1995)
41. E.Y. Jiang, D.C. Sun, C. Lin, M.B. Tian, H.L. Bai, S.L. Ming, Facing targets sputtered Fe-N gradient films. *J. Appl. Phys.* **78**(4), 2596–2600 (1995)
42. R.A. Street, *Hydrogenated amorphous silicon* (Cambridge University Press, Cambridge, 1991)
43. I. Chambouleyron, A.R. Zanatta, Nitrogen in germanium. *J. Appl. Phys.* **84**(1), 1–30 (1998)
44. P. Hammer, N.M. Victoria, F. Alvarez, Electronic structure of hydrogenated carbon nitride films. *J. Vac. Sci. Technol. A-Vac. Surf. Films* **16**(5), 2941–2949 (1998)
45. D.C. Reynolds, D.C. Look, B. Jogai, H. Morkoc, Similarities in the bandedge and deep-centre photoluminescence mechanisms of ZnO and GaN. *Solid State Commun.* **101**(9), 643–646 (1997)
46. I.G. Austin, W.A. Jackson, T.M. Searle, P.K. Bhat, R.A. Gibson, Photoluminescence properties of a-SiN_x: H-alloys. *Philos. Mag. B-Phys. Condens. Matter Stat. Mech. Electron. Opt. Magn. Prop.* **52**(3), 271–288 (1985)

47. A.R. Zanatta, I. Chambouleyron, Nitrogen in the amorphous-germanium network: from high dilution to the alloy phase. *Phys. Rev. B* **48**(7), 4560–4570 (1993)
48. J. Vilcarromero, F.C. Marques, Influence of the deposition conditions on the properties of amorphous germanium nitrogen alloys. *Phys. Status Solidi B-Basic Res.* **192**(2), 543–547 (1995)
49. S. Hasegawa, M. Matsuda, Y. Kurata, Bonding configuration and defects in amorphous Si_Nx-H films. *Appl. Phys. Lett.* **58**(7), 741–743 (1991)
50. C.Q. Sun, Oxidation electronics: bond-band-barrier correlation and its applications. *Prog. Mater. Sci.* **48**(6), 521–685 (2003)
51. D. Jin, P. Hing, C.Q. Sun, Growth dynamics and electric properties of PbTi_{0.1}Zr_{0.9}O₃ ceramics doped with cerium oxide. *J. Phys. D-Appl. Phys.* **33**(6), 744–752 (2000)
52. C.Q. Sun, D. Jin, J. Zhou, S. Li, B.K. Tay, S.P. Lau, X.W. Sun, H.T. Huang, P. Hing, Intense and stable blue-light emission of Pb(ZrxTi1-x)O-3. *Appl. Phys. Lett.* **79**(8), 1082–1084 (2001)
53. G.A. Hirata, J. McKittrick, D. Devlin, Growth and analysis of red, green and blue luminescent oxide thin films. *Surf. Rev. Lett.* **5**(1), 413–417 (1998)
54. A. Kudo, H. Yanagi, H. Hosono, H. Kawazoe, SrCu₂O₂: a p-type conductive oxide with wide band gap. *Appl. Phys. Lett.* **73**(2), 220–222 (1998)
55. Y.D. Jiang, F.L. Zhang, C.J. Summers, Z.L. Wang, Synthesis and properties of Sr₂CeO₄ blue emission powder phosphor for field emission displays. *Appl. Phys. Lett.* **74**(12), 1677–1679 (1999)
56. K.J. Price, L.R. Sharpe, L.E. McNeil, E.A. Irene, Electroluminescence in silicon oxynitride films. *J. Appl. Phys.* **86**(5), 2638–2641 (1999)
57. Y.Q. Wang, T.P. Zhao, J. Liu, G.G. Qin, Near-ultraviolet and near-infrared electroluminescence from an indium-tin-oxide film native Si oxide/p-Si structure. *Appl. Phys. Lett.* **74**(25), 3815–3817 (1999)
58. S. Yuan, C. Jagadish, Y. Kim, Y. Chang, H.H. Tan, R.M. Cohen, M. Petracic, L.V. Dao, M. Gal, M.C.Y. Chan, E.H. Li, O. Jeong-Seok, P.S. Zory, Anodic-oxide-induced intermixing in GaAs-AlGaAs quantum-well and quantum-wire structures. *IEEE J. Sel. Top. Quantum Electron.* **4**(4), 629–635 (1998)
59. C.X. Xu, X.W. Sun, B.J. Chen, C.Q. Sun, B.K. Tay, S.X.S. Li, Aligned ZnO nanofibre array prepared by vapour transport in air. *Chin. Phys. Lett.* **20**(8), 1319–1322 (2003)
60. M.L. Brongersma, A. Polman, K.S. Min, E. Boer, T. Tambo, H.A. Atwater, Tuning the emission wavelength of Si nanocrystals in SiO₂ by oxidation. *Appl. Phys. Lett.* **72**(20), 2577–2579 (1998)
61. A.M. Liu, Microstructure and photoluminescence spectra of porous InP. *Nanotechnology* **12**(3), L1–L3 (2001)
62. M.A. Monclus, D.C. Cameron, A. Chowdhury, R. Barkley, M. Collins, Investigation of the valence band states of reactively sputtered carbon nitride films. *Thin Solid Films* **355**, 79–84 (1999)
63. J.J. Li, W.T. Zheng, C.Z. Gu, Z.S. Jin, Y.N. Zhao, X.X. Mei, Z.X. Mu, C. Dong, C.Q. Sun, Field emission enhancement of amorphous carbon films by nitrogen-implantation. *Carbon* **42**(11), 2309–2314 (2004)
64. T. Sugino, T. Yamamoto, C. Kimura, H. Murakami, M. Hirakawa, Field emission characteristics of carbon nanofiber improved by deposition of boron nitride nanocrystalline film. *Appl. Phys. Lett.* **80**(20), 3808–3810 (2002)
65. E. Hernandez, C. Goze, P. Bernier, A. Rubio, Elastic properties of C and B_xC_yN_z composite nanotubes. *Phys. Rev. Lett.* **80**(20), 4502–4505 (1998)
66. J. Robertson, Mechanisms of electron field emission from diamond, diamond-like carbon, and nanostructured carbon. *J. Vac. Sci. Technol., B* **17**(2), 659–665 (1999)
67. A.T. Sowers, B.L. Ward, S.L. English, R.J. Nemanich, Field emission properties of nitrogen-doped diamond films. *J. Appl. Phys.* **86**(7), 3973–3982 (1999)

68. S.C. Lim, R.E. Stallcup, I.A. Akwani, J.M. Perez, Effects of O-2, H-2, and N-2 gases on the field emission properties of diamond-coated microtips. *Appl. Phys. Lett.* **75**(8), 1179–1181 (1999)
69. L.K. Cheah, X. Shi, E. Liu, B.K. Tay, Electron field emission properties of tetrahedral amorphous carbon films. *J. Appl. Phys.* **85**(9), 6816–6821 (1999)
70. C. Bandis, B.B. Pate, Simultaneous field emission and photoemission from diamond. *Appl. Phys. Lett.* **69**(3), 366–368 (1996)
71. M.W. Geis, N.N. Efremow, K.E. Krohn, J.C. Twichell, T.M. Lyszczarz, R. Kalish, J.A. Greer, M.D. Tabat, A new surface electron-emission mechanism in diamond cathodes. *Nature* **393**(6684), 431–435 (1998)
72. W. Zhu, G.P. Kochanski, S. Jin, Low-field electron emission from undoped nanostructured diamond. *Science* **282**(5393), 1471–1473 (1998)
73. A. Beiser, *Perspective of Modern Physics*, 18th edn. (McGraw-Hill, Singapore, 1988)
74. M.J. Rutter, J. Robertson, Ab initio calculation of electron affinities of diamond surfaces. *Phys. Rev. B* **57**(15), 9241–9245 (1998)
75. G.A.J. Amaratunga, S.R.P. Silva, Nitrogen containing hydrogenated amorphous carbon for thin-film field emission cathodes. *Appl. Phys. Lett.* **68**(18), 2529–2531 (1996)
76. P.R. Briddon, R. Jones, Theory of impurities in diamond. *Phys. B* **185**(1–4), 179–189 (1993)
77. W.T. Zheng, C.Q. Sun, B.K. Tay, Modulating the work function of carbon by N or O addition and nanotip fabrication. *Solid State Commun.* **128**(9–10), 381–384 (2003)
78. H. Riege, I. Boscolo, J. Handerek, U. Herleb, Features and technology of ferroelectric electron emission. *J. Appl. Phys.* **84**(3), 1602–1617 (1998)
79. I. Stolichnov, A.K. Tagantsev, E.L. Colla, N. Setter, Cold-field-emission test of the fatigued state of Pb(ZrxTi1-x)O-3 films. *Appl. Phys. Lett.* **73**(10), 1361–1363 (1998)
80. W.E. Pickett, Negative electron-affinity and low work function surface: cesium on oxygenated diamond(100). *Phys. Rev. Lett.* **73**(12), 1664–1667 (1994)
81. L.W. Lin, The role of oxygen and fluorine in the electron-emission of some kinds of cathodes. *J. Vac. Sci. Technol., A Vac. Surf. Films* **6**(3), 1053–1057 (1988)
82. N. Park, S.W. Han, J. Ihm, Effects of oxygen adsorption on carbon nanotube field emitters. *Phys. Rev. B* **64**(12), 125401 (2001)
83. S.C. Kung, K.C. Hwang, I.N. Lin, Oxygen and ozone oxidation-enhanced field emission of carbon nanotubes. *Appl. Phys. Lett.* **80**(25), 4819–4821 (2002)
84. A. Wadhawan, R.E. Stallcup, K.F. Stephens, J.M. Perez, I.A. Akwani, Effects of O-2, Ar, and H-2 gases on the field-emission properties of single-walled and multiwalled carbon nanotubes. *Appl. Phys. Lett.* **79**(12), 1867–1869 (2001)
85. C.E. Johnson, J.M. Bennett, M.P. Nadler, Oxidation of diamond windows. *J. Mater. Res.* **10**(10), 2555–2563 (1995)
86. A. Joshi, R. Nimmagadda, J. Herrington, Oxidation-kinetics of diamond, graphite, and chemical vapor-deposited diamond films by thermal gravimetry. *J. Vac. Sci. Technol., A Vac. Surf. Films* **8**(3), 2137–2142 (1990)
87. W. Zhu, X.H. Wang, D.J. Pickrell, A.R. Badzian, R. Messier, The oxidation of CVD diamond films. *Carbon* **28**(6), 796 (1990)
88. K. Bobrov, H. Schechter, A. Hoffman, M. Folman, Molecular oxygen adsorption and desorption from single crystal diamond (111) and (110) surfaces. *Appl. Surf. Sci.* **196**(1–4), 173–180 (2002)
89. K. Böer, *Survey of Semiconductor Physics*, vol. II (Van Nostrand Reinhold, New York, 1992)
90. N.S. Xu, Y. Tzeng, R.V. Latham, Similarities in the cold electron-emission characteristics of diamond-coated molybdenum electrodes and polished bulk graphite surfaces. *J. Phys. D-Appl. Phys.* **26**(10), 1776–1780 (1993)
91. L.K. Pan, H.B. Li, Z. Sun, C.Q. Sun, Surface metalization on the photo-emission, photo-absorption and core-level shift of nanosolid silicon. *Surf. Rev. Lett.* **16**(2), 265–270 (2009)
92. P. Hartman, Non-uniform distribution of faces in a zone. *Z. Kristall.* **121**(1), 78–80 (1965)

93. F.K. de Theije, E. van Veenendaal, W.J.P. van Enkevort, E. Vlieg, Oxidative etching of cleaved synthetic diamond 111 surfaces. *Surf. Sci.* **492**(1–2), 91–105 (2001)
94. C.Q. Sun, H. Xie, W. Zhang, H. Ye, P. Hing, Preferential oxidation of diamond {111}. *J. Phys. D-Appl. Phys.* **33**(17), 2196–2199 (2000)
95. Y.K. Kim, K.Y. Lee, J.Y. Lee, Texture-controlled diamond films synthesized by microwave plasma-enhanced chemical vapour deposition. *Thin Solid Films* **272**(1), 64–70 (1996)
96. H.T. Ye, C.Q. Sun, H.T. Huang, P. Hing, Dielectric transition of nanostructured diamond films. *Appl. Phys. Lett.* **78**(13), 1826–1828 (2001)
97. C.Q. Sun, The sp hybrid bonding of C, N and O to the fcc(001) surface of nickel and rhodium. *Surf. Rev. Lett.* **7**(3), 347–363 (2000)
98. C.Q. Sun, Y.Q. Fu, B.B. Yan, J.H. Hsieh, S.P. Lau, X.W. Sun, B.K. Tay, Improving diamond-metal adhesion with graded TiCN interlayers. *J. Appl. Phys.* **91**(4), 2051–2054 (2002)
99. Y.Q. Fu, C.Q. Sun, H.J. Du, B.B. Yan, Crystalline carbonitride forms harder than the hexagonal Si-carbonitride crystallite. *J. Phys. D-Appl. Phys.* **34**(9), 1430–1435 (2001)
100. Y.Q. Fu, C.Q. Sun, H.J. Du, B.B. Yan, From diamond to crystalline silicon carbonitride: effect of introduction of nitrogen in CH₄/H₂ gas mixture using MW-PECVD. *Surf. Coat. Technol.* **160**(2–3), 165–172 (2002)
101. D.H. Lu, M. Yi, S.K. Mo, A.S. Erickson, J. Analytis, J.H. Chu, D.J. Singh, Z. Hussain, T.H. Geballe, I.R. Fisher, Z.X. Shen, Electronic structure of the iron-based superconductor LaOFeP. *Nature* **455**(7209), 81–84 (2008)
102. C.Q. Sun, Dominance of broken bonds and nonbonding electrons at the nanoscale. *Nanoscale* **2**(10), 1930–1961 (2010)
103. I. Novak, B. Kovac, L. Klasinc, V.A. Ostrovski, Nitrogen lone pair interactions in organic molecules: a photoelectron spectroscopic study. *Spectroc. Acta Pt. A-Molec. Biomolec. Spectr.* **59**(8), 1725–1731 (2003)

Chapter 9

Concluding Remarks

- *Achieved consistent insight into the 3B dynamics and quantitative information of surfaces with chemisorbed C, N, O, and C₂H₂.*
- *Essential events in surface adsorption include bond contraction and sp-orbit hybridization. Bond and non-bond formation result in all the observations.*
- *The 3B approach enhances the capabilities of existing experimental techniques to reveal the 3B and electronic dynamics comprehensively.*
- *Developed knowledge has enabled materials and processes design for practical applications.*

9.1 General Understanding

9.1.1 Essential Events on a Surface

The nature, order, length, and energy of the chemical bond determine the properties of a substance. The formation, dissociation, relaxation, and vibration of the bond and non-bond, and the associated dynamics of electron densification, localization, entrapment, and polarization are the key of tuning the property change. The underlying mechanism and the consequences of the surface events are useful in practice:

- A chemical bond contracts on a surface or at sites surrounding defects where the atomic CN reduces. An extension of the concept of ‘atomic size shrinks with its CN reduction,’ initiated by Goldschmidt and Pauling, to solid surfaces results in the BOLS correlation mechanism, which dictates the tunable properties of a nanosolid of which the portion of surface atoms increases with reducing particle size.
- A surface consisting up to three atomic layers forms the high density, elastic, and chemically and thermally active skin phase. The BOLS correlation modifies both the cohesive energy of an atom on a surface and the binding energy density

in the relaxed surface region. The BOLS correlation makes impact on the fields of nanometric materials and surface science.

- C, N, and O atoms hybridize their sp orbitals upon reacting with atoms disregarding the structure phases to form the CH_4 , NH_3 , and H_2O -like tetrahedron structures. The reaction not only causes bond and non-bond reformation but also modifies the valence band and the surface potential barrier with generation of lone-pair non-bonding, electron-hole pair, H-like bonding, and dipole antibonding.
- The combination of BOLS and 3B mechanisms form comprehensive sources that determine the unusual behavior of a surface. Bond contraction perturbs the Hamiltonian that defines the entire band structure and the related properties of a solid; chemical reaction causes a repopulation of valence electrons in the valence band and modifies the binding energy. Chemical reaction changes the bond nature while the coordination reduction changes the bond length and energy. All the physical properties should be derivatives of the Hamiltonian of the system or the DOS distribution in the valence band of the solid.

9.1.2 Bond Nature and Bond-Forming Kinetics

Surface chemisorption is a kinetic process in which O^{-1} forms first and then the O^{-2} follows with sp -orbital hybridization and, H-like bond formation, if necessary. An oxide tetrahedron forms intrinsically, which is independent of the bonding environment or the nature of the host element. A host atom may donate more than one electron to different oxygen atoms while one oxygen atom can never catch more than one electron from a specific host atom because of the directional specificity of the hybridized orbits. The sp orbits of an oxygen atom cannot hybridize until its two bonding orbitals are fully occupied. The two bonding orbits can be occupied by sharing electrons with atoms of a metal or a non-metal, or even by dragging the electron cloud of dipoles, thereby, being able to stabilize the primary M_2O tetrahedron. The production of the non-bonding lone pairs and the induced dipoles are also intrinsic, and they are independent of the environment or the nature of the bonding constituents.

One oxide surface may contain atoms with different valences: O^{-1} , O^{-2} , M^+ , M^{+2} , M^p , M^{+p} , and M^{vac} . An oxide system is composed of various chemical bonds: the ionic or polar-covalent bond between the oxygen and the host atom, the non-bonding lone pair of oxygen, antibonding host dipoles, host ions, and the H-like bond. Covalent bond and antibond can never form between the adsorbate and the host substrate atom due to the huge difference in electronegativity between them [1]. These often overlooked bonding events and the corresponding atomic valences play crucial roles in the process of reaction and in determining the properties of a chemisorbed system.

An oxide tetrahedron forms in the following discrete stages:

1. An ionic or polar-covalent bond forms and contracts first. The ions polarize their surrounding atoms.
2. The second contraction bond follows.
3. The *sp* orbitals of oxygen hybridize with the production of non-bonding lone pairs.
4. Interaction develops between the adsorbate and the antibonding dipoles through lone pairs.
5. At high oxygen coverage, H-like bond forms annihilating the electron cloud of the dipoles to the bonding orbits of the oxygen adsorbate.

The bonding process is reversible by heating or by bombardment of energetic particles. Bond switching is responsible for the oxygen-attacked rusting of bulk metals and for oxygen floating in the process of epitaxial growth of metal on oxygen pre-covered metals. Oxide tetrahedron formation causes atomic dislocation, phase formation and transition, and charge and mass transportation.

The dynamics of *sp*-orbit hybridization applies to the reaction of carbon and nitrogen with a Ni(001) surface. Patterns of geometrical reconstruction and surface morphology for the O–Rh(001) and the (C, N)–Ni(001) surfaces are the same, the valences of surface atoms, the bond stress, and the driving forces for these surfaces are different. This is simply due to the variation in the adsorbate valences. A ‘rhombi-chain’ model or a $c(4\sqrt{2} \times 4\sqrt{2})R45-16O^{-2}$ (N^{-3} , C^{-4}) phase structure could describe these ‘p4g’ reconstructions well.

9.1.3 Orientation Specificity of the Tetrahedron

Formation of the oxide tetrahedron and its kinetics is common while the adsorbate-site selectivity, the order of the ionic bonds formation, and the orientation of the oxide tetrahedron vary with the bonding environment. Except for the initial stage of oxidation, the oxygen adsorbate prefers a position inside a tetrahedron. However, the scale and geometry of the lattice, and the electronegativity of the host determine the bond formation order and the site-and-orientation specificity of the tetrahedron.

- Oxygen prefers the next-nearest-neighboring C_{4v} hollow site of the fcc(001) surface. However, the orders of the ionic bond formation on the Cu(001) and (Rh, V, Ag)(001) surfaces are opposite owing to their different atomic sizes and their values of electronegativity. Different patterns of reconstruction of the O–Rh(001) and the O–Cu(001) surfaces arise from nothing more than the minor difference in their atomic radius [$1.342(\text{Rh}) - 1.277(\text{Cu}) = 0.065 \text{ \AA}$] and electronegativity [$2.2(\text{Rh}) - 1.9(\text{Cu}) = 0.3$]. Due to the small size of hollow [$d = 2R(\sqrt{2} - 1) = 1.058 \text{ \AA}$] and the low electronegativity of the Cu(001) surface, the oxygen [$d = 1.32 \text{ \AA}$] bond to one Cu on the surface first, and then

to another Cu underneath. However, with a wider hollow [1.112 Å] and the higher electronegativity of the Rh(001) surface than that of the Cu(001) surface, oxygen is able to sink into the hollow and form the first bond to the Rh atom underneath.

- The inverse orders of ionic bond formation generate entirely different patterns of reconstruction and morphology, as well as the different surface atomic valences and phase structures on the fcc(001) surface of Cu, Rh, V, and Ag. Adsorption of oxygen to the Rh(001) surface creates the Rh₅O radial pyramid and then the Rh₄O tetrahedron that gives the ‘p4g’ clockwise reconstruction and the ‘rhombi-chain’ fashion. Oxygen reaction with the Cu(001) surface gives rise to the off-centered pyramid and then the missing row structure in which the pairing ‘Cu^P:O⁻²:Cu^P’ strings form. The pairing Cu^P-Cu^P crosses over the missing-row vacancy. Alternation of the valence of oxygen from O⁻¹ to O⁻² gives rise to the off-centered CuO₂ pairing pyramid into the Cu₃O₂ pairing tetrahedron on the Cu(001) surface. The analysis also applies to the phase transition of O-V(001) and O-Ag(001) surfaces.
- The fcc(110) surface of Cu, Ni, Ag, and Pt fits the oxide tetrahedron ideally by locating the adsorbate at the long-bridge hollow site with ‘missing-row’ production. However, the slightly opened fcc(110) surfaces of Rh and Pd allow the oxygen to locate at the fcc(111) facet site in a zigzag fashion along the close-packed direction without atom missing. The former produces the alternative rows of metal vacancies and the single ‘M^P:O⁻²:M^P’ string. The latter forms the M₅O, M₄O, and M₃O structures in the sequential phases with production of, respectively. The observable differences on these fcc(110) surfaces resulting from nothing more than the difference in the atomic size and electronegativity.
- The slight geometrical difference between the (Rh, Pd)-fcc(110) surface and the (Co, Ru)-hcp(10 $\bar{1}$ 0) surface allows the oxygen adsorbates to prefer the troughs in different ways. Oxygen adsorbate prefers the fcc(111) trough located beside a certain close-packed metal row on the fcc(110) surface. In contrast, the adsorbate locates in the same fcc(111) facet trough but at site between two neighboring metal rows on the hcp(10 $\bar{1}$ 0) surface. Such a difference in the adsorbate’s site-specificity generates entirely different patterns in STM observations. The zigzagged dipole row is seen at the (Rh, Pd)(110) surface but the grouped octopoles appear at the (Ru, Co)(10 $\bar{1}$ 0) surfaces at 0.5 ML oxygen coverage.
- Oxygen prefers the hcp(0001) hollow site on both the (Rh, Al)(111) surfaces and the Ru(0001) surface. Although the basic tetrahedron remains during the course of reaction, the electronic configurations of the constituent atoms alternate in the process of oxidation. Electron transportation leads to the ‘C_{3v}-radial’ and then the ‘pairing-row’ type reconstruction and, finally, H-like bonds domination at the surface. In comparison, oxidation of the Cu(111) and the Pd(111) [2] surfaces gives rather complicated patterns of reconstruction.
- At the O⁻¹-induced precursor phases, O⁻¹ forms one bond to a host atom nearby and polarizes its surroundings. The O⁻¹-induced dipoles interact with the O⁻¹

adsorbate through the electrostatic $O^{-1} \cdot M^P$ Coulomb interaction that is rather weak as revealed with EELS from the O–Ru and O–Rh surfaces at the initial stages of oxidation. Oxygen tends to form the first bond with an atom on the transition metal surface such as the Cu(001) and Co($10\bar{1}$, 0) surfaces because of the low electronegativity (<2.0) and short atomic radius ($<1.3 \text{ \AA}$). The O^{-1} – O^{-1} dimer rests atop Co atoms forming the ‘II’-shaped Co_2O_2 bond with two Co atoms on the Co($10\bar{1}$, 0) surface because of the dimension of the C_{2v} hollow of Co($10\bar{1}$, 0) (dimension of $2.50 \times 4.06 \text{ \AA}^2$). The O^{-1} locates $\leq 0.4 \text{ \AA}$ eccentrically ($\sim 0.18 \text{ \AA}$) above the Cu(001) hollow ($2.55 \times 3.61 \text{ \AA}^2$) and forms the CuO_2 off-centered pyramid on the surface. In contrast, oxygen sinks into the hollow site and bonds firstly to the noble metal (Ag, Rh, Pd, and Ru) atom underneath. Therefore, it is safe to say that O^{-1} prefers the on-surface position of a transition metal and then the O^{-2} buckles in, and that the O^{-1} and the O^{-2} locate at a sub-surface position underneath the surfaces of noble metals throughout the course of reaction.

- In the O^{-2} valence situations, the *sp*-orbital hybridization allows the O^{-2} to seek four suitable neighbors to form a stable quasi-tetrahedron. Oxygen prefers the nearly central position of the tetrahedron rather than any other alternatives. Therefore, difference in the bonding environment determines the orientation of the tetrahedron of which the lone pairs tend to point into the open end of the surface. The Cu(001) surface supports the pairing Cu_3O_2 tetrahedron, while the (Cu, Ni, Ag, Pt)(110) surface supports the primary Cu_2O tetrahedron. The Rh(001) surface supports the single Rh_2O tetrahedron with rotation, which forms the rhombi chain along the $\langle 11 \rangle$ direction. The O–Cu(001) surface differs only from the O–Cu(110) surface in that the O–Cu–O chain rotates itself by $\pm 45^\circ$ to fit the crystal $\langle 110 \rangle$ orientation. The V(001) surface allows the ‘radial’ and then the short ordered ($\sqrt{2} \times 3\sqrt{2}$) $R45^\circ$ – $4O^{-2}$ reconstruction. Oxygen reaction with Ag(001) surface forms the same structure phase to that of Cu(001) but in opposite order. The missing row-type Ag_3O_2 structure is more stable at low temperature while the ‘radial’ $Ag_5O(O^{-1})$ is stable at room temperature and above.
- Oxygen can penetrate into the bulk or float back to the surface subjecting to external conditions, such as heating and changing constituent concentration, through bond switching. Oxide tetrahedron formation shows strong geometric selectivity on the surfaces of the hardest material, diamond, and the diamond (111) plane is preferable throughout the course of reaction. The eroding of the weakly bound dipoles is responsible for the rusting of a substance.

9.1.4 Consequences of Bond Forming

The external conditions determine the site-and-orientation specificity of the basic oxide tetrahedron, which generate versatile patterns of observation. The main identities of oxide surfaces are the following:

- $O^{-2}:M^P:O^{-2}$ protruding chains form at most of the surfaces. All $O^{-2}:M^P:O^{-2}$ chains are zigzagged by the lone-pair non-bonding states rather than by any other kinds of chemical bonds. The dipoles do not belong to the M_2O tetrahedron bonding, as these dipoles exchange no electrons with the O^{-2} . Those ions belonging to the M_2O molecule are perpendicularly connected to the chain and they cannot be detected using STM imaging because of the reduced size and lowered energy levels of occupancy.
- The missing-row forms on a limited number of surfaces due to oxygen chemisorption. The missing atoms on the $O-(Cu, Ag)(001)$ surface and the $O-(Cu, Ni, Ag, Pt)(110)$ surfaces are isolated during bond formation as the metallic neighbors of the missing-row atoms have combined with oxygen adsorbates. These 'extra' atoms for tetrahedron formation are readily squeezed away from their regular positions by a small disturbance such as being dragged out by the two neighboring O^{-1} at the initial stage of $Cu(001)$ surface reaction.
- H-like bond formation is, however, more general than the missing row on the surfaces. The process of H-like bond formation compensates for the lack of an atom for the tetrahedron formation, in which the adsorbate drags the electron cloud of the dipoles to its bonding orbits. This process sharpens the 'tip' of the 'honeycomb' protrusions such as in the $(Co, Ru)(10\bar{1}0)-c(2 \times 4)-4O^{-2}$ phase. There are no atoms to be missing. Importantly, the H-like bond lowers the STM protrusions and stabilizes the system by reducing the dipole moment on the surface, as do the phases of $(Co, Ru)(10\bar{1}0)-(2 \times 1)p2mg-2O^{-2}$, $(Rh, Pd)(110)-(2 \times 1)p2mg-2O^{-2}$, and $Ru(0001)-(1 \times 1)-O^{-2}$. Except for those phases induced by O^{-1} and indicated by 'missing row' in Table 3.1, all the phases contain the H-like bonds. At increased oxygen coverage, the H-like bonds interlock all the surface atoms. Such bond interlocking prevents the top layer from diffusing of guest atom into the bulk, which acts as a barrier that should be of use in anticorrosion.
- Because of oxygen penetrating into the top layer for tetrahedron formation, the first interlayer spacing expands. The production of metal ions in the second layer strengthens the interaction between the ionic second layer and the third metallic layer. Therefore, the spacing between the second and third atomic layer often contracts.

9.1.5 Driving Forces Behind Reconstruction

It is known that the binding energy is about -1.0 eV for a metallic bond and about -3.0 for an ionic bond. The energies for the H-like bond and the non-bonding lone pair are around -0.05 to -0.10 eV. Disregarding the minor energies for the weak bound states, the transition of metallic bond to the contracted ionic bond is associated with a gain in energy:

$$\Delta E = 3.0/(1 - Q) - (1.0) = (2 + Q)/(1 - Q) < 2.0 \text{ (eV/bond)}.$$

The net gain in energy provides forces that drive reconstruction, though the orbit hybridization and the antibonding formation consume some amount of energy. Analysis of the Rh(001)-O⁻² clock reconstruction indicates that the driving force for the atomic dislocation also comes from other sources such as the alternative electrostatic repulsion and attraction along the ⟨11⟩ rhombi chain, and a response of bond tension that stabilizes the clock rotation.

9.1.6 Factors Controlling Bond Formation

The *sp* orbitals of an oxygen atom hybridize intrinsically at the full occupancy of the bonding orbitals. Formation of an oxide tetrahedron is independent of the nature of the host element and the geometrical environment. However, external factors determine the site-and-orientation of the oxide tetrahedron and the formation order of the ionic bonds of the tetrahedron. The extrinsic dominating factors are:

1. Difference in electronegativity between the bond constituents
2. Lattice geometrical orientation and the scale of lattice constant of the host
3. Valences of the oxygen adsorbate
4. Substrate temperature and oxygen exposure as well as aging conditions.

Only the last condition is controllable. The valences of oxygen can be changed by varying oxygen exposure or by annealing the sample at a certain temperature. The multi-phase ordering on the metal surfaces results from the variation in the oxygen valence under various bonding circumstances.

9.2 Capability Enhancement of Probing Techniques

Developed knowledge has enhanced the capabilities of the following techniques in terms of probing atomic valence, bond geometry, valence DOS, bond strength, and bond-forming kinetics.

9.2.1 STM and STS

- The 3B premise enables the STM and STS to probe individual atomic valence, which assists formulation of the reaction kinetics. Electron clouds of metal dipoles, induced by either the O⁻¹ or the non-bonding lone pairs of the O⁻², dominate the STM protrusions; ions of guest or oxygen (M⁺, O⁻¹ or O⁻²) or vacancies of missing atoms produce STM depressions. Even though it locates

well above the surface atomic plane, the oxygen adsorbate is still not detectable by an STM because the occupied energy states of the oxygen are still lower than the E_F of the metal hosts, albeit the enlarged adsorbate. The M^+ is undetectable because of both the reduced atomic size and the lowered energy states of occupancy.

- The various shapes of STM protrusions represent the configuration of dipoles. For example, (1) a single dipole forms on the Cu(110)-O⁻² surface; (2) an engaged-cogwheel and paired dipoles (quadruple) grow on the Cu(001)-O⁻¹ surface; and, (3) the grouped dipoles (octupole) form a congested array on the (Co, Ru)(10 $\bar{1}$ 0)-c(2 × 4)-4O⁻² and the V(001)-($\sqrt{2} \times 3\sqrt{2}$)R45°-4O⁻² surfaces.
- The unique STS profiles covering energies of $E_F \pm 2.5$ eV from the O-Cu(110) surface give the on-site DOS information about the lone pairs ($<E_F$) and antibonding dipoles ($>E_F$). The STS features from O-Nb(110) show the resonant features due to the surface-image potential, which is in accordance with observations using the inverse PES.

9.2.2 PES, TDS, EELS, and VLEED

Spectral identities of STS, PES, TDS, EELS, and VLEED correspond to individual processes of bond formation or their consequences on the energetic behavior of valence electrons. Oxygen-induced phase ordering and structure patterning vary indeed from situation to situation. However, formation of the primary tetrahedron, the DOS features, and the bond-forming kinetics are naturally common for all the analyzed representatives.

- The four valence DOS features in a PES correspond to the oxygen-host bonding (~ -5 eV), non-bonding lone-pairs of oxygen (~ -2 eV), electron holes of the host ($\leq E_F$), and the antibonding host dipoles ($\geq E_F$), rather than simply the addition of the 2s or 2p states of the isolated oxygen to the valence DOS of the host.
- The change of work function corresponds to the bandwidth of the antibonding dipole states, which provides information about the dipole formation and H-like bond formation. Dipole formation widens the bandwidth of the antibonding states and reduces the work function; H-like bond formation narrows the antibonding sub-band and restores the work function, which stabilizes the entire system. The reduced work function could be of use in the cold-cathode electron emission but the H-like bond formation effects adversely.
- TDS provides information about the activation energy for individual bond breaking. The oscillation of the TDS signatures of the O-Rh and O-Pd surfaces corresponds to the sequential events of bonding, non-bonding, and the H-like bonding contribution.
- The energy increase of the dipole-stretch mode in EELS relates directly to the strength of non-bonding interaction that varies from the O⁻¹·M^p electrostatic to

the $O^{-2}:M^P$ lone pair and to the $O^{-2}:M^{P+}$ H-bond-like contribution. The vibration energy increases accordingly, in the range of 50–80 meV.

- Raman spectroscopy gives information at low frequencies about the non-bonding lone-pair interaction, being similar to that revealed by EELS. As the weaker part of a hydrogen bond, the lone-pair interaction exists in oxides, nitrides, and bio-molecules such as protein and DNA chains.
- LEED at very low energy (<16 eV) provides a unique means that collects nondestructive information from the top atomic layer and covers the valence band in energy. VLEED gives simultaneous information about the surface morphology, lattice geometry, and valence DOS, though sophisticated decoding and a proper model are required.

9.3 Advancement in Applications

The 3B and BOLS premises led to a systematic understanding of the effects of chemical bond formation and the physical relaxation on the performance of substance, which enables the process design for strengthening diamond–metal adhesion, functional materials for photo and electron emission, photonic crystal with tunable optical bandgap, etc.

9.4 Recommendations

This part has thus far discussed with evidence and suggestions of potential applications, the significance of the non-bonding lone-electron pairs and the lone-pair-induced dipoles associated with the process of tetrahedron bond formation of C, N, O, and F and the undercoordination-induced quantum entrapment of the core and bonding electrons and lone-electron polarization. The impact of these often overlooked interactions and the associated energy states in the midgap region is enormous in particular at the nanoscale. These weak interactions and charge can never be neglected when one attend to substances with adsorption. These weak interactions and non-bonding electrons also form basic function groups in the biologic, organic, and inorganic species. Table 9.1 features the classification, origins, functions and possible applications of the bonds and non-bonds.

Utilizing the concepts of these unconventional types of weak interactions and their energetics, one can look forward to designing and synthesizing new functional materials. The approach of studying the formation, dissociation, relaxation, and vibration of bonds and non-bonds, and associated energetics and dynamics of electron transportation, polarization, localization, and densification effects on a microscopic level is essential to facilitating a deeper understanding of the macroscopic behavior of functional materials. Finding and grasping with factors controlling the non-bonding states and making them of use in functional materials

Table 9.1 Origin, functionality, and possible applications of broken bonds and non-bonding electrons

| Bond and DOS | Origin | Functions and applications |
|---|--|---|
| Regular bonds ($\ll E_F$) | Strong interaction, charge sharing | Hamiltonian; atomic cohesive energy; band structure; dispersion; allowed DOS in valence band and below; mainly bulk properties |
| Electronic hole ($< E_F$) | Charge transition in reaction, positive ions | Compound band gap formation; semiconductor band gap expansion; photon emission and absorption, photonic sensor |
| Antibonding dipole ($> E_F$) | Induced by lone-pair polarization or undercoordination-induced local core-charge densification | Impurity states generation; work function reduction; surface dipole-layer formation; surface energy density gain; electron cold-field emission; super-hydrophobicity; defect magnetism, etc. |
| Non-bonding lone pair ($< E_F$) | N, O and F <i>sp</i> -orbital hybridization | Polarizing, functional groups in organic and biological molecules, impurity states generation; hardness and elastic modulation; quantum friction; Infrared activity; magnetic modulation; drug design; density anomalies of ice, NTE, 4S; etc. |
| H-like and C–H-like bonds | Bond formation between dipole and electronegative elemental atoms | Dipole-state annihilation; work function recovery, impurity states annihilation; Surface stabilization; surface passivation; antioxidation |
| Non-bonding lone electron ($\sim E_F$) | Defect, <i>sp</i> ² -hybridization in C, half-filled s-orbit of noble metals | Midgap defect states; Dirac resonance; defect magnetism; end and edge states; 4S; Graphite electrical conductivity; catalytic enhancement, etc. |
| Broken bonds | Undercoordination | Modulation of bulk properties; structure relaxation; Hamiltonian, cohesive energy, electro-affinity modulation; Local densification of charge, energy and mass; Lone-electron polarization; size dependency of all bulk detectable properties; Bandgap opening; etc. |

design will form, in the near future, a subject area of ‘Non-bonding Electronics and Energetics,’ which would be even more challenging, fascinating, promising, and rewarding than dealing with the core or valence electrons alone.

The 3B-forming dynamics is probably the only wise that could generalize various observations of chemisorption occurring on different surfaces. Further efforts toward bond and electronic engineering would be even more encouraging and rewarding.

- In crystallographic studies of chemisorbed surfaces, it might not be essential to locate precisely the static positions of the host atoms on a surface since the reaction is a kinetic process in which charge transportation dominates and all the involved atoms move collectively and continually. Identifying the nature, the dynamics and kinetics of bond formation, and their consequences on observations and practical applications should be a foremost concern in practice. The bond angle and bond length are retractable depending on surface coordinates and the bonding environment. During the reaction, all atoms change their sizes and valences, and hence, the hard-sphere models limit advancement of knowledge. In fact, a tiny variation in oxygen positions in the O–Cu(110) surface gives an entirely different physical picture. Therefore, in decoding the diffraction data, it would be necessary to replace the traditional trial–error wisdom of individual displacement of the hard spheres with variation of bond geometry and atomic valence states.
- Due to the correlation among the parameters, the number of numerical solutions may not be unique and physical constraints are necessary. It would be more realistic in theoretical approaches to consider the actual occupancy of the hybridized orbits by the lone pairs and antibonding dipoles, in particular. The interatomic potential for the $O^{-2}:M^P$ (lone pair) differs from that for the $O^{-2}-M^+$ (ionic bond). Such modifications improve the outcome of calculations such as minimizing the system total energy. Bond contraction is also an intrinsic process on the surface and a bond-switching mechanism would be necessary. Exercises in terms of rigid sphere trapped in the potential well at the surface without breaking the barrier are inadequate in chemisorption studies. The shortened bond lengths of CO, NO, and NH_3 molecules (by up to 0.79 Å) on a Ni(001) and a NiO(001) indicate true bond formation, instead of simply electrostatic interaction [3].
- Chemisorption is a dynamics process in which charge transportation dominates. Atomic dislocation is only one of the numerous consequences of bond formation. Therefore, it is necessary to examine the system by all the effective means, and their correlation in terms of crystallography, morphology, desorption, and electronic spectroscopy to avoid misinterpreting the observations.
- The *sp*-orbital hybridization may extend to reactions involving other electronegative elements. Interestingly, based on DFT pseudo-potential and tight-binding theoretical calculations, Lefebvre et al. [4] pointed out that the electronic structures of the tin monochalcogenide (SnX , $X = O, S, Se, \text{ or } Te$) family possesses similar DOS features that are consistent with the presence of a lone pair. This observation indicates the essentiality of *sp*-orbital hybridizations for other electronegative additives. The weak non-bonding interaction, such as the lone pair and the H-like bond, plays critical, yet often overlooked, role in bioelectronics such as the folding, signaling, and regulating of protein and DNA chains as well as cell binding. The non-bonding weak interaction and the dipole formation also contribute to the mechanism for medicine-cell interaction, such as messaging and regulation of NO.

- Furnished with the BOLS and 3B correlations, the knowledge about the mentioned bonding events and the factors controlling bond switching, one would be able to develop methods for controllable bond making and breaking toward designing materials with anticipated functions in the near future. Progress made in practical applications indicates that the ways of analyzing and activities of approaching are in correct and efficient tracks, which should bring along new findings. Further efforts, I am sure, toward materials design based on the BOLS and 3B correlations would be even more challenging, fascinating, promising, and rewarding.

References

1. J.M.D. Coey, H. Sun, Improved magnetic-properties by treatment of iron-based rare-earth intermetallic compounds in ammonia. *J. Magn. Magn. Mater.* **87**(3), L251–L254 (1990)
2. E. Lundgren, G. Kresse, C. Klein, M. Borg, J.N. Andersen, M. De Santis, Y. Gauthier, C. Konvicka, M. Schmid, P. Varga, Two-dimensional oxide on Pd(111). *Phys. Rev. Lett.* **88**(24), 246103 (2002)
3. J.T. Hoefl, M. Kittel, M. Polcik, S. Bao, R.L. Toomes, J.H. Kang, D.P. Woodruff, M. Pascal, C.L.A. Lamont, Molecular adsorption bond lengths at metal oxide surfaces: failure of current theoretical methods. *Phys. Rev. Lett.* **87**(8), 086101 (2001)
4. I. Lefebvre, M.A. Szymanski, J. Olivier-Fourcade, and J.C. Jumas, Electronic structure of tin monochalcogenides from SnO to SnTe. *Phys. Rev. B.* **58**(4), 1896–1906 (1998)

Part I

O, N, and C Chemisorption

A.1 Highlights

- O, N, and C prefer tetrahedron geometry upon chemisorbing to a solid skin evolving its valence from one to the highest valence n with production of the $n-4$ electron lone pairs.
- Chemisorption involves at least the outermost two atomic layers with the adsorbate sitting in between in most cases.
- Chemisorption roughens the surface potential barrier and morphology by formation of ions, dipoles, and missing vacancies.
- Chemisorption results in generally four valence states representing the bonding electron pairs, nonbonding lone pairs, empty holes, and antibonding dipoles.
- Solid skin forms a strained phase that is elastic but chemically and thermally less stable
- Patterns of relaxation and reconstruction may change from situation to situation, the nature of the bonds and the attributes of the valence states are common.
- STSM/S, LEED, PES, EELS, Raman, and TDS provide comprehensive information regarding the formation, relaxation, and vibration of the bonds and nonbonds and the associated charge entrapment and polarization.
- Oxidation proceeds in four discrete stages of O^{1-} , O^{2-} , sp-orbit hybridization, and structural relaxation.
- Factors dominating the bond making and breaking are the electronegativity, crystal geometry, pressure, and temperature of operation.

Part II

Size Matter

Abstract Atomic undercoordination shortens and stiffens the remnant bonds to yield local quantum entrapment, densification, and polarization, which discriminate defects, skins, and nanostructures from the bulk, particularly in the size dependence and size-induced emergence behavior.

Part II deals with atomic undercoordination-induced bond relaxation and nonbonding electron polarization. Relaxation of bonds between undercoordinated atoms results in bond strength gain and strong localization-entrapment, densification, and polarization, which modifies the Hamiltonian, atomic cohesive energy, local binding energy density, work function, and electroaffinity. These fundamental attributes unify the unusual performance of adatoms, defects, surfaces, and size dependency of nanostructures, including mechanical strength, thermal stability, acoustic, photonic, electronic, magnetic, and dielectric properties. Such skin effect plays the core role in dictating the size dependency of nanostructures, whereas atoms in the core interior remain as they are in the bulk. The polarization of nonbonding electrons takes the responsibility for the emerging properties that the bulk does never show. The emerging properties include the conductor-insulator transition, catalytic conversion and enhancement, nanoplasmonics, dilute magnetism, and the superhydrophobicity, superlubricity, superfluidity, and super-solidity at nanosized contacts.

Chapter 10

Introduction

- *Defects, surfaces, 1D atomic chains, 2D atomic sheets, and nanostructures of various shapes share the same nature of bond order deficiency.*
- *All detectable properties remain no longer bulk constant but change with variation of solid size at the nanoscale.*
- *Properties that bulk materials never show merge at the nanoscale such as conductor-insulator transition, dilute magnetism, Dirac-Fermi polarons, catalytic conversion and enhancement, superhydrophobicity, superfluidity, superlubricity, and supersolidity.*
- *Clarification, correlation, formulation, and quantification of the size dependency of the known bulk properties and the emerging properties at the nanoscale form the focus of this part.*
- *Bond and nonbond formation, dissociation, relaxation and vibration and the associated energetics and dynamics of electron densification, localization, polarization and transportation should be the factors of dominance.*

10.1 Scope

Part II starts in this chapter with a brief overview on the intriguing behavior of a nanometer-sized solid. [Chapter 11](#) introduces the atomic coordination number (CN) and atomic radius (bond-order-length, BOL) correlation premise of Pauling [1] and Goldschmidt [2]. Extending the BOL to include the bond energy and electron relaxation leads to the bond-order-length-strength (BOLS) correlation for the unusual performance of the undercoordinated atoms. This section also introduces the non-bonding electron polarization (NEP) [3] by the densely entrapped bonding and core electrons. The NEP at site with even lower atomic CN than that of a flat surface is responsible for the emerging properties such as the catalytic ability enhancement of noble metals, dilute magnetism, conductor-insulator transition, etc. A combination of the core-shell configuration of nanostructures and the local band average (LBA) approach yields a general scaling relationship for the

shape and size dependence of a nanosolid. Chapters 12–20 implement the BOLS to formulate and quantify the physical properties of nanostructures in terms of bond strength, atomic cohesive energy, electroaffinity, and energy in the region of surface skin. Chapter 21 features the progress with prospects on extensions of the knowledge.

10.2 Overview: Size Fascinations

Nanosolids, or so-called nanoparticles, nanoclusters, nanocrystallites, nanograins, etc., are defined as substance or device that is in the shape of a spherical dot, a cylindrical rod, a thin plate, or a void of any irregular shape smaller than 10^2 nm across or substances consisting of such voids or grains that are weakly interconnected [4]. Monatomic chains and monolayer atomic sheets are ideal cases of the one- and the two-dimensional systems at the nanoscale. The substance of a nanosolid can be composites, compounds, alloys, or element media. From a fundamental point of view, nanostructures bridge the gap between an isolated atom and its bulk counterpart with the size dependency of known bulk properties and emerging properties that bulk materials do not have.

The key difference between a solid and its elementally isolated atom is the involvement of interatomic interaction that varies with the coordination number (CN, z) of an atom. Without interatomic interaction, neither a solid nor even a liquid could form. The interatomic interaction causes a solid to be completely different from an isolated atom in performance. Compared with its bulk counterpart, on the other hand, a nanosolid has a high proportion of undercoordinated atoms ($0 < z < 12$) in the surface skin. For a spherical dot of one micrometer across, the volume sum of all surface atoms is only 1 % of the volume of the entire solid. For a 10 nm-sized dot, the surface-to-volume ratio is 25 % and it reaches 100 % when the solid is around one nm across or consists of three atomic shells or less. The atomic CN is two in the atomic chain interior or at the edge of a single-layer graphene. Therefore, interaction between the undercoordinated atoms and the high fraction of such undercoordinated atoms form the key discriminating in nature a nanosolid from an isolated atom or from its bulk parent.

The discovery of nanosolids of various shapes and their assemblies is quite surprising, which has thus generated enormously ever-increasing interest for new knowledge and technological thrusts. Properties of solids determined by their shapes and sizes are indeed fascinating, which laid the basis of the emerging fields of nanoscience and nanotechnology that is the key area of significance in concurrent science, technology, and economics.

Nanoscaled materials are offering a variety of novel features such as the size dependency of known bulk properties and emerging properties that the bulk parent does not have. New physical and chemical properties occur in such systems because of the unusual bonds between the undercoordinated atoms and the associated entrapment or polarization of electrons.

The study of nanocrystalline materials is an active area of research in physics, chemistry, and materials engineering as well as biomedical engineering [5, 6]. The striking significance of miniaturizing a solid to the nanometer scale is the tunability of the measurable quantities of the solid in all aspects. In transport dynamics, quantized and resonant features due to size effect become apparent. In addition to the large surface-to-volume ratios, the surface, interface, and quantum effects take on a significance that is normally inconsequential for bulk materials.

Varieties of physical properties such as mechanical strength, plasticity [7], sintering and alloying ability [8], diffusivity [9], chemical reactivity [10, 11], as well as the mode of crystal growth (self-assembly) are dependent upon particle size. Property tunability also includes thermodynamics (critical temperatures for phase transitions such as liquidation, evaporation, and heat transport), acoustics (optical and acoustic modes of lattice vibration), optics (photoemission and absorption) [12–14], electronics (work function, energy-level positions, electron–phonon coupling, workfunction, electroaffinity) [15, 16], magnetic (magnetization tailoring or enhancement), and dielectric performance. Surfaces passivated by electronegative additives such as C, N, and O, also affect the performance of the nanosolids [17]. Not only the size-dependent phase transition but also the chemical interaction between the core of the nanoparticle and its surfactant molecules are responsible for the observed X-ray absorption fine structure (XAFS) spectral changes [18].

Materials composed of nanosolids possess unusually new features [19–21]. For instances, formation of the surface skin modifies the structural and physical properties, resulting from a breaking of lattice periodicity or forming surface-dangling bonds, giving rise to site-specific surface anisotropy, weakened exchange coupling, and surface spin disorder [22]. The spin–spin coupling at the interface and interaction between the surface and the core magnetic structures give rise to exchange anisotropy [23].

Pt containing a network of nanometer-sized pores could generate reversible strain with amplitudes comparable with those of commercially available actuators through surface-charging effects under potentials of about 1 V [24]. The conversion of an external electrical signal into a volume change, and a mechanical force, known as actuation, is of importance to small-scale devices.

Solid size reduction increases the sinterability of a zeolite crystal at the ambient temperature. On heating nanocrystallites of 40–80 nm at 80 °C, solution-mediated mass transport results in additional substantial crystal growth that occurs at $10^2\text{--}3$ °C for large bulk [8]. A single-walled carbon nanotube (SWCNT) is 2.6 times stiffer than the bulk graphite [25, 26] but it melts at $\sim 1,600$ K [27] being 0.42 times the melting point ($T_m(\infty) = 3,800$ K) of a bulk graphite or a diamond. Atoms in the open edge of an SWCNT coalesce at 1,593 K and, a ~ 280 % extensibility of the CNT occurs at $\sim 2,000$ K. Under the flash of an ordinary camera, the SWCNT burns (fully oxidized) under the ambient conditions [28].

A CdS nanodot of ~ 2.5 nm across melts at 600 K [12], being much lower than the bulk value of 1,675 K. The size-induced T_m suppression is quite common to nanosolids [14, 29].

Grains of semiconductors of a few nanometers across emit blue-shifted light but the larger chunks of the same material do not [30, 31]. The band gap (E_G) of CdSe can be tuned from deep red (1.7 eV) to green (2.4 eV) by simply reducing the solid diameter from 20 to 2 nm [32]. The E_G [33, 34] and the core-level shift (ΔE_V) [35] of nanosemiconductors increase whereas the dielectric susceptibility (χ) decreases when the solid size is reduced. Without triggering the electron–phonon (e–p) interaction or electron–hole (e–h) production, STS/M revealed that at 4 K the E_G expands from 1.1 to 3.5 eV when the diameter of Si nanorod reduces from 7.0 to 1.3 nm associated with some 10 % of Si–Si surface-bond contraction [36].

Size reduction can enhance or tail the magnetic properties of nanocomposites at different temperatures [37]. At low temperatures, the saturation magnetization (M_S) of a small solid is higher than that of the bulk with oscillation features when the solid size is reduced; however, at the ambient temperatures, the trend is the opposite.

Nitriding occurs at a much lower temperature within a shorter period (300 °C for 9 h) for a Fe surface covered with nanoparticles compared with that for a smooth Fe surface where nitriding occur at 500 °C or higher for more than 48 h under an atmospheric pressure of ammonia [38]. Reducing the Au particle size can raise the diffusivity of Ag into Au nanoparticles at the ambient [39]. Decreasing the size of tin oxide particles in the range of 10–35 nm increases its sensitivity to toxic gases [40]. Nanometerization (27 nm) of SrTiO₃ lowers the operation temperature for sensor from 970 to 310 K, close to the temperature of human body [41]. Size reduction not only enhances gas sensitivity of SnO₂ [40] but also the ionicity of Cu₂O nanoparticles [42]. The single atoms accounted for ~ 70 % of the total activity of catalysts containing single atoms, subnanoclusters, and nanoparticles, thus serving as the most important active sites. The Ir single atoms greatly enhance the reducibility of the FeO_x support and generation of oxygen vacancies, leading to the excellent performance of the Ir₁/FeO_x single-atom catalyst [43].

Introducing ferroelectric materials of different sizes into a photonic crystal could modulate its refractive index and the photonic band gap, E_G , which is sensitive not only to the operation temperature or the applied electric field, but also to the particle sizes [44, 45]. Filled up the crystal matrix of SiO₂ with BaTiO₃ and PbLaZrO₃ can modulate the phase-transition point of BaTiO₃ (100–150 °C). The photonic E_G of the resultant assembly is strongly temperature dependent. At the Curie point (T_C), the E_G undergoes a 20 nm redshift, and the E_G shifts to even longer wavelength with the increase of the applied electric field. Both the refractive index and the T_C are tunable by changing the solid size and the applied voltage.

The thermal expansion coefficient, the electric resistivity, and the specific heat of metallic nanosolids or alloys increase inversely with solid size whereas the temperature coefficient of resistivity and the critical temperature for magnetic transition drop inversely with solid size [46]. The emerging freedom of size

changes many physical and chemical properties that are conventionally constant for a bulk [47–56].

The size-induced property change of nanostructures has inspired numerous theoretical models discussed from various perspectives. For instance, the following models describe the size-induced blueshift in the photoluminescence (PL) of semiconductor nanosolids:

1. Quantum confinement theory [57–60] suggests that the Coulomb potential energy and the kinetic energy of excitons (electron–hole pairs) are responsible for the intrinsic E_G expansion, which dictates the PL blueshift observed.
2. The free-exciton collision model [61] proposes that, during the PL measurement, the excitation laser heats the free excitons which then collide with the boundaries of the nanometer-sized fragments. The PL blueshift originates from the activation of hot-phonon-assisted electronic transitions, instead of quantum confinement.
3. The impurity luminescent center model [62] assumes that different impurity centers in the solid take responsibility for the PL blueshift. The densities and types of impurity centers vary with particle size.
4. Surface states and surface alloying mechanisms [63] consider that the extent of surface reaction and measurement temperature determine the PL blueshift and the passivation effect varies with the processing parameters and aging conditions [64].
5. An intercluster interaction and oxidation [65] argument claims the origin for the size-reduction-induced PL blueshift.

Another significant phenomenon is the size dependence of thermal stability. The critical temperature of melting (T_m) of an isolated nanosolid, or a system with weakly linked nanoparticles, generally drops with solid size (called as undercooling). The T_m may rise (called as overheating) for an embedded nanometric system due to the interfacial effect. The T_m was characterized by either the Lindemann criterion [66] of the magnitude abruptness of atomic vibration or Born's criterion [67] of absence of the shear modulus at melting. The following schemes model the nanosolid melting: (1) homogeneous melting and growth [68, 69], (2) liquid shell nucleation [70–73], (3) liquid nucleation and growth [70, 74, 75], (4) random fluctuation melting [76]. The origin for nanosolid melting is ascribed as: (1) lattice-vibrational instability [29, 77–81], (2) liquid-drop formation [82], or (3) surface-phonon instability [83–85].

10.3 Challenge

Overwhelming contributions have been made for the development of nanotechnology by the advent of methods such as atomic imaging and manipulating, nanosolid synthesizing, functioning, and characterizing as well as structural

patterning for device fabrication. However, challenge remains on the physical insight into the nature behind and factors dominating the general trend of the tunability and the emerging of new properties of substance at the nanoscale. It is quite often that there are numerous models for a certain phenomenon, but in fact, all anomalies due to size should results from the same origin of atomic CN reduction.

Predictable design and controllable growth of nanostructured materials or devices are of foremost importance to scientific and technological communities. One needs not only to understand the performance but also to know the origin, the trend, and the limitation of the change and the interdependence of various properties in order to harnessing the performance of materials and devices. Furthermore, structural miniaturization provides one with an additional freedom that not only allows the tunable properties of a solid by changing its shape and size but also challenges one to gain quantitative information by making use of the new freedom of size.

10.4 Objectives

This part aims to present a consistent understanding of the undercoordinated systems such as point defects, adatoms, flat surfaces, and nanostructures of various shapes from the perspective of atomic undercoordination that induces local bond-relaxation and charge quantum entrapment and polarization in terms of the BOLS correlation and the NEP. For simplicity, the dimensionless form of change (%) of a detectable quantity and the dimensionless form of size K (being the number of atoms lined along the radius of a sphere or across the thin film) are used unless indicated otherwise. The dimensionless approach also allows the generality of the formulation and minimizes the contribution from impurities and artifacts in measurement. Attempt is made to minimize and simplify numerical expressions with focus more on physical understanding.

References

1. L. Pauling, Atomic radii and interatomic distances in metals. *J. Am. Chem. Soc.* **69**(3), 542–553 (1947)
2. V.M. Goldschmidt, Crystal structure and chemical correlation. *Ber. Deut. Chem. Ges.* **60**, 1263–1296 (1927)
3. C.Q. Sun, Dominance of broken bonds and nonbonding electrons at the nanoscale. *Nanoscale* **2**(10), 1930–1961 (2010)
4. M.F. Ashby, T.J. Lu, Metal foams: a survey. *Sci. China Ser. B-Chem.* **46**(6), 521–532 (2003)
5. A.S. Edelstein, R.C. Cammarata, *Nanomaterials: Synthesis, Properties and Applications* (Institute of Physics, Bristol, 1996)
6. H. Gleiter, Nanocrystalline materials. *Prog. Mater Sci.* **33**(4), 223–315 (1989)
7. L. Lu, M.L. Sui, K. Lu, Superplastic extensibility of nanocrystalline copper at room temperature. *Science* **287**(5457), 1463–1466 (2000)

8. S. Mintova, N.H. Olson, V. Valtchev, T. Bein, Mechanism of zeolite a nanocrystal growth from colloids at room temperature. *Science* **283**(5404), 958–960 (1999)
9. S. Horch, H.T. Lorenzen, S. Helveg, E. Laegsgaard, I. Stensgaard, K.W. Jacobsen, J.K. Nørskov, F. Besenbacher, Enhancement of surface self-diffusion of platinum atoms by adsorbed hydrogen. *Nature* **398**(6723), 134–136 (1999)
10. O.K. Tan, W. Zhu, Q. Yan, L.B. Kong, Size effect and gas sensing characteristics of nanocrystalline $x\text{SnO}(2)-(1-x)\alpha\text{-Fe}_2\text{O}_3$ ethanol sensors. *Sens. Actuator B-Chem.* **65**(1–3), 361–365 (2000)
11. C.N.R. Rao, G.U. Kulkarni, P.J. Thomas, P.P. Edwards, Size-dependent chemistry: properties of nanocrystals. *Chem.-a Eur. J.* **8**(1), 29–35 (2002)
12. A.N. Goldstein, C.M. Echer, A.P. Alivisatos, Melting in semiconductor nanocrystals. *Science* **256**(5062), 1425–1427 (1992)
13. H.K. Christenson, Confinement effects on freezing and melting. *J. Phys.: Condens. Matter* **13**(11), R95–R133 (2001)
14. Z. Zhang, J.C. Li, Q. Jiang, Modelling for size-dependent and dimension-dependent melting of nanocrystals. *J. Phys. D-Appl. Phys.* **33**(20), 2653–2656 (2000)
15. T. van Buuren, L.N. Dinh, L.L. Chase, W.J. Siekhaus, L.J. Terminello, Changes in the electronic properties of Si nanocrystals as a function of particle size. *Phys. Rev. Lett.* **80**(17), 3803–3806 (1998)
16. A.D. Yoffe, Semiconductor quantum dots and related systems: electronic, optical, luminescence and related properties of low dimensional systems. *Adv. Phys.* **50**(1), 1–208 (2001)
17. C.Q. Sun, H.Q. Gong, P. Hing, H.T. Ye, Behind the quantum confinement and surface passivation of nanoclusters. *Surf. Rev. Lett.* **6**(2), 171–176 (1999)
18. H. Modrow, Tuning nanoparticle properties—the X-ray absorption spectroscopic point of view. *Appl. Spectrosc. Rev.* **39**(2), 183–290 (2004)
19. J.I. Brauman, Clusters. *Science* **271**(5251), 889 (1996)
20. R.F. Service, Semiconductor clusters, nanoparticles, and quantum dots. *Science* **271**, 890 (1996)
21. R.T. Collins, P.M. Fauchet, M.A. Tischler, Porous silicon: from luminescence to LEDs. *Phys. Today* **50**(1), 24–31 (1997)
22. R.H. Kodama, A.E. Berkowitz, E.J. McNiff, S. Foner, Surface spin disorder in NiFe_2O_4 nanoparticles. *Phys. Rev. Lett.* **77**(2), 394–397 (1996)
23. A.E. Berkowitz, K. Takano, Exchange anisotropy: a review. *J. Magn. Magn. Mater.* **200**(1–3), 552–570 (1999)
24. J. Weissmuller, R.N. Viswanath, D. Kramer, P. Zimmer, R. Wurschum, H. Gleiter, Charge-induced reversible strain in a metal. *Science* **300**(5617), 312–315 (2003)
25. E.W. Wong, P.E. Sheehan, C.M. Lieber, Nanobeam mechanics: elasticity, strength, and toughness of nanorods and nanotubes. *Science* **277**(5334), 1971–1975 (1997)
26. Y. Ren, Y.Q. Fu, K. Liao, F. Li, H.M. Cheng, Fatigue failure mechanisms of single-walled carbon nanotube ropes embedded in epoxy. *Appl. Phys. Lett.* **84**(15), 2811–2813 (2004)
27. B. An, S. Fukuyama, K. Yokogawa, M. Yoshimura, Surface superstructure of carbon nanotubes on highly oriented pyrolytic graphite annealed at elevated temperatures. *Jpn. J. Appl. Phys.* **37**(6B), 3809–3811 (1998). Part 1-Regular Papers Short Notes & Review Papers
28. P.M. Ajayan, M. Terrones, A. de la Guardia, V. Huc, N. Grobert, B.Q. Wei, H. Lezec, G. Ramanath, T.W. Ebbesen, Nanotubes in a flash—ignition and reconstruction. *Science* **296**(5568), 705 (2002)
29. F.G. Shi, Size-dependent thermal vibrations and melting in nanocrystals. *J. Mater. Res.* **9**(5), 1307–1313 (1994)
30. G. Allan, C. Delerue, M. Lannoo, E. Martin, Hydrogenic impurity levels, dielectric-constant, and coulomb charging effects in silicon crystallites. *Phys. Rev. B* **52**(16), 11982–11988 (1995)

31. X.S. Chen, J.J. Zhao, G.H. Wang, X.C. Shen, The effect of size distributions of Si nanoclusters on photoluminescence from ensembles of Si nanoclusters. *Phys. Lett. A* **212**(5), 285–289 (1996)
32. A.P. Alivisatos, Semiconductor clusters, nanocrystals, and quantum dots. *Science* **271**(5251), 933–937 (1996)
33. L.K. Pan, C.Q. Sun, B.K. Tay, T.P. Chen, S. Li, Photoluminescence of Si nanosolids near the lower end of the size limit. *J. Phys. Chem. B* **106**(45), 11725–11727 (2002)
34. C.Q. Sun, S. Li, B.K. Tay, T.P. Chen, Upper limit of blue shift in the photoluminescence of CdSe and CdS nanosolids. *Acta Mater.* **50**(18), 4687–4693 (2002)
35. C.Q. Sun, L.K. Pan, Y.Q. Fu, B.K. Tay, S. Li, Size dependence of the 2p-level shift of nanosolid silicon. *J. Phys. Chem. B* **107**(22), 5113–5115 (2003)
36. D.D.D. Ma, C.S. Lee, F.C.K. Au, S.Y. Tong, S.T. Lee, Small-diameter silicon nanowire surfaces. *Science* **299**(5614), 1874–1877 (2003)
37. J. Shi, S. Gider, K. Babcock, D.D. Awschalom, Magnetic clusters in molecular beams, metals, and semiconductors. *Science* **271**(5251), 937–941 (1996)
38. W.P. Tong, N.R. Tao, Z.B. Wang, J. Lu, K. Lu, Nitriding iron at lower temperatures. *Science* **299**(5607), 686–688 (2003)
39. T. Shibata, B.A. Bunker, Z.Y. Zhang, D. Meisel, C.F. Vardeman, J.D. Gezelter, Size-dependent spontaneous alloying of Au-Ag nanoparticles. *J. Am. Chem. Soc.* **124**(40), 11989–11996 (2002)
40. M.K. Kennedy, F.E. Kruijs, H. Fissan, B.R. Mehta, S. Stappert, G. Dumpich, Tailored nanoparticle films from monosized tin oxide nanocrystals: particle synthesis, film formation, and size-dependent gas-sensing properties. *J. Appl. Phys.* **93**(1), 551–560 (2003)
41. Y. Hu, O.K. Tan, W.Q. Cao, W.G. Zhu, Fabrication and characterization of nano-sized SrTiO₃-based oxygen sensor for near room-temperature operation. *IEEE Sens. J.* **5**(5), 825–832 (2005)
42. B. Balamurugan, B.R. Mehta, S.M. Shivaprasad, Surface-modified CuO layer in size-stabilized single-phase Cu₂O nanoparticles. *Appl. Phys. Lett.* **79**(19), 3176–3178 (2001)
43. J. Lin, A. Wang, B. Qiao, X. Liu, X. Yang, X. Wang, J. Liang, J. Li, J. Liu, T. Zhang, Remarkable performance of Ir/FeO_x single-atom catalyst in water gas shift reaction. *J. Am. Chem. Soc.* **135**(41), 15314–15317 (2013)
44. J. Zhou, C.Q. Sun, K. Pita, Y.L. Lam, Y. Zhou, S.L. Ng, C.H. Kam, L.T. Li, Z.L. Gui, Thermally tuning of the photonic band gap of SiO₂ colloid-crystal infilled with ferroelectric BaTiO₃. *Appl. Phys. Lett.* **78**(5), 661–663 (2001)
45. B. Li, J. Zhou, L.F. Hao, W. Hu, R.L. Zong, M.M. Cai, M. Fu, Z.L. Gui, L.T. Li, Q. Li, Photonic band gap in (Pb, La)(Zr, Ti)O₃ inverse opals. *Appl. Phys. Lett.* **82**(21), 3617–3619 (2003)
46. K. Lu, Nanocrystalline metals crystallized from amorphous solids: nanocrystallization, structure, and properties. *Mater. Sci. Eng. R-Rep.* **16**(4), 161–221 (1996)
47. N. Agrait, A.L. Yeyati, J.M. van Ruitenbeek, Quantum properties of atomic-sized conductors. *Phys. Rep.-Rev. Sec. Phys. Lett.* **377**(2–3), 81–279 (2003)
48. W.P. Halperin, Quantum size effects in metal particles. *Rev. Mod. Phys.* **58**(3), 533–606 (1986)
49. C. Binns, Nanoclusters deposited on surfaces. *Surf. Sci. Rep.* **44**(1–2), 1–49 (2001)
50. F. Baletto, R. Ferrando, Structural properties of nanoclusters: energetic, thermodynamic, and kinetic effects. *Rev. Mod. Phys.* **77**(1), 371–423 (2005)
51. B. Baretzky, M.D. Baro, G.P. Grabovetskaya, J. Gubicza, M.B. Ivanov, Y.R. Kolobov, T.G. Langdon, J. Lendvai, A.G. Lipnitskii, A.A. Mazilkin, A.A. Nazarov, J. Nogues, I.A. Ovidko, S.G. Protasova, G.I. Raab, A. Revesz, N.V. Skiba, J. Sort, M.J. Starink, B.B. Straumal, S. Surinach, T. Ungar, A.P. Zhilyaev, Fundamentals of interface phenomena in advanced bulk nanoscale materials. *Rev. Adv. Mater. Sci.* **9**(1), 45–108 (2005)
52. C. Noguera, Insulating oxides in low dimensionality: a theoretical review. *Surf. Rev. Lett.* **8**(1–2), 121–167 (2001)
53. P. Moriarty, Nanostructured materials. *Rep. Prog. Phys.* **64**(3), 297–381 (2001)

54. M. Fernandez-Garcia, A. Martinez-Arias, J.C. Hanson, J.A. Rodriguez, Nanostructured oxides in chemistry: characterization and properties. *Chem. Rev.* **104**(9), 4063–4104 (2004)
55. C.N.R. Rao, F.L. Deepak, G. Gundiah, A. Govindaraj, Inorganic nanowires. *Prog. Solid State Chem.* **31**(1–2), 5–147 (2003)
56. C.X. Wang, G.W. Yang, Thermodynamics of metastable phase nucleation at the nanoscale. *Mater. Sci. Eng. R-Rep.* **49**(6), 157–202 (2005)
57. P.F. Trwoga, A.J. Kenyon, C.W. Pitt, Modeling the contribution of quantum confinement to luminescence from silicon nanoclusters. *J. Appl. Phys.* **83**(7), 3789–3794 (1998)
58. A.L. Efros, Interband absorption of light in a semiconductor sphere. *Sov. Phys. Semiconductors-Ussr* **16**(7), 772–775 (1982)
59. L.E. Brus, On the development of bulk optical-properties in small semiconductor crystallites. *J. Lumin.* **31**, 381–384 (1984)
60. Y. Kayanuma, Quantum-size effects of interacting electrons and holes in semiconductor microcrystals with spherical shape. *Phys. Rev. B* **38**(14), 9797–9805 (1988)
61. Y.D. Glinka, S.H. Lin, L.P. Hwang, Y.T. Chen, N.H. Tolk, Size effect in self-trapped exciton photoluminescence from SiO₂-based nanoscale materials. *Phys. Rev. B* **64**(8): art. no.-085421 (2001)
62. G.G. Qin, H.Z. Song, B.R. Zhang, J. Lin, J.Q. Duan, G.Q. Yao, Experimental evidence for luminescence from silicon oxide layers in oxidized porous silicon. *Phys. Rev. B* **54**(4), 2548–2555 (1996)
63. F. Koch, V. Petrovakoch, T. Muschik, A. Nikolov, V. Gavrilenko, Some perspectives on the luminescence mechanism via surface-confined states of porous Si, in *Microcrystalline Semiconductors : Materials Science and Devices*, eds. by P.M. Fauchet et al. (Materials Research Soc, Pittsburgh, 1993), pp. 197–202
64. S.M. Prokes, Surface and optical properties of porous silicon. *J. Mater. Res.* **11**(2), 305–320 (1996)
65. T.S. Iwayama, D.E. Hole, I.W. Boyd, Characteristic photoluminescence band in Si⁺ - implanted SiO₂ grown on Si wafer. *Microelectron. Reliab.* **40**(4–5), 849–854 (2000)
66. F.A. Lindemann, The calculation of molecular natural frequencies. *Physikalische Zeitschrift* **11**, 609–612 (1910)
67. M. Born, Thermodynamics of crystals and melting. *J. Chem. Phys.* **7**(8), 591–603 (1939)
68. P. Buffat, J.P. Borel, Size effect on melting temperature of gold particles. *Phys. Rev. A* **13**(6), 2287–2298 (1976)
69. P. Pawlow, The dependency of the melting point on the surface energy of a solid body. (Supplement.). *Zeitschrift Fur Physikalische Chemie–Stoichiometrie Und Verwandtschaftslehre.* **65**(5), 545–548 (1909)
70. H. Reiss, P. Mirabel, R.L. Whetten, Capillarity theory for the coexistence of liquid and solid clusters. *J. Phys. Chem.* **92**(26), 7241–7246 (1988)
71. H. Sakai, Surface-induced melting of small particles. *Surf. Sci.* **351**(1–3), 285–291 (1996)
72. A.R. Ubbelohde, *The Molten State of Materials* (Wiley, New York, 1978)
73. K.J. Hanszen, Theoretische untersuchungen uber den schmelzpunkt kleiner kugelchen—ein beitrag zur thermodynamik der grenzflächen. *Z. Angew. Phys.* **157**(5), 523–553 (1960)
74. P.R. Couchman, W.A. Jesser, Thermodynamic theory of size dependence of melting temperature in metals. *Nature* **269**(5628), 481–483 (1977)
75. R.R. Vanfleet, J.M. Mochel, Thermodynamics of melting and freezing in small particles. *Surf. Sci.* **341**(1–2), 40–50 (1995)
76. B. Vekhter, R.S. Berry, Phase coexistence in clusters: an ‘‘experimental’’ isobar and an elementary model. *J. Chem. Phys.* **106**(15), 6456–6459 (1997)
77. Q. Jiang, L.H. Liang, J.C. Li, Thermodynamic superheating and relevant interface stability of low-dimensional metallic crystals. *J. Phys.: Condens. Matter* **13**(4), 565–571 (2001)
78. Q. Jiang, H.Y. Tong, D.T. Hsu, K. Okuyama, F.G. Shi, Thermal stability of crystalline thin films. *Thin Solid Films* **312**(1–2), 357–361 (1998)
79. Q. Jiang, H.X. Shi, J.C. Li, Finite size effect on glass transition temperatures. *Thin Solid Films* **354**(1–2), 283–286 (1999)

80. Z. Wen, M. Zhao, Q. Jiang, The melting temperature of molecular nanocrystals at the lower bound of the mesoscopic size range. *J. Phys.-Condens. Matter* **12**(41), 8819–8824 (2000)
81. Q. Jiang, L.H. Liang, M. Zhao, Modelling of the melting temperature of nano-ice in MCM-41 pores. *J. Phys.-Condens. Matter* **13**(20), L397–L401 (2001)
82. K.K. Nanda, S.N. Sahu, S.N. Behera, Liquid-drop model for the size-dependent melting of low-dimensional systems. *Phys. Rev. A* **66**(1), 013208 (2002)
83. M. Wautelet, Estimation of the variation of the melting temperature with the size of small particles, on the basis of a surface-phonon instability model. *J. Phys. D-Appl. Phys.* **24**(3), 343–346 (1991)
84. Q. Jiang, Z. Zhang, J.C. Li, Superheating of nanocrystals embedded in matrix. *Chem. Phys. Lett.* **322**(6), 549–552 (2000)
85. R. Vallee, M. Wautelet, J.P. Dauchot, M. Hecq, Size and segregation effects on the phase diagrams of nanoparticles of binary systems. *Nanotechnology* **12**(1), 68–74 (2001)

Chapter 11

Theory: BOLS and NEP

- *Atomic undercoordination shortens and stiffens the remaining bonds between undercoordinated atoms, which follow the BOLS correlation.*
- *Local densification and quantum entrapment of energy and electrons take places, of which the extent increases with the lowering of atomic CN.*
- *Polarization happens to the non-bonding electrons (non-bonding electron polarization, NEP) by the densely entrapped core and bonding electrons, which exemplifies Anderson's localization due to bond order deficiency.*
- *The polarized electrons neither follow the Hamiltonian nor obey the standard dispersion, but form impurity states in the mid-bandgap region, which splits and screens the local interatomic potentials.*
- *Core-shell configuration and the local bond average (LBA) are necessary to overcome limitations faced by classical continuum or quantum methods in dealing with the strongly localized nature of undercoordinated atoms.*

11.1 Broken Bond

11.1.1 Barrier Confinement

Termination of the lattice periodicity in the surface normal direction has two effects. One is the creation of the surface potential barrier (SPB, related to work function), and the other is the reduction in the CN of atoms in the skin. The former confines electrons moving inside the body, while the latter shortens and strengthens bonds in the skin region. Local densification and quantum entrapment of bonding electrons, bond energy, and mass and polarization of the non-bonding electrons take places, which modify the atomic cohesive energy and the crystal potential in the Hamiltonian. The entrapment enlarges electroaffinity and polarization lowers the work function.

The work function, $\Phi = E_0 - E_F(n(E)^{2/3})$ [1], is the separation between the vacuum level, E_0 , and the Fermi energy, E_F . The value of Φ depends on both the charge density $n(E)$ in the surface region and the energy that the valence density of state (DOS) is centered. Dipole formation that raises the energy and the density of the high-energy electrons reduces the Φ of a metal surface. Non-bonding electron polarization (NEP) by the densely entrapped core electrons also lowers the SPB and the work function [2]. On the other hand, nitrogen or oxygen chemisorption also lowers the work function by some 1.2 eV [3]. However, if hydrogen bond like forms with more addition of the adsorbates at the surface, the Φ will restore to the original value or even higher because the metal dipoles donate their polarized electrons to the additional electronegative additives to form a '+/p' at the surface [4].

The SPB confines only electrons that are freely moving inside the solid. The SPB has nothing to do with the *strongly localized* electrons in the core bands or with those shared in the bonding orbits. According to the principle of quantum uncertainty, reducing the dimension (D) of the space inside which energetic particles are moving increases the fluctuation, rather than the average value of the momentum p , or the kinetic energy E_k , of the moving particles:

$$\begin{aligned} \Delta p &\propto \hbar/D; & p &= \bar{p} \pm \Delta p \\ E_k &= \bar{p}^2/(2m) \end{aligned} \quad (11.1)$$

where \hbar , being the reduced Planck constant, corresponds to the minimal quanta in energy and in momentum spaces, and m is the mass of the moving particle. SPB confinement causes energy rise of neither the freely moving carriers nor the localized ones. Therefore, the kinetic energies of carriers or e-h pairs change little with solid dimension according to the principle of quantum uncertainty.

11.1.2 Atomic CN Reduction

The CN of an atom in a highly curved surface is lower than that of an atom at a flat surface. For a negatively curved surface (such as the inner side of a pore or a bubble), the CN is greater than that of a flat surface. Therefore, from the atomic CN imperfection point of view, there is no difference in nature between a nanosolid, a nanosized pore, and a flat surface. This premise extends to the structural defects or faults such as voids surrounding which atoms experience a CN loss with respect to the ideal bulk standard of 12.

Figure 11.1 illustrates situations of atomic CN imperfection. The CN is two for an atom in the interior of a monatomic chain or an atom at the open edge of a SWCNT or a graphene sheet; while in the CNT wall and graphene interior, the CN is three. At the atomic chain ends, it is one. For an atom in the fcc unit cell, the CN varies from site to site. The CN of an atom at the edge or corner differs from the CN of an atom in the plane or inside the unit cell. The CN imperfection is not limited to the CN loss but covers situations of bond angle distortion. The effective

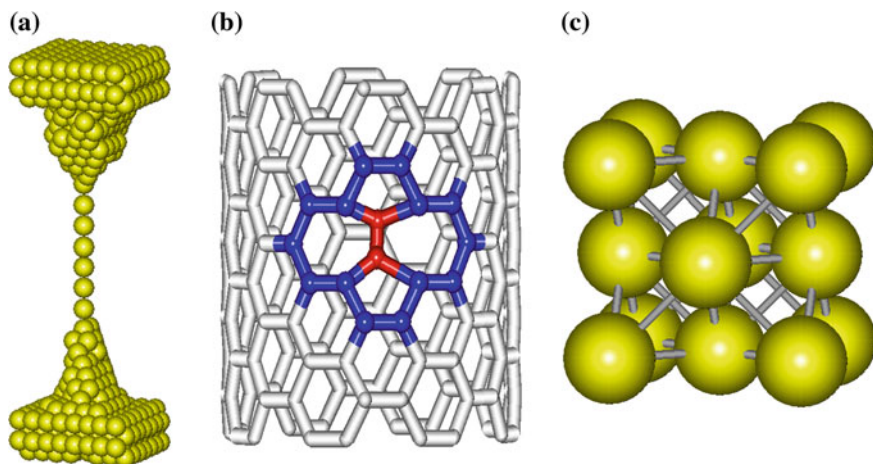


Fig. 11.1 Atomic CN of **a** monatomic chain ($z = 2$), **b** SWCNT ($z = 2, 3$), and **c** an fcc unit cell (z varies from site to site) (Reprinted with permission from [5])

CN imperfection is irrespective of the bond nature or the crystal structure. For example, the CN of an atom in diamond or silicon is 12 as the diamond structure is an interlock of two fcc unit cells.

11.2 Bond Relaxation in Length and Energy

11.2.1 Atomic CN-Radius Correlation

Pauling [6] and Goldschmidt [7] indicated that, if the CN of an atom is reduced, the ionic and the metallic radius of an atom would shrink spontaneously. Therefore, the CN imperfection will shorten the remaining bonds between undercoordinated atoms, which is independent of the nature of the specific chemical bond [8] or the structural phase. Bond order loss-induced bond contraction applies to a liquid surface, gaseous phase, and homo- and hetero-junction interface in addition to atoms at the vacuum–solid interface.

11.2.2 BOLS Notation

Figure 11.2a shows the CN dependence of the bond contraction coefficient C_z . The solid curve formulates Goldschmidt notation indicating that an ionic radius contracts by 12, 4, and 3 % if the CN of the atom is reduced from 12 to 4, 6 and 8, respectively, with respect to that of the fcc structure standard. Feibelman [9] noted

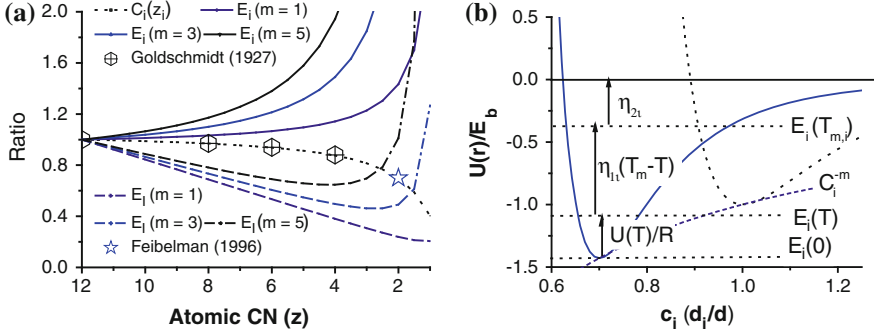


Fig. 11.2 Illustration of the BOLS correlation. **a** CN dependence of the normalized bond length $d_i/d = C_i(z_i)$, and the CN and bond nature dependence of bond energy $E_i/E_b = C_i^{-m}$ and the atomic cohesive energy $E_i/E_B = z_{ib}C_i^{-m}$. The scattered data are from Goldschmidt and Feibelman. The $C_i(z_i)$ curve also matches the measurement from Au clusters. **b** Atomic CN imperfection causes the remaining bonds of the undercoordinated atom to contract from one unit (in d) to C_i and to increase the cohesive energy per coordinate from one unit (in E_b) to C_i^{-m} . Separation between the $E_i(T)$ and the $E_i(0)$ is the thermal vibration or internal energy, and the separation between $E_i(T)$ and $E_i = 0$ (at evaporation) corresponds to energy for thermal or mechanical rupture of the pairing bond and the elastic modulus. $T_{m,i}$ is the melting point, which is proportional to atomic cohesive energy, $E_{C,i}$. η_{1i} is the specific heat per bond, and η_{2i} is $1/z_i$ fold energy required for evaporating an atom in the molten state (Reprinted with permission from [5]). The coordinates (d_z , E_z) at equilibrium is much more important than the shape of a particular interatomic potential

a 30 % contraction of Ti and Zr dimer bond, and a 40 % contraction of vanadium dimer bond, which is in line with the BOLS formulation that includes the bond energy change:

$$\begin{cases} C(z) = d_z/d_0 = 2/\{1 + \exp[(12 - z)/(8z)]\} & \text{(BOLS-coefficient)} \\ E_z = C_z^{-m}E_b & \text{(Single-bond-energy)} \\ E_{B,z} = zE_z & \text{(Atomic-coherency)} \end{cases} \quad (11.2)$$

The bond nature index m correlates the bond energy to the bond length. For Au, Ag, Ni, and Cu metals, $m \equiv 1$; for alloys and compounds, m is around four; for C and Si, the optimal m value is 2.56 [10] and 4.88 [11], respectively. The m value may change with the coordination environment of group III and group IV elements [12]. The $C(z)$ is anisotropic and varies with the effective CN rather than the apparent CN value. The z_i labels the atomic CN of atoms in the i th layer of a substance. The curvature dependent z_i takes the following form [11]:

$$\begin{aligned} z_1 &= \begin{cases} 4(1 + 0.75/K) & \text{curved-surface} \\ 4 & \text{flat-surface} \end{cases}; \\ z_2 &= z_1 + 2 \\ z_3 &= 12 \end{aligned} \quad (11.3)$$

The curvature K^{-1} takes all possible values from infinity to negative infinity. The BOLS correlation illustrated in Fig. 11.2 is independent of the particular form of the pairing potential as the approach involves only atomic distance and bond energy at equilibrium $u(d_z, E_z)$.

11.2.3 Pauling's Notation

From a study of interatomic distances of the C–C bond in organic chemistry, Pauling derived [6]

$$r(1) - r(v/z_0) = 0.030 \log(v/z_0) \text{ (nm)} \quad (11.4)$$

where $r(1)$ is the length of a dimer bond. The $r(v/z)$ is the radius of an atom with v -fold bond z -coordinate.

As an illustration of the use of this relation, the radius of the hcp-structured Ti was from the data of the bcc-structured Ti. The radius of the bcc-structured Ti is 0.1442 nm, and there are eight bonds of each atom. The length of the next six shortest bonds is 0.1667 nm. These values were calculated from the known bcc lattice parameter of 0.333 nm. The valence, v , of a Ti atom is four. The problem is to determine what fraction of these four bonds is associated with the eight nearest neighbors and with the six next-nearest others. From Eq. (11.4),

$$r(1) - r(x/8) = 0.030 \log(x/8) \quad (11.5)$$

and, for the next-nearest neighbors,

$$r(1) - r[(4 - x)/6] = 0.030 \log[(4 - x)/6] \quad (11.6)$$

where x is the number of bonds associated with the eight near neighbors and $(4 - x)$ the number associated with the other six. Subtracting (11.5) from (11.6) and using the value $(0.1667 - 0.1442)$ obtained from the lattice parameter, one can find that $x = 3.75$ and the dimer bond length $r(1) = 0.13435$ nm which contracts by 0.00985 nm. The bond number v/z is 4/12 in the hcp of CN = 12, and the corresponding bond length is $r(4/12) = 0.13435 - 0.03 \log(4/12) = 0.1486$ nm. From Eq. (11.4), one can also deduce the bond length of an atom with a reduced CN(z):

$$r(v/z) = r(v/z_0) + 0.030 \log(z/z_0) \quad (11.7)$$

Appendix A2 lists the electronegativity (η), metallic (ionic) valencies, and metallic (ionic) radii of all elements. Pauling's theory introduced here contains numerous assumptions and it is somewhat empirical in nature. Compared to Eq. (11.4), Pauling's notation is d_0 and valence value dependent and somewhat complicated, which gives

$$C(z) = 1 + 0.060 \log(z/z_0)/d_0(v/z_0) \quad (11.8)$$

This notation does give surprisingly good answers in certain cases [8]. Both Eqs. (11.4) and (11.8) are valid, but relation (11.2) is universal and sufficient for the purely CN effect.

11.2.4 Physical BOLS

11.2.4.1 Potential Well Depression

An extension of Goldschmidt's notation to including bond energy and atomic cohesive energy results in the BOLS correlation premise. Figure 11.2b illustrates schematically the BOLS correlation using the pairing atomic potential, $u(r)$. When the CN of an atom is reduced, the equilibrium atomic distance will contract from one unit (in d_0) to C_z and the cohesive energy of the shortened bond will increase in magnitude from one unit (in E_b) to C_z^{-m} . The solid and the broken $u(r)$ curves correspond to potentials of the pairing atoms with and without the CN imperfection effect being involved. The $u(r)$ curve glides downward along the C_z^{-m} line. The bond length–strength correlation herein is consistent with the trend reported in Bahn and Jacobsen [13] albeit the extents of bond contraction and energy enhancement. It is true that the shorter the bond becomes, the stronger the bond will be.

There are several characteristic energies in Fig. 11.2b, which correspond to the following facts:

1. The local melting point $T_{m,z}$ is proportional to the cohesive energy of the z -coordinated atom, $zE_z(0)$ [14, 15].
2. The separation between $E = 0$ and $E_z(T_m)$, or η_{2z} , is $1/z$ -fold energy that is required for atomization of an atom in molten state.
3. Separation between $E = 0$ and $E_z(T)$, or $\eta_{1z}(T_{m,z} - T) + \eta_{2z}$, corresponds to the cohesive energy per coordinate, E_z , at T , being required for fracturing a bond mechanically or thermally. η_{1z} is the specific heat per coordinate.
4. The spacing between $E_z(T)$ and $E_z(0)$ is the thermal vibration energy.
5. The energy contributing to the mechanical strength is the separation between the $E_z(T_m)$ and the $E_z(T)$, or $\eta_{1z}(T_{m,z} - T)$, as a molten phase is extremely soft and highly compressible with zero shear modulus [16].

Values of the η_{1z} and the η_{2z} can be determined with the known C_z^{-m} and the bulk η_{1b} and η_{2b} values given in Table 11.1 and Fig. 11.3 for various crystal structures. The z -resolved η_1 and η_2 follow the relations

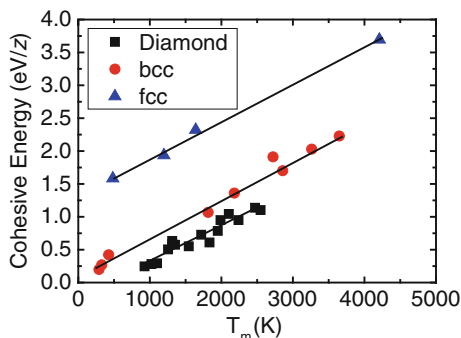
$$\begin{cases} \eta_{1z} = z_0\eta_{1b}/z \\ \eta_{2z} = C_z^{-m}\eta_{2b} \end{cases}$$

Table 11.1 Correlation between the bond energy and the T_m of various structures

| | fcc | bcc | Diamond |
|-------------------------------|-------|--------|---------|
| η_{1b} (10^{-4} eV/K) | 5.542 | 5.919 | 5.736 |
| η_{2b} (eV) | -0.24 | 0.0364 | 1.29 |

$E_b = \eta_{1b}T_m + \eta_{2b}$ [17]. The value of $\eta_{2b} < 0$ for an fcc structure means that the energy required for breaking all the bonds of an atom in molten state is included in terms of $\eta_{1b}T_m$, and therefore, the η_{2b} deviates from the true specific heat per CN. The η_{2b} for the fcc structure should be linear dependence on T_m

Fig. 11.3 Correlation of the crystal structure, the bond energy, and the T_m of elemental solids [17–19]



11.2.4.2 Quantum Entrapment and Densification

As the relaxation (either contraction or expansion) is a spontaneous process, the potential well become deeper, according to the general rule of energy minimization. The energy of the relaxed bond will be greater. Bond expansion might happen, but the process must proceed toward lowering the binding energy of the entire system, unless the relaxation is under external stimulus such as heating, pressing, or stretching.

Figure 11.4 illustrates the potential well of a nanosolid with involvement of the BOLS effect at edges. Compared with the quantum confinement convention that extends the monocenter trapping potential of an isolated atom d to the scale of particle size D , the BOLS potential includes the multi trapping centers of all the involved atoms and, importantly, the BOLS effect in the skin consisting of three atomic layers. The shortening and strengthening of the edge bonds deepen the well of the pairing potentials in the skin in a radial way. Therefore, the density of charge, energy, and mass in the relaxed skin are higher than they are in the bulk interior. Meanwhile, the energy levels of the core and the bonding electrons will shift as the potential well deepens, which leads to the quantum entrapment. This convention applies to monoatomic chains, atomic defects, terrace edges, and flat surfaces, where atomic CN undergoes reduction. Because of the reduced CN, the atomic cohesive energy will drop if the zE_z could not compensate for the z_bE_b loss.

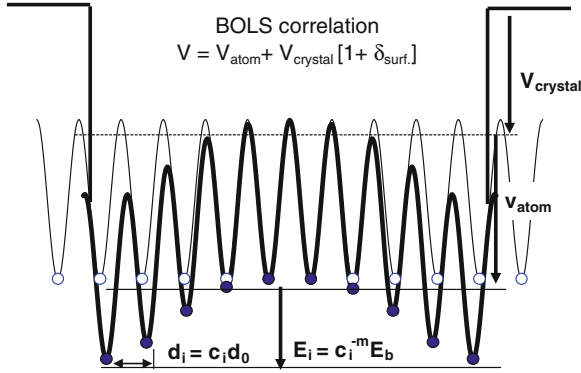


Fig. 11.4 Schematic illustration of the BOLS derived nanosolid potential with multi-trap centers and CN imperfection induced local strain and quantum entrapment at the terminating edges [20, 21]. In the relaxed skin, the density of charge, energy, and mass will be higher than they are in the bulk interior [22]. However, atomic cohesive energy for the undercoordinated atoms will drop (Reprinted with permission from [5])

11.2.5 Chemical BOLS

The physical BOLS describes the effect atomic CN deficiency, which is different from that defined for chemical reaction in which the bond order refers to the number of chemical bonds formed between a pair of atoms. The bond energy E , bond length d , and bond order n for chemical reaction are correlated as [6, 23]

$$\begin{cases} d/d_s = 1 - 0.26 \ln(n)/d_s \\ E/E_s = \exp[c(d_s - d)] = n^p \end{cases} \quad (11.9)$$

where subscript s stands for ‘single bond,’ c and p are empirical constants. This model allows prediction of quantities in gas-surface reactions, namely [24–27] (1) binding energies for molecular adsorbed species, (2) binding energies for atomically adsorbed species, (3) activation energies to chemisorption, and (4) activation energies to dissociative chemisorption.

11.3 Non-Bonding Electron Polarization

11.3.1 Attributes of Non-Bonding Electrons

The ‘non-bonding’ electrons are referred to these non-bonding lone pairs, anti-bonding dipoles, non-bonding unpaired electrons (such as the π -bond in graphite, the dangling bond in Si surface, and those in the half-filled s -orbitals of noble metals at the nanoscale), as well as H-like and C–H-like bonds. An ionic impurity also

induces dipoles [4, 28]. The van der Waals bond that has a maximal energy of several tenths of an eV should be in this category as it represents dipole–dipole interaction instead of charge sharing. Such non-bonding electrons are only active when they are in positions adjacent to the broken bonds at the open edges of a substance.

Unlike the core electrons in the deeper bands or the bonding electrons in the valence band, the non-bonding electrons do add impurity states in the energy between the conduction and the valence band or create tails to these bands. Being strongly localized and rather weakly bound with energy being equivalent to that of human body temperature, the electrons neither contribute significantly to the Hamiltonian nor follow the regular dispersion relations, but they demonstrate fascinating properties such as those seen at the edges of graphenes and at the ends of atomic chains. This kind of electrons is readily polarized by the neighboring densely entrapped charge or they polarize the surroundings. The polarized states split and screen locally the crystal potential that determines the energy band such as the XPS core-level shift. These electrons are however hardly describable in quantum computation because of the localized and the weak bound nature. However, they dictate the performance of a substance when interacting with the environment. The presence of these non-bonding states near the broken bonds dominates unexpectedly the fascinating behavior of biologic and organic molecules and functional materials at the nanoscale.

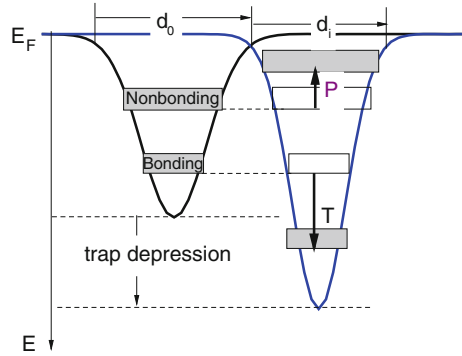
11.3.2 Non-Bonding Electron Polarization

According to Anderson [29], bond order loss causes a localization of electrons. The bond contraction raises the local density of electrons in the core bands and electrons shared in the bonds. The core band will shift accordingly as the potential well deepens (called entrapment, T). The densification and entrapment of the core and bonding electrons in turn polarize the non-bonding electrons, raising their energy closer to E_F . The polarize electrons will split and screen the potential.

This sequential happening of bond contraction, densification, entrapment, and polarization (bonding–non-bonding electron repulsion and strong correlation) may elaborate the ‘Strong localization’ of Anderson for systems with bond order loss [2].

At the terminating end of a solid, the characteristics of the non-bonding states become even more pronounced. Polarization occurs to the lone electrons, if exist, by the densely trapped bonding and core electrons of the undercoordinated atoms, as illustrated in Fig. 11.5.

Fig. 11.5 Schematic illustration of the polarization of the non-bonding states (P) by the densely entrapped bonding and core charges (T), because of the BOLS. This sequence of processes modulates the Hamiltonian by crystal potential splitting and charge distribution in all bands (Reprinted with permission from [2])



11.4 Shape and Size Dependency

11.4.1 Core–Shell Configuration: Skin Volume Fraction

The surface-to-volume ratio, γ_i , determines the trend of size dependency. Taking a sphere with radius R as a sample, the γ_1 for the first atomic shell of d_{z1} thick is

$$\gamma_1 = d(\ln V) = \frac{\int_{v_1}^{v_2} dV}{V} = \frac{4\pi \int_{R-d_{z1}}^R R^2 dR}{4\pi R^3/3} \approx 1 - 3 \left(\frac{R - d_{z1}}{R} \right) = \frac{3C_{z1}}{K} \quad (11.10)$$

where K is the number of atoms lined along the radius of the nanosphere or across the thickness of a thin film or the wall thickness of a nanotubes. C_{z1} is the bond contraction coefficient. Generally, $\gamma_i = \tau K^{-1} C_i$. $\tau = 1, 2,$ and 3 corresponds to a thin plate, a cylindrical rod, and a spherical dot, respectively. For a hollow system, one has to introduce a size L that is the number of atomic layers not occupied by atoms in a hollow structure. In this situation, the sum of γ_i should count both external and internal sides of the hollow system. For a solid system, $L = 0$; while for a hollow sphere or a hollow tube, $L < K$. For a hollow system, with reduced particle size, the performance of surface atoms will dominate because at the smallest size ($K \rightarrow 3$) γ_1 approaches unity. At $K = 1$, the solid will degenerate into an isolated atom. If all bonds in the nanocrystal contribute to the size effect, the integral over the entire sphere will be unity. Therefore, the K^{-1} dependence of observations indicates clearly that bonds in the skin of limited thickness dominate the size-induced property change.

The definition of dimensionality herein differs from conventional in transport considerations in which a nanosphere is defined as zero dimension, a rod as one dimension, and a plate as two dimension. Figure 11.6b, c illustrates the derivation of the surface-to-volume ratio. As the K is an integer, the property change will show quantized oscillation features at small particle sizes, which varies from structure to structure, as illustrated in Fig. 11.6c.

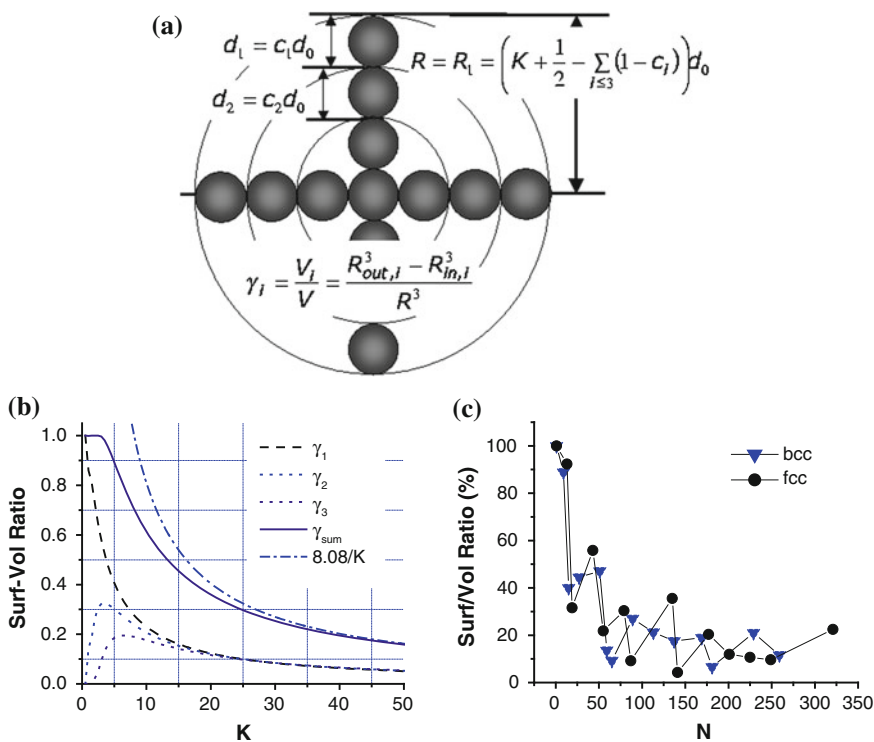


Fig. 11.6 **a** Surface-to-volume ratio (γ_i) of a nanosolid. **b** The γ_i drops from unity to infinitely small when the solid grows from atomic scale, $K = 1$, to infinitely large, $K = \infty$. At the lower end of the size limit, the solid degenerates into an isolated atom. **c** The number ratio shows oscillatory features for fcc and bcc small solids (Reprinted with permission from [5])

11.4.2 Local Bond Average

For a given specimen whether it is crystal, non-crystal, with or without defects or impurities being involved, the nature and the total number of bonds of the specimen do not change under an external stimulus before phase transition. However, the length and strength of all the involved bonds or their average will response to the externally applied stimulus, unless bond unfolding or breaking taking place. If the functional dependence of a detectable quantity on the bonding identities is properly formulated, one would know the performance of the entire specimen under external stimulus by focusing on the response of the length and strength of the representative bond. These considerations form the base of the local bond average (LBA) approach.

The LBA approach [30] is substantially the same to the volume partitioning approximation implemented by Delph and co-workers [31, 32] who have opened a way in improving the calculation of local quantities. The volume averaging

provides a reasonable and correct way to obtain physically meaningful stress and elastic properties of complex microstructures. They derived the absolute values of local stress and elastic constants for a region containing a fixed number of atoms that is part of a large body. By means of an expansion of the local interatomic potential energy, they derived expressions for the local second Piola–Kirchhoff stress. Using this approach, they have obtained good agreement with the suitably averaged continuum solutions in the far-field regime.

Unlike the volume partition approximation, the LBA approach seeks for the relative change in a quantity with respect to the known bulk value under the applied stimulus. The LBA approach focuses merely on the performance of the local representative bonds disregarding the exact number of bonds that will not change in the given specimen under a certain circumference. The presence of the broken bonds, defects, impurities, or the non-crystallinity will affect the reference values of concern rather than the nature of observations. Contribution from long-range-order interactions or from the high-order coordinates can be simplified by folding them into the bonds of the specific atom to the nearest neighbors. The LBA approach represents the true situations of measurements in terms of energy of the reciprocal spaces and theoretical computations that collect statistic information from large number of atoms or bonds. Furthermore, compared with the measurement and computation, the LBA could discriminate the behavior of local bonds at different sites. Furnished with the LBA approximation, the difficulties encountered by the classical and quantum approaches in particular for the small object could be readily solved [33].

11.5 Scaling Relations

11.5.1 LBA Scaling Relation

The relative change in a measurable quantity $Q(K)$ of a nanosolid-containing N atoms, with dimension K , is related to the $Q(\infty) = Nq_0$ for the same solid without the CN imperfection effect in the following form:

$$Q(K) = Nq_0 + \sum_{i \leq 3} N_i(q_i - q_0) \quad (11.11)$$

where subscript i denotes an atom in the i th atomic layer, which counts up to three from the outermost atomic layer inward as no CN reduction is expected for $i > 3$. The q_0 and q_i correspond to the local density of Q inside the bulk and in the i th atomic layer, respectively. Eq. (11.11) yields the immediate relation:

$$\frac{Q(K) - Q(\infty)}{Q(\infty)} = \begin{cases} bK^{-1} & \text{(measurement)} \\ \Delta_q & \text{(theory)} \end{cases}$$

$$\Delta_q = \sum_{i \leq 3} \gamma_i (\Delta q_i / q) \quad (11.12)$$

$$\gamma_i = \frac{N_i}{N} = \frac{V_i}{V} = \frac{\tau C_i}{K} \leq 1$$

The slope $b \equiv Q(\infty) \times \Delta_q \times K = Q(\infty) \times \sum_{i \leq 3} \tau C_i \Delta q_i / q_0 \cong \text{constant}$, which is the core physics of nanoscience. The $\Delta_q \propto K^{-1}$ varies simply with the $\gamma_i(\tau, K, C_i)$ if the functional dependence of $q(z_i, C_i, m)$ on the atomic CN, bond length, and bond energy is given. The weighting factor, γ_i , represents the geometrical contribution from the dimension (K, L) and the dimensionality (τ) of the solid, which determines the magnitude of the change. The quantity $\Delta q_i / q_0$ in the skin is the origin of change. The static dimensionality τ represents the factor of shape. No zero dimensionality is necessary.

The overall surface-to-volume ratio, $\sum_{i \leq 3} \gamma_i = \sum_{i \leq 3} \tau K^{-1} C_i$, drops in a K^{-1} fashion from unity to infinitely small when the solid dimension grows from atomic level to infinitely large. The γ_1 for a sphere is greater than that of a rod and a plane of the same scale. At $K < 3$, the performance of the surface atoms will dominate because at the smallest size the γ_1 approaches unity. For a spherical dot at the lower end of the size limit, $K = 1.5$ ($Kd_0 = 0.43$ nm for an Au spherical dot example), $\gamma_1 = 1$, $\gamma_2 = \gamma_3 = 0$, and $z_1 = 2$, which is identical in situation to an atom in a monatomic chain despite the orientation of the bond. Atoms in the atomic chain are identical in situation to an atom in a monatomic chain despite the geometrical orientation of the two interatomic bonds in the atomic chain. Actually, the bond orientation is not involved in the BOLS modeling iteration. Therefore, the performance of an atom in the fcc unit cell is identical to the same atom in a monatomic chain from the perspective of bond order loss. At the lower end of the size limit, the property change in a nanosolid relates directly to the behavior of single bond, which forms the starting point of the current ‘bottom-up’ approach. Most importantly, this expression covers the whole range of solid sizes, from monatomic chain to the infinite large bulk. The variable, besides the size effect, the T is critical as all the bonds in the substance response to the temperature change.

The layer-counting premise in Fig. 11.7a represents that atoms in the surface skins dictate the size-induced property change, yet atoms in the core interior remain as they are in the bulk because of the broken-bond-induced local strain and quantum entrapment.

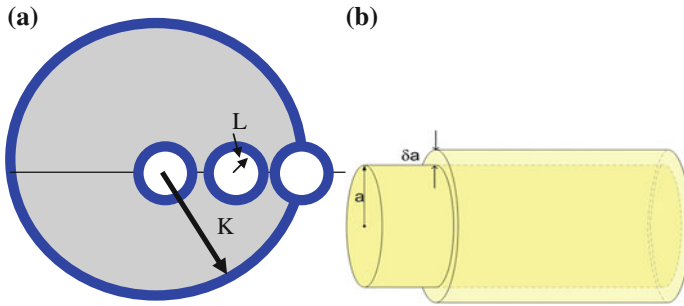


Fig. 11.7 Schematic illustration of the surface-to-volume ratio of **a** a sphere with $4\pi(n + 1/2)^3/3$ cavities and **b** the core-shell structure of a cylindrical nanorods. Only atoms in the skin of Δz thick contribute to the property change, yet atoms in the core interior remain their bulk nature (Reprinted with permission from [5])

11.5.2 Surface-to-Volume Ratio

The difference between a positively curved surface and a negatively curved surface is nothing more than the surface-to-volume ratio, γ_i , and the slight difference in the coordinating environment of the undercoordinated atoms. Considering a sphere of K radius with $(n + 1/2)$ spherical cavities of L_j radius lined along the K radius, as illustrated in Fig. 11.7b, the total number of voids is $4\pi(n + 1/2)^3/3$ inside the K sphere. For the hollow sphere ($n = 0$) with only one void in the center, this expression needs slight revision. We can estimate the volume V_0 occupied by atoms as the entire volume of the sphere less the voids. The sum of the volume of skins of the voids and the sphere surface is V_i . The V_0 and the V_i are calculated as follows:

$$V_0 = \frac{4\pi}{3} \left[K^3 - \frac{4\pi}{3} \left(n + \frac{1}{2} \right)^3 L^3 \right]$$

$$V_i = 4\pi \left[K^2 C_{io} + \frac{4\pi}{3} \left(n + \frac{1}{2} \right)^3 L^2 C_{ii} \right]$$

where C_{ii} and C_{io} represent the bond contraction coefficient for atoms in the inner negatively curved skins of the cavities and atoms at the outer positively curved surface of the sphere, respectively. The ratio between the volume sum of the skins and the volume occupied by atoms is

$$\begin{aligned}
r_i(n, L, K) &= \frac{V_i}{V_0} = \frac{3}{K} 3 \frac{3C_{io} + 4\pi(n+1/2)^3(L/K)^2 C_{ii}}{1 - 4\pi(n+1/2)^3(L/K)^3} \\
&= \frac{3}{K} \begin{cases} \frac{3C_{io} + 4\pi(n+1/2)^3(L/K)^2 C_{ii}}{3 - 4\pi(n+1/2)^3(L/K)^3} & \text{(Porous - sphere)} \\ C_{io} & \text{(Solid - sphere)} \\ \frac{3C_{io} + 4\pi(L/K)^2 C_{ii}}{3 - 4\pi(L/K)^3} & \text{(Hollow - sphere)} \end{cases} \quad (11.13)
\end{aligned}$$

The parameters of n , L , and K are constrained by the relation: $2(L+1)(n+1/2) \leq K-2$ because of the allowed maximum number of cavities aligned along the radius K . $2(L+1)$ represents the diameter of the void including the one layer of surface skin and $K-2$ the radius of the sphere excluding the surface skin. This expression covers situations of a solid sphere, a hollow sphere, and a sphere with uniformly distributed cavities of the same size. This relation also applies to a solid rod, a hollow tube, and a porous nanowire as well.

With the derived $r_i(n, L, K)$ relation and the given expressions for the $q(z_i, d_i(t), E_i(t))$, one can readily predict the size, cavity density, and temperature dependence of the Q of a system with large fraction of undercoordinated atoms without involving hypothetical parameters.

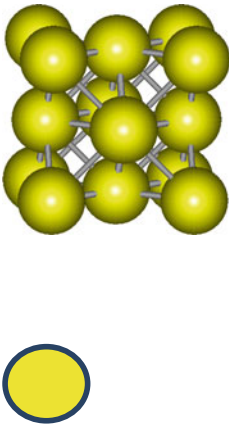

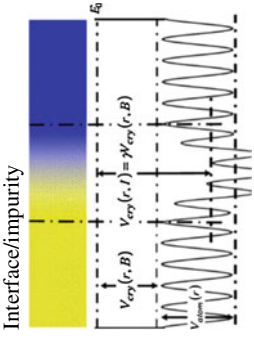
11.6 Summary

This section addressed the event of atomic CN imperfection and its effect on the bond length, bond strength, charge entrapment, and polarization of the undercoordinated atoms. In using the BOLS correlation, one needs to consider the cohesive energy per bond or per discrete atom in dealing with thermally activated process such as phase transition and crystal growth. One also needs to consider the binding energy density in the surface skin in dealing with the Hamiltonian of the system that dictates the change in the entire band structure of a nanosolid. Some properties, such as mechanical strength and magnetization, both atomic cohesion and energy density come into competition. An additionally quantum entrapment in the skin is critical to transport dynamics. The performance of a material is determined by the bond and binding electrons. The size-induced emergence of properties that the bulk parent does not demonstrate is more important to the size dependency of the known bulk properties. Table 11.2 features the classification, origin, notation, and the size-induced tunability and the emerging properties at edges, skins, interfaces, and solid at the nanoscale.

The following sections will focus on the size dependency of the known bulk properties and the emerging properties of nanostructures toward consistent insight into the nature of the size- and shape-induced property change in nanosolids.

Physical quantities of a bulk solid can normally be categorized as follows:

Table 11.2 Classification, origin, notation, and the size dependency and size emergency of possible properties of substances at the nanoscales, edges, skins, and interfaces (with potential trap or barrier formation)

| | | | | |
|-----------------------------|---|--|---|---|
| Isolated atom exists at 0 K | Atomic chain, sheet, tube, wire, dot, skin, Ideal bulk nanocrystals, etc. |  |  |  |
| Interatomic interaction | 0 | 1 | 1 | 1 |
| Coordination number | 0 | <12 (under) | =12 (full) | Hetero |
| Notations | Interaction between undercoordinated atoms differs in nature nanostructures from an isolated atom or the bulk in performance—skin dominance | | | |
| Size limits | Defects, skins, adatoms, nanostructures of various shapes share the same attribute | | | |
| Size dependency | Bond between undercoordinated atoms becomes shorter and stronger | | | |
| | Skin atoms/bonds dictate size dependency | | | |
| | Interface potential barrier/trap formation with charge entrapment and polarization | | | |
| | From a dimer to considerable large bulk with skin | | | |
| | Tunable properties that the parent bulk demonstrate (skin entrapment): | | | |
| | Elastic modulus Y , | | | |
| | Melting point T_m , | | | |
| | Band gap E_G | | | |
| | XPS core-level shift | | | |
| | Dielectric constant ϵ_r | | | |
| | Work function ϕ , etc. | | | |

(continued)

Table 11.2 (continued)

| | | |
|-----------------------------|---|--------------------|
| Isolated atom exists at 0 K | Atomic chain, sheet, tube, wire, dot, skin, Ideal bulk nanocrystals, etc. | Interface/impurity |
| Size emergency | Emerging properties that the bulk parent never demonstrate (non-bonding electron polarization): | |
| | Dilute magnetism | |
| | Catalytic ability | |
| | Superhydrophobicity | |
| | Thermoelectricity | |
| | Drug delivery (biosolubility) | |
| | Giant magnetoresistance | |
| | Strong correlation: high- T_C superconductors, topological insulators, thermoelectric materials, electricity generators, etc. | |

1. Quantities that are related directly to bond length, such as the mean lattice constant, mass density, binding energy density, and the mean free path in transport.
2. Quantities that depend on atomic cohesive energy, $E_{B,z} = \sum_{z_i} E_i = z_i E_i$, such as self-organization growth, thermal stability, Coulomb blockade, critical temperature for liquidation, evaporation and phase transition of a nanosolid and the activation energy for atomic dislocation, diffusion, and bond unfolding [34].
3. Properties that vary with the binding energy density in the relaxed continuum region such as the Hamiltonian that determines the entire band structure and related properties such as bandgap, core-level energy, magnetization, and phonon frequency. The binding energy density is proportional to the single-bond energy E_i because the number of bonds per circumferential area between neighboring atomic layers in the relaxed region does not change.
4. Properties related to the electroaffinity such as reactivity, iconicity, and toxicity.
5. Properties contributed from the joint effect of the binding energy density and atomic cohesive energy such as mechanical strength, Young's modulus, surface energy, surface stress, extensibility and compressibility of a nanosolid, and the magnetic performance of a ferromagnetic nanosolid.
6. Transport dynamics and scattering process such as thermal conductivity, electric conductivity, relate to the trapping potential well of depth. The localized and depressed potential well will govern the transport processes.

Therefore, if one knows the functional dependence of the q on atomic separation or its derivatives, the size dependence of the quantity Q is then definite. This approach means that one can design a nanomaterial with desired functions based on the prediction as such by simply tuning the shape and size of the solid.

References

1. D.J. Wales, Structure, dynamics, and thermodynamics of clusters: tales from topographic potential surfaces. *Science* **271**(5251), 925–929 (1996)
2. C.Q. Sun, Dominance of broken bonds and nonbonding electrons at the nanoscale. *Nanoscale* **2**(10), 1930–1961 (2010)
3. C.Q. Sun, Oxygen-reduced inner potential and work function in VLEED. *Vacuum* **48**(10), 865–869 (1997)
4. C.Q. Sun, Oxidation electronics: bond-band-barrier correlation and its applications. *Prog. Mater. Sci.* **48**(6), 521–685 (2003)
5. C.Q. Sun, Size dependence of nanostructures: Impact of bond order deficiency. *Prog. Solid State Chem.* **35**(1), 1–159 (2007)
6. L. Pauling, Atomic radii and interatomic distances in metals. *J. Am. Chem. Soc.* **69**(3), 542–553 (1947)
7. V.M. Goldschmidt, Crystal structure and chemical correlation. *Ber. Deut. Chem. Ges.* **60**, 1263–1296 (1927)
8. M.J. Sinnott, *The Solid State for Engineers* (Wiley, New York, 1963)
9. P.J. Feibelman, Relaxation of hcp(0001) surfaces: a chemical view. *Phys Rev B* **53**(20), 13740–13746 (1996)

10. S. Li, T.H. Yip, C.Q. Sun, S. Widjaja, M.H. Liang, in *Origin of Self-Aligned Nano-domains in MgB₂, 3rd Asian meeting on electroceramics (AMEC-3)*, Singapore, 2003
11. C.Q. Sun, L.K. Pan, Y.Q. Fu, B.K. Tay, S. Li, Size dependence of the 2p-level shift of nanosolid silicon. *J. Phys. Chem. B* **107**(22), 5113–5115 (2003)
12. C.Q. Sun, C.M. Li, H.L. Bai, E.Y. Jiang, Melting point oscillation of a solid over the whole range of sizes. *Nanotechnology* **16**(8), 1290–1293 (2005)
13. S.R. Bahn, K.W. Jacobsen, Chain formation of metal atoms. *Phys. Rev. Lett.* **87**(26), 266101 (2001)
14. C.Q. Sun, Y. Wang, B.K. Tay, S. Li, H. Huang, Y.B. Zhang, Correlation between the melting point of a nanosolid and the cohesive energy of a surface atom. *J. Phys. Chem. B* **106**(41), 10701–10705 (2002)
15. U.F. Kocks, A.S. Argon, M.F. Ashby, Thermodynamics and kinetics of slip. *Prog. Mater. Sci.* **19**, 1–281 (1975)
16. M. Born, Thermodynamics of crystals and melting. *J. Chem. Phys.* **7**(8), 591–603 (1939)
17. K.K. Nanda, S.N. Sahu, S.N. Behera, Liquid-drop model for the size-dependent melting of low-dimensional systems. *Phys. Rev. A* **66**(1), 013208 (2002)
18. C. Kittel, *Introduction to Solid State Physics*, 8th edn. (Wiley, New York, 2005)
19. W.A. Harrison, in *Electronic Structure and the Properties of Solids*, ed. by A.J. Freeman (San Francisco, 1980)
20. W.J. Huang, R. Sun, J. Tao, L.D. Menard, R.G. Nuzzo, J.M. Zuo, Coordination-dependent surface atomic contraction in nanocrystals revealed by coherent diffraction. *Nat. Mater.* **7**(4), 308–313 (2008)
21. Y. Wang, Y.G. Nie, L.L. Wang, C.Q. Sun, Atomic-layer- and crystal-orientation-resolved 3d_{5/2} binding energy shift of Ru(0001) and Ru(1010) surfaces. *J. Chem. Phys. C* **114**(2), 1226–1230 (2010)
22. C.Q. Sun, Surface and nanosolid core-level shift: impact of atomic coordination-number imperfection. *Phys. Rev. B* **69**(4), 045105 (2004)
23. H.S. Johnston, C. Parr, Activation energies from bond energies: 1. Hydrogen transfer reactions. *J. Am. Chem. Soc.* **85**(17), 2544–2551 (1963)
24. W.H. Weinberg, The bond-energy bond-order (BEBO) model of chemisorption. *J. Vac. Sci. Technol.* **10**(1), 89 (1973)
25. E. Shustorovich, Chemisorption phenomena: analytic modeling based perturbation theory and bond-order conservation. *Surf. Sci. Rep.* **6**, 1–63 (1986)
26. H. Gross, C.T. Campbell, D.A. King, Metal-carbon bond energies for adsorbed hydrocarbons from calorimetric data. *Surf. Sci.* **572**(2–3), 179–190 (2004)
27. W.H. Weinberg, R.P. Merrill, Crystal-field surface orbital—bond-energy bond-order (CFSO-BEBO) model for chemisorption—application to hydrogen adsorption on a platinum (111) surface. *Surf. Sci.* **33**(3), 493–515 (1972)
28. B.C. Stipe, M.A. Rezaei, W. Ho, Single-molecule vibrational spectroscopy and microscopy. *Science* **280**(5370), 1732–1735 (1998)
29. E. Abrahams, P.W. Anderson, D.C. Licciardello, T.V. Ramakrishnan, Scaling theory of localization: absence of quantum diffusion in two dimensions. *Phys. Rev. Lett.* **42**(10), 673–676 (1979)
30. C.Q. Sun, Thermo-mechanical behavior of low-dimensional systems: the local bond average approach. *Prog. Mater. Sci.* **54**(2), 179–307 (2009)
31. T.J. Delph, Local stresses and elastic constants at the atomic scale. *Proc. R. Soc. A-Math. Phys. Eng. Sci.* **461**(2058), 1869–1888 (2005)
32. J. Cormier, J.M. Rickman, T.J. Delph, Stress calculation in atomistic simulations of perfect and imperfect solids. *J. Appl. Phys.* **89**(1), 99–104 (2001)
33. M.X. Gu, Y.C. Zhou, L.K. Pan, Z. Sun, S.Z. Wang, C.Q. Sun, Temperature dependence of the elastic and vibronic behavior of Si, Ge, and diamond crystals. *J. Appl. Phys.* **102**(8), 083524 (2007)
34. D. Tomanek, S. Mukherjee, K.H. Bennemann, Simple theory for the electronic and atomic-structure of small clusters. *Phys. Rev. B* **28**(2), 665–673 (1983)

Chapter 12

Skin Bond Relaxation and Nanosolid Densification

- *Surface consisting of a few number of atomic layers forms the skin of a substance.*
- *The skin shell forms a high-density phase that is more elastic, stiffer, chemically and thermally less stable with entrapped electrons, and subjective polarization.*
- *Bond relaxation happens only in the skin in a radial way. The extent and depth of bond relaxation increase with surface curvature.*
- *In placing with the conventional concept of surface free energy, the energy density and the atomic cohesive energy in the skin region determine the performance of a surface.*
- *BOLS notation holds for defects, skins of solids and liquids, as well as molecules in gaseous phases.*

12.1 Skin Bond Relaxation

12.1.1 Monolayer Relaxation

There has been huge database of skin bond contraction for flat surfaces (Table 12.1 and Fig. 11.2b). Atomic undercoordination-induced bond contraction derived interlayer relaxation and intra-plane reconstruction are common. For instance, LEED and DFT revealed some 10 % reduction in the first-layer spacing (d_{12}) of the hcp(10 $\bar{1}$ 0) surface of Ru [1], Co [2], and Re [3]. The d_{12} of diamond (111) surface is \sim 30 % smaller than the (111) spacing in the bulk, which results in a substantial reduction in the surface energy [4]. VLEED revealed that the O–Cu bond contraction from 4 to 12 % forms one of the four discrete stages of the Cu₃O₂ bonding kinetics on the Cu(001) surface [5] and about 10 % contraction of the O–Cu bond in the O–Cu(110) surface [6–8]. A 12–14 % bond contraction

Table 12.1 Bond length relaxation for typical covalent, metallic, and ionic solids and its effect on the physical properties of the corresponding solid or surface

| Bond nature | Medium | C_1 | Effect |
|---------------------|---|-----------|---|
| Covalent | Diamond [14, 4] | 0.7 | Surface energy decrease |
| Metallic | hcp (10 $\bar{1}$ 0) surface of Ru, [1] Co, [2] and Re, [3] | 0.9 | |
| | Fe–W, Fe–Fe [15] | 0.88 | Atomic magnetic momentum enhancement by (25–27) % |
| | Fe(310) [16], Ni(210) [17] | 0.85–0.9 | Cohesive energy rises by 0.3 eV per bond |
| | Al(001) [18] | | |
| | Ni, Cu, Ag, Au, Pt, and Pd dimer [12] | 0.7 | Single-bond energy increases by 2–3 times |
| | Ti, Zr [19] | 0.6 | |
| | V [19] | | |
| Ionic | O–Cu(001) [5] | 0.88–0.96 | |
| | O–Cu(110) [6] | 0.9 | |
| | TiCrN [9] | 0.86–0.88 | 100 % rise in hardness |
| Extraordinary cases | (Be, Mg) (0001) surface Zn, Cd, and Hg dimer bond [19], Nb [20] | >1.0 | No report is available about its effects on physical properties |

Where d_0 and d_1 are the bond lengths for atoms inside the bulk and for atoms at the surface, respectively. The C_1 is the bond contraction coefficient

enhances the surface stress and Young's modulus of TiCrN films [9]. Interatomic distance drops significantly [10] associated with rise of cohesive energy per bond as the dimensionality decreases from three to one for Ag, Au, and Cu nanosolids, see Fig. 12.1. Kara and Rahman [11] found that distances between neighboring atoms of Ag, Cu, Ni, and Fe in different CNs follow a strong BOL correlation. The bond lengths of Ag, Cu, Ni, and Fe diameters are 2.53, 2.22, 2.15, and 2.02 Å, respectively [11], being 12.5 % for Ag, 13.2 % for Cu, 13.6 % for Ni, and 18.6 % for Fe shorter than they are in the respective bulk.

However, the d_{12} of the hcp(0001) surface of Be and Mg and the dimer bonds of the II-b elements of Zn, Cd, and Hg have been reported to expand. With a reduction in Se grain size from 70 to 13 nm, the a lattice was found to expand by 0.3 %, but the c lattice spacing decreases slightly, which expands the unit-cell volume by about 0.7 % at $D = 13$ nm [13]. The reported expansion appears off line with notations of Goldschmidt and Pauling who emphasized that the global bond contraction depends uniquely on the reduction in atomic CN, and it is independent of the bond nature or the particular constituent elements (Appendix A2) (Table 12.2).

Fig. 12.1 DFT-derived BOLS relation from bulk fcc crystals to atomic chains (reprinted with permission from [12]). The bond length contracts and the cohesive energy per bond in the chains are about 2–3 times that of the bulk fcc crystals, which is in accordance with the BOLS correlation albeit the absolute amounts of variation

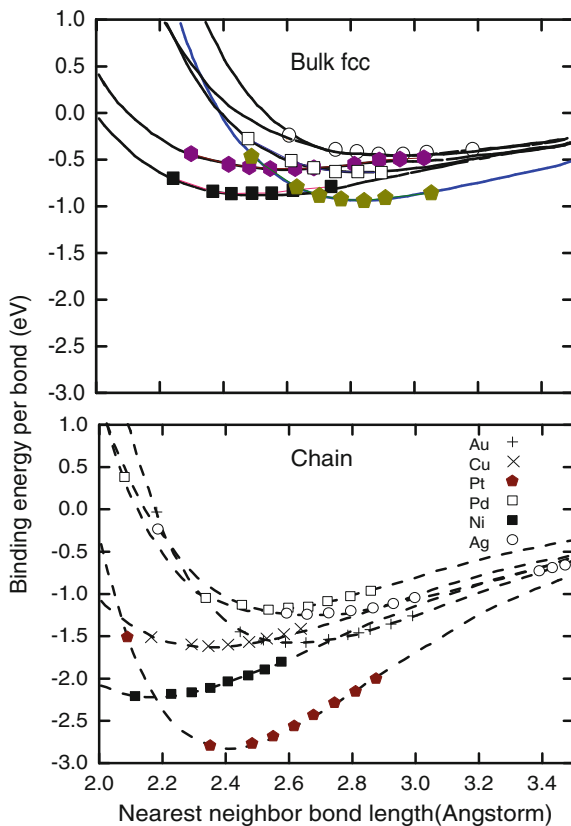


Table 12.2 Surface interlayer relaxation of clean metal surfaces

| Metal | Method | $\Delta d_{12}/d_{12}$ | Metal | Method | $\Delta d_{12}/d_{12}$ (%) |
|-------------------|---------------|------------------------|---------|--------------------|----------------------------|
| Rh(001) | LEED [21, 22] | -1.2; -1.4 | Fe(210) | LEED [23] | -22 |
| W(001) | DFT [24] | -5.7 | Fe(310) | LEED [23] | -16 |
| W(110) | LEED [22, 25] | -3.0 | Pd(310) | DFT [26] | -14.1 |
| W(320) | DFT [27] | -22.3 | Pt(210) | LEED/EAM [28] | -23.0/-31; |
| Al(001) | DFT [18] | -10 | Cu(331) | DFT [29, 30] | -22.0; -13.8 |
| | | | | RSGF [31] | -10.4 |
| Al(210) | LEED [32] | -16 | Cu(551) | RSGF* [31] | -9.8 |
| Ti/Zr(0001) | DFT [19] [33] | -6.1 to -7.8 | Cu(211) | DFT [29, 31, 34] | -14.4; -28.4; |
| | | | | | -10.8 |
| | LEED [22] | -4.9 | | LEED [35] | -14.9 |
| Ag/Cu/ Ni(110) | [36, 37] | -6 to -9 | Cu(117) | LEED [38] DFT [39] | -13.0; -9.5 |
| Ag/Cu/ Ni(111) | LEED [40] | -1 to -2 | Al(113) | DFT [41] | -6.8 |
| Ag/Cu/ Ni(100) | [42] | -2 to -3 | Al(115) | DFT [41] | -8.0 |
| Fe/W(110) | DFT [11, 43] | -10.0; -13.0 | Al(117) | DFT [41] | -8.3 |

12.1.2 Multilayer Relaxation

Numerical calculations and diffraction optimizations also suggest coexistence of bond contraction and expansion extending to deeper atomic layers for a number of metals [44]. Multilayer relaxation happens to Ag(410) and Cu(320) surfaces [45]. The multilayer relaxation is subject to the data processing iteration. The same set of Ag(410) LEED database gives rise different conclusions. One is non-measurable relaxation and the other is a 36 % contraction of the d_{23} and a 18 % expansion of d_{34} [46]. Theoretical calculations clarified this discrepancy with a 11.6, 5.3, and 9.9 % contraction of the Ag(410) outermost three interlayer separations and followed by 2.1 and 6.7 % expansion subsequently. A combination of LEED, DFT, and MD [47] investigation turned out that the d_{12} of Ag(110) surface contracts by 8 % at 133 K and by 0.2 % at 673 K associated with a rise in the Debye temperature from 150 ± 65 to 170 ± 100 K compared with the bulk value of 225 K.

For a Cu(320) surface, a 13.6 and 9.2 % contraction of the first two interlayers are followed by an expansion of 2.9 %, and then an 8.8 % contraction, and finally a 10.7 % expansion for the subsequent three [45]. The d_{12} of the Au(110) surface is reduced by 13.8 %, the d_{23} is expanded by 6.9 %, and finally the d_{34} is reduced by 3.2 % [48]. On the other hand, LEED measurements of Cu(320) revealed a 24 % contraction for d_{12} and 16 % contraction for d_{23} , followed by 10 % expansion for d_{34} . Therefore, physical constraints are necessary to specify a unique solution from these derived by mathematically geometrical optimizations.

12.2 Liquid Skin, Gas Phase, and Interface

Bond contraction also happens in liquid skins and gaseous molecules. For instances, bonds at methanol skin contracts by 4.5 % but the hydrogen bond expands by 5.9 % at water surface at room temperature [49]. The spacing between the first and the second atomic layers of liquid Sn, Hg, Ga, and In contracts by 10 % [50]. Phase change occurs at the droplet surface of *n*-alkane indicates the formation of a monolayer thick solid solution of the oil phase [51]. Bond contraction at liquid skin results in the surface strain and surface stress that drives and sustains liquid drop and gas-bubble formation. X-ray crystallography revealed that a Cr–Cr bond length contracts by 31.5 % from the bulk value of 0.255 to 0.174 nm for a Cr₂ anion protected by three bidentate amidinate ligands [52] and 0.175 nm [53] for a neutral Cr₂ complex.

Bond contraction also happens to the hetero-coordinated atoms. Extended X-ray absorption fine structure (EXAFS) and X-ray absorption near edge spectroscopy (XANES) measurements revealed a 8 % contraction of distance between the As impurity (acceptor dopant) and the Te sub-lattice in CdTe [54]. At Al twin grain boundaries, homo-junction dislocations have either compact or dissociated interlayers. The minimum stress (σ_p) required for moving an edge dislocation is

approximately 20 times higher for the compact dislocations than for the equivalent dissociated dislocations [55]. The homo-junction interface and the hetero-junction interface bond contraction provide insight into the deformation of ultrafine-grained metals and the twin grain boundaries.

However, exceptional cases exist. Based on the fine structure of boron and carbon K -edges in EELS and TEM, Lu et al. [56] found local C–C bond expansion at sites with local high B content in the diamond grain.

A few layer NB atomic sheet shows asymmetric interlayer relaxation effect. The sp -orbit hybridization of N and B results in an empty orbit of B and a lone-pair-filled orbit of N . The interlayer relaxation proceeds with the lone pair and empty orbit. At the side of B outward, the interface contracts substantially while the other side of N outward show strong expansion [57].

12.3 Nanosolid Densification

12.3.1 Known Facts

The lattice constants of an isolated nanosolid or a complex consisting of highly dispersed nanosolids are often shorter [58, 59] than that of the bulk while for a nanosolid embedded in a matrix of different materials or passivated chemically, the lattice constant may expand [60]. For example, oxygen chemisorption could expand the first metallic interlayer by up to 10–25 % due to the penetration of oxygen atoms into the interlayer spacing for tetrahedron bond formation [61]. Lattice expansion happens in nanocrystalline copper [62]. A 0.4-nm-thick oxide skin induced the lattice expansion associated with magnetization moment (M_s) suppression of Ni nanosolids in the diameter range of 6–27 nm [63, 64]. The M_s of 16 nm $\text{La}_{0.7}\text{Sr}_{0.3}\text{MnO}_3$ nanoparticles is significantly lower than that of a bulk sample [65]. The nearest-neighbor atomic distance demonstrate noticeable contraction in silver particles of 2.5–13 nm sizes isolated in solid Ar and in Pd particles of 1.4–5.0 [66, 67]. The lattice constant of 14 nm FePt nanoparticles embedded in an amorphous carbon matrix contracts by 4 % [68]. The mean lattice constants of Sn and Bi nanoparticles decreases with the particle size, and the absolute amount of contraction of the c -axis lattice is more significant than that of the a -axis lattice, showing anisotropy of lattice contraction [69]. A 12.5 nm-sized ZnMnTe nanosolid demonstrates a ~ 8 % lattice contraction [70]. The Cu–Cu distance contracts with solid size in a D^{-1} fashion, and the Cu–Cu dimer bond is reduced by 13 % from 0.2555 to 0.2210 nm of the 0.7 nm-sized particle [71]. However, an effective-medium theory approximation [72] suggested that the bond lengths of small (100–1,000 atoms) Cu particles at various temperatures suffer only slight changes. DFT calculations [73] predicted that the atomic distance of Ge and Si expands in the central sites while the bond length contracts in the surface

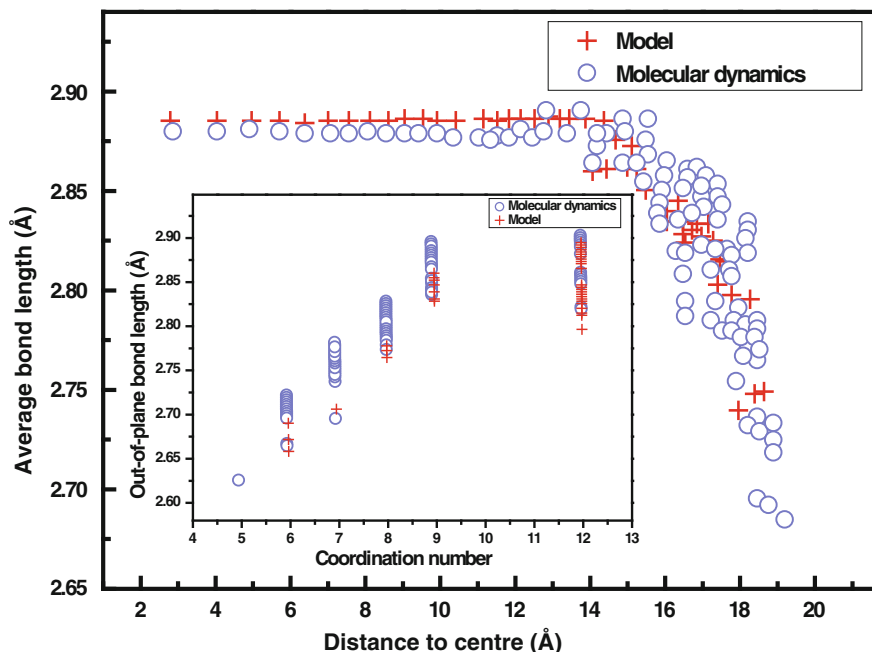


Fig. 12.2 Au–Au bond strain extends to only the outermost two atomic layers for gold nanoclusters (reprinted with permission from [74])

skins, and therefore, the mean lattice constants of the whole Ge and Si nanosolids are smaller than the bulk values.

Using a combination of the MD calculations, Pauling’s correlation, and the coherent electron diffraction, Huang et al. [74, 75] revealed that inhomogeneous relaxations occurring at the outermost two atomic layers of Au nanocrystals (Fig. 12.2). The relaxation is dominated by large out-of-plane bond length contractions for the edge atoms (~ 0.02 nm, $\sim 7\%$); a significant contraction (~ 0.013 nm, 4.5%) for the (100) surface atoms; and a much smaller contraction (~ 0.005 nm, 2%) for atoms in the (111) facets. EXAFS measurement [76] revealed the same results of coordination dependence of Au–Au bond contraction that is independent of the substrate support type. The coordination dependence of Au–Au bond length determined in Refs [74, 96] is in good accordance with the BOLS premise. However, the observed Au–Au bond length expansion of an Au_{102} cluster coated with thiolated organic ligands [77] should arise from the diffusion of S atoms into the atomic layer to form Au–S bond that expands the Au–S–Au separation, being the same to oxygen chemisorption.

Undercoordination-induced global bond contraction in solid and liquid skins, terrace edges, gaseous phases, skins of nanosolids, and associated with impurities and interfaces are in accordance with the BOLS correlation mechanism—bonds between the undercoordinated atoms are shorter and stronger.

12.3.2 Possible Mechanisms

Nanosolid lattice contraction is often ascribed to the effect of hydrostatic pressure of the surface stress [78] and the intrinsic compressibility that is anisotropic [66, 79–81]. The mean lattice strain is also explained in terms of incorporation of impurities such as hydrogen, carbon, and oxygen, or pseudo morphism in the case of crystalline supports [67]. The anisotropic lattice contraction of Bi and Sn nanocrystals demonstrates the anisotropy of both the compressibility and the thermal expansion coefficient of the corresponding bulk counterpart in the c and in the a -axis [82]. The size-induced lattice contraction is also related to the Laplace–Young’s equation and the solid–liquid interfacial energy [83, 84]. Supersaturation of the vacant lattice sites inside the particle also change the lattice constant of nanocrystal [69]. Nevertheless, all the modeling arguments could fit the experimental data well despite different physical origins.

Actually, surface stress and surface energy result intrinsically from, rather than in, the bond contraction as no external pressure is applied to the surface. For instance, the thermal expansion coefficient and hydrostatic compressibility follow the following relations, with Y being the Young’s modulus and u the interatomic potential energy,

$$\beta = -\frac{1}{V} \left(\frac{\partial V}{\partial P} \right) \Big|_T = \left(-V \frac{\partial^2 u}{\partial V^2} \Big|_T \right)^{-1} \propto Y^{-1}; \quad \alpha = \frac{1}{V} \left(\frac{\partial V}{\partial T} \right) \Big|_P \quad (12.1)$$

The compressibility and thermal expansibility are the intrinsic of a solid and they depend functionally on the interatomic interaction and atomic size. These measurable quantities describe the response of the lattice ($V \propto d^3$) to the change of the external stimuli such as hydrostatic pressure, ΔP , or temperature, ΔT .

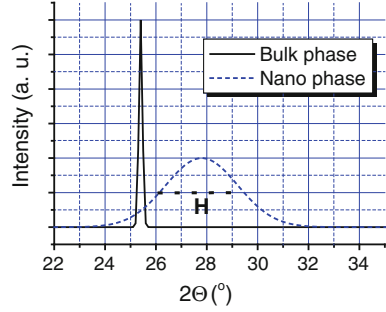
$$\frac{\Delta V}{V} = 3 \frac{\Delta d}{d} = \begin{cases} \beta \times \Delta P \\ \alpha \times \Delta T \end{cases}$$

External stimulus simply provides a probe detecting the responses: compression or expansion. It is inadequate to assume a constant compressibility or a constant thermal expansibility in dealing with a nanometric solid. In fact, the surface stress and interfacial energy are derivatives of the binding energy that is enhanced at the surface by the spontaneous bond contraction.

12.3.3 BOLS Formulation

The BOLS notation indicates that the contraction of the mean lattice constant of the entire solid originates from the CN imperfection-induced bond contraction of surface atoms and the fraction of the surface atoms of the entire solid. The following expressions formulate the surface strain and nanosolid densification [82, 83]:

Fig. 12.3 XRD determination of the lattice constant and grain size in nanostructures materials



$$\frac{\Delta d(K)}{d_0(\infty)} = \begin{cases} \Delta_d = \tau K^{-1} \sum_{i \leq 3} C_i (C_i - 1) < 0 & \text{(BOLS)} \\ -(2\beta\sigma)/(3K) & \text{(liquid-drop)} \\ -(\beta\gamma_{s-1}d_0)^{1/2}/K & \text{(surface-stress)} \end{cases} \quad (12.2)$$

where β is the compressibility and σ the surface stress of the corresponding bulk solid. $\gamma_{s-1} = (2d_0 S_{\text{vib}} \cdot H_m)/(3VR)$ is the solid–liquid interfacial energy, which is a function of the bulk melting enthalpy, H_m , and Molar volume, V , and the vibrational part of melting entropy, S_{vib} . The relative change in the mean lattice constant of a particle in the BOLS premise simply depends on the shape and size of the solid and the bond contraction coefficient C_i without needing other quantities that may vary with solid size.

Among several methods, XRD is the most efficient method to determine the crystal size D and the lattice constant d for a bulk and nanostructured materials, as illustrated in Fig. 12.3, based on Bragg diffraction and Scherrer's equation,

$$\begin{cases} 2d \sin \theta = n\lambda \\ D = \lambda(H \cos \theta)^{-1} \end{cases}$$

where λ is the X-ray wavelength, θ is the diffraction angle, and H the width of the peak at half maximum. The n is the order of diffraction.

Given the shape and size of a solid and the known atomic diameters of the constituent atoms, one can easily predict the lattice contraction of the nanosolid using Eq. (12.2). For the ZnMnTe spherical nanosolid instance [70], the diameters of the constituent atoms are 0.1306(Zn), 0.1379(Mn), and 0.1350(Te) nm, and the effective CN of the outermost three atomic layers are taken as 4, 6, and 8, respectively. The resultant bond length is $\langle d \rangle = \sum x d_x$ with x being the fraction of the component element. Calculation results agree fairly well with the observation ($\sim 8\%$ contraction for 12.5 nm-sized ZnMnTe solid) and show that the lattice constant reaches its bulk value only when the solid dimension is sufficiently large. At the lower end of the size limit, the mean lattice contraction of the solid approaches the value for a dimer of the same atomic constituents. Furthermore, predictions based on the BOLS premise also agree with the observed trends of lattice contraction for ZnS:Mn films [85] and Sn and Bi nanoparticles [69].

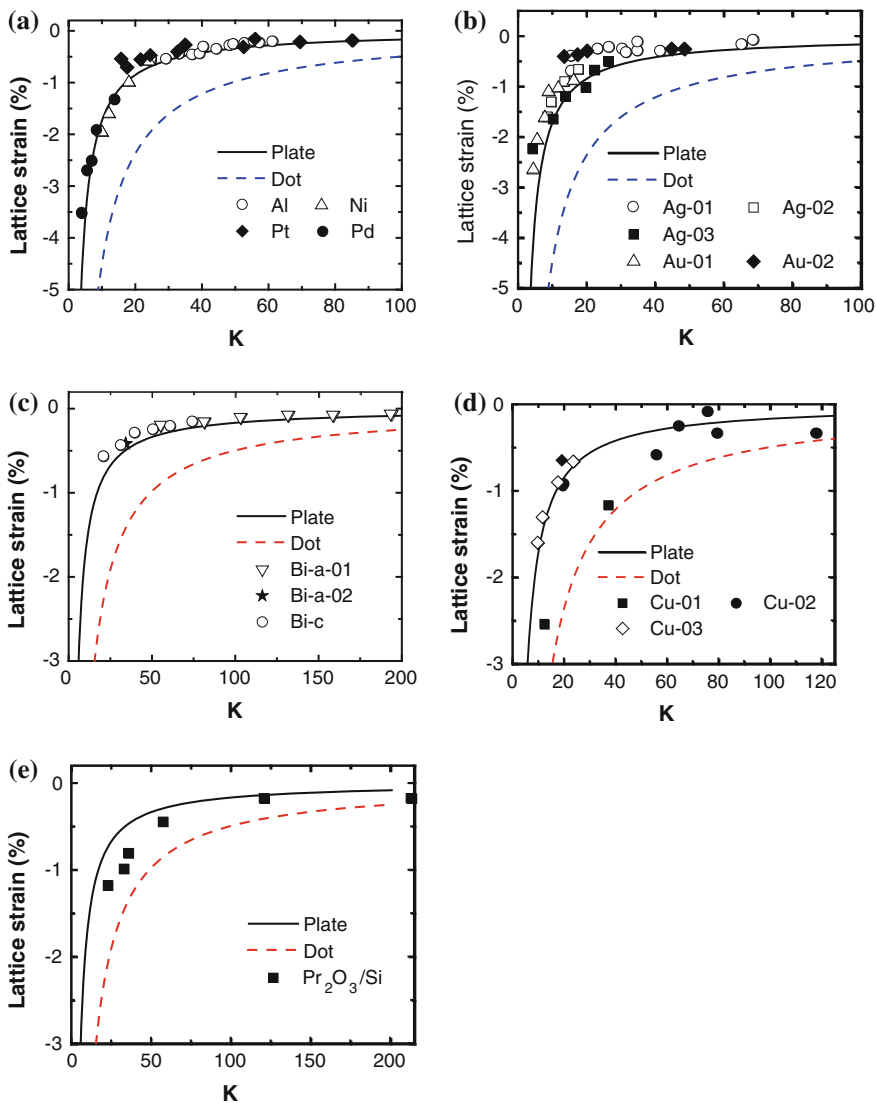


Fig. 12.4 BOLS reproduction of the measured size dependency of the mean lattice contraction of **a** Al [86], Ni [11], Pd [67], and Pt [87], **b** Ag-01 [81], Ag-02 [11], Ag-03 [66], Au-01 [79], Au-02 [88], **c** Bi-a-01 [69], Bi-a-02 [89], Bi-c [69], **d** Cu-01 [90], Cu-02 [91], Cu-03 [11] nanoparticles. **e** Thickness dependence of lattice constant of Pr_2O_3 films on Si substrate [92]. The strain $\Delta a/a$ and $\Delta c/c$ for Bi nanosolid are homogeneous (reprinted with permission from [93])

Measurements [11] show that for the 2.0, 2.5, and 3.5 nm-sized Ag crystals, the Ag–Ag atomic distance is shorter than the bulk value. For the 5.0 nm crystal, 60 % of the atoms have the bulk value but 40 % have shorter atomic distances.

Figure 12.4 shows the lattice contraction for a number of metals. The average atomic distance for Ag, Cu, and Ni shortens by 1.6–2.0 % for small crystals and about 0.6 % for relatively larger ones, compared with the bulk value. The observed anisotropy of Bi lattice contraction does not exist if one considers the relative change of the c and the a -axis, $\Delta a/a$ and $\Delta c/c$, instead of the absolute amount of variation.

12.3.4 Strain-Induced Stiffness

BOLS indicates that nanoparticles have bulk-like interior structure with spontaneous surface relaxation [59, 94, 95] rather than the homogeneous relaxation throughout the particles [96, 97]. Combining the pair distribution function (PDF) derived from wide-angle X-ray scattering and EXAFS analyses, Gilbert et al. [98] found the structural coherence loss happens in a distance of 2 nm. Figure 12.5 shows that the PDF profile for the real ZnS nanoparticles is distinct from that of an ideally computed ZnS nanoparticle in the following aspects [98]:

1. The PDF peak intensity of the first shell for the real particle is lower than that for the ideal case.
2. PDF peak intensities of the real case at higher correlation distances diminish more rapidly than the ideal nanoparticle.
3. PDF peak widths for the real case are broader than the ideal one.
4. The PDF peak positions shift closer to the reference atom, which is more apparent at $r = 1.0$ and 1.4 nm (shortened by 0.008 and 0.02 nm, respectively), indicating a contraction of the mean bond length of the real nanoparticle.
5. The frequency of lattice vibration shift from the bulk value of 7.1 to 11.6 THz, implying bond stiffening.

The stiffening of the strained ZnS nanosolid evidences the dominance of the shorter and stronger bonds in the surface skin. The PDF-intensity attenuation results from the volume change of the high-order CN loss of atoms. The PDF peak shifting and broadening arise from the broad range of bond contraction in the outermost two or three atomic layers and the inhomogeneous sizes. As the XRD and the EXAFS probe statistic information from a collection of nanosolids, one could only tell the existence of structure deviation but hardly conclude whether the structure distortion arises from the skin or from the core region. However, the diameter difference of $(3.4-2.0)$ 1.4 nm coincide with the thickness of the skins composing the outermost atomic capping and surface layers [99] $(3 \text{ (layer)} \times 2 \text{ (sides)} \times 0.255 \text{ (diameter)}) = 1.5$ nm) of which atoms are subject to CN imperfection. Compared with the PDF of an amorphous solid of which the structure coherence extends only to a few atomic distances [100], the detected PDF of ZnS nanosolid coincides with the core size of the measured solid. Therefore, the surface layers should dominate the bond length distortion.

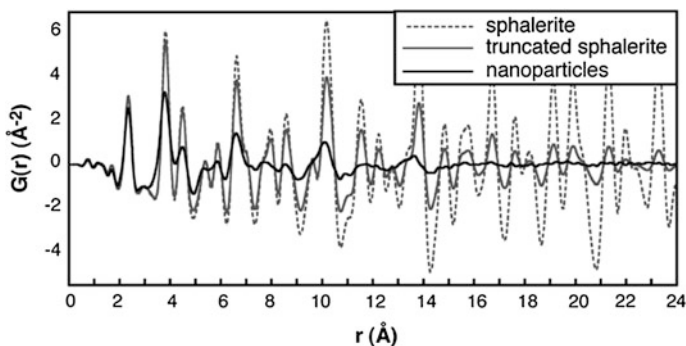


Fig. 12.5 Comparison of the pair distribution function of ZnS bulk solid, calculation for ideal nanosolid, and the measurement for real nanosolid show the cohesive length loss of nanosolid (reprinted with permission from [98])

The difference between a solid composed of nanoparticles and a solid in an amorphous state is the distribution of atoms with CN imperfection. Undercoordinated atoms are located only at the surface of a nanosolid but distribute randomly inside the amorphous solid. The distribution of CN imperfection is sensitive to processing conditions of amorphous states. In probing statistical information, the low-CN atoms contribute identically irrespective of their locations. It is anticipated that the PDF correlation length, or core size, increases with nanocrystal size. Further verification by measuring different sizes would affirm the shell-strain-induced stiffness.

12.4 Energy Entrapment

Undercoordination-induced bond contraction at a surface has indeed enormous effects on various physical properties of a nanosolid because of the local densification and entrapment of electrons and energies in the skins and the lower atomic coherency. Besides the magnetic enhancement [15–17], the relaxation of Al, Ag, Cu, and Pd surfaces yield energy shift of the surface states and localization of the states [101]. For Ag nanocrystals, densification stiffens the atomic force constants by up to 120 % when compared to that for bulk silver [11]. The vibrational energy and the heat capacity of the step and the terrace atoms on the Cu(711) surface are sensitive to the local atomic environment, and vibrational contribution to the excessive free energy of the step atoms near room temperature is a significant fraction of the kink formation energy [102]. The Al(001) surface relaxation expands the bandwidth for the relaxed monolayer by 1.5 eV compared with the value for the bulk-truncated monolayer with 0.3 eV enhancement of atomic cohesive energy [18]. The lattice constant of Au nanoparticles capped in n-dodecanethiol contracts by 1.4, 1.1, and 0.7 % shift the 4f core level by 0.36, 0.21, and 0.13 eV for the 1.6, 2.4, and 4.0 nm-sized Au particles [103]. Therefore,

the impact on physical properties of atomic CN imperfection and the associated bond-strength gain is indeed enormous especially for a system with large proportion of undercoordinated atoms.

12.5 Summary

Bond between undercoordinated atoms becomes shorter and stronger. The shorter bond increases the local density of charge, energy and mass; the stronger bond deepens the local potential that entraps charge and energy. The locally densely entrapped bonding electrons polarize the nonbonding electrons. The local strain, entrapment and polarization results in the abnormal behavior of defects, skins, and nanostructures in terms of size dependence and size emergence.

References

1. A. Baraldi, S. Lizzit, G. Comelli, G. Paolucci, Oxygen adsorption and ordering on Ru(10 $\bar{1}$ 0). *Phys. Rev. B* **63**(11), 115410 (2001)
2. H. Over, G. Kleinle, G. Ertl, W. Moritz, K.H. Ernst, H. Wohlgemuth, K. Christmann, E. Schwarz, A LEED structural-analysis of the Co(1010) surface. *Surf. Sci.* **254**(1–3), L469–L474 (1991)
3. H.L. Davis, J.B. Hannon, K.B. Ray, E.W. Plummer, Anomalous interplanar expansion at the (0001) surface of Be. *Phys. Rev. Lett.* **68**(17), 2632–2635 (1992)
4. T. Halicioglu, Calculation of surface energies for low index planes of diamond. *Surf. Sci.* **259**(1–2), L714–L718 (1991)
5. C.Q. Sun, Exposure-resolved VLEED from the O-Cu(001): bonding dynamics. *Vacuum* **48**(6), 535–541 (1997)
6. C.Q. Sun, Origin and processes of O–Cu(001) and the O–Cu(110) biphas ordering. *Int. J. Mod. Phys. B* **12**(9), 951–964 (1998)
7. C.Q. Sun, O–Cu(001): I. Binding the signatures of LEED, STM and PES in a bond-forming way. *Surf. Rev. Lett.* **8**(3–4), 367–402 (2001)
8. C.Q. Sun, O–Cu(001): II. VLEED quantification of the four-stage Cu₃O₂ bonding kinetics. *Surf. Rev. Lett.* **8**(6), 703–734 (2001)
9. C.Q. Sun, B.K. Tay, S.P. Lau, X.W. Sun, X.T. Zeng, S. Li, H.L. Bai, H. Liu, Z.H. Liu, E.Y. Jiang, Bond contraction and lone pair interaction at nitride surfaces. *J. Appl. Phys.* **90**(5), 2615–2617 (2001)
10. T. Nautiyal, S.J. Youn, K.S. Kim, Effect of dimensionality on the electronic structure of Cu, Ag, and Au. *Phys. Rev. B* **68**(3), 033407 (2003)
11. A. Kara, T.S. Rahman, Vibrational properties of metallic nanocrystals. *Phys. Rev. Lett.* **81**(7), 1453–1456 (1998)
12. S.R. Bahn, K.W. Jacobsen, Chain formation of metal atoms. *Phys. Rev. Lett.* **87**(26), 266101 (2001)
13. Y.H. Zhao, K. Zhang, K. Lu, Structure characteristics of nanocrystalline element selenium with different grain sizes. *Phys. Rev. B* **56**(22), 14322–14329 (1997)
14. J. Cormier, J.M. Rickman, T.J. Delph, Stress calculation in atomistic simulations of perfect and imperfect solids. *J. Appl. Phys.* **89**(1), 99–104 (2001)

15. X. Qian, W. Hubner, First-principles calculation of structural and magnetic properties for Fe monolayers and bilayers on W(110). *Phys. Rev. B* **60**(23), 16192–16197 (1999)
16. W.T. Geng, A.J. Freeman, R.Q. Wu, Magnetism at high-index transition-metal surfaces and the effect of metalloid impurities: Ni(210). *Phys. Rev. B* **63**(6), 064427 (2001)
17. W.T. Geng, M. Kim, A.J. Freeman, Multilayer relaxation and magnetism of a high-index transition metal surface: Fe(310). *Phys. Rev. B* **63**(24), 245401 (2001)
18. I.P. Batra, Lattice-relaxation in aluminum monolayers. *J. Vac. Sci. Technol. a-Vac. Surf. Films* **3**(3), 1603–1606 (1985)
19. P.J. Feibelman, Relaxation of hcp(0001) surfaces: a chemical view. *Phys. Rev. B* **53**(20), 13740–13746 (1996)
20. R. Banerjee, E.A. Sperling, G.B. Thompson, H.L. Fraser, S. Bose, P. Ayyub, Lattice expansion in nanocrystalline niobium thin films. *Appl. Phys. Lett.* **82**(24), 4250–4252 (2003)
21. A.M. Begley, S.K. Kim, F. Jona, P.M. Marcus, Surface relaxation of Rh (001). *Phys. Rev. B* **48**(16), 12326–12329 (1993)
22. G. Teeter, J.L. Erskine, Studies of clean metal surface relaxation experiment-theory discrepancies. *Surf. Rev. Lett.* **6**(5), 813–817 (1999)
23. J. Sokolov, F. Jona, P.M. Marcus, Multilayer relaxation of the Fe(210) surface. *Phys. Rev. B* **31**(4), 1929–1935 (1985)
24. C.L. Fu, S. Ohnishi, E. Wimmer, A.J. Freeman, Energetics of surface multilayer relaxation on W (001)—evidence for short-range screening. *Phys. Rev. Lett.* **53**(7), 675–678 (1984)
25. G. Teeter, J.L. Erskine, F. Shi, M.A. Van Hove, Surface roughness and LEED crystallography: analysis of flat and vicinal W (110). *Phys. Rev. B* **60**(3), 1975–1981 (1999)
26. Y.S. Li, F. Jona, P.M. Marcus, Low-energy-electron-diffraction study of multilayer relaxation on a Pb(311) surface. *Phys. Rev. B* **44**(15), 8267–8273 (1991)
27. J.H. Cho, D.H. Oh, L. Kleinman, Core-level shifts of low coordination atoms at the W(320) stepped surface. *Phys. Rev. B* **64**(11), 115404 (2001)
28. X.G. Zhang, M.A. Vanhove, G.A. Somorjai, P.J. Rous, D. Tobin, A. Gonis, J.M. Maclaren, K. Heinz, M. Michl, H. Lindner, K. Muller, M. Ehsasi, J.H. Block, Efficient determination of multilayer relaxation in the Pt(210) stepped and densely kinked surface. *Phys. Rev. Lett.* **67**(10), 1298–1301 (1991)
29. W.T. Geng, A.J. Freeman, Multilayer relaxation of Cu(331). *Phys. Rev. B* **64**(11), 115401 (2001)
30. Y. Tian, K.W. Lin, F. Jona, Anomalous multilayer relaxation on a Cu{331} surface. *Phys. Rev. B* **62**(19), 12844–12848 (2000)
31. S. Durukanoglu, A. Kara, T.S. Rahman, Local structural and vibrational properties of stepped surfaces: Cu(211), Cu(511), and Cu(331). *Phys. Rev. B* **55**(20), 13894–13903 (1997)
32. D.L. Adams, V. Jensen, X.F. Sun, J.H. Vollesen, Multilayer relaxation of the Al(210) surface. *Phys. Rev. B* **38**(12), 7913–7931 (1988)
33. J.H. Cho, K. Terakura, Plane-wave-basis pseudopotential calculations of the surface relaxations of Ti(0001) and Zr(0001). *Phys. Rev. B* **56**(15), 9282–9285 (1997)
34. C.Y. Wei, S.P. Lewis, E.J. Mele, A.M. Rappe, Structure and vibrations of the vicinal copper (211) surface. *Phys. Rev. B* **57**(16), 10062–10068 (1998)
35. T. Seyller, R.D. Diehl, F. Jona, Low-energy electron diffraction study of the multilayer relaxation of Cu(211). *J. Vac. Sci. Technol. A-Vac. Surf. Films* **17**(4), 1635–1638 (1999)
36. K.P. Bohnen, K.M. Ho, Structure and dynamics at metal-surfaces. *Surf. Sci. Rep.* **19**(3–6), 99–120 (1993)
37. A.M. Rodriguez, G. Bozzolo, J. Ferrante, Structure and energetics of high-index Fe, Al, Cu and Ni surfaces using equivalent crystal theory. *Surf. Sci.* **307**, 625–631 (1994)
38. S. Walter, H. Baier, M. Weinelt, K. Heinz, T. Fauster, Quantitative determination of Cu(117) multilayer surface relaxations by LEED. *Phys. Rev. B* **63**(15), 155407 (2001)
39. Z.J. Tian, T.S. Rahman, Energetics of stepped Cu surfaces. *Phys. Rev. B* **47**(15), 9751–9759 (1993)

40. S.B. Qadri, J. Yang, B.R. Ratna, E.F. Skelton, J.Z. Hu, Pressure induced structural transitions in nanometer size particles of PbS. *Appl. Phys. Lett.* **69**(15), 2205–2207 (1996)
41. P.A. Grivil, S. Holloway, Roughening and melting of stepped aluminum surfaces. *Phys. Rev. B* **53**(16), 11128–11145 (1996)
42. J.W.M. Frenken, J.F. Vanderveen, G. Allan, Relation between surface relaxation and surface force-constants in clean and oxygen-covered Ni(001). *Phys. Rev. Lett.* **51**(20), 1876–1879 (1983)
43. H.L. Meyerheim, D. Sander, R. Popescu, J. Kirschner, P. Steadman, S. Ferrer, Surface structure and stress in Fe monolayers on W(110). *Phys. Rev. B* **64**(4), 045414 (2001)
44. D.A. Walko, I.K. Robinson, Structure of Cu(115): clean surface and its oxygen-induced facets. *Phys. Rev. B* **59**(23), 15446–15456 (1999)
45. S. Durukanoglu, T.S. Rahman, Structure of Ag(410) and Cu(320). *Phys. Rev. B* **67**(20), 205406 (2003)
46. F. Jona, P.M. Marcus, E. Zanazzi, M. Maglietta, Structure of Ag{410}. *Surf. Rev. Lett.* **6**(3–4), 355–359 (1999)
47. V.B. Nascimento, E.A. Soares, V.E. de Carvalho, E.L. Lopes, R. Paniago, C.M.C. de Castilho, Thermal expansion of the Ag(110) surface studied by low-energy electron diffraction and density-functional theory. *Phys. Rev. B* **68**(24), 245408 (2003)
48. I. Galanakis, N. Papanikolaou, P.H. Dederichs, Applicability of the broken-bond rule to the surface energy of the fcc metals. *Surf. Sci.* **511**(1–3), 1–12 (2002)
49. K.R. Wilson, R.D. Schaller, D.T. Co, R.J. Saykally, B.S. Rude, T. Catalano, J.D. Bozek, Surface relaxation in liquid water and methanol studied by X-ray absorption spectroscopy. *J. Chem. Phys.* **117**(16), 7738–7744 (2002)
50. O.G. Shpyrko, A.Y. Grigoriev, C. Steimer, P.S. Pershan, B.H. Lin, M. Meron, T. Graber, J. Gerbhardt, B. Ocko, M. Deutsch, Anomalous layering at the liquid Sn surface. *Phys. Rev. B* **70**(22), 224206 (2004)
51. M.J.W. Povey, S.A. Hindle, A. Aarflot, H. Hoiland, Melting point depression of the surface layer in n-alkane emulsions and its implications for fat destabilization in ice cream. *Cryst. Growth Des.* **6**(1), 297–301 (2006)
52. Y.C. Tsai, C.W. Hsu, J.S.K. Yu, G.H. Lee, Y. Wang, T.S. Kuo, Remarkably short metal-metal bonds: a lantern-type quintuply bonded Dichromium(I) complex. *Angew. Chem. Int. Ed.* **47**(38), 7250–7253 (2008)
53. A. Noor, F.R. Wagner, R. Kempe, Metal-metal distances at the limit: a coordination compound with an ultrashort chromium–chromium bond. *Angew. Chem.-Int. Edit.* **47**(38), 7246–7249 (2008)
54. H.E. Mahnke, H. Haas, E. Holub-Krappe, V. Koteski, N. Novakovic, P. Fochuk, O. Panchuk, Lattice distortion around impurity atoms as dopants in CdTe. *Thin Solid Films* **480**, 279–282 (2005)
55. S.G. Srinivasan, X.Z. Liao, M.I. Baskes, R.J. McCabe, Y.H. Zhao, Y.T. Zhu, Compact and dissociated dislocations in aluminum: Implications for deformation. *Phys. Rev. Lett.* **94**(12), 125502 (2005)
56. Y.-G. Lu, S. Turner, J. Verbeeck, S.D. Janssens, K. Haenen, G. Van Tendeloo, Local bond length variations in boron-doped nanocrystalline diamond measured by spatially resolved electron energy-loss spectroscopy. *Appl. Phys. Lett.* **103**(3), 032105 (2013)
57. J. Li, H.D. Li, Asymmetric interlayer relaxation of the few-layer NB atomic sheets, Private communications
58. I. Aruna, B.R. Mehta, L.K. Malhotra, Faster H recovery in Pd nanoparticle layer based Gd switchable mirrors: size-induced geometric and electronic effects. *Appl. Phys. Lett.* **87**(10), 103101 (2005)
59. H.H. Liu, E.Y. Jiang, H.L. Bai, P. Wu, Z.Q. Li, Impact of atomic shells on the structure of cluster. *Chem. Phys. Lett.* **412**(1–3), 195–199 (2005)
60. C.Q. Sun, *Theory of size, confinement, and oxidation effects*. ed. by Rodríguez, M. Fernandez, J.A. Garcia. *Synthesis and Applications of Oxide Nanoparticles*, (Wiley, New York, 2007)

61. C.Q. Sun, Oxidation electronics: bond-band-barrier correlation and its applications. *Prog. Mater. Sci.* **48**(6), 521–685 (2003)
62. Y. Champion, F. Bernard, N. Millot, P. Perriat, Surface adsorption effects on the lattice expansion of copper nanocrystals. *Appl. Phys. Lett.* **86**(23), 231914 (2005)
63. Y.W. Duan, J.G. Li, Structure study of nickel nanoparticles. *Mater. Chem. Phys.* **87**(2–3), 452–454 (2004)
64. J.G. Li, Y. Qin, X.L. Kou, J.J. Huang, Microstructure and magnetic properties of $\text{Fe}_x\text{Ni}_{1-x}$ alloy nanoplatelets. *J. Nanosci. Nanotechnol.* **5**(10), 1699–1706 (2005)
65. Y.W. Duan, X.L. Kou, J.G. Li, Size dependence of structure and magnetic properties of $\text{La}_{0.7}\text{Sr}_{0.3}\text{MnO}_3$ nanoparticles. *Phys. B-Condens. Matter.* **355**(1–4), 250–254 (2005)
66. P.A. Montano, W. Schulze, B. Tesche, G.K. Shenoy, T.I. Morrison, Extended X-ray-absorption fine-structure study of Ag particles isolated in solid argon. *Phys. Rev. B* **30**(2), 672–677 (1984)
67. R. Lamber, S. Wetjen, N.I. Jaeger, Size dependence of the lattice-parameter of small palladium particles. *Phys. Rev. B* **51**(16), 10968–10971 (1995)
68. W.B. Mi, Z.Q. Li, P. Wu, E.Y. Jiang, H.L. Bai, D.L. Hou, X.L. Li, *Facing-target sputtered Fe-C granular films: Structural and magnetic properties.* *J. Appl. Phys.* **97**(4), 043903 (2005)
69. X.F. Yu, X. Liu, K. Zhang, Z.Q. Hu, The lattice contraction of nanometre-sized Sn and Bi particles produced by an electrohydrodynamic technique. *J. Phys.-Condens. Matter* **11**(4), 937–944 (1999)
70. D.R. Reddy, B.K. Reddy, Laser-like mechanoluminescence in ZnMnTe-diluted magnetic semiconductor. *Appl. Phys. Lett.* **81**(3), 460–462 (2002)
71. P.A. Montano, G.K. Shenoy, E.E. Alp, W. Schulze, J. Urban, Structure of copper microclusters isolated in solid argon. *Phys. Rev. Lett.* **56**(19), 2076–2079 (1986)
72. L.B. Hansen, P. Stoltze, J.K. Nørskov, B.S. Clausen, W. Niemann, Is there a contraction of the interatomic distance in small metal particles. *Phys. Rev. Lett.* **64**(26), 3155–3158 (1990)
73. H.C. Weissker, J. Furthmüller, F. Bechstedt, Structural relaxation in Si and Ge nanocrystallites: influence on the electronic and optical properties. *Phys. Rev. B* **67**(24), 245304 (2003)
74. W.J. Huang, R. Sun, J. Tao, L.D. Menard, R.G. Nuzzo, J.M. Zuo, Coordination-dependent surface atomic contraction in nanocrystals revealed by coherent diffraction. *Nat. Mater.* **7**(4), 308–313 (2008)
75. I. Robinson, Coherent diffraction: giant molecules or tiny crystals? *Nat. Mater.* **7**(4), 275–276 (2008)
76. J.T. Miller, A.J. Kropf, Y. Zha, J.R. Regalbutto, L. Delannoy, C. Louis, E. Bus, J.A. van Bokhoven, The effect of gold particle size on Au–Au bond length and reactivity toward oxygen in supported catalysts. *J. Catal.* **240**(2), 222–234 (2006)
77. P.D. Jadzinsky, G. Calero, C.J. Ackerson, D.A. Bushnell, R.D. Kornberg, Structure of a thiol monolayer-protected gold nanoparticle at 1.1 angstrom resolution. *Science* **318**(5849), 430–433 (2007)
78. D. Buttard, G. Dolino, C. Faivre, A. Halimaoui, F. Comin, V. Formoso, L. Ortega, Porous silicon strain during in situ ultrahigh vacuum thermal annealing. *J. Appl. Phys.* **85**(10), 7105–7111 (1999)
79. C.W. Mays, J.S. Vermaak, D. Kuhlmann, On surface stress and surface tension: II. determination of surface stress of gold. *Surf. Sci.* **12**(2), 134–140 (1968)
80. A.M. Stoneham, Comment on the lattice contraction of nanometre-sized Sn and Bi particles produced by an electrohydrodynamic technique. *J. Phys. Condens. Matter* **11**(42), 8351–8352 (1999)
81. H.J. Wasserman, J.S. Vermaak, On determination of a lattice contraction in very small silver particles. *Surf. Sci.* **22**(1), 164–172 (1970)
82. K.K. Nanda, S.N. Behera, S.N. Sahu, The lattice contraction of nanometre-sized Sn and Bi particles produced by an electrohydrodynamic technique. *J. Phys. Condens. Matter* **13**(12), 2861–2864 (2001)

83. Q. Jiang, L.H. Liang, D.S. Zhao, Lattice contraction and surface stress of fcc nanocrystals. *J. Phys. Chem. B* **105**(27), 6275–6277 (2001)
84. L.H. Liang, J.C. Li, Q. Jiang, Size-dependent melting depression and lattice contraction of Bi nanocrystals. *Phys. B-Condens. Matter* **334**(1–2), 49–53 (2003)
85. T. Toyama, D. Adachi, H. Okamoto, Electroluminescent devices with nanostructured ZnS: Mn emission layer operated at 20. *Mater. Res. Symp. Proc.* **621**(1) (2000)
86. J. Woltersdorf, A.S. Nepijko, E. Pippel, Dependence of lattice-parameters of small particles on the size of the nuclei. *Surf. Sci.* **106**(1–3), 64–69 (1981)
87. M. Zhao, X.H. Zhou, Q. Jiang, Comparison of different models for melting point change of metallic nanocrystals. *J. Mater. Res.* **16**(11), 3304–3308 (2001)
88. H. Müller, C. Opitz, K. Strickert, L.Z. Skala, *Phys. Chem. Leipzig.* **268**, 634 (1987)
89. G. Kellermann, A.F. Craievich, Structure and melting of Bi nanocrystals embedded in a B_2O_3 - Na_2O glass. *Phys. Rev. B* **65**(13), 134204 (2002)
90. G. Apai, J.F. Hamilton, J. Stohr, A. Thompson, Extended X-ray-absorption fine-structure of small Cu and Ni clusters—binding-energy and bond-length changes with cluster size. *Phys. Rev. Lett.* **43**(2), 165–169 (1979)
91. H.J. Wasserman, J.S. Vermaak, Determination of surface stress of copper and platinum. *Surf. Sci.* **32**(1), 168–174 (1972)
92. J.P. Liu, P. Zaumseil, E. Bugiel, H.J. Osten, Epitaxial growth of Pr_2O_3 on Si(111) and the observation of a hexagonal to cubic phase transition during postgrowth N-2 annealing. *Appl. Phys. Lett.* **79**(5), 671–673 (2001)
93. C.Q. Sun, Size dependence of nanostructures: Impact of bond order deficiency. *Prog. Solid State Chem.* **35**(1), 1–159 (2007)
94. K. Leung, K.B. Whaley, Surface relaxation in CdSe nanocrystals. *J. Chem. Phys.* **110**(22), 11012–11022 (1999)
95. L.W. Wang, A. Zunger, Pseudopotential calculations of nanoscale CdSe quantum dots. *Phys. Rev. B* **53**(15), 9579–9582 (1996)
96. E. Rabani, Structure and electrostatic properties of passivated CdSe nanocrystals. *J. Chem. Phys.* **115**(3), 1493–1497 (2001)
97. A. Puzder, A.J. Williamson, F.A. Reboredo, G. Galli, Structural stability and optical properties of nanomaterials with reconstructed surfaces. *Phys. Rev. Lett.* **91**(15), 157405 (2003)
98. B. Gilbert, F. Huang, H.Z. Zhang, G.A. Waychunas, J.F. Banfield, Nanoparticles: strained and stiff. *Science* **305**(5684), 651–654 (2004)
99. J. Nanda, D.D. Sarma, Photoemission spectroscopy of size selected zinc sulfide nanocrystallites. *J. Appl. Phys.* **90**(5), 2504–2510 (2001)
100. R.A. Street, *Hydrogenated amorphous silicon* (Cambridge University Press, Cambridge, 1991)
101. I.Y. Sklyadneva, G.G. Rusina, E.V. Chulkov, Vibrational states on vicinal surfaces of Al, Ag, Cu, Pd. *Surf. Sci.* **416**(1–2), 17–36 (1998)
102. A. Kara, S. Durukanoglu, T.S. Rahman, Local thermodynamic properties of a stepped metal surface: Cu(711). *Phys. Rev. B* **53**(23), 15489–15492 (1996)
103. P. Zhang, T.K. Sham, X-ray studies of the structure and electronic behavior of alkanethiolate-capped gold nanoparticles: the interplay of size and surface effects. *Phys. Rev. Lett.* **90**(24), 245502 (2003)

Chapter 13

End and Edge States: Entrapment and Polarization

- *The effective atomic CN of adatoms, atoms at terrace edges, and the ends of atomic chains is even lower than that of the flat surface (4 instead of 6).*
- *Quantum entrapment is global and polarization is subjective, depending on the electronic configuration in the valence band.*
- *Defects and edges are associated with local bond strain, entrapment, and the subjective polarization.*
- *Graphite monolayer skin only shows entrapment but the atomic van der Waals shows both entrapment and polarization—one neighbor short makes a great difference.*
- *Pt and Co islands exhibit entrapment dominance while Au, Ag, Rh, W edges and islands show both, which could be of use in classifying the catalytic nature of the undercoordinated specimens.*

13.1 Atomic Chains, Nanowires, and Clusters

13.1.1 Quantum Entrapment with Polarization

13.1.1.1 Au and Ag

Electron polarization frequently happens at sites surrounding atoms with even lower atomic CNs than that of a flat surface, namely four. As a consequence of the local polarization and entrapment, transition from conductor to semiconductor happens to small clusters such as ~ 3 -nm-sized Al nanoclusters deposited on Si substrate [1]. The broken-bond-induced densification and localization of electrons with lowered binding energy in the traps have been observed as defect states [2], chain end states [3, 4], terrace edge states [5–7], and surface states [8–10]. Strong localization of excess electrons also happens to the surface of ice [11] and metal films [12].

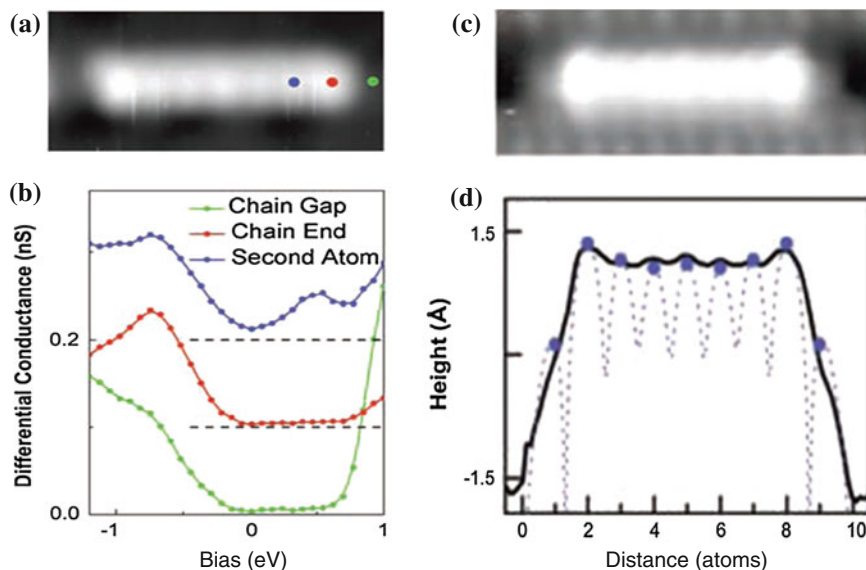


Fig. 13.1 STM/S profiles of **a** protrusions, **b** end states at -0.7 eV, **c** apparent height, and **d** the line scan difference between the ends and the chain interior of Au–Au atomic chain (reprinted with permission from [4])

Such polarization is responsible for the emerging properties of substance at the nanoscale, such as the extraordinary ability of catalysis, dilute magnetism, creation of Dirac–Fermi polarons, superhydrophobicity, etc.

Figure 13.1 shows the STM/S (a) image, (b) energy states, (c) apparent height, and (d) the line scan difference between the ends and the interior of an Au–Au chain [4]. The states at -0.7 eV at associated with the ends that are 0.02 – 0.03 nm higher in scale. The high protrusions and the edge states represent a high saturation and high energy of the surface charge, being the same to the dipoles induced by oxygen chemisorption [13]. The elevation of binding energy and saturation result from the localized polarization of the otherwise conduction electrons by electrons densely entrapped in the core and bonding orbits. STM/S profiles of (a) an Au nanowire and (b) the line scans crossing the wire at the different sites and the (c) corresponding dI/dV spectra, in Fig. 13.2, show the same trend to the chain ends. The narrow cross section enhances the polarization [14].

DFT calculations of Cubooctahedral (CO-13, 55, 147) and Marks Decahedral (MD-13, 49,75) gold clusters [15] result in the LDOS shown in Fig. 13.3. The size-induced polarization is consistent with STM/S observations and BOLS prediction. Calculations also confirmed the BOLS expected lattice strain, charge transfer in real space from the inner to the outermost atomic layer, and valence charge polarization from the lower to the higher binding energies of the well-

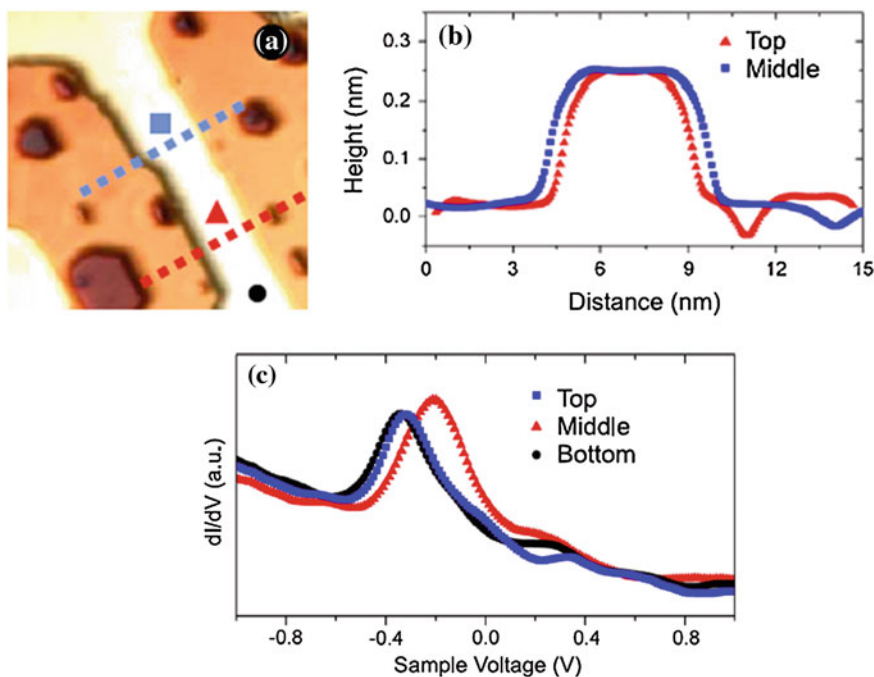


Fig. 13.2 STM/S profiles **a** of an Au nanowire and **b** the line scans crossing the wire at the *top*, *middle*, and *bottom* sites of different widths, and **c** the dI/dV spectra recorded at the respective locations demonstrate the width effect on the polarization of the occupied LDOS (reprinted with permission from [14])

defined gold clusters. Bonds between the less coordinated atoms at corners or at edges contract more significantly than those in the cluster interior. The Au–Au distance contracts up to 30 %, being in line with experimental observations of the Au cluster [16] and Au–Au chain bonds [17]. Meanwhile, the charge flows from the inner shell to the outermost of the clusters by an amount up to 1.5 electrons per atom, which agrees with the STM/S measurement from Au–Au chains deposited on NiAl(110) surface [18].

Figure 13.4 shows the STM/S profiles of a Ag monomer, Ag quasi-dimer, and Ag_2 dimer under positive bias [19]. The unoccupied states shift from 3.0 to 2.7 and to 2.4 eV with an increase in the effective CN of the system. Ag quasi-dimer remains somewhat the monomer nature, while the dimer exhibits the weakest polarization effect. The STS spectra in Fig. 13.4d acquired from clean Ag(111) surface, monomers (Ag_1), dimers (Ag_2), trimers (Ag_3), tetramers (Ag_4), pentamers (Ag_5), and a compact silver assembly (Ag_n) with $n = 10$ show the same trend of the undercoordination-induced polarization [20].

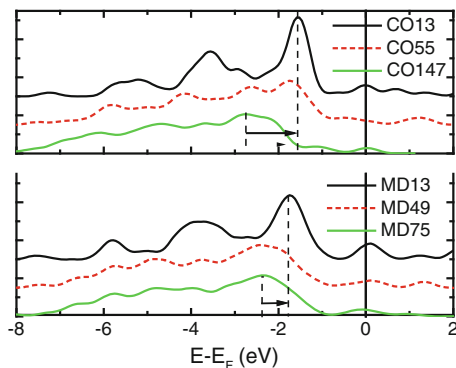


Fig. 13.3 Size-resolved valence LDOS of Au-MD and Au-CO clusters shows that as the number of atoms is reduced, the LDOS moves up toward E_F (positioned at 0) (reprinted with permission from [15]). The polarization trend agrees with STM/S observations of gold islands of different sizes [14] and gold monatomic chain [4]. The polarization is most significant of the lowest coordinated atoms

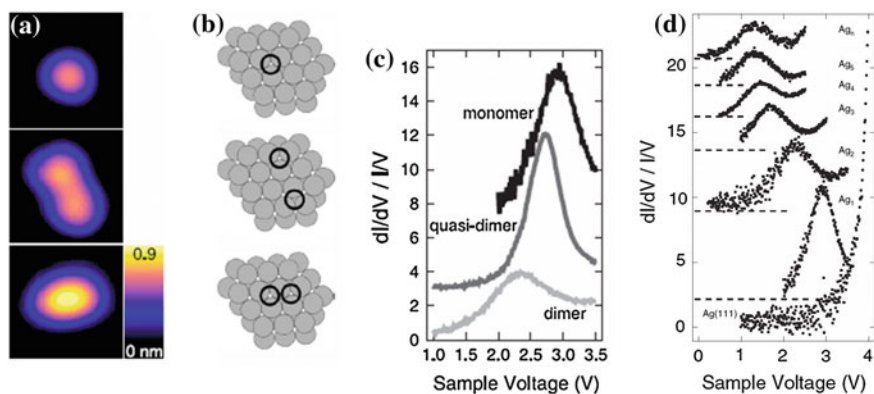


Fig. 13.4 STM/S profiles of **a** the undercoordination effect on the polarization of the unoccupied state of **b** a Ag monomer, Ag quasi-dimer, and a Ag_2 dimer under positive bias [19] with states **c** energies at 3.0, 2.7, and 2.4 eV for the unoccupied states. **d** Normalized STS spectra acquired from clean Ag(111) surface and Ag_n ($n = 1-5, 10$) clusters. The *dashed lines* indicate the respective zero of the spectra (reprinted with permission from [20])

13.1.1.2 Rh and W

The zone-selective XPS (ZPS) technique is able to distill the coordination-resolved electronic binding energy of adatoms or at sites surrounding defects, surfaces, interfaces, and solid skin with and without adsorption [21]. The ZPS is obtained by subtracting from the XPS profiles collected from the conditioned surfaces the referential XPS spectrum collected from the ideally perfect surface of the same substance. Before subtraction, all spectral peaks are background corrected and

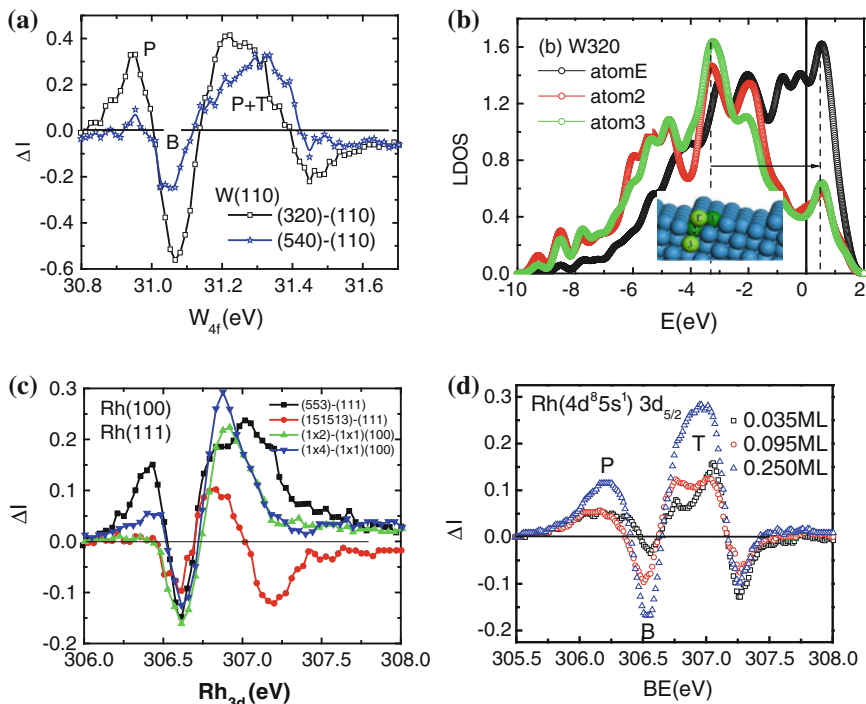
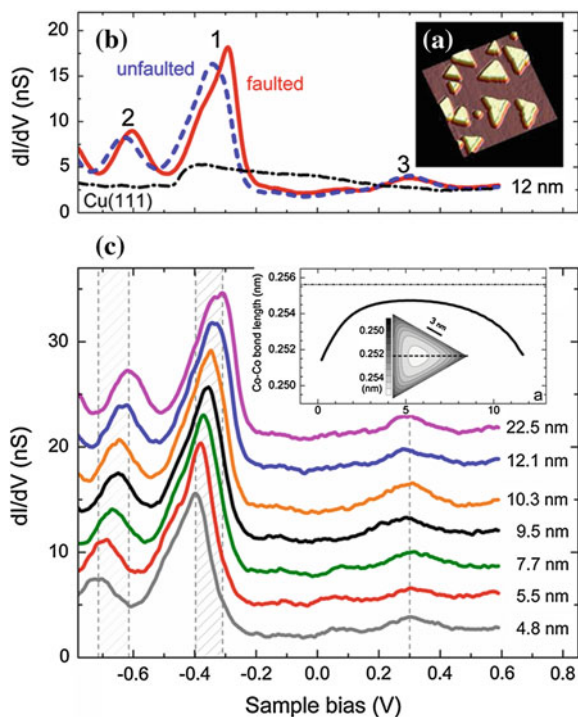


Fig. 13.5 ZPS profiles for **a** the W(540) (0.16 ML) and the W(320) (0.28 ML) surfaces with respect to the W(110) surface [24–27], **b** coordination-resolved valence LDOS of W(320) surface atoms [28], **c** Rh(111) vicinal (553) (0.26 ML) and (151,513) (0.07 ML) surfaces [29] and the missing-row type reconstructed Rh(100) surfaces. The reconstructed Rh(100) surfaces have the same edge density (0.5 ML) but slightly different atomic CNs [30]. ZPS profiles **d** of Rh atoms added on Rh(100) surface in different coverage [22]. Peaks above the bulk valley arise from the valence charge polarization that screens and splits the crystal potential and hence produces the T and P components. The valley at the bottom edge of the band represents the coupling effect of T and P

peak area normalized. Figure 13.5 shows the ZPS of undercoordinated W(110) and Rh(111) vicinal surfaces with different amounts of edge atoms, and Rh($5s^1$) adatoms on the Rh(001) surface [22] as well as the valence LDOS for the W(320) surface atoms [23].

All ZPS profiles show respectively a main valley corresponding to the bulk component. The peak above the valley results from polarization (P) of the otherwise valence electrons by the densely entrapped electrons (T) in the bonding and core orbits. The second peak and the second valley at the bottom edge of the bands result from the joint effects of entrapment and polarization. The locally polarized electrons screen and split the crystal potential and hence split the core band into the P and the T components, which has no effect on the bulk component. The valence LDOS of W(320) atoms exhibits apparently the CN-resolved polarization of W atom at the terrace edge, which is the same to the Au clusters in Fig. 13.3.

Fig. 13.6 Site-resolved Co–Co bond length and island size dependence of quantum entrapment of the valence states of Co islands [32]. Constant energy of the unoccupied states at 0.3 eV indicates absence of polarization effect.



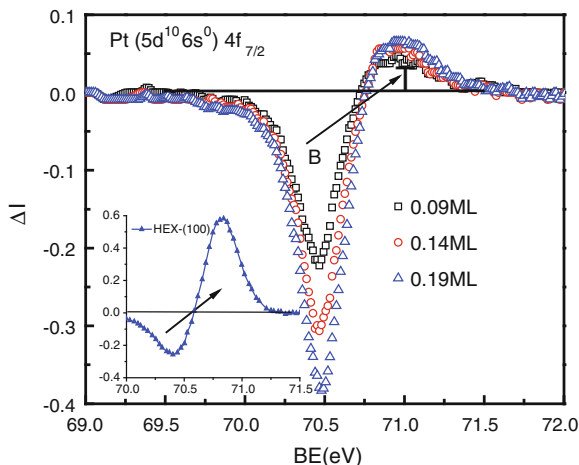
13.1.2 Entrapment Without Polarization

13.1.2.1 Co and Pt

Low-temperature STM/S profiles of Co nanoislands deposited on Cu(111) surface in Fig. 13.6 revealed that the occupied states shift downward from -0.3 to -0.4 eV as the island size is decreased from 22.5 to 4.5 nm. Inset shows that the lattice constant of Co islands contracts by 6 % from the bulk value of 0.251 to 0.236 nm at edges [31]. The presence of the entrapment and the absence of polarization of Co islands indicate that Co ($3d^7 4s^2$) atom lacks the unpaired valence electrons for being polarized. These results show the quantum entrapment without polarization.

Figure 13.7 shows the ZPS profiles of Pt atoms on the Pt(111) surface and the hexagonally reconstructed Pt(001) surface with vacancy edges [33]. Only the entrapped state presents without polarization. The valley at 70.5 eV corresponds to the bulk. The slight difference in the T peak between the adatoms (71.0 eV) and the vacancy edges (70.7 eV) indicates that Pt adatoms have effective CNs that are smaller than the vacancy edge atoms. The absence of polarization results from the lacking of the unpaired $5d^{10} 6s^0$ electrons of Pt.

Fig. 13.7 ZPS of Pt($5d^{10}6s^0$) adatoms (coverage in ML) revealed the entrapment without polarization (reprinted with permission from [22]). Valley B at 70.5 eV corresponds to the bulk component. Inset is the ZPS for the hexagonally reconstructed Pt(001) surface with denser edges [33]. The peak centered at 71.0 eV arises from the adatom-induced entrapment



13.2 Graphite Monolayer Skin and GNR Edges

13.2.1 Defect and Edge: Entrapment with Polarization

Upon the sp^2 -orbit hybridization, three sp^2 electrons of each carbon atom form σ bonds to its neighboring atoms in a C_{3v} symmetry and the non-bonding unpaired electron of the carbon develops into the π and π^* states at the corner of the Brillouin zone. The unrolled SWCNTs or called graphene nanoribbons (GNRs) [34] with open edges with two-coordinated carbon atoms. There are typically two types of GNRs classified by the shapes of edges. One is the armchair-edged AGNR with larger bandgap and semiconductive nature, and the other is the zigzag-edged ZGNR possessing the localized edge states with energy being at the Fermi level or above with more metallic feature. The E_G is roughly proportional to the inverse width of the GNRs. Atomic distances along the edges are different. For the AGNR edge, atomic separation is alternatively d and $2d$; for the ZGNR, it is $\sqrt{3}d$ identically.

Electrons of GNR are usually delocalized and dominate the electrical conductivity and the low-temperature thermal conductivity. However, near the edge of surface, these electrons are strongly localized and polarized by the deeply trapped bonding electrons, see Fig. 13.8a [35]. When the STM tip moves from the GNR interior toward the edge, the polarization becomes more pronounced and the Dirac peak moves nearer to E_F . As the vehicle of topological insulator, the edge Dirac states give rise to many unusual phenomena such as the unconventional magnetism that enables the carbon-only ferromagnetism, spin glass state, half-integer quantum Hall effect [36–39], ultrahigh electric and thermal mobility [40, 41], extremely low effective mass, and a group velocity of 1/300 times that of the light traveling in vacuum. However, the AGNR edge shows no polarization because the π -like

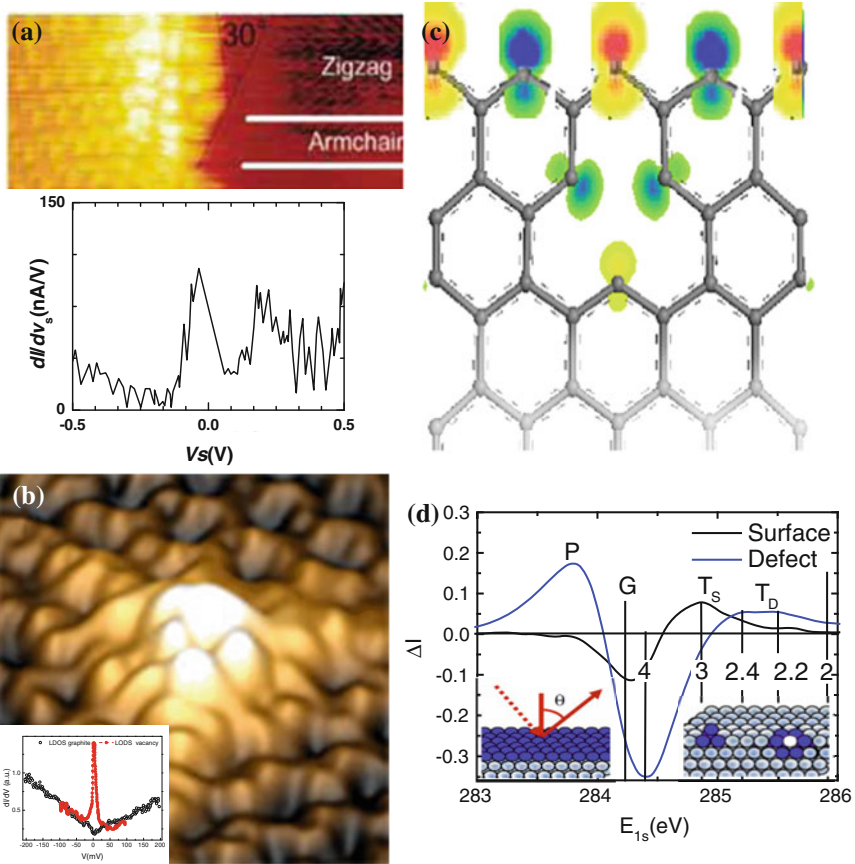


Fig. 13.8 STM/S profiles of **a** GNR with different edges (reprinted with permission from [44]), **b** graphite surface with and without vacancy defect (reprinted with permission from [45]), **c** the polarization of the z -edge and vacancy, and **d** the C1s ZPS profiles of the monolayer skin and the point defect of graphite (0001) surface. High protrusions and resonant states at E_F are the polarized dangling- σ -bond electrons. Armchair edge, graphite surface, and GNR interior show no signatures of polarization. C1s ZPS profiles indicate screening and splitting of the crystal potential by the defect dipoles create the T_S (surface, $z \sim 3.1$), T_D (defect, $z \sim 2.2 \sim 2.4$) entrapped components and the P states. The valley of the skin profile corresponds to the bulk component of graphite ($z = 5.335$). Defects were generated with $9 \times 10^{14} \text{ cm}^{-2}$ dosed Ar^+ spray, and the skin ZPS is the difference between spectra collected at 75° and 25°

bond formation between the nearest C atoms along the edge annihilates the dangling-bond electrons. Only a slight difference in separation between atoms lined along the AGNR and the ZGNR edges means a lot. One is semiconductor like and the other metallic like.

Atomic vacancy generated by Ar^+ spraying at a graphite surface [42] shares the same LODS features to that of the edge of ZGNR [43], as shown in Fig. 13.8: high STM protrusion and Dirac resonant peak at zero bias. The mobility of the vacancy

states is lower than the edge states. No such features can be resolved from graphite surface or from the GNR interior. Only one neighbor short makes a great difference between the defect and the surface in the electronic configuration. The ZPS profiles indicate indeed that the surface bonds are shorter and stronger than the bonds in the bulk; the bonds nearby defects are even shorter and stronger.

13.2.2 Monolayer Skin: Entrapment Without Polarization

Figure 13.8d compares the ZPS profiles of the monolayer skin and the vacancy defect of graphite. The skin ZPS shows only one entrapment without polarization, which is the same to the ZPS of Pt adatoms. However, the defect ZPS shows an entrapment peak that is even lower in energy and an additional polarization peak, which is similar to the Rh adatoms and W edges. A combination of the STM/S and the ZPS profiles provides a comprehensive picture on what has happened to the monolayer skin and the point defect of graphite, and the GNR edges:

1. Bonds between undercoordinated C atoms are shorter and stronger than that inside the bulk graphite.
2. Bonds at edges of defects of GNR are even shorter and stronger because of one more neighbor loss.
3. The edge dangling- σ -bond electrons in the vacant and ZGNR edge are polarized by electrons that are densely entrapped in the core and bonding orbits, which create the high STM protrusions and the resonant Dirac–Fermi states at E_F .
4. The polarons screen and split the local interatomic potential, resulting in the entrapped T and the polarized P states in the C1s band.
5. Because of the alternative d and $2d$ distances along the AGNR edge and the reconstructed-ZGNR edge, quasi- π -bond forms between the dangling-bond electrons and therefore no polarization happens at AGNR edges that perform like semiconductor.

13.2.3 CN-Resolved Bond Energy

Using an aberration corrected TEM, Girit et al. [46] uncovered that the minimal energy (7.5 eV/bond) required for breaking a 2-coordinated carbon atom near a vacancy is 32 % higher than that (5.67 eV/bond) required for breaking a 3-coordinated carbon atom in graphene interior. This finding is in line with the BOLS prediction that the broken bonds shorten and strengthen the neighboring bonds. Intensive XPS and Raman analyses and numerical calculations confirmed the BOLS prediction on the C–C bond attributes in different situations, see Table 13.1 [47–50].

Table 13.1 The length d_z and energy E_z of C–C bond and the electronic binding energy of the C1s band E_z of z -coordinated carbon atoms

| | z | C_z | d_z (nm) | E_z (eV) | C1s (eV) | P (eV) |
|------------------|-------|-------|------------|------------|----------|----------|
| Atom | 0 | – | – | – | 282.57 | |
| GNR edge | 2.00 | 0.70 | 0.107 | 1.548 | 285.89 | |
| Graphite | 2.20 | 0.73 | 0.112 | 1.383 | 285.54 | 283.85 |
| Vacancy | 2.40 | 0.76 | 0.116 | 1.262 | 285.28 | |
| GNR interior | 3.00 | 0.81 | 0.125 | 1.039 | 284.80 | |
| Graphite surface | 3.10 | 0.82 | 0.127 | 1.014 | 284.75 | |
| Graphite | 5.335 | 0.92 | 0.142 | 0.757 | 284.20 | |
| Diamond | 12.00 | 1.00 | 0.154 | 0.615 | 283.89 | |

$C_z = d_z/0.154$ is the bond contraction coefficient (reprinted with permission from [51])

13.2.4 DFT-TB Derivatives: Dirac–Fermi Polarons

Figure 13.9 shows the BOLS-TB (tight binding)-derived LDOS of edge-hydrogenated AGNR with an atomic vacancy. The vacancy creates a sharp resonant peak at E_F as demonstrated by graphite surface vacancy [45]. Arrows indicate that the separation between the bonding and the antibonding bands of the p_z electrons increases in magnitude once one moves from the inner to the edge and then to the vacancy site of the AGNR. Therefore, the extents of entrapment and polarization increase with the reduction in atomic z . This coordination trend of quantum entrapment is in accordance with the ZPS C1s energy shift [47]. The polarization of the unpaired non-bonding electrons by the densely entrapped bonding electrons results in the Dirac–Fermi polarons.

13.3 Summary

All undercoordinated systems demonstrate the electronic feature of global quantum entrapment and the subjective polarization. Undercoordinated atoms of Au, Ag, Rh, and W show both entrapment and polarization, while the undercoordinated Co and Pt atoms show only entrapment. One neighbor short makes the C atom at the defect site and the ZGNR edge to be completely different from that in the flat graphite surface and in the GNR interior and AGNR edge.

The ZPS bridges the STM/S and the XPS to clarify the physical origin of the end and edge states in various bands at the atomic scale. The physical picture for undercoordinated atoms is that the broken bond induces local strain and bond energy gain with an association of densification and entrapment of the core charge and energy; the densely and deeply trapped charge polarizes in turn the otherwise conducting electrons, leading to the STM/S-mapped protrusions and the Dirac resonant E_F states. The polarization of the non-bonding electrons will screen partially in turn and split the crystal potential, giving rise to the P states in the core

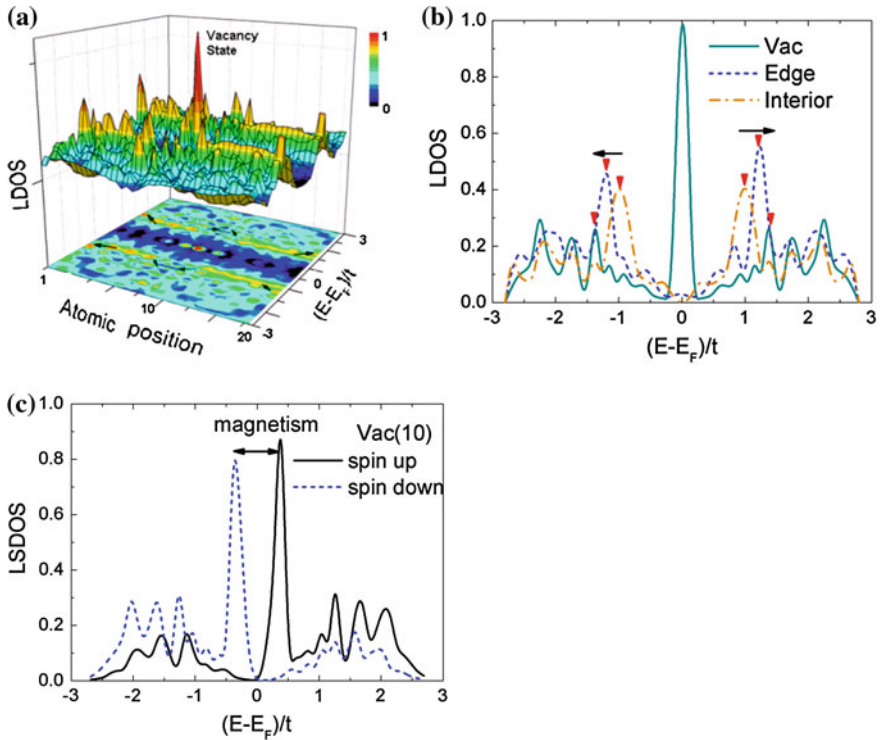


Fig. 13.9 **a** BOLS-TB-derived LDOS of the AGNR shows the E_F resonant peak at vacancy, being the same to that of graphite surface vacancy [45] and the ZGNR edge [52]. **b** The polarization and entrapment effect is more significant at vacancy site than that at the edge and at the GNR interior as arrows indicated. **c** The vacancy shows the spin-resolved LDOS features (reprinted with permission from [50])

bands. This procedure holds general for undercoordinated systems with non-bonding electrons such as the otherwise conduction electrons in the unpaired valence electrons of $\text{Ag}(5s^1)$, $\text{Au}(6s^1)$, $\text{Rh}(5s^1)$, etc. Situation reverses if the non-bonding electrons are absent such as $\text{Co}(3d^74s^2)$ and $\text{Pt}(6d^{10}5s^0)$. Anomalous states also exist such as $\text{W}(5d^46s^2)$ because of the mixed bands of valence charge of the higher quantum numbers.

References

1. Y. Jiang, K.H. Wu, J. Ma, B. Wu, E.G. Wang, P. Ebert, Quantum size effects in the nonmetal to metal transition of two-dimensional Al Islands. *Phys. Rev. B* **76**(23), 235434 (2007)
2. Y. Niimi, T. Matsui, H. Kambara, H. Fukuyama, STM/STS measurements of two-dimensional electronic states trapped around surface defects in magnetic fields. *Physica E* **34**(1–2), 100–103 (2006)

3. V.S. Stepanyuk, A.N. Klavsyuk, L. Niebergall, P. Bruno, End electronic states in Cu chains on Cu(111): ab initio calculations. *Phys. Rev. B* **72**(15), 153407 (2005)
4. J.N. Crain, D.T. Pierce, End states in one-dimensional atom chains. *Science* **307**(5710), 703–706 (2005)
5. Y. Kobayashi, K. Kusakabe, K. Fukui, T. Enoki, STM/STS observation of peculiar electronic states at graphite edges. *Physica E* **34**(1–2), 678–681 (2006)
6. K. Nakada, M. Fujita, G. Dresselhaus, M.S. Dresselhaus, Edge state in graphene ribbons: nanometer size effect and edge shape dependence. *Phys. Rev. B* **54**(24), 17954–17961 (1996)
7. S. Mattila, J.A. Leiro, M. Heinonen, T. Laiho, Core level spectroscopy of MoS₂. *Surf. Sci.* **600**(24), 1168–1175 (2006)
8. G. Fanchini, A. Tagliaferro, N.M.J. Conway, C. Godet, Role of lone-pair interactions and local disorder in determining the interdependency of optical constants of a—CN:H thin films. *Phys. Rev. B* **66**(19), 195415 (2002)
9. J. Ciston, L.D. Marks, R. Feidenhans'l, O. Bunk, G. Falkenberg, E.M. Lauridsen, Experimental surface charge density of the Si(100)-2 × 1H surface. *Phys. Rev. B* **74**(8), 085401 (2006)
10. T. Fauster, C. Reuss, I.L. Shumay, M. Weinelt, F. Theilmann, A. Goldmann, Influence of surface morphology on surface states for Cu on Cu(111). *Phys. Rev. B* **61**(23), 16168–16173 (2000)
11. A. Hermann, P. Schwerdtfeger, W.G. Schmidt, Theoretical study of the localization of excess electrons at the surface of ice. *J. Phys. Condens. Matter* **20**(22), 225003 (2008)
12. Z. Abbas, C. Labbez, S. Nordholm, E. Ahlberg, Size-dependent surface charging of nanoparticles. *J. Chem. Phys. C* **112**(15), 5715–5723 (2008)
13. C.Q. Sun, Oxidation electronics: bond–band–barrier correlation and its applications. *Prog. Mater. Sci.* **48**(6), 521–685 (2003)
14. K. Schouteden, E. Lijnen, D.A. Muzychenko, A. Ceulemans, L.F. Chibotaru, P. Lievens, C.V. Haesendonck, A study of the electronic properties of Au nanowires and Au nanoislands on Au(111) surfaces. *Nanotechnology* **20**(39), 395401 (2009)
15. X. Zhang, J.L. Kuo, M.X. Gu, X.F. Fan, P. Bai, Q.G. Song, C.Q. Sun, Local structure relaxation, quantum trap depression, and valence charge polarization induced by the shorter-and-stronger bonds between under-coordinated atoms in gold nanostructures. *Nanoscale* **2**(3), 412–417 (2010)
16. W.J. Huang, R. Sun, J. Tao, L.D. Menard, R.G. Nuzzo, J.M. Zuo, Coordination-dependent surface atomic contraction in nanocrystals revealed by coherent diffraction. *Nat. Mater.* **7**(4), 308–313 (2008)
17. C.Q. Sun, H.L. Bai, S. Li, B.K. Tay, C. Li, T.P. Chen, E.Y. Jiang, Length, strength, extensibility, and thermal stability of a Au–Au bond in the gold monatomic chain. *J. Phys. Chem. B* **108**(7), 2162–2167 (2004)
18. N. Nilius, M.V. Ganduglia-Pirovano, V. Brázdová, M. Kulawik, J. Sauer, H.J. Freund, Electronic properties and charge state of gold monomers and chains adsorbed on alumina thin films on NiAl(110). *Phys. Rev. B* **81**, 045422 (2010)
19. A. Sperl, J. Kroger, R. Berndt, A. Franke, E. Pehlke, Evolution of unoccupied resonance during the synthesis of a silver dimer on Ag(111). *N. J. Phys.* **11**(6), 063020 (2009)
20. A. Sperl, J. Kroger, N. Neel, H. Jensen, R. Berndt, A. Franke, E. Pehlke, Unoccupied states of individual silver clusters and chains on Ag(111). *Phys. Rev. B* **77**(8), 085422–085427 (2008)
21. C.Q. Sun, Atomic scale purification of electron spectroscopic information. USA patent: publication: 22 Dec 2011: WO 2011/159252, 2011: USA
22. C.Q. Sun, Y. Wang, Y.G. Nie, Y. Sun, J.S. Pan, L.K. Pan, Z. Sun, Adatoms-induced local bond contraction, quantum trap depression, and charge polarization at Pt and Rh surfaces. *J. Chem. Phys. C* **113**(52), 21889–21894 (2009)
23. Y. Wang, X. Zhang, Y. Nie, C.Q. Sun, Under-coordinated atoms induced local strain, quantum trap depression and valence charge polarization at W stepped surfaces. *Physica B* **407**(1), 49–53 (2012)

24. G.K. Wertheim, P.H. Citrin, Surface-atom core-level shifts of W(111). *Phys. Rev. B* **38**(11), 7820–7823 (1988)
25. A.M. Shikin, A. Varykhalov, G.V. Prudnikova, V.K. Adamchuk, W. Gudat, O. Rader, Photoemission from stepped W(110): initial or final state effect? *Phys. Rev. Lett.* **93**(14), 146802 (2004)
26. D.M. Riffe, B. Kim, J.L. Erskine, Surface core-level shifts and atomic coordination at a stepped W(110) surface. *Phys. Rev. B* **50**(19), 14481–14488 (1994)
27. K.G. Purcell, J. Jupille, G.P. Derby, D.A. King, Identification of underlayer components in the surface core-level spectra of W(111). *Phys. Rev. B* **36**(2), 1288–1291 (1987)
28. Y. Wang, X. Zhang, Y.G. Nie, C.Q. Sun, Under-coordinated atoms induced local strain, quantum trap depression and valence charge polarization at W stepped surfaces. *Physica B-Condens. Matter* **407**(1), 49–53 (2012)
29. J. Gustafson, M. Borg, A. Mikkelsen, S. Gorovikov, E. Lundgren, J.N. Andersen, Identification of step atoms by high resolution core level spectroscopy. *Phys. Rev. Lett.* **91**(5), 056102 (2003)
30. A. Baraldi, S. Lizzit, F. Bondino, G. Comelli, R. Rosei, C. Sbraccia, N. Bonini, S. Baroni, A. Mikkelsen, J.N. Andersen, Thermal stability of the Rh(110) missing-row reconstruction: combination of real-time core-level spectroscopy and ab initio modeling. *Phys. Rev. B* **72**(7), 075417 (2005)
31. O. Mironets, H.L. Meyerheim, C. Tusche, V.S. Stepanyuk, E. Soyka, P. Zschack, H. Hong, N. Jeutter, R. Felici, J. Kirschner, Direct evidence for mesoscopic relaxations in cobalt nanoislands on Cu(001). *Phys. Rev. Lett.* **100**(9), 096103 (2008)
32. M.V. Rastei, B. Heinrich, L. Limot, P.A. Ignatiev, V.S. Stepanyuk, P. Bruno, J.P. Bucher, Size-dependent surface states of strained cobalt nanoislands on Cu(111). *Phys. Rev. Lett.* **99**(24), 246102–246104 (2007)
33. A. Baraldi, E. Vesselli, L. Bianchettin, G. Comelli, S. Lizzit, L. Petaccia, S. de Gironcoli, A. Locatelli, T.O. Menten, L. Aballe, J. Weissenrieder, J.N. Andersen, The $(1 \times 1) \rightarrow$ hexagonal structural transition on Pt(100) studied by high-energy resolution core level photoemission. *J. Chem. Phys.* **127**(16), 164702 (2007)
34. K.S. Novoselov, A.K. Geim, S.V. Morozov, D. Jiang, Y. Zhang, S.V. Dubonos, I.V. Grigorieva, A.A. Firsov, Electric field effect in atomically thin carbon films. *Science* **306**(5696), 666–669 (2004)
35. Y. Kobayashi, K. Fukui, T. Enoki, K. Kusakabe, Edge state on hydrogen-terminated graphite edges investigated by scanning tunneling microscopy. *Phys. Rev. B* **73**(12), 125415 (2006)
36. Y.B. Zhang, Y.W. Tan, H.L. Stormer, P. Kim, Experimental observation of the quantum Hall effect and Berry's phase in graphene. *Nature* **438**(7065), 201–204 (2005)
37. X. Du, I. Skachko, F. Duerr, A. Luican, E.Y. Andrei, Fractional quantum Hall effect and insulating phase of Dirac electrons in graphene. *Nature* **462**(7270), 192–195 (2009)
38. K.I. Bolotin, F. Ghahari, M.D. Shulman, H.L. Stormer, P. Kim, Observation of the fractional quantum Hall effect in graphene. *Nature* **462**(7270), 196–199 (2009)
39. K.S. Novoselov, Z. Jiang, Y. Zhang, S.V. Morozov, H.L. Stormer, U. Zeitler, J.C. Maan, G.S. Boebinger, P. Kim, A.K. Geim, Room-temperature quantum hall effect in graphene. *Science* **315**(5817), 1379 (2007)
40. K.I. Bolotin, K.J. Sikes, Z. Jiang, M. Klima, G. Fudenberg, J. Hone, P. Kim, H.L. Stormer, Ultrahigh electron mobility in suspended graphene. *Solid State Commun.* **146**(9–10), 351–355 (2008)
41. A.A. Balandin, S. Ghosh, W. Bao, I. Calizo, D. Teweldebrhan, F. Miao, C.N. Lau, Superior thermal conductivity of single-layer graphene. *Nano Lett.* **8**(3), 902–907 (2008)
42. T. Enoki, Y. Kobayashi, K.I. Fukui, Electronic structures of graphene edges and nanographene. *Int. Rev. Phys. Chem.* **26**(4), 609–645 (2007)
43. Y. Niimi, T. Matsui, H. Kambara, K. Tagami, M. Tsukada, H. Fukuyama, Scanning tunneling microscopy and spectroscopy of the electronic local density of states of graphite surfaces near monoatomic step edges. *Phys. Rev. B* **73**(8), 085421–085428 (2006)

44. Y. Kobayashi, K. Fukui, T. Enoki, K. Kusakabe, Y. Kaburagi, Observation of zigzag and armchair edges of graphite using scanning tunneling microscopy and spectroscopy. *Phys. Rev. B* **71**(19), 193406 (2005)
45. M.M. Ugeda, I. Brihuega, F. Guinea, J.M. Gómez-Rodríguez, Missing atom as a source of carbon magnetism. *Phys. Rev. Lett.* **104**, 096804 (2010)
46. C.O. Girit, J.C. Meyer, R. Ermi, M.D. Rossell, C. Kisielowski, L. Yang, C.H. Park, M.F. Crommie, M.L. Cohen, S.G. Louie, A. Zettl, Graphene at the edge: stability and dynamics. *Science* **323**(5922), 1705–1708 (2009)
47. C.Q. Sun, Y. Sun, Y.G. Nie, Y. Wang, J.S. Pan, G. Ouyang, L.K. Pan, Z. Sun, Coordination-resolved C–C bond length and the C1s binding energy of carbon allotropes and the effective atomic coordination of the few-layer graphene. *J. Chem. Phys. C* **113**(37), 16464–16467 (2009)
48. X.X. Yang, J.W. Li, Z.F. Zhou, Y. Wang, L.W. Yang, W.T. Zheng, C.Q. Sun, Raman spectroscopic determination of the length, strength, compressibility, Debye temperature, elasticity, and force constant of the C–C bond in graphene. *Nanoscale* **4**(2), 502–510 (2012)
49. W.T. Zheng, C.Q. Sun, Underneath the fascinations of carbon nanotubes and graphene nanoribbons. *Energy Environ. Sci.* **4**(3), 627–655 (2011)
50. X. Zhang, Y.G. Nie, W.T. Zheng, J.L. Kuo, C.Q. Sun, Discriminative generation and hydrogen modulation of the Dirac–Fermi polarons at graphene edges and atomic vacancies. *Carbon* **49**(11), 3615–3621 (2011)
51. C.Q. Sun, Y. Nie, J. Pan, X. Zhang, S.Z. Ma, Y. Wang, W. Zheng, Zone-selective photoelectronic measurements of the local bonding and electronic dynamics associated with the monolayer skin and point defects of graphite. *RSC Adv.* **2**(6), 2377–2383 (2012)
52. K. Nakada, M. Fujita, K. Wakabayashi, K. Kusakabe. Localized electronic states on graphite edge. in 21st International Conference on Low Temperature Physics (LT 21). Prague, Czech Republic (1996)

Chapter 14

Thermal Stability: Atomic Cohesive Energy

- *Critical temperature for phase transition depends on the atomic cohesive energy that is the product of bond number and bond energy.*
- *The skin of a solid generally melts prior to the bulk (supercooling) and some interfaces melt at temperatures higher than the bulk melting point (superheating).*
- *Group IIIa and IVa atomic clusters show superheating because of the bond nature evolution.*
- *A dual-shell model describes the T_C for ferromagnetic, ferroelectric, and superconductive phase transitions because of the involvement of both the long- and the short-range interactions.*
- *Activation energy for diffusion and epitaxial growth is proportional to the atomic cohesive energy; growing temperature controls the crystal size and associated properties.*

14.1 Cohesive Energy

14.1.1 Definition

The cohesive energy of a solid (E_{coh}) is an important quantity used to accounting for the binding strength of a crystal. The E_{coh} is equal to the energy dividing the entire crystal into the individually isolated atoms by breaking all bonds involved. The E_{coh} is given as: $E_{\text{coh}}(N) = NE_B = Nz_bE_b$, if no atomic CN imperfection is considered. The cohesive energy for an atom in the bulk, or atomic coherency, E_B , is the sum of the bond energy E_b over all its atomic CN, $E_B = z_bE_b$, for a specific atom in the bulk, $E_{Bz} = zE_z$ is the cohesive energy for an atom with z neighbors.

The heat required for releasing an atom from a solid is the right atomic cohesive energy. Phase transition by loosening the atom requires energy that is a fraction of the E_B . The atomic E_B varies with, not only the atomic CN, but also the CN

reduction induced bond strength gain. The under-coordinated surface atoms will be generally less thermally stable than those inside the core interior, unless the strength gain of the remaining bonds overcomes the effect of coordination reduction, $E_{Bz} > E_B$. For large bulk materials, effects of surface CN imperfection is negligible but, for small particles, surface effects become dominant because of the appreciably large fraction of such under-coordinated atoms at the surface.

The mean value of the E_{Bz} is responsible for the fall (undercooling) or rise (overheating) of the T_m of a surface and a nanosolid. The E_{Bz} is also responsible for other thermally activated behavior such as phase transition, catalytic reactivity, crystal structural stability, alloy formation (segregation and diffusion), and stability of electrically charged particles (Coulomb explosion), as well as the crystal growth and atomic diffusion, atomic gliding displacement that determine the ductility of nanosolids.

14.1.2 Known Mechanisms

14.1.2.1 Surface Area Difference

One approach to determine the E_{coh} of a nanosolid is to consider the difference between the surface area of the entire particle and the overall surface area of all the constituent atoms being isolated one from another [1]. For a spherical dot with R radius and N atoms of diameter d_0 , the E_{coh} equals to the energy required to generate the area difference, ΔS , between the isolated N atoms and the nanodot without changing the volume:

$$\begin{cases} N4\pi(d_0/2)^3/3 = 4\pi(R)^3/3 & \text{(volume-conservation)} \\ \Delta S = \pi[Nd_0^2 - (2R)^2] & \text{(Surface-area-difference)} \end{cases}$$

Letting the surface energy per unit area at 0 K be γ_0 , and then the overall $E_{coh}(N)$ is,

$$\begin{cases} E_{coh}(K) = \gamma_0 \Delta S & = \pi N d_0^2 \gamma_0 (1 - N^{-1/3}) \\ & = E_{coh}(\infty) (1 - \alpha/K) \end{cases}$$

$E_{coh}(\infty) = \pi N d_0^2 \gamma_0$ is the cohesive energy of the N atoms without the effect of atomic CN imperfection. The factor α varies with the shape and dimensionality of the solid. For a cube, the factor is 9/4 [1]; for a spherical dot, it is 1/2.

Considering situations of both the isolated and the embedded nanosolids with involvement of the interface and surface contributions [2]:

$$E_{B,s} = [E_B + 3\beta(E_B/2 + kE_m/2)]/4$$

yields the mean atomic cohesive energy,

$$\begin{aligned} E_B(K) &= E_B + \gamma_0(E_{B,S} - E_B) \\ &= E_B + 3\gamma_0[k\beta E_m - (2 - \beta)E_B]/8 \end{aligned}$$

where β is the ratio of the interface area to the entire surface area, k denotes the degree of cohesion between the nanocrystal and the matrix with atomic cohesive energy E_B . For a nanocrystal wholly embedded in the matrix, $\beta = 1$ and $k = 1$; for an isolated crystal, $\beta = 0$ and $k = 0$ [3].

14.1.2.2 Atomic CN Difference

By considering the effect of surface CN imperfection, Tomanek et al. [4] derived the E_B for an individual atom denoted i :

$$E_{B,i} = (z_i/z_b)^{1/2}E_B(\infty) + E_R$$

E_R representing the repulsive interaction is negligible at equilibrium. The mean E_B in a nanosolid is obtainable by summing all bonds over all the N atoms:

$$\langle E_B(N) \rangle = \sum_{\langle i,N \rangle} (z_i)^{1/2} E_i / N$$

A theory established based on the framework of the latent heat and the size-dependent cohesive energy agrees with experimental data results of W and Mo nanosolids [5].

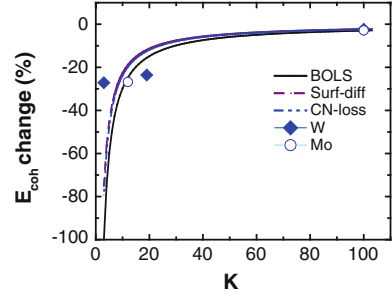
14.1.3 BOLS Formulation

The BOLS notation considers variation of atomic E_{coh} from atoms in the skin only. Using the same spherical dot containing N atoms with N_i atoms in the i th surface shell, the average $\langle E_{\text{coh}}(N) \rangle$, or $\langle E_B(N) \rangle$ is,

$$\begin{aligned} \langle E_{\text{coh}}(N) \rangle &= Nz_b E_b + \sum_{i \leq 3} N_i (z_i E_i - z_b E_b) \\ &= NE_B(\infty) + \sum_{i \leq 3} N_i z_b E_b (z_{ib} E_{ib} - 1) \\ &= E_{\text{coh}}(\infty) \left[1 + \sum_{i \leq 3} \gamma_i (z_{ib} C_i^{-m} - 1) \right] \\ &= E_{\text{coh}}(\infty) (1 + \Delta_B) \end{aligned} \tag{14.1}$$

or, $\langle E_B(N) \rangle = E_B(\infty) (1 + \Delta_B)$

Fig. 14.1 Comparison of the modeling predictions with experimental results on the size-dependent E_B of Mo and W nanosolids [6]. Numerical agreement is nearly identical for the compared models albeit the different physical origins (Reprinted with permission from [7])



where $E_{\text{coh}}(\infty) = Nz_b E_b$ represents the ideal situation without CN imperfection. The $z_{ib} = z_i/z_b$ is the normalized CN and $E_{ib} = E_i/E_b \cong C_i^{-m}$ is the binding energy per coordinate of a surface atom normalized by the bulk value. For a free surface, $\Delta_B < 0$; for an intermixed interface, Δ_B may vary depending on the interfacial bond energy.

The following scaling relationships formulate the size dependence of E_B ,

$$\frac{\Delta E_B(K)}{E_B(\infty)} = \begin{cases} \sum_{i \leq 3} \gamma_i (z_{ib} c_i^{-m} - 1) = \Delta_B & \text{(BOLS)} \\ \sum_{i \leq 3} \gamma'_i [(z_{ib})^{1/2} - 1] = \Delta'_B & \text{(CN-loss)} \\ -\alpha/K = \delta_B & \text{(Area-difference)} \end{cases} \quad (14.2)$$

where $\gamma_i \sim \tau C_i/K$ and $\gamma'_i \sim \tau_i/K$ are the surface-to-volume ratio in the corresponding formulations. Figure 14.1 shows the match between these notations and measurements of the size-dependent $\langle E_B(K) \rangle$ of Mo and W nanosolids [6]. From a numerical viewpoint, one could hardly tell which model is preferred to others though physical indications of the compared models are different.

14.1.4 Atomic Vacancy Formation

As an element of structural defects, atomic vacancies, or point defects are very important in materials and have remarkable effect on the physical properties of a material such as electrical resistance, heat capacity, and mechanical strength. A vacancy formation is associated with local strain, densification, quantum entrapment, and polarization.

Atomic vacancy formation needs energy to break all the bonds of the specific atom to its surroundings, which is the same to the atomic E_B though structure deformation or relaxation is involved upon vacancy formation. However, the structural deformation or relaxation costs no additionally external energy. Vacancy volume should be greater than the atomic size because of the atomic CN imperfection induced contraction of bonds surrounding the vacancy. The measured E_B is subject to accuracy. For instance, the E_B of a Mo atom varies from 2.24 to 3.30 eV [8].

Theoretical efforts can predict the E_B of limited numbers of metals and alloys, but the theories are rather complicated [9].

14.1.4.1 Brook's Convention

Brooks [10] assumed the crystal is isotropic and considered the formation of a vacancy as an equivalent to creating new surface, equal to the area of one unit cell, being approximately the spherical surface of the atomic volume. He also assumed that the surface tension of the hole would shrink the vacancy size by distorting the rest of the crystal elastically. Then, the E_B for atomic vacancy formation inside a bulk solid equals the minimum of the sum of the increased surface energy and distortion energy,

$$E_B = \pi d_0^3 \gamma_0 G (\gamma_0 + G d_0)^{-1}$$

G is the shear modulus and γ_0 the surface energy per unit area surrounding the vacancy. Introducing the size effect to the d_0 , G , and γ_0 , the relative change in the mean E_B in a nanoparticle becomes,

$$\frac{E_p - E_B}{E_B} = \frac{d_p^3}{d_0^3} \left(\frac{G d_0 + \gamma_0}{G d_p + \gamma_0} \right) - 1$$

where E_p and d_p are the corresponding vacancy formation energy and mean atomic diameter in the nanosolid.

An extension of Brook's approach to nanostructures assumed that the G and the γ_0 of a nanosolid remain the bulk values [11]. The key factor influencing the E_p of a spherical dot of diameter D is the size-dependent atom size. Assuming that a small shrink of εD ($\varepsilon \ll 1$) results from the hole volume contraction, the surface energy variation $\Delta\gamma$, and the strain-dependent elastic energy f of the particle become,

$$\begin{aligned} \Delta\gamma &= \pi D^2 \left[(1 - \varepsilon)^2 - 1 \right] \gamma_0 \\ f &= \pi G D^3 \varepsilon^2 \end{aligned} \quad (14.3)$$

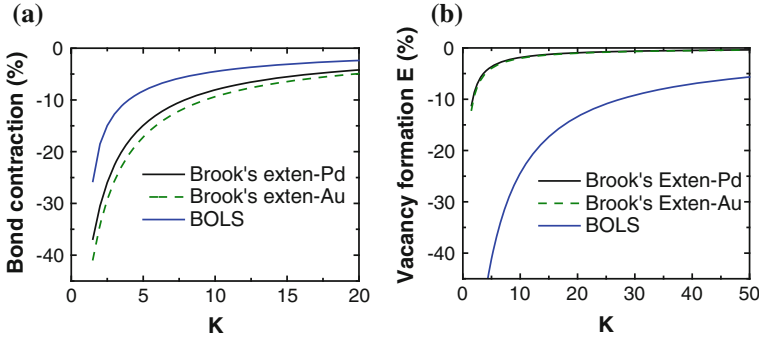
At equilibrium, the total energy F , or the sum of $\Delta\gamma$ and f , is minimal, that is, $dF/d\varepsilon = 0$, and then, the strain of the particle becomes

$$\varepsilon = [1 + (G/\gamma_0)D]^{-1}$$

The average size d_p of an atom shrinks due to the presence of G and γ_0 , $d_p = d_0(1 - \varepsilon)$.

Table 14.1 Shear modulus, surface energy and the calculated α values for Pd and Au

| | G (10^{10} N/m ²) [12] | γ_0 (J/m ²) [13] | α /nm | K_{Ec}/K_{dc} |
|----|---|-------------------------------------|--------------|-----------------|
| Pd | 4.36 | 2.10 | 0.104 | 0.1894/0.8770 |
| Au | 2.60 | 1.55 | 0.119 | 0.2066/1.035 |

**Fig. 14.2** Comparison of **a** the bond (particle size) contraction and **b** atomic vacation-formation energy derived from the BOLS premise and from Brook's approach for Pd and Au nanosolids (Reprinted with permission from [7])

14.1.4.2 BOLS Formulation

The following compares Brook's approximation and the BOLS correlation on the bond strain of a nanosolid:

$$\frac{\Delta d_p}{d_0} = \begin{cases} -[1 + (G/\gamma_0)D]^{-1} \cong -K_{dc}/(K + K_{dc}) & \text{(Brook)} \\ \sum_{i \leq 3} \gamma_i (C_i - 1) = \Delta_d & \text{(BOLS)} \end{cases}$$

where $K_{dc} = \gamma_0/(2d_0G)$ is the critical value and K remains its usual meaning of dimensionless form of size. Further simplification of Eq. (14.3) leads to the atomic vacancy formation energy in a nanometric system as given in comparison with the BOLS derivative:

$$\frac{\Delta E_B(K)}{E_B(\infty)} = \begin{cases} -(1 + K/\alpha)^{-1} \cong -K_{Ec}/(K_{Ec} + K) \\ \sum_{i \leq 3} \gamma_i (z_{ib} C_i^{-m} - 1) = \Delta_B \end{cases} \quad (14.4)$$

where $\alpha = (2gd_0 + 3)/[2d_0(g^2d_0 + g)]$ ($\sim 10^{-1}$ level) and $g = G/\gamma_0 \sim 10$ nm⁻¹. $K_{Ec} = \alpha/(2d_0)$ is the critical value of K . For Pd and Au nanosolids, the critical K_{Ec} and E_{dc} values are calculated based on the given G and γ_0 bulk values, as listed in Table 14.1.

Figure 14.2 compares the predictions of the two models. At the lower end of the size limit ($K = 1.5$), the particle diameter contracts by 40 % associated with 12 % reduction in the E_B according to Brook's convention [11]. In comparison, the

BOLS correlation predicts a 25 % bond contraction and 70 % lower of the E_B for the smallest size. The approximation based on Brook's relation overestimates the bond contraction and underestimates the E_B suppression because of the assumption of size-independent G and γ_0 . Actually, the atomic vacancy should expand instead as the remaining bonds of the surrounding atoms contract. The strain of the entire nanoparticle arises from surface bond contraction and has little to do with the atomic void inside. One may note that E_B varies from site to site due to the difference of atomic CN environment at various locations of the solid.

14.2 Liquid–Solid Phase Transition

14.2.1 Undercooling: Skin Pre-Melting

Undercooling and overheating are the mostly attended activities of materials at the nanoscale. In many cases, surface liquidation and evaporation often occur at temperatures lower than the corresponding bulk values [14–16]. Likewise, liquid surface freezes at lower temperatures [17]. For substrate-supported nanosolids with relatively free surfaces, the T_m decreases with particle size (termed as undercooling). In contrast, as per the existing experimental evidence for embedded nanosolids, the T_m can be lower than the bulk T_m for some matrices. However, the same nanosolid embedded in some other different matrices may melt at temperatures higher than the bulk T_m (overheating). Overheating of 115 K occurs to Pb(111) films confined in an Al(111) matrix [18]. The T_m suppression for a free surface corresponds to the reduced degree of confinement and the increased entropy of the molecules at the surface compared with atoms in the bulk, whereas the T_m elevation or depression of the embedded nanosolids depends on the coherency between the nanosolids and the embedding matrix [19, 20].

There is an extensive database describing surface and nanosolid T_m suppression [21–26]. For instance, a photoelectron emission study [27] confirmed that lithium (110) surface melting occurs 50 K below the bulk T_m (454 K). A temperature-resolved XRD analysis revealed that the T_m of nanometer-sized drugs (polymer) also drops (by 33 and 30 K for 7.5-nm-sized griseofulvin and 11.0-nm-sized nifedipine, respectively) in a 1/R fashion [28]. STM measurements of a reversible, temperature-driven structural surface phase transition of Pb/Si(111) nanoislands indicates that the transition temperature decreases with inverse of domain size and the phase transition is independent of the processes of cooling or heating [29].

The T_m of a Pd nanowire is lower than the bulk value but higher than that of the cluster with countable number of atoms proceeding in a surface pre-melting manner. A quasi-liquid skin grows from the surface radially inward for both cluster and wire, followed by a breakdown of order in the remaining solid core at the transition temperature [30].

The size effect on the nanosolid melting has been modeled in terms of classical thermodynamics and atomistic MD simulations [31–46]. In general, the size-dependent $T_m(K)$ follows the empirical scaling relationship:

$$\frac{\Delta T_m(K)}{T_m(\infty)} = -\frac{K_C}{K}, \quad (14.5)$$

where K_C is the critical size at which the nanosolid melts completely, or the $T_m(K_C) = 0$ K. The physics behind the K_C is the focus of modeling studies.

14.2.1.1 Classical Thermodynamics

Classical thermodynamics based on the surface Laplace and the Gibbs–Duhem equations [43] have derived that K_C obeys the following relations [41, 44]:

$$K_C = \frac{-2}{H_m(\infty)} \times \begin{cases} \sigma_{sv} - \sigma_{lv}(\rho_s/\rho_l)^{2/3}, & \text{(HGM)} \\ \sigma_{sl}(1 - K_0/K)^{-1} + \sigma_{lv}(1 - \rho_s/\rho_l), & \text{(LSM)} \\ [\sigma_{sl}, 3(\sigma_{sv} - \sigma_{lv}\rho_s/\rho_l)/2] & \text{(LNG)} \end{cases}$$

where H_m is the latent heat of fusion. ρ is the mass density and σ the interfacial energy. Subscripts s , l , and v represent the phases of solid, liquid, and vapor, respectively. The critical value of $R_C (= K_C d_0)$ is normally several nanometers. These expressions correspond to three outstanding mechanisms in terms of classical thermodynamics:

1. The homogeneous melting and growth (HMG) model [32, 33] considers the equilibrium between the entire solid and the entire molten particle, which suggests that the melt proceeds throughout the solid simultaneously. This model describes well the case of smallest nanoparticle with K_C equal to three or less or otherwise to larger values with void defects being involved.
2. The liquid shell nucleation (LSN) model [34] assumes that a liquid layer of thickness K_0 is in equilibrium at the surface, which indicates that the surface melts before the core of the solid.
3. The liquid nucleation and growth (LNG) model [37, 38] suggests that melting starts by the nucleation of a liquid layer at the surface and moves into the solid as a slow process with a definite activation energy. The LSN and the LNG are valid to the melting of a flat surface or a larger nanoparticle.

14.2.1.2 Atomistic Models

Models based on atomistic/MD attribute the critical R_C to:

$$R_C = \begin{cases} 5,230 v_0 \gamma, & (v_0 = 4\pi d_0^3/3) & \text{(Liquid-drop)} \\ \alpha_m d_0, & (\alpha_m - \text{constant}) & \text{(Surf-phonon)} \\ R_0 \left(\frac{1-\beta}{1-R_0/R} \right), & & \text{(Surf-RSMD)} \end{cases} \quad (14.6)$$

The liquid-drop model [47] relates the T_m to the E_{coh} of the entire particle of N atoms. With the involvement of surface, the E_{coh} equals the difference between the volume cohesive energy (NE_B) and the surface energy ($4\pi d_0^2 N^{2/3} \gamma$). The mean cohesive energy per atom with volume v_0 in the solid is $E_B(R) = E_B - E_{B,S} N^{-1/3}$, where $E_{B,S} = 4\pi d_0^2 \gamma$ is the cohesive energy for an atom at the surface. The relation between the E_B and the $E_{B,S}$ is given empirically as, $E_{B,S} = 0.82 E_B$ [48]. Based on the Lindemann's criterion of melting, the T_m of the bulk material follows [49],

$$T_m(\infty) = n f_c^2 E_B / (3k_B Z) \propto E_B \quad (14.7)$$

where n is the exponent of the repulsive part of the interaction potential between constituent atoms, Z is the valence of the atom, which is different from the atomic CN (z). The coefficient f_c is the thermal expansion magnitude of an atom at T_m . At T_m , the f_c is less than 5 % [50, 51]. The T_m depends simply on the mean atomic $\langle E_B(K) \rangle$ of the solid. Replacing the E_B with the size-resolved $E_B(K)$, Nanda et al. [47] derived the liquid-drop model for the $T_m(K)$ based on the relation:

$$E_b(\infty) = \eta_{1b} T_m(\infty) + \eta_{2b} \quad (14.8)$$

where the constant η_{2b} represents $1/z$ -fold of the enthalpy of fusion and atomization, which is required for evaporating an atom from the molten state. η_{1b} is the specific heat per coordinate in the bulk. The η_{1b} and η_{2b} values are tabulated in Table 14.1 [47]. According to the liquid-drop notation, the critical radius at which $T_m(K_C)$ approaches 0 K is in the range of 0.34 (for Mn) and 1.68 nm (for Ga) [47].

The surface-phonon instability model [40, 52, 53] suggests that the $T_m(K)$ varies with $T_m(\infty)$ and with the energy for defect formation at the surface. Within the thermodynamic limit (particle radius larger than 2 nm), the effects of size reduction and electronic excitation combine [54].

The lattice-vibration instability model [40, 55–59] extends Lindemann's vibrational-lattice instability criterion [60]. The melting behavior of a nanosolid is related to the ratio (β) of the root-mean-square displacement (RMSD, δ^2) of an atom at the surface to the RMSD of an atom inside a spherical dot. β is a size-independent parameter:

$$\beta = \delta_s^2(D) / \delta_b^2(D) = \delta_s^2(\infty) / \delta_b^2(\infty)$$

The K_C is determined by $K_0 = \tau$ (dimensionality) at which all the constituent atoms have surface features. This model indicates that if $\beta > 1$, the surface melts below the bulk T_m , and vice versa. According to the RMSD, a nanosolid of $K_C = \tau$ radius will melt at 0 K.

14.2.2 Overheating: Interface Effect

In the case of embedded nanosolids, the coefficient of surface energy will be replaced by the interfacial energy if surfaces are completely saturated with atoms of the surrounding matrix. Nanda et al. [47] introduced the ratio as a perturbation of surface energy between the matrix and the embedded specimen,

$$\frac{\Delta T_m(K)}{T_m(\infty)} = -\frac{K_C}{K} \left(1 - \frac{\gamma_{Mat}}{\gamma} \right)$$

If the surface energy of the matrix $\gamma_{Mat} > \gamma$, the core nanosolid melts at a temperature that is higher than its bulk counterpart. This expression matches the experimental data of Pb particles embedded in an Al matrix but overestimates the T_m for Indium particles embedded in an Al matrix by some 10–20 K using the known γ and γ_{Mat} values.

Based on the size-dependent magnitudes of the atomic vibrations, Jiang et al. [40, 61] extended the $T_m(K)$ model for the overheating, according to which overheating is possible if the diameter of the matrix atoms is smaller than the atomic diameter of the embedded nanosolid. Therefore, adjusting the β value in the *RMSD* model describes both overheating and undercooling of a nanosolid. Overheating happens when $\beta < 1$, which means that the matrix confines the vibration of the interfacial atoms.

However, MD simulations [62] suggest that atoms in the bulk interior of a freestanding nanosolid melt prior to the surface that melts at relatively higher temperatures. This prediction seems to be conflicting with existing database but as discussed shortly for the overheating of the smallest Ge⁺ and Sn clusters. In contrast, MD calculations [63] of the melting evolution, atomic diffusion and vibrational behavior of bcc metal vanadium nanoparticles with diameters around 2–9 nm suggest that the melting proceeds in two stages. A stepwise pre-melting of the skin of two or three atomic layers happens first and then an abrupt melting of the entire cluster follows. The heat of fusion of nanoparticles is also inversely proportional to the nanoparticle size.

The models of LSN, HMG and LNG suit only the cases of T_m suppression ($\Delta T_m < 0$) while the liquid-drop and the RMSD models cover both the undercooling and the overheating. For particles larger than several nanometers, all the models worked sufficient well despite the disputable mechanisms.

14.2.3 BOLS Formulation

A Taylor's series of the binding energy of a pair of atoms can be decomposed as energies of binding at 0 K, $E_b(d_0)$, and the thermal vibration energy, $E_V(T)$:

$$\begin{aligned}
E_{\text{total}}(r, T) &= \sum_n \left(\frac{d^n u(r)}{n! dr^n} \right)_{r=d_0} (r - d_0)^n \\
&= u(d_0) + 0 + \frac{d^2 u(r)}{2! dr^2} \Big|_{d_0} (r - d_0)^2 + \frac{d^3 u(r)}{3! dr^3} \Big|_d (r - d_0)^3 \dots \\
&= E_b(d_0) + \frac{k}{2} (r - d_0)^2 + \frac{k'}{6} (r - d_0)^3 + \dots \\
&= E_b(d_0) + E_V(T) = \begin{cases} 0, & (\text{Evaporation}) \\ E_C, & (\text{Critical} - T_C) \end{cases}
\end{aligned} \tag{14.9}$$

The term of $n = 0$ corresponds to the minimal binding energy at $T = 0$ K, $E_b(d_0) < 0$. The term $n = 1$ is the force $[\partial u(r)/\partial r]_{d_0} = 0$ at equilibrium and terms with $n \geq 2$ correspond to the thermal vibration energy, $E_V(T)$. The T_C can be any critical temperature for event such as liquid–solid, liquid–vapor, or other phase transition, like magnetic and ferroelectric transitions. By definition, the thermal vibration energy of a bond is,

$$\begin{aligned}
E_V(T) &= \frac{d^2 u(r)}{2! dr^2} \Big|_d (r - d)^2 + \frac{d^3 u(r)}{3! dr^3} \Big|_d (r - d)^3 \dots \\
&\cong \mu \omega^2 (r - d)^2 / 2 + 0[(r - d)^{n > 2}] \\
&\approx k_v (r - d)^2 / 2 = \eta_1 T
\end{aligned} \tag{14.10}$$

where $r - d_0$ is the magnitude of lattice vibration. μ is the reduced mass of a dimer of concern. The term $q_v = \mu \omega^2$ is the force constant for lattice vibration with an angular frequency ω .

The physical argument for the BOLS iteration is that, if one wishes to peel off or loosen an atom in the solid thermally, one must supply sufficient thermal energy to overcome the cohesion that binds the specific atom to its surrounding neighbors. The thermal energy required to loosen one bond is the separation of $E_b(T_C) - E_b(T)$, see Sect. 14.2. If the $E_V(T)$ is sufficiently large, all the bonds of the specific atom will break and this atom will leave the solid. At the evaporating point of any kind of solid, $E_{\text{total}} = 0$; at the critical point, $E_{\text{total}} = E_C$. One may consider step-by-step the energies required for melting (or dissociating) a bond, an atom, and then shell-by-shell of a nanosolid of radius lined with K atoms.

The thermal energy required for loosening a bond of an atom in the bulk by raising the temperature from T to T_C equals,

$$E_T = E_b(T_C) - E_b(T) = \eta_1 (T_C - T) \propto E_b(0) \tag{14.11}$$

The energy required for melting the entire atom in a bulk is proportional to the $E_B(0)$, which is a sum of the single bond energy over all the coordinates.

Melting a nanosolid comprising N atoms in a shell-by-shell manner requires thermal energy that is proportional to the cohesive energy of the entire solid:

$$T_m(K) \propto E_{\text{coh}}(K) = N z_b E_b + \sum_{i \leq 3} N_i (z_i E_i - z_b E_b) \quad (14.12)$$

If the bond nature in the solid is homogenous, the E_{coh} may vary from material to material, but for a specific sample, the fraction of the E_{coh} needed for the phase transition is fixed for a specific process occurring to the specimen [49]. The relative change in $T_m(K)$ and $T_C(K)$ is then:

$$\frac{\Delta T_m(K)}{T_m(\infty)} = \frac{\Delta T_C(K)}{T_C(\infty)} = \frac{\Delta E_B(K)}{E_B(\infty)} = \sum_{i \leq 3} \gamma_i (z_{ib} c_i^{-m} - 1) = \sum_{i \leq 3} \gamma_i (\alpha - 1) = \Delta_B \quad (14.13)$$

The temperature is always the same throughout the specimen in operation whereas the intrinsic $T_{C,i}$ may vary from site to site if the sample contains atoms with different CN, such as atoms at the surface, grain boundary, or sites surrounding voids or stacking faults.

This mechanism explains why the latent heat of fusion of a solid has a broad range of measured values rather than appearing as a sharp peak [41, 64]. For a solid with numerous randomly distributed defects, the mechanism of random fluctuation melting [39] could dominate because energies required for breaking one bond or dissociating an individual atom with different CN are different. This mechanism also explains the broad temperature range for glass transition of an amorphous state as the random distribution of atomic CN imperfection in the amorphous solid. Glass transition happens in a range of temperatures and it is material processing condition dependent [65].

On the other hand, from a classical thermodynamic point of view, the thermal energy E_T required for the liquid–solid phase transition can be estimated by integrating the specific heat over the entire solid with and without CN imperfection from zero to the T_m :

$$\frac{\Delta E_T(K)}{E_T(\infty)} = \frac{\int_0^{T_m(K)} C_p(K_j, T) dT}{\int_0^{T_m(\infty)} C_p(\infty, T) dT} - 1 \cong \frac{\Delta T_m(K_j)}{T_m(\infty)} = \Delta_B \quad (14.14)$$

with the assumption of $C_p(K, T) \cong C_p(\infty, T) \cong C_v(\infty, T) = \text{constant}$ in the entire temperature range [66]. It is true in fact that $C_p(K, T) \neq C_p(\infty, T) \neq C_v(\infty, T) \neq \text{constant}$. The Debye temperature and therefore the specific heat C_p are size and temperature dependent [56, 67]. This effect results in a 3–5 % deviation of the C_p value. Besides, $(C_p - C_v)/C_v \sim 3\%$ [66]. Compared with the precision in determining the size and shape of a nanosolid, such errors are negligible.

Actually, measurements [68–70] revealed that the C_p varies insignificantly with the particle size in the measuring temperature range. Therefore, it is acceptable to simplify the C_p as a constant in the integration. Such simplification may lead to slight deviation in the integration in Eq. (14.14) from the true value. Nevertheless, one should particularly note that the deviation of the integration from true value

only affects the precision of the m value or the effective z_{ib} , and it does not change the nature of the phenomenon.

14.2.4 Verification: Liquidation and Evaporation

Equation (14.13) indicates that the size-dependent $\Delta T_m(K)/T_m(\infty)$ originates from the relative change in the $E_{B,i}$ of a surface atom to the bulk value. The $\Delta T_m(K)/T_m(\infty)$ follows the scaling law given in Sect. 14.2. Figure 14.3 compares predictions using parameters given in Table 14.2 with the measured size-dependent melting behavior of metals, semiconductors, inert gases, and methyl chloride polymer (m-Cl), as well as embedded systems showing overheating effects. The size-dependent evaporating temperatures (T_{eva}) of Ag and CdS nanosolids also follow the trend of prediction.

The matching between BOLS prediction and measurements provides additional information about the mode of epitaxial crystal growth and the bonding status between the nanosolid and the substrate. Results show that Al nanosolids grown on a SiN substrate are more plate-like ($\tau = 1$) throughout the measured size but Sn on SiN and Au on C are more spherical-like ($\tau = 3$) at particle sizes smaller than 10 nm. The melting profiles show that at the smaller size range, Au/W interface promotes more significantly the melting of Au (undercooling) than the Au/C interface. The silica matrix causes a slight overheating of the embedded Au solid compared with the curves for Au on the other two substrates. The deviation from theory and experiment also provides information about the difference in interfacial energy between the particles and the substrates.

The BOLS premise indicates that the overheating of In/Al ($T_{m,In}/T_{m,Al} = 530/932$), Pb/Al (600/932), Pb/Zn (600/692), and Ag/Ni (1235/1726) [71] results from the interfacial bond strengthening. An atom performs differently at a free surface from this atom at the interface. Although the coordination ratio at the interfaces suffers little change ($z_{ib} \sim 1$), formation of the interfacial compound or alloy alters the nature of the interatomic bond that should be different in strength. In this case, one may replace the $z_{ib}C_i^{-m}$ with a parameter α to describe the interfacial bond enhancement, as indicated in panel (g).

Numerical fitting turns out the α value of 1.8, which indicates that an interfacial bond is 80 % stronger than the bond in the parent bulk. If one considers the bond contraction, $0.90 \sim 0.92$ [72], as the As and Bi impurities in CdTe compound, the m value is around 5.5–7.0. The high m value indicates that bond nature indeed evolves from a compound with m around four to a value of more covalent nature. Therefore, the deformed and shortened interfacial bond is much stronger. This finding means that electrons at an interface are deeply entrapped and densified. Therefore, it is understandable that twins of nanograins [73] and the multilayered structures [74] are stronger and thermally more stable.

It is anticipated therefore that a thin insulating layer could form in a hetero-junction interface because of the interfacial bond nature alteration and the charge

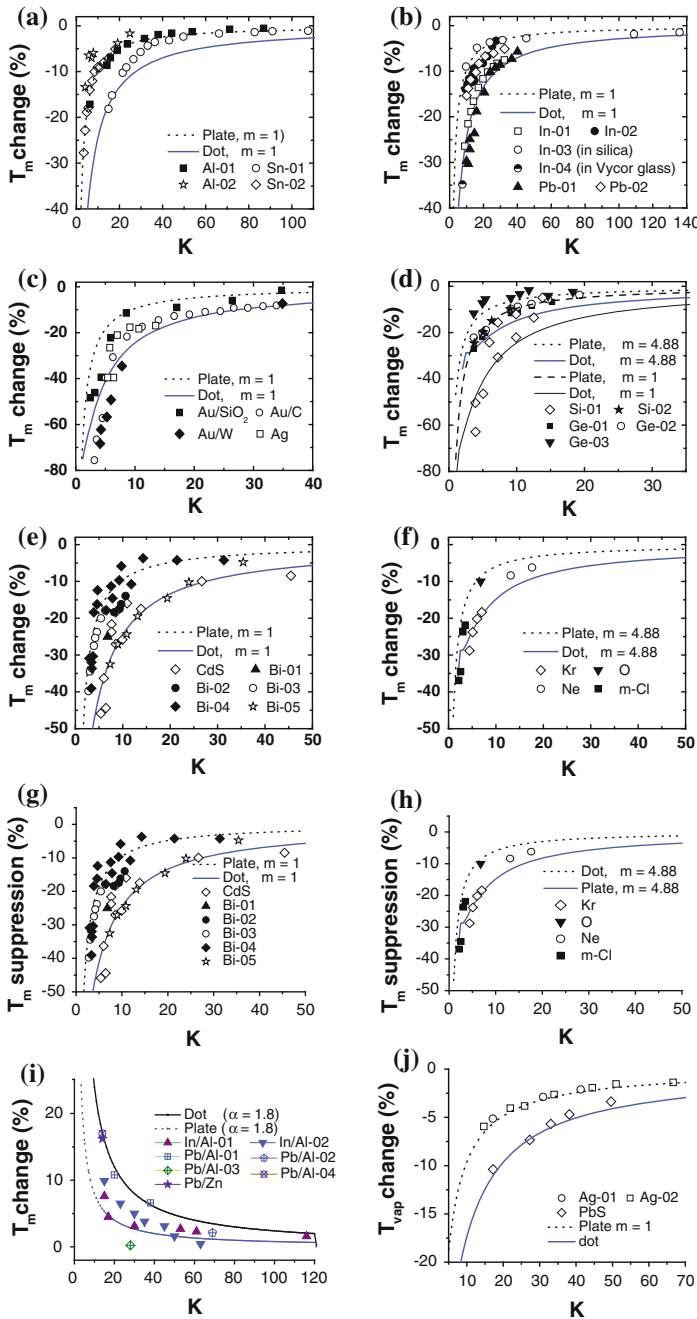


Fig. 14.3 Agreement between predictions (*solid lines*) and experimental observations of the size- and shape-dependence of the T_m suppression of **a** Sn and Al on Si_3N_4 substrate [66, 70], **b** In and Pd, **c** Au on C [33], W [32] and embedded in Silica [78], **d** Ge and Si, **e** Bi and CdS, **f** Kr, Ne and O, and m-Cl, **g** overheating of embedded In and Pb, **h** T_{eva} of Ag and PbS nanosolids [79]. Parameters and references are given in Table 14.2 (Reprinted with permission from [7])

Table 14.2 Parameters used in calculations presented in Fig. 14.3

| Medium | $T_m(\infty)$ | T_m intercept | Data sources (Ref.) |
|---------------------------|---------------|-----------------|---------------------|
| Al-01 (on SiN) | 933.25 | | [69] |
| Al-02 | | | [80] |
| Sn-01 (on SiN) | 505.06 | | [81] |
| Sn-02 | | | [82] |
| Au/C | 1337.33 | | [33] |
| Au/SiO ₂ | | | [78] |
| Au/W | | 947 | [32] |
| Ag | 1,234 | | |
| In-01 | 429.76 | 438.9 | [24] |
| In-02 | | 433 | [82] |
| In-03 | | 443 | [83] |
| Pb-01 | 600.6 | 632.6 | [84] |
| Pb-02 | 600.6 | 607 | [24] |
| Si-01 | 1,685 | 1,510 | [85] |
| Si-02 | | | [86] |
| Ge-01 (beginning) | 930 | 910 | [87] |
| Ge-02 (ending) | – | 1023.3 | |
| Ge-03 (recrystallization) | | 1260.8 | |
| CdS | 1,678 | 1,346 | [14] |
| Bi-01 | 544.52 | | [24] |
| Bi-02 | | 618.9 | [82] |
| Bi-03 | | 559.9 | [88] |
| Bi-04 | | 587.6 | [89] |
| Bi-05 | | 557.8 | [90] |
| Kr | 116 | 109.2 | [91] |
| O | 54.4 | | [92] |
| Ne | 24.6 | | [85] |
| Methyl chloride (m-Cl) | 175.6 | | [91] |
| In/Al-01 | 429.76 | 433 | [93] |
| In/Al-02 | 429.76 | 423.8 | [82] |
| Pb/Al-01 | 933.25 | 613.2 | [19] |
| Pb/Al-02 | | | [94] |
| Pb/Al-03 | | | [95] |
| Pb/Al-04 | | | [96] |
| Pb/Zn | 692.73 | | [92] |

T_m is the intercept of least-root-mean-square linearization of the experimental data that calibrate the measurements. Atomic sizes are referred to Appendix A2

For metals, $m = 1$. For embedded system, the $z_{ib}C_i^m$ is replaced with a constant α that describes the bond strength enhancement due to the alloying at the interfaces

trapping effect. This anticipation explains the high interfacial stress (σ_p) of junction dislocations in aluminum [75] and provides new insight into the deformation of ultrafine-grained metals. The interface bond strengthening also explains the fact that a monolayer GaAs coating on a Ge(110) surface could raise the T_m (1211 K)

with an association of a dramatic drop of the diffusion coefficient of the Ge atoms. In contrast, a Ge monolayer coating on a GaAs(110) surface lowers the T_m of GaAs (1,540 K) by 300 K. Therefore, overheating is subject to the configuration of the hetero-junction interface and their respective $T_m(\infty)$ as well.

The T_m of Si and CdS nanosolids appeared to be lower than the expected values with $m = 4.88$ for Si. The reason of the deviation could be the definition of melting temperature that may refer to temperature of coalescence or complete melting. For instance, MD calculations revealed that [76] coalescence occurs at temperatures lower than the cluster T_m , and that the temperature difference between coalescence and melting increases with cluster size reduction. In the normalization of the scaling relation, the coalescence temperature is lower than the T_m and the coalescence T drops faster than T_m with solid size. The size-dependent T_m of Kr, Ne, and O solids follow the curve of $m = 4.88$ as well, despite the accuracy of measurement. The In particle encapsulated in silica exhibits overheating while the In embedded in Vycor glass shows no overheating effect. From the *RMSD* instability point of view, the interfacial binding constrains the *RMSD* of the interfacial atom to be smaller than that of a bulk atom [40].

Equation (14.13) indicates that the quantity $\alpha = z_i/z_b C_i^{-m}$ dictates the process of overheating ($\alpha > 1$, T_m elevation for chemically capped nanosolids) or undercooling ($\alpha < 1$, T_m suppression of freestanding nanosolids). For a capped nanosolid, $z_i/z_b \sim 1$, the α represents the interfacial bond strength. For a freestanding nanosolid, there are two possibilities for $\alpha > 1$. One is that the m increases as z_i is reduced and the other is that the C_i is much lower than the prediction [77].

14.2.5 T_m Oscillation

14.2.5.1 Observations

The hardness of a bulk material is proportional to its T_m . However, the skin of a solid is generally harder, but the melts more easily than the core interior. XRD in ultrahigh vacuum [44] reveals that the T_m of Pb nanosolids drops with crystallite size, which follows the liquid-skin melting mechanism. Such melting behavior is demonstrated via the reversible growth of a 0.5-nm (2 atomic diameters)-thick liquid skin on 50-nm-sized crystallites.

It is surprising, however, that a freestanding nanosolid at the lower end of the size limit, or clusters containing 10–50 atoms of Ga^+ or IV-A elements, melts at temperatures that are 10–100 % or even higher than the bulk $T_m(\infty)$ [29, 97–100]. For example, Ga_{39-40}^+ clusters melt at about 550 K, while a Ga_{17}^+ cluster does not melt even up to 700 K compared with the $T_m(\infty)$ of 303 K [97]. Small Sn clusters with 10–30 atoms melt at least 50 K above the $T_m(\infty)$ of 505 K [22]. Numerical optimizations suggest that Ga_{13}^+ and Ga_{17}^+ clusters melt at 1,400 and 650 K [98]

and Sn_n ($n = 6, 7, 10$ and 13) clusters melt at 1,300, 2,100, 2,000, and 1,900 K, respectively [100]. For a Sn_{10} cluster, the structural transition happens at 500 and 1,500 K and the structural transition of a Sn_{20} cluster occurs at 500 and 1,200 K [101]. The Sn_{10}^+ and Sn_{11}^+ clusters survive up to 1,073 K while Sn clusters containing $n > 19$ and $n < 8$ atoms are less thermally stable as melting occurs at 773 K or below [102]. Sn_{19} can remain solid up to 673 K while Sn_{20} melts below 673 K.

Calculations [99] suggested that the IV-A elements, C_n , Si_n , Ge_n , and Sn_n ($n \sim 13$) clusters melt at temperatures higher than their $T_m(\infty)$. The measured T_m for Bi particles of 7 nm in radius was similar, being up to 50 K above the value predicted by the homogeneous melting model [103]. The C_{13} cluster prefers a monocyclic ring or a tadpole structure, which is most probable to appear in the simulated annealing when the temperature is between 3,000 and 3,500 K. Numerical calculations, suggested that at the smallest sizes, carbon atoms tend to form tubes or fullerene rather than tetrahedron diamond. Although the T_m may be overestimated to some extent for the smallest clusters [100], the calculated T_m elevation follows the trend of measurement.

The T_m elevation of the smallest Ga and Sn nanosolid corresponded either to the bond nature alteration from covalent-metallic to pure covalent with slight bond contraction [98, 104], or to the significant geometrical reconstruction as Ge, Si, and Sn clusters are found to be stacks of stable tricapped trigonal prism units [105].

14.2.5.2 BOLS Formulation

The generality of the atomic clusters is the atomic CN that is one or two lower than the atomic CN at a flat surface, four. As demonstrated in Sect. 14.3, only one CN loss makes a great difference—the bond is much shorter and stronger than the bonds at the surface.

The T_m oscillation over the whole range of sizes for Sn and Ga^+ clusters can be formulated by varying the bond nature index m as a function of z . Optimization leads to the relation that expresses the m value over the range from seven at $z = 2$ to one at $z > 4$:

$$m(z) = 1 + 12/\{1 + \exp[(z - 2)/1.5]\}$$

Figure 14.4 shows that the T_m curves drop generally with size and then bends up at $K > 3$ ($\text{Log}(K) > 0.5$, or $z > 3$) for higher m values. If the T_m rise originates from the C_z deviation without bond nature change, the bond will contract to $C_z = 0.7^7 = 0.082$. A 92 % bond contraction is impossible. Therefore, the m value, or the bond nature, must change with CN for these elemental solids. As the smallest clusters are not spherical in shape, the equivalent size might be subject to adjustment.

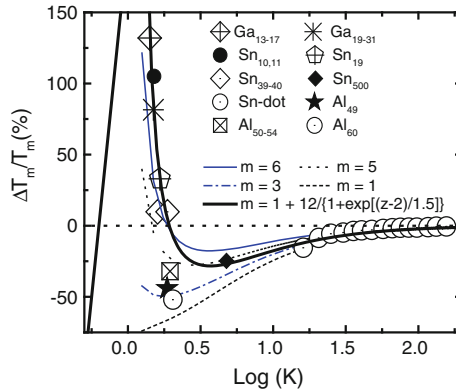


Fig. 14.4 Comparison of the predicted T_m ossification with those measured from Ga_{13-17}^+ [91, 97], Sn_{10-19}^+ [102], Sn_{19-31}^+ [22], Ga_{39-40}^+ [97], Sn_{500} [112], and Sn nanosolid on Si_3N_4 substrate [64]. The T_m deviation of Al_{50-60}^+ clusters [109] from the predictions indicates that the bond nature alteration of Al is less significant compared to Sn and Ga bonds. Ideal fit is reached with a function of $m(z) = 1 + 12/[1 + \exp((z-2)/1.5)]$ to let m transit from 7 at $z = 2$ to 1 when $z > 4$ [113]

The $m(z)$ modification matches closely the measurement of Ga_{17}^+ , Ga_{39-40}^+ , Sn_{19-31} , and Sn_{500} clusters, and Sn nanosolids deposited on Si_3N_4 substrate as well [64]. Calculations [100] show that the T_m transition for Sn_{6-13} happens at Sn_7 . Results indicate that the nature of the Sn–Sn and the Ga–Ga bond indeed evolves from metallic covalent to pure covalent as atomic CN reduces to much lower values, as expected by Chacko et al. [98].

This bond nature evolution also complies with findings that the Al–Al bond for under-coordinated or distorted Al atoms at grain boundaries [106] and at free surfaces [107] becomes shorter ($\sim 5\%$) and stronger with increasing covalent character [108]. However, bond nature evolution in Al_{49-60}^+ clusters appears not as significant as occurred in Sn and Ga, as the T_m for Al_{49-63}^+ is 300 K lower than the $T_m(\infty)$. The abrupt T_m rise (~ 180 K) for Al_{51-54}^+ , Sn_{10-11}^+ and Sn_{19-20}^+ clusters [109] may be partly due to the closed shell structures that are highly thermally stable [110, 111].

Results show that bonding to two neighbors is stronger for an IV-A atom than bonding with three or more due to the bond nature evolution. This mechanism explains why a C_{13} cluster prefers a ring or a tadpole structure with each atom having two bonds, or tubes, or GNR sheet, or fullerene having three neighbors rather than the densely packed tetrahedron structure of four neighbors [99]. For the covalent, Si ($m = 4.88$) and C ($m = 2.56$) clusters should also show the T_m elevation (bending up) at $K < 3$ with fewer than four neighbors.

The bond nature evolution may be the unique property of the III-A and IV-A elements with a larger number of electrons as compared to Al ($m \sim 2$), Ga ($m = 6-7$), C ($m = 2.56$), Si ($m = 4.88$), and Sn ($m = 6-7$).

14.2.6 Remarks

The BOLS premise has reconciled the undercooling, overheating, and oscillating of the T_m over the whole range of sizes of various specimens to the effect of atomic CN imperfection and bond nature alteration. Atomic CN revised cohesive energy of the under-coordinated system determines the geometrical reconstruction, surface lattice/phonon instability, and surface energy. Actually, the surface and interfacial energy, surface stress, the local mass density of liquid and solid are all functions of atomic separation and bond energy that are subject to the BOLS correlation.

The T_m suppression is directly related to the atomic CN imperfection and its effect on the bond strength. The T_m elevation of embedded system is related to the strengthening of the interfacial bond. The T_m oscillation over the whole range of size of III-A and IV-A elements results from atomic CN variation and bond nature evolution.

14.3 Solid Phase Transition

14.3.1 Observations

With reduction in a solid size, the phase stability of the solid becomes lower as well. The T_C of ferromagnetic [114–116], ferroelectric [117–119], and superconductive [120–122] nanosolids can be modified by adjusting the shape and size of the nanosolid. The tunable T_C will be an advantage for sensors or switches that can be functioning in a designed temperature range.

14.3.1.1 Ferromagnetic T_C

For ferromagnetic nanosolids, such as Fe, Co, and Ni and their alloys or compounds [123–125], the T_C reduces with the particle size or with the thickness of the films [114, 116, 126–133]. The T_C of Prussian blue nanowire is also reduced with respect to the bulk [134] due to the diminution of the average number of nearest magnetic neighbors and magnetic exchange interaction constants. According to the scaling theory [135], a spin–spin correlation length (SSCL, or ξ) limitation model [136, 137] defines the SSCL as the distance from a point beyond which there is no further correlation of a physical property associated with that point. Values for a given property at distances beyond the SSCL are purely random. The SSCL depends functionally on temperature as $\xi = \xi_0(1 - T/T_C)^{-\nu}$, with ν being a universal critical exponent. The SSCL premise indicates that the ξ is limited by the film thickness. If the ξ exceeds the film thickness K , the T_C will be lower than the bulk value. The SSCL mechanism gives rise to the power-law form of $T_C(K)$ that

involves two freely adjustable parameters, λ and C (or C_0). The λ value varies from unity to 1.59 for the mean-field approximation and the three-dimensional Ising model, respectively [127, 135, 137]:

$$\frac{\Delta T_C(K)}{T_C(\infty)} = (C_0 K)^{-\lambda} \quad (14.15)$$

An alternative non-continuous form based on the mean-field approximation covers the thinner scales [138]:

$$\frac{\Delta T_C(K)}{T_C(\infty)} = \begin{cases} -\left(\frac{\xi+1}{2K\xi}\right)^\lambda, & (K > \xi) \\ \frac{K-1}{2\xi} - 1, & (K < \xi) \end{cases} \quad (14.16)$$

This relation shows that T_C varies linearly with K and approaches to zero at $K = 1$ (single atom). If $\lambda \neq 1$, there is a discontinuity at $K = \xi$.

The T_C change in a spherical nanosolid is often related to the counts of surface bonds [139]. If the number of exchange bonds per unit volume inside the bulk is z , the number of bonds for the magnetically active surface atom is $z/2$ or less. The T_C is proportional to the mean number of exchange bonds per unit volume, and then, the relative change in the T_C is:

$$\frac{\Delta T_C(K)}{T_C(\infty)} = -\frac{\tau \Delta K}{2K} \quad (14.17)$$

where ΔK is the thickness of the layer with half-depleted exchange bonds. The quantity ΔK is an average that characterizes the features of the surface CN-deficient structure of a nanosolid. If ΔK is independent of the particle radius K , the T_C drops with K and the critical K_C at which T_C is zero is $\tau \Delta K/2$. This relation characterizes qualitatively the interrelation between the degree of magnetic structure disorder and the particle size for Fe_3O_4 spherical dots [140] by setting the critical thickness ΔK of half (for larger size) and two (for the smallest size) atomic sizes.

14.3.1.2 Superconductive T_C

Highly dispersed superconducting nanosolids can be coupled due to the proximity effect when the interparticle spacing is of the order of twice the penetration length of the superconducting order parameter in the normal phase [141, 142]. The electronic energy levels of the sample are discrete, with a mean-level spacing of Kobo gap δ_K for fine metallic particles [143, 144]: $\delta_K = 4E_F/3n \propto 1/V \propto K^{-3}$. As pointed out by Anderson [145], superconductivity would not be possible when δ_K becomes larger than the bulk E_G . Thus, the relation between the superconducting phase transition and the energy-level spacing for spherical granules follows the relation [146, 147]:

$$\ln(T_C(K_j)/T_C(\infty)) = \sum [2/(2m_j + 1)] \times [\tanh[(\pi/2)((2m_j + 1)2\pi k_B T_C/\delta_K)] - 1]$$

Index m_j is the magnetic quantum number. Estimation using this relation yields a 2.5 nm critical size for the disappearance of superconductivity of Pb nanosolid. Experiments of Giaver and Zeller [122] on Sn confirmed the existence of a metastable energy gap only for particles larger than 2.5 nm. However, the T_C for Pb is detectable when the grown Pb atomic layers on Si substrate are four and more [148]. The T_C suppression of Pb embedded in the Al-Cu-V matrix [121] does not follow this relation but the following:

$$T_C(K) = T_C(\infty) \exp(-K_C/K)$$

with $T_C(\infty) = 7.2$ K for Pb [120]. Due to the finite number of electrons in each particle (between 1,000 and 64,000 depending upon the grain size), the conventional BCS approach loses its validity because the bulk BCS theory of superconductivity assumes an infinite number of electrons. Small size implies fewer electrons at the Fermi surface and the increased separation of Kubo levels. Additionally, energy-level spacing may be larger compared to thermal energy $k_B T$. Therefore, the assumption of metallic behavior of these particles is subject to examination.

The T_C of superconductive MgB_2 thin films decreases and the residual resistance increases when the epitaxial MgB_2 thin films become thinner [120, 149]. At sizes larger than 300 nm, the T_C saturates at 41.8 K. The resistivity also saturates to the bulk value of 0.28 Ω cm at 300 nm. A possible explanation of higher T_C is the strain in the film, while the grain size is not likely to be the direct cause of the thickness dependence of T_C . XRD revealed that the a lattice expands from the bulk value of 0.3086 to 0.3095 nm while the c lattice contracts from 0.3524 to 0.3515 nm for a 230-nm-thick MgB_2 film [150]. Hur et al. [151] reported a higher-than-bulk T_C in MgB_2 films on boron crystals and suggested that it is due to tensile strain. A T_C elevation is possible by compressing the c -axis [152]

14.3.1.3 Ferroelectric T_C

Unlike ferromagnetic and superconductive nanosolids that show smaller critical sizes for $T_C = 0$ K, a ferroelectric nanosolid often shows larger critical size at which the ferroelectric feature disappears [153]. Reducing the grain size from 1,200 to 50 nm results in a progressive reduction in tetragonal distortion, heat of transition, T_C , and relative dielectric constant of BaTiO_3 crystal [154]. The critical size for ferroelectricity disappearance is in the range of 10–30 nm. A combination of the size effect and the size-dependent ‘dilution’ effect of a grain boundary ‘dead’ layer could be the cause depressing the relative permittivity. The remnant polarization of the nanoscaled $\text{Pb}(\text{Zr}, \text{Ti})\text{O}_3$ thin films decreases from 6.0 to 2.5 $\mu\text{C}/\text{cm}^2$,

while the coercive field increases from 50 to 150 kV/cm, with the decrease in film thickness from 152 to 32 nm [155].

Theoretical approaches for the ferroelectric depression include: (1) pseudospin theory based on the Ising model in a transverse field, (2) macroscopic Landau theory with consideration of surface effects, and (3) a polaron model for the very-long-wavelength region. The Landau-type model of Zhong et al. [156] considers the surface and non-equilibrium energy by introducing a surface extrapolation length δ to the size-depressed T_C of ferroelectric nanosolids, expressed using the Ising premise, $J_{ij} = J/r_{ij}^\sigma$. $\sigma = 0$ corresponds to an infinite-range interaction and $\sigma = \infty$ to a nearest-neighbor interaction [157].

Bursill et al. [158] assumed that the Landau-Ginzburg-Devonshire (LGD) coefficients in the Gibbs energy change with particle size. Huang et al. [159] combined the LGD theory and the BOLS correlation to study the size effect of ferroelectrics. The model assumes that the surface bond contraction is the origin for the size effect [160], which was confirmed by measurements. For example, barium titanate particles consist of a shell of cubic material surrounding a core of tetragonal material [161–163].

The following scaling relation is widely used to fit the T_C suppression of ferroelectric nanosolids [118],

$$\Delta T_C(K)/T_C(\infty) = C/(K - K_C) \quad (14.18)$$

where C and the K_C are adjustable parameters. The proper form of the dividend seems to be $K + K_C$ instead of $K = K_C$. Jiang et al. [164] adopted their model for T_m suppression to the size-dependent T_C of the ferroelectric nanosolids as:

$$\begin{cases} T_C(K)/T_C(\infty) = \exp\left\{-2S_0[3R_S(K/K_C - 1)]^{-1}\right\} \\ K_C = \alpha_{90}(2k_B\alpha\beta^2)^{-1} \end{cases}$$

where S_0 is the transition entropy and R_S is the ideal gas constant. α is the thermal expansion coefficient and β the compressibility. The constant α_{90} denotes the density of 90° domain walls. This relation reproduces the measured T_C suppression of BaTiO_3 and PbTiO_3 nanosolids with the known S_0 values.

14.3.1.4 Antiferromagnetic Transition

When a sufficiently large magnetic field is applied along the preferred axis, the so-called spin-flop reorientation occurs, i.e., a 90° rotation of the sublattice vectors, in the antiferromagnetic $\alpha\text{-Fe}_2\text{O}_3$ nanosolids [165]. Both the spin-flop field, H_{S-F} ($T = 0$), and the Morin transition temperature (T_M) decrease with particle size in a K^{-1} way and approach to zero when the diameter is smaller than 8 nm, for spherical particles [166]. Table 14.3 features the size-dependent H_{S-F} and T_M values.

Table 14.3 Size dependence of the Morin temperature (T_M) and the spin-flop transition field at $T = 0$ ($H_{S-F,0}$) for the heminatite nanosolids [165]

| D/nm | T_M/K | $H_{S-F,0}/\text{Tesla}$ |
|---------------|----------------|--------------------------|
| 36.4 | 186 | 1.7 |
| 40.0 | 200 | 2.5 |
| 82.7 | 243 | 5.4 |
| 159.0 | 261 | 6.6 |

The CN of the surface spins determines a variety of reversal paths and in turn affects both the exchange and anisotropy fields [165]. Therefore, the surface spins undergo spin-flop instability at field that is much lower than the field for the bulk. For Ho films, the helical antiferromagnetic ordering temperature, called Néel temperature (T_N), decreases with film thickness [167]. The offset thickness is 11 ML for metallic Ho films in comparison with the value of 16 ML for Cr in sputtered, epitaxial Fe/Cr(001) superlattice [168]. In the $\text{Pr}_{0.5}\text{Ca}_{0.5}\text{MnO}_3$ nanowires, a ferromagnetic transition occurs at ~ 105 K; the antiferromagnetic transition happens at 175 K; and the charge ordering transition is suppressed from the bulk value of 245 K [169].

14.3.2 BOLS Formulation

An extension of the BOLS correlation into the Ising model could improve the insight into size-induced T_C suppression of ferromagnetic, ferroelectric, and superconductive nanosolids as well as the T_M and H_{S-F} for antiferromagnetic heminatite.

14.3.2.1 Ising Model

The Hamiltonian of an Ising spin system in an external field B is expressed as [138],

$$H_{\text{ex}} = \sum_{\langle i,j \rangle} J_{ij} S_i S_j - g \mu_B B \sum_{i=1}^N S_i \propto z_i d_i^{-1}$$

The H_{ex} is identical to the atomic E_B under zero external field, $B = 0$. S_i and S_j is the spin operator in site i and site j , respectively. J_{ij} is the exchange strength between spins, which is inversely proportional to atomic distance. The sum is over all the possible coordinates, z_i . For phase transition, the thermal energy required is in equilibration with a certain portion of the exchange energy. This mechanism leads to the case being the same as for T_m suppression as described in Eq. (14.13).

14.3.2.2 High-Order CN Imperfection: The Dual-Shell Model

For ferroelectric systems, the exchange energy also follows the Ising model, but the S_j here represents the quanta of a dipole or an ion (called quasi-dipole) that is responsible for the ferroelectric performance. The difference in the correlation length is that the dipole system is longer than that of a ferromagnetic spin–spin system. Usually, dipole–dipole Van der Waals interaction follows the r^{-6} type whereas the superparamagnetic interaction follows an r^{-3} relation. Hence, it is insufficient to count only the exchange bonds within the nearest neighbors for atoms with distant interaction in a ferroelectric system.

A dual-shell model describing the short- and the long-range interactions in the ferromagnetic nanosolid is necessary [170]. A critical exchange correlation radius K_C can be defined to count contributions from all atoms within the sphere of radius K_C . Therefore, the sum in Eq. (14.13) changes from the z_i neighbors to atoms within the K_C -sized correlation volume.

For a ferroelectric spherical dot with radius K , one needs to consider the interaction between the specific central atom and its neighbors within the critical volume $V_C = 4\pi K_C^3/3$, in addition to the BOLS correlation limited to the skin. The ferroelectric property drops down from the bulk value to a value smaller than 5/16 (estimated from Fig. 14.5) when one goes from the central atom to the edge along the radius. If the surrounding volume of the central atom is smaller than the critical V_C , the ferroelectric feature of the central atom attenuates; otherwise, the bulk value remains. For an atom in the i th surface layer, the number of the exchange bonds loss is proportional to the volume V_{vac} that is the volume difference between the two caps of the V_C -sized sphere as illustrated in Fig. 14.5a. Therefore, the relative change in the ferroelectric exchange energy of an atom in the i th atomic layer to that of a bulk atom due to volume loss becomes,

$$\frac{\Delta E_{exc,i}}{E_{exc}(\infty)} = \frac{V_C - V_{vac,i}}{V_C} - 1 = -\frac{V_{vac,i}}{V_C} = \delta_{V,i} \quad (14.19)$$

14.3.2.3 Generalization of T_C Suppression

Considering the BOLS correlation for the nearest neighbors and the volume loss of long-order CN imperfection, we have a generalized form for the T_C suppression for the ferromagnetic, ferroelectric, and superconductive nanosolids ($m = 1$ in the Ising model):

$$\frac{\Delta T_C(K)}{T_C(\infty)} = \frac{\Delta E_{exc}(K)}{E_{exc}(\infty)} = \begin{cases} \sum_{i \leq 3} \gamma_i (z_{ib} C_i^{-1} - 1) = \Delta_B & \text{(short-order-loss)} \\ \sum_{i \leq K_C} \gamma_i \delta_{V,i} + \Delta_B = \Delta_{COH} & \text{(long-order-loss)} \end{cases} \quad (14.20)$$

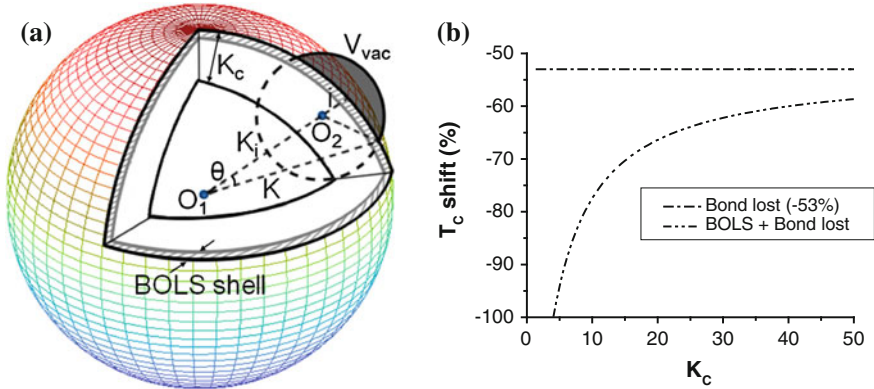


Fig. 14.5 The dual-shell model for the short- and long-range interactions in nanosolid ferroelectric nanosolid. **a** Schematic of the high-order exchange bonds loss of an atom in a spherical nanosolid with radius K . K_C is the critical correlation radius. The V_{vac} loss (the shaded portion) is the difference between volumes of the two spherical caps: $V_{vac,i} = \pi(K_C + K_i - K \cos \theta)^2 (K_C - \frac{K_C + K_i - K \cos \theta}{3}) - \pi(K - K \cos \theta)^2 (K - \frac{K - K \cos \theta}{3})$, where the angle θ is determined by the triangle O_1O_2A . **b** Correlation radius K_C dependence of the T_C shift of ferroelectric and superconductive nanosolids. For $K_C = 5$ example, BOLS lowers the T_C by -41.1% , the high-order bond loss contributes to the T_C suppression by -53% , and the overall T_C shift is -94% . $K_C \leq 4$, $T_C = 0$ [171] (Reprinted with permission from [7])

For a short-order spin–spin interaction, the sum is over the outermost three atomic layers in terms of BOLS whereas for a long-order dipole–dipole interaction, the sum is within the sphere of the critical volume V_C . Therefore, ΔK in Eq. (14.17) is not a constant. In the BOLS premise, the γ_i is not always proportional to the inverse radius, which drops instead from unity to infinitely small when the particle grows from atomic scale to macroscopic size. Meanwhile, the z_i and the C_i vary with the curvature of the sphere.

Figure 14.5b shows the general K_C dependence of the ferroelectric T_C shift involving both the volume loss and the BOLS effect. For $K_C = 5$ example, bond contraction lowers the T_C by -41.1% and the volume loss lowers the T_C by -53% and the overall T_C shift is -94% .

14.3.3 Verification: Critical Size

Least-root-mean-square linearization of the measured size-dependent T_C represented by Eq. (14.20) gives the slope B' and an intercept that corresponds to the bulk $T_C(\infty)$. The $B' = K\Delta_{COH}$ for a ferroelectric system. For a ferromagnetic system, $B' = K\Delta_B$ is a constant without needing numerical optimization. Calculations based on Eq. (14.20) were conducted using the average bond length (appendix A2) and the known $T_C(\infty)$ values listed in Table 14.4.

Table 14.4 BOLS predicted critical correlation radius (K_C) in comparison with the documented R'_C of magnetic, ferroelectric, superconductive, and antimagnetic nanosolids

| Materials | $T_C(\infty)/K$ | $K_C/R_C(\text{nm})$ | R'_C/nm (Ref.) |
|--|-----------------|----------------------|-------------------------|
| Fe | 1,043 | 1 | 0 [116] |
| Co | 1,395 | 1 | 0 [114] |
| Ni | 631 | 1 | 0 [114] |
| Fe ₃ O ₄ | 860 | 1 | 0 [140] |
| PbTiO ₃ | 773 | 4/1.04 | 6.3 [118], 4.5 [117] |
| SrBi ₂ Ta ₂ O ₉ | 605 | 4/1.0 | 1.3 [119] |
| PbZrO ₃ | 513 | 8/2.3 | 15 [174] |
| BaTiO ₃ | 403 | 100/24.3 | 24.5 [177], 55 [173] |
| MgB ₂ | 41.7 | 3.5/1.25 | 1.25 [175] |
| Pb | 7.2 | 3.5/1.25 | 1.25 [121] |

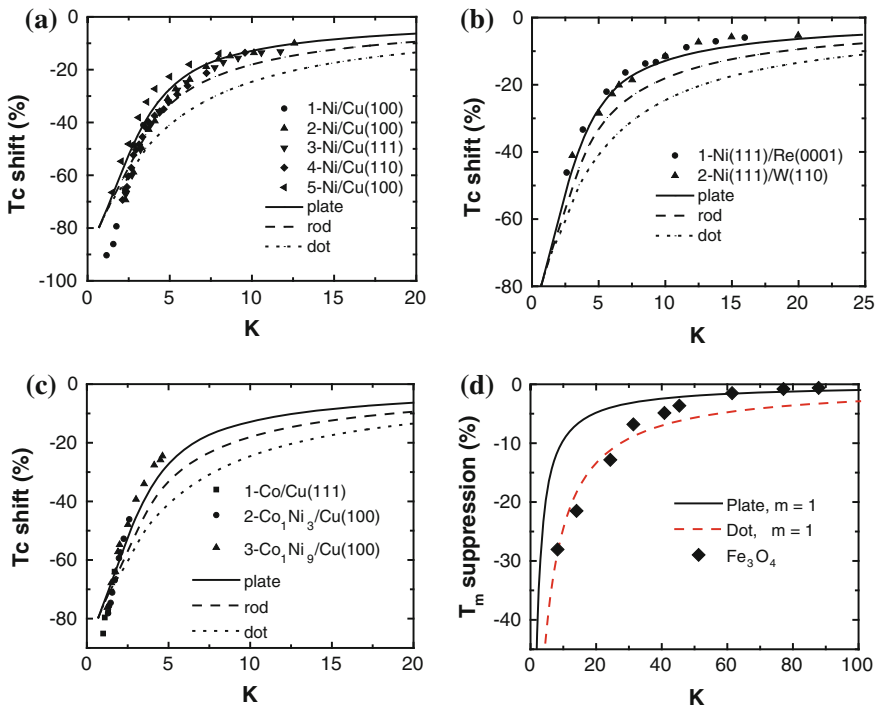
**Fig. 14.6** Comparison of the predicted T_C suppression with observations of **a** Ni thin films: data 1 [130], data 2, 3, and 4 [138], data 5 [114], **b** data 1 [172] and data 2 [129], **c** Co films [114], and **d** Fe₃O₄ nanosolids [140] (Reprinted with permission from [7])

Fig. 14.7 T_C suppression of ferroelectric PbTiO_3 [117], $\text{SrBi}_2\text{Ta}_2\text{O}_9$ [119], BaTiO_3 [173], and antiferroelectric PbZrO_3 [174] nanosolids with different K_C values (Reprinted with permission from [7])

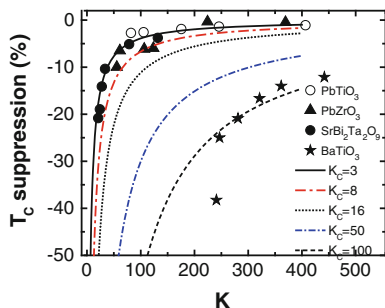


Figure 14.6 shows the T_C suppression for ferromagnetic Ni, Co, and Fe_3O_4 nanosolids. For ultrathin films, the measured data are closer to the predicted curve for a spherical dot. This coincidence indicates that at the beginning of film growth, the films prefer island patterns that transform gradually into a continuous slab. For a ferroelectric system, we need to optimize the K_C value by in computation to match theoretical curves to the measured data.

Figure 14.7 shows the T_C suppression of ferroelectric PbTiO_3 [117], $\text{SrBi}_2\text{Ta}_2\text{O}_9$ [119], BaTiO_3 [173], and antiferroelectric PbZrO_3 [174] nanosolids. For ferroelectric and superconductive nanosolids, $T_C = 0$ K occurs at $V_{\text{vac}} = V_C$, which means that K_C corresponds not to $T_C = 0$ K, but to a value that is much lower than room temperature. The difference in the optimized K_C by different approaches, as compared to Table 14.4, lies in that the γ_i is not a constant but changes with particle size.

Comparing the BOLS prediction to the measured T_C suppression of superconductive MgB_2 nanosolids in Fig. 14.8 leads to an estimation of the critical radius $K_C = 3.5$ of measurement ($R_C \sim 1.25$ nm) [175]. For the smallest MgB_2 crystals, the relative Bragg intensities of the allowed reflections can only match during Rietveld refinement by introducing statistically distributed B-vacancies, with the refined value falling from 1 to $2/3$. This fact means that the average CN of Mg to B atoms falls from 12 to 8, which indicates the loss of superconductivity due to the under-coordination effect [176]. Therefore, long-range interaction is important to the superconductive T_C . For an Al–Cu–V embedded Pb nanosolid [121], the K_C is around 1, being the same to the ferromagnetic solid. For the antiferromagnetic $\alpha\text{-Fe}_2\text{O}_3$, a spin-flop transition at a critical size of 8 nm results also from the high-order CN imperfection. Therefore, the long-order interaction dominates the T_C for all the ferroelectric, antiferroelectric, and superconductive nanocompounds.

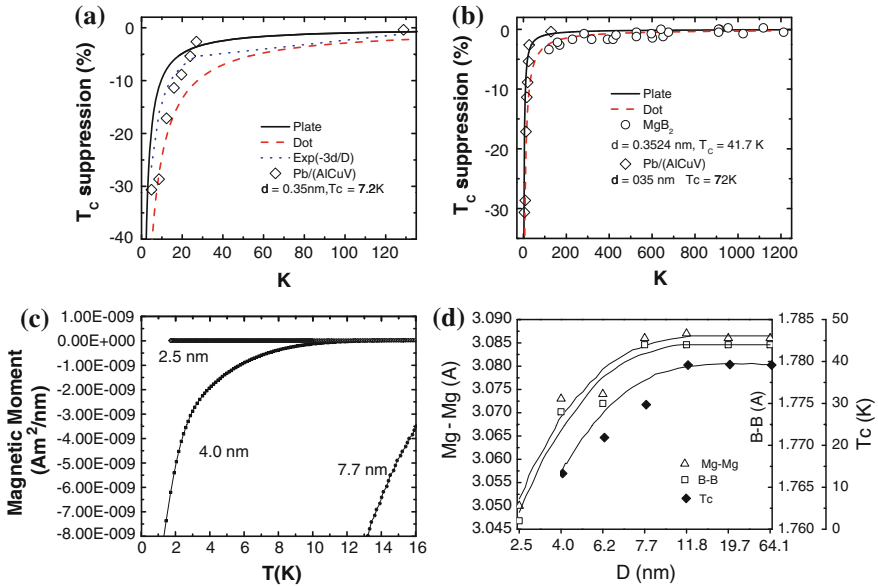


Fig. 14.8 Superconductive T_c suppression of **a** Pb particles embedded in Al-Cu-V matrix [120]. **b** MgB₂ films [120]. **c** Size and temperature dependence of the magnetism of MgB₂ superconducting nanosolids. **d** Size-induced T_c and bond length suppression of MgB₂ nanosolids [175] (Reprinted with permission from [7])

14.4 Diffusion and Crystal Growth

14.4.1 Diffusivity

14.4.1.1 Observations

The kinetics of diffusion occurring in nanostructured materials is a subject of intensive study [178, 179]. Materials at the nanoscale showed sharp acceleration of diffusion [180], indicating the lowered activation energy of diffusion. The activation enthalpies for the interfacial diffusion are comparable to those for surface diffusion, which are much lower than those for diffusion along grain boundaries [181, 182].

Measuring grain boundary diffusion fluxes of Cu and creep behavior of coarse-grained and nanostructured Ni samples at 423 and 573 K [183] revealed that the creep acceleration behavior is grain size-dependent because of the high diffusivity in the finer grain material. Fe-tracer diffusion in submicrocrystalline Pd powders demonstrates that interfacial diffusion occurs at relatively low temperatures accompanied by a substantial recovery of grain growth [184]. Atomic defects trigger the recovery processes and the crystal growth occurring in a main recovery stage at 500 K. The under-coordinated atoms surrounding the defects are

responsible for the onset of diffusion in the interfaces as these atoms are mobile in this temperature regime.

By means of surface mechanical attrition treatment (SMAT) to a pure iron plate, Wang et al. [185] fabricated a 5- μm -thick Fe surface layer composed of 10–25-nm-sized grains without porosity or contamination on the Fe plate. They measured Cr diffusion kinetics within a temperature range of 573–653 K in the nano-Fe-coated plate. The diffusivity of Cr in the nanocrystalline Fe is 7–9 orders higher in magnitude than that in a Fe lattice and 4–5 orders higher than that in the grain boundaries (GBs) of α -Fe. The activation energy (E_A) for Cr diffusion in the Fe nanophase is comparable to that of the GB diffusion, but the pre-exponential factor is much higher. The enhanced diffusivity of Cr in Fe corresponded to a large volume fraction of non-equilibrium GBs and a considerable amount of triple junctions in the presence of the nanocrystalline Fe samples.

Under the given conditions, copper atoms were not detectable in the coarse-grained Ni even at a depth of 2 μm . However, the diffusive copper fluxes in nanostructured Ni penetrate into a depth greater than 25 and 35 μm at 423 and 573 K, respectively [183]. This information leads to the GB diffusion coefficients of copper in nanostructured nickel as derived as follows.

As no migration of the GBs in nanostructured Ni was observed at 423 K, the diffusion coefficient, D_b , can be determined using the equation describing the change in the GB impurity concentration versus time t of the diffusion at annealing [186]:

$$c(x, t) = c_0 \operatorname{erfc} [x / (2\sqrt{D_b t})]$$

where c_0 is the concentration of copper in the skin. The depth x is the distance from the surface at which $\log c = -1$ ($c = 0.1\%$, which corresponds to the resolution limit of the SIMS unit). An extrapolation of the experimental concentration curve at $x \rightarrow 0$ gives the value of c_0 . In this case, $D_b = 1 \times 10^{-14} \text{ m}^2/\text{s}$ ($t = 3 \text{ h}$).

Grain growth occurs in nanostructured nickel annealed at 573 K, and the grain boundary migration occurs at the velocity of $V \sim 7 \times 10^{-11} \text{ m}^2/\text{s}$. In this case, the D_b follows [186]:

$$c(x, V, \beta) = c_0 \exp\left(-x\sqrt{V/D_b\beta_b}\right)$$

Considering the diffusion width of the boundary $\beta_b = 10^{-8} \text{ m}$, one can obtain the $D_b = 1.4 \times 10^{-12} \text{ m}^2/\text{s}$, which is two orders higher than that for the same sample annealed at 423 K. These experimental data demonstrate the increase in the GB diffusion coefficient of copper in nanostructured Ni in comparison with that happens in the coarse-grained nickel.

The interdiffusion between Ag and Au is enhanced when the Au particle size is reduced [187]. For the very small particles (<4.6 nm initial Au-core size), these two metals are almost randomly distributed within the particle; for larger particles, the diffusion boundary is only one monolayer. These results are beyond the scope

of surface pre-melting effect. Defects at the bimetallic interface seemed to enhance the radial migration of one metal into the other [187].

In situ four-point probe measurements of the onset temperature at which the electrical resistivity deviates from linearity during the temperature ramping [188] revealed that at the deviation point, the Ag thin films become unstable due to void formation and growth during annealing. In vacuum, Ag thin films thicker than 85 nm on SiO₂ substrates are thermally stable. Using the Arrhenius relation in terms of onset temperature and film thickness, an E_A of 0.326 ± 0.02 eV is obtained for the onset of Ag agglomeration ramped at a rate of 0.1 °C per second. This value is consistent with the E_A for surface diffusion of Ag in a vacuum. Therefore, Ag agglomeration and surface diffusion share the same E_A , both of which depend on the atomic cohesive energy.

The high diffusivity at the nanoscale also enhances diffusion of a liquid into the nanosolid [189]. Powder nanosolids as electrodes in chemical sensors show much improved diffusion efficiency (10 – 10^4) [189]. Further, the powder ultramicro-electrode can significantly enhance the mass transportation rate from solution to the nanosolids surface, being irrespective of particular catalytic material [190, 191].

14.4.1.2 BOLS Formulation

According to the BOLS, atomic CN imperfection suppresses the E_B that is responsible for the E_A loss in atomic diffusion, agglomeration, and glide dislocation. The diffusivity D follows the Arrhenius relation,

$$D(\infty, T) = D_0 \exp(-E_A(\infty)/k_B T) \quad (14.21)$$

where the activation enthalpy of diffusion is $E_A(\infty) = 1.76$ eV and the pre-exponential factor is $D_0 = 0.04$ cm² s⁻¹ for gold. Incorporating the BOLS into the interdiffusion and nanoalloying by letting $E_A \propto E_B$ and hence the E_A is atomic CN dependent.

Diffusing an atom into the solid requires energy to relax partially the bonds for atom dislocations. Applying Eq. (14.12)–(14.21) by considering the size effect, one has,

$$\begin{aligned} \frac{D(K, T)}{D(\infty, T)} &= \exp\left(-\frac{E_A(K) - E_A(\infty)}{k_B T}\right) \\ &= \exp\left(-\frac{E_A(\infty)}{k_B T} \left[\frac{E_B(K)}{E_B(\infty)} - 1\right]\right) \\ &= \exp\left(\frac{-E_A(\infty)}{k_B T} \Delta_B\right) \\ D(K, T) &= D_0 \exp\left(\frac{-E_A(\infty)}{k_B T} \frac{T_m(K)}{T_m(\infty)}\right) = D_0 \exp\left(\frac{-E_A(\infty)}{k_B T} [1 + \Delta_B]\right) \end{aligned} \quad (14.22)$$

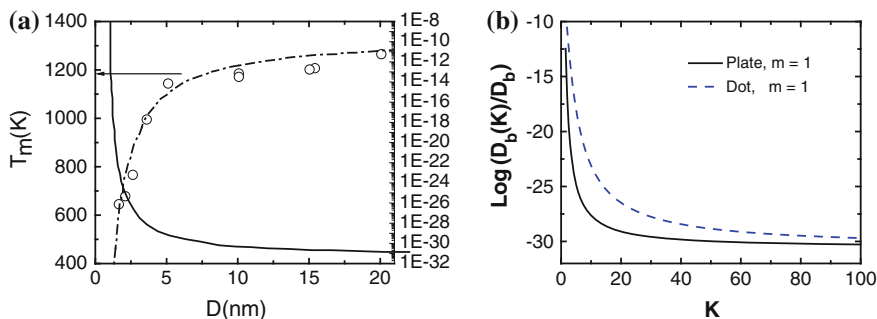


Fig. 14.9 Size dependence of the T_m and the diffusivity of silica-encapsulated gold particles. **a** The solid curve (right-hand side axis) is the calculated Au self-diffusion coefficient [78]. **b** BOLS predicted size-dependent diffusivity

Therefore, the nanodiffusivity increases at the nanoscale because of the reduced atomic E_B . The $D(K, T)$ drops with the $T_m(K)/T_m(\infty)$ ratio in an exponential way. This formulation provides a feasible mechanism for the nanoalloying, nanodiffusion, and nanoreaction in the grain boundaries where under-coordinated atoms dominate.

However, oxidation resistance of a Si nanorod exhibits oscillation features [192]. At the lower end of the size limit, Si nanorod can hardly be oxidized, as oxide tetrahedron formation is strongly subject to the atomic geometrical environment. For instance, oxidation happens preferentially at the densely packed diamond [111] plane of C_{3v} symmetry rather than the loosely packed (110) surface [193]. The high surface curvature of Si nanorod and the shortened surface bond resists the formation of an oxide tetrahedron.

Figure 14.9 compares the measured size-dependent T_m suppression and diffusion-coefficient enhancement of silica-encapsulated gold particles [78] in comparison with BOLS prediction. The trend similarity shows the correlation between the diffusivity and activity in terms of activation energy.

14.4.2 Crystal Growth

14.4.2.1 Liquid–Solid Epitaxy

Knowing the initial stages of growth of nanometer-sized crystals from the molten or amorphous matrix is a challenging issue. This process largely determines the resulting microstructure of a polycrystalline material, which is extremely difficult to study experimentally due to the small size of the clusters and the short time period involved. MD simulation results on the homoepitaxial growth and melting of Si provide an example for the understanding in terms of the transition-state theory of crystal growth.

According to transition-state theory, the driving force, F_C , for the movement of the liquid–crystal interface is the free energy difference between the liquid and bulk crystal. This difference is approximately proportional to the magnitude of the undercooling, $T_m - T$. The velocity of the moving interface, V , is proportional to the driving force $V = kF_C$, where k is the mobility of the liquid–crystal interface. This interfacial mobility determined by the movement of the atoms in the liquid phase as atoms residing in the crystalline phase are far less mobile. Therefore, this mobility is proportional to the thermally activated atomic diffusion in the liquid phase. As is well established, T_m suppression happens in a cluster of finite size due to atomic CN imperfection, which contributes to the free energy of the liquid–crystal interface.

The T_m drop with solid size is a reflection of the reduced atomic E_B and the mobility activation energy E_A (\propto atomic E_B) of the liquid–crystal interface, which is essentially the same to that for liquid diffusion. In the study of growth and melting of Si, the crystal front velocity follows the Stillinger–Weber (SW) potential that consists of additive two-body and three-body energy terms. The three-body term is zero for the perfect-crystal structure at $T = 0$ K, but even at high temperature, the three-body term is relatively low in the crystalline phase (e.g., the three-body energy is about 0.1 eV/atom at $T = 1,200$ K). In contrast, the liquid phase is characterized by a larger three-body energy (-1 eV/atom). Using this large difference, Koblinski [86] calculated the amount of crystal and liquid phase present in the simulated cell simply by monitoring the total three-body energy and using it as reference for the corresponding values of the bulk liquid and bulk solid at the same temperature.

The size-dependent $T_m(K)$ contributes to the growth/melt behavior of clusters with various initial sizes as a function of temperature. The free energy of the cluster results from the surface and the bulk contributions. The surface contribution, U_S , approximates the product of the surface area and the liquid–solid interfacial free energy, γ_{ls} , such that $U_S = A\gamma_{ls}K^2$, where A is a geometrical constant (for a spherical dot, $A = 4\pi d_0^2$). The bulk contribution, U_B , approximates the product of the volume of the cluster and the difference in free energy densities between solid and liquid, Δu , such that $U_B = B\Delta uK^3$, where B is another geometrical constant (for a spherical cluster $B = 4\pi d_0^3/3$).

The difference between crystal and liquid free energy densities in the vicinity of the T_m is proportional to the magnitude of undercooling (or overheating), $\Delta u = u_0(T - T_m(K))$, where u_0 is a constant (Δu correctly vanishes at T_m). For a given temperature, the critical cluster size corresponds to the maximum of the free energy $U = U_S + U_B$. By differentiating the free energies with respect to the cluster size K , one finds the maximum at $T = T_m(K) - c\gamma_{sl}/K$, where c is a constant depending on A , B , and u_0 . The linear dependence of the T_m on the inverse of the crystalline size implies that the interfacial energy, γ_{sl} , does not change significantly with temperature, from the first-order approximation. In reality, the interfacial energy varies with both size and temperature.

In order to understand the temperature dependence of the growth rate in terms of undercooling and thermally activated interfacial mobility, one may assume that

in the classical nucleation theory, growth takes place on an atom-by-atom basis. Hence, the average rates of crystallization and dissolution are [86]:

$$v_{\pm} = v_0 \exp\{\pm[(\Delta u - \Delta A\gamma_{sl})/(2k_B T)] - E_A/k_B T\}$$

where $\Delta A = A_{n+1} - A_n$ is an increase in the interfacial area due to the attachment of an atom to the crystal. The v is the thermal vibration frequency of the interfacial atom. The cluster growth velocity resulting from the difference between v_+ and v_- , which yields

$$\begin{aligned} V_{\text{grow}} &\sim \exp(-E_A/k_B T) \sinh\{[\Delta u - \Delta A\gamma_{sl}]/(2k_B T)\} \\ &\cong \{[\Delta u - \Delta A\gamma_{sl}]/(2k_B T)\} \exp(-E_A/k_B T) \end{aligned} \quad (14.23)$$

The argument of the hyperbolic sine is small near the T_m (it is exactly zero at the $T_m(K)$). Equation (14.23) indicates that the rate of the growth/melting is driven by the lowering of the free energy, $\Delta u - \Delta A\gamma_{sl}$, while the interfacial mobility is determined by the E_A for diffusion jumps of the interfacial atoms. Noting that ΔA is proportional to K^{-1} and $\Delta u = u_0(T - T_m(K))$, and then, the scaling law for melting applies $\Delta T_m(K) \sim \gamma_{sl}/K$. ($T_m(K)$ is the temperature at which $V_{\text{grow}} = 0$.) For planar growth, the interfacial contribution to the free energy disappears; thus, V_{grow} is zero exactly at the $T_m(\infty)$ ($\Delta u = 0$).

For a given cluster size, the free energy term can be expanded around its $T_m(K)$ such that

$$V_{\text{grow}}(K) \sim [(T_m(K) - T)/T] \exp(-E_A/k_B T) \quad (14.24)$$

This process describes the kinetics of liquid-nanosolid dissolution and growth. The E_A obtained from the best fits are 0.75 ± 0.05 eV for 2.0- and 2.6-nm solids and 0.85 ± 0.05 eV for 3.5-nm solids, respectively. This result complies with the BOLS expectation that the mean atomic E_B increases with solid size. Incorporating the BOLS correlation to the $T_m(K)$ and $E_A(K)$, Eq. (14.24) becomes,

$$\begin{aligned} \frac{\Delta E_A(K)}{E_A(\infty)} &= \frac{\Delta T_m(K)}{T_m(\infty)} = \Delta_B \\ V_{\text{grow}}(D) &\sim [(T_m(\infty)(1 + \Delta_B) - T)/T] \exp\{-[E_A(\infty)(1 + \Delta_B)]/k_B T\} \end{aligned} \quad (14.25)$$

The exponential part is the same to the diffusivity (see Eq. (14.22)). Size-induced perturbation appears twice in this formulation. Results in Fig. 14.9a show the mobility of the liquid–solid interface that is determined by diffusion in the adjacent bulk liquid, which is exactly the case of homoepitaxial growth.

14.4.2.2 Vapor Phase Deposition

The knowledge of size-dependent melting provides guidelines for controlling the size of nanosolid growth on heated substrates in vapor deposition and modulating the crystal size by annealing. For a given substrate temperature (T_S), there will be a

minimum critical size of the grown particle. Thus, any particle larger than this critical size will grow and remain. If the incident sourcing cluster size is smaller than the critical size, the particles will melt upon deposition and they will coagulate to produce clusters equal to the critical size or larger. If the T_S is higher than the T_m , the landed clusters merge and then evaporate [79]. This intuition implies that the T_S should be as low as possible if one wants to obtain smaller particles.

This mechanism also applies to controlling the sinterability of nanosolids. In fact, the solid size of an oxide increases with annealing temperature [195] and agglomeration happens at a certain size range at room temperature in the process of ball milling [196, 197]. The T_S -related nucleation and agglomeration explains why the topmost Bi layers on graphite start to lose long-range order at 10–15 K below the $T_m(\infty)$ of Bi, 544.52 K and why nucleation occurs at ~ 125 K below the $T_m(\infty)$. The temperature of melting and solidification of the same surface is different [198].

Normally, the $T_S(K)$ for growth is around 0.3 times the $T_m(K)$ [194, 199],

$$T_S(\tau, K_C) = 0.3T_m(\tau, K) = 0.3T_m(\infty)(1 + \Delta_B)$$

$$\Delta_B = \text{triangle}_B \cong \Delta'_B / K_C,$$

which gives the thermally stable critical size at the given T_S :

$$K_C = \frac{-\Delta'_B}{1 - T_S(\tau, K)/[0.3T_m(\infty)]} = \frac{\tau \sum_3 C_i (1 - z_{ib} C_i^{-m})}{1 - T_S(\tau, K)/[0.3T_m(\infty)]} \quad (14.26)$$

The constant $\Delta'_B = -2.96$ for a spherical metallic dot ($m = 1$; $\tau = 3$; $K_C > 3$). The critical size and the number of atoms in the deposited nanosolid depend on the $T_S(\tau, K)/0.3T_m(\infty)$ ratio.

Figure 14.10b formulates the $R_C (= K_C d)$ dependence on the T_S . With the known atomic size d and $T_m(\infty)$, one is able to control the crystal size [200]. This relation predicts that a monatomic layer of metals ($\tau = 1$) could only growth at $T_S = 0$ K or nearby. This prediction is in accordance with observations, For instance, monolayer Pd forms on Si surface only at 4 K or below [148].

14.4.3 Thermally Control of Crystal Size and Bandgap

Grain size that determines the bandgap of a nanosolid semiconductor is controllable by programming the growing or annealing temperature T_S [195]. For the post-annealing process, the as-grown particle size (K_0) and threshold temperature (T_{th}) are involved. The high-energy grain boundary does not gain mobility until reaching T_{th} , at which grains grow upon heating to minimize the overall energy.

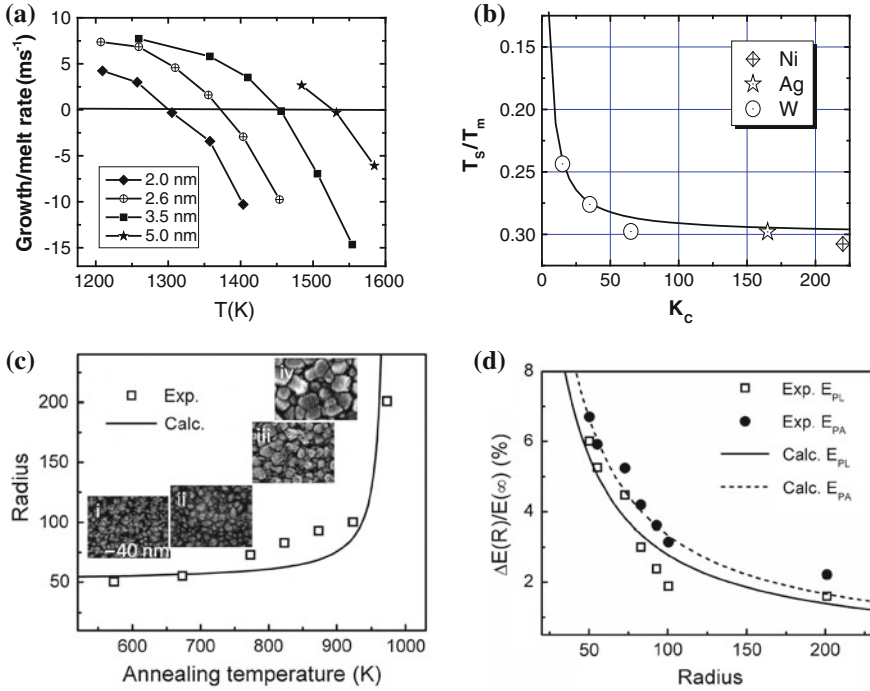


Fig. 14.10 **a** MD simulation of size and temperature dependence of Si nanosolid melting (negative) and growth (positive) [86]. **b** Agreement between BOLS predictions with measurements [194] of $T_s = 0.3T_m$ dependence of critical sizes for W ($T_m(\infty) = 3,695$ K), Ni (1,728 K), and Ag (1,235 K) nanocrystal growth. ZnO Size control of **c** the crystal size and **d** the E_{PL} and E_{PA} by a programmable annealing at: (1) as-grown, (2) 773 K, (3) 873 K, and (4) 923 K (Reprinted with permission from [7])

With T_{th} and K_0 being taken into consideration, Eq. (14.26) evolves into the form describing the T_a dependent of the critical size:

$$\begin{cases} T_a - T_{th} = 0.3T_m(K) = 0.3T_m(\infty)(1 + K^{-1}\Delta'_B) \\ K - K_0 = \frac{\Delta'_B}{(T_a - T_{th})/[0.3T_m(\infty)] - 1} = \frac{|\Delta'_B|}{1 - (T_a - T_{th})/[0.3T_m(\infty)]} \end{cases}$$

This relation indicates that the crystal size is dominated by the term $(T_a - T_{th})/[0.3T_m(\infty)]$; grain grows as T_a rises when $T_a > T_{th}$. The grain radius K is hence controllable by tuning the T_a .

The inset in Fig. 14.10 shows the SEM micrograph of spontaneous grain growth at different temperatures. Both the crystal size and the bandgap agree with the BOLS expectation on the T_a dependence of the physical properties.

14.5 Summary

The BOLS correlation has enabled the thermodynamic behavior of a nanosolid to be consistently formulated and understood in terms of atomic cohesive energy modulation. The difference between the cohesive energy of an atom at the surface and that of an atom inside the solid determines the fall or rise of the T_m of a surface and a nanosolid. The T_C suppression for ferromagnetic, ferroelectric, and superconducting nanosolids follows the same trend of T_m whose change follows the BOLS prediction including the short- and the long-range interactions.

Numerical match between predictions and measurements for a number of specimens reveals that the short spin–spin correlation dominates the exchange interaction in the ferromagnetic Fe, Co, Ni, and Fe_3O_2 nanosolids, whereas the long-range interaction dominates the exchange energy for the ferroelectric PbTiO_3 , PbZrO_3 , $\text{SrBi}_2\text{Ta}_2\text{O}_9$, and BaTiO_3 , and the superconductive MgB_2 nanosolids.

The BOLS premise also reconciles the activation energy for diffusion, agglomeration, and nucleation in crystal growth and the temperature dependence of the crystal size in annealing and vapor–solid epitaxial growth. It is possible to tune the crystal size and properties such as the band gap of noncrystallite by controlling the processing temperatures.

References

1. W.H. Qi, M.P. Wang, Size effect on the cohesive energy of nanoparticle. *J. Mater. Sci. Lett.* **21**(22), 1743–1745 (2002)
2. D. Xie, M.P. Wang, W.H. Qi, A simplified model to calculate the surface-to-volume atomic ratio dependent cohesive energy of nanocrystals. *J. Phys.-Condens. Matter* **16**(36), L401–L405 (2004)
3. W.H. Qi, M.P. Wang, G.Y. Xu, The particle size dependence of cohesive energy of metallic nanoparticles. *Chem. Phys. Lett.* **372**(5–6), 632–634 (2003)
4. D. Tomanek, S. Mukherjee, K.H. Bennemann, Simple theory for the electronic and atomic-structure of small clusters. *Phys. Rev. B* **28**(2), 665–673 (1983)
5. Q. Jiang, J.C. Li, B.Q. Chi, Size-dependent cohesive energy of nanocrystals. *Chem. Phys. Lett.* **366**(5–6), 551–554 (2002)
6. H.K. Kim, S.H. Huh, J.W. Park, J.W. Jeong, G.H. Lee, The cluster size dependence of thermal stabilities of both molybdenum and tungsten nanoclusters. *Chem. Phys. Lett.* **354**(1–2), 165–172 (2002)
7. C.Q. Sun, Size dependence of nanostructures: Impact of bond order deficiency. *Prog. Solid State Chem.* **35**(1), 1–159 (2007)
8. T. Gorecki, Vacancies and changes of physical-properties of metals at melting-point. *Z. Metallk.* **65**(6), 426–431 (1974)
9. M.W. Finnis, The Harris functional applied to surface and vacancy formation energies in aluminum. *J. Phys.-Condens. Matter* **2**(2), 331–342 (1990)
10. H. Brooks, *Impurities and Imperfection* (American Society for Metals, Cleveland, 1955)
11. W.H. Qi, M.P. Wang, Size dependence of vacancy formation energy of metallic nanoparticles. *Phys. B-Condens. Matter* **334**(3–4), 432–435 (2003)
12. E.A. Brands, *Smithells Metals Reference Book*, 6th edn. (Butterworths, London, 1983)

13. A.R. Miedema, Surface energies of solid metals. *Z. Metallk.* **69**(5), 287–292 (1978)
14. A.N. Goldstein, C.M. Echer, A.P. Alivisatos, Melting in semiconductor nanocrystals. *Science* **256**(5062), 1425–1427 (1992)
15. J.G. Dash, History of the search for continuous melting. *Rev. Mod. Phys.* **71**(5), 1737–1743 (1999)
16. J. Penfold, The structure of the surface of pure liquids. *Rep. Prog. Phys.* **64**(7), 777–814 (2001)
17. V.P. Modak, H. Pathak, M. Thayer, S.J. Singer, B.E. Wyslouzil, Experimental evidence for surface freezing in supercooled n-alkane nanodroplets. *Phys. Chem. Chem. Phys.* **15**(18), 6783–6795 (2013)
18. J.I. Akhter, Size-dependent superheating in confined Pb(111) films. *J. Phys.-Condens. Matter* **17**(1), 53–60 (2005)
19. H.W. Sheng, G. Ren, L.M. Peng, Z.Q. Hu, K. Lu, Superheating and melting-point depression of Pb nanoparticles embedded in Al matrices. *Philos. Mag. Lett.* **73**(4), 179–186 (1996)
20. H.W. Sheng, G. Ren, L.M. Peng, Z.Q. Hu, K. Lu, Epitaxial dependence of the melting behavior of In nanoparticles embedded in Al matrices. *J. Mater. Res.* **12**(1), 119–123 (1997)
21. Y. Lereah, G. Deutscher, P. Cheyssac, R. Kofman, A direct observation of low-dimensional effects on melting of small lead particles. *Europhys. Lett.* **12**(8), 709–713 (1990)
22. A.A. Rouse, J.B. Bernhard, E.D. Sosa, D.E. Golden, Variation of field emission and photoelectric thresholds of diamond films with average grain size. *Appl. Phys. Lett.* **75**(21), 3417–3419 (1999)
23. N. Hamada, S. Sawada, A. Oshiyama, New one-dimensional conductors—graphitic microtubules. *Phys. Rev. Lett.* **68**(10), 1579–1581 (1992)
24. V.P. Skripov, V.P. Koverda, V.N. Skokov, Size effect on melting of small particle. *Phys. Status Solidi A-Appl. Res.* **66**(1), 109–118 (1981)
25. J.F. Pocza, A. Barna, P.B. Barna, Formation processes of vacuum-deposited indium films and thermodynamical properties of submicroscopic particles observed by in situ electron microscopy. *J. Vacuum Sci. Technol.* **6**(4), 472–474 (1969)
26. Y.J. Lee, E.K. Lee, S. Kim, R.M. Nieminen, Effect of potential energy distribution on the melting of clusters. *Phys. Rev. Lett.* **86**(6), 999–1002 (2001)
27. S.C. Santucci, A. Goldoni, R. Larciprete, S. Lizzit, M. Bertolo, A. Baraldi, C. Masciovecchio, Calorimetry at surfaces using high-resolution core-level photoemission. *Phys. Rev. Lett.* **93**(10), 106105 (2004)
28. P. Bergese, I. Colombo, D. Gervasoni, L.E. Depero, Melting of nanostructured drugs embedded into a polymeric matrix. *J. Phys. Chem. B* **108**(40), 15488–15493 (2004)
29. I.S. Hwang, S.H. Chang, C.K. Fang, L.J. Chen, T.T. Tsong, Observation of finite-size effects on a structural phase transition of 2D nanoislands. *Phys. Rev. Lett.* **93**(10), 106101 (2004)
30. L. Miao, V.R. Bhethanabotla, B. Joseph, Melting of Pd clusters and nanowires: A comparison study using molecular dynamics simulation. *Phys. Rev. B* **72**(13), 134109 (2005)
31. F.G. Shi, Size-dependent thermal vibrations and melting in nanocrystals. *J. Mater. Res.* **9**(5), 1307–1313 (1994)
32. P. Buffat, J.P. Borel, Size effect on melting temperature of gold particles. *Phys. Rev. A* **13**(6), 2287–2298 (1976)
33. P. Pawlow, The dependency of the melting point on the surface energy of a solid body (Supplement). *Zeitschrift Fur Physikalische Chemie–Stoichiometrie Und Verwandtschaftslehre* **65**(5), 545–548 (1909)
34. H. Reiss, P. Mirabel, R.L. Whetten, Capillarity theory for the coexistence of liquid and solid clusters. *J. Phys. Chem.* **92**(26), 7241–7246 (1988)
35. H. Sakai, Surface-induced melting of small particles. *Surf. Sci.* **351**(1–3), 285–291 (1996)
36. K.J. Hanszen, Theoretische untersuchungen uber den schmelzpunkt kleiner kugelchen—ein beitrage zur thermodynamik der grenzflächen. *Z. Angew. Phys.* **157**(5), 523–553 (1960)

37. P.R. Couchman, W.A. Jesser, Thermodynamic theory of size dependence of melting temperature in metals. *Nature* **269**(5628), 481–483 (1977)
38. R.R. Vanfleet, J.M. Mochel, Thermodynamics of melting and freezing in small particles. *Surf. Sci.* **341**(1–2), 40–50 (1995)
39. B. Vekhter, R.S. Berry, Phase coexistence in clusters: an “experimental” isobar and an elementary model. *J. Chem. Phys.* **106**(15), 6456–6459 (1997)
40. Q. Jiang, Z. Zhang, J.C. Li, Superheating of nanocrystals embedded in matrix. *Chem. Phys. Lett.* **322**(6), 549–552 (2000)
41. M. Zhang, M.Y. Efremov, F. Schiettekatte, E.A. Olson, A.T. Kwan, S.L. Lai, T. Wisleder, J.E. Greene, L.H. Allen, Size-dependent melting point depression of nanostructures: nanocalorimetric measurements. *Phys. Rev. B* **62**(15), 10548–10557 (2000)
42. Z.H. Jin, P. Gumbsch, K. Lu, E. Ma, Melting mechanisms at the limit of superheating. *Phys. Rev. Lett.* **87**(5), 055703 (2001)
43. R. Defay, I. Prigogine, *Surface Tension and Adsorption* (Wiley, New York, 1951)
44. K.F. Peters, J.B. Cohen, Y.W. Chung, Melting of Pb nanocrystals. *Phys. Rev. B* **57**(21), 13430–13438 (1998)
45. U. Tartaglino, T. Zykova-Timan, F. Ercolessi, E. Tosatti, Melting and nonmelting of solid surfaces and nanosystems. *Phys. Rep.-Rev. Sec. Phys. Lett.* **411**(5), 291–321 (2005)
46. Q.W. Yang, R.Z. Zhu, J.A. Wei, Y.H. Wen, Surface-induced melting of metal nanoclusters. *Chin. Phys. Lett.* **21**(11), 2171–2174 (2004)
47. K.K. Nanda, S.N. Sahu, S.N. Behera, Liquid-drop model for the size-dependent melting of low-dimensional systems. *Phys. Rev. A* **66**(1), 013208 (2002)
48. J.H. Rose, J.R. Smith, J. Ferrante, Universal features of bonding in metals. *Phys. Rev. B* **28**(4), 1835–1845 (1983)
49. J. Tateno, Empirical relation on melting temperature of some ionic-crystals. *Solid State Commun.* **10**(1), 61–62 (1972)
50. M.A. Omar, *Elementary Solid State Physics: Principles and Applications* (Addison-Wesley, New York, 1993)
51. B. Pluis, D. Frenkel, J.F. Vanderveen, Surface-induced melting and freezing II. A semi-empirical landau-type model. *Surf. Sci.* **239**(3), 282–300 (1990)
52. M. Wautelet, Estimation of the variation of the melting temperature with the size of small particles, on the basis of a surface-phonon instability model. *J. Phys. D-Appl. Phys.* **24**(3), 343–346 (1991)
53. R. Vallee, M. Wautelet, J.P. Dauchot, M. Hecq, Size and segregation effects on the phase diagrams of nanoparticles of binary systems. *Nanotechnology* **12**(1), 68–74 (2001)
54. M. Wautelet, Phase stability of electronically excited Si nanoparticles. *J. Phys.-Condens. Matter* **16**(12), L163–L166 (2004)
55. Q. Jiang, L.H. Liang, J.C. Li, Thermodynamic superheating and relevant interface stability of low-dimensional metallic crystals. *J. Phys.: Condens. Matter* **13**(4), 565–571 (2001)
56. Q. Jiang, H.Y. Tong, D.T. Hsu, K. Okuyama, F.G. Shi, Thermal stability of crystalline thin films. *Thin Solid Films* **312**(1–2), 357–361 (1998)
57. Q. Jiang, H.X. Shi, J.C. Li, Finite size effect on glass transition temperatures. *Thin Solid Films* **354**(1–2), 283–286 (1999)
58. Z. Wen, M. Zhao, Q. Jiang, The melting temperature of molecular nanocrystals at the lower bound of the mesoscopic size range. *J. Phys.-Condens. Matter* **12**(41), 8819–8824 (2000)
59. Q. Jiang, L.H. Liang, M. Zhao, Modelling of the melting temperature of nano-ice in MCM-41 pores. *J. Phys.-Condens. Matter* **13**(20), L397–L401 (2001)
60. F.A. Lindemann, The calculation of molecular natural frequencies. *Physikalische Zeitschrift* **11**, 609–612 (1910)
61. Z. Zhang, J.C. Li, Q. Jiang, Modelling for size-dependent and dimension-dependent melting of nanocrystals. *J. Phys. D-Appl. Phys.* **33**(20), 2653–2656 (2000)
62. J.L. Wang, X.S. Chen, G.H. Wang, B.L. Wang, W. Lu, J.J. Zhao, Melting behavior in ultrathin metallic nanowires. *Phys. Rev. B* **66**(8), 085408 (2002)

63. W.Y. Hu, S.G. Xiao, J.Y. Yang, Z. Zhang, Melting evolution and diffusion behavior of vanadium nanoparticles. *Eur. Phys. J. B* **45**(4), 547–554 (2005)
64. S.L. Lai, J.Y. Guo, V. Petrova, G. Ramanath, L.H. Allen, Size-dependent melting properties of small tin particles: Nanocalorimetric measurements. *Phys. Rev. Lett.* **77**(1), 99–102 (1996)
65. Q. Jiang, X.Y. Lang, Glass transition of low-dimensional polystyrene. *Macromol. Rapid Commun.* **25**(7), 825–828 (2004)
66. X.Z. Ding, X.H. Liu, The Debye temperature of nanocrystalline titania measured by two different methods. *Phys. Status Solidi A-Appl. Res.* **158**(2), 433–439 (1996)
67. M. Schmidt, R. Kusche, B. von Issendorff, H. Haberland, Irregular variations in the melting point of size-selected atomic clusters. *Nature* **393**(6682), 238–240 (1998)
68. S.L. Lai, J.R.A. Carlsson, L.H. Allen, Melting point depression of Al clusters generated during the early stages of film growth: nanocalorimetry measurements. *Appl. Phys. Lett.* **72**(9), 1098–1100 (1998)
69. C.E. Bottani, A.L. Bassi, B.K. Tanner, A. Stella, P. Tognini, P. Cheyssac, R. Kofman, Melting in metallic Sn nanoparticles studied by surface Brillouin scattering and synchrotron-x-ray diffraction. *Phys. Rev. B* **59**(24), 15601–15604 (1999)
70. J. Zhong, L.H. Zhang, Z.H. Jin, M.L. Sui, K. Lu, Superheating of Ag nanoparticles embedded in Ni matrix. *Acta Mater.* **49**(15), 2897–2904 (2001)
71. O.G. Shpyrko, A.Y. Grigoriev, C. Steimer, P.S. Pershan, B.H. Lin, M. Meron, T. Graber, J. Gerbhardt, B. Ocko, M. Deutsch, Anomalous layering at the liquid Sn surface. *Phys. Rev. B* **70**(22), 224206 (2004)
72. L. Lu, R. Schwaiger, Z.W. Shan, M. Dao, K. Lu, S. Suresh, Nano-sized twins induce high rate sensitivity of flow stress in pure copper. *Acta Mater.* **53**(7), 2169–2179 (2005)
73. S. Veprek, M.G.J. Veprek-Heijman, P. Karvankova, J. Prochazka, Different approaches to superhard coatings and nanocomposites. *Thin Solid Films* **476**(1), 1–29 (2005)
74. S.G. Srinivasan, X.Z. Liao, M.I. Baskes, R.J. McCabe, Y.H. Zhao, Y.T. Zhu, Compact and dissociated dislocations in aluminum: Implications for deformation. *Phys. Rev. Lett.* **94**(12), 125502 (2005)
75. F. Ding, A. Rosen, K. Bolton, Size dependence of the coalescence and melting of iron clusters: a molecular-dynamics study. *Phys. Rev. B* **70**(7), 075416 (2004)
76. C.Q. Sun, Y. Shi, C.M. Li, S. Li, T.C.A. Yeung, Size-induced undercooling and overheating in phase transitions in bare and embedded clusters. *Phys. Rev. B* **73**(7), 075408 (2006)
77. M.J. Sinnott, *The solid state for engineers* (Wiley, New York, 1963)
78. K. Dick, T. Dhanasekaran, Z.Y. Zhang, D. Meisel, Size-dependent melting of silica-encapsulated gold nanoparticles. *J. Am. Chem. Soc.* **124**(10), 2312–2317 (2002)
79. K.K. Nanda, A. Maisels, F.E. Kruijs, H. Fissan, S. Stappert, Higher surface energy of free nanoparticles. *Phys. Rev. Lett.* **91**(10), 106102 (2003)
80. J. Eckert, J.C. Holzer, C.C. Ahn, Z. Fu, W.L. Johnson, Melting behavior of nanocrystalline aluminum powders. *Nanostruct Mater* **2**(4), 407–413 (1993)
81. S.L. Lai, G. Ramanath, L.H. Allen, P. Infante, Heat capacity measurements of Sn nanostructures using a thin-film differential scanning calorimeter with 0.2 nJ sensitivity. *Appl. Phys. Lett.* **70**(1), 43–45 (1997)
82. G.L. Allen, W.W. Gile, W.A. Jesser, The melting temperature of micro-crystals embedded in a matrix. *Acta Metall.* **28**(12), 1695–1701 (1980)
83. K.M. Unruh, T.E. Huber, C.A. Huber, Melting and freezing behavior of indium metal in porous glasses. *Phys. Rev. B* **48**(12), 9021–9027 (1993)
84. T. Bendavid, Y. Lereah, G. Deutscher, R. Kofman, P. Cheyssac, Solid-liquid transition in ultra-fine lead particles. *Philos. Mag. A-Phys. Condens. Matter Struct. Defects Mech. Prop.* **71**(5), 1135–1143 (1995)
85. A.N. Goldstein, The melting of silicon nanocrystals: Submicron thin-film structures derived from nanocrystal precursors. *Appl. Phys. A-Mater. Sci. Process.* **62**(1), 33–37 (1996)

86. P. Kebabinski (1999) Thermodynamics and kinetics of melting and growth of crystalline silicon clusters, in *Microcrystalline and Nanocrystalline Semiconductors-1998*, ed. by L.T. Canham et al., pp 311–316
87. Y.Y. Wu, P.D. Yang, Melting and welding semiconductor nanowires in nanotubes. *Adv. Mater.* **13**(7), 520–523 (2001)
88. G. Kellermann, A.F. Craievich, Structure and melting of Bi nanocrystals embedded in a B_2O_3 - Na_2O glass. *Physical Review B* **65**(13), 134204 (2002)
89. S.J. Peppiatt, Melting of small particles II. Bismuth. *Proc. R. Soc. London Ser. A-Math. Phys. Eng. Sci.* **345**(1642), 401–412 (1975)
90. H. Itoigawa, T. Kamiyama, Y. Nakamura, Bi precipitates in Na_2O - B_2O_3 glasses. *J. Non-Cryst. Solids* **210**(1), 95–100 (1997)
91. K. Morishige, K. Kawano, Freezing and melting of nitrogen, carbon monoxide, and krypton in a single cylindrical pore. *J. Phys. Chem. B* **104**(13), 2894–2900 (2000)
92. E. Molz, A.P.Y. Wong, M.H.W. Chan, J.R. Beamish, Freezing and melting of fluids in porous glass. *Phys. Rev. B* **48**(9), 5741–5750 (1993)
93. H. Saka, Y. Nishikawa, T. Imura, Temperature dependence of the stacking fault energy in silver-base alloys. *Phil. Mag. A* **57**, 859–868 (1983)
94. L. Grabaek, J. Bohr, E. Johnson, A. Johansen, L. Sarholt-kristensen, H.H. Andersen, Superheating and supercooling of lead precipitates in aluminum. *Phys. Rev. Lett.* **64**(8), 934–937 (1990)
95. L. Zhang, Z.H. Jin, L.H. Zhang, M.L. Sui, K. Lu, Superheating of confined Pb thin films. *Phys. Rev. Lett.* **85**(7), 1484–1487 (2000)
96. K. Chattopadhyay, R. Goswami, Melting and superheating of metals and alloys. *Prog. Mater. Sci.* **42**(1–4), 287–300 (1997)
97. G.A. Breaux, R.C. Benirschke, T. Sugai, B.S. Kinnear, M.F. Jarrold, Hot and solid gallium clusters: too small to melt. *Phys. Rev. Lett.* **91**(21), 215508 (2003)
98. S. Chacko, K. Joshi, D.G. Kanhere, S.A. Blundell, Why do gallium clusters have a higher melting point than the bulk? *Phys. Rev. Lett.* **92**(13), 135506 (2004)
99. Z.Y. Lu, C.Z. Wang, K.M. Ho, Structures and dynamical properties of C-n, Si-n, Ge-n, and Sn-n clusters with n up to 13. *Phys. Rev. B* **61**(3), 2329–2334 (2000)
100. F.C. Chuang, C.Z. Wang, S. Ogut, J.R. Chelikowsky, K.M. Ho, Melting of small Sn clusters by ab initio molecular dynamics simulations. *Phys. Rev. B* **69**(16), 165408 (2004)
101. K. Joshi, D.G. Kanhere, S.A. Blundell, Abnormally high melting temperature of the Sn-10 cluster. *Phys. Rev. B* **66**(15), 155329 (2002)
102. G.A. Breaux, C.M. Neal, B.P. Cao, M.F. Jarrold, Tin clusters that do not melt: Calorimetry measurements up to 650 K. *Phys. Rev. B* **71**(7), 073410 (2005)
103. E.A. Olson, M.Y. Efremov, M. Zhang, Z. Zhang, L.H. Allen, Size-dependent melting of Bi nanoparticles. *J. Appl. Phys.* **97**(3), 034304 (2005)
104. R.O. Jones, Simulated annealing study of neutral and charged clusters—Al(n) and Ga(n). *J. Chem. Phys.* **99**(2), 1194–1206 (1993)
105. A.A. Shvartsburg, B. Liu, Z.Y. Lu, C.Z. Wang, M.F. Jarrold, K.M. Ho, Structures of germanium clusters: Where the growth patterns of silicon and germanium clusters diverge. *Phys. Rev. Lett.* **83**(11), 2167–2170 (1999)
106. G.H. Lu, S.H. Deng, T.M. Wang, M. Kohyama, R. Yamamoto, Theoretical tensile strength of an Al grain boundary. *Phys. Rev. B* **69**(13), 134106 (2004)
107. K. Carling, G. Wahnstrom, T.R. Mattsson, A.E. Mattsson, N. Sandberg, G. Grimvall, Vacancies in metals: from first-principles calculations to experimental data. *Phys. Rev. Lett.* **85**(18), 3862–3865 (2000)
108. S. Ogata, J. Li, S. Yip, Ideal pure shear strength of aluminum and copper. *Science* **298**(5594), 807–811 (2002)
109. G.A. Breaux, C.M. Neal, B. Cao, M.F. Jarrold, Melting, premelting, and structural transitions in size-selected aluminum clusters with around 55 atoms. *Phys. Rev. Lett.* **94**(17), 173401 (2005)

110. H.H. Liu, E.Y. Jiang, H.L. Bai, P. Wu, Z.Q. Li, C.Q. Sun, Possible paths towards magic clusters formation. *THEOCHEM* **728**(1–3), 203–207 (2005)
111. H. Haberland, T. Hippler, J. Donges, O. Kostko, M. Schmidt, B. von Issendorff, Melting of sodium clusters: where do the magic numbers come from? *Phys. Rev. Lett.* **94**(3), 035701 (2005)
112. T. Bachels, H.J. Guntherodt, R. Schafer, Melting of isolated tin nanoparticles. *Phys. Rev. Lett.* **85**(6), 1250–1253 (2000)
113. C.Q. Sun, C.M. Li, H.L. Bai, E.Y. Jiang, Melting point oscillation of a solid over the whole range of sizes. *Nanotechnology* **16**(8), 1290–1293 (2005)
114. F. Huang, G.J. Mankey, M.T. Kief, R.F. Willis, Finite-size-scaling behavior of ferromagnetic thin-films. *J. Appl. Phys.* **73**(10), 6760–6762 (1993)
115. G.G. Kenning, J.M. Slaughter, J.A. Cowen, Finite-size effects in a CuMn spin-glass. *Phys. Rev. Lett.* **59**(22), 2596–2599 (1987)
116. Z.Q. Qiu, J. Pearson, S.D. Bader, Asymmetry of the spin reorientation transition in ultrathin Fe films and wedges grown on $\text{Ag}(100)$. *Phys. Rev. Lett.* **70**(7), 1006–1009 (1993)
117. W.L. Zhong, B. Jiang, P.L. Zhang, J.M. Ma, H.M. Cheng, Z.H. Yang, L.X. Li, Phase-transition in PbTiO_3 ultrafine particles of different sizes. *J. Phys.: Condens. Matter* **5**(16), 2619–2624 (1993)
118. K. Ishikawa, K. Yoshikawa, N. Okada, Size effect on the ferroelectric phase-transition in PbTiO_3 ultrafine particles. *Phys. Rev. B* **37**(10), 5852–5855 (1988)
119. T. Yu, Z.X. Shen, W.S. Toh, J.M. Xue, J. Wang, Size effect on the ferroelectric phase transition in $\text{SrBi}_2\text{Ta}_2\text{O}_9$ nanoparticles. *J. Appl. Phys.* **94**(1), 618–620 (2003)
120. A.V. Pogrebnnyakov, J.M. Redwing, J.E. Jones, X.X. Xi, S.Y. Xu, Q. Li, V. Vaithyanathan, D.G. Schlom, Thickness dependence of the properties of epitaxial MgB_2 thin films grown by hybrid physical-chemical vapor deposition. *Appl. Phys. Lett.* **82**(24), 4319–4321 (2003)
121. A.P. Tsai, N. Chandrasekhar, K. Chattopadhyay, Size effect on the superconducting transition of embedded lead particles in an Al-Cu-V amorphous matrix. *Appl. Phys. Lett.* **75**(11), 1527–1528 (1999)
122. I. Giaever, H.R. Zeller, Superconductivity of small TiN particles measured by tunneling. *Phys. Rev. Lett.* **20**(26), 1504–1508 (1968)
123. M. Stampanoni, A. Vaterlaus, M. Aeschlimann, F. Meier, Magnetism of epitaxial bcc iron on $\text{Ag}(001)$ observed by spin-polarized photoemission. *Phys. Rev. Lett.* **59**(21), 2483–2485 (1987)
124. M.N. Baibich, J.M. Broto, A. Fert, F.N. Vandau, F. Petroff, P. Eitenne, G. Creuzet, A. Friederich, J. Chazelas, Giant magnetoresistance of $(001)\text{Fe}/(001)\text{Cr}$ magnetic superlattices. *Phys. Rev. Lett.* **61**(21), 2472–2475 (1988)
125. C. Liu, E.R. Moog, S.D. Bader, Polar Kerr-effect observation of perpendicular surface anisotropy for ultrathin fcc Fe grown on $\text{Cu}(100)$. *Phys. Rev. Lett.* **60**(23), 2422–2425 (1988)
126. C.M. Schneider, P. Bressler, P. Schuster, J. Kirschner, J.J. Demiguel, R. Miranda, Curie-temperature of ultrathin films of fcc cobalt epitaxially grown on atomically flat $\text{Cu}(100)$ surfaces. *Phys. Rev. Lett.* **64**(9), 1059–1062 (1990)
127. X. Hu, Y. Kawazoe, Mean-field theory for critical phenomena in bilayer systems. *Phys. Rev. B* **50**(17), 12647–12658 (1994)
128. J.T. Ou, F.R. Wang, D.L. Lin, Critical behavior of magnetic films in the Ising model. *Phys. Rev. E* **56**(3), 2805–2810 (1997)
129. Y. Li, K. Baberschke, Dimensional crossover in ultrathin $\text{Ni}(111)$ films on $\text{W}(110)$. *Phys. Rev. Lett.* **68**(8), 1208–1211 (1992)
130. M. Tischer, D. Arvanitis, T. Yokoyama, T. Lederer, L. Troger, K. Baberschke, Temperature-dependent moxd measurements of thin Ni films on $\text{Cu}(100)$. *Surf. Sci.* **307**, 1096–1101 (1994)
131. L.H. Tjeng, Y.U. Idzerda, P. Rudolf, F. Sette, C.T. Chen, Soft-x-ray magnetic circular-dichroism—a new technique for probing magnetic-properties of magnetic-surfaces and ultrathin films. *J. Magn. Magn. Mater.* **109**(2–3), 288–292 (1992)

132. J.S. Jiang, C.L. Chien, Magnetization and finite-size effects in Gd/W multilayers. *J. Appl. Phys.* **79**(8), 5615–5617 (1996)
133. J.S. Jiang, D. Davidovic, D.H. Reich, C.L. Chien, Oscillatory superconducting transition-temperature in Nb/Gd multilayers. *Phys. Rev. Lett.* **74**(2), 314–317 (1995)
134. P.H. Zhou, D.S. Xue, Finite-size effect on magnetic properties in Prussian blue nanowire arrays. *J. Appl. Phys.* **96**(1), 610–614 (2004)
135. M.E. Fisher, M.N. Barber, Scaling theory for finite-size effects in critical region. *Phys. Rev. Lett.* **28**(23), 1516–1519 (1972)
136. D.S. Ritchie, M.E. Fisher, Finite-size and surface effects in Heisenberg films. *Phys. Rev. B* **7**(1), 480–494 (1973)
137. M.N. Barber, in *Phase Transitions and Critical Phenomena*, ed. by C. Domb, J. Lebowita, Vol. 8 (Academic, New York, 1983)
138. R.J. Zhang, R.F. Willis, Thickness-dependent Curie temperatures of ultrathin magnetic films: Effect of the range of spin–spin interactions. *Phys. Rev. Lett.* **86**(12), 2665–2668 (2001)
139. V.I. Nikolaev, A.M. Shipilin, The influence of breaking of exchange bonds on the Curie temperature. *Phys. Solid State* **45**(6), 1079–1080 (2003)
140. B. Sadeh, M. Doi, T. Shimizu, M.J. Matsui, Dependence of the Curie temperature on the diameter of Fe₃O₄ ultra-fine particles. *J Magn Soc Jpn* **24**, 511–514 (2000)
141. P.G. Degennes, *Superconductivity of Metals and Alloys* (Benjamin, New York, 1966)
142. R. Goswami, S. Banerjee, K. Chattopadhyay, A.K. Raychaudhuri, Superconductivity in rapidly quenched metallic systems with nanoscale structure. *J. Appl. Phys.* **73**(6), 2934–2940 (1993)
143. C.Q. Sun, Surface and nanosolid core-level shift: Impact of atomic coordination-number imperfection. *Phys. Rev. B* **69**(4), 045105 (2004)
144. R. Kubo, Electronic properties of metallic fine particles. I. *J. Phys. Soc. Jpn.* **17**(6), 975–979 (1962)
145. P.W. Anderson, Theory of dirty superconductors. *J. Phys. Chem. Solids* **11**(1–2), 26–30 (1959)
146. M. Strongin, R.S. Thompson, O.F. Kammerer, J.E. Crow, Destruction of superconductivity in disordered near-monolayer films. *Phys. Rev. B* **1**(3), 1078–1090 (1970)
147. B. Muhlschl, Dj Scalapin, R. Denton, *Thermodynamic properties of small superconducting particles*. *Phys. Rev. B* **6**(5), 1767 (1972)
148. Y. Guo, Y.F. Zhang, X.Y. Bao, T.Z. Han, Z. Tang, L.X. Zhang, W.G. Zhu, E.G. Wang, Q. Niu, Z.Q. Qiu, J.F. Jia, Z.X. Zhao, Q.K. Xue, Superconductivity modulated by quantum size effects. *Science* **306**(5703), 1915–1917 (2004)
149. A.V. Pogrebnnyakov, J.M. Redwing, S. Raghavan, V. Vaithyanathan, D.G. Schlom, S.Y. Xu, Q. Li, D.A. Tenne, A. Soukiassian, X.X. Xi, M.D. Johannes, D. Kasinathan, W.E. Pickett, J.S. Wu, J.C.H. Spence, Enhancement of the superconducting transition temperature of MgB₂ by a strain-induced bond-stretching mode softening. *Phys. Rev. Lett.* **93**(14), 147006 (2004)
150. J. Nagamatsu, N. Nakagawa, T. Muranaka, Y. Zenitani, J. Akimitsu, Superconductivity at 39 K in magnesium diboride. *Nature* **410**(6824), 63–64 (2001)
151. N. Hur, P.A. Sharma, S. Guha, M.Z. Cieplak, D.J. Werder, Y. Horibe, C.H. Chen, S.W. Cheong, High-quality MgB₂ films on boron crystals with onset T-c of 41.7 K. *J. Appl. Phys. Lett.* **79**(25), 4180–4182 (2001)
152. T. Yildirim, O. Gulseren, A simple theory of 40 K superconductivity in MgB₂: first-principles calculations of T-c its dependence on boron mass and pressure. *J. Phys. Chem. Solids* **63**(12), 2201–2206 (2002)
153. V. Hornebecq, C. Huber, M. Maglione, M. Antonietti, C. Elissalde, Dielectric properties of pure (BaSr)TiO₃ and composites with different grain sizes ranging from the nanometer to the micrometer. *Adv. Funct. Mater.* **14**(9), 899–904 (2004)

154. Z. Zhao, V. Buscaglia, M. Viviani, M.T. Buscaglia, L. Mitoseriu, A. Testino, M. Nygren, M. Jonsson, P. Nanni, Grain-size effects on the ferroelectric behavior of dense nanocrystalline BaTiO₃ ceramics. *Phys. Rev. B* **70**(2), 024107 (2004)
155. J. Hong, H.W. Song, J. Choi, S.K. Kim, Y. Kim, K. No, Dependence of ferroelectricity on film thickness in nano-scale Pb(Zr, Ti)O₃ thin films. *Integr. Ferroelectr.* **68**, 157–159 (2004)
156. W.P. Tong, N.R. Tao, Z.B. Wang, J. Lu, K. Lu, Nitriding iron at lower temperatures. *Science* **299**(5607), 686–688 (2003)
157. C.L. Wang, Y. Xin, X.S. Wang, W.L. Zhong, Size effects of ferroelectric particles described by the transverse Ising model. *Phys. Rev. B* **62**(17), 11423–11427 (2000)
158. B. Jiang, L.A. Bursill, Phenomenological theory of size effects in ultrafine ferroelectric particles of lead titanate. *Phys. Rev. B* **60**(14), 9978–9982 (1999)
159. H.T. Huang, C.Q. Sun, T.S. Zhang, P. Hing, Grain-size effect on ferroelectric Pb(Zr_{1-x}Ti_x)O₃ solid solutions induced by surface bond contraction. *Phys. Rev. B* **63**(18), 184112 (2001)
160. H.T. Huang, C.Q. Sun, P. Hing, Surface bond contraction and its effect on the nanometric sized lead zirconate titanate. *J. Phys.: Condens. Matter* **12**(6), L127–L132 (2000)
161. M. Tanaka, Y. Makino, Finite size effects in submicron barium titanate particles. *Ferroelectr. Lett. Sect.* **24**(1–2), 13–23 (1998)
162. A. Munkholm, S.K. Streiffer, M.V.R. Murty, J.A. Eastman, C. Thompson, O. Auciello, L. Thompson, J.F. Moore, G.B. Stephenson, Antiferrodistortive reconstruction of the PbTiO₃(001) surface. *Phys. Rev. Lett.* **88**(1), 016101 (2002)
163. H.T. Huang, L.M. Zhou, J. Guo, H.H. Hng, J.T. Oh, P. Hing, F spots and domain patterns in rhombohedral PbZr_{0.90}Ti_{0.10}O₃. *Appl. Phys. Lett.* **83**(18), 3692–3694 (2003)
164. Q. Jiang, X.F. Cui, M. Zhao, Size effects on Curie temperature of ferroelectric particles. *Appl. Phys. A-Mater. Sci. Process.* **78**(5), 703–704 (2004)
165. R.D. Zysler, D. Fiorani, A.M. Testa, L. Suber, E. Agostinelli, M. Godinho, Size dependence of the spin-flop transition in hematite nanoparticles. *Phys. Rev. B* **68**(21), 212408 (2003)
166. N. Amin, S. Arajs, Morin temperature of annealed submicronic alpha-Fe₂O₃ particles. *Phys. Rev. B* **35**(10), 4810–4811 (1987)
167. E. Weschke, H. Ott, E. Schierle, C. Schussler-Langeheine, D.V. Vyalikh, G. Kaindl, V. Leiner, M. Ay, T. Schmitte, H. Zabel, P.J. Jensen, Finite-size effect on magnetic ordering temperatures in long-period antiferromagnets: holmium thin films. *Phys. Rev. Lett.* **93**(15), 157204 (2004)
168. E.E. Fullerton, K.T. Riggs, C.H. Sowers, S.D. Bader, A. Berger, Suppression of biquadratic coupling in Fe/Cr(001) superlattices below the neel transition of Cr. *Phys. Rev. Lett.* **75**(2), 330–333 (1995)
169. S.S. Rao, K.N. Anuradha, S. Sarangi, S.V. Bhat, Weakening of charge order and antiferromagnetic to ferromagnetic switch over in Pr_{0.5}Ca_{0.5}MnO₃ nanowires. *Appl. Phys. Lett.* **87**(18), 182503 (2005)
170. S.Z. Ma, X.H. Wang, J. Zhou, L.T. Li, C.Q. Sun, Thermal stability of the nanostructured BaTiO₃ determined by long and short range interactions: a dual-shell model. *J. Appl. Phys.* **107**(6), 064102 (2010)
171. W.H. Zhong, C.Q. Sun, B.K. Tay, S. Li, H.L. Bai, E.Y. Jiang, Curie temperature suppression of ferromagnetic nanosolids. *J. Phys.: Condens. Matter* **14**(23), L399–L405 (2002)
172. R. Bergholz, U. Gradmann, Structure and magnetism of oligatomic Ni(111)-films on Re(0001). *J. Magn. Magn. Mater.* **45**(2–3), 389–398 (1984)
173. K. Uchina, Y. Sadanaga, T. Hirose, *J Am Ceram Soc.* **72**, 1555 (1999)
174. S. Chattopadhyay, P. Ayyub, V.R. Palkar, A.V. Gurjar, R.M. Wankar, M. Multani, Finite-size effects in antiferroelectric PbZrO₃ nanoparticles. *J. Phys.-Condens Matter* **9**(38), 8135–8145 (1997)
175. S. Li, T. White, J. Plevart, C.Q. Sun, Superconductivity of nano-crystalline MgB₂. *Supercond. Sci. Technol.* **17**(9), S589–S594 (2004)

176. S. Li, T. White, C.Q. Sun, Y.Q. Fu, J. Plevert, K. Lauren, Discriminating lattice structural effects from electronic contributions to the superconductivity of doped MgB_2 with nanotechnology. *J. Phys. Chem. B* **108**(42), 16415–16419 (2004)
177. S. Schlag, H.F. Eicke, W.B. Stern, Size driven phase transition and thermodynamic properties of nanocrystalline BaTiO_3 . *Ferroelectr. Lett. Sect.* **173**, 351–369 (1995)
178. R.Z. Valiev, R.K. Islamgaliev, I.V. Alexandrov, Bulk nanostructured materials from severe plastic deformation. *Prog. Mater. Sci.* **45**(2), 103–189 (2000)
179. G. Ouyang, C.X. Wang, G.W. Yang, Anomalous interfacial diffusion in immiscible metallic multilayers: a size-dependent kinetic approach. *Appl. Phys. Lett.* **86**(17), 171914 (2005)
180. I.M. Razumovskii, L.G. Kornelyuk, R.Z. Valiev, V.I. Sergeev, Diffusion along nonequilibrium grain-boundaries in a nickel-base superalloy. *Mater. Sci. Eng., A: Struct. Mater. Prop. Microstruct and Processing* **167**(1–2), 123–127 (1993)
181. J. Horvath, Diffusion in nanocrystalline materials diffusion and defect data—Solid State Data. Part A: Defect Diffus. Forum **66–69**, 207–227 (1989)
182. T. Mutschele, R. Kirchheim, Segregation and diffusion of hydrogen in grain-boundaries of palladium. *Scr. Metall.* **21**(2), 135–140 (1987)
183. Y.R. Kolobov, G.P. Grabovetskaya, I.V. Ratochka, E.V. Kabanova, E.V. Naidenkin, T.C. Lowe, Effect of grain-boundary diffusion fluxes of copper on the acceleration of creep in submicrocrystalline nickel. *Ann. Chim.-Sci. Mat.* **21**(6-7), 483–491 (1996)
184. R. Wurschum, A. Kubler, S. Gruss, P. Acharwaechter, W. Frank, R.Z. Valiev, R.R. Mulyukov, H.E. Schaeffer, Tracer diffusion and crystallite growth in ultra-fine-grained Pd prepared by severe plastic deformation. *Ann. Chim.-Sci. Mat.* **21**(6-7), 471–482 (1996)
185. Z.B. Wang, N.R. Tao, W.P. Tong, J. Lu, K. Lu, Diffusion of chromium in nanocrystalline iron produced by means of surface mechanical attrition treatment. *Acta Mater.* **51**(14), 4319–4329 (2003)
186. Y.M. Mishin, I.M. Razumovskii, Development of boundary diffusion-models. *Scr. Metall. Materialia* **25**(6), 1375–1380 (1991)
187. T. Shibata, B.A. Bunker, Z.Y. Zhang, D. Meisel, C.F. Vardeman, J.D. Gezelter, Size-dependent spontaneous alloying of Au-Ag nanoparticles. *J. Am. Chem. Soc.* **124**(40), 11989–11996 (2002)
188. H.C. Kim, T.L. Alford, D.R. Allee, Thickness dependence on the thermal stability of silver thin films. *Appl. Phys. Lett.* **81**(22), 4287–4289 (2002)
189. C.M. Li, C.S. Cha, Powder microelectrodes I. Reversible systems. *Acta Phys. Chim. Sin.* **4**(2), 167–171 (1988)
190. C.S. Cha, C.M. Li, H.X. Yang, P.F. Liu, Powder microelectrodes. *J. Electroanal. Chem.* **368**(1–2), 47–54 (1994)
191. C.M. Li, C.S. Cha, Porous carbon composite/enzyme glucose microsensor. *Front. Biosci.* **9**, 3324–3330 (2004)
192. D.D.D. Ma, C.S. Lee, F.C.K. Au, S.Y. Tong, S.T. Lee, Small-diameter silicon nanowire surfaces. *Science* **299**(5614), 1874–1877 (2003)
193. C.Q. Sun, H. Xie, W. Zhang, H. Ye, P. Hing, Preferential oxidation of diamond {111}. *J. Phys. D-Appl. Phys.* **33**(17), 2196–2199 (2000)
194. M.L. Alymov, E.I. Maltina, Y.N. Stepanov, *Nanostruct. Mater.* **4** (1994)
195. S. Ma, H. Liang, X. Wang, J. Zhou, L. Li, C.Q. Sun, Controlling the band gap of ZnO by programmable annealing. *J. Phys. Chem. C* **115**(42), 20487–20490 (2011)
196. Y. Hu, O.K. Tan, W.Q. Cao, W.G. Zhu, Fabrication and characterization of nano-sized SrTiO_3 -based oxygen sensor for near room-temperature operation. *IEEE Sens. J.* **5**(5), 825–832 (2005)
197. Y. Hu, O.K. Tan, J.S. Pan, X. Yao, A new form of nanosized SrTiO_3 material for near-human-body temperature oxygen sensing applications. *J. Phys. Chem. B* **108**(30), 11214–11218 (2004)

198. M.K. Zayed, H.E. Elsayed-Ali, Condensation on (002) graphite of liquid bismuth far below its bulk melting point. *Phys. Rev. B* **72**(20), 205426 (2005)
199. Q. Jiang, F.G. Shi, Size-dependent initial sintering temperature of ultrafine particles. *J. Mater. Sci. Technol.* **14**(2), 171–172 (1998)
200. H. Roder, E. Hahn, H. Brune, J.P. Bucher, K. Kern, Building one-dimensional and 2-dimensional nanostructures by diffusion-controlled aggregation at surfaces. *Nature* **366**(6451), 141–143 (1993)

Chapter 15

Lattice Dynamics: Phonon Relaxation

- *Frequency of lattice vibration fingerprints the stiffness (Yd) of a peculiarly representative bond in real space in the form of $\omega \propto z/d(E/\mu)^{1/2} \propto (Yd)^{1/2}$ with involvement of the bond order (z), bond length (d), bond energy (E), and the reduced mass of a dimer.*
- *The process of phonon scattering contributes less to the intrinsic vibration.*
- *Atomic undercoordination softens the optical phonons of nanostructures.*
- *Intergrain interaction results in emerging of the low-frequency phonons whose frequency undergoes blueshift with reduction in solid size.*
- *The D and $2D$ modes in carbon arise from interaction of a certain atoms with all of its z neighbors; while the G mode in carbon and the E_g mode (144 cm^{-1}) in TiO_2 are dominated by dimer interaction only.*

15.1 Background

Vibration of atoms at a surface is of high interest because the behavior of phonons influences directly the electrical and optical properties of materials, such as electron–phonon coupling, photoabsorption, photoemission, and transport dynamics in devices [1]. With miniaturization of a solid down to the nanometer scale, the transverse and the longitudinal optical (TO/LO) Raman modes shift toward lower frequency (phonon softening) [2], accompanied with generation of low-frequency Raman (LFR) acoustic modes at wave numbers of a few or a few tens cm^{-1} . The LFR frequency shifts up (phonon stiffening) when the solid size is reduced [3, 4]. Theoretical studies are based on the continuum dielectric mechanism [5, 6] or from microscopic lattice dynamics point of view [4, 7]. Multi-phonon resonant scattering exists throughout the course of measurements.

The size-dependent Raman shifts follow empirically the relation [2, 4],

$$\omega(K) = \omega(\infty) + A_f(d_0/K)^K,$$

where A_f and κ are adjustable parameters used to fit the measurement. For the optical redshift, $A_f < 0$. For Si example, $\omega(\infty) = 520 \text{ cm}^{-1}$ corresponds to a wavelength of $2 \times 10^4 \text{ nm}$. The index κ varies from 1.08 to 1.44. The d_0 is the lattice size that should contract with the solid dimension [8]. For the LFR mode blueshift, $A_f > 0$, $\kappa = 1$. The LFR mode disappears when the particle size approaches infinity, $\omega(\infty) = 0$.

15.1.1 Acoustic Phonon Stiffening

15.1.1.1 Quadrupolar Vibration

The LFR is in acoustic category, which is associated with the vibration of the nanoparticle. The phonon energies are size dependent and vary with materials of the host matrix. The LFR scattering from silver nanoclusters embedded in porous Al_2O_3 [9] and SiO_2 [10] seemed arise from the quadrupolar vibration modes that are enhanced by the excitation of the surface plasmas of the encapsulated Ag particles. The selection of modes by LFR scattering is due to the stronger plasmon–phonon coupling for these modes. For an Ag particle smaller than 4 nm, the size dependence of the LFR peak frequency approximates Lamb’s theory [11], which gives vibrational frequencies of a homogeneous elastic body in a spherical form.

The mechanism for the LFR mode enhancement is analogous to the case of surface-plasma-enhanced Raman scattering from molecules adsorbed on rough metal surfaces. The surface acoustic phonons are eigenfrequencies of a homogeneous elastic sphere under stress-free boundary conditions, which give rise to a low-frequency ω that is in the range of a few to a few tens of cm^{-1} . The LFR mode corresponds to the spheroidal and the torsional mode of vibrations of a spherical or an ellipsoidal particle. Spheroidal motions are associated with dilation, and it depends strongly on the cluster material through the transverse and the longitudinal sound velocities, v_t and v_l , respectively. The sound velocity in a medium depends functionally on the Young’s modulus and the mass density, i.e., $v \sim (Y/\rho)^{0.5} \sim \sqrt{E_b}$, where E_b is the cohesive energy per coordinate [12]. No volume change is assumed in the torsional motion of the particle. These modes are characterized by indices l and n , where l is the angular momentum quantum number and n is the branch number, and $n = 0$ represents the surface modes. The spheroidal modes with $l = 0$ and 2 are Raman active, and the torsional modes are Raman inactive [13]. The surface quadrupole mode ($l = 2$) appears in both polarized and depolarized geometry, whereas the surface symmetric mode ($l = 0$) appears only in the polarized geometry. The relation between the particle size and the frequency of the polarized acoustic phonon follows [14]:

$$\sin(\xi) = 4n_{\text{eff}}^2 j_1(\xi)$$

with complex argument,

$$\xi = R(\omega + i\Gamma)/v_1 \quad (15.1)$$

where ω and Γ are the phonon frequency and bandwidth, respectively, for the polarization-confined acoustic phonon of the first order. The term $j_1(\xi)$ is the spherical Bessel function of the first kind with order one, n_{eff} is an effective internal acoustic index given by,

$$n_{\text{eff}}^2 = n_p^2 - f_c \left\{ n_m^2 - (k\xi)^2 / \{4[1 - i(k\xi)]\} \right\} \quad (15.2)$$

where n_p and n_m are the ratios of transverse-to-longitudinal sound velocities in the particle and in the matrix, respectively, k is the ratio between the v_1 in the particle to that in the matrix, and f_c is a coupling constant between the particle and the matrix,

$$f_c = \rho_m / (k^2 \rho_p)$$

with ρ_m and ρ_p being the mass densities for the matrix and for the particle, respectively. By substituting n_{eff} in Eq. (15.2) into Eq. (15.1), the relation between particle radius R and the phonon frequency ω can be obtained from the real part of Eq. (15.1). The eigenfrequencies for the torsional modes and the spheroidal modes with $n = 0$ can be written as [15]:

$$\begin{cases} \omega_t^1 = 0.815v_t/Rc, & \omega_t^2 = 0.4v_t/Rc & \text{(Torsional)} \\ \omega_s^0 = 0.18v_1/Rc, & \omega_s^1 = 0.585v_1/Rc, & \omega_s^2 = 0.42v_1/Rc & \text{(spheroidal)} \end{cases}$$

where c is the velocity of light in vacuum. For bulk Ag, $v_t = 1,660$ m/s and $v_1 = 3,650$ m/s, the ω is around 10^2 cm^{-1} level. This approach fits the measured LFR data for Ag embedded in Al_2O_3 and SiO_2 matrix [14, 15].

The polarized and depolarized LFR peaks can also be ascribed as the confined LA-like and TA-like acoustic phonons, respectively [16]. Interface between the nanoparticle and the matrix leads to a redshift for both the polarized and the depolarized LFR peaks. This approach improves the fit to the measurement compared with Lamb's model. Atomistic simulations [17] suggested that the morphology of nanoscopic Ag grains (twinned icosahedra, Mark's decahedra, and irregular nanograins) introduces a high degree of complexity into the phonon spectra with total and partial vibrational density of states and phonon localization. For the low energy, single-crystalline grains present torsional and radial phonon modes. When compared to faceted grains of the same size, high-energy, spherical models that present regular protrusions on the surface have a smaller acoustic gap and a higher total acoustic DOS. The twinned icosahedra have a breathing mode. Nanograins with grain boundaries and surface disorder do not have degenerate frequencies, and the acoustic gap is significantly reduced.

15.1.1.2 Lattice Strain

Lattice contraction induced strain is suggested to be responsible for the LFR blueshift. $\text{CdS}_x\text{Se}_{1-x}$ nanocrystals embedded in a borosilicate ($\text{B}_2\text{O}_3\text{-SiO}_2$) glass matrix undergo the size-dependent compressive strain [18]. The lattice strain causes the surface tension to increase when the crystal size is reduced. The compressive stress overcoming the redshift caused by phonon confinement with negative dispersion is suggested to drive the LFR blueshift. The LFR blueshift is also related to the bond length and energy that are functionally dependent on the entropy, latent heat of fusion, and the melting point [19].

15.1.2 Optical Phonon Softening

The high-frequency Raman shift has usually been suggested to be activated by surface disorder [20] and explained in terms of surface stress [21, 22], phonon quantum confinement [23, 24], and surface chemical effect. The Raman shifts of TiO_2 particles are attributed to the effects of decreasing particle size on the force constants and vibrational amplitudes of the nearest neighbor bonds [25]. However, the effect of stress can usually be ignored for hydrogenated silicon [26, 27], in which hydrogen atoms terminate the surface dangling bonds to reduce the bond strains and hence the residual stress.

The phonon confinement model [23] attributes the redshift of the asymmetric Raman line to relaxation of the q -vector selection rule for the excitation of the Raman active phonons due to their localization. The relaxation of the momentum conservation rule arises from the finite crystalline size and the diameter distribution of the nanosolid in the films. When the size is decreased, the rule of momentum conservation will be relaxed and the Raman active modes will not be limited at the center of the Brillouin zone [21]. The large surface-to-volume ratio of a nanodot strongly affects the optical properties mainly due to introducing surface polarization states [28].

Particle size reduction softens the phonons for all glasses, and the phonon frequencies of CdSe nanodots vary with the composition of host glasses. Models based on assumptions that the materials are homogeneous and isotropic are valid only in the long-wavelength limit. When the size of the nanosolid is in the range of a few nanometers, the continuum dielectric models exhibit limitations.

Hwang et al. [29] consider the effect of lattice contraction in explaining the versatile phonon redshifts of nanosolid CdSe embedded in different glass matrices. The following expresses the K -dependent phonon shift with inclusion of lattice contraction,

$$\omega(K) = \omega_L + \Delta\omega_D(K) + \Delta\omega_C(K) \quad (15.3)$$

where ω_L is the LO phonon frequency of the bulk. $\Delta\omega_D(K)$ is the peak shift due to phonon dispersion, and $\Delta\omega_C(K)$ the peak shift due to lattice contraction. The phonon dispersion $\Delta\omega_D(K)$ follows

$$\Delta\omega_D(K) = \left[\omega_L^2 - \beta_L^2 \left(\frac{\mu_{np}}{Kd_0} \right)^2 \right]^{1/2} - \omega_L \cong - \left(\frac{\beta_L^2}{2\omega_L} \right) \left(\frac{\mu_{np}}{Kd_0} \right)^2 \quad (15.4)$$

where the parameter β_L describes the phonon dispersion assumed to be parabolic and μ_{np} is the nonzero n_p the root of the equation of $\tan(\mu_{np}) = \mu_{np}$. The $\Delta\omega_C(K)$ is given as [18]:

$$\Delta\omega_C(K) = \omega_L \left[\left(1 + \frac{3\Delta d(K)}{d} \right)^{-\gamma} - 1 \right] \cong -3\gamma\omega_L \frac{\Delta d(K)}{d}$$

where

$$\begin{aligned} \frac{\Delta d(K)}{d} &= (\alpha' - \alpha)(T - T_g) - \frac{2\beta_c}{3} \left(\frac{\sigma_\infty}{Kd_0} + \frac{b}{2(Kd_0)^2} \right) \\ &\cong (\alpha' - \alpha)(T - T_g) - \frac{\beta_c b}{3(Kd_0)^2} \end{aligned} \quad (15.5)$$

γ is the Grüneisen parameter, α' and α are the linear thermal expansion coefficients of the host glass and the nanodot, respectively. T and T_g are the testing and the heat treatment temperature, respectively. β_c and σ_∞ are the compressibility and the surface tension of the bulk, respectively, and b is the parameter describing the size-dependent surface tension of the crystal. The surface tension for bulk crystals is small. The first term describes lattice contraction by thermal expansion mismatch between the glass matrix and the crystal, and the second term arises from the increase in surface tension with the decrease in crystal size. Substituting Eq. (15.5) into (15.4), the phonon frequency change at a given temperature is obtained,

$$\begin{aligned} \frac{\Delta\omega(K)}{\omega_L} &= -3\gamma(\alpha' - \alpha)(T - T_g) - \left[\frac{1}{2} \left(\frac{\beta_L \mu_{np}}{\omega_L} \right)^2 - \gamma\beta_c b \right] (Kd_0)^{-2} \\ &= A - BK^{-2} \end{aligned} \quad (15.6)$$

For a free surface, $\alpha' = \alpha$, and $b = 0$. There are some difficulties however to use this equation, as remarked on by Hwang et al. [29] since the thermal expansion coefficient within the temperature range $T - T_g$ is hardly detectable. The value of B in Eq. (15.6) is given by the difference of the phonon negative dispersion and the size-dependent surface tension. Thus, a positive value of B indicates that the phonon negative dispersion exceeds the size-dependent surface tension and consequently causes the redshift of phonon frequency. On the contrary, if the size-dependent surface tension is stronger than the phonon negative dispersion, blue-shift occurs. In case of balance of the two effects, i.e., $B = 0$, the size dependence

disappears. Furthermore, the parameter b introduced by the size-dependent surface tension is unknown. At the lower end of the size limit, the $\omega(K) \rightarrow -\infty$ diverges in a K^{-2} way.

15.2 BOLS Formulation

15.2.1 Scattering by Vibrations

Raman scattering arises from the radiating dipole moment induced by the electric field of incident electromagnetic radiation. The laws of momentum and energy conservation govern the interaction between a phonon and a photon. When we consider a solid containing numerous Bravais unit cells and each cell contains n atoms, there will be $3n$ modes of vibrations. Among the $3n$ modes, there will be three acoustic modes, LA, TA₁ and TA₂ and $3(n - 1)$ optical modes. The acoustic mode represents the in-phase motion of the mass center of the unit cell or the entire solid.

Therefore, the LFR should arise from the vibration of the entire nanosolid interacting with the host matrix. For a freestanding nanosolid, the LFR corresponds to intercluster interaction. The optical mode is the relative motion of the individual atoms in a complex unit cell that contains more than one atom. For elemental solids with a simple such as the fcc structure of Ag, there presents only acoustic modes. The structure for silicon or diamond is an interlock of two fcc structures that contain in each cell two atoms in non-equivalent positions, so there will be three acoustic modes and three optical modes. The complex structure of compound ensures multiple optical modes.

15.2.2 Frequency of Lattice Vibration

The solution to the Hamiltonian of a vibration system is a Fourier series with multiple terms of frequencies being fold of that of the primary mode [30]. For example, the frequency of the secondary 2D mode should be twofold that of the primary D mode of diamond. Instead of the multi-phonon resonant scattering, Raman frequencies are the characteristics of the solution. Generally, one can measure the Raman frequency of a particular x mode as $\omega_x = \omega_{x0} + \Delta\omega_x$, where ω_{x0} is the reference point from which the Raman shift $\Delta\omega_x$ proceeds. The ω_{x0} may vary with the frequency of the incident radiation and substrate conditions, but not the nature and the trends induced by the applied stimuli. By expanding the interatomic potential in a Taylor series at its equilibrium and considering the effective atomic z , one can derive the vibration frequency shift of a harmonic system,

$$\begin{aligned}
u(r) &= \sum_{n=0} \left(\frac{d^n u(r)}{n! dr^n} \right)_{r=d_z} (r - d_z)^n \\
&\cong E_z + 0 + \frac{d^2 u(r)}{2! dr^2} \Big|_{r=d_z} (r - d_z)^2 + 0 \left((r - d_z)^{n \geq 3} \right) \\
&= E_z + \frac{\mu \omega^2 (r - d_z)^2}{2} + 0 \left((r - d_z)^{n \geq 3} \right).
\end{aligned}$$

From the dimensionality analysis, the term $\partial u^2(r)/\partial r^2|_{r=d}$ is proportional to $E_z^{1/2}/d_z$. The $E_z^{1/2}/d_z \cong \sqrt{Y_z d_z}$; ($Y_z \approx E_z/d_z^3$) is rightly the square root of the stiffness being the product of the Young's modulus and the bond length [31].

Equating the vibration energy to the third term in the Taylor series and omitting the higher-order terms yields

$$\frac{1}{2} \mu (\Delta \omega)^2 x^2 \cong \frac{1}{2} \frac{\partial u(r)}{\partial r^2} \Big|_{r=d} x^2 \propto \frac{1}{2} \frac{E_z}{d^2} x^2$$

As the first-order approximation, the lattice vibration frequency ω can be detected as Raman shift $\Delta \omega_x(z, d_z, E_z, \mu)$ from the reference point, $\omega_x(1, d_b, E_b, \mu)$, which depends functionally on the order z , length d_z , and energy E_z of the representative bond for the entire specimen and the reduced mass of the dimer atoms of the representative bond with $\mu = m_1 m_2 / (m_1 + m_2)$,

$$\begin{aligned}
\Delta \omega_x(z, d_z, E_z, \mu) &= \omega_x(z, d_z, E_z, \mu) - \omega_x(1, d_b, E_b, \mu) \\
&= \omega = \sqrt{\frac{d^2 u(r)}{\mu dr^2} \Big|_{r=d_z}} \propto \frac{1}{d_z} \left(\frac{E_z}{\mu} \right)^{1/2} \times \begin{cases} 1 \\ z \end{cases} \quad (15.7)
\end{aligned}$$

Considering the coordination-resolved mode vibration, the z takes the values of $z = 1$ and z . For instance, for the D and the 2D modes of graphene, z is the number of neighboring atoms, and for the G mode of graphene, and the 141 cm^{-1} mode of TiO_2 , $z = 1$ [32, 33].

The vibration amplitude is $x = r - d_0$. The high-order terms contributes to the nonlinear behavior. If the vibration is a dimer dominance, $z = 1$; otherwise, the short-range interaction on each atom results from its neighboring coordinating atoms, and the atomic vibrating dislocation is the contribution from all the surrounding coordinates, z . Since the vibration amplitude $x \ll d_0$, the mean contribution from each coordinate to the force constant and to the magnitude of dislocation as the first-order approximation

$$k_1 = k_2 = \dots = k_z = \mu_i (c\omega)^2,$$

and,

$$x_1 = x_2 = \dots = x_z = (r - d_0)/z.$$

Therefore, the total energy of a certain atom with z coordinates is the sum over all coordinates [34]

$$u(r) = -zE_b + \frac{zd^2u(r)}{2!dr^2} \Big|_{d_0} (r - d_0)^2 + \dots \quad (15.8)$$

This relation leads to an expression for the phonon frequency as a function of bond order, bond length, and bond energy

$$\omega \propto \frac{z(E_b)^{1/2}}{d_0}, \text{ and } \frac{\omega_z}{\omega} = z_{ib} C_z^{-(m/2+1)} \quad (15.9)$$

15.2.3 Size Dependence

Combining Eqs. (15.9) and (15.10) gives the size-dependent redshift of optical mode of a nanosolid [where $Q(\infty) = \omega(\infty) - \omega(1)$]:

$$\begin{aligned} \omega(K) - \omega(1) &= [\omega(\infty) - \omega(1)](1 + \Delta_R) \\ \text{or, } \frac{\omega(K) - \omega(\infty)}{\omega(\infty) - \omega(1)} &= \Delta_R < 0 \\ \Delta_R &= \sum_{i \leq 3} \gamma_i \left(\frac{\omega_i}{\omega_b} - 1 \right) = \begin{cases} \sum_{i \leq 3} \gamma_i \left(z_{ib} C_i^{-(m/2+1)} - 1 \right) & (z = z) \\ \sum_{i \leq 3} \gamma_i \left(C_i^{-(m/2+1)} - 1 \right) & (z = 1) \end{cases} \end{aligned} \quad (15.10)$$

where ω_{x0} and ω_{xi} correspond to the vibration frequency of an atom inside the bulk and in the i th surface atomic shell. $\omega_x(1)$ is the vibrational frequency of an isolated dimer, which is the reference point for the optical redshift upon nanosolid and bulk formation. The frequency decreases from the dimer value with the number of atomic CN and then reaches the bulk value ($z = 12$) that is experimentally detectable.

15.3 Verification and Quantification

15.3.1 CN-Resolved Optical Phonon Softening

The $\omega(\infty)$ and $\omega(K)$ in Eq. (15.10) are measured values. Based on the size notation and measurements, one is able to determine the $\omega(1)$ or the $\omega(\infty) - \omega(1)$ by matching the measured data of size dependence to the theoretically predicted

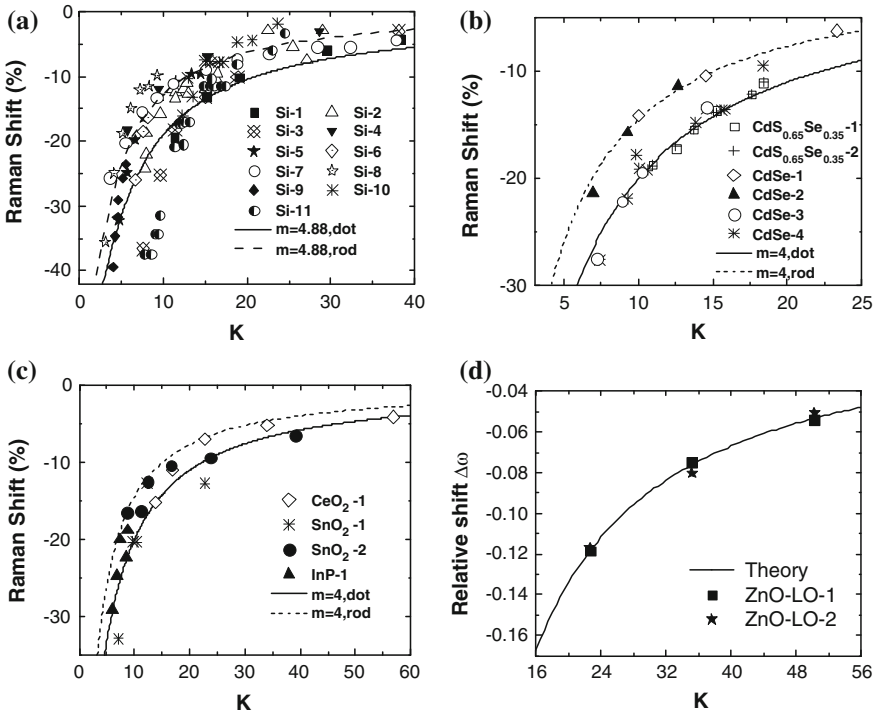


Fig. 15.1 Size-softened LO phonons of **a** Si [2, 4, 21, 35–39], **b** CdS_{0.65}Se_{0.35} [40] and CdSe [29, 41], **c** CeO₂ [20, 42, 43] and InP-1[44], **d** ZnO [45, 46] nanoparticles (Reprinted with permission from [31])

line, $\omega(\infty) - \omega(1) \equiv -A'/(\Delta_R K)$. Matching prediction to the measurement turns out $k = 1$ because $\Delta_R \propto K^{-1}$.

Figure 15.1 shows typical examples of size-softened optical phonons, which justifies the validity of the BOLS with derived information about the corresponding dimer vibration is given in Table 15.1. The size-softened phonons arise from the involvement of the interaction between the specific atom and its surrounding neighbors [32, 33].

15.3.2 LFR: Intercluster Interaction

Figure 15.2 shows the size-dependent LFR for different nanosolids. The LFR frequency depends linearly on the inverse K ,

$$\Delta\omega(K) = \omega(K) - \omega(\infty) = -A'K^{-1}$$

Table 15.1 Vibration frequencies of isolated dimers of various nanosolids and their redshift upon bulk formation derived from simulating the size-dependent redshift of Raman optical modes, as shown in Fig. 15.1

| Material | Mode | $\omega(\infty)(\text{cm}^{-1})$ | $\omega(1) (\text{cm}^{-1})$ |
|--|---------------------------|----------------------------------|------------------------------|
| Si | | 520.0 | 502.3 |
| CdS _{0.65} Se _{0.35} | LO ₁ CdSe-like | 203.4 | 158.8 |
| | LO ₂ CdS-like | 303 | 257.7 |
| CdSe | LO | 210 | 195.2 |
| CeO ₂ | | 464.5 | 415.1 |
| SnO ₂ | A _{1g} | 638 | 602.4 |
| InP | LO | 347 | 333.5 |

The zero intercept at the vertical axis, $\omega(\infty) = 0$, indicates that when K approaches infinity, the LFR disappears, which implies that the LFR modes and their blueshift result from vibration of the individual nanoparticle as a whole, as represented in the quadruple vibration mechanism. This notation treats the nanoparticle as an individual body in vibration, which gives information about the strength of the interparticle interaction, as summarized in Table 15.2. The mechanical coupling between nanoclusters is the key to the LFR [47].

15.3.3 Amplitude and Frequency of Skin Atom Vibration

At a given temperature, the vibrational amplitude and frequency of a given atom follow Einstein's relation, $\mu(c\omega x)^2/2z = k_B T$, which yields the magnitude of vibration: $x \propto z^{1/2}\omega^{-1}$. The frequency and magnitude of vibration for an surface atom ($z = 4$) follows

$$\begin{aligned}
 \frac{\omega_1}{\omega_b} &= z_{ib} C_1^{-(m/2+1)} = \begin{cases} 0.88^{-3.44}/3 = 0.517 & (\text{Si}) \\ 0.88^{-3/2}/3 = 0.404 & (\text{Metal}) \end{cases} \\
 \frac{x_1}{x_b} &= (z_1/z_b)^{1/2} \omega_b/\omega_1 = (z_b/z_1)^{1/2} C_1^{(m/2+1)} \\
 &= \begin{cases} \sqrt{3} \times 0.88^{3.44} = 1.09 & (\text{Si}) \\ \sqrt{3} \times 0.88^{3/2} = 1.43 & (\text{Metal}) \end{cases}
 \end{aligned} \tag{15.11}$$

The vibrational amplitude of an atom at the surface is indeed greater [54, 55] than that of a bulk atom while the frequency is lower. The magnitude and frequency are sensitive to the m value and vary insignificantly with the curvature of a spherical dot when $K > 3$.

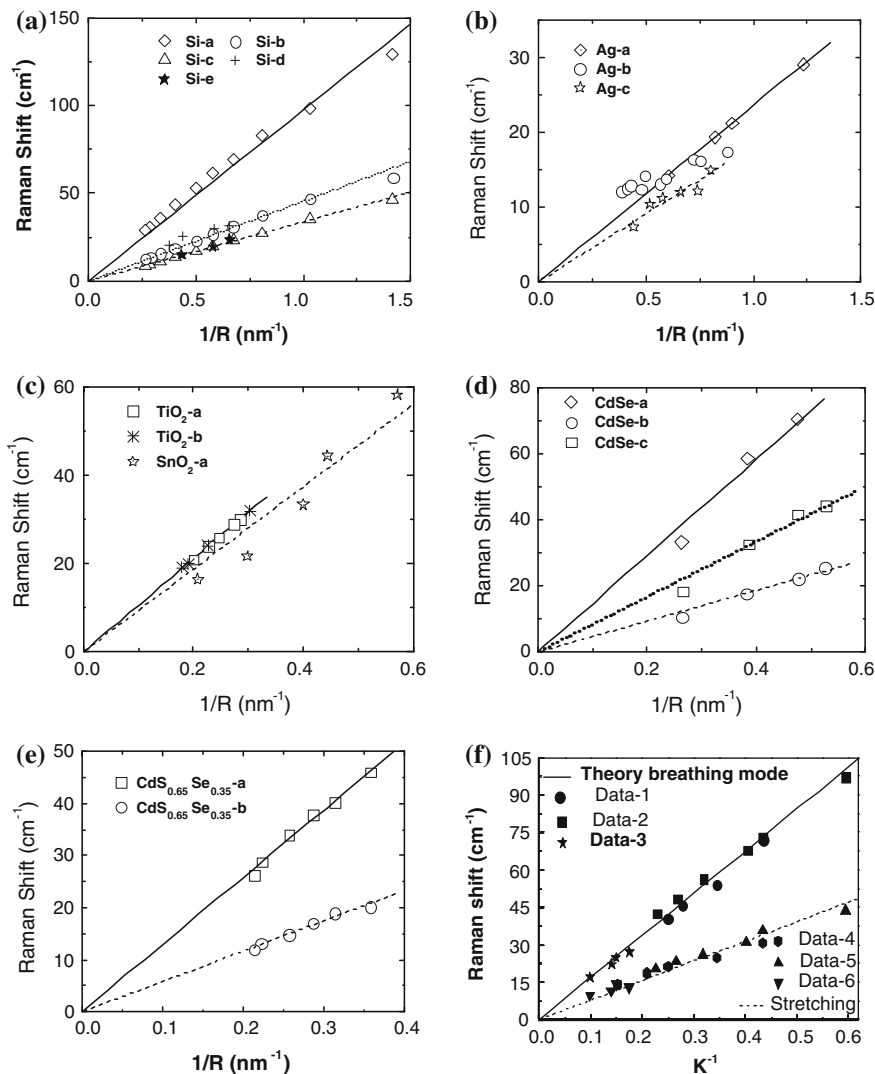


Fig. 15.2 LFR blueshift of **a** Si [3, 4], **b** Ag-a (in SiO₂) [48], Ag-b (in SiO₂) [10], and Ag-c (in Al₃O₂) [9], **c** TiO₂[49] and SnO₂ [20], **d** CdSe-a ($l = 0, n = 2$), CdSe-b ($l = 2, n = 1$), and CdSe-c ($l = 0, n = 1$) [50], **e** CdS_{0.65}Se_{0.35}-a (in glass) [40], **f** ZnO [51–53] nanoparticles (Reprinted with permission from [31])

Table 15.2 Linearization of the LFR acoustic modes of various nanosolids

| Sample | A' |
|--------------|------------------|
| Ag-a & Ag-b | 23.6 ± 0.72 |
| Ag-c | 18.2 ± 0.56 |
| TiO-a, TiO-b | 105.5 ± 0.13 |
| SnO-a | 93.5 ± 5.43 |
| CdSe-1-a | 146.1 ± 6.27 |
| CdSe-1-b | 83.8 ± 2.84 |
| CdSe-1-c | 46.7 ± 1.39 |
| CdSSe-a | 129.4 ± 1.18 |
| CdSSe-b | 58.4 ± 0.76 |
| Si | 97.77 |
| Si | 45.57 |
| Si | 33.78 |

15.4 Summary

The BOLS correlation and the scaling relation correlate the size-created and stiffened LFR phonons to the intergrain interaction. The size-softened optical phonons result from interaction between the undercoordinated neighboring atoms in the skin. The coordination reduction enhancement of the phonon frequencies of the E_g mode of TiO_2 and the G mode of GNR is dictated by the interaction between undercoordinated dimers. The size-induced phonon relaxation follows a K^{-1} fashion. Decoding the size dependency of the Raman optical redshift leads to vibrational information of Si, InP, CdS, CdSe, TiO_2 , CeO_2 , and SnO_2 dimers and their bulk shifts.

References

1. T. Takagahara, Electron-phonon interactions and excitonic dephasing in semiconductor nanocrystals. *Phys. Rev. Lett.* **71**(21), 3577–3580 (1993)
2. J. Zi, H. Buscher, C. Falter, W. Ludwig, K.M. Zhang, X.D. Xie, Raman shifts in Si nanocrystals. *Appl. Phys. Lett.* **69**(2), 200–202 (1996)
3. M. Fujii, Y. Kanzawa, S. Hayashi, K. Yamamoto, Raman scattering from acoustic phonons confined in Si nanocrystals. *Phys. Rev. B* **54**(12), R8373–R8376 (1996)
4. W. Cheng, S.F. Ren, Calculations on the size effects of Raman intensities of silicon quantum dots. *Phys. Rev. B* **65**(20), 205305 (2002)
5. M.C. Klein, F. Hache, D. Ricard, C. Flytzanis, Size dependence of electron-phonon coupling in semiconductor nanospheres—the case of CdSe. *Phys. Rev. B* **42**(17), 11123–11132 (1990)
6. C. Trallero-Giner, A. Debernardi, M. Cardona, E. Menendez-Proupin, A.I. Ekimov, Optical vibrons in CdSe dots and dispersion relation of the bulk material. *Phys. Rev. B* **57**(8), 4664–4669 (1998)
7. X.H. Hu, J. Zi, Reconstruction of phonon dispersion in Si nanocrystals. *J. Phys. Condens. Matter* **14**(41), L671–L677 (2002)
8. C.Q. Sun, S. Li, B.K. Tay, Laser-like mechanoluminescence in ZnMnTe-diluted magnetic semiconductor (vol 81, pg 460, 2002). *Appl. Phys. Lett.* **82**(20), 3568–3569 (2003)

9. B. Palpant, H. Portales, L. Saviot, J. Lerme, B. Prevel, M. Pellarin, E. Duval, A. Perez, M. Broyer, Quadrupolar vibrational mode of silver clusters from plasmon-assisted Raman scattering. *Phys. Rev. B* **60**(24), 17107–17111 (1999)
10. M. Fujii, T. Nagareda, S. Hayashi, K. Yamamoto, Low-frequency Raman-scattering from small silver particles embedded in SiO₂ thin-films. *Phys. Rev. B* **44**(12), 6243–6248 (1991)
11. H. Lamb, *Proc. London Math. Soc.* **13** (1882)
12. M.A. Omar, *Elementary Solid State Physics: Principles and Applications* (Addison-Wesley, New York, 1993)
13. E. Duval, Far-infrared and Raman vibrational transitions of a solid sphere—selection-rules. *Phys. Rev. B* **46**(9), 5795–5797 (1992)
14. P. Verma, W. Cordts, G. Irmer, J. Monecke, Acoustic vibrations of semiconductor nanocrystals in doped glasses. *Phys. Rev. B* **60**(8), 5778–5785 (1999)
15. M. Ferrari, F. Gonella, M. Montagna, C. Tosello, Detection and size determination of Ag nanoclusters in ion-exchanged soda-lime glasses by waveguided Raman spectroscopy. *J. Appl. Phys.* **79**(4), 2055–2059 (1996)
16. J. Zi, K.M. Zhang, X.D. Xie, Microscopic calculations of Raman scattering from acoustic phonons confined in Si nanocrystals. *Phys. Rev. B* **58**(11), 6712–6715 (1998)
17. G.A. Narvaez, J. Kim, J.W. Wilkins, Effects of morphology on phonons in nanoscopic silver grains. *Phys. Rev. B* **72**(15), 155411 (2005)
18. G. Scamarcio, M. Lugara, D. Manno, Size-dependent lattice contraction in CdS_{1-x}Se_x nanocrystals embedded in glass observed by Raman-scattering. *Phys. Rev. B* **45**(23), 13792–13795 (1992)
19. L.H. Liang, C.M. Shen, X.P. Chen, W.M. Liu, H.J. Gao, The size-dependent phonon frequency of semiconductor nanocrystals. *J. Phys. Condens. Matter* **16**(3), 267–272 (2004)
20. A. Dieguez, A. Romano-Rodriguez, A. Vila, J.R. Morante, The complete Raman spectrum of nanometric SnO₂ particles. *J. Appl. Phys.* **90**(3), 1550–1557 (2001)
21. Z. Iqbal, S. Veprek, Raman-scattering from hydrogenated microcrystalline and amorphous-silicon. *J. Phys. C-Solid State Phys.* **15**(2), 377–392 (1982)
22. E. Anastassakis, E. Liarokapis, Polycrystalline Si under strain—elastic and lattice-dynamic considerations. *J. Appl. Phys.* **62**(8), 3346–3352 (1987)
23. H. Richter, Z.P. Wang, L. Ley, The one phonon Raman-spectrum in microcrystalline silicon. *Solid State Commun.* **39**(5), 625–629 (1981)
24. I.H. Campbell, P.M. Fauchet, The effects of microcrystal size and shape on the one phonon Raman-spectra of crystalline semiconductors. *Solid State Commun.* **58**(10), 739–741 (1986)
25. H.C. Choi, Y.M. Jung, S.B. Kim, Size effects in the Raman spectra of TiO₂ nanoparticles. *Vib. Spectrosc.* **37**(1), 33–38 (2005)
26. X. Wang, D.M. Huang, L. Ye, M. Yang, P.H. Hao, H.X. Fu, X.Y. Hou, X.D. Xie, Pinning of photoluminescence peak positions for light-emitting porous silicon—an evidence of quantum-size effect. *Phys. Rev. Lett.* **71**(8), 1265–1267 (1993)
27. J.L. Andujar, E. Bertran, A. Canillas, C. Roch, J.L. Morenza, Influence of pressure and radio-frequency power on deposition rate and structural-properties of hydrogenated amorphous-silicon thin-films prepared by plasma deposition. *J. Vac. Sci. Technol. A-Vac. Surf. Films* **9**(4), 2216–2221 (1991)
28. L. Banyai, S.W. Koch, *Semiconductor Quantum Dots* (World Scientific, Singapore, 1993)
29. Y.N. Hwang, S.H. Shin, H.L. Park, S.H. Park, U. Kim, H.S. Jeong, E.J. Shin, D. Kim, Effect of lattice contraction on the Raman shifts of CdSe quantum dots in glass matrices. *Phys. Rev. B* **54**(21), 15120–15124 (1996)
30. W.G. Han, C.T. Zhang, A theory of nonlinear stretch vibrations of hydrogen-bonds. *J. Phys.: Condens. Matter* **3**(1), 27–35 (1991)
31. C.Q. Sun, Size dependence of nanostructures: Impact of bond order deficiency. *Prog. Solid State Chem.* **35**(1), 1–159 (2007)
32. X.X. Yang, J.W. Li, Z.F. Zhou, Y. Wang, L.W. Yang, W.T. Zheng, C.Q. Sun, Raman spectroscopic determination of the length, strength, compressibility, debye temperature, elasticity, and force constant of the C–C bond in graphene. *Nanoscale* **4**(2), 502–510 (2012)

33. X.J. Liu, L.K. Pan, Z. Sun, Y.M. Chen, X.X. Yang, L.W. Yang, Z.F. Zhou, C.Q. Sun, Strain engineering of the elasticity and the Raman shift of nanostructured TiO₂. *J. Appl. Phys.* **110**(4), 044322 (2011)
34. L.K. Pan, C.Q. Sun, C.M. Li, Elucidating Si–Si dimmer vibration from the size-dependent Raman shift of nanosolid Si. *J. Phys. Chem. B* **108**(11), 3404–3406 (2004)
35. G. Viera, S. Huet, L. Boufendi, Crystal size and temperature measurements in nanostructured silicon using Raman spectroscopy. *J. Appl. Phys.* **90**(8), 4175–4183 (2001)
36. P.M. Fauchet, I.H. Campbell, Raman-spectroscopy of low-dimensional semiconductors. *Crc Crit. Rev. Solid State Mater. Sci.* **14**, S79–S101 (1988)
37. A.K. Sood, K. Jayaram, D.V.S. Muthu, Raman and high-pressure photoluminescence studies on porous silicon. *J. Appl. Phys.* **72**(10), 4963–4965 (1992)
38. C. Ossadnik, S. Veprek, I. Gregora, Applicability of Raman scattering for the characterization of nanocrystalline silicon. *Thin Solid Films* **337**(1–2), 148–151 (1999)
39. G.X. Cheng, H. Xia, K.J. Chen, W. Zhang, X.K. Zhang, Raman measurement of the grain-size for silicon crystallites. *Phys. Status Solidi A-Appl. Res.* **118**(1), K51–K54 (1990)
40. P. Verma, L. Gupta, S.C. Abbi, K.P. Jain, Confinement effects on the electronic and vibronic properties of CdS_{0.65}Se_{0.35} nanoparticles grown by thermal annealing. *J. Appl. Phys.* **88**(7), 4109–4116 (2000)
41. A. Tanaka, S. Onari, T. Arai, Raman-scattering from CdSe microcrystals embedded in a germanate glass matrix. *Phys. Rev. B* **45**(12), 6587–6592 (1992)
42. J.E. Spanier, R.D. Robinson, F. Zheng, S.W. Chan, I.P. Herman, Size-dependent properties of CeO_{2-y} nanoparticles as studied by Raman scattering. *Phys. Rev. B* **64**(24), 245407 (2001)
43. C.H. Shek, G.M. Lin, J.K.L. Lai, Effect of oxygen deficiency on the Raman spectra and hyperfine interactions of nanometer SnO₂. *Nanostruct. Mater.* **11**(7), 831–835 (1999)
44. M.J. Seong, O.I. Micic, A.J. Nozik, A. Mascarenhas, H.M. Cheong, Size-dependent Raman study of InP quantum dots. *Appl. Phys. Lett.* **82**(2), 185–187 (2003)
45. H.-M. Cheng, K.-F. Lin, C.H. Hsu, C.-J. Lin, L.-J. Lin, W.-F. Hsieh, Enhanced resonant Raman scattering and electron–phonon coupling from self-assembled secondary ZnO nanoparticles. *J. Phys. Chem. B* **109**(39), 18385–18390 (2005)
46. J.W. Li, S.Z. Ma, X.J. Liu, Z.F. Zhou, C.Q. Sun, ZnO meso-mechano-thermo physical chemistry. *Chem. Rev.* **112**(5), 2833–2852 (2012)
47. M. Talati, P.K. Jha, Low-frequency acoustic phonons in nanometric CeO₂ particles. *Phys. E* **28**(2), 171–177 (2005)
48. P. Gangopadhyay, R. Kesavamoorthy, K.G.M. Nair, R. Dhandapani, Raman scattering studies on silver nanoclusters in a silica matrix formed by ion-beam mixing. *J. Appl. Phys.* **88**(9), 4975–4979 (2000)
49. P. Gotic, M. Ivanda, A. Sekulic, S. Music, S. Popovic, A. Turkovic, K. Furic, Microstructure of nanosized TiO₂ obtained by sol-gel synthesis. *Mater. Lett.* **28**(1–3), 225–229 (1996)
50. L. Saviot, B. Champagnon, E. Duval, I.A. Kudriavtsev, A.I. Ekimov, Size dependence of acoustic and optical vibrational modes of CdSe nanocrystals in glasses. *J. Non-Cryst. Solids* **197**(2–3), 238–246 (1996)
51. P.M. Chassaing, F. Demangeot, N. Combe, L. Saint-Macary, M.L. Kahn, B. Chaudret, Raman scattering by acoustic phonons in wurtzite ZnO prismatic nanoparticles. *Physical Review B* **79**(15), 155314–155315 (2009)
52. N. Combe, P.-M. Chassaing, F. Demangeot, Surface effects in zinc oxide nanoparticles. *Phys. Rev. B* **79**(4), 045408–045409 (2009)
53. H.K. Yadav, V. Gupta, K. Sreenivas, S.P. Singh, B. Sundarakannan, R.S. Katiyar, Low frequency Raman scattering from acoustic phonons confined in ZnO nanoparticles. *Phys. Rev. Lett.* **97**(8), 085502 (2006)
54. F.G. Shi, Size-dependent thermal vibrations and melting in nanocrystals. *J. Mater. Res.* **9**(5), 1307–1313 (1994)
55. Q. Jiang, Z. Zhang, J.C. Li, Superheating of nanocrystals embedded in matrix. *Chem. Phys. Lett.* **322**(6), 549–552 (2000)

Chapter 16

Electrons: Entrapment and Polarization

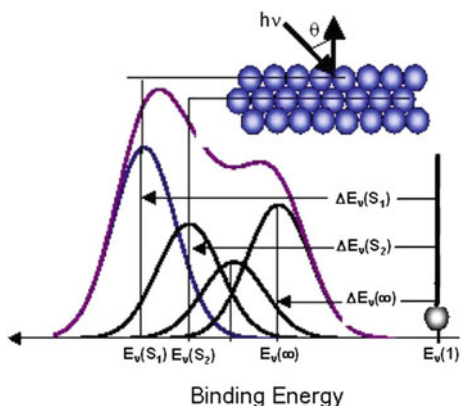
- *The core-level binding energy shifts from that of an isolated atom upon inter-atomic interaction being involved.*
- *The exchange integral that is proportional to the single bond energy at equilibrium determines the amount of shift.*
- *The energy level shift is always positive unless polarization is involved.*
- *Atomic undercoordination induced quantum entrapment not only deepens the core level but also enlarges the electroaffinity of a substance. The latter represents the ability of the specimen holding electrons captured from its partner that has lower electronegativity.*
- *Nonbonding electron polarization not only lowers the work function but also splits and screens the local interatomic potential.*
- *Complementing STM/S and PES, ZPS collects coordination-resolved information of bond length, bond energy, binding energy density, atomic cohesive energy and the extent of polarization at sites of defects, monolayer skins, terrace edges, hetero-junction interfaces.*

16.1 Known Facts

16.1.1 Core-Level Shift

Unlike the valence DOS that provides direct information about charge transportation kinetics during reaction [1], the energy shift of a core level of an isolated atom gives profound information about the strength of crystal binding that is dominated by inter-atomic interaction. Alteration of bond nature and variation of bond strength will affect the crystal potential and hence shift the core level by a certain extent. The strengthening of the bond will shift the core level positively; if the crystal potential is screened or the bond becomes weaker, the shift is negative.

Fig. 16.1 Illustration of the positive shift (S_1, S_2, \dots, B) of the core-band components with respect to the energy level of an isolated atom, $E_v(0)$. $\Delta E_v(S_i) = \Delta E_v(\infty)[1 + \Delta_i]$. The intensities of the low-energy bulk component often increase with incident beam energy and the decrease in the polar angle between the incident beam and surface normal (Reprinted with permission from [3])



Being able to discriminate the crystal binding core-level shift (CLS) from the atomic potential trapping (core level of an isolated atom) of a core electron under various physical and chemical environment is a great challenge. Combining the most advanced laser cooling technology and XPS, one can measure the energy separation between different energy levels of the slowly moving gaseous atoms trapped by the laser beams, but the core-level energy of an isolated atom is hardly applicable [2]. What one can measure using XPS are the convoluted broad peaks of the core bands contributing from atomic potential trapping, crystal binding, crystal orientation, surface relaxation or nanosolid formation, and the effect of surface passivation.

In addition to the well-known chemical shift caused by the core-hole ‘screening’ due to charge transportation in reaction, relaxed interlayer spacings at a surface can split the core level of a specimen into a few components, as illustrated in Fig. 16.1. However, specification of the origin of reference from which the shift proceeds, the direction of the shift, and the surface components is quite controversial, as summarized in Table 16.1. With the widely used sign convention, a positive shift relates the low-energy component (away from E_F) to the surface contribution (S_i , $i = 1, 2, \dots, B$) while the high-energy component relates to the bulk origin (B) (Fig. 16.1). The resultant peak is often located in between the components, and the exact position of the resultant peak varies with experimental conditions, which results in the core-level energy of a specimen vary from source to source.

The intensity of the high-energy component in an XPS spectrum often increases with the incident beam energy or with decreasing the polar angle between the incident beam and the surface normal (Fig. 16.1) [4–8]. The intensity of the high-energy component also increases with decreasing the surface atomic density under the same beam conditions (energy and incident angle). For example, Pd(110, 100, 111) surfaces demonstrate two $3d_{5/2}$ components at 334.35 and 334.92 eV. The intensity of high-energy 334.35 eV peak decreases when the surface geometry turns from (110) to (111) [9] (with atomic density $n_{110} : n_{100} : n_{111} = 1/\sqrt{2} : 1 : 2/\sqrt{3}$). The 306.42 eV component of the Rh(111) $3d_{5/2}$ level measured

Table 16.1 Specifications and the possible origins of the surface-induced core-level splitting

| Specification | Samples |
|--|---|
| Positive shift: (low \rightarrow high \rightarrow E_F) S_1, S_2, \dots , and B | Nb(001) [4, 6], graphite [5], Tb(0001)-4f [7], Ta(001)-4f [8], Ta(110) [10], Mg(10 $\bar{1}$ 0) [11], Ga(0001) [12] |
| Negative shift: B, S_4, S_3, S_2 , and S_1 B, S_2, S_3, S_4 , and S_1 | Be(0001) [13], Be(10 $\bar{1}$ 0) [11, 14, 15], Ru(10 $\bar{1}$ 0) [16], Mo(110) [17], Al(001) [18], W(110) [19], W(320) [20], Pd(110,100, 111) [9] |
| Mixed shift: $S_1, B, S_{\text{dimer-up}}, S_{\text{dimer-down}}$ S_2, B, S_1 S_1, B, S_2 $S_2, S_3 + S_4, S_1, B$ | Si(111) [21], Si(113) [22], Ge(001) [23], Ru(0001) [24], Be(10 $\bar{1}$ 0) [25] |

under 380 eV beam energy is relatively higher than the same peak of the Rh(110) measured using 370 eV beam energy compared with the high-energy component at 307.18 eV [9].

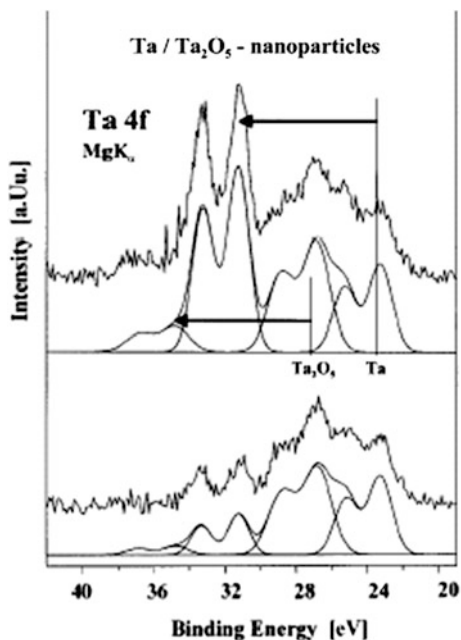
The energy of individual component should be intrinsic, but the resultant peak changes with crystal orientation due to the convoluted contribution from the involved peaks. The dependence of the high-energy-component intensity on the beam conditions and on the atomic density implies that the surface relaxation induces a positive shift.

Upon reacting with electronegative elements such as oxygen, the core level also splits with the production of low-energy satellites. Such ‘chemical shift’ arises from core-hole production due to bond formation that weakens the ‘screening’ of the crystal potential acting on the specific core electrons. The effects of surface relaxation and chemical reaction enhance each other. For instance, Ru(0001) shows two distinct Ru-3d_{5/2} components of surface relaxation. Both components then shift deeply simultaneously by up to 1.0 eV upon oxygen adsorption [21]. Rh(100)-3d_{5/2} has a component of 0.65 eV away from the main peak of the bulk. Oxygen addition shifts both components 0.40 eV downward [26].

Figure 16.2 shows the XPS Ta-4f spectra taken after removing about 30 % (upper) and 50 % (lower) of the surface nanoparticles of a gate device by sputtering [27]. The first doublets (Ta-4f_{5/2} and Ta-4f_{7/2}) at (23.4 and 26.8 eV) arise from TaSi_x and Ta₂O₅. The second doublets at (31.6 and 34.5 eV) are size-induced shift of the first doublets (arrows indicated). Removing the nanoparticles weakens the size effect. Therefore, both surface relaxation and chemical reaction shift the core level positively by an amount that varies not only with the original core-level position but also with the extent of reaction.

When a solid reduces its size down to the nanometer scale, the entire core-level features (both the main peak and the chemical satellites) move simultaneously toward lower binding energy and the amounts of shift depend not only on the

Fig. 16.2 Intensity and energy shift of Ta-4f doublets upon 30 % (*upper*) and 50 % (*lower*) of the surface nanoparticles being removed of a Ta/Si gate device (Reprinted with permission from [27]). The first pair of doublets ($4f_{5/2}$ and $4f_{7/2}$) at 23.4 and 26.8 eV arises from $TaSi_x$ and Ta_2O_5 . The second pair of doublets at 31.6 and 34.5 eV is the size-induced shift of the first doublets (*arrows indicated*)



original core-level position but also on the shape-and-size of the particle. Fig 16.3 compares with the mono-peak of S-2p and S-2s core bands of a bulk solid, ZnS and CdS nanosolids exhibit three components of each the S-2p and S-2s core band [28, 29]. These components have been ascribed as the contribution, from low to high binding energy, from the outermost capping layer (0.2–0.3 nm thick), surface layer (0.2–0.3 nm thick), and the core of the nanosolid, as shown in Fig. 16.3a and b. This specification is in accordance with the surface positive CLS. The energy value of each component changes slightly with particle size but the peak intensity of each component and the resultant peak vary considerably with the fraction of atoms in the capping, the surface, and the core of the nanosolid. The intensity of the capping component grows at the cost of the intensity of the core component, as the solid size is reduced. The intensity increase in the capping component follows the size dependence of the surface-to-volume ratio of a nanosolid [28, 29].

Generally, the CLS of a nanosolid follows the scaling relation with a slope B that changes depending on surface treatment, particle dimensionality, and particle–substrate interaction [30]. The highly oriented pyrolytic graphite (HOPG) shows two $C1s$ components separated by 0.12 eV [5]. The low-energy component of the $C1s$ corresponds to surface and the other to the bulk. The $2p_{3/2}$ peak of Cu nanosolids deposited on HOPG and CYLC (polymer) [31], the 4f peak of Au nanosolids deposited on Octanedithiol [32], TiO_2 [33], and Pt(001) [34] as well as the Pd/HOPG [35] follow exactly the scaling law. Therefore, surface relaxation and nanosolid formation play an equivalent role in splitting and shifting the core-level energy.

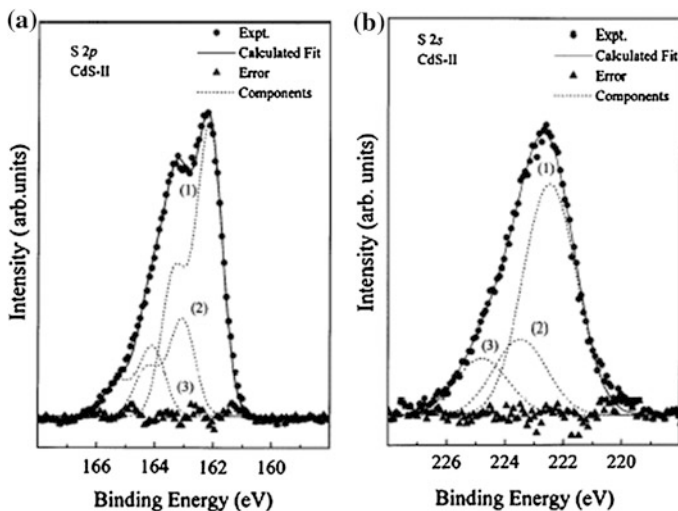


Fig. 16.3 The core (1), surface (2), and capping (3) components of **a** S-2p and **b** S-2s spectra of CdS nanosolids. Particle-size reduction lowers the intensity of the core (1) and increases the intensities of surface and capping component (Reprinted with permission from [28, 29]) because of the atomic fraction change in the respective layers

16.1.2 Known Mechanisms

The following arguments provide possible mechanism for the surface- and size-induced CLS:

1. Surface interlayer contraction creates the low-energy component of the CLS [8]. For example, a 12 % contraction of the first-layer spacing Nb(001) shifts the $3d_{3/2}$ by 0.50 eV [4]; a (10 ± 3) % contraction of the first-layer spacing of Ta(001) offsets the $4f_{5/2(7/2)}$ by 0.75 eV [8]. The surface bond contraction enhanced interlayer charge density, and resonant diffraction of the incident light is supposed to be responsible for the positive energy shift [4, 8].
2. The thermo-chemical or the ‘initial (neutral, un-ionized specimen with n electrons)–final (radiation beam ionized specimen with $n - 1$ electrons) states’ relaxation dominates the CLS [6, 7]. The energy required for removing a core electron from a surface atom is different from the energy required for a bulk atom. The surface atom is assumed as a ‘ $Z + 1$ impurity’ sitting on the substrate metal of Z atomic number. The energy states of atoms at a flat surface or at a curved surface are expected to increase/decrease while the initial states of atoms in the bulk decreases/increase when the particle size is reduced. This mostly adopted mechanism creates the positive, negative, or mixed surface shift in theoretical calculations.

3. Size-enhanced ionicity of copper and oxygen contributes to the 2p energy shift of CuO nanosolid [36]. Oxygen atoms bond more strongly to the Cu atoms in a nanosolid than they do inside the bulk.
4. Other models such as the interfacial dipole formation [27], metal-non-metal transition [35, 37–39], and interfaces oxygen vacancies [40] account for the size-induced CLS.

Briefly, surface relaxation, defect creation, adatom epitaxy, atomic chain and ribbon formation, and nanosolid formation share a common yet unclear origin in splitting and shifting the core level to lower binding energy. However, definition of the XPS peak components is quite confusing and the origin for the under-coordination induced CLS is under debate.

16.2 BOLS-TB Formulation

16.2.1 Hamiltonian and Energy Dispersion

The Hamiltonian and the wave function describing an electron moving in the v th orbit of an atom in the bulk solid is [41],

$$\begin{aligned}
 H &= H_0 + H' \\
 \text{with } \begin{cases} H_0 = -\frac{\hbar^2 \nabla^2}{2m} + V_{\text{atom}}(r) & \text{(Intra-atomic interaction)} \\ H' = V_{\text{cryst}}(r) & \text{(Inter-atomic interaction)} \end{cases} & \quad (16.1) \\
 \phi_{v,i}(r) \cong |v, i\rangle \exp(ikr) \approx |v, i\rangle & \quad \text{(Wave-function)}
 \end{aligned}$$

H_0 is the Hamiltonian for an isolated atom, which consists the kinetic energy and the intra-atomic potential, $V_{\text{atom}}(r) = V_{\text{atom}}(r + R) < 0$. The H' is the crystal potential, $V_{\text{crystal}}(r) = V_{\text{crystal}}(r + R) < 0$. The $V_{\text{cryst}}(r)$ sums over the interatomic potentials of all neighbors. Both the intra- and the crystal potentials are periodic in real space with R being the lattice constant. Because of the strong localization nature of the core electrons, the plain wave prefactor $\exp(ikr)$ of the Bloch function is often omitted [41]. Therefore, the wave function for the tightly bound core electron approximates an electron of an isolated atom. The eigen wave function $|v, i\rangle$ meets the following requirement with i and j denoting atomic positions:

$$\langle v, j | v, i \rangle = \delta_{ij} = \begin{cases} 1 & (i = j) \\ 0 & (i \neq j) \end{cases}$$

The energy dispersion of an electron in an ideal bulk ($z_b = 12$ for an fcc standard) is:

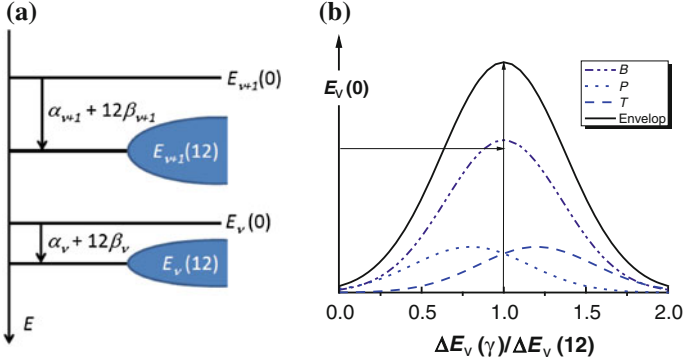


Fig. 16.4 **a** Evolution of the v th atomic energy level from $E_v(0)$ to the v th band $E_{v(z_b = 12)}$ with a shift of $\Delta E_v(z_b) = \alpha_v + z_b \beta_v$ and a width of $E_{vW} = 2z_b \beta_v \Phi_v(k, R)$ upon bulk formation. The amounts of energy shift and band expansion depend on the cohesive energy per bond at equilibrium and the quantum number v of the band. **b** A typical XPS spectrum of the core band with addition of entrapment (T) and polarization (P) components to the bulk (B) shift. (Reprinted with permission from [3])

$$E_v(z_b) = E_v(0) + (\alpha_v + z_b \beta_v) + 2z_b \beta_v \Phi_v(k, R)$$

$$\text{with } \begin{cases} E_v(0) &= -\langle v, i | H_0 | v, i \rangle & (\text{Atomic core level}) \\ \alpha_v &= -\langle v, i | H' | v, i \rangle \propto E_b & (\text{Exchange integral}) \\ \beta_v &= -\langle v, i | H' | v, j \rangle \propto E_b & (\text{Overlap integral}) \end{cases} \quad (16.2)$$

The interaction between the ion-core and the particular electron determines the energy level of an isolated atom, $E_v(0)$. Being an intrinsic constant irrespective of the chemical or the coordination environment, the $E_v(0)$ reduces its value from 10^3 to 10^0 eV until the vacuum level $E_0 = 0$ as the v increases, or if one-step out from the nearest orbit outward of the atom. Once the crystal potential is involved, or a bulk or a liquid is formed, the core level $E_v(0)$ will deepen by an amount of $\Delta E_v(z_b) = E_v(z_b) - E_v(0) = \alpha_v + z_b \beta_v$ associated with band broadening. Both the exchange integral α_v and the overlap integral β_v are proportional to the cohesive energy per bond at equilibrium, E_b . As illustrated in Fig. 16.4, if one moves from the valance band downward, the $\Delta E_v(z_b)$ will turn from 10^0 to 10^{-1} eV and the E_{vW} approach a line of spin-resolved energy level, such as the $1s$, $2p_{1/2}$, and $2p_{3/2}$ levels of Cu. The shape of the core band follows the form of $2z_b \beta_v \Phi_v(k, R) \sim \sin^2(kR/2)$, for an fcc structure, is often approximated using the Gaussian or the Lorentz functions in decomposing the spectrum.

Typically, $z_b \beta_v / \alpha_v < 3\%$. the bond energy E_b dominates the CLS from the first-order approximation. Any perturbation to the interatomic potential at equilibrium, or any variation of the interatomic bond will directly change the bandwidth and the CLS changes with the effective atomic CN (z). If the z increases from zero (an isolated atom) to 12 (an infinite size), the CLS deepens from that of an isolated atom to a maximum at $z = 2$ (an fcc unit cell) and then recovers gradually to the

bulk shift E (12). The measured 2p level of Cr_N ($N = 2-13$ corresponds to $z = 2$) [42] does follow the expected CN trend.”

16.2.2 BOLS: Coordination Resolution

The modification of crystal potential deepens the core level by an amount of $\Delta E_v(z_b)$. The perturbation Δ_H will shift the bulk component positively ($\Delta_H > 0$, entrapment (T) or shifting away from E_f) or negatively ($\Delta_H < 0$, polarization (P) or moving toward E_f), see Fig. 16.4b. A mixed shift may happen if both entrapment and polarization simultaneously come into play. Assuming that the wave function changes insignificantly for the strongly localized core electrons, Eq. (16.1) turns to be the following form with replacing z_b with x representing the effect of atomic CN(z) variation or polarization,

$$H' = V_{\text{cryst}}(r)(1 + \Delta_H)$$

$$E_v(x) = E_v(0) + \alpha_{vx}(1 + x\beta_{vx}/\alpha_{vx}) + 2x\beta_{vx}\Phi_v(k, R)$$

$$\text{with } \begin{cases} E_v(0) &= -\langle v, i | H_0 | v, i \rangle & \text{(atomic core level)} \\ \alpha_{vx} &= -\langle v, i | H' | v, i \rangle \propto E_b(1 + \Delta_H) \propto E_x & \text{(Exchange integral)} \\ \beta_{vx} &= -\langle v, i | H' | v, j \rangle \propto E_b(1 + \Delta_H) \propto E_x & \text{(Overlap integral)} \end{cases} \quad (16.3)$$

According to the energy band theory and the BOLS correlation, the surface- and the size-induced energy shift of the energy level of an isolated atom $E_v(0)$ follows the relation:

$$\begin{cases} V(\Delta_H) = V_{\text{atom}}(r) + V_{\text{cry}}(r)[1 + \Delta_H] & (a) \\ E_v(\Delta_H) = E_v(0) + [E_v(\infty) - E_v(0)](1 + \Delta_H), & \text{or} \\ E_v(\Delta_H) = E_v(\infty) + [E_v(\infty) - E_v(0)]\Delta_H & (b) \end{cases} \quad (16.4)$$

where $E_v(0)$ and $E_v(\infty)$ are intrinsic quantities of a specimen. Neither chemical reaction nor bond relaxation changes these two quantities. The perturbation Δ_H follows,

$$\Delta_H = \begin{cases} \Delta_H(z) = \frac{E_z - E_b}{E_b} = C_z^{-m} - 1 & \text{(Site specificity of defect and surface)} \\ \Delta_H(K, \tau) = \tau K^{-1} \sum_{i \leq 3} C_i \Delta_H(z_i) & \text{(Shell resolved in } \tau \text{ - shaped nanosolid)} \end{cases} \quad (16.5)$$

Δ_H is the site-specific contribution for defect and surface and the weighted sum over the outermost two or three atomic layers of nanosolid. At the lower end of the size limit, the perturbation to the Hamiltonian of a nanosolid relates directly to the behavior of the representative bond, being the case of the outermost surface layer and a monatomic chain. The following relation holds,

$$\begin{aligned} \frac{E_v(\Delta_l) - E_v(0)}{E_v(\Delta_{l'}) - E_v(0)} &= \frac{1 + \Delta_l}{1 + \Delta_{l'}}, (l' \neq l), \text{ or} \\ \frac{E_v(\Delta_l) - E_v(\infty)}{E_v(\Delta_{l'}) - E_v(\infty)} &= \frac{\Delta_l}{\Delta_{l'}}, (l' \neq l) \end{aligned} \quad (16.6)$$

Δ_l can be either form of Eq. (16.5). Given an XPS profile with clearly identified $E_v(S_i)$ and $E_v(\infty)$ of a surface, or a set of XPS data collected from a certain type of nanosolid of different sizes, one can obtain the $E_v(0)$ and $\Delta E_v(\infty)$, and the CN-dependent shift, based on the following relations derived from Eq. (16.6):

$$\begin{cases} E_v(0) &= \frac{(1+\Delta_{H'})E_v(\Delta_H) - (1+\Delta_H)E_v(\Delta_{H'})}{\Delta_{H'} - \Delta_H}, \quad (H \neq H') \\ \Delta E_v(\infty) &= E_v(\infty) - E_v(0) \\ E_v(0) &= E_v(\infty) - [E_v(\Delta_H) - E_v(\infty)]\Delta_H^{-1} \quad (\text{Atomic } v\text{th level}) \\ E_v(\Delta_H) &= E_v(0) + [E_v(0) - E_v(\infty)](1 + \Delta_H) \quad (\text{Perturbation - respolved}) \\ E_v(z) &= E_v(0) + [E_v(0) - E_v(\infty)]C_z^{-m} \quad (\text{CN - resolved}) \end{cases} \quad (16.7)$$

The XPS spectra of a certain substance of various orientations or different sizes contain a total number of $l (>2)$ peak components; $E_v(0)$ and the $\Delta E_v(\infty)$ will take the mean value of the $N = C_l^2 = l! / [(l-2)!2!]$ combinations with a standard deviation σ , and the CN-dependent CLS follows:

$$\begin{cases} \langle E_v(0) \rangle &= [\sum_N E_v(0)] / N \quad (\text{Atomic } v\text{th level}) \\ \sigma &= \sqrt{[\sum_N (E_v(0) - \langle E_v(0) \rangle)^2] / [N(N-1)]} \quad (\text{Perturbation-respolved}) \\ E_v(z) &= \langle E_v(0) \rangle \pm \sigma + [\langle E_v(0) \rangle - E_v(\infty)]C_z^{-m} \quad (\text{CN - resolved}) \end{cases} \quad (16.8)$$

Accuracy of the determination is subject to the XPS data calibration and the bond length that may not always follow exactly the BOLS specification. Nevertheless, furnished with this approach, one is able to elucidate, in principle, the coordination dependence of the core-level position of substance with all possible atomic CN values from $z = 0$ to $z = 12$.

Therefore, the BOLS-TB approach uniquely defines the reference origin, the physical origin, the direction, and the correlation among the core-level components for under-coordination systems. By doing so, one is also able to determine the locally effective atomic CN and the associated bond strain ε_z , binding-energy density E_D , and atomic cohesive energy E_C [43, 44]:

$$\begin{cases} \varepsilon_z = d_z/d_0 - 1 &= C_z - 1 \\ E_D(z)/E_D(12) &= C_z^{-(m+3)} \\ E_C(z)/E_C(12) &= z_{ib}C_z^{-m} \end{cases} \quad (16.9)$$

16.3 Coordination-Resolved Electronic Binding Energy

16.3.1 Surface: Skin-Resolved Quantum Entrapment

Figures 16.5 and 16.6 show the decomposition of the XPS data for the Rh, Pd, and Ag surfaces of different orientations. The Pd $3d_{5/2}$ spectra demonstrate one symmetric convoluted peak but the Rh $3d_{5/2}$ spectra show two majors. The asymmetry at the deeper edge corresponds to the presence of even under-coordinated defects, according to the BOLS-TB premise. The XPS spectral pattern difference among the spectra arises from the electronic configurations of Pd($5s^04d^{10}$), Rh($5s^14d^8$), and Ag($5s^14d^{10}$) [45].

Likewise, decoding the XPS spectra of the bcc-structured (a) W(100) [49], (b) (110), and (c) (111) [50] surfaces, the hcp-structured Re, Ru, and Be surfaces derived quantitative information is summarized in Table 16.6. The apparent atomic CN in the bcc bulk is 8 instead of 12 for the fcc standard. However, one can normalize the CN by $z = 12 \times \text{CN}_{\text{bcc}}/8$. The derived z values are the effective instead of the apparent value. XPS spectra from the well-faceted W skins were decomposed with respect to the reported best-fit results²⁵ using the components of B , S_2 , and S_1 . The order of the B , S_2 , and S_1 components and the separation between them follow the same constraints, as mentioned above.

Results indicate that the bonds in the outermost layer are shortest and strongest in comparison to those in the subsequent sublayers, which agrees with what discovered by Matsui et al. [60] from Ni surface. They found that the Ni 2p levels of the outermost three atomic layers shift positively to lower BE distinctly, with the outermost atomic layer shifting the most.

16.3.2 Surface Energetics

Figure 16.7 shows atomic CN (orientation and sublayer)-resolved bond strain, binding-energy shift, E_C , and E_D of the solid skins. These derivatives empower the XPS in revealing such information that is critical to materials devices.

For a flat fcc(001) surface as standard, $z_1 = 4$, $z_2 = 5.73$, and $z_{i \geq 3} = 12$, and correspondingly, the bond contraction coefficient of $C_1 = 0.88$, $C_2 = 0.92$, and $C_{i \geq 3} = 1$. Table 16.2 lists the effective CNs for other surfaces. For metals such as Au, Ag, and Cu, $m = 1$; for carbon, $m = 2.56$; and for Si, $m = 4.88$. For other alloys and compounds, the m may vary. Averaging the sum over the top two atomic layers, one can obtain the mean energy density per unit area within the two atomic layers and the mean energy remain per discrete atom in the top two atomic layers at $T \sim 0$ K. With the given bond energy for Cu (4.39 eV/atom), Diamond

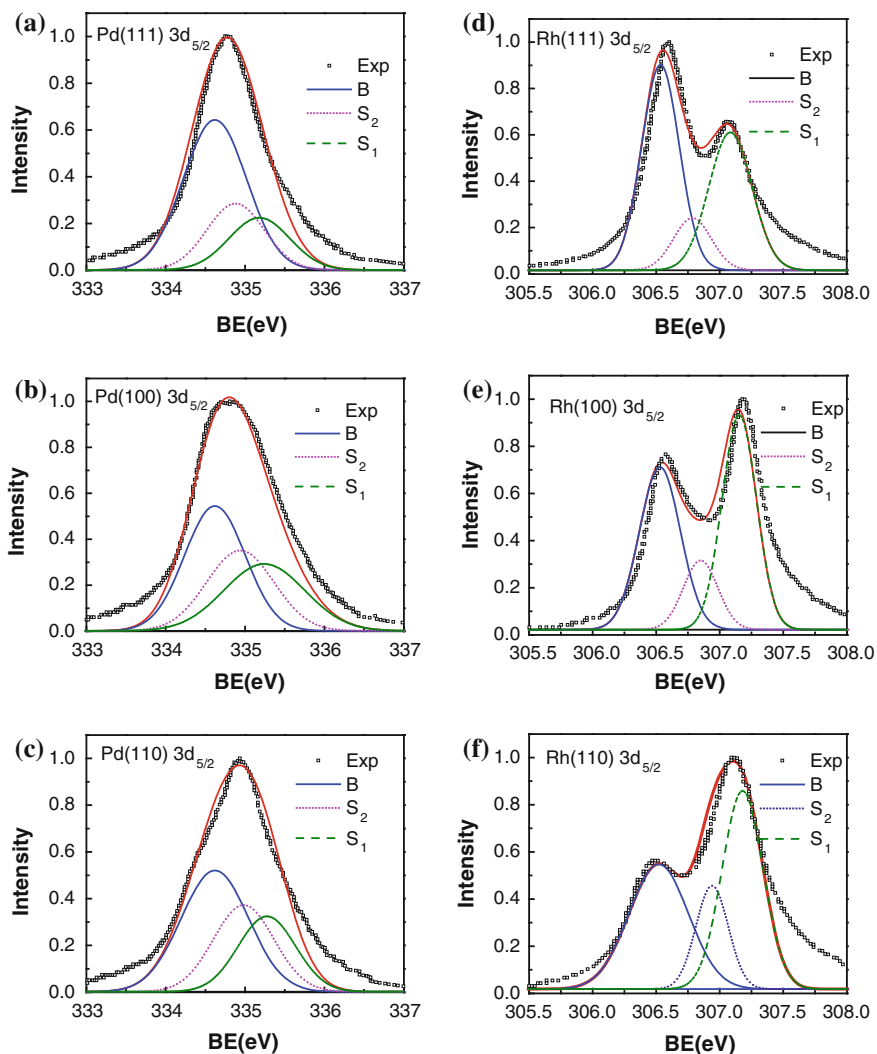


Fig. 16.5 Decomposition of the XPS $3d_{5/2}$ spectra for the fcc(111), (100), and (110) solid skins of **a-c** Pd and **d-f** Rh [9, 46] using S_1 , S_2 , and B components with derived information summarized in Table 16.2. The asymmetric tails at the deeper edge indicate the defect or adatom-induced entrapment (Reprinted with permission from [45])

(7.37 eV/atom), and Si (4.63 eV/atom) [61], we can easily calculate the energy density and atomic cohesive energy in the skin, as shown in Table 16.3. Results show that at $T = 0$, the surface energy density (in eV/nm³ unit) is always higher and the surface atomic coherency (in eV/atom unit) lower than the corresponding bulk values.

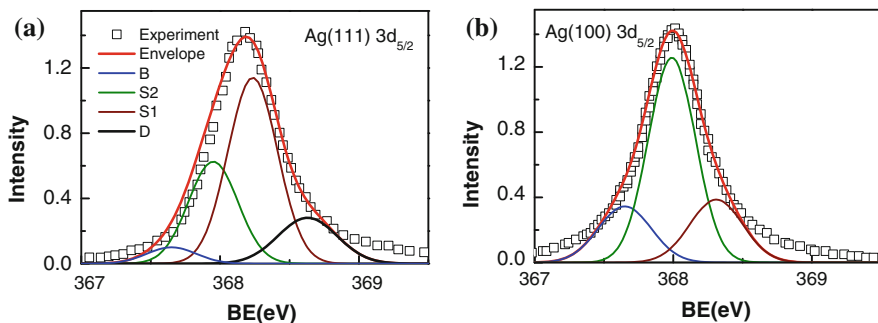


Fig. 16.6 Decomposition of the XPS $3d_{5/2}$ spectra for **a** Ag(111) [9] and **b** Ag(100) [47] skins with Gaussian components each representing the bulk B , S_2 and S_1 sublayers and defect D from higher to lower BE [48]

16.4 Nanosolid CLS

BOLS prediction yields a simple form for elucidating the $E_v(0)$ from a set of data of size-dependent CLSs, which follows the scaling law (Eq. 11.12). The $Q(\infty) = \Delta E_v(\infty) - \Delta E_v(0) = B/(\Delta_H K)$ varies simply with the parameter m and the given dimensionality (τ) and size (K) of the solid because $\Delta_H \propto K^{-1}$. There are only two independent variables, m and $\Delta E_v(\infty)$, involved in calculations. If a certainly known quantity $Q(\infty)$ in the scaling law, such as the $T_m(\infty)$ or the bandgap $E_G(\infty)$, and the measured size-dependent $Q(K)$ of the considered system are given, the m can be obtained by equaling both the theoretical and experimental scaling relations. With the determined m , any other unknown quantities $Q(\infty)$ such as the crystal binding intensity, $\Delta E_v(\infty)$, of the same system, and then, the energy level of an isolated atom, $E_v(0)$, can be determined.

Figure 16.8a illustrates the CLS change with cluster size (effective atomic CN). If the solid increases from an isolated atom to an infinite size, the CLS shifts along the line in the lower side of (a). The core level deepens to a maximal that corresponds to $z = 2$ (an fcc unit cell) and then recovers in a K_{-1} fashion to the bulk shift ΔE_v (12). The experimental results in panel (b) for the 2p level of C_{TN} ($N = 2-13$) clusters [42] and the C 1s level at $z > 2$ [81] do follow the expected size trend.

16.4.1 Skin, Size, and Edge Entrapment

Figure 16.9 plots the (a, b) skin-resolved 2p core levels spectra of Si surfaces [63, 64], (c, d) size-resolved energy shift of the 2p core level and the valence band of Si^n ($N = 5 - 92$) [65], and (e) DFT optimized valence DOS of the Si (100) and the (210) stepped surfaces. Results show consistently that under-coordination of atoms in the surface skin of clusters and the terrace-edge entrapped electrons and deepen

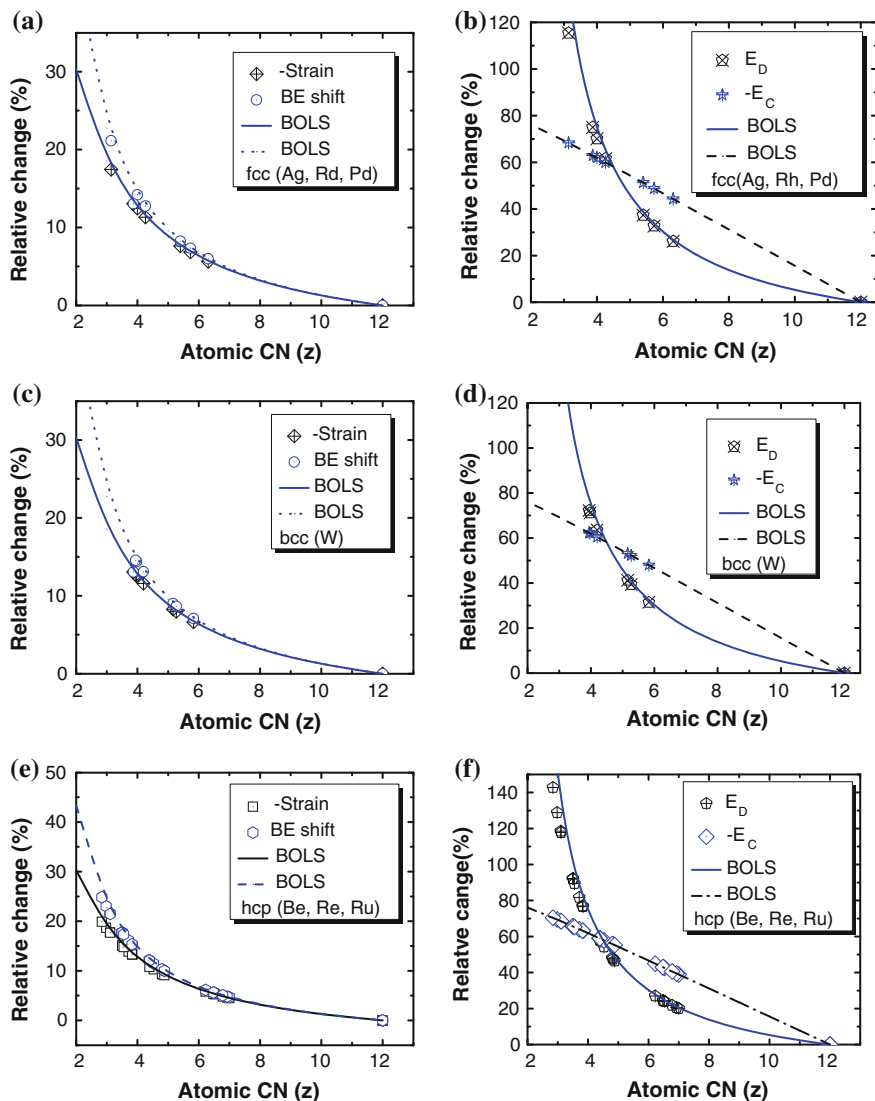


Fig. 16.7 Coordination-resolved (orientation and sublayer) bond strain, BE shift, E_C , and E_D of (a, b) fcc, (c, d) bcc, and (e, f) hcp-structured solid skins

the binding energy of both the 2p and the valence bands of Si. Table 16.2 summarizes information derived from the XPS of Si surfaces and clusters.

$$\begin{cases} E_{2p}(K) = E_{2p}(\infty) + b/K = 99.06 + 9.68/K & [\text{nano-Si}] \\ E_{2p}(K) = 102.60 + 13.8/n^{1/3} = 102.60 + 10.69/K & [\text{Si}_n^+] \\ E_{vb}(K) = 4.20 + 10.89/K & [\text{Si}_n^+] \end{cases}$$

Table 16.2 a The effective $CN(z)$, energy of component (eV), lattice strain ($\varepsilon = C_z^{-1}(\%)$), relative BE shift $\delta E_z = \Delta E(z)/\Delta E(12) - 1 = (C_z^{-1} - 1)(\%)$, relative atomic cohesive energy ($E_C = E_C(z)/E_C(12) - 1 = (z_{ib}C_z^{-1} - 1)(\%)$), and the relative BE density ($E_D = E_D(z)/E_D(12) = (C_z^{-4} - 1)(\%)$) in various registries of Pd [9], Rh [46], and Ag [47] skins [45, 48] ($m = 1.0$); **b** the bcc-structured W surfaces [49–52] ($m = 1.0$); **c** hcp-structured Re [53–56], Be [53, 54, 57], and Ru [24, 58, 59] surfaces ($m = 1.0$); **d** Si surfaces [63, 64] and $Si_N^{\dagger}(N = 5 - 92)$ [65] ($m = 4.88$)

| | z | Pd3d _{5/2} | Rh3d _{5/2} | Ag3d _{5/2} | $-\varepsilon_z$ (%) | δE_z | δE_D | $-\delta E_C$ |
|------------------|-------|---------------------|----------------------|---------------------|-------------------------|---------------|--------------|---------------|
| a | | | | | | | | |
| $E_v(0)$ | 0 | 330.261 | 302.163 | 363.022 | – | – | – | – |
| $E_v(12)$ | 12 | 334.620 | 306.530 | 367.650 | 0 | 0 | 0 | 0 |
| $\Delta E_v(12)$ | – | 4.359 | 4.367 | 4.628 | – | – | – | – |
| fcc(111) | S_2 | 334.88 | 306.79 | 367.93 | 5.63 | 5.97 | 26.08 | 44.28 |
| | S_1 | 335.18 | 307.08 | 368.24 | 11.31 | 12.75 | 61.60 | 59.97 |
| | D | – | – | 368.63 | 17.45 | 21.15 | 115.39 | 68.30 |
| fcc(100) | S_2 | 334.94 | 306.85 | 367.99 | 6.83 | 7.33 | 32.70 | 48.75 |
| | S_1 | 335.24 | 307.15 | 368.31 | 12.44 | 14.20 | 70.09 | 61.93 |
| fcc(110) | S_2 | 334.98 | 306.89 | – | 7.62 | 8.25 | 37.33 | 51.29 |
| | S_1 | 335.28 | 307.18 | – | 13.05 | 13.05 | 74.99 | 62.91 |
| | z | $W_{4f7/2}$ | $-\varepsilon_z$ (%) | δE_z | δE_D | $-\delta E_C$ | | |
| b | | | | | | | | |
| $E_v(0)$ | 0 | 28.910 | – | – | – | – | – | – |
| $E_v(12)$ | 12 | 31.083 | 0 | 0 | 0 | 0.00 | 0.00 | 0.00 |
| $\Delta E_v(12)$ | – | 2.173 | – | – | – | – | – | – |
| bcc(100) | S_2 | 31.283 | 8.26 | 9.01 | 9.01 | 41.20 | 53.12 | 53.12 |
| | S_1 | 31.398 | 12.57 | 14.38 | 14.38 | 71.18 | 62.16 | 62.16 |
| bcc(110) | S_2 | 31.240 | 6.61 | 7.07 | 7.07 | 31.44 | 47.99 | 47.99 |
| | S_1 | 31.402 | 12.71 | 14.56 | 14.56 | 72.22 | 62.37 | 62.37 |
| bcc(111) | S_2 | 31.275 | 7.96 | 8.65 | 8.65 | 39.37 | 52.28 | 52.28 |
| | S_1 | 31.370 | 11.58 | 13.09 | 13.09 | 63.58 | 60.46 | 60.46 |

(continued)

Table 16.2 (continued)

| | | <i>z</i> | $Re_{\text{ref}}/s/2$ | $Ru_{3d5/2}$ | Be_{1s} | $-e_z$ (%) | δE_z | δE_D | $-\delta E_C$ |
|------------------|----------|----------|-----------------------|--------------|---------------|---------------|--------------|---------------|---------------|
| c | | | | | | | | | |
| $E_v(0)$ | - | 0 | 40.015 | 275.883 | 106.416 | - | - | - | - |
| $E_v(12)$ | <i>B</i> | 12 | 42.645 | 279.544 | 111.110 | 0 | 0 | 0 | 0 |
| $\Delta E_v(12)$ | | - | 2.630 | 3.661 | 4.694 | - | - | - | - |
| hcp(0001) | S_3 | 6.50 | 42.794 | 279.749 | 111.370 | 5.32 | 5.62 | 24.44 | 42.97 |
| | S_2 | 4.39 | 42.965 | 279.992 | 111.680 | 10.79 | 12.10 | 57.90 | 58.99 |
| | S_1 | 3.50 | 43.110 | 280.193 | 111.945 | 15.06 | 17.73 | 92.14 | 65.66 |
| (10 $\bar{1}0$) | S_4 | 6.97 | - | 279.719 | 111.330 | 4.57 | 4.79 | 20.57 | 39.48 |
| | S_3 | 4.80 | - | 279.921 | 111.590 | 9.35 | 10.31 | 48.08 | 55.88 |
| | S_2 | 3.82 | - | 280.105 | 111.830 | 13.30 | 15.35 | 77.01 | 63.28 |
| | S_1 | 3.11 | - | 280.329 | 112.122 | 17.68 | 21.47 | 117.74 | 68.52 |
| (11 $\bar{2}0$) | S_4 | 6.22 | - | - | 111.400 | 5.80 | 6.16 | 27.01 | 44.97 |
| | S_3 | 4.53 | - | - | 111.650 | 10.27 | 11.45 | 54.26 | 57.93 |
| | S_2 | 3.71 | - | - | 111.870 | 13.88 | 16.11 | 81.76 | 64.10 |
| (12 $\bar{3}1$) | S_1 | 2.98 | - | - | 112.190 | 18.70 | 22.99 | 128.84 | 69.46 |
| | S_4 | 6.78 | 42.779 | - | - | 4.81 | 5.05 | 21.79 | 40.65 |
| | S_3 | 4.88 | 42.910 | - | - | 9.09 | 10.00 | 46.43 | 55.27 |
| | S_2 | 3.55 | 42.100 | - | - | 14.77 | 17.33 | 89.49 | 65.29 |
| | S_1 | 2.84 | 43.305 | - | - | 19.89 | 24.83 | 142.80 | 70.46 |
| d | | | | | | | | | |
| | | <i>z</i> | $2p_{1/2}$ | $2p_{3/2}$ | $-e_z$ (%) | δE_z | δE_D | $-\delta E_C$ | |
| $E_v(0)$ | | 0 | 96.740 | 96.170 | - | - | - | - | |
| $E_v(12)$ | <i>B</i> | 12 | 99.220 | 98.630 | 0 | 0 | 0 | 0 | |
| $\Delta E_v(12)$ | | - | 2.460 | 2.460 | - | - | - | - | |
| Si(100) | S_2 | 5.5 | 99.750 | 99.160 | 7.37 | 45.32 | 82.85 | 33.40 | |
| | S_1 | 4 | 100.287 | 99.697 | 12.44 | 91.18 | 184.74 | 36.27 | |
| Si(111) | S_2 | 5.64 | 99.720 | 99.130 | 7.04 | 42.77 | 77.70 | 32.90 | |
| | S_1 | 4.24 | 100.161 | 99.570 | 11.39 | 80.41 | 159.30 | 36.25 | |

Table 16.3 Predicted bond nature (m) dependence of ratios of energy density (eV/nm^3), $\langle\gamma_d\rangle$, and atomic cohesive energy (eV/atom , free energy), $\langle\gamma_f\rangle$, of a surface with respect to the bulk values

| m | $E_C(B)$ | $E_D(B)$ | $\langle\gamma_{ds}/\gamma_{db}\rangle$ | $E_D(S)$ | $\langle\gamma_{fs}/\gamma_{fb}\rangle$ | $E_C(S)$ |
|---------------|----------|----------|---|----------|---|----------|
| 1 (metal, Cu) | 4.39 | 155.04 | 1.468 | 198.60 | 0.455 | 2.00 |
| 2.56(diamond) | 7.37 | 1307.12 | 1.713 | 2262.63 | 0.524 | 3.86 |
| 4.88 (Si) | 4.63 | 164.94 | 2.165 | 357.09 | 0.649 | 3.00 |

Subscript 1 and 2 refers to the top first and second layers. $\langle\gamma_{ss}/\gamma_{sb}\rangle$ is approximately equal to $1 - \langle\gamma_{fs}/\gamma_{fb}\rangle$ according to the traditional definitions [62]

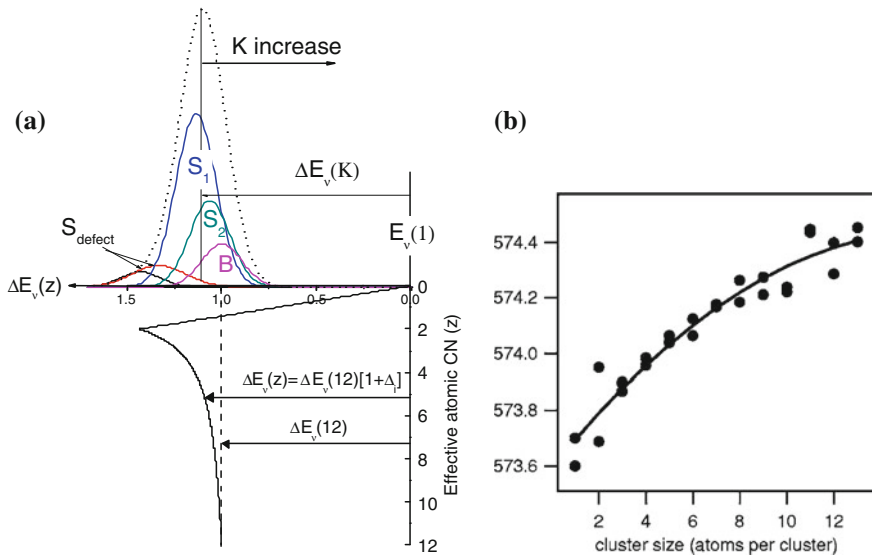


Fig. 16.8 **a** Correspondence between the cluster size (effective atomic CN) and the CLS. **b** The number-of-atom resolved Cr_{2p} energy shifts from the E_{2p} ($n = 1$) = 537.5 eV to E_{2p} ($n = 13$ with an effective CN of 2) = 574.4 eV [42], which follows the predicted trend at $z < 2$. (refer to Fig. 16.12)

With respect to the known bulk $E_{2p}(\infty)$ value at -99.2 eV, a 0.14 eV ($= 99.2 - 99.06$) correction and a -3.4 ($99.2 - 102.6$) eV correction are made. This correction does not influence the value of the shift, $\Delta E_{2p}(\infty) = E_{2p}(\infty) - E_{2p}(0)$. In processing the data reported in [65], the cluster size $n = 4\pi K^3/3$ is converted to $K^{-1} = (3n/4\pi)^{-1/3} = 1.29n^{-1/3}$. A slight deviation in the slopes arises from the accuracy in measurements. The missing of one electron in Si_n^+ weakens the screening effect on the crystal potential. For the smaller clusters, the bond shortens and strengthens more than in those of the larger particles. Matching theory to the measurements, with the known $m = 4.88$ [66] for Si, gives rise to the $2p$ level of an isolated Si atom $E_{2p}(0)$ of -96.74 eV and the bulk shift $\Delta E_{2p}(\infty)$ of -2.46 eV.

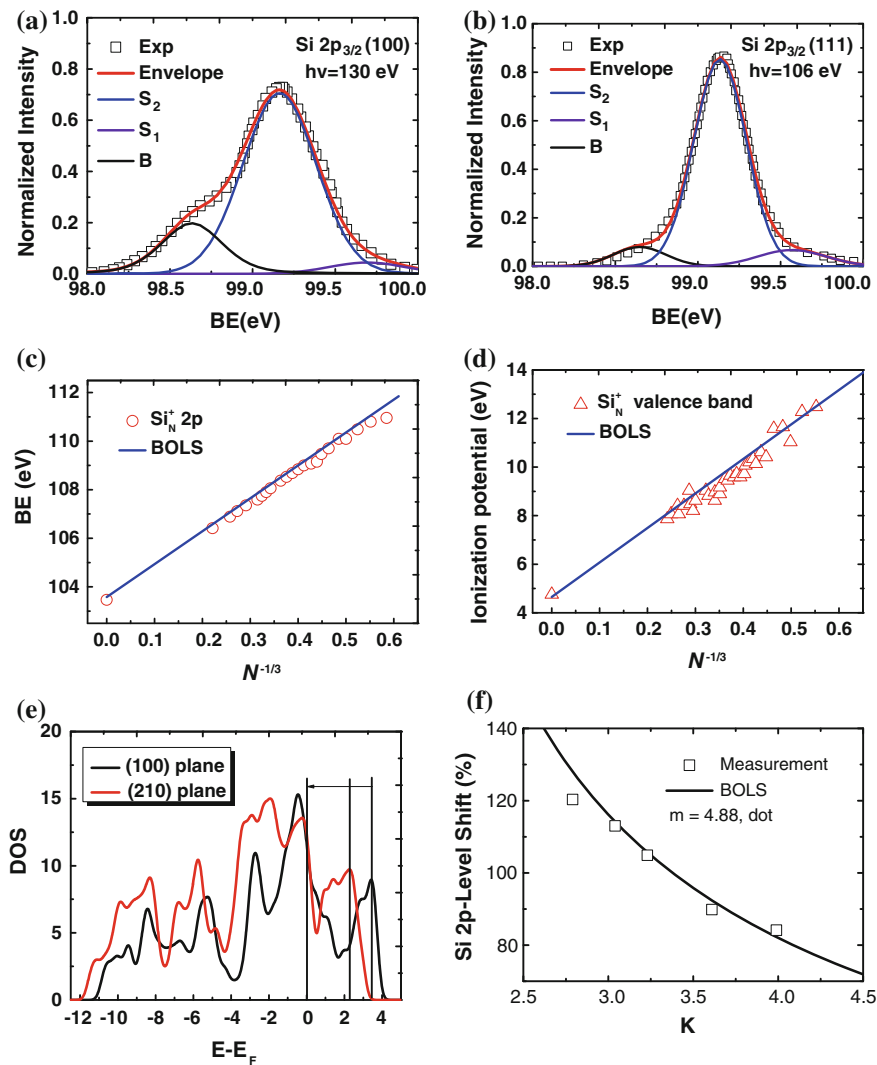


Fig. 16.9 Skin-, size-, and edge-resolved electronic binding-energy shifts of Si. The 2p spectra for **a** Si(100) [63] and **b** Si(111) [64] surfaces with the bulk B, S₂, and S₁ components; size dependence of the **c** 2p and **d** the valence band of Si_N⁺ clusters [65], and **e** edge-induced quantum entrapment of the valence DOS of Si(210) surface with respect to the Si(100) surface (Reprinted with permission from [67])

16.4.2 Core–Shell Discriminative Entrapment

Figure 16.10 shows size dependence of the binding energy shift for Cu-2p, Au-4f, and Pd-3d nanosolids. Linearization of the $E_v(K)$ versus K^{-1} relation derives the slope and the $E_v(\infty)$ values. The atomic trapping energy $E_{2p}(0) = 931.0$ eV and the $\Delta E_{2p}(\infty) = 1.70$ eV. Taking the obtained Cu- $\Delta E_{2p}(\infty)$ value as reference in simulating the measured size-dependent $\Delta E_{2p}(K)$ for Cu on CYCL gives $m = 1.82$, which adds the contribution from the interface between Cu and CYCL polymer substrate to the $m = 1$.

For the Au nanosolid, $m = 1$ has been confirmed in decoding the size-dependent T_m of Au nanoparticles deposited on C and W substrates [68]. Fitting the measured $\Delta E_{4f}(K)$ of Au/Octan with $m = 1$ gives $E_{4f}(0) = 81.50$ eV for an isolated Au atom and $\Delta E_{4f}(\infty) = 2.86$ eV for the Au bulk. Taking $\Delta E_{4f}(\infty) = -2.86$ eV as reference, comparison confirms that Au grows on TiO_2 and on Pt(001) substrates in a layer-by-layer mode [33, 34]. Reproduction of the XPS peak change in Pd/HOPG nanosolids [35] results in the value of $\Delta E_{\text{Pd-3d}}(\infty) = 4.00 \pm 0.02$ eV and $E_{\text{Pd-3d}}(0) = 330.34$ eV [69], compared with that derived from Pd surface of 4.36 and 330.26 eV, respectively.

Calculation results from counting the capping, surface, and the core of the ZnS and CdS nanosolids show that the crystal binding to S-2p of ZnS is stronger than that of CdS, as compared in Table 16.4, because the Zn-S bond³⁰ is shorter than the Cd-S⁴⁸ bond. The measured S-2s and S-2p peaks of CdS should shift up or down consistently against the same peaks of ZnS. Compared with the measured S-2s and S-2p peaks from CdS, it can be found that the S-2p peak from ZnS goes slightly down while the S-2s peak floats up with respect to those of CdS. This may cause the $E_{2p}(0)$ values of S in the two samples to vary slightly.

Assuming $m = 4$ for O-Cu, we can use the measured data [36] to estimate the $E_{2p}(0)$ and the $\Delta E_{2p}(\infty)$ of bulk Cu and bulk CuO, as given in Table 16.4. The estimated values seem to be too large to be reasonable compared with those obtained from Cu/HOPG or Cu/CYCL. As mentioned earlier, the accuracy is strictly subject to the precision of the XPS data. The modeling predictions agree also with the trends of the CLS for O-Sn and O-Ta compound nanosolids, of which both the satellites and the main peaks in the XPS profiles shift toward higher binding energy with reducing particle size (Table 16.5).

16.4.3 Number-of-Layer Dependence of Graphene

The C1s spectrum of graphene exhibits components corresponding to the GNR edge at 285.97, surface layer at 284.80 and graphite bulk at 284.20 eV [71]. The intensity of the bulk component deepens and the resultant peak shifts from the bulk value of 284.40–284.85 eV for the single-layer graphene [72]. C₆₀ deposited on CuPc substrate demonstrates the same trends of thickness dependence of the work

Table 16.4 Atomic $E_v(0)$ and $\Delta E_C(\infty)$ and the standard deviation σ for different nanosolids based on the available XPS database ($m = 4$)

| Nanosolid | XPS measurement E_v | | | Calculated | | |
|--|---------------------------|-------------------|-----------------|------------|----------------------|--------------|
| | $S_1(z_1 = 4)$ | $S_2(z_2 = 6)$ | B | $E_v(0)$ | $\Delta E_v(\infty)$ | σ |
| CdS-S 2p [29] | 163.9 | 162.7 | 161.7 | 158.56 | 3.14 | 0.002 |
| ZnS-S 2p [28] | 164.0 | 162.4 | 161.4 | 157.69 | 3.71 | 0.002 |
| CdS-S 2s [29] | 226.0 | 224.7 | 223.8 | 220.66 | 3.14 | 0.001 |
| ZnS-S 2s [28] | 229.0 | 227.3 | 226.3 | 222.32 | 3.92 | 0.001 |
| CuO-Cu 2p _{3/2} [36] | 936.0/934.9 (4/6 nm) | 932.9 (25 nm) | 932.1 (Bulk) | 919.47 | 12.63 | 0.36 (2.8 %) |
| CuO-Cu 2p _{3/2} Refined data | 935.95/934.85 (4/6 nm) | 932.95 (25 nm) | 932.1 (Bulk) | 919.58 | 12.52 | 0.30 (2.4 %) |

Table 16.5 Bond nature (m), dimensionality (τ), and binding-energy information of Au, Cu, Pd, and Si nanocrystals

| | Au/Octan | Au/TiO ₂ | Au/Pt | Cu/HOPG | Cu/CYCL | Si 2p | Pd 3d |
|----------------------|-----------|---------------------|--------|-----------|---------|-------|--------|
| m | 1 | | | | 1.82 | 4.88 | 1 |
| τ | 3 | 1 | 1 | 3 | 3 | 3 | 3 |
| d_0/nm | 0.288 | | | 0.256 | | 0.263 | 0.273 |
| $E_v(\infty)$ | 84.37(4f) | | | 932.7(2p) | | 99.20 | 334.35 |
| $E_v(0)$ | 81.504 | 81.506 | 81.504 | 931.0 | | 96.74 | 330.34 |
| $\Delta E_v(\infty)$ | 2.866 | 2.864 | 2.866 | 1.70 | | 2.46 | 3.98 |

Table 16.6 Coordination-resolved C1s binding energies of carbon allotropes

| Atomic CN | 0 | 2 | 3 | 5.335 | 12 |
|------------------|--------|-------------|--------------------|----------------|-----------------------|
| BOLS derivatives | 282.57 | 285.89 | 284.80 | 284.20 | 283.89 |
| Measurements | – | 285.97 [71] | 284.80 [71] | 284.20 [71] | 283.50–289.30 [78–80] |
| | | | 284.42 [5] | 284.30 [5, 74] | |
| | | | 284.90 [74] | 284.35 [76] | |
| | | | 284.53–284.74 [75] | 284.45 [77] | |

$z = 0$ and 12 correspond to an isolated C atom and a C atom in the diamond bulk, respectively. $z = 2, 3, 4,$ and 5.335 correspond to the atomic CN of graphene/CNT edge, graphene interior, diamond surface and bulk graphite, respectively

function and C1s shift [73]. Table 16.6 shows the coordination-resolved C1s energy shift. These observations result from the coordination-resolved coupling of quantum entrapment and polarization.

Combining the measurements [71] and the BOLS-TB premise [81] results in the following expressions, and the CN-resolved C1s energy shift,

$$E_{1s}(z) = E_{1s}(0) + [E_{1s}(12) - E_{1s}(0)]C_z^{-2.56} = 282.57 + 1.32C_z^{-2.56}(\text{eV}) \quad (16.10)$$

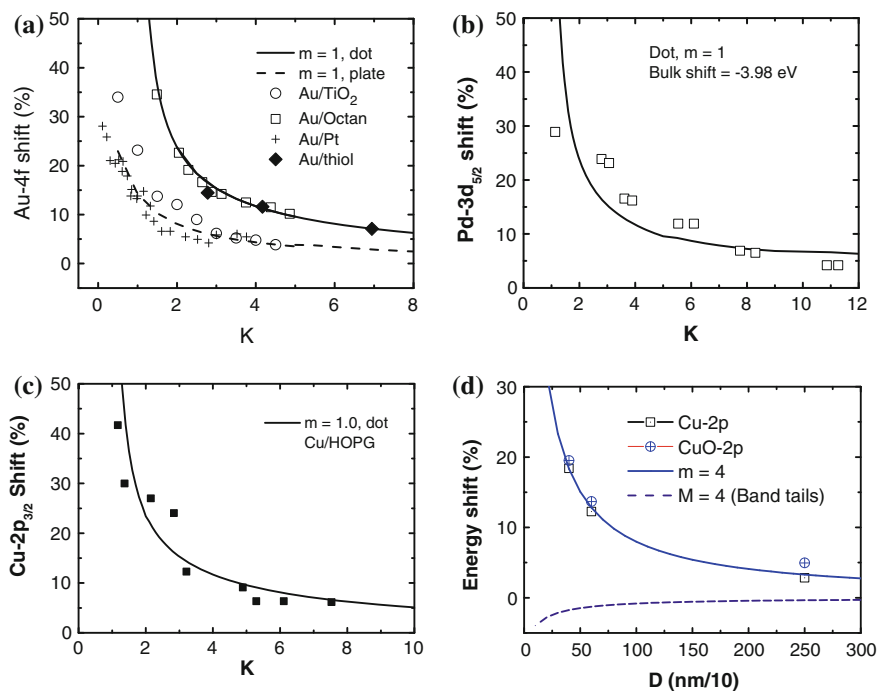


Fig. 16.10 Size dependence of the core-level shift of Au, Pd, Cu, and CuO nanocrystals. **a** Au [70] encapsulated in Thiol and Au on Octan [32] show three-dimensional features while Au on TiO₂ [33] and on Pt [34] show plate pattern of formation. **b** Pd on HOPG substrate [35]. The different m values in **c** of Cu on HOPG and CYCL [31] indicate the contribution from the reaction between Cu nanosolid and polymer CYCL substrate. **d** Core-level shift and bandwidth of CuO nanoparticles (Reprinted with permission from [3])

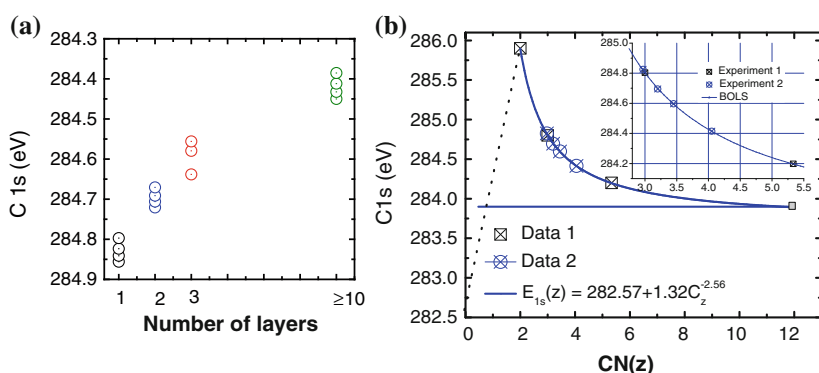


Fig. 16.11 **a** Number-of-layer-resolved C1s energy [82, 83] and **b** CN-resolved C1s shift of graphene (data 1) [71] and the correlation between the number-of-layer and effective CN (data 2) [82] (Reprinted with permission from [81])

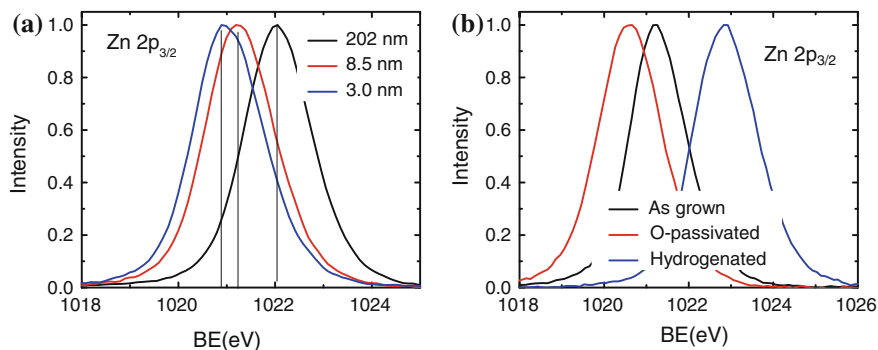


Fig. 16.12 Normalized Zn- $2p_{3/2}$ spectra showing **a** cluster size-induced polarization (*upward shift*) that screens in turn the crystal potential and shift the core level negatively [85]. **b** Annealing under the ambient of $0.21\text{O}_2 + 0.79\text{N}_2$ shifting the peak from 1,021.2 to 1,020.8 eV but under $0.03\text{H}_2 + 0.97\text{Ar}$ ambient annihilates the polarization shifting the peak of 1,020.8–1,022.9 eV (Reprinted with permission from [86, 87])

Figure 16.11 plots CN dependence of the C1s energy $E_{1s}(z)$ of carbon allotropes. Matching the number-of-layer-resolved C1s-level shift [82] results in the correlation between the number-of-layer and the effective atomic CN of the few-layer graphene (inset): 1($z = 2.97$), 2(3.2), 3(3.45), and 10(4.05).

The positive C1s-level shift is associated with a reduction in work function from the bulk value of 4.6–4.3 eV for the single-layer GNR [84]. The work function reduction indicates the enhancement of edge polarization and charge densification by bond contraction. The fraction of surface and edge atoms increases and the number of layer is reduced. Hence, the associated work function reduction and the C1s shift evidence the coexistence of entrapment and polarization.

16.4.4 Size-Induced Polarization

Figure 16.12 shows a negative shift of the Zn $2p_{3/2}$ binding energy by 1.2 eV upon ZnO crystal being reduced from 200 to 3.0 nm [85] as a result of polarization. Hydrogen passivation eliminates the polarization states and shifts the $2p$ -level shift to lower binding energy. Annealing the ZnO at temperature up to 900 °C under the ambient pressure of H_2 3 % + Ar 97 % (I) and O_2 21 % + N_2 79 % (II) for 24 h creates two kinds of defects [86]. Type I shows the PL energy at 2.46 eV and type II at 2.26 eV.

Unlike other metals that demonstrate positive shift with size reduction, Zn $2p_{3/2}$ level in ZnO shifts oppositely—size reduction raises the core level. O-passivation enhances the positive shift but hydrogen passivation shifts the core level adversely.

Annealing under 100 % O₂ at the ambient pressure lowers the PL peak from 2.46 to 2.15 eV [87].

As both the core level and bandgap depend on the crystal potential, bond contraction deepens the potential and polarization elevates it by screen weakening. Particle-size reduction enhances the polarization of the non-bonding electrons by the densely entrapped core electrons, which happens at the highly curved surfaces.

The screening of the crystal potential by the O-induced dipoles narrows the bandgap and shifts the core level negatively. However, hydrogenation annihilates the unpaired electron dipoles. The competition of polarization and entrapment determines both the bandgap and the CLS [88, 89].

Size reduction-induced polarization happens in compounds containing N, O, and F and metals with the outermost s-orbit filled with unpaired electrons like Ag, Au, Rh, while happens not to metals with such s-orbit that is empty or filled with paired electrons, such as Pt and Co. Such polarization of substance at the nanoscale creates properties that the bulk counterpart never demonstrates such as the dilute magnetism, catalysis, superhydrophobicity, fluidity, lubricity, as will be addressed in later section.

16.5 Electroaffinity and Work Function

16.5.1 Electroaffinity Modulation: Valance Entrapment

Electroaffinity is the separation between the vacuum level, E_0 , and the conduction-band bottom edge, which represents the ability of holding the bonding electrons. In comparison, the difference in electro-negativity between two elements represents the capability of the more electro-negative element catching electrons from the less electro-negative one. One specimen with a larger value of electronegativity has higher tendency to hold the caught electrons more firmly.

The enlargement of electroaffinity of the specimen results from the conduction-band entrapment. The affinity change follows the relation:

$$\begin{aligned}\Delta\varepsilon(\tau, K) &= \Delta E_C(\tau, K) - \Delta E_C(\infty) - \Delta E_G(\tau, K)/2 \\ &= [\Delta E_C(\infty) - \Delta E_G(\infty)/2] \times \Delta_H(\tau, K)\end{aligned}\quad (16.11)$$

The conduction-band edge drops sharply from the $E_C(0)$ to a maximum at $E_C(K \sim 1.5)$ and then recovers in a K^{-1} manner until the bulk value of $\Delta E_C(\infty)$ is reached. $K = 1.5$ corresponds to $z = 2$, which is the case of a monatomic chain ($\tau = 1$) or a unit cell ($\tau = 3$) containing 12 atoms of an fcc structure, for instance. With the $\Delta E_C(\infty)$ data obtained as above [31, 90], the maximal $\Delta\varepsilon_M$ value, or the valence DOS shift of Cu_{3d} ($\Delta E_{3d}(\infty) = 2.12$ eV, $\Delta\varepsilon_M = 0.99$ eV) and Au_{4f} nanospheres are ($\Delta E_{3d}(\infty) = 2.87$ eV; $\Delta\varepsilon_m = 1.34$ eV) based on the parameters of $\tau = 3$, $m = 1.0$, and $\Delta_H(1.5) = 0.7^{-1} - 1 = 43$ %. For a semiconductor Si nanosphere ($\tau = 3$ and $m = 4.88$), the electroaffinity will be enlarged at most by

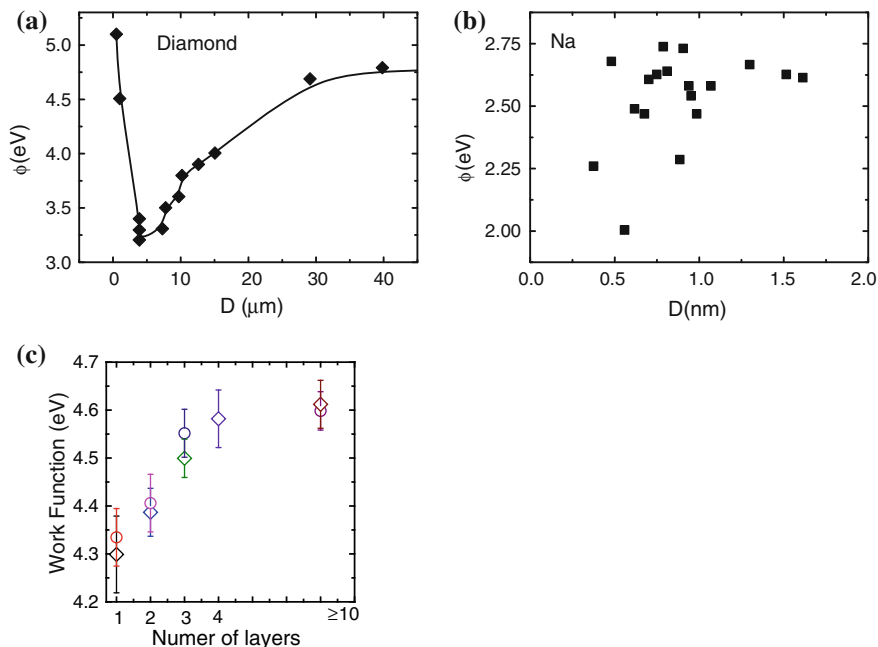


Fig. 16.13 Size modulated work function in **a** diamond [91] and **b** Na [94] nanocrystals and **c** graphene ribbon [82, 83]. Recovery of the work function is due to the geometrical flatness [96] (Reprinted with permission from [3])

$\Delta_H(1.5) = 0.7^{-4.88} - 1 = 470\%$. Employing the $\Delta E_{2p}(\infty) = 2.46$ eV and $E_G(\infty) = 1.12$ eV, the estimated $\Delta\varepsilon_M$ for Si at least is 5.8 eV.

However, a competition between the entrapment and the polarization of the dangling bond minimizes the expectation, see Fig. 16.9. At a flat surface ($z_1 = 4$), the energy level shifts by $0.88^{-1} - 1 = 13.6\%$ for metals, which contribute to the enlargement of the electronegativity. The enlarged electroaffinity explains why the bond nature alteration occurs in the III-A nanosolids and why the IV-A covalent bond becomes even stronger at $z_i \leq 3$. The valence DOS entrapment is responsible for the ionicity of O and Cu at the nanoscale. Affinity enlargement should be responsible for the toxicity that nanocrystals demonstrate.

16.5.2 Workfunction: Polarization or Entrapment

16.5.2.1 Geometrical Modulation: Charge Densification

Bond contraction deepens the interatomic potential well and enhances the charge density in the relaxed surface region. The locally confined electrons near the

surface edge become denser. In addition to polarization, the densification lowers the work function.

For an isolated nanosolid of size K , the Φ satisfies ($V \propto d^\tau$):

$$\Phi = E_0 - E_F; \text{ and } E_F \propto n^{2/3} = (N_e/V)^{2/3} \propto (\bar{d})^{-2\tau/3} \quad (16.12)$$

The total number of electrons N_e of a nanosolid conserves. At the lower end of the size limit of a spherical or semispherical dot ($R \sim 1$ nm, $\tau = 3$), the average bond length is around 80 % of that in the bulk, and hence, the Φ will reduce from the original value by 30 % (E_F shifts up by $0.8^{-2} - 1$), according to Eq. (16.12).

Figure 16.13 shows that the Φ of the diamond (111) surface decreases from the bulk value of 4.8 eV to a minimum of 3.2 eV at an average grain size of about 4 μm . The Φ restores to a maximum of 5.1 eV at a diamond particle size of 0.32 μm [91] because of the dominance of entrapment at the curved surface. No dipole could form at diamond surface. The threshold for field emission drops from 3.8 to 3.4 V/ μm for polycrystalline diamond films on molybdenum tips as the average grain size of diamond decreases from 6.0 to 0.25 μm . The work function of an InAs dot on GaAs(001) surface is lower than that of an InAs wetting layer, and increases with decreasing dot height [92, 93].

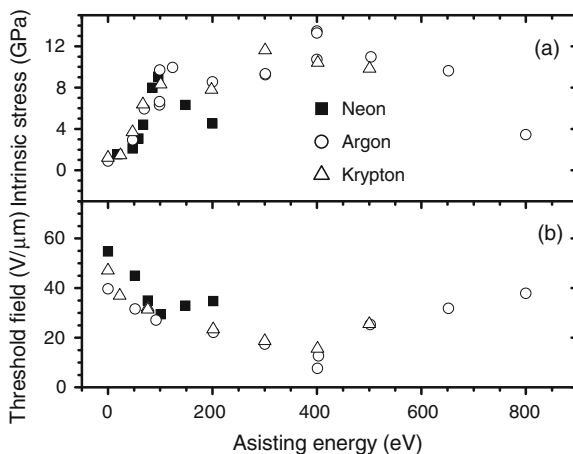
The Φ of Na particles around 0.4–2.0 nm size varies inversely with the size R and lowered from the bulk value of 2.75 to 2.25 eV (by 18 %) [94]. Carbon nanotubes have a Φ of 4.6–4.8 eV at the tips, which is 0.2–0.4 eV lower than that of carbon (graphite) bulk. A small fraction of the nanotubes have a Φ value of ~ 5.6 eV. This discrepancy results from the metallic and semiconductive characteristics of the nanotubes. The average Φ of porous Si increases as the crystalline size decreases because of etching the impurity Si–H, Si–O, and Si–H–O bonds at the surface [95].

The hydrogen-rich and oxygen-contained precursors promote electron emission from discrete diamond particles and *non-continuous* diamond films but not for high quality and continuous diamond films, nanocrystalline diamond, or glassy carbon coatings even if they contain conductive graphitic carbon [96]. The Φ at the tips of individual multi-walled carbon nanotubes shows no significant dependence on the diameter of the nanotubes in the range of 14–55 nm [97]. This phenomenon indicates the significance of CN imperfection on the Φ reduction that is subject to the separation between the nanoparticles and surface chemical states.

16.5.2.2 Mechanical Modulation

Amorphous carbon (a-C) films have a uniquely intrinsic stress (~ 12 GPa) that is almost one order of magnitude higher than those found in other amorphous materials such as *a*-Si, *a*-Ge, or metals (<1 GPa) [98]. Applying pressure to a material, one can modify its electronic properties, e.g., band structure, resistivity, work function, due to the stress [99]. Poa et al. [98, 100] found a correlation between the stress and the threshold field for electron emission, as shown in Fig. 16.14.

Fig. 16.14 Stress dependence of the threshold field of amorphous carbon as a function of the assisting energy when bombarded by different noble gases (Reprinted with permission from [100])



Increasing the internal stresses from 1 to 12 GPa suppresses the threshold field for electron emission. The enhanced stress squeezes the π and the π^* bands together. Such a band overlap increases the electron conductivity and hence the drop of the threshold. On the other hand, the 'c-axis' spacing of the sp^2 clusters is likely to be smaller than that of crystalline graphite under the intrinsic stress. The reduced lattice spacing will densify the charge in the compressed region, which suppresses internally the threshold field. Applying an external stress by bending a-C films or carbon nanotubes has the same effect on reducing the threshold for electron emission [101]. However, the threshold field will restore when it reaches to a critical value under further tensile stress.

Lacerda et al. [102] examined the effect of trapping noble gases (Ar, Kr, and Xe) in an a-C matrix on the internal stress of the a-C films. Controlling the size of the pores within which noble gases are trapped could increase the internal stress from 1 to 11 GPa, and meanwhile, elevates the core-level binding energy of the entrapped gases by 1 eV associated with 0.05 nm expansion of the atomic distance of the noble gases. For Ar(Xe), the first interatomic separation varies from 0.24 (0.29) nm to 0.29(0.32) nm in the 1–11 GPa pressure range. This observation indicates that the interfacial C–C bonds contract which amplify the pores and the molecular separation between the entrapped gases.

An external pressure around 11 GPa suppresses the interplanar distance of graphite by $\sim 15\%$ [103], gathering the core/valence electrons and carbon atoms denser. The resistivity of a-C films decreases when the external hydrostatic pressure is increased [104]. A dense, metallic, and rigid form of graphitic carbon forms under compression [105]. However, the spontaneous lattice contraction of other materials could raise the resistivity; instead, the densified charge is strongly trapped within the lowered potential well though both the intrinsic and extrinsic pressure could densify the mass, charge, and the stress (energy) of a highly sp^2 rich a-C film.

The BOLS provides a mechanism for the stress-enhanced threshold field of carbon films. Nanopore formation creates under-coordinated atoms at the interfaces between the entrapped gas and the a-C matrix. The CN imperfection shortened lattice of the host matrix, which will expand the pore size and elongate the intermolecular distance of the gases. The bond expansion of the entrapped gases is associated with weakening of interatomic binding of the gas atoms confined in the pores. The interfacial C–C bond contraction enhances both the charge density and the internal stress, associated with a drop of the local work function by as high as 30 %. Therefore, the internal stress affects the work function by enhancing the local charge density trapped in the deep potential well. From this perspective, a sp^2 cluster with a shortened bond (≤ 0.142 nm) would be beneficial to the field emission properties when compared with a sp^3 cluster (0.154 nm bond length) despite the less localized van der Waals bond electrons that should add a DOS feature in the mid gap.

In contrast, external tensile stress could raise the atomic binding and the total energy between a pair of atoms, being the same in effect as heating and thus weakening the bond. Heating or pressing should raise the $N(E)$ higher and, as a consequence, minimize the gap between the π and π^* bands. Overstressing the specimen tends to break C–C bonds to form dangling bonds. The dangling bond electrons add DOS features in the midgap. This process restores the threshold upon the specimen being overstressed.

The mechanism for the external pressure lowered Φ is different from that of the intrinsic stress though the effects are the same. The intrinsic compressive stress increases the charge density and raises the resistivity because of the entrapment, whereas the external stress ‘pumps’ the $N(E)$ up and raises the conductivity by polarization. This mechanism is in accordance with observations that the resistivity of an as-grown nanostructure increases with the inverse of solid size but, under stretching, the electrical conductivity remains comparable to that of bulk copper [106, 107].

16.6 Summary

The BOLS correlation premise has unified the CLS induced by surface relaxation and nanosolid formation into the same origin of atomic CN imperfection. Atomic CN imperfection also enhances the ionicity of the constituent atoms such as oxygen and metals and the toxicity as a consequence [36]. The coordination imperfection provides a new dimension that allows one to determine the core-level energies of an isolated atom and hence discriminate the contribution of crystal binding from the effect of intra-atomic trapping to the core electrons at energy levels shifted by bulk formation, surface relaxation, or nanosolid formation. The work function of a surface can be lowered by size reduction or curvature enhancement, chemisorption, compression, and tension by either raising the local charge density or polarization.

References

1. C.Q. Sun, Oxidation electronics: bond-band-barrier correlation and its applications. *Prog. Mater. Sci.* **48**(6), 521–685 (2003)
2. W.D. Phillips, Laser cooling and trapping of neutral atoms. *Rev. Mod. Phys.* **70**(3), 721–741 (1998)
3. C.Q. Sun, Size dependence of nanostructures: Impact of bond order deficiency. *Prog. Solid State Chem.* **35**(1), 1–159 (2007)
4. B.S. Fang, W.S. Lo, T.S. Chien, T.C. Leung, C.Y. Lue, C.T. Chan, K.M. Ho, Surface band structures on Nb(001). *Phys. Rev. B* **50**(15), 11093–11101 (1994)
5. T. Balasubramanian, J.N. Andersen, L. Wallden, Surface-bulk core-level splitting in graphite. *Phys. Rev. B* **64**, 205420 (2001)
6. M. Alden, H.L. Skriver, B. Johansson, Ab-initio surface core-level shifts and surface segregation energies. *Phys. Rev. Lett.* **71**(15), 2449–2452 (1993)
7. E. Navas, K. Starke, C. Laubschat, E. Weschke, G. Kaindl, Surface core-level shift of 4f states for Tb(0001). *Phys. Rev. B* **48**(19), 14753 (1993)
8. R.A. Bartynski, D. Heskett, K. Garrison, G. Watson, D.M. Zehner, W.N. Mei, S.Y. Tong, X. Pan, The 1st interlayer spacing of Ta(100) determined by photoelectron diffraction. *J. Vac. Sci. Technol. a-Vac. Surf. Films* **7**(3), 1931–1936 (1989)
9. J.N. Andersen, D. Hennig, E. Lundgren, M. Methfessel, R. Nyholm, M. Scheffler, Surface core-level shifts of some 4d-metal single-crystal surfaces: experiments and ab initio calculations. *Phys. Rev. B* **50**(23), 17525–17533 (1994)
10. D.M. Riffe, G.K. Wertheim, Ta(110) surface and subsurface core-level shifts and 4f_{7/2} line-shapes. *Phys. Rev. B* **47**(11), 6672–6679 (1993)
11. J.H. Cho, K.S. Kim, S.H. Lee, M.H. Kang, Z.Y. Zhang, Origin of contrasting surface core-level shifts at the Be(10 $\bar{1}$ 0) and Mg(10 $\bar{1}$ 0) surfaces. *Phys. Rev. B* **61**(15), 9975–9978 (2000)
12. A.V. Fedorov, E. Arenholz, K. Starke, E. Navas, L. Baumgarten, C. Laubschat, G. Kaindl, Surface shifts of 4f electron-addition and electron-removal states in Gd(0001). *Phys. Rev. Lett.* **73**(4), 601–604 (1994)
13. L.I. Johansson, H.I.P. Johansson, J.N. Andersen, E. Lundgren, R. Nyholm, 3 Surface-shifted core levels on Be(0001). *Phys. Rev. Lett.* **71**(15), 2453–2456 (1993)
14. S. Lizzit, K. Pohl, A. Baraldi, G. Comelli, V. Fritzsche, E.W. Plummer, R. Stumpf, P. Hofmann, Physics of the Be(10 $\bar{1}$ 0) surface core level spectrum. *Phys. Rev. Lett.* **81**(15), 3271–3274 (1998)
15. H.I.P. Johansson, L.I. Johansson, E. Lundgren, J.N. Andersen, R. Nyholm, Core-level shifts on Be(10 $\bar{1}$ 0). *Phys. Rev. B* **49**(24), 17460–17463 (1994)
16. A. Baraldi, S. Lizzit, G. Comelli, A. Goldoni, P. Hofmann, G. Paolucci, Core-level subsurface shifted component in a 4d transition metal: Ru(10 $\bar{1}$ 0). *Phys. Rev. B* **61**(7), 4534–4537 (2000)
17. E. Lundgren, U. Johansson, R. Nyholm, J.N. Andersen, Surface core-level shift of the Mo(110) surface. *Phys. Rev. B* **48**(8), 5525–5529 (1993)
18. R. Nyholm, J.N. Andersen, J.F. Vanacker, M. Qvarford, Surface core-level shifts of the Al(100) and Al(111) surfaces. *Phys. Rev. B* **44**(19), 10987–10990 (1991)
19. D.M. Riffe, B. Kim, J.L. Erskine, Surface core-level shifts and atomic coordination at a stepped W(110) surface. *Phys. Rev. B* **50**(19), 14481–14488 (1994)
20. J.H. Cho, D.H. Oh, L. Kleinman, Core-level shifts of low coordination atoms at the W(320) stepped surface. *Phys. Rev. B* **64**(11), 115404 (2001)
21. C.J. Karlsson, E. Landemark, Y.C. Chao, R.I.G. Uhrberg, Atomic origins of the surface components in the Si 2p core-level spectra of the Si(111)7 × 7 surface. *Phys. Rev. B* **50**(8), 5767–5770 (1994)
22. S.M. Scholz, K. Jacobi, Core-level shifts on clean and adsorbate-covered Si(113) surfaces. *Phys. Rev. B* **52**(8), 5795–5802 (1995)

23. T.W. Pi, J.F. Wen, C.P. Ouyang, R.T. Wu, Surface core-level shifts of Ge(100)-2X1. *Phys. Rev. B* **63**(15), 153310 (2001)
24. S. Lizzit, A. Baraldi, A. Groso, K. Reuter, M.V. Ganduglia-Pirovano, C. Stampl, M. Scheffler, M. Stichler, C. Keller, W. Wurth, D. Menzel, Surface core-level shifts of clean and oxygen-covered Ru(0001). *Phys. Rev. B* **63**(20), 205419 (2001)
25. P.A. Glans, L.I. Johansson, T. Balasubramanian, R.J. Blake, Assignment of the surface core-level shifts to the surface layers of Be(10(1)over-bar0). *Phys. Rev. B* **70**(3), 033408 (2004)
26. M. Zacchigna, C. Astaldi, K.C. Prince, M. Sastry, C. Comincioli, R. Rosei, C. Quaresima, C. Ottaviani, C. Crotti, A. Antonini, M. Matteucci, P. Perfetti, Photoemission from atomic and molecular adsorbates on Rh(100). *Surf. Sci.* **347**(1–2), 53–62 (1996)
27. D. Schmeisser, O. Bohme, A. Yfantis, T. Heller, D.R. Batchelor, I. Lundstrom, A.L. Spetz, Dipole moment of nanoparticles at interfaces. *Phys. Rev. Lett.* **83**(2), 380–383 (1999)
28. J. Nanda, D.D. Sarma, Photoemission spectroscopy of size selected zinc sulfide nanocrystallites. *J. Appl. Phys.* **90**(5), 2504–2510 (2001)
29. J. Nanda, B.A. Kuruville, D.D. Sarma, Photoelectron spectroscopic study of CdS nanocrystallites. *Phys. Rev. B* **59**(11), 7473–7479 (1999)
30. C.Q. Sun, L.K. Pan, H.L. Bai, Z.Q. Li, P. Wu, E.Y. Jiang, Effects of surface passivation and interfacial reaction on the size-dependent 2p-level shift of supported copper nanosolids. *Acta Mater.* **51**(15), 4631–4636 (2003)
31. D.Q. Yang, E. Sacher, Initial- and final-state effects on metal cluster/substrate interactions, as determined by XPS: copper clusters on Dow Cyclotene and highly oriented pyrolytic graphite. *Appl. Surf. Sci.* **195**(1–4), 187–195 (2002)
32. T. Ohgi, D. Fujita, Consistent size dependency of core-level binding energy shifts and single-electron tunneling effects in supported gold nanoclusters. *Phys. Rev. B* **66**(11), 115410 (2002)
33. A. Howard, D.N.S. Clark, C.E.J. Mitchell, R.G. Egdell, V.R. Dhanak, Initial and final state effects in photoemission from Au nanoclusters on TiO₂(110). *Surf. Sci.* **518**(3), 210–224 (2002)
34. M. Salmeron, S. Ferrer, M. Jassar, G.A. Somorjai, Core-band and valence-band energy-level shifts in small two-dimensional islands of gold deposited on Pt(100)—the effect of step edge, surface, and bulk atoms. *Phys. Rev. B* **28**(2), 1158–1160 (1983)
35. H.N. Aiyer, V. Vijayakrishnan, G.N. Subbanna, C.N.R. Rao, Investigations of Pd clusters by the combined use of HREM, STM, high-energy spectroscopies and tunneling conductance measurements. *Surf. Sci.* **313**(3), 392–398 (1994)
36. K. Borgohain, J.B. Singh, M.V.R. Rao, T. Shripathi, S. Mahamuni, Quantum size effects in CuO nanoparticles. *Phys. Rev. B* **61**(16), 11093–11096 (2000)
37. C.N.R. Rao, G.U. Kulkarni, P.J. Thomas, P.P. Edwards, Size-dependent chemistry: properties of nanocrystals. *Chem.-a Eur. J.* **8**(1), 29–35 (2002)
38. V. Vijayakrishnan, A. Chainani, D.D. Sarma, C.N.R. Rao, Metal-insulator transitions in metal-clusters: a high-energy spectroscopy study of Pd and Ag clusters. *J. Phys. Chem.* **96**(22), 8679–8682 (1992)
39. M.G. Mason, in *Cluster Models for Surface and Bulk Phenomena*, ed. by G. Pacchioni (Plenum, New York, 1992)
40. Z.X. Yang, R.Q. Wu, Origin of positive core-level shifts in Au clusters on oxides. *Phys. Rev. B* **67**(8), 081403 (2003)
41. M.A. Omar, *Elementary Solid State Physics: Principles and Applications* (Addison-Wesley, New York, 1993)
42. M. Reif, L. Glaser, M. Martins, W. Wurth, Size-dependent properties of small deposited chromium clusters by X-ray absorption spectroscopy. *Phys. Rev. B* **72**(15), 155405 (2005)
43. C.Q. Sun, Y. Shi, C.M. Li, S. Li, T.C.A. Yeung, Size-induced undercooling and overheating in phase transitions in bare and embedded clusters. *Phys. Rev. B* **73**(7), 075408 (2006)

44. X.J. Liu, J.W. Li, Z.F. Zhou, L.W. Yang, Z.S. Ma, G.F. Xie, Y. Pan, C.Q. Sun, Size-induced elastic stiffening of ZnO nanostructures: skin-depth energy pinning. *Appl. Phys. Lett.* **94**, 131902 (2009)
45. Y. Wang, Y.G. Nie, J.S. Pan, L.K. Pan, Z. Sun, L.L. Wang, C.Q. Sun, Orientation-resolved $3d(5/2)$ binding energy shift of Rh and Pd surfaces: anisotropy of the skin-depth lattice strain and quantum trapping. *PCCP* **12**(9), 2177–2182 (2010)
46. A. Baraldi, L. Bianchettin, E. Vesselli, S. de Gironcoli, S. Lizzit, L. Petaccia, G. Zampieri, G. Comelli, R. Rosei, Highly under-coordinated atoms at Rh surfaces: interplay of strain and coordination effects on core level shift. *N. J. Phys.* **9**(143), 12 (2007)
47. M. Rocca, L. Savio, L. Vattuone, U. Burghaus, V. Palomba, N. Novelli, F.B. de Mongeot, U. Valbusa, R. Gunnella, G. Comelli, A. Baraldi, S. Lizzit, G. Paolucci, Phase transition of dissociatively adsorbed oxygen on Ag(001). *Phys. Rev. B* **61**(1), 213–227 (2000)
48. M.P. Goertz, X.Y. Zhu, J.E. Houston, Exploring the liquid-like layer on the ice surface. *Langmuir: The ACS J. Surf. Colloids* **25**(12), 6905–6908 (2009)
49. J. Jupille, K.G. Purcell, D.A. King, W(100) clean surface phase transition studied by core-level-shift spectroscopy: order-order or order-disorder transition. *Phys. Rev. B* **39**(10), 6871–6879 (1989)
50. K.G. Purcell, J. Jupille, G.P. Derby, D.A. King, Identification of underlayer components in the surface core-level spectra of W(111). *Phys. Rev. B* **36**(2), 1288–1291 (1987)
51. X.B. Zhou, J.L. Erskine, Surface core-level shifts at vicinal tungsten surfaces. *Phys. Rev. B* **79**(15), 155422 (2009)
52. Y.G. Nie, X. Zhang, S.Z. Ma, Y. Wang, J.S. Pan, C.Q. Sun, XPS revelation of tungsten edges as a potential donor-type catalyst. *PCCP* **13**(27), 12640–12645 (2011)
53. N. Martensson, H.B. Saalfeld, H. Kuhlenbeck, M. Neumann, Structural dependence of the 5d-metal surface energies as deduced from surface core-level shift measurements. *Phys. Rev. B* **39**(12), 8181–8186 (1989)
54. A.S.Y. Chan, G.K. Wertheim, H. Wang, M.D. Ulrich, J.E. Rowe, T.E. Madey, Surface atom core-level shifts of clean and oxygen-covered Re(1231). *Phys. Rev. B* **72**(3), 035442 (2005)
55. R. Ducros, J. Fusy, Core level binding energy shifts of rhenium surface atoms for a clean and oxygenated surface. *J. Electron Spectrosc. Relat. Phenom.* **42**(4), 305–312 (1987)
56. Y.G. Nie, J.S. Pan, W.T. Zheng, J. Zhou, C.Q. Sun, Atomic scale purification of Re surface kink states with and without oxygen chemisorption. *J. Chem. Phys.* **115**(15), 7450–7455 (2011)
57. Y. Wang, Y.G. Nie, J.S. Pan, L.K. Pan, Z. Sun, C.Q. Sun, Layer and orientation resolved bond relaxation and quantum entrapment of charge and energy at Be surfaces. *PCCP* **12**(39), 12753–12759 (2010)
58. Y. Wang, Y.G. Nie, L.L. Wang, C.Q. Sun, Atomic-layer- and crystal-orientation-resolved $3d_{5/2}$ binding energy Shift of Ru(0001) and Ru(1010) surfaces. *J. Chem. Phys. C* **114**(2), 1226–1230 (2010)
59. A. Baraldi, S. Lizzit, G. Comelli, G. Paolucci, Oxygen adsorption and ordering on Ru(10(1)over-bar-0). *Phys. Rev. B* **63**(11), 115410 (2001)
60. F. Matsui, T. Matsushita, Y. Kato, M. Hashimoto, K. Inaji, F.Z. Guo, H. Daimon, Atomic-layer resolved magnetic and electronic structure analysis of Ni thin film on a Cu(001) surface by diffraction spectroscopy. *Phys. Rev. Lett.* **100**(20), 207201 (2008)
61. C. Kittel, *Introduction to Solid State Physics*, 8th edn. (Wiley, New York, 2005)
62. M. Zhao, W.T. Zheng, J.C. Li, Z. Wen, M.X. Gu, C.Q. Sun, Atomistic origin, temperature dependence, and responsibilities of surface energetics: an extended broken-bond rule. *Phys. Rev. B* **75**(8), 085427 (2007)
63. F. Himpsel, P. Heimann, T. Chiang, D. Eastman, Geometry-dependent Si(2p) surface core-level excitations for Si(111) and Si(100) surfaces. *Phys. Rev. Lett.* **45**(13), 1112–1115 (1980)
64. F. Himpsel, G. Hollinger, R. Pollak, Determination of the Fermi-level pinning position at Si(111) surfaces. *Phys. Rev. B* **28**(12), 7014–7018 (1983)

65. M. Vogel, C. Kasigkeit, K. Hirsch, A. Langenberg, J. Rittmann, V. Zamudio-Bayer, A. Kulesza, R. Mitrić, T. Möller, B. Issendorff, J. Lau, 2p core-level binding energies of size-selected free silicon clusters: chemical shifts and cluster structure. *Phys. Rev. B* **85**(19), 195454 (2012)
66. L.K. Pan, C.Q. Sun, Coordination imperfection enhanced electron-phonon interaction. *J. Appl. Phys.* **95**(7), 3819–3821 (2004)
67. L.K. Pan, S.Q. Xu, W. Qin, X.J. Liu, Z. Sun, W.T. Zheng, C.Q. Sun, Skin dominance of the dielectric-electronic-phononic-photonics attribute of nanostructured silicon. *Surf. Sci. Rep.* **68**(3–4), 418–455 (2013)
68. P. Buffat, J.P. Borel, Size effect on melting temperature of gold particles. *Phys. Rev. A* **13**(6), 2287–2298 (1976)
69. C.Q. Sun, Atomic-coordination-imperfection-enhanced Pd-3d(5/2) crystal binding energy. *Surf. Rev. Lett.* **10**(6), 1009–1013 (2003)
70. P. Zhang, T.K. Sham, X-ray studies of the structure and electronic behavior of alkanethiolate-capped gold nanoparticles: the interplay of size and surface effects. *Phys. Rev. Lett.* **90**(24), 245502 (2003)
71. K.J. Kim, H. Lee, J.H. Choi, Y.S. Youn, J. Choi, T.H. Kang, M.C. Jung, H.J. Shin, H.J. Lee, S. Kim, B. Kim, Scanning photoemission microscopy of graphene sheets on SiO₂. *Adv. Mater.* **20**(19), 3589–3591 (2008)
72. K.V. Emtsev, F. Speck, T. Seyller, L. Ley, J.D. Riley, Interaction, growth, and ordering of epitaxial graphene on SiC{0001} surfaces: a comparative photoelectron spectroscopy study. *Phys. Rev. B* **77**(15), 155303 (2008)
73. H.Y. Mao, R. Wang, H. Huang, Y.Z. Wang, X.Y. Gao, S.N. Bao, A.T.S. Wee, W. Chen, Tuning of C[sub 60] energy levels using orientation-controlled phthalocyanine films. *J. Appl. Phys.* **108**(5), 053706 (2008)
74. Y.M. Shulga, T.C. Tien, C.C. Huang, S.C. Lo, V. Muradyan, N.V. Polyakova, Y.C. Ling, R.O. Loutfy, A.P. Moravsky, XPS study of fluorinated carbon multi-walled nanotubes. *J. Electron Spectrosc. Relat. Phenom.* **160**(1–3), 22–28 (2007)
75. A. Goldoni, R. Laricprete, L. Gregoratti, B. Kaulich, M. Kiskinova, Y. Zhang, H. Dai, L. Sangaletti, F. Parmigiani, X-ray photoelectron microscopy of the C 1 s core level of free-standing single-wall carbon nanotube bundles. *Appl. Phys. Lett.* **80**(12), 2165–2167 (2002)
76. P. Bennich, C. Puglia, P.A. Bruhwiler, A. Nilsson, A.J. Maxwell, A. Sandell, N. Martensson, P. Rudolf, Photoemission study of K on graphite. *Phys. Rev. B* **59**(12), 8292–8304 (1999)
77. C.S. Yannoni, P.P. Bernier, D.S. Bethune, G. Meijer, J.R. Salem, NMR determination of the bond lengths in C₆₀. *J. Am. Chem. Soc.* **113**(8), 3190–3192 (1991)
78. G. Speranza, N. Laidani, Measurement of the relative abundance of sp(2) and sp(3) hybridised atoms in carbon based materials by XPS: a critical approach. Part I. *Diamond Relat. Mater.* **13**(3), 445–450 (2004)
79. S. Takabayashi, K. Motomitsu, T. Takahagi, A. Terayama, K. Okamoto, T. Nakatani, Qualitative analysis of a diamondlike carbon film by angle-resolved X-ray photoelectron spectroscopy. *J. Appl. Phys.* **101**, 103542 (2007)
80. K.G. Saw, J. du Plessis, The X-ray photoelectron spectroscopy C 1 s diamond peak of chemical vapour deposition diamond from a sharp interfacial structure. *Mater. Lett.* **58**(7–8), 1344–1348 (2004)
81. C.Q. Sun, Y. Sun, Y.G. Nie, Y. Wang, J.S. Pan, G. Ouyang, L.K. Pan, Z. Sun, Coordination-resolved C–C bond length and the C 1 s binding energy of carbon allotropes and the effective atomic coordination of the few-layer graphene. *J. Chem. Phys. C* **113**(37), 16464–16467 (2009)
82. H. Hibino, H. Kageshima, M. Kotsugi, F. Maeda, F.-Z. Guo, Y. Watanabe, Dependence of electronic properties of epitaxial few-layer graphene on the number of layers investigated by photoelectron emission microscopy. *Phys. Rev. B* **79**, 125431 (2009)
83. T. Filleter, K.V. Emtsev, T. Seyller, R. Bennewitz, Local work function measurements of epitaxial graphene. *Appl. Phys. Lett.* **93**(13), 133117 (2008)

84. U. Starke, C. Riedl, Epitaxial graphene on SiC(0001) and SiC(0001)over-bar): from surface reconstructions to carbon electronics. *J. Phys.: Condens. Matter* **21**(13), 134016 (2009)
85. Y.Y. Tay, S. Li, C.Q. Sun, P. Chen, Size dependence of Zn 2p 3/2 binding energy in nanocrystalline ZnO. *Appl. Phys. Lett.* **88**(17), 173118 (2006)
86. Y.Y. Tay, T.T. Tan, M.H. Liang, F. Boey, S. Li, Specific defects, surface band bending and characteristic green emissions of ZnO. *Phys. Chem. Chem. Phys.* **12**(23), 6008–6013 (2010)
87. Y.Y. Tay, T.T. Tan, F. Boey, M.H. Liang, J. Ye, Y. Zhao, T. Norby, S. Li, Correlation between the characteristic green emissions and specific defects of ZnO. *Phys. Chem. Chem. Phys.* **12**(10), 2373–2379 (2010)
88. C.Q. Sun, Dominance of broken bonds and nonbonding electrons at the nanoscale. *Nanoscale* **2**(10), 1930–1961 (2010)
89. J.W. Li, S.Z. Ma, X.J. Liu, Z.F. Zhou, C.Q. Sun, ZnO meso-mechano-thermo physical chemistry. *Chem. Rev.* **112**(5), 2833–2852 (2012)
90. C.Q. Sun, L.K. Pan, T.P. Chen, X.W. Sun, S. Li, C.M. Li, Distinguishing the effect of crystal-field screening from the effect of valence recharging on the 2P(3/2) and 3d(5/2) level energies of nanostructured copper. *Appl. Surf. Sci.* **252**(6), 2101–2107 (2006)
91. P. Abbott, E.D. Sosa, D.E. Golden, Effect of average grain size on the work function of diamond films. *Appl. Phys. Lett.* **79**(17), 2835–2837 (2001)
92. A.A. Rouse, J.B. Bernhard, E.D. Sosa, D.E. Golden, Variation of field emission and photoelectric thresholds of diamond films with average grain size. *Appl. Phys. Lett.* **75**(21), 3417–3419 (1999)
93. T. Yamauchi, M. Tabuchi, A. Nakamura, Size dependence of the work function in InAs quantum dots on GaAs(001) as studied by Kelvin force probe microscopy. *Appl. Phys. Lett.* **84**(19), 3834–3836 (2004)
94. M.M. Kappes, R.W. Kunz, E. Schuhmacher, Production of large sodium clusters (Nax, x < 65) by seeded-beam expansions. *Chem. Phys. Lett.* **91**:413–418 (1982)
95. T.M. Bhave, S.V. Bhoraskar, Surface work function studies in porous silicon. *J. Vac. Sci. Technol. B* **16**(4), 2073–2078 (1998)
96. Y. Tzeng, C. Liu, A. Hirata, Effects of oxygen and hydrogen on electron field emission from microwave plasma chemically vapor deposited microcrystalline diamond, nanocrystalline diamond, and glassy carbon coatings. *Diam. Relat. Mat.* **12**(3–7), 456–463 (2003)
97. R.P. Gao, Z.W. Pan, Z.L. Wang, Work function at the tips of multiwalled carbon nanotubes. *Appl. Phys. Lett.* **78**(12), 1757–1759 (2001)
98. C.H.P. Poa, R.G. Lacerda, D.C. Cox, F.C. Marques, S.R.P. Silva, Effects of stress on electron emission from nanostructured carbon materials. *J. Vac. Sci. Technol. B* **21**(4), 1710–1714 (2003)
99. C. Uher, R.L. Hockey, E. Benjacob, Pressure-dependence of the c-axis resistivity of graphite. *Phys. Rev. B* **35**(9), 4483–4488 (1987)
100. C.H. Poa, R.G. Lacerda, D.C. Cox, S.R.P. Silva, F.C. Marques, Stress-induced electron emission from nanocomposite amorphous carbon thin films. *Appl. Phys. Lett.* **81**(5), 853–855 (2002)
101. C.H.P. Poa, R.C. Smith, S.R.P. Silva, C.Q. Sun, Influence of mechanical stress on electron field emission of multiwalled carbon nanotube-polymer composites. *J. Vac. Sci. Tech. B* **23**(2), 698–701 (2005)
102. R.G. Lacerda, M.C. dos Santos, L.R. Tessler, P. Hammer, F. Alvarez, F.C. Marques, Pressure-induced physical changes of noble gases implanted in highly stressed amorphous carbon films. *Phys. Rev. B* **68**(5), 054104 (2003)
103. R.W. Lynch, H.G. Drickame, Effect of high pressure on lattice parameters of diamond graphite and hexagonal boron nitride. *J. Chem. Phys.* **44**(1), 181–184 (1966)
104. S. Bhattacharyya, S.V. Subramanyam, Metallic conductivity of amorphous carbon films under high pressure. *Appl. Phys. Lett.* **71**(5), 632–634 (1997)
105. K. Umamoto, S. Saito, S. Berber, D. Tomanek, Carbon foam: spanning the phase space between graphite and diamond. *Phys. Rev. B* **64**(19), 193409 (2001)

106. L. Lu, M.L. Sui, K. Lu, Superplastic extensibility of nanocrystalline copper at room temperature. *Science* **287**(5457), 1463–1466 (2000)
107. K. Lu, Nanocrystalline metals crystallized from amorphous solids: nanocrystallization, structure, and properties. *Mater. Sci. Eng. R-Rep.* **16**(4), 161–221 (1996)

Chapter 17

Bandgap Expansion: Photon Emission and Absorption

- *The E_G of a semiconductor is proportional to the first Fourier series coefficient of the interatomic potential.*
- *Skin-resolved bond contraction and entrapment perturb that the Hamiltonian originates and the increased fraction of undercoordinated atoms expands the E_G .*
- *Energies of photon emission and photon absorption are superposition of the interatomic binding energy and the electron–phonon coupling i.e., Stokes shift.*
- *Polarization of the dangling bond electrons creates the mid-gap states and band tails, which lowers the quantum efficiency of photon emission; hydrogenation could annihilate such defect states.*
- *Graphenes with arm-chaired or reconstructed zigzag edges are semiconductor like because of the annihilation of the edge polarization by quasi- π bond formation between the nearest carbon atoms along the edges; graphenes with zigzag edges behave like metal because of the edge localized and polarized states in the mid-gap region.*

17.1 Observations

The Hamiltonian determines and correlates the properties intrinsically, and therefore, it is appropriate to consider the change of all the properties relating to the Hamiltonian rather than separate one phenomenon at a time from another. The size-induced quantum entrapment and polarization modulates the Hamiltonian, and therefore, the entire band structure of nanostructured semiconductors [1]:

1. Bandgap E_G expansion gives rise to the blueshift in the PL and photoabsorbance (PA) energy of nanometric semiconductors such as Si [2], Si oxides [3–6], III-V [7] (GaN [8, 9], InAs [10], GaP and InP [11, 12]), and II-VI (CdS [13–15], ZnS [16], CdSe [17, 18], ZnTe [19], CdTe/CdZnTe [20]) compounds. The energy shifts are controllable by changing the particle size or by pore formation. When the crystal size is reduced or the specimen's shape is changed

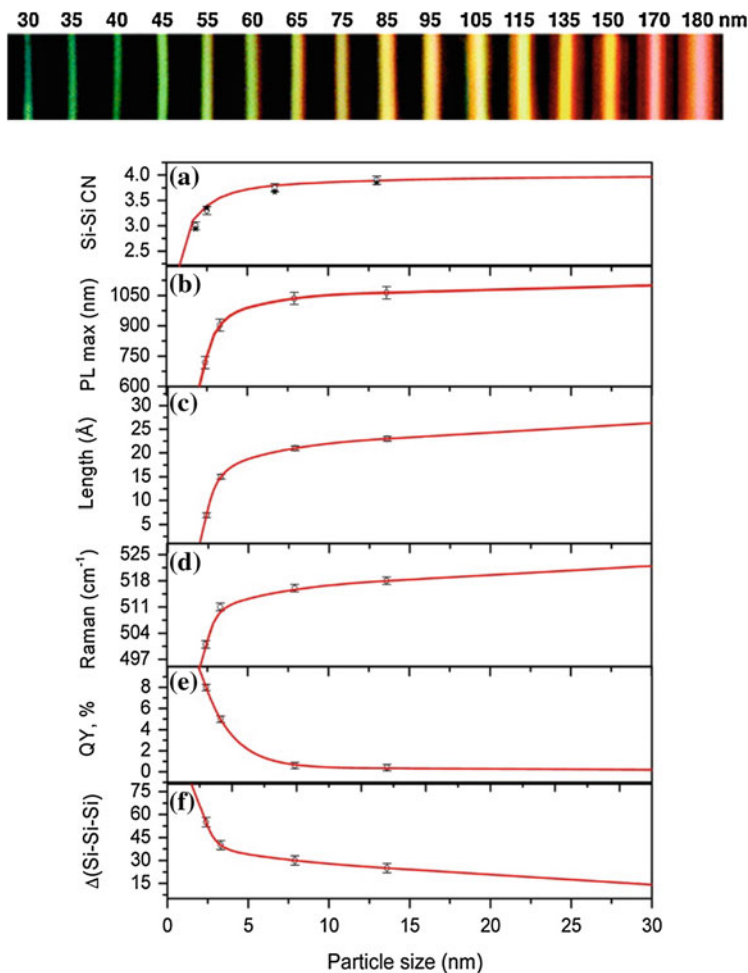


Fig. 17.1 Scalable fabrication of p-Si modulates the color of the PL (*upper panel*) showing the size dependency of emission wavelength (reprinted with permission from [22]). Experimental (*solid stars*) and computed (*open circles*) **a** first coordination numbers (CN) of Si atoms; **b** experimental photoluminescence (PL) peak positions (*symbols*); **c** experimental length of structural coherence (*symbols*); **d** experimental Raman peak position (*symbols*); **e** experimental quantum yield (*symbols*); and **f** $\Delta(\text{Si-Si-Si})$ bond angle distributions (*symbols*) as a function of particle size. *Solid lines (in red)* are nonlinear fits to the respective experimental data (reprint with permission from [26]. Copyright (2013) American Chemical Society)

from one to two and to three dimensions of the same feature size [21], these energies will increase. As shown in Fig. 17.1, porous Si with nanostructured frames emits a tunable, wide spectrum of colors under white light illumination at room temperature [22].

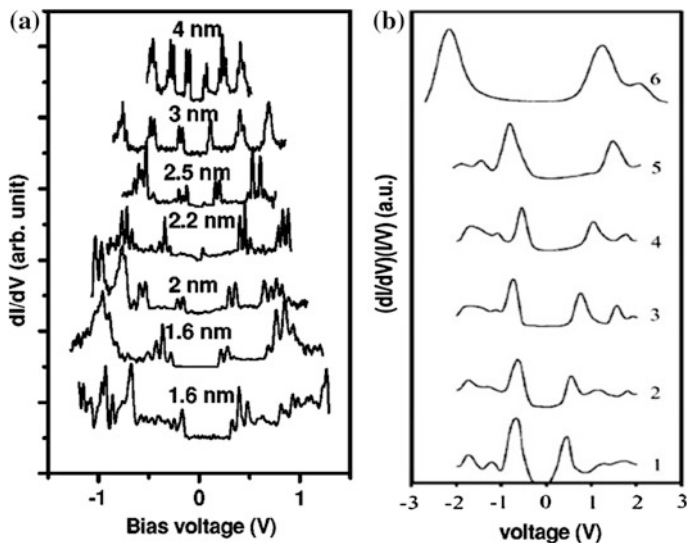


Fig. 17.2 STS conductance of **a** crystalline Pd particles (reprinted with permission from [29]) and of **b** Si nanowires with diameter decreases from 7 (curve 1) to 1.3 nm (curve 6) (reprinted with permission from [2]). Crystal size reduction creates **(a)** and expands **(b)** the bandgap at the nanoscale

2. Electron–phonon coupling shifts the intrinsic bandgap E_G to the E_{PA} or the E_{PL} by an addition or subtraction of the Stokes shift that also changes with solid size [23].
3. The E_G expansion suppresses the complex dielectric constant of a nanometric semiconductor [24]. The dielectric suppression enhances the Coulomb interaction among electrons, holes, and ionized shallow impurities in nanometric devices and enhances the exciton binding energy [25].
4. Figure 17.1 also shows a comprehensive set of data revealed using the high-energy synchrotron X-ray diffraction coupled to atomic pair distribution function analysis and computer simulations of the oxide-free Si nanoparticles [26]. These data show clearly the particle size dependency of the average first coordination numbers, length of structural coherence, and degree of local bond angle distortions in comparison with the optical properties such as photoluminescence emission energy, quantum yield, and Raman frequency of nanostructured Si.

The size-induced quantum entrapment and polarization splits the valence band of metals to generate an artificial bandgap, which turns a metal at the nanoscale to be an insulator [27]. The artificial bandgaps for Au [28] and Pd [29] clusters increase when the number of Au and Pd atoms is reduced in the clusters. Figure 17.2 shows the evolution of the STS spectra for Pd and Si nanowires.

Without igniting electron–phonon interaction at $T = 4$ K nor exciton production and combination, the E_G of Si nanorods increases from 1.1 to 3.5 eV when the wire

diameter is reduced from 7.0 to 1.3 nm and that the surface Si–Si bond contracts by $\sim 12\%$ from the bulk value (0.263 nm) to ~ 0.23 nm [2]. This observation concurs with the BOLS expectation: CN imperfection shortens and strengthens the remaining bonds of the lower-coordinated atoms associated with E_G expansion that is proportional to the single bond energy. Likewise, the size-enlarged E_G of Si nanorods, Si nanodots, Ge nanostructures, and other III–V and II–VI semiconductors at the nanoscale follows the same rule without involving electron–hole interaction, electron–phonon coupling or quantum confinement [30–32].

17.2 Known Mechanisms

“Quantum confinement (QC)” theory [33, 34] describes the PL blueshift in terms of E_G expansion by radius R reduction:

$$\begin{aligned} E_G(R) &= E_G(\infty) + \pi^2 \hbar^2 / (2\mu R^2) - 1.786 e^2 / (\epsilon_r R) + 0.284 E_R \\ E_R &= \mu e^4 / (2\epsilon_r^2 \epsilon_0^2 \hbar^2) = 13.56\mu / \epsilon_r^2 m_e \text{ (eV)} \end{aligned} \quad (17.1)$$

where μ ($1/\mu = 1/m_h^* + 1/m_e^*$) being the reduced mass of an electron–hole (e–h) pair (exciton). The potential [35, 36] and the kinetic energy [33, 34] of the e–h pairs that are separated by a distance of the particle dimension or the quantum well size dictates the E_G expansion. The Rydberg correlation energy E_R is the background contribution. The effective dielectric constant ϵ_r and the effective mass, μ , describe the effect of the homogeneous medium in the quantum box, which is a monocentral of trapping potential extended from that of an isolated atom by expanding atomic size to the dimension of the solid. The dictating factor for the QC convention is the production and motion of e–h pairs. For CdS example [36, 37], $\epsilon_r = 5.5$, $m_e^* = 0.19$, and $m_h^* = 0.8$.

According to the QC theory, the potential barrier of the surface confines electrons in the conduction band and holes in the valence band. Alternatively, the potential well of the quantum box entraps them moving inside. Because of the confinement, optical transition energy of electrons and holes between the valence and the conduction band increases, with enlarges effectively the E_G . The sum of kinetic and potential energy of the freely moving carriers is responsible for the E_G expansion, and therefore, the width of the confined E_G grows as the characteristic dimensions of the crystallite decrease [34].

In contrary, surface dielectric function model [38] suggests that photon emission of sized quantum dot (QD) depends on changes to dielectric function in the ‘superficial skin’ rather than the entire dot as QC theory refers. The dielectric function in the core interior of a QD remains as that of the bulk material, but in a small dot, the differences are greater near the grain boundary.

A free-exciton collision model [3] proposes that thermally activated phonons in the grain boundaries rather than the QC effect contribute to E_G expansion. During PL measurement, the excitation laser heats the free excitons that then collide with

the boundaries of the nanometer-sized fragments. The laser heating the free excitons up to the temperature in excess of the activation energy required for the self-trapping gives rise to the extremely hot self-trapping excitons (STEs). Because the resulting temperature of the STEs is much higher than the lattice temperature, the cooling of the STEs is dominated by emitting phonons. However, if the STE temperature comes into equilibrium with the lattice temperature, the absorption of lattice phonons becomes possible. As a result, blueshift of the STE-PL band happens upon the hot-phonon-assisted electronic transitions taking place. The energy gained from laser heating of the exciton increases with decreasing nanosolid diameter in an $\exp(1/R)$ form.

Other phenomenological models for the PL blueshift of nanosolids include the impurity centers [39], surface states [40], surface alloying [41], cluster interaction, and oxidation effect.

17.3 BOLS Formulation

17.3.1 Energy Band Formation

Figure 17.3 illustrates the evolution of the energy level of an isolated atom to the energy band of a bulk solid that contains N atoms. Electrons of an isolated atom confined by the intra-atomic trapping potential, $V_{\text{atom}}(r) = \text{constant}$ or $-\infty$, move around the central ion core in a standing wave form inside the potential well. The eigen wave functions and the eigen energies are as follows:

$$\phi_n(r) \propto \sin^2(2\pi nr/d_0) \quad \text{and} \quad E(n) = 2(n\pi\hbar)^2 / (m_e d_0^2), \quad n = 1, 2, 3, \dots$$

where the atomic diameter d_0 corresponds to the dimension of the potential well of the isolated atom. The quantum numbers (n) correspond to different energy levels. The energy separation between the closest two levels depends on $(n+1)^2 - n^2 = 2n + 1$.

When a system contains two atoms, the single energy level splits into two sublevels and the interatomic binding energy determines the separation between the sublevels. Meanwhile, the presence of interatomic interaction shifts the center of the two levels down. Increasing the number of atoms up to N , the single energy level will expand into a band within which there are N sublevels. The number of atoms N in the solid determines the number of the sublevels in a particular energy band. What distinguishes a nanosolid from a bulk solid is that for the former the N is accountable, while for the latter the N is too large to be accounted.

Therefore, the classical band theories are valid for a nanometric solid that contains at least two atoms. As detected using XPS, the DOS of a core band for a nanosolid exhibits band-like features rather than the discrete spectral lines of an isolated atom. If the N is sufficiently small, the separation between the sublevels is

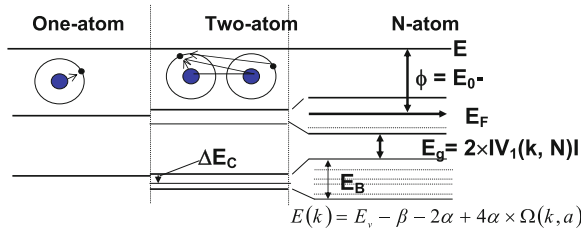


Fig. 17.3 Evolution of an energy level into the band when particle grows from an isolated atom to a bulk solid that contains N atoms. Indicated is the work function ϕ , bandgap E_G , core-level shift ΔE_v , bandwidth E_B . The number of allowed sublevels in a certain band equals the number of atoms of the solid. The sublevel spacing, or Kubo gap, is $4E_F/3N$, with E_F being the Fermi level of the bulk [44] (reprinted with permission from [30])

resolvable. The energy level spacing of the successive sublevels in the valence band, known as the Kubo gap ($\delta_K = 4E_F/3N$), decreases with increasing number of valence electrons of the system [42]. For a system containing 1,000 silver atoms, the Kubo gap would be 5–10 meV. At room temperature, $k_B T \cong 25$ meV, a 3-nm-sized particle containing 500 atoms or more would be metallic ($k_B T > \delta_K$). At low temperatures, however, the level spacings especially in a small particle may become comparable to $k_B T$ or higher, rendering them nonmetallic [42]. Because of the presence of the δ_K in an individual nanosolid, properties such as electron conductivity and magnetic susceptibility exhibit quantized features [43]. The resultant discreteness of energy sublevels also brings about fundamental changes in the characteristic spectral features of the nanosolids, especially those related to the valence band.

According to the band theory, the Hamiltonian for an electron inside a solid is in the form [45]:

$$\hat{H} = \hat{H}_0 + \hat{H}' = -\frac{\hbar^2 \nabla^2}{2m} + V_{\text{atom}}(r) + V_{\text{cry}}(r + R_C) \quad (17.2)$$

where the $V_{\text{atom}}(r)$ is the intra-atomic trapping potential of an isolated atom, and the $\hat{H}' = V_{\text{cry}}(r) = V_{\text{cry}}(r + R_C)$ is the periodic potential of the crystal, i.e., the interatomic interaction. R_C is the lattice constant. According to the nearly free-electron approximation, the E_G originates from the crystal potential and the width of the gap is simply twice of the first Fourier coefficient of the crystal potential

$$E_G = 2|V_1(k_1)| \quad (17.3)$$

Therefore, the E_G , the energy shift $\Delta E_v(\infty) = -(\beta + 2\alpha)$ of the $E_v(0)$ and the bandwidth ΔE_B (Chap. 16) are dependent on crystal potential. Any perturbation to the crystal potential will vary these quantities. Without the crystal potential, neither the E_G expansion nor the core-level shift would be possible; without the interatomic binding, neither a solid nor even a liquid could form.

17.3.2 Hamiltonian Perturbation

Considering an assembly composed of n particles of a mean size K and with each particle, there are N atoms, the total binding energy, $V(r, n, N)$ [46]:

$$\begin{aligned}
 V(r, n, N) &= \sum_n \sum_{l \neq i} \sum_i v(r_{li}) \\
 &= \frac{n}{2} \left[N \sum_{i=1} v(r_{ii}) + \sum_{k \neq j} V(K_k) \right] \\
 &\cong \frac{n}{2} [N^2 v(d_0) + nV(K)]
 \end{aligned} \tag{17.4}$$

$V(r, n, N)$ sums over all the nN atoms and the n particles. The high-order r_{li} is a certain fold of the nearest atomic spacing, d_0 . Besides, interaction between the nearest clusters, k and j , $V(K_k)$, should be taken into account. If K_k is considerably large (such as the case of porous Si, or highly dispersed particles), the last term is negligible, which is the case of an isolated particle. Normally, the intercluster interaction, $V(K)$, is much weaker than the interatomic interaction. For example, if the cluster is taken as an electrical dipole or a magnetic dipole, the van der Waals or the superparamagnetic potential is much weaker. If the intercluster interaction is significant, Eq. (17.4) evolves into the following form in terms of a core-shell structure:

$$\begin{aligned}
 V_{\text{cry}}(r, n, N) &= \frac{nN}{2} \left[N_i v(d_i) + (N - N_i) v(d_0) + \frac{n}{N} V(K) \right] \\
 &= \frac{nN^2 v(d_0)}{2} \left[\frac{N_i v(d_i)}{N v(d_0)} + \left(1 - \frac{N_i}{N} \right) + \frac{nV(K)}{N^2 v(d_0)} \right] \\
 &= V_{\text{cry}}(d_0, n, N) \{ 1 + \gamma_i [v(d_i)/v(d_0) - 1] + \delta_k(K) \} \\
 \frac{\Delta V_{\text{cry}}(N)}{V_{\text{cry}}(\infty)} &= \sum_{i \leq 3} \gamma_i \frac{\Delta v}{v} + \delta'_k(K) = \sum_{i \leq 3} \gamma_i (C_i^{-m} - 1) + \delta'_k(K) \\
 \delta_k &= \frac{nV(K)}{N^2 v(d_0)}
 \end{aligned} \tag{17.5}$$

The i counts from the outermost inward up to three of the nanosolid. $V_{\text{cryst}}(d_0, n, N)$ is the crystal potential of the system without the effect of atomic CN imperfection or the intercluster interaction. The pair interatomic binding energy at equilibrium atomic separation, $v(d_i) \propto E_i = C_i^{-m} E_b$. This leads to the perturbation to the crystal binding energy (the energy per bond in the relaxed region rather than the atomic cohesive energy) upon assembly of the nanosolids. The perturbation covers the weighted sum of contribution from the individual surface layers ($C_i^{-m} - 1$) over the outermost three atomic layers of a nanosolid, and the intercluster interaction, $\delta_k(K)$ that is negligible if the particle size is sufficiently large.

The crystal potential in Eq. (17.2) becomes $V_{\text{cryst}}(\Delta_H) = V_{\text{cry}}(r)[1 + \Delta_H]$. In conjunction with the corresponding Bloch wave functions, the atomic trapping potential, $V_{\text{atom}}(r)$, defines the discrete core-level energies of an isolated atom, $E_v(0)$. The crystal binding $V_{\text{cryst}}(r)$ defines not only the E_G , but also the shift of the core-level energy away from the original position, $\Delta E_v(\infty) = E_v(\infty) - E_v(0)$, as well as other quantities such as the bandwidth and band tails. The dimensionless Δ_H , being independent of the particular form of the interatomic potential, is the contribution from binding energy in the relaxed surface region.

The perturbation to the Hamiltonian will cause the changes of E_G and $E_v(K)$, which follows the scaling relation:

$$\frac{\Delta E_G(K)}{E_G(\infty)} = \frac{\Delta E_v(K) - \Delta E_v(\infty)}{\Delta E_v(\infty)} = \Delta_H \quad (17.6)$$

In the quantum theory the key elements are the Hamiltonian and the Bloch wave functions. Nanosolid densification modifies the wave functions slightly as, in this case, no chemical reaction occurs.

17.4 Process of Photon Emission and Absorption

17.4.1 Electron–Phonon Coupling

The joint effect of crystal binding and electron–phonon coupling determines the PL or PA energies, as illustrated in Fig. 17.4. The energies of the ground state (E_1) and the excited state (E_2) are expressed as follows [47]:

$$\begin{cases} E_1(q) = Aq^2 \\ E_2(q) = A(q - q_0)^2 + E_G \end{cases} \quad (17.7)$$

Constant A is the slope of the parabolas with q being the wavevector. The vertical distance between the two minima is the intrinsic E_G that depends uniquely on the crystal potential. The e–p coupling offsets laterally the $E_2(q)$ curve, which can be strengthened by enhancing lattice vibration. Therefore, the blueshift in the E_{PL} and in the E_{PA} is the joint contribution from the change of crystal binding and e–p coupling. At a surface, the CN-imperfection-enhanced bond strength affects both the frequency and magnitude [48, 49] of lattice vibration. Hence, at a surface, the e–p coupling, and hence, the Stokes shift will be enhanced.

In the process of carrier formation and recombination, an electron is excited by a photon with $E_{\text{PL}} = E_G + W$ energy from the ground minimum to the excited state with creation of an electron–hole pair exciton. The excited electron then undergoes a thermalization, moves to the minimum of the excited state, and eventually transmits to the ground combining with the hole. The carrier recombination is associated with emission of a photon with energy $E_{\text{PL}} = E_G - W$. The

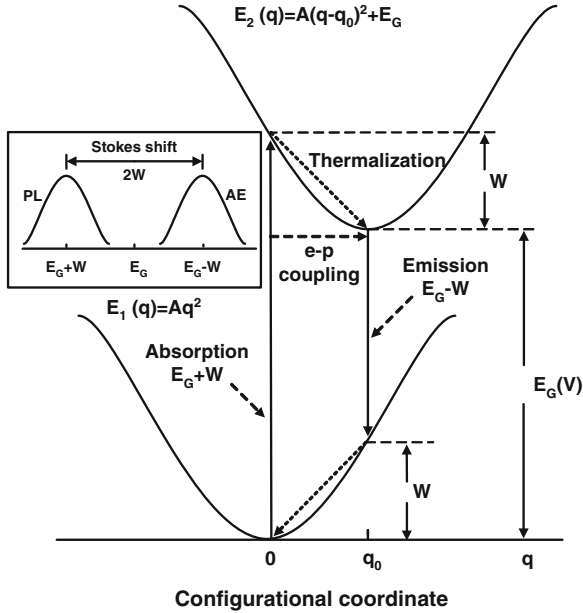


Fig. 17.4 Correlation between the bandgap E_G , Stokes shift (W) and the photonic bandgap of E_{PA} and E_{PL} . Crystal potential determines E_G , and electron–phonon coupling determines W . Inset illustrates the Stokes shift from E_{PA} to E_{PL} . An electron is excited by absorbing a photon with energy $E_{PA} = E_G + W$ from the ground minimum to the excited state and then undergoes a thermalization to the excited minimum prior to recombination with the hole in the ground, emitting a photon with energy $E_{PL} = E_G - W$ [47] (reprinted with permission from [30])

transition processes (exciton production and recombination) follow the rule of momentum and energy conservation though the conservation law is subject to relaxation for the short-ordered nanosolid. Such conservation law relaxation is responsible for the broad peaks in the E_{PA} and E_{PL} .

The inset illustrates the Stokes shift, $2W = 2Aq_0^2$, from E_{PL} to E_{PA} . The q_0 is inversely proportional to atomic distance d_i , and hence, $W_i = A/(C_i d_i)^2$, in the surface region. Thus, the blueshift of the E_{PL} , the E_{PA} , and the W are correlated with the bond contraction [31]:

$$\left. \begin{aligned} \frac{\Delta E_{PL}(K)}{E_{PL}(\infty)} \\ \frac{\Delta E_{PA}(K)}{E_{PA}(\infty)} \end{aligned} \right\} = \frac{\Delta E_G(K) \mp \Delta W(K)}{E_G(\infty) \mp W(\infty)} \cong \sum_{i \leq 3} \gamma_i [(C_i^{-m} - 1) \mp B(C_i^{-2} - 1)] \quad (17.8)$$

$$\left(B = \frac{A}{E_G(\infty)d^2}; \frac{W(\infty)}{E_G(\infty)} \approx \frac{0.007}{1.12} \approx 0 \right)$$

Compared with the bulk $E_G(\infty) = 1.12$ eV, the $W(\infty) \sim 0.007$ eV [50] is negligible. One can easily calculate the size-dependent E_{PL} , E_{PA} , and

$E_G = (E_{PL} + E_{PA})/2$ using Eq. (17.8). Matching theory to measurement turns out values of m and A for a specific semiconductor.

17.4.2 E_G Expansion

The BOLS formulation reproduces the size dependency of both the $E_{PL}(K)$ and the $E_{PA}(K)$ of porous Silicon (p-Si) [31]. Figure 17.5a, b show that the reflectivity and absorption coefficient varies with size in the wavelengths of 200–900 nm, which is related to the change of dimension and geometry of columns and voids on the p-Si surface. The reflection spectra give the absorption coefficient [51] and the E_{PA} value [52, 53]. Figure 17.5c shows the size dependence of the E_G , E_{PL} , E_{PA} , and the E_{2p} of p-Si. Matching the predictions with the measured E_{PA} and E_{PL} data (a) gives coefficient $B = 0.91$ and $m = 4.88$.

It is important to note that an STS collects *localized* DOS information without needing any energetic stimulus. The bias ($|V_b| < 2$ eV) between the tip and the sample surface is not sufficiently large to break the Si–Si bond. What happens upon being biased is that the tip introduces holes or electrons into the sample rather than produces electron–hole pairs inside the specimen. As such, neither electron excitation from the ground to the excited states nor electron–hole pair production or carrier recombination occurs during STS measurement. What contributes to the STS- E_G are states occupied by the covalent bonding electrons and the empty states that are strongly localized at the probed site rather than the Coulomb interaction between the excited electron–hole or kinetic energies of the mobile carriers moving inside, or being confined by, the nanosolid. Without causing e–h pair (exciton) production and recombination [44], STS- E_G continues expanding upon the size being reduced. A surface hydride may form upon the sample being passivated using hydrogen. However, hydride formation reduces the mid-gap impurity DOS and hence improves the quantum efficiency in the irradiation recombination, and hence, the surface hydride formation could never expand the E_G [47]. As shown in Fig. 17.6c, the size-enlarged E_G of Si nanorods (STS derived) [2] and Si nanodots (mean value of E_{PA} and E_{PL}) follows the BOLS prediction which involves no events of electron–hole interaction, e–p coupling, or quantum confinement.

17.4.3 PL Blueshift

Figure 17.7 shows the size-induced PL blueshift for InP, InAs, CdS, and CdSe nanosolids. This size trend agrees with the E_G expansion of Si:H nanosolids [67]. All the data follow the similar trend of $m = 4–6$. The cluster interaction appears to

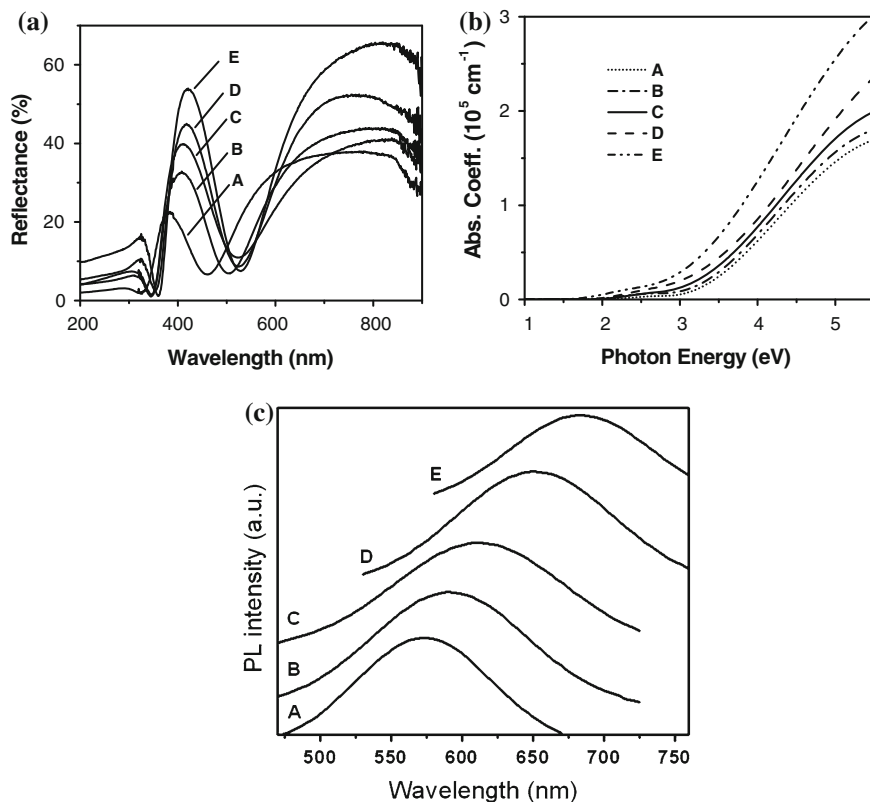


Fig. 17.5 **a** Reflection and **b** absorption spectra of p-Si of different particle sizes measured at ambient temperature. E_{PA} is obtained with the Tauc plot fitting of the reflection and absorption data. Size dependence of **c** PL spectra in particle size range of $R = 1.4\text{--}2.1$ nm [31] (reprinted with permission from [30])

play an insignificant role in the PL blueshift, which coincides with BOLS predictions. The general dimensionless trend of PL blueshift indicates that the size effect on the bandgap varies little with materials or with the particular crystal structures, wurtzite and zinc-blende structures in Fig. 17.7b [68].

The E_G value for a bulk compound varies with the extent of chemical reaction [69, 70]. For example, the E_G for the SiO_x varies from 1.12 (Si) to 9.0 (SiO_2) eV. It is not realistic to fit the measured data perfectly without considering the effect of surface passivation. One should focus on the trends of change and their physical origins.

Figures 17.6 and 17.7 compare the PL blueshift of nanometric semiconductors at the lower end of the size. The PL blueshift of Si, CdS [13], CdSe [71–75], and InP [11, 76, 77] nanosolids ($D < 5$ nm) are in accordance with BOLS prediction.

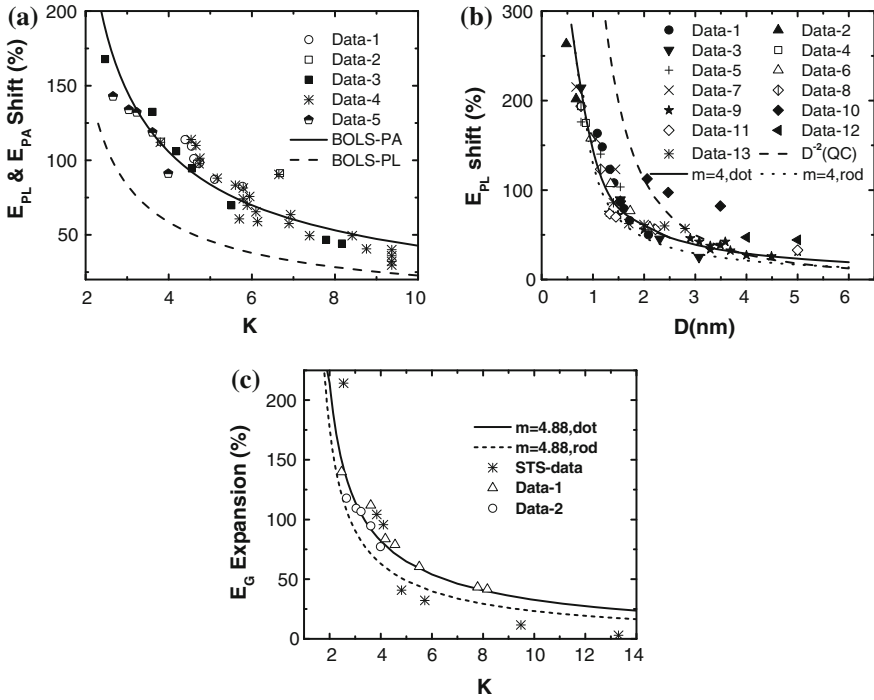


Fig. 17.6 Size-reduction-induced blueshift of **a** E_{PA} [54–58], **b** E_{PL} [4, 50, 54, 56, 58–65], **c** E_G [2, 54, 66] of p-Si (reprinted with permission from [30])

Figure 17.7 also plots curves of $R^{-1.04}$ and $100 \times (5.8D^2 + 27.2D + 10.4)^{-1}$ for comparison [78].

Figure 17.8 shows the BOLS reproduction of the measured size dependence of [79]: (a) photoabsorption energy E_{PA} with inset showing an offset to fit $\Delta E_{PA}/E_{PA} \equiv 0$; (b) photoluminescence energy E_{PL} ; (c) bandgap E_G ; and (d) Stokes shift $W = (E_{PL} - E_{PA})/2$.

17.5 Bandwidth and Band Tails

17.5.1 Bandwidth: Charge Densification

The BOLS-TB premise indicates that both the crystal potential and the effective atomic CN determine the bandwidth that shrinks with reducing particle size:

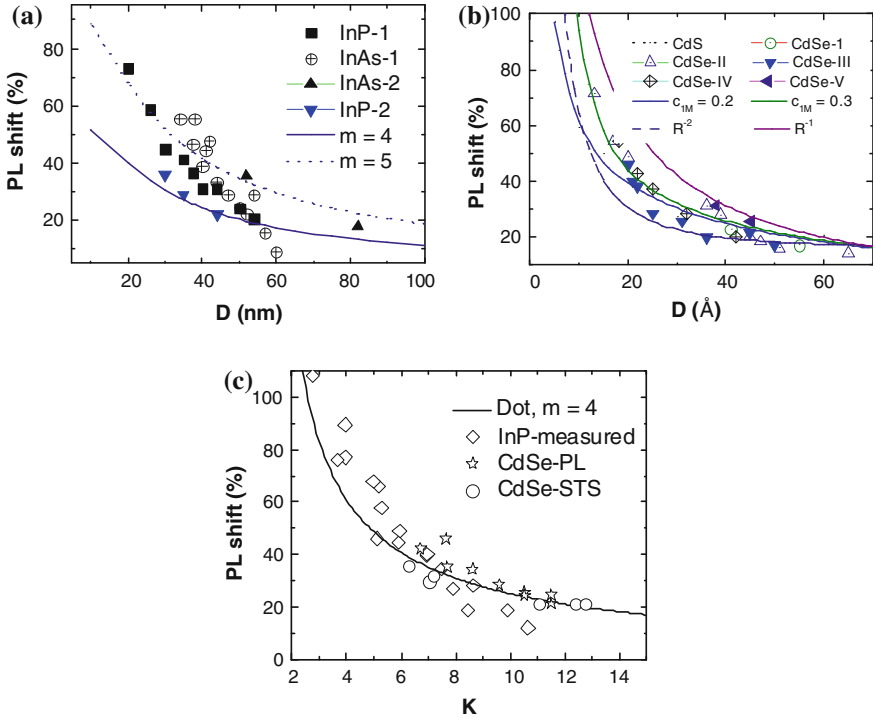


Fig. 17.7 Size-induced PL blueshift of **a** InAs [10], InP-01 [12, 76], **b** Zn-blende-I and wurtzite structure-II of CdS and CdSe [7], CdS-I [13], CdSe [71–75], and **c** InP [11, 76] and CdSe [80] nanostructures. The R^{-1} and R^{-2} curves diverge at the lower end of the size limit (reprinted with permission from [30])

$$\frac{\Delta E_B(K)}{E_B(\infty)} = \sum_{i \leq 3} \gamma_i \left(\frac{\Delta \alpha_i}{\alpha} + \frac{\Delta z}{z} \right) \tag{17.9}$$

$$E_B(K) = z \alpha \Omega(k_l, r, z)$$

$$\alpha = -\langle \phi_v(r) | V_{\text{cry}}(r) | \phi_v(r - R_C) \rangle$$

where α is the overlap integral (only a few percentile of the exchange integral), and $\Omega(x)$ is a $\sin^2(x)$ form function for the fcc structure for instance. CuO nanocrystals show this size trend of the bandwidth narrowing [88]. Particle size reduction increases the peak intensity but narrows the base of the peak (rather than the full width at half maximum that describes the distribution of the occupied DOS in the core band). If the z reduces to one or two, the bandwidth will degenerate into the single energy level of an isolated atom.

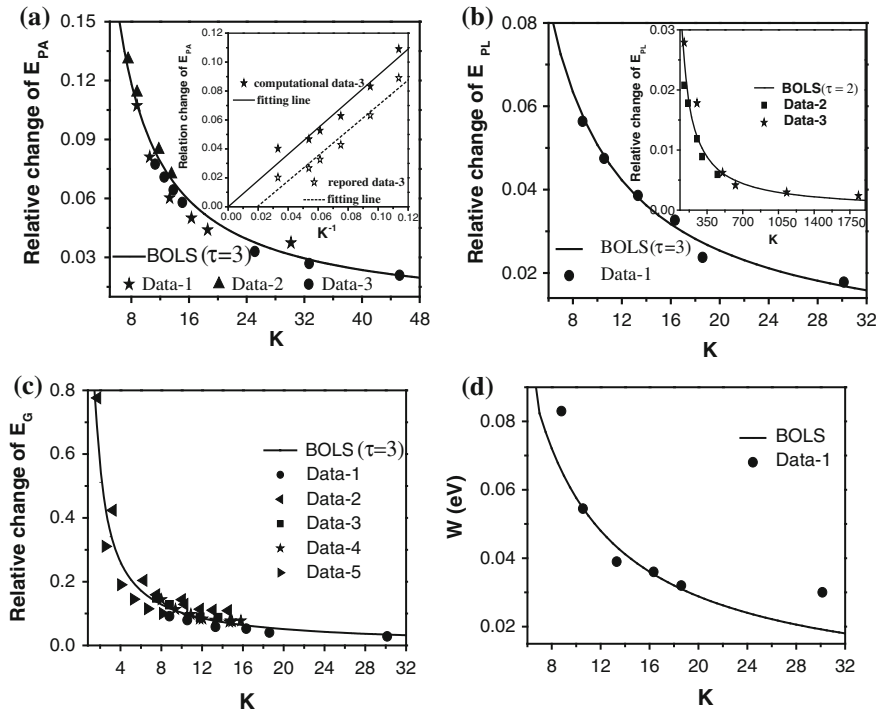


Fig. 17.8 BOLS reproduction of the measured size dependence of: **a** E_{PA} with Data 1–3 from Refs. [81–83]. Inset shows an offset to fit $\Delta E_{PA}/E_{PA} \equiv 0$. **b** E_{PL} with Data 1–3 from Refs. [81, 84, 85]. **c** E_G with Data 1–5 from Refs. [81, 82, 86, 87], and **d** Stokes shift $W = (E_{PL} - E_{PA})/2$ with data from Refs. [82] of ZnO [79] (reprinted with permission from [30])

17.5.2 Surface States and Band Tails

There are two kinds of surface states: entrapment and polarization. The dangling bonds or surface impurities are subject to polarization, which add impurity states within the E_G of semiconductors. Termination of the dangling bonds by H adsorption could minimize the impurity states. The other is the entrapment in the relaxed surface region, which offsets the entire band structure down associated with E_G enlargement and the presence of band tails.

The difference between an assembly of nanosolids and a bulk solid in amorphous state is the distribution of defects of the same nature. In the amorphous phase, the randomly distributed CN deficiency causes the bond length and angle of the specific atom to distort in a non-predictable way, which adds traps randomly in depth inside the bulk. In an amorphous solid, the number of the undercoordinated atoms is hardly controllable as the amorphous state depends heavily on the processing conditions. For a nanosolid or nanocrystallite, CN deficiency only happens

in an ordered way at the surface and the number of sites of CN deficiency is controllable by adjusting the shape and size of the nanosolids.

The CN deficiency in both amorphous and nanosolid states bends the energy near the conduction and the valence band edges with production of band tails occupied by the localized states. Resultant of the band tails gives the Urbach edge appearing in the photoabsorption spectra [47]. According to the BOLS premise, the Urbach edge of a nanosolid resulting from bond contraction due to the CN imperfection in the surface region, which is comparable to the random traps inside the amorphous bulk solid. The deepened potential traps near the surface edges are responsible for the localization of carriers in the band tails of nanosolids. Therefore, the CN-imperfection-enhanced interatomic interaction in the surface skin of a nanosolid should also produce such band tails that are identical to the band tails of an amorphous solid though the tail states originate from different sites in real space. Photoabsorption spectra of InAs [10], InP [11], and XPS spectra for Si:H nanosolids [67] demonstrate such Urbach edges.

17.6 E_G Expansion of GNRs

17.6.1 *Experimental and Numerical Inconsistency*

Armchair-edged or the reconstructed zigzag-edged graphene nanoribbons (GNRs), demonstrate semiconductor like with tunable bandgaps because of the alternative C–C distances along the edges [89]. Formation of the quasi- π bond between the nearest neighbors annihilates the impurity states in the mid- E_G [90]. The E_G of the AGNR expands with its inverse width [91–94]. Electron transport dynamics measurement [93] at temperatures below 200 K revealed that the E_G varies with the GNR width W in a way of: $E_G = 0.2/(W - 16 \text{ nm})$. When the GNR is narrower than 16 nm, the E_G increases abruptly to several eV and then approaches the values derived from DFT calculations [92, 95]. The E_G in the electrically gated bilayer graphene can be tunable up to 250 meV [96].

Figure 17.9 compares the DFT calculated [92] and the measured [93] width dependence of E_G expansion. Calculations suggested that the E_G of the AGNR expands from some 0.25 to 2.5 eV when the K is decreased from 20 to 1.5 with the feature of $3n$ periodicity. However, the conductance measurements revealed that the apparent E_G increases from several meV to 2.0 eV when the width of the GNR is decreased from $K = 40$ to $K = 5$. The measured data show neither the DFT-derived $3n$ oscillation nor the orientation dependence. This inconsistency indicates that mechanisms behind the measurements in real situations and calculations under ideal conditions are different.

Despite the magnitude difference between the measurements [93] and the theoretical calculations [92, 94, 98], the energetic origin for the width-dependent E_G expansion is under debate. The E_G expansion corresponds to carrier

confinement [92, 97, 99, 100], edge distortion [91], edge energy pinning [94, 100, 101], doping [102], defects forming [103], symmetry breaking [104], substrate interaction [105], and quantum confinement [106]. By introducing a hopping parameter t_1 for the nearest neighbor hopping integral to represent various chemical edge modifications, in the tight-binding calculations, Wang et al. [100] found that if the t_1 is identical to that in the ribbon interior, no significant E_G expansion occurs.

Therefore, the E_G expansion originates from the hopping integral t_1 at edges should be certainly greater than those in the GNR interior [99, 100]. A relaxation of the edge structure of AGNR is crucial to obtaining a non-metallic bandgap [107]. Conductance calculations suggested that edge disorder [108] in AGNRs could cause short localization lengths which could make expected semiconducting GNR devices insulating. One isolated edge defect could even induce localized states and consequently zero-conductance dips [109]. The edge and defect states are therefore critical to the performance of GNRs [91] inspite of the edge chemical passivation by boron [110], nitrogen [111], oxygen [112], or fluorine [113]. When the spin polarization is considered, both symmetric and asymmetric ZGNRs present semiconductor behavior, which is different from spin-unpolarized result showing metallic nature [114]. A combination of both radial and axial deformation can cause transition between semiconductor and conductor like [115]. Folding the graphene also modulates the bandgap and conductance [116]. These addends not only change the band structures of the AGNRs but also result in observable conductor-to-insulator transition.

It is unexpected that the BOLS, the DFT, and the experimentally measured results are inconsistent [95, 97]. Being able to resolve the size dependence of the thermal stability, mechanical strength, bandgap and core-level shift of numerous specimens including SWCNT, graphene, and graphite, the BOLS appears uncertain to reproduce the width trends of the E_G for GNRs. The inconsistency indicates however the impact of the nonbonding mid-gap states and the inhomogeneous stress caused by edge chemisorption, which can hardly be represented at the present in theoretical computations. The nonbonding states dominate the apparent E_G as one can measure transition of electrons from the mid-gap impurity states to the tail of the conduction band rather than from the valence to the conduction band directly [47]. From this perspective, experiments measure the true but not the intrinsic E_G . The measured trend of E_G expansion gives information about the change of the separation between the upper edge of nonbonding states and the conduction band tail, instead.

17.6.2 Impurity States

In fact, the E_G is determined intrinsically by the crystal potential the Hamiltonian matrix, while the density and energy of carriers in GNR play their roles in the transport dynamics. To verify the contribution of edge strain and quantum

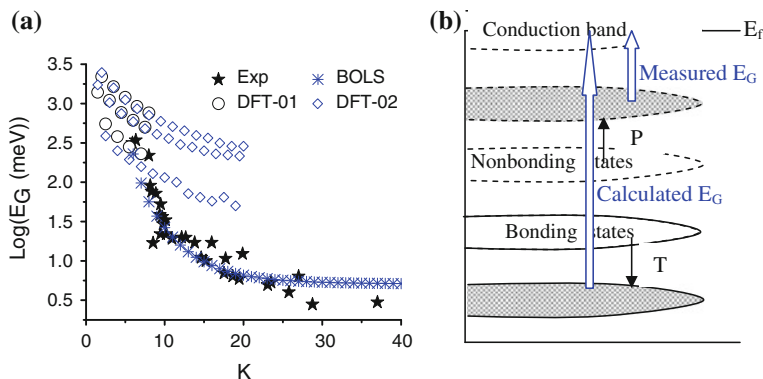


Fig. 17.9 a Discrepancy between the DFT calculated [92] and the conductance-measured [93] E_G expansion of GNRs. Numerical fit based on BOLS consideration can be realized by employing a width dependence of non-constant m values [95]. The DFT describes more intrinsic E_G under ideal conditions, while the experimental presents more on the apparent E_G mediated by the mid-gap impurity states (b) (reprinted with permission from [97])

entanglement to the bandgap expansion, Zhang et al. [97] performed DFT calculations on various carbon structures with different atomic CNs to gain the valence DOS and C–C bond lengths and the E_G expansion, see Fig. 17.9. However, DFT-derived extent of C–C bond contraction follows not well the BOLS expectation in particular at the lower CN values though the calculated E_G reproduces the results reported in ref [92]. As such, the calculated charge densification is lower than that the BOLS expected. By considering the unusual edge strain-and-trap boundary conditions, that is, a potential barrier followed immediately by the deep potential trap, quantum calculations may produce the BOLS expected results.

17.6.3 BOLS-TB: Edge Quantum Entrapment

Inspired by the BOLS, DFT, and experimental discrepancy, Zhang [97] developed an edge-modified BOLS-TB approach to examine the E_G expansion of the AGNR(II) and the rec-ZGNR(I), as illustrated in Fig. 17.10. An atomic vacancy is also shown at the $N = 11$ point. The t is the overlap integral between two adjacent atoms in the ribbon interior; t_1 and t_2 are the integrals at edges [97]. Table 17.1 lists the BOLS-derived strains and overlap integrals.

Figure 17.11 compares the band structure of an AGNR-11 obtained using (a) the conventional TB, (b) the BOLS-TB, with the strain and overlap integrals as given in Table 17.1, and (c) the DFT calculation results. A high DOS degeneracy at $E = \pm 2.7$ eV in (a) suggests that the system is unstable. This frustration can be avoided by using the modified BOLS-TB and DFT methods. Since there are 22 unpaired p_z electrons in the AGNR-11 unit cell, 22 double-degenerated bands will

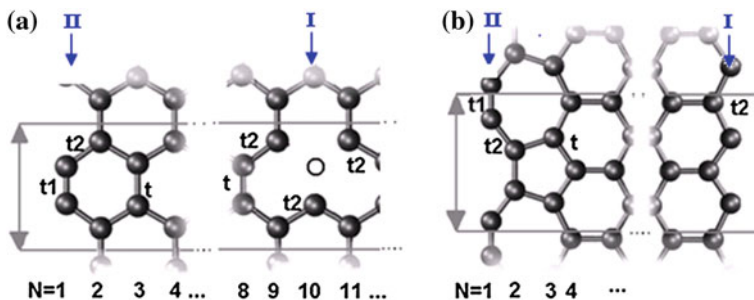


Fig. 17.10 Atomic structures of **a** the ZGNR (I) AGNR(II) and **b** the rec-ZGNR(II) edges of infinitely long ribbons with N represent the atomic positions. The t is the overlap integrals between two adjacent atoms in the ribbon interior; t_1 and t_2 are the integrals at edges. (reprinted with permission from [97])

Table 17.1 BOLS-TB parameters for calculating the E_G of AGNR and rec-ZGNR. The strain is set with respect to bond length of diamond according to the z -dependent contraction coefficient [97]

| Bond position | t_1 | t_2 | H-C edge | Interior | Graphite [117] | Diamond [117] |
|---------------|---------|---------|----------|-----------------------------|----------------|---------------|
| z | 2 | 2.5 | 2.125 | 3 | 5.335 | 12 |
| Strain (%) | -30.2 | -23.6 | -11.5 | -18.5 | -7.8 | 0 |
| Integral | $1.49t$ | $1.17t$ | $1.11t$ | $t = -$ 2.4 eV | | |

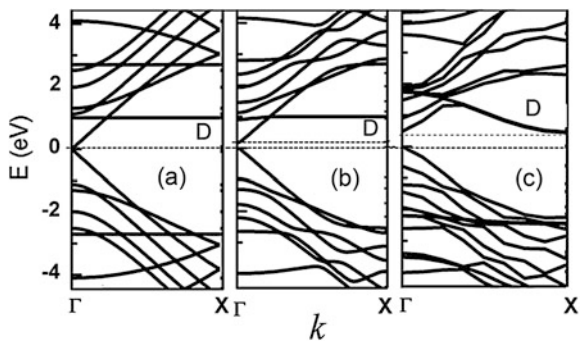


Fig. 17.11 Band structures of the AGNR-11 calculated using **a** the conventional TB, **b** the BOLS-TB, and **c** the DFT methods. The dangling bond electrons provide impurity states (*broken lines*) near the Fermi energy, indicated by D. An E_G is generated in **(b)** and **(c)**, and the dangling bond states do not affect the E_G in calculations (reprinted with permission from [97])

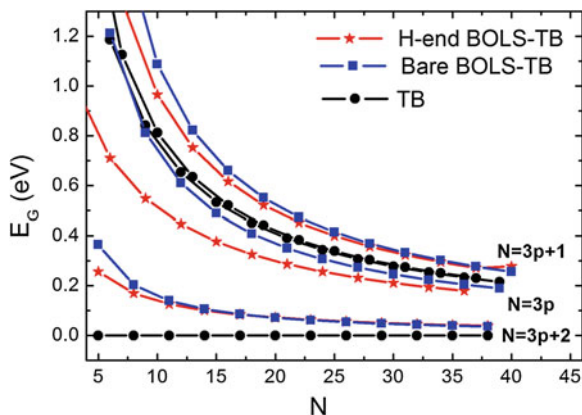


Fig. 17.12 Comparison of the width dependence of the E_G in bare and H -passivated AGNRs shows the absence of E_G expansion for the $N = 3p + 2$ in the conventional TB approach. The BOLS-TB results have the same trend to that of DFT [92], clarifying the origin of the width trends of E_G expansion. H -termination changes insignificantly the bandgap [47] (reprinted with permission from [97])

be present. The Fermi level lies at the middle of the E_G . The E_G opening can be observed in the BOLS-TB (b) and the DFT (c) derivatives. The dangling bond electrons provide impurity level closing to the Fermi energy, which has no significant effect on E_G [47, 118].

Figure 17.12 compares the E_G of both the bare and the H -adsorbed AGNRs as a function of the ribbon width N . The conventional TB results in the zero E_G when $N = 3p + 2$ (p is an integer); while the modified BOLS-TB results in the E_G opening, which is consistent with the reported DFT [92, 94] and experimental observations [93]. The edge hydrogenation does not affect the E_G generation or the E_G expansion trend significantly. Findings confirm further that the edge strain and quantum entrapment originate the E_G expansion of GNR with and without H -termination [100]. The effect of H -passivation on the width of the E_G is the same as the hydrogenation of amorphous silicon [47]. The hydrogenation of GNR edges annihilates the dangling bond states and hence minimizes the mid-gap impurity states without affecting the bandgap substantially. Likewise, calculations of the rec-ZGNR with and without H -passivation using these three methods derived the similar results. A very small E_G (~ 0.1 eV) is generated near the Γ point using the latter two methods [97].

17.6.4 Dispersion Linearization

As the GNRs C–C bond contracts by up to $C_{z=2} - 1 = 0.3$, the corresponding reciprocal lattice and the Brillouin zone edge will expand by $0.7^{-1}(\sim 1.4)$, the

bandwidth also expands by $0.7^{-2.56} = 2.52$. This reciprocal reconfiguration will stretch the dispersion relation $E_v(k)$ for the valence band and below with a certain extent of linearization [95]. The energy dispersion determined by the Hamiltonian determines the effective mass, $\hbar^2 [\nabla_k^2 E_v(k)]^{-1}$, and the group velocity, $\nabla_k E_v(k)/\hbar$, of bonding electrons. The stretching and linearization of the dispersion may result in a lowered group velocity, $\nabla_k E_v(k)$, and enlarged effective mass of bonding electrons instead because of the drop of $\nabla_k^2 E_v(k)$ with the linearization, which behave oppositely to the Dirac-Fermions. The smaller effective mass and the higher group velocity evidence that the Dirac-Fermi polarons located at the corner of the Brillouin zone of the GNRs, which neither follow the linear dispersion nor occupy the allowed states in the valence band and below, as one expected.

The BOLS-TB algorithm has enabled clarification of the energetic origin of the width dependence of the GNR E_G expansion. The shorter and stronger bonds between the undercoordinated edge atoms and the associated edge quantum entrapment, which perturb the Hamiltonian and initiate the E_G opening with the nonbonding states meditation. The dangling bond electrons form the quasi- π bond to remove the impurity states in the mid- E_G energy. DFT expectations and experimental observations are inconsistent because the involvement of the nonbonding states in experiment. H -passivation can remove the mid-gap non-bonding states while the passivation has no influence on the intrinsic bandgap. In the conductance measurements, however, the mid-gap states contribute to the real E_G . The bond contraction will stretch the Brillouin zone and linearize the energy dispersion curve, which lowers the group velocity and enlarges the effective mass of the bonding electrons, opposing to the trend that the nonbonding states demonstrate.

17.7 Summary

In terms of BOLS perturbation to the Hamiltonian of an extended solid, one is able to reconcile the change of E_G , E_{PL} , E_{PA} , bandwidth, core-level shift, and the charge entrapment and polarization induced by crystal size reduction. Introducing the effect of CN imperfection in the surface skin to the convention of an extended solid evolves the entire band structure of a nanometric semiconductor. This approach allows one to discriminate the contribution from crystal binding from the effect of e-p coupling in determining the E_G expansion and PL blueshift.

The presence of the edge nonbonding states in experiment and the absence in DFT calculation discriminate the discrepancy of E_G expansion in measurements and calculation. The edge bond contraction and quantum entrapment dictate the E_G creation and expansion of the AGNR and the rec-ZGNR ribbons.

In addition, the conventional band theories are valid for a nanosolid that contains numerous atoms in the form of multiple trapping centers in the energy box. The spontaneous contraction of the chemical bond at the surface is the origin of the

size dependency of a nanosolid as all the detectable quantities are functions of interatomic binding energy. Therefore, the CN-imperfection-induced bond contraction and the rise in the surface-to-volume ratio with reducing particle size changes the band features of nanometric semiconductors and the performance of electrons, phonons, and photons in the small particles.

References

1. A.P. Alivisatos, Semiconductor clusters, nanocrystals, and quantum dots. *Science* **271**(5251), 933–937 (1996)
2. D.D.D. Ma, C.S. Lee, F.C.K. Au, S.Y. Tong, S.T. Lee, Small-diameter silicon nanowire surfaces. *Science* **299**(5614), 1874–1877 (2003)
3. Y.D. Glinka, S.H. Lin, L.P. Hwang, Y.T. Chen, N.H. Tolk, Size effect in self-trapped exciton photoluminescence from SiO₂-based nanoscale materials. *Phys. Rev. B.* **64**(8), art. no.-085421 (2001)
4. S. Schuppler, S.L. Friedman, M.A. Marcus, D.L. Adler, Y.H. Xie, F.M. Ross, Y.J. Chabal, T.D. Harris, L.E. Brus, W.L. Brown, E.E. Chaban, P.F. Szajowski, S.B. Christman, P.H. Citrin, Size, shape, and composition of luminescent species in oxidized si nanocrystals and H-passivated porous Si. *Phys. Rev. B* **52**(7), 4910–4925 (1995)
5. L. Heikkila, T. Kuusela, H.P. Hedman, Electroluminescence in Si/SiO₂ layer structures. *J. Appl. Phys.* **89**(4), 2179–2184 (2001)
6. B. Garrido, M. Lopez, O. Gonzalez, A. Perez-Rodriguez, J.R. Morante, C. Bonafos, Correlation between structural and optical properties of Si nanocrystals embedded in SiO₂: The mechanism of visible light emission. *Appl. Phys. Lett.* **77**(20), 3143–3145 (2000)
7. A. Tomasulo, M.V. Ramakrishna, Quantum confinement effects in semiconductor clusters. *J. Chem. Phys.* **105**(9), 3612–3626 (1996)
8. S.C. Jain, M. Willander, J. Narayan, R. Van Overstraeten, III-nitrides: growth, characterization, and properties. *J. Appl. Phys.* **87**(3), 965–1006 (2000)
9. P. Ramvall, S. Tanaka, S. Nomura, P. Riblet, Y. Aoyagi, Observation of confinement-dependent exciton binding energy of GaN quantum dots. *Appl. Phys. Lett.* **73**(8), 1104–1106 (1998)
10. A.A. Guzelian, U. Banin, A.V. Kadavanich, X. Peng, A.P. Alivisatos, Colloidal chemical synthesis and characterization of InAs nanocrystal quantum dots. *Appl. Phys. Lett.* **69**(10), 1432–1434 (1996)
11. O.I. Micic, J. Sprague, Z.H. Lu, A.J. Nozik, Highly efficient band-edge emission from InP quantum dots. *Appl. Phys. Lett.* **68**(22), 3150–3152 (1996)
12. J.M. Ferreyra, C.R. Proetto, Quantum size effects on excitonic Coulomb and exchange energies in finite-barrier semiconductor quantum dots. *Phys. Rev. B* **60**(15), 10672–10675 (1999)
13. Y. Wang, N. Herron, Quantum size effects on the exciton energy of CdS clusters. *Phys. Rev. B* **42**(11), 7253–7255 (1990)
14. M.V.R. Krishna, R.A. Friesner, Exciton spectra of semiconductor clusters. *Phys. Rev. Lett.* **67**(5), 629–632 (1991)
15. P.E. Lippens, M. Lannoo, Comparison between calculated and experimental values of the lowest excited electronic state of small CdSe crystallites. *Phys. Rev. B* **41**(9), 6079–6081 (1990)
16. D.S. Chuu, C.M. Dai, Quantum size effects in CdS thin-films. *Phys. Rev. B* **45**(20), 11805–11810 (1992)
17. V. Albe, C. Jouanin, D. Bertho, Confinement and shape effects on the optical spectra of small CdSe nanocrystals. *Phys. Rev. B* **58**(8), 4713–4720 (1998)

18. M.G. Bawendi, W.L. Wilson, L. Rothberg, P.J. Carroll, T.M. Jedju, M.L. Steigerwald, L.E. Brus, Electronic-structure and photoexcited-carrier dynamics in nanometer-size CdSe clusters. *Phys. Rev. Lett.* **65**(13), 1623–1626 (1990)
19. S. Hayashi, H. Sanda, M. Agata, K. Yamamoto, Resonant Raman-scattering from ZnTe microcrystals—evidence for quantum size effects. *Phys. Rev. B* **40**(8), 5544–5548 (1989)
20. C. Gourgon, L.S. Dang, H. Mariette, C. Vieu, F. Muller, Optical-properties of CdTe/CdZnTe wires and dots fabricated by a final anodic-oxidation etching. *Appl. Phys. Lett.* **66**(13), 1635–1637 (1995)
21. M.F. Ng, R.Q. Zhang, Dimensionality dependence of optical properties and quantum confinement effects of hydrogenated silicon nanostructures. *J. Phys. Chem. B* **110**(43), 21528–21535 (2006)
22. L. Cao, P. Fan, E.S. Barnard, A.M. Brown, M.L. Brongersma, Tuning the color of silicon nanostructures. *Nano Lett.* **10**, 2649–2654 (2010)
23. C.Q. Sun, L.K. Pan, Y.Q. Fu, B.K. Tay, S. Li, Size dependence of the 2p-level shift of nanosolid silicon. *J. Phys. Chem. B* **107**(22), 5113–5115 (2003)
24. R. Tsu, D. Babic, L. Ioriatti, Simple model for the dielectric constant of nanoscale silicon particle. *J. Appl. Phys.* **82**(3), 1327–1329 (1997)
25. C.Q. Sun, X.W. Sun, B.K. Tay, S.P. Lau, H.T. Huang, S. Li, Dielectric suppression and its effect on photoabsorption of nanometric semiconductors. *J. Phys. D-Appl. Phys.* **34**(15), 2359–2362 (2001)
26. V. Petkov, C.M. Hessel, J. Ovtchinnikoff, A. Guillaussier, B.A. Korgel, X.F. Liu, C. Giordano, Structure-properties correlation in Si nanoparticles by total scattering and computer simulations. *Chem. Mater.* **25**(11), 2365–2371 (2013)
27. E. Roduner, Size matters: why nanomaterials are different. *Chem. Soc. Rev.* **35**(7), 583–592 (2006)
28. B. Wang, X.D. Xiao, X.X. Huang, P. Sheng, J.G. Hou, Single-electron tunneling study of two-dimensional gold clusters. *Appl. Phys. Lett.* **77**(8), 1179–1181 (2000)
29. B. Wang, K.D. Wang, W. Lu, J.L. Yang, J.G. Hou, Size-dependent tunneling differential conductance spectra of crystalline Pd nanoparticles. *Phys. Rev. B* **70**(20), 205411 (2004)
30. C.Q. Sun, Size dependence of nanostructures: impact of bond order deficiency. *Prog. Solid State Chem.* **35**(1), 1–159 (2007)
31. L.K. Pan, C.Q. Sun, Coordination imperfection enhanced electron-phonon interaction. *J. Appl. Phys.* **95**(7), 3819–3821 (2004)
32. L.K. Pan, Z. Sun, C.Q. Sun, Coordination imperfection enhanced electron-phonon interaction and band-gap expansion in Si and Ge nanocrystals. *Scripta Mater.* **60**(12), 1105–1108 (2009)
33. A.L. Efros, Interband absorption of light in a semiconductor sphere. *Sov. Phys. Semiconductors-USSR* **16**(7), 772–775 (1982)
34. A.I. Ekimov, A.A. Onushchenko, Quantum size effect in the optical-spectra of semiconductor micro-crystals. *Sov. Phys. Semiconductors-USSR* **16**(7), 775–778 (1982)
35. L.E. Brus, On the development of bulk optical-properties in small semiconductor crystallites. *J. Lumin.* **31**, 381–384 (1984)
36. Y. Kayanuma, Quantum-size effects of interacting electrons and holes in semiconductor microcrystals with spherical shape. *Phys. Rev. B* **38**(14), 9797–9805 (1998)
37. M.L. Steigerwald, L.E. Brus, Semiconductor crystallites—a class of large molecules. *Accounts Chem. Res.* **23**(6), 183–188 (1990)
38. L.W. Wang, A. Zunger, Dielectric-constants of silicon quantum dots. *Phys. Rev. Lett.* **73**(7), 1039–1042 (1994)
39. G.G. Qin, H.Z. Song, B.R. Zhang, J. Lin, J.Q. Duan, G.Q. Yao, Experimental evidence for luminescence from silicon oxide layers in oxidized porous silicon. *Phys. Rev. B* **54**(4), 2548–2555 (1996)
40. X.Y. Wang, L.H. Qu, J.Y. Zhang, X.G. Peng, M. Xiao, Surface-related emission in highly luminescent CdSe quantum dots. *Nano Lett.* **3**(8), 1103–1106 (2003)

41. E. Koch, V. Petrovakocho, T. Muschik, A. Nikolov, V. Gavrilenko, Some perspectives on the luminescence mechanism via surface-confined states of porous Si, in *Microcrystalline Semiconductors: Materials Science & Devices*, ed. by P.M. Fauchet, et al. (Materials Research Soc, Pittsburgh, 1993), pp. 197–202
42. C.N.R. Rao, G.U. Kulkarni, P.J. Thomas, P.P. Edwards, Size-dependent chemistry: properties of nanocrystals. *Chem. Eur. J.* **8**(1), 29–35 (2002)
43. H.N. Aiyer, V. Vijayakrishnan, G.N. Subbanna, C.N.R. Rao, Investigations of Pd clusters by the combined use of HREM, STM, high-energy spectroscopies and tunneling conductance measurements. *Surf. Sci.* **313**(3), 392–398 (1994)
44. C.Q. Sun, T.P. Chen, B.K. Tay, S. Li, H. Huang, Y.B. Zhang, L.K. Pan, S.P. Lau, X.W. Sun, An extended ‘quantum confinement’ theory: surface-coordination imperfection modifies the entire band structure of a nanosolid. *J. Phys. D-Appl. Phys.* **34**(24), 3470–3479 (2001)
45. M.A. Omar, *Elementary Solid State Physics: Principles and Applications* (Addison-Wesley, New York, 1993)
46. C.Q. Sun, H.Q. Gong, P. Hing, H.T. Ye, Behind the quantum confinement and surface passivation of nanoclusters. *Surf. Rev. Lett.* **6**(2), 171–176 (1999)
47. R.A. Street, *Hydrogenated Amorphous Silicon* (Cambridge University Press, Cambridge, 1991)
48. F.G. Shi, Size-dependent thermal vibrations and melting in nanocrystals. *J. Mater. Res.* **9**(5), 1307–1313 (1994)
49. Q. Jiang, Z. Zhang, J.C. Li, Superheating of nanocrystals embedded in matrix. *Chem. Phys. Lett.* **322**(6), 549–552 (2000)
50. G.D. Sanders, Y.C. Chang, Theory of optical-properties of quantum wires in porous silicon. *Phys. Rev. B* **45**(16), 9202–9213 (1992)
51. W. Theiss, in *Scout Thin Film Analysis Software Handbook, Hard and Software*, ed. by M. Theiss (Aachen, Germany) (www.mtheiss.com)
52. S. Furukawa, T. Miyasato, Quantum size effects on the optical band-gap of microcrystalline Si-H. *Phys. Rev. B* **38**(8), 5726–5729 (1988)
53. S. Guha, P. Steiner, W. Lang, Resonant Raman scattering and photoluminescence studies of porous silicon membranes. *J. Appl. Phys.* **79**(11), 8664–8668 (1996)
54. L.K. Pan, C.Q. Sun, B.K. Tay, T.P. Chen, S. Li, Photoluminescence of Si nanosolids near the lower end of the size limit. *J. Phys. Chem. B* **106**(45), 11725–11727 (2002)
55. S. Furukawa, T. Miyasato, Quantum size effects on the optical band-gap of microcrystalline Si-H. *Phys. Rev. B* **38**(8), 5726–5729 (1988)
56. Y. Kanemitsu, H. Uto, Y. Masumoto, T. Matsumoto, T. Futagi, H. Mimura, Microstructure and optical-properties of freestanding porous silicon films—size dependence of absorption-spectra in Si nanometer-sized crystallites. *Phys. Rev. B* **48**(4), 2827–2830 (1993)
57. J. von Behren, T. van Buuren, M. Zacharias, E.H. Chimowitz, P.M. Fauchet, Quantum confinement in nanoscale silicon: the correlation of size with bandgap and luminescence. *Solid State Commun.* **105**(5), 317–322 (1998)
58. L. Canham, *Properties of Porous Silicon: INSPEC1997*, London
59. X. Wang, D.M. Huang, L. Ye, M. Yang, P.H. Hao, H.X. Fu, X.Y. Hou, X.D. Xie, Pinning of photoluminescence peak positions for light-emitting porous silicon—an evidence of quantum-size effect. *Phys. Rev. Lett.* **71**(8), 1265–1267 (1993)
60. L. Dorigoni, O. Bisi, F. Bernardini, S. Ossicini, Electron states and luminescence transition in porous silicon. *Phys. Rev. B* **53**(8), 4557–4564 (1996)
61. M.S. Hybertsen, M. Needels, 1st-principles analysis of electronic states in silicon nanoscale quantum wires. *Phys. Rev. B* **48**(7), 4608–4611 (1993)
62. T. Ohno, K. Shiraishi, T. Ogawa, Intrinsic origin of visible-light emission from silicon quantum wires—electronic-structure and geometrically restricted exciton. *Phys. Rev. Lett.* **69**(16), 2400–2403 (1992)
63. C.Y. Yeh, S.B. Zhang, A. Zunger, Confinement, surface, and chemisorption effects on the optical-properties of Si quantum wires. *Phys. Rev. B* **50**(19), 14405–14415 (1994)

64. A.J. Read, R.J. Needs, K.J. Nash, L.T. Canham, P.D.J. Calcott, A. Qteish, 1st-principles calculations of the electronic-properties of silicon quantum wires. *Phys. Rev. Lett.* **69**(8), 1232–1235 (1992)
65. L. Pavesi, G. Giebel, F. Ziglio, G. Mariotto, F. Priolo, S.U. Campisano, C. Spinella, Nanocrystal size modifications in porous silicon by preanodization ion-implantation. *Appl. Phys. Lett.* **65**(17), 2182–2184 (1994)
66. I.H. Campbell, P.M. Fauchet, The effects of microcrystal size and shape on the one phonon Raman-spectra of crystalline semiconductors. *Solid State Commun.* **58**(10), 739–741 (1986)
67. T. van Buuren, L.N. Dinh, L.L. Chase, W.J. Siekhaus, L.J. Terminello, Changes in the electronic properties of Si nanocrystals as a function of particle size. *Phys. Rev. Lett.* **80**(17), 3803–3806 (1998)
68. A.D. Yoffe, Semiconductor quantum dots and related systems: electronic, optical, luminescence and related properties of low dimensional systems. *Adv. Phys.* **50**(1), 1–208 (2001)
69. S. Hasegawa, M. Matsuda, Y. Kurata, Bonding configuration and defects in amorphous SiNx-H films. *Appl. Phys. Lett.* **58**(7), 741–743 (1991)
70. M.L. Brongersma, A. Polman, K.S. Min, E. Boer, T. Tambo, H.A. Atwater, Tuning the emission wavelength of Si nanocrystals in SiO₂ by oxidation. *Appl. Phys. Lett.* **72**(20), 2577–2579 (1998)
71. M. Nogami, S. Suzuki, K. Nagasaka, Sol-gel processing of small-sized CdSe crystal-doped silica glasses. *J. Non-Cryst. Solids* **135**(2–3), 182–188 (1991)
72. M.G. Bawendi, P.J. Carroll, W.L. Wilson, L.E. Brus, Luminescence properties of CdSe quantum crystallites—resonance between interior and surface localized states. *J. Chem. Phys.* **96**(2), 946–954 (1992)
73. J.E.B. Katari, V.L. Colvin, A.P. Alivisatos, X-Ray photoelectron-spectroscopy of CdSe nanocrystals with applications to studies of the nanocrystal surface. *J. Phys. Chem.* **98**(15), 4109–4117 (1994)
74. W. Hoheisel, V.L. Colvin, C.S. Johnson, A.P. Alivisatos, Threshold for quasi-continuum absorption and reduced luminescence efficiency in CdSe nanocrystals. *J. Chem. Phys.* **101**(10), 8455–8460 (1994)
75. A.P. Alivisatos, T.D. Harris, L.E. Brus, A. Jayaraman, Resonance Raman-scattering and optical-absorption studies of CdSe microclusters at high-pressure. *J. Chem. Phys.* **89**(10), 5979–5982 (1988)
76. O.I. Micic, H.M. Cheong, H. Fu, A. Zunger, J.R. Sprague, A. Mascarenhas, A.J. Nozik, Size-dependent spectroscopy of InP quantum dots. *J. Phys. Chem. B* **101**(25), 4904–4912 (1997)
77. O.I. Micic, K.M. Jones, A. Cahill, A.J. Nozik, Optical, electronic, and structural properties of uncoupled and close-packed arrays of InP quantum dots. *J. Phys. Chem. B* **102**(49), 9791–9796 (1998)
78. S. Sapra, R. Viswanatha, D.D. Sarma, An accurate description of quantum size effects in InP nanocrystallites over a wide range of sizes. *J. Phys. D-Appl. Phys.* **36**(13), 1595–1598 (2003)
79. J.W. Li, S.Z. Ma, X.J. Liu, Z.F. Zhou, C.Q. Sun, ZnO meso-mechano-thermo physical chemistry. *Chem. Rev.* **112**(5), 2833–2852 (2012)
80. D. Katz, T. Wizansky, O. Millo, E. Rothenberg, T. Mokari, U. Banin, Size-dependent tunneling and optical spectroscopy of CdSe quantum rods. *Phys. Rev. Lett.* **89**(8), 086801 (2002)
81. R. Viswanatha, S. Sapra, B. Satpati, P.V. Satyam, B.N. Dev, D.D. Sarma, Understanding the quantum size effects in ZnO nanocrystals. *J. Mater. Chem.* **14**(4), 661–668 (2004)
82. K.F. Lin, H.M. Cheng, H.C. Hsu, L.J. Lin, W.F. Hsieh, Band gap variation of size-controlled ZnO quantum dots synthesized by sol-gel method. *Chem. Phys. Lett.* **409**(4–6), 208–211 (2005)
83. E.A. Meulenkaamp, Synthesis and growth of ZnO nanoparticles. *J. Phys. Chem. B* **102**(29), 5566–5572 (1998)

84. Y.H. Yang, X.Y. Chen, Y. Feng, G.W. Yang, Physical mechanism of blue-shift of UV luminescence of a single pencil-like ZnO nanowire. *Nano Lett.* **7**(12), 3879–3883 (2007)
85. H.L. Cao, X.F. Qian, Q. Gong, W.M. Du, X.D. Ma, Z.K. Zhu, Shape- and size- controlled synthesis of nanometre ZnO from a simple solution route at room temperature. *Nanotechnology* **17**(15), 3632 (2006)
86. J.B. Li, L.W. Wang, Band-structure-corrected local density approximation study of semiconductor quantum dots and wires. *Phys. Rev. B* **72**(12), 125325 (2005)
87. G.-C. Yi, C.R. Wang, W.I. Park, ZnO nanorods: synthesis, characterization and applications. *Semiconductor. Sci. Technol.* **20**(4), S22 (2005)
88. K. Borgohain, J.B. Singh, M.V.R. Rao, T. Shripathi, S. Mahamuni, Quantum size effects in CuO nanoparticles. *Phys. Rev. B* **61**(16), 11093–11096 (2000)
89. W.T. Zheng, C.Q. Sun, Underneath the fascinations of carbon nanotubes and graphene nanoribbons. *Energy Environ. Sci.* **4**(3), 627–655 (2011)
90. X. Zhang, Y.G. Nie, W.T. Zheng, J.L. Kuo, C.Q. Sun, Discriminative generation and hydrogen modulation of the Dirac-Fermi polarons at graphene edges and atomic vacancies. *Carbon* **49**(11), 3615–3621 (2011)
91. D. Gunlycke, C.T. White, Tight-binding energy dispersions of armchair-edge graphene nanostrips. *Phys. Rev. B* **77**, 115116 (2008)
92. Y.W. Son, M.L. Cohen, S.G. Louie, Energy gaps in graphene nanoribbons. *Phys. Rev. Lett.* **97**(21), 216803 (2006)
93. M.Y. Han, B. Ozyilmaz, Y.B. Zhang, P. Kim, Energy band-gap engineering of graphene nanoribbons. *Phys. Rev. Lett.* **98**, 206805 (2007)
94. S.S. Yu, Q.B. Wen, W.T. Zheng, Q. Jiang, Electronic properties of graphene nanoribbons with armchair-shaped edges. *Mol. Simul.* **34**(10–15), 1085–1090 (2008)
95. C.Q. Sun, S.Y. Fu, Y.G. Nie, Dominance of broken bonds and unpaired nonbonding pi-electrons in the band gap expansion and edge states generation in graphene nanoribbons. *J Chem Phys C* **112**(48), 18927–18934 (2008)
96. Y.B. Zhang, T.T. Tang, C. Girit, Z. Hao, M.C. Martin, A. Zettl, M.F. Crommie, Y.R. Shen, F. Wang, Direct observation of a widely tunable bandgap in bilayer graphene. *Nature* **459**(7248), 820–823 (2009)
97. X. Zhang, J.L. Kuo, M.X. Gu, P. Bai, C.Q. Sun, Graphene nanoribbon band-gap expansion: Broken-bond-induced edge strain and quantum entrapment. *Nanoscale* **2**(10), 2160–2163 (2010)
98. S. Reich, J. Maultzsch, C. Thomsen, P. Ordejo, Tight-binding description of graphene. *Phys. Rev. B* **66**(3), 035412 (2002)
99. L. Liu, Z. Shen, Bandgap engineering of graphene: a density functional theory study. *Appl. Phys. Lett.* **95**(25), 252103–252104 (2009)
100. Z.F. Wang, Q.X. Li, H.X. Zheng, H. Ren, H.B. Su, Q.W. Shi, J. Chen, Tuning the electronic structure of graphene nanoribbons through chemical edge modification: a theoretical study. *Phys. Rev. B* **75**, 113406 (2007)
101. F. Zheng, K.I. Sasaki, R. Saito, W. Duan, B.L. Gu, Edge states of zigzag boron nitride nanoribbons. *J. Phys. Soc. Jpn.* **78**(7), 074713 (2009)
102. I. Zanella, S. Guerini, S.B. Fagan, J. Mendes, A.G. Souza, Chemical doping-induced gap opening and spin polarization in graphene. *Phys. Rev. B* **77**, 073404 (2008)
103. E. Rotenberg, A. Bostwick, T. Ohta, J.L. McChesney, T. Seyller, K. Horn, Origin of the energy bandgap in epitaxial graphene. *Nat. Mater.* **7**(4), 258–259 (2008)
104. S.Y. Zhou, D.A. Siegel, A.V. Fedorov, F. El Gabaly, A.K. Schmid, A.H.C. Neto, D.H. Lee, A. Lanzara, Origin of the energy bandgap in epitaxial graphene—reply. *Nat. Mater.* **7**(4), 259–260 (2008)
105. S.Y. Zhou, G.H. Gweon, A.V. Fedorov, P.N. First, W.A. De Heer, D.H. Lee, F. Guinea, A.H.C. Neto, A. Lanzara, Substrate-induced bandgap opening in epitaxial graphene. *Nat. Mater.* **6**(10), 770–775 (2007)
106. T. Enoki, Y. Kobayashi, K.I. Fukui, Electronic structures of graphene edges and nanographene. *Int. Rev. Phys. Chem.* **26**(4), 609–645 (2007)

107. D. Finkenstadt, G. Pennington, M.J. Mehl, From graphene to graphite: a general tight-binding approach for nanoribbon carrier transport. *Phys. Rev. B* **76**(12), 121405 (2007)
108. D. Gunlycke, D.A. Areshkin, C.T. White, Semiconducting graphene nanostrips with edge disorder. *Appl. Phys. Lett.* **90**, 142104 (2007)
109. T.C. Li, S.P. Lu, Quantum conductance of graphene nanoribbons with edge defects. *Phys. Rev. B* **77**(8), 085408 (2008)
110. B. Zheng, P. Hermet, L. Henrard, Scanning tunneling microscopy simulations of nitrogen- and boron-doped graphene and single-walled carbon nanotubes. *ACS Nano* **4**(7), 4165–4173 (2010)
111. S.S. Yu, W.T. Zheng, Q.B. Wen, Q. Jiang, First principle calculations of the electronic properties of nitrogen-doped carbon nanoribbons with zigzag edges. *Carbon* **46**(3), 537–543 (2008)
112. S.S. Yu, W.T. Zheng, Q. Jiang, Oxidation of graphene nanoribbon by molecular oxygen. *IEEE Trans. Nanotechnol.* **7**(5), 628–635 (2008)
113. D. Gunlycke, J. Li, J.W. Mintmire, C.T. White, Edges bring new dimension to graphene nanoribbons. *Nano Lett.* **10**(9), 3638–3642 (2010)
114. Y. Ren, K.Q. Chen, Effects of symmetry and Stone-Wales defect on spin-dependent electronic transport in zigzag graphene nanoribbons. *J. Appl. Phys.* **107**(4), 044514 (2010)
115. Y. Ren, K.Q. Chen, Q. Wan, B.S. Zou, Y. Zhang, Transitions between semiconductor and metal induced by mixed deformation in carbon nanotube devices. *Appl. Phys. Lett.* **94**(18), 183506 (2009)
116. Y.E. Xie, Y.P. Chen, J.X. Zhong, Electron transport of folded graphene nanoribbons. *J. Appl. Phys.* **106**(10), 103714 (2009)
117. C.Q. Sun, Y. Sun, Y.G. Nie, Y. Wang, J.S. Pan, G. Ouyang, L.K. Pan, Z. Sun, Coordination-resolved C–C bond length and the C 1s binding energy of carbon allotropes and the effective atomic coordination of the few-layer graphene. *J. Chem. Phys. C* **113**(37), 16464–16467 (2009)
118. V. Barone, O. Hod, G.E. Scuseria, Electronic structure and stability of semiconducting graphene nanoribbons. *Nano Lett.* **6**(12), 2748–2754 (2006)

Chapter 18

Dielectric Suppression: Electron Polarization

- *Complex dielectric constant relates to transition of electrons from the valence band to the conduction band.*
- *Skin-resolved bond contraction, interatomic interaction, and electron-phonon coupling determine the change in the dielectric constant.*
- *Dielectric constant changes roughly with the square inverse of the bandgap.*
- *Dielectric constant drops with solid size or porosity enhancement.*
- *Lowered refractive index and absorption coefficient in skin up to three atomic layers may find application for waveguides, cavity lasing, and high reflectivity in optical devices.*

18.1 Background

The complex dielectric constant, $\epsilon_r(\omega) = \text{Re}[\epsilon_r(\infty)] + i\text{Im}[\epsilon_r'(\omega)]$, is a direct measure of electron polarization response to external electric field, which has enormous impact on the electrical and optical performance of a solid and related devices. For example, low $\epsilon_r(\infty)$ media are required for the replacement of Al with Cu in microelectronic circuitry to prevent the ‘cross-talk’ between connections; however, media of higher $\epsilon_r(\infty)$ are required for the miniaturized conductor-metal-oxide-semiconductor gate devices. Miniaturizing a semiconductor solid to the nanometer scale often lowers the $\epsilon_r(\text{K})$ [1, 2]. The $\epsilon_r(\text{K})$ reduction enhances the Coulomb interaction between charged particles such as electrons, holes, and ionized shallow impurities in nanometric devices, leading to abnormal responses. The increase in exciton activation energy in nanosemiconductors due to $\epsilon_r(\text{K})$ reduction would significantly influence optical absorption and transport properties of the devices. Both the AC conductivity and dielectric susceptibility of amorphous Se films drop with thickness in the range of 15–850 [3]. The complex dielectric constant decreases with increasing the frequency or lowering the temperature of operation.

Carrier motion could be the dominant mechanism in both ac polarization and dc conduction. A thermodynamic analysis [4] suggests a drastic variation in the polarization near the dislocation due to the coupling of the stress field of the dislocation and the polarization. These polarization gradients result in strong depolarizing fields that suppress the polarization in a region that extends over several nanometers. In epitaxial ferroelectric films, these polarization gradients should result in the formation of dead layers that severely degrade ferroelectric properties. The detrimental effect of such regions will be enhanced in ultrathin ferroelectric thin films and hence play a critical extrinsic role in the size effect studies of ferroelectrics. A progressive reduction in tetragonal distortion, heat of transition, Curie temperature, and relative dielectric constant has been observed on the dense BaTiO₃ ceramics with grain size decreasing from 1200 to 50 nm [5]. The critical size for ferroelectricity disappearance is in the range of 10–30 nm. The combination of the intrinsic size effect and of the size-dependent ‘dilution’ effect of a grain boundary ‘dead’ layer depresses strongly the relative permittivity of nanocrystalline ceramics.

The relative changes in the dielectric susceptibility, $\chi = \epsilon_r - 1$, is modeled as follows:

$$\Delta\chi(K)/\chi(\infty) = \begin{cases} -\left[1 + (K/\alpha)^\lambda\right]^{-1} & \text{(Penn)} \\ \frac{-2\Delta E_G(K)}{E_G(\infty)} & \text{(Tsu)} \\ \frac{-2}{1-(E/E_G(\infty))^2} \left(\frac{\Delta E_G(K)}{E_G(\infty)}\right) & \text{(Chen)} \end{cases}$$

where α and λ in the Penn’s empirical model [6] are freely adjustable parameters that vary from situation to situation as listed in Table 18.1. Tsu and Babic [7] related the susceptibility change directly to the offset of $E_G(K)$. Considering the contribution from incident photon energy, $E = \hbar\omega$, Chen et al. [8, 9] modified Tsu’s model and studied the dielectric response of nanosolid Si embedded in a SiO₂ matrix using ellipsometry. They suggested that the dielectric suppression varies with the photon beam energy that should be lower than the intrinsic $E_G(\infty)$ of Si. Delerue et al. [10] deposited PbSe nanocrystals of several nanometers in height on an Au(111) substrate and measured the thickness-dependent dielectric function. Compared with electronic structure calculations of the imaginary part of the dielectric function of PbSe nanocrystals, they suggested that quantum confinement at well-identifiable points in the Brillouin zone, instead of the bandgap transition, determines the size-dependent variation of the dielectric function.

The size-induced decrease in the average dielectric response is also suggested to be mainly due to the breaking of the polarizable bonds at the surface [11] rather than the E_G expansion or quantum confinement. First-principle calculations suggested that the dielectric response is bulk like inside the nanocrystal, and the reduction in the macroscopic dielectric constants is surface dominance [12]. This finding indicates that the nanocrystal are more ‘superficial’ than first thought in terms of quantum confinement [13]. A theoretical study [14] of the third-order susceptibility for an Ag dielectric composite suggests the saturation of optical

Table 18.1 Simulation results in Penn's model

| | ϵ_r (bulk) | α/nm | λ |
|--------------|---------------------|--------------------|-----------|
| CdSe [16] | 6.2 | 0.75 | 1.2 |
| Si-a [7, 17] | 11.4 | 2.2 | 2 |
| Si-b [18] | 11.4 | 1.84 | 1.18 |
| Si-c [18] | 10.38 | 0.85 | 1.25 |
| Si-d [18] | 9.5 | 0.69 | 1.37 |

transitions between discrete states of conduction electrons in metal dots. Saturation effects lead to a decrease in the local field enhancement factor that is of particular importance for surface-enhanced phenomena, such as Raman scattering and nonlinear optical responses.

The modified models [7, 8] suit only the cases where $\Delta E_G(K)/E_G(\infty) < 0.5$, otherwise, $\chi < 0$, which is physically forbidden. Generally, the E_G often expands beyond this critical value such as the case of Si nanorods with $E_G = 3.5$ eV [15]. Therefore, understanding of dielectric suppression of nanosolid semiconductors is still under debate. Furthermore, the size dependence of the imaginary part of the dielectric constant and of the photoabsorption coefficient needs yet to be established. Therefore, deeper and consistent insight into the origin and a clearer and complete expression for the size dependence of the complex dielectric constant of a nanosolid semiconductor is necessary.

18.2 BOLS Formulation

18.2.1 Electron Polarization

Electronic polarization through a process of transition from the lower ground states (valence band, or the mid-gap impurity states) to the upper excited states in the conduction band takes the responsibility for complex dielectrics. This process is subject to the selection rule of energy and momentum conservation, which determines the optical response of semiconductors and reflects how strongly the electrons in ground states are coupling with the excited states that shift with lattice phonon frequencies [19]. Therefore, the ϵ_r of a semiconductor is directly related to its bandgap E_G at zero temperature, as no lattice vibration occurs at 0 K.

Since the involvement of electron-phonon coupling, electron excitation from the ground states to the excited upper states is complicated, as illustrated in Fig. 17.4. The energy for photon absorption, or energy difference between the upper excited state $E_2(q)$ and the lower ground state $E_1(q)$, at q is as follows:

$$\begin{aligned}
 \hbar\omega &= E_2(q) - E_1(q) \\
 &= E_G - Aq_0^2 + 2Aqq_0 \\
 &= E_{\text{PL}} + 2Aqq_0.
 \end{aligned}
 \tag{18.1}$$

The imaginary part, $\varepsilon_r'(\omega)$, describes the electromagnetic wave absorption and is responsible for the energy loss of incident irradiation through the mechanism of electron polarization. The $\varepsilon_r'(\omega)$ can be obtained by inserting the gradient of Eq. (18.1) into the relation [20, 21],

$$\begin{aligned}\varepsilon_r'(\omega) &= \frac{F}{\omega^2} \int ds \frac{f_{CV}}{|\nabla[E_C(q) - E_V(q)]|} \\ &= \frac{\pi F f_{CV}}{A \omega^2} q \\ &= \frac{\pi F f_{CV}}{2A^2} \frac{\hbar\omega - E_{PL}}{q_0 \omega^2} \propto \frac{\hbar\omega - E_{PL}}{q_0 \omega^2},\end{aligned}$$

where the gradient and the elemental area for integral are derived as follows [22]:

$$\begin{aligned}\nabla[E_C(q) - E_V(q)] &= 2Aq_0 \\ ds &= 2\pi q_0 dq\end{aligned}\tag{18.2}$$

The s is the area difference of the two curved surfaces in q space of the upper excited band and the lower ground band. F is a constant. f_{CV} , the probability of intersub-band (Kubo gap) transition, is size dependent. However, the size-induced change in transition probability between the sublevels is negligibly small, and for the first-order approximation, f_{CV} is taken as a constant.

18.2.2 Complex Dielectrics

18.2.2.1 Dielectric susceptibility

The Kramers–Kronig relation correlates the real part to the imaginary part of the complex dielectric function by [23],

$$\begin{aligned}\varepsilon_r(\infty) - 1 = \chi &= \frac{2}{\pi} \int_{\omega_0}^{\infty} \frac{\varepsilon_r'(\omega)}{\omega} d\omega \quad \left(\omega_0 = \frac{E_{PL}}{\hbar} \right) \\ &= \frac{F f_{CV}}{A^2 q_0} \int_{\omega_0}^{\infty} \frac{\hbar\omega - E_{PL}}{\omega^3} d\omega \\ &= \frac{G}{q_0 E_{PL}}, \quad \left(G = \frac{\hbar^2 F f_{CV}}{2A^2} \right)\end{aligned}\tag{18.3}$$

where $\hbar\omega - E_{PL} = 2Aq_0$ as given in Eq. (18.1). Hence, the size-suppressed dielectric susceptibility depends functionally on the characteristics of e–p interaction and the PL energy. Using the relation of $\Delta E_{PL}(K)/E_{PL}(\infty) = \Delta_H - B\Delta_{e-p}$ (Chap. 17), the size-induced relative change in both the χ and the $\varepsilon_r'(\omega)$ follows:

$$\begin{aligned}
\frac{\Delta\chi(K)}{\chi(\infty)} &= -\frac{\Delta E_{\text{PL}}(K)}{E_{\text{PL}}(\infty)} - \frac{\Delta q_0(K)}{q(\infty)} \\
&= -\frac{\Delta E_{\text{PL}}(K)}{E_{\text{PL}}(\infty)} + \frac{\Delta d_i(K)}{d_0} \\
&= -(\Delta_H - B\Delta_{e-p}) + \Delta_d, \tag{18.4} \\
\frac{\Delta\epsilon'_r(K, \omega)}{\epsilon'_r(\infty)} &= \frac{-E_{\text{PL}}(\infty)}{\hbar\omega - E_{\text{PL}}(\infty)} \frac{\Delta E_{\text{PL}}(K)}{E_{\text{PL}}(\infty)} + \frac{\Delta d_i(K)}{d_0} \\
&= \frac{-E_{\text{PL}}(\infty)}{\hbar\omega - E_{\text{PL}}(\infty)} (\Delta_H - B\Delta_{e-p}) + \Delta_d
\end{aligned}$$

where B is the e-p coupling coefficient. Δ_H and Δ_{e-p} represent the contribution from the CN-imperfection-perturbed Hamiltonian and the e-p coupling in the relaxed surface skin. The last term is the bond length change ($q \propto d^{-1}$). They are given as follows [24]:

$$\begin{cases}
\Delta_H &= \sum_{i \leq 3} \gamma_i (C_i^{-m} - 1), & (\text{Hamiltonian-perturbation}) \\
\Delta_{e-p} &= \sum_{i \leq 3} \gamma_i (C_i^{-2} - 1), & (e-p\text{-coupling}) \\
\Delta_d &= \sum_{i \leq 3} \gamma_i (C_i - 1), & (\text{bond-contraction})
\end{cases} \tag{18.5}$$

For a spherical silicon dot, $B = 0.91$, $m = 4.88$, $z_2 = 6$, and $z_3 = 12$. Compared with the relations given in (18.4), the complex dielectric performance of a nanosolid semiconductor depends functionally on crystal binding energy and e-p coupling strength. The imaginary dielectric constant depends also functionally on the photon energy. Both components drop with solid size, which follow the BOLS correlation.

18.2.2.2 Direct and indirect band transition

For direct and indirect bandgap optical transition, the $\epsilon'_r(\omega)$ can be traditionally simplified as [25, 26]

$$\begin{aligned}
\epsilon'_r(\omega) &= \begin{cases} \frac{B'}{\omega^2} (\hbar\omega - E_G)^{1/2} & (\text{direct} - E_G) \\ A'(T) (\hbar\omega - E_G)^2 & (\text{indirect} - E_G) \end{cases} \tag{18.6} \\
B' &= \pi (2\mu/\hbar^2)^{\frac{3}{2}} f_{\text{cv}} A. \\
&\quad (\hbar\omega > E_G),
\end{aligned}$$

where $A'(T)$ containing parameters for band structure and temperature describes the momentum contribution of phonons to the indirect E_G transition. The probability of interband transition, f_{cv} and $A'(T)$, should also vary with the particle size. It would be reasonable to assume that the size-induced transition probability change is negligibly small despite the availability of the exact correlation of the transition probability to the Kubo gaps.

Compared with Eq. (18.4), the traditional form of size-dependent $\epsilon_r'(\omega)$ varies with the E_G and the incident beam energy:

$$\frac{\Delta[\epsilon_r'(K, \omega)]}{\epsilon_r'(\infty, \omega)} = \frac{\alpha' E_G(\infty)}{E_G(\infty) - \hbar\omega} \left(\frac{\Delta E_G(K)}{E_G(\infty)} \right) = \frac{\alpha' E_G(\infty)}{E_G(\infty) - \hbar\omega} \Delta_H \quad (18.7)$$

where $\alpha' = 1/2$ and 2 correspond to direct and indirect E_G transition, respectively. The traditional form of dielectric constant at a certain optical energy, $\hbar\omega > E_G(\infty)$, decreases with E_G expansion, Δ_H , without involvement of bond contraction and e-p interaction.

18.2.2.3 Photon absorption

The absorption coefficient, α , the refractive index, $n (= \sqrt{\epsilon_r})$, and the complex dielectric function are correlated as follows: $\alpha(\omega) = 2\pi\epsilon_r'(\omega)/n\lambda$, and the transmittance of light is given as $T \propto \exp(-\alpha x)$, where x is the thickness of the medium for light transmission. This relation leads to the size-induced change of α as

$$\begin{aligned} \frac{\Delta\alpha(K, \omega)}{\alpha(\infty, \omega)} &= \frac{\Delta\epsilon_r'(K, \omega)}{\epsilon_r'(\infty, \omega)} - \frac{\Delta\epsilon_r(K)}{2\epsilon_r(\infty)} \\ &= - \left[\frac{\chi(\infty)}{\chi(\infty)+1} + \frac{\alpha' E_G(\infty)}{\hbar\omega - E_G(\infty)} \right] \Delta_H \quad (\text{convention}) \\ \text{or} &= \left[\frac{\chi(\infty)}{2[\chi(\infty)+1]} - \frac{E_{PL}(\infty)}{\hbar\omega - E_{PL}(\infty)} \right] \times (\Delta_H - B\Delta_{e-p}) + \frac{\chi(\infty)+2}{2[\chi(\infty)+1]} \times \Delta_d \quad (\text{BOLS}) \end{aligned} \quad (18.8)$$

The traditional form $[\Delta\chi(K)/\chi(\infty) = -2\Delta_H]$ discriminates the direct and indirect E_G transition by the α' , while the BOLS form $[\Delta\chi(K)/\chi(\infty) = \Delta_d - (\Delta_H - B\Delta_{e-p})]$ counts the contribution from e-p coupling, lattice relaxation, and crystal binding.

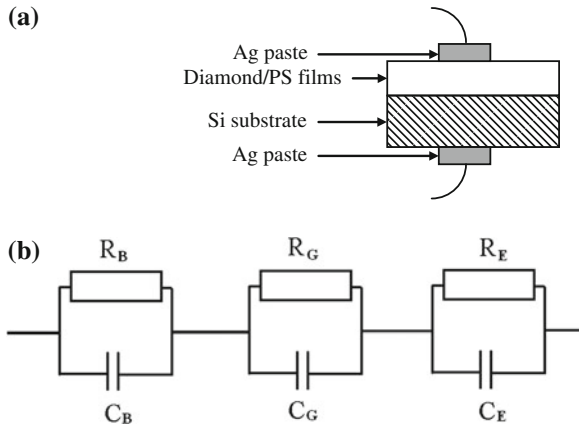
18.3 Numerical Verification

18.3.1 Dielectric Suppression

It is possible to discriminate the dielectric contribution of the nanosolid Si backbone from the measured effective ϵ_{eff} of p-Si by matching the prediction with the measured impedance spectra. P-Si samples were prepared, and their impedance was measured at ambient temperature in the frequency range of 50 Hz–1.0 MHz under 100 mV potential. Silver paste is generally used for an ohmic contact.

The impedance behavior can be described by Debye's formula for a serial-parallel resistor-capacitor (RC) circuit [27] with elements that correspond to the dielectric behavior of different components. The high-temperature impedance behavior can be described by a series of triple parallel RC circuit elements [27]

Fig. 18.1 **a** RC circuit and **b** representations for the impedance measurement of a sample containing several components



that correspond to the dielectric behavior of grain interior, grain boundary, and electrode/film interface, respectively, as shown in Fig. 18.1. The complex impedance response commonly exhibits semicircular forms in the measured Cole–Cole plot [28] as shown in Fig. 18.2. At higher temperatures, two or more semicircles present corresponding different transition mechanisms [29]. The grain boundary resistance is normally higher than the grain interior, and the electrode/film interface resistance is higher than that of the boundary. The larger radius of the Cole–Cole plot in frequency space corresponds to contribution from a constituent of lower resistance. Therefore, the first semicircle in the high-frequency region corresponds to the behavior of grain interior, while the intermediate and tertiary semicircles in the lower-frequency region correspond to the grain boundary and the electrode/film interface, respectively.

The complex impedance Z^* measured by RCL meter can be expressed as [30]

$$\begin{cases} Z^* = Z' - jZ'' \\ Z' = \sum_l \frac{R_l}{1 + \omega^2 R_l^2 C_l^2}; \quad Z'' = \sum_l \frac{\omega R_l^2 C_l}{1 + \omega^2 R_l^2 C_l^2} \end{cases} \quad (18.9)$$

where ω is the angular frequency. The resistance R_l represents ionic or electronic conduction mechanisms, while the capacitance C_l represents the polarizability of the sample from different components labeled l , which are related to grain interior, grain boundary, and electrode or interface [22]. Curves A–E in Fig. 18.2 denote the responses of different samples (Table 18.2) measured at the ambient temperature. The complex impedance plots show only one depressed single semicircular arc, indicating that only one primary mechanism, corresponding to the bulk grain behavior, dominates the polarization and easy path for conductance within the specimen. The second intercept on the lateral real axis made by the semicircle corresponds to the resistance in the bulk grain. As it is seen, the intercept of the semicircles shifts away from the origin as the solid size decreases, indicating an increase in the nanograin resistance, due to the lowering of the atomic potential well that traps the electrons in the surface region.

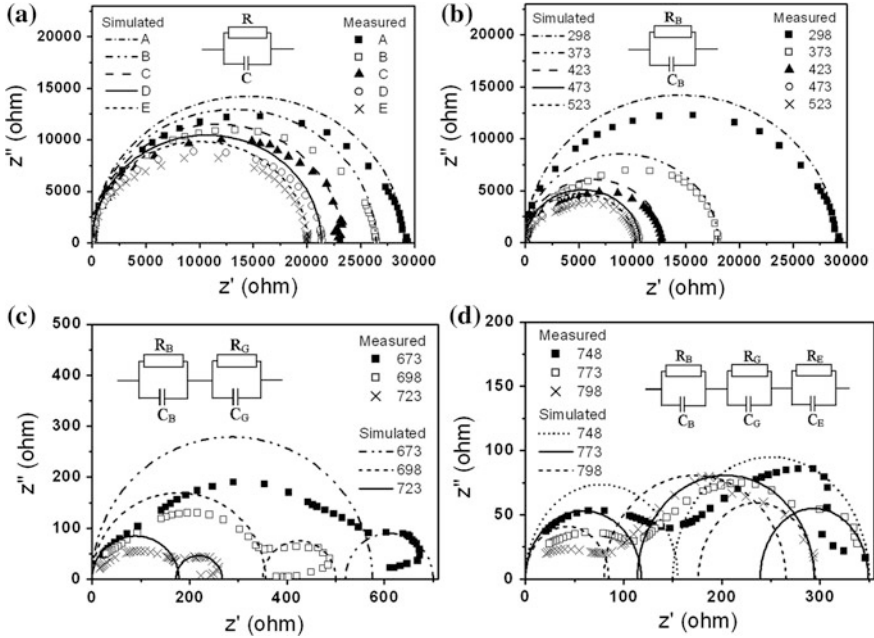


Fig. 18.2 Simulated and measured **a** size (see Table 18.2) and **b-d** temperature (annotated) dependence of Cole–Cole plots of p–Si and the RC parallel circuit model (inset) for typical dielectric materials (Reprinted with permission from [22])

The capacitance and dielectric constant are extracted by using the relation: $Z'' = 1/(\omega C)$ from the data measured in the high-frequency range of 10^5 – 10^6 Hz [31]. The bulk grain capacitance C of the sample is given by the slope of the straight line determined by the variation in Z'' as a function of $1/\omega$. Then, the effective dielectric constant ϵ_{eff} of the porous structure is calculated based on the equation: $\epsilon_{\text{eff}} = Cx/(\epsilon_0 S)$. With the measured ϵ_{eff} , we can calculate the $\epsilon_{\text{nano-Si}}$ based on the Looyenga approximation [32]:

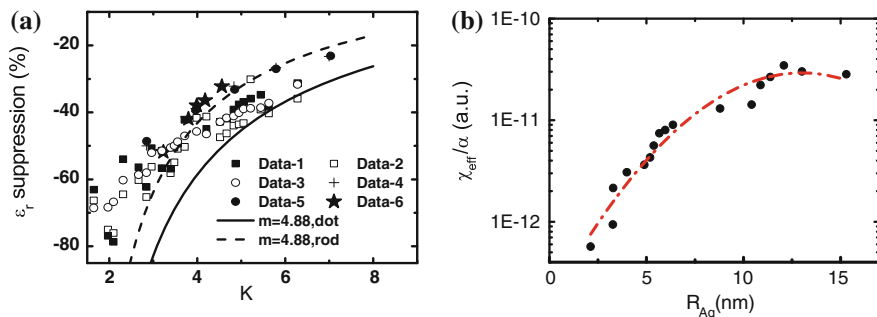
$$\epsilon_{\text{eff}}^{1/3} = (1 - p)\epsilon_{\text{nano-Si}}^{1/3} + p\epsilon_{\text{air}}^{1/3},$$

where $\epsilon_{\text{air}} (\approx 1)$ is the dielectric constant of air, and p is the porosity of the p–Si. Results in Table 18.2 show that the $\epsilon_{\text{nano-Si}}$ decreases with solid size.

Figure 18.3 compares the $\epsilon_{\text{nano-Si}}$ derived herein and other sophisticated calculations of nanosolid Si and the third-order dielectric susceptibility of Ag nanodots. Although the dielectric susceptibility does not follow the BOLS prediction, it shows the suppressed trend. Consistency in trends between BOLS predictions and the measured results evidences that the BOLS correlation describes adequately the true situation in which atomic CN imperfection dictates the $\epsilon_{\text{nano-Si}}$ suppression. Other factors may contribute to dielectric suppression, which makes the prediction deviate from measurement compared with other

Table 18.2 Summary of the D-dependent $\epsilon_{\text{nano-Si}}$ derived from the measured E_{PL} , porosity, and ϵ_{eff} , p-Si

| Sample | D (nm) | E_{PL} (eV) | Porosity (%) | ϵ_{eff} | $\epsilon_{\text{nano-Si}}$ |
|--------|----------|----------------------|--------------|-------------------------|-----------------------------|
| A | 1.7 | 2.08 | 85 | 1.43 | 6.27 |
| B | 2.0 | 1.82 | 76 | 1.84 | 7.29 |
| C | 2.1 | 1.81 | 71 | 2.11 | 7.7 |
| D | 2.2 | 1.79 | 68 | 2.28 | 7.86 |
| E | 2.4 | 1.76 | 66 | 2.45 | 8.29 |

**Fig. 18.3** Comparison of the BOLS predictions with the sophisticated calculation and measurement results on the size-dependent dielectric constants of (a) silicon nanosolids with calculated Data—1, 2, 3 [18]; Data—4 and 5[1] and Data—6 [22]; and (b) the third-order dielectric susceptibility of Ag nanosolid [14]. Note that a logarithmic y-axis has been used in b for clarity (Reprinted with permission from [33])

simulations reported in previous sections. The apparent factors are the accuracy and uniformity of the shape and size of porous Si and the porosity. Atomic CN at a negatively curved surface of a pore is higher than that at the positively curved surface of a dot. As the numerical solution sums the contribution from crystal binding (E_G expansion), electron-phonon coupling, and bond contraction, errors accumulate from the three aspects, contributing to the observed deviation. However, from a physical and chemical insight point of view, the first (main)-order approximation would be acceptable as other artifacts from measurement or from impurities are hardly controllable.

18.3.2 Blueshift of Photoabsorption Coefficient

Equation (18.8) describes the size dependence of the coefficient of photon absorption. For Si, $\chi(\infty) = 10.4$ and $E_{\text{PL}}(\infty) \sim E_G(\infty) = 1.12$ eV. It is surprising that, as shown in Fig. 18.4, a blueshift of the absorption edge takes place for the nano-Si. The threshold of absorption for the indirect bandgap is slightly

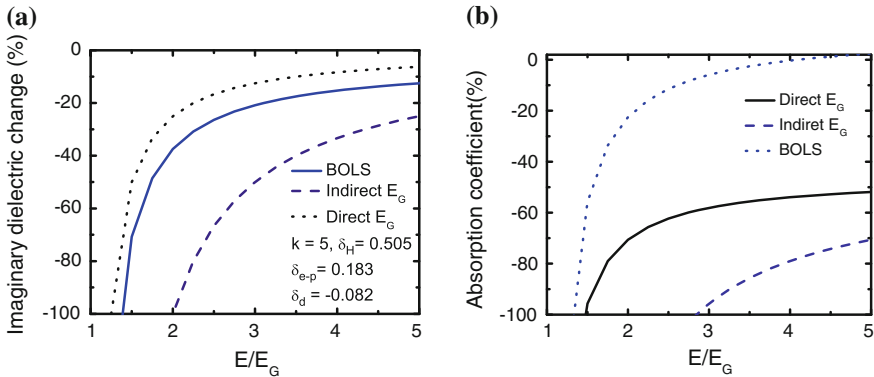


Fig. 18.4 Energy dependence of **a** imaginary dielectrics and **b** photoabsorption coefficient in conventional and BOLS approaches. Spherical size $K = 5$ is used corresponding to $\Delta_H = 0.506$, $\Delta_{e-p} = 0.182$, and $\Delta_d = -0.083$ (Reprinted with permission from [33])

higher than that of the direct bandgap materials. Such a blueshift of absorption edges should be advantageous in designing devices for optical communication of nanometer-scaled wires, tubes or superlattice structures. The lowered absorption coefficient and refractive index make a nanometer-sized adsorbate more transparent, which may form the basis of quantum lasers, as observed at room temperature from nanostructured ZnO tubes that emit ultraviolet laser at 393 ± 3 nm under 355-nm optical excitation [34].

18.4 Summary

The BOLS correlation has enabled numerical solutions to unifying the complex dielectric constants and the coefficient of photoabsorption of nanosemiconductors to the often-overlooked event of atomic CN imperfection and its effect on crystal binding and electron-phonon coupling. The solution applies to the whole range of measuring energies. The dielectric constant drops dramatically at the surface edge of the solid due to bond order loss. The lowered dielectric constant, refractive index, and the low absorption coefficient could be useful to trap and amplify light within the nanosolid by internal reflection, which provides a possible mechanism for random lasers. Understanding could be of use in designing photonic crystals with thermally and electrically tunability for optical switches and in fabricating waveguides for light trapping and amplifying device applications [35]. In addition, the BOLS correlation has also allowed formulation the dielectric suppression, dispersion, and conductivity and dielectric transition of nanosemiconductors. Examination of the effect of temperature and frequency on the dielectric transition and relaxation of nanosolid Si and nanodiamond derived the activation energy for conductivity and dielectric transition of both nanodiamond and nanosilicon, giving

information about the impurity mid-gap states of the corresponding systems [22, 29, 36].

References

1. L.W. Wang, A. Zunger, Dielectric-constants of silicon quantum dots. *Phys. Rev. Lett.* **73**(7), 1039–1042 (1994)
2. J.P. Walter, M.L. Cohen, Wave-vector-dependent dielectric function for Si, Ge, GaAs, and ZnSe. *Phys. Rev. B* **2**(6), 1821 (1970)
3. D. Deger, K. Ulutas, Conduction and dielectric polarization in Se thin films. *Vacuum* **72**(3), 307–312 (2003)
4. S.P. Alpay, I.B. Misirlioglu, V. Nagarajan, R. Ramesh, Can interface dislocations degrade ferroelectric properties? *Appl. Phys. Lett.* **85**(11), 2044–2046 (2004)
5. Z. Zhao, V. Buscaglia, M. Viviani, M.T. Buscaglia, L. Mitoseriu, A. Testino, M. Nygren, M. Johnsson, P. Nanni, Grain-size effects on the ferroelectric behavior of dense nanocrystalline BaTiO₃ ceramics. *Phys. Rev. B* **70**(2), 024107 (2004)
6. D.R. Penn, Wave-number-dependent dielectric function of semiconductors. *Phys. Rev.* **128**(5), 2093 (1962)
7. R. Tsu, D. Babic, Doping of a quantum-dot. *Appl. Phys. Lett.* **64**(14), 1806–1808 (1994)
8. T.P. Chen, Y. Liu, M.S. Tse, O.K. Tan, P.F. Ho, K.Y. Liu, D. Gui, A.L.K. Tan, Dielectric functions of Si nanocrystals embedded in a SiO₂ matrix. *Phys. Rev. B* **68**(15), 153301 (2003)
9. T.P. Chen, Y. Liu, M.S. Tse, P.F. Ho, G. Dong, S. Fung, Depth profiling of Si nanocrystals in Si-implanted SiO₂ films by spectroscopic ellipsometry. *Appl. Phys. Lett.* **81**(25), 4724–4726 (2002)
10. Z. Hens, D. Vanmaekelbergh, E.S. Kooij, H. Wormeester, G. Allan, C. Delerue, Effect of quantum confinement on the dielectric function of PbSe. *Phys. Rev. Lett.* **92**(2), 026808 (2004)
11. C. Delerue, M. Lannoo, G. Allan, Concept of dielectric constant for nanosized systems. *Phys. Rev. B* **68**(11), 115411 (2003)
12. X. Cartoixa, L.W. Wang, Microscopic dielectric response functions in semiconductor quantum dots. *Phys. Rev. Lett.* **94**(23), 236804 (2005)
13. H. Winn, Quantum dot may be more “superficial” than first thought. *SPIE OE Mag.* **8**, (2005)
14. V.P. Drachev, A.K. Buin, H. Nakotte, V.M. Shalaev, Size dependent $\chi(3)$ for conduction electrons in Ag nanoparticles. *Nano Lett.* **4**(8), 1535–1539 (2004)
15. D.D.D. Ma, C.S. Lee, F.C.K. Au, S.Y. Tong, S.T. Lee, Small-diameter silicon nanowire surfaces. *Science* **299**(5614), 1874–1877 (2003)
16. L.W. Wang, A. Zunger, Pseudopotential calculations of nanoscale CdSe quantum dots. *Phys. Rev. B* **53**(15), 9579–9582 (1996)
17. R. Tsu, D. Babic, L. Ioriatti, Simple model for the dielectric constant of nanoscale silicon particle. *J. Appl. Phys.* **82**(3), 1327–1329 (1997)
18. M. Lannoo, C. Delerue, G. Allan, Screening in semiconductor nanocrystallites and its consequences for porous silicon. *Phys. Rev. Lett.* **74**(17), 3415–3418 (1995)
19. L. Canham, Properties of porous silicon: INSPEC1997, London
20. M.A. Omar, *Elementary Solid State Physics: Principles and Applications* (Addison-Wesley, New York, 1993)
21. D.L. Greenway, G. Harbeke, *Optical Properties and Band Structure of Semiconductors* (Pergamon Press, New York, 1968)
22. L.K. Pan, H.T. Huang, C.Q. Sun, Dielectric relaxation and transition of porous silicon. *J. Appl. Phys.* **94**(4), 2695–2700 (2003)
23. F.G. Brown, *The Physics of Solids* (Benjamin Press, New York, 1968)

24. L.K. Pan, C.Q. Sun, B.K. Tay, T.P. Chen, S. Li, Photoluminescence of Si nanosolids near the lower end of the size limit. *J. Phys. Chem. B* **106**(45), 11725–11727 (2002)
25. C.Q. Sun, X.W. Sun, B.K. Tay, S.P. Lau, H.T. Huang, S. Li, Dielectric suppression and its effect on photoabsorption of nanometric semiconductors. *J. Phys. D Appl. Phys.* **34**(15), 2359–2362 (2001)
26. F.J. Blatt, *Physics of Electronic Conduction in Solids* (McGraw-Hill, New York, 1967)
27. J.R. Macdonald, *Impedance Spectroscopy* (ed. by J. Wiley, New York, 1987)
28. J.W. Orton, M.J. Powell, The Hall-effect in polycrystalline and powdered semiconductors. *Rep. Prog. Phys.* **43**(11), 1263–1307 (1980)
29. H.T. Ye, C.Q. Sun, H.T. Huang, P. Hing, Dielectric transition of nanostructured diamond films. *Appl. Phys. Lett.* **78**(13), 1826–1828 (2001)
30. M. Kleitz, J.H. Kennedy, *Fast Ion Transport in Solids*, ed. by P. Vashishta et al. (Elsevier, North Holland, 1979)
31. S. Lanfredi, J.F. Carvalho, A.C. Hernandez, Electric and dielectric properties of Bi₂TiO₂ single crystals. *J. Appl. Phys.* **88**(1), 283–287 (2000)
32. H. Looyenga, Dielectric constants of heterogeneous mixtures. *Physica* **31**(3), 401–406 (1965)
33. C.Q. Sun, Size dependence of nanostructures: Impact of bond order deficiency. *Prog. Solid State Chem.* **35**(1), 1–159 (2007)
34. X.W. Sun, S.F. Yu, C.X. Xu, C. Yuen, B.J. Chen, S. Li, Room-temperature ultraviolet lasing from zinc oxide microtubes. *Jpn. J. Appl. Phys. Part 2 Lett.* **42**(10B), L1229–L1231 (2003)
35. J. Zhou, Y. Zhou, S.L. Ng, H.X. Zhang, W.X. Que, Y.L. Lam, Y.C. Chan, C.H. Kam, Three-dimensional photonic bandgap structure of a polymer-metal composite. *Appl. Phys. Lett.* **76**(23), 3337–3339 (2000)
36. L.K. Pan, S.Q. Xu, W. Qin, X.J. Liu, Z. Sun, W.T. Zheng, C.Q. Sun, Skin dominance of the dielectric-electronic-phononic-photonic attribute of nanostructured silicon. *Surf. Sci. Rep.* **68**(3–4), 418–455 (2013)

Chapter 19

Magnetic Modulation: Atomic CN and Thermal Coupling

- *Interspin interaction and the spin momentum dictate the magnetism of nanoferromagnetic system, following the BOLS notation, Ising premise, and Brillouin functions.*
- *The T_C drops with solid size because of the increased fraction of surface atoms and the associated depression of atomic cohesive energy.*
- *At extremely low temperature, the $M_S(K, T)$ increases with oscillatory features as the solid size is reduced. Surface spins associated with the entrapment of the 3d and 4f electrons and the polarization of the non-bonding electrons contribute and raise the surface magnetism.*
- *At the mid-Tregion, the M_S drops with size. The spin direction will fluctuate due to thermal agitation, and the magnetization becomes lower with solid size.*
- *The H_C increases with the shrink of particle size because of the enhancement of interdomain interaction.*

19.1 Background

19.1.1 Observations

A ferromagnetic solid changes its magnetic properties once its size is reduced or it is measured at different temperatures. For example, the Curie temperature T_C drops [1–3] and the coercivity (H_C) increases for embedded nanograins, whereas for an isolated nanosolid, the H_C drops [4–7]. Generally, the saturation magnetization (M_S) increases at low temperature with quantized features, whereas the M_S drops at ambient temperatures when the solid size is reduced [5–11]. When the size of the ferromagnetic (Pt/Co)-antiferromagnetically (FeMn) coupled nanostructure is reduced, the exchange biasing field and the blocking temperature decrease, while the H_C increases [12, 13]. Figure 19.1 a and b show the magnetic oscillation of small Ni and Rh particles at temperatures closing to 0 K.

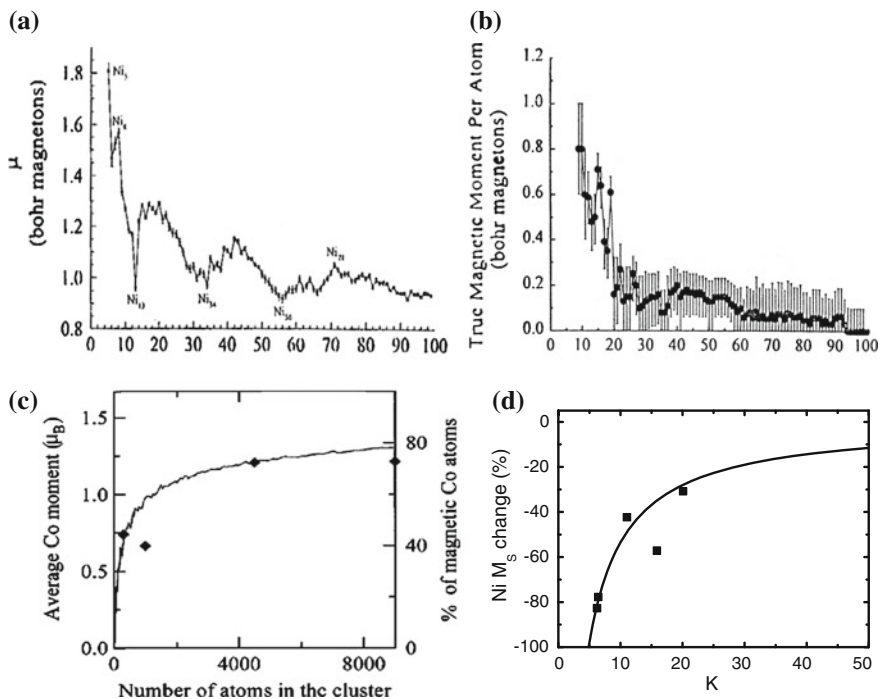


Fig. 19.1 Size dependence of magnetic moments of **a** Ni_n [29] and **b** Rh_n [30] particles measured at low temperature shows the size-enhanced and quantized $M_S(N)$ with oscillating features, **c** cobalt particles [11] and **d** Ni thin films [6] measured at room temperature show size-tailed $M_S(K)$, instead (reprinted with permission from [31])

19.1.1.1 Surface Magnetron

In the case of surfaces and thin films, the magnetic moment of an atom (μ_i) in the surface region is larger than the corresponding bulk value (μ_b) [14, 15]. For instance, compared to the bcc Fe bulk moment of $2.2 \mu_B$, the μ for a surface Fe atom has been found theoretically to be enhanced: (1) by 15 % to $2.54 \mu_B$ for one monolayer (ML) Fe on 5 ML W(110) and (2) by 29 % to $2.84 \mu_B$ for 2 ML Fe on 5 ML W(110) surface. The significant surface relaxation (-12 %) of Fe(310) [16] and Ni(210) [17] surfaces has also been found to enhance the atomic μ by up to 27 %. The μ_B is the Bohr magnetron.

19.1.1.2 Nanosolid at Low Temperature

The surface effects become stronger in the case of a nanosolid since a larger fraction of atoms is located at the curved surface. However, controversy remains in the measured trend of the $M_S(K)$ values [8–11, 18–21]. One trend in measurement

shows that at temperatures below 200 K, the $M_S(K)$ increases with the inverse of size [21–25]. For example, the M_S per atom of Fe, Co, and Ni (at 78–120 K) was measured [25] to increase up to the value of the free atom when the solid size was reduced to a cluster that contains 30 atoms or less. As the size is increased up to 700 atoms, the magnetic moment approaches to the bulk limit. The M_S of Ni clusters also increase inversely with size at temperature between 73 and 198 K [26]. Co_n particles of 1.8–4.4 nm sizes carry magnetic moments that are $\sim 20\%$ higher than the bulk value [26]. The moment of a Co surface atom is enhanced by 32% compared to the bulk value of $1.73 \mu_B$ [27]. In the temperature range of 77–570 K, the M_S of Fe–Ni alloy films increase gradually when the film thickness is decreased from 75 to 35 nm [28]. In a Stern–Gerlach experiment conducted at ~ 20 K, Cox et al. [19] measured the magnetic properties of isolated iron-atom clusters containing 2–17 atoms and Fe monoxides and dioxides clusters and found that the spin per atom of iron clusters was larger than that of the bulk counterpart. It was therefore widely accepted that size reduction could enhance the magnetization of the small ferromagnetic particles.

19.1.1.3 Nanosolid at the Ambient Temperature

Since the observation of Cox in 1985 [19], numerous experiments have been conducted on various ferromagnetic nanosolids. Repeating the same Stern–Gerlach deflections of Fe clusters in a molecular beam, Heer et al. [8] found instead that the average magnetic moments for small iron clusters (50–230 atoms) drops with the number of atoms when the molecular beam nozzle temperatures are around 300 K. This trend is similar to those observed at room temperature of Co [11], $Pd_{96}Fe_4$ [9, 10], $Pd_{97.1}Fe_{2.9}$ [10], $NiFe_2O_4$ [32], and Ni_3Fe [18] alloy particles. Similarly, a remarkable reduction in magnetization for Fe–Ni invar alloy (<40 nm) [33] and Ni thin films has been observed at room temperature [6, 34]. The M_S for Fe_3O_4 thin films [35] drops rapidly when the film decreases from 70 nm. For $\gamma-Fe_2O_3$ nanoparticles, M_S also increases with particle size [36]. Figure 19.1c and d shows the magnetic suppression of Co clusters [11, 18] and Ni films. Small $Pd_{100-x}Fe_x$ grains with $x = 4, 6, 8, 12$ and a radius of approximately 5 nm at 4.2, 100, and 295 K show typical superparamagnetic features with M_S values that are substantially smaller than those observed for the bulk [9]. However, for MnBi films [37], the magnetic momentum changes with neither thickness nor chemical composition. Therefore, it was surprising that some measurements give conflicting data and show magnetic elevation, whereas some show suppression without considering the operating temperature.

19.1.1.4 Coercive Performance

An isolated magnetic domain or highly dispersed ones often show no hysteresis at any temperature. When the size of an isolated ferromagnetic solid is reduced to a

certain critical size, the coercivity of the isolated nanosolid will approach to zero [38]. $\text{Fe}_{69}\text{Ni}_9\text{CO}_2$ powders of 10–15 nm grain sizes show almost no hysteresis, being indicative of superparamagnetic characteristics [39]. However, when the particles get closer together, the superparamagnetic behavior vanishes and the coercivity is present [38, 40]. The coercivity increases with the inverse of grain size, which follows a $H_C \sim 1/K$ relation [5, 38, 41]. Investigation on the $\text{Fe}_{74.5-x}\text{Cu}_x\text{Nb}_3\text{Si}_{13.5}\text{B}_9$ ($x = 0\text{--}1$ at %) ribbons with grain sizes between 10 and 300 nm suggests that the H_C increases following a K^6 dependence and then drops in a $1/K$ fashion at the critical size of 50 nm. A similar trend of transition has been observed for Fe, Ni, and Co metal films, with corresponding critical sizes of 20, 40, and 30 nm [42]. Figure 19.2a shows the size-enhanced H_C of Ni thin films consisting of 3–10 nm grains. Panel b shows the CN-imperfection-enhanced magnetization of Ni, Fe, and Co particles and panel c the Monte Carlo simulated $M_S(T, N)$ profiles [43].

19.1.2 Known Mechanisms

19.1.2.1 Magnetization

A number of outstanding theories have been developed to explain the unusual behavior of ferromagnetic nanosolids, in particular the oscillatory behavior at low T (see Fig. 19.1a, b) [21, 25] and the inconsistent trends of M_S measured at different temperature ranges. Several shell structural models have been proposed for the size-enhanced magnetization [25, 45] which suggested that the magnetic moment of an individual atom is determined by its atomic CN [45]. By assuming bulk-like structures (such as fcc and bcc) and different global cluster shapes (cube, octahedron, and cube octahedron), the average magnetic moment was found to oscillate with the cluster size, agreeing with observations. Therefore, the magnetic ‘shell structure’ reflects the progressive formation of concentric atomic layers [46].

Without considering the effect of temperature, the magnetic properties of transition metals are described by using a simple rectangular d-band assumption [23] together with the second moment approximation, as the first-order approximation [47]. It was assumed that the d-band splitting between the major and the minor spin caused by exchange interaction is invariant for the cluster to the bulk solid, leading to the following expression [15]:

$$\frac{\mu_z}{\mu_b} = \begin{cases} \mu_{\text{dim}}/\mu_b, & \text{if } z \leq z_b(\mu_{\text{dim}}/\mu_b)^2 \\ (z_b/z)^{1/2}, & \text{otherwise} \end{cases} \quad (19.1)$$

where μ_{dim} is the magnetic moment of one atom with one neighbor. In the case of Fe, $\mu_b = 2.22 \mu_B$ [48] and $\mu_{\text{dim}} = 3.2 \mu_B$ [44]. If $z_b = 12$, the step function transits at $z = 5.775$. The magnetic moment of an atom will take the dimer value if its CN is six or less. Considering the geometrical arrangement of atoms in different lattice

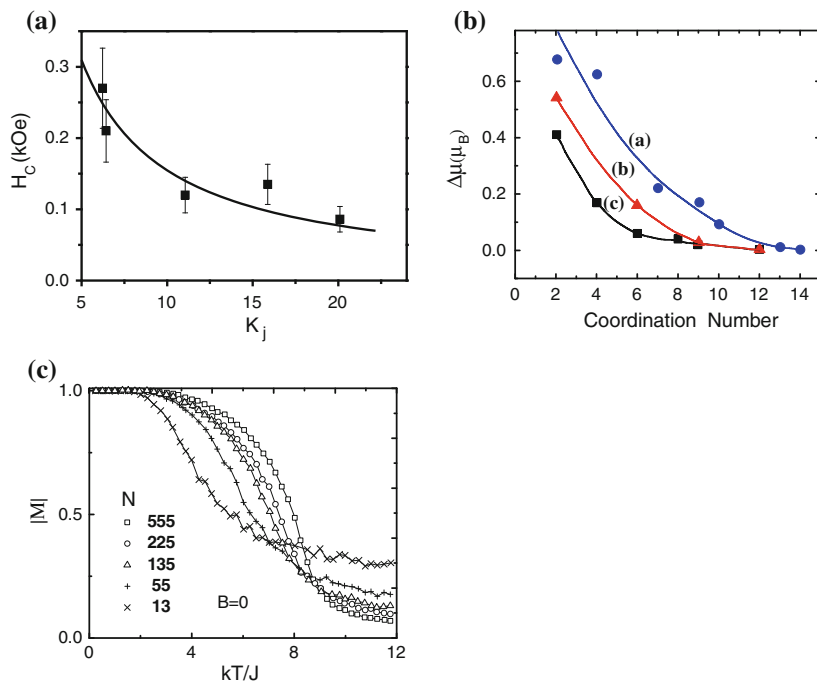


Fig. 19.2 **a** Size-enhanced H_C of Ni films [6] measured at room temperature. **b** CN dependence of the magnetic moment in (a) Fe, (b) Co, and (c) Ni as a function of nearest neighbor coordination (in various structures) [44]. **c** Monte Carlo simulated $M_S(T, N)$ profiles [43] (reprinted with permission from [31])

structures of various shapes, the oscillation features could be reproduced using the core–shell structure [15, 49]. Calculations using the tight-binding theory [44] also show that the magnetic moment of Fe, Co, and Ni atoms increases toward the atomic value when the CN is reduced, as shown in Fig. 19.2b.

The following mechanisms explain the M_S suppression at mid- T regime:

1. Surface spins are weakly coupled and more disordered at the ambient temperatures compared to the bulk spins. Spins in the bulk interior dominates the magnetization. Solid size reduction lowers the number of bulk spins [50].
2. The suppression of the T_C lowers the M_S . In the core–shell structure, the surface layer is magnetically molten, which contributes little to the total M_S of the system [43].
3. Fe^{3+} ions redistribute as the size is reduced in Fe_3O_2 [36].
4. As shown in Fig. 19.2c, the M_S of a small cluster is never higher than the bulk value because of the reduction in the surface exchange bonds. Based on an assumption that the clusters undergo a superparamagnetic relaxation, Khanna

and Linderoth [51] derived that the effective M_S of small Fe and Co clusters decrease with size, as a consequence of fluctuations due to thermal vibration and rotation effects on the domain when the domain is considered as a giant spinner.

19.1.2.2 Coercivity

The Ising model is sufficient for the first-order approximation to describe the interspin interaction within a domain and the intergrain interaction within a solid composed of nanograins. Considering a domain as a giant spinner with a moment J , the exchange energy of the spinner ($E_{\text{exc}, i}$) interacting with its z nearest giant spin neighbors follows the Ising relation. The d_i is then replaced with grain diameter, D (also structural correlation length), if the uniform grain size is assumed. The following equation formulates the $H_C(D)$ transition from D^6 to D^{-1} [52], which represents the lattice strain that increases with the decrease in particle size [53],

$$H_C \sim \frac{1}{20} \frac{K_2^4 D^6}{A^3 M_0} \Rightarrow H_C \propto \frac{1}{2} H_S \propto E'_{\text{exc}} \propto z D^{-1}$$

where K_2 is the strength of local uniaxial anisotropy, and M_0 is the magnitude of the local magnetization vector. A is the exchange stiffness parameter. The former corresponds to the random anisotropy mechanism of domain wall pinning at grain boundaries; the latter relates to the intergrain and grain–substrate interaction [52].

The following presents the understanding of the size and temperature dependence of $M_S(K, T)$ and the $M_S(K \sim 0, T \sim 0)$ oscillation in experimental and theoretical observations by incorporating the BOLS mechanism to the Ising model and Brillouin function with Monte Carlo calculations and measurements support.

19.2 BOLS Formulation

19.2.1 Charge Localization

The CN-imperfection-enhanced bond energy deepens the interatomic potential well of the under coordinated atom from one unit to C_i^{-m} . The deepened potential well entraps and localizes the electrons. If the localization probability is proportional to the potential well depth, then the densely localized electrons contribute to the μ_i of the undercoordinated atom. The corresponding change of the mean $\mu(K)$ varies monotonically with the coefficient of bond contraction:

$$\begin{cases} \mu_i(z_i) = C_i^{-m} \mu_b & \text{(atomic site)} \\ \frac{\Delta\mu(K)}{\mu_b} = \sum_{i \leq 3} r_i (C_i^{-m} - 1) & \text{(core-shell structure)} \end{cases} \quad (19.2)$$

The effective magnetic momentum along the applied field of a z_i coordinated atom is $\mu_{iz} = Jg_J\mu_B$. The Lande g -factor ($g_J = 1-2$) is a function of the orbital (L) and the spin (S_p) angular momenta: $g_J = 1 + [J(J+1) + S_p(S_p+1) - L(L+1)]/[2J(J+1)]$. The CN imperfection also affects g_J . However, in the first-order approximation, one can neglect this effect. For a dimer Fe atom ($z_i = 2$, $C_i \sim 0.7$), $\mu_i = 0.7^{-1}\mu_b = 3.25\mu_B$, which is 1.43 times the bulk value, coinciding with measured value of $\mu_{\text{dim}} = 3.2\mu_B$.

Compared with the known model in Eqs. (19.1), (19.2) employs a smooth function rather than a step function transiting at $z_i \sim 6$, despite different physical origins. As the effective CN of an atom at a flat or a curved surface is four or lower, the BOLS premise predicts a $0.88^{-1} = 12\%$ or higher magnetic enhancement of a surface atom at 0 K [17, 54]. Therefore, atomic CN imperfection deepens the interatomic potential that traps the electrons with high probability of localization. The entrapment of the 3d electrons for transition metals or 4f electrons for rare earth metals and the polarization of the non-bonding electrons contribute to the μ_i of the undercoordinated surface atom at extremely low temperature. By taking the effect of atomic CN imperfection and the pronounced portion of surface atoms into consideration, the magnetic properties of the ferromagnetic nanosolids should differ from those of the bulk.

19.2.2 Brillouin Function

The interspin interaction dominates the order of the spin system and hence the M_S and the T_C . At low temperatures, the total angular moment of an atom changes its direction in a quantum tunneling process [55]. At higher temperatures, the spin direction will fluctuate due to thermal agitation. The strength of interspin coupling that varies with atomic CN determines the ease of fluctuation. Because of fluctuation, the magnetic momentum will reduce and eventually vanish at the T_C . In the first-order approximation to the size and temperature dependence of the $\mu_S(T, K)$, we use the concept of ‘molecular field,’ to describe the spontaneous magnetization at T in terms of Brillouin function, $B_J(y)$ [56]:

$$\begin{cases} \mu(T) = g_J J \mu_B B_J(y) \\ B_J(y) = \frac{2J+1}{2J} \coth \frac{2J+1}{2J} y - \frac{1}{2J} \coth \frac{y}{2J} \\ y = \frac{Jg_J\mu_B}{k_B T} H_m \end{cases} \quad (19.3)$$

where g_J is the Lande g -factor, J is the total angular momentum, and $E_{\text{exc}} \sim E_{\text{coh}}$ is the molecular field. When T approaches to $0.8 T_C$, $\mu(T) \approx \mu_S(T)$. Therefore, the $\mu_S(K, T)$ can be obtained by replacing the bulk J and H_m with the size-dependent $J(K)$ and $E_{\text{exc}}(K)$ that are given as follows:

$$\begin{aligned} E_{\text{exc}}(K) &= E_{\text{exc}}(\infty) \left[1 + \sum_{i \leq 3} \gamma_i (z_{\text{ib}} C_i^{-m} - 1) \right] \\ J(K) &= J \left[1 + \sum_{i \leq 3} \gamma_i (C_i^{-m} - 1) \right] \end{aligned} \quad (19.4)$$

Differentiating Eq. (19.3) against $E_{\text{exc}}(K)$ leads to the size- and temperature-dependent $\mu_S(K, T)$:

$$\begin{aligned} \frac{\Delta \mu_S(K, T)}{\mu_S(\infty, T)} &= \left\{ \frac{1}{2J} \csc h^2 \left[\frac{2g_J \mu_B}{2k_B T} A E_{\text{exc}}(\infty) \right] - \frac{2J+1}{2J} \csc h^2 \left[\frac{(2J+1)g_J \mu_B}{2k_B T} A E_{\text{exc}}(\infty) \right] \right\} \\ &\times \frac{\Delta E_{\text{exc}}(K)}{E_{\text{exc}}(\infty)} \\ &= \alpha(T) \sum_{i \leq 3} \gamma_i (z_{\text{ib}} C_i^{-m} - 1) \end{aligned} \quad (19.5)$$

where parameter $\alpha(T)$ is T and material dependent. Equation (19.5) indicates that for a specific ferromagnetic solid and at a given temperature, the $\mu_S(K, T)$ changes with the atomic cohesive energy. One needs to note that Eq. (19.5) does not apply to an isolated atom without exchange interaction being involved though the isolated atom possesses intrinsically higher magnetic momentum.

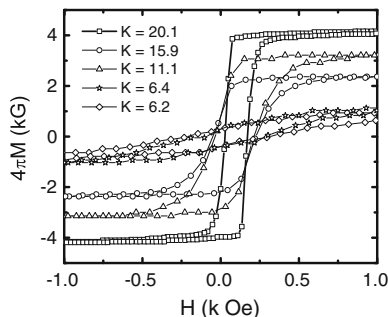
19.3 Experimental and Numerical Verification

19.3.1 Ni Films at the Ambient Temperature

Ni films with grain sizes in the range of 3–10 nm were grown on Si(100) substrates using physical vapor deposition. The in-plane magnetic properties were measured using vibrational sample magnetometer at room temperature [6].

Figures 19.1d and 19.2a compare the predicted with $m = 1$ and the measured size dependence of the M_S and the H_C for the Ni films. The match of $M_S(K)$ at 300 K is realized with $\alpha(J, T) = 4.0$. When the particle size is reduced to $K = 5$ ($D = 2.5$ nm), $M_S = 0$. This result is consistent with the findings of the size-induced T_C suppression of ferromagnetic nanosolids [3]. For a Ni particle of $K = 5$, the T_C drops by ~ 51 % from 631 to 309 K and the M_S is not detectable [2]. The magnetic hysteretic loops of N particles of different sizes in Fig. 19.3 show that at the room temperature, the M_s drops, while the H_c increases with reduction in particle size, which agrees with expectations.

Fig. 19.3 Magnetic hysteretic loops of Ni films of different grain sizes measured at room temperature (reprinted with permission from [6])



19.3.2 Monte Carlo Computation

Monte Carlo simulation based on the BOLS incorporated Ising convention matches the results of modified Brillouin function [56]. Varying the spin value S_i^l for each atom represents the effect of atomic CN-imperfection-enhanced magnetic moment. Six kinds of nanosolids with completely filled outermost shells were employed to investigate the size, shape, and crystal structure effects on the μ_S at various temperatures. The fcc spherical dots are formed in such a way that layers of successive atoms are added to the initial central atom. Figure 19.4a shows, for example, the fcc spherical dot containing N_{141} atoms with $S = 9$ shells and $K = 3.3$. The rod and the plate systems are formed based on the fcc lattice along the $\langle 100 \rangle$ direction. The length of the rod is maintained at $K = 28.3$, and the variation in this has an insignificant effect on the result. The radius of the rod ranges from $S = 1$ to 11 ($K = 0.5$ – 3.66). The width and length of the plate are maintained at $K = 28.3$. The thickness ranges from $S = 1$ to 14 ($K = 0.5$ – 5.1). Figure 19.4b and c illustrate an fcc rod and plate with $S = 3$, $K = 1.9$ and $S = 2$, $K = 1.7$, respectively.

Calculations also examine the ordered structures of icosahedra, decahedra, and the close-packed fcc truncated octahedra that are favored from the energetic point of view. Figure 19.4d–f show the close-packed structures with a total number of N_{101} , N_{147} , and N_{201} atoms, respectively. Icosahedra and decahedra are non-crystalline structures that cannot form in bulk crystals because of the fivefold symmetry. Icosahedra are quasi-spherical, where atoms are arranged in the concentric shells. Marks-truncated decahedra have reentrant (111) facets that are introduced via a modified Wulff construction. fcc truncated octahedra possess a crystalline structure and have the open (100) facets.

Calculations were conducted by using cool state initialization at low temperature ($k_B T/J_{\text{exc}} < 6$) and hot state initialization at relatively high temperature ($k_B T/J_{\text{exc}} \geq 6$) [56]. In the hot state, spins orientate randomly; and in the cool state, spins align parallel to the applied magnetic field. For a certain spin system, the value of the Hamiltonian $H_{\text{ex},k-1}$ was calculated. A spin S_i chooses random value, and the orientation flips from S_i^l to $S_{i,\text{trial}}$. The $H_{\text{ex},k}$ was optimized to satisfy the Metropolis criterion [57]:

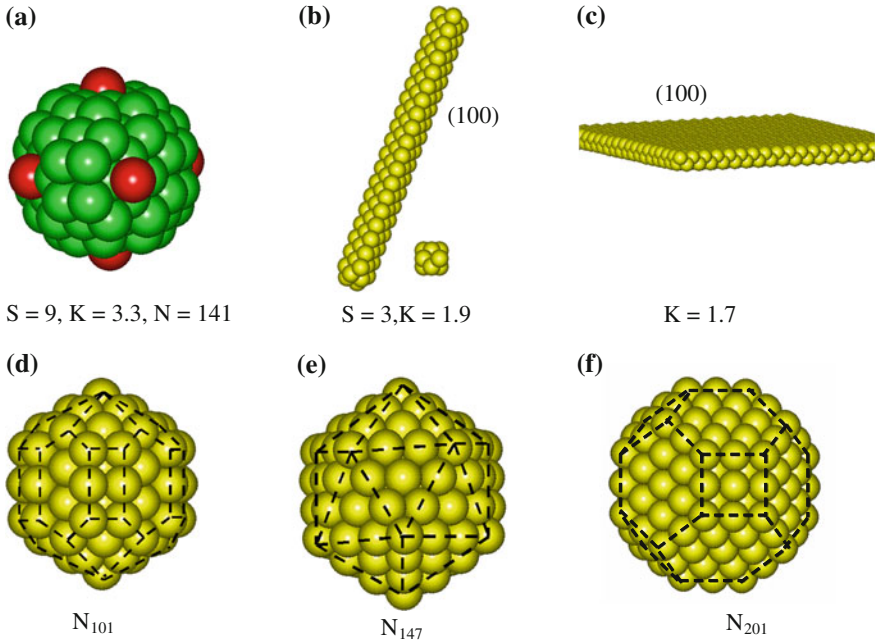


Fig. 19.4 Atomic configurations of **a** an fcc dot of 9 shells with $K = 3.3$, **b** an fcc rod of 3 shells with $K = 1.9$, and **c** an fcc plate of $K = 1.7$ thick, **d** an icosahedron with N_{147} atoms, **e** a marks decahedron with N_{101} , and **f** an fcc truncated octahedron with N_{201} atoms (reprinted with permission from [56])

$$\begin{cases} \exp(-\Delta H_{\text{ex}}/kT) > \delta_{\text{mc}} \\ \Delta H_{\text{ex}} = H_{\text{ex},k} - H_{\text{ex},k-1} \end{cases}$$

The ΔH_{ex} is the energy change for a spin re-orientation, and the δ_{mc} is a uniform random deviate. After MC steps of sweeping over all lattice sites of the spin system, the spin system of a specific size at a specific temperature reaches thermal equilibrium. In the MC simulation, each atom serves as an independent spin with μ_i in unit of the bulk μ_b . For the bulk value, S takes the values of $+1$ or -1 for the up and down flip. The energy changes for the spin flip from $k-1$ to k step due to thermal vibration: $\Delta H_{\text{ex}} = H_{\text{ex},k} - H_{\text{ex},k-1}$. At a given temperature, the system reaches to equilibrium after sufficient steps of operation. The magnetization is then calculated based on the relation: $\langle M \rangle = \left[\sum_N M(s_1^{(i)}, s_2^{(i)}, \dots, s_N^{(i)}) \right] / N$ with 5,000 thermalization steps for each spin to reach the thermal equilibrium state.

Figure 19.5 shows the MC simulated $M_S(K, T)$ curves at zero applied magnetic field for (a) an fcc dot, (b) an fcc rod, (c) an fcc plate, and (d) an icosahedra spin system. Generally, at very low temperature region ($k_B T / J_{\text{exc}} < 3$), the $M_S(K, T)$ increases with oscillatory features as the solid size is reduced. At the mid- T region ($k_B T / J_{\text{exc}} \sim 6$), the M_S drops with size. In the paramagnetic region, the

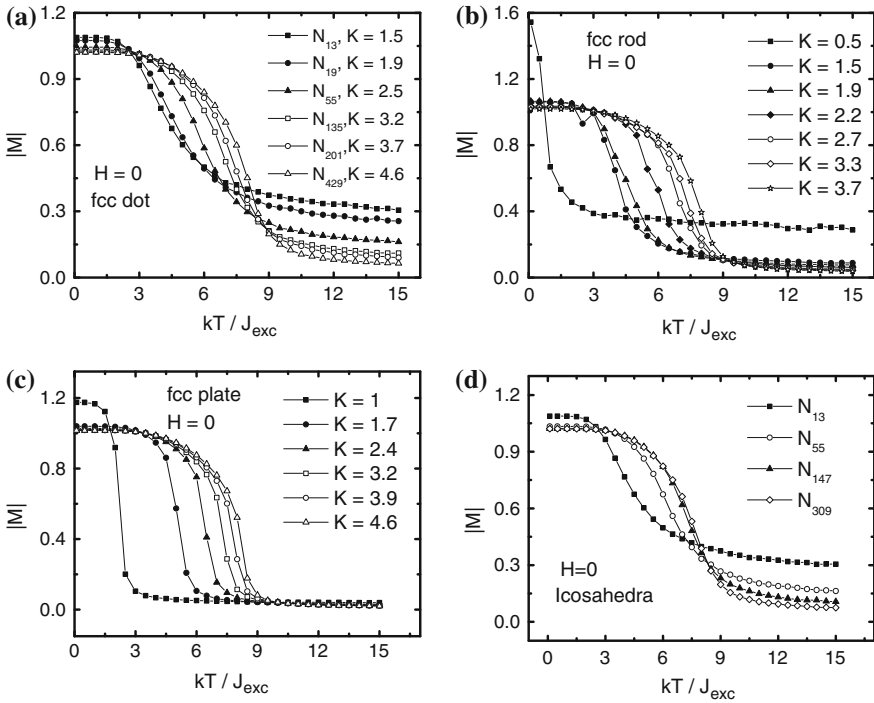
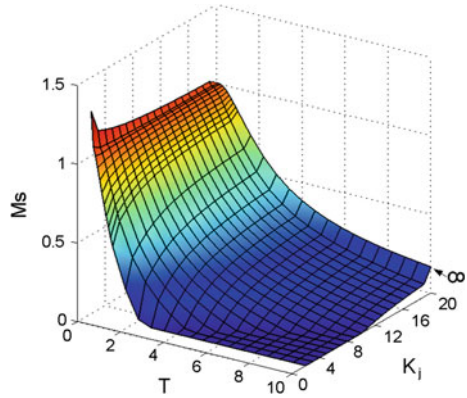


Fig. 19.5 Temperature ($k_B T/J_{exc}$) and size, shape, and size dependence of the M_S for **a** an fcc dot, **b** an fcc rod, **c** an fcc plate, and **d** an icosahedral spin system (reprinted with permission from [31])

Fig. 19.6 Counterplot of the BOLS predicted $M_S(T, K)$, which shows that M_S increases with inverse size at low temperature and decreases with size at mid temperature. The M_S is normalized by $M_S(T=0, K=\infty)$, and T is normalized by $AE_{exc}(\infty)$ (reprinted with permission from [31])



residual M_S increases as the size is reduced. These features are intrinsically common depending less on the shape and the crystal structure of the specimen.

Figure 19.6 shows the $M_S(K, T)$ counterplot for a spherical dot. The surface-to-volume ratio gives a smooth function without oscillatory features.

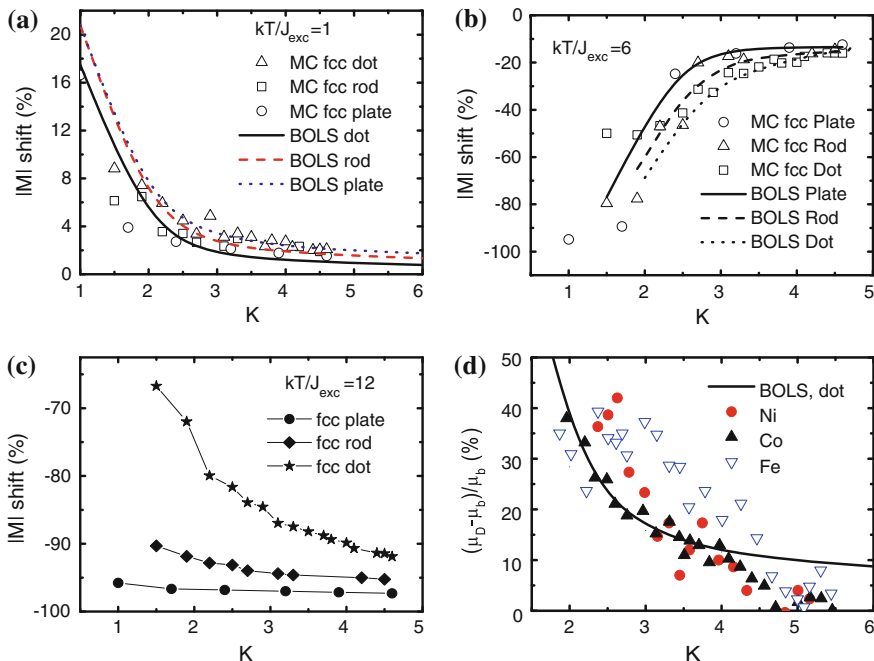


Fig. 19.7 Comparison of BOLS predictions with measured size dependence of M_S at low T . **a** $k_B T/J_{exc} = 1$, **b** $k_B T/J_{exc} = 6$, **c** $k_B T/J_{exc} = 12$ for fcc nanosolids shows three outstanding regions, where $|MI$ shift = $[|M(K) - |M(\infty)|]/|M(\infty)| \times 100\%$, and **d** low temperature $M_S(K)$ of Fe, Ni, and Co particles (reprinted with permission from [25])

19.3.2.1 $M_S(K, T \sim 0 \text{ K})$ Enhancement

Figure 19.5a shows that for a specific size K , the M_S of the fcc dot is higher than that of the fcc plate because a spherical dot has higher γ_i value. The dimensionality of a dot is three, but for a plate, it is unity. When $T \rightarrow 0$, $y \rightarrow \infty$, and then $B_J(y) \rightarrow 1$, Eq. (19.3) approximates. $\mu_S(T \rightarrow 0) = Jg_j\mu_B$. Using a core-shell structure in the BOLS correlation that calculates the magnetic moment of every atom layer-by-layer leads to the size-enhanced M_S for a nanosolid at very low temperature, which follows Eq. (19.2).

Figure 19.7 compares BOLS predictions with measured size dependence of M_S at low T . As the measured data are much scattered, it is hard to reach a conclusion though the trends generally match; however, the close match of $T_C(K)$ suppression and lattice contraction, as shown earlier in this report evidences sufficiently the validity of the BOLS formulation as the origin of the unusual magnetic behavior of the ferromagnetic nanosolids at different temperatures.

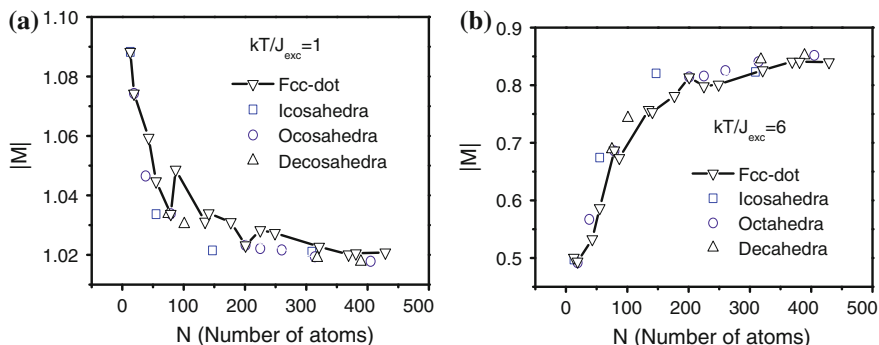


Fig. 19.8 Magnetic oscillation features of different crystal structures at **a** low and **b** high temperatures due to the ‘magic number’ effect (reprinted with permission from [31])

19.3.2.2 $M_S(K, T \sim T_C)$ Suppression

Figure 19.7 shows the matching between BOLS predictions with $\alpha(J, T) = 1.4$ and the MC simulated results at different temperatures. The calculated trend is consistent with the measurement with $\alpha(J, T)$ value that is different from Ni sample. The calculation takes the surface CN to the half number of the bulk (12), but in the BOLS premise, the effective surface CN is four or less. In the paramagnetic phase as shown in Fig. 19.7c, the remnant magnetism is higher for smaller particles, which results from the slower temperature decay in the MC study and to the increasing fluctuations with decrease in cluster size [43].

19.3.2.3 $M_S(K)$ Oscillation and Structural Stability

The oscillation behavior of M_S of smaller clusters, as shown in Fig. 19.8, depends less on the crystal structures. This relation suggests that the oscillatory originates from the surface-to-volume number ratios because some particles have fewer atoms in the surface shells with smaller γ_i value than those of the adjacent larger or smaller sizes, as illustrated in Chap. 11 for the ‘magic number’ of fcc and bcc structures [29]. Therefore, it is not surprising to resolve the M_S oscillation in the low temperature measurement of smaller nanostructures with quantized surface-to-volume number ratios.

The physical properties of nanosolids in molecular regime typically exhibit a very irregular dependence on their aggregate size, namely magic numbers, while they behave in a regular way in the mesoscopic regime. The icosahedron, Marks decahedron, and the fcc truncated octahedron have lower M_S in the low- T region, especially the small icosahedral particles of N_{55} and N_{147} atoms, compared to other structures. An icosahedron has fewer low-CN atoms at the surface with most compact structures. The mass spectra of nanosolids usually exhibit especially abundant sizes that often reflect particularly stable structures, especially reactive

nanosolids, or closed electronic shells [58]. These sizes of ‘magic number’ are of theoretical interest since many of them correspond to compact structures that are especially stable. The simulative results show the magic numbers of N_{13} , N_{55} , N_{147} for icosahedron magnetic nanoparticles [24]. However, when the N is larger than 300, the fcc truncated octahedron is magnetically most stable compared with the decahedra, icosahedra, and the fcc spherical dot. The MC simulation results are consistent with experimental findings that the icosahedral structure transits at ~ 3.8 nm to the fcc truncated structure when the particle size is increased [59]. The competition between the surface remnant atomic cohesive energy and the binding energy density determines the structural stability. Therefore, icosahedra are the most stable at small sizes due to their low surface energy and good quasi-spherical structures, while decahedra are favorable at intermediate sizes, and regular crystalline structures are favored for large objects.

19.4 Summary

Incorporating the BOLS notation to the Ising premise and the Brillouin function has led to clarification and formulation of the shape, size, and temperature dependence of the magnetism of ferromagnetic clusters. Monte Carlo simulations and measurements verify the formulations. Reproduction of all the observable features at various temperatures, including the oscillatory ones gives clear physical insight into the origin of the changes:

1. For a ferromagnetic nanosolid, the magnetic moment at very low temperature increases with the inverse of size compared with the bulk value due to the deepening of the intra-atomic potential well that entraps and polarizes the surface spins contributing to the angular momentum of the under coordinated atoms of a nanosolid.
2. The M_S at temperature around T_C reduces. The decrease in exchange energy dominates the thermal stability and therefore the T_C of a nanosolid.
3. The M_S oscillates with the total number of atoms arise from nothing more than the surface-to-volume number ratio of the solid.
4. Intergrain interaction dictates the H_C .
5. Structure transition from icosahedron to fcc truncated octahedron happens at size containing 300 atoms, which is common to observations using other means.

Consistency in the MC calculations, BOLS predictions, and experimental observations not only clarifies the confusion on magnetic behavior of a ferromagnetic nanosolid at various temperatures. The joint contribution from the CN imperfection and the associated bond energy rise lowers the exchange energy that tailors the temperature of phase transition. Therefore, it is not surprising that some measurements show the enhanced M_S at low temperature, while some observed the tailoring of the M_S at temperature close to the T_C [60–62].

References

1. Y. Li, K. Baberschke, Dimensional crossover in ultrathin Ni(111) films on W(110). *Phys. Rev. Lett.* **68**(8), 1208–1211 (1992)
2. W.H. Zhong, C.Q. Sun, B.K. Tay, S. Li, H.L. Bai, E.Y. Jiang, Curie temperature suppression of ferromagnetic nanosolids. *J. Phys.: Condens. Matter* **14**(23), L399–L405 (2002)
3. C.Q. Sun, W.H. Zhong, S. Li, B.K. Tay, H.L. Bai, E.Y. Jiang, Coordination imperfection suppressed phase stability of ferromagnetic, ferroelectric, and superconductive nanosolids. *J. Phys. Chem. B* **108**(3), 1080–1084 (2004)
4. E. Tronc, M. Nogues, C. Chanec, F. Lucari, F. D’Orazio, J.M. Greneche, J.P. Jolivet, D. Fiorani, A.M. Testa, Magnetic properties of gamma-Fe₂O₃ dispersed particles: size and matrix effects. *J. Magn. Magn. Mater.* **272**, 1474–1475 (2004)
5. M.S. Seehra, A. Punnoose, Particle size dependence of exchange-bias and coercivity in CuO nanoparticles. *Solid State Commun.* **128**(8), 299–302 (2003)
6. W.H. Zhong, C.Q. Sun, S. Li, Size effect on the magnetism of nanocrystalline Ni films at ambient temperature. *Solid State Commun.* **130**(9), 603–606 (2004)
7. J.G. Li, Y. Qin, X.L. Kou, J.J. Huang, The microstructure and magnetic properties of Ni nanoplatelets. *Nanotechnology* **15**(8), 982–986 (2004)
8. W.A. Deheer, P. Milani, A. Chatelain, Spin relaxation in small free iron clusters. *Phys. Rev. Lett.* **65**(4), 488–491 (1990)
9. M. Guzman, J.L. Delplancke, G.J. Long, J. Delwiche, M.J. Hubin-Franskin, F. Grandjean, Morphologic and magnetic properties of Pd_{100-x}Fe_x nanoparticles prepared by ultrasound assisted electrochemistry. *J. Appl. Phys.* **92**(5), 2634–2640 (2002)
10. T. Taniyama, E. Ohta, T. Sato, M. Takeda, Magnetic properties of Pd-2.9 at % Fe fine particles. *Phys. Rev. B* **55**(2), 977–982 (1997)
11. Y. Qiang, R.F. Sabiryanov, S.S. Jaswal, Y. Liu, H. Haberland, D.J. Sellmyer, Magnetism of Co nanocluster films. *Phys. Rev. B* **66**(6), 064404 (2002)
12. J. Sort, B. Dieny, M. Fraune, C. Koenig, F. Lunnebach, B. Beschoten, G. Guntherodt, Perpendicular exchange bias in antiferromagnetic-ferromagnetic nanostructures. *Appl. Phys. Lett.* **84**(18), 3696–3698 (2004)
13. V. Baltz, J. Sort, B. Rodmacq, B. Dieny, S. Landis, Size effects on exchange bias in sub-100 nm ferromagnetic-antiferromagnetic dots deposited on prepatterned substrates. *Appl. Phys. Lett.* **84**(24), 4923–4925 (2004)
14. L.M. Falicov, D.T. Pierce, S.D. Bader, R. Gronsky, K.B. Hathaway, H.J. Hopster, D.N. Lambeth, S.S.P. Parkin, G. Prinz, M. Salamon, I.K. Schuller, R.H. Victora, Surface, interface, and thin-film magnetism. *J. Mater. Res.* **5**(6), 1299–1340 (1990)
15. F. Aguilera-granja, J.L. Moranlopez, Ising-model of phase-transitions in ultrathin films. *Solid State Commun.* **74**(3), 155–158 (1990)
16. W.T. Geng, A.J. Freeman, R.Q. Wu, Magnetism at high-index transition-metal surfaces and the effect of metalloidal impurities: Ni(210). *Phys. Rev. B* **63**(6), 064427 (2001)
17. W.T. Geng, M. Kim, A.J. Freeman, Multilayer relaxation and magnetism of a high-index transition metal surface: Fe(310). *Phys Rev B* **63**(24), 245401 (2001)
18. C.N. Chinnasamy, A. Narayanasamy, N. Ponpandian, K. Chattopadhyay, M. Saravanakumar, Order–disorder studies and magnetic properties of mechanically alloyed nanocrystalline Ni₃Fe alloy. *Mater. Sci. Eng., A-Structural Mater. Prop. Microstruct. Process.* **304**, 408–412 (2001)
19. D.M. Cox, D.J. Trevor, R.L. Whetten, E.A. Rohlfing, A. Kaldor, Magnetic-behavior of free-iron and iron-oxide clusters. *Phys. Rev. B* **32**(11), 7290–7298 (1985)
20. J.P. Bucher, D.C. Douglass, L.A. Bloomfield, Magnetic-properties of free cobalt clusters. *Phys. Rev. Lett.* **66**(23), 3052–3055 (1991)
21. I.M.L. Billas, J.A. Becker, A. Chatelain, W.A. Deheer, Magnetic-moments of iron clusters with 25–700 atoms and their dependence on temperature. *Phys. Rev. Lett.* **71**(24), 4067–4070 (1993)

22. S. Ohnishi, A.J. Freeman, M. Weinert, Surface magnetism of Fe(001). *Phys. Rev. B* **28**(12), 6741–6748 (1983)
23. G.M. Pastor, J. Dorantesdávila, K.H. Bennemann, Size and structural dependence of the magnetic-properties of small 3d-transition-metal clusters. *Phys. Rev. B* **40**(11), 7642–7654 (1989)
24. C.Y. Yang, K.H. Johnson, D.R. Salahub, J. Kaspar, R.P. Messmer, Iron clusters-electronic-structure and magnetism. *Phys. Rev. B* **24**(10), 5673–5692 (1981)
25. I.M.L. Billas, A. Chatelain, W.A. Deheer, Magnetism from the atom to the bulk in iron, cobalt, and nickel clusters. *Science* **265**(5179), 1682–1684 (1994)
26. A.P. Tsai, N. Chandrasekhar, K. Chattopadhyay, Size effect on the superconducting transition of embedded lead particles in an Al–Cu–V amorphous matrix. *Appl. Phys. Lett.* **75**(11), 1527–1528 (1999)
27. A. Ney, P. Pouloupoulos, K. Baberschke, Surface and interface magnetic moments of Co/Cu(001). *Europhys. Lett.* **54**(6), 820–825 (2001)
28. M. Konno, Anomalous thickness dependence of the saturation magnetization in Fe–Ni invar alloy-films. *J. Phys. Soc. Jpn.* **49**(3), 1185–1186 (1980)
29. S.E. Apsel, J.W. Emmert, J. Deng, L.A. Bloomfield, Surface-enhanced magnetism in nickel clusters. *Phys. Rev. Lett.* **76**(9), 1441–1444 (1996)
30. A.J. Cox, J.G. Louderback, S.E. Apsel, L.A. Bloomfield, Magnetic in 4d-transition metal-clusters. *Phys. Rev. B* **49**(17), 12295–12298 (1994)
31. C.Q. Sun, Size dependence of nanostructures: impact of bond order deficiency. *Prog. Solid State Chem.* **35**(1), 1–159 (2007)
32. R.H. Kodama, A.E. Berkowitz, E.J. McNiff, S. Foner, Surface spin disorder in NiFe₂O₄ nanoparticles. *Phys. Rev. Lett.* **77**(2), 394–397 (1996)
33. K. Sumiyama, T. Sato, G.M. Graham, Thickness dependence of magnetization in Fe–Ni invar alloy film. *Solid State Commun.* **19**(5), 403–404 (1976)
34. G. Wedler, H. Schneck, Galvanomagnetic and magnetic-properties of evaporated thin nickel films. II. Thickness dependence of hall-coefficients, magnetoresistivity and saturation magnetization. *Thin Solid Films* **47**(2), 147–153 (1977)
35. S. Ohta, A. Terada, Y. Ishii, and S. Hattori, Thickness dependence of magnetic properties and read-write characteristics for iron oxide thin films. *Trans. Inst. Electr. Commun. Eng. Jpn.* **E68** (1985)
36. M.D. Mukadam, S.M. Yusuf, P. Sharma, S.K. Kulshreshtha, Particle size-dependent magnetic properties of gamma-Fe₂O₃ nanoparticles. *J. Magn. Magn. Mater.* **272**, 1401–1403 (2004)
37. K. Kempter, I. Maurer, H. Harms, Saturation magnetization of MnBi films with different thicknesses and composition. *Appl. Phys.* **7**(1), 7–9 (1975)
38. A. Manaf, R.A. Buckley, H.A. Davies, M. Leonowicz, Enhanced magnetic-properties in rapidly solidified Nd–Fe–B based alloys. *J. Magn. Magn. Mater.* **101**(1–3), 360–362 (1991)
39. K. Shafi, A. Gedanken, R. Prozorov, A. Revesz, J. Lendvai, Preparation and magnetic properties of nanosized amorphous ternary Fe–Ni–Co alloy powders. *J. Mater. Res.* **15**(2), 332–337 (2000)
40. J. Degauque, B. Astie, J.L. Porteseil, R. Vergne, Influence of the grain-size on the magnetic and magnetomechanical properties of high-purity iron. *J. Magn. Magn. Mater.* **26**(1–3), 261–263 (1982)
41. G. Herzer, Grain-size dependence of coercivity and permeability in nanocrystalline ferromagnets. *IEEE Trans. Magn.* **26**(5), 1397–1402 (1990)
42. F. Sato, N. Tezuka, T. Sakurai, T. Miyazaki, Grain diameter and coercivity of Fe, Ni, and Co metals. *IEEE Trans Magn Jpn* **9**, 100–106 (1994)
43. J. Merikoski, J. Timonen, M. Manninen, P. Jena, Ferromagnetism in small clusters. *Phys. Rev. Lett.* **66**(7), 938–941 (1991)
44. M.R. Press, F. Liu, S.N. Khanna, and P. Jena, Magnetism and local order. II. Self-consistent cluster calculations. *Phys. Rev. B.* **40**(1), 399–406 (1989)

45. P.J. Jensen, K.H. Bennemann, Theory for the atomic shell structure of the cluster magnetic-moment and magnetoresistance of a cluster ensemble. *Z. Phys. D-Atoms Mol. Clusters* **35**(4), 273–278 (1995)
46. F. Aguilera-Granja, J.M. Montejano-Carrizales, J.L. Moran-Lopez, Magnetic moments of iron clusters: a simple theoretical model. *Phys. Lett. A* **242**(4–5), 255–260 (1998)
47. J.J. Zhao, X.S. Chen, Q. Sun, F.Q. Liu, G.H. Wang, A simple d-band model for the magnetic property of ferromagnetic transition-metal clusters. *Phys. Lett. A* **205**(4), 308–312 (1995)
48. C. Kittel, *Introduction to Solid State Physics*. 8th edn. (Wiley, New York, 2005)
49. J.M. MontejanoCarrizales, F. AguileraGranja, J.L. MoranLopez, Direct enumeration of the geometrical characteristics of clusters. *Nanostruct. Mater.* **8**(3), 269–287 (1997)
50. D.H. Han, J.P. Wang, H.L. Luo, Crystallite size effect on saturation magnetization of fine ferrimagnetic particles. *J. Magn. Magn. Mater.* **136**(1–2), 176–182 (1994)
51. S.N. Khanna, S. Linderoth, Magnetic-behavior of clusters of ferromagnetic transition-metals. *Phys. Rev. Lett.* **67**(6), 742–745 (1991)
52. R. Alben, J.J. Becker, M.C. Chi, Random anisotropy in amorphous ferromagnets. *J. Appl. Phys.* **49**(3), 1653–1658 (1978)
53. M. Lopez, P. Marin, T. Kulik, A. Hernando, Influence of measuring temperature in size dependence of coercivity in nano structured alloys. *J. Magn. Magn. Mater.* **290**, 171–174 (2005)
54. X. Qian, W. Hubner, First-principles calculation of structural and magnetic properties for Fe monolayers and bilayers on W(110). *Phys. Rev. B* **60**(23), 16192–16197 (1999)
55. C. Sangregorio, T. Ohm, C. Paulsen, R. Sessoli, D. Gatteschi, Quantum tunneling of the magnetization in an iron cluster nanomagnet. *Phys. Rev. Lett.* **78**(24), 4645–4648 (1997)
56. W.H. Zhong, C.Q. Sun, S. Li, H.L. Bai, E.Y. Jiang, Impact of bond-order loss on surface and nanosolid magnetism. *Acta. Mater.* **53**(11), 3207–3214 (2005)
57. N. Metropolis, A.W. Rosenbluth, M.N. Rosenbluth, A.H. Teller, E. Teller, Equation of state calculations by fast computing machines. *J. Chem. Phys.* **21**(6), 1087–1092 (1953)
58. M. Sakurai, K. Watanabe, K. Sumiyama, K. Suzuki, Magic numbers in transition metal (Fe, Ti, Zr, Nb, and Ta) clusters observed by time-of-flight mass spectrometry. *J. Chem. Phys.* **111**(1), 235–238 (1999)
59. D. Reinhard, B.D. Hall, P. Berthoud, S. Valkealahti, R. Monot, Size-dependent icosahedral-to-fcc structure change confirmed in unsupported nanometer-sized copper clusters. *Phys. Rev. Lett.* **79**(8), 1459–1462 (1997)
60. Y.W. Du, J. Wu, H.X. Lu, T.X. Wang, Z.Q. Qiu, H. Tang, J.C. Walker, Magnetic-properties of fine iron particles. *J. Appl. Phys.* **61**(8), 3314–3316 (1987)
61. S. Gangopadhyay, G.C. Hadjipanayis, C.M. Sorensen, K.J. Klabunde, Magnetic-properties of ultrafine Co particles. *IEEE Trans. Magn.* **28**(5), 3174–3176 (1992)
62. R.D. Sanchez, J. Rivas, P. Vaqueiro, M.A. Lopez-Quintela, D. Caeiro, Particle size effects on magnetic garnets prepared by a properties of yttrium iron sol-gel method. *J. Magn. Magn. Mater.* **247**(1), 92–98 (2002)

Chapter 20

Functionalities of Non-Bonding Electrons: Size Emergence

- *The coupling of the entrapment and the polarization of the nonbonding lone electrons by the densely entrapped core and bonding electrons derives emerging properties that the bulk counterpart does not show.*
- *imilar to the lone pairs and dipoles, the polarized lone electrons neither follow the dispersion relationships nor occupy the allowed states in the valence band and below but they generate the midgap impurity states near E_F .*
- *Polarization happens at sites with even lower atomic CN, which gives rise to the non-zero spin (carrier of topologic insulator), conductor-insulator transition, surface plasmonic enhancement, and the superhydrophobicity, superfluidity, superlubricity, and supersolidity.*
- *The dominance of entrapment derives the acceptor type catalysis and the dominance of polarization results in donor-type catalyst of metals at the nanoscale.*
- *These emerging attributes become more significant when the atomic CN is even lower. UV irradiation, hydrogenation or contamination may annihilate these features.*

20.1 Significance of Non-Bonding Electrons

Although they exist ubiquitously in the human bodies and our surroundings, the impact of the non-bonding lone electrons and lone-electron pairs has long been underestimated. In addition to the shorter and stronger bonds between undercoordinated atoms that initiate the size trends of the otherwise constant bulk properties when a substance turns into the nanoscale, the presence of the lone electrons nearby the broken bonds generate the fascinating phenomena that bulk materials do not show. The lone-electron pairs and the lone-pair-induced dipoles associated with C, N, O, and F tetrahedral coordination bonding form functional groups in the biologic, organic, and inorganic specimens. This section will focus on the development and applications of theory regarding the energetics and dynamics of non-bonding electrons, aiming to raise the awareness of their revolutionary impact to

the society. Discussion will also extend to the prospective impacts of the non-bonding unpaired electrons on mysteries such as the catalytic enhancement and catalysts design, the dilute magnetism, conductor–insulator transition, and the superhydrophobicity, fluidity, lubricity, and solidity at the nanoscaled contacts. Meanwhile, it is essential and effective to understand the properties of substances from the perspective of bond and non-bond formation, dissociation, relaxation and vibration, and the associated energetics and dynamics of charge repopulation, polarization, densification, and localization. Finding and grasping with factors controlling the non-bonding states and making them of use in functional materials design and identifying their limitations will form, in the near future, a subject area of ‘Nonbonding Electronics and Energetics,’ which would be even more challenging, fascinating, promising, and rewarding than dealing with the core or valence electrons alone.

20.2 Diluted Magnetism: Defect Locked Dipoles

20.2.1 *Nonmagnetic Metals at the Nanoscale*

It has been surprising that nanoclusters consisting non-magnetic element such as Rh [1], Pd [2], and Pt [3] exhibit magnetism, as shown in Fig. 20.1, which is beyond the expectation of traditional magnetism theory [4]. The size trend of Rh magnetization suggests the dominance of the number ratio of surface atoms [5]. Magnetization measurements of Pt clusters consisting of 13 ± 2 atoms well characterized and monodispersed in a zeolite confirmed the predicted extraordinary magnetic polarization with up to eight unpaired electrons on a cluster, corresponding to a magnetic moment of $0.65(5)\mu_B$ per atom. However, the effect is partly quenched by hydrogen chemisorption [6]. The magnetization of Pt nanoparticles also decreases with the increase in particle diameter, as shown in Fig. 20.1b [7]. The effects of hydrogen desorption and size change on the magnetization indicate that only atoms in the surface contribute.

In a bulk specimen, the ratio of such unpaired surface electrons is extremely low and therefore its magnetism is hardly detectable. From the maximum magnetoresistance change, the conduction electron polarization of the Pd nanoparticle superlattice is estimated to be similar to 4 %. The ferromagnetism of Pd nanoparticles is evolved into ferromagnetism without protective agents; therefore, the origin of ferromagnetism in the chemically prepared Pd nanoparticles is associated with the intrinsic characteristics of the Pd nanoparticles, but not the effect of the existence of a protective agent [2]. Because the s -orbit of $Pt(6s^0)$ and $Pd(5s^0)$ are empty, no magnetization is supposed to exhibit. However, the polarization may extend to the f or d electrons and then situation changes.

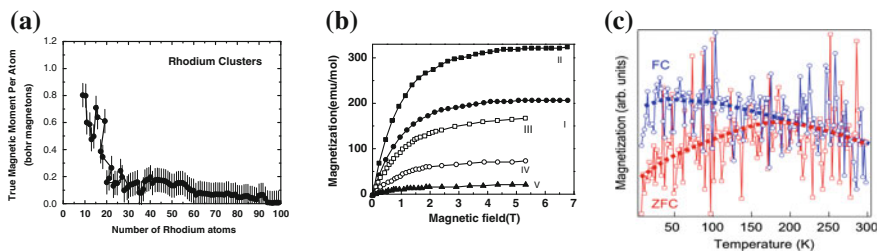


Fig. 20.1 **a** Size dependence of the magnetic moments of $\text{Rh}_n(5s^1)$ particles measured at low temperature shows the size-enhanced and quantized $M_S(N)$ with oscillating features [1, 8]. **b** Molar magnetization at 1.8 K of Pt_{13} clusters on NaY substrate before (I) and after (II) hydrogen desorption [6], compared with that of Pt nanoparticles of 2.3 nm (420 atoms, III), 3.0 nm (940 atoms, IV), and 3.8 nm (1,900 atoms, V) [7]. **c** Temperature dependence of $\text{Pd}(5s^04d^{10})$ nanoparticle magnetizations under zero-field cooling (ZFC) and field cooling (FC) [2] (Reprinted with permission from [9])

20.2.2 Graphite Vacancy and GNR Edges

Wang et al. [10] measured at 2 and 300 K the magnetism of graphene fabricated at (a) 400 and (b) 600 °C and suggested that the magnetism is associated with defects on the graphene because the higher defect density presents to the sample fabricated at high temperature. It has also been found that weak magnetic momentum is detectable to the graphite nanostructures at 4 K under a maximum applied field of 20 kOe [11]. From a systematic calculations using a combination of mean-field Hubbard model and first principles on the magnetic properties of disordered graphene and irradiated graphite, Yazyev [12] concluded that only single-atom defects can induce ferromagnetism in graphene-based materials.

To confirm the defect magnetism of GNR, Zhang et al. [14] calculated the effect of quantum entrapment and polarization on the magnetism of graphene vacancy and edges of the AGNR, ZGNR, and rec-ZGNR, using the BOLS-incorporated tight-binding mean-field Hubbard model. Results in Sect. 13.2 suggest that in addition to the global quantum entrapment of the undercoordinated vacancy and edges, the Dirac resonant peak presents only to the vacancy and the ZGNR edges. The mid-gap Dirac states are associated with nonzero magnetism, the spins oriented alternatively up and down. We also found from the calculations that the zigzag edges exhibit E_F resonant states with nonzero spin, and it is more significant to the reconstructed GNR edge.

20.2.3 Oxides and Nitrides

The most surprising finding in magnetism is that non-magnetic semiconductors such as ZnO and GaN [15], CuO, and TiO_2 [16] become ferromagnetic at room temperature and above when they are doped with just a few percent of transition

metal cations such as V, Cr, Mn, Fe, Co, or Ni [17]. Dilute magnetic oxides are transparent and wide-bandgap materials. Defects have been identified to promote the magnetism in ZnO [18]. This dilute magnetism presents in thin films and nanocrystals, but not in the well-crystallized bulk material. Slight nitrogen substitution for oxygen raises the Curie temperature and lowers the coercivity. The magnetic moment decays with a characteristic decay time of weeks or months. UV irradiation can recover the decay of the magnetization.

Such undercoordination-associated dilute magnetism cannot be understood in terms of the conventional superexchange or double-exchange interactions theory of magnetism in insulators; nor can a carrier-mediated ferromagnetic exchange mechanism account for the magnitude of the Curie temperatures, which are well in excess of 400 K (1/30 eV).

According to Coey et al. [19], the shallow donor electrons that form bound magnetic polarons, which overlap to create a mid-gap spin-split impurity band, mediate the ferromagnetic exchange in dilute ferromagnetic oxides and nitrides. High Curie temperatures arise only when empty minority-spin or majority-spin d states lie at the Fermi level in the impurity band. The d^0 ferromagnetism exists in nitrides, hexaborides, thiol-coated noble metal nanoparticles, purely organic systems, and even for silicon, with a spin-split impurity band near the E_F , being coincidence with that generated by the lone pairs or the dipole states [13].

20.2.4 Edge States Versus Dilute Magnetism

The dilute magnetism associated with atomic undercoordination arises from the locally locked and polarized non-bonding electrons including the lone s-electrons in metal and the sp^2 dangling-bond electron in C; the lone electron induced dipoles in oxide and nitrides. These localized and paired electrons exhibit no spin. However, near the broken bonds, situations change entirely. These electrons will be locally pinned and polarized by the deeply and densely trapped bonding and core electrons. These locked electrons contribute no longer to the conductivity but demonstrate measurable magnetism.

In contrast to the magnetism displayed by nanoclusters of noble metals and graphene nanoribbons, the diluted magnetism displayed by nanostructured oxides results mainly from dipoles at surfaces instead of the locked dipoles due to polarization of unpaired electrons. However, in the presence of additional O atoms, these dipoles give away the polarized electrons to form bonds with the former, which leads to a reduction in the magnetic character, being the same to the function of hydrogen surface termination. The Curie temperature higher than 400 K corresponds to the lone-pair interaction of ~ 0.05 eV (600 K), UV radiation reversion corresponds to the removal of surface contamination or dehybridization of sp orbitals, which diminish the surface dipoles. The presence of antibonding dipoles at the open surface may correspond to and elaborate the oxygen vacancy effect as one often refers.

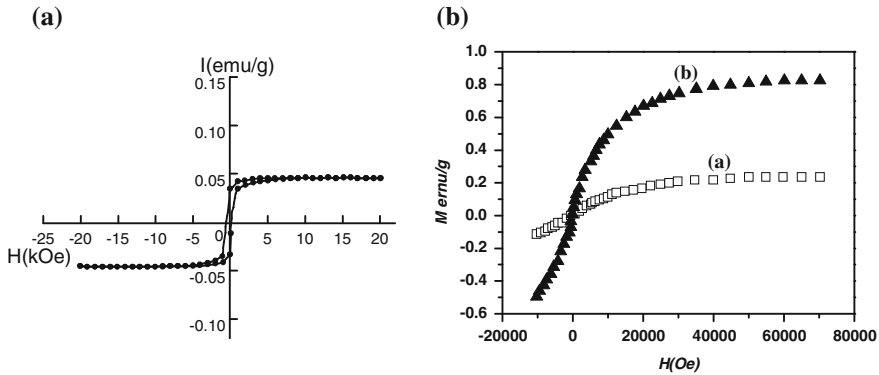


Fig. 20.2 Magnetization curves of **a** the graphite nanostructures prepared by pyrolysis of PVC 1,273 K and measured at 4 K by a SQUID magnetometer under a maximum applied field of 20 kOe [11] and **b** graphene samples fabricated at **a** 400 and **b** 600 °C measured at 2 K [10]. High-temperature preparation generates more defects (Reprinted with permission from [13])

However, there are three reservations on the undercoordination-induced dipole magnetism for practical applications [13]. Firstly, the stability of the magnetrons with energy in the Fermi level and the binding energy is in meV level. Any perturbation by UV irradiation or thermal excitation may demolish them. Secondly, chemisorption by exposing the sample to the environment may decrease the magnetism. Finally, the intensity, as shown in Figs. 20.1 and 20.2, depends on the total number of defects. The weak magnetism may not suffice to the sensitivity requirement of practical devices.

20.3 Conductor-Insulator Transition: E_G Opening and Surface Plasmonics

By combining STM and high-resolution EELS, Jiang et al. [20] found that the bandgap of two-dimensional Al islands grown on Si(111) substrates increases with decreasing island size. On the other hand, these originally highly conductive materials are no longer conducting; they become insulators instead when the solid size is reduced to 2–3 nm [21]. Furthermore, the conduction band splits into two branches in ultrathin films such as Ag, Au, Pd, etc. [22–24]. The separation between the branches expands with the inverse of film thickness.

The transition from conductor to insulator of noble metal clusters corresponded to the expansion of the Kubo gap: $\delta k = 4E_F/3N$, where E_F corresponds to the Fermi energy of the bulk and N to the total number of atoms in the cluster. If the δk is greater than the energy kT at room temperature (1/40 eV), electrons cannot

transit from the lower sublevel to the next higher one, conductor–insulator transition takes place [21]. The bandgap opening was also attributed purely to the size effect arising from the lateral confinement of free electrons in a 2D potential well formed by the islands [20].

As intrinsic contribution, the polarization of the valence electrons near the upper valance edge by the densely trapped bonding and core charges could not be ignored. The mechanism of band splitting by the quantum entrapment and polarization may complement the aforementioned mechanisms. The conductor–insulator transition evidences the strong localization, quantum entrapment and polarization of the conductive electrons. Therefore, both the conductor–insulator transition and the magnetism presence of metal clusters arise from the same origin.

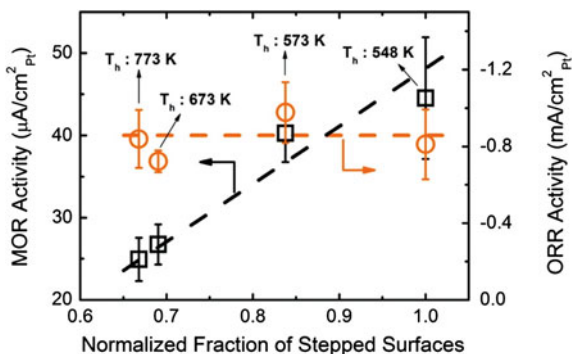
The observed conduction band splitting provides possible mechanism for the surface plasma generation of nanoclusters of noble metals such as Ag and Au with oscillation frequency that is dependent upon the dielectric constant, ϵ_L , charge density, n , and effective mass of electron, m^* , in the surface skin. The plasmonic frequency can be derived as $\omega_p = \sqrt{ne^2/\epsilon_L m^*} \propto eE_G \sqrt{n/m^*}$ as the real part of the dielectric constant ϵ_L is inversely proportional to the square of the bandgap roughly [25, 26]. Therefore, the observed edge and surface states due to band splitting may be responsible for the tunable plasmonic frequency or the surface-enhanced Raman shift intensity of selected metal surfaces and nanostructures. In addition to the classical model of surface plasma oscillation, the model of valence band splitting may provide a band structure perspective, as optical properties of a material are related to the band structure.

20.4 Catalytic Conversion and Enhancement

Automobiles emit pollution mostly in the first 5 min after start-up because Pt- or Pd-based catalysts currently used in automobile exhaust cleanup are inactive below a temperature of 200 °C. The low-temperature gold catalysts are very inactive unless the gold is in the form of particles smaller than 8 nm in diameter. However, self-ignition of Pt nanoparticles happens at room temperature by exposing the particles to methanol/air or ethanol/air gas mixtures. Designing efficient catalysts working at low temperature for both oxidation and reduction is greatly desired for environment protection.

Atomic undercoordination or hetero-coordination forms an optimal way though mechanism remains yet to be clear. With the every third row of Au atoms adding to a fully Au-covered TiO₂ surface could improve the efficiency of CO oxidation at room temperature by a factor of 50 compared with the otherwise fully Au-covered surface [27]. In the case of N₂ dissociation on Ru(0001) surface, the activation energy is 1.5 eV lower at step edges than that on the flat surface, yielding at 500 K an desorption rate that is at least nine orders of magnitude higher on the terraces,

Fig. 20.3 Step-density dependence of the oxygen reduction reaction (ORR, *right axis*) and methanol oxidation reaction (MOR, *left axis*) of 2-nm Pt particles (Reprinted with permission from [40])



as the dissociation is largely influenced by the presence of steps [28]. Similar results have been found for NO decomposition on Ru(0001) [29, 30], H₂ dissociation on Si(001) [31], and low-temperature nitridation of nanopatterned Fe surface [32]. An adatom concentration of a few percent is sufficient to dominate the overall reaction rate in a catalytic process because of the higher reaction rate or the lower activation energies of the undercoordinated atoms. For instance, the first methane dehydrogenation process is highly favored at the Rh-adatom site on Rh(111) surface with respect to step or terrace sites [33, 34]; adatoms deposited on oxides can activate the C–H bond scission [35], the acetylene cyclomerization [36], and the CO oxidation [37]. Preferential ON uptake occurs at Rh(311) and (533) edges [38].

The presence of defects opens new pathways which significantly decrease the thermal stability of the reconstructed Rh(110) surfaces [39]. Although the activity of electrochemical oxidation of carbon monoxide and methanol electro-oxidation can be increased by increasing surface steps on Pt nanoparticles, the oxygen reduction reaction activity of the 2-nm-sized Pt nanoparticle has been found insensitive to the step area, as shown in Fig. 20.3 [40], in contrast to the methanol oxidation reaction activity.

Another relevant contribution determining the chemical reactivity is the surface strain. Jakob et al. [41] and Gsell et al. [42], found preferential oxygen and carbon monoxide adsorption on the stretched regions obtained through subsurface argon implantation on Ru(0001). Winterlin et al. [43] measured an enhanced NO dissociation probability at the local expanded areas of the Ru(0001) dislocations. In the case of a supported nanoparticle catalyst, adsorption on small clusters can induce a considerable stress in the surface region [44]. In any case, the existence of strain, originated by surface defects or by the interaction with the support, seems to be a general feature of surface catalysts. Using an indirect nanoplasmonic sensing method, Langhammer et al. [45] observed strong size effect in studying the hydriding and dehydriding kinetics of Pd nanoparticles in the size range 1.8–5.4 nm. The size trend agrees well with the simulated diffusion-controlled hydriding

kinetics. They attributed this trend to surface tension on hydrogen desorption from the surface layer.

A possible mechanism for the undercoordinated Au catalyst enhancement was proposed as follows [27]. The catalytic activity of gold corresponded entirely to the presence of neutral gold adatoms. These adatoms differ from atoms on bulk gold in three ways that *might* enhance their catalytic activity: (1) They have fewer nearest-neighbor atoms and *possibly* a special bonding geometry to other gold atoms that creates a more reactive orbital. (2) They exhibit quantum size effects that *may* alter the electronic band structure of gold nanoparticles. (3) They *may* undergo electronic modification by interactions with the underlying oxide that cause partial electron donation to the gold cluster. It is noted that the undercoordination-enhanced CO oxidation catalytic reactivity of Au/TiO₂ monatomic chains and Au/oxide [27] nanosolid agrees with the BOLS prediction of the size dependence of diffusivity with activation energy being proportional to atomic cohesive energy or the critical temperature of melting. The similarity in the trends of atomic diffusivity and chemical reactivity indicates that these two identities are correlated in terms of activation energy, though the former is related to atomic dislocation while the latter to charge capturing.

Obviously, the ability of accepting or donating charge of a catalyst plays a key role in the process of catalytic reaction [4]. The directions of electronic transfer between gold atom and the underlying oxide, and between the gold and the CO gas need to be clear, which may form the key to the catalytic activity of these undercoordinated catalysts. An atomic-level understanding of the local energetic behavior of electrons of low-dimensional systems and their mechanical properties become especially important in systems with a large number of highly undercoordinated atoms.

The objective of catalytic enhancement and catalyst design is to modulate the electronic structure in the upper edge of the valence band. One can create vacancies on the valence band edge or can raise the occupied valence states toward the E_F . Therefore, the catalyst can serve as acceptor and donor, respectively, to catching or offering electrons. According to the BOLS-NEP notation, the undercoordination-induced quantum entrapment and non-bonding charge polarization provide a possible means. Strain or stress is a consequence of the surface bond contraction and quantum trapping, and therefore, valence DOS and strain are correlated. Therefore, the involvement of the broken bonds and the non-bonding paired and unpaired electrons play significance roles in the complex process such as $\text{CO} \leftrightarrow \text{Au} \leftrightarrow \text{Oxide}$ reaction.. Suitable size range may exist for Pt and Pd catalysts to be reactive at room temperature without ignition. The electroaffinity is tunable by the cluster size through valence charge polarization or quantum trapping [46]. The stress is related to the quantum entrapment through interatomic binding energy variation. Hence, the ability of accepting or donating charge of a catalyst is controllable by varying atomic coordination.

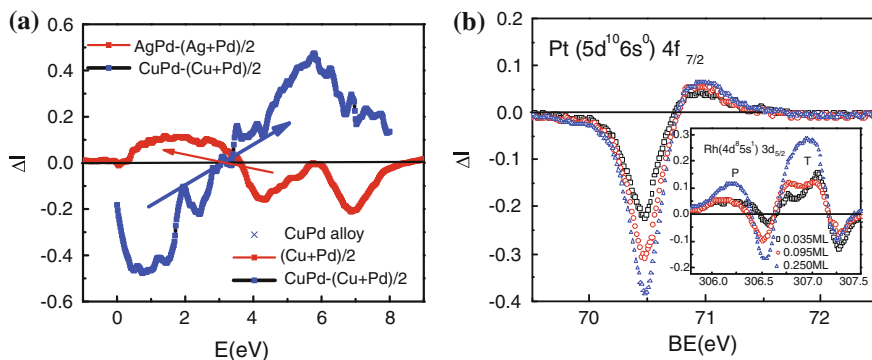


Fig. 20.4 ZPS-purified **a** valence DOS showing the charge flow directions upon Ag/Pd and Cu/Pd alloy formation [47] and **b** core-level DOS of Pt and Rh adatoms [48]. Results suggest that AgPd alloy and Rh adatoms serve as donor-type catalysts because of the polarization while Pt adatoms and CuPd alloy as acceptor-type catalysts because of the dominance of quantum entrapment in the process of catalytic reaction

The purified energy states of the valence DOS of Ag/Pd and Cu/Pd alloys [47], and the core band of Pt and Rh adatoms [48], shown in Fig. 20.4, clarify why these catalysts perform differently. The undercoordinated Pt adatoms and hetero-coordinated CuPd alloy tend to catch electrons from the gaseous specimen other than to donate, which may explain the active oxidation and the inactive reduction and the charge flow direction between the Pt nanocatalyst and the gaseous specimen in the processes of reduction and oxidation (Fig. 20.3). Likewise, CuPd performs the same in the process of reaction. In contrast, Rh adatoms and Ag/Pd alloy donate their valence charge to the gaseous specimen in reaction, a way opposing to Pt and Cu/Pd alloy. This finding provides guidelines and efficient means for the catalyst design and new catalyst identification. As shown in Chap. 13, graphite surface and cobalt clusters may serve as acceptor-type catalysts, while graphite point defects and *W* terrace edges may serve as donor-type catalysts.

DFT calculation results in Fig. 20.5 show the polarization of the valence electrons of gold solid clusters and hollow cages and the activation energies for CO oxidation [49]. The lower the effective atomic CN is, the stronger the polarization and the lower the activation energy will be for CO oxidation of the gold catalyst, which is in accordance with observations for Pt catalysts shown in Fig. 20.3. Bond contraction, core electron entrapment, and valence charge polarization happen only to the outermost two atomic layers [49–51].

Therefore, a high degree of atomic undercoordination by size reduction or proper hetero-coordination by alloy or compound formation could be effective approaches for the efficient catalyst design because the broken-bond- and interface-bond-induced quantum trapping and polarization that determines the direction and extent of valence charge flow between the gaseous specimen and the catalyst.

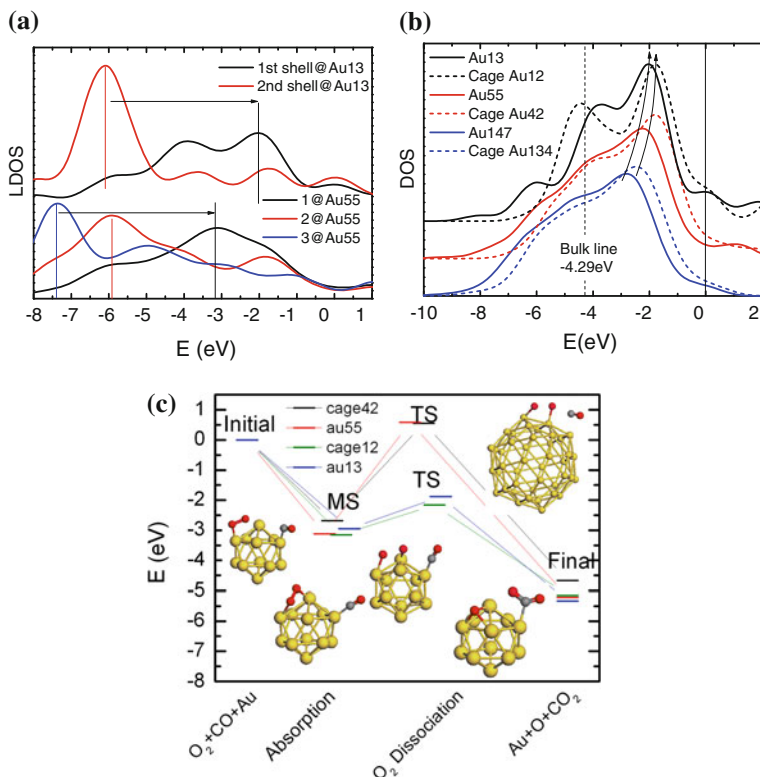


Fig. 20.5 **a** Shell-resolved LDOS of Au₁₃ and Au₅₅ clusters; **b** size-resolved DOS of Au_{13,55,147} solid clusters and Ag_{12,42,134} hollow cages; and **c** activation energies for CO oxidation pertained to different geometric structures of gold [49]

20.5 Superhydrophobicity, Superfluidity, Superlubricity, and Supersolidity

The phenomena of superhydrophobicity, superfluidity, superlubricity, and supersolidity (4S) at the nanometer-sized contacts of liquid–solid or solid–solid share the common characteristics of chemically nonstick, mechanically elastic, and kinetically frictionless in motion. Although the 4S occurrences have been extensively investigated, mechanism behind the common characteristics remains a problem. The BOLS-NEP notation provides an energetic and electronic mechanism indicating that Coulomb repulsion between the ‘electric dipoles pinned in the elastic skins or the solid-like covering sheets of liquid droplets’ dictates the 4S. The localized energy densification makes the skin stiffer, and the densely and tightly trapped bonding charges polarize the non-bonding electrons, if exist, to form locked dipoles. In addition, the *sp* orbit hybridization of F, O, N, or C upon reacting with solid atoms generates non-bonding lone pairs or unpaired edge electrons that

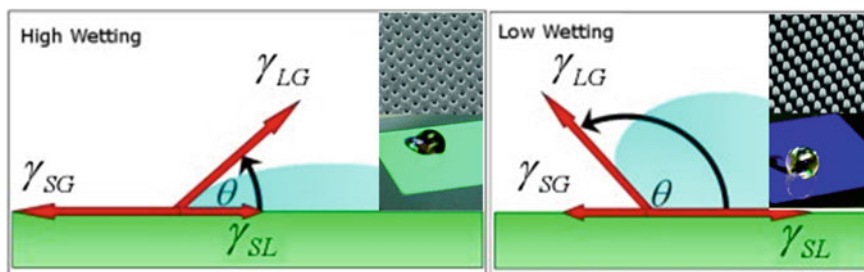


Fig. 20.6 Substrate patterns and the superhydrophobicity of water droplets [59] and the derivative of the Young equation. On the *left*, there is much wetting and the contact angle is small. On the *right*, little wetting and the contact angle is large. The drawing derives Young force equations, $\gamma_{SG} - \gamma_{SL} = \gamma_{LG} \cos \theta$ [60]

induce dipoles directing into the open end of a surface. The dipoles can be, however, demolished by UV radiation, thermal excitation, or excessively applied compression due to ionization or sp orbit dehybridization. Such a Coulomb repulsion between the negatively charged skins of the contacting objects not only lowers the effective contacting force and the friction but also prevents charge from being exchanged between the counterparts of the contact. Being similar to magnetic levitation, such Coulomb repulsion provides the force driving the 4S.

20.5.1 Observations

20.5.1.1 Superhydrophobicity–Hydrophilicity Transition

Superhydrophobic materials have surfaces that are extremely difficult to wet, with water contact angles in excess of 150° or even greater, see Fig. 20.6 shows that surfaces with ultrahydrophobicity have aroused much interest with their potential applications in self-cleaning coatings, microfluidics, and biocompatible materials and so on. Many physical–chemical processes, such as adsorption, lubrication, adhesion, dispersion, friction, etc., are closely related to the wettability of materials surfaces [52, 53]. Examples of hydrophobic molecules include alkanes, oils, fats, wax, and greasy and organic substances with C, N, O, or F as the key constituent element.

Many of these superhydrophobic materials found in nature display characteristics fulfilling Cassie–Baxters’ law [54] stating that the surface contact angle can be increased by simply roughing up the surface, i.e., the surface roughness and the contact area are suggested to be the factors of dominance. For instance, fluids can slip frictionlessly past pockets of air between textured surfaces with micrometer-scale grooves or posts of tiny distances [55]. The slip length for water is almost ten times longer than previously achieved, indicating that engineered surfaces can significantly reduce drag in fluid systems. On the base of Cassie–Baxters’ law and

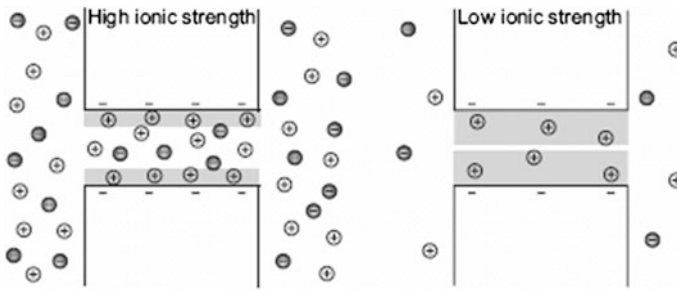


Fig. 20.7 Electrical double-layer (EDL) mechanism, shaded in gray, at high ionic strength, it is thin, allowing co-ions and counterions to pass through the nanochannel. At low ionic strength, the EDL thickness increases, resulting in a counterion-selective nanochannels [65]

thermodynamics considerations, Fang et al. [56] and Li et al. [57] designed tunable superhydrophobic surfaces to control the directional motion of water droplets by varying the pillar width and spacing simultaneously. Varying the gradient of the stiffness of a microbeam could also drive directional movement of liquid droplets on a microbeam [58].

A water strider statically standing on water can bear a load up to ten times its body weight with its middle and hind legs, which tread deep puddles without piercing the water surface [61]. This fact illustrates the superhydrophobicity of the water strider legs due to 'biowax' coatings. Another comparative experiment [62] using the real water strider legs and artificial legs made of wax-coated steel wires revealed that the adaptive deformation capacity of the real leg through its three joints makes a more important contribution to the superior load-bearing ability than the superhydrophobicity.

What is even more amazing is that the hydrophobic surface can switch reversibly between superhydrophobicity and superhydrophilicity when the solid surface is subject to UV radiation [63], which results in electron-hole pair creation [64]. After being stored in the dark over an extended period, the hydrophilicity is once again lost.

20.5.1.2 Superfluidity in Nanochannels

The transport of fluid in and around nanometer-sized objects with at least one characteristic dimension below 100 nm enables the superfluidic occurrence that is impossible on bigger length scales [65]. Nanofluids have significantly greater thermal and mass conductivity in nanochannels compared with their base fluids [66]. The difference between the nanofluid and the base fluid is the high value of surface-to-volume ratio that increases with the miniaturization of the dimensions of both the fluid and the channel cavity in which the fluid is flowing. This high ratio in nanochannels results in surface-charge-governed transport, which allows ion separation and is described by an electrokinetic theory of electrical double layer (EDL)

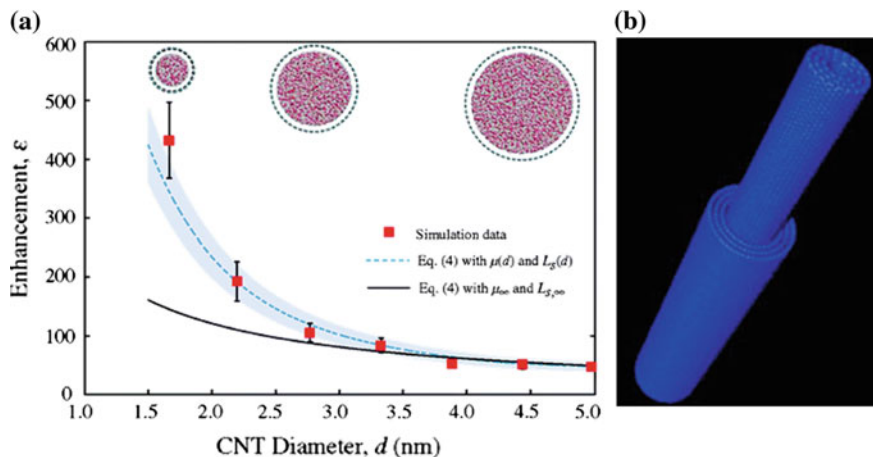


Fig. 20.8 **a** Superfluidity of water droplet in CNTs of different diameters [68] and **b** ultralow-friction nanoscale linear bearing made of multi-walled CNT [69]

scheme, as illustrated in Fig. 20.7 [67]. The EDL channel can be operated as field-effect transistors to detect chemical and biological species label free, and transport through nanochannels leads to analyte separation and new phenomena when the EDL thickness becomes comparable to the smallest channel opening.

On the other hand, the rate of the pressure-driven water flow through carbon nanotubes (CNTs) is orders higher than predictions by conventional fluid flow theory, see Fig. 20.8 [68]. The thinner the channel cavity is, the faster the fluid flow rate will be under the same pressure [70]. This high fluid velocity results from an almost frictionless interface between the CNT wall and the fluid droplets [71, 72]. A MD calculation [73] suggested that water flow in CNT could generate a constant voltage difference of several mV between the two ends of a CNT, due to interactions between the water dipole chains and charge carriers in the CNT, which might also contribute to the abnormal frictionless fluid flow in the CNT.

20.5.1.3 Superlubricity in Dry Sliding: Atomistic Friction

More observations that are fascinating include the ultralow-friction linear bearing of CNTs and the superlubricity at dry nanocontacts sliding in high vacuum [74, 75]. TEM revealed that the inner walls of a multi-walled CNT can slide back and forth with respect to the outer walls of the CNT, being free from wear for all cycles of motion (see Fig. 20.8b) [69]. Surface energy calculations suggested that the force retracting the core nanotubes back into the outer tubes was 9 nN, being much lower than the van der Waals forces pulling the core nanotubes back into their sheath. The removal of the outer walls of the MWCNT corresponded to the highly localized dissipation at defect scattering sites, located primarily at the ends of the tube.

The demonstration of ultralow friction between multi-walled CNT layers is a valuable confirmation that they will be useful mechanical components in molecular nanotechnology such as molecular bearing.

The occurrence of quantum friction is a kinetic process of energy dissipation ($E = f_r \cdot s$ with f_r being the friction force and s the sliding distance) due to the phonon (heat) and electron excitation (electron–hole pair production) during sliding [76]. A state of ultralow friction is reached when a sharp tip slides over a flat surface and the applied pressure is below a certain threshold, whose value is dependent on the surface potential sensed by the tip and the stiffness of the contacting materials [73, 77, 78].

A comparative study of hydrogen- and deuterium-terminated single-crystal diamond and silicon surfaces revealed that the hydrogenated surface (terminated with H^+) exhibited higher friction than the surface passivated with $^2H^+$. The additional neutron in the $^2H^+$ should play a certain yet unclear role of significance because of the possible adsorbate size difference [76]. A remarkable dependence of the friction force on carrier type and concentration has been discovered by Park et al. [79] on doped silicon substrates. An experiment of a biased conductive TiN-coated tip of an atomic force microscope sliding on a Si substrate with patterned p and n stripes revealed that charge depletion or accumulation results in substantial differences in the friction force. A positive bias applied to the p region causes a substantial increase in the friction force compared to the n region because of the accumulation of holes (+charged) in the p region. No variation of friction force was resolvable between n and p regions under negative bias. Both observations [76, 79] indicate clearly that the positively charged (H^+) tip or substrate (electronic holes +) would induce high friction force.

The superlubricity phenomenon was explained using the classical Prandtl–Tomlinson (PT) model [80, 81] and its extensions, including thermal activation, temporal and spatial variations of the surface corrugation, and multiple contact effects [77]. Progress suggests that the friction force depends linearly on the number of atoms that interact chemically across the contact [82]. According to the one-dimensional PT model, the slider atoms feel the periodic potential of the substrate surface atoms as they slide over them, experiencing a net force that is the sum of individual instantaneous friction force on each atom resulting from the gradient of the periodic potential.

20.5.1.4 Supersolidity of 4He : Superelasticity and Superfluidity

At temperature below 200 mK [83], Helium 4 (4He) crystal is readily decoupled into fragments in a torsional oscillator to exhibit superfluidic nature—frictionless motion without viscosity [84, 85]; meanwhile, the 4He crystal fragments are stiffer than expected and hence react elastically to a shear stress [86]. The individual segment of the 4He crystal would be thus both superelastic and superfluidic in motion.

The superfluidity of 4He solid is usually described in terms of Bose–Einstein condensation or quantum statistics in energy space. All particles occupy the lowest

energy states simultaneously. A scenario in real space is lacking though the crystal defect has been recognized as the key to the supersolidity [87]. The quantum defects such as atomic vacancies are of the order of one nm size or thereabouts [88], and the supersolidity is related to structural disorders [89] such as dislocations, vacancies, grain boundaries, or ill-crystallized regions where the undercoordinated atoms dominate. According to Anderson [87], the observations are conjectured to be describable in terms of a rarified Gross-Pitaevskii superfluid of vacancies, with a transition temperature of about 50 mK, whose density is locally enhanced by crystal imperfections. The observations can be affected by this density enhancement. Therefore, disorder and defects that could enhance the local density appear to play an important yet uncertain role in the supersolidity of ^4He crystals [90].

The superfluidity of ^4He solid is related to the quantum defects such as atomic vacancies of 1 nm size or around [91], and the supersolidity is related to structural disorder [89] such as dislocations, grain boundaries, or ill-crystallized regions. According to Pollet et al. [91], inside a dislocation or a grain boundary, the local stress is anisotropic, which is sufficient to bring the vacancy energy to zero, so that the defect is invaded by vacancies that are mobile and superfluidic. Solid ^4He could contain a network of defects, and if these defects are connected to each other, mass could flow from one side of the crystal to the other without friction. On the other hand, the disorder-induced stiffening could be the result of dislocations becoming pinned by isotopic impurities (i.e., ^3He atoms even at very small concentrations).

20.5.2 Known Mechanisms

The following theories describe the underlying mechanism for the 4S:

1. Young's theory in terms of surface tension and interface energies [92].
2. Wenzel-Cassie-Baxters' law [93, 94] of surface roughness for superhydrophobicity.
3. EDL scheme for the superfluidity [67].
4. PT theory [81, 95] of the superposition of the slope of atomic potential and multiple contact effects [77] for atomic scale quantum friction.
5. Anderson's theory [87] of local vacancy density enhancement of crystal imperfections and the Bose–Einstein condensation theory for the superelasticity and superfluidity of the individual segment of the ^4He crystal supersolidity.

For instance, Young equation formulates the surface wetting from the perspective of force equilibrium, as illustrated in Fig. 20.6:

$$\cos \theta = \frac{\gamma_{\text{SG}} - \gamma_{\text{SL}}}{\gamma_{\text{LG}}}$$

where S, L, and G represents the solid, liquid, and gaseous phases, respectively, and γ is the surface tension resulting from energy densification in the surface skin.

These models are working well for certain occurrences such as a water droplet resting on the repellent lotus leaf [96] and a water strider standing on the water surface [61, 62]. However, some amazing observations are beyond the expectation of these theories.

The 4S occurrences result from the reduction in the friction force ($f_r = \mu N$ with μ being the friction coefficient and N the contacting force). The lowering of the f_r will reduce the process of friction or the extent of phonon and electron excitation. One surprising fact is that these 4S effects share a general identity of nonstick and frictionless motion with lowered effective contacting pressure and reduced friction coefficient. The 4S phenomena must share a common elastic and repulsive origin in addition to the energetic and geometric descriptions of the existing models. Considerations from the perspectives of surface roughness, air pocket, and surface energy seem insufficient because the chemistry and the charge identities do alter at the surface skin up to two interatomic spacings [97]. In particular, the hydrophobicity–hydrophilicity recycling effect caused by UV irradiation and the subsequent dark aging is beyond the scope of Cassie’s law and the PT mechanism of air pocket dominance. Furthermore, the superhydrophobicity of alkanes, oils, fats, wax, and the greasy and organic substances is independent of the surface roughness. Although the crystal defects have been recognized as the key to the super-solidity of ^4He solid, correlation between the defects and the superelasticity and superfluidity is yet to be established. Therefore, a deeper insight into the chemical nature of the surfaces is necessary for one to gain a consistent understanding of the origin for the 4S.

20.5.3 BOLS-NEP Formulation

The currently described knowledge about localized charge entrapment and polarization associated with the skin of both the liquid and the solid specimen provides an electronic mechanism for the 4S. According to the BOLS-NEP notation, the small fluidic drop can be viewed as a liquid core covered with a solid-like, densely charged, and elastic sheet with pinned dipoles. The energy density, charge density, polarizability, and the trap depth are bond order dependence.

At the surface of skin depth, the curvature (K^{-1}) dependence of the effective atomic CN (z_i), bond length (d_i), charge density (n_i), elastic modulus (B_i) or energy density, and the potential trap depth (E_i) follow the relations:

$$\left\{ \begin{array}{ll} z_1 = 4(1 - 0.75 \text{ K}^{-1}); z_2 = z_1 + 2 & \text{(Effective-coordination)} \\ d_i = C_i d = 2d[1 + \exp((12 - z_i)/(8z_i))]^{-1} & \text{(Bond-contraction- coefficient)} \\ n_i = n C_i^{-3} & \text{(Charge-density)} \\ B_i = \mathbf{B} C_i^{-(m+3)} & \text{(Bulk-modulus)} \\ E_i = E_b C_i^{-m} & \text{(Potential-trap-depth)} \end{array} \right.$$

Repellant force exists between the densely trapped, the consequently polarized surface, and the wall of the channel or the patterned nanostructures. In the outermost two atomic layers of a smaller droplet, the energy density is higher and the energy level is deeper, the effect of core electron entrapment and dipole pinning is even more significant. Therefore, a solid-like shell with densely trapped and polarized electrons interacts with the environment in a different manner from that of bigger drops. Accordingly, the inner surface of the microchannel also got a high-density charge because of the broken-bond-induced entrapment. Progress [98] suggested that the surface charge density increases with the inverse of the droplet size. This mechanism also applies to the inner wall of the pipe.

20.5.4 Electrolevitation

20.5.4.1 Dipole Formation and Elastic Enhancement

The spontaneous lattice strain and bond energy gain will enhance the surface elasticity by $\Delta B_i/B_b = C_i^{-(m+3)} - 1 > 0$, charge density by $\Delta n_i/n_b = C_i^{-3} - 1 > 0$, and the potential well depth by $\Delta E_i/E_b = C_i^{-m} - 1 > 0$. If taking $z_1 = 4$ and $m = 4$ for a flat compound surface, $C_1 = 0.88$, the B_1 in the first atomic spacing is $B_1/B_b = 0.88^{-7} \sim 2.5$ times that of the bulk. Similarly, the charge density is $n_i/n_b = C_i^{-3} = 0.88^{-3} = 1.47$ times that of the bulk. The potential well trap depth is $E_i/E_b = C_i^{-m} = 1.14$ for $m = 1$ and 1.67 for $m = 4$ times the original depth. MD calculations [99] suggested that the dynamic wetting and electrowetting proceed through the formation of a nonslip and solid-like monolayer precursor water film on gold substrate, which coincides with the BOLS-NEP expectation on the 4S: solid-like elastic skin with electric force dominance. Bond contraction, core electron entrapment, and valence charge polarization happen only to the outermost two atomic layers [49–51].

Figure 20.9a shows the theoretically predicted curvature (K^{-1}) dependence of the skin charge density, elasticity (energy density), and potential trap depth of the outermost shell of a spherical dot. The volume average corresponds to the size dependence of the elastic modulus such as ZnO [100] and the core-level shift of nanostructures [101]. As illustrated in Fig. 20.9b, the likely charged (green dots) drop and the wall surface are repel each other. The droplet will lose its viscosity and becomes frictionless unless the surface dipoles are removed. Such a system runs in a way more like a ‘magnetic levitation train.’ Water confined between silica plates maintains the lubricity under the normal pressure of 1.7 MPa for the untreated silica at pull, but the lubricity increases at 0.4 MPa for the treated silica plate [102]. This finding indicates that hydrophilic interface produces no surface effect and the interface between the untreated silica and water is indeed hydrophobic. Using specular X-ray reflectivity analysis, Uysal et al. [103] confirmed that gap exists between the water the hydrophobic substrate. Therefore, the repelling of

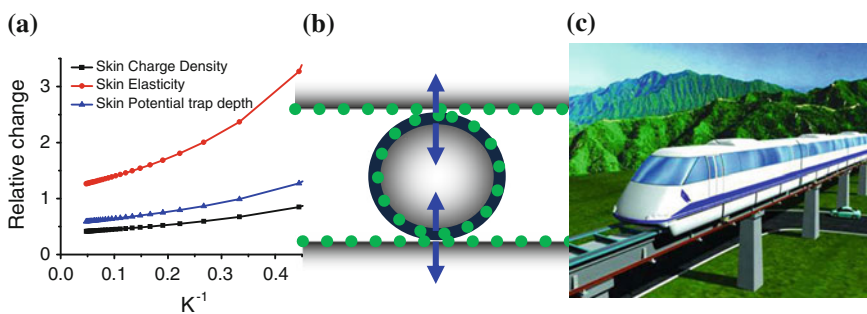


Fig. 20.9 ‘Electric levitation’ mechanism for the 4S. **a** Curvature (K^{-1}) dependence of the skin charge density, elasticity (energy density), and potential trap depth of the outermost shell of a spherical dot. **b** Repulsion between like charges (*dots*) of dipoles pinned in the surfaces. **c** ‘Electric levitation’ mechanism suggests that surface dipoles induced by the local strain and quantum entrapment or by the lone pairs of O, N, and F play important roles in the skin supersolidity and the 4S

the like charges at both the channel and the solid-like drop surfaces governs the observed superfluidity.

The superhydrophobicity phenomenon can be explained from the viewpoints of surface chemistry, energy, and charge density enhancement. If the air pockets beneath a droplet on a sinusoidal substrate are open to the atmosphere, the superhydrophobic state can exist only when the substrate is hydrophobic, and the geometric parameters of the microstructure have a great influence on the wetting behavior. Being similar to the superfluidity, polarization of the surface or the presence of lone-pair electrons happens to both the fluidic drop and the material. The charged surface repels the ambient charged particles, such as water molecules, to result in superhydrophobicity. The UV radiation removes the polarized charges, and the dark storage recovers the surface dipoles, being the same as the surface magnetism of noble metal clusters and the dilute magnetism of oxide nanostructures [4, 17].

The mechanism of interface electric repulsion also applies to the frictionless CNT linear bearing and the superlubricity of nanocontacts. In fact, the bond contraction happens to the CNT of limited number of walls. Bonds near the open ends contract even further. Densification of both the σ - and π -electrons takes place to all the walls; the repulsion between the densely packed and localized like charges will reduce the friction force substantially, while the electrostatic forces of the additionally densely charged CNT ends may provide force of retraction motion and oscillation. In the nanocontacts, the saturated potential barrier due to the skin charge trapping of the nanocontacts also provide a repulsion force between the contacts.

The Coulomb repulsion between the ‘locked dipoles in the stiffened skins’ of the small grains could help in understanding the puzzle of ^4He crystal supersolidity in real space. The densification of energy corresponds to the enhancement of elasticity, which stiffens the solid skin allowing the ^4He segment to react elastically to a shear stress; the repulsion between the charged surfaces makes the

frictionless motion. The extremely weak interatomic interaction between the He atoms makes the ^4He atoms or grains nonstick—more like hard spheres with close-filled electronic shells. The nonstick interaction between grains will lower the friction coefficient. Lattice contraction of the supersolid ^4He segments is expected to happen, though this contraction may be too tiny [84] and needs to be verified experimentally.

20.5.4.2 Surface Dipole Depletion

The UV radiation with excitation energy around 3.0 eV could break chemical bonds and ionize surface atoms, which could turn the hydrophobic surface to be hydrophilic, as it has widely been observed. Ar^+ sputtering the surface is expected to have the same function of removing dipole or monopole temporarily. If the polarized electrons were removed by UV irradiation, sputtering, or thermal excitation, the 4S characteristics would be lost. Aging of the specimen will recover the surface charges. The effect of UV radiation reversing effect is the same as that observed in the surface magnetism of noble metal clusters and the dilute magnetism of oxide nanostructures [4, 6, 17]. Thermal annealing at temperatures of 600 K or above, oxygen orbital dehybridization takes place and the lone pair induced Cu surface dipoles vanish [104]. However, aging the samples in the ambient will recover the sp hybridization and the dipoles as well. Surface bias to a certain extent may also cause the depletion of the locked charges though this expectation is subject to verification. Overloaded pressure in the dry sliding will overcome the Coulomb repulsion, as the energy dissipation by phonon and electron excitation could occur under the applied pressure. On the other hand, a sufficiently large difference in the electroaffinity between the contact media, chemical bond may form under a certain conditions such as heating, pressure, or electric field, the interface will be adherent.

20.5.4.3 Superfluidity and Supersolidity of ^4He Crystal

Encouragingly, the understanding of superfluidity, superhydrophobicity, and superlubricity at nanometer-scale contacts discussed here could provide a supplementary mechanism for the superfluidity and supersolidity of ^4He crystal. Repulsion between the ‘electric monopoles locked in the stiffened skins’ of the small grains could help in solving this puzzle. Broken-bond-induced local strain and quantum entrapment lead to a densification of charge and energy in the skin of a few atomic layer thick. The densification of energy corresponds to the enhancement of the elasticity, which stiffens the solid skin allowing the ^4He segment to react elastically to a shear stress. The repulsion between the densely entrapped electrons makes the motion frictionless. ^4He crystals lack the non-bonding electrons because of the close atomic shells. Therefore, the broken bonds serve as not only centers that initiate structure failure but also provide sites for

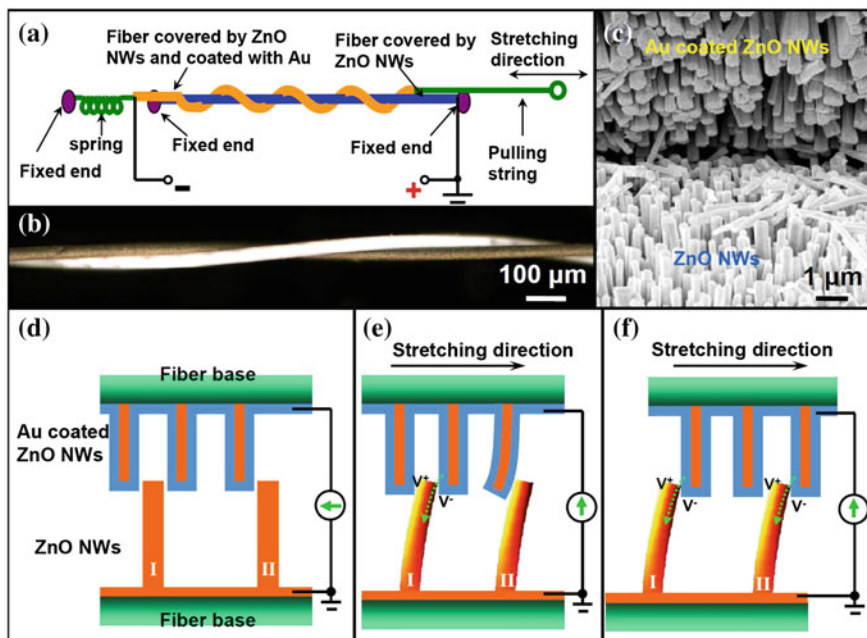


Fig. 20.10 Illustration of the electricity harvesting device based on **a** tooth-like friction of two wires with **b** and **c** brushes made of nanofibres (printed with permission from [106]). A low-frequency, external vibration/friction/pulling force drives the textile-fiber based piezoelectric nanogenerator. **b** An optical image of a pair of entangled fibers, one of which is coated with Au (in darker contrast). **c** SEM image at the “teeth-to-teeth” interface of two fibers covered by NWs, with the top one coated with Au. **d** The NWs and top fiber are completely covered by a layer of Au. **e-f** Dislocation of the brushes creates piezoelectric potential across the NW I and II.

pinning dislocations by charge and energy entrapment, which could be responsible for the superfluidity and supersolidity as observed.

The interatomic ‘bond’ breaks easily for ^4He crystals, which requires energy at the critical point of 4.2 K for liquid–vapor transition in the order of $1/3,000$ eV, much smaller than a typical van der Waals bond of 0.1 eV or around. The extremely weak interatomic interaction through charge sharing makes the ^4He atoms or grains nonstick.

20.6 Electric Energy Harvesting

ZnO nanocrystals demonstrate strong polarization, see Fig. 16.11 [105], which ensures nano-ZnO a material with dilute magnetism and catalytic active. Meanwhile, nano-ZnO exhibits piezoelectricity, which has been used for energy harvesting devices. Fig. 20.10 illustrates the fiber nanogenerator of electricity by

making use of the low frequency mechanical movements [106]. Two entangled fibers form a pair of “teeth-to-teeth” brushes, with one fiber covered with Au coated nanowires and the other is made of bare ZnO nanowires. A relative brushing of the NWs seeded at the two fibers produces electricity owing to a coupled piezoelectric-semiconductor, which is effective only at the nanoscale. Using a bundle of NW yarns can improve fiber’s conductivity and the output current. Stretching the ZnO nanowire could enhance the piezoelectric effect and generates up to 209 V with inclusion of vertically aligned PZT nanofibers [107], which is large enough to directly lighten up a commercial light-emitting diode without energy storage process [108].

20.7 Summary

The undercoordination- and hetero-coordination-induced quantum entrapment and polarization of the non-bonding lone-electron pairs by the entrapped core electrons are indeed significant. The impact of these often overlooked interactions and the associated energy states in the mid-gap region is enormous in particular at the nanoscale. These weak interactions and non-bonding charge can never be neglected when we attend to substances at the nanoscale. The following summarizes the understandings of the emerging properties of substance at the nanoscale:

1. Undercoordination induces global entrapment by subjective polarization depending on the electronic configuration of the outermost electron shell of the substance.
2. The localization and polarization of the non-bonding electrons with nonzero spin are responsible for the dilute magnetism and conductor–insulator transition at the nanoscale.
3. The dominance of entrapment or polarization creates the catalytic attributes of the otherwise inert noble metals at the nanoscale.
4. The coupling of energy densification (solid like and high elasticity), quantum entrapment, and polarization dictates the interface 4S.
5. Curvature enhancement, or lowers the atomic CN could strengthen these emerging properties; however, Hydrogenation and UV irradiation could annihilate the lone electrons and hence eliminates the emerging properties of dilute magnetism, catalytic ability, and the 4S—electric levitation.
6. These weak interactions and non-bonding electrons also form basic function groups in the biologic, organic, and inorganic species.
7. Localized polarization of nonbonding electrons by both the lone pairs in compounds and by the skin and edge entrapped bonding electrons should contribute to the edge and surface states that form the key to the topological insulator, high-TC superconductors, and thermoelectric devices.

Utilizing the concepts of these unconventional types of weak interactions and their energetics, we can look forward to designing and synthesizing new functional materials. The approach of studying the formation, dissociation, relaxation, and vibration of bonds and non-bonds, and associated energetics and dynamics of electron transportation, polarization, localization, and densification effects on a microscopic level is essential to facilitating a deeper understanding of the macroscopic behavior of functional materials. Finding and grasping with factors controlling the non-bonding states and making them of use in functional materials design will form, in the near future, a subject area of ‘Nonbonding Electronics and Energetics,’ which would be even more challenging, fascinating, promising, and rewarding than dealing with the core or valence electrons alone.

References

1. A.J. Cox, J.G. Louderback, S.E. Apsel, L.A. Bloomfield, Magnetic in 4d-transition metal-clusters. *Phys. Rev. B* **49**(17), 12295–12298 (1994)
2. T. Okamoto, H. Maki, Y. Oba, S. Yabuuchi, T. Sato, E. Ohta, Electrical detection of ferromagnetism in Pd nanoparticles by magnetoresistance measurement. *J. Appl. Phys.* **106**(2), 023908 (2009)
3. J. Bartolome, F. Bartolome, L.M. Garcia, E. Roduner, Y. Akdogan, F. Wilhelm, A. Rogalev, Magnetization of Pt-13 clusters supported in a NaY zeolite: a XANES and XMCD study. *Phys. Rev. B* **80**(1), 014404 (2009)
4. E. Roduner, Size matters: why nanomaterials are different. *Chem. Soc. Rev.* **35**(7), 583–592 (2006)
5. W.H. Zhong, C.Q. Sun, S. Li, H.L. Bai, E.Y. Jiang, Impact of bond-order loss on surface and nanosolid magnetism. *Acta Mater.* **53**(11), 3207–3214 (2005)
6. X. Liu, M. Bauer, H. Bertagnolli, E. Roduner, J. van Slageren, F. Phillipp, Structure and magnetization of small monodisperse platinum clusters. *Phys. Rev. Lett.* **97**(25), 253401 (2006)
7. Y. Yamamoto, T. Miura, Y. Nakae, T. Teranishi, M. Miyake, H. Hori, Magnetic properties of the noble metal nanoparticles protected by polymer. *Phys. B-Condens. Matter* **329**, 1183–1184 (2003)
8. A.J. Cox, J.G. Louderback, L.A. Bloomfield, Experimental-observation of magnetism in Rhodium clusters. *Phys. Rev. Lett.* **71**(6), 923–926 (1993)
9. C.Q. Sun, Size dependence of nanostructures: impact of bond order deficiency. *Prog. Solid State Chem.* **35**(1), 1–159 (2007)
10. Y. Wang, Y. Huang, Y. Song, X.Y. Zhang, Y.F. Ma, J.J. Liang, Y.S. Chen, Room-temperature ferromagnetism of graphene. *Nano. Lett.* **9**(1), 220–224 (2009)
11. T. Saito, Magnetic properties of carbon materials prepared from polyvinyl chloride. *J. Appl. Phys.* **105**(1), 013902 (2009)
12. O.V. Zazyev, Magnetism in disordered graphene and irradiated graphite. *Phys. Rev. Lett.* **101**(3), 037203 (2008)
13. C.Q. Sun, Dominance of broken bonds and nonbonding electrons at the nanoscale. *Nanoscale* **2**(10), 1930–1961 (2010)
14. X. Zhang, Y.G. Nie, W.T. Zheng, J.L. Kuo, C.Q. Sun, Discriminative generation and hydrogen modulation of the Dirac-Fermi polarons at graphene edges and atomic vacancies. *Carbon* **49**(11), 3615–3621 (2011)
15. C. Liu, F. Yun, H. Morkoc, Ferromagnetism of ZnO and GaN: a review. *J. Mater. Sci.-Mater. Electron.* **16**(9), 555–597 (2005)

16. Y. Matsumoto, M. Murakami, T. Shono, T. Hasegawa, T. Fukumura, M. Kawasaki, P. Ahmet, T. Chikyow, S. Koshihara, H. Koinuma, Room-temperature ferromagnetism in transparent transition metal-doped titanium dioxide. *Science* **291**(5505), 854–856 (2001)
17. J.M.D. Coey, Dilute magnetic oxides. *Curr. Opin. Solid State Mater. Sci.* **10**(2), 83–92 (2006)
18. F. Pan, C. Song, X.J. Liu, Y.C. Yang, F. Zeng, Ferromagnetism and possible application in spintronics of transition-metal-doped ZnO films. *Mater. Sci. Eng. R-Reports* **62**(1), 1–35 (2008)
19. J.M.D. Coey, M. Venkatesan, C.B. Fitzgerald, Donor impurity band exchange in dilute ferromagnetic oxides. *Nat. Mater.* **4**(2), 173–179 (2005)
20. Y. Jiang, K.H. Wu, J. Ma, B. Wu, E.G. Wang, P. Ebert, Quantum size effects in the nonmetal to metal transition of two-dimensional Al islands. *Phys. Rev. B* **76**(23), 235434 (2007)
21. C.N.R. Rao, G.U. Kulkarni, P.J. Thomas, P.P. Edwards, Size-dependent chemistry: properties of nanocrystals. *Chem. -a Eur. J.* **8**(1), 29–35 (2002)
22. B. Wang, X.D. Xiao, X.X. Huang, P. Sheng, J.G. Hou, Single-electron tunneling study of two-dimensional gold clusters. *Appl. Phys. Lett.* **77**(8), 1179–1181 (2000)
23. B. Wang, K.D. Wang, W. Lu, J.L. Yang, J.G. Hou, Size-dependent tunneling differential conductance spectra of crystalline Pd nanoparticles. *Phys. Rev. B* **70**(20), 205411 (2004)
24. I. Matsuda, C. Liu, T. Hirahara, M. Ueno, T. Tanikawa, T. Kanagawa, R. Hobarra, S. Yamazaki, S. Hasegawa, Electron-phonon interaction and localization of surface-state carriers in a metallic monolayer. *Phys. Rev. Lett.* **99**(14), 146805 (2007)
25. M.A. Omar, *Elementary Solid State Physics: Principles and Applications* (Addison-Wesley, New York, 1993)
26. L.K. Pan, C.Q. Sun, T.P. Chen, S. Li, C.M. Li, B.K. Tay, Dielectric suppression of nanosolid silicon. *Nanotechnology* **15**(12), 1802–1806 (2004)
27. M.S. Chen, D.W. Goodman, The structure of catalytically active gold on Titania. *Science* **306**(5694), 252–255 (2004)
28. S. Dahl, A. Logadottir, R.C. Egeberg, J.H. Larsen, I. Chorkendorff, E. Tornqvist, J.K. Nørskov, Role of steps in N-2 activation on Ru(0001). *Phys. Rev. Lett.* **83**(9), 1814–1817 (1999)
29. B. Hammer, Bond activation at monatomic steps: NO dissociation at corrugated Ru(0001). *Phys. Rev. Lett.* **83**(18), 3681 (1999)
30. T. Zambelli, J. Winterlin, J. Trost, G. Ertl, Identification of the “active sites” of a surface-catalyzed reaction. *Science* **273**(5282), 1688–1690 (1996)
31. P. Kratzer, E. Pehlke, M. Scheffler, M.B. Raschke, U. Hofer, Highly site-specific H-2 adsorption on vicinal Si(001) surfaces. *Phys. Rev. Lett.* **81**(25), 5596–5599 (1998)
32. W.P. Tong, N.R. Tao, Z.B. Wang, J. Lu, K. Lu, Nitriding iron at lower temperatures. *Science* **299**(5607), 686–688 (2003)
33. G. Fratesi, S. de Gironcoli, Analysis of methane-to-methanol conversion on clean and defective Rh surfaces. *J. Chem. Phys.* **125**(4), 044701 (2006)
34. A. Kokalj, N. Bonini, C. Sbraccia, S. de Gironcoli, S. Baroni, Engineering the reactivity of metal catalysts: a model study of methane dehydrogenation on Rh(111). *J. Am. Chem. Soc.* **126**(51), 16732–16733 (2004)
35. S. Abbet, A. Sanchez, U. Heiz, W.D. Schneider, A.M. Ferrari, G. Pacchioni, N. Rosch, Acetylene cyclotrimerization on supported size-selected Pd_n clusters (1 ≤ n ≤ 30): one atom is enough! *J. Am. Chem. Soc.* **122**(14), 3453–3457 (2000)
36. S. Abbet, U. Heiz, H. Hakkinen, U. Landman, CO oxidation on a single Pd atom supported on magnesia. *Phys. Rev. Lett.* **86**(26), 5950–5953 (2001)
37. C.J. Zhang, P. Hu, The possibility of single C–H bond activation in CH₄ on a MoO₃-supported Pt catalyst: a density functional theory study. *J. Chem. Phys.* **116**(10), 4281–4285 (2002)
38. F. Esch, A. Baraldi, C. Comelli, S. Lizzit, M. Kiskinova, P.D. Cobden, B.E. Nieuwenhuys, Atomic nitrogen on steps: a fast x-ray photoelectron spectroscopy study of the NO uptake on Rh(533), Rh(311), and Rh(111). *J. Chem. Phys.* **110**(8), 4013–4019 (1999)

39. A. Baraldi, S. Lizzit, F. Bondino, G. Comelli, R. Rosei, C. Sbraccia, N. Bonini, S. Baroni, A. Mikkelsen, J.N. Andersen, Thermal stability of the Rh(110) missing-row reconstruction: Combination of real-time core-level spectroscopy and ab initio modeling. *Phys. Rev. B* **72**(7), 075417 (2005)
40. S.W. Lee, S. Chen, J. Suntivich, K. Sasaki, R.R. Adzic, Y. Shao-Horn, Role of surface steps of Pt nanoparticles on the electrochemical activity for oxygen reduction. *J. Phys. Chem. Lett.* **1**, 1316–1320 (2010)
41. P. Jakob, M. Gsell, D. Menzel, Interactions of adsorbates with locally strained substrate lattices. *J. Chem. Phys.* **114**(22), 10075–10085 (2001)
42. M. Gsell, P. Jakob, D. Menzel, Effect of substrate strain on adsorption. *Science* **280**(5364), 717–720 (1998)
43. J. Wintterlin, T. Zambelli, J. Trost, J. Greeley, M. Mavrikakis, Atomic-scale evidence for an enhanced catalytic reactivity of stretched surfaces. *Angew. Chem. Int. Ed.* **42**(25), 2850–2853 (2003)
44. B. Richter, H. Kuhlenbeck, H.J. Freund, P.S. Bagus, Cluster core-level binding-energy shifts: the role of lattice strain. *Phys. Rev. Lett.* **93**(2), 026805 (2004)
45. C. Langhammer, V.P. Zhdanov, I. Zorić, B. Kasemo, Size-dependent kinetics of hydriding and dehydriding of Pd nanoparticles. *Phys. Rev. Lett.* **104**(13), 135502 (2010)
46. C.Q. Sun, Y. Shi, C.M. Li, S. Li, T.C.A. Yeung, Size-induced undercooling and overheating in phase transitions in bare and embedded clusters. *Phys. Rev. B* **73**(7), 075408 (2006)
47. C.Q. Sun, Y. Wang, Y.G. Nie, B.R. Mehta, M. Khanuja, S.M. Shivaprasad, Y. Sun, J.S. Pan, L.K. Pan, Z. Sun, Interface charge polarization and quantum trapping in AgPd and CuPd bimetallic alloy catalysts. *PCCP* **12**, 3131–3135 (2010)
48. C.Q. Sun, Y. Wang, Y.G. Nie, Y. Sun, J.S. Pan, L.K. Pan, Z. Sun, Adatoms-induced local bond contraction, quantum trap depression, and charge polarization at Pt and Rh surfaces. *J. Chem. Phys. C* **113**(52), 21889–21894 (2009)
49. X. Zhang, J.L. Kuo, M.X. Gu, X.F. Fan, P. Bai, Q.G. Song, C.Q. Sun, Local structure relaxation, quantum trap depression, and valence charge polarization induced by the shorter-and-stronger bonds between under-coordinated atoms in gold nanostructures. *Nanoscale* **2**(3), 412–417 (2010)
50. W.J. Huang, R. Sun, J. Tao, L.D. Menard, R.G. Nuzzo, J.M. Zuo, Coordination-dependent surface atomic contraction in nanocrystals revealed by coherent diffraction. *Nat. Mater.* **7**(4), 308–313 (2008)
51. J.T. Miller, A.J. Kropf, Y. Zha, J.R. Regalbuto, L. Delannoy, C. Louis, E. Bus, J.A. van Bokhoven, The effect of gold particle size on Au–Au bond length and reactivity toward oxygen in supported catalysts. *J. Catal.* **240**(2), 222–234 (2006)
52. W. Li, A. Amirfazli, Superhydrophobic surfaces: adhesive strongly to water? *Adv. Mater.* **19**(21), 3421–3422 (2007)
53. X.M. Li, D. Reinhoudt, M. Crego-Calama, What do we need for a superhydrophobic surface? A review on the recent progress in the preparation of superhydrophobic surfaces. *Chem. Soc. Rev.* **36**(8), 1350–1368 (2007)
54. A.B.D. Cassie, S. Baxter, *Trans. Faraday Soc.* **40**, 546 (1944)
55. C. Lee, C.H. Choi, C.J. Kim, Structured surfaces for a giant liquid slip. *Phys. Rev. Lett.* **101**(6), 064501 (2008)
56. G.P. Fang, W. Li, X.F. Wang, G.J. Qiao, Droplet motion on designed microtextured superhydrophobic surfaces with tunable wettability. *Langmuir* **24**(20), 11651–11660 (2008)
57. W. Li, G.P. Fang, Y.F. Lij, G.J. Qiao, Anisotropic wetting behavior arising from superhydrophobic surfaces: parallel grooved structure. *J. Phys. Chem. B* **112**(24), 7234–7243 (2008)
58. X.P. Zheng, H.P. Zhao, L.T. Gao, J.L. Liu, S.W. Yu, X.Q. Feng, Elasticity-driven droplet movement on a microbeam with gradient stiffness: a biomimetic self-propelling mechanism. *J. Colloid Interface Sci.* **323**(1), 133–140 (2008)

59. E. Martines, K. Seunarine, H. Morgan, N. Gadegaard, C.D.W. Wilkinson, M.O. Riehle, Superhydrophobicity and superhydrophilicity of regular nanopatterns. *Nano. Lett.* **5**(10), 2097–2103 (2005)
60. F. Mugele, J.C. Baret, Electrowetting: from basics to applications. *J. Phys.-Condens. Matter* **17**(28), R705–R774 (2005)
61. X.F. Gao, L. Jiang, Water-repellent legs of water striders. *Nature* **432**(7013), 36 (2004)
62. Q.S. Zheng, Y. Yu, X.Q. Feng, The role of adaptive-deformation of water strider leg in its walking on water. *J. Adhes. Sci. Technol.* **23**(3), 493–501 (2009)
63. G. Caputo, R. Cingolani, P.D. Cozzoli, A. Athanassiou, Wettability conversion of colloidal TiO₂ nanocrystal thin films with UV-switchable hydrophilicity. *PCCP* **11**, 3692–3700 (2009)
64. R.D. Sun, A. Nakajima, A. Fujishima, T. Watanabe, K. Hashimoto, Photoinduced surface wettability conversion of ZnO and TiO₂ thin films. *J. Phys. Chem. B* **105**(10), 1984–1990 (2001)
65. R.B. Schoch, J.Y. Han, P. Renaud, Transport phenomena in nanofluidics. *Rev. Mod. Phys.* **80**(3), 839–883 (2008)
66. K.F.V. Wong, T. Kurma, Transport properties of alumina nanofluids. *Nanotechnology*. **19**(34), 345702 (2008)
67. F. Baldessari, Electrokinetics in nanochannels—part I. Electric double layer overlap and channel-to-well equilibrium. *J. Colloid Interface Sci.* **325**(2), 526–538 (2008)
68. J.A. Thomas, A.J.H. McGaughey, Reassessing fast water transport through carbon nanotubes. *Nano. Lett.* **8**(9), 2788–2793 (2008)
69. J. Cumings, A. Zettl, Low-friction nanoscale linear bearing realized from multiwall carbon nanotubes. *Science* **289**(5479), 602–604 (2000)
70. M. Whitby, L. Cagnon, M. Thanou, N. Quirke, Enhanced fluid flow through nanoscale carbon pipes. *Nano. Lett.* **8**(9), 2632–2637 (2008)
71. M. Majumder, N. Chopra, R. Andrews, B.J. Hinds, Nanoscale hydrodynamics: enhanced flow in carbon nanotubes. *Nature* **438**(7064), 44 (2005)
72. H.G. Park, Y. Jung, Carbon nanofluidics of rapid water transport for energy applications. *Chem. Soc. Rev.* (2014). doi:[10.1039/C1033CS60253B](https://doi.org/10.1039/C1033CS60253B)
73. Q.Z. Yuan, Y.P. Zhao, Hydroelectric voltage generation based on water-filled single-walled carbon nanotubes. *J. Am. Chem. Soc.* **131**(18), 6374 (2009)
74. A. Socoliuc, E. Gnecco, S. Maier, O. Pfeiffer, A. Baratoff, R. Bennewitz, E. Meyer, Atomic-scale control of friction by actuation of nanometer-sized contacts. *Science* **313**(5784), 207–210 (2006)
75. E. Gnecco, S. Maier, E. Meyer, Superlubricity of dry nanocontacts. *J. Phys.: Condens. Matter* **20**(35), 354004 (2008)
76. R.J. Cannara, M.J. Brukman, K. Cimatu, A.V. Sumant, S. Baldelli, R.W. Carpick, Nanoscale friction varied by isotopic shifting of surface vibrational frequencies. *Science* **318**(5851), 780–783 (2007)
77. A. Socoliuc, R. Bennewitz, E. Gnecco, E. Meyer, Transition from stick-slip to continuous sliding in atomic friction: entering a new regime of ultralow friction. *Phys. Rev. Lett.* **92**(13), 134301 (2004)
78. A. Erdemir, J.M. Martin (eds.), *Superlubricity* (Elsevier, Amsterdam, 2007)
79. J.Y. Park, D.F. Ogletree, P.A. Thiel, M. Salmeron, Electronic control of friction in silicon pn junctions. *Science* **313**(5784), 186 (2006)
80. G.A. Tomlinson, *Philos. Mag.* **7**, 905 (1929)
81. L. Prandtl, Mind model of the kinetic theory of solid bodies. *Zeitschrift Fur Angewandte Mathematik Und Mechanik* **8**, 85–106 (1928)
82. Y.F. Mo, K.T. Turner, I. Szlufarska, Friction laws at the nanoscale. *Nature* **457**(7233), 1116–1119 (2009)
83. E. Kim, M.H.W. Chan, Probable observation of a supersolid helium phase. *Nature* **427**(6971), 225–227 (2004)

84. S. Balibar, F. Caupin, Supersolidity and disorder. *J. Phys.-Condens. Matter* **20**(17), 173201 (2008)
85. B. Hunt, E. Pratt, V. Gadagkar, M. Yamashita, A.V. Balatsky, J.C. Davis, Evidence for a superglass state in solid 4He. *Science* **324**, 632–636 (2009)
86. J. Day, J. Beamish, Low-temperature shear modulus changes in solid He-4 and connection to supersolidity. *Nature* **450**(7171), 853–856 (2007)
87. P.W. Anderson, A gross-Pitaevskii treatment for supersolid helium. *Science* **324**, 631–632 (2009)
88. L. Pollet, M. Boninsegni, A.B. Kuklov, N.V. Prokof'ev, B.V. Svistunov, M. Troyer, Local stress and superfluid properties of solid He-4. *Phys. Rev. Lett.* **101**(9), 097202 (2008)
89. S. Sasaki, R. Ishiguro, F. Caupin, H.J. Maris, S. Balibar, Superfluidity of grain boundaries and supersolid behavior. *Science* **313**(5790), 1098–1100 (2006)
90. J. Saunders, A glassy state of supersolid helium. *Science* **324**, 601–602 (2009)
91. L. Pollet, M. Boninsegni, A.B. Kuklov, N.V. Prokof'ev, B.V. Svistunov, M. Troyer, Local stress and superfluid properties of solid He-4. *Phys. Rev. Lett.* **101**(9), 097202 (2008)
92. N.K. Adam, Use of the term 'Young's equation' for contact angles. *Nature* **180**, 809–810 (1957)
93. G. Whyman, E. Bormashenko, T. Stein, The rigorous derivation of Young, Cassie-Baxter and Wenzel equations and the analysis of the contact angle hysteresis phenomenon. *Chem. Phys. Lett.* **450**(4–6), 355–359 (2008)
94. A.B.D. Cassie, S. Baxter, Wettability of porous surfaces. *Trans. Faraday Soc.* **40**, 0546–0550 (1944)
95. G.A. Tomlinson, Molecular cohesion. *Philos. Maga.* **6**(37), 695 (1928)
96. A. Lafuma, D. Quere, Superhydrophobic states. *Nat. Mater.* **2**, 457–460 (2003)
97. F. Matsui, T. Matsushita, Y. Kato, M. Hashimoto, K. Inaji, F.Z. Guo, H. Daimon, Atomic-layer resolved magnetic and electronic structure analysis of Ni thin film on a Cu(001) surface by diffraction spectroscopy. *Phys. Rev. Lett.* **100**(20), 207201 (2008)
98. Z. Abbas, C. Labbez, S. Nordholm, E. Ahlberg, Size-dependent surface charging of nanoparticles. *J. Chem. Phys. C* **112**(15), 5715–5723 (2008)
99. B. Zheng, P. Hermet, L. Henrard, Scanning tunneling microscopy simulations of nitrogen- and boron-doped graphene and single-walled carbon nanotubes. *ACS Nano.* **4**(7), 4165–4173 (2010)
100. M. Zhao, W.T. Zheng, J.C. Li, Z. Wen, M.X. Gu, C.Q. Sun, Atomistic origin, temperature dependence, and responsibilities of surface energetics: an extended broken-bond rule. *Phys. Rev. B* **75**(8), 085427 (2007)
101. C.Q. Sun, Surface and nanosolid core-level shift: impact of atomic coordination-number imperfection. *Phys. Rev. B* **69**(4), 045105 (2004)
102. M. Kasuya, M. Hino, H. Yamada, M. Mizukami, H. Mori, S. Kajita, T. Ohmori, A. Suzuki, K. Kurihara, Characterization of water confined between silica surfaces using the resonance shear measurement. *J. Phys. Chem. C* **117**(26), 13540–13546 (2013)
103. A. Uysal, M. Chu, B. Stripe, A. Timalina, S. Chattopadhyay, C.M. Schlepütz, T.J. Marks, P. Dutta, What x rays can tell us about the interfacial profile of water near hydrophobic surfaces. *Phys. Rev. B* **88**(3), 035431 (2013)
104. C.Q. Sun, Oxidation electronics: bond-band-barrier correlation and its applications. *Prog. Mater. Sci.* **48**(6), 521–685 (2003)
105. Y.Y. Tay et al., Size dependence of Zn 2p 3/2 binding energy in nanocrystalline ZnO. *Appl. Phys. Lett.* **88**(17), 173118 (2006)
106. Y. Qin, X.D. Wang, Z.L. Wang, Microfibre-nanowire hybrid structure for energy scavenging. *Nature.* **451**(7180), 809–813 (2008)
107. R.S. Yang et al., Power generation with laterally packaged piezoelectric fine wires. *Nat. Nanotechnol.* **4**(1), 34–39 (2009)
108. L. Gu et al., Flexible fiber nanogenerator with 209 V output voltage directly powers a light-emitting diode. *Nano Lett.* **13**(1), 91–94 (2013)

Chapter 21

Concluding Remarks

21.1 Attainment

Bond relaxation in length and energy and the associated local quantum and polarization dictate the property change of a substance. The BOLS correlation notation is able to reconcile the performance of undercoordinated systems such as defects, surfaces, and nanostructures, in particular, the size dependency and emergence of nanostructures. The atomic CN or skin-resolved bond relaxation in length and energy and the associated bonding electron entrapment and non-bonding electron polarization are the key. The core-shell configuration and the LBA approach provides the universal ingredients to formulate the coordination-resolved property change:

$$\begin{aligned}
 C_i &= 2\{1 + \exp[(12 - z_i)/(8z_i)]\}^{-1} && \text{(Bond length)} \\
 C_i^{-m} &= E_i/E_b && \text{(Bond energy)} \\
 z_1 &= 4(1 - 0.75K^{-1}); z_2 = z_1 + 2; z_3 = z_3 + 4 && \text{(Effective CN)} \\
 \gamma_i &= \tau C_i K^{-1} && \text{(Skin volume ratio)} \\
 \frac{\Delta Q(K)}{Q(\infty)} &= \sum_{i \leq 3} \gamma_i \frac{\Delta q_i(z_i, m, d_i, E_i)}{q_0(12, m, d_i, E_i)} && \text{(Size dependency)}
 \end{aligned}$$

For defect, surface, atomic chains, or atomic sheets, the summation turns to only one term that describes the local properties at the atomic scale. Δq_i is the origin and the surface-to-volume ratio ($\tau K^{-1} C_i$) determines the extent of change. As tabulated below, the $q_i(z_i, m, d_i, E_i)$ connects the macroscopically detectable quantities to the bond parameters. The bond nature indicator m discriminates one (group) of material(s) from others in description such as ZnO, graphene, TiO₂, group III-V, II-VI, and group IV semiconductors and metals [1–15]:

| Q | q | $\Delta q/q_0$ | Quantity |
|-------|------------------|-----------------------|---|
| T_m | zE_z | $z_{ib}C_z^{-m} - 1$ | Melting point (m is the bond nature index, z_{ib} is the relative atomic CN) |
| Y_z | $d_z^{-\tau}E_z$ | $C_z^{-(m+\tau)} - 1$ | Elastic modulus |

(continued)

| (continued) | | | |
|-------------------------------|--|---|---|
| $\Delta\omega$ | $\frac{z}{d} \left(\frac{E_z}{\mu}\right)^{1/2}$ | $z_{ib} C_z^{-(m/2)+1} - 1$ | Raman shift |
| ΔE_v | E_z | $C_z^{-m} - 1$ | Core-level shift; |
| E_G | | | bandgap |
| W | d^{-2} | $B(C_i^{-2} - 1)$ | Stokes shift (e - p coupling, B is a constant) |
| E_{PA} | $E_G \pm W$ | $(C_z^{-m} - 1) \pm B(C_z^{-2} - 1)$ | Photon absorption (PA) and |
| E_{PL} | | | luminescence (PL) |
| $\varepsilon_r(0) - 1 = \chi$ | $\frac{d}{E_G - W}$ | $-(\Delta_H - B\delta_{e-p}) + \sum_{i \leq 3} \gamma_i (C_{iz} - 1)$ | Dielectric susceptibility (δ_{e-p} is electron-phonon interaction) |
| $\varepsilon_r'(\omega)$ | $\frac{\hbar\omega - E_{PL}}{q_0 A^2 \omega^2}$ | - | Imaginary dielectric constant ($\hbar\omega$ is incident photon energy, A constant, q_0 the wave vector) |

As demonstrated, the impact of the often overlooked event of atomic CN imperfection and the associated local quantum entrapment and polarization is indeed profoundly tremendous. The BOLS and NEP notations enable one to view the performance of a defect, surface, a nanosolid, and a solid in amorphous state consistently in a way from the perspective of bond and non-bond formation, dissociation, relaxation, and vibration and the energetic and dynamic process of electron densification, localization, polarization, and redistribution. The following features the progress made in this part:

1. The relaxation of bonds between atoms with fewer neighbors than the ideal in bulk play the same significant role in science pertaining to defect, surface, and nanostructures of various shapes.
2. The BOLS-NEP clarifies the nature difference between nanostructures and bulk of the same substance.
3. Bonds between undercoordinated atoms become shorter and stronger; bond shortening increases the local density of bonding electrons and binding energy while bond strengthening deepens the interatomic potential wells and results in quantum entrapment globally for undercoordinated systems.
4. The densely and locally entrapped bonding electrons polarize in turn the weakly bound non-bonding electrons to form Dirac-Fermi polarons with creation of emerging properties that the bulk materials never demonstrate.
5. Interaction between undercoordinated atoms in the skin and the fraction of such undercoordinated atoms determine the unusual behavior of nanostructures. The BOLS correlation clarifies the common origin for the unusual performance of defects, surfaces, grain boundaries, and nanostructures of various shapes in chemistry, dielectrics, electronics, magnetism, mechanics, thermodynamics, phononics, and photonics.
6. The LBA approach, core-shell configuration, BOLS-NEP premise reconcile the size and shape dependence of known bulk properties and the emerging anomalies of materials at the nanoscale.

7. A well-ordered, solid-like, and elastic sheet covers the liquid surface; the elastic repulsion between the densely charged surfaces could dominate the superfluidity in nanochannels, the superhydrophobicity of nanostructures, and the frictionless linear bearing of CNT.
8. The size degree of freedom results in determination of the energy levels of an isolated atom, the specific heat per bond, etc., by matching predictions to the observed size and shape dependence of the XPS data. This attempt enhances in turn the capability of the XPS, providing an effective way of discriminating the contribution from intraatomic trapping from the contribution of crystal binding to the specific electrons. Attainment is beyond the scope of a combination of XPS and laser cooling that measures the energy level separation of the slowly moving atoms/clusters in gaseous phase.
9. Quantitative information about dimer vibration and e–p interaction can be elucidated by matching predictions to the measured shape and size dependence of Raman and photoemission/absorption spectra of Si and other III–V and II–VI compounds. The CN imperfection of different orders unifies the phase stability of ferromagnetic, ferroelectric, and superconductive nanosolids. In conjunction with the previous bond-band-barrier correlation mechanism, the present approach allows us to distinguish the extent of oxidation and contribution of surface passivation to the dielectric susceptibility of porous silicon [16].
10. Polarization of the non-bonding electrons is responsible for the size emergence of defect and nanostructures with properties that the bulk material does not demonstrate. This kind properties include dilute magnetism, catalysis, Dirac–Fermi polaron, magnetoresistance, etc.

Consistency between the BOLS prediction and the measurements evidences not only the essentiality and validity of the BOLS-NEP notation but also the significance of atomic CN imperfection to the low-dimensional and disordered systems that are dominated by atomic CN deficiencies. Understanding gained insofar should be able to help us in predicting nanosolid performance and hence provide guideline in designing process and fabricating materials with desired functions.

21.2 Limitations

The significance of the approach is that it covers the whole range of sizes from a dimer bond to the bulk solid and covers the states of surface, amorphous, and nanosolid of various shapes to bulk solid with defects inside, with almost no assumptions or freely adjustable parameters. Almost all of the imaginable and detectable quantities are consistently related to the BOLS correlation and the population of the undercoordinated atoms as well. For instance, the surface energy, interfacial energy, surface stress, the local mass density of liquid and solid are all functions of atomic separation and bond energy that are subject to the effect of

atomic CN imperfection. The difficulties encountered by other theories in describing the photoluminescence blueshift at the lower end of the size limit and the melting point oscillation over the whole range of sizes have been completely resolved. The parameters involved are just the bond nature represented by the parameter m and the corresponding bulk values of quantities of concern, which is independent of the particularity of element, crystal structures, or the form of interatomic potentials.

One may wonder that there is often competition between various origins for a specific phenomenon. As demonstrated in the context, the atomic CN imperfection affects almost all the aspects of concern, and therefore, the atomic CN imperfection should dominate the performance of a nanosolid through the competition factors. For instance, the atomic cohesive energy dictates the phase transition or melting while the binding energy density dominates angular momentum and mechanical strength. These two competition factors determine the unusual behavior of a nanosolid in magnetism and mechanical strength under various conditions.

One may also wonder about the effect of impurities such as surface oxidation on the measurement. Although XRD and XPS revealed no impurities in the Ni samples, for instance, one cannot exclude the existence of trace impurities. However, if all the samples were prepared and measured under the same conditions and we use the relative change of the quantities, artifacts caused by impurities should be minimized, and the results are purely size dependent.

The BOLS-NEP premise applies to the so-called dangling bond, as a dangling bond is not a real bond that forms between two neighboring atoms. It is true that the concept of localized bond is not applicable to metallic systems due to the demoralized valence electrons whose wave function often extends to the entire solid. However, the demoralized valence electrons are often treated as a Fermi sea and the metal ions are arranged regularly in the Fermi-sea background. As a standard practice, the metallic bond length corresponds to the equilibrium atomic separation and the bond energy is defined as the division of the atomic cohesive energy E_B by the atomic CN in a real system. For the tetrahedral bond of diamond and Si, the full CN is not four as the tetrahedron is an interlock of fcc structures. Therefore, the BOLS premise is valid for any solid disregarding the nature of the chemical bond. The pair interatomic potential for metallic interatomic interaction also holds, as the pair potential represents the resultant effect of various orders of coordination and the charge-density distribution. DFT calculations on the dimer bond contraction and bond strength gain of Ni, Cu, Ag, Au, Pt, and Pd evidence sufficiently the validity of the current BOLS correlation for metallic systems.

Stimuli in measurement may affect the data acquired. For example, in mechanical strength detection, the stress-strain profiles of a nanosolid may not be symmetric under tension and compression, and the flow stress is strain rate, loading mode, and materials compactness as well as size distribution dependent. However, one could not expect to cover the fluctuations of mechanical (strain rate, stress direction, loading mode, etc), thermal (self-heating during process and electron bombardment in TEM), crystal structure orientation, or grain-size

distributions in a theoretical model, as these fluctuations add random artifacts that are hardly controllable. These effects can be minimized in the present approach using relative changes that are intrinsic in physics.

As the current approach is the first (but main)-order approximation, there is still plenty of room for improvement by involving other high-order effects that contribute to the physical properties. If counting atom-by-atom in a specific crystal structure, the theoretical curves at the lower end of the size limit should show oscillation features with ‘magic number’ of atoms due to the surface-to-volume ratio. For illustration purpose, it would be adequate to employ the smooth function for the surface-to-volume ratio in the present approach, as one should focus, in the first place, on the nature, trend, and origins for the size-induced changes and to grasp with factors controlling the property change.

It should be emphasized that all the models mentioned in the context are successful from different physical perspectives, and with the BOLS correlation as complementary origin, they would be complete and in good accordance.

21.3 Prospects

Although the imaginable and detectable quantities of a nanosolid have been formulated and verified experimentally and computationally, there are still exciting challenges ahead of us:

1. Further attention is needed to address the joint effect of physical size and chemical reaction. At an interface, no significant CN imperfection is expected but chemical bonds may evolve when an alloy or a compound is formed. The chemical effect alters the nature of the bond while the physical size causes the bond contraction. Both will modify the atomic trapping, crystal binding, electron–phonon coupling, which should be origin for the detectable physical properties of a solid including transport properties. Switching between superhydrophilicity and superhydrophobicity of chemically treated nanostructure could be successful samples for the joint effect of the BOLS and 3B proposals.
2. Traditional practice in theoretical calculations may be subject to modification at the lower end of the size limit to involve the effect of CN imperfection. Consideration of the real boundary conditions with atomic CN imperfection instead of the ideal periodic boundary conditions would be necessary. As demonstrated, the atomic CN imperfection and the large portion of surface/interface atoms play the key roles in determining the performance of small structures.
3. Formulation is needed for the interdependence of various physical properties pertain to nanocrystals. For instance, the T_C and the valence DOS measurement of atomic-layered growth of superconductive Pb on stepped Si substrate [16] shows oscillation of both T_C and the valence DOS peak near the E_F when the film thickness was increased by one atomic layer at a time. The T_C increases

gradually to the bulk value at about 30 layers in a saw-tooth-like oscillatory fashion. The oscillation is in about 0.5 K in magnitude and in a period of every other layer. The two DOS peaks at 0 and 0.3 eV below E_F dominate alternatively with the layer-by-layer growth.

4. Transport in thermal conductivity and electric conductivity play an important role in the performance of nanostructured devices, which would be more challenging. Employing the BOLS local potential for a nanosolid and for an assembly of nanosolids could improve the understanding on the kinetic and dynamic performance of a nanosolid under external stimuli.
5. Determination of the multiple fields coupling effect on certain physical properties is expected. Application of the BOLS and its derivative to process and materials design is important in practical applications. If we know what is intrinsic and what the limit is, we may save our spirit and resources in fabricating devices and materials. For example, those working in microelectronics often expect to expand the limit of dielectrics to the lower end for interconnection and to the higher end for Gate devices by changing the grain size. The BOLS derivative is able to tell us that it is unlikely to raise the dielectrics by reducing the particle size and one has to seek other chemical routes for the objectives. One cannot expect proper functioning of a ferromagnetic, ferroelectric, and a superconductive nanosolid when the solid size is smaller than 2.5 nm, as derived in the present work.
6. The strongly correlated systems, such as high- T_c super conductors, topologic insulators, thermoelectric emitters, etc., show strong edge effects with polarized states near the E_F , which could result from the combination of undercoordination-induced entrapment and polarization and the chemically-induced localization and polarization.

These topics would form challenging branches of study toward profound knowledge and practical applications and this part just scratches the skin of this vast field while further investigation is in progress. Consideration from the perspective of bond and non-bond formation, dissociation, relaxation, and vibration and the energetic and dynamic process of electron densification, localization, polarization, and redistribution would be more fascinating, promising, revealing, and rewarding.

References

1. C.Q. Sun, Y. Sun, Y.G. Nie, Y. Wang, J.S. Pan, G. Ouyang, L.K. Pan, Z. Sun, Coordination-resolved C–C bond length and the C 1 s binding energy of carbon allotropes and the effective atomic coordination of the few-layer Graphene. *J. Chem. Phys. C.* **113**(37), 16464–16467 (2009)
2. X.X. Yang, J.W. Li, Z.F. Zhou, Y. Wang, L.W. Yang, W.T. Zheng, C.Q. Sun, Raman spectroscopic determination of the length, strength, compressibility, debye temperature, elasticity, and force constant of the C–C bond in Graphene. *Nanoscale* **4**(2), 502–510 (2012)

3. W.T. Zheng, C.Q. Sun, Underneath the fascinations of carbon nanotubes and Graphene nanoribbons. *Energy Environ. Sci.* **4**(3), 627–655 (2011)
4. C.Q. Sun, Y. Nie, J. Pan, X. Zhang, S.Z. Ma, Y. Wang, W. Zheng, Zone-selective photoelectronic measurements of the local bonding and electronic dynamics associated with the monolayer skin and point defects of graphite. *RSC Adv.* **2**(6), 2377–2383 (2012)
5. S. Ma, H. Liang, X. Wang, J. Zhou, L. Li, C.Q. Sun, Controlling the band gap of ZnO by programmable annealing. *J. Phys. Chem. C* **115**(42), 20487–20490 (2011)
6. X.J. Liu, L.K. Pan, Z. Sun, Y.M. Chen, X.X. Yang, L.W. Yang, Z.F. Zhou, C.Q. Sun, Strain engineering of the elasticity and the Raman shift of nanostructured TiO₂. *J. Appl. Phys.* **110**(4), 044322 (2011)
7. J.W. Li, S.Z. Ma, X.J. Liu, Z.F. Zhou, C.Q. Sun, ZnO meso-mechano-thermo physical chemistry. *Chem. Rev.* **112**(5), 2833–2852 (2012)
8. Y.M. Chen, J.W. Li, X.X. Yang, Z.F. Zhou, C.Q. Sun, Band gap modulation of the IV, III-V, and II-VI semiconductors by controlling the solid size and dimension and the temperature of operation. *J. Chem. Phys. C.* **115**(47), 23338–23343 (2011)
9. Y. Nie, Y. Wang, X. Zhang, J. Pan, W. Zheng, C.Q. Sun, Catalytic nature of under- and hetero-coordinated atoms resolved using zone-selective photoelectron spectroscopy (ZPS). *Vacuum* **100**, 87–91 (2014)
10. X.X. Yang, Z.F. Zhou, Y. Wang, J.W. Li, N.G. Guo, W.T. Zheng, J.Z. Peng, C.Q. Sun, Raman spectroscopic determination of the length, energy, debye temperature, and compressibility of the C–C bond in carbon allotropes. *Chem. Phys. Lett.* **575**, 86–90 (2013)
11. X.X. Yang, Z.F. Zhou, Y. Wang, R. Jiang, W.T. Zheng, C.Q. Sun, Raman spectroscopy determination of the debye temperature and atomic cohesive energy of CdS, CdSe, Bi₂Se₃, and Sb₂Te₃ nanostructures. *J. Appl. Phys.* **112**(8), 4759207 (2012)
12. W. Qin, Y. Wang, Y.L. Huang, Z.F. Zhou, C. Yang, C.Q. Sun, Bond order resolved 3d(5/2) and valence band chemical shifts of Ag surfaces and nanoclusters. *J. Phys. Chem. A.* **116**(30), 7892–7897 (2012)
13. E.S.M. Goh, T.P. Chen, H.Y. Yang, Y. Liu, C.Q. Sun, Size-suppressed dielectrics of Ge nanocrystals: skin-deep quantum entrapment. *Nanoscale* **4**(4), 1308–1311 (2012)
14. E.S.M. Goh, T.P. Chen, S.F. Huang, Y.C. Liu, C.Q. Sun, Bandgap expansion and dielectric suppression of self-assembled Ge nanocrystals. *J. Appl. Phys.* **109**(6), 064307 (2011)
15. J.W. Li, L.W. Yang, Z.F. Zhou, P.K. Chu, X.H. Wang, J. Zhou, L.T. Li, C.Q. Sun, Bandgap modulation in ZnO by size, pressure, and temperature. *J. Chem. Phys. C.* **114**(31), 13370–13374 (2010)
16. L.K. Pan, S.Q. Xu, W. Qin, X.J. Liu, Z. Sun, W.T. Zheng, and C.Q. Sun, Skin dominance of the dielectric-electronic-phononic-photon attribute of nanostructured silicon. *Surface Science Reports*, 2013. **68**(3-4), 418–455 (2013)
17. Y. Guo, Y.F. Zhang, X.Y. Bao, T.Z. Han, Z. Tang, L.X. Zhang, W.G. Zhu, E.G. Wang, Q. Niu, Z.Q. Qiu, J.F. Jia, Z.X. Zhao, Q.K. Xue, Superconductivity modulated by quantum size effects. *Science* **306**(5703), 1915–1917 (2004)

Part II

Size Matter

A.1 Highlights

- Bonds between undercoordinated atoms and the performance of local electrons differentiate in nature the less-coordinated atoms from those isolated or fully coordinated ones
- A broken bond shortens and strengthens its neighbors globally and spontaneously, which follows the BOLS notation, irrespective of structural phase of a substance.
- Local densification and entrapment of bonding electrons, energy, and mass happens accordingly.
- Densely entrapped bonding and core electrons polarize the nonbonding electrons (NEP) of chain ends, defects, defect edges, and nanocrystals, which yield properties that a bulk substance never demonstrates, such as Dirac–Fermi polaron creation, dilute magnetism, catalytic ability, conductor–insulator transition, hydrophobicity of liquid and solid surfaces.
- Entrapment of valence charge enlarges the electroaffinity and the polarization lowers the work function of a substance.
- The core–shell configuration, BOLS-NEP premise, and the local bond average (LBA) approach reconcile the size dependency of nanostructures in chemical and thermal stability, mechanical strength, phonon relaxation dynamics, phonon emissibility and absorbance, dielectric relaxation, magnetic modulation, etc.
- The theory-driven numerical approaches empower XPS and Raman to gain coordination-resolved information such as local bond length, bond energy, bond stiffness, binding energy density, atomic cohesive energy, and their interdependence.

Part III

Atomistic Solid Mechanics

Abstract Atomic hetero- and under-coordination, mechano- and thermo-activation relax the bonds, energy density, and cohesive energy, which discriminate defects, liquid and solid skins, nanostructures from the bulk in the elasticity, plasticity, and mechanical strength.

Part III deals with the hydro-, nano-, and thermo- effects on bond length and energy and the mechanical properties of substances in the form of monatomic chains, hollow tubes, liquid and solid skins, nanocavities, nanowires, and nanograins, as well as interfaces on the base of the LBA approach and the BOLS premise. Differentiating from the classical continuum and contemporary quantum methods, the LBA approach correlates the measurable quantities of a specimen to the energetic responses of identities (bond nature, order, length and strength) of its representative bond to external stimuli, such as changes in temperature, pressure, and coordination environments. The shorter and stronger bonds between under-coordinated atoms and the consequent local strain and quantum entrapment dictate, intrinsically, the mechanical behavior of systems with a high proportion of such atoms. The hydrostatic compression-induced shortening and strengthening of the bond stiffens the substance. The thermally driven bond expansion and weakening soften the specimen. The competition between the energy density gain and the residual atomic cohesive energy in the relaxed skin region determines, intrinsically, the mechanical performance of a mesoscopic specimen under compression; the competition between the activation and inhibition of atomic dislocations motion dominates, extrinsically, the yield strength of the specimen during plastic deformation. The coupling of the thermo-, mechanical-, and meso-effects takes place only in the skin region. Therefore, the mechanical behavior of a specimen depends on its shape, size, the nature of the bonds involved, surface and interface conditions, and the temperature at which the physical properties of the specimen is measured. This bond relaxation premise has thus reconciled the hydro-meso-thermal mechanical properties of low-dimensional systems, including

elasticity and extensibility, inverse Hall-Petch relationship. Furthermore, quantification of these properties has led to quantitative information regarding the bond identities in monatomic chains and carbon nanotubes, as well as the factors dominating the sizes at which a nanograin is strongest.

Chapter 22

Introduction

- *Monatomic chains (MCs), nanotubes (NTs), nanowires (NWs), solid and liquid surface skins, nanocavities, and nanograins share considerable similarities in the thermo-mechanical behavior.*
- *Emerging problems due to the change of solid size and operating pressure and temperature challenge existing continuum and quantum approaches.*
- *Atomistic comprehension of the elastic and plastic deformation of substance in the full size scales is of great importance.*
- *A new approach combining theory and experiment from the perspective of bond formation, dissociation, relaxation, and vibration is highly desirable.*

22.1 Scope

Part III starts with a brief overview on the unusual mechanical behavior of the mesoscopic systems including Cs, nanotubes (NTs), nanowires (NWs), solid and liquid skins, nanocavities, and solids in nanometer and micrometer regimes. A brief summary outlines opening questions and emerging problems that pose a challenge for a consistent understanding. Chapter 23 presents theoretical considerations of the local bond average (LBA) and the effect of broken bonds on the behavior of the remaining ones of the undercoordinated atoms. To deal with the size, pressure, and temperature dependence of the mechanical properties of the mesoscopic systems, the BOLS is extended to the relaxation of bond length and energy due to thermal and mechanical activation. The effects of the coupling of size, strain, pressure, temperature are formulated, which happens only in the skin region. Chapters 24–30 extend the analytical solutions to the functional dependence of mechanical properties in various situations on the bond-relaxation dynamics. Solutions are applied to typical situations in which the size and temperature determine the intrinsic properties, such as the elasticity, the extensibility, and the plasticity in which extrinsic factors come into play. Wherever possible, existing modeling considerations and understandings from various perspectives are

discussed comparatively. The LBA analysis showed consistently that the shortened and stiffened bonds of the undercoordinated atoms or bond relaxation by compression dictate the mechanical behavior of a mesoscopic substance, which is quite different from that of its isolated constituent atoms or its bulky counterpart. Agreement between predictions and experimental observations on the mechanical properties of MCs, solid and liquid skins, NTs, NWs, nanocavities, and the inverse Hall–Petch relationship (IHPR) is realized with consistent understanding of the commonly intrinsic origin behind the observations. Chemisorption-induced surface stress and its effect on the surface tension of liquids are also discussed from the perspective of charge repopulation and polarization upon adsorbate-bond making. The LBA treatment in terms of bonding energetics has led to quantitative information about bonding identities and an improved understanding of the factors governing the intrinsically mechanical performance of mesoscopic systems. Artifacts are very important in the indentation test of plastic deformation, and hence the observed IHPR arises from two competitions within the intrinsic and the extrinsic contributions. Atomic vacancies of nanocavities play dual roles in determining the mechanical properties. The broken-bond-induced strain and quantum entrapment surrounding the defects not only serve as centers inhibiting the motion of atomic dislocations but also provide sites initializing structure failure in plastic deformation. The interface bond strain, the associated energy pinning, and the bond nature alteration upon alloy or compound formation are responsible for the mechanical strengthening of the twin grains and interface mixing. Chapter 31 presents a discussion on the attainments and limitations of the development. Prospects of further extension of the developed approaches to atomic defects, impurities, adsorbed surfaces, liquid surfaces, junction interfaces, and systems under other stimuli such as electronic, and magnetic fields are briefly addressed. Some open problems and continuing challenges, pertaining plastic deformation in particular are also highlighted in Chap. 31.

22.2 Overview

22.2.1 *Basic concepts*

As there is a bridge between the atomistic and macroscopic scales, the nanoscopic systems have attracted tremendous interest because of their intriguing properties from a basic scientific viewpoint, as well as from their great potential in upcoming technological applications such as nanomechano-electronic devices [1]. The significance of a nanoscopic specimen is the tunability in physical properties compared with the corresponding more bulky samples of which the proportion of the undercoordinated surface atoms is negligible. The coordination deficiency differs the nanoscopic systems substantially from the isolated atoms of their constituent elements or the corresponding bulk counterparts in performance. Because of the reduction in the mean atomic CN nanoscopic systems display novel mechanical,

thermal, acoustic, optical, electronic, dielectric, and magnetic properties [2–5]. However, the unusual behavior of a nanostructure goes beyond the expectation and description of the classical theories in terms of the continuum medium mechanics and the statistic thermodynamics. Quantities such as the Young's modulus and the extensibility of a solid remain no longer constant but change with the solid size. In general, the mechanical properties of a solid vary with the temperature and the pressure of operation. Thermal softening and pressure hardening are very common. It is fascinating that the new degree of the freedom of size and its combination with temperature or pressure not only offer one with opportunities to tune the physical properties of a nanosolid but also allow one to gain information that is beyond the scope of conventional approaches.

In dealing with the mechanical behavior of the mesoscopic systems, the following concepts could be of importance:

1. Surface energetics can be categorized as follows: (1) excessive energy stored per unit area of the skin of a certain thickness, (2) residual cohesive energy per discrete atom at the surface and, (3) the conventional definition of surface energy that refers to energy consumed (loss) for making a unit area of surface.
2. Surface stress (σ) is the change of surface energy with respect to surface strain, corresponding to the first-order differential of the binding energy with respect to volume. Surface stress, being the same in dimension (in unit of J/m^3 or N/m^2) to surface energy and hardness (H), reflects intrinsically the internal energy response to volume change at a given temperature. Hardness is the ability of one material to resist being scratched or dented by another in plastic deformation. The stress often applies to elastic regime, while the hardness or flow or yield stress applies to plastic deformation where creeps, grain glide, dislocation movements, and strain-gradient work hardening are competitively involved [6, 7].
3. Elastic bulk modulus (B) is the second-order differential of the binding energy with respect to volume strain and is proportional to the sum of binding energy per unit volume from the perspectives of both dimensionality and rigorous solutions. Differing from the definition of bulk modulus, Young's modulus (Y) gives the elastic response of a material to an applied uniaxial stress and is therefore directionally dependent on the orientation of the defect structure and/or crystal. The product of the Young's modulus and the sample dimension represents the stiffness of the material, which correlates with the atomic structure. The Y value also relates to other quantities such as Debye temperature, sound velocity, specific heat at constant volume, and the thermal conductivity of a substance.
4. Compressibility (β , also called extensibility) is theoretically proportional to the inverse of the elastic modulus. The stiffness of a specimen refers to its elastic strength that is the product of Young's modulus and the thickness of the specimen; the toughness of a specimen refers to its yield strength in plastic deformation that involves activation and inhibition of atomic dislocations motion, bond unfolding, grain gliding, and work hardening during deformation. A specimen that is stiffer may not be tougher, and vice versa, although both the

elastic and the plastic strength are in principle proportional to the binding energy density.

5. Surface tension (τ) referring to the surface energy of a liquid phase is one of the important physical quantities that control the growth of a material on a substrate as well as different phenomena at a liquid surface, such as coalescence, melting, evaporation, phase transition, crystal growth, chemical reaction, and so on. Temperature dependence of the surface tension gives profound information in particular for the surfaces with adsorbed molecules or with multi-components for alloying or compound forming.
6. Critical temperatures (T_C) that are related to atomic cohesive energy represent the thermal stability of a specimen such as solid–liquid, liquid–vapor, or ferromagnetic, ferroelectric, and superconductive phase transitions, or glass transition in amorphous states.

From an experimental point of view, the values of the bulk modulus B and stress σ can be measured by equaling the external mechanical stimulus to the responses of the interatomic bonding of the solid,

$$\left\{ \begin{array}{l} \sigma = \frac{F}{A} = \frac{E}{V} \propto - \left. \frac{\partial u(r)}{\partial V} \right|_{r \neq d} \propto \frac{u(r)}{r^3} \text{ (Stress)} \\ B = V \left. \frac{\partial P}{\partial V} \right|_{r=d} \propto -V \left. \frac{\partial^2 u(r)}{\partial V^2} \right|_{r=d} \propto \frac{E_b}{d^3} \text{ (Bulk modulus)} \\ \beta = \frac{\partial V}{V \partial P} = B^{-1}; \beta' = \frac{\partial^2 V}{V \partial P^2} \text{ (Compressibility)} \end{array} \right. \quad (22.1)$$

where the parameters F , V , and A correspond, respectively, to force, volume, and the area on which the F is acting. The function $u(r)$ is a pairing interatomic potential, and r is the atomic distance. At equilibrium, $r = d$, σ is zero.

The σ , B , and Y are proportional to the binding energy per unit volume under given status,

$$[\sigma] \propto [B] \propto [Y] \propto \frac{E}{d^3}; \text{ (Pa)} \quad (22.2)$$

The aim of using the proportional relation is to focus on the relative change of σ and B with respect to their given bulk values. According to the LBA approach [8], the elasticity and the stress of a specimen can be related to the bond length (volume) and the bond energy of the representative bonds, as the nature and the total number of bonds in the given specimen do not change during measurement unless phase transition occurs.

From an atomistic and dimensional point of view, the terms of B , Y , and σ as well as the surface tension and surface energy are the same in dimension (Pa, or Jm^{-3}) because they are all intrinsically proportional to the sum of bond energy per unit volume. The numerical expressions in Eq. (22.2) apply in principle to any substance in any phase and any deformation processes including elastic, plastic, recoverable, or non-recoverable without contribution from extrinsic artifacts. The fact that the

hardness for various carbon materials, silicon, and SiC [9] varies linearly with elastic modulus evidences for this relation. Nanoindentation revealed that the hardness and modulus of Ni films are linearly dependent [10]. Counter examples exist such as polycrystalline metals whose Young's modulus is independent of grain size, but whose hardness varies following the inverse Hall–Petch relationship (IHPR) [11] because the involvement of artifacts as extrinsic factors becomes dominant in the contact measurement for the latter. Artifacts such as purity, strain rate, creep rate, load scale, and direction will come into play as an addition. Artifacts are unavoidable in detecting methods such as nanoindentation or the Vickers microhardness measurements. Chapter 28 will show that contributions of such artifacts are more significant to nanograins than to the surfaces of thin films. Therefore, the measured results are a collection of intrinsic and extrinsic changes of the mechanical performance, which make it difficult to discriminate intrinsic information from extrinsic contributions to the mechanical behavior of the mesoscopic systems.

Many techniques have been developed to measure the Young's modulus and the stress of the mesoscopic systems [12, 13]. Besides the traditional Vickers microhardness test, techniques mostly used for nanostructures are tensile test using an atomic force microscope (AFM) cantilever, a nanotensile tester, a transmission electron microscopy (TEM)-based tensile tester, an AFM nanoindenter, an AFM three-point bending tester, an AFM wire free-end displacement tester, an AFM elastic–plastic indentation tester, and a nanoindentation tester. Surface acoustic waves (SAWs), ultrasonic waves, atomic force acoustic microscopy (AFAM), and electric field-induced oscillations in AFM and in TEM are also used. Comparatively, the methods of SAWs, ultrasonic waves, field-induced oscillations, and an AFAM could minimize the artifacts because of their nondestructive nature though these techniques collect statistic information from responses of all the chemical bonds involved [14].

22.2.2 Challenges

As the nanoscopic mechanics is an emerging field of study, fundamental progress is lagging far behind the experimental exploitations. Many questions and challenges are still open for discussion. The following features a few samples regarding the mechanical puzzles of the mesoscopic systems.

1. Size dependence of elasticity and yield strength

Measurements have revealed that the elasticity and the strength of a nanosolid changes with solid size exhibiting three seemingly conflicting trends, as summarized in Table 22.1. Sophisticated theoretical models from various perspectives explained the intriguing mechanical performance of the mesoscopic systems. For instances, the followings provide possible mechanisms for the elastic response and mechanical strength of nanostructures. These models include the nonlinear effects [15], surface reconstruction [16] and relaxation [17, 18], surface stress or surface

Table 22.1 A summary of the experimentally observed changes in elastic modulus or mechanical strength at a surface or for a nanosolid upon size reduction with respect to the bulk values [40]

| Observed trends | Specimens and references | Methods used |
|---------------------------|---|-------------------------|
| Hardening | TiCrN [41], AlGaN [42], a-C and a-C:N surface [43, 44] | Nanoindentation |
| | Ni [45, 46], Ag, Ni, Cu, Al α_2 -TiAl and γ -TiAl surfaces [47] | |
| | Au and Ag films [48] | |
| | TiC, ZrC, and HfC surfaces [49] | |
| | Nanograined steel [50] | AFM |
| | ZnO nanobelts [51–53] wires [54], and surface [55, 56] | |
| | Ag wires [57] | SAW |
| | Poly(L-lactic acid) fibers [58] | DFT |
| | | AFM |
| | SiTiN fibers [59] | |
| | Au–Au bond [60] | |
| | SWCNT, MWCNT, and SiC wire [61] | Nanoindentation |
| | CNT-spun fibers [62] | |
| Ag and Pd wires [63] | | |
| GaN wires [64] | | |
| Softening | Ni surface [62] and nanocrystals [25] | AFAM |
| | Polymer surface [65] | AFM |
| | Polystyrene surface [66] | |
| | ZnO nanobelts/wires [67–70] | AFM three-point bending |
| | Cr [71] and Si [72] nanocantilevers | AFM |
| ZnS nanofilaments [73] | Force deflection spectroscopy | |
| Retention or irregularity | ZnS nanobelts hardness increase yet elasticity decreases [74] | AFM |
| | Au wires [75] | |
| | SiO ₂ wires [76] | |
| | Silver nanowires [77] | Nanoindenter |
| | 20–80 nm Ge wires [78] | |

tension [19–23], excessive surface and edge stress [24]. The skin mechanics also ascribed as surface shell high compressibility [25], dislocation starvation [26, 27], the stochastic of dislocation source lengths [28], mismatch stress [29], grain volume relaxation [30], competition between bond loss and bond saturation [31], and stronger bonds between undercoordinated atoms [32–34].

Large-scale atomistic simulations [35, 36] of the plastic deformation of nanocrystalline materials suggest that both the inter- and intra-granular deformation processes under uniaxial tensile and compressive stress in nanoindentation are leading conditions. In the scoping studies [37, 38], various parametric effects on the stress state and kinematics have been quantified. The considered parameters

include crystal orientation (single slip, double slip, quadruple slip, and octal slip), temperature, applied strain rate, specimen size, specimen aspect ratio size, deformation path (compression, tension, shear, and torsion), and material (Ni, Al, and Cu). Although the thermodynamic force (stress) varies at different size scales, the kinematics of deformation is similar based on atomistic simulations, finite element simulations, and physical experiments. Atomistic simulations, that inherently include extreme strain rates and size scales, give results that agree with the phenomenological attributes of plasticity observed in macroscale experiments. These include strain rate dependence of the flow stress into a rate independent regime, approximate Schmidt-type behavior; size-scale dependence on the flow stress, and kinematic behavior of large deformation plasticity. However, an atomistic understanding and analytical expressions in terms of the intrinsically key factors for the size and temperature dependence of the strength and extensibility of nanostructures are yet lacking though molecular dynamics (MD) simulations [39] suggest that surface atoms play an important, yet unclear, role in nanomechanics.

2. Surface energy, strength, and thermal stability

Normally, the skin of an inorganic solid is harder at temperatures far below the melting point (T_m) but the hard skin melts more easily in a shell-resolved manner [79, 80]. For Si(111) surface ($T_m = 1,687$ K), surface pre-melting is initiated in the temperature range 1,473–1,493 K at surface step bunches and boundaries of step-free regions [81]. However, surface hardening does not occur so often for specimens with lower T_m values. In comparison, the surface of a liquid solidifies first associated with lattice contraction and crystallization in the outermost atomic layers [82]. Although a critical-depth mechanism [83, 84] has been developed to ascribe the surface hardening as a surface effect, strain-gradient work hardening, and non-dislocation mechanisms of deformation [85], these phenomena appear beyond the scope of classical theory considerations in terms of entropy, enthalpy, or free energy. An atomic scale understanding of the origin of surface tension and its temperature and adsorbate dependence is highly desirable [86, 87]. Furthermore, conventional definition of surface energetics with involvement of classical statistic thermodynamics and continuum medium considerations for larger scales may need revision because the discrete quantized nature in nanoscopic scales becomes dominant.

3. Thermally induced softening

Thermally induced softening of a substance has been widely seen for substances disregarding its shape and size. Generally, when the testing temperature is raised, the compressibility/extensibility of the solid increases rendering the mechanical strength as observed in the cases of nanograined Al [88] and diamond films [89]. At higher temperatures, the bending stiffness and the apparent Young's modulus of diamond beams (wires) drastically reduced to one-third of the initial value before fracture. The flexural strength and the modulus of the hydrosilylated and condensed curable silicone resins also decrease when the testing temperature is raised [90]. The yield strength of Mg nanosolid [91] of a given size drops when the

temperature is increased. An atomic scale simulation [92] suggests that the material becomes softer in both the elastic and the plastic regimes as the operating temperature is raised. When measured at 200 °C, the strength of the 300 nm-sized Cu nanograins is lowered by 15 % and the ductility increases substantially [93]. The biaxial Young's modulus of Si(111) and Si(100) drops linearly when the temperature (T) is increased [94, 95]. The Young's modulus of the TiN/Mo_xC multilayer films drops when the temperature is raised from 100 to 400 °C though the modulus increases with the decrease in the modulation period of the multilayers [96]. An MD investigation suggested that the longitudinal Young's modulus and the shear modulus for both the armchair and the zigzag NTs change in different trends over the temperature range of 300–1,200 K. The Y value drops while the shear modulus increases as the temperature is increased [97].

The Y values often drop nonlinearly at very low temperatures and then linearly at higher temperatures [8, 98]. When the operation temperature is increased from room temperature to 400 °C, the ductility of the ultrafine-grained FeCo₂V samples of 100–290 nm size increases from 3 to 13 % or even to 22 % associated with strength reduction [99]. Superplasticity of individual single-walled CNTs [100] has been observed at elevated temperatures of $\sim 2,000$ K [101]. The ductility of a nanosolid increases exponentially with temperature up to almost infinity at T_m . An analytical expression for the thermally driven softening and the thermally enhanced ductility is also yet lacking.

4. Monatomic chain forming and breaking

A MC is an ideal prototype for mechanical testing as no processes of bond unfolding or atomic glide dislocating are involved in the deformation. It is intriguing that at 4.2 K and under UHV conditions, the maximal length at breaking of an Au–Au bond in the Au–MC is about 0.23 nm, being 20 % shorter than the equilibrium Au–Au distance of 0.29 nm in the bulk [102]. At room temperature, the breaking limits vary from 0.29 to 0.48 nm [103]. However, the controllable formation of an MC of other metals is rare. Theoretical reproduction of the scattered data of measurement, in particular, the extreme values of 0.23 and 0.48 nm have been hardly possible although the mechanisms of fuzzy imaging [104], atomistic impurity mediation [1], and charge mediation [105] in the state-of-the-art computational approaches have made some progress in understanding.

5. Stiffness and thermal stability at the nanoscale

For bulk materials, the elastic modulus is proportional to the melting point. At the nanoscale, this rule breaks. For example, carbon nanotubes and nanocompounds such as ZnO and SiC nanowires exhibit extremely high strength yet relatively lower thermal stability compared with their bulk counterparts. The elastic modulus of the single-walled CNT (SWCNT) varies from 0.5 to 5.5 TPa depending on the presumption of the wall thickness of the CNT. The Young's modulus of the multi-walled CNTs (MWCNTs) drops with the inverse number of walls (or wall thickness), and it is less sensitive to the outermost radius of the MWCNTs if the wall thickness remains unchanged [106]. Atoms in the open edge

of as SWCNT coalesce at 1,593 K and a ~ 280 % extensibility of the CNT occurs at $\sim 2,000$ K. Under the flash of an ordinary camera, the SWCNT burns under the ambient conditions.

6. Inverse Hall–Petch relationship

Under a tensile or compressive stress, the hardness or the plastic flow stress of crystals in the size range of 100 nm or higher is subject to the classical temperature-independent Hall–Petch relationship (HPR) [11]. The hardness increases linearly with the inverse square root of solid size. With further size reduction, the mechanical strength of the solid continues increasing but deviates from the initially linear HPR until a critical size of the strongest hardness, of the order of 10 nm, is reached. At the critical grain size, the slope of the inverse IHPR curve will change from positive to negative and then the nanosolid turns to be softer. Although there is a growing body of experimental evidence pointing to the unusual IHPR deformation in the nanometer regime, the underlying atomistic mechanisms behind are yet unclear [11, 38, 63]. The factors dominating the critical size at which the HPR transits are far from clear. The HPR–IHPR transition seems to be a topic of endless discussions because of the competition between the intrinsic contributions and the extrinsic artifacts that involve the activation and inhabitation of grain-boundary sliding due to the difficulty of partial dislocation movement.

7. Vacancy defect and nanocavity induced hardening and thermal instability

It is expected that atomic vacancies reduce the number of chemical bonds and therefore the strength of a porous material becomes lower. However, the hardness of a specimen does not follow this simple intuitive picture of coordination counting. Vacancies not only act as pinning centers inhibiting dislocation motion and thus enhancing the mechanical strength within a certain concentration but also provide sites initiating structure failure. An introduction of a limited amount of atomic vacancies or nanocavities could indeed enhance the mechanical strength of the porous specimen. Atomic vacancies or discretely distributed nanometer-sized cavities could not only enhance the mechanical strength of the specimen, but also cause a substantial depression of the temperature of melting. Metallic foams of 40 \sim 60 % mass density are several times harder yet lighter compared with the standard materials, providing new kinds of materials that are lighter and stronger for energy management. However, excessive amount of cavities or large pores are detrimental to the mechanical strength of the specimen. For instance, the Young's modulus of a defected nanotube is reduced gradually with each atomic defect, and the plastic strength of the NTs is catastrophically influenced by the existence of just a few atomic defects [107]. Understanding the discrepancy between expectations and observations of cavity-induced hardening and melting is also a challenge.

8. Adsorbate-induced surface stress

The surface tension of a liquid drops linearly when the measuring temperature is raised. However, contamination, or adsorption, may change the slope of the

temperature coefficient. Adsorbate-bond making at a solid surface could alter the surface stress in various ways. For instance, hydrogen addition could embrittle the metals and C addition usually induces compressive stress at the surface. Even on the same surface, different adsorbents such as C, N, O, S, and CO, result in different kinds of stress. The adsorbate-induced stress may change its sign with the coverage of the specific adsorbate. A specific adsorbate may induce different kinds of stress at different faces of the same material. An understanding of the adsorbate-induced surface stress and its correlation to the adsorbate-induced slope inflection of the T -dependent surface tension from the perspective of charge polarization and repopulation upon bond making is necessary.

9. Interface and nanocomposite

Mechanical strengthening of a material can occur using multilayer formation of different kinds of compounds or by composite formation with nanostructured fillers such as carbon nanotubes, fibers, or clays inserted into the polymer matrix. The roles of the interface mixing, the dissociated interface skins, or the hard in fillers are yet unclear in the process of nanocomposite reinforcement.

10. Limitations of the classical and quantum approximations

Classical approaches in terms of the Gibbs free energy or the continuum medium mechanics can account for the physical properties of a macroscopic system. For instances, the detectable quantities are related directly to the external stimulus such as temperature (T) and entropy (S), pressure (P) and volume (V), surface area A and surface energy γ , chemical potential μ_i and composition n_i , charge quantity q and electric field, magnetic momentum μ_B and magnetic field, etc., without needing consideration of atomistic origin:

$$G(T, P, A, n_i, E, B, \dots) = \Omega(ST, VP, \gamma A, \mu_i n_i, qE, \mu_B B, \dots)$$

At the atomic scale, quantum effect becomes dominant, which can reproduce the physical properties of a small object by solving the Schrödinger equations for the behavior of electrons or the Newtonian's motion equations for the atoms with a sum of averaged interatomic potentials as key factors to the single-body systems:

$$\begin{cases} H_i = T_i + v_i(r) + V_{\text{crystal}}(r + R_{ij}) & \text{(Quantum mechanics)} \\ F = -\nabla[V_{\text{crystal}}(r + R_{ij})] = Mr'' & \text{(Molecular dynamics)} \end{cases}$$

where H is the Hamiltonian and F the force. T_i is the kinetic energy, v_i the intra-atomic potential, and V_{crystal} is the periodic crystal potential. R_{ij} is the atomic distance. M is the mass of the atom.

However, for a small system at the manometer regime, both the classical and the quantum approaches encountered severe difficulties. For instances, the statistic mechanics is conducted over a large number of atoms, N , with a standard deviation that is proportional to $N^{-1/2}$. Quantities such as the entropy, the volume, the surface energy, and the chemical potential of a particular element remain no longer constant but change with the solid size [108–111]. Quantum approaches are facing

the boundary-condition problems that are the core of nanoscience. The broken-bond-induced local strain and skin quantum entrapment and the consequent charge, energy, and mass densification in the surface skin play a role of significance. In fact, the real system is atomic site anisotropic, kinetic, with strongly localized nature. Describing the effect of skin trapping using an average of interatomic potentials and under the periodic or free boundary conditions in quantum mechanical approaches may be too ideal. Therefore, to complement the classical and quantum theories, a set of analytical expressions from the perspective of LBA for the size, temperature, pressure, and bond nature dependence of the intrinsic mechanical properties of a specimen is necessary.

22.3 Objectives

Authoritative overviews [100, 112–116] and monographs [117–119] have provided the understanding of the origin of solid mechanics with models based on analyses and simulations at different levels from continuum to atomistic scales. Complementing these contributions, this part aims to address the following:

1. To reconcile experimental and theoretical observations on the size and temperature dependences of the elastic and plastic deformation of nanoscopic systems including atomic chains, NTs, liquid and solid skins, thin films, multilayers, nanocavities, nanograins, and nanocomposites to provide with consistent understanding.
2. To present analytical solutions for predicative observation of the size, temperature, pressure, and bond nature dependence of the intrinsic mechanical behavior of systems from atomic chain to macrospecimen as mentioned above from the perspective of bond formation, dissociation, relaxation, and vibration by extending the BOLS correlation theory to the temperature and pressure domain. It could be possible to employ the LBA approach to connect the macroscopic properties of a specimen to the atomistic factors (e.g., bond nature, bond order, bond length, and bond strength) of the representative local bonds. Establishment of the functional dependence of the detectable quantities on the bonding identities and the response of the bonding identities to external stimulus such as coordination environment (BOLS effect), temperature (thermal expansion and vibration), and stress field (deformation and deformation energy). A combination of the LBA approach and the BOLS correlation theory could complement the classical continuum and quantum approaches.
3. To gain atomistic insight into the origin of the size, pressure, and temperature dependence of the nanoscopic mechanics. Deeper insight into the consequences of bond making and breaking and a grasp of the factors controlling bond making and bond breaking are necessary to improve works in other fields such as nano- and microelectronics, catalytic electronics, and nanobiotechnology.

4. To find factors dominating the mechanical performance of the mesoscopic systems and the interdependence of various quantities from the perspective of bond making and bond breaking to provide guideline for nanomechanical device design. Discriminating the intrinsic contributions from the extrinsic artifacts involved in the indentation test may allow one to understand the correlation between the elastic and the plastic deformations. Importantly, besides the performance and its origin, one needs to know the trends and the limitations of the changes and interdependence of various properties.
5. To elucidate information such as single-bond energy, maximum strain, in particular, the length, strength, extensibility, breaking limit, specific heat, and melting point of the single bond in MCs and CNTs, by matching the theoretical predictions to experimental observations. The new degree of freedom of size not only allows one to tune the physical properties of a specimen but also provides one with opportunities to gain information such as the energy levels of an isolated atom [120, 121] and the vibration frequency of an isolated dimer [122, 123]. A combination of the degrees of freedom of size, pressure, and temperature may allow one to gain more information such the cohesive energy per bond in various systems under various conditions. All these quantities are of elemental importance to surface and materials sciences.

References

1. N. Agrait, A.L. Yeyati, J.M. van Ruitenbeek, Quantum properties of atomic-sized conductors. *Phys. Rep.-Rev. Sec. Phys. Lett.* **377**(2–3), 81–279 (2003)
2. C.Q. Sun, Size dependence of nanostructures: impact of bond order deficiency. *Prog. Solid State Chem.* **35**(1), 1–159 (2007)
3. C. Binns, Nanoclusters deposited on surfaces. *Surf. Sci. Rep.* **44**(1–2), 1–49 (2001)
4. B. Cappella, G. Dietler, Force-distance curves by atomic force microscopy. *Surf. Sci. Rep.* **34**(1–3), 1–+ (1999)
5. A.I. Rusanov, Surface thermodynamics revisited. *Surf. Sci. Rep.* **58**(5–8), 111–239 (2005)
6. Y. Huang, H. Gao, W.D. Nix, J.W. Hutchinson, Mechanism-based strain gradient plasticity—II. Analysis. *J. Mech. Phys. Solids* **48**(1), 99–128 (2000)
7. N.A. Fleck, J.W. Hutchinson, Strain gradient plasticity, in *Advances in Applied Mechanics*, vol. 33 (Academic Press Inc, San Diego, 1997), pp. 295–361
8. M.X. Gu, Y.C. Zhou, L.K. Pan, Z. Sun, S.Z. Wang, C.Q. Sun, Temperature dependence of the elastic and vibronic behavior of Si, Ge, and diamond crystals. *J. Appl. Phys.* **102**(8), 083524 (2007)
9. Y. Gogotsi, S. Welz, D.A. Ersoy, M.J. McNallan, Conversion of silicon carbide to crystalline diamond-structured carbon at ambient pressure. *Nature* **411**(6835), 283–287 (2001)
10. Z.S. Ma, S.G. Long, Y. Pan, Y.C. Zhou, Indentation depth dependence of the mechanical strength of Ni films. *J. Appl. Phys.* **103**(4), 043512 (2008)
11. S. Yip, Nanocrystalline metals: mapping plasticity. *Nat. Mater.* **3**(1), 11–12 (2004)
12. E.P.S. Tan, C.T. Lim, Mechanical characterization of nanofibers: a review. *Compos. Sci. Technol.* **66**(9), 1102–1111 (2006)

13. Y.N. Xia, P.D. Yang, Y.G. Sun, Y.Y. Wu, B. Mayers, B. Gates, Y.D. Yin, F. Kim, Y.Q. Yan, One-dimensional nanostructures: synthesis, characterization, and applications. *Adv. Mater.* **15**(5), 353–389 (2003)
14. X.D. Han, Z. Zhang, Z.L. Wang, Experimental nanomechanics of one-dimensional nanomaterials by in situ microscopy. *NANO* **2**(5), 249–271 (2007)
15. H.Y. Liang, M. Upmanyu, H.C. Huang, Size-dependent elasticity of nanowires: nonlinear effects. *Phys. Rev. B* **71**(24), 241403 (2005)
16. H.W. Shim, L.G. Zhou, H.C. Huang, T.S. Cale, Nanoplate elasticity under surface reconstruction. *Appl. Phys. Lett.* **86**, 151912(15), 151912 (2005)
17. J.G. Guo, Y.P. Zhao, The size-dependent elastic properties of nanofilms with surface effects. *J. Appl. Phys.* **98**(7), 074306 (2005)
18. J.G. Guo, Y.P. Zhao, The size-dependent bending elastic properties of nanobeams with surface effects. *Nanotechnology* **18**(29), 295701 (2007)
19. S. Cuenot, C. Fretigny, S. Demoustier-Champagne, B. Nysten, Surface tension effect on the mechanical properties of nanomaterials measured by atomic force microscopy. *Phys. Rev. B* **69**(16), 165410 (2004)
20. V.B. Shenoy, Atomistic calculations of elastic properties of metallic fcc crystal surfaces. *Phys. Rev. B* **71**(9), 094104 (2005)
21. G. Stan, S. Krylyuk, A.V. Davydov, M. Vaudin, L.A. Bendersky, R.F. Cook, Surface effects on the elastic modulus of Te nanowires. *Appl. Phys. Lett.* **92**(24), 241908 (2008)
22. G.X. Cao, X. Chen, Size dependence and orientation dependence of elastic properties of ZnO nanofilms. *Int. J. Solids Struct.* **45**(6), 1730–1753 (2008)
23. J. He, C.M. Lilley, Surface effect on the elastic behavior of static bending nanowires. *Nano Lett.* **8**(7), 1798–1802 (2008)
24. T.Y. Zhang, M. Luo, W.K. Chan, Size-dependent surface stress, surface stiffness, and Young's modulus of hexagonal prism 111 beta-SiC nanowires. *J. Appl. Phys.* **103**(10), 104308 (2008)
25. Y. Zhao, T.D. Shen, J.Z. Zhang, High P-T nano-mechanics of polycrystalline nickel. *Nanoscale Res. Lett.* **2**(10), 476–491 (2007)
26. J.R. Greer, W.D. Nix, Size dependence of mechanical properties of gold at the sub-micron scale. *Appl. Phys. A-Mater. Sci. Process.* **80**(8), 1625–1629 (2005)
27. J.R. Greer, W.C. Oliver, W.D. Nix, Size dependence of mechanical properties of gold at the micron scale in the absence of strain gradients. *Acta Mater.* **53**(6), 1821–1830 (2005)
28. T.A. Parthasarathy, S.I. Rao, D.M. Dimiduk, M.D. Uchic, D.R. Trinkle, Contribution to size effect of yield strength from the stochastics of dislocation source lengths in finite samples. *Scripta Mater.* **56**(4), 313–316 (2007)
29. Y. Choi, S. Suresh, Size effects on the mechanical properties of thin polycrystalline metal films on substrates. *Acta Mater.* **50**(7), 1881–1893 (2002)
30. G. Guisbiers, O. Van Overschelde, M. Wautelet, Nanoparticulate origin of intrinsic residual stress in thin films. *Acta Mater.* **55**(10), 3541–3546 (2007)
31. L.G. Zhou, H. Huang, Elastic softening and stiffening of metals surfaces. *Int. J. Multiscale Comput. Eng.* **4**(1), 19–28 (2006)
32. G.H. Lu, S.H. Deng, T.M. Wang, M. Kohyama, R. Yamamoto, Theoretical tensile strength of an Al grain boundary. *Phys. Rev. B* **69**(13), 134106 (2004)
33. L. Qiao, X.J. Zheng, Elastic property of fcc metal nanowires via an atomic-scale analysis. *Appl. Phys. Lett.* **92**(23), 231908 (2008)
34. G. Ouyang, X.L. Li, X. Tan, G.W. Yang, Size-induced strain and stiffness of nanocrystals. *Appl. Phys. Lett.* **89**(3), 031904 (2006)
35. H. Van Swygenhoven, Size effects in plasticity: experiments and simulations, in *Nanomaterials by Severe Plastic Deformation*, ed. Z. Horita (Trans Tech Publications Ltd, Zurich-Uetikon, 2006), pp. 193–200
36. H. Van Swygenhoven, P.M. Derlet, A. Hasnaoui, Atomistic modeling of strength of nanocrystalline metals. *Adv. Eng. Mater.* **5**(5), 345–350 (2003)

37. M.F. Horstemeyer, M.I. Baskes, S.J. Plimpton, Computational nanoscale plasticity simulations using embedded atom potentials. *Theor. Appl. Fract. Mech.* **37**(1–3), 49–98 (2001)
38. K.S. Kumar, H. Van Swygenhoven, S. Suresh, Mechanical behavior of nanocrystalline metals and alloys. *Acta Mater.* **51**(19), 5743–5774 (2003)
39. H.A. Wu, Molecular dynamics study on mechanics of metal nanowire. *Mech. Res. Commun.* **33**(1), 9–16 (2006)
40. C.Q. Sun, Thermo-mechanical behavior of low-dimensional systems: the local bond average approach. *Prog. Mater. Sci.* **54**(2), 179–307 (2009)
41. C.Q. Sun, B.K. Tay, S.P. Lau, X.W. Sun, X.T. Zeng, S. Li, H.L. Bai, H. Liu, Z.H. Liu, E.Y. Jiang, Bond contraction and lone pair interaction at nitride surfaces. *J. Appl. Phys.* **90**(5), 2615–2617 (2001)
42. D. Caceres, I. Vergara, R. Gonzalez, E. Monroy, F. Calle, E. Munoz, F. Omnes, Nanoindentation on AlGaIn thin films. *J. Appl. Phys.* **86**(12), 6773–6778 (1999)
43. E. Liu, X. Shi, H.S. Tan, L.K. Cheah, Z. Sun, B.K. Tay, J.R. Shi, The effect of nitrogen on the mechanical properties of tetrahedral amorphous carbon films deposited with a filtered cathodic vacuum arc. *Surf. Coat. Technol.* **120**, 601–606 (1999)
44. X. Shi, B.K. Tay, D.I. Flynn, Z. Sun, Tribological properties of tetrahedral carbon films deposited by filtered cathodic vacuum arc technique, in *Thin Films: Stresses and Mechanical Properties VI*, eds. by W.W. Gerberich, et al. (Materials Research Society, Warrendale, 1997), pp. 293–298
45. R.A. Mirshams, P. Parakala, Nanoindentation of nanocrystalline Ni with geometrically different indenters. *Mater. Sci. Eng. A Struct. Mater. Prop. Microstruct. Process.* **372**(1–2), 252–260 (2004)
46. C.D. Gu, J.S. Lian, Z.H. Jiang, Q. Jiang, Enhanced tensile ductility in an electrodeposited nanocrystalline Ni. *Scripta Mater.* **54**(4), 579–584 (2006)
47. M.H. Zhao, W.S. Slaughter, M. Li, S.X. Mao, Material-length-scale-controlled nanoindentation size effects due to strain-gradient plasticity. *Acta Mater.* **51**(15), 4461–4469 (2003)
48. Y.F. Cao, S. Allameh, D. Nankivil, S. Sethiaraj, T. Oti, W. Soboyejo, Nanoindentation measurements of the mechanical properties of polycrystalline Au and Ag thin films on silicon substrates: effects of grain size and film thickness. *Mater. Sci. Eng. A-Struct. Mater. Prop. Microstruct. Process.* **427**(1–2), 232–240 (2006)
49. D. Ferro, R. Teghil, S.M. Barinov, L. D’Alessio, G. DeMaria, Thickness-dependent hardness of pulsed laser ablation deposited thin films of refractory carbides. *Mater. Chem. Phys.* **87**(2–3), 233–236 (2004)
50. M.Y. Liu, B. Shi, J.X. Guo, X. Cai, H.W. Song, Lattice constant dependence of elastic modulus for ultrafine grained mild steel. *Scripta Mater.* **49**(2), 167–171 (2003)
51. H. Ni, X.D. Li, Young’s modulus of ZnO nanobelts measured using atomic force microscopy and nanoindentation techniques. *Nanotechnology* **17**(14), 3591–3597 (2006)
52. A.J. Kulkarni, M. Zhou, F.J. Ke, Orientation and size dependence of the elastic properties of zinc oxide nanobelts. *Nanotechnology* **16**(12), 2749–2756 (2005)
53. M. Lucas, W.J. Mai, R.S. Yang, Z.L. Wang, E. Riedo, Size dependence of the mechanical properties of ZnO nanobelts. *Phil. Mag.* **87**(14–15), 2135–2141 (2007)
54. C.Q. Chen, Y. Shi, Y.S. Zhang, J. Zhu, Y.J. Yan, Size dependence of Young’s modulus in ZnO nanowires. *Phys. Rev. Lett.* **96**(7), 075505 (2006)
55. L.X. Zhang, H.C. Huang, Young’s moduli of ZnO nanoplates: Ab initio determinations. *Appl. Phys. Lett.* **89**(18), 183111 (2006)
56. G. Cao, X. Chen, Energy analysis of size-dependent elastic properties of ZnO nanofilms using atomistic simulations. *Phys. Rev. B* **76**(16), 165407 (2007)
57. G.Y. Jing, H.L. Duan, X.M. Sun, Z.S. Zhang, J. Xu, Y.D. Li, J.X. Wang, D.P. Yu, Surface effects on elastic properties of silver nanowires: contact atomic-force microscopy. *Phys. Rev. B* **73**(23), 235409 (2006)

58. E.P.S. Tan, C.T. Lim, Nanoindentation study of nanofibers. *Appl. Phys. Lett.* **87**(12), 123106 (2005)
59. F. Vaz, S. Carvalho, L. Rebouta, M.Z. Silva, A. Paul, D. Schneider, Young's modulus of (Ti, Si)N films by surface acoustic waves and indentation techniques. *Thin Solid Films* **408**(1–2), 160–168 (2002)
60. G. Rubio-Bollinger, S.R. Bahn, N. Agrait, K.W. Jacobsen, S. Vieira, Mechanical properties and formation mechanisms of a wire of single gold atoms. *Phys. Rev. Lett.* **87**(2), 026101 (2001)
61. E.W. Wong, P.E. Sheehan, C.M. Lieber, Nanobeam mechanics: elasticity, strength, and toughness of nanorods and nanotubes. *Science* **277**(5334), 1971–1975 (1997)
62. A.B. Dalton, S. Collins, E. Munoz, J.M. Razal, V.H. Ebron, J.P. Ferraris, J.N. Coleman, B.G. Kim, R.H. Baughman, Super-tough carbon-nanotube fibres: these extraordinary composite fibres can be woven into electronic textiles. *Nature* **423**(6941), 703 (2003)
63. R.E. Miller, V.B. Shenoy, Size-dependent elastic properties of nanosized structural elements. *Nanotechnology* **11**(3), 139–147 (2000)
64. G. Feng, W.D. Nix, Y. Yoon, C.J. Lee, A study of the mechanical properties of nanowires using nanoindentation. *J. Appl. Phys.* **99**(7), 074304 (2006)
65. W.J. Price, S.A. Leigh, S.M. Hsu, T.E. Patten, G.Y. Liu, Measuring the size dependence of Young's modulus using force modulation atomic force microscopy. *J. Phys. Chem. A* **110**(4), 1382–1388 (2006)
66. K. Miyake, N. Satomi, S. Sasaki, Elastic modulus of polystyrene film from near surface to bulk measured by nanoindentation using atomic force microscopy. *Appl. Phys. Lett.* **89**(3), 031925 (2006)
67. J.H. Song, X.D. Wang, E. Riedo, Z.L. Wang, Elastic property of vertically aligned nanowires. *Nano Lett.* **5**(10), 1954–1958 (2005)
68. X.D. Bai, P.X. Gao, Z.L. Wang, E.G. Wang, Dual-mode mechanical resonance of individual ZnO nanobelts. *Appl. Phys. Lett.* **82**(26), 4806–4808 (2003)
69. K. Yum, Z.Y. Wang, A.P. Suryavanshi, M.F. Yu, Experimental measurement and model analysis of damping effect in nanoscale mechanical beam resonators in air. *J. Appl. Phys.* **96**(7), 3933–3938 (2004)
70. A.V. Desai, M.A. Haque, Mechanical properties of ZnO nanowires. *Sens. Actuator A-Phys.* **134**(1), 169–176 (2007)
71. S.G. Nilsson, X. Borriese, L. Montelius, Size effect on Young's modulus of thin chromium cantilevers. *Appl. Phys. Lett.* **85**(16), 3555–3557 (2004)
72. X.X. Li, T. Ono, Y.L. Wang, M. Esashi, Ultrathin single-crystalline-silicon cantilever resonators: fabrication technology and significant specimen size effect on Young's modulus. *Appl. Phys. Lett.* **83**(15), 3081–3083 (2003)
73. Q.H. Xiong, N. Duarte, S. Tadigadapa, P.C. Eklund, Force-deflection spectroscopy: a new method to determine the Young's modulus of nanofilaments. *Nano Lett.* **6**(9), 1904–1909 (2006)
74. X.D. Li, X.N. Wang, Q.H. Xiong, P.C. Eklund, Mechanical properties of ZnS nanobelts. *Nano Lett.* **5**(10), 1982–1986 (2005)
75. B. Wu, A. Heidelberg, J.J. Boland, Mechanical properties of ultrahigh-strength gold nanowires. *Nat. Mater.* **4**(7), 525–529 (2005)
76. H. Ni, X.D. Li, H.S. Gao, Elastic modulus of amorphous SiO₂ nanowires. *Appl. Phys. Lett.* **88**(4), 043108 (2006)
77. X.D. Li, H.S. Hao, C.J. Murphy, K.K. Caswell, Nanoindentation of silver nanowires. *Nano Lett.* **3**(11), 1495–1498 (2003)
78. L.T. Ngo, D. Almecija, J.E. Sader, B. Daly, N. Petkov, J.D. Holmes, D. Erts, J.J. Boland, Ultimate-strength germanium nanowires. *Nano Lett.* **6**(12), 2964–2968 (2006)
79. A. Siavosh-Haghighi, D.L. Thompson, Melting point determination from solid-liquid coexistence initiated by surface melting. *J. Phys. Chem. C* **111**(22), 7980–7985 (2007)
80. Y.G. Chushak, L.S. Bartell, Melting and freezing of gold nanoclusters. *J. Phys. Chem. B* **105**(47), 11605–11614 (2001)

81. V. Ignatescu, J.A. Blakely, Morphological evidence for surface pre-melting on Si(111). *Surf. Sci.* **601**(23), 5459–5465 (2007)
82. O.G. Shpyrko, A.Y. Grigoriev, C. Steimer, P.S. Pershan, B.H. Lin, M. Meron, T. Graber, J. Gerbhardt, B. Ocko, M. Deutsch, Anomalous layering at the liquid Sn surface. *Phys. Rev. B* **70**(22), 224206 (2004)
83. T.Y. Zhang, W.H. Xu, Surface effects on nanoindentation. *J. Mater. Res.* **17**(7), 1715–1720 (2002)
84. W.H. Xu, T.Y. Zhang, Surface effect for different types of materials in nanoindentation, in *Advances in Fracture and Failure Prevention, Pts 1 and 2*, eds. by K. Kishimoto, et al. (Trans Tech Publications Ltd, Zurich-Uetikon, 2004), pp. 1587–1592
85. E. Manika, J. Maniks, Size effects in micro- and nanoscale indentation. *Acta Mater.* **54**(8), 2049–2056 (2006)
86. I. Egry, The surface tension of binary alloys: Simple models for complex phenomena. *Int. J. Thermophys.* **26**(4), 931–939 (2005)
87. R.N. Shimizu, N.R. Demarquette, Evaluation of surface energy of solid polymers using different models. *J. Appl. Polym. Sci.* **76**(12), 1831–1845 (2000)
88. M.A. Haque, M.T.A. Saif, Thermo-mechanical properties of nano-scale freestanding aluminum films. *Thin Solid Films* **484**(1–2), 364–368 (2005)
89. F. Szuecs, M. Werner, R.S. Sussmann, C.S.J. Pickles, H.J. Fecht, Temperature dependence of Young's modulus and degradation of chemical vapor deposited diamond. *J. Appl. Phys.* **86**(11), 6010–6017 (1999)
90. Y.H. Wu, F.J. McGarry, B.Z. Zhu, J.R. Keryk, D.E. Katsoulis, Temperature effect on mechanical properties of toughened silicone resins. *Polym. Eng. Sci.* **45**(11), 1522–1531 (2005)
91. N. Ono, R. Nowak, S. Miura, Effect of deformation temperature on Hall–Petch relationship registered for polycrystalline magnesium. *Mater. Lett.* **58**(1–2), 39–43 (2004)
92. J. Schiotz, T. Vegge, F.D. Di Tolla, K.W. Jacobsen, Atomic-scale simulations of the mechanical deformation of nanocrystalline metals. *Phys. Rev. B* **60**(17), 11971–11983 (1999)
93. N.A. Krasilnikov, Z. Pakiel, W. Lojkowski, R.Z. Valiev, Grain refinement and mechanical properties of nickel subjected to severe plastic deformation, in *Interfacial Effects and Novel Properties of Nanomaterials*, eds. by W. Lojkowski, J.R. Blizzard (Trans Tech Publications Ltd., Zurich-Uetikon, 2003)
94. P. Kury, M. Horn-von Hoegen, Impact of thermal dependence of elastic constants on surface stress measurements. *Rev. Sci. Instrum.* **75**(5), 1357–1358 (2004)
95. Y.A. Burenkov, Nikanoro.Sp, Temperature-dependence of elastic-constants of silicon. *Fiz. Tverd. Tela* **16**(5), 1496–1498 (1974)
96. Q. Liu, X.P. Wang, F.J. Liang, J.X. Wang, Q.F. Fang, Hardness enhancement and oxidation resistance of nanocrystalline TiN/MoxC multilayer films. *Mater. Res. Bull.* **41**(8), 1430–1436 (2006)
97. C.L. Zhang, H.S. Shen, Temperature-dependent elastic properties of single-walled carbon nanotubes: prediction from molecular dynamics simulation. *Appl. Phys. Lett.* **89**(8), 081904 (2006)
98. R. Dingreville, J.M. Qu, M. Cherkaoui, Surface free energy and its effect on the elastic behavior of nano-sized particles, wires and films. *J. Mech. Phys. Solids* **53**(8), 1827–1854 (2005)
99. A. Duckham, D.Z. Zhang, D. Liang, V. Luzin, R.C. Cammarata, R.L. Leheny, C.L. Chien, T.P. Weihs, Temperature dependent mechanical properties of ultra-fine grained FeCo-2 V. *Acta Mater.* **51**(14), 4083–4093 (2003)
100. P.H. Mayrhofer, C. Mitterer, L. Hultman, H. Clemens, Microstructural design of hard coatings. *Prog. Mater. Sci.* **51**(8), 1032–1114 (2006)
101. J.Y. Huang, S. Chen, Z.Q. Wang, K. Kempa, Y.M. Wang, S.H. Jo, G. Chen, M.S. Dresselhaus, Z.F. Ren, Superplastic carbon nanotubes: conditions have been discovered that

- allow extensive deformation of rigid single-walled nanotubes. *Nature* **439**(7074), 281 (2006)
102. C. Untiedt, A.I. Yanson, R. Grande, G. Rubio-Bollinger, N. Agrait, S. Vieira, J.M. van Ruitenbeek, Calibration of the length of a chain of single gold atoms. *Phys. Rev. B* **66**(8), 085418 (2002)
 103. S.B. Legoas, D.S. Galvao, V. Rodrigues, D. Ugarte, Origin of anomalously long interatomic distances in suspended gold chains. *Phys. Rev. Lett.* **88**(7), 076105 (2002)
 104. H. Hakkinen, R.N. Barnett, A.G. Scherbakov, U. Landman, Nanowire gold chains: formation mechanisms and conductance. *J. Phys. Chem. B* **104**(39), 9063–9066 (2000)
 105. A. Ayuela, M.J. Puska, R.M. Nieminen, J.A. Alonso, Charging mechanism for the bond elongation observed in suspended chains of gold atoms. *Phys. Rev. B* **72**(16), 161402 (2005)
 106. L.F. Wang, Q.S. Zheng, J.Z. Liu, Q. Jiang, Size dependence of the thin-shell model for carbon nanotubes. *Phys. Rev. Lett.* **95**(10), 105501 (2005)
 107. M. Sammalkorpi, A. Krashennnikov, A. Kuronen, K. Nordlund, K. Kaski, Mechanical properties of carbon nanotubes with vacancies and related defects. *Phys. Rev. B* **70**(24), 245416 (2004)
 108. V.N. Singh, B.R. Mehta, Nanoparticle size-dependent lowering of temperature for phase transition from In(OH)(3) to In₂O₃. *J. Nanosci. Nanotechnol.* **5**(3), 431–435 (2005)
 109. S. Kala, B.R. Mehta, Size-dependent structural, optical and hydrogenation properties of Pr nanoparticle layers. *J. Alloy. Compd.* **431**(1–2), 10–15 (2007)
 110. S. Tripathi, R. Brajpuriya, A. Sharma, A. Soni, G.S. Okram, S.M. Chaudhari, T. Shripathi, Thickness dependent structural, electronic, and optical properties of Ge nanostructures. *J. Nanosci. Nanotechnol.* **8**(6), 2955–2963 (2008)
 111. H. Modrow, Tuning nanoparticle properties: the X-ray absorption spectroscopic point of view. *Appl. Spectrosc. Rev.* **39**(2), 183–290 (2004)
 112. N. Karak, Polymer (epoxy) clay nanocomposites. *J. Polym. Mater.* **23**(1), 1–20 (2006)
 113. F. Hussain, M. Hojjati, M. Okamoto, R.E. Gorga, Review article: polymer-matrix nanocomposites, processing, manufacturing, and application: an overview. *J. Compos. Mater.* **40**(17), 1511–1575 (2006)
 114. M. Okamoto, Recent advances in polymer/layered silicate nanocomposites: an overview from science to technology. *Mater. Sci. Technol.* **22**(7), 756–779 (2006)
 115. Y. Tanaka, J.P. Gong, Y. Osada, Novel hydrogels with excellent mechanical performance. *Prog. Polym. Sci.* **30**(1), 1–9 (2005)
 116. C.S. Lu, Y.W. Mai, Y.G. Shen, Recent advances on understanding the origin of superhardness in nanocomposite coatings: a critical review. *J. Mater. Sci.* **41**(3), 937–950 (2006)
 117. B. Wang, *Mechanics of Advanced Functional Materials* (Springer-Zhejiang University press, 2012)
 118. Y.P. Zhao, *Physical Mechanics of Surface and Interface* (Beijing: Scientif Press, 2012)
 119. Q. Jiang, Z. Wen, *Thermodynamics of Materials* (SPringer-High Education press, 2010)
 120. C.Q. Sun, Surface and nanosolid core-level shift: impact of atomic coordination-number imperfection. *Phys. Rev. B* **69**(4), 045105 (2004)
 121. C.Q. Sun, L.K. Pan, T.P. Chen, X.W. Sun, S. Li, C.M. Li, Distinguishing the effect of crystal-field screening from the effect of valence recharging on the 2P(3/2) and 3d(5/2) level energies of nanostructured copper. *Appl. Surf. Sci.* **252**(6), 2101–2107 (2006)
 122. C.Q. Sun, L.K. Pan, C.M. Li, S. Li, Size-induced acoustic hardening and optic softening of phonons in InP, CeO₂, SnO₂, CdS, Ag, and Si nanostructures. *Phys. Rev. B* **72**(13), 134301 (2005)
 123. M.X. Gu, L.K. Pan, B.K. Tay, C.Q. Sun, Atomistic origin and temperature dependence of Raman optical redshift in nanostructures: a broken bond rule. *J. Raman Spec.* **38**(6), 780–788 (2007)

Chapter 23

Theory: Multiple-Field Coupling

- Variation of atomic CN, pressure, and temperature relax the bond length and bond energy with an association of densification of charge, energy, and mass. Multiple fields coupling takes place in the skin region.
- Localized densification of energy by size reduction and compression contributes to the mechanical strength; bond order loss and heating and softening modifies the atomic cohesive energy, both of which dominate the detectable quantities of a substance.
- The performance of the entire specimen can be viewed as the attribute of one bond averaged over all the bonds involved.
- A detectable quantity can be connected to the averaged bond and its geometric and energetic response to the externally applied stimulus such as coordination environment, temperature, pressure, etc.

23.1 Pressure-, Strain-, and Temperature-Resolved BOLS

23.1.1 BOLS Formulation

If the effects of atomic CN deficiency, strain, stress, and temperature come into play simultaneously, the length, $d(z, \varepsilon, T, P)$, and the energy, $E_I(z, \varepsilon, T, P)$, of the representative bond will change accordingly. Therefore, based on the LBA approach, we can extend the BOLS correlation to temperature and pressure domains, leading to the BOLS modification,

$$\begin{cases} d(z, \varepsilon, P, T) = d_0 \Pi_J (1 + \varepsilon_J) = d_b \left[(1 + (C_z - 1)) \left(1 + \int_0^\varepsilon d\varepsilon \right) \left(1 + \int_{T_0}^T \alpha(t) dt \right) \left(1 - \int_{P_0}^P \beta(p) dp \right) \right] \\ E(z, \varepsilon, P, T) = E_0 (1 + \sum_J \Delta_J) = E_b \left[1 + \frac{(C_z^m - 1) - d_z^2 \int_0^\varepsilon \kappa(\varepsilon) d\varepsilon - \int_{T_0}^T \eta(t) dt - \int_{P_0}^P p(v) dv}{E_b} \right] \end{cases} \quad (23.1)$$

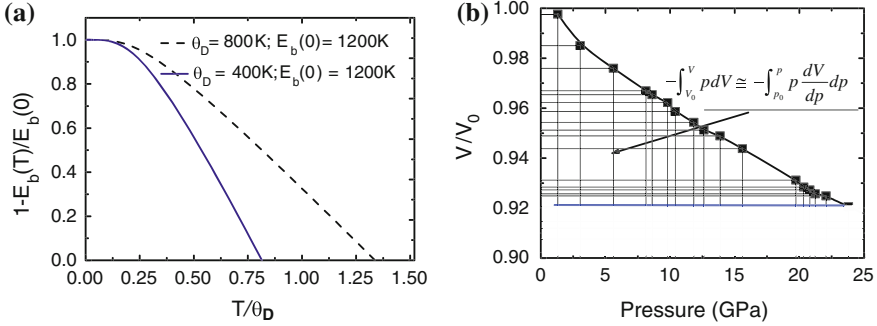


Fig. 23.1 **a** Temperature dependence of bond energy $E_b(T)/E_b(0) = 1 - U(T/\theta_D)/E_b(0)$ with $U(T/\theta_D)$ being the thermal or internal vibration energy per coordinate in the bulk of Debye approximation. $E_b(T)/E_b(0)$ depends linearly on temperature at $T > \theta_D/3$, and the slope changes with the $E_b(0)$ values. **b** Typical V - P profile and the pressure-induced energy density gain of the entire body, represented by the gridded area in the V - P profile (Reprinted with permission from [7])

T_0 and P_0 are the references at the ambient conditions. Δ_J is the energy perturbation and ε_J the strain caused by the applied stimuli. The summation and the production are preceded over all the J stimuli of (z, ε, P, T) . The $\alpha(t)$ is the temperature-dependent thermal expansion coefficient (TEC). $\beta = -\partial v / (v \partial p)$ is the compressibility ($p < 0$ compressive stress) or extensibility ($p > 0$ tensile stress) that is proportional to the inverse of elastic bulk modulus. The $k(\varepsilon)$ is the effective force constant. $\eta(t)$ is the T -dependent specific heat of the representative bond, which approximates Debye approximation, $C_v(T/\theta_D)$, for a z -coordinated atom. Generally, the thermal measurement is conducted under constant pressure and the $\eta(t)$ is related to the C_p . However, there is only a few percent difference between the C_p and C_v [1].

These expressions indicate that the mechanical work hardening by compression or by the compressive strain will shorten and strengthen but the thermal vibration or the tensile strain will elongate and weaken the bond. Atomic CN reduction shortens and strengthens the bond, according to the BOLS correlation. The generalized form indicates that one can consider all the stimuli either individually or collectively, depending on the experimental conditions.

Figure 23.1a illustrates the temperature and Debye temperature dependence of the inner bond energy. In the V - P profile, as illustrated in Fig. 23.1b, only the gridded part $-\int_{V_0}^V p dV \cong -\int_{p_0}^p p \frac{dV}{dp} dp$ contributes to the energy density of the entire body [2]. For the single bond, the atomic volume, $v(z, t, p)$, is replaced by the bond length, $d(z, t, p)$, and the p is replaced by the force, f . The $\beta(p)$ remains constant at constant temperature within the regime of elastic deformation and then the integration $\int_0^P \beta(p) dp = \beta P$ can be simplified, unless phase transition occurs [3–5]. If the compressibility varies with pressure, the third-order Birch-Murnaghan isothermal equation of state is applied [6],

$$p(V) = \frac{3B_0}{2} \left(\xi^{-7/3} - \xi^{-5/3} \right) \left\{ 1 + \frac{3}{4} (B'_0 - 4) \left(\xi^{-2/3} - 1 \right) \right\}$$

where B_0 is the static bulk modulus and B'_0 the first-order pressure derivative of the B_0 ; the $\xi = v/v_0$ is the ratio of volume of unit cell addressed after and before being compressed.

23.1.2 Thermal Expansion

The $\alpha(t)$ depends nonlinearly on temperature in the low-temperature range, and the $\alpha(t)$ decreases with the feature sizes of nanostructures [8, 9]. EXAFS investigations [10] revealed that in small gold particles, the temperature dependence of the first neighbor distance is different from that of the macrocrystalline counterpart. In the largest size samples, a reduction in the thermal expansion happens, whereas in the smallest ones, a crossover from an initial thermal expansion to a thermal contraction presents.

According to Cardona [11], the lattice thermal expansion of a cubic crystal could be expressed in terms of the Grüneisen mode parameter, γ_q , and lattice vibration in the frequency of ω_q

$$\begin{aligned} \frac{\Delta d}{d_0} = \alpha T &= \frac{\hbar}{3BV} \sum_q \gamma \omega_q \left[n_B(\omega_q) + \frac{1}{2} \right] \\ &\propto \begin{cases} \frac{2kT}{BV_C} \langle \gamma_q \rangle & (T > \theta_D) \\ \int_0^{\omega_D} \langle \gamma_q \rangle \omega^3 \left\{ [\exp(\hbar\omega/kT) - 1]^{-1} + 1/2 \right\} d\omega & (\text{else}) \end{cases} \quad (23.2) \\ \gamma_q &= - \frac{\partial \text{Ln}(\omega_q)}{\partial \text{Ln}(V)} \end{aligned}$$

where B is the bulk modulus and V the volume. V_C is the volume of the primary unit cell and $\langle \gamma_q \rangle$ the average of γ_q over all branches of the Brillouin zone. The $n_B(\omega_q)$ is the Bose–Einstein population function.

From the phonon nonlinearities, Grüneisen [12] derived the expression for the volume TEC that is proportional to the product of the specific heat and Grüneisen parameter,

$$\alpha = \frac{\gamma C_v}{VB_T}$$

From the perspective of LBA, the $\alpha(t)$ for the representative bond can be derived from the differential of the thermal expansion relation [13],

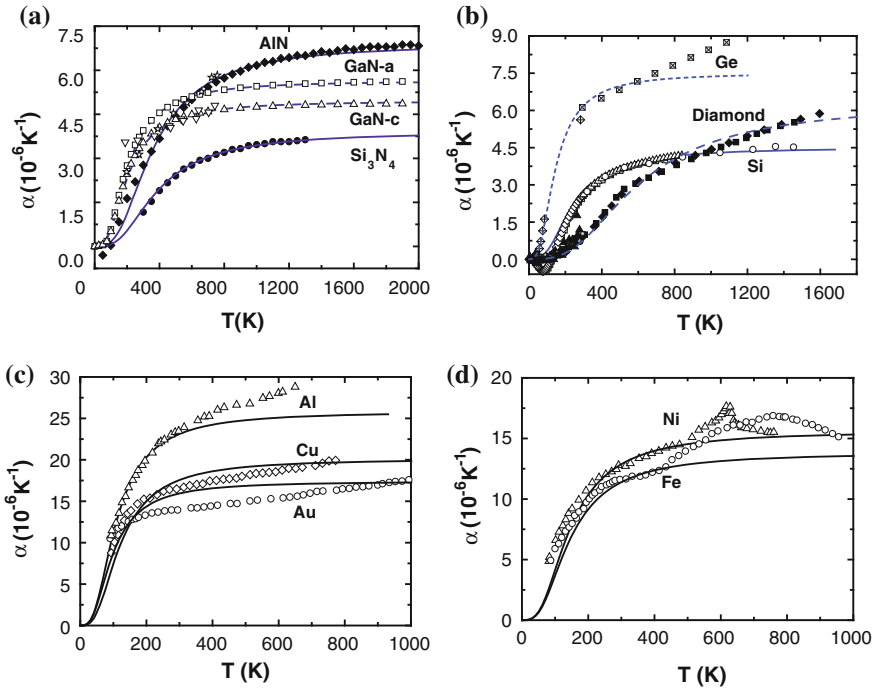


Fig. 23.2 LBA reproduction (*solid lines* [13]) of the temperature dependence of (a) TECs of (a) AlN [21], Si₃N₄ [21], and GaN [15, 22]), and (b) Si [23–25], Ge [26] and Diamond [14, 27–29]; (c) Au, Cu, and Al [30]; (d) Ni and Fe [30]. (Reprinted with permission from [13])

$$L = L_0 \left(1 + \int_0^T \alpha(t) dt \right), \text{ and,} \quad (23.3)$$

$$\alpha(t) \cong \frac{dL}{L_0 dt} = \frac{1}{L_0} \left(\frac{\partial L}{\partial u} \right) \frac{du}{dt} \propto - \frac{\eta_1(t)}{L_0 F(r)} = A(r) \eta_1(t)$$

where $(\partial L / \partial u) = -F^{-1}$ is the inverse of interatomic force in dimension at a non-equilibrium atomic distance. The value $A(r) = (-L_0 F(r))^{-1}$ can be obtained by matching theory to measurement. The smaller expansion coefficient for small particles [8–10, 14, 15] indicates an increased value of the gradient of the interatomic potential, which is consistent with the narrowed shape of the BOLS-related interatomic potential (see Chap. 11). The derived TEC follows approximately the trend of Debye specific heat, being consistent with experimental observations.

In fact, Eqs. (23.2) and (23.3) are substantially the same following the Debye or Einstein population. Normally, the $\alpha(t > \theta_D)$ is in the order of $10^{-(6 \sim 7)} \text{ K}^{-1}$. Figure 23.2 and Table 23.1 show the reproduction of the measured thermal expansion of Si and some nitrides according to Eq. (23.3).

The present form is much simpler and straightforward without the parameters of B , V , or γ_q being involved. The current approach covers the general trend for T -

Table 23.1 Parameters derived from fitting to the TECs and lattice parameters [13]

| | [31, 32] | $\alpha(t)$ | | $l(t)$ | | | Mean | |
|--------------------------------|----------------|----------------|--------|----------------|----------------------|----------------|----------------|--------|
| | θ_D (K) | θ_D (K) | $A(r)$ | θ_D (K) | $A(r)$ | l_0 (Å) | θ_D (K) | $A(r)$ |
| Si | 647 | 1,000 | 0.579 | 1,100 | 0.579 | 5.429 | 1,050 | 0.579 |
| Ge | 360 | 600 | 0.966 | 500 | 1.035 | 5.650 | 550 | 1.001 |
| C | 1,860 | 2,500 | 0.811 | 2,150 | 0.792 | 3.566 | 2,325 | 0.802 |
| AlN | 1,150 | 1,500 | 0.888 | 1,500 | 0.946(a) 0.881(c) | 3.110 4.977 | 1,500 | 0.882 |
| Si ₃ N ₄ | 1,150 | 1,600 | 0.502 | 1,400 | 0.888 | 7.734 | 1,500 | 0.695 |
| GaN | 600 | 850 | 0.637 | 800 | 0.637(a) 0.618(c) | 3.189 5.183 | 825 | 0.631 |
| Au | 170 | 400 | 2.241 | 400 | 2.105 | 4.070 | 400 | 2.173 |
| Cu | 315 | 500 | 2.588 | 500 | 2.588 | 3.600 | 500 | 2.588 |
| Al | 420 | 450 | 3.322 | 500 | 3.554 | 4.036 | 475 | 3.438 |
| Ni | 375 | 600 | 2.009 | 600 | 2.144 | 3.513 | 600 | 2.076 |
| Fe | 460 | 600 | 1.777 | 600 | 20.09 | 2.820 | 600 | 10.93 |

a and c represents a-axis and c-axis of the crystal, respectively

dependent $\alpha(T)$ showing exceedingly good agreement with the measured data for AlN, Si₃N₄, and GaN. However, the observed negative TECs in group-IV elements at extremely low temperatures could not be reproducible. Generally, most materials expand upon being heated, although some expand upon cooling like graphite [16], graphene oxide paper [17], ZrWO₃ [18, 19], and other compounds composed of N, F, and O [20]. The unusual behavior of materials having negative TECs is often attributed to the negative Grüneisen parameters of the transverse acoustic phonons near the Brillouin zone boundary. In metals, in addition to the phonon contribution to the thermal expansion, free electrons also play a role in T -dependent change in lattice constant. The current model gives better prediction for the lattice behavior at low temperatures than at high temperatures for some pure metals, such as Au, Cu, and Al. The TECs of these pure metals still keep increasing with temperature even at very high temperature ($T \gg \theta_D$). This deviation may arise from the thermal contribution from electrons. For the ferromagnetic Ni and Fe, the measured TECs exhibit an abrupt feature at the Curie temperature T_c , which corresponds to a phase transition from ferromagnetic to paramagnetic, and this abrupt feature may arise from spin contribution to the specific heat. It is not surprising that these unexpected features are beyond the scope of the current model because we used an ideal case of the phonon density of states derived from long wavelength at the Brillouin zone center and only the phonon contribution is considered. The contribution from electrons, or spins, or phase transition is not included. The Debye approximation of the specific heat assumes that the phonon density of states in an elastic medium is ideally proportional to ω^2 . In reality, one has to consider the exact form of the phonon density of states that is a quantity of measurement using neutron diffraction and it is beyond the scope of theory. Nevertheless, the phonon contribution to the thermal properties is dominant, and a precise prediction of the T -dependent TECs can be

made if the exact density of states $g(\omega)$ is given. The reproduction of the general trend of T -dependent TECs may evidence the validity of the current LBA approach in describing the thermally induced bond expansion.

The $\eta_1(t)$ and the integration of $\eta_1(t)$ with respect to T , or the conventionally termed internal or vibration energy, $U(T/\theta_D)$, follow the relation

$$\eta_1(t/\theta_D) = \frac{C_v(T/\theta_D)}{zR} = \frac{\kappa^2}{z} \left(\frac{T}{\theta_D} \right)^\kappa \int_0^{\theta_D/T} \frac{x^{\kappa+1} \exp(x)}{(e^x - 1)^2} dx$$

$$U(T/\theta_D) = \begin{cases} = \int_0^T \eta_1(t) dt & = \kappa \left(\frac{T}{\theta_D} \right)^{\kappa+1} \int_0^{\theta_D/T} \frac{x^\kappa dx}{e^x - 1} \\ \cong \sum_{n>1} \frac{1}{n!} \left. \frac{\partial^n u(x)}{\partial x^n} \right|_{x=0} x^n & \sim \omega^2 x^2 / 2 + u'''(r) x^3 / 6 + 0(x^n > 4) \end{cases} \quad (23.4)$$

with $x = \hbar\omega/k_B T$ and κ the dynamic dimensionality considered in transport dynamics (for a spherical dot, $\kappa = 0$; for atomic chains and thin wires, $\kappa = 1$; for thin surface slabs, $\kappa = 2$; and for large bulk, $\kappa = 3$). The $U(T/\theta_D)$ corresponds to the internal bond energy including all acoustic and optical modes of harmonic and inharmonic vibrations. The $U(T/\theta_D)$ is the amount of energy for the bond weakening.

23.1.3 High-Temperature and Low-Stress Approximation

At temperature higher than the Debye temperature, the $\eta_1(T > \theta_D)$ equals unity. In addition, at sufficiently lower stress, the compressibility approaches constant. Therefore, the absolute value of $E_i(z, T, P)$ can be simplified as

$$E_i(z_i, T, P) = E_i(z, 0, 0) - \eta_1 T + d_i(z, T, 0)[1 + \beta P/2]P$$

$$\stackrel{T < \theta_D}{\cong} \eta_2 + \eta_1(T_{mi} - T) + d_i(z, T, 0)[1 + \beta P/2]P \quad (23.5)$$

η_2 is the latent heat per coordinate of atomization for an atom in the molten state. At $T > \theta_D$, the integral will degenerate into the linear relation as given by Nanda [33], $E_b(0) = \eta_2 + \eta_1 T_m$.

Therefore, the magnitude of the net binding energy in Eq. (23.5) contains three parts: (1) the binding energy per bond at 0 K, $E_i(z, 0, 0)$; (2) the internal or thermal energy, $U(T/\theta_D) = \eta_1 T$, and (3) the deformation energy due to the field of stress, $d_i(z, T, 0)[1 + \beta P/2]P$. For an atom, the last two terms have to be revised to $z\eta_1 T$ and $d_i^3(z, T, 0)[1 + 3\beta P/2]P$ because of the three-dimensional nature. The deformation energy is estimated rather small (at 10^{-1} to 10^{-2} eV levels), and it is negligible in comparison with the bond energy in the order of 10^0 eV.

Figure 23.1a illustrates the temperature dependence of the reduced bond energy for an atom in the bulk. Considering the single bond, one has to divide the values by the atomic CN. The $E_b(0)$ and the θ_D are so important that they determine the

slope of the $E_b(T)/E_b$ -T curve and the transition point (about $\theta_D/3$) at which the $E_b(T)/E_b$ approaches to a linear temperature dependence.

For the bond of an undercoordinated atom, $E_i = \eta_{2i} + \eta_{1i}T_{mi}$. Because $T_m \propto z_b E_b$, $T_{mi} \propto z_i E_i$, and $E_i = C_i^{-m} E_b$, one has the relations of $\eta_{2i} + \eta_{1i}T_{mi} = -C_i^{-m}(\eta_2 + \eta_1 T_m)$ and

$$\begin{aligned}\frac{T_{mi}}{T_m} &= z_{ib} C_i^{-m} = 1 + \Delta_i; \\ \frac{\eta_{2i}}{\eta_2} &= C_i^{-m}; \\ \frac{\eta_{1i}}{\eta_1} &= \frac{z_b}{z_i} = z_{bi}.\end{aligned}\quad (23.6)$$

for the quantities between the localized and the bulk standard. The Δ_i is the perturbation to atomic cohesion energy.

23.2 Multi-Field Coupling

The joint effect of multiple fields on the cohesive energy of nanocrystals can be integrated based on the rule of energy superposition [20]. Variation in these external stimuli provides perturbations in the crystal cohesive energy, based on the core-shell configuration,

$$E_{\text{coh}}(K, P, T) = z_b E_b \left(N - \sum_{i \leq 3} N_i \right) + \sum_{i \leq 3} N_i z_i E_i$$

where

$$\begin{cases} E_i = E_{i0} + \sum_x \Delta E_i^x \\ E_b = E_{b0} + \sum_x \Delta E_b^x \end{cases} \quad (23.7)$$

E_{i0} and E_{b0} are the cohesive energy per bond in the i th atomic site and in the bulk without other stimuli. ΔE_i^x corresponds to the term of $\sum_J \Delta J$ in Eq. (23.1). The multiple field coupling yields the following relations based on the relation of $E_{\text{coh}}(\infty, 0, 0) = N z_b E_{b0}$,

$$\begin{aligned}E_{\text{coh}}(K, x_i) &= z_b \left(E_{b0} + \sum_x \Delta E_b^x \right) \left(N - \sum_{i \leq 3} N_i \right) + \sum_{i \leq 3} N_i z_i \left(E_{i0} + \sum_x \Delta E_i^x \right) \\ \frac{E_{\text{coh}}(K, x_i)}{E_{\text{coh}}(\infty, 0, 0)} &= \left(1 + \frac{\sum_x \Delta E_b^x}{E_{b0}} \right) \left(1 - \sum_{i \leq 3} \gamma_i \right) + \sum_{i \leq 3} \gamma_i z_{ib} \left(C_i^{-m} + \frac{\sum_x \Delta E_i^x}{E_{b0}} \right) \\ &= \left(1 + \frac{\sum_x \Delta E_b^x}{E_{b0}} \right) + \sum_{i \leq 3} \gamma_i \left\{ \left(z_{ib} C_i^{-m} - 1 + z_{ib} \frac{\sum_x \Delta E_i^x}{E_{b0}} - \frac{\sum_x \Delta E_b^x}{E_{b0}} \right) \right\} \\ &= \left[1 + \sum_{i \leq 3} \gamma_i (z_{ib} C_i^{-m} - 1) \right] + \frac{\sum_x \Delta E_b^x}{E_{b0}} \left\{ 1 + \left[\sum_{i \leq 3} \gamma_i \left(z_{ib} \frac{\sum_x \Delta E_i^x}{\sum_x \Delta E_b^x} - 1 \right) \right] \right\}.\end{aligned}\quad (23.8)$$

The first part represents purely the effect of size and the second part the joint effect of other stimuli. The effect of multi-filed coupling proceeds only in the skin, as seen from the sum in the second part.

23.3 Factors Dominating Mechanical Strength

As indicated in Eq. (22.2), the stress and modulus have the same dimension being proportional to the sum of binding energy per unit volume. According to the expression, mechanical elasticity strengthening only takes place once the bond energy increases and/or the bond length contracts. No other factors contribute intrinsically. Therefore, a superhard covalent crystal should be reached with the factors of higher bond density or electronic density, shorter bond length, and greater degree of bond covalency [34–37].

According to Born's criterion [38], the shear modulus disappears when a solid is in molten state. If Born's criterion holds, the latent heat of atomization, η_2 , contributes little to the elasticity and the yield strength. However, an elastic modulus should be present in the liquid and even in the gaseous phases because of the nonzero sound velocity in these phases. The sound velocity depends functionally on the elastic constant and the mass density of the specimen in the form of $(Y/\rho)^{1/2}$. However, the η_2 contributes indeed to the extensibility of atomic wires [39]. In fact, the tensile strength of alloys drops from the bulk values to approximately zero when the temperature is approaching T_m [40, 41]. Therefore, Born's criterion is more suitable to situations where the extensibility and plastic deformation happen.

Instead of the classical Gibbs free energy [$G(T, P, n_i, A) = U - TS + PV + \sum \mu_i n_i + \sigma A$], Helmholtz free energies [$F(T, V, n_i, A) = U - TS + PV + \sum \mu_i n_i + \sigma A$], internal energy $U(S, V)$, or enthalpy [$H(S, P) = U + PV$], or the continuum solid mechanics, the LBA approach in terms of bond length and bond energy and their response to atomic CN, temperature, and stress are appropriate for substances at all scales. Instead of the classical statistic thermodynamic quantities such as entropy S that is suitable for a body with infinitely large number of atoms, here considers only the reduced specific heat per bond, $\eta(T/\theta_D)$. Neither the chemical potential μ_i for the component n_i nor the tension σ of a given surface are needed in the current approach. Here one needs considering only the specific heat per coordinate.

Reproduction of the measured temperature dependence of (1) the redshift of the Raman optical modes [42–44], (2) surface tension of liquid [45], (3) elastic modulus [42], and (4) lattice expansion [13] of solid materials evidence the validity of the LBA approach for the thermally induced mechanical behavior of materials.

23.4 Summary

The BOLS correlation applies to the temperature and pressure domains based on the LBA approximation. The often overlooked event of bond broken and its effect on the behavior of the remaining bonds of the undercoordinated atoms dictate the behavior of low-dimensional systems. All the detectable quantities can be connected to the representative bonds and their response to the external stimulus. The coordination environment affects bonds only in the outermost two atomic layers yet temperature and pressure will affect all the bonds in the specimen. The multiple field coupling happens in the skin region only. Given the known functional dependence of the detectable quantities on the bond length and bond energy and the shape and size, one would be able to predict the trends of the performance of nanostructures and to gain physical insight into the unusual behavior of small objects without needing hypothetical parameters.

References

1. C.Q. Sun, Y. Wang, B.K. Tay, S. Li, H. Huang, Y.B. Zhang, Correlation between the melting point of a nanosolid and the cohesive energy of a surface atom. *J. Phys. Chem. B* **106**(41), 10701–10705 (2002)
2. G. Ouyang, C.Q. Sun, W.G. Zhu, Pressure-stiffened Raman phonons in group III nitrides: A local bond average approach. *J. Phys. Chem. B* **112**(16), 5027–5031 (2008)
3. B. Gilbert, H. Zhang, B. Chen, M. Kunz, F. Huang, J.F. Banfield, Compressibility of zinc sulfide nanoparticles. *Phys. Rev. B* **74**(11), 115405 (2006)
4. M. Pravica, Z. Quine, E. Romano, X-ray diffraction study of elemental thulium at pressures up to 86 GPa. *Phys. Rev. B* **74**(10), 104107 (2006)
5. B. Chen, D. Penwell, L.R. Benedetti, R. Jeanloz, M.B. Kruger, Particle-size effect on the compressibility of nanocrystalline alumina. *Phys. Rev. B* **66**(14), 144101 (2002)
6. F. Birch, Finite elastic strain of cubic crystals. *Phys. Rev.* **71**(11), 809–824 (1947)
7. Z.W. Chen, C.Q. Sun, Y.C. Zhou, O.Y. Gang, Size dependence of the pressure-induced phase transition in nanocrystals. *J. Chem. Phys. C* **112**(7), 2423–2427 (2008)
8. J.L. Hu, W.P. Cai, C.C. Li, Y.J. Gan, L. Chen, *In situ x-ray diffraction study of the thermal expansion of silver nanoparticles in ambient air and vacuum*. *Appl. Phys. Lett.* **86**(15), 151915 (2005)
9. L. Li, Y. Zhang, Y.W. Yang, X.H. Huang, G.H. Li, L.D. Zhang, *Diameter-dependent thermal expansion properties of Bi nanowire arrays*. *Appl. Phys. Lett.* **87**(3), 031912 (2005)
10. T. Comaschi, A. Balerna, S. Mobilio, Temperature dependence of the structural parameters of gold nanoparticles investigated with EXAFS. *Physical Review B* **77**(7), 075432 (2008)
11. M. Cardona, M.L.W. Thewalt, Isotope effects on the optical spectra of semiconductors. *Rev. Mod. Phys.* **77**(4), 1173–1224 (2005)
12. E. Grüneisen, The state of a body. *Handb. Phys.* **10**, 1–52. NASA translation RE2-18-59 W (1926)
13. M.X. Gu, Y.C. Zhou, C.Q. Sun, Local bond average for the thermally induced lattice expansion. *J. Phys. Chem. B* **112**(27), 7992–7995 (2008)
14. G.A. Slack, S.F. Bartram, *Thermal expansion of some diamond-like crystals*. *J. Appl. Phys.* **46**(1), 89–98 (1975)

15. R.R. Reeber, K. Wang, Lattice parameters and thermal expansion of GaN. *J. Mater. Res.* **15**(1), 40–44 (2000)
16. Q.H. Tang, T.C. Wang, B.S. Shang, and F. Liu, Thermodynamic properties and constitutive relations of crystals at finite temperature. *Sci. China-Phys. Mech. Astron.* **G 55**, 933, (2012)
17. Y.J. Su, H. Wei, R.G. Gao, Z. Yang, J. Zhang, Z.H. Zhong, Y.F. Zhang, Exceptional negative thermal expansion and viscoelastic properties of graphene oxide paper. *Carbon* **50**(8), 2804–2809 (2012)
18. C. Martinek, F.A. Hummel, Linear thermal expansion of 3 tungstates. *J. Am. Ceram. Soc.* **51**(4), 227 (1968)
19. T.A. Mary, J.S.O. Evans, T. Vogt, A.W. Sleight, Negative thermal expansion from 0.3 to 1050 Kelvin in ZrW_2O_8 . *Science* **272**(5258), 90–92 (1996)
20. C.Q. Sun, Dominance of broken bonds and nonbonding electrons at the nanoscale. *Nanoscale* **2**(10), 1930–1961 (2010)
21. R.J. Bruls, H.T. Hintzen, G. de With, R. Metselaar, J.C. van Miltenburg, The temperature dependence of the Gruneisen parameters of $MgSiN_2$, AlN and β - Si_3N_4 . *J. Phys. Chem. Solids* **62**(4), 783–792 (2001)
22. A.U. Sheleg, W.A. Savastenko, *Fiz. Mat. Nauk* **3**, 126 (1976)
23. J. Kim, J.A. Freitas, P.B. Klein, S. Jang, F. Ren, S.J. Pearton, The effect of thermally induced stress on device temperature measurements by Raman spectroscopy. *Electrochem. Solid State Lett.* **8**(12), G345–G347 (2005)
24. K.G. Lyon, G.L. Salinger, C.A. Swenson, G.K. White, Linear thermal-expansion measurements on silicon from 6 to 340 K. *J. Appl. Phys.* **48**(3), 865–868 (1977)
25. R.B. Roberts, Thermal-expansion reference data—silicon 300–850 K. *J. Phys. D-Appl. Phys.* **14**(10), L163–L166 (1981)
26. H.P. Singh, Determination of thermal expansion of germanium rhodium and iridium by x-rays. *Acta Crystallogr. Sect. A* **A 24**, 469 (1968)
27. T. Sato, K. Ohashi, T. Sudoh, K. Haruna, H. Maeta, Thermal expansion of a high purity synthetic diamond single crystal at low temperatures. *Phys. Rev. B* **65**(9), 092102 (2002)
28. C. Giles, C. Adriano, A.F. Lubambo, C. Cusatis, I. Mazzaro, M.G. Honnicke, Diamond thermal expansion measurement using transmitted X-ray back-diffraction. *J. Synchrotron Radiat.* **12**, 349–353 (2005)
29. K. Haruna, H. Maeta, K. Ohashi, T. Koike, Thermal-expansion coefficient of synthetic diamond single-crystal at low-temperatures. *Jpn. J. Appl. Phys. Part 1-Regul. Pap. Short Notes Rev Pap.* **31**(8), 2527–2529 (1992)
30. F.C. Nix, D. MacNair, The thermal expansion of pure metals copper, gold, aluminum, nickel, and iron. *Phys. Rev.* **60**(8), 597–605 (1941)
31. C. Kittel, *Introduction to Solid State Physics*. 8 edn. (New York, Wiley, 2005)
32. <http://www.infoplease.com/periodictable.php>
33. K.K. Nanda, S.N. Sahu, S.N. Behera, Liquid-drop model for the size-dependent melting of low-dimensional systems. *Phys. Rev. A* **66**(1), 013208 (2002)
34. Z.W. Chen, M.X. Gu, C.Q. Sun, X.Y. Zhang, R.P. Liu, Ultrastiff carbides uncovered in first principles. *Appl. Phys. Lett.* **91**(6), 061905 (2007)
35. Y.J. Tian, B. Xu, D.L. Yu, Y.M. Ma, Y.B. Wang, Y.B. Jiang, W.T. Hu, C.C. Tang, Y.F. Gao, K. Luo, Z.S. Zhao, L.M. Wang, B. Wen, J.L. He, Z.Y. Liu, Ultrahard nanotwinned cubic boron nitride. *Nature* **493**(7432), 385–388 (2013)
36. F.M. Gao, J.L. He, E.D. Wu, S.M. Liu, D.L. Yu, D.C. Li, S.Y. Zhang, Y.J. Tian, Hardness of covalent crystals. *Phys. Rev. Lett.* **91**(1), 015502 (2003)
37. X.J. Guo, L. Li, Z.Y. Liu, D.L. Yu, J.L. He, R.P. Liu, B. Xu, Y.J. Tian, H.T. Wang, Hardness of covalent compounds: Roles of metallic component and d valence electrons. *J. Appl. Phys.* **104**(2), 2956594 (2008)
38. M. Born, Thermodynamics of crystals and melting. *J. Chem. Phys.* **7**(8), 591–603 (1939)
39. C.Q. Sun, C.M. Li, S. Li, B.K. Tay, Breaking limit of atomic distance in an impurity-free monatomic chain. *Phys. Rev. B* **69**(24), 245402 (2004)

40. D.G. Eskin, Suyitno, L. Katgerman, Mechanical properties in the semi-solid state and hot tearing of aluminium alloys. *Prog. Mater. Sci.* **49**(5), 629–711 (2004)
41. J. Campbell, *Castings*. (Butterworth-Heinemann, Oxford, 1991)
42. M.X. Gu, Y.C. Zhou, L.K. Pan, Z. Sun, S.Z. Wang, C.Q. Sun, Temperature dependence of the elastic and vibronic behavior of Si, Ge, and diamond crystals. *J. Appl. Phys.* **102**(8), 083524 (2007)
43. M.X. Gu, L.K. Pan, B.K. Tay, C.Q. Sun, Atomistic origin and temperature dependence of Raman optical redshift in nanostructures: a broken bond rule. *J. Raman Spec.* **38**(6), 780–788 (2007)
44. M.X. Gu, L.K. Pan, T.C.A. Yeung, B.K. Tay, C.Q. Sun, Atomistic origin of the thermally driven softening of Raman optical phonons in group III nitrides. *J. Chem. Phys. C* **111**(36), 13606–13610 (2007)
45. M. Zhao, W.T. Zheng, J.C. Li, Z. Wen, M.X. Gu, C.Q. Sun, Atomistic origin, temperature dependence, and responsibilities of surface energetics: An extended broken-bond rule. *Phys. Rev. B* **75**(8), 085427 (2007)

Chapter 24

Liquid and Solid Skins

- *The concepts of (1) energy density gain per unit volume, (2) residual cohesive energy per discrete surface atom replace essentially the conventional concept of surface energy or the energy loss per unit area or per atom in breaking one body into two halves.*
- *The excessive surface energy, stress, and tension results from the broken-bond-induced bond contraction and the associated bond strength gain; the residual atomic cohesive energy results from the product of bond order remain and bond energy gain.*
- *A liquid surface solidifies easier than the liquid core; a solid skin is generally harder than the core interior.*
- *A strained, solid-like, and well-ordered liquid skin serves as an elastic covering sheet for a liquid drop or a gas bubble formation; the skin is covered with locked dipoles due to charge polarization by the densely trapped core electrons.*
- *Temperature dependence of surface tension reveals the atomic cohesive energy at the surface; the temperature dependence of elastic modulus gives the mean atomic cohesive energy of the specimen.*
- *Pressure dependence of elastic modulus reveals the binding energy density of the specimen.*
- *Charge repopulation and polarization dominates the adsorbate-induced stress change.*
- *The non-bonding states of nitrogen and oxygen play an important role in determining the stress of a chemisorbed surface.*

24.1 Observations

24.1.1 Surface Energetics: Classical Concepts

24.1.1.1 Surface Free Energy

Surface energetics, including the terms of surface energy, surface free energy, surface tension, surface stress, and their correlations, plays the central role in surface and nanosolid sciences. Despite confusions about these terms, the surface energetics is of great importance to a qualitative and sometimes even quantitative understanding of the microscopic and mesoscopic processes at a surface of liquid or solid. The surface energetics links the atomistic bonding configuration at the interfacial region with its macroscopic properties, such as strength, elasticity, wettability, reactivity, diffusivity, and adhesion [1, 2]. Without the surface or surface energetics, neither a liquid drop nor a gas bubble could form.

During the last few decades, tremendous attention has been paid to the energetically induced surface processes such as reconstruction, relaxation, interfacial mixing, segregation, self-organization, adsorption, and melting at the solid surfaces. Increased knowledge about the surface stress or surface energy of clean and adsorbate-covered metals has been established by the development of experimental and theoretical methods such as Raman shift, X-ray glancing diffractions, and the microcantilever sensors that allows the detection of extremely small amounts of substances in gases or liquids [3].

However, detailed knowledge about the dynamics of surface energetic identities is yet lacking [1, 2, 4], in particular, the atomistic and electronic origin, temperature and adsorbate dependence, and the analytical description of the interdependence between surface energetic identities and the energetically driven phenomena and processes.

Traditionally, the surface energy (γ_s), or the surface free energy for a solid, is defined as the energy needed to cut a given crystal into two halves, or energy consumed (loss) in making a unit area of surface [5]. The surface energy or stress is involved in the Helmholtz or Gibbs free energy in the classical statistic thermodynamics [6]

$$\begin{aligned} dF &= -SdT - PdV + \sum \mu_i dn_i + \sigma dA && \text{(Helmholtz)} \\ dG &= -SdT + VdP + \sum \mu_i dn_i + \sigma dA && \text{(Gibbs)} \end{aligned}$$

with parameters of entropy (S), chemical potential (μ_i) of the i th component (n_i), surface tension (σ), and the surface area A being involved.

Usually, unrelaxed structures at zero temperature are considered in the discussion of surface energies. The values obtained are then corrected for relaxations of the surface atoms, without mentioning reconstructions of the surface. In some cases, these corrections are thought very small, so a simplified model can be made without including relaxations. The temperature dependence involves the phonons and their modification on the surface; the vibrational effects sometimes have to be taken into account when the temperature dependence is studied.

The following explains conventionally the atomistic origin of the surface energy. A surface atom has fewer neighboring atoms and experiences fewer attractive interaction forces from its surroundings than a fully coordinated atom in the bulk interior. Consequently, the atoms at the surface experience a net force pointing into the bulk, or in other words, the potential energy of a surface atom is higher than that of a bulk atom because of the lowered atomic coordination. If one wants to create two new surfaces with a total area of A by cutting a solid at constant elastic strain (ε_{ij}) and constant temperature, one requires the surface energy

$$\gamma_s = (F_S - F_0)_{\varepsilon_{ij}, T} / A$$

where F_S and F_0 are, respectively, the system free energy after and before the cut.

The simplest approach to get a rough estimation of the surface energy is to determine the number of bonds that have to be broken in order to create a unit area of surface. One can cut a crystal along a certain crystallographic plane and multiply this number of broken bonds with the energy per bond without considering the bond energy change caused by the reduction in atomic coordination. The following summarize typical approaches for the defined surface energy [2, 7–9]:

$$\gamma_s = \begin{cases} \frac{W_s - W_B}{20} n_d (n_d - 10) & \text{(Galanakis)} \\ (1 - z_s/z_b) E_B & \text{(Haiss)} \\ (1 - \sqrt{z_s/z_b}) E_B & \text{(Desjonqueres)} \\ \frac{[2 - z_s/z_b - (z_s/z_b)^{1/2}] + \lambda [2 - z'_s/z'_b - (z'_s/z'_b)^{1/2}]}{2 + 2\lambda} E_B & \text{(Jiang)} \end{cases} \quad (24.1)$$

- Galanakis et al. [9] correlated the surface energy of some d-metals to the broken bond in the tight-binding approximation. The n_d is the number of d-electrons. W_S and W_B are the bandwidths for the surface and the bulk density of states, which took in rectangular forms.
- Haiss et al. [2] related the surface energy directly to the multiplication of the number of broken bonds and the cohesive energy per bond $E_b = E_B/z_b$ at 0 K. The γ_s values are estimated by determining the broken bond number $z_{\text{hkl}} = z_b - z_s$ for creating a unit surface area by cutting a crystal along a certain crystallographic plane with a Miller index (hkl), where z_s is the CN of a surface atom and z_b the corresponding bulk atomic CN.
- A second-moment tight-binding approximation conducted by Desjonquères et al. [9] suggested that the surface energy gain is proportional to $\sqrt{z_s}$, instead of z_s , because of the lowering of the occupied surface energy states or the surface-induced positive core-level shift as observed using XPS [10]. According to this approximation, the rearrangement of the electronic charge does not practically change the nature of the remaining bonds if one bond breaks. Thus, the energy needed to break a bond is independent of the surface orientation, so that the γ_s value is proportional to the square root of the number of the nearest-neighboring bonds.

- In order to obtain a more general expression, Jiang et al. [8] suggested that an average of the approximations of Haiss and Desjonquères and an extension to counting the contribution from the next-nearest neighbors could be more inclusive. The prime in the expression denotes the next-nearest neighbors of the surface atoms, and λ is the total bond strength ratio between the next-nearest neighbor and the nearest one.
- In addition, Xie et al. [11] derived an expression for the size dependence of surface energy of nanostructures: $\gamma_s = E_B/\pi d^2$ with d being the mean atomic radius and E_B the atomic vacancy formation energy [12].

Besides the thermodynamic considerations, the kinetic processes of lattice vibration play significant roles in the anisotropy of surface properties [13]. The amplitudes and frequencies of atomic vibrations [14], as well as the bond lengths and strengths at a surface are different from their corresponding bulk values because of the effect of bond broken [15]. During the growth of a thin film, adatoms and atomic vacancies also contribute to the surface energy. With these contributing factors, the surface energetics becomes even more complicated.

24.1.1.2 Surface Stress

In contrast to the surface energy, relating to energy change during the plastic deformation of a unit area of surface, the surface stress (σ_{ij}) is related to energy changes during the elastic stretching of a preexisting surface. Since the surface stress in general may be dependent on the direction of the stretching, the term σ_{ij} is a second-rank tensor and the stretching has to be expressed by the elastic strain tensor ε_{ij} ,

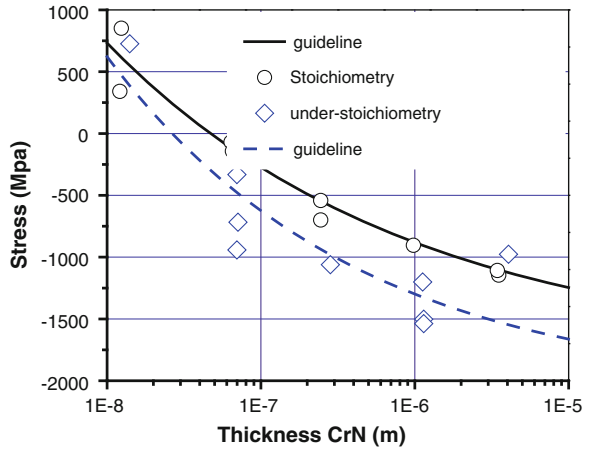
$$\sigma_{ij} = \frac{\partial \gamma_s}{\partial \varepsilon_{ij}}$$

where the γ_s is the free energy at any strain. If γ_s is lowered for negative strain values, the surface tends to shrink and the surface stress has a positive sign. In this situation, the stress is ‘tensile.’ If the surface tends to expand, the corresponding stress is ‘compressive’ with a negative sign.

According to Haiss [2], the surface stress originates physically from the atomic CN reduction in surface atoms and the corresponding charge redistribution. The charge redistribution alters the nature of the chemical bonds and the equilibrium interatomic distances. Hence, the surface atoms attempt to assume their equilibrium interatomic distances and exert forces on the bulk, as long as the potential corrugation of the underlying atomic layer holds the topmost atoms in registry with the bulk lattice. The surface stress can be quantified as the sum of such forces.

It has been found [16] that the stress in CrN films varies with film thickness, see Fig. 24.1, which corresponds to the sum of the tensile stress generated at the grain boundaries, compressive stress due to ion peening in deposition, and thermal stress due to the difference in thermal expansion between the coating and the substrate.

Fig. 24.1 Thickness dependence of CrN film stress [16] showing dominance of the surface and the influence of chemical stoichiometry (reprinted with permission from [111])



The tensile part due to grain boundaries is thickness dependent. The other two contributions are thickness independent. Summation of the three components leads to a stress gradient in the coating.

24.1.1.3 Surface Tension

Surface tension is expressed either as the force per unit length or as the energy per unit area of the interface between air and liquid, which results from the force of cohesion between liquid molecules or from the attraction of molecules to one another on a liquid surface. Thus, a potential barrier emerges between the air and the liquid. The elastic-like force between surface molecules tends to minimize or constrict the area of the surface. In physics, surface tension is an effect within the surface layer of a liquid that causes the layer to behave as an elastic sheet with higher strength and higher elasticity of the liquid. However, it is unclear yet why the liquid skin is more elastic and stronger than the liquid core interior although the surface tension of an organic specimen was suggested [17] to be proportional to the product of molecular weight and the topological Wiener index to a power of 3/2, $MW^{3/2}$. The topological Wiener index is the sum of all the shortest distance in the molecular crystallography, and the $MW^{3/2}$ is treated as characterizing the moment of inertia of the rotational motion of the molecules.

24.1.2 Solid Skin Rectification

The elasticity and hardness of a skin depend on several factors [18]: (1) the surface curvature, (2) the nature of the bond involved, and (3) the ratio between the operating temperature and the skin melting point. Normally, the surface of a solid

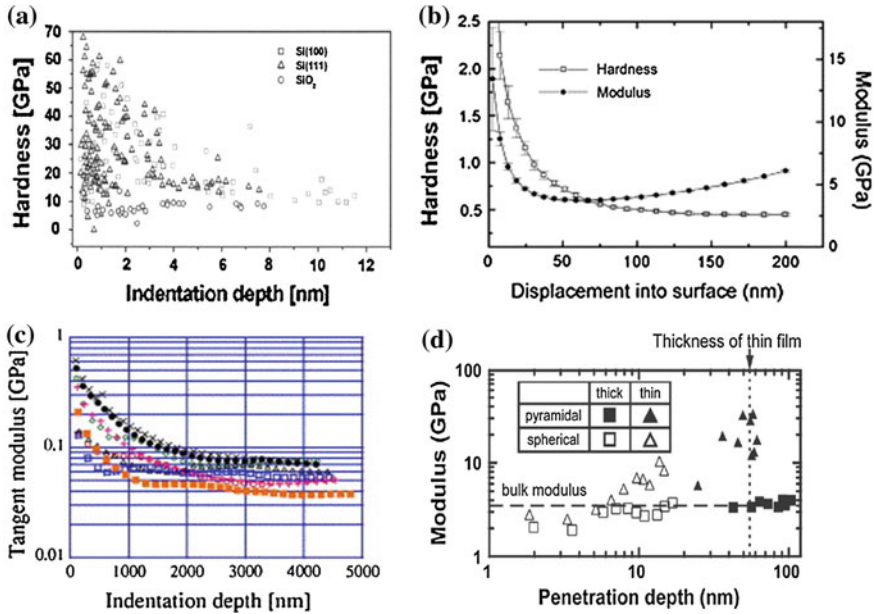


Fig. 24.2 Skin hardening of **a** the Si(001), Si(111), and SiO₂ skins [19], **b** the silica-based low-dielectric films [20], and **c** the modulus-depth profile of a CNT turf showing one order higher in magnitude at the skins. Indentations are taken at different distances from the edge of the turf. The more compliant cases correspond to indentations closer to the edge [31]. Skin softening of **d** polymer [33], measured using AFM indentation. *Outlined* and *filled* symbols correspond to the values estimated using the *pyramidal diamond* and *spherical* indenters, respectively, for thick (*squares*) and thin (*triangles*) polymer films (reprinted with permission from [111])

is harder than the bulk interior at temperature far below the skin melting point. For instance, as shown in Fig. 24.2a, the hardness measurements of Si skins, with penetration depths as small as 1 nm yield $H \sim 25$ GPa, showing a drastic increase to 75 GPa with penetration depths to 5 nm compared with the bulk value of 12 GPa [19]. Figure 24.2b shows the relation between the hardness and elastic modulus of the silica-based low-dielectric films [20].

Similarly, the maximum hardness for nano- and microcrystalline pure nickel films is also peaked at a penetration depth of ~ 5 nm [21, 22]. The hardness of Ni films varies in a range from 6 to 20 GPa depending not only on the geometrical shapes (conical, Berkovich, and cube-corner) of the indenter tips but also on the strain rate in measurement. The peak position (5 nm in depth) changes with neither the shape of the indenter tips nor the strain rates nor the particular specimen, which indicates the intrinsic nature of surface hardening. The values of both the Y and the σ for nitrogen-doped amorphous carbon (a-C) films [23] at the ambient temperature also show maximum hardness near the surface. The maximum hardness is 3–4 times higher than the bulk values, whereas the peak positions in the hardness-depth profiles remain unchanged when the nitrogen content or film thickness

changes. The hardness of TiCrN films at 5–10-nm depth [24] reaches a maximum of 50 GPa, being twice the bulk value. The same trend holds for a-C [25] and AlGaN [26] films with peaks positioned at several nanometers in depth that corresponds to the surface roughness.

Surfaces of Ag, Ni, Cu, and Al thin films are 4 ± 0.5 times harder than the bulk interior, and the hardness of α_2 -TiAl and γ -TiAl surfaces is ~ 2 times the corresponding bulk values [27]. The hardness of Ti, Zr, and Hf carbide films on silicon substrate increases from the bulk value of 18–45 GPa when the film thickness is decreased from 9,000 to 300 nm [28]. The Young's modulus of nanograined steel was determined to increase from 218 to 270 GPa associated with a mean lattice contraction from 0.2872 to 0.2864 nm when the grain size is reduced from 700 to 100 nm [29]. These observations evidence the skin hardening effect arising from the shortened and strengthened bonds between the undercoordinated atoms. Furthermore, surface passivation with electronegative elements could alter the bond nature in the surface skins and hence change the surface stress. A combination of the DFT and MD calculations [30] suggested that a surface could be softer or stiffer depending on the competition between electron redistribution and the atomic coordination on surfaces. Results show that the Young's modulus along the $\langle 110 \rangle$ direction on (100) surface is higher than its bulk counterpart; meanwhile, it is smaller along the $\langle 100 \rangle$ direction on (100) surface.

As shown in Fig. 24.2c, the tangent modulus of a CNT turf (a complex structure of intertwined nanotubes cross-linked by adhesive contact) was measured to be one order higher near the surface and the modulus drops with the penetration depth [31]. The modulus near the terrace edge is even higher than the flat surface.

In contrast, skin softening occurs to some polymers or materials of lower melting points. An AFM room temperature indentation measurement [32] revealed that the local Young's modulus of the organic thin films that can evaporate at ~ 150 °C decreases with particle size. The elastic modulus of polystyrene films increases with the penetration depth [33]. When the penetration depth is less than 5 nm, the elastic modulus of the films is smaller than that of the bulk. The elastic modulus approaches the bulk value when the depth is more than 10 nm, as shown in Fig. 24.2d. These observations suggest the significance of the difference between the temperature of melting and the temperature of testing to the measured values.

Ideally, an enhancement of the elasticity and hardness are readily observed from the skins of compounds, alloys, or specimens with high melting points, whereas the enhancement is not seen so often using indentation method for specimens with lower melting points such as Sn, Zn, Al, and organic specimens unless they are chemically passivated [34].

The measured skin hardening or softening also varies with methods of detection. For instance, the modulus of nanocrystalline of 50–800-nm-thick Ni films, measured using acoustic AFM [35], is lower than that of the bulk, as no artifacts such as accumulation of dislocations are involved in the non-contact acoustic AFM method. SiTiN films are measured approximately 10–20 % harder using nanoindentation than the values obtained using SAWs methods [36]. The additional pressure due to compression will cause deviation of the intrinsic values. Therefore,

the hard materials may be measured even harder and the soft one may be even softer using the indentation methods. During the contact measurements, heat released during bond unfolding could raise the specimen by 40–50 °C [37, 38], which softens the sample.

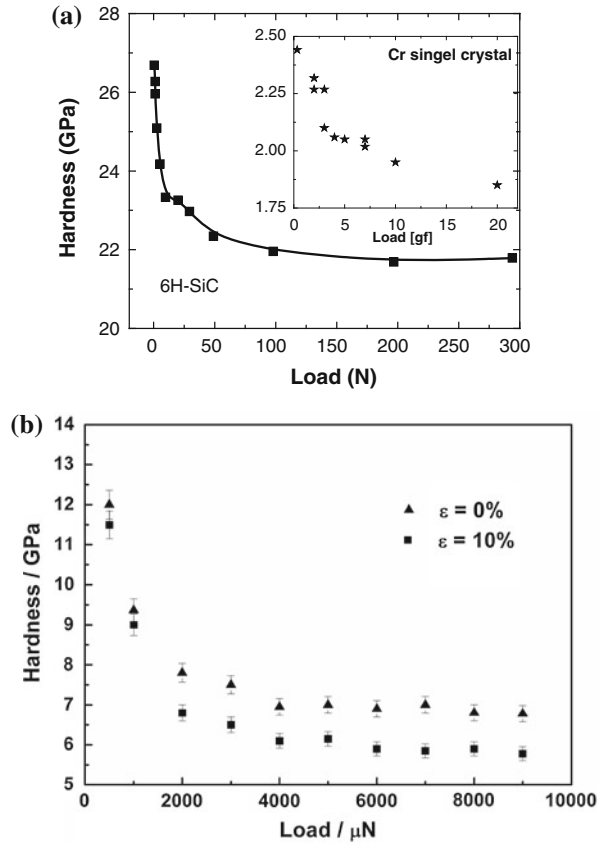
Normally, deformation resistance from the effect of the pile up of dislocations, strain gradient work hardening, and the artifacts due to indentation tip shapes, strain rates, loading scales and directions, etc., involved in the contact mode of indentation would play a role of significance [39]. The surface smoothness has less influence on the measurement [40].

Figure 24.3 shows the measured hardness dependence of Cr [41], 6H–SiC [39], and Ni [42] films on the load scales in the indentation methods. The hardness of the single-crystal moissanite (6H–SiC) obtained by 10-second loading parallel to the crystallographic c axis varies with the loading magnitude. If the load is 0.5 N, the derived hardness is 26 GPa, whereas, loading at 29 and 50 N, the corresponding hardness values are 22.5 and 22 GPa, respectively [39]. Therefore, it is difficult to be certain of the hardness of a material because of the joint contribution from the intrinsic and extrinsic processes. However, a careful calibration of the area function over the contact depth range prior to nanoindentation tests may improve the accuracy of the derived information [43].

Hence, one should tell that a specimen is harder or softer compared with the bulk standards with indicating the conditions of surface passivation, temperature of operation, and the testing methods used. Artifacts always presents in practice. What one is concerned about is the intrinsic change in the mechanical properties with temperature, solid size, and the nature of the bond involved. Therefore, one has to minimize contributions from artifacts in modeling considerations.

Several models exist on the mechanism for the skin hardening or softening. For instance, Zhang and co-workers [44, 45] proposed a critical-depth mechanism stating that the apparent surface stress plays an important role in the depth-dependent hardness for various types of materials, such as metals, ceramics, and polymers and there exists a critical indentation depth. The bulk deformation predominates when the indentation depth is deeper than the critical depth; otherwise, surface deformation predominates. However, the origin of this critical depth is unknown. The trend of hardness versus indentation depth after the peak is described using the mechanism of strain gradient [46] or attributed to the contributions from surface energy and the increase in dislocation density with the depth [47]. The surface hardening has also been attributed to the surface effect, strain gradient work hardening, and non-dislocation mechanisms of deformation [41], besides the currently proposed T-BOLS correlation [48] that attributes the surface hardening to the broken-bond-induced shortening and strengthening of the remaining bonds, or the binding energy density pertained to the undercoordinated atoms. The surface softening to the small difference of $T_m - T$. Operation temperature closing to the T_m of the specimen will trigger the situation described by Born's criterion.

Fig. 24.3 Load dependence of **a** the microhardness of Cr crystal (*insert*) [41] and 6H-SiC [39] and **b** the nanohardness of Ni films of $\sim 3\text{-}\mu\text{m}$ thickness under zero and 10 % tensile strain [42], showing the general trend of hardness in indentation methods (reprinted with permission from [111])



24.1.3 Liquid Skin Elasticity: Adsorption and Thermal Excitation

The surface tension for a liquid takes on an important part in the formation of liquid drop, bubble, or gas bubble in a liquid. Compared with the solid skin pre-melting, a liquid surface tends to solidify at temperatures below the bulk melting point. Normally, the temperature dependence of the surface tension of a molten substance follows a linear relation to the temperature of testing [49–54]:

$$\begin{aligned} \gamma_s(T) &= \gamma_s(T_m) + \alpha_t(T_m - T) = \gamma_s(0) - \alpha_t T \quad (\text{J/m}^2) \\ \gamma_s(0) &= \gamma_s(T_m) + \alpha_t T_m \end{aligned} \quad (24.2)$$

where $\gamma_s(T_m)$ is the γ_s value at melting. α_t is the thermal coefficient or the slope of variation. For pure metals or alloys, the surface tension drops linearly with the increase in temperature. However, the surface tension is very sensitive to the chemical environment or contamination [55, 56]. The surface tension of an alloy

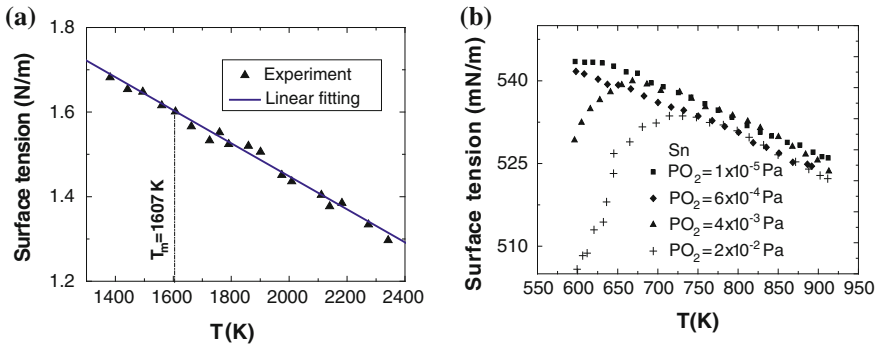


Fig. 24.4 Temperature dependence of surface tension of **a** CoSi liquid [57] and **b** Sn liquid under different oxygen partial pressures [58]. The inflection of the coefficient results from a competition between the adsorbate-induced compressive stress and the broken-bond-induced tensile stress according to the present understanding (reprinted with permission from [111])

also varies with composition. Typical samples in Fig. 24.4 show the linear temperature dependence of surface tension of a CoSi alloy [57] and the inflected temperature dependence of the surface tension of a Sn surface under different ambient of oxygen [58]. With the given composition, the surface tension drops linearly with the increase in temperature. However, the temperature coefficient inflects from negative to positive at a certain temperature and then drops following that of the ideal situations.

The turning point changes with oxygen dosage. As discussed later, the slope inflection can be envisioned as the contribution from the additionally compressive or tensile stress induced by surface adsorption to compensate or enhance the original surface tension of the liquid. For a specimen with a melting point much higher than the temperature of desorption of the specific adsorbate, such slope inflection may not be readily seen because of the thermal desorption of the electronegative additives, which occurs at temperature below 1,200 K for oxygen, for instance [59]. The inflection of the temperature coefficient of Sn surface tension induced by O addition [60], as shown in Fig. 24.4, results from adsorbate-induced compressive stress that compensates for the surface tension.

A huge database has been established regarding the temperature coefficient of surface tension for metals, alloys, and polymers. Tables 24.1a and 24.1b tabulate the data for some typical samples and includes information derived and discussed later in Sect. 24.4.2. The temperature dependence of surface tension provided an opportunity for one to derive information regarding atomic cohesive energy in the bulk and with possible mechanism for the adsorbate-induced surface stress. The latter could be a challenging topic of research on adsorption of various adsorbates to liquid surfaces of relatively low- T_m metals.

Table 24.1a Information of the mean atomic cohesive energy $E_B(0)$ (in bold case) derived from fitting the measured T -dependent surface tension, as shown in detail later in Sect. 24.4.2 with the measured surface tension and its temperature coefficient as listed in the first two columns

| | $\gamma_s(T_m)$ (mJ/m ²) | α_γ (mJ/ (m ² K)) | α_i^a (10 ⁻⁶ K ⁻¹) | $\theta_D(K)$ | T_m (K) | ΔT (K) | $E_B(0)$ (eV) | $E_B(0)$ [112] |
|--|---|---|---|---------------|-----------|----------------|------------------|-------------------|
| Hg [52] | 493 | 0.2 | 60.4 | 100 | 234.32 | 273–523 | 1.47 | 0.67 |
| Si [113] | 783.5 | 0.65 | 2.6 | 647 | 1,687 | 1,350–1,900 | 5.33 | 4.63 |
| Si [114] | 735 | 0.074 | | | | 1,457–1,890 | 2.04 | |
| Si [54] | 763 | 0.219 | | | | 1,690–1,750 | 1.15 | |
| Ga-added Si [115] | 777 | 0.243 | | | | 1,680–1,760 | 2.12 | |
| B-added Si [54] | 721 | 0.098 | | | | 1,690–1,750 | 3.92 | |
| Al ₂ O ₃ [54] | 640 | 0.082 | | 1,045 | 2,327 | 2,190–2,500 | 4.39 | |
| Al ₂ O ₃ [57] | 550 – 700 | 0.082 – 0.48 | | | | | | |
| Co ₂₅ Si ₇₅ [115] | 1,604 | 0.4 | | | 1,607 | 1,384–2,339 | 2.43 | |
| Ni [51] | 1,823 | 0.46 | 1.6 | 375 | 1,728 | | 3.645 | 4.44 |
| Ni [116] | 1,868 | 0.22 | | | | 1,300–1,625 | 6.03 | |
| Ni [117] | 1,854 | 0.364 | | | | | 4.02 | |
| Ni [118] | 1,846 | 0.25 | | | | | 5.38 | |
| Co [119] | 1,875 | 0.348 | 13 | 385 | 1,768 | | 4.22 | 4.39 |
| Co [120] | 1,881 | 0.34 | | | | | 4.31 | |
| Co [121] | 1,887 | 0.33 | | | | | 4.42 | |
| Co [67] | 1,930 | 0.33 | | | | 1,500–2,000 | 4.49 | |
| Ag [122] | 925.4 | 0.228 | 18.9 | 215 | 1,234.78 | 1,250–1,500 | 3.12 | 2.95 |
| Ta [123] | 2,150 | 0.21 | 6.3 | 225 | 3,269 | 2,970–3,400 | 7.98 | 8.1 |
| W [124] | 2,478 | 0.31 | 4.5 | 310 | 3,695 | 3,360–3,700 | 6.90 | 8.9 |
| Ga [70] | 718.2 | 0.062 | 18 | 240 | 302.77 | 823–993 | 7.01 | 2.81 |
| In [122] | 573.5 | 0.099 | 32.1 | 129 | 429.6 | 500–1,400 | 3.67 | 2.52 |
| In [70] | 546.8 | 0.082 | | | | 673–993 | 4.32 | |
| Sn [70] | 545.66 | 0.066 | 22 | 170 | 504.93 | 723–993 | 5.18 | 3.14 |
| Sn [122, 125] | 547.17 | 0.065 | | | | 500–1,300 | 5.26 | |
| Bi [70] | 378.9 | 0.070 | 13.4 | 120 | 544.5 | 773–873 | 3.51 | 2.18 |
| Pb [70] | 445.54 | 0.089 | 28.9 | 88 | 600.46 | 757–907 | 2.95 | 2.03 |
| H ₂ O [68] | 75.4 | 0.162 | – | 192 | 273 | 273–373 | 0.38 | |

The bond energy $E_b(0)$ is available by dividing the atomic cohesive energy $E_B(0)$ with bulk coordination z_b (=12) for elemental specimen. θ_D and T_m are the Debye temperature and melting point as input in calculations. $\Delta T(K)$ is the temperature range of testing. Scattered data for a specific substance and the deviation from the reference values show the sensitivity of the LBA-derived $E_B(0)$ to the extrinsic factors such as surface contamination in comparison with the reference data

^a Coefficient of linear thermal expansion at 25 °C in K⁻¹ (Handbook of chemistry and physics)

Table 24.1b Thermal expansion coefficients are not available and therefore not used in the practices on polymers. Experimental data are sourced from Ref. [69] $E_B(0)$ in bold are derivatives from the fitting

| | $\gamma_s(T_m)$ (mJ/m ²) | α_t (mJ/(m ² K)) | ΔT (°C) | T_m (K) | $E_B(0)$ (eV) |
|------------------------------------|--------------------------------------|------------------------------------|-----------------|-----------|---------------|
| Hexadecane (C16) | 29 | 0.094 | 298–373 | 291 | 0.30 |
| PE (C2000) | 35.6 | 0.065 | 403–493 | 407 | 0.41 |
| PEO | 46.7 | 0.08 | 343–463 | 333 | 0.40 |
| PCAP | 44.4 | 0.068 | 373–398 | 333 | 0.43 |
| PEKK | 63.8 | 0.08 | 571–618 | 578 | 0.60 |
| PBT, poly (butylene terephthalate) | 59.3 | 0.08 | 493–523 | 496 | 0.54 |
| Poly (trimethylene terephthalate) | 53.8 | 0.067 | 538–562 | 496 | 0.56 |
| PET | 54.2 | 0.0646 | 513–593 | 528 | 0.59 |
| Poly (amide ester) copolymer | 60.4 | 0.08 | 433–463 | 433 | 0.52 |
| Nylon 66 | 64 | 0.115 | 543–563 | 533 | 0.47 |
| Polyamide MPMD-12 | 54.55 | 0.081 | 463–623 | 463 | 0.49 |

24.2 Atomistics of Surface Energetics

24.2.1 Motivation

By definition, the dimensions of surface energy, surface stress, and surface tension are expressed in terms of energy per unit area, eV/nm²; however, according to the coordinate-counting premise, the unit of the surface energy is in eV/atom. The former represents the energy density per unit area of surface without considering thickness, whereas the latter reflects the energy remain per discrete atom upon a surface being made. Observations show that the surface energy in terms of eV/nm² is often higher, while the surface energy in terms of eV/atom is lower in magnitude compared with the bulk values because of the difference in definition. Such inconsistency has caused confusion about the definition of surface energetics. On the other hand, the atomistic origin, temperature dependence, and the responsibility of the surface energy in terms of either eV/atom or eV/nm² are yet unclear. Most importantly, the effect of a broken bond on the length and strength of the remaining bonds between the undercoordinated atoms in the surface skin has been overlooked conventionally.

The shortened and strengthened bonds are indeed crucial to surface energetics. For example, a considerable percentage contraction occurs to the first and the second layer of the diamond surface, which leads to a substantial reduction in the surface energy according to MD calculations [61]. The contraction varies from 11.2 to 56.2 % depending on the surface plane and the potential function used in computation. Furthermore, the classical theories of continuum medium mechanics and the statistic thermodynamics deal with only the consequence but the atomistic origin of the mesoscopic mechanics.

In fact, the performance of a surface is dictated by the energy gain per unit volume in the skin or by the cohesive energy remnant per bond of the undercoordinated surface atoms instead of the energy cost for surface formation. The surface energy density gain arising from surface relaxation or bond contraction causes the reconstruction according to the BOLS notation. Meanwhile, the surface bond strain causes the surface stress other than the stress induces the strain, as one may percept intuitively. Therefore, a formulation taking the bond nature, strain, and temperature dependence of surface energetics is necessary.

24.2.2 Atomistic Definition

In reality, the remaining energies in the surface skin or by the residual bond energy of the discrete surface atoms instead of the energy loss upon surface formation govern the performance of a surface. The following concepts describe the surface energetics effectively:

1. The surface is envisioned as a sheet or a skin of a certain thickness (two-to-three atomic layers) rather than an ideal two-dimensional sheet without thickness.
2. The energy density gain (γ_{ds}) refers to the energy stored per unit volume (in the units of eV/nm³) in the skin upon making the surface.
3. The residual atomic cohesive energy (γ_{fs}) represents the cohesive energy per discrete surface atom (in the units of eV/atom) upon the surface bond being broken, which equals the multiplication of the remaining number of bonds with a bond energy that varies with the number of the bonds broken.
4. The conventional definition of surface energy refers to the energy cost (loss) for formation of unit surface area, which has little to do with surface phenomena or surface processes.

From the analytical expression of binding energy per unit area, $E_b d^{-2}$, and the current T-BOLS notation, the shortened and strengthened bonds of the undercoordinated surface atoms dictate the surface tension, surface stress, and surface energy. Correspondingly, one may also clarify the difference between surface stress and surface tension as the energy gradient in the surface normal and in the surface plane directions, respectively, as summarized in Table 24.2. The $d_i(z_i, T)$ and $E_i(z_i, T)$ follow the temperature and size $z_i(K, T)$ dependence, as discussed in Chap. 23. From the atomistic perspective, the surface tension is a vector with x and y components because $\partial F_x / \partial y = \partial F_y / \partial x = 0$ instead of a second-rank tensor.

Table 24.2 Proposed terms of curvature $K^{-1}(z_i)$ and T dependence of surface energetics arising from the effect of a broken bond represented by the T-BOLS correlation and their expressions, atomistic origins, and their responsibilities for the surface phenomena and processes [66]

| Definitions | T -dependent expression | Atomistic origin | Functionality |
|--|--|---|--|
| Surface energy density (γ_{ds}) (eV/nm ³) | $\gamma_{ds} = \frac{\sum_{i \leq 2} E_i(z_i, T) / d_i^3(z_i, T) \times d_i(z_i, T)}{\sum_{i \leq 2} d_i(z_i, T)}$ | Energy gain per unit area of $(d_1 + d_2)$ thick due to the broken-bond-induced strain and bond strength gain | Surface stress; elasticity; Hamiltonian; surface optics; dielectrics; surface trapping states; electron and photon transport dynamics; work function, etc. |
| Surface atomic cohesive energy (γ_{fs}) (eV/atom) | $\gamma_{fs} = \frac{\sum_{i \leq 2} z_i E_i(z_i, T)}{2}$ | Binding energy remnant per discrete atom upon surface formation | Thermal stability; melting and evaporating ability; wettability; diffusivity; reactivity; acoustics; self-assembly; reconstruction |
| Energy cost for surface formation (γ_s) (eV/atom) | $\gamma_s = z_b E_b - \gamma_{fs}$ or equivalent to the forms in Eq. 24.1 | Traditional definition of energy loss per atom upon surface formation | |
| Surface stress (P) (eV/nm ²) | $\frac{\partial F_x}{\partial x} j + \frac{\partial F_y}{\partial y} j + \frac{\partial F_z}{\partial z} k$ | Force gradient in the surface | Surface relaxation, strength, hardness |
| Surface tension (τ) (eV/nm ²) | $\frac{\partial F_x}{\partial x} i + \frac{\partial F_y}{\partial y} j$ | Force per unit length in the surface $x - y$ plane | Surface reconstruction, strength, hardness |

24.3 Analytical Expressions

24.3.1 Surface Energetics

According to Eq. (23.4), the curvature and temperature dependence of surface energy density, γ_{di} , and the surface atomic cohesive energy, γ_{fi} , follow the relations:

$$\begin{aligned}\gamma_{di}(z_i, T) &\propto \frac{E_i(z_i, T)}{d_i^3(z_i, T)} = \frac{E_i(0) - \int_0^T \eta_{1i}(t) dt}{d_i^3(1 + \alpha_i T)^3} \\ \gamma_{fi}(z_i, T) &\propto z_i E_i(z_i, T) = z_i \left[E_i(0) - \int_0^T \eta_{1i}(t) dt \right]\end{aligned}\quad (24.3)$$

The internal energy $\int_0^T \eta_{1i}(t) dt \cong \omega^2 x^2 / 2 + u'''(r)x^3 / 3 + 0(x^n > 3)$ corresponds to the thermal vibration of various modes, harmonic and anharmonic, which weakens the bond strength. The ω and x represent the frequency and amplitude of vibration, respectively. The relative values of the surface energetics in the i th atomic layer to the bulk values of γ_{db} and γ_{fb} , measured at $T_0 = 0$ K, follows:

$$\begin{aligned}\frac{\gamma_{di}(z_i, m, T)}{\gamma_d(z_b, m, 0)} &= \frac{d^3}{d_i^3(1 + \alpha_i T)^3} \times \frac{E_i(0) - \int_0^T \eta_{1i}(t) dt}{E_b(0)} \\ &= \frac{C_i^{-(3+m)}}{(1 + \alpha_i T)^3} \left(1 - \frac{\int_0^T \eta_{1i}(t) dt}{z_{ib} C_i^{-m} E_b(0)} \right) \\ \frac{\gamma_{fi}(z_i, m, T)}{\gamma_f(z_b, m, 0)} &\cong z_{ib} C_i^3 (1 + \alpha_i T)^3 \frac{\gamma_{di}(z_i, m, T)}{\gamma_d(z_b, m, 0)}\end{aligned}\quad (24.4)$$

At $T = 0$ K, the surface energy density is always higher and the surface atomic cohesive energy is always lower than the corresponding bulk values.

24.3.2 Elasticity and Yield Strength

The surface stress, or surface tension, and bulk modulus at a specific atomic site share the same dimension of the surface energy density [Eq. (22.1)]:

$$\begin{aligned}\sigma_i(T, P) &= -\frac{\partial u(r)}{\partial V} \propto Y_i(T, P) \propto B_i(T, P) \\ B_i(T, P) &= -V \left. \frac{\partial^2 u(r)}{\partial V^2} \right|_{r=d_i} \propto \frac{E_i(T, P)}{d_i^3} \propto \gamma_{di}(T, P)\end{aligned}\quad (24.5)$$

This expression formulates the correspondence between surface energy density and the mechanical properties. Precisely, the B and σ are the derivatives of

interatomic potential. However, there exists uncertainty in choosing the exact form of $u(r)$. What one is concerned with is the relative change of the B and P to the bulk values. No particular form of the $u(r)$ is involved in the present exercise, as one needs only the values of (E_i, d_i) at the equilibrium. The Y_i is referred only to the equilibrium but the σ to any states. It would be sufficient to consider the equilibrium positions (bond length and energy) and the temperature-induced energy change. An exact solution may be obtainable in the first-principle calculations, but the outcome will also be subject to the form of the $u(r)$ chosen.

Equation (24.5) indicates that the Y_i and σ_i enhancement depends uniquely on the shortened and the strengthened bonds. The relative values for the local Y_i , σ_i and γ_{di} to those of the bulk measured at $T_0 = 0$ K follow the same relation

$$\left. \begin{array}{l} \frac{Y_i(m, z_i, T, P)}{Y(m, z, 0, 0)} \\ \frac{\sigma_i(m, z_i, T, P)}{\sigma(m, z, 0, 0)} \\ \frac{\gamma_{di}(m, z_i, T, P)}{\gamma_d(m, z, 0, P)} \end{array} \right\} = \frac{C_i^{-(3+m)}}{(1 + \alpha_i T + \beta_i P)^3} \times \left[1 - \frac{\int_0^{T/\theta_D} \eta_1(t) dt}{z_{ib} C_i^{-m} E_b(0)} - \frac{\int_1^{V/V_0} P(x) dx}{E_b(0)/V_0} \right] \quad (24.6)$$

Numerical reproduction of these quantities derives the quantities of atomic cohesive energy $z_{ib} E_i(0)$, binding energy density $E_b(0)/V_0$, Debye temperature θ_D , compressibility β , thermal expansion coefficient α , etc.

24.4 Strain-Induced Skin Elasticity and Stress

24.4.1 Bond Nature and Surface Curvature

24.4.1.1 Flat Surface

For a flat surface, $z_1 = 4$, $z_2 = 6$, and the effective $z_{i \geq 3} = 12$. The corresponding bond contraction coefficient $C_i(z) = 2/(1 + \exp((12 - z)/(8z)))$ leads to $C_1 = 0.88$, $C_2 = 0.94$, and $C_{i \geq 3} = 1$. For the diamond cubic materials, the effective z_b is 12 though they have a first neighbor coordination of four because an interlock of two fcc structures forms the complex unit cell in diamond. Averaging the sum over the top two atomic layers, one can obtain the mean energy density gain per unit area of $(d_1 + d_2)$ thick and the remaining cohesive energy per discrete atom in the top two atomic layers of a flat surface at low temperatures:

$$\begin{aligned} \langle \gamma_{ds} \rangle &= \left(\sum_{i \leq 2} \gamma_{di} d_i \right) / \left(\sum_{i=2} d_i \right), \quad (\text{eV/nm}^3) \\ \langle \gamma_{fs} \rangle &= \left[\sum_{i \leq 2} \gamma_{fi} \right] / 2, \quad (\text{eV/atom}) \end{aligned}$$

moreover, the relative changes of these quantities for a flat surface

Table 24.3 Bond nature (m) dependence of the ratios of surface energy density, $\langle\gamma_{ds}\rangle$, per unit area and surface cohesion (free energy), $\langle\gamma_f\rangle$, per atom with respect to the bulk values

| m | γ_{d1}/γ_{db} | γ_{d2}/γ_{db} | $\langle\gamma_{ds}/\gamma_{db}\rangle$ | γ_{f1}/γ_{fb} | γ_{f2}/γ_{fb} | $\langle\gamma_{fs}/\gamma_{fb}\rangle$ |
|-----|---------------------------|---------------------------|---|---------------------------|---------------------------|---|
| 1 | 1.668 | 1.281 | 1.39 | 0.379 | 0.532 | 0.46 |
| 3 | 2.153 | 1.45 | 1.73 | 0.489 | 0.602 | 0.56 |
| 5 | 2.981 | 1.68 | 2.16 | 0.632 | 0.681 | 0.67 |

Subscripts 1 and 2 refer to the top first and the second atomic layers in a flat surface. $\langle\gamma_{ss}/\gamma_{sb}\rangle$ is approximately equal to $1 - \langle\gamma_{fs}/\gamma_{fb}\rangle$

$$\begin{aligned} \left\langle \frac{\Delta\gamma_{ds}}{\gamma_{db}} \right\rangle &= \sum_{i \leq 2} \left(C_i^{-(m+2)} - 1 \right) / (C_1 + C_2) \\ \left\langle \frac{\Delta\gamma_{fs}}{\gamma_{fb}} \right\rangle &= \sum_{i \leq 2} (z_{ib} C_i^{-m} - 1) / 2 \end{aligned} \quad (24.7)$$

Table 24.3 compares the estimated ratios of the defined surface energy density, surface atomic cohesive energy, and the traditionally defined surface energy. Results show that the $\langle\gamma_{ds}\rangle$ is always higher and the $\langle\gamma_{fs}\rangle$ is always lower than the bulk values. Therefore, it is not surprising that measurements show inconsistent values of surface energy because of the definitions.

24.4.1.2 Nanosolid: Curvature and Bond Nature Dependences

Considering the outermost two atomic layers of a spherical dot, it is possible to derive the T -independent $\langle\gamma_{ds}/\gamma_{db}\rangle$ and $\langle\gamma_{fs}/\gamma_{fb}\rangle$ as a function of the bond nature and the curvature by using, $z_1 = 4 \times (1 - 0.75/K)$ and $z_2 = z_1 + 2$. According to the core-shell structure, the size-dependent relative change in a measurable quantity Q follows the scaling relation with the following quantities:

$$q_i = \begin{cases} \gamma_{di} &= E_i/d_i^3 \propto Y_i \\ \gamma_{fi} &= z_i E_i \propto T_{Ci} \end{cases} \quad (24.8)$$

On the basis of Eq. (24.8), one can predict the trend of bond nature and curvature dependence of the surface energetics, as shown in Fig. 24.5a and b. These quantities are not simply a linear dependence of the curvature or solid size because of the nonlinear dependence of the bond contraction coefficient on atomic CN. The surface energetics changes slightly with the curvature. The volume average of the energy density gain agrees with the observed size dependence of the Young's modulus of ZnO₂ nanowires [62]. The size dependence of residual cohesive energy is consistent with the measured trends of critical temperature for evaporation T_C (T_{onset}) of Ag, Au, and PbS nanostructures [63], as shown in Fig. 24.5c and d.

Ideally, the T_C for Au and Ag nanosolid should follow the $m = 1$ curve and that of PbS follow the curve of $m = 4$. However, contamination during heating should alter the surface bond nature and energy. Therefore, it is no surprising why the measured data for Au and Ag not follow the $m = 1$ curve exactly. Measurements

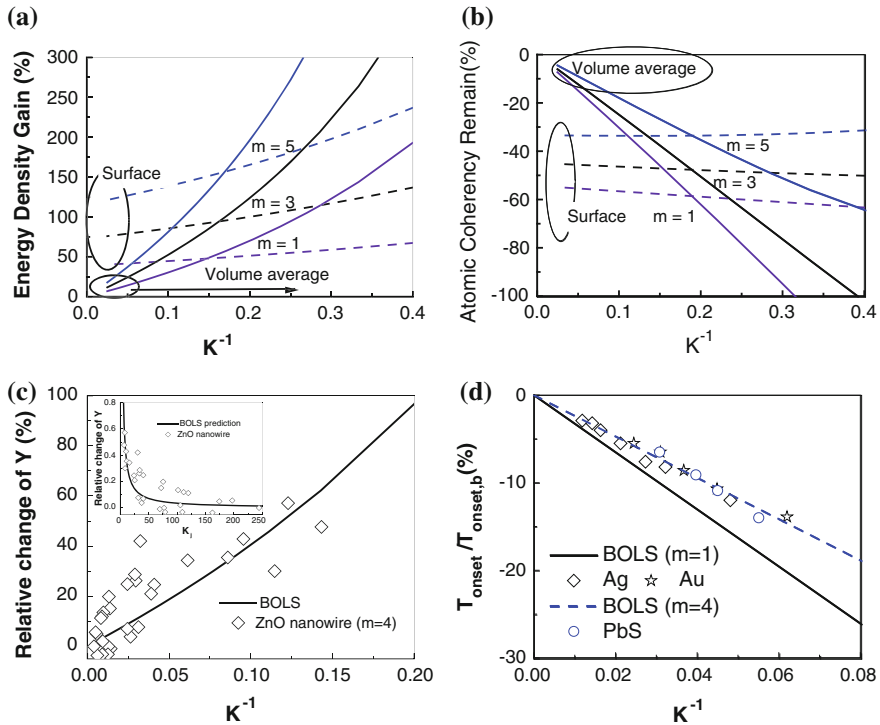


Fig. 24.5 Prediction of curvature-induced **a** energy density gain per unit volume and **b** the remnant cohesive energy per discrete atom averaged over the surface skins (surface) of two atomic layer thickness and averaged over the entire *spherical* solid (volume average or size dependence). The former increases, whereas the latter drops with the decrease in solid size. The volume average of **a** determines the size dependence of strength and elasticity, and the volume average of **b** dictates the thermal stability of nanostructures. Panels **c** and **d** compare the predictions with the measured size-dependent relative change of Young's modulus (energy density) of ZnO nanowires [62] and the cohesive energy (evaporation temperature) for PbS, Ag, and Au nanosolids [63]. *Insert* in **c** is the same set of data expressed in Y - K wise [66] (reprinted with permission from [111])

under ultrahigh vacuum may rectify the deviation. The predicted size dependence of the remaining cohesive energy also agrees with the measured size effect on the binding energy per atom of Ag particles [64] and the structural phase transition temperature for Pb nanoislands on Si substrate [65].

24.4.2 T -Dependent Liquid Skin Tension

The z_i , m , and T dependence of the mean surface energy density, $\langle \gamma_{\text{ds}} \rangle$ and mean atomic cohesive energy, $\langle \gamma_{\text{fs}} \rangle$ can be expressed as [66]

$$\langle \gamma_{ds} \rangle = \frac{\sum_{i \leq 2} E_i(z_i, T) / d_i^3(z_i, T) \times d_i(z_i, T)}{\sum_{i \leq 2} d_i(z_i, T)} \text{ (eV/nm}^3\text{)}$$

$$\langle \gamma_{fs} \rangle = \frac{\sum_{i \leq 2} z_i E_i(z_i, T)}{2} \text{ (eV/atom),}$$

Under the given conditions of $\alpha T_m \ll 1$ and $T \gg \theta_D$, the $\langle \gamma_{ds} \rangle$ can be reduced as

$$\left\langle \frac{\gamma_{ds}(T)}{\gamma_{ds}(0)} \right\rangle \stackrel{T \gg \theta_D}{\cong} \left[\frac{C_1^{-(m+2)} + C_2^{-(m+2)}}{C_1 + C_2} - \frac{z_{b1} C_1^{-2} + z_{b2} C_2^{-2}}{C_1 + C_2} \frac{\eta_1 T}{E_b(0)} \right] \frac{1}{(1 + \alpha T)^3}$$

$$\stackrel{\alpha T_m \ll 1}{\cong} \frac{C_1^{-(m+2)} + C_2^{-(m+2)}}{C_1 + C_2} - \frac{z_{b1} C_1^{-2} + z_{b2} C_2^{-2}}{C_1 + C_2} \frac{\eta_1 T}{E_b(0)} \quad (24.9)$$

To be in line with the current definition of surface energy density, one needs to assume a thickness $D (= d_1 + d_2)$ to apply to the classical expression for surface tension or stress, $\gamma_s(T)/D$. The introduction of D does not vary the reduced form of surface tension and thus one has

$$\frac{\gamma_s(T)}{\gamma_b(0)} = \frac{\gamma_s(T_m)}{\gamma_b(0)} + \frac{\alpha_t T_m}{\gamma_b(0)} \left(1 - \frac{T}{T_m} \right) = \frac{\gamma_s(0)}{\gamma_b(0)} - \frac{\alpha_t T}{\gamma_b(0)} \quad (24.10)$$

Equating Eqs. (24.9)–(24.10) leads to an estimation of the single bond energy $E_b(0)$ and the bulk energy density, $\gamma_b(0)/D$, with the measured temperature dependence of surface tension:

$$\begin{cases} \gamma_b(0) & \alpha_t T \ll 1 \frac{(C_1 + C_2) \times (\gamma_s(T_m) + \alpha_t T_m)}{C_1^{-(m+2)} + C_2^{-(m+2)}} = A_1(m) [\gamma_s(T_m) + \alpha_t T_m] = A_1(m) \gamma_s(0) \\ E_b(0) & \alpha_t T \ll 1 \frac{z_{b1} C_1^{-2} + z_{b2} C_2^{-2}}{C_1 + C_2} \times \frac{\eta_1 \gamma_b(0)}{\alpha_t} \end{cases} \quad (24.11)$$

where $A_1(m)$ is bond nature dependent. The calculated $A_1 (m = 1) = 0.6694$ and $A_2 = 3.4174$. A careful fitting to the measured surface tension with the given Debye temperature and the known coefficient of thermal expansion can derive the precise value of $E_b(0)$ for a specimen. Based on this relation, one can reproduce the measured temperature dependence of surface energy, surface tension, and Young's modulus with derivatives of the $E_b(0)$ that represents the mean bond energy of the entire solid. Involvement of artifacts and impurities will cause deviation of the $E_b(0)$ from the true values.

Figure 24.6 shows the reproduction of the measured temperature dependence of surface tension of (a) liquid Hg [52] and Ni [51], (b) Co [67] and H₂O [68], and (c) hexadecane and polyethylene [69]. With the Debye temperature and the thermal expansion coefficient for the corresponding specimens as input parameters, the $E_b(0)$ is derived. No other parameters are involved. Tables 24.1a and 24.1b summarize information of the estimated results for several specimens.

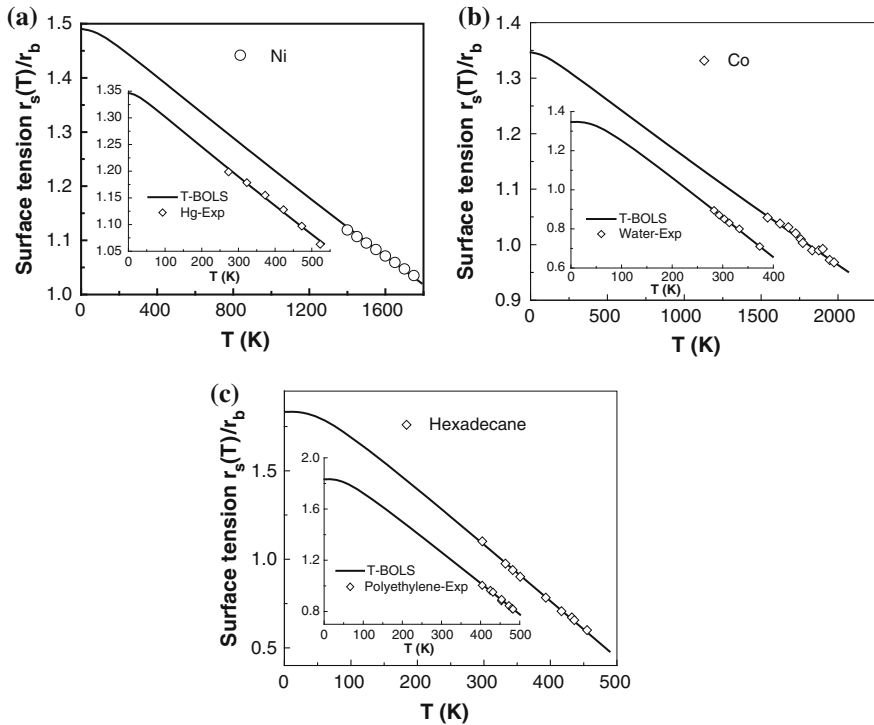


Fig. 24.6 Estimation of $E_b(0)$ by reproducing the measured temperature dependence of surface tension for **a** Hg [52] and Ni [51] liquid, **b** Co [67] and H₂O [68], and **c** hexadecane and polyethylene [69]. Tables 24.1a and 24.1b list the input and output parameters (reprinted with permission from [111])

Therefore, reproduction of the temperature and atomic CN dependence of surface tension results in information regarding the mean atomic cohesive energy in the bulk. The accuracy of the derivatives can be improved by increasing the droplet size or minimizing the curvature and by improving the sample purity [70, 71] because artifacts such as surface contamination and sample purity may lead to error to the derived $E_b(0)$ value. The high sensitivity of the derived $E_b(0)$ to the chemical condition of the liquid and solid surfaces could be an advantage of this approach, which offers a promising way to detect chemical reactions of a specimen by attaching other guest atoms such as biomolecules and cells to the surface of low- T_m specimens.

Adatoms or atomic vacancies during crystal growth will affect the surface energy in a dynamic way by introducing additional traps nearby because of the bond order deficiency, which is within the BOLS expectation [72, 73]. However, the dynamic behavior of adatoms and vacancies is not immediate concern in the present case. The present approach derives information of bond energy limiting only to elemental specimens. For compounds or alloys, one can obtain the mean value of atomic cohesive energy. The accuracy of estimation is strictly subject to

the measurement. Other factors such as materials purity, defect concentration, and testing techniques may lead to the accuracy of the derived $E_b(0)$ values. Discriminating the contribution of defect concentration, surface chemical contamination, or artifacts due to experimental techniques from the intrinsically true contribution to the derived $E_b(0)$ would be even more interesting. Nevertheless, results given here and progress made insofar may demonstrate that the current T-BOLS approach could represent the true situation of observations.

24.4.3 Strain-Induced Skin Elasticity and Strength

Incorporating the nanoindentation measurement of the hardness (stress) for TiCrN [24] and Si [19] surfaces yield the relationships

$$(\sigma_s - \sigma)/\sigma = C_i^{-(m+3)} - 1 = \begin{cases} \frac{(50-25)}{25} = 1 & (\text{TiCrN}; C_i = 0.9; m = 4) \\ \frac{(70-12)}{12} = 4.7 & (\text{Si}; C_i = 0.84; m = 4.88) \end{cases}$$

This relation derives the m values and the extent of bond contraction using Eq. (24.6). For the TiCrN surface, the C_i value is estimated to be ~ 0.9 and the associated $m = 4$. The C_i for Si is estimated at 0.84 with the given $m = 4.88$. Similarly, for amorphous carbon films [23], the C_i is around 0.8 ± 0.2 with the given $m = 2.56$. Predictions also agree with the theoretically calculated thickness dependence of Young's modulus for Ni, Cu, and Ag thin films at $T \ll T_m$ [74, 75].

Incorporating the maximum Y values and the lattice contraction [29] to the BOLS expression ($Y_i/Y_b = C_i^{-(m+3)}$ with $m = 1$) leads to a C_i value of 0.95 for steel. Unfortunately, the high $\sigma_i/\sigma > 4$ values for Ag, Ni, Cu, and Al ($m = 1$) thin films [27] are beyond the BOLS expectation. The exceedingly high surface hardness may result from artifacts such as surface passivation that alters the nature of the initially metallic surface bonds to a compound with m value greater than four.

The Y -suppression of an organic specimen indicates the importance of the $(T_m - T)$ contribution to the mechanical strength. The Y value drops for polymers with size, according to the empirical relation $Y = 0.014 \times \ln(x) + 0.903 \pm 0.045$ [32], with x being the particle size in nm. The Y -suppression of polymers results from the low T_m (~ 450 K) of the specimen. The ambient testing temperature is only $2/3$ of the T_m .

24.5 Adsorbate-Induced Skin Stress: Bonding Effect

24.5.1 Observations

Atoms at the pure metal surfaces relax inwardly and reconstruct in the surface planes because of the spontaneous bond contraction and the derived tensile stress. The stress-induced inward relaxation is quite common despite the discrepancy in

the number of layers being involved. Occasionally, surface tension breaks bonds between surface atoms, and then, atoms may move away from the surface without being disturbed by external stimulus. For instance, missing rows could often form at the Au, Pt, Ag, Pd, and Rh surfaces, in particular, in the (110) plane [76–80] with least mass density in the plane compared with the (100) and the (111) planes. The surface relaxation and reconstruction are consequences of bond order deficiency according to the BOLS notation.

However, adsorbate could induce various kinds of stresses accompanied with versatile patterns of relaxation and reconstruction [59, 81, 82]. The spacing between the first and the second atomic layers expands if an adsorbate such as C, N, and O buckles into space between the atomic layers even if there is contraction of bonds between the adsorbates and the host atoms [81]. For example, H, C, N, O, S, and CO adsorbates on a metal surface could change the surface stress and cause surface reconstruction because of bond making and breaking. Surface adsorption of sodium ions also increases the stiffness of a microcantilever [83].

The adsorbate-induced stress is versatile and capricious. One kind of adsorbate can induce different kinds of stresses at different planes of the same specimen, and different kinds of adsorbates can induce different stresses at a specific surface. The adsorbate-induced stress may change its sign when the adsorbate coverage changes. For example, one monolayer (ML) of oxygen on a Si(111) surface could induce -7.2 N/m compressive stress while, on the O–Si(001) surface, the adsorbate produces a tensile stress of 0.26 N/m [84]. One ML S, O, and C addition to the Ni(100) surface could induce a $c(2 \times 2)$ reconstruction with compressive stress of -6.6 , -7.5 , and -8.5 N/m, respectively [85]. The C, O, and S adsorbate-induced stresses provide driving forces for the Ni(111) surface reconstruction upon adsorption [86]. An STM bending bar measurement [87] suggested that the (2×1) -O phase induces compressive stress on the Cu(110) surface and the stress varies significantly with oxygen coverage. Using the cantilever vibration method, Hwang et al. [88] studied the correlation between bimolecular interactions and the dynamical response of nanocantilevers in terms of the resonant frequency shift. They found that the surface stress increases linearly with the concentration of antigen, driven by the specific protein–protein interactions.

Room temperature adsorption of CO molecules could induce exclusively a compressive stress on the Ni(111) surface. The stress is tensile on the Ni(100) surface at a CO coverage below 0.2 ML [89]. The tensile stress passes through a maximum of 0.96 N/m at a coverage of $\theta = 0.09$ and then becomes compressive for $\theta > 0.25$ with a value of -0.54 N/m at $\theta = 0.5$, as compared in Fig. 24.7. The latter value is small compared with the stress produced by other more strongly chemisorbed adsorbates on the same surface. The sign reversal of the CO–Ni(100) surface stress corresponded to a coverage-dependent variation in the net charge transfer between the metal surface atoms and the adsorbates, involving an enhanced splitting of the bonding and the $\text{CO}-2\pi^*$ antibonding orbitals of neighboring molecules at higher adsorbate coverage [89]. Nitrogen addition is often more beneficial to the mechanical and corrosion properties of a metallic surface because N could induce different kinds of stress [90, 91].

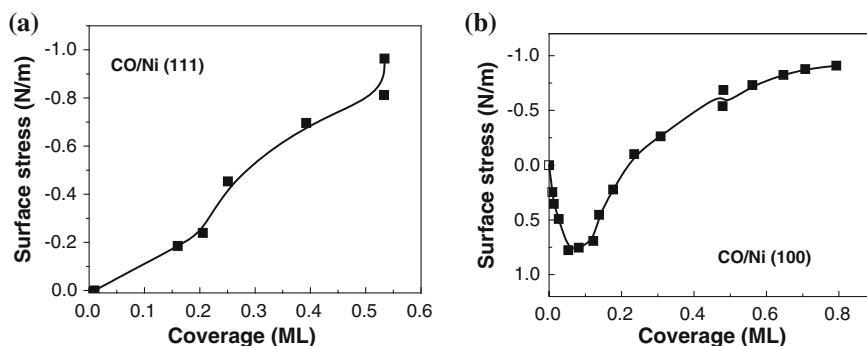


Fig. 24.7 Coverage dependence of CO-induced **a** Ni(111) and **b** Ni(100) surface stress [89]. CO turns the Ni(111) surface to be compressive, and CO changes the Ni(100) stress from tensile to compressive with the increase in CO coverage (reprinted with permission from [111])

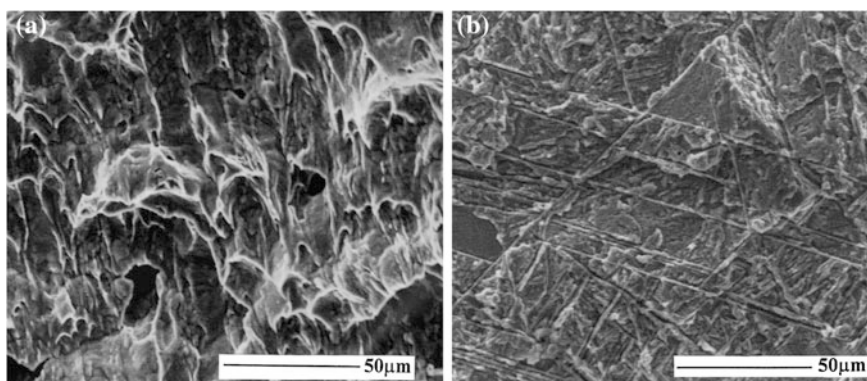


Fig. 24.8 Fracture cross-sectional SEM morphologies of **a** pure Ti and **b** hydrogen plasma-sputtered Ti showed the hydrogen-induced transformation from ductile to fragile modes of failure (reprinted with permission from [92])

A full understanding of the adsorbate-induced stress may help to explain the adsorbate-induced slope change in the temperature dependence of the surface tension such as Sn liquid, as shown in Fig. 24.4. Charge repopulation and polarization upon chemisorption should provide forces driving the observed reconstruction and the measured stress.

Figure 24.8 shows that hydrogen plasma sputtering embrittles Ti surface and causes a detrimental effect on the toughness of a Ti specimen that would otherwise behave as a ductile material when breaking [92]. Nanovoids about two nm in diameter are formed on the epitaxial GaN layers upon high-dose hydrogen implantation and subsequent annealing, while large microcracks of 150–200 nm long occurred after 1 h annealing at 700 °C, leading to surface blistering [93]. The nanovoids also serve as precursors to the microcrack formation and the blistering

Table 24.4 Residual stresses (GPa) of Ti, TiC, and diamond coatings deposited with CH₄/H₂ = 196: 4 at a plasma power of 1 kW [97]

| | | Diamond film thickness (μm) | 3.8 | 6.4 | 8.1 | 9.2 |
|----------------|--------------------------------|-----------------------------|--------|--------|--------|--------|
| Diamond | XRD (311) | | -3.42 | -3.19 | -2.85 | -2.41 |
| | Raman (1,332 m ⁻¹) | | -3.5 | -3.1 | -3.2 | -2.1 |
| TiC interlayer | XRD (420) | | -0.505 | -0.280 | -0.344 | -0.303 |
| Ti substrate | XRD (420) | | 0.267 | 0.120 | 0.118 | 0.105 |

process at Si [94] and AlN [95] surfaces as well. These observations manifest the special function of hydrogen atoms can only bonds to one atom each in terminating the metallic bonding networks because of the presence of H⁺ valence. A better understanding of H⁺ termination of bonding may explain the results of Na⁺- and Ca²⁺-induced embrittlement of Al grain boundaries [96].

XRD and Raman measurement of the residual stresses of the Ti/TiC/diamond interfaces at different stages in diamond growth revealed that carbon addition could change the tensile stress of the Ti specimen into compressive [97]. As shown in Table 24.4, the tensile stress dominates in the pure Ti surface and the carbon turns the tensile surface stress of the Ti into compression upon TiC interlayer formation. The compressive stress in the TiC interlayer and the tensile stress of the Ti are reduced gradually with the thickness increases in the grown diamond films.

Broken-bond-induced bond contraction and bond strength gain create surface tensile stress of pure metals. However, the mechanism for the adsorbate-induced stress, being a long historical issue, is yet unclear. Particularly, how the surface stress changes its sign upon increasing the dosage of adsorbate and why different adsorbates cause different kinds of stress at a given surface. Apparently, the processes of adsorbate-induced stress cannot be explained in terms of the potential wells of adsorption [59] but atomic valance variation during reaction [81].

24.5.2 *Electronic Origin: Charge Entrapment and Polarization*

Adsorbate-induced charge redistribution and polarization is responsible for the adsorbate-induced surface stress and the corresponding reconstruction [59, 81]. Atomic valance variation is responsible for the stress evolution including the sign change. The bond making dynamics described in Part I may illustrate the evolution of bond stress during adsorbate bond making.

24.5.2.1 O¹⁻-Induced Stress at the Cu(001) and the Rh(001) Surfaces

STM imaging and the corresponding c(2 × 2)-2O¹⁻ bond configurations at the Cu(001) and the Rh(001) surfaces (Part I) indicate that in both cases, O¹⁻ adsorbate occupies the fourfold hollow site. Because of the difference in lattice

size ($d_{\text{Cu}} = 0.255$ nm; $d_{\text{Rh}} = 0.268$ nm) and the electronegativity ($\zeta_{\text{Cu}} = 2.5$; $\zeta_{\text{Rh}} = 2.2$), O^{1-} prefers one bond forming with a Cu atom on the surface and polarizes the remaining three Cu atoms nearby in the surface plane. A group of four O^{1-} ions and a pair of O^{1-} ions form two domains (depressed patches in dark) with walls consisting of the interlocked dipoles (bright protrusions). Therefore, the $\text{Cu}(001)\text{-c}(2 \times 2)\text{-}2\text{O}^{1-}$ surface is fully occupied by the interlocked dipoles and the atoms attract one another. The surface stress tends to be tensile.

However, the O^{1-} forms a bond with an Rh atom immediately underneath and polarizes the remaining four atoms in the surface. The dipoles point to the open end of the surface. The surface dipoles repel one another, and therefore, compressive stress dominates in the $\text{Rh}(001)\text{-c}(2 \times 2)\text{-}2\text{O}^{1-}$ surface with a ‘radial outgoing’ pattern of reconstruction. The $\text{Rh}(001)\text{-c}(2 \times 2)\text{-}2\text{O}^{1-}$ scenario holds for the $\text{Ni}(001)\text{-c}(2 \times 2)\text{-}2\text{C}^{1-}$ surface as well with compressive stress dominance. Therefore, the same O^{1-} adsorbate induces an opposite stress on the fcc(001) surface of Cu and Rh because of the difference in the electronegativity and the lattice size of the host elements.

24.5.2.2 $\text{Cu}(001)\text{-(}2 \times 2\sqrt{2}\text{)R}45^\circ\text{-}2\text{O}^{2-}$ Compressive Stress

On further relaxation of the O-adsorbed Cu(001) surface, the O adsorbate varies its valence value from -1 to -2 accompanied with a $\text{Cu}(001)\text{-(}2 \times 2\sqrt{2}\text{)R}45^\circ\text{-}2\text{O}^{2-}$ ‘missing-row’-type reconstruction. The sp-orbit hybridization of oxygen leads to a tetrahedron with involvement of two bonding and two non-bonding orbitals. The non-bonding lone pairs polarize the neighboring Cu atoms to be Cu^{p} dipole. The Cu_3O_2 pairing tetrahedron is formed with antibonding dipoles that are coupled oppositely, crossing over the missing row atoms. Because of the dipole–dipole repulsion, compressive stress becomes dominant at the $\text{Cu}(001)\text{-(}2 \times 2\sqrt{2}\text{)R}45^\circ\text{-}2\text{O}^{2-}$ surface. Therefore, the evolution of the O^{1-} to the O^{2-} turns the Cu(001) surface stress from tensile to compressive because of charge redistribution and polarization upon adsorbate bond making.

24.5.2.3 C^{4-} -, N^{3-} -, and O^{2-} -Induced fcc(001) Surface Stress

Likewise, N^{3-} results in tensile, while C^{4-} leads to compressive stress on the Ni(001) surface. The sp-orbit hybridization of N gives one, and the sp-orbit hybridization gives one non-bonding lone pair to the N- but none to the C-centered tetrahedron, because of their different valences. The N–Ni(001) surface produces the $\text{Ni}^+\text{-Ni}^+\text{-Ni}^{+/p}\text{-Ni}^{+/p}$ chain, and the C–Ni(001) produces the $\text{Ni}^+\text{-Ni}^+\text{-Ni}^{2+}\text{-Ni}^{2+}$ chain along the $\langle 11 \rangle$ surface direction. The repulsion between the like charges and the attraction between the unlike ones causes a tensile response of the N–Ni(001) surface bonds. The repulsion throughout the rhombus chain leads to the

compressive response of the bonds at the C–Ni(001) surface [98]. The bond stress response gives rise to the tensile or the compressive stress for the O^{2-} , N^{3-} , and C^{4-} -induced reconstruction systems.

Therefore, adsorbate may induce positive or negative surface stress, depending on the substrate geometry and importantly the atomic valence and polarization. These electronic scenarios improve understanding of the adsorbate-induced surface stress and the adsorbate-induced slope change in the temperature dependence of the surface tension of liquid metals.

24.6 Nitrogen-Enhanced Elasticity and Hardness

24.6.1 Observations

Nitrogenation of metals has been a fully developed technology for hardness and elasticity enhancement of a surface [99–105]. Even though the hardness and elasticity of nitrides has been intensively investigated and widely utilized, neither the local bonding structure nor the microstructure corresponding to the observed mechanical properties, are well established [90, 106].

The joint effect of surface bond contraction, bond nature alteration, and the involvement of non-bonding lone pair is crucial to the hardness and elasticity of the nitride surfaces [24]. Nanoindentation measurements revealed that the elastic recovery of TiCrN and GaAlN surfaces could reach as high as 100 % and the nitride films are harder under a relatively lower indentation load (<1.0 mN) than the amorphous carbon (a-C) films that are slightly softer and less elastic at the same load scale of indentation [107]. At a nanoindentation load of 1 mN and below, the hydrogenated CN:H film is harder and more elastic (75 % elastic recovery) compared with that of a-C:H (60 % elastic recovery). However, at higher indentation load, nitride films are softer than the a-C films or polycrystalline diamond. For C and Ti nitride films, the elastic recovery ranges from 65 to 85 % at higher indentation load (5 mN) [106]. The friction coefficient of the nitride films increases suddenly at critical loads for TiN and CN (5 N), indicating the breaking of the surface bonds. Similarly, sapphire (α -Al₂O₃) with lone-pair presence [108] exhibits a pop-in (a sudden shape change of the stress-depth profile shape) critical load at 1.0 mN below which the elastic recovery of the specimen is 100 % under nanoindentation [43]. The higher pop-in critical load of sapphire may indicate the breaking the high-density lone pairs in the oxide.

24.6.2 Atomistic Mechanism

The typical case in which the N reacts with metal atoms in a surface of C_{3v} symmetry, such as the fcc(111) and hcp(0001) planes [90, 109]. The N^{3-} ion is

located in between the top two atomic layers with the lone pair directing into the substrate. The smaller M^+ and the saturate bonded N^{3-} ionic cores with densely packed electrons surface form the skin ionic bonding network. Charge transportation upon bond formation empty the outermost shells of the M^+ ions. Therefore, the top surface layer should be chemically inert as it is hard for one additional acceptor to catch electrons from the deeper energy levels of the M^+ ions. Electrons in the saturated bond should be more stable compared with the otherwise unbounded ones in the neutral host atoms.

The high intra-surface strength due to the ionic networking could be responsible for the hardness of the top atomic layer. On the other hand, the $N^{3-}-M^+$ network at the surface is connected to the substrate mainly through the non-bonding lone pairs. The non-bonding interaction is rather weak (~ 0.05 eV per bond) compared with the initially metallic bonds (~ 1.0 eV per bond) or the intra-surface ionic bond (2–3 eV per bond). The weak interlayer interaction due to lone-pair formation should be highly elastic within a certain range of loads, which makes the two adjacent surface layers more elastic at an indent load lower than a critical value at which the lone pairs will break. Therefore, the enhanced intra-layer strength makes a nitride usually harder, and the weakened interlayer bonding makes the nitride highly elastic and self-lubricating. Results of indentation at various loads and the sliding friction measurements agree with the anticipated high elasticity and high hardness at lower indent load and the existence of the critical scratching load [24].

The surface ionic layer determines the hardness of a nitride coating and the surface bond contraction further enhances the hardness at the surface. The lone pairs are responsible for the high elasticity and self-lubrication of the nitride. Therefore, the strength of the previously predicted hardest C_3N_4 phase is lower than diamond or cubic boron nitride by a surprisingly large amount, while the C_3N_4 phase is highly elastic because of the excessive electrons on the N atoms, consistent with the current understanding [110]. The excessive electrons exist in the states of non-bonding lone pairs, which play a key role in determining the high elasticity and low hardness, and hence, no nitride should be harder than a diamond. Nitride multilayers could be a different case because of the interface mixing where bond contraction, energy densification, and pinning effect will take place.

Briefly, nitrogen could enhance the hardness of a metal surface because of the bond nature alteration and surface bond contraction. An N–M bond is shorter than a C–M bond because of the ionic radius of C^{4-} and N^{3-} . The involvement of lone pairs makes the nitride more elastic but readily broken under a critical load. Such an interpretation may provide a possible mechanism for the atomistic friction and self-lubrication of a nitride specimen.

24.7 Summary

An application of the T-BOLS correlation with the liquid and solid skins has led to a consistent insight into the atomistic mechanism for the surface energetics and its derivatives on the elasticity and strength. Major conclusions drawn from this Chapter are the following:

1. The broken bond may not contribute directly to the surface energetics, but the broken bond causes the remaining ones to contract spontaneously associated with bond strength gain. The shortened and strengthened bonds between the undercoordinated surface atoms dictate the surface energetics and the mechanical behavior of liquid and solid skins. The bond strain induces surface stress rather than the inverse: Surface stress compresses the surface bond to contract. The strain-induced stress is always tensile, giving rise to the observed pinning and trapping effect in the surface skins.
2. The energy density gain and the cohesive energy remnant per discrete atom are suggested essential to classify the origin and temperature dependence of surface energetics and their responsibilities for surface processes and phenomena. These new concepts may provide a complementary to the classical theories of continuum medium mechanics and statistic thermodynamics.
3. A solid surface melts first and a liquid surface solidifies easier than the liquid core. A strained, solid-like, and well-ordered liquid skin serves as an elastic covering sheet for a liquid drop or a gas bubble formation; a solid skin is generally harder than the core interior.
4. Functional dependence of the surface energetics on the bonding identities represents the true situation that the variation of surface energetics from the bulk values arises from the shortened and strengthened bonds between the undercoordinated atoms.
5. The predicted volume average of the energy density gain and the residual atomic cohesive energy agrees with the measured size dependence of Young's modulus and the critical temperatures for evaporation, melting, and phase transition.
6. The thermal expansion and vibration weaken surface energetics through the internal energy, which follows the integration of the specific heat. This approach allows us to estimate the bond energy by reproducing the measured temperature dependence of surface tension and Young's modulus. The accuracy of estimation is strictly subject to the experimental data.
7. Adsorbate-induced inflection of the temperature coefficient of the surface tension and the adsorbate-induced surface stress evolution of a solid surface can be consistently understood in terms of adsorbate bond making that causes charge redistribution and polarization and the corresponding patterns of reconstructions. The adsorbate-induced stress may change from situation to situation depending on the configuration of surface bonding networks. The involvement of non-bonding lone pairs and the bond nature alteration in nitrogenation makes a nitride surface highly elastic and robust at relatively lower indentation or scratching load.

References

1. H. Ibach, The role of surface stress in reconstruction, epitaxial growth and stabilization of mesoscopic structures. *Surf. Sci. Rep.* **29**(5–6), 195–263 (1997)
2. W. Haiss, Surface stress of clean and adsorbate-covered solids. *Rep. Prog. Phys.* **64**(5), 591–648 (2001)
3. R. Berger, E. Delamarche, H.P. Lang, C. Gerber, J.K. Gimzewski, E. Meyer, H.J. Guntherodt, Surface stress in the self-assembly of alkanethiols on gold. *Science* **276**(5321), 2021–2024 (1997)
4. M.N. Magomedov, The surface energy of nanocrystals. *Russ. J. Phys. Chem.* **79**(5), 711–720 (2005)
5. R. Dingreville, J.M. Qu, M. Cherkaoui, Surface free energy and its effect on the elastic behavior of nano-sized particles, wires and films. *J. Mech. Phys. Solids* **53**(8), 1827–1854 (2005)
6. W. Vogelsberger, Thermodynamics of homogeneous nucleation under different constraints. *Z. Phys. Chemie-Int. J. Res. Phys. Chem. Chem. Phys.* **215**, 1099–1120 (2001)
7. M.C. Desjonquères, D. Spanjaard, in *Concepts in Surface Physics*. Springer Series in Surface, vol. 30 (Springer, Berlin, 1993)
8. Q. Jiang, H.M. Lu, M. Zhao, Modelling of surface energies of elemental crystals. *J. Phys.: Condens. Matter* **16**(4), 521–530 (2004)
9. I. Galanakis, N. Papanikolaou, P.H. Dederichs, Applicability of the broken-bond rule to the surface energy of the fcc metals. *Surf. Sci.* **511**(1–3), 1–12 (2002)
10. C.Q. Sun, Surface and nanosolid core-level shift: Impact of atomic coordination-number imperfection. *Phys Rev B* **69**(4), 045105 (2004)
11. D. Xie, M.P. Wang, L.F. Cao, A simplified model to calculate the higher surface energy of free-standing nanocrystals. *Phys. Status Solidi B-Basic Solid State Phys.* **242**(8), R76–R78 (2005)
12. D. Xie, M.P. Wang, W.H. Qi, A simplified model to calculate the surface-to-volume atomic ratio dependent cohesive energy of nanocrystals. *J. Phys.-Condens. Matter* **16**(36), L401–L405 (2004)
13. O.L. Alerhand, J.D. Joannopoulos, E.J. Mele, Thermal amplitudes of surface atoms on Si(111) 2×1 and Si(001) 2×1 . *Phys. Rev. B* **39**(17), 12622–12629 (1989)
14. C.Q. Sun, L.K. Pan, C.M. Li, S. Li, Size-induced acoustic hardening and optic softening of phonons in InP, CeO₂, SnO₂, CdS, Ag, and Si nanostructures. *Phys. Rev. B* **72**(13), 134301 (2005)
15. C.Q. Sun, Size dependence of nanostructures: impact of bond order deficiency. *Prog. Solid State Chem.* **35**(1), 1–159 (2007)
16. G. Janssen, F.D. Tichelaar, C.C.G. Visser, Stress gradients in CrN coatings. *J. Appl. Phys.* **100**(9), 093512 (2006)
17. V.G. Uryadov, N.V. Aristova, E.N. Ofitserov, The temperature dependence of the surface tension of organic nonelectrolytes. *Russ. J. Phys. Chem.* **79**(12), 2016–2019 (2005)
18. Z.Q. Cao, X. Zhang, Size-dependent creep behaviour of plasma-enhanced chemical vapour deposited silicon oxide films. *J. Phys. D-Appl. Phys.* **39**(23), 5054–5063 (2006)
19. S. Garcia-Manyes, A.G. Guell, P. Gorostiza, F. Sanz, Nanomechanics of silicon surfaces with atomic force microscopy: an insight to the first stages of plastic deformation. *J. Chem. Phys.* **123**(11), 114711 (2005)
20. Y.H. Wang, M.R. Moitreyee, R. Kumar, S.Y. Wu, J.L. Xie, P. Yew, B. Subramanian, L. Shen, K.Y. Zeng, The mechanical properties of ultra-low-dielectric-constant films. *Thin Solid Films* **462**, 227–230 (2004)
21. R.A. Mirshams, P. Parakala, Nanoindentation of nanocrystalline Ni with geometrically different indenters. *Mater. Sci. Eng. A-Struct. Mater. Prop. Microstruct. Process.* **372**(1–2), 252–260 (2004)

22. C.D. Gu, J.S. Lian, Z.H. Jiang, Q. Jiang, Enhanced tensile ductility in an electrodeposited nanocrystalline Ni. *Scripta Mater.* **54**(4), 579–584 (2006)
23. E. Liu, X. Shi, H.S. Tan, L.K. Cheah, Z. Sun, B.K. Tay, J.R. Shi, The effect of nitrogen on the mechanical properties of tetrahedral amorphous carbon films deposited with a filtered cathodic vacuum arc. *Surf. Coat. Technol.* **120**, 601–606 (1999)
24. C.Q. Sun, B.K. Tay, S.P. Lau, X.W. Sun, X.T. Zeng, S. Li, H.L. Bai, H. Liu, Z.H. Liu, E.Y. Jiang, Bond contraction and lone pair interaction at nitride surfaces. *J. Appl. Phys.* **90**(5), 2615–2617 (2001)
25. X. Shi, B.K. Tay, D.I. Flynn, Z. Sun, in *Tribological Properties of Tetrahedral Carbon Films Deposited by Filtered Cathodic Vacuum Arc Technique*, ed. by W.W. Gerberich et al. *Thin Films: Stresses and Mechanical Properties VI*, (Materials Research Society, Warrendale, 1997) pp. 293–298
26. D. Caceres, I. Vergara, R. Gonzalez, E. Monroy, F. Calle, E. Munoz, F. Omnes, Nanoindentation on AlGaIn thin films. *J. Appl. Phys.* **86**(12), 6773–6778 (1999)
27. M.H. Zhao, W.S. Slaughter, M. Li, S.X. Mao, Material-length-scale-controlled nanoindentation size effects due to strain-gradient plasticity. *Acta Mater.* **51**(15), 4461–4469 (2003)
28. D. Ferro, R. Teghil, S.M. Barinov, L. D'Alessio, G. DeMaria, Thickness-dependent hardness of pulsed laser ablation deposited thin films of refractory carbides. *Mater. Chem. Phys.* **87**(2–3), 233–236 (2004)
29. M.Y. Liu, B. Shi, J.X. Guo, X. Cai, H.W. Song, Lattice constant dependence of elastic modulus for ultrafine grained mild steel. *Scripta Mater.* **49**(2), 167–171 (2003)
30. L.G. Zhou, H.C. Huang, Are surfaces elastically softer or stiffer? *Appl. Phys. Lett.* **84**(11), 1940–1942 (2004)
31. S.D. Mesarovic, C.M. McCarter, D.F. Bahr, H. Radhakrishnan, R.F. Richards, C.D. Richards, D. McClain, J. Jiao, Mechanical behavior of a carbon nanotube turf. *Scripta Mater.* **56**(2), 157–160 (2007)
32. W.J. Price, S.A. Leigh, S.M. Hsu, T.E. Patten, G.Y. Liu, Measuring the size dependence of Young's modulus using force modulation atomic force microscopy. *J. Phys. Chem. A* **110**(4), 1382–1388 (2006)
33. K. Miyake, N. Satomi, S. Sasaki, Elastic modulus of polystyrene film from near surface to bulk measured by nanoindentation using atomic force microscopy. *Appl. Phys. Lett.* **89**(3), 031925 (2006)
34. M.X. Gu, C.Q. Sun, Z. Chen, T.C.A. Yeung, S. Li, C.M. Tan, V. Nosik, Size, temperature, and bond nature dependence of elasticity and its derivatives on extensibility, Debye temperature, and heat capacity of nanostructures. *Phys Rev B* **75**(12), 125403 (2007)
35. M. Kopycinska-Muller, R.H. Geiss, J. Muller, D.C. Hurley, Elastic-property measurements of ultrathin films using atomic force acoustic microscopy. *Nanotechnology* **16**(6), 703–709 (2005)
36. F. Vaz, S. Carvalho, L. Rebouta, M.Z. Silva, A. Paul, D. Schneider, Young's modulus of (Ti, Si)N films by surface acoustic waves and indentation techniques. *Thin Solid Films* **408**(1–2), 160–168 (2002)
37. Y. Yan, H. Yin, Q.P. Sun, Y. Huo, Rate dependence of temperature fields and energy dissipations in non-static pseudoelasticity. *Continuum Mech. Thermodyn.* **24**(4–6), 675–695 (2012)
38. A. Amini, W.Y. Yan, Q.P. Sun, Depth dependency of indentation hardness during solid-state phase transition of shape memory alloys. *Appl. Phys. Lett.* **99**(2), 3603933 (2011)
39. V. Brazhkin, N. Dubrovinskaia, A. Nicol, N. Novikov, R. Riedel, R. Solozhenko, Y. Zhao, What does 'harder than diamond' mean? *Nat. Mater.* **3**(9), 576–577 (2004)
40. S.M. Chung, A.U.J. Yap, Effects of surface finish on indentation modulus and hardness of dental composite restoratives. *Dent. Mater.* **21**(11), 1008–1016 (2005)
41. E. Manika, J. Maniks, Size effects in micro- and nanoscale indentation. *Acta Mater.* **54**(8), 2049–2056 (2006)

42. Z.S. Ma, S.G. Long, Y. Pan, Y.C. Zhou, Indentation depth dependence of the mechanical strength of Ni films. *J. Appl. Phys.* **103**(4), 043512 (2008)
43. C. Lu, Y.W. Mai, P.L. Tam, Y.G. Shen, Nanoindentation-induced elastic-plastic transition and size effect in α -Al₂O₃(0001). *Philos. Mag. Lett.* **87**(6), 409–415 (2007)
44. T.Y. Zhang, W.H. Xu, Surface effects on nanoindentation. *J. Mater. Res.* **17**(7), 1715–1720 (2002)
45. W.H. Xu, T.Y. Zhang, in *Surface Effect for Different Types of Materials in Nanoindentation*, ed. by K. Kishimoto et al. *Advances in Fracture and Failure Prevention*, Pts 1 and 2 (Trans Tech Publications Ltd, Zurich-Uetikon, 2004), pp. 1587–1592
46. W.D. Nix, H.J. Gao, Indentation size effects in crystalline materials: a law for strain gradient plasticity. *J. Mech. Phys. Solids* **46**(3), 411–425 (1998)
47. S. Graca, R. Colaco, R. Vilar, Indentation size effect in nickel and cobalt laser clad coatings. *Surf. Coat. Technol.* **202**(3), 538–548 (2007)
48. C.Q. Sun, S. Li, C.M. Li, Impact of bond order loss on surface and nanosolid mechanics. *J. Phys. Chem. B* **109**(1), 415–423 (2005)
49. H. Fujii, T. Matsumoto, S. Izutani, S. Kiguchi, K. Nogi, Surface tension of molten silicon measured by microgravity oscillating drop method and improved sessile drop method. *Acta Mater.* **54**(5), 1221–1225 (2006)
50. Q. Zhao, Y. Liu, E.W. Abel, Effect of temperature on the surface free energy of amorphous carbon films. *J. Colloid Interface Sci.* **280**(1), 174–183 (2004)
51. F. Xiao, R.H. Yang, C. Zhang, Surface tension of molten Ni–W and Ni–Cr alloys. *Mater. Sci. Eng. B-Solid State Mater. Adv Technol.* **132**(1–2), 183–186 (2006)
52. S. Halas, T. Durakiewicz, Temperature dependence of the surface energy of mercury from 0 to 250 degrees C. *J. Phys.-Condens. Matter* **14**(47), L735–L737 (2002)
53. H.M. Lu, Q. Jiang, Surface tension and its temperature coefficient for liquid metals. *J. Phys. Chem. B* **109**(32), 15463–15468 (2005)
54. H. Nakanishi, K. Nakazato, K. Terashima, Surface tension variation of molten silicon measured by ring tensiometry technique and related temperature and impurity dependence. *Japan. J. Appl. Phys. Part 1-Regul. Pap. Short Notes Rev. Pap.* **39**(12A), 6487–6492 (2000)
55. J. Lee, W. Shimoda, T. Tanaka, Temperature and oxygen partial pressure dependences of the surface tension of liquid Sn–Ag and Sn–Cu lead-free solder alloys. *Mon. Chem.* **136**(11), 1829–1834 (2005)
56. M. Rosner-Kuhn, W.H. Hofmeister, G. Kuppermann, R.J. Bayuzick, M.G. Froberg, Investigations of the influence of oxygen on the surface tension of zirconium by the oscillating drop technique. *Surf. Sci.* **443**(3), 159–164 (1999)
57. H.P. Wang, W.J. Yao, C.D. Cao, B. Wei, Surface tension of superheated and undercooled liquid Co–Si alloy. *Appl. Phys. Lett.* **85**(16), 3414–3416 (2004)
58. L. Fiori, E. Ricci, E. Arato, P. Costa, Dynamic surface tension measurements on a molten metal-oxygen system: the behaviour of the temperature coefficient of the surface tension of molten tin. *J. Mater. Sci.* **40**(9–10), 2155–2159 (2005)
59. C.Q. Sun, Oxidation electronics: bond–band–barrier correlation and its applications. *Prog. Mater Sci.* **48**(6), 521–685 (2003)
60. J. Solon, J. Pecreaux, P. Girard, M.C. Faure, J. Prost, P. Bassereau, Negative tension induced by lipid uptake. *Phys. Rev. Lett.* **97**(9), 098103 (2006)
61. T. Halicioglu, Calculation of surface energies for low index planes of diamond. *Surf. Sci.* **259**(1–2), L714–L718 (1991)
62. C.Q. Chen, Y. Shi, Y.S. Zhang, J. Zhu, Y.J. Yan, Size dependence of Young’s modulus in ZnO nanowires. *Phys. Rev. Lett.* **96**(7), 075505 (2006)
63. K.K. Nanda, Bulk cohesive energy and surface tension from the size-dependent evaporation study of nanoparticles. *Appl. Phys. Lett.* **87**, 021909(2), 021909 (2005)
64. Y.P. Chiu, L.W. Huang, C.M. Wei, C.S. Chang, T.T. Tsong, Magic numbers of atoms in surface-supported planar clusters. *Phys. Rev. Lett.* **97**(16), 165504 (2006)
65. I.S. Hwang, S.H. Chang, C.K. Fang, L.J. Chen, T.T. Tsong, Observation of finite-size effects on a structural phase transition of 2D nanoislands. *Phys. Rev. Lett.* **93**(10), 106101 (2004)

66. M. Zhao, W.T. Zheng, J.C. Li, Z. Wen, M.X. Gu, C.Q. Sun, Atomistic origin, temperature dependence, and responsibilities of surface energetics: an extended broken-bond rule. *Phys. Rev. B* **75**(8), 085427 (2007)
67. W.J. Yao, X.J. Han, M. Chen, B. Wei, Z.Y. Guo, Surface tension of undercooled liquid cobalt. *J. Phys.-Condens. Matter* **14**(32), 7479–7485 (2002)
68. Temperature dependence of water surface tension <http://hyperphysics.phy-astr.gsu.edu/hbase/surten.html#c3>
69. B.B. Sauer, G.T. Dee, Surface tension and melt cohesive energy density of polymer melts including high melting and high glass transition polymers. *Macromolecules* **35**(18), 7024–7030 (2002)
70. T. Tanaka, M. Nakamoto, R. Oguni, J. Lee, S. Hara, Measurement of the surface tension of liquid Ga, Bi, Sn, In and Pb by the constrained drop method. *Z. Metallk.* **95**(9), 818–822 (2004)
71. M.N. Magomedov, Dependence of the surface energy on the size and shape of a nanocrystal. *Phys. Solid State* **46**(5), 954–968 (2004)
72. C.Q. Sun, Y. Wang, Y.G. Nie, Y. Sun, J.S. Pan, L.K. Pan, Z. Sun, Adatoms-induced local bond contraction, quantum trap depression, and charge polarization at Pt and Rh surfaces. *J. Chem. Phys. C* **113**(52), 21889–21894 (2009)
73. C.Q. Sun, Y. Nie, J. Pan, X. Zhang, S.Z. Ma, Y. Wang, W. Zheng, Zone-selective photoelectronic measurements of the local bonding and electronic dynamics associated with the monolayer skin and point defects of graphite. *RSC Adv.* **2**(6), 2377–2383 (2012)
74. F.H. Streitz, R.C. Cammarata, and K. Sieradzki, Surface-stress effects on elastic properties. I. Thin metal-films. *Phys. Rev. B* **49**(15), 10699–10706 (1994)
75. B.W. Dodson, Many-body surface strain and surface reconstructions in fcc transition-metals. *Phys. Rev. Lett.* **60**(22), 2288–2291 (1988)
76. A. Nduwimana, X.G. Gong, X.Q. Wang, Relative stability of missing-row reconstructed (110) surfaces of noble metals. *Appl. Surf. Sci.* **219**(1–2), 129–135 (2003)
77. M.J. Rost, S.B. van Albada, J.W.M. Frenken, Thermally activated domain boundary formation on a missing row reconstructed surface: Au(110). *Surf. Sci.* **547**(1–2), 71–84 (2003)
78. I.K. Robinson, M.C. Saint-Lager, P. Dolle, S. Boutet, M. De Santis, R. Baudoing-Savois, Relaxations in the 1×5 reconstruction of Pt(110). *Surf. Sci.* **575**(3), 321–329 (2005)
79. A. Baraldi, S. Lizzit, F. Bondino, G. Comelli, R. Rosei, C. Sbraccia, N. Bonini, S. Baroni, A. Mikkelsen, J.N. Andersen, Thermal stability of the Rh(110) missing-row reconstruction: combination of real-time core-level spectroscopy and ab initio modeling. *Phys. Rev. B* **72**(7), 075417 (2005)
80. J.M. Zhang, H.Y. Li, K.W. Xu, Reconstructed (110) surfaces of FCC transition metals. *J. Phys. Chem. Solids* **67**(8), 1623–1628 (2006)
81. C.Q. Sun, The sp hybrid bonding of C, N and O to the fcc(001) surface of nickel and rhodium. *Surf. Rev. Lett.* **7**(3), 347–363 (2000)
82. C.Q. Sun, Electronic process of Cu(Ag, V, Rh)(001) surface oxidation: atomic valence evolution and bonding kinetics. *Appl. Surf. Sci.* **246**(1–3), 6–13 (2005)
83. S. Kim, K.D. Kihm, Effect of adsorption-induced surface stress change on the stiffness of a microcantilever used as a salinity detection sensor. *Appl. Phys. Lett.* **93**(8), 081911 (2008)
84. D. Sander, H. Ibach, Experimental-determination of adsorbate-induced surface stress—oxygen on Si(111) and Si(100). *Phys. Rev. B* **43**(5), 4263–4267 (1991)
85. D. Sander, U. Linke, H. Ibach, Adsorbate-induced surface stress—sulfur, oxygen and carbon on Ni(100). *Surf. Sci.* **272**(1–3), 318–325 (1992)
86. A. Grossmann, W. Erley, H. Ibach, Adsorbate-induced surface stress and surface reconstruction—oxygen, sulfur and carbon on Ni(111). *Surf. Sci.* **337**(3), 183–189 (1995)
87. C. Bombis, M. Moiseeva, H. Ibach, Adsorbate-induced surface stress and self-assembly of $(2 \times 1)\text{O}$ on Cu(110) measured with an STM. *Phys. Rev. B* **72**(24), 245408 (2005)

88. K.S. Hwang, K. Eom, J.H. Lee, D.W. Chun, B.H. Cha, D.S. Yoon, T.S. Kim, J.H. Park, Dominant surface stress driven by biomolecular interactions in the dynamical response of nanomechanical microcantilevers. *Appl. Phys. Lett.* **89**(17), 173905 (2006)
89. A. Grossmann, W. Erley, H. Ibach, Adsorbate-induced surface stress—Co on Ni(100) and Ni(111). *Surf. Sci.* **313**(1–2), 209–214 (1994)
90. W.T. Zheng, C.Q. Sun, Electronic process of nitriding: mechanism and applications. *Prog. Solid State Chem.* **34**(1), 1–20 (2006)
91. V.G. Gavriljuk, Nitrogen in iron and steel. *ISIJ Int.* **36**(7), 738–745 (1996)
92. Y.Q. Fu, B.B. Yan, N.L. Loh, C.Q. Sun, P. Hing, Deposition of diamond coating on pure titanium using micro-wave plasma assisted chemical vapor deposition. *J. Mater. Sci.* **34**(10), 2269–2283 (1999)
93. I. Radu, R. Singh, R. Scholz, U. Gosele, S. Christiansen, G. Bruderl, C. Eichler, V. Harle, Formation of nanovoids in high-dose hydrogen implanted GaN. *Appl. Phys. Lett.* **89**(3), 031912 (2006)
94. J.K. Lee, Y. Lin, Q.X. Jia, T. Hochbauer, H.S. Jung, L. Shao, A. Misra, M. Nastasi, Role of strain in the blistering of hydrogen-implanted silicon. *Appl. Phys. Lett.* **89**(10), 101901 (2006)
95. R. Singh, R. Scholz, S.H. Christiansen, U. Gosele, Formation of nanovoids/microcracks in high dose hydrogen implanted AlN. *Phys. Status Solidi A-Appl. Mater. Sci.* **205**(11), 2683–2686 (2008)
96. G.H. Lu, Y. Zhang, S. Deng, T. Wang, M. Kohyama, R. Yamamoto, F. Liu, K. Horikawa, M. Kanno, Origin of intergranular embrittlement of Al alloys induced by Na and Ca segregation: grain boundary weakening. *Phys. Rev. B* **73**(22), 224115 (2006)
97. Y.Q. Fu, C.Q. Sun, B.B. Yan, H.J. Du, Carbon turns the tensile surface stress of Ti to be compressive. *J. Phys. D-Appl. Phys.* **34**(24), L129–L132 (2001)
98. H. Ibach, Adsorbate-induced surface stress. *J. Vac. Sci. Technol. A-Vac. Surf. Films* **12**(4), 2240–2243 (1994)
99. F. Berberich, W. Matz, U. Kreissig, N. Schell, A. Mucklich, Mechanism of degradation of surface hardening at elevated temperature in TiAlV-alloys by in situ synchrotron radiation diffraction. *Nucl. Instrum. Methods Phys. Res. Sect. B-Beam Interact. Mater. Atoms* **199**, 54–58 (2003)
100. R.A. Andrievski, Particulate nanostructured silicon nitride and titanium nitride. *ACS symposium series* (1996), **622**
101. S. Veprek, The search for novel, superhard materials. *J. Vac. Sci. Technol. A-Vac. Surf. Films* **17**(5), 2401–2420 (1999)
102. P. Schaaf, Laser nitriding of metals. *Prog. Mater. Sci.* **47**(1), 1–161 (2002)
103. S. Veprek, A.S. Argon, Towards the understanding of mechanical properties of super- and ultrahard nanocomposites. *J. Vac. Sci. Tech. B* **20**(2), 650–664 (2002)
104. S. PalDey, S.C. Deevi, Single layer and multilayer wear resistant coatings of (Ti, Al)N: a review. *Mater. Sci. Eng. A-Struct. Mater. Prop. Microstruct. Process.* **342**(1–2), 58–79 (2003)
105. X.M. Bai, W.T. Zheng, T. An, Superhard nano-multilayers and nanocomposite coatings. *Prog. Nat. Sci.* **15**(2), 97–107 (2005)
106. H. Sjoström, S. Stafström, M. Boman, J.E. Sundgren, Superhard and elastic carbon nitride thin-films having fullerene-like microstructure. *Phys. Rev. Lett.* **75**(7), 1336–1339 (1995)
107. C. Wang, S.R. Yang, H.X. Li, J.Y. Zhang, Elastic properties of a-C : N : H films. *J. Appl. Phys.* **101**(1), 013501 (2007)
108. Z.W. Zhao, B.K. Tay, C.Q. Sun, V. Ligatchev, Oxygen lone-pair states near the valence band edge of aluminum oxide thin films. *J. Appl. Phys.* **95**(8), 4147–4150 (2004)
109. C.Q. Sun, A model of bonding and band-forming for oxides and nitrides. *Appl. Phys. Lett.* **72**(14), 1706–1708 (1998)
110. Y. Zhang, H. Sun, C.F. Chen, Strain dependent bonding in solid C₃N₄: high elastic moduli but low strength. *Phys. Rev. B* **73**(6), 064109 (2006)

111. C.Q. Sun, Thermo-mechanical behavior of low-dimensional systems: the local bond average approach. *Prog. Mater. Sci.* **54**(2), 179–307 (2009)
112. C. Kittel, *Introduction to Solid State Physics*. 8th ed. (Wiley, New York, 2005)
113. M. Przyborowski, T. Hibiya, M. Eguchi, I. Egry, Surface-tension measurement of molten silicon by the oscillating drop method using electromagnetic-levitation. *J. Cryst. Growth* **151**(1–2), 60–65 (1995)
114. H. Fujii, T. Matsumoto, N. Hata, T. Nakano, M. Kohno, K. Nogi, Surface tension of molten silicon measured by the electromagnetic levitation method under microgravity. *Metall. Mater. Trans. A-Phys. Metall. Mater. Sci.* **31**(6), 1585–1589 (2000)
115. P.F. Paradis, T. Ishikawa, Surface tension and viscosity measurements of liquid and undercooled alumina by containerless techniques. *Jpn. J. Appl. Phys.* **44**, 5082–5085 (2005)
116. S. Sauerland, G. Lohofer, I. Egry, Surface-tension measurements on levitated aspherical liquid nickel drops. *Thermochim. Acta* **218**, 445–453 (1993)
117. B.J. Keene, K.C. Mills, R.F. Brooks, Surface-properties of liquid-metals and their effects on weldability. *Mater. Sci. Technol.* **1**(7), 568–571 (1985)
118. J. Schade, A. McLean, W.A. Miller, in *Surface Tension Measurements on Oscillating Droplets of Undercooled Liquid Metals and alloys*, ed. by E.W. Collins, C.C. Koch. Proceedings of 115th Annual Meeting of IUS-AIME, New Orleans, 1986, p. 233
119. X.J. Han, N. Wang, B. Wei, Thermophysical properties of undercooled liquid cobalt. *Philos. Mag. Lett.* **82**(8), 451–459 (2002)
120. B.J. Keene, Review of data for the surface-tension of pure metals. *Int. Mater. Rev.* **38**(4), 157–192 (1993)
121. R.A. Eichel, I. Egry, Surface tension and surface segregation of liquid cobalt-iron and cobalt-copper alloys. *Z. Metallk.* **90**(5), 371–375 (1999)
122. J. Lee, W. Shimoda, T. Tanaka, Temperature dependence of surface tension of liquid Sn–Ag, In–Ag and In–Cu alloys. *Meas. Sci. Technol.* **16**(2), 438–442 (2005)
123. P.F. Paradis, T. Ishikawa, S. Yoda, Surface tension and viscosity of liquid and undercooled tantalum measured by a containerless method. *J. Appl. Phys.* **97**(5), 053506 (2005)
124. P.F. Paradis, T. Ishikawa, R. Fujii, S. Yoda, Physical properties of liquid and undercooled tungsten by levitation techniques. *Appl. Phys. Lett.* **86**(4), 041901 (2005)
125. J. Lee, W. Shimoda, T. Tanaka, Surface tension and its temperature coefficient of liquid Sn–X (X = Ag, Cu) alloys. *Mater. Trans.* **45**(9), 2864–2870 (2004)

Chapter 25

Monatomic Chains: Strength and Extensibility

- *With involvement of neither atomic gliding nor bond unfolding, monatomic chain forms an ideal prototype for knowledge of bond stretching.*
- *A bond in a monatomic chain contracts by 30 % at equilibrium, and the metallic bond energy increases by 43 % compared with the bond in the bulk counterpart.*
- *A monatomic chain melts at $0.42 T_m$; metallic chains could form at $0.4 T_m$ with caution in operation.*
- *The breaking limit of the bond varies exponentially with the inverse separation ($T_m - T$) between the melting point of the chain and the temperature of operation.*

25.1 Observations

25.1.1 Temperature-Dependent Strain Limit

A metallic monatomic chain (MC) is an ideal prototype of a nanowire for studying the extensibility and mechanical strength as the extension of an MC involves only the process of bond stretching. Processes such as bond unfolding or atomic gliding take place in coarse-grained metallic chunks under mechanical stretching [1]. The intriguing phenomena appearing in MCs include the quantum conductance, higher chemical reactivity, lower thermal stability, and the unusually high mechanical strength at low temperatures and high ductility at slightly higher temperatures. Temperature of operation is an important factor to the performance of atomic chains. The quantum conductance of MCs has been understood as arising from the enlarged sublevel separation, known as the Kubo gap, $\delta_k = 4E_F/3N$, where E_F is the Fermi energy of the bulk and N is the total number of atoms of the cluster [2, 3]. Atomic chains of Au and Ag exhibit semiconductor features with a bandgap of 1.3 eV for Au and 0.8 eV for Ag with reasons yet to be clear [4]. This transition of conductor–insulator happens to metal clusters at ~ 2 nm scale. Knowledge about the equilibrium bond length, strength, extensibility, maximum strain, specific heat,

and the thermal and chemical stability of the MC bond is essential to understanding the process of superplasticity of atomic wires at the nanoscale.

The breaking limit of the Au–Au distance in the MC varies from range of 0.29 nm [5], 0.36 nm ($\pm 30\%$) [6], 0.35–0.40 nm [2], and even on a single occasion as 0.48 nm [7], measured using TEM at room temperature. The atomic distance in the stress-free Au atomic wires also varies from 0.24 to 0.34 nm with an estimated average of 0.26 ± 0.02 nm at room temperature [8]. However, at 4.2 K, the breaking limit of the Au–Au bond is reduced to 0.23 ± 0.04 nm as measured using STM and to 0.26 ± 0.04 nm as measured using mechanically controllable break junctions [9]. The standard bulk value of the Au–Au distance is 0.288 nm.

Likewise, STM measurement [10] revealed at 4.2 K that the Ir-MC and the Pt-MC breaks at 0.22 ± 0.02 and 0.23 ± 0.02 nm, respectively, being substantially shorter than the corresponding bulk values of 0.271 and 0.277 nm. Low-temperature measurements of the MCs show a commonly large extent of bond contraction with respect to the bulk values despite the applied tensile stress.

Numerical calculations for the impurity-free Au-MC have yielded a maximum Au–Au distance of 0.31 nm under tension [11–14], which hardly match the values measured at the ambient or at the extremely low temperatures in ultrahigh vacuum.

An EXRAFS study [15] revealed that the covalent bond in the Tellurium MC (0.2792 nm) is shorter and stronger than the bond (0.2835 nm) in the trigonal Te (t-Te) bulk structure. The Debye–Waller factor (square of the mean amplitude of lattice vibration) of the Te chain is larger than that of the bulk, but the thermal evolution of the Debye–Waller factor is slower than that of the bulk, which suggests the Te–Te bond in the chain is stronger than it is in the bulk, see Fig. 25.1a.

Figure 25.1b shows the temperature dependence of the interplanar spacing d of the (220) plane for the annealed Ni nanowire arrays (45 nm) and the annealed bulk Ni [16]. The results indicate that the bonds between atoms for Ni nanowires are stronger than bonds in the bulk. These findings demonstrate evidently the shorter and stronger bonds with greater amplitude of vibration and slower thermal expansion of the bonds between the undercoordinated atoms. The slope of the T dependence is inversely proportional to the atomic cohesive energy [17].

Figure 25.2a and b show the elastic modulus and the yield stress of Au nanostructures measured at room temperature [18, 19]. At the size corresponding to atomic chain, the elastic modulus is enhanced by 4–6 times with respect to the bulk value of 79 GPa. The yield stress rises sharply in the limit of a single-atom bridge to the value of ~ 150 GPa and over 4 orders than the yield stress of single crystal. The atomic-scale necks of gold tip in an atomic force microscopy were pushed into a flat gold surface. An examination of these tiny, gold bridges revealed that they were stiffest when they comprised just a single atom under compression.

Similarly, the yield stress of Ag atomic bridge reaches ~ 14 –25 GPa compared to that of single crystal Ag, ~ 0.5 MPa. The strength difference between Au and Ag atomic image arises from the melting point that is estimated to be 294 K for Ag and 318 K for Au atomic chains. These findings are consistent with the measured enhancement of Young's modulus, yield strength, and ultimate tensile strength as the silver nanowire diameter is decreased [20].

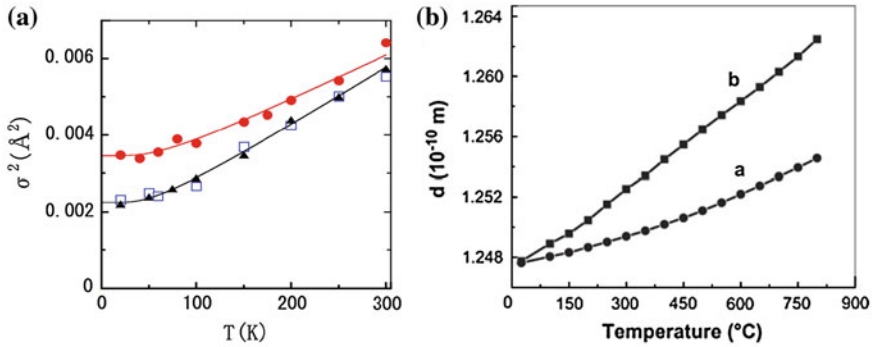


Fig. 25.1 **a** Size and temperature dependence of the Debye–Waller factor σ^2 (amplitude of lattice vibration) of the nearest neighbor within chains for Te systems. *Solid lines* are the respective correlated Einstein model fit to t-Te in the 0.5-nm-thick films (*solid circles*). The *triangles* denote σ^2 for bulk t-Te; the *squares* denote σ^2 for the 300-nm-thick films (reprinted with permission from [15]), and **b** the temperature dependences of the interplanar spacing d of the (220) plane for the annealed Ni nanowire arrays (*curve a*) and the annealed bulk Ni (*curve b*) show the same trend of size and temperature dependence (reprinted with permission from [16])

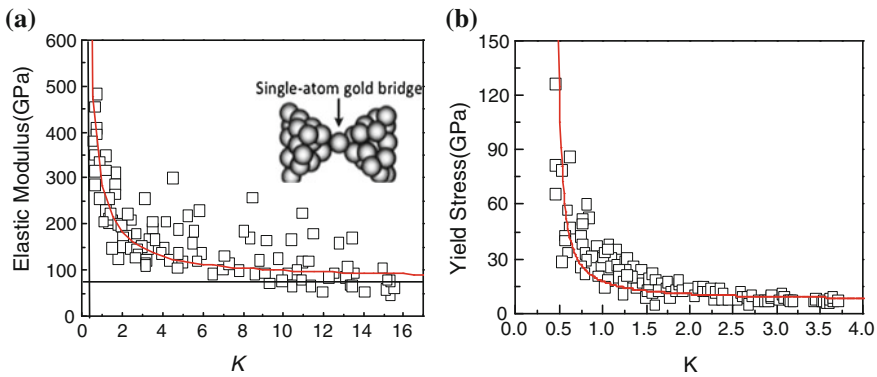


Fig. 25.2 Size dependence of **a** Young’s modulus and **b** yield stress of Au nanostructures down to the lower end of the size limit as being the monatomic chain ($K = 1.5$, indicated by the *broken lines* [41]) (reprint with permission from [18, 19, 42])

25.1.2 Known Mechanisms

The following explains the Au-MC elongation in terms of structural, chemical, or electronic effects:

- The fuzzy image mechanism [11] suggested that the MC elongation results from an artifact linked to a rotatable zigzag structure of the atomic chain. For an MC with an odd number of atoms, every other one is at fixed position along the chain

axis, while the atoms between the fixed ones rotate rapidly around the axis, offering a fuzzy image that TEM imaging could hardly catch. This mechanism works merely for the MCs consisting odd number of atoms [21, 22].

- The impurity mediation mechanism [23] proposed that artificial mediation with impurities of light atoms such as X (= H, He, B, C, N, O, S, CH, CH₂, and CO) being inserted into the Au–Au chain in calculations is responsible for all the observed elongations because the light atoms cannot be seen in the TEM. The light atom insertion has indeed led to gold separation in the Au–X–Au chain that could match the observed Au–Au distances. For instance, the insertion of a carbon atom leads to the stretched Au–C–Au distance of 0.39 nm just before breaking; wires containing B, N, and O displayed even larger distances under tension. The Au–H–Au distance, 0.36 nm, matches one of the experimentally measured values, and the anomalously large distance of 0.48 nm matches the separation between gold atoms in an Au–S–Au chain [24].
- The charge mediation mechanism [25] assumed that the enlarged electronegativity and electroaffinity of the undercoordinated Au-MC atom enables the Au atom to catch selected number of electrons from the TEM radiation. Then, this charging effect modifies the shape of the interatomic pairing potential with the presence of a potential maximum or force zero (transition point at the second-order differential of the potential curve), at a distance being attributed to the breaking limit. It was derived that the states of Au₂¹⁻, Au₃²⁻, Au₄²⁻, and Au₄³⁻ could lead to the maximum Au–Au distances of 0.49, 0.41, 0.49, and 0.35 nm, respectively. Unfortunately, this argument could not explain the Au–Au distances shorter than 0.35 nm. In fact, charging effect exists only for thick insulating samples in the TEM measurement because of the non-conductive character of the specimen, according to Egerton et al. [26]. The energetic electrons ($E > 10^5$ eV) in the TEM readily transmit through insulating specimens thinner than 100 nm, and the charging effect for conductors or thinner insulators becomes negligible though an increase in the electroaffinity does occur to the undercoordinated Au atoms by 1.34 eV (25 %) [27].

The Au–Au, Pt–Pt, and Ir–Ir distances at low temperatures are 15–20 % shorter than the bulk values, which are beyond the scope of these mechanisms. Therefore, mechanism for the MC elongation is still open for debate. Encouragingly, sophisticated DFT calculations [28] suggest that the pairing potential is valid and the Au–Au equilibrium distance (without the presence of an external stimulus) is between 0.232 and 0.262 nm and the cohesive energy per bond increases by 200 % from –0.51 to –1.59 eV. MCs of Pt, Cu, and Ag follow the same trend in theory though experimental observation of such MC formation at room temperature has been infrequent.

According to the ab initio calculations and STM measurements [29], the mechanical strength of the Au–Au bond is about twice that of the bulk value. Results from a combination of high-resolution TEM and MD simulation [30]

suggested that different initial crystallographic orientations lead to differentiated linear Au atomic chain formations, which suggested that the kinetic aspects such as temperatures and elongation rates strongly affect the morphology and chance of MC formation. In addition to the DFT approaches, Jiang et al. [31] correlated the formation tendency of a MC under tensile stress to the ratio between the Peierls stress of a bulk crystal having dislocations and the theoretical shear breaking stress of the MC. They suggested that the metallic elements having the largest Poisson's ratio hold the largest MC-forming ability since such metals have the smallest elastic energy storage within the crystals and can thus endure the largest plastic deformation. Experiment using electron cohesive diffraction [32], MD [33] and DFT [34] computations revealed consistently the skin-resolved Au–Au bond contraction in Au nanocrystals because of the bond order loss.

25.2 T-BOLS Formulation

25.2.1 Chain Melting Energetics

The temperature of melting an atom with z_i coordinates, $T_{m,i}$, is proportional to the atomic cohesive energy, $T_{m,i} \propto z_i E_i$ [35, 36]. If one wants to melt or thermally rupture the bond, one has to provide thermal energy that is a certain proportion of the entire binding energy. In contrast, breaking a bond mechanically at a temperature T needs energy that equals to the net bond energy at T :

$$\begin{aligned}
 E_b(T) &= \begin{cases} E_b(0) - \int_0^T \eta_1(t) dt & (T \leq \theta_D) \\ \approx \eta_2 + \eta_1(T_m - T) & (T > \theta_D) \end{cases} \\
 E_i(T) &= E_i(0) - \int_0^T \eta_1(t) dt = \eta_{2i} + \int_T^{T_m} \eta_{1i}(t) dt \\
 &= \begin{cases} C_i^{-m} E_b(0) - z_{bi} \int_0^T \eta_1(t) dt & (T \leq \theta_D) \\ \approx C_i^{-m} \eta_2 + z_{bi} \eta_1(T_m - T) & (T > \theta_D) \end{cases}
 \end{aligned} \tag{25.1}$$

The constant η_{2i} is the $1/z_i$ -fold energy that is required for evaporating a molten atom in the MC with $z_i = 2$. η_{1i} and η_{2i} can be determined with the known C_i^{-m} and the known bulk values of η_1 and η_2 that vary with crystal structures [37],

$$\begin{cases} \eta_{1i} &= z_{bi} \eta_1 \\ \eta_{2i} &= C_i^{-m} \eta_2 \end{cases} .$$

25.2.2 Elasticity and Extensibility

The effect of heating on the strength and compressibility (under compressive stress) or extensibility (under tensile stress) at a given temperature follows [38, 39]

$$P_i(z_i, T) = -\frac{\partial u(r, T)}{\partial V} \sim B_i(z_i, T) = -V \left. \frac{\partial^2 u(r, T)}{\partial V^2} \right|_{d_i} \propto \frac{N_i E_i(T)}{d_i^3(T)} \quad (25.2)$$

$$\beta_i(z_i, T) = -\left. \frac{\partial V}{V \partial P} \right|_T \propto [B_i(z_i, T)]^{-1}$$

Theoretically, β is in an inverse of the bulk modulus in dimension. However, η_{2i} does not contribute to the extensibility for the molten state as it approaches infinity at T_m . The N_i is the total number of bonds in the d_i^3 volume. Calibrated with the bulk value at T_0 , the reduced temperature dependence of the linear extensibility for the MC at $T \gg \theta_D$ will be

$$\frac{\beta_i(z_i, T)}{\beta_0(z, T_0)} = \frac{d_i(1 + \alpha_i T)}{d(1 + \alpha T_0)} \times \frac{\eta_1(T_m - T_0)}{\eta_{1i}(T_{mi} - T)}. \quad (25.3)$$

Note that the bond number density in the relaxed region does not change upon relaxation ($N_i \cong N_{\text{bulk}}$). For instance, bond relaxation never changes the bond number between the neighboring atoms in an MC ($\tau = 1$) whether it is suspended or embedded in the bulk, nor does it change the number density between the circumferential atomic layers of a solid.

25.2.3 Strain Limit

Introducing the following effects: (1) atomic CN-imperfection-induced bond contraction, (2) thermal expansion (with linear coefficient α_i), and (3) the temperature dependence of extensibility (with coefficient β_i), leads to an analytical expression for the distance between two nearest atoms in the interior of a MC, as a function of atomic CN, mechanical (P), and thermal (T) stimuli:

$$d_i(z_i, T, P) = d \times C(z_i)(1 + \alpha_i T)[1 + \beta_i(z_i, T)P]$$

or the maximal strain at constant T ,

$$\frac{\Delta d_{iM}(z_i, T, P)}{d_i(z_i, T, 0)} = \beta_i(z_i, T)\bar{P} \quad (25.4)$$

where $d_i(z_i, T, 0) = d \times C(z_i)(1 + \alpha_i T)$ is the bond length at T without mechanical stretching. At the bulk T_m , the linear thermal expansion ($\alpha_i \times T_m$) is around 3 % for most metals, which is negligibly small compared with C_i . Equating the energy for mechanical rupture to that for thermal rupture, as given in Eq. (25.1), yields

$$\begin{aligned}
 E_i(T) &= \int_{d_i(z_i, T, 0)}^{d_{iM}(z_i, T, P)} P dx = \bar{P} [d_{iM}(z_i, T, P) - d_i(z_i, T, 0)] = \bar{P} \Delta d_{iM}(z_i, T, P) \quad (25.5) \\
 &= \eta_{2i} + \eta_{1i}(T_{mi} - T)
 \end{aligned}$$

The mechanical rupture energy equals the thermal energy required for evaporating the same atom by warming it up from the initial T . One can approximate the P to the mean \bar{P} , if the $d_{iM}(z_i, T, P)$ represents the breaking limit, as the integral is a constant. Combining Eqs. (25.4) and (25.5) yields

$$\bar{P} = \pm \left\{ \frac{E_i(T)}{\beta(z_i, T) \times d_i(z_i, T, 0)} \right\}^{1/2} \quad (25.6)$$

For tensile stress, \bar{P} takes a positive value; for compressive stress, \bar{P} is negative. The combination of Eqs. (25.3) and (25.6) yields the maximal strain of a bond in the MC:

$$\begin{aligned}
 \frac{\Delta d_{iM}(z_i, T, P)}{d_i(z_i, T, 0)} &= \beta_i(z_i, T) \bar{P} = \left\{ \frac{\beta(z_i, T) \times E_i(T)}{d_i(z_i, T, 0)} \right\}^{1/2} \\
 &= \left[\frac{\eta_{1i} d_i(z_i, T, 0) \times \beta_0(z, T_0)}{\eta_{1i} d \times d_i(z_i, T, 0)} \times \left(\frac{T_m - T_0}{T_{m,i} - T} \right) \times [\eta_{1i}(T_{m,i} - T) + \eta_{2i}] \right]^{1/2} \\
 &= \left[\frac{\beta_0 \eta_{1i} (T_m - T_0)}{d} \left(1 + \frac{\eta_{2i}}{\eta_{1i} (T_{m,i} - T)} \right) \right]^{1/2} \\
 &\cong \left(\frac{\beta_0 \eta_{1i} (T_m - T_0)}{d} \right)^{1/2} \exp \left\{ \frac{\eta_{2i} / \eta_{1i}}{2[T_m - T / (1 + \Delta_i)]} \right\} = B \times \exp \left\{ \frac{A}{T_m - T / (1 + \Delta_i)} \right\} \quad (25.7)
 \end{aligned}$$

where $1 + \Delta_i = z_{ib} C_i^{-m}$. For a metallic MC with $z_i = 2$ and $m = 1$, the melting point is $T_{m,i} \propto z_{ib} C_i^{-1} T_m = T_m / 4.185 = 0.239 T_m$. If the η_{2i} is taken into consideration in the extensibility of Eq. (25.3), the strain will remain constant without features of temperature dependence:

$$\frac{\Delta d_{iM}(z_i, T, P)}{d_i(z_i, T, 0)} = \left[\frac{z_{ib} \beta_0(z, T_0)}{d} \times \frac{E_b(T_0)}{E_i(T)} \times E_i(T) \right]^{1/2} = \text{const.}$$

This derivative validates Born's criterion of shear modulus disappearance at melting. The η_{2i} contributes to the plasticity but not to the elasticity.

The analytical expression of the maximal strain varies not apparently with the extrinsic parameter P or the strain rate, but depends intrinsically on the inverse of the $T_{m,i} - T$ in an exponential way. When the temperature approaches $T_{m,i}$, the strain will approach infinity. The constant $A = \eta_{2i} / 2\eta_{1i}$ is crystal structure dependent. The factor B depends on the nature of the material and varies with the bulk extensibility (at T_0), bond length, and T_m as well as the specific heat per bond in the bulk.

25.3 Bonding Identities

25.3.1 MC Bonding Identities

The MC is an equivalent of the crystal at the lower end of size limit, that is, the unit cell of an fcc structure with the effective size of $K = 1.5$ and $z = 2$ ($R = Kd = 0.43$ nm for an Au spherical dot or an equivalent of an fcc unit cell). At $z = 2$, the Au–Au distance contracts by $C_2 - 1 = 30\%$ from 0.288 to ~ 0.201 nm, the XPS 4f binding energy shift by $C_2^{-1} - 1 = 43\%$ from the bulk value of 2.86–4.09 eV and the melting point drops by $z_{2,12}C_2^{-1} - 1 = -76\%$ from 1,337.33 to 320 K ($0.239 T_m$, see Part II).

Therefore, the value of 0.23 ± 0.04 nm of Au–Au breaking limit measured at 4.2 K under tension [9] is simply a $\sim 15\%$ strain response to the tensile stress of the original equilibrium bond length, 0.201 nm. Similarly, the values of 0.22 ± 0.02 nm for Ir and 0.23 ± 0.02 nm for Pt [10] MC measured at 4.2 K are also 16 and 19% strain response to the tensile stress of the equilibrium MC bond length (0.190 and 0.194 nm, respectively) that are 30% shorter than the respective bulk values of 0.271 and 0.277 nm.

25.3.2 Specific Heat and Breaking Limit

With the known values of thermal expansion coefficient $\alpha = 14.7 \times 10^{-6} \text{ K}^{-1}$, $T_m = 1,337.33$ K, and $d = 0.2878$ nm, one can find the maximal strain of the Au-MC using Eq. (25.7). Calibrated using the breaking limits of $d_{iM}(4.2 \text{ K}) = 0.23$ nm [9], and the mean $d_{iM}(300 \text{ K}) = 0.35$ nm [2, 5, 6], Eq. (25.7) results in the $\beta_0 = 5.0 \text{ TPa}^{-1}$ and $\eta_{2i}/\eta_{1i} = 64$ K.

Using the relation $E_i = C_i^{-1}E_b$, or, $\eta_{1i}T_{m,i} + \eta_{2i} = C_i^{-1}(\eta_1T_m + \eta_2)$ and the given $\eta_1 = 0.0005542 \text{ eV/K}$ and $\eta_2 = -0.24 \text{ eV}$ for the fcc structures [37] turns out $\eta_{1i} = 0.0033325 \text{ eV/K}$ and $\eta_{2i} = 0.2128 \text{ eV}$. The bulk value of $\eta_2 = C_i\eta_{2i} = 0.14897 \text{ eV}$, being compatible to that of diamond structures of $\eta_2 = 0.24 \text{ eV}$. The $\eta_2 < 0$ in [37] means that the actual latent of atomization energy of the molten atom is included in the term of η_1T_m , and therefore, the η_1 may not represent the true value of the specific heat per coordinate. Accuracy of solutions gained herewith is subject strictly to the given η_1 and η_2 values and the precision of the measured $d_{iM}(T \neq 0)$ values used for calibration, as no freely adjustable parameters are involved in calculations.

Figure 25.3a compares the calculated maximum strain versus T/T_m with the measured values for the Au-MC at various temperatures. The theoretical curve covers all the divergent values measured at 4.2 K (0.23 ± 0.04 nm) and at the ambient temperatures (298 ± 6 K, 0.29–0.48 nm). The divergent data are actually centered at some 22 K below the melting point, 320 K, of the Au-MC with a 6-K fluctuation. The fluctuation may arise from differences in the temperature of

testing, or the strain rate applied during measurement. Therefore, all reported values of Au–Au bond breaking are true, but the measurements might have been conducted in different seasons or different locations.

According to Egerton et al. [26], the temperature rise of a TEM specimen in micrometer size caused by electron beam radiation in the TEM is less than 2 K. The heat energy released from bond stretching may contribute to the actual temperature of the specimen, but it is expected to be insignificant for the small samples and is common to all measurements.

Likewise, the 16–19 % elongation limits of Ir-MC and Pt-MC measured using an STM at 4.2 K are also within the framework. The divergent values of the breaking limits measured at the ambient temperature are dominated by the extensibility factor that increases exponentially with temperature and reaches infinity at $T_{m,i}$. The thermal and mechanical fluctuations in the measurement become significant.

Figure 25.3a also suggests that the dominant factor T_m has slight influences on the breaking mode of a MC. The bond of a low- T_m specimen breaks more readily at low temperature than the bond of a high- T_m specimen; the bond of the low- T_m specimen is more easily extended as T approaches $T_{m,i}$ than the ones with higher T_m values.

The above scenario for metallic MC elongation also applies to the elongation of organic molecular chains. A curve shown in Fig. 25.3b for the monomer persistence length versus temperature of a single polymer chain adsorbed on an Au(111) substrate showed a similar trend of temperature-dependent extensibility to that for the Au-MC despite the complexity of polymer extension because of the involvement of worm-like extension and bond unfolding [40]. The rupture occurs at 315 K, and the monomer increases its length from 0.18 to 0.38 nm in an exponential way when the temperature is increased from 300 to 315 K though the rupture is a stochastic process and depends on many factors such as pulling speed, bond strength, and the temperature of operation.

25.3.3 Criteria for MC Formation

Equation (25.7) indicates that a metallic MC melts at a temperature of $1/4.185$ (0.239) of the bulk T_m . Observations suggest that a metallic MC could be readily made at a temperature that is $\sim 20 \pm 6$ K lower than its melting point, $T_{m,i}$. Therefore, if one wants to make a MC of a certain specimen extendable at the ambient temperature (300 K), one has to work with the material whose T_m satisfies $(300 + 20) \times 4.185 = 1,343$ K or a value close to this point. However, an extendable MC can hardly form at room temperature or above if the bulk T_m of a specific metal is below $300 \times 4.185 = 1,260$ K, such as Sn (505.1 K), Pb (600.6 K), and Zn (692.7 K). An extendable Ti-MC (with $T_m = 1,941$ K) may form at ~ 440 K, slightly lower than its $T_{m,i} = T_m/4.185 = 462$ K. Therefore, it is possible to make a specific MC by operating the MC at a carefully controlled range of temperatures.

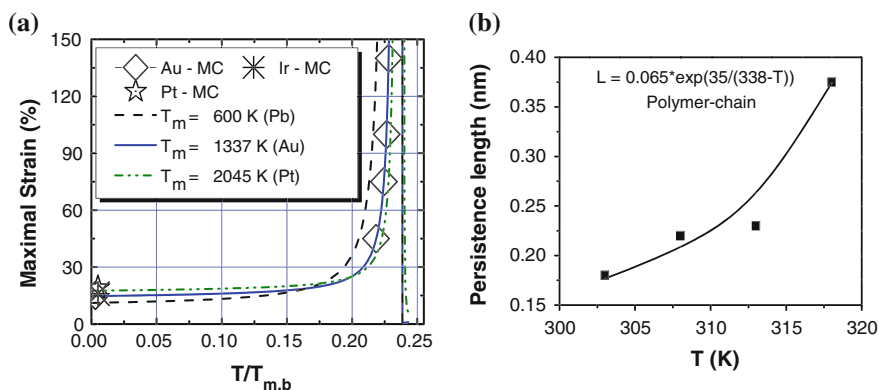


Fig. 25.3 **a** Temperature dependence of an MC breaking limit in comparison with values for an Au-MC measured at 4.2 K (0.23 ± 0.04 nm) and at ambient (298 ± 6 K, 0.29–0.48 nm) indicates that the scattered data arise from temperature-dependent extensibility and the thermal and mechanical fluctuations near the melting point of the Au-MC. Varying the T_m changes slightly the ease of MC bond breaking at different temperatures. The 16–19 % elongation of Ir and Pt measured using STM at 4.2 K [10] is also within the prediction. **b** Temperature dependence of polymer extension also shows the exponential dependence of elongation before breaking [40] (reprinted with permission from [43])

Au is favorable for such MC formation at the ambient temperature, whereas the well-known ductile metals of Ag ($T_m = 1,235$ K), Al ($T_m = 933.5$ K), and Cu ($T_m = 1,356$ K) are unlikely to form extendable MCs though they could form superplastic NWs at the ambient temperatures. Although the electronic structure may need to be considered in making an MC [10], the operating temperature would be most critical. The high extensibility is apparent in the temperature range that corresponds to the quasi-molten state that is much softer and highly extendable than the bulk.

25.4 Summary

The T-BOLS correlation has enabled calibration of the length, strength, extensibility, and thermal stability of the Au-MC bond under the conditions with and without thermal and mechanical stimuli. Major findings are summarized as follows:

1. Without external stimuli, the metallic bond in an MC contracts by ~ 30 %, associated with ~ 43 % magnitude rise of the bond energy and 1/4.2 times of the melting point compared with the bulk standard. The electroaffinity (separation between the vacuum level and the band edge of the 4f conduction band) of the Au-MC is 1.34 eV greater than the bulk, which is responsible for the high chemical reactivity of the undercoordinated MC.

2. The analytical solution shows that the strain limit of a metallic bond in a MC under tension does not apparently vary with the mechanical stress or the strain rate but apparently with temperature in the form $\exp [A/(T_m/4.2 - T)]$. This relation governs the tendency for a metallic MC to form or break, and therefore, an MC of other elements could be made by operating it at properly controlled range of temperatures. However, as extrinsic factors, the stress field and the strain rate could be important in the experiments relating to MC elongation.
3. Matching the calculated Au–Au distance to all the insofar measured values indicates that the divergency in measurements originates from thermal and mechanical fluctuations and the extremely high extensibility near the melting point.

Therefore, the coordination-imperfection-enhanced binding intensity, mechanical strength, the suppressed thermal stability, and the compressibility/extensibility of a MC are correlated, which could be extended to the thermal and mechanical behavior of other metallic nanowires. The developed approach provides an effective way of determining the bulk 0 K extensibility, β_0 , the effective specific heat η_{1i} per coordinate, and the energy (η_{2i}) required for evaporating an atom from the molten MC. Practical data would be helpful to give information on the MC bonding identities and the single-electron energy level of an isolated atom, one of the challenging tasks for nanometrology.

References

1. Y. Champion, C. Langlois, S. Guerin-Mailly, P. Langlois, J.L. Bonnetien, M.J. Hytch, Near-perfect elastoplasticity in pure nanocrystalline copper. *Science* **300**(5617), 310–311 (2003)
2. H. Ohnishi, Y. Kondo, K. Takayanagi, Quantized conductance through individual rows of suspended gold atoms. *Nature* **395**(6704), 780–783 (1998)
3. C.N.R. Rao, G.U. Kulkarni, P.J. Thomas, P.P. Edwards, Size-dependent chemistry: properties of nanocrystals. *Chem. Eur. J.* **8**(1), 29–35 (2002)
4. F. Fioravante, R.W. Nunes, Semiconducting chains of gold and silver. *Appl. Phys. Lett.* **91**(22), 223115 (2007)
5. Y. Takai, T. Kawasaki, Y. Kimura, T. Ikuta, R. Shimizu, Dynamic observation of an atom-sized gold wire by phase electron microscopy. *Phys. Rev. Lett.* **87**(10), 106105 (2001)
6. A.I. Yanson, G.R. Bollinger, H.E. van den Brom, N. Agrait, J.M. van Ruitenbeek, Formation and manipulation of a metallic wire of single gold atoms. *Nature* **395**(6704), 783–785 (1998)
7. S.B. Legoas, D.S. Galvao, V. Rodrigues, D. Ugarte, Origin of anomalously long interatomic distances in suspended gold chains. *Phys. Rev. Lett.* **88**(7), 076105 (2002)
8. T. Kizuka, Atomic configuration and mechanical and electrical properties of stable gold wires of single-atom width. *Phys. Rev. B* **77**(15), 155401 (2008)
9. C. Untiedt, A.I. Yanson, R. Grande, G. Rubio-Bollinger, N. Agrait, S. Vieira, J.M. van Ruitenbeek, Calibration of the length of a chain of single gold atoms. *Phys. Rev. B* **66**(8), 085418 (2002)
10. R.H.M. Smit, C. Untiedt, A.I. Yanson, J.M. van Ruitenbeek, Common origin for surface reconstruction and the formation of chains of metal atoms. *Phys. Rev. Lett.* **87**(26), 266102 (2001)

11. H. Hakkinen, R.N. Barnett, A.G. Scherbakov, U. Landman, Nanowire gold chains: formation mechanisms and conductance. *J. Phys. Chem. B* **104**(39), 9063–9066 (2000)
12. M.R. Sorensen, M. Brandbyge, K.W. Jacobsen, Mechanical deformation of atomic-scale metallic contacts: Structure and mechanisms. *Phys. Rev. B* **57**(6), 3283–3294 (1998)
13. D. Sanchez-Portal, E. Artacho, J. Junquera, P. Ordejon, A. Garcia, J.M. Soler, Stiff monatomic gold wires with a spinning zigzag geometry. *Phys. Rev. Lett.* **83**(19), 3884–3887 (1999)
14. J.A. Torres, E. Tosatti, A. Dal Corso, F. Ercolessi, J.J. Kohanoff, F.D. Di Tolla, J.M. Soler, The puzzling stability of monatomic gold wires. *Surf. Sci.* **426**(3), L441–L446 (1999)
15. H. Ikemoto, T. Miyanaga, Extended x-ray absorption fine structure study of local structure and atomic correlations of tellurium nanoparticles. *Phys. Rev. Lett.* **99**(16), 165503 (2007)
16. X.W. Wang, G.T. Fei, B. Wang, M. Wang, L. De Zhang, In situ X-ray diffraction study on the interatomic force of Ni nanowires. *Solid State Sci.* **10**(9), 1185–1188 (2008)
17. J.W. Li, S.Z. Ma, X.J. Liu, Z.F. Zhou, C.Q. Sun, ZnO meso-mechano-thermo physical chemistry. *Chem. Rev.* **112**(5), 2833–2852 (2012)
18. J.N. Armstrong, S.Z. Hua, H.D. Chopra, Mechanics of quantum and Sharvin conductors. *Phys. Rev. B* **83**(23), 235422 (2011)
19. J.N. Armstrong, R.M. Schaub, S.Z. Hua, H.D. Chopra, Channel saturation and conductance quantization in single-atom gold constrictions. *Phys. Rev. B* **82**(19), 195416 (2010)
20. Y. Zhu, Q. Qin, F. Xu, F. Fan, Y. Ding, T. Zhang, B.J. Wiley, Z.L. Wang, Size effects on elasticity, yielding, and fracture of silver nanowires: in situ experiments. *Phys. Rev. B* **85**(4), 045443 (2012)
21. V. Rodrigues, D. Ugarte, Real-time imaging of atomistic process in one-atom-thick metal junctions. *Phys. Rev. B* **63**(7), 073405 (2001)
22. H. Koizumi, Y. Oshima, Y. Kondo, K. Takayanagi, Quantitative high-resolution microscopy on a suspended chain of gold atoms. *Ultramicroscopy* **88**(1), 17–24 (2001)
23. N. Agrait, A.L. Yeyati, J.M. van Ruitenbeek, Quantum properties of atomic-sized conductors. *Phys. Rep.-Rev. Sec. Phys. Lett.* **377**(2–3), 81–279 (2003)
24. F.D. Novaes, A.J.R. da Silva, E.Z. da Silva, A. Fazzio, Effect of impurities in the large Au–Au distances in gold nanowires. *Phys. Rev. Lett.* **90**(3), 036101 (2003)
25. A. Ayuela, M.J. Puska, R.M. Nieminen, J.A. Alonso, Charging mechanism for the bond elongation observed in suspended chains of gold atoms. *Phys. Rev. B* **72**(16), 161402 (2005)
26. R.F. Egerton, P. Li, M. Malac, Radiation damage in the TEM and SEM. *Micron* **35**(6), 399–409 (2004)
27. C.Q. Sun, Y. Shi, C.M. Li, S. Li, T.C.A. Yeung, Size-induced undercooling and overheating in phase transitions in bare and embedded clusters. *Phys. Rev. B* **73**(7), 075408 (2006)
28. S.R. Bahn, K.W. Jacobsen, Chain formation of metal atoms. *Phys. Rev. Lett.* **87**(26), 266101 (2001)
29. G. Rubio-Bollinger, S.R. Bahn, N. Agrait, K.W. Jacobsen, S. Vieira, Mechanical properties and formation mechanisms of a wire of single gold atoms. *Phys. Rev. Lett.* **87**(2), 026101 (2001)
30. P.Z. Coura, S.B. Legoas, A.S. Moreira, F. Sato, V. Rodrigues, S.O. Dantas, D. Ugarte, D.S. Galvao, On the structural and stability features of linear atomic suspended chains formed from gold nanowires stretching. *Nano Lett.* **4**(7), 1187–1191 (2004)
31. Q. Jiang, M. Zhao, J.C. Li, Formation of monoatomic chains of metallic elements. *Appl. Surf. Sci.* **206**(1–4), 331–335 (2003)
32. W.J. Huang, R. Sun, J. Tao, L.D. Menard, R.G. Nuzzo, J.M. Zuo, Coordination-dependent surface atomic contraction in nanocrystals revealed by coherent diffraction. *Nat. Mater.* **7**(4), 308–313 (2008)
33. W.H. Qi, B.Y. Huang, M.P. Wang, Bond-length and -energy variation of small gold nanoparticles. *J. Comput. Theor. Nanosci.* **6**(3), 635–639 (2009)
34. X. Zhang, J.L. Kuo, M.X. Gu, X.F. Fan, P. Bai, Q.G. Song, C.Q. Sun, Local structure relaxation, quantum trap depression, and valence charge polarization induced by the shorter-

- and-stronger bonds between under-coordinated atoms in gold nanostructures. *Nanoscale* **2**(3), 412–417 (2010)
35. U.F. Kocks, A.S. Argon, M.F. Ashby, Thermodynamics and kinetics of slip. *Prog. Mater. Sci.* **19**, 1–281 (1975)
 36. F.G. Shi, Size-dependent thermal vibrations and melting in nanocrystals. *J. Mater. Res.* **9**(5), 1307–1313 (1994)
 37. K.K. Nanda, S.N. Sahu, S.N. Behera, Liquid-drop model for the size-dependent melting of low-dimensional systems. *Phys. Rev. A* **66**(1), 013208 (2002)
 38. C.Q. Sun, C.M. Li, S. Li, B.K. Tay, Breaking limit of atomic distance in an impurity-free monatomic chain. *Phys. Rev. B* **69**(24), 245402 (2004)
 39. N. Agrait, A.L. Yeyati, J.M. van Ruitenbeek, Quantum properties of atomic-sized conductors. *Phys. Rep.-Rev. Sec. Phys. Lett.* **377**(2–3), 81–279 (2003)
 40. K. Nakajima, H. Watabe, T. Nishi, Single polymer chain rubber elasticity investigated by atomic force microscopy. *Polymer* **47**(7), 2505–2510 (2006)
 41. Z.S. Ma, Z.F. Zhou, Y.L. Huang, Y.C. Zhou, C.Q. Sun, Mesoscopic superelasticity, superplasticity, and superrigidity. *Sci. China G: Phys., Mech. Astron.* **55**(6), 963–979 (2012)
 42. J.N. Armstrong, S.Z. Hua, H.D. Chopra, Strength of metals at the Fermi length scale. *Phys. Status Solidi* **9**, 99–101 (2012)
 43. C.Q. Sun, Thermo-mechanical behavior of low-dimensional systems: the local bond average approach. *Prog. Mater. Sci.* **54**(2), 179–307 (2009)

Chapter 26

Atomic Sheets, Nanotubes, and Nanowires

- *The elastic modulus is proportional to the binding energy density (E_z/d_z^3), while the melting point to the atomic cohesive energy (zE_z), which causes the paradox in observations at the nanoscale.*
- *With the known stiffness of 0.368 TPa-nm and the tip-end melting point of 1,593 K, the C–C bond in the SWCNT is determined to be ~ 0.142 nm thick and ~ 0.125 nm long with a 68 % magnitude rise in binding energy, the edge C–C bond is 0.108 nm long and 152 % times stronger, in comparison with the bulk diamond values.*
- *The Young's modulus of SWNT and graphene is 2.60 TPa, 2.5 times the bulk value of 1.02 TPa.*
- *The Young's modulus of a hollow tube increases with the inverse of wall thickness, rather than its radius; a hollow tube is more elastic than a solid rod of the same radius because of the relatively high proportion of surface atoms.*

26.1 Observations

26.1.1 Stiffness and Elasticity

The strong bonds between adjacent carbon atoms make individual nanotube one of the toughest materials ever known. A rather stiff CNT gel can be made by physically grinding up SWCNTs with ionic liquids. The gels showed good thermal and dimensional stability and could be shaped into conductive sheets to enhance the mechanical properties. Using a coagulation-based CNT spinning technique, Dalton et al. [1] spun surfactant-dispersed SWCNTs from a rotating bath of aqueous polyvinyl alcohol to produce CNT gel fibers that they then converted to solid nanotube composite fibers. The resulting 100-m-long fibers were 50 μm thick and contained around 60 % nanotubes by weight. The composite has a tensile strength of 1.8 GPa and an energy-to-break value of 570 J/g. The static fatigue

strength of SWCNT ropes is at least twice that of graphite fiber within 10^4 s and is similar to that of graphite fiber at longer times, while the dynamic fatigue strength is twice that of the graphite fiber to up to 10^7 cycles [2]. The fibers, which are suitable for weaving into electronic cloth, are four times tougher than spider silk and 17 times tougher than the Kevlar fibers used in bulletproof vests. The fibers also have twice the stiffness and strength and 20 times the toughness of the same weight of a steel wire.

However, precision determination of the Young's modulus of the CNTs is a long challenge [3]. For instance, a TEM nanorobotic manipulator measurement suggested that the Y value varies over a range of 0.5–5.5 TPa being subject to the presumption of the wall thickness [4–11]. If one assumes the equilibrium interlayer spacing of graphite sheet as $t_1 = 0.34$ nm, to represent the single-wall (bond) thickness, the derived Y_1 value is ~ 1.1 TPa [12, 13]. If $t_1 = 0.066$ nm, which is close to the radius of a free carbon atom (0.0771–0.0914 nm), the Y_1 is derived as 5.5 TPa [14–17]. The apparent thickness may change slightly due to the thermal vibration [18], which should be limited to 5 % or lower of the bond length at the temperature of melting [19]. The Y value for the bulk graphite or diamond is 1.02 TPa. However, the measured Y_1 varies insignificantly with the tube diameter or the tube helicity of the SWCNT though the curvature-induced strain may contribute [20].

In practice, one can only measure the product of the Young's modulus and the wall thickness, or called stiffness, $(Yt)_1$, of the SWCNT, rather than the individual component, Y_1 or t_1 . Although the measured values of t_1 and Y_1 are widely scattered, the product of $(Yt)_1$ surprisingly approaches a constant value of 0.368 ± 0.005 TPa·nm [21]. Therefore, discriminating the Y_1 value from the product of $(Yt)_1$ is essential.

In contrast, the multi-walled (MW) CNTs demonstrate two typical trends of the change in Y values:

- The Y value remains almost constant for a given number of walls without change in the tube diameter [12] and
- The Y value increases as the number of walls (λ) or wall thickness is reduced [22].

26.1.2 Thermal and Chemical Stability

On the other hand, the CNTs are less chemically and thermally stable compared with the bulk graphite or diamond crystal. Atoms at the open edge of a SWCNT could even melt or coalesce prior to that for atoms in the tube body at temperature much lower than the melting point of the bulk graphite ($T_m = 3,800$ K). The coalescent temperature of the MWCNT increases as the number of walls increases, being opposite in trend to the elastic modulus. Coalescence of the SWCNT happens at 1,073 K under energetic (1.25 MeV) electron beam irradiation, and the

coalescence starts at sites surrounding atomic vacancies via a zipper-like mechanism [23], indicating that the undercoordinated atoms melt more easily and the vacancy provides site for thermally induced structure failure.

The STM tip-end that is made of SWCNT starts to melt at 1,593 K in ultrahigh vacuum [24]. The tip-end of the SWCNTs melts first and then is followed by the wall of the SWCNT. The electron beam irradiation lowers at least the melting point by some 500 K due mainly to the impulse of the energetic electrons, according to Egerton [25]. Annealing at 1,670–1,770 K under medium–high vacuum, or in flowing Ar and N₂ atmospheres, 60 % SWCNTs coalesce with their neighbors [26]. Heating under an Ar flow in the temperature range of 1,873–2,273 K results in a progressive destruction of the SWCNT bundle, and this is followed by the coalescence of the entire CNT bundle [27]. Coalescence starts at the edge of CNT bundles [28]. SWCNTs transform at 2,473 K or higher to MWCNTs with external diameter of several nanometers. Fe–C impurity bonds can be completely removed from the CNTs at 2,523 K [29]. MWCNTs are more thermally stable than the SWCNTs, and the stability of the MWCNTs increases with the number of walls (λ) [9, 30, 31], opposing to the change trend of modulus. On the other hand, an ordinary camera flash [32] could burn the SWCNT at the ambient conditions, showing the higher chemical reactivity for oxidation of the SWCNT.

Lee et al. [33] measured the elastic properties and intrinsic breaking strength of a freestanding monolayer graphene ribbon (GNR) by nanoindentation in an AFM. They found that the force–displacement behavior is nonlinearly elastic and yields second- and third-order elastic stiffness of 340 Nm⁻¹ (Nm⁻¹ = TPa·nm) and -690 Nm⁻¹, respectively. The breaking strength is 42 Nm⁻¹ and represents the intrinsic strength of a defect-free GNR sheet. These quantities correspond to a $Y = 1.0$ TPa, a third-order elastic stiffness of $D = -2.0$ TPa, compared with the intrinsic strength of $\sigma_{\text{int}} = 130$ GPa for bulk graphite. These experiments established graphene as the strongest material ever measured and showed that atomically perfect nanoscale materials can be mechanically tested to deformations well beyond the linear regime [34].

With an aberration-corrected TEM being capable of simultaneously atomic spatial resolution and one-second temporal resolution, Girit et al. [35] observed in situ the dynamics of carbon atoms at the edge of a hole in a suspended, single atomic layer of graphene. The rearrangement of bonds and beam-induced ejection of carbon atoms is recorded as the hole grows. They demonstrated the edge reconstruction and the stability of the ‘zigzag’ edge configuration, revealing the complex behavior of atoms preferentially occurring at the edge boundary. Most strikingly, they discovered that breaking a C–C bond of 3-coordinated carbon atom in the graphene requires a minimal energy of 5.67 eV per bond and breaking a C–C bond of a 2-coordinated carbon atom near atomic vacancy needs 7.50 eV per bond. The ratio $E_2/E_3 = 7.50/5.67 = 1.32$ approaches the BOLS prediction, $E_2/E_3 = (C_2/C_3)^{-2.56} = 1.49$.

These observations evidence consistently the lowered chemical and thermal stability albeit the higher mechanical strength of the CNTs and the graphene at the ambient temperature.

26.2 BOLS Formulation

The striking difference between the bulk diamond and a SWCNT/graphene is that the effective atomic CN of a C atom reduces from a bulk value of 12 to 3 and the sp orbit hybridization transits from the sp^3 to the sp^2 type upon SWCNT formation. For an atom near to the defect vacancy or at the open edge of a CNT or a GNR, the CN is 2. One of the sp^2 σ -bonds becomes dangling with the generation of an unpaired electron in addition to the unpaired π -bond electrons. The difference between CNT and GNR is the number of the 2-coordinated edge atoms.

With the specified atomic CN for diamond, graphite, and the CNT and graphene edges, one can readily determine the bond length (d_z), the bond energy (E_z), and the cohesive energy ($E_{\text{coh}} = zE_z$) of a single atom as well as the binding energy density ($E_d = n_z E_z$) in a specific atomic site. The value n_i is the bond number per unit volume. Since the cohesive energy defines the thermal stability [36], and the energy density determines the mechanical strength [37], the functional dependence of $Y(z)$ and $T_m(z)$ on the atomic CN and the bond energy at the equilibrium is given as

$$\begin{cases} Y(z) \propto n_z E_z = d_z^{-2} E_z \\ T_m(z) \propto E_{\text{coh}}(z) = z E_z \end{cases} \quad (26.1)$$

For a SWCNT or a monolayer GNR, $n_z \propto d_z^{-2}$ is the bond number per unit area, which is independent of the wall thickness. Obviously, no other argument could change the Y value except the bond length and bond energy. Heating to the melting point will lengthen and weaken the bonds between the undercoordinated atoms; the undercoordinated atoms will coalesce with their neighbors.

26.3 Verification

26.3.1 CN-Resolved C–C Bond Length

Table 26.1 compares the BOLS-predicted bond strain in comparison with the evaluated values for C allotropes [21]. On the other hand, the C–C bond was suggested to contract varying from 11.2 to 39.8 % in the first interlayer spacing of diamond, according to MD computations [38]. The mechanical transverse deformation of single-layer and bilayer graphene under central loading using a mixed atomistic continuum—finite element technique—suggested that the C–C bond length is within the range of 0.111–0.116 nm for the bilayer [39] and 0.10 nm

Table 26.1 Comparison of BOLS predicted with the measured and the DFT-calculated CN dependence of C–C bond train

| | | | | |
|--------------|--------------|-----------------------|-----------------------|--------------|
| Atomic CN | 2 | 3 | 4 | 5.335 |
| BOLS [42] | −0.3027 [21] | −0.1853 [21] | −0.1243 | −0.0779 [43] |
| Experimental | | −(0.091 − 0.058) [44] | −(0.112 − 0.398) [38] | |
| DFT [41] | −0.1649 | −0.1104 | −0.0926 | −0.0758 |

$z = 2, 3, 4,$ and 5.335 correspond to the atomic CN of graphene/CNT edge, graphene interior, diamond surface, and bulk graphite, respectively. The BOLS prediction has been confirmed by decoding the thermal stability and elasticity of SWCNT [21] and the C 1 s core-level shift of carbon allotropes [42]

for the single-layer graphene [40], agreeing with the BOLS expectation. The DFT-optimized C–C bond lengths [41] follow the BOLS-predicted trend, but the extent deviates at smaller CN values. The effect of the deviation is enormous as all the quantities discussed herewith depend on the extent of bond contraction.

26.3.2 C–C Bond Energy and Elasticity

Correlation between the measured stiffness $(Yt)_{z=3}$ (0.368 TPa·nm) and the melting point $T_m(z = 2)$ (1,593 K) for a SWCNT with the corresponding values for bulk diamond ($T_m(12) = 3,800$ K, $Y(12) = 1.02$ TPa) satisfies the relations [21]:

$$\left\{ \begin{array}{l} \frac{T_m(2)}{T_m(12)} = \frac{1,593}{3,800} = \frac{2}{12} c(2)^{-m} = \frac{0.6973^{-m}}{6} \quad (\text{tip} - \text{bulk}) \\ \frac{T_m(2)}{T_m(3)} = \frac{1,593}{T_m(3)} = \frac{2}{3} \left(\frac{c(2)}{c(3)} \right)^{-m} = \frac{2 \times 0.8559^{-m}}{3} \quad (\text{wall} - \text{tip}) \\ \frac{(Y \cdot t)_{z=3}}{Y(12)t_{z=3}} = \frac{0.368}{1.02t_{z=3}} = c(3)^{-(2+m)} = 0.8147^{-(2+m)} \quad (\text{CNT} - \text{wall}) \end{array} \right. \quad (26.2)$$

This set of equations resolves the quantities of $m = 2.5585 \cong 2.56$, $t_{z=3} = 0.142$ nm, and the tube wall melting point, $T_m(3) = 1,605$ K, as listed in Table 26.2. It is seen that the bond energy enhancement for the 2- and 3-coordinated carbons is 2.52 and 1.69 times ($2.52/1.69 = 1.49$) the bulk values, respectively, being comparable to the experimental value [35] of $7.5/5.67 = 1.32$ with a 10 % tolerance.

Furthermore, the activation energy for chemical reaction is also proportional to the atomic cohesive energy. Therefore, the chemical stability of the undercoordinated atoms is lower than that of the atoms in the bulk, which may explain why the CNT could burn using an ordinary camera flash under the ambient conditions. Conclusion on the CN dependence of C–C bonding identities applies to GNR as well as the curvature effect is weak. Comparing the derivative from the SWCNT to the measured modulus of 1.0 TPa under the assumption of 0.335 nm thick of the monolayer graphene [33], the elastic modulus of the graphene is $1.0 \times 0.335/0.142 = 2.36$ TPa, which is substantially the same to that of the SWCNT (2.56 TPa) [45].

Table 26.2 With the measured $(Yt)_{z=3} = 0.368$ TPa-nm and $T_m(2) = 1,593$ K data as input, Eq. (26.2) yields the unique solutions to the C–C bond length, thickness, energy, m value, elastic modulus, and the wall interior melting point, which in turn verifies that the input data represent true values

| | |
|--|---------------------|
| $(Yt)_{z=3}$ | 0.368 TPa-nm |
| Tip-end $T_m(2)$ | 1,593 K |
| m | 2.5585 |
| Tube wall $T_m(3)$ | 1,605 K |
| Elastic modulus Y | 2.595 TPa |
| CNT effective thickness $t(3)$ | 0.142 nm |
| Bond length $d(2)$ ($c(2) = 0.6973$) | 0.107 nm |
| Bond length $d(3)$ ($c(3) = 0.8147$) | 0.126 nm |
| Bond energy enhancement, $E(2)/E(12)$ | 2.52 |
| Bond energy enhancement, $E(3)/E(12)$ | 1.69 |

The accuracy of the numerical solutions is subject to the initial input of the measured $T_m(2)$ and $(Yt)_{z=3}$ values. Errors in measurement or due to structural defects of the CNT may affect the accuracy of the solutions, but they never alter the nature of the observations. However, in the current iteration, any variation in the input parameters leads to solutions that are physically forbidden [21]. Therefore, the solution is unique.

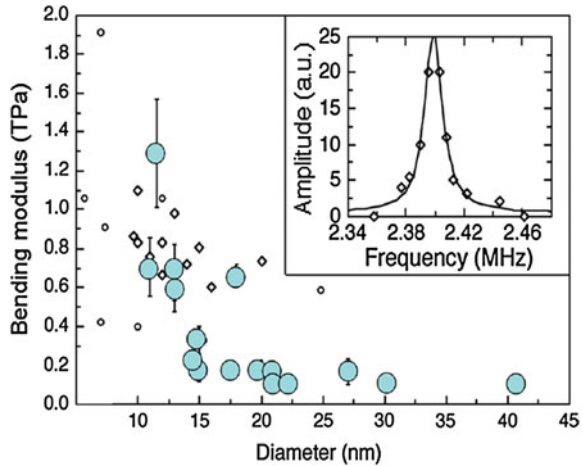
26.3.3 Elasticity: Wall Thickness Dependence

For the hollow or solid nanobeams (nanorods and MWCNTs), the relative change in a measurable quantity (denoted as Q), which is dependent on shape and size, of a nanosystem with dimension K can be quantized with the core–shell configuration as [21]:

$$\left\{ \begin{array}{l} \frac{\Delta Q(K)}{Q(\infty)} = \sum_{i \leq 3} \gamma_i \frac{\Delta q_i(d_i, z_i, E_i)}{q(d, z_b, E_b)} \\ \gamma_i = \frac{\int_{K-i}^K x dx + \int_{K-\lambda}^{K-\lambda+i} x dx}{\int_{K-\lambda}^K x dx} = \frac{i\{(2K-i) + [2(K-\lambda) + i]\}}{\lambda(2K-\lambda)} = \frac{2(2K-\lambda)i}{\lambda(2K-\lambda)} \propto \frac{1}{\lambda} \end{array} \right. \quad (26.3)$$

where q_i being the density of quantity Q on an atomic scale is functionally dependent on the bond length d_i , the effective z_i , and the bond energy E_i . The difference in Δq_i between the surface region and the bulk originates the change in the value Q ; the surface-to-volume ratio, γ_i , of a nanosolid dominates the trends of Q change. The index value i counts from the vacuum sides inward up to a value of 3. Therefore, it is not surprising that, for a solid rod or a MWCNT with K and λ , the overall $\Delta Q(K)/Q(\infty)$ varies with the inverse radius ($1/K$) and the $\Delta Q(K)/Q(\infty)$

Fig. 26.1 Diameter (*wall thickness*) dependence of the elastic modulus of MWCNT. Data in *solid circles* are sourced from [46]; diamonds from [47]; and *open circles* from [12, 17]. The drop at 8 nm in bending modulus corresponds to the wrinkling effect of the wall of the nanotube during bending [46]. Inset shows no remarkable change in the Lorentzian line shape of the resonance for tubes in measurement



value differs from the corresponding bulk value ($\Delta Q(K)/Q(\infty) = 0$). For a hollow MWCNT of λ thickness, the $\Delta Q(K)/Q(\infty)$ varies with the wall thickness instead of the diameter of the MWCNT.

These predictions agree with the observed trends in the Y enhancement (see Fig. 26.1) and the T_m suppression of the nanobeams. The direct evidence for the λ dependence is that the Y value was calculated to vary over a range of 4.7–1.04 TPa when the wall number λ increases from unity to infinity. AFM measurements [12] of the K dependence of the Young's modulus of SiC nanorods and MWCNTs revealed that the MWCNTs are about twice as stiff as the SiC nanorods and that the strengths of the SiC nanorods are substantially greater than those found for large SiC structures (600 GPa). The Young's modulus is 610 and 660 GPa for SiC rods of 23.0 and 21.5 nm, respectively. For MWCNTs, the modulus is 1.28 ± 0.59 TPa without apparent dependence on the diameter of the nanotubes. The broad range of measured values should be more attributable to the scattered number of walls of the nanotubes than to the error in measurement.

26.3.4 Superplasticity of CNT

The theoretical maximum tensile strain, or elongation, of a SWCNT is almost 20 % [48, 49], but in practice, only 6 % [50] has been achieved at room temperatures. However, at high temperatures (estimated at 2,000 K might be too high with respect to Ref. [24]), individual SWCNTs can undergo a superplastic deformation, becoming nearly 280 % longer and 15 times thinner, from 12 to 0.8 nm, before tensile failure [51].

The temperature in the middle of the SWCNT is more than 2,270 K as estimated during deformation at a bias of 2.3 V with a current flow. Despite the

apparent discrepancy of this estimation compared with the STM measurements showing that the tube body melts at 1,605 K, the nanotube appears to be completely ductile near the melting point, according to the findings for Au-MC [140 % elongation near the $T_m(2)$]. Compared to the Au-MC, kinks and point defects in the CNT are involved and fully activated, resulting in the possible superplastic deformation of CNT at the elevated temperatures. The kink motion evidences the kink-mediated plasticity at high temperatures. The processes of kink nucleation and motion and atom diffusion are important during superplastic deformation, which help to heal defects such as vacancies and to prevent the formation of large dislocation loops that might initiate cracks and lead to failure of the strained nanotubes.

Such large plastic strains in nanotubes demonstrate their ductile nature at high temperatures [52–54], which concurs with BOLS predictions that the strain limit is exponentially proportional to the inverse of separation between the melting point and the temperature of operation. In contrast, tensile-pulling experiments at room temperature without any bias showed that almost all nanotubes failed at a tensile strain of less than 15 %. Superplasticity of MWCNT could be possible in vacuum at elevated temperatures as the T_m for the MWCNT is higher than that for the SWCNT.

26.4 Nanowires

26.4.1 Elasticity and Strength

Figure 26.2 shows the Young's modulus enhancement of TiO₂ nanorods [55], Ag, Pd, [56], and ZnO nanobelts [57] and nanowires [58]. The Young's modulus of Ag nanowires [59] of 20–100 nm diameter increases when the diameter is decreased, which corresponded to the effects of surface stress, oxidation surface layers, and surface roughness. ZnS nanobelts are 79 % harder but 52 % lower in elastic modulus compared to the bulk ZnS [60]. The ZnS nanobelts also exhibit significant creep under a constant indentation load at room temperature.

However, an opposite trend has been measured using AFM bending methods in the (0001)-oriented ZnO nanobelts/wires and showed a lower modulus than that of bulk ZnO (measured at 140 GPa) varying from 29 ± 8 [61] to 100 GPa, [62] [63]. The modulus of Cr [64] and Si [65] nanocantilevers also decreases sharply with decreasing diameter. In contrast, amorphous Si nanowires [66] and Au [67] and Ag [68] nanowires show no apparent change with size. Therefore, it appears quite confusing that, even for the same materials such as Ni, Ag, ZnO, and Si, the Y value changes in different ways, depending on the experimental techniques and operation conditions.

This is similar to the variation in the skin hardening and softening as discussed in Sect. 24.3. For instance, the Y value of ZnO nanobelts of 50–140 nm thick and

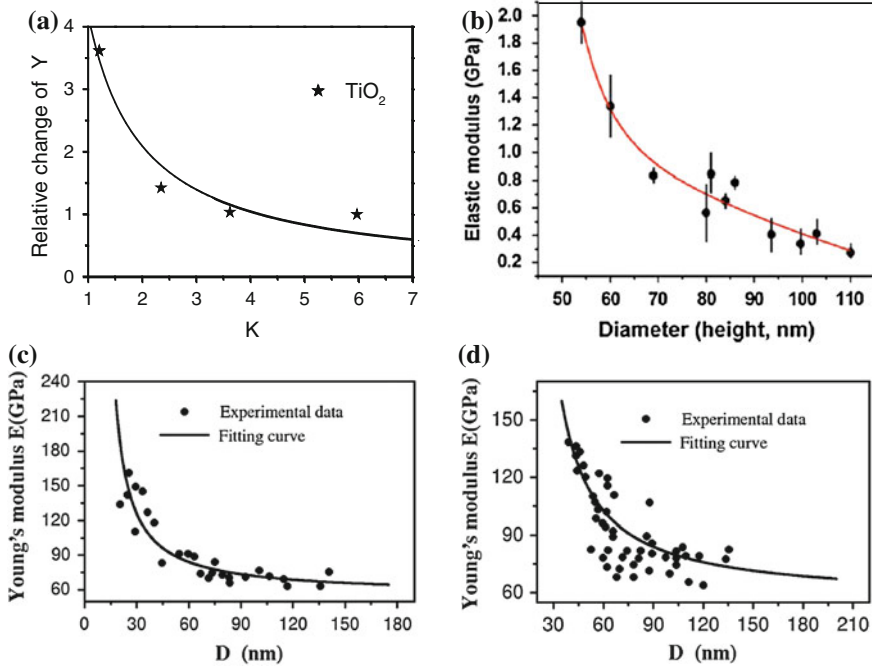


Fig. 26.2 Size (scattered data) dependence of the elastic modulus of **a** TiO₂ nanowires [55], **b** poly (2-acrylamido-2-methyl-1-propanesulfonic acid) polymer nanowires [71], and **c** Ag [75] and **d** Pb [76] nanowires

270–700 nm wide was measured using an AFM three-point bending method to be 38.2 ± 1.8 GPa, which is about 20 % higher than the Young's modulus of 31.1 ± 1.3 GPa obtained using nanoindentation [69]. A modeling study of the size effect on the elastic behavior of solid and hollow polymer nanofibers under uniaxial tension [70] shows that fiber radius has appreciable effect on the elastic response of polymer nanofibers. At nanometer scale, solid nanofibers show less the effect of surface tension coupling. However, hollow nanofibers show greater axial stiffening effect with increasing axial stretch because of the coupling of surface tension depending on the combination of the fiber exterior and interior radii and the material properties.

The elastic modulus of single polymer nanofibers increases exponentially as the diameter of the polymer nanofibers decreases to a few tens of nanometers (Fig. 26.2b) [71] being opposite to the measured trend of polymers using the indentation method. The unusual behavior of nanobeams corresponded to the microstructure and confinement [68].

The defect-free nanotubes are ideal cases of cylindrical nanocavities with defect-free shells that are much stronger than the bulk materials unless excessive defects are presented in the unreconstructed walls [12]. Defects in the walls of nanotubes serve as centers initiating the failure in particular for the plastic

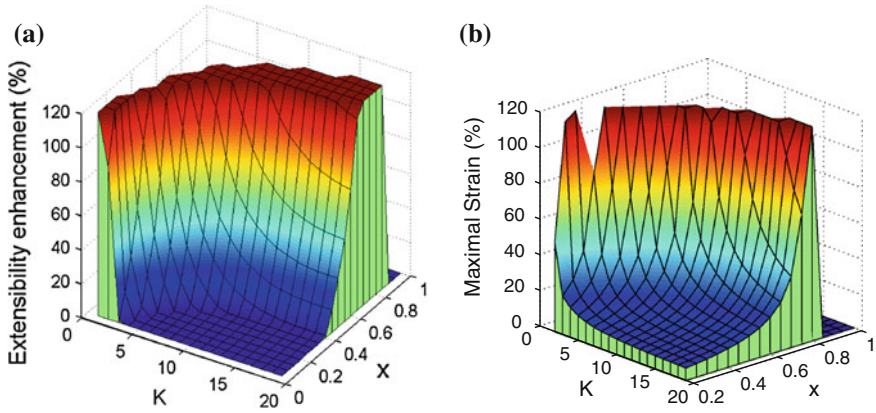


Fig. 26.3 Illustrative counterplots for the K - and $x (= T/T_m)$ -dependent **a** extensibility, and **b** maximum strain of defect-free Au-NWs. The extensibility and the maximum strain increase rapidly when T approaches to $T_m(K)$ which, in turn, drops with K (reprinted with permission from [90])

deformation. For instances, the Young's modulus of a defected nanotube is reduced gradually with each atomic defect and the strength of the nanotubes is catastrophically influenced by the existence of just a few atomic defects [72]. A theoretical calculation [73] of the tensile strength of nanotube mats and fibers predicted that the stiffness and strength of the mats could be increased at least by an order of magnitude through small dose irradiation with energetic particles to break some bonds and generate some new kinds of bonds between the interfaces of the nanotubes [74].

26.4.2 Nanowire Superplasticity: Bond Unfolding

One may extend the extensibility of MC and CNT to the case of nanowires by replacing the $T_{m,i}$ and the η_{2i}/η_{1i} for an MC in Eqs. (25.3) and (25.7) with the size-dependent $T_m(K)$ and $\eta_2(K)/\eta_1(K)$, which turns out [77]:

$$\frac{\Delta\beta_i(z_i, K, T)}{\beta_0(z_b, 0)} = \frac{\eta_{1b}C(K)T_m}{\eta_1(K)[T_m(K) - T]} - 1 \quad (26.4)$$

$$\frac{\Delta d_M(K, T, P)}{d(K, T, 0)} \cong B \exp\left\{\frac{\eta_2(K)}{2\eta_1(K)[T_m(K) - T]}\right\}.$$

The counterplots in Fig. 26.3 illustrate the size- and T/T_m -dependent extensibility and the maximum strain of impurity-free Au-NWs with the parameters determined for the Au-MC. The ratio $\eta_1(K)/\eta_1 = 1 + 10/(1 + \exp((K - 1.5)/20))$ is assumed to change from $\eta_{1i}/\eta_1 = z_{bi} = 6$ to 1 (at $K = \infty$) gradually. The mean

bond contraction coefficient $C(K)$ drops from 1 to 0.7 and the $T_m(K)/T_m(\infty)$ drops from 1 to 0.239 when a NW of infinite size shrinks into an MC. Equation (26.4) indicates that the extensibility enhancement happens ($\Delta\beta_i > 0$) when $[T_m(K) - T] < \eta_1 C(K) T_m / \eta_1(K)$; otherwise, the extensibility is lower than the bulk value. When T approaches $T_m(K)$, the extensibility increases exponentially up to infinity.

Measurements have shown that the detectable maximum strain of a suspended impurity-free Au-MC bond is less than 140 % $((0.48 - 0.20)/0.20)$ compared with the equilibrium Au-Au bond length in the MC, which is much lower than the detected strain (10^3) of nanograin Cu and Al NWs forming at room temperature or at the subambient temperatures [78–80]. Therefore, bond stretching discussed herewith is not the factor dominating the high extensibility of a NW. The factors dominating the NWs extensibility could be the bond unfolding, atomic gliding dislocations, and creep and grain boundary movement [78–81]. However, the present understanding further confirms that the barrier or the activation energy for atomic dislocation and diffusion of the undercoordinated atoms at the grain boundaries is lower than that of the fully coordinated ones in the ideal bulk, as these activities are subject to the atomic cohesion, which, in turn, drops with atomic CN.

Han et al. [82] observed in situ by a high-resolution TEM the unusually large strain plasticity (125 % strain with 450 % diameter reduction) of Si (15–70 nm in diameter) and SiC (~ 80 nm in diameter) [83] nanowires (NWs) at room temperature. They found that the dislocation activation energy drops with the diameter of the NWs. The continuous plasticity of the SiC-NWs is accompanied by a process of increasing dislocation density at an early stage, followed by an obvious lattice distortion, and finally reaches an entire structure amorphization at the most strained region of the NW. An AFM measurement [84] of the length of gold nanowire structures during extension and compression cycles revealed that nanowires elongate under force in quantized steps of up to three integer multiples of 1.76 Å and that they shorten spontaneously in steps of 1.52 Å under slight compression.

MD calculations [85] revealed that the mechanical strengths of the Au nanowires decrease with the increasing temperature. However, defects improved the mechanical strength under a wide range of temperature. Comparing to the single-crystal nanowire, the existence of the atomic defects extends the elastic deformation showing a larger yield strain. The breaking behavior of the nanowire is sensitive to the atomic defects when the defect ratio is 5 % at 100 K, whereas the ratio is 1 % when temperatures are 300 and 500 K. Measurements using the bending, buckling, and stretching methods confirmed that the presence of fewer mechanical defects per unit length offers high strength to Au-NWs [86].

These findings indicate that the sliding of crystal planes within the gold nanowires creates stacking faults that change the local structure from face-centered cubic to hexagonal close packed. These experiments provide direct evidence for the unfolding mechanism underlying the plastic deformation of a nanowire. In the process of bond unfolding, phase transition, the specimen also releases energy that raises the effective temperature of operation [87–89].

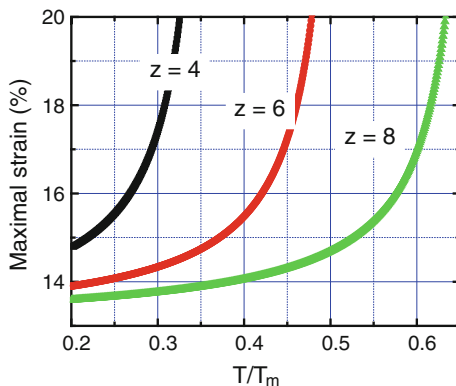


Fig. 26.4 Temperature and CN (z) dependence of the Au–Au bond maximum strain show the order of melting at a curved surface of a nanowire and infers the breaking mode of a nanowire at different temperature ranges. At higher T , core bond breaks first because of with ductile manner because of the lower extensibility; at lower T , skin bond break first with fragile manner because of the shorter skin bond (reprinted with permission from [103])

26.4.3 Breaking Modes of Nanowires

Figure 26.4 showing the atomic CN and temperature dependence of maximum bond strain indicates that the melting of a nanosolid starts from the first atomic shell ($z_1 = 4$) and then the second ($z_2 = 6$) when the temperature is elevated, as observed in many cases. For instances, it has been confirmed that a flat or a curved surface melts at temperatures of 50 K [91] to 100 K [92] lower than the bulk interior. A quasi-molten skin grows radially inward from the surface into the core center for both clusters and wires. The surface melting is followed by a breakdown of order in the remaining solid core. The melting of an impurity-free vanadium nanosolid proceeds in a stepwise way, i.e., the surface layer of 2–3 lattice-constant thick region melts first and then the abrupt overall melting of the entire cluster follows [92].

An MD computation [93] of the shell-resolved fluctuation of the root mean square bond length of a 147-atom Leonard-Jones cluster revealed that the process of surface melting starts from the migrating of the vertex atoms on the surface. Although the melting process of LJ147 cluster could be divided into stages of surface melting and general melting, the melting still exhibits a continuous process from the surface shell to the core interior. Therefore, a tiny cluster could not manifest the layer-by-layer feature of surface melting. This surface pre-melting was in the ‘liquid skin nucleation and growth’ mode [94–96] and follows the ‘liquid drop’ [97] and the ‘surface phonon instability’ [98] and the current BOLS models [36], as well as other outstanding models [99].

At temperatures close to the $T_{m,1}$ of the surface, the maximum strain and the extensibility of the surface layer approach infinity, whereas the strain limit of the

core interior remains at the limited bulk values because of the higher bulk melting point. At temperatures near surface melting or above, bond breaking under tension should start from the NW interior, because the inner bonds firstly reach their strain limits that are lower than that of the surface skin bonds at the same temperature. However, at temperatures far below $T_{m,1}$, bond breaking may start from the outermost atomic shell and the nanosolid manifests brittle character, as the shortened surface bonds break first. At very low temperatures, the theoretically allowed maximum strains for the entire NW should be constant.

If one deforms the entire nanowire by an amount t of xd , the strain of the bonds in the respective shells will be $\varepsilon_i = x/C_i$. Because $C_1 < C_2 < C_3$, the actual applied strains are in this order, $\varepsilon_3 < \varepsilon_2 < \varepsilon_1$, which indicates that the skin bond breaks first at low T . Therefore, the breaking mode of a nanowire at low T is expected to be opposite to that at higher T . At very low T , the surface bond breaks before the bulk ones, while at $T \sim T_{m1}$ or higher, the skin bond breaks after the ones in the core interior.

It has been measured using a ‘nanostretching stage’ located within a STM at room temperature that the MWCNTs break in the outermost shell [100]. This ‘sword-in-sheath’ failure mode, or inner bonds break first, agrees with the expectation of the current BOLS approach as the operating temperature is far below the tube melting temperature at 1,600 K [21]. The helical multi-shell gold nanowires [101] become thinner and thinner without breaking the outer shell atomic bond under tension at room temperature, as the Au-NW breaking starts from the inner shell according to the current understanding. Tight-binding calculations [102] suggest that 90 % atoms composing the linear atomic chains come from outermost atomic layers of gold specimen in the stretching at ~ 350 K, indicating the relatively high mobility of the undercoordinated atoms.

26.5 Summary

With the known $(Yt)_{z=3}$ value and the known temperature of tip-end melting for a SWCNT, the T-BOLS function enables the quantification of the bonding identities, the dimension, and energy of a single C–C bond in SWCNT. The C–C bond of the SWCNT contracts by ~ 18.5 % with an energy rise by ~ 68 %. The effectively static thickness of the C–C bond is ~ 0.142 nm, which is the diameter of a C atom, rather than the graphite sheet separation (0.34 nm) or the diameter of a free carbon atom (0.132 nm). The melting point of the tube wall is slightly (~ 12 K) higher than that of the tube end. The unique solution clarifies that the quoted $T_m(2)$ and the Yt values are truly correct for a SWCNT in which the Young’s modulus is 2.5 times and the melting point is 0.42 times that of bulk graphite.

Predictions of the wall thickness dependence of the T_m suppression and Y enhancement of the nanobeams agree well with the insofar-observed trends documented. Bond unfolding, atomic gliding dislocations, and creep and kink formation dominate the superplasticity of nanograined crystals or the SWCNTs in

quasi-molten states because the detectable maximal strains of an ideal bond are limited to 140 % at melting. Understandings extend to atomic sheets and nanowires with consideration of the core-shell configurations.

References

1. A.B. Dalton, S. Collins, E. Munoz, J.M. Razal, V.H. Ebron, J.P. Ferraris, J.N. Coleman, B.G. Kim, R.H. Baughman, Super-tough carbon-nanotube fibres—these extraordinary composite fibres can be woven into electronic textiles. *Nature* **423**(6941), 703 (2003)
2. G. Ma, Y. Ren, J. Guo, T. Xiao, F. Li, H.M. Cheng, Z.R. Zhou, K. Liao, How long can single-walled carbon nanotube ropes last under static or dynamic fatigue? *Appl. Phys. Lett.* **92**(8), 083105 (2008)
3. P.M. Agrawal, B.S. Sudalayandi, L.M. Raff, R. Komanduri, A comparison of different methods of Young's modulus determination for single-wall carbon nanotubes (SWCNT) using molecular dynamics (MD) simulations. *Comput. Mater. Sci.* **38**(2), 271–281 (2006)
4. K. Asaka, T. Kizuka, Atomistic dynamics of deformation, fracture, and joining of individual single-walled carbon nanotubes. *Phys. Rev. B* **72**(11), 115431 (2005)
5. M. Nakajima, F. Arai, T. Fukuda, In situ measurement of Young's modulus of carbon nanotubes inside a TEM through a hybrid nanorobotic manipulation system. *IEEE Trans. Nanotechnol.* **5**(3), 243–248 (2006)
6. A. Krishnan, E. Dujardin, T.W. Ebbesen, P.N. Yianilos, M.M.J. Treacy, Young's modulus of single-walled nanotubes. *Phys. Rev. B* **58**(20), 14013–14019 (1998)
7. K. Enomoto, S. Kitakata, T. Yasuhara, N. Ohtake, T. Kuzumaki, Y. Mitsuda, Measurement of Young's modulus of carbon nanotubes by nanoprobe manipulation in a transmission electron microscope. *Appl. Phys. Lett.* **88**(15), 153115 (2006)
8. F. Scarpa, S. Adhikari, A mechanical equivalence for Poisson's ratio and thickness of C–C bonds in single wall carbon nanotubes. *J. Phys. D-Appl. Phys.* **41**(8), 085306 (2008)
9. E. Hernandez, C. Goze, P. Bernier, A. Rubio, Elastic properties of C and BxCyNz composite nanotubes. *Phys. Rev. Lett.* **80**(20), 4502–4505 (1998)
10. B.I. Yakobson, C.J. Brabec, J. Bernholc, Nanomechanics of carbon tubes: instabilities beyond linear response. *Phys. Rev. Lett.* **76**(14), 2511–2514 (1996)
11. T. Vodenitcharova, L.C. Zhang, Effective wall thickness of a single-walled carbon nanotube. *Phys. Rev. B* **68**(16), 165401 (2003)
12. E.W. Wong, P.E. Sheehan, C.M. Lieber, Nanobeam mechanics: elasticity, strength, and toughness of nanorods and nanotubes. *Science* **277**(5334), 1971–1975 (1997)
13. M.R. Falvo, G.J. Clary, R.M. Taylor, V. Chi, F.P. Brooks, S. Washburn, R. Superfine, Bending and buckling of carbon nanotubes under large strain. *Nature* **389**(6651), 582–584 (1997)
14. E.T. Thostenson, Z.F. Ren, T.W. Chou, Advances in the science and technology of carbon nanotubes and their composites: a review. *Compos. Sci. Technol.* **61**(13), 1899–1912 (2001)
15. J.P. Salvetat, G.A.D. Briggs, J.M. Bonard, R.R. Bacsca, A.J. Kulik, T. Stockli, N.A. Burnham, L. Forro, Elastic and shear moduli of single-walled carbon nanotube ropes. *Phys. Rev. Lett.* **82**(5), 944–947 (1999)
16. J.P. Lu, Elastic properties of carbon nanotubes and nanoropes. *Phys. Rev. Lett.* **79**(7), 1297–1300 (1997)
17. M.M.J. Treacy, T.W. Ebbesen, J.M. Gibson, Exceptionally high Young's modulus observed for individual carbon nanotubes. *Nature* **381**(6584), 678–680 (1996)
18. G. Zhang, B.W. Li, Wall "thickness" effects on Raman spectrum shift, thermal conductivity, and Young's modulus of single-walled nanotubes. *J. Phys. Chem. B* **109**(50), 23823–23826 (2005)

19. M.A. Omar, *Elementary Solid State Physics: Principles and Applications* (Addison-Wesley, New York, 1993)
20. X. Zhou, J.J. Zhou, Z.C. Ou-Yang, Strain energy and Young's modulus of single-wall carbon nanotubes calculated from electronic energy-band theory. *Phys. Rev. B* **62**(20), 13692–13696 (2000)
21. S. Li, T.H. Yip, C.Q. Sun, S. Widjaja, M.H. Liang, *Origin of self-aligned nano-domains in MgB₂*. in *3rd Asian Meeting on Electroceramics (AMEC-3)*. Singapore, (2003)
22. Z.C. Tu, Z. Ou-Yang, Single-walled and multiwalled carbon nanotubes viewed as elastic tubes with the effective Young's moduli dependent on layer number. *Phys. Rev. B* **65**(23), 233407 (2002)
23. M. Terrones, H. Terrones, F. Banhart, J.C. Charlier, P.M. Ajayan, Coalescence of single-walled carbon nanotubes. *Science* **288**(5469), 1226–1229 (2000)
24. B. An, S. Fukuyama, K. Yokogawa, M. Yoshimura, Surface superstructure of carbon nanotubes on highly oriented pyrolytic graphite annealed at elevated temperatures. *Jpn. J. Appl. Phys. Part 1-Regul. Pap. Short Notes Rev. Pap.* **37**(6B), 3809–3811 (1998)
25. R.F. Egerton, P. Li, M. Malac, Radiation damage in the TEM and SEM. *Micron* **35**(6), 399–409 (2004)
26. P. Nikolaev, A. Thess, A.G. Rinzler, D.T. Colbert, R.E. Smalley, Diameter doubling of single-wall nanotubes. *Chem. Phys. Lett.* **266**(5–6), 422–426 (1997)
27. K. Metenier, S. Bonnamy, F. Beguin, C. Journet, P. Bernier, M.L. de La Chapelle, O. Chauvet, S. Lefrant, Coalescence of single-walled carbon nanotubes and formation of multiwalled carbon nanotubes under high-temperature treatments. *Carbon* **40**(10), 1765–1773 (2002)
28. J. Sloan, A.I. Kirkland, J.L. Hutchison, M.L.H. Green, Structural characterization of atomically regulated nanocrystals formed within single-walled carbon nanotubes using electron microscopy. *Acc. Chem. Res.* **35**(12), 1054–1062 (2002)
29. R. Andrews, D. Jacques, D. Qian, E.C. Dickey, Purification and structural annealing of multiwalled carbon nanotubes at graphitization temperatures. *Carbon* **39**(11), 1681–1687 (2001)
30. S. Bandow, S. Asaka, Y. Saito, A.M. Rao, L. Grigorian, E. Richter, P.C. Eklund, Effect of the growth temperature on the diameter distribution and chirality of single-wall carbon nanotubes. *Phys. Rev. Lett.* **80**(17), 3779–3782 (1998)
31. D. Bom, R. Andrews, D. Jacques, J. Anthony, B.L. Chen, M.S. Meier, J.P. Selegue, Thermogravimetric analysis of the oxidation of multiwalled carbon nanotubes: evidence for the role of defect sites in carbon nanotube chemistry. *Nano Lett.* **2**(6), 615–619 (2002)
32. P.M. Ajayan, M. Terrones, A. de la Guardia, V. Huc, N. Grobert, B.Q. Wei, H. Lezec, G. Ramanath, T.W. Ebbesen, Nanotubes in a flash—ignition and reconstruction. *Science* **296**(5568), 705 (2002)
33. C. Lee, X.D. Wei, J.W. Kysar, J. Hone, Measurement of the elastic properties and intrinsic strength of monolayer graphene. *Science* **321**(5887), 385–388 (2008)
34. E. Cadelano, P.L. Palla, S. Giordano, L. Colombo, Nonlinear elasticity of monolayer graphene. *Phys. Rev. Lett.* **102**(23), 235502 (2009)
35. C.O. Girit, J.C. Meyer, R. Erni, M.D. Rossell, C. Kisielowski, L. Yang, C.H. Park, M.F. Crommie, M.L. Cohen, S.G. Louie, A. Zettl, Graphene at the edge: stability and dynamics. *Science* **323**(5922), 1705–1708 (2009)
36. C.Q. Sun, Y. Wang, B.K. Tay, S. Li, H. Huang, Y.B. Zhang, Correlation between the melting point of a nanosolid and the cohesive energy of a surface atom. *J. Phys. Chem. B* **106**(41), 10701–10705 (2002)
37. C.Q. Sun, B.K. Tay, S.P. Lau, X.W. Sun, X.T. Zeng, S. Li, H.L. Bai, H. Liu, Z.H. Liu, E.Y. Jiang, Bond contraction and lone pair interaction at nitride surfaces. *J. Appl. Phys.* **90**(5), 2615–2617 (2001)
38. T. Halicioglu, Calculation of surface energies for low index planes of diamond. *Surf. Sci.* **259**(1–2), L714–L718 (1991)

39. F. Scarpa, S. Adhikari, R. Chowdhury, The transverse elasticity of bilayer graphene. *Phys. Lett. A* **374**(19–20), 2053–2057 (2010)
40. F. Scarpa, S. Adhikari, A.J. Gil, C. Remillat, The bending of single layer graphene sheets: the lattice versus continuum approach. *Nanotechnology* **21**(12), 125702 (2010)
41. C.Q. Sun, S.Y. Fu, Y.G. Nie, Dominance of broken bonds and unpaired nonbonding pi-electrons in the band gap expansion and edge states generation in graphene nanoribbons. *J Chem Phys C* **112**(48), 18927–18934 (2008)
42. C.Q. Sun, Y. Sun, Y.G. Nie, Y. Wang, J.S. Pan, G. Ouyang, L.K. Pan, Z. Sun, Coordination-resolved C–C bond length and the C 1 s binding energy of carbon allotropes and the effective atomic coordination of the few-layer graphene. *J. Chem. Phys. C* **113**(37), 16464–16467 (2009)
43. P. Bennich, C. Puglia, P.A. Bruhwiler, A. Nilsson, A.J. Maxwell, A. Sandell, N. Martensson, P. Rudolf, Photoemission study of K on graphite. *Phys. Rev. B* **59**(12), 8292–8304 (1999)
44. C.S. Yannoni, P.P. Bernier, D.S. Bethune, G. Meijer, J.R. Salem, NMR determination of the bond lengths in C60. *J. Am. Chem. Soc.* **113**(8), 3190–3192 (1991)
45. W.T. Zheng, C.Q. Sun, Underneath the fascinations of carbon nanotubes and graphene nanoribbons. *Energy & Environ. Sci.* **4**(3), 627–655 (2011)
46. X.D. Han, Z. Zhang, Z.L. Wang, Experimental nanomechanics of one-dimensional nanomaterials by in situ microscopy. *Nano* **2**(5), 249–271 (2007)
47. J.P. Salvetat, A.J. Kulik, J.M. Bonard, G.A.D. Briggs, T. Stockli, K. Metenier, S. Bonnamy, F. Beguin, N.A. Burnham, L. Forro, Elastic modulus of ordered and disordered multiwalled carbon nanotubes. *Adv. Mater.* **11**(2), 161–165 (1999)
48. Q.Z. Zhao, M.B. Nardelli, J. Bernholc, Ultimate strength of carbon nanotubes: a theoretical study. *Phys. Rev. B* **65**(14), 144105 (2002)
49. M.B. Nardelli, B.I. Yakobson, J. Bernholc, Mechanism of strain release in carbon nanotubes. *Phys. Rev. B* **57**(8), R4277–R4280 (1998)
50. D.A. Walters, L.M. Ericson, M.J. Casavant, J. Liu, D.T. Colbert, K.A. Smith, R.E. Smalley, Elastic strain of freely suspended single-wall carbon nanotube ropes. *Appl. Phys. Lett.* **74**(25), 3803–3805 (1999)
51. J.Y. Huang, S. Chen, Z.Q. Wang, K. Kempa, Y.M. Wang, S.H. Jo, G. Chen, M.S. Dresselhaus, Z.F. Ren, Superplastic carbon nanotubes—conditions have been discovered that allow extensive deformation of rigid single-walled nanotubes. *Nature* **439**(7074), 281 (2006)
52. M.B. Nardelli, B.I. Yakobson, J. Bernholc, Brittle and ductile behavior in carbon nanotubes. *Phys. Rev. Lett.* **81**(21), 4656–4659 (1998)
53. D. Orlikowski, M.B. Nardelli, J. Bernholc, C. Roland, Ad-dimers on strained carbon nanotubes: a new route for quantum dot formation? *Phys. Rev. Lett.* **83**(20), 4132–4135 (1999)
54. P. Calvert, Nanotube composites: a recipe for strength. *Nature* **399**(6733), 210–211 (1999)
55. L. Dai, C.H. Sow, C.T. Lim, W.C.D. Cheong, V.B.C. Tan, Numerical investigations into the tensile behavior of TiO₂ nanowires: structural deformation, mechanical properties, and size effects. *Nano Lett.* **9**(2), 576–582 (2009)
56. R.E. Miller, V.B. Shenoy, Size-dependent elastic properties of nanosized structural elements. *Nanotechnology* **11**(3), 139–147 (2000)
57. A.J. Kulkarni, M. Zhou, F.J. Ke, Orientation and size dependence of the elastic properties of zinc oxide nanobelts. *Nanotechnology* **16**(12), 2749–2756 (2005)
58. C.Q. Chen, Y. Shi, Y.S. Zhang, J. Zhu, Y.J. Yan, Size dependence of Young's modulus in ZnO nanowires. *Phys. Rev. Lett.* **96**(7), 075505 (2006)
59. G.Y. Jing, H.L. Duan, X.M. Sun, Z.S. Zhang, J. Xu, Y.D. Li, J.X. Wang, D.P. Yu, Surface effects on elastic properties of silver nanowires: contact atomic-force microscopy. *Phys. Rev. B* **73**(23), 235409 (2006)
60. X.D. Li, X.N. Wang, Q.H. Xiong, P.C. Eklund, Mechanical properties of ZnS nanobelts. *Nano Lett.* **5**(10), 1982–1986 (2005)

61. J.H. Song, X.D. Wang, E. Riedo, Z.L. Wang, Elastic property of vertically aligned nanowires. *Nano Lett.* **5**(10), 1954–1958 (2005)
62. X.D. Bai, P.X. Gao, Z.L. Wang, E.G. Wang, Dual-mode mechanical resonance of individual ZnO nanobelts. *Appl. Phys. Lett.* **82**(26), 4806–4808 (2003)
63. K. Yum, Z.Y. Wang, A.P. Suryavanshi, M.F. Yu, Experimental measurement and model analysis of damping effect in nanoscale mechanical beam resonators in air. *J. Appl. Phys.* **96**(7), 3933–3938 (2004)
64. S.G. Nilsson, X. Borriase, L. Montelius, Size effect on Young's modulus of thin chromium cantilevers. *Appl. Phys. Lett.* **85**(16), 3555–3557 (2004)
65. X.X. Li, T. Ono, Y.L. Wang, M. Esashi, Ultrathin single-crystalline-silicon cantilever resonators: fabrication technology and significant specimen size effect on Young's modulus. *Appl. Phys. Lett.* **83**(15), 3081–3083 (2003)
66. C. Gaire, D.X. Ye, F. Tang, R.C. Picu, G.C. Wang, T.M. Lu, Mechanical testing of isolated amorphous silicon slanted nanorods. *J. Nanosci. Nanotechnol.* **5**(11), 1893–1897 (2005)
67. B. Wu, A. Heidelberg, J.J. Boland, Mechanical properties of ultrahigh-strength gold nanowires. *Nat. Mater.* **4**(7), 525–529 (2005)
68. B. Wu, A. Heidelberg, J.J. Boland, J.E. Sader, X.M. Sun, Y.D. Li, Microstructure-hardened silver nanowires. *Nano Lett.* **6**(3), 468–472 (2006)
69. H. Ni, X.D. Li, Young's modulus of ZnO nanobelts measured using atomic force microscopy and nanoindentation techniques. *Nanotechnology* **17**(14), 3591–3597 (2006)
70. X.F. Wu, Y.A. Dzenis, Size effect in polymer nanofibers under tension. *J. Appl. Phys.* **102**(4), 044306 (2007)
71. M.K. Shin, S.I. Kim, S.J. Kim, S.K. Kim, H. Lee, G.M. Spinks, Size-dependent elastic modulus of single electroactive polymer nanofibers. *Appl. Phys. Lett.* **89**(23), 231929 (2006)
72. M. Sammalkorpi, A. Krasheninnikov, A. Kuronen, K. Nordlund, K. Kaski, Mechanical properties of carbon nanotubes with vacancies and related defects. *Phys. Rev. B* **70**(24), 245416 (2004)
73. J.A. Astrom, A.V. Krasheninnikov, K. Nordlund, Carbon nanotube mats and fibers with irradiation-improved mechanical characteristics: a theoretical model. *Phys. Rev. Lett.* **93**(21), 215503 (2004)
74. A. Kis, G. Csanyi, J.P. Salvetat, T.N. Lee, E. Coureau, A.J. Kulik, W. Benoit, J. Brugger, L. Forro, Reinforcement of single-walled carbon nanotube bundles by intertube bridging. *Nat. Mater.* **3**(3), 153–157 (2004)
75. N.E. Dowling, *Mechanical Behavior of Materials: Engineering Methods for Deformation, Fracture, and Fatigue* (Prentice-Hall, NJ, 1999)
76. M.F. Ashby, D.R.H. Jones, *Engineering Materials*, vol. 1 (Pergamon, Oxford, 1980)
77. J.G. Dash, History of the search for continuous melting. *Rev. Mod. Phys.* **71**(5), 1737–1743 (1999)
78. L. Lu, M.L. Sui, K. Lu, Superplastic extensibility of nanocrystalline copper at room temperature. *Science* **287**(5457), 1463–1466 (2000)
79. Y.M. Wang, E. Ma, M.W. Chen, Enhanced tensile ductility and toughness in nanostructured Cu. *Appl. Phys. Lett.* **80**(13), 2395–2397 (2002)
80. R.Z. Valiev, R.K. Islamgaliev, I.V. Alexandrov, Bulk nanostructured materials from severe plastic deformation. *Prog. Mater. Sci.* **45**(2), 103–189 (2000)
81. Y. Champion, C. Langlois, S. Guerin-Mailly, P. Langlois, J.L. Bonnetien, M.J. Hytch, Near-perfect elastoplasticity in pure nanocrystalline copper. *Science* **300**(5617), 310–311 (2003)
82. X.D. Han, K. Zheng, Y.F. Zhang, X.N. Zhang, Z. Zhang, Z.L. Wang, Low-temperature in situ large-strain plasticity of silicon nanowires. *Adv. Mater.* **19**(16), 2112–2118 (2007)
83. X.D. Han, Y.F. Zhang, K. Zheng, X.N. Zhang, Z. Zhang, Y.J. Hao, X.Y. Guo, J. Yuan, Z.L. Wang, Low-temperature in situ large strain plasticity of ceramic SiC nanowires and its atomic-scale mechanism. *Nano Lett.* **7**(2), 452–457 (2007)

84. P.E. Marszalek, W.J. Greenleaf, H.B. Li, A.F. Oberhauser, J.M. Fernandez, Atomic force microscopy captures quantized plastic deformation in gold nanowires. *Proc. Natl. Acad. Sci. U. S. A.* **97**(12), 6282–6286 (2000)
85. F.Y. Wang, W. Sun, H.B. Wang, J.W. Zhao, M. Kiguchi, C.Q. Sun, Investigation on the effect of atomic defects on the breaking behaviors of gold nanowires. *J. Nanopart. Res.* **14**(9), 1082 (2012)
86. M. Chang, X. Liu, F.-C. Chang, J.R. Deka, Mechanical characterization of a single gold nanowire. *J. Nanosci. Nanotechnol.* **13**(8), 5832–5839 (2013)
87. Y. Yan, H. Yin, Q.P. Sun, Y. Huo, Rate dependence of temperature fields and energy dissipations in non-static pseudoelasticity. *Continuum Mech. Thermodyn.* **24**(4–6), 675–695 (2012)
88. A. Amini, W.Y. Yan, Q.P. Sun, Depth dependency of indentation hardness during solid-state phase transition of shape memory alloys. *Appl. Phys. Lett.* **99**(2), 3603933 (2011)
89. F.Y. Wang, W. Sun, Y.J. Gao, Y.H. Liu, J.W. Zhao, C.Q. Sun, Investigation on the most probable breaking behaviors of copper nanowires with the dependence of temperature. *Comput. Mater. Sci.* **67**, 182–187 (2013)
90. C.Q. Sun, Thermo-mechanical behavior of low-dimensional systems: the local bond average approach. *Prog. Mater. Sci.* **54**(2), 179–307 (2009)
91. S.C. Santucci, A. Goldoni, R. Larciprete, S. Lizzit, M. Bertolo, A. Baraldi, C. Masciovecchio, Calorimetry at surfaces using high-resolution core-level photoemission. *Phys. Rev. Lett.* **93**(10), 106105 (2004)
92. W.Y. Hu, S.G. Xiao, J.Y. Yang, Z. Zhang, Melting evolution and diffusion behavior of vanadium nanoparticles. *Eur. Phys. J. B* **45**(4), 547–554 (2005)
93. H.H. Liu, E.Y. Jiang, H.L. Bai, P. Wu, Z.Q. Li, C.Q. Sun, Shell-resolved melting kinetics of icosahedral cluster. *J. Nanosci. Nanotechnol.* **9**(3), 2051–2054 (2009)
94. H. Reiss, I.B. Wilson, The effect of surface on melting point. *J. Colloid Sci.* **3**(6), 551–561 (1948)
95. H. Sakai, Surface-induced melting of small particles. *Surf. Sci.* **351**(1–3), 285–291 (1996)
96. C.R.M. Wronski, Size dependence of melting point of small particles of TiN. *Br. J. Appl. Phys.* **18**(12), 1731–1734 (1967)
97. K.K. Nanda, S.N. Sahu, S.N. Behera, Liquid-drop model for the size-dependent melting of low-dimensional systems. *Phys. Rev. A* **66**(1), 013208 (2002)
98. M. Wautelet, Phase stability of electronically excited Si nanoparticles. *J. Phys.-Condens. Matter* **16**(12), L163–L166 (2004)
99. D. Ganguli, Size effect in melting: a historical overview. *Trans. Indian Ceram. Soc.* **67**(2), 49–62 (2008)
100. M.F. Yu, O. Lourie, M.J. Dyer, K. Moloni, T.F. Kelly, R.S. Ruoff, Strength and breaking mechanism of multiwalled carbon nanotubes under tensile load. *Science* **287**(5453), 637–640 (2000)
101. Y. Kondo, K. Takayanagi, Synthesis and characterization of helical multi-shell gold nanowires. *Science* **289**(5479), 606–608 (2000)
102. F. Sato, A.S. Moreira, P.Z. Coura, S.O. Dantas, S.B. Legoas, D. Ugarte, D.S. Galvao, Computer simulations of gold nanowire formation: the role of outlayer atoms. *Appl. Phys. A-Mater. Sci. Process.* **81**(8), 1527–1531 (2005)
103. C.Q. Sun, H.L. Bai, S. Li, B.K. Tay, C. Li, T.P. Chen, E.Y. Jiang, Length, strength, extensibility, and thermal stability of a Au–Au bond in the gold monatomic chain. *J. Phys. Chem. B* **108**(7), 2162–2167 (2004)

Chapter 27

Nanograins: I. Elasticity and Compressibility

- *Skin-resolved energy density determines the elasticity of nanograins. Skin-resolved cohesive energy loss depresses the thermal stability.*
- *Elasticity of a specimen may rise or drop with size reduction, depending on the separation between the melting point and the temperature of operation, $T_m - T$.*
- *Heating lengthens and softens the representative bond and hence lowers the energy density and elasticity. Compression shortens and stiffens the representative bond and raises the elasticity.*
- *Raman shift is proportional to the square root of stiffness, $\omega \propto (Yd)^{1/2}$.*
- *Theory reproduction of heating effect turns out thermal expansion coefficient, Debye temperature, and atomic cohesive energy.*
- *Theory reproduction of compressing effect derives compressibility and binding energy density.*

27.1 Known Mechanisms

27.1.1 Size Dependence

The size dependence of the elastic modulus was also attributed to the total strain energy of a nanocrystalline [1, 2] that can be decomposed into the strain energy of the bulk (U_b) and the surface, (U_s), i.e., $U = U_b + U_s$. Minimizing the total strain energy of nanocrystals will deform from the bulk crystal lattice into the self-equilibrium state of crystals. The strain in a self-equilibrium state in nanocrystals can be calculated by $\partial U / V_0 \partial \varepsilon_{ij} = 0$, in which V_0 and ε_{ij} ($i, j = 1, 2, 3$) are the volume and the elastic strain, respectively. The size-dependent Y modulus of spherical nanocrystals based on the size-dependent surface free energy was derived as [1],

$$\frac{Y(K)}{Y(\infty)} = (1 - K)^5 + \frac{5Y_s}{3Y(\infty)} (3K - 6K^2 + 4K^3),$$

where Y_s denotes the surface Y modulus and K is the dimensionless form of the nanocrystal's size. Theoretical analysis suggested that the elastic modulus are anisotropic depending on the crystal orientation [3].

27.1.2 Temperature Dependence

The thermal effect on the Young's modulus was modeled based on the third law of thermodynamics as anharmonic effects of the lattice vibrations [4]. Wachtman et al. and Champion et al. suggested an empirical equation for the temperature effect on the Young's modulus [5],

$$Y(T) = Y_0 - b_1 T \exp(-T_0/T) \quad (27.1)$$

where $Y(T)$ and Y_0 are the Young's modulus at T and 0 K, respectively. T_0 and b_1 are freely adjustable parameters. This model worked well at high temperatures where the $Y(T)$ shows linear dependent on temperature. However, below the Debye temperature, θ_D , the measured data manifest nonlinear nature [6–8]. Andersen derived an alternative by introducing the Mie–Grüneisen equation [9],

$$\begin{cases} Y = Y_0 - \frac{3R\gamma\delta T}{V_0} H\left(\frac{T}{\theta_D}\right) \\ H\left(\frac{T}{\theta_D}\right) = 3\left(\frac{T}{\theta_D}\right)^3 \int_0^{\theta_D/T} \frac{x^3}{e^x - 1} dx \end{cases} \quad (27.2)$$

with R being the ideal gas constant, γ is the Grüneisen parameter, and δ is the Anderson constant that is temperature independent. V_0 is the specific volume per mole of atoms at 0 K. According to Anderson, the term $b_1 T \exp(-T_0/T)$ in Eq. (27.1) is virtually the inner energy of the Debye approximation,

$$\frac{\Delta B(T)}{B_0} \cong \frac{\Delta Y(T)}{Y_0} = -\frac{\gamma\delta R\theta_D}{B_0 V_0} \int_0^T C_V dT = -\frac{\gamma\delta R\theta_D}{B_0 V_0} H(T/\theta_D) \quad (27.3)$$

This expression correlates the mechanical property B to the specific heat C_V or the internal vibration energy, $H(T/\theta_D)$. Equation (27.3) satisfies the Nernst's theorem, where the temperature derivatives of the elastic constants must vanish at 0 K. The B correlates to Y by $Y/B = 3 \times (1 - 2\nu)$, where ν denoting the Poisson ratio is negligibly small, and therefore $Y \approx 3B$. This relation could reproduce the measured $Y(T)$ reasonably well at low temperatures by taking the $\gamma\delta R\theta_D/(B_0 V_0)$ as an adjusting parameter.

From the perspective of classical thermodynamics, Garai and Laugier [10] derived a solution for fitting the temperature dependence of the bulk modulus,

$$B_T^0 = B_0^0 \exp \left[\int_{T=0}^T \alpha \alpha_{V_p} dt \right]$$

where superscript 0 denotes the quantities gained at 1 bar pressure. B_0^0 is the modulus at 0 K. α is a constant depending on the material; α_{Vp} is the volume thermal expansion coefficient.

The Young's modulus determines both the Eigen frequency $\omega(Y)$ and the force constant k_1 of a homogeneous nanocantilever with uniform cross section $A = \omega t$ (width and thickness) in the following relations [11, 12]:

$$\begin{cases} \omega = 1.0149 \frac{t}{L^2} \sqrt{\frac{Y}{\rho}} \\ k_1 = \frac{Yw}{4} \left(\frac{t}{L}\right)^3 \end{cases}$$

where ρ is the density, L the length, w the width, and t the thickness of the cantilever. Neglecting the thermally induced geometrical change of the cantilever, one can measure the vibration frequency and the Y–T relationship. Using this approach, Gysin et al. [4] determined the vibration frequency of a silicon cantilever and derived $Y_0 = 167.5$ GPa and $\theta_D = 634$ K. The derived values correspond to the documented Y value for the $\langle 110 \rangle$ direction and the documented $\theta_D = 645$ K of Si.

27.1.3 Pressure Dependence

The pressure dependence of the bulk modulus, and Raman shift as well, under compression are usually described using the quadratic functions [13],

$$Q(P) = Q(0) + aP + bP^2$$

where a and b are freely adjustable parameters; $Q(0)$ represents the Raman frequency or the elastic modulus under 0 Pa pressure.

27.2 TP-BOLS Formulation

27.2.1 Size, Pressure, and Temperature Dependence

When the solid size, operating temperature, or pressure changes, the length, $d(z_i, T, P)$, and the energy, $E_i(z_i, T, P)$, of the representative bond will change simultaneously. Based on the LBA approach, we can extend the BOLS correlation to temperature and pressure domains, leading to the temperature- and pressure-dependent bond length and bond energy,

$$\begin{cases} d(z_i, T, P) = \prod(1 + \Delta d_i) = C_i d_b \left(1 + \int_0^T \alpha_i(t) dt \right) \left(1 + \int_0^P \beta_i dp \right) \\ E(z_i, T, P) = E_0 \left(1 + \sum_i \Delta E_i \right) = E_0 \left[1 + (C_i^{-m} - 1) + \frac{\Delta E_T + \Delta E_P}{E_0} \right] \end{cases} \quad (27.4)$$

where $\alpha(t)$ is the thermal expansion coefficient, β_i is the compressibility. E_0 is the bond energy in the bulk at the ambient. ΔE_T and ΔE_P are the energy perturbation over all the surface layers caused by the applied temperature and pressure.

The ΔE_P is the pressure perturbation of energy, which can be expressed as [14],

$$\Delta E_P = - \int_{V_0}^V p(v) dv = \begin{cases} \int_0^P v dp - VP \\ \int_0^P \frac{dv}{dp} p dp \end{cases} \quad (27.5)$$

(either way works. note : $d(vp) = v dp + p dv$)

where the V and P are correlated with the Birch–Murnaghan (BM) equation of states [15]

$$p(x) = \frac{3B_0}{2} \left(x^{-7/3} - x^{-5/3} \right) \left\{ 1 + \frac{3}{4} (B'_0 - 4) \left(x^{-2/3} - 1 \right) \right\} \quad (27.6)$$

V_0 is the volume of unit cell under the standard reference conditions. $x = V/V_0$ is the volume ratio of the unit cell upon the cell being compressed. B_0 is the static bulk modulus and B'_0 is the first-order pressure derivative of the B_0 [16]. Figure 27.1 presents the d/d_0 - P and V/V_0 - P curve with the BM equation and the match of the experimental results of ZnO [16–18] with an optimal polynomial form of $V/V_0 = 1 + \beta p + \beta' p^2 = 1 - 6.55 \times 10^{-3} p + 1.25 \times 10^{-4} p^2$. Using the relationship of $x = V/V_0 = 1 - \beta p + \beta' p^2$, one can find (see Fig. 23.1b)

$$\begin{cases} \Delta E_P = - \int_{V_0}^V p(v) dv = -V_0 \int_1^x p(x) dx = V_0 P^2 \left(\frac{1}{2} \beta - \frac{2}{3} \beta' P \right) \\ x(P) = V_0 = 1 - \beta P + \beta' P^2; \frac{dx}{dp} = -\beta + 2\beta' P \end{cases}$$

According to Debye approximation, temperature elevation weakens the bond energy ΔE_T in the form of,

$$\begin{aligned} \Delta E_T(T/\theta_D) &= \int_0^T \eta_1(T) dt = \int_0^T \frac{C_V(T/\theta_D)}{z} dt \\ &= \int_0^T \int_0^{\theta_D/T} \frac{9R}{z} \left(\frac{T}{\theta_D} \right) \frac{x^4 \exp(x)}{(e^x - 1)^2} dx dt \\ &= \frac{9RT}{z} \left(\frac{T}{\theta_D} \right)^3 \int_0^{\theta_D/T} \frac{x^3}{e^x - 1} dx \end{aligned} \quad (27.7)$$

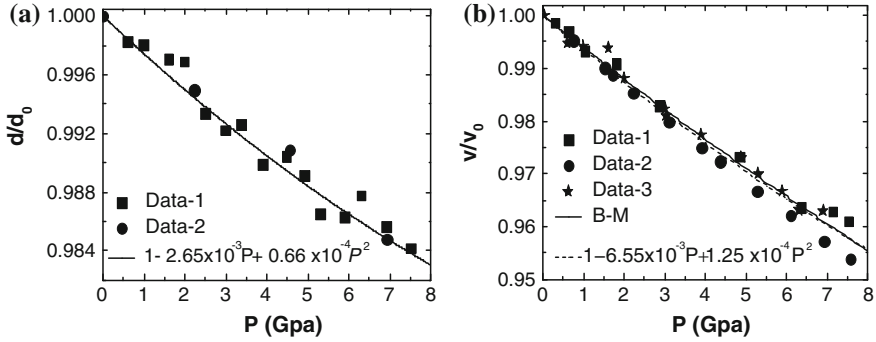


Fig. 27.1 Fitting to the experimental P dependent **a** bond length using polynomial form [16, 17] and **b** volume [16–18] of ZnO with derivatives of the linear and volume compressibility with nonlinear contributions [19]

where $\eta_1(T) = C_v/z(T)$ is the specific heat per bond that is assumed to follow Debye approximation $C_v(T/\theta_D)$, of constant volume and approaches a constant value of $3R$ (R is the ideal gas constant) at high temperature. At $T > \theta_D$, the integration of the specific heat or the specific internal energy depends linearly on T . At low temperatures, on the other hand, the integration shows nonlinearity with respect to the temperature in a T^4 manner.

Using the core–shell configuration, the bond nature (m), solid shape (τ), solid size (K), pressure (P), and temperature (T) dependence of the relative change of the energy density can be obtained by summing contributions toward the outermost three atomic layers. The relative change of the Y that is proportional to the energy density (E_{Den}) of a solid to the values at measured $T_0 = 0$ K can be expressed as,

$$\left\{ \begin{array}{l} \frac{E_{Den}(K, x_i)}{E_{Den}(\infty, 0, 0)} = [1 + \sum_{i \leq 3} \gamma_i (\lambda C_i^{-m} - 1)] + \frac{\sum_x \Delta E_b^x}{E_{b0}} \left[1 + \sum_{i \leq 3} \gamma_i \left(\lambda \frac{\sum_x \Delta E_i^x}{\sum_x \Delta E_b^x} - 1 \right) \right] \\ \lambda = [C_i \times (1 + \int_0^T \alpha_i dt + \int_0^P \beta_i dp)] / (1 + \int_0^T \alpha dt + \int_0^P \beta dp)^{-\tau} \end{array} \right. \quad (27.8)$$

The first part represents purely the effect of size, and the second part the joint effect of other stimuli. The effect of multi-filed coupling proceeds only in the surface up to skin depth, as seen from the second term in the second part. The undercoordinated atoms in the surface skin dictate the relative change of the elasticity and extensibility of the entire nanosolid whereas atoms in the core interior retain their bulk features.

For the bulk materials ($C_i = 1$ and $\Delta_i = 0$), the skin effect can be omitted. The Y then turns to be P and T dependent only. The thermally driven softening and mechanically stiffening exhibit the bulk feature, and no summation over the surface layers is necessary. Apart from the effect of thermal expansion, the present form agrees with Anderson’s model of T -dependent Y with further identification of

$\gamma\delta R\theta_D/(B_0V_0) = 1/E_b(0)$ and the internal vibration energy, $3RT \times F(T/\theta_D) = H(T/\theta_D)$. The Y value drops nonlinearly with T at $T \ll \theta_D$ because of the involvement of the nonlinear specific heat in Debye approximation. At $T > \theta_D$, Y drops linearly with T in spite of the contribution from thermal expansion.

27.2.2 Debye Temperature and Specific Heat

The Debye temperature, defined as $\theta_D = \hbar\omega_D/k_B$, is a key parameter that determines the specific heat capacity and thermal transport dynamics. The θ_D is actually not a constant but changes with the object size [20–24] and the temperature of testing [25–27] as the θ_D depends functionally on Y . Earlier contributions [20] suggested that the size-dependent θ_D result from the finite cutoff of frequency and the surface stress, especially, if the size is smaller than 20 nm. Ballerina and Mobile [21] confirmed the predicted size dependence of θ_D . Calculations of the temperature-dependent θ_D of some fcc and bcc metals [25] revealed that θ_D drops when the measuring temperature is increased because of the temperature dependence of elastic constants and the sound velocity of the solid. Discrepancy remains regarding the T_m dependence of the θ_D . One opinion is that θ_D varies linearly with T_m [25], and the other suggests a square root dependence of θ_D on T_m according to Lindermann's [28] criterion of melting.

Since $\theta_D = \hbar\omega_D/k_B \propto \omega_D \propto \sqrt{Yd} \propto \sqrt{E}/d$. The multiple field effect on the θ_D is generalized as,

$$\begin{aligned} \frac{\theta_D(z_i, m, T, P)}{\theta_D(z_b, m, 0, 0)} &= \frac{\omega_D(z_i, m, T, P)}{\omega_D(z_b, m, 0, 0)} = \frac{(v_s d)(z_i, m, T, P)}{(v_s d_i)(z_b, m, 0, 0)} \\ &= \frac{C_i^{-1}}{1 + \alpha_i T + \beta_i P} \left(\frac{E_i(z_i, m, T, P)}{E_b(z_b, m, 0, 0)} \right)^{1/2} \end{aligned} \quad (27.9)$$

Replacing the $E_b(T)$ with $E_b(T) \approx \eta_2 + \eta_1(T_m - T)$ yields the form,

$$\theta_D = \sqrt{\eta_2 + \eta_1(T_m - T)}/d. \quad (27.10)$$

which agrees with the square root dependence of the T independent θ_D on T_m : $\theta_D \propto T_m^{1/2}/d$ [28]. For nanostructures, the θ_D drops with size because of T_m depression.

Generally, the specific heat is regarded as a macroscopic quantity integrated over all bonds of the specimen and is the amount of energy required to raise the temperature of the substance by 1 K. However, in dealing with the representative bond of the entire specimen, one has to consider the specific heat per bond that is obtained by dividing the bulk-specific heat by the total number of bonds involved. Depending critically on the θ_D and the Y , the specific heat varies with both object size and the temperature of measurement. The effect of body size on the specific

heat capacity has received considerable attention [29–32]. For instance, Novotny et al. [29] measured the low-temperature heat capacity of 2.2 and 3.7-nm-sized lead particles and observed the enhancement of heat capacity below 5 K. Lu [33] demonstrated that the specific heat of metallic or alloying nanosolids increases with the inverse of solid size. However, an ac microcalorimeter measurement [30] showed the opposite trend for Al films where the specific heat drops with the thickness of the Al film from 370 to 13.5 nm.

The rise of the absorption and the loss of thermal waves with specific wave vectors explain the decrease of specific heat in the small volumes. Lu et al. [31] calculated the size effects on the specific heat of Al thin films by employing the Prasher's approach [34] and derived that the reduction of phonon states was not the main reason causing the size effect on specific heat; but a thin layer of Al oxide was responsible for it.

The heat capacity per unit volume is defined as the ratio of an infinitely small amount of heat δE added to the body to the corresponding small increase in its temperature δT when the volume remains unchanged. The specific heat approximates the extended Debye model:

$$C_v = \left(\frac{\partial E}{\partial T} \right)_V = \kappa^2 R \left(\frac{T}{\theta_D} \right)^\kappa \int_0^{\theta_D/T} \frac{x^{\kappa+1} \exp(x)}{(\exp(x) - 1)^2} dx \quad (27.11)$$

where $x = \hbar\omega/k_B T$. When $\kappa = 3$, Eq. (27.11) is reduced to the three-dimensional standard form of Debye model. For $T \gg \theta_D$, the integration in gives $(1/\kappa)(\theta_D/T)^\kappa$. The heat capacity C_v is simplified as κR , in agreement with the Dulong–Petit law in the case of $\kappa = 3$. At higher temperatures, the C_v approaches a constant.

At $T \ll \theta_D$, the upper limit of the integral of Eq. (27.11) approaches infinity and the integration gives $\int_0^\infty x^{\kappa+1} e^x / (e^x - 1)^2 dx \approx 3.290, 7.212$ and 25.976 , for $\kappa = 1, 2$, and 3 , respectively. Therefore, the heat capacity in the low-temperature limit becomes:

$$\begin{cases} C_v &= A\kappa^2 \left(\frac{T}{\theta_D} \right)^\kappa \\ \theta_D &= \sqrt{\eta_2 + \eta_1(T_m - T)}/d \end{cases} \quad (27.12)$$

where A is a fixed value. Equations (27.11) and (27.12) indicate that θ_D has a strong effect on the heat capacity. Using the same core–shell structure for a nanosolid, one can simplify the expression for the specific heat dependence on the size, shape, and bond nature at very low temperatures ($T \sim 0$) [35]:

$$\begin{aligned} \frac{\Delta C_v(m, T, K)}{C_v(m, T_0, \infty)} &= \sum_{i \leq 3} \frac{\tau C_i}{K} \left[C_i^{(1+m/2)\kappa} \left(\frac{1 - T/T_m(1 + \Delta_i)}{1 - T_0/T_m} \right)^{-\kappa/2} - 1 \right] \\ &\cong \sum_{i \leq 3} \frac{\tau C_i}{K} \left[C_i^{(1+m/2)\kappa} (1 - T_0/T_m)^{\kappa/2} - 1 \right] < 0 \quad (T \sim 0) \end{aligned} \quad (27.13)$$

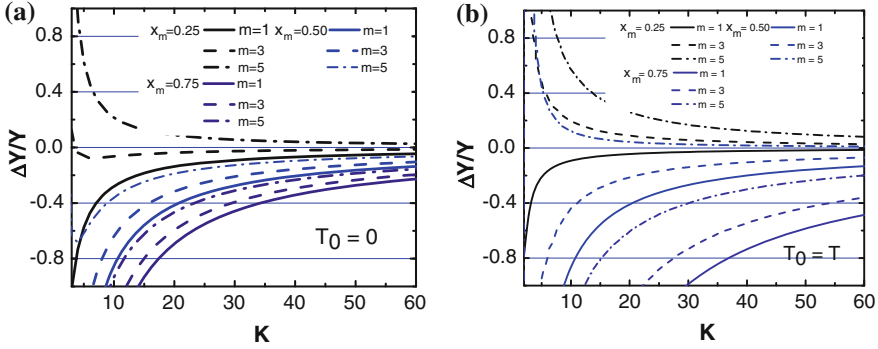


Fig. 27.2 Prediction of size K dependence of Young’s modulus with **a** $T_0 = 0$ and **b** $T_0 = T$ of different bond natures and $x_m(T/T_m)$ values. Young’s modulus enhancement occurs at the combinations of $(x_m, m) = (<0.25, >3)$ for $T_0 = 0$ and $(x_m, m) = (<0.5, >3)$ for $T_0 = T$. The Y retention may happen at critical $(T/T_m, m)$ combinations (reprinted with permission from [37])

Since the coefficient of bond contraction C_i is always smaller than unity, the heat capacity is always lower than the bulk value at lower temperatures. The heat capacity decreases with the inverse size (K). At temperatures close to θ_D , the heat capacity should be evaluated using Eq. (27.11), where the θ_D is size, temperature, and bond nature dependent.

27.2.3 Raman Shift Versus Young’s Modulus

As discussed in Chap. 15, the solution to the Hamiltonian of a vibration system is a Fourier series with multiple terms of frequencies being fold of that of the primary mode [36]. Any perturbation to the Hamiltonian causes the Raman frequencies to shift from the initially ideal values. Therefore, applied strain, pressure, temperature, or the atomic CN variation can modulate the length and energy of the involved bonds, or their representative, and hence the phonon frequencies in terms of bond relaxation and vibration.

From the dimensional analysis, the vibration frequency is proportional to the square root of the bond stiffness. Equaling the vibration energy of an ideal harmonic oscillator to the corresponding term in the Taylor series of the interatomic potential around its equilibrium, one can find,

$$\begin{cases} \frac{1}{2} \mu (\Delta\omega)^2 x^2 \cong \frac{1}{2} \frac{\partial \mu(r)}{\partial r^2} \Big|_{r=d} x^2 \propto \frac{1}{2} \frac{E_s}{d^2} x^2 \\ (\Delta\omega)^2 = \frac{E_s}{d^2} = Yd \end{cases}$$

The elastic modulus correlates thus with the Raman shift of the specimen.

27.3 TP-BOLS Expectations

27.3.1 Elasticity and Extensibility

Using Eq. (24.10), one is able to predict the bond nature, the shape and size, and the T/T_m dependence of the Young's modulus and extensibility of a solid. For illustration purpose, we selected $m = 1$ (for metals), 3 (carbon, 2.56), and 5 (Si, 4.88), $x_m (T/T_m) = 0.25, 0.5,$ and 0.75 and the dimensionality $\tau = 3$ (for a sphere) in calculations. The T_0 was set at 0 K and T , respectively. For temperature dependence, we used $K = 10$ and 50 sizes by fixing other parameters. η_{21} was taken as zero for illustration purpose, otherwise a small offset would be achieved that could hardly be identified in the predicted trends of the relative changes.

Figure 27.2a shows that either elevation or depression of the Young's modulus with decreasing sizes may occur depending on the combination of the (x_m, m) values. For example, Y elevation occurs in the situations of $(x_m, m) = (<0.25, >3)$. Y retention may happen at critical (x_m, m) combinations such as $(x_m, m) = (\sim 0.25, \sim 3)$. The critical combination of (x_m, m) can be obtained by allowing Eq. (24.10) to approach zero. If we select $T = T_0$, Y elevation also occurs in the situations of $(x_m, m) = (<0.5, >5)$. Y value may also remain constant at $(T/T_m, m) = (0.25, \sim 2)$ and $(0.5, \sim 4)$.

It is therefore not surprising that the modulus may rise, drop, or remain constant when the solid size is reduced, depending on the bond nature indicator m , the temperature ratio x_m , and the testing techniques as well. The predicted low-temperature stiffening agrees with the findings that the impact toughness of nanostructured Ti is enhanced at low temperatures of 200 and 77 K, a unique phenomenon that contradicts the observations in coarse-grained materials. The size-induced compressibility modulation of Au and Ag nanostructures is also understandable based on the theory consideration.

According to the prediction, the Y values for pure metallic ($m = 1$) nanoparticle always drop with size at $T > 0.25 T_m$. However, the surface chemical passivation, defects, and the artifacts in measurement could promote the measured values. For instance, surface adsorption alters the surface metallic bonds ($m = 1$) to new kinds of bonds with $m > 1$. Surface compound formation or surface alloying alters the m value from one to a value around 4.

Figure 27.3 shows the predicted temperature-induced relative change of (a) Y values and (b) the extensibility for $K = 10$ and $m = 1, 3,$ and 5 samples. If $T_0 = T$, Y drops nonlinearly with T until T_m is reached. The insertion shows the case of $T_0 = 0$ in which the Y drops linearly with T . Detailed calculation with consideration of the thermal coefficient of expansion and the nonlinear T dependence of the specific heat will give the nonlinear form at very low temperatures, as detailed in next section. The extensibility approaches infinity at $T \sim T_m(K)$. The inset in (b) shows singularities because of the shell-by-shell configuration. If we treat the outermost two atomic layers as the skin with a mean $z_i = (4 + 6)/2$, the singularity occurs at the melting point that drops in value with the characteristic size.

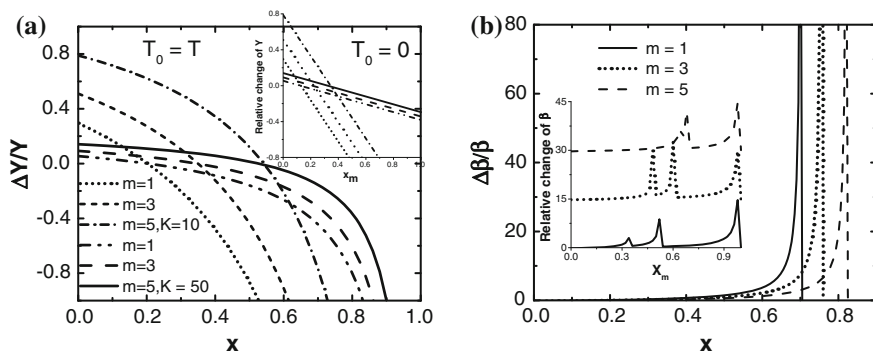


Fig. 27.3 Prediction of $x = T/T_m$ dependence of **a** Young's modulus and **b** extensibility of a spherical nanosolid with different m and T/T_m ratios. For illustration purposes, we only present here the linear T dependence for the high temperature approximation. The inset shows the cases of $T_0 = 0$. The Y values of a nanosolid of lower m values and smaller sizes drop faster when the test temperature is raised. The extensibility approaches infinity at the T_m . The singularities in the inset exhibit the shell-by-shell melting features (reprinted with permission from [37])

On the other hand, a smaller nanosolid with lower m value is more easily extensible at elevated temperatures.

The predicted m , K , and T/T_m dependence of modulus and extensibility covers all the possible trends as observed. For example, the predicted Y -depression agrees well with the measured trends of Al ($m = 1$, $T/T_m = 300/650 \sim 0.5$) [38] and polymers ($T_g = 300/450 \sim 2/3$) [39]. Predictions agree well with the measured size dependence of the compressibility, or the inverse of Young's modulus, for nanostructures. Nanocrystalline α -Al₂O₃ with particle sizes of 67, 37, 20 and 6 nm under pressure up to 60 GPa shows a systematic decrease in the compressibility and transition pressure with an increase in particle size. In addition, a high-pressure phase appeared at pressure values of 51 and 56 GPa for 67 and 37-nm-sized α -Al₂O₃, respectively [40]. The compressibility of both Ni and Mo also decreases with particle sizes [41]. Predictions also agree with the observed trends of temperature dependence of Young's modulus of CVD nanodiamond films [42], the silicone resins [39], and the yield stress (linearly proportional to modulus) of Mg nanosolid [43] of a given size. A compensation of the pressure-induced T_C elevation to the size-induced T_C depression has been verified to be the physical origin for the observed size and pressure effect on the solid–solid phase transition at room temperature of a number of nanostructured specimens [14].

The ductility increases exponentially with temperature until infinity at the T_m value that drops with solid size. The extensibility of nanometer-scaled Al–Cu alloys in the quasi-molten state [44], nanometer-scaled Al₂O₃ [40], and PbS [45] at room temperature increases generally with grain refinement. The m values for compounds or alloys are around 4 or higher, and their T/T_m ratios are relatively lower. The increase in compressibility/extensibility of Al₂O₃ and PbS nanosolids is associated with a decrease in Young's modulus as temperature rises. The

superplasticity of materials such as Cu wires ($m = 1$, $T/T_m \sim 1/2$) [46] with grain size less than tens of nanometers in the temperature range $0.5\text{--}0.6 T_m$ [47] also agrees with the predictions. The Y elevation of Si nanosphere ($m = 4.88$, $T/T_m \sim 1/6$) [48] is also within the prediction because of their high m values and low T/T_m ratios.

However, the discrepancy for ZnO wires [49] and Si spheres [48] and Si belts [50] in the size dependence of elastic modulus may arise from different T/T_m of operation or different experimental conditions or methods. It is anticipated that modulus enhancement, as observed from TiCrN and GaAlN surfaces [51], may not be observable at room temperature for the low- T_m metals such as Sn, Pb, Al, Zn, Mg, and In.

27.3.2 Debye Temperature and Specific Heat

Using Eq. (27.10), one is able to predict the bond nature, size, and temperature dependence of $\theta_D(m, K, \text{ and } T)$. Figure 27.4 shows the relative change in θ_D for nanowires ($\tau = 2$, $\kappa = 1$) with $m = 1, 3, 5$, and $x(T/T_m) = 0, 0.25$, and 0.50 . When the measuring temperature is much lower than the melting point ($T/T_m \ll 1$), θ_D is increased when the K is decreased; while θ_D increases faster at larger m values. On the other hand, θ_D is decreased when the operating temperature is raised and the relative change in θ_D is greater for smaller m values. A close examination of (a) and Eq. (27.10) could lead to a conclusion that, for a certain ($T/T_m, m$) combination, θ_D may vary insignificantly with particle size, as for the insignificant change in Young's modulus.

Figure 27.4b shows the temperature-induced relative change in θ_D for nanowires ($\tau = 2$, $\kappa = 1$) of size $K = 10$ and 50 . If we set $T_0 = T$, θ_D decreases nonlinearly with T until the T approaches T_{mi} (local melting temperature of the i th atomic site). The two transition points for each of (m, K) combinations arise from the loss of bonds, which happens only to the outermost two discrete atomic layers. Moreover, the variation in θ_D with the temperature and size is more pronounced for larger m and smaller K values.

Figure 27.5 compares the predictions with various theoretical or experimental data (a) for Au particles and (b) θ_D from Debye–Waller parameter measurement for Se nanoclusters. Couchman and Karasz's approach [20] shows that the change in θ_D involves the particle size K and cutoff acoustic wavevectors K_0 : $\Delta\theta_D/\theta_0 \approx -3\pi/(8KK_0)$, without temperature being involved. By applying Eq. (27.10), with $T_0 = 0.245T_m$ and $T = 0.16T_m$, agreement between the T-BOLS prediction and Couchman and Karasz's estimation has been reached. If we set $T_0 = 0.224T_m$ and $T = 0.204T_m$, The T-BOLS premise agrees well with the measured data of Balerna and Mobilio, as shown in Figure 27.5a.

Figure 27.5b predicts the general trend of θ_D with respect to size though the precise agreement is not satisfied. However, since the measurement was conducted at $T = 293$ K that is higher than the local melting temperature of the outermost

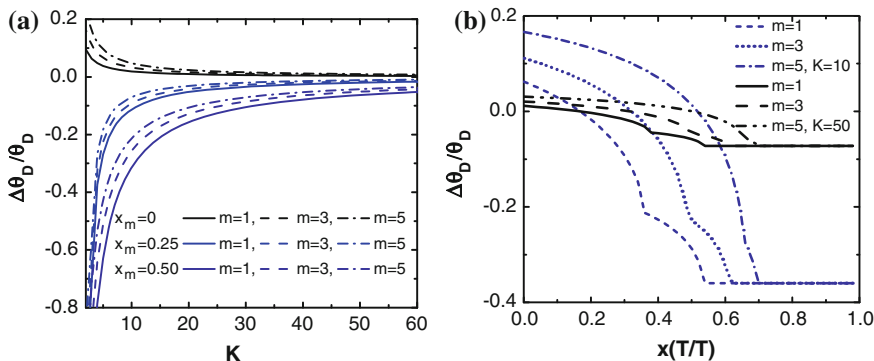


Fig. 27.4 Prediction of **a** size (K) and **b** temperature $x(T/T_m)$ dependence of θ_D for different bond natures (m). The θ_D increases with the decreasing in size at very low T , and the θ_D decreases with decreasing the size for high temperature. The θ_D of nanowires with higher m values and smaller size drops faster when the temperature is elevated. The transition points correspond to local melting temperature of the outermost two atomic layers [35] (reprinted with permission from [37])

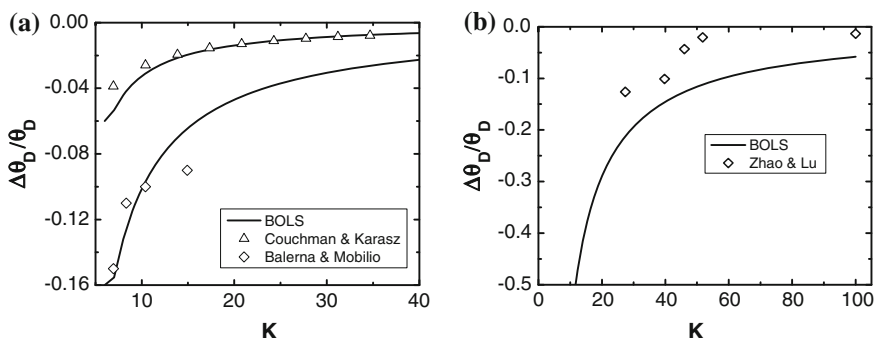


Fig. 27.5 Comparison of the T-BOLS predictions with the observations based on **a** Couchman and Karasz's model (with $T_0 = 0.245 T_m$, $T = 0.16 T_m$, and $T_m = 1337$ K) [20] and Balerna and Mobile's measurement (with $T_0 = 0.224 T_m$ and $T = 0.204 T_m$) [21] for Au particles and, **b** Zhao and Lu's measurement of Se particles (with $T_0 = T = 0.6 T_m$ and $T_m = 494$ K) [22]

two atomic layers, about $0.6T_m$ (for Se $T_m = 494$ K), the features measured are dominated by the core interior with an insignificant contribution from the temperature dependence.

As indicated in Eq. (27.13), the specific heat capacity depends unambiguously on θ_D and hence on the size, temperature, and the bond nature involved. Figure 27.6a shows the reduced C_v (in units of the gas constant R) versus temperature (T/θ_{D0}) for Si nanowires ($m = 4.88$) and Al nanowires ($m = 1$) of different diameters ($K = 5, 10$, and 20). The shape of the C_v curve is similar to that of the bulk but the size induces a depression over the whole temperature range. For the same K at a given T/θ_{D0} , the reduction in heat capacity increases with the m value.

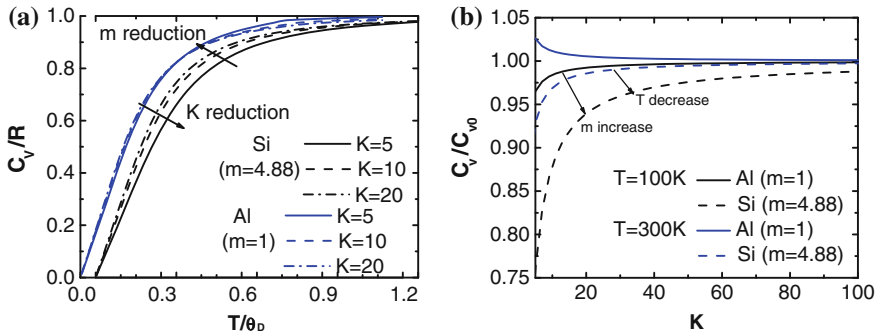


Fig. 27.6 a Prediction of the temperature (T/θ_{D0}) and size dependence of heat capacity (in units of R) for Si nanowires ($m = 4.88$) and Al nanowires ($m = 1$) with $K = 5, 10$ and 20 and at $T = 100\text{ K}$ and 300 K , in panels (a) and (b). The heat capacity approaches R at very high temperature and decreases with solid size. The reduction in heat capacity is more pronounced for larger m values at a given T/θ_{D0} . The heat capacity generally reduces with solid size and reduces faster at lower temperature and larger m values [35] (reprinted with permission from [37])

(b) plots C_v/C_{v0} (where C_{v0} is the bulk heat capacity at a given temperature) versus K at $T = 100\text{ K}$ and 300 K for Al and Si nanowires.

The heat capacity decreases with the size at fixed temperature (except for Al nanowires measured at room temperature, where the heat capacity is very close to the bulk C_v value obtained when $K > 15$ and increases slightly with decreasing size). For a given size, the reduction in the heat capacity is more significant at lower temperatures or larger m values. In this analysis, we set $T_0 = T$. If T_0 is assumed 0 K , the general trend of heat capacity is preserved, but the reduction in heat capacity is more pronounced.

27.4 $K, P,$ and T Dependence of Elasticity and Vibration Frequency

27.4.1 Au and Ag Metals

Figure 27.7 shows the T-BOLS reproduction of the size and temperature dependence of the elastic modulus and the pressure dependence of the compressibility of Au and Ag of different sizes. Reproduction of the measurements derives the Debye temperature of 170 K and 160 K and the Atomic cohesive energy of 1.64 and 1.24 eV for Au and Ag crystals. An XRD with synchrotron radiation at pressures up to 30 GP revealed that silver (10 nm) and gold (30 nm) nanoparticles are stiffer than the corresponding bulk materials. The bulk modulus of n-Au increases by 60% [52]. The unexpected high modulus corresponded to the polysynthetic domain twinning and lamellar defects as the main origin for the strong decrease in compressibility.

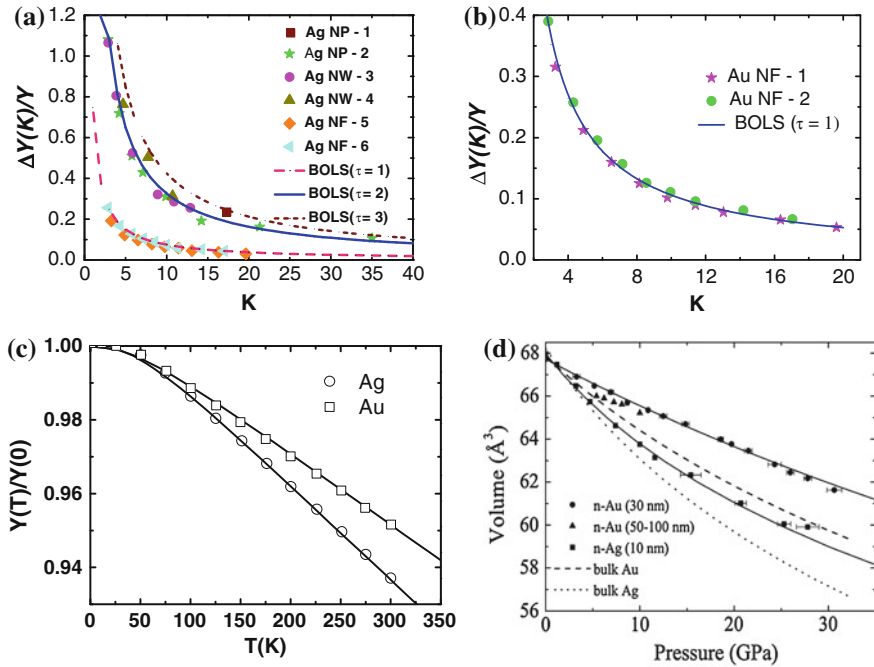


Fig. 27.7 Size-dependent elastic modulus of **a** Ag nanoparticles (NP) and nanowires (NW) [53–55] and **b** Au nanofilms (NF) [54]. **c** Temperature dependence of the elastic modulus [10, 56] and **d** pressure dependence of the unit-cell volume of less compressible n-Ag and n-Au compared with the bulk materials. The data for n-Au (50–100 nm) is taken from [57]. Dotted and dashed lines represent for bulk case of Ag [58] and Au [59], respectively

27.4.2 Group IV Elements

- Si, Ge, and Carbon Allotropes

Figure 27.8 shows the reproduction of the temperature dependence of the Raman shift and Young's modulus of bulk solid for group IV elements with derived information of $E_B(0)$ given in Table 24.6. Deviation between derivatives of the atomic cohesive energy exists but the E_c for Ge is consistently derived from both the temperature-dependent Raman shift and elastic modulus (Table 27.1).

- Carbon allotropes

Bond-order variation and the pattern change in sp-orbit hybridization make carbon allotropes a group of versatile materials varying from diamond, graphite, C_{60} , nanotube (CNT), nanobud (CNB), graphene, and graphene nanoribbons (GNRs) with properties that are amazing. For instances, graphite is an opaque conductor but diamond is an insulator transparent to light almost all wavelengths; the former shares non-bonding unpaired (or π -bond) electrons due to sp^2 -

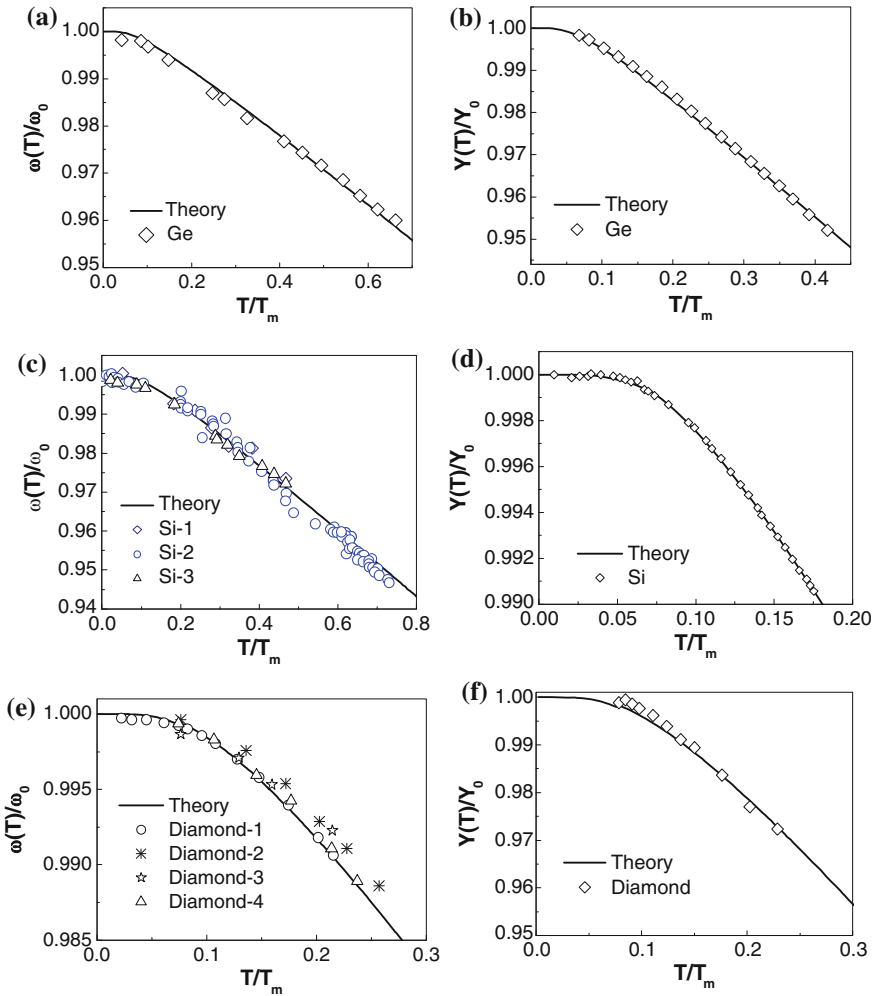


Fig. 27.8 Agreement between predictions and the measured temperature dependence of the Raman shift and Young's modulus of Ge (a [60], b [61]), Si (c [60, 62, 63], d [63]), and Diamond (e [64–67], f [68]) with derived information of $E_B(0)$ given in Table 27.6 (reprinted with permission from [69])

hybridization compared with the latter of ideally sp^3 hybridized. CNT and graphene demonstrate anomalous properties including high tensile strength, electrical conductivity, ductility, and thermal conductivity. GNR performs, however, quite differently from CNT or the infinitely large graphene because of the involvement of the two-coordinated edge atoms and the associated Dirac Fermions [71–75]. Raman phonons relax with the applied stimuli such as the temperature and pressure as well as the allotropic coordination environment [76, 77].

Table 27.1 List of the input data, such as melting temperature, T_m , the Debye temperature, θ_D , T -dependent thermal expansion coefficient, $\alpha(T)$, and the derived atomistic cohesive energy $E_B(0)$ from fitting to the temperature dependence of Y and ω for Si, Ge, and Diamond

| | T_m (K) | θ_D (K) | $E_B(0)$ (eV) | | | [141] |
|---------|--------------|-------------------|---------------|------|------|-------|
| | | | Raman | Y | Mean | |
| Si | 1,647 | 647 | 2.83 | 4.33 | 3.58 | 4.03 |
| Ge | 1,210 | 360 | 2.52 | 2.65 | 2.58 | 3.85 |
| Diamond | 3,820 | 1,860 | 6.64 | 5.71 | 6.18 | 7.37 |

Accuracy is subject to the measurement where artifacts contribute. Therefore, extra caution is needed in the measurement

Taking $z_g = 5.335$ for the bulk graphite as a reference and with the aid of $z = 3$ for graphene, the $\omega_x(1)$ is derived [77],

$$\begin{aligned}
 C_x(z, z_g) &= \frac{\omega_x(z) - \omega_x(1)}{\omega_x(z_g) - \omega_x(1)} = \left(\frac{C_z}{C_{z_g}} \right)^{-(m/2+1)} \begin{cases} \frac{z}{z_g} & (\text{D, 2D}) \\ 1 & (\text{G}) \end{cases} \\
 &= \left(\frac{0.8147}{0.9220} \right)^{-2.28} \times \begin{cases} \frac{3.0}{5.335} & = 0.7456 \quad (\text{D, 2D}; z = 3) \\ 1 & = 1.3260 \quad (\text{G}; z = 3) \end{cases} \quad (27.14)
 \end{aligned}$$

Based on the known 2D mode shifting from 2,720 to 2,680 cm^{-1} and D mode from 1,367 to 1,344 cm^{-1} , and the G mode shifting from 1,582 to 1,587 cm^{-1} , when the graphite ($z_g = 5.335$) turns into the monolayer ($z = 3$) graphene [78–82], we can obtain the reference $\omega_x(1)$ for the D, 2D, and G modes from Eq. (23.5),

$$\begin{aligned}
 \omega_x(1) &= \frac{\omega_x(z) - \omega_x(z_g)C_x(z, z_g)}{1 - C_x(z, z_g)} = \frac{\omega_x(3) - \omega_x(z_g)C_x(3, z_g)}{1 - C_x(3, z_g)} \\
 &= \begin{cases} 1276.8 & (\text{D}) \\ 1566.7 & \text{G} \\ 2562.6 & \text{2D} \end{cases} \quad (\text{cm}^{-1})
 \end{aligned}$$

Based on these derivatives, one can reproduce the T - and P -dependent Raman shift with the quantified Debye temperature, mode cohesive energy, compressibility, and binding energy density as given in Table 27.2.

Figure 27.9a shows the reproduction of the z -dependent Raman frequencies of (a) the D/2D modes [78, 83, 84] and the G mode. When the n is greater than 6, the z reaches and then maintains almost the bulk graphite value of 5.335. The consistency between predictions and measurements of the z -dependent Raman shifts for the three modes evidences the essentiality and appropriateness of the proposed mechanisms for the lattice vibration in graphene. Size-reduction-induced phonon shift of the G mode contribute by only one neighbor ($z = 1$) [36].

Figure 27.9b and c show the reproduction (solid line) of the measured T -dependent D and G modes for diamond, graphite, graphene, SWCNT, C_{60} , and CNB. Results show that at $T < \theta_D/3$, the slow drop of the Raman shift arises from the small $\int_0^T \eta dt$ values as the specific heat $\eta(t)$ is proportional to T^τ . From the

Table 27.2 Quantitative information derived from reproducing the measured temperature and pressure independence of Raman shift for graphene, SWCNT, C_{60} , CNB, graphite, and diamond

| Parameters | Graphene G mode | SWCNT | Graphite | C_{60} | CNB | Diamond D/2D |
|--|--------------------|--------------|---------------------|-------------|-------------|---------------------|
| CN | 3 | 3 | 5.335 1582.7 | 2.465 | 5.605 | 12 |
| $\omega(1)$ | | | 1566.7 | | | 1367.0/2820.0 |
| A (ω - T slope) | 0.019 [88] | 0.024 [91] | 0.028 [89] | 0.0165 [87] | 0.0273 [86] | 1276.8/2562.6 |
| $\alpha(10^{-6} \text{ K}^{-1})$ | 9 | 8 | 8 [98] | 1 | 5 | 0.033 [65] |
| B_0/B'_0 ($\text{GPa}/-$) | 890/5.0 | 865/5.0 | 39 [100]/10.0 [100] | - | - | 0.8 [99] |
| $d(\text{nm})$ | 0.125 | 0.125 | 0.142 | 0.118 | 0.143 | 446 [101]/3.6 [101] |
| E_b (eV) | 1.038 | 1.038 | 0.756 | 1.22 | 0.743 | 0.154 |
| $E_{\text{in-cot}}$ (eV) | 1.032 | 0.817 | 0.700 | 1.188 | 0.718 | 0.614 [70] |
| θ_D | 540 | 600 | 1,000 | 650 | 550 | 0.594 |
| $\beta/\beta'(10^{-3} \text{ GPa}^{-1}/\text{GPa}^{-2})$ | 1.145/0.0763 | 1.156/0.0770 | 18,440/0.4427 | - | - | 2230 [102] |
| E_{den} (eV/nm ³) | 466.19 | 456.32 | 347.68 | - | - | 2.120/0.0035 |
| | | | | - | - | 249.59 |

2D mode frequency is twofold of that of the primary D mode, instead of the double-phonon resonant effect [36]

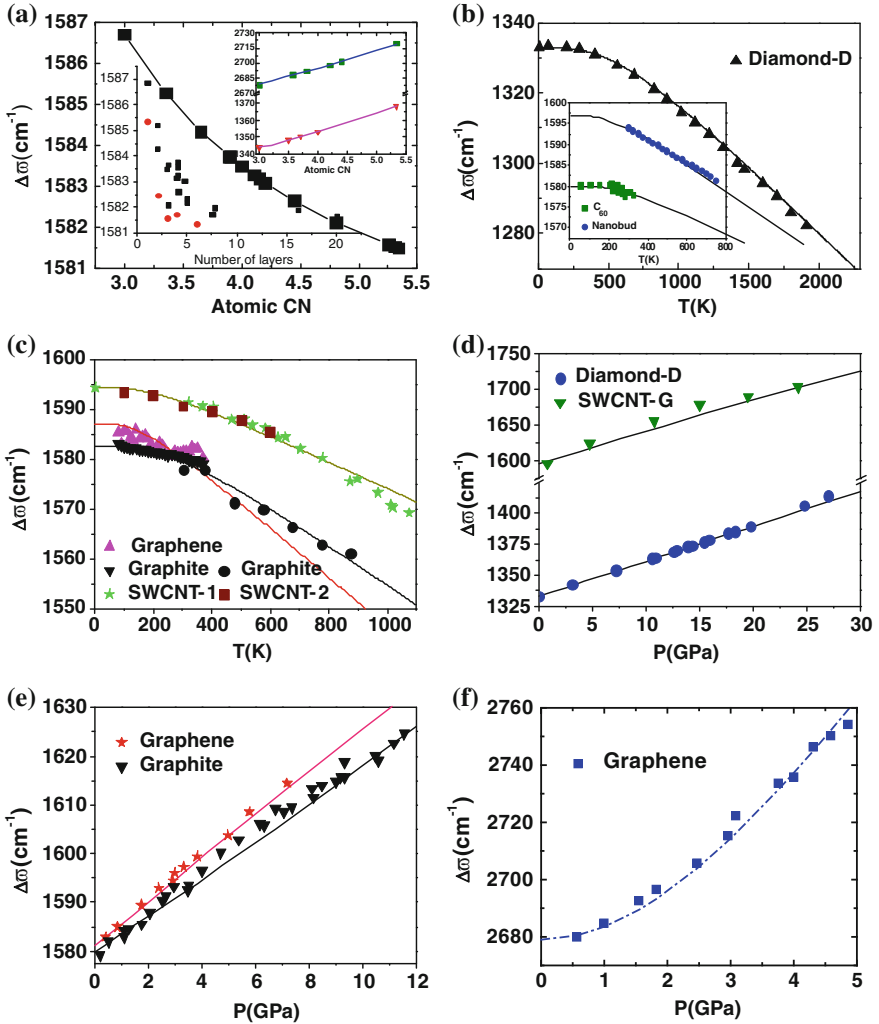


Fig. 27.9 a CN dependence of the G modes (inset) [78, 79] and D/2D mode (inset) [78, 81] of graphene [36]. T -dependent Raman shifts of b diamond [65], CNB [86], and C_{60} [87] (inset), c graphene [88], graphite [89, 90], and SWCNT [91, 92], at the ambient pressure. P -dependent Raman shifts of d diamond [93] and SWCNT [94], e graphene [95] and graphite [96], and f graphene [95] at room temperature with derived information summarized in Table 27.2 [36, 97] (reprinted with permission from [36, 97])

matching, we can obtain the Debye temperature θ_D that determines the width of the shoulder. At $T \geq \theta_D/3$, the relative Raman shift turns from nonlinear to linear. The high temperature ω - T slope, A , for each phase was obtained by fitting the experimental data. Here, the mode cohesive energy $E_{m\text{-coh}}(0)$ is defined as the different Raman modes corresponding to bond energy, $E_b(0)$. Therefore, we can

also obtain the $E_{m\text{-coh}}(0)$ that determines the slope of the $\omega(T)$ curve at high temperature ($T \geq \theta_D/3$). By the known relation $E_{m\text{-coh}}(z) = C_z^m E_{m\text{-coh}}(b)$ and the known bulk mode cohesive energy as well as the fixed m value, we also can estimate the effective CN of the C_{60} and CNB phase, as given in Table 27.2.

Results above show that the mode cohesive energy is generally lower than the atomic cohesive energy and varies from phase to phase for the same phonon mode. For instance, the G mode cohesive energy is 0.594 eV while the atomic cohesive energy is 7.37 eV for diamond. The former corresponds to energy activating the specific mode vibration while the latter to the energy of atomic evaporation of the specific crystal. From the derivatives, the C_{60} has lower CN than graphene. The bond energy, atomic cohesive energy, and mode cohesive energy of C_{60} are the highest among all the phases. Therefore, the C_{60} is the strongest. The Debye temperatures of other phases are substantially lower than that of diamond, 2,230 K.

Figure 27.9d–f shows the consistency between BOLS predictions and the experimental results of the P -dependent Raman shifts for carbon allotropes. By matching the measured P -dependent Raman shift, we can obtain the binding energy density (E_{den}) and the compressibility (β), as tabulated in Table 27.2. Results show that the energy densities of graphene and SWCNT's are higher than that of diamond, which is consistent with that discovered using XPS [85]. Since the elastic modulus is proportional to the binding energy density, the elastic modulus of graphene and SWCNT are higher and hardly compressed in comparison to diamond. The elastic modulus for C_{60} and CNB will be available provided with the P -dependent Raman shift data.

27.4.3 II–VI Semiconductors

- ZnO

Figure 27.10 shows the theoretical match to the measured size dependence of the relative change in $Y(K)$ for ZnO nanowires, nanorods [103, 104], nanotubes [105], and nanofilms [49, 104]. Only the outermost three atomic layers contribute to the strength change for ZnO nanowires, nanorods, and nanofilms but for ZnO nanotubes, contribution of both the outer and the inner shells should be included.

Figure 27.11 shows the theoretical match to the measured temperature dependence of the (a) $Y(T)$, (b) $\omega(T)$, $E_G(T)$ (inset), and pressure dependence of the (c) elastic modulus and (d) Raman shift of various modes of ZnO. Compared with the thermally softened ZnO Young's modulus, the pressure-induced elastic stiffening results from bond compression and bond strengthening owing to mechanical work hardening.

Figure 27.11d presents theoretical match with the measured pressure-dependent Raman shift of $E_1(\text{LO}, 595 \text{ cm}^{-1})$, $E_2(\text{high}, 441.5 \text{ cm}^{-1})$, $E_1(\text{TO}, 410 \text{ cm}^{-1})$, $A_1(\text{TO}, 379 \text{ cm}^{-1})$, and $B_1(\text{LO}, 302 \text{ cm}^{-1})$ phonon modes for ZnO at room temperature [109, 110]. Agreement between predictions and experimental

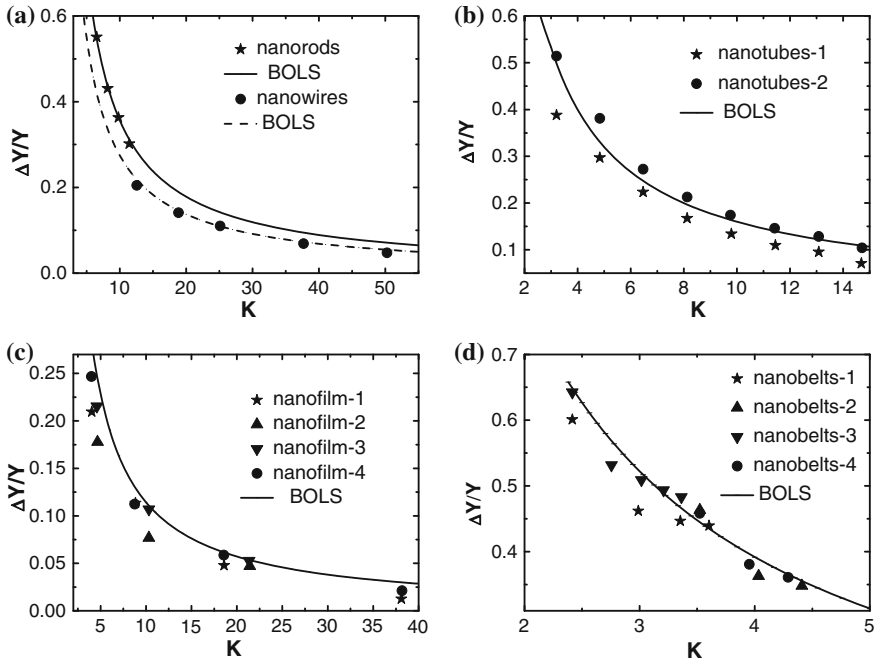


Fig. 27.10 Theoretical (solid lines) reproduction of the computed and measured (scattered) Young's modulus for ZnO **a** nanowires and nanorods [103, 104], **b** nanotubes [105], **c** nanofilms [106, 107], and **d** nanobelts [108] as a function of size K (reprinted with permission from [19])

observations allows us to determine the $\omega(1)$ of $E_1(\text{LO}, 510 \text{ cm}^{-1})$, $E_2(\text{high}, 380 \text{ cm}^{-1})$, $E_1(\text{TO}, 355 \text{ cm}^{-1})$, $A_1(\text{TO}, 330 \text{ cm}^{-1})$, and $B_1(\text{LO}, 271 \text{ cm}^{-1})$ modes. The change of the bond energy is dependent on the ambient temperature and pressure. Therefore, the competition between the thermal expansion and the pressure-induced compression determines the blue shift of Raman peaks.

- CdSe, CdS, BiSe, and BeTe

Figure 27.12 presents the T-BOLS reproduction of the size and temperature-dependent Raman shift of II–VI semiconductors. Table 27.3 features information of the atomic cohesive energy (E_{Coh}), Debye temperature (θ_{D}), and reference frequencies $\omega(1)$ derived from the reproduction, with comparison of the documented θ_{D} .

27.4.4 III–V Semiconductors

Figure 27.13 presents the TP-BOLS reproduction of the pressure and temperature-dependent Raman shift of III–V semiconductors. Table 27.4 features information

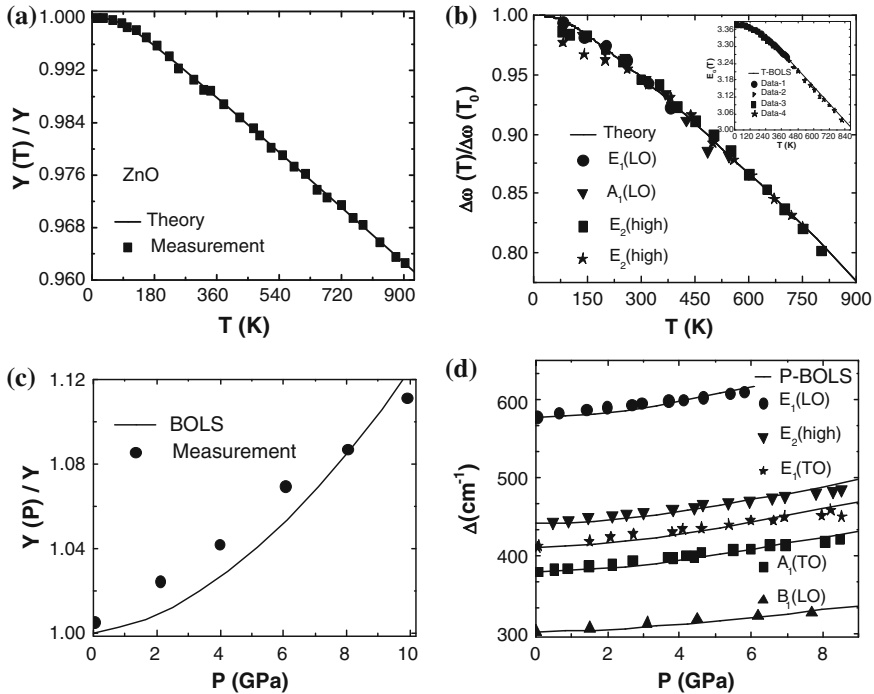


Fig. 27.11 Temperature dependence of **a** the Young’s modulus [7] and **b** the Raman shifts at the atmospheric pressure for ZnO with confirmation of $\theta_D = 310$ K and derivative of $E_b = 0.75$ eV per bond, which is in accordance with that derived from T -dependent bandgap change (inset **b** [111–114]) of ZnO [19]. Pressure dependence of **c** elastic modulus [115] and **d** optical modes [$E_1(\text{LO})$, $E_2(\text{high})$, $E_1(\text{TO})$, $A_1(\text{TO})$, and $B_1(\text{LO})$] for ZnO [109, 110] with derivative of the binding energy density (E_d) of 0.097 eV/Å³ (reprinted with permission from [19])

of the reference frequencies $\omega(1)$ and mode cohesive energy ($E_{\text{mod-coh}}$) derived from the reproduction. Debye temperature θ_D , melting point, and thermal expansion coefficient are input parameters.

27.4.5 Other Compounds

- TiO_2

The anatase TiO_2 has six Raman active modes of $3E_g$ (144, 196, and 639 cm^{-1}), $2B_{1g}$ (397 and 519 cm^{-1}), and $1A_{1g}$ (513 cm^{-1}). The rutile TiO_2 has only four Raman active modes of A_{1g} (612 cm^{-1}), B_{1g} (143 cm^{-1}), E_g (447 cm^{-1}), and B_{2g} (826 cm^{-1}). Generally, the frequency of the transverse optical (TO) phonon undergoes a red shift upon the radius R of nanosolid being decreased and almost all the modes are stiffened under high pressure and softened at elevated

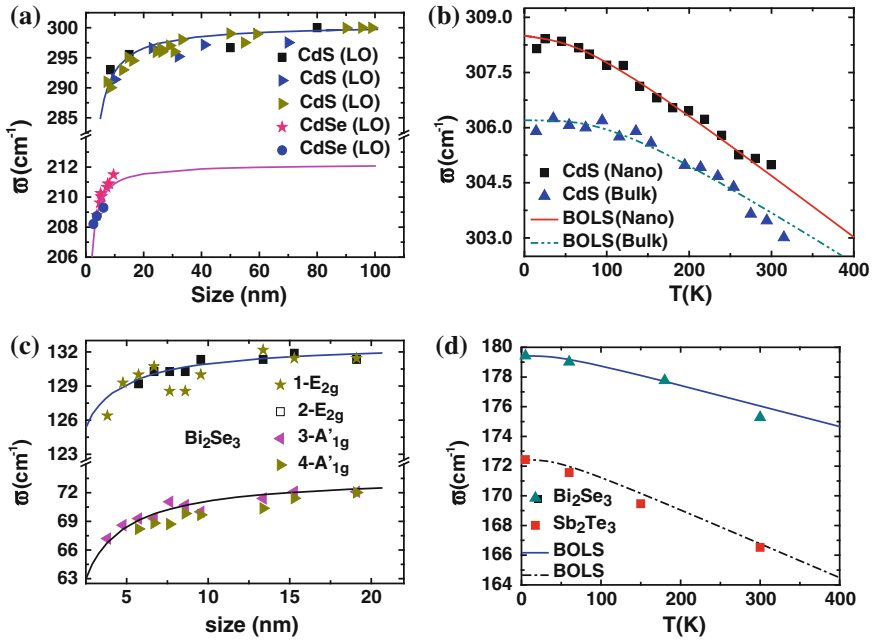


Fig. 27.12 a Size and b temperature dependence of Raman shift for CdS and CdSe [116] and c Bi₂Se₃ [117–120] and d Sb₂Te₃ [121] with derived information as given in Table 27.3

Table 27.3 Atomic cohesive energy (E_{Coh}), Debye temperature (θ_D), and reference frequencies $\omega(1)$ derived from the reproduction of the T -dependent Raman shift of Bi₂Se₃, Sb₂Te₃, and CdS bulk [122]

| | Mode | E_{Coh} (eV) | $\omega(1)$ (cm ⁻¹) | θ_D (K) | |
|---------------------------------|------------------------------|-----------------------|---------------------------------|-------------------|-----------|
| | | | | Output references | |
| CdS (bulk) | LO | 2.13 | 106.57 | 450 | 460 [123] |
| CdS (nano) | LO | 1.72 | 106.57 | 300 | 300 [123] |
| Sb ₂ Te ₃ | A _{1g} ² | 1.09 | 30.65 | 165 | 162 [124] |
| Bi ₂ Se ₃ | A _{1g} ² | 1.24 | 40.57 | 185 | 182 [125] |

temperatures [141–143]. However, for the TiO₂, the A_{1g}(612 cm⁻¹) mode of rutile phase undergoes a red shift while the E_g(144 cm⁻¹) mode of anatase phase undergoes a blue shift when the solid size is reduced [143–146].

TP-BOLS matching of the measured and calculated size [144, 147], temperature [141, 148], and pressure [148] dependence of the B and $\Delta\omega$ [149] for TiO₂ at room temperature, as shown in Fig. 27.14 allows us to verify the developed solutions and extract information as given in Table 27.5. Reproduction of TiO₂ phonons turns out $m = 5.34$ [150]. Reproduction of the E_g mode of TiO₂, shown in Fig. 27.14, revealed that the respective phonon frequency is contributed by only one neighbor ($z = 1$).

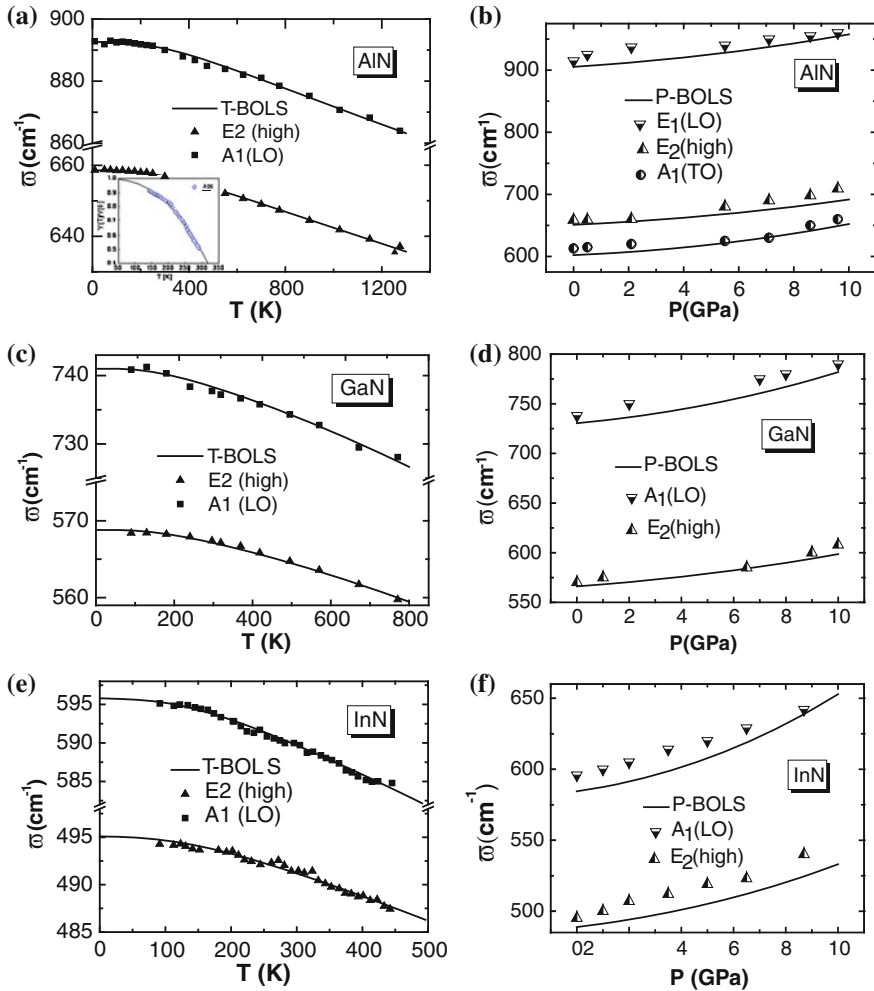


Fig. 27.13 Pressure and temperature-dependent Raman shift of (a, b) for AlN [126–129] (c, d) GaN [130–133], and (e, f) InN [134, 135]. Extracted intrinsic phonon frequency $\omega(1)$ and mode cohesive energies $E_p(0)$ for various modes are tabulated in Table 27.4 (reprinted with permission from [136])

Theoretical reproduction of the measured size dependence of (a) $Y(K)$ [147], (b) $\Delta\omega(K)$ [146] of the $E_g(144\text{ cm}^{-1})$ mode of anatase phase, and (c) $\Delta\omega(K)$ [144] of the $A_{1g}(612\text{ cm}^{-1})$ mode of rutile phase for TiO_2 at the room temperature and the atmospheric pressure with the optimized m value of 5.34 [150]. The $A_{1g}(612\text{ cm}^{-1})$ mode of rutile phase undergoes a red shift and $E_g(144\text{ cm}^{-1})$ of anatase phase goes a blue shift with size reduction [143–145].

The size-induced blue shift of Raman frequency is governed by a different mechanism that involves the coordination number $z \equiv 1$. Therefore, the Raman

Table 27.4 Melting temperature (T_m), Debye temperature (θ_D), and the temperature-dependent thermal expansion coefficient ($\alpha(T)$).

| | T_m/K | θ_D/K | α (Ref) | Raman mode | $\omega(1)$ (cm^{-1}) | $E_{\text{mod-coh}}(0)$ (eV) |
|-----|----------------|---------------------|----------------|--------------------|----------------------------------|------------------------------|
| AlN | 3,273 | 1,150 | [138] | $E_2(\text{high})$ | 658.6 | 1.13 |
| | | | | $A_1(\text{LO})$ | 892.6 | 1.21 |
| | | | | $A_1(\text{TO})$ | 613 | 0.71 |
| | | | | $E_1(\text{LO})$ | 914.7 | 1.31 |
| | | | | $E_1(\text{TO})$ | 671.6 | 1.19 |
| GaN | 2,773 | 600 | [139] | $E_2(\text{high})$ | 570.2 | 1.44 |
| | | | | $A_1(\text{LO})$ | 738 | 0.97 |
| | | | | $A_1(\text{TO})$ | 534 | 1.26 |
| | | | | $E_1(\text{LO})$ | 745 | 0.95 |
| | | | | $E_1(\text{TO})$ | 561.2 | 1.59 |
| InN | 1,373 | 600 | [140] | $E_2(\text{high})$ | 495.1 | 0.76 |
| | | | | $A_1(\text{LO})$ | 595.8 | 0.50 |

The intrinsic Raman frequency at $\omega(1)$ is extrapolated from experimental data to 0 K. The fitting results, that is the *mode* cohesive energy at 0 K, $E_{\text{mod-coh}}(0)$ of various Raman active modes [136, 137]

mode red shift arises from atomic cohesive energy weakening of the lower coordinated atoms in the surface region of nanograin, whereas the LFR blue shift is predominated by intergrain interactions. The dimer bond interaction without involvement of the neighboring numbers governs the blue shift of the $E_g(144 \text{ cm}^{-1})$ mode of anatase. Decoding the measured size dependence of the Raman optical shift turned out the vibrational information on TiO_2 dimers $\omega(1) = 610.25 \text{ cm}^{-1}$ and their bulk shifts of 1.75 cm^{-1} for the A_{1g} mode of rutile phase, and $\omega(1) = 118.35 \text{ cm}^{-1}$ and their bulk shifts of 25.65 cm^{-1} for the E_g mode of anatase phase, which is beyond the scope of direct measurement.

In the T -dependent curves, the shoulder is related to the θ_D and the slope at higher temperature depends on the atomic cohesive energy, $E_c = zE_z$. Matching the two sets of $B(T)$ and the $\Delta\omega(T)$ data will improve the reliability of the derivatives. The theoretical match of the measured T -dependent $B(T)$ [148] and the $\Delta\omega(T)$ [141] of the $E_g(639 \text{ cm}^{-1})$ mode for anatase phase TiO_2 in Fig. 27.14 leads to the $\omega(1) = 600 \text{ cm}^{-1}$ and the θ_D of 768 K, which is in good agreement with the reported value of 778 K [152]. The cohesive energy E_c is derived as 1.56 eV. At $T \leq \theta_D/3$, the relative B and $\Delta\omega$ turns from nonlinear to linear when the temperature is increased.

Theoretical reproduction of the P dependence leads to quantitative information of the compressibility and the binding energy density. Reproduction of the experimental x - P curve [149, 154, 155] derived the values of $\beta = 6.84 \times 10^{-3} \text{ GPa}^{-1}$, $\beta' = -1.21 \pm 0.05 \times 10^{-4} \text{ GPa}^{-2}$, $B_0 = 143 \text{ GPa}$, and $\beta'_0 = 8.86$ [151].

Matching the prediction to the measurement derives the binding energy density $0.182 \text{ eV}/\text{\AA}^3$. The theoretical $\Delta\omega(P)$ curve based on the relation $[\Delta\omega]^2/[Yd] \equiv 1$ showed consistency between theory and prediction of the P -dependent $B(P)$ [148] and $\Delta\omega(P)$ [143] for the $E_g(639 \text{ cm}^{-1})$ mode for anatase phase TiO_2 .

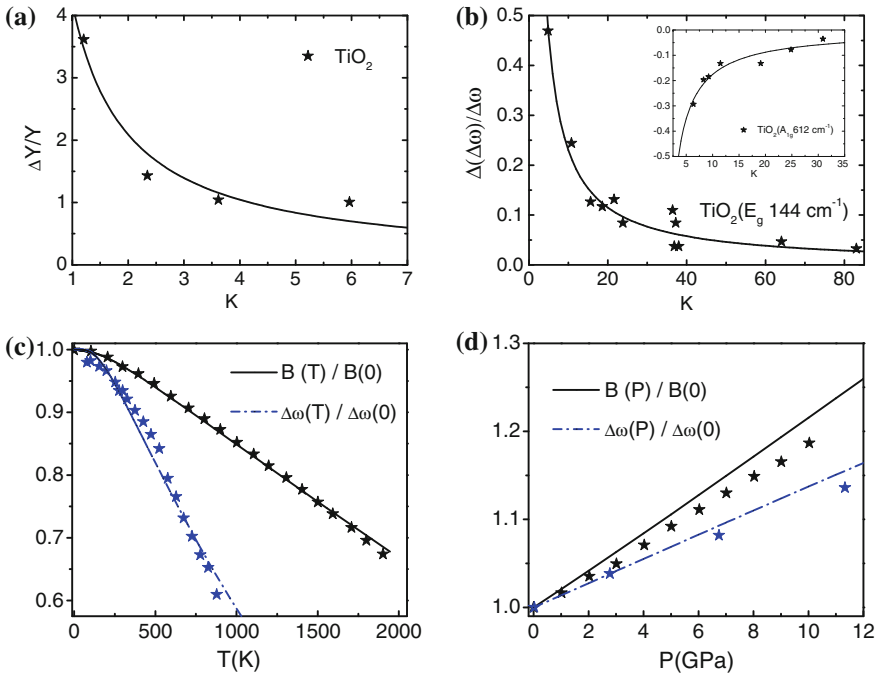


Fig. 27.14 Size dependence of **a** the elastic modulus [147] and **b** the Raman shifts [144, 146], **c** temperature [141, 148], and **d** pressure [143, 148] dependence of the bulk modulus and Raman shift A_{1g} mode (inset $E_g - 639 \text{ cm}^{-1}$) of TiO_2 [144, 151]. The paradox in the size-induced shift trends arises from the involvement of the different numbers of atomic CN of the specific atom. Theoretical matching gives rise to the mode cohesive energy and Debye temperature as listed in Table 27.5 (Reprinted with permission from [151])

Table 27.5 Parameters derived from theoretical reproduction of the size, pressure, and temperature dependence of the bulk modulus and the Raman shift for TiO_2 [151]

| Stimulus | Quantity | Value | References |
|----------|---|--|-------------|
| K | Bond nature indicator, m | 5.34 | 5.34 [150] |
| | Dimer vibration frequency, $\omega(0)(\text{cm}^{-1})$ | 610.25(A_{1g} 612) 600(E_g 639) 118.35(E_g 144) | – |
| | | | |
| T | Cohesive energy $E_c = z_p E_0(\text{eV/atom})$ | 1.56 | – |
| | Debye temperature, θ_D (K) | 768 | 778 [152] |
| P | Bulk modulus, $B_0/B'_0(\text{GPa}/-)$ | 143/8.86 | 167/- [153] |
| | Compressibility, β/β' ($\text{Gpa}^{-1}/\text{Gpa}^{-2}$) | 6.84×10^{-3} $(1.21 \pm 0.05) \times 10^{-4}$ | – |
| | Energy density, E_{den} ($\text{eV}/\text{\AA}^3$) | 0.182 | – |

Table 27.6 Parameters derived from fitting to the T dependent of the Young's modulus for given materials

| Sample | T_m (K) | θ_D (K) | $E_b(0)$ (eV) |
|------------------------------------|-----------|----------------|---------------|
| KCl [10] | 1,044 | 214 | 0.57 |
| MgSO ₄ [10] | 1,397 | 711 | 2.80 |
| Al ₂ O ₃ [5] | 2,303 | 986 | 3.90 |
| MgO [10] | 3,100 | 885 | 1.29 |
| BaTiO ₃ [156] | 1,862 | 580 | 2.50 |
| BaZrO ₃ [156] | 2,873 | 680 | 0.74 |
| BaNbO ₃ [156] | | 740 | 1.10 |

The T_m and θ_D for bulk are input and the atomic cohesive energy $E_b(0)$ are derived from the fitting [69, 56]

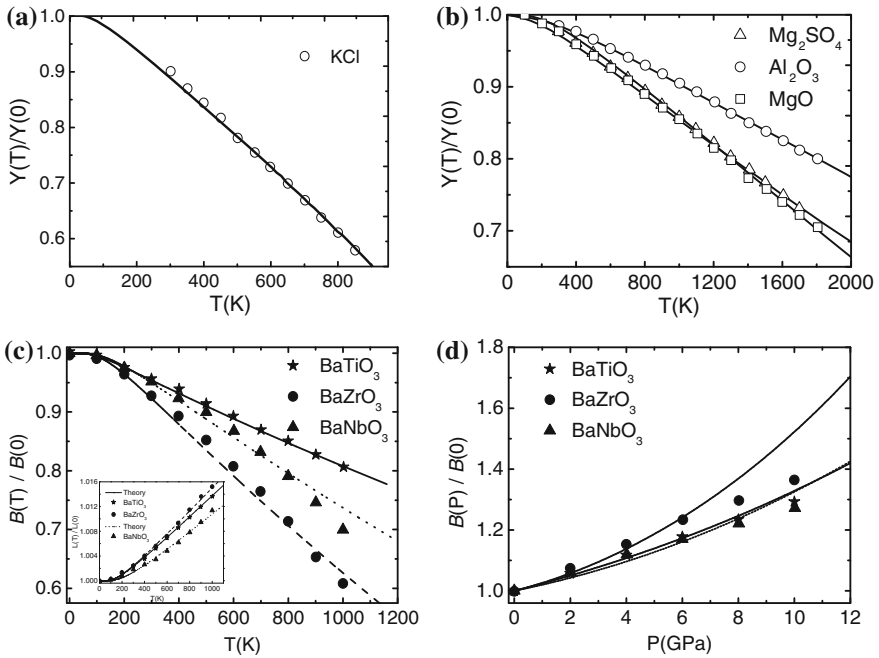


Fig. 27.15 Theoretical reproduction (solid lines) of the measured (scattered data) **a-c** T dependent and **d** P dependent of Young's modulus for various specimens [156], with derived information of mean atomic cohesive energy as listed in Table 27.6 [157]

- KCl, Al₂O₃, MgO, Mg₂SO₄, and BaXO₄

Figure 27.15 shows the match between predictions and the measured T -dependent Young's modulus for Al₂O₃, MgSO₄, MgO, and KCl with T_m and θ_D as input and atomic cohesive energy E_b as derivative. The accuracy of the derive $E_b(0)$ is subject to many factors such as surface finishing and measurement techniques.

27.5 Summary

A set of analytical expressions enables theoretical unification of the size, pressure, temperature, and bond nature dependence of elastic modulus and Raman shift to be reproduced with derivatives of the atomic cohesive energy, binding energy density, Debye temperature, specific heat, and the reference frequency of Raman shift for bulk and nanostructures. The bond relaxation in length and energy determines the correlation between these quantities and their interdependence. The followings conclude:

1. The BOLS correlation and LBA approach correlate the Young's modulus to the Raman shift.
2. The Young's modulus of a nanosolid may drop, rise, or remain unchanged with size reduction, depending on the temperature of operation, the nature of the bond involved, and experimental techniques and conditions. It is therefore not surprising to observe the elastic modulus change in different trends for different materials measured under different conditions.
3. The thermal softening arises from thermal expansion and vibration that weakens the bond through the increase in internal energy that follows Debye approximation.
4. One could not consider a single parameter on its own without addressing the rest when discussing the mechanical and thermal properties of a material, especially for a small object. One should not separate the mechanical performance from the thermal response in dealing with small objects, as they are interdependent.
5. The Debye temperature θ_D has a square root dependence on $(T_m - T)^{1/2}/d$, rather than a linear or square root dependence on T_m .
6. The specific heat capacity generally decreases when the solid size is reduced. The reduction in the specific heat capacity is more pronounced for larger m values at lower temperatures.
7. The elastic modulus correlates to the Raman frequency whose shift is proportional to the square root of the bond stiffness.
8. Reproduction of the T- and P-dependence of the Raman shift and elastic modulus derives the bond length, bond energy, energy density, atomic cohesive energy and the Debye temperature.

Therefore, the macroscopically measurable B and $\Delta\omega$ connect directly to the bond length and energy of the specimen and their response to the intrinsic coordination imperfection and the applied stimuli through the BOLS correlation and the LBA approach. Exercises lead to derived information of the cohesive energy and Debye temperature, energy density, compressibility, the bulk modulus and their first-order derivatives, and the analytical correlation between the B and $\Delta\omega$.

The LBA and BOLS would provide a useful yet simple way to unify the mechanical and vibration properties of a specimen under the change of atomic coordination, thermal, and mechanical activation. With the developed premise, one can predict the changing trends of all the concerned properties and can derive quantitative information as such from any single measurement alone.

References

1. G. Ouyang, X.L. Li, X. Tan, G.W. Yang, Size-induced strain and stiffness of nanocrystals. *Appl. Phys. Lett.* **89**(3), 031904 (2006)
2. G. Ouyang, X. Tan, G.W. Yang, Thermodynamic model of the surface energy of nanocrystals. *Phys. Rev. B* **74**(19), 195408 (2006)
3. Y.L. Liu, Y. Zhang, H.B. Zhou, G.H. Lu, M. Kohyama, Theoretical strength and charge redistribution of fcc Ni in tension and shear. *J. Phys. Condens. Matter* **20**(33), 335216 (2008)
4. U. Gysin, S. Rast, P. Ruff, E. Meyer, D.W. Lee, P. Vettiger, C. Gerber, Temperature dependence of the force sensitivity of silicon cantilevers. *Phys. Rev. B* **69**(4), 045403 (2004)
5. J.B. Wachtman, W.E. Tefft, D.G. Lam, C.S. Apstein, Exponential temperature dependence of young's modulus for several oxides. *Phys. Rev.* **122**(6), 1754 (1961)
6. G.A. Alers, D.L. Waldorf, Variation of the elastic moduli at the superconducting transition. *Phys. Rev. Lett.* **6**(12), 677–679 (1961)
7. A.K. Swarnakar, L. Donzel, J. Vleugels, O. Van der Biest, High temperature properties of ZnO ceramics studied by the impulse excitation technique. *J. Eur. Ceram. Soc.* **29**(14), 2991–2998 (2009)
8. R. Chang, L.J. Graham, Low-temperature elastic properties of ZrC and TiC. *J. Appl. Phys.* **37**(10), 3778–3783 (1966)
9. O.L. Anderson, Derivation of Wachtman's equation for the temperature dependence of elastic moduli of oxide compounds. *Phys. Rev.* **144**(2), 553–557 (1966)
10. J. Garai, A. Laugier, The temperature dependence of the isothermal bulk modulus at 1 bar pressure. *J. Appl. Phys.* **101**(2), 2424535 (2007)
11. S. Rast, C. Wattering, U. Gysin, E. Meyer, Dynamics of damped cantilevers. *Rev. Sci. Instrum.* **71**(7), 2772–2775 (2000)
12. U. Rabe, K. Janser, W. Arnold, Vibrations of free and surface-coupled atomic force microscope cantilevers: Theory and experiment. *Rev. Sci. Instrum.* **67**(9), 3281–3293 (1996)
13. J. Liu, Y.K. Vohra, Raman modes of 6H polytype of silicon carbide to ultrahigh pressures: a comparison with silicon and diamond. *Phys. Rev. Lett.* **72**(26), 4105 (1994)
14. Z.W. Chen, C.Q. Sun, Y.C. Zhou, O.Y. Gang, Size dependence of the pressure-induced phase transition in nanocrystals. *J. Chem. Phys. C* **112**(7), 2423–2427 (2008)
15. S. Desgreniers, High-density phases of ZnO: Structural and compressive parameters. *Phys. Rev. B* **58**(21), 14102 (1998)
16. H. Sowa, H. Ahsbahs, High-pressure X-ray investigation of zincite ZnO single crystals using diamond anvils with an improved shape. *J. Appl. Crystallogr.* **39**(2), 169–175 (2006)
17. F. Decremps, F. Datchi, A.M. Saitta, A. Polian, S. Pascarelli, A. Di Cicco, J.P. Iti, F. Baudalet, Local structure of condensed zinc oxide. *Phys. Rev. B.* **68**(10), 015502 (2003)
18. H. Karzel, W. Potzel, M. Köfferlein, W. Schiessl, M. Steiner, U. Hiller, G.M. Kalvius, D.W. Mitchell, T.P. Das, P. Blaha, K. Schwarz, M.P. Pasternak, Lattice dynamics and hyperfine interactions in ZnO and ZnSe at high external pressures. *Phys. Rev. B* **53**(17), 11425–11438 (1996)
19. J.W. Li, S.Z. Ma, X.J. Liu, Z.F. Zhou, C.Q. Sun, ZnO meso-mechano-thermo physical chemistry. *Chem. Rev.* **112**(5), 2833–2852 (2012)

20. P.R. Couchman, F.E. Karasz, Effect of particle-size on Debye temperature. *Phys. Lett. A* **62**(1), 59–61 (1977)
21. A. Balerna, S. Mobilio, Dynamic properties and debye temperatures of bulk au and au clusters studied using extended x-ray-absorption fine-structure spectroscopy. *Phys. Rev. B* **34**(4), 2293–2298 (1986)
22. Y.H. Zhao, K. Lu, Grain-size dependence of thermal properties of nanocrystalline elemental selenium studied by x-ray diffraction. *Phys. Rev.B* **56**(22), 14330–14337 (1997)
23. C.C. Yang, M.X. Xiao, W. Li, Q. Jiang, Size effects on Debye temperature, Einstein temperature, and volume thermal expansion coefficient of nanocrystals. *Solid State Commun.* **139**(4), 148–152 (2006)
24. M.A. Shandiz, Effective coordination number model for the size dependency of physical properties of nanocrystals. *J. Phys. Condens. Matter* **20**(32), 325237 (2008)
25. R.C.G. Killean, E.J. Lisher, Debye temperatures of cubic elements and their relationship to melting points. *J. Phys. C-Solid State Phys.* **8**(21), 3510–3520 (1975)
26. S.A. Peng, G. Grimvall, Bonding and Debye temperatures in alkali earth-metal halides. *J. Phys. Chem. Solids* **55**(8), 707–710 (1994)
27. C.J. Martin, D.A. Oconnor, Experimental test of Lindemanns melting law. *J. Phys. C-Solid State Phys.* **10**(18), 3521–3526 (1977)
28. F.A. Lindemann, The calculation of molecular natural frequencies. *Physikalische Zeitschrift* **11**, 609–612 (1910)
29. V. Novotny, J.H.P. Watson, P.P.M. Meincke, Effect of size and surface on specific-heat of small lead particles. *Phys. Rev. Lett.* **28**(14), 901 (1972)
30. Q.L. Song, Z. Cui, S.H. Xia, S.F. Chen, An ac microcalorimeter for measuring specific heat of thin films. *Microelectron. J.* **35**(10), 817–821 (2004)
31. Y. Lu, Q.L. Song, S.H. Xia, Calculation of specific heat for aluminium thin films. *Chin. Phys. Lett.* **22**(9), 2346–2348 (2005)
32. J. Yu, Z.A. Tang, F.T. Zhang, G.F. Wei, L.D. Wang, Investigation of a microcalorimeter for thin-film heat capacity measurement. *Chin. Phys. Lett.* **22**(9), 2429–2432 (2005)
33. K. Lu, Nanocrystalline metals crystallized from amorphous solids: Nanocrystallization, structure, and properties. *Mater. Sci. Eng. R-Rep.* **16**(4), 161–221 (1996)
34. R.S. Prasher, P.E. Phelan, Non-dimensional size effects on the thermodynamic properties of solids. *Int. J. Heat Mass Transf.* **42**(11), 1991–2001 (1999)
35. M.X. Gu, C.Q. Sun, Z. Chen, T.C.A. Yeung, S. Li, C.M. Tan, V. Nosik, Size, temperature, and bond nature dependence of elasticity and its derivatives on extensibility, Debye temperature, and heat capacity of nanostructures. *Phys Rev B* **75**(12), 125403 (2007)
36. X.X. Yang, J.W. Li, Z.F. Zhou, Y. Wang, L.W. Yang, W.T. Zheng, C.Q. Sun, Raman spectroscopic determination of the length, strength, compressibility, Debye temperature, elasticity, and force constant of the C–C bond in graphene. *Nanoscale* **4**(2), 502–510 (2012)
37. C.Q. Sun, Thermo-mechanical behavior of low-dimensional systems: The local bond average approach. *Prog. Mater. Sci.* **54**(2), 179–307 (2009)
38. M.A. Haque, M.T.A. Saif, Thermo-mechanical properties of nano-scale freestanding aluminum films. *Thin Solid Films* **484**(1–2), 364–368 (2005)
39. Y.H. Wu, F.J. McGarry, B.Z. Zhu, J.R. Keryk, D.E. Katsoulis, Temperature effect on mechanical properties of toughened silicone resins. *Polym. Eng. Sci.* **45**(11), 1522–1531 (2005)
40. B. Chen, D. Penwell, L.R. Benedetti, R. Jeanloz, M.B. Kruger, Particle-size effect on the compressibility of nanocrystalline alumina. *Phys. Rev.B* **66**(14), 144101 (2002)
41. S. Vennila, S.R. Kulkarni, S.K. Saxena, H.P. Liermann, S.V. Sinogeikin, Compression behavior of nanosized nickel and molybdenum. *Appl. Phys. Lett.* **89**(26), 261901 (2006)
42. F. Szuecs, M. Werner, R.S. Sussmann, C.S.J. Pickles, H.J. Fecht, Temperature dependence of Young's modulus and degradation of chemical vapor deposited diamond. *J. Appl. Phys.* **86**(11), 6010–6017 (1999)
43. N. Ono, R. Nowak, S. Miura, Effect of deformation temperature on Hall-Petch relationship registered for polycrystalline magnesium. *Mater. Lett.* **58**(1–2), 39–43 (2004)

44. D.G. Eskin, A. Suyitno, L. Katgerman, Mechanical properties in the semi-solid state and hot tearing of aluminium alloys. *Prog. Mater. Sci.* **49**(5), 629–711 (2004)
45. S.B. Qadri, J. Yang, B.R. Ratna, E.F. Skelton, J.Z. Hu, Pressure induced structural transitions in nanometer size particles of PbS. *Appl. Phys. Lett.* **69**(15), 2205–2207 (1996)
46. L. Lu, M.L. Sui, K. Lu, Superplastic extensibility of nanocrystalline copper at room temperature. *Science* **287**(5457), 1463–1466 (2000)
47. K.S. Siow, A.A.O. Tay, P. Oruganti, Mechanical properties of nanocrystalline copper and nickel. *Mater. Sci. Technol.* **20**(3), 285–294 (2004)
48. W.W. Gerberich, W.M. Mook, C.R. Perrey, C.B. Carter, M.I. Baskes, R. Mukherjee, A. Gidwani, J. Heberlein, P.H. McMurry, S.L. Girshick, Superhard silicon nanospheres. *J. Mech. Phys. Solids* **51**(6), 979–992 (2003)
49. C.Q. Chen, Y. Shi, Y.S. Zhang, J. Zhu, Y.J. Yan, Size dependence of Young's modulus in ZnO nanowires. *Phys. Rev. Lett.* **96**(7), 075505 (2006)
50. X.X. Li, T. Ono, Y.L. Wang, M. Esashi, Ultrathin single-crystalline-silicon cantilever resonators: Fabrication technology and significant specimen size effect on Young's modulus. *Appl. Phys. Lett.* **83**(15), 3081–3083 (2003)
51. C.Q. Sun, B.K. Tay, S.P. Lau, X.W. Sun, X.T. Zeng, S. Li, H.L. Bai, H. Liu, Z.H. Liu, E.Y. Jiang, Bond contraction and lone pair interaction at nitride surfaces. *J. Appl. Phys.* **90**(5), 2615–2617 (2001)
52. Q.F. Gu, G. Krauss, W. Steurer, F. Gramm, A. Cervellino, Unexpected high stiffness of Ag and Au nanoparticles. *Phys. Rev. Lett.* **100**(4), 045502 (2008)
53. M.X. Gu, Y.C. Zhou, C.Q. Sun, Local bond average for the thermally induced lattice expansion. *J. Phys. Chem. B* **112**(27), 7992–7995 (2008)
54. F.H. Streitz, R.C. Cammarata, K. Sieradzki, Surface-stress effects on elastic properties I Thin metal-films. *Phys. Rev. B* **49**(15), 10699–10706 (1994)
55. M.T. McDowell, A.M. Leach, K. Gaill, On the elastic modulus of metallic nanowires. *Nano Lett.* **8**(11), 3613–3618 (2008)
56. J. Li, Y.X. Li, X. Yu, W.J. Ye, C.Q. Sun, Local bond average for the thermally driven elastic softening of solid specimens. *J. Phys. D-Appl. Phys.* **42**(4), 045406 (2009)
57. C.D. Martin, S.M. Antao, P.J. Chupas, P.L. Lee, S.D. Shastri, J.B. Parise, Quantitative high-pressure pair distribution function analysis of nanocrystalline gold. *Appl. Phys. Lett.* **86**(6), 061910 (2005)
58. K. Syassen, W.B. Holzapfel, Isothermal compression of Al and Ag to 120 KBar. *J. Appl. Phys.* **49**(8), 4427–4430 (1978)
59. D.L. Heinz, R. Jeanloz, The equation of state of the gold calibration standard. *J. Appl. Phys.* **55**(4), 885–893 (1984)
60. J. Menendez, M. Cardona, Temperature-dependence of the 1st-order raman-scattering by phonons in Si, Ge, and a-Sn-anharmonic effects. *Phys. Rev. B* **29**(4), 2051–2059 (1984)
61. M.E. Fine, Elasticity and thermal expansion of germanium between 195 deg-C 275 deg-C. *J. Appl. Phys.* **24**(3), 338–340 (1953)
62. T.R. Hart, R.L. Aggarwal, B. Lax, Temperature dependence of Raman scattering in silicon. *Phys. Rev. B-Solid State* **1**(2), 638 (1970)
63. M. Balkanski, R.F. Wallis, E. Haro, Anharmonic effects in light-scattering due to optical phonons in silicon. *Phys. Rev. B* **28**(4), 1928–1934 (1983)
64. M.S. Liu, L.A. Bursill, S. Prawer, R. Beserman, Temperature dependence of the first-order Raman phonon line of diamond. *Phys. Rev. B* **61**(5), 3391–3395 (2000)
65. J.B. Cui, K. Amtmann, J. Ristein, L. Ley, Noncontact temperature measurements of diamond by Raman scattering spectroscopy. *J. Appl. Phys.* **83**(12), 7929–7933 (1998)
66. H. Herchen, M.A. Cappelli, 1 st-order Raman-spectrum of diamond at high-temperatures. *Phys. Rev. B* **43**(14), 11740–11744 (1991)
67. E.S. Zouboulis, M. Grimsditch, Raman-scattering in diamond up to 1900-K. *Phys. Rev. B* **43**(15), 12490–12493 (1991)

68. D.A. Czaplewski, J.P. Sullivan, T.A. Friedmann, J.R. Wendt, Temperature dependence of the mechanical properties of tetrahedrally coordinated amorphous carbon thin films. *Appl. Phys. Lett.* **87**(16), 2108132 (2005)
69. M.X. Gu, Y.C. Zhou, L.K. Pan, Z. Sun, S.Z. Wang, C.Q. Sun, Temperature dependence of the elastic and vibronic behavior of Si, Ge, and diamond crystals. *J. Appl. Phys.* **102**(8), 083524 (2007)
70. C. Kittel, *Introduction to Solid State Physics*, 8th edn. (Wiley, New York, 2005)
71. C.O. Girit, J.C. Meyer, R. Erni, M.D. Rossell, C. Kisielowski, L. Yang, C.H. Park, M.F. Crommie, M.L. Cohen, S.G. Louie, A. Zettl, Graphene at the edge: Stability and dynamics. *Science* **323**(5922), 1705–1708 (2009)
72. W.T. Zheng, C.Q. Sun, Underneath the fascinations of carbon nanotubes and graphene nanoribbons. *Energy Environ. Sci.* **4**(3), 627–655 (2011)
73. X. Zhang, Y.G. Nie, W.T. Zheng, J.L. Kuo, C.Q. Sun, Discriminative generation and hydrogen modulation of the Dirac-Fermi polarons at graphene edges and atomic vacancies. *Carbon* **49**(11), 3615–3621 (2011)
74. K.S. Novoselov, Z. Jiang, Y. Zhang, S.V. Morozov, H.L. Stormer, U. Zeitler, J.C. Maan, G.S. Boebinger, P. Kim, A.K. Geim, Room-temperature quantum hall effect in graphene. *Science* **315**(5817), 1379 (2007)
75. K.S. Novoselov, A.K. Geim, S.V. Morozov, D. Jiang, Y. Zhang, S.V. Dubonos, I.V. Grigorieva, A.A. Firsov, Electric field effect in atomically thin carbon films. *Science* **306**(5696), 666–669 (2004)
76. X.X. Yang, J.W. Li, Z.F. Zhou, Y. Wang, W.T. Zheng, C.Q. Sun, Frequency response of graphene phonons to heating and compression. *Appl. Phys. Lett.* **99**(13), 133108 (2011)
77. Y. Wang, X.X. Yang, J.W. Li, Z.F. Zhou, W.T. Zheng, C.Q. Sun, Number-of-layer discriminated graphene phonon softening and stiffening. *Appl. Phys. Lett.* **99**(16), 163109 (2011)
78. D. Graf, F. Molitor, K. Ensslin, C. Stampfer, A. Jungen, C. Hierold, L. Wirtz, Spatially resolved raman spectroscopy of single- and few-layer graphene. *Nano Lett.* **7**(2), 238–242 (2007)
79. A. Gupta, G. Chen, P. Joshi, S. Tadigadapa, P.C. Eklund, Raman scattering from high-frequency phonons in supported n-graphene layer films. *Nano Lett.* **6**(12), 2667–2673 (2006)
80. H. Wang, Y. Wang, X. Cao, M. Feng, G. Lan, Vibrational properties of graphene and graphene layers. *J. Raman Spectrosc.* **40**(12), 1791–1796 (2009)
81. A.K. Gupta, T.J. Russin, H.R. Gutierrez, P.C. Eklund, Probing graphene edges via Raman scattering. *ACS Nano* **3**(1), 45–52 (2008)
82. C. Thomsen, S. Reich, Double resonant Raman scattering in graphite. *Phys. Rev. Lett.* **85**(24), 5214–5217 (2000)
83. T.M.G. Mohiuddin, A. Lombardo, R.R. Nair, A. Bonetti, G. Savini, R. Jalil, N. Bonini, D.M. Basko, C. Galiotis, N. Marzari, K.S. Novoselov, A.K. Geim, A.C. Ferrari, Uniaxial strain in graphene by Raman spectroscopy: G peak splitting, Gruneisen parameters, and sample orientation. *Phys. Rev. B* **79**(20), 205433 (2009)
84. F. Ding, H. Ji, Y. Chen, A. Herklotz, K. Dorr, Y. Mei, A. Rastelli, O.G. Schmidt, Stretchable Graphene: A close look at fundamental parameters through biaxial straining. *Nano Lett.* **10**(9), 3453–3458 (2010)
85. C.Q. Sun, Y. Sun, Y.G. Nie, Y. Wang, J.S. Pan, G. Ouyang, L.K. Pan, Z. Sun, Coordination-resolved C–C bond length and the c 1s binding energy of carbon allotropes and the effective atomic coordination of the few-layer Graphene. *J. Chem. Phys. C* **113**(37), 16464–16467 (2009)
86. M. He, E. Rikkinen, Z. Zhu, Y. Tian, A.S. Anisimov, H. Jiang, A.G. Nasibulin, E.I. Kauppinen, M. Niemela, A.O.I. Krause, Temperature dependent Raman spectra of carbon nanobuds. *J. Phys. Chem. C* **114**(32), 13540–13545 (2010)
87. M. Matus, H. Kuzmany, Raman spectra of single-crystal C < sub > 60 </sub>. *Appl. Phys. A Mater. Sci. Process.* **56**(3), 241–248 (1993)

88. I. Calizo, A.A. Balandin, W. Bao, F. Miao, C.N. Lau, Temperature Dependence of the Raman Spectra of Graphene and Graphene Multilayers. *Nano Lett.* **7**(9), 2645–2649 (2007)
89. N.J. Everall, J. Lumsdon, D.J. Christopher, The effect of laser-induced heating upon the vibrational raman spectra of graphites and carbon fibres. *Carbon* **29**(2), 133–137 (1991)
90. I. Calizo, F. Miao, W. Bao, C.N. Lau, A.A. Balandin, Variable temperature Raman microscopy as a nanometrology tool for graphene layers and graphene-based devices. *Appl. Phys. Lett.* **91**(7), 071913–071916 (2007)
91. Z. Zhou, X. Dou, L. Ci, L. Song, D. Liu, Y. Gao, J. Wang, L. Liu, W. Zhou, S. Xie, D. Wan, Temperature dependence of the Raman spectra of individual carbon nanotubes. *J. Phys. Chem. B* **110**(3), 1206–1209 (2006)
92. S. Chiashi, Y. Murakami, Y. Miyauchi, S. Maruyama, Temperature dependence of raman scattering from single-walled carbon nanotubes: Undefined radial breathing mode peaks at high temperatures. *Jap. J. Appl. Phys.* **47**(4), 2010–2015 (2008)
93. H. Boppart, J. van Straaten, I.F. Silvera, Raman spectra of diamond at high pressures. *Phys. Rev. B* **32**(2), 1423–1425 (1985)
94. A. Merlen, N. Bendiab, P. Toulemonde, A. Aouizerat, A. San Miguel, J.L. Sauvajol, G. Montagnac, H. Cardon, P. Petit, Resonant Raman spectroscopy of single-wall carbon nanotubes under pressure. *Phys. Rev. B* **72**(3), 035409–035415 (2005)
95. J.E. Proctor, E. Gregoryanz, K.S. Novoselov, M. Lotya, J.N. Coleman, M.P. Halsall, High-pressure Raman spectroscopy of graphene. *Phys. Rev. B.* **80**(7), 073408 (2009)
96. M. Hanfland, H. Beister, K. Syassen, Graphite under pressure: Equation of state and first-order Raman modes. *Phys. Rev. B* **39**(17), 12598–12603 (1989)
97. X.X. Yang, Z.F. Zhou, Y. Wang, J.W. Li, N.G. Guo, W.T. Zheng, J.Z. Peng, C.Q. Sun, Raman spectroscopic determination of the length, energy, Debye temperature, and compressibility of the C–C bond in carbon allotropes. *Chem. Phys. Lett.* **575**, 86–90 (2013)
98. F.C. Marques, R.G. Lacerda, A. Champi, V. Stolojan, D.C. Cox, S.R.P. Silva, Thermal expansion coefficient of hydrogenated amorphous carbon. *Appl. Phys. Lett.* **83**(15), 3099–3101 (2003)
99. R. Kalish, Ion-implantation in diamond and diamond films: Doping, damage effects and their applications. *Appl. Surf. Sci.* **117**, 558–569 (1997)
100. S. Reich, C. Thomsen, P. Ordejon, Elastic properties of carbon nanotubes under hydrostatic pressure. *Phys. Rev. B* **65**(15), 153407–153411 (2002)
101. D.L. Farber, J. Badro, C.M. Aracne, D.M. Teter, M. Hanfland, B. Canny, B. Couzinet, Experimental evidence for a high-pressure isostructural phase transition in osmium. *Phys. Rev. Lett.* **93**(9), 095502–095506 (2004)
102. W.R. Panero, R. Jeanloz, X-ray diffraction patterns from samples in the laser-heated diamond anvil cell. *J. Appl. Phys.* **91**(5), 2769–2778 (2002)
103. R. Agrawal, B. Peng, E.E. Gdoutos, H.D. Espinosa, Elasticity size effects in ZnO nanowires—a combined experimental-computational approach. *Nano Lett.* **8**(11), 3668–3674 (2008)
104. J. Wang, A.J. Kulkarni, F.J. Ke, Y.L. Bai, M. Zhou, Novel mechanical behavior of ZnO nanorods. *Comput. Meth. Appl. Mech. Eng.* **197**(41–42), 3182–3189 (2008)
105. W. Moon, H. Hwang, Atomistic study of structures and elastic properties of single crystalline ZnO nanotubes. *Nanotechnology* **19**(22), 225703 (2008)
106. G. Cao, X. Chen, Energy analysis of size-dependent elastic properties of ZnO nanofilms using atomistic simulations. *Phys. Rev. B* **76**(16), 165407 (2007)
107. G.X. Cao, X. Chen, Size dependence and orientation dependence of elastic properties of ZnO nanofilms. *Int. J. Solids Struct.* **45**(6), 1730–1753 (2008)
108. J.S. Qi, D.N. Shi, J.M. Jia, First-principles studies of the electronic and mechanical properties of ZnO nanobelts with different dominant surfaces. *Nanotechnology* **19**(43), 435707 (2008)
109. F. Decremps, J. Pellicer-Porres, A.M. Saitta, J.-C. Chervin, A. Polian, High-pressure Raman spectroscopy study of wurtzite ZnO. *Phys. Rev. B* **65**(9), 092101 (2002)

110. J. Serrano, A.H. Romero, F.J. Manjon, R. Lauck, M. Cardona, A. Rubio, Pressure dependence of the lattice dynamics of ZnO: An ab initio approach. *Phys. Rev.B* **69**(9), 094306 (2004)
111. H. Alawadhi, S. Tsoi, X. Lu, A.K. Ramdas, M. Grimsditch, M. Cardona, R. Lauck, Effect of temperature on isotopic mass dependence of excitonic band gaps in semiconductors: ZnO. *Phys. Rev.B* **75**(20), 205207 (2007)
112. V.V. Ursaki, I.M. Tiginyanu, V.V. Zalamai, E.V. Rusu, G.A. Emelchenko, V.M. Masalov, E.N. Samarov, Multiphonon resonant Raman scattering in ZnO crystals and nanostructured layers. *Phys. Rev.B* **70**(15), 155204 (2004)
113. S.H. Eom, Y.M. Yu, Y.D. Choi, C.S. Kim, Optical characterization of ZnO whiskers grown without catalyst by hot wall epitaxy method. *J. Cryst. Growth* **284**(1–2), 166–171 (2005)
114. R. Hauschild, H. Priller, M. Decker, J. Bruckner, H. Kalt, C. Klingshirn, Temperature dependent band gap and homogeneous line broadening of the exciton emission in ZnO. *Phys. Status Solidi C* **3**(4), 976–979 (2006)
115. Y. Fei, S. Cheng, L.B. Shi, H.K. Yuan, Phase transition, elastic property and electronic structure of wurtzite and rocksalt ZnO. *J. Synth. Cryst.* **38**(6), 1527–1531 (2009)
116. E.S.F. Neto, N.O. Dantas, S.W.d Silva, P.C. Morais, M.A.P.d Silva, A.J.D. Moreno, V.L. Richard, G.E. Marques, C.T. Giner, Temperature-dependent Raman study of thermal parameters in CdS quantum dots. *Nanotechnology* **23**(12), 125701 (2012)
117. J. Zhang, Z. Peng, A. Soni, Y. Zhao, Y. Xiong, B. Peng, J. Wang, M.S. Dresselhaus, Q. Xiong, Raman spectroscopy of few-quintuple layer topological insulator Bi₂Se₃ nanoplatelets. *Nano Lett.* **11**(6), 2407–2414 (2011)
118. D.S. Chuu, C.M. Dai, Quantum size effects in CdS thin films. *Phys. Rev. B* **45**(20), 11805–11810 (1992)
119. A. Tanaka, S. Onari, T. Arai, Raman scattering from CdSe microcrystals embedded in a germanate glass matrix. *Phys. Rev. B* **45**(12), 6587 (1992)
120. Y.N. Hwang, S.H. Park, D. Kim, Size-dependent surface phonon mode of CdSe quantum dots. *Phys. Rev. B* **59**(11), 7285 (1999)
121. Y. Kim, X. Chen, Z. Wang, J. Shi, I. Miotkowski, Y.P. Chen, P.A. Sharma, A.L.L. Sharma, M.A. Hekmaty, Z. Jiang, D. Smirnov, Temperature dependence of Raman-active optical phonons in Bi[_{sub} 2]Se[_{sub} 3] and Sb[_{sub} 2]Te[_{sub} 3]. *Appl. Phys. Lett.* **100**(7), 071907 (2012)
122. X.X. Yang, Z.F. Zhou, Y. Wang, R. Jiang, W.T. Zheng, C.Q. Sun, Raman spectroscopy determination of the Debye temperature and atomic cohesive energy of CdS, CdSe, Bi₂Se₃, and Sb₂Te₃ nanostructures. *J. Appl. Phys.* **112**(8), 4759207 (2012)
123. J. Rockenberger, L. Tröger, A. Kornowski, T. Vossmeier, A. Eychmüller, J. Feldhaus, H. Weller, EXAFS studies on the size dependence of structural and dynamic properties of CdS nanoparticles. *J. Phys. Chem. B* **101**(14), 2691 (1997)
124. J.S. Dyck, W. Chen, C. Uher, Č. Drašar, and P. Lošt'ák, Heat transport in Sb₂(2-x)V_xTe₃ single crystals. *Phys. Rev. B.* **66**(12), 125206 (2002)
125. G.E. Shoemaker, J.A. Rayne, R.W.J. Ure, Specific heat of n- and p-type Bi₂Te₃ from 1.4 to 90°K. *Phys. Rev.* **185**(3), 1046 (1969)
126. P. Perlin, A. Polian, T. Suski, Raman-scattering studies of aluminum nitride at high-pressure. *Phys. Rev. B* **47**(5), 2874–2877 (1993)
127. M. Kuball, J.M. Hayes, A.D. Prins, N.W.A. van Uden, D.J. Dunstan, Y. Shi, J.H. Edgar, Raman scattering studies on single-crystalline bulk AlN under high pressures. *Appl. Phys. Lett.* **78**(6), 724–726 (2001)
128. M. Ueno, A. Onodera, O. Shimomura, K. Takemura, X-ray-observation of the structural phase-transition of aluminium nitride under high-pressure. *Phys. Rev. B* **45**(17), 10123–10126 (1992)
129. M. Kuball, J.M. Hayes, Y. Shi, J.H. Edgar, A.D. Prins, N.W.A. van Uden, D.J. Dunstan, Raman scattering studies on single-crystalline bulk AlN: temperature and pressure dependence of the AlN phonon modes. *J. Cryst. Growth* **231**(3), 391–396 (2001)

130. M.P. Halsall, P. Harmer, P.J. Parbrook, S.J. Henley, Raman scattering and absorption study of the high-pressure wurtzite to rocksalt phase transition of GaN. *Phys. Rev. B* **69**(23), 235207 (2004)
131. P. Perlin, C. Jaubertiecarillon, J.P. Itie, A. SanMiguel, I. Grzegory, A. Polian, Raman-scattering and x-ray-absorption spectroscopy in gallium nitride under high-pressure. *Phys. Rev. B* **45**(1), 83–89 (1992)
132. S. Limpijumng, W.R.L. Lambrecht, Homogeneous strain deformation path for the wurtzite to rocksalt high-pressure phase transition in GaN. *Phys. Rev. Lett.* **86**(1), 91–94 (2001)
133. A. Link, K. Bitzer, W. Limmer, R. Sauer, C. Kirchner, V. Schwegler, M. Kamp, D.G. Ebling, K.W. Benz, Temperature dependence of the E-2 and A(1)(LO) phonons in GaN and AlN. *J. Appl. Phys.* **86**(11), 6256–6260 (1999)
134. C. Pinquier, F. Demangeot, J. Frandon, J.C. Chervin, A. Polian, B. Couzinet, P. Munsch, O. Briot, S. Ruffenach, B. Gil, B. Maleyre, Raman scattering study of wurtzite and rocksalt InN under high pressure. *Phys. Rev. B* **73**(11), 115211 (2006)
135. X.D. Pu, J. Chen, W.Z. Shen, H. Ogawa, Q.X. Guo, Temperature dependence of Raman scattering in hexagonal indium nitride films. *J. Appl. Phys.* **98**(3), 2006208 (2005)
136. M.X. Gu, L.K. Pan, T.C.A. Yeung, B.K. Tay, C.Q. Sun, Atomistic origin of the thermally driven softening of Raman optical phonons in group III nitrides. *J. Chem. Phys. C* **111**(36), 13606–13610 (2007)
137. G. Ouyang, C.Q. Sun, W.G. Zhu, Pressure-stiffened Raman phonons in group III nitrides: A local bond average approach. *J. Phys. Chem. B* **112**(16), 5027–5031 (2008)
138. L.K. Pan, C.Q. Sun, C.M. Li, Elucidating Si–Si dimmer vibration from the size-dependent Raman shift of nanosolid Si. *J. Phys. Chem. B* **108**(11), 3404–3406 (2004)
139. R.R. Reeber, K. Wang, Lattice parameters and thermal expansion of GaN. *J. Mater. Res.* **15**(1), 40–44 (2000)
140. G.A. Slack, S.F. Bartram, Thermal expansion of some diamond-like crystals. *J. Appl. Phys.* **46**(1), 89–98 (1975)
141. Y.L. Du, Y. Deng, M.S. Zhang, Variable-temperature Raman scattering study on anatase titanium dioxide nanocrystals. *J. Phys. Chem. Solids* **67**(11), 2405–2408 (2006)
142. A.Y. Kuznetsov, R. Machado, L.S. Gomes, C.A. Achete, V. Swamy, Size dependence of rutile TiO₂ lattice parameters determined via simultaneous size, strain, and shape modeling. *Appl. Phys. Lett.* **94**, 193117 (2009)
143. V. Swamy, A. Kuznetsov, L.S. Dubrovinsky, R.A. Caruso, D.G. Shchukin, B.C. Muddle, Finite-size and pressure effects on the Raman spectrum nanocrystalline anatase TiO₂. *Phys. Rev. B* **71**(18), 184302 (2005)
144. V. Swamy, Size-dependent modifications of the first-order Raman spectra of nanostructured rutile TiO₂. *Phys. Rev. B* **77**(19), 195414 (2008)
145. S. Sahoo, A.K. Arora, V. Sridharan, Raman line shapes of optical phonons of different symmetries in anatase TiO₂ nanocrystals. *J. Phys. Chem. C* **113**(39), 16927–16933 (2009)
146. V. Swamy, D. Menzies, B.C. Muddle, A. Kuznetsov, L.S. Dubrovinsky, Q. Dai, V. Dmitriev, Nonlinear size dependence of anatase TiO₂ lattice parameters. *Appl. Phys. Lett.* **88**(24), 243103 (2006)
147. L. Dai, C.H. Sow, C.T. Lim, W.C.D. Cheong, V.B.C. Tan, Numerical Investigations into the Tensile Behavior of TiO₂ Nanowires: Structural Deformation, Mechanical Properties, and Size Effects. *Nano Lett.* **9**(2), 576–582 (2009)
148. J. Zhu, J.X. Yu, Y.J. Wang, X.R. Chen, F.Q. Jing, First-principles calculations for elastic properties of rutile TiO₂ under pressure. *Chin. Phys. B* **17**(6), 2216 (2008)
149. V. Swamy, A.Y. Kuznetsov, L.S. Dubrovinsky, A. Kurnosov, V.B. Prakapenka, Unusual Compression Behavior of Anatase TiO₂ Nanocrystals. *Phys. Rev. Lett.* **103**(7), 75505 (2009)
150. X.J. Liu, L.W. Yang, Z.F. Zhou, P.K. Chu, C.Q. Sun, Inverse Hall-Petch relationship of nanostructured TiO₂: Skin-depth energy pinning versus surface preferential melting. *J. Appl. Phys.* **108**, 073503 (2010)

151. X.J. Liu, L.K. Pan, Z. Sun, Y.M. Chen, X.X. Yang, L.W. Yang, Z.F. Zhou, C.Q. Sun, Strain engineering of the elasticity and the Raman shift of nanostructured TiO₂. *J. Appl. Phys.* **110**(4), 044322 (2011)
152. A.Y. Wu, R.J. Sladek, Elastic Debye temperatures in tetragonal crystals: Their determination and use. *Phys. Rev. B* **25**(8), 5230 (1982)
153. B. Chen, H. Zhang, K. Dunphy-Guzman, D. Spagnoli, M. Kruger, D. Muthu, M. Kunz, S. Fakra, J. Hu, Q. Guo, J. Banfield, Size-dependent elasticity of nanocrystalline titania. *Phys. Rev. B* **79**(12), 125406 (2009)
154. F. Birch, Finite elastic strain of cubic crystals. *Phys. Rev.* **71**(11), 809–824 (1947)
155. F.D. Murnaghan, The compressibility of media under extreme pressures. *Proc. Nat. Acad. Sci.* **30**(9), 244–247 (1944)
156. N. Iles, A. Kellou, K.D. Khodja, B. Amrani, F. Lemoigno, D. Bourbie, H. Aourag, Atomistic study of structural, elastic, electronic and thermal properties of perovskites Ba(Ti, Zr, Nb)O₃. *Comput. Mater. Sci.* **39**(4), 896–902 (2007)
157. X.J. Liu, L.K. Pan, Z. Sun, X.H. Wang, J. Zhou, L.T. Li, C.Q. Sun, Mechanically stiffened and thermally softened bulk modulus of BaXO₃ (X = Ti, Zr, Nb) cubic perovskites. *J. Appl. Phys.* **109**(3), 033511 (2011)

Chapter 28

Nanograins: II. Plasticity and Yield Stress

- *The competition between the energy density gain and the cohesive energy loss in the skin dictates intrinsically the IHPR.*
- *The competition between the activation and the inhibition of dislocation motion activates the IHPR.*
- *The critical size in the IHPR is determined by: (1) the nature of the bonds involved and (2) the temperature of operation.*
- *Superplasticity takes place in the quasi-molten phase.*
- *The skin governs the multi-field coupling effect on the physical anomalies of nanostructures.*

28.1 Hall–Petch Relationship

In plastic deformation tests, the measured flow stress, or hardness, of nanograins changes with its grain size in a trend quite different from the predicted monotonic features of the elastic response because of the involvement of extrinsic factors including artifacts in the contact mode of measurement. The flow stress of the solid grains increases under the mechanical stimulus when the grain size is reduced. For brittle materials, such as intermetallic compounds and ceramics, the ductility increases with grain refinement because of the increased grain boundary (GB) volume fraction, GB sliding, and GB dislocation accumulation [1]. The plastic deformation results from the couple of mechanical deformation controlled by the stress field applied, chemical reaction determined by the external loading environment, and mechanical–chemical interaction governed by both loading type and environment [2]. Temperature rise accelerates the penetration of oxygen into the grain interior and reduces the critical stress for plastic yielding. When the chemical effect is avoided, the initiation of plasticity is enabled by octahedral shear stress but the further development of plastic deformation is influenced by hydrostatic stress. Plasticity of silicon in the form of phase transitions, e.g., from the diamond to amorphous or from the amorphous to bcc structures, is determined by loading

history. The elastic deformation of the two-phase alloy obeys the rule of mixtures for a composite; the plastic deformation is governed by the softer matrix but enhanced, in part, by the deflection of shear bands by the globular harder phase [3].

The size-induced mechanical hardening of nanograins is divided into three size regions, as illustrated in Fig. 28.1a. Region I corresponds to the classical Hall–Petch relationship (HPR) [4–6]. Regions II and III are known as the inverse Hall–Petch relationship (IHPR) [7–12]. Postulated explanations for the HPR-IHPR behavior include dislocation-based models, diffusion-based models, grain boundary-shearing models, two-phase-based models, and dislocation absorption-based models [13]. The observations are also explained by considering two alternative and complementary rate mechanisms of plasticity, grain boundary shear, and dislocation plasticity, each contributing to the overall strain rate in proportion to the volume fraction of the material in which they operate [14].

The mechanical strengthening with grain refinement in the size range of 100 nm or larger (region I) has traditionally been rationalized with the so-called T-independent HPR that can be simplified in a dimensionless form being normalized by the bulk strength, $\sigma(\infty)$, measured at the same temperature and under the same conditions:

$$\sigma(K)/\sigma(\infty) = 1 + AK^{-0.5} = 1 + A'\mu(b/K)^{0.5} \quad (28.1)$$

The slope A or A' is an adjustable parameter for fitting to measurements, which represents both the intrinsic properties and the extrinsic artifacts such as defects, the pileup of dislocations, shapes of indentation tips, strain rates, load scales, and directions in the test. The μ and b correspond, respectively, to the shear modulus and the Burger's vector modulus reduced by atomic size, d . The bulk modulus B is related to the shear modulus μ and the Poisson ratio ν by: $\mu = B/[2(1 + \nu)]$. Using the dimensionless form of the normalized, yield strength aims to minimizing the contribution from artifacts due to processing conditions, crystal orientations, and the purity of the specimens if the measurement is conducted under the identical conditions throughout the course of the experiment. For convenience, we use both $x = K^{-0.5}$ and K as indicators of the dimensionless form of sizes.

As the crystal is refined from the micrometer regime into the nanometer regime (Region II), the classical HPR process invariably breaks down and the yield strength versus grain size relationship departs markedly from that seen at larger grain sizes (Region I). With further grain refinement, the yield stress peaks in many cases at a mean grain size in the order of 10 nm or so. A further decrease in grain size (Region III) can cause softening of the solid, instead, and then the HPR slope turns from positive to negative at a critical size, or called the strongest grain size [17].

There has been a concerted global effort underway using a combination of novel processing routes, the state-of-the-art experimental measurements, and large-scale computations to develop deeper insight into the IHPR phenomena. For example, by squeezing Si nanospheres of different sizes between a diamond-tipped probe and the sapphire surface, Gerberich et al. [18] determined at room

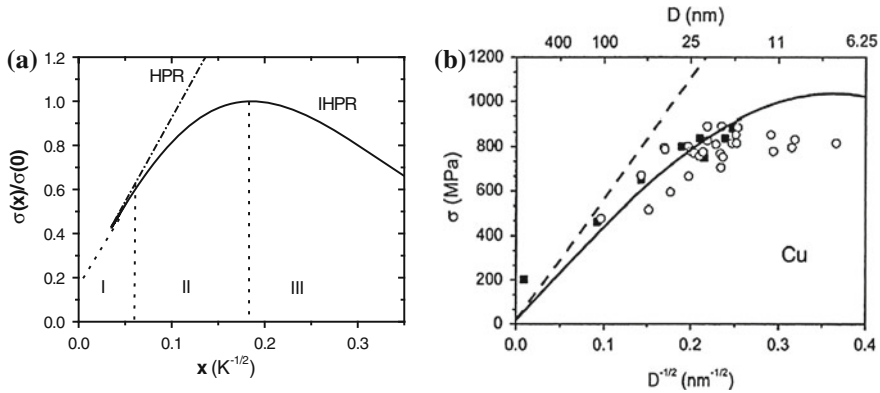


Fig. 28.1 **a** Illustration of the three regions of hardness transition from the classical HPR to the IHPR [15]. **b** The typical best fit of the IHPR for Cu nanograins by Zhao et al. [16]

temperature that a defect-free silicon nanoparticle with a diameter of 40 nm is ~ 3 times (50 GPa) harder than bulk silicon (12 GPa), while it was around 20 GPa with a diameter of 100 nm. The smaller the sphere, the harder it was. Tensile tests of the electrodeposited nanocrystalline Ni–W alloys with grain sizes of 20, 12, 8, and 5 nm revealed that the strongest grain size is at 8–10 nm that is an essential characteristics of the nanocrystalline Ni–W alloys [19–21]. The softening of nanograins is also attributed to the increase in intercrystalline volume fraction, especially the fraction associated with the triple junction [22]. The IHPR effect has also been experimentally observed in SiC [23], Ni–P [24], melt-spun AlMnCe, and AlCrCeCo alloys [25], see more examples in Table 28.1. Progress in fabrication, characterization, and the understanding of the HPR–IHPR relations of nanocrystalline materials have been reviewed by many specialists [26–36].

28.2 Mesoscopic Models

Numerous models elaborate the HPR and IHPR effects. The possible mechanisms for the plastic deformation of nanograins include the pileup breakdown, GB sliding, core and mantle structures, GB rotation, grain coalescence, shear-band formation, and gradient and twinning effects. The IHPR appears because of the increased porosity at small grain sizes, suppression of dislocation pileups, and dislocation motion through multiple grains, enhanced grain boundary diffusion, or absence of dislocations in the small grains without the mirror forces in the next grain being involved. It appears that the mechanism for the HPR and the IHPR is a topic of endless debate because of the complicated factors. The following discusses typical mechanisms for the HPR, IHPR, and the transition from HPR to IHPR and the critical grain size.

Table 28.1 Comparison of the measured and predicted strongest critical grain sizes for IHPR transition with $f = 0.5, 0.668$ and $m = 1$ otherwise as indicated

| Element | d/nm | T_m/K | P_M | Measured D_C/nm | Predicted D_C/nm ($f = 0.5; 0.663$) |
|----------------------------------|---------|---------|-------|---------------------------|---|
| Mg | 0.32 | 923 | – | | 18.2; 17.3 |
| Ca | 0.394 | 1,115 | – | | 22.41; 22.41 |
| Ba | 0.443 | 1,000 | – | | 25.2; 23.9 |
| Ti | 0.293 | 1,941 | – | | 23.6; 23.6 |
| Zr | 0.319 | 2,182 | – | | 29.3; 29.3 |
| V | 0.2,676 | 2,183 | – | | 24.6; 24.6 |
| Ta | 0.2914 | 2,190 | – | | 26.8; 26.8 |
| Fe | 0.252 | 1,811 | 9,765 | 18.2 | 19.1 |
| Co | 0.2552 | 1,728 | – | | 19.3 |
| Ni | 0.2488 | 1,728 | 7,042 | 17.5; 13 [59] | 18.8 |
| Cu | 0.2555 | 1,358 | 890 | 14 [76]; 14.9; 25–30 [77] | 16.1 |
| Zn | 0.2758 | 693 | 1,034 | 17.2; 10; [78] 11 [9] | 18.5; 16.5 |
| Pd | 0.2746 | 1,825 | 3,750 | 19.9 | 20.8 |
| Ag | 0.2884 | 1,235 | – | | 17.3 |
| Pt | 0.277 | 1,828 | – | | 21.0 |
| Au | 0.288 | 1,337 | – | | 17.3 |
| Al | 0.286 | 993 | – | 18 [76] | 16.3; 15.4 |
| C | 0.154 | 3,800 | – | | 20.5 ($m = 2.56$) |
| Si | 0.2632 | 1,683 | 4 | 9.1 | 10.6 ($m = 4.88, f = 0.1$) |
| Ge | 0.2732 | 1,211 | – | | 11.5 ($m = 4.88, f = 0.1$) |
| Sn | 0.384 | 505.1 | – | | 47.2; 40.6 |
| Pb | 0.3492 | 600.6 | – | | 28.0; 24.9 |
| Bi | 0.34 | 544.4 | – | | 36.0; 29.2 |
| Ni ₈₀ P ₂₀ | 0.2429 | 1,184 | 7,063 | 7.9 ($m = 4$) | 8.9 |
| NiZr ₂ | 0.4681 | 1,393 | 7,093 | 17.0 ($m = 4$) | 19.8 |
| TiO ₂ | 0.3860 | 2,098 | 7,432 | 22.5 ($m = 5.34$) | 23.1 ($f = 0.01$) |

The predicted critical sizes agree with measurement as derived from Fig. 28.3 unless with given references. Changing the f value only affects the $D_C = (2K_C d)$ of a material with T_m below 1,000 K [75]

28.2.1 HPR-I: Linear Hardening

- **GB barriers-limited dislocations** [37–40]. For large grain sizes, most of the models using a mechanism based on dislocation pileup account for the grain size dependence of the macroscopic plastic flow stress. In deriving the HPR, the role of GBs as a barrier to dislocation motion is considered in various models. One type of models [39] regards the GBs as barriers to the pileup of dislocations. The GB stress of one grain concentrates the dislocations, which activates the dislocation sources in the neighboring grains, thus initiating slip from grain to grain. The other type of models [40] regards the GBs as dislocations barriers limiting the mean free path of the dislocations, thereby increasing strain hardening, resulting in the HPR [41]. The conventional dislocation theory for the HPR gives a linear dependence of σ on $K^{-1/2}$ only when there are a large

number of dislocations in a pileup, which is equivalent to assuming that the grain sizes in the polycrystalline material under consideration is large. Deformation mechanism at larger scales is believed to occur through the production and motion of dislocations within the individual grains [42].

28.2.2 IHPR-II: HPR Deviation

- **Intra-granular transition of GB-sourced dislocations** [43]. The first theoretical attempt proposed that dislocations in nanograins are nucleated at the GBs, travel across the grain, and annihilate on the opposite GBs, and therefore, intra-granular transition dominates the HPR deviation.
- **Intergranular GB** stacking fault drained dislocations [42, 44]. As the grain size is decreased, dislocations are expected to pileup at the GBs and become less mobile because of the role of the stacking fault energy, essentially a misfit energy caused by atomic planes stacked out of sequence, thus leading to increased strength. Therefore, the IHPR corresponds to the GBs that serve as a dislocation drains rather than sources. In the nanometer regime, GBs are occupying a significant fraction of the material's volume, deformation proceeds by a mechanism that is intergranular rather than intra-granular, as argued above.

28.2.3 IHPR-III: Softening

- **GB migration and diffusion** mechanism suggests that the GB migration and diffusion dominate the size-induced softening. When the grain size is below the critical values of 10–20 nm, more than 50 % of atoms are associated with GBs or interfacial boundaries. Therefore, GB atoms play the dominating roles in the softening of nanocrystalline materials. Nanocrystalline materials exhibit creep and superplasticity at lower temperatures than do micrograined counterparts. Similarly, plastic deformation of nanocrystalline coatings is considered to be associated with GB sliding assisted by GB diffusion or rotation. MD calculation using the embedded atom method [45] and the effective medium theory [46] suggested that GB migration and sliding are predominant instead of the mechanism of diffusion switching [47]. An intricate interplay between GB sliding and GB diffusion may occur, and therefore, the IHPR effect arises from sliding accommodated GB diffusion creep [28, 48].
- **Soft GBs-embedded hard cores.** This composite core-shell structure model suggests that the IHPR-deformed bulk metallic glass can be treated as a composite of hard amorphous grains surrounded by a shell of soft GBs [49, 50]. The grain interior deforms elastically under external stresses, while the plastic deformation of the GB layer is governed by a Maxwell's equation. In such a

microstructure, the deformation of the GB shell contributes significantly to the overall deformation. Nieh and Wang [51] indicated that the apparent IHPR in the BeN alloy is actually an artifact as it is caused by the presence of relatively soft amorphous Be–B phases when the grain size of Be is significantly refined by B alloying. When the grain size was less than 10 nm, the GBs were thicker than those of coarser-grained materials. The interface region of the nanocrystallites having a structure of non-periodic atomic array expanded into the center region. Factors such as residual porosity, impurities, residual stresses, minor surface flaws, and/or narrow shear bands are suggested to lower and scatter the tensile strength values [52]. Similarly, a phase mixture model [22, 53] treats a polycrystalline material as a mixture of two phases: the grain interior material whose plastic deformation is governed by dislocation and diffusion mechanisms and the GB ‘phase’ whose plastic flow is controlled by a GB diffusion mechanism [54, 55]. The reduction in dislocation mean free path through GBs diffusion rather than dislocation nucleation governs the size effect in this range [56]. The softening in plastic deformation was also ascribed as a large number of small ‘sliding’ events of atomic planes at the GBs, with only a minor part being caused by dislocation activity in the grains; the softening at small grain sizes is therefore due to the larger fraction of atoms at the GBs [16]. An acoustic emission spectroscopic study [57] suggested that a peculiar deformation behavior, due to the competition between different deformation mechanisms such as dislocation pileups in nanocrystalline grains and grain sliding-grain rotation within amorphous boundaries, plays a vital role in the deformation of superhard nanostructures.

28.2.4 HPR-IHPR Transition

- **Grain size triggers collective motion of dislocations.** This mechanism [58] suggests that the classical HPR arises from the collective motion of interacting dislocations yet the breakdown for nanometric grains stems from the loss of such a collective behavior as the grains start deforming by successive motion of individual dislocations. Mohamed [59] interpreted the nanometer-scaled softening in terms of dislocation-accommodated boundary sliding. The HPR breakdown may lead to three possible behaviors according to the patterns of dislocations:
 - If dislocations are nucleated at vertices, the IHPR will bend down showing softening characteristics;
 - If dislocations are at the GB triple junctions, the IHPR curve will turn to be flat without softening or hardening taking place.
 - If dislocations occur at the GBs, the IHPR will remain the classical HPR trend and there will be no IHPR.
- **Dislocation absorption.** Carlton and Ferreira [13] revised the HPR with a statistical probability of dislocation absorption by grain boundaries, showing

that the yield strength is dependent on strain rate and temperature and deviates from the HPR below a critical grain size.

The HPR becomes IHPR in the way of,

$$\sigma(K)/\sigma(\infty) = 1 + A((1 - \sigma_{\text{dis}})/K)^{0.5},$$

where σ_{dis} is the probability of a dislocation being absorbed by the GB.

- **Core–shell role exchange.** The IHPR slope transition is also suggested to arise from the role exchange of the grain interior and the GBs [60]. The thermally activated GB shear [9] and the excessive volume of the undercoordinated GB atoms [61] are suggested to be responsible for the IHPR softening [62, 63]. A switch in the microscopic deformation mechanism from dislocation-mediated plasticity in the coarse-grain interior to the GB sliding in the nanocrystalline regime is suggested to be responsible for the maximum strength [64]. In the HPR regime, crystallographic slips in the grain interiors govern the plastic behavior of the polycrystallite; while in the IHPR regime, GBs dominate the plastic behavior. During the transition, both the grain interiors and the GBs contribute competitively. The slope in the HPR is suggested to be proportional to the work required to eject dislocations from GBs, and the GB strain energy has to be taken into consideration [65]. The transition with decreasing grain size from a GB dislocation to a GB-based deformation mechanism in the nanocrystalline fcc metals provides also a possible mechanism [66].

28.2.5 Strongest Grain Size

The following approaches estimate the strongest grain size. One approach is to assume that the plastic deformation of a nanocrystal switches abruptly from the pileup of dislocations to the GB-relaxation mechanism at a grain size, $d = d_c$ [53],

$$\sigma(K_c)/\sigma(\infty) = 1 + AK_c^{-0.5} = 1 + g\left(\frac{d_c}{w} - 1\right)$$

where g is an adjustable parameter depending on grain morphology and w the GB width that is approximately three times the Burgers vector, b , i.e., $w \approx 3b$. According to this model, the strength of the IHPR material decreases linearly with its grain size below a certain threshold. The d_c was estimated to be 25 nm for Cu, in comparison with the reported values of 14 nm [67], 18 nm [68], and 50 nm [69].

Another approach for the flow stress of an A–B alloy suggests that the strongest grain size represents the emergence of GB diffusion that causes the HPR breakdown. For the A–B alloy, the critical grain size is given by [21]:

$$d_{\text{AB}}^i = \left[\frac{D_{\text{B}}}{D_{\text{A}}} (1 - c) + c \right]^{2/7} d_{\text{A}}^i$$

the critical grain size for pure A is d_A^i , D_B and D_A are the diffusivity of atom B in A and the self-diffusivity of A, respectively. The c is the atomic ratio of B to A. A prediction of the strongest grain size for the W/Ni alloys (with 13–19.6 at % W and a presumption of $d_{Ni}^i = 12$ nm) shows acceptable agreement with the measured critical size of around 8–10 nm [19].

28.2.6 $T_m(K)$ Dependent IHPR

Zhao et al. [16] proposed an atomistic analytical expression for reproducing the yield strength over the whole HPR and IHPR size range. They modified the T-independent HPR by introducing the activation energy for atomic dislocation to the HPR slope. The activation energy was related directly to the melting point suppression, $T_m(K) \propto E_A(K)$ [70]. The IHPR turns to be,

$$\sigma(K) = \sigma_0 + \left(A_1 + A_2 K^{-1/2} \right) \exp\left(\frac{T_m(K)}{2T_0} \right)$$

where σ , A_1 , and A_2 are adjustable parameters. T_0 is the reference temperature of measurement, and $T_m(K)$ is the K -dependent melting point. The $T_m(K)$ drops with the inverse size of the nanoparticle, K . This approach with inclusion of the essential fact of the size-induced T_m depression could reproduce the IHPR observations quite reasonably for a number of specimens, as shown for a sample of such cases in Fig. 28.1b.

28.3 T-BOLS Formulation: Dual Competition

The measured size and temperature dependence of the yield strength and compressibility of a nanosolid can be obtained by substituting the size and bond nature-dependent $\eta_1(K)$, $d(K)$, and $T_m(K, m)$ for the atomic η_{1i} , d_i , and $T_{m,i}$. The solution is:

$$\frac{\sigma(K, T)}{\sigma(\infty, T_0)} = \begin{cases} \frac{\eta_1(K)}{\eta_1(\infty)} \times \left(\frac{d}{d(K, T)} \right)^3 \times \frac{T_m(K, m) - T}{T_m - T_0} & = \frac{\sigma(K)}{\sigma(\infty)} \phi(K, m, T) \quad (\text{Born-criterion}) \\ \left(\frac{d}{d(K, T)} \right)^3 \times \frac{\eta_2(K) + \eta_1(K)[T_m(K, m) - T]}{\eta_2(\infty) + \eta_1(\infty)(T_m - T_0)} & (\text{Full-energy}) \end{cases} \quad (28.2)$$

In Born's criterion, the additional term $\phi(K, m, T)$ includes contributions from bond nature, bond length, and the separation of $[T_m(m, K) - T]$ to the yield strength of a solid in the T-independent HPR treatment. The term $[T_m(m, K) - T]$ in the Born's criterion is replaced by the net energy difference in the full-energy approximation. Numerically, these approximations are substantially the same because the addition of η_2 leads to only an insignificant offset of the relative

σ values. However, according to the fact that the mechanical strength approaches zero at melting, the term of η_2 can be ruled out and the Born's criterion applies. Therefore, the full-energy consideration can be ignored in the case of plastic deformation for the first-order approximation.

By comparing the currently derived form of Eq. (28.2) with the traditional HPR of Eq. (28.1), one can readily find that the ratio of the size-dependent specific heat per bond follows the traditional T-independent HPR, $\eta_1(K)/\eta_1(\infty) = \sigma(K)/\sigma(\infty) = 1 + AK^{-0.5}$. Incorporating the activation energy, $E_A(K) \propto T_m(K)$ [16, 70, 71], for atomic dislocation into the pre-factor A, leads to an analytical expression for the size- and T-dependent HPR in terms of energy density ratio:

$$\begin{aligned} \frac{\sigma(K, T)}{\sigma(\infty, T)} &= \frac{\eta_1(K)}{\eta_1(\infty)} \left\{ \left(\frac{d(\infty)}{d(K)} \right)^3 \times \frac{T_m(K, m) - T}{T_m - T_0} \right\} \\ &= [1 + AK^{-0.5}] \times \left\{ [1 + \Delta_d(K)]^{-3} \times \frac{T_m(K, m) - T}{T_m - T_0} \right\} \\ &= \varphi(A(T, T_m(K, m)), K) \times \phi(K, T, T_m(K, m)) \end{aligned} \quad (28.3a)$$

where

$$\begin{aligned} A &= A(T, T_m(K, m)) = f' \times \exp C \left[\frac{T_m(K, m)}{T} - 1 \right] = f \times \exp \left[\frac{T_m(K, m)}{T} \right] \\ \Delta_d(K) &= \sum_{i \leq 3} \gamma_i (C_i - 1) \end{aligned} \quad (28.3b)$$

The activation energy for dislocation motion is proportional to the size and bond nature dependence of the atomic cohesive energy, or the temperature difference between melting and operation,

$$\begin{cases} E_A(K, m, T) \propto T_m(K, m) - T = T_m(\infty, m)[1 + \Delta_C(K)] - T \\ \Delta_C(K, m) = \sum_{i \leq 3} \gamma_i (z_{ib} C_i^{-m} - 1) \end{cases} \quad (28.3c)$$

The pre-factor f is an adjustable parameter, which should cover both intrinsic and extrinsic contributions. The $\Delta_d(K)$ is the contraction of the mean bond length, and $\Delta_C(K, m)$ the perturbation to the mean cohesive energy of a nanograin.

The difference in the $T_m(K, m) - T$ or the ratio of the $T_m(K, m)/T$ is critical as it appears in both parts of ϕ and φ . Equation (28.3a) represents two types of competition in the IHPR:

1. The intrinsic competition between the remaining atomic cohesive energy and the energy density gain in the GBs and their temperature dependence, in terms of the separation of $T_m(m, K) - T$. If T remains unchanged during the measurement, a size reduction will decrease the $T_m(m, K)$ and hence the value of $T_m(m, K) - T$. Thus, the strength of the solid will drop with solid size. The term of $\eta_1(K)/\eta_1(\infty) = z/z(K)$ represents the energy density gain, which is

inversely proportional to the average coordination, as discussed in the section dealing with MC elongation. In nanograins, the deviations from both the energy density and atomic cohesive energy arise from GB atoms as atoms in the grain interior retain their bulk nature.

2. The competition between the activation and inhibition of dislocations motion dictate extrinsically. The exponential form of $T_m(m, K)/T$ represents the easiness of activating dislocations. Because the $T_m(m, K)$ drops with solid size, the dislocation motion becomes easier to form at smaller sizes because of the undercoordinated GB atoms, agreeing with observations of Han et al. [72]. The counterpart of competition comes from dislocation accumulation and strain gradient work hardening that inhibit further sliding dislocations, which complies with the traditional establishment in the T-independent HPR of $AK^{-0.5}$. The factors such as impurities or defects, shapes of indenter tips, strain rates and directions, and loading directions and scales also contribute to the yield strength measured [73].

Therefore, the intrinsic competition between the remaining atomic cohesive energy and the binding energy density gain in the GBs and the extrinsic competition between the activation and the resistance of dislocations determine the entire process of HPR and IHPR, which depends on temperature of operation because of the thermally driven bond expansion and bond weakening. The analytical form also represents that the undercoordinated atoms in the surface skin dictate the IHPR, whereas atoms in the core interior retain their bulk features and that both the bond length and bond strength are temperature dependent.

According to this solution, the grain boundary is harder at temperatures far below the surface $T_{m,1}$ because of the dominance of bond strength gain, whereas at temperatures close to the $T_{m,1}$, the GB is softer than the grain interior because of the dominance of bond order loss that lowers the barrier for atomic dislocation motion, concurring with the mechanism of core-shell role exchange. When operating at a given temperature, solid-size reduction lowers the $T_m(K, m)$. When K is sufficiently large, the analytical form degenerates into the traditional HPR, of which the slope is now clearly seen to be dominated by the term $f \times \exp(T_m(m, \infty)/T)$ that relates to the specific heat or activation energy for atomic dislocation.

The derived form is in accordance and further formulates the known mechanism of core-shell role exchange [49–65] and the composite or the mixed phase-structure model [49, 56] for the IHPR. The T-BOLS approximation clarifies that the competition between the atomic cohesive energy (T_m) remnant, and energy density (stress) gain in the GB region dictates intrinsically the mechanical behavior at GBs, which is sensitive to the temperature of operation. As the solid size is decreased, transition from the dominance of energy density gain to the dominance of remaining atomic cohesive energy occurs at the critical size at which both mechanisms contribute competitively. It is emphasized that all the afore-mentioned models give reasonable explanations of the HPR/IHPR transition but, with the currently proposed temperature dependence of the T-BOLS consideration as the atomistic and intrinsic origin, all the approaches would be correct and complete.

28.4 Verification

28.4.1 Strongest Sizes in the IHPR

By equaling the differential of the natural logarithm of Eq. (28.3a) to zero $d(\text{Ln}(\sigma/\sigma_0))/dx = 0$, one can determine the critical size $K_C(f, T_m(x), T, m)$ with the slope of HPR transiting from positive to negative, which distinguishes factors dominating the K_C value. For calculation convenience, one can simplify $x = K^{-0.5}$, $\theta(x) = T/T_m(x)$, and $\theta(0) = T/T_m(\infty)$. σ and σ_0 represent $\sigma(x, T)$ and $\sigma(0, T_0)$, respectively. The numerical processing leads to the following relation:

$$\frac{d(\text{Ln}(\sigma/\sigma_0))}{d\text{Ln}(x)} = A(x, \theta(x), m) \times \frac{\theta(0)+2\Delta_C(x,m)}{\theta(0)(1+A(x,\theta(x),m))} - \frac{6\Delta_d(x)}{1+\Delta_d(x)} + \frac{2\Delta_C(x,m)}{1+\Delta_C(x,m)-\theta(0)} = 0 \quad (28.4)$$

This solution indicates that the critical size depends on the bond nature indicator m , $T/T_m(x)$, and the pre-factor f in A. Solving this equation numerically gives rise to the critical sizes x_C of different materials, agreeing with measurements, as listed in Table 28.1.

28.4.2 T_C for Phase Transition

It is necessary to define the critical temperatures, T_C , and the corresponding critical size, K_C , for the transition from solid-to-quasi-molten phase and T_m for transition from quasi-molten-to-liquid using the relations:

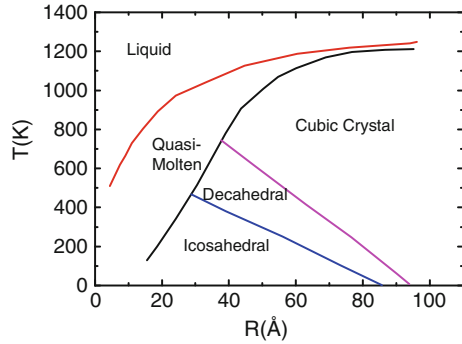
$$\frac{\sigma(K, T_C)}{\sigma(\infty, T_C)} = \frac{1 + A(K, \theta(K), m)}{[1 + \Delta_d(K)]^3} \times \frac{T_m(K, m) - T_C}{T_m - T_C} \begin{cases} \leq 1 & \text{(Quasi-molten)} \\ = 0 & \text{(Liquid)} \end{cases} \quad (28.5)$$

The quasi-molten state is defined thus that at a temperature higher than $T_C(K, f, m)$, the solid of critical size K_C is softer and easily compressible compared with the bulk counterpart at $T = T_C(K, f, m)$. At the melting point, $T_m(x, m)$, the quasi-molten state becomes a liquid associated with zero hardness and infinite compressibility. T_C is lower than the T_m for the same size. This definition complies Born's criterion indicating the absence of shear modulus at melting, and that defined by Marks [74], as illustrated in Fig. 28.2.

28.4.3 Strongest Grain Size

By incorporating the value of $\eta_1(x)/\eta_1(0) = 0.00187/0.0005542 = 3.3742$ for an impurity-free gold MC into Eq. (28.3a), one can estimate the value of f for the gold

Fig. 28.2 Phase diagram for small gold clusters shows the size-depressed critical temperatures for melting and quasi-molten (Reprinted with permission from [74])



MC with the parameters of $z_i = 2$, $K = 1.5$, $x = 1/\sqrt{K} = 1.223$, $m = 1$, $T = 298$ K, and $T_m(x) = 1337.33/4.1837 = 318$ K:

$$f = \frac{\left[\frac{\eta_1(x)}{\eta_1(0)} - 1 \right]}{\left[x \times \exp \left[\frac{T_m(x)}{T} \right] \right]} = 2.3742 / \left\{ 1.223 \times \exp \left[\frac{318}{298} \right] \right\} = 0.668 \quad (28.6)$$

The f value is intrinsic for the elongation test of the impurity-free Au-MC. However, in the test of nanograins plastic deformation, artifacts such as the external stress or strain rate or structural defects will contribute to the yield strength and hence the pre-factor f value. The f term is an adjustable parameter that may change when the nature of the bond is altered, such as in the cases of Si and TiO_2 that will be shown shortly.

Table 28.1 lists the strongest sizes x_C of selected nanosolids with the known bond length d and bulk melting point T_m as the input. All the nanograins were taken as being in spherical shape. The pre-factor f is adjusted under the constraint that the HPR slope should match the observations and intercept at the positive side of the vertical axis. Only positive intercept in measurement is physically acceptable. The theoretical curves were normalized with the calculated peak values at the transition point, x_C , and the experimental data measured at room temperature were normalized with the measured maximum P_M .

Figure 28.3 compares the theoretically produced IHPR with the measured data of typical nanocrystals. Insets in panel (e) show the size dependence of the elastic modulus and melting point of TiO_2 [79]. The straight lines are the traditional HPR and their slopes are obtained by adjusting the f values in Eq. (28.3a). The dashed lines only consider the extrinsic competition between activating and blocking dislocation motions represented by the activation energy without involving the contribution from the intrinsic competition, with $\varphi(d, m, T) = 1$. The solid lines are the current T-BOLS predictions covering both intrinsic and extrinsic competitions without using any other adjustable parameters. The scattered data are experimental results documented in the literature. All the panels were fitted at $T = 300$ K with $f = 0.5$ unless otherwise as indicated. Agreement indicates that

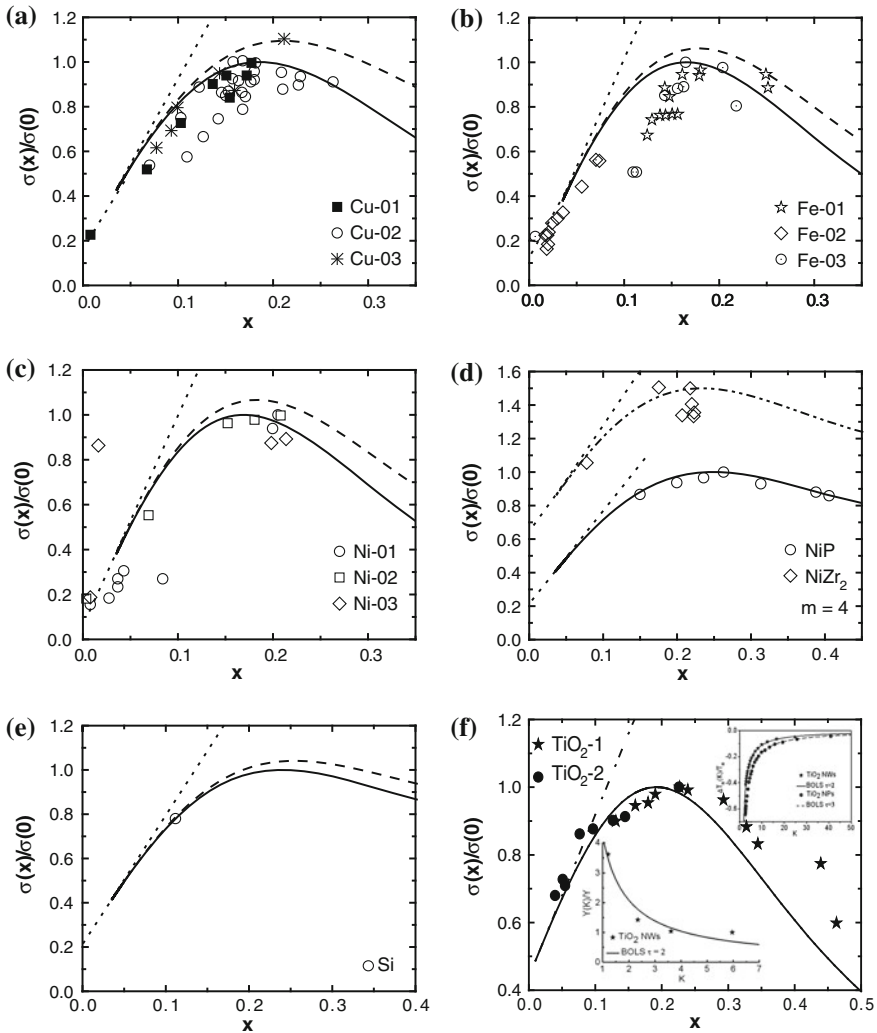
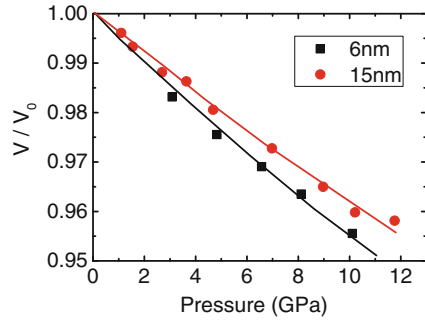


Fig. 28.3 Theoretical reproduction (*solid line*) of the measured IHPR (*scattered data*) of **a** Cu [80–82], **b** Fe [80], **c** Ni [10, 83], **d** NiP [84] and NiZr [85], **e** Si [18], and **f** TiO₂ [86, 87] with insets showing the size reduction-enhanced elastic modulus (energy density) and depressed melting point (atomic cohesive energy) of TiO₂ [88]. The *straight lines* are traditional HPR representing $1 + f \times x \times \exp(T_m(0)/T)$ and its intercept at the y-axis corresponds to the normalized hardness of the bulk counterparts. The *solid curves* represent the complete T-IHPR form, $[1 + f \times x \times \exp(T_m(x)/T)]\phi(d, m, T)$. The *dashed curves* are the modified HPR, $[1 + f \times x \times \exp(T_m(x)/T)]$. The slope $f = 0.5$ was optimized unless otherwise indicated for all the samples (Reprinted with permission from [15])

Fig. 28.4 The V–P profile for nanostructured TiO₂ shows the IHPR transition at 15 nm size, as the slope is inversely proportional to the bonding energy density of yield stress, according to the present T-BOLS notation. (Reprinted with permission from [89])



the IHPR is dominated by the extrinsic competition of activating and inhibiting dislocation motion whereas the intrinsic competition between the energy density gain and the atomic cohesive energy remnant in the skin plays a less significant role in plastic deformation.

The T-BOLS predictions match reasonably well to all measurements. The perfect match of the IHPR for NiP alloy and TiO₂ compound may adequately evidence that the current T-BOLS and LBA approaches are close to the true situations of IHPR involving both intrinsic and extrinsic contributions. As can be seen from Table 28.1, changing the f values from 0.5 to 0.668 has no effect on the critical size for materials with $T_m(0) > 1,000$ K, or $T/T_m(0) < 1/3$, and therefore, for the examined samples, using $f = 0.5$ or 0.663 makes no difference. The small f values for TiO₂(0.01) and Si(0.1) may be dominated by the bond nature alteration that lowers the $T_m(x, m)$ insignificantly.

Strikingly, one datum point of measurement is sufficient to calibrate the IHPR of a specimen. For example, applying the measured relative hardness of the defect-free 40-nm silicon nanosphere to the IHPR equation results in the maximum hardness of Si nanosolid at room temperature being 5 times the bulk value and the IHPR critical size being at 9–10 nm. The calibration using one datum point and the known bulk value should be one of the advantages of the current approach in predicting and calibrating the IHPR of a solid. Applying $m = 4.88$ for Si to Eq. (28.3a) gives immediately the bond contraction coefficient of $C_1 = (85 \pm 1)\%$ and the corresponding $z_1 \approx 3.60 \pm 0.25$. The z_1 for the spherical Si is slightly lower than $z_1 = 4$ for the flat surface, and the C_1 is slightly lower than a flat surface (88 %) because of the positive curvature of the sphere.

Insets in Fig. 28.3f show the cluster-size reduction-enhanced energy density (elastic modulus) and the depressed atomic cohesive energy (melting point) of TiO₂, evidencing the competition of both entities at the small scale. However, under compression, the elastic modulus of TiO₂ increase till 15 nm and then drops because of the contacting measurements [89], see Fig. 28.4.

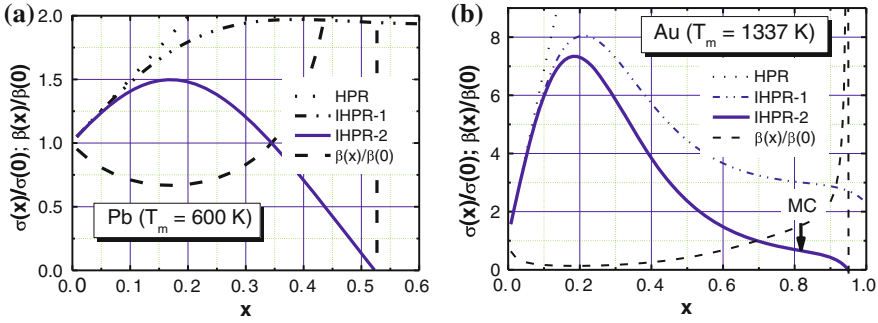


Fig. 28.5 Comparison of the IHPR-2 (solid line) transition and critical sizes for solid-to-quasi-molten and quasi-molten-to-liquid transition at 300 K for **a** Pb ($m = 1$, $T_m = 600.6$ K, and $f = 0.668$) and **b** Au ($m = 1$, $T_m = 1337.33$ K, $f = 0.668$). $\sigma/\sigma_0 = 1$ corresponds to quasi-molten state with critical temperature $T_C(x)$; $\sigma/\sigma_0 = 0$ corresponds to quasi-molten-to-liquid transition $T_m(x)$. Broken lines represent the reduced compressibility that drops first and then bends up until the bulk value at $T_C(x)$ and then goes up to infinity at $T_m(x)$. The Au–MC is in quasi-molten state at 300 K, which clarifies further the high extensibility of Au–MC at the ambient temperature. The curve of IHPR-1 could not reach the quasi-molten or the liquid states (Reprinted with permission from [15])

28.4.4 The Strongest Size

Figure 28.5 shows that, as the inverse of yield strength, the normalized compressibility drops first and then bends up at the IHPR critical point until it reaches the bulk value at $T_C(x)$. The compressibility then goes up to infinity at $T_m(x)$. This trend agrees with the breaking limits of metallic MC and polymer chains approaching T_m .

Results show that the Pb nanosolid of $x = 0.34$ ($D = 6$ nm) size becomes quasi-molten and of $x = 0.52$ ($D = 2.6$ nm) becomes liquid at 300 K because of the lower bulk melting point (600 K). In contrast, the Au nanosolid of $x = 0.68$ ($D = 1.25$ nm) becomes quasi-molten and $x = 0.95$ ($D = 0.64$ nm being smaller than one fcc unit cell) becomes liquid at 300 K. Therefore, the gold MC (or an fcc unit cell) is in the quasi-molten state at 300 K, which clarifies further why the Au–MC is highly extendable at the ambient temperature.

Figure 28.6 demonstrates the f , m , and $T/T_m(0)$ dependence of the strongest size x_C . The critical size varies significantly with the temperature of operation ($T/T_m(0)$) and the bond nature m . In the range of $f = 0.1$ and 1.0, x_C depends less on the f values if the $T/T_m(0)$ ratio is smaller than 0.15. There exist two temperatures for one x_C value in both panels (a) and (b). For the $x_C = 0.15$ example, the temperature reads as $T = 0.17T_m$ and $0.65T_m$ for the $f = 1$ curve in panel (a); and the T reads 0.1 and $0.7 T_m$ for $m = 5$ in panel (b). This result means that the same critical size can be obtained by measuring the specimen at different temperatures but the corresponding values of hardness are completely different; the specimen at low T is much harder than it is at higher T , as demonstrated in Fig. 28.7a.

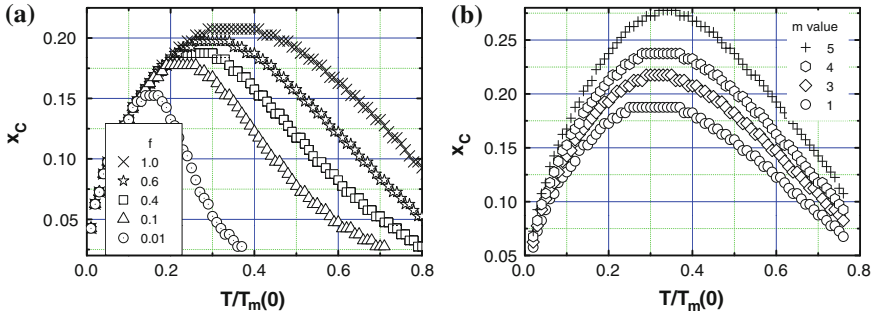


Fig. 28.6 Dependence of the strongest size $x_C(m, f, T/T_m(0))$ on **a** the extrinsic factor f and **b** the intrinsic bond nature indicator m . At $T/T_m(0) < 0.15$, x_C depends insignificantly on the f ; the m influences the x_C over the whole range of temperature. One critical size x_C can be obtained at two temperatures with different hardness (Reprinted with permission from [15])

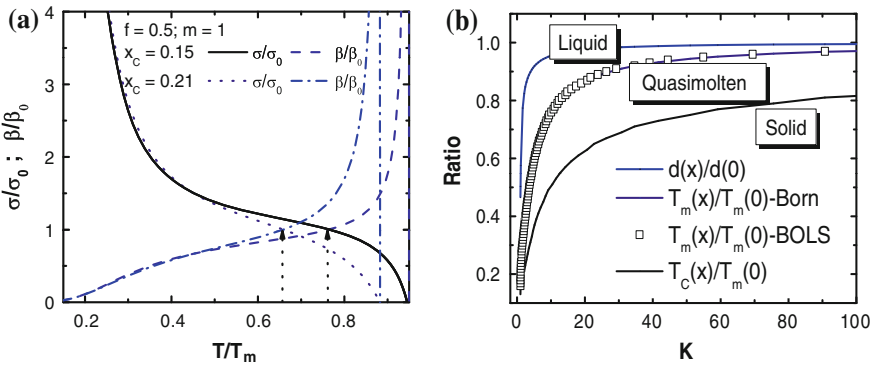


Fig. 28.7 **a** T/T_m dependence of the mechanical strength and ductility of nanocrystals of size $x_C = 0.15$ and 0.21 , and **b** comparison of the size dependence of the phase diagram showing the critical temperatures for solid-quasi-molten transition, $T_C(x)/T_m(0)$, and quasi-molten-liquid transition of metallic nanosolid ($m = 1$) and the size dependence of bond length contraction, $d(x)/d(0)$. $T_m(x)/T_m(0)$ -BOLS curve overlaps the $T_m(x)/T_m(0)$ -Born (Reprinted with permission from [15])

28.4.5 Size Effect on $T_C(x)$ and $T_m(x)$

The T/T_m and the size dependence of the strength and ductility in Fig. 28.7a reveal the following trends in general:

1. For a given material of a given size, the normalized mechanical strength drops from infinity to zero when T increases from zero to $T_m(x, m)$, associated with an increase in ductility until a singularity is reached at $T_m(x)$. Meanwhile, the $T_m(x)$ drops with size by 5 and 15 %, respectively, for the $x_C = 0.15$ and 0.21 examples.

- Both σ and β reach their bulk values (or transits into quasi-molten state) at $T_C = 0.75 T_m$ and $0.65 T_m$ for $x_C = 0.15$ and 0.21 , respectively. When $T > T_C$, σ drops, and β rises in an exponential way.

A comparison of the size dependence to the normalized atomic distance $d(x)/d(0)$, melting point, $T_m(x, m = 1)/T_m(0)$, and the ratio of $T_C(x, f, m = 1)/T_m(0)$ for solid-quasi-molten transitions shown in Fig. 28.7b indicates that the $T_C(x, f)$ drops more rapidly with size than the $T_m(x, m)$. The bulk T_C value is about 20 % lower than that of the bulk T_m . This trend agrees with the findings of Marks as shown in Fig. 28.2, which clarifies the distinguishable separation between the T_m and T_C in the whole range of solid size.

The currently defined $T_m(x)/T_m(0)$ -BOLS curve overlaps the curve derived from Born's criterion, $T_m(x)/T_m(0)$ -Born, which indicates the consistency in the respective physical mechanisms of melting. BOLS notation suggests that the melting is governed by the skin-resolved depression of the atomic cohesive energy ($T_m \propto zE_z$) but the Born's criterion Eq. (28.5) requires that the shear modulus or mechanical strength disappears at T_m [90]. The trend of the $T_m(x)/T_m(0)$ curves also agree with the models derived from Lindermann's criterion of atomic vibration [91–93], surface lattice/phonon instability [94, 95], liquid drop [96], and surface area difference [97]. Therefore, all the models are correct despite different perspectives.

28.4.6 Quasi-Molten State and Superplasticity

The presence of the quasi-molten state improves the understanding of the superplasticity of the nanograined solid. Superplasticity, an excessive strain of 10^3 without any substantial necking region when loaded in tension, is generally observed in materials with grain size less than 10 nm in the temperature range of 0.5 – $0.6 T_m$ [98]. Si and SiC nanowires of several 10 nm in diameter exhibit plasticity with about 150 % elongation [72, 99]. Because of the large GB volume fraction and the high self-diffusivity, superplasticity is achievable at lower temperatures and/or higher strain rates for some nanocrystalline materials. For a Cu nanosolid example with $K = 10$ (5 nm in diameter) size, the bond length contracts by a mean value of 5 %, associated with a 25 % drop of T_m and a 50 % drop of T_C with respect to the bulk $T_m(0)$ value of 1,358 K. The 5-nm-sized Cu solid is in a quasi-molten state at 680 K according to Fig. 28.7b. The self-heating in operation due to energy released from the process of bond breaking and unfolding raise the actual temperature of the specimen by some 40–50 K [100]. Hence, the size-induced T_C suppression and the bond breaking/unfolding-induced self-heating provide additional mechanism for the high ductility of Cu nanowires [101] at the ambient temperatures, which is dominated by bond unfolding and atomic gliding dislocations through creep and kink formation, instead of bond stretching, as discussed previously.

The predicted m , f , and $T/T_m(0)$ dependence of x_C , $T_C(x)$, and the trends of mechanical strength and compressibility/extensibility coincide exceedingly well with the cases as reported by Eskin et al. [102] on the grain size dependence of the tensile elongation (extensibility) of Al–Cu alloys in the quasi-molten state [103]. The ductility increases exponentially to infinity with temperature up to T_m that drops with solid size. On the other hand, the ductility increases generally with grain refinement. This is also frequently observed in cases such as alumina [104] and PbS [105] in the nanometer range at room temperature [106, 107]. The compressibility of Al_3O_2 and PbS solid increases but the Young's modulus decreases as the solid size is decreased. The predicted trends also agree with experimental observations [108] of the temperature dependence of the yield stress of Mg nanosolids of a given size showing that the yield strength drops as the operating temperature is elevated [108]. Temperature dependence of the tensile properties of ultrafine-grained ordered $FeCo_2V$ samples with grain sizes of 100, 150, and 290 nm revealed extremely high yield strengths (up to 2.1 GPa) present at room temperature with appreciable ductility of 3–13 %. The measured strengths declined gradually as the testing temperature was increased to 400 °C, while ductility was generally enhanced, up to 22 % [109]. At $T > 0.7 T_m$, the mechanical strength decreases rapidly with increasing temperature and with decreasing strain rate [110].

28.5 Elasticity Versus Hardness

Theoretically, the dimensionality for elasticity, stress and hardness is identical in Pascal unit (energy density) but at different states. The ideal form represents the intrinsic property change without experimental artifacts being involved. However, the softening and the slope transition in the IHPR plastic deformation arises from the extrinsic competition between activation of and resistance to glide dislocations, which is absent in the elastic deformation in particular using the non-contact measurement such as SWA techniques and Raman measurements.

A measurement of the size dependence of the hardness, shear stress, and elastic modulus of copper nanoparticles, as shown in Fig. 28.8a, confirmed this expectation. The shear stress and elastic modulus of Cu reduce monotonically with the solid size but the hardness shows the strong IHPR. Therefore, the extrinsic factors become dominant in the plastic deformation of nanocrystals, which triggers the HPR and IHPR being actually a response to the contacting detection. However, as compared in Fig. 28.8b and c, the hardness and Young's modulus of Ni films are linearly interdependent. This observation indicates that extrinsic factors dominating the IHPR of nanograins contribute little to the nanoindentation test of film materials.

By definition, the Young's modulus is for the regime of elastic deformation, while its inverse, or the extensibility/compressibility, covers both elastic and plastic types of deformation. However, either the elastic or the plastic process is

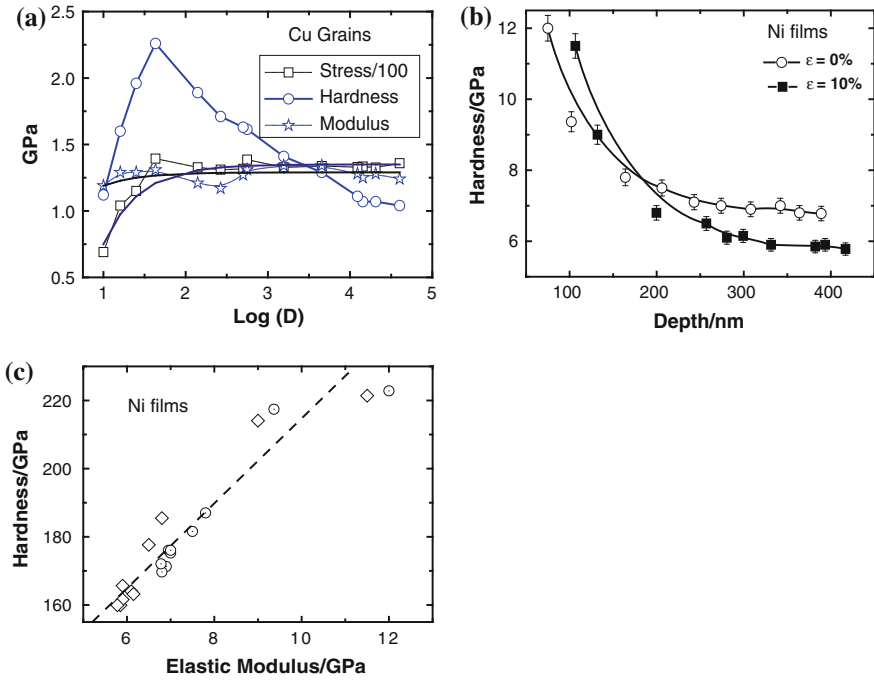


Fig. 28.8 **a** Comparison of the measured size dependence of elasticity, shear stress and hardness of Cu nanostructures [77], and the nanoindentation depth dependence of **b** the hardness and **c** the correlation between the hardness and elastic modulus of Ni films [111], indicating the significance of extrinsic factors on the hardness measurement of nanocrystals but contribute little to films (Reprinted with permission from [15])

related to the process of bond distortion, including bond unfolding, stretching, or breaking, that consumes energy (obtained by integrating the stress with respect to strain) each process being a certain portion of the entire binding energy. No matter how complicated the actual process of bond deformation (with linear or nonlinear response) or recovery (reversible or irreversible) is, a specific process consumes a fixed portion of bond energy, and the exact portion for the specific process does not come into play in the numerical expressions for the relative change. Therefore, the analytical expression of the elastic modulus is valid for describing the intrinsic properties for any substance of any scale of size and in any phase.

However, for plastic deformation, the competition between dislocation activation and dislocation resistance becomes dominant, which presents a difference in the plastic deformation from the elastic response in terms of the IHPR features. In the nanoindentation test, errors may arise because of the shapes and sizes of the tips. The stress–strain profiles of a nanosolid are not symmetrical when comparing the situation under tension to that under compression [112]. The flow stress is dependent of strain rate, loading mode and duration, and material compactness, as well as size distribution. These factors may influence measured data that are seen

to be quite scattered and vary from source to source. As the Young's modulus and mechanical strength are quantities of intensity, they are volume less. Therefore, it is not appropriate to think about the stress or elasticity of a certain atom, instead, at a specific atomic site.

28.6 Size and Pressure Compensation on T_C

28.6.1 *Known Identities*

Phase stability of nanostructures has been one of the central issues in nanoscience and technology. For a given specimen of a fixed size, phase transition takes place when the temperature is raised to a certain degree. The value of the critical temperature (T_C) varies with the actual process of phase transition. The T_C values are different for the magnetic–paramagnetic, ferroelectric–non-ferroelectric, solid–solid, solid–liquid, and liquid–vapor phase transitions of the same specimen. Generally, solid-size reduction depresses the T_C of a nanosolid because atomic undercoordination lowers cohesive energy of atomics in the skin.

However, compression elevates the T_C because the mechanical work stores energy to the individual bond to raise the energy density of the entire body of the specimen of usual materials. Overheating does occur when the measurement is conducted under applied pressure that shortens and strengthens the bonds. When the pressure is increased to a critical value of P_C , solids transform from the less densely packed geometry to denser solid phases disregarding the solid size. Conventionally, studies of phase transitions in condensed phases have generally assumed that the stimuli of pressure, temperature, and the composition of the specimen are the variables of dominance in determining the stable states of a substance.

Studies of clusters in the condensed phases have led to numerous instances in which one bond-geometry appears to be favored over others in finite size, as compared with the bulk, because of the altered atomic cohesive energy upon solid-size change. A huge database showing consistently that the critical pressure (P_C) for the transition from the less coordinated structural phase to the denser structures increases with the reduction in crystal size [113–123]. For the bulk CdSe instance, the transition pressure is 2.5 GPa but when the size is reduced to 1 to 3 nm across, the transition pressure increases to a value of 5 GPa. The size trend for the pressure-induced γ -Fe₂O₃ (maghemite) to α -Fe₂O₃ (hematite) transition showed that 7-nm nanocrystals transforms at 27 GPa, 5 nm ones at 34 GPa, and 3 nm ones at 37 GPa [114].

28.6.2 Known Mechanisms

Numerous mechanisms explain the solid–solid phase transition from various perspectives [126–132]. Classical statistic thermodynamics in terms of Gibbs free energy could describe the phase transition without needing consideration of atomistic origin. However, the introduction of the new degree of the freedom of solid size has proven to tune the physical extent of a material, adding another important variable in determining the transition behavior [113, 114]. At the nanometer regime, both the thermodynamics and kinetics may come into play in the transformation, which goes beyond the scope of classical theory as the entropy, for instance, is based on statistics of large sample size. Furthermore, all the detectable properties such as the Debye temperature, the specific heat, and the thermal expansion coefficient remain no longer constant but become tunable with the particle size. Despite the importance of the solid–solid transition of materials, the microscopic mechanisms of the solid–solid phase transition of solid in the nanometer regime are much more complicated due to the inhomogeneous kinetic effect taking place in the skin and in the bulk regions.

28.6.3 BOLS Formulation

This phenomenon is a typical example for the multi-field-coupling effect in nanostructures. Equation (23.8) in Sect. 23.2,

$$\Delta T_c = \frac{\Delta T_c(K, p, T)}{T_c(\infty, 0, 0)} = \frac{E_{\text{coh}}(K, p, T)}{E_{\text{coh}}(\infty, 0, 0)} - 1$$

yields

$$E_{b0}\Delta T_c - \Delta E_b^p = K^{-1} \sum_{i \leq 3} \tau C_i [\Delta E_b^p (z_{ib} C_i^{-m} - 1) + (z_{ib} \Delta E_i^p - \Delta E_b^p)]$$

or

$$K_C = \frac{\sum_{i \leq 3} \tau C_i [\Delta E_b^p (z_{ib} C_i^{-m} - 1) + (z_{ib} \Delta E_i^p - \Delta E_b^p)]}{E_{b0}\Delta T_c - \Delta E_b^p} \cong \frac{A(K_C, P_C)}{P_C} \geq 0$$

where

$$\begin{cases} \Delta E_i^p &= - \int_{P_0}^{P_c} \frac{dv_i}{v_0} p dp = - \left(\beta_i P + 0.5 \beta'_i P^2 \right) \Big|_{P_0}^{P_c} / V_0 \\ \Delta E_b^p &= - \int_{P_0}^{P_c} \frac{dv_b}{v_0} p dp = - \left(\beta_b P + 0.5 \beta'_b P^2 \right) \Big|_{P_0}^{P_c} / V_0 = -P \left(\beta_b + 0.5 \beta'_b P \right) / V_0 \end{cases} \quad (28.7)$$

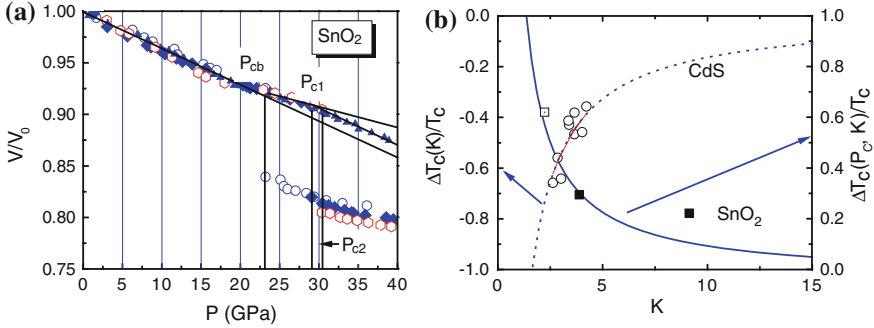


Fig. 28.9 **a** The V - P profile for SnO_2 nanocrystals showing the size and pressure dependence of the phase transition from rutile to cubic structures taking place at room temperature [89]. The *square*, *diamond*, *circle*, and *up-triangle* symbols represent the *bulk*, 14, 8, and 3-nm SnO_2 samples, respectively. Corresponding critical transition pressures are denoted as p_{Cb} , p_{C1} , and p_{C2} while the p_{c3} for the 3 nm crystal is beyond the measured pressure range. **b** Comparison of the P-BOLS predicted (*solid curves*) with the measured (*scattered symbols*) pressure-elevated T_C for solid–solid transition of SnO_2 nanocrystals derived from (a) and the size-induced T_C depression for solid–liquid transition of CdS nanocrystals [124], showing compensation of the relative changes. The empty square is an extrapolation of the 3-nm SnO_2 solid. The transition pressure for the 3-nm SnO_2 is predicted to be 43 GPa [125]

E_{b0} is the equilibrium bond energy. τ is the dimensionality. β and β' are the compressibility and its first derivative. Subscript i and b denotes the i th atomic layer and the bulk. If $\Delta T_C \rightarrow 0$, $\Delta T_C = 0$; $\beta_b \gg 0.5\beta'_b P$.

This relation indicates that the coupling effect dominates only in the skins, and the size and pressure do compensate the following:

1. The skin dictates the multi-field-coupling effect on the T_C . If $z_{ib} = 1$, the sum equals zero. Neither size dependency nor multi-field effect takes place.
2. The K_C is inversely proportional to the additional energy $E_{b0}\Delta T_C$ due to size reduction and the mechanical work $-\Delta E_b^p$. Mechanical compression compensates size reduction in the thermal stability.
3. If the critical temperature remain unchanged $\Delta T_C = 0$, the K_C can be simplified at $K_C P_C \equiv A(K, P_C)$. The $A(K, P_C)$ approximates a constant that is modulated by the size and the critical pressure.

28.6.4 Verification

The BOLS formulation enables reproduction of the measured P_C - K_C . Figure 28.9a shows the typical V - P profiles [89] measured at the ambient temperature for SnO_2 bulk and powders of 14, 8, and 3 nm across, which demonstrates clearly the size

Table 28.2 Information derived from Fig. 28.9 for SnO₂ nanocrystals

| | Bulk | 14 nm | 8 nm | 3 nm |
|-----------------------------------|-------|-------|-------|-------|
| $\beta(10^{-3} \text{ GPa}^{-1})$ | -3.53 | -2.35 | -2.35 | -3.3 |
| ΔE^P | 22.26 | 5.39 | 6.54 | 10.38 |
| P_c (GPa) | 23.0 | 29.0 | 31.0 | 43.0 |
| A | 23.0 | 23.46 | 23.47 | 23.49 |
| ΔT_C | 0 | 0.242 | 0.294 | 0.611 |

β is the slope of the V - P profile, ΔE^P is the integration of the V - P curve. The meaning of A and ΔT_C are given in the context

dependence of the critical pressure for phase transition [89]. The critical pressures for phase transition change with both K and P . The P_C is higher for the smaller solid. The V - P profile could be well represented by the relation of $V/V_0 = 1 + \beta P + \beta' P^2$ ($\beta'' \ll \beta$) at $V/V_0 > 0.8$, being substantially the same in value to the description of the third-order Birch–Murnaghan equation of state. The slope of the V - P profile, $\beta = dV/(V_0 dp)$, corresponds to bulk compressibility. The β values derived from the V - P profile at different regions change slightly, as listed in Table 28.2. As the β is the inverse of bulk modulus, the slightly lowered β value in the size range of 8 and 14 nm corresponds to turning point of the IHPR for the size dependence of the mechanical strength of nanostructures. By nature, the mechanical strength and the elastic modulus of a specimen are both intrinsically proportional to the sum of bond energy per unit volume though artifacts may be involved in the plastic deformation. Therefore, the lowered β in the size region of 8–14 nm is consistent with the strongest size in the IHPR.

Figure 28.9b shows the consistence between predictions (solid curve) and the measured (scattered symbols) size and pressure dependence of T_C . The T_C for the solid-solid transition of SnO₂ nanocrystals increases under the compressive stress when the solid size is reduced. The T_C for the solid-liquid transition of CdS nanocrystals drops with solid size at the ambient pressure. The exceedingly good agreement between predictions and observations in the two situations evidences the validity of the considerations from the perspective of atomic cohesive energy. The critical pressure for the 3 nm SnO₂ transition is predicted to be 43 GPa that is beyond the range of the referred measurement. It is apparent that the pressure-induced T_C elevation compensates for the size-induced T_C depression, which determines the observed size trend of the pressure induced phase transition. If the solid size induces a T_C elevation, the critical pressure will drop to compensate for the size-induced overheating. Therefore, the critical pressure for phase transition at a given temperature may increase or decrease subjecting to the size effect.

Figure 28.10 reproduces the measured P_c - K data for CdSe transforming from the 4-nearest coordinated Wurtzite to the 6-nearest coordinated cubic rock-salt structure, and the transition of Fe₂O₃ from γ to α phase. The exceedingly good

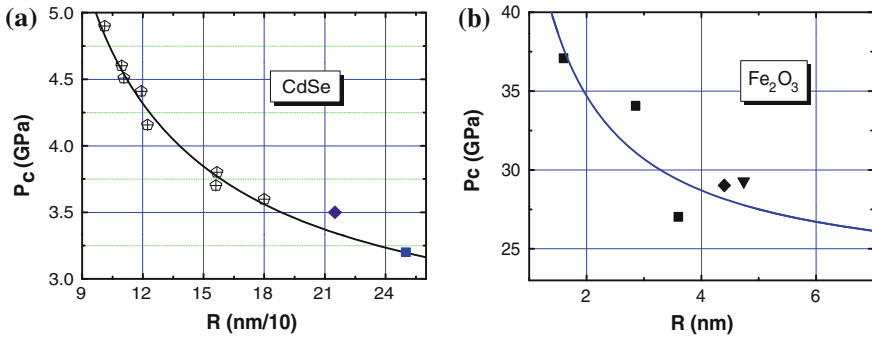


Fig. 28.10 P–K correlation for the solid–solid phase transition occurring at room temperature for **a** CdS [115, 118] and **b** Fe_2O_3 [114] in comparison with that for SnO_2 nanocrystals (Fig. 28.9b). **b** Theoretical reproduction of the size and pressure dependence of the phase transition of CdSe nanocrystals at room temperature ($\Delta T_C = 0$) [125]. Agreement between predictions and observations in these situations evidences the validity of the P-BOLS considerations from the perspective of atomic cohesive energy. The critical pressure for the 3-nm SnO_2 transition is predicted to be 43 GPa that is beyond the range of the referred measurement. Indeed, the pressure-induced T_C elevation compensates for the size-induced T_C depression (Reprinted with permission from [125])

agreement between the predictions and the measured trends in both cases demonstrates the effectiveness of the formulation and the validity of the physical considerations.

28.7 Summary

The extensibility and plastic yield strength of a solid over the whole range of sizes can be formulated based on the T-BOLS correlation and LBA mechanism, which has enabled the reproduction of the observed HPR and IHPR effect and identification of factors dominating the strongest sizes. Matching predictions to observations reveals the following:

1. The IHPR originates from the intrinsic competition between the energy density gain in the skin and the cohesive energy remnant of the undercoordinated surface atoms and the extrinsic competition between activation and prohibition of atomic dislocations. The activation energy is proportional to the atomic cohesive energy that drops with solid size whereas the prohibition of atomic dislocation arises from dislocation accumulation and strain gradient work hardening, which increases with the indentation depth. As the solid size decreases, a transition from dominance of energy density gain to dominance of cohesive energy remnant occurs at the IHPR critical size because of the increased proportion of the undercoordinated atoms. During the transition, contributions from both processes are comparative.

2. The IHPR critical size is predictable, which can be calibrated with a few measured datum points for a specific system. The critical size is dominated intrinsically by the bond nature, the T/T_m ratio, and extrinsically by experimental conditions or other factors such as size distribution and impurities that are represented by the factor f .
3. The IHPR at larger solid size converges to the normal HPR that holds its conventional meaning of the accumulation of atomic dislocations that resist further atomic displacements in plastic deformation. The slope in the traditional HPR is proportional to $\exp(T_m/T)$, which addresses the relationship between the hardness and the activation energy for atomic dislocations. The $K^{-0.5}$ term in the conventional HPR represents the accumulation of atomic dislocations that resists further dislocations.
4. This understanding of the process provides an additional explanation for the high ductility of a metallic nanosolid as the critical temperature for the solid-to-quasi-molten transition is much lower than the bulk melting point and the self-heating during detection should raise the actual temperature of the small specimen.
5. Compression-elevated bond energy compensates for the size reduction-lowered atomic cohesive energy to maintain the thermal stability. The energetic disparity between the skin and the bulk originate such anomalies, which bulk materials do not demonstrate, and the mechanism is beyond the scope of the classical theories of thermodynamics.

References

1. R.W. Siegel, G.E. Fougere, Mechanical properties of nanophase metals. *Nanostruct. Mater.* **6**(1–4), 205–216 (1995)
2. L.C. Zhang, I. Zarudi, Towards a deeper understanding of plastic deformation in monocrystalline silicon. *Int. J. Mech. Sci.* **43**(9), 1985–1996 (2001)
3. A. Concustell, N. Mattern, H. Wendrock, U. Kuehn, A. Gebert, J. Eckert, A.L. Greer, J. Sort, M.D. Baro, Mechanical properties of a two-phase amorphous Ni–Nb–Y alloy studied by nanoindentation. *Scripta Mater.* **56**(2), 85–88 (2007)
4. E.O. Hall, The deformation and ageing of mild steel: III discussion of results. *Proc. Phys. Soc. London Sect. B* **64**(381), 747–753 (1951)
5. N.J. Petch, The cleavage strengthening of polycrystals. *J. Iron Steel Inst.* **174**(1), 25–28 (1953)
6. M.F. Ashby, Deformation of plastically non-homogeneous materials. *Phil. Mag.* **21**(170), 399–424 (1970)
7. Y.M. Wang, M.W. Chen, F.H. Zhou, E. Ma, High tensile ductility in a nanostructured metal. *Nature* **419**(6910), 912–915 (2002)
8. D. Jang, M. Atzmon, Grain-size dependence of plastic deformation in nanocrystalline Fe. *J. Appl. Phys.* **93**(11), 9282–9286 (2003)
9. H. Conrad, J. Narayan, Mechanism for grain size softening in nanocrystalline Zn. *Appl. Phys. Lett.* **81**(12), 2241–2243 (2002)
10. H.S. Kim, A composite model for mechanical properties of nanocrystalline materials. *Scripta Mater.* **39**(8), 1057–1061 (1998)

11. H. Van Swygenhoven, P.M. Derlet, A. Hasnaoui, Atomic mechanism for dislocation emission from nanosized grain boundaries. *Phys. Rev. B* **66**(2), 024101 (2002)
12. S.G. Zaichenko, A.M. Glezer, Disclination mechanism of plastic deformation of nanocrystalline materials. *Interface Sci.* **7**(1), 57–67 (1999)
13. C.E. Carlton, P.J. Ferreira, What is behind the inverse Hall–Petch effect in nanocrystalline materials? *Acta Mater.* **55**(11), 3749–3756 (2007)
14. A.S. Argon, S. Yip, The strongest size. *Philos. Mag. Lett.* **86**(11), 713–720 (2006)
15. C.Q. Sun, Thermo-mechanical behavior of low-dimensional systems: The local bond average approach. *Prog. Mater. Sci.* **54**(2), 179–307 (2009)
16. M. Zhao, J.C. Li, Q. Jiang, Hall–Petch relationship in nanometer size range. *J. Alloy. Compd.* **361**(1–2), 160–164 (2003)
17. J. Schiotz, F.D. Di Tolla, K.W. Jacobsen, Softening of nanocrystalline metals at very small grain sizes. *Nature* **391**(6667), 561–563 (1998)
18. W.W. Gerberich, W.M. Mook, C.R. Perrey, C.B. Carter, M.I. Baskes, R. Mukherjee, A. Gidwani, J. Heberlein, P.H. McMurry, S.L. Girshick, Superhard silicon nanospheres. *J. Mech. Phys. Solids* **51**(6), 979–992 (2003)
19. Y. Giga, Y. Kimoto, Demonstration of an inverse Hall–Petch relationship in electrodeposited nanocrystalline Ni–W alloys through tensile testing. *Scripta Mater.* **55**(2), 143–146 (2006)
20. H. Somekawa, T.G. Nieh, K. Higashi, Instrumented indentation properties of electrodeposited Ni–W alloys with different microstructures. *Scripta Mater.* **50**(11), 1361–1365 (2004)
21. C.A. Schuh, T.G. Nieh, H. Iwasaki, The effect of solid solution W additions on the mechanical properties of nanocrystalline Ni. *Acta Mater.* **51**(2), 431–443 (2003)
22. T. Yamasaki, P. Schlossmacher, K. Ehrlich, Y. Ogino, Formation of amorphous electrodeposited Ni–W alloys and their nanocrystallization. *Nanostruct. Mater.* **10**(3), 375–388 (1998)
23. S. Guicciardi, D. Sciti, C. Melandri, A. Bellosi, Nanoindentation characterization of submicro- and nano-sized liquid-phase-sintered SiC ceramics. *J. Am. Ceram. Soc.* **87**(11), 2101–2107 (2004)
24. Y. Zhou, U. Erb, K.T. Aust, G. Palumbo, The effects of triple junctions and grain boundaries on hardness and Young’s modulus in nanostructured Ni–P. *Scripta Mater.* **48**(6), 825–830 (2003)
25. A. Inoue, H.M. Kimura, M. Watanabe, A. Kawabata, Work softening of aluminum base alloys containing nanoscale icosahedral phase. *Mater. Trans. JIM* **38**(9), 756–760 (1997)
26. S.C. Tjong, H. Chen, Nanocrystalline materials and coatings. *Mater. Sci. Eng. R-Rep.* **45**(1–2), 1–88 (2004)
27. I.A. Ovid’ko, Deformation and diffusion modes in nanocrystalline materials. *Int. Mater. Rev.* **50**(2), 65–82 (2005)
28. D. Wolf, V. Yamakov, S.R. Phillpot, A. Mukherjee, H. Gleiter, Deformation of nanocrystalline materials by molecular-dynamics simulation: Relationship to experiments? *Acta Mater.* **53**(1), 1–40 (2005)
29. D. Sherman, D. Brandon, Mechanical properties of hard materials and their relation to microstructure. *Adv. Eng. Mater.* **1**(3–4), 161–181 (1999)
30. R.A. Andrievskii, A.M. Glezer, Size effects in nanocrystalline materials: II Mechanical and physical properties. *Fiz. Metallov Metalloved.* **89**(1), 91–112 (2000)
31. A.I. Gusev, The effects of the nanocrystalline state in solids. *Uspekhi Fiz. Nauk* **168**(1), 55–83 (1998)
32. G.S. Was, T. Foecke, Deformation and fracture in microlaminates. *Thin Solid Films* **286**(1–2), 1–31 (1996)
33. C. Suryanarayana, Nanocrystalline materials. *Int. Mater. Rev.* **40**(2), 41–64 (1995)
34. V.G. Gryaznov, L.I. Trusov, Size effects in micromechanics of nanocrystals. *Prog. Mater. Sci.* **37**(4), 289–401 (1993)

35. G.A. Malygin, Plasticity and strength of micro- and nanocrystalline materials. *Phys. Solid State* **49**(6), 1013–1033 (2007)
36. M.A. Meyers, A. Mishra, D.J. Benson, Mechanical properties of nanocrystalline materials. *Prog. Mater. Sci.* **51**(4), 427–556 (2006)
37. J.C.M. Li, Y.T. Chou, Role of dislocations in flow stress grain size relationships. *Metall. Trans.* **1**(5), 1145–1148 (1970)
38. J.A. Knapp, D.M. Follstaedt, Hall–Petch relationship in pulsed-laser deposited nickel films. *J. Mater. Res.* **19**(1), 218–227 (2004)
39. R.W. Armstrong, A.K. Head, Dislocation queueing and fracture in an elastically anisotropic material. *Acta Metall.* **13**(7), 759–764 (1956)
40. N. Louat, Alloys, strong at room and elevated-temperatures from powder-metallurgy. *Acta Metall.* **33**(1), 59–69 (1985)
41. A. Lasalmonie, J.L. Strudel, Influence of grain-size on the mechanical-behavior of some high-strength materials. *J. Mater. Sci.* **21**(6), 1837–1852 (1986)
42. V. Yamakov, D. Wolf, S.R. Phillpot, A.K. Mukherjee, H. Gleiter, Deformation-mechanism map for nanocrystalline metals by molecular-dynamics simulation. *Nat. Mater.* **3**(1), 43–47 (2004)
43. J.C. Li. Transactions of the society of petroleum engineers of the American Institute of Mining, Metallurgical, and Petroleum Engineers Inc. 227 (239)1963
44. C.S. Pande, B.B. Rath, M.A. Imam, Effect of annealing twins on Hall–Petch relation in polycrystalline materials. *Mater. Sci. Eng. A-Struct. Mater. Prop. Microstruct. Process.* **367**(1–2), 171–175 (2004)
45. Y. Mishin, D. Farkas, M.J. Mehl, D.A. Papaconstantopoulos, Interatomic potentials for monoatomic metals from experimental data and ab initio calculations. *Phys. Rev. B* **59**(5), 3393–3407 (1999)
46. K.W. Jacobsen, J.K. Norskov, M.J. Puska, Interatomic interactions in the effective-medium theory. *Phys. Rev. B* **35**(14), 7423–7442 (1987)
47. M.F. Ashby, R.A. Verrall, Diffusion-accommodated flow and superplasticity. *Acta Metall.* **21**(2), 149–163 (1973)
48. H. Van Swygenhoven, P.M. Derlet, A.G. Froseth, Stacking fault energies and slip in nanocrystalline metals. *Nat. Mater.* **3**(6), 399–403 (2004)
49. H. Bei, S. Xie, E.P. George, Softening caused by profuse shear banding in a bulk metallic glass. *Phys. Rev. Lett.* **96**(10), 105503 (2006)
50. G.J. Fan, H. Choo, P.K. Liaw, E.J. Lavernia, A model for the inverse Hall–Petch relation of nanocrystalline materials. *Mater. Sci. Eng.* **409**(1–2), 243–248 (2005). *Structural Materials Properties Microstructure and Processing*
51. T.G. Nieh, J.G. Wang, Hall–Petch relationship in nanocrystalline Ni and Be–B alloys. *Intermetallics* **13**(3–4), 377–385 (2005)
52. E. Ma, Instabilities and ductility of nanocrystalline and ultrafine-grained metals. *Scr. Mater.* **49**(7), 663–668 (2003)
53. H.S. Kim, Y. Estrin, Phase mixture modeling of the strain rate dependent mechanical behavior of nanostructured materials. *Acta Mater.* **53**(3), 765–772 (2005)
54. Z.H. Jiang, X.L. Liu, G.Y. Li, Q. Jiang, J.S. Lian, Strain rate sensitivity of a nanocrystalline Cu synthesized by electric brush plating. *Appl. Phys. Lett.* **88**(14), 143115 (2006)
55. J.S. Lian, C.D. Gu, Q. Jiang, Z.H. Jiang, Strain rate sensitivity of face-centered-cubic nanocrystalline materials based on dislocation deformation. *J. Appl. Phys.* **99**(7), 076103 (2006)
56. S. Lefebvre, B. Devincere, T. Hoc, Simulation of the Hall–Petch effect in ultra-fine grained copper. *Mater. Sci. Eng.* **400**, 150–153 (2005). *Structural Materials Properties Microstructure and Processing*
57. C. Lu, Y.W. Mai, Y.G. Shen, Optimum information in crackling noise. *Phys. Rev. E* **72**(2), 027101 (2005)

58. F. Louchet, J. Weiss, T. Richeton, Hall–Petch law revisited in terms of collective dislocation dynamics. *Phys. Rev. Lett.* **97**(7), 075504 (2006)
59. F.A. Mohamed, Interpretation of nanoscale softening in terms of dislocation-accommodated boundary sliding. *Metall. Mater. Trans. A-Phys. Metall. Mater. Sci.* **38A**(2), 340–347 (2007)
60. H.W. Song, S.R. Guo, Z.Q. Hu, A coherent polycrystal model for the inverse Hall–Petch relation in nanocrystalline materials. *Nanostruct. Mater.* **11**(2), 203–210 (1999)
61. S. Cheng, J.A. Spencer, W.W. Milligan, Strength and tension/compression asymmetry in nanostructured and ultrafine-grain metals. *Acta Mater.* **51**(15), 4505–4518 (2003)
62. P.P. Chattopadhyay, S.K. Pabi, I. Manna, On the inverse Hall–Petch relationship in nanocrystalline materials. *Z. Metallk.* **91**(12), 1049–1051 (2000)
63. B. Jiang, G.J. Weng, A generalized self-consistent polycrystal model for the yield strength of nanocrystalline materials. *J. Mech. Phys. Solids* **52**(5), 1125–1149 (2004)
64. J. Schiotz, K.W. Jacobsen, A maximum in the strength of nanocrystalline copper. *Science* **301**(5638), 1357–1359 (2003)
65. V. Bata, E.V. Pereloma, An alternative physical explanation of the Hall–Petch relation. *Acta Mater.* **52**(3), 657–665 (2004)
66. V. Yamakov, D. Wolf, S.R. Phillpot, A.K. Mukherjee, H. Gleiter, Deformation mechanism crossover and mechanical behaviour in nanocrystalline materials. *Philos. Mag. Lett.* **83**(6), 385–393 (2003)
67. R.A. Masumura, P.M. Hazzledine, C.S. Pande, Yield stress of fine grained materials. *Acta Mater.* **46**(13), 4527–4534 (1998)
68. A.A. Fedorov, M.Y. Gutkin, I.A. Ovid’ko, Triple junction diffusion and plastic flow in fine-grained materials. *Scr. Mater.* **47**(1), 51–55 (2002)
69. E. Arzt, Overview no. 130—Size effects in materials due to microstructural and dimensional constraints: A comparative review. *Acta Mater.* **46**(16), 5611–5626 (1998)
70. U.F. Kocks, A.S. Argon, M.F. Ashby, Thermodynamics and kinetics of slip. *Prog. Mater. Sci.* **19**, 1–281 (1975)
71. X.Y. Qin, X.G. Zhu, S. Gao, L.F. Chi, J.S. Lee, Compression behaviour of bulk nanocrystalline Ni–Fe. *J. Phys. Condens. Matter* **14**(10), 2605–2620 (2002)
72. X.D. Han, K. Zheng, Y.F. Zhang, X.N. Zhang, Z. Zhang, Z.L. Wang, Low-temperature in situ large-strain plasticity of silicon nanowires. *Adv. Mater.* **19**(16), 2112–2118 (2007)
73. V. Brazhkin, N. Dubrovinskaia, A. Nicol, N. Novikov, R. Riedel, R. Solozhenko, Y. Zhao, What does ‘harder than diamond’ mean? *Nat. Mater.* **3**(9), 576–577 (2004)
74. L.D. Marks, Experimental studies of small-particle structures. *Rep. Prog. Phys.* **57**(6), 603–649 (1994)
75. C.Q. Sun, S. Li, C.M. Li, Impact of bond order loss on surface and nanosolid mechanics. *J. Phys. Chem. B* **109**(1), 415–423 (2005)
76. S. Yip, Nanocrystalline metals: Mapping plasticity. *Nat. Mater.* **3**(1), 11–12 (2004)
77. S.Y. Chang, T.K. Chang, Grain size effect on nanomechanical properties and deformation behavior of copper under nanoindentation test. *J. Appl. Phys.* **101**(3), 033507 (2007)
78. J. Narayan, R.K. Venkatesan, A. Kvit, Structure and properties of nanocrystalline zinc films. *J. Nanopart. Res.* **4**(3), 265–269 (2002)
79. X.J. Liu, L.W. Yang, Z.F. Zhou, P.K. Chu, C.Q. Sun, Inverse Hall–Petch relationship of nanostructured TiO₂: Skin-depth energy pinning versus surface preferential melting. *J. Appl. Phys.* **108**, 073503 (2010)
80. P.G. Sanders, J.A. Eastman, J.R. Weertman, Elastic and tensile behavior of nanocrystalline copper and palladium. *Acta Mater.* **45**(10), 4019–4025 (1997)
81. H.H. Fu, D.J. Benson, M.A. Meyers, Analytical and computational description of effect of grain size on yield stress of metals. *Acta Mater.* **49**(13), 2567–2582 (2001)
82. P.G. Sanders, C.J. Youngdahl, J.R. Weertman, The strength of nanocrystalline metals with and without flaws. *Mater. Sci. Eng.* **23A**, 77–82 (1997). *Structural Materials Properties Microstructure and Processing*

83. C.A. Schuh, T.G. Nieh, T. Yamasaki, Hall–Petch breakdown manifested in abrasive wear resistance of nanocrystalline nickel. *Scr. Mater.* **46**(10), 735–740 (2002)
84. G. Palumbo, U. Erb, K.T. Aust, Triple line disclination effects on the mechanical-behavior of materials. *Scr. Metall. Mater.* **24**(12), 2347–2350 (1990)
85. K. Lu, Nanocrystalline metals crystallized from amorphous solids: Nanocrystallization, structure, and properties. *Mater. Sci. Eng. R-Rep.* **16**(4), 161–221 (1996)
86. B. Chen, H. Zhang, K. Dunphy-Guzman, D. Spagnoli, M. Kruger, D. Muthu, M. Kunz, S. Fakra, J. Hu, Q. Guo, J. Banfield, Size-dependent elasticity of nanocrystalline titania. *Phys. Rev. B* **79**(12), 125406 (2009)
87. H.J. Hofler, R.S. Averback, Grain-growth in nanocrystalline TiO₂ and its relation to vickers hardness and fracture-toughness. *Scr. Metall. Mater.* **24**(12), 2401–2406 (1990)
88. Y. He, J.F. Liu, W. Chen, Y. Wang, H. Wang, Y.W. Zeng, G.Q. Zhang, L.N. Wang, J. Liu, T.D. Hu, H. Hahn, H. Gleiter, J.Z. Jiang, High-pressure behavior of SnO₂ nanocrystals. *Phys. Rev. B* **72**(21), 212102 (2005)
89. M. Born, Thermodynamics of crystals and melting. *J. Chem. Phys.* **7**(8), 591–603 (1939)
90. F.G. Shi, Size-dependent thermal vibrations and melting in nanocrystals. *J. Mater. Res.* **9**(5), 1307–1313 (1994)
91. Q. Jiang, Z. Zhang, J.C. Li, Superheating of nanocrystals embedded in matrix. *Chem. Phys. Lett.* **322**(6), 549–552 (2000)
92. Q. Jiang, C.C. Yang, Size effect on the phase stability of nanostructures. *Curr. Nanosci.* **4**(2), 179–200 (2008)
93. R. Vallee, M. Wautelet, J.P. Dauchot, M. Hecq, Size and segregation effects on the phase diagrams of nanoparticles of binary systems. *Nanotechnology* **12**(1), 68–74 (2001)
94. G. Guisbiers, M. Kazan, O. Van Overschelde, M. Wautelet, S. Pereira, Mechanical and thermal properties of metallic and semiconductive nanostructures. *J. Chem. Phys. C* **112**(11), 4097–4103 (2008)
95. K. Nakada, M. Fujita, G. Dresselhaus, M.S. Dresselhaus, Edge state in graphene ribbons: Nanometer size effect and edge shape dependence. *Phys. Rev. B* **54**(24), 17954–17961 (1996)
96. W.H. Qi, M.P. Wang, G.Y. Xu, The particle size dependence of cohesive energy of metallic nanoparticles. *Chem. Phys. Lett.* **372**(5–6), 632–634 (2003)
97. K.S. Siow, A.A.O. Tay, P. Oruganti, Mechanical properties of nanocrystalline copper and nickel. *Mater. Sci. Technol.* **20**(3), 285–294 (2004)
98. X.D. Han, Y.F. Zhang, K. Zheng, X.N. Zhang, Z. Zhang, Y.J. Hao, X.Y. Guo, J. Yuan, Z.L. Wang, Low-temperature in situ large strain plasticity of ceramic SiC nanowires and its atomic-scale mechanism. *Nano Lett.* **7**(2), 452–457 (2007)
99. Y. Yan, H. Yin, Q.P. Sun, Y. Huo, Rate dependence of temperature fields and energy dissipations in non-static pseudoelasticity. *Continuum Mech. Thermodyn.* **24**(4–6), 675–695 (2012)
100. L. Lu, M.L. Sui, K. Lu, Superplastic extensibility of nanocrystalline copper at room temperature. *Science* **287**(5457), 1463–1466 (2000)
101. D.G. Eskin, L. Katgerman, Mechanical properties in the semi-solid state and hot tearing of aluminium alloys. *Prog. Mater. Sci.* **49**(5), 629–711 (2004)
102. J. Campbell, *Castings* (Butterworth-Heinemann, Oxford, 1991)
103. B. Chen, D. Penwell, L.R. Benedetti, R. Jeanloz, M.B. Kruger, Particle-size effect on the compressibility of nanocrystalline alumina. *Phys. Rev. B* **66**(14), 144101 (2002)
104. S.B. Qadri, J. Yang, B.R. Ratna, E.F. Skelton, J.Z. Hu, Pressure induced structural transitions in nanometer size particles of PbS. *Appl. Phys. Lett.* **69**(15), 2205–2207 (1996)
105. M.R. Gallas, G.J. Piermarini, Bulk modulus and Youngs modulus of nanocrystalline gamma-alumina. *J. Am. Ceram. Soc.* **77**(11), 2917–2920 (1994)
106. J. Zhao, G.R. Hearne, M. Maaza, F. Laher-Lacour, M.J. Witcomb, T. Le Bihan, M. Mezouar, Compressibility of nanostructured alumina phases determined from synchrotron X-ray diffraction studies at high pressure. *J. Appl. Phys.* **90**(7), 3280–3285 (2001)

107. N. Ono, R. Nowak, S. Miura, Effect of deformation temperature on Hall–Petch relationship registered for polycrystalline magnesium. *Mater. Lett.* **58**(1–2), 39–43 (2004)
108. A. Duckham, D.Z. Zhang, D. Liang, V. Luzin, R.C. Cammarata, R.L. Leheny, C.L. Chien, T.P. Weihs, Temperature dependent mechanical properties of ultra-fine grained FeCo–2V. *Acta Mater.* **51**(14), 4083–4093 (2003)
109. N. Agrait, A.L. Yeyati, J.M. van Ruitenbeek, Quantum properties of atomic-sized conductors. *Phys. Rep.-Rev. Sec. Phys. Lett.* **377**(2–3), 81–279 (2003)
110. Z.S. Ma, S.G. Long, Y. Pan, Y.C. Zhou, Indentation depth dependence of the mechanical strength of Ni films. *J. Appl. Phys.* **103**(4), 2885090 (2008)
111. A.C. Lund, T.G. Nieh, C.A. Schuh, Tension/compression strength asymmetry in a simulated nanocrystalline metal. *Phys. Rev. B* **69**(1), 012101 (2004)
112. G. Abudukelimu, G. Guisbiers, M. Wautelet, Theoretical phase diagrams of nanowires. *J. Mater. Res.* **21**(11), 2829–2834 (2006)
113. S.M. Clark, S.G. Prilliman, C.K. Erdonmez, A.P. Alivisatos, Size dependence of the pressure-induced gamma to alpha structural phase transition in iron oxide nanocrystals. *Nanotechnology* **16**(12), 2813–2818 (2005)
114. K. Jacobs, D. Zaziski, E.C. Scher, A.B. Herhold, A.P. Alivisatos, Activation volumes for solid–solid transformations in nanocrystals. *Science* **293**(5536), 1803–1806 (2001)
115. M. Bruchez, M. Moronne, P. Gin, S. Weiss, A.P. Alivisatos, Semiconductor nanocrystals as fluorescent biological labels. *Science* **281**(5385), 2013–2016 (1998)
116. V.L. Colvin, M.C. Schlamp, A.P. Alivisatos, Light-emitting-diode from Cadmium selenide nanocrystals and a semiconducting polymer. *Nature* **370**(6488), 354–357 (1994)
117. S.H. Tolbert, A.P. Alivisatos, Size dependence of a first-order solid–solid phase-transition—the wurtzite to rock-salt transformation in CdSe nanocrystals. *Science* **265**(5170), 373–376 (1994)
118. J.N. Wickham, A.B. Herhold, A.P. Alivisatos, Shape change as an indicator of mechanism in the high-pressure structural transformations of CdSe nanocrystals. *Phys. Rev. Lett.* **84**(5), 923–926 (2000)
119. D. Zaziski, S. Prilliman, E.C. Scher, M. Casula, J. Wickham, S.M. Clark, A.P. Alivisatos, Critical size for fracture during solid–solid phase transformations. *Nano Lett.* **4**(5), 943–946 (2004)
120. L. Manna, L.W. Wang, R. Cingolani, A.P. Alivisatos, First-principles modeling of unpassivated and surfactant-passivated bulk facets of wurtzite CdSe: A model system for studying the anisotropic growth of CdSe nanocrystals. *J. Phys. Chem. B* **109**(13), 6183–6192 (2005)
121. K. Jacobs, J. Wickham, A.P. Alivisatos, Threshold size for ambient metastability of rocksalt CdSe nanocrystals. *J. Phys. Chem. B* **106**(15), 3759–3762 (2002)
122. Z.W. Wang, K. Finkelstein, C. Ma, Z.L. Wang, Structure stability, fracture, and tuning mechanism of CdSe nanobelts. *Appl. Phys. Lett.* **90**(11), 2713172 (2007)
123. A.N. Goldstein, C.M. Echer, A.P. Alivisatos, Melting in semiconductor nanocrystals. *Science* **256**(5062), 1425–1427 (1992)
124. Z.W. Chen, C.Q. Sun, Y.C. Zhou, O.Y. Gang, Size dependence of the pressure-induced phase transition in nanocrystals. *J. Chem. Phys. C* **112**(7), 2423–2427 (2008)
125. M. Grunwald, E. Rabani, C. Dellago, Mechanisms of the wurtzite to rocksalt transformation in CdSe nanocrystals. *Phys. Rev. Lett.* **96**(25), 255701 (2006)
126. D. Zahn, Y. Grin, S. Leoni, Mechanism of the pressure-induced wurtzite to rocksalt transition of CdSe. *Phys. Rev. B* **72**(6), 064110 (2005)
127. F. Shimojo, S. Kodiyalam, I. Ebbsjo, R.K. Kalia, A. Nakano, P. Vashishta, Atomistic mechanisms for wurtzite-to-rocksalt structural transformation in cadmium selenide under pressure. *Phys. Rev. B* **70**(18), 184111 (2004)
128. B.J. Morgan, P.A. Madden, Pressure-driven sphalerite to rock salt transition in ionic nanocrystals: A simulation study. *Nano Lett.* **4**(9), 1581–1585 (2004)

129. V. Swamy, A. Kuznetsov, L.S. Dubrovinsky, P.F. McMillan, V.B. Prakapenka, G. Shen, B.C. Muddle, Size-dependent pressure-induced amorphization in nanoscale TiO_2 . *Phys. Rev. Lett.* **96**(13), 135702 (2006)
130. M.S. Miao, W.R.L. Lambrecht, Universal transition state for high-pressure zinc blende to rocksalt phase transitions. *Phys. Rev. Lett.* **94**(22), 225501 (2005)
131. F. Calvo, J.P.K. Doye, Pressure effects on the structure of nanoclusters. *Phys. Rev. B* **69**(12), 125414 (2004)
132. C.C. Chen, A.B. Herhold, C.S. Johnson, A.P. Alivisatos, Size dependence of structural metastability in semiconductor nanocrystals. *Science* **276**(5311), 398–401 (1997)

Chapter 29

Atomic Vacancy, Nanocavity, and Porous Foams

- *Bonds between undercoordinated atoms in the inner surfaces of nanopores perform the same as those in the skins of the bulk and of a nanosolid.*
- *A broken bond not only serves as a center initiating mechanical failure but also provides a site pinning dislocations and trapping energy.*
- *Atomic vacancies, point defects, and nanometer-sized pores result in the unusual properties of the specimens—they are of lightweight and high strength yet thermally or chemically less stable.*

29.1 Observations

29.1.1 Atomic Vacancies and Point Defects

It is expected intuitively that atomic vacancies or point defects reduce the number of chemical bonds of nearby atoms and hence lowers the strength of the entire body of a material. However, the hardness of transition metal carbides and nitrides does not follow this simple picture of bond counting. Vacancies or point defects not only provide sites initiating structure failure [1] but also act as pinning centers inhibiting the motion of dislocations and hence enhancing the mechanical strength of the material [2]. The hardness of iron aluminides (FeAlN) is proportional to the square root of the vacancy concentration [3]. About 4 % nitrogen atomic vacancies could stabilize the rocksalt structure of MnN substantially [4]. With the increase in C vacancies in the WAIC compounds, the mass density decreases, whereas the hardness increases monotonically up to a maximum at 35 % of C vacancies, as shown in Fig. 29.1a [5]. Fracture measurement and modeling analysis indicated that a small number of atomic defects modulate the strength of the WS₂ nanotubes [6]. An atomic defect has an enormous influence on the Young's modulus and tensile strength of the nanotubes [7]. The excessive voids presented in the wall of the unreconstructed nanotubes serve as centers initiating structure failure in plastic

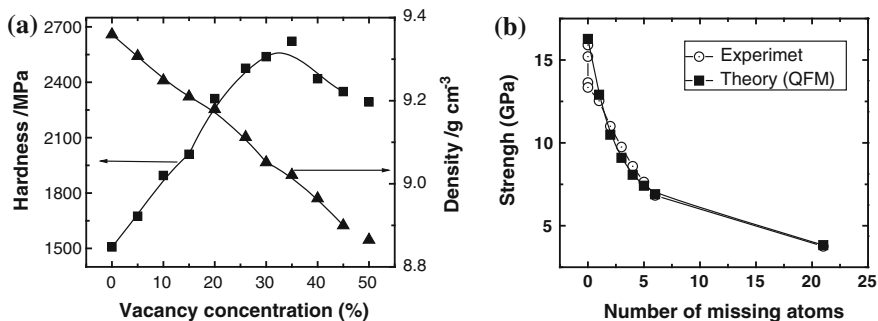


Fig. 29.1 Mechanical hardening by creation of (a) carbon vacancy density in $(W_{0.5}Al_{0.5})_x C_{1-x}$ compound [5] and (b) point defect in WS_2 nanotubes [6] (reprinted with permission from [9])

deformation. Figure 29.1b shows the strength versus the number of missing atoms in the critical defect according to the quantized fracture mechanics (QFM) approximation [8].

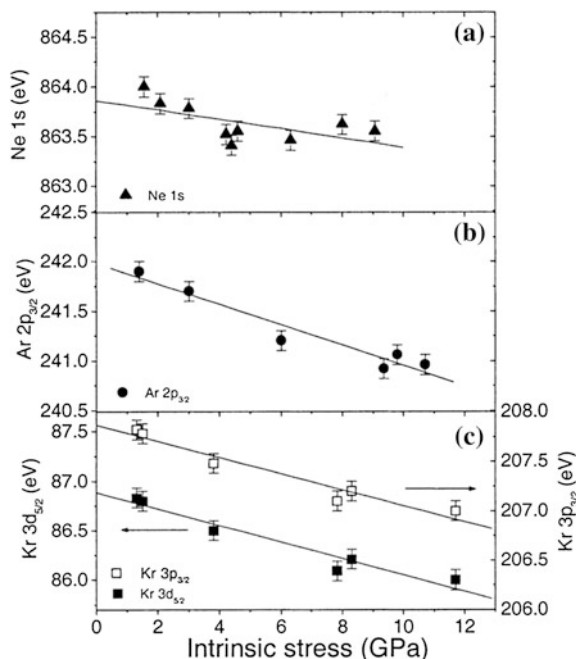
An *ab initio* calculation of shear elastic stiffness and electronic structures suggested that the vacancy produces entirely different effects on the mechanical strength of group IVb nitrides and group Vb carbides. The occupation of the shear-unstable metallic *d*-*d* bonding states changes essentially in an opposite way for the carbides and nitrides in the presence of vacancies, resulting in different responses to shear stress [10]. Experimentally, the hardness and the elastic modulus of group IVb nitrides such as TiN_x , ZrN_x , and HfN_x decrease as the concentration of the nonmetal vacancy increases [11, 12]. In contrast, the hardness of the Vb carbides such as NbC_x and TaC_x increases consistently and reproducibly as the vacancy concentration increases up to a modest value and reaches a maximum at a vacancy concentration of about 12 % [13].

DFT calculations [14] also suggested that the boron doping of $ScRh_3B_x$ could enhance the cohesive energy monotonically due to the strong covalent bonding between B-2p and Rh-4d states. However, at $x = 0.5$, a configuration is achieved in which each boron is surrounded by vacancies at the cube centers. This configuration reduces the strain in the structure and shortens the Rh-B bonds, leading to a maximum in the bulk modulus. The density of states at the Fermi energy is also minimum for $x = 0.5$ which adds further stability to the structure.

29.1.2 Nanocavity

Formation of nanometer-sized cavities could also enhance the mechanical properties of solid materials to a certain extent [14–16]. For instance, Si atomic vacancy could trap oxygen atom to reduce its diffusivity [17]. He implantation induces ~ 1 -nm-sized bubbles that enhance the hardness of Ni layers by

Fig. 29.2 Binding energy shifts of the noble gases entrapped in a-C nanopores as a function of the compressive stress of the a-C films (reprinted with permission from [33]), evidencing the weakening atomic interaction of the entrapped gases



approximately seven times that of untreated Ni, up to 8.3 ± 0.6 GPa, indicating that the bubbles provide centers for pinning dislocation motion strongly [18].

Amorphous carbon (a-C) films have a uniquely intrinsic stress (~ 12 GPa) which is almost one order in magnitude higher than those found in other amorphous materials such as a-Si, a-Ge, or metals (<1 GPa) [19]. The internal stress of the a-C films can be modulated by changing the sizes of nanopores that are produced by the bombardment of noble gases (Ar, Kr, and Xe) during formation [20, 21]. Using extended near-edge XAFS and XPS, Lacerda et al. [20] investigated the effect of the trapping of noble gases in the a-C matrix on the internal stress of the a-C films and the energy states of the trapped gases. They found that the internal stress could be raised from 1 to 11 GPa by controlling the sizes of the pores within which noble gases are trapped. Meanwhile, they found an approximate ~ 1 eV lowering (smaller in magnitude) of the core level (Kr-3p, 3d, Ne-1s, and Ar-2p), binding energy of the entrapped gases (Fig. 29.2) associated with 0.03–0.05 nm expansion of the atomic distance of the noble gases trapped. The measured core-level shift is of the same order as those measured for noble gases implanted in Ge [22], Al [23], Cu, Ag, Au [24, 25], and Xe implanted in Pd hosts [26]. The interatomic separation of Ar(Xe) increases from 0.24 (0.29) to 0.29 (0.32) nm when the stress of the host a-C is increased from 1 to 11 GPa [27]. Examination [18] of the dependence of yield strength on He concentration, bubble size, and bubble density suggests that the bubbles pin dislocation motion as strongly as the hard second-phase precipitates do.

The bubble-induced internal stress has the similar effect to applying mechanical stress to the specimen. Compressing the organic layers in organic light-emitting diode (OLED) has been found to be an effective process for improving the performance of organic electroluminescent devices [28]. This process involves applying physical pressure to the organic layers of the device. The OLED fabricated using this method shows a notable increase in luminance intensity and current efficiency when it is compared with a compression-free device, and the current efficiency has been almost doubled.

Comparatively, an external hydrostatic pressure around 11 GPa could suppress the interplanar distance of microcrystalline graphite by $\sim 15\%$ [29], gathering the core/valence electrons of carbon atoms closer together. An increase in the external hydrostatic pressure lowers the resistivity of a-C films [30]. These results are in accordance with the work of Umemoto et al. [31] who proposed a dense, metallic, and rigid form of graphitic carbon with similar characteristics. The effect of hydrostatic pressure is very much the same to the pore-induced internal stress using noble gas sputtering and implanting.

The binding energy weakening and atomic distance expansion of the entrapped gases indicate clearly the gas-entrapped pore size expansion and the interfacial C–C bond contraction. The pore-entrapped gases undergo a pressure that is lower than the atmosphere. The interfacial C–C bonds contribute to the extraordinary mechanical strength of the entire a-C films. The excessive stress induced by pore creation plays the same role as the external hydrostatic pressure causing densification, metallization, and strengthening of the graphite by lattice compression. The surface interstitial nanovoids of 2–3 nm size induced by He⁺ implantation in crystalline Si could remarkably reduce the diffusivity of B atoms, whereas these nanovoids do not hinder the B electrical activation [32]. This finding evidences the elevation of the activation energy, or barrier, for atomic diffusion and the densified charge for the higher conductivity due to the local strain in the negatively curved skins of voids.

29.1.3 Metallic Foams

Metal foams with excessive amount of discretely distributed nanocavities have formed a class of new materials, which offer a variety of applications in fields such as lightweight construction or crash energy management, as well as sensing, catalysis, and other applications which benefit from their characteristic high surface area per unit volume [34, 35]. Despite the versatility of geometrical forms of the pores [36–38], the significance of the foams is the large proportion of undercoordinated atoms.

Foams can be fabricated by dissolution in acid, anode oxidation in liquid, or simply using powder-metallurgy sintering with or without placeholder or scaffolds [35–37]. For example, nanoporous gold is made by the dissolution in acid of silver atoms from an Au/Ag alloy; during dissolution, gold atoms in the lattice of the

parent phase dynamically rearrange to form a three-dimensional crystalline random porous structure with uniform ligament size [39]. Application of anodic potential to the alloy in this dealloying process enhances the silver dissolution rate relative to the gold diffusion rate, leading to smaller ligament sizes. The foams can be envisioned as a three-dimensional network of ultrahigh-strength nanowires or spherical holes in a matrix, thus bringing together two seemingly paradox properties: high strength and high porosity yet lighter and thermally less stable. The foamed materials are expected to be stiffer at low temperatures and tougher at raised temperatures compared with bulk crystals.

Figure 29.3 shows the typical open-cell structure and the ligament size of Au nanofoams and the size and surface effect on the stiffness of Au foams of $\sim 30\%$ relative density samples [40]. Foams of the smaller ligament sizes are stronger and that the surface skin of the ligand is even stronger, which agrees with previously discussed skin mechanics and indentation depth features of the continuum thin films. Decreasing ligament size, especially below 10 nm, causes a dramatic rise in the effective Young's modulus of nanoporous Au [41] and the strength of the ligand [42].

Characterization [43] of the size-dependent mechanical properties of nanoporous Au using a combination of nanoindentation, column pillar microcompression, and MD simulations suggested that nanoporous gold could be as strong as bulk Au and that the ligaments in nanoporous gold approach the theoretical yield strength of bulk gold, or even harder [40]. At a relative density of 42 %, porous Au manifests a sponge-like morphology of interconnecting ligaments on a length scale of similar to 100 nm. The material is polycrystalline with grain sizes of 10–60 nm. Microstructural characterization of the residual indentation reveals a localized densification via ductile (plastic) deformation under compressive stress. A mean hardness of 145 MPa and a Young's modulus of 11.1 GPa have been derived from the analysis of the load-displacement curves. The hardness of the investigated nanoporous Au has a value some 10 times higher than the hardness predicted by the scaling laws of open-cell foams [44]. The compacted nanocrystalline Au ligaments exhibit an average grain size of <50 nm and hardness values ranging from 1.4 to 2.0 GPa, which were up to 4.5 times higher than the hardness values obtained from polycrystalline Au [45]. A decrease in ligament size resulted in an increase in the yield stress. The yield stress of the nanometer-sized Au ligament was much higher than that of bulk polycrystalline gold. Therefore, the size and surface effects, such as a reduction in the number of defects in grains, are important to the strengthening of nanoporous Au [46]. Using scaling laws for foams, the yield strength of the 15-nm-diameter ligaments is estimated to be 1.5 GPa, close to the theoretical strength of Au. This value agrees well with extrapolations of the HPR yield strength at submicron scales [47].

Similarly, the strength of Al foams increases by 60–75 % upon thermal treatment and age hardening after foaming [48]. The hardness of the Al foam is twice as high as pure Al, and the hardness decreases with increasing temperature [49].

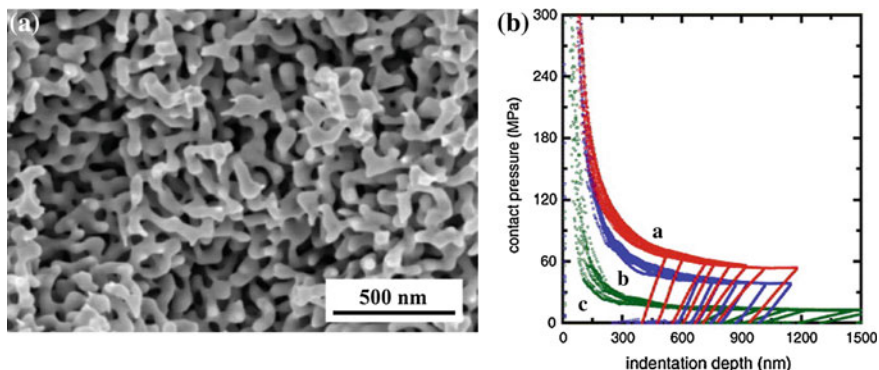


Fig. 29.3 **a** The open-cell structure of Au nanofoams and **b** the size and surface effect on the hardness in the nanoindentation load–depth profiles for 30 % relative density samples, given distinct ligament sizes in panel **b**: (a) 60 nm; (b) 160 nm; and (c) 480 nm (reprinted with permission from [40])

Figure 29.4a shows the porosity dependence of the stress–strain curves of the aluminum foams with a relative density of 14.6–48.5 %, where the pore size is between 1.6 and 2.0 mm. If the foam density was high, then the constant-stress plateau was short. On the other hand, foam of lower density exhibited a longer, flatter plateau because the structure affords more opportunity for cell walls to collapse and deform [50]. Foams with smaller pore sizes should follow the same trend of hardness change in smaller ligands.

However, nanoindentation measurement [51] revealed that the mechanical properties, such as the modulus and hardness, of anodic Al oxide structures decrease monotonically as the pore size is increased from 30 to 80 nm, see Fig. 29.4b. Although the elastic modulus, hardness, and viscosity are different mechanical properties, a similar behavior was observed for all these properties, being the same to polymers [52]. The same trend of change in the seemingly different quantities indicates clearly their common origin and interdependence from the perspective of energy density, according to the BOLS correlation.

The porous structure is light yet thermally less stable. MD simulation [53] of the size effect on melting in solids containing nanovoids revealed four typical stages in void melting that are different from the melting of bulk materials and nanoparticles. Melting in each of the stages is governed by the interplay among different thermodynamic mechanisms arising from the changes in the interfacial free energies, the curvature of the interface, and the elastic energy induced by the density change at melting. As a result, the local melting temperatures show a strong dependence on the void size, which is the cause of the observed complex hierarchical melting sequence.

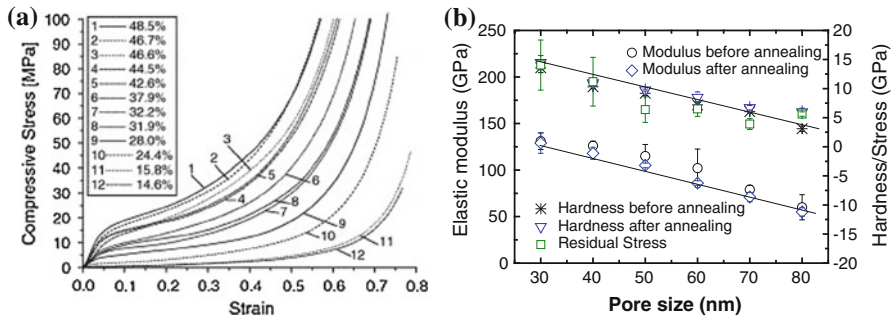


Fig. 29.4 **a** Compressive stress–strain curves of Al foams with different relative density (pore size: 1.60–2.00 mm) and **b** pore size dependence of modulus, hardness, and residual stress anodic Al oxide foams, which follow the same trend of change [51], indicating the common origin of these seemingly different quantities from the perspective of energy density, according to the BOLS premise (reprinted with permission from [9])

29.2 Known Mechanism

There have been multiple models regarding the cavity hardening of nanovoided systems. Quantize fracture mechanics (QFM) in terms of the classical continuum medium mechanics and the Gibbs free energy considers that a discrete number of defects arising from a few missing atoms in a nanostructure could contribute to the mechanical strength. Another theoretical approach considers the electronic structure around the Fermi energy [54]. Theoretical calculations suggested that the presence of two unsaturated electronic bands near the Fermi level respond, which oppositely to shear stress to enhance the hardness of the voided systems. This system behaves in an unusual way as the number of electrons in a unit cell changes. These proposals agree with the BOLS notation indicating that the density of states will shift to energy deeper away from the E_F because of the broken-bond-induced quantum entrapment. The deepened potential well provides also an atomistic understanding of the effect of defect pinning that inhibits atomic dislocation motion.

The macroscopic stresses are suggested to be composed of two parts, representing dynamic and quasi-static components [55]. The dynamic part controls the movement of the dynamic yield surface in stress space, while the quasi-static part determines the shape of the dynamic yield surface. The matrix material is idealized as a rigid-perfect plastic. Two major effects of point defects are proposed to lead to significant anomalies in mechanical properties: spontaneous stress and stiffness. Among the two, one is the direct effects caused by non-interacting point defects and the other is the collective effects induced by interacting point defects [56]. The first group includes the following: (1) changes in the linear dimensions of a solid in response to a change in defect concentration and (2) stress induced by an inhomogeneous distribution of point defects, a so-called chemical stress. The second

group includes the following: (1) defect order–disorder transitions accompanied by self-strain and (2) deviations from the linear elastic behavior because of the dissociation/association of point defects. All of the above effects become important if the concentration of point defects is sufficiently high (above 10^{21} cm^{-3}).

For metal foams, there are also a number of models. According to Gibson and Ashby [57] and Hodge et al. [45], the relationship between the yield strength (σ) and the relative density (ρ_f/ρ_b) of a foam material follows the scaling law

$$\sigma_f = \sigma_b \times \begin{cases} (\rho_f/\rho_b)^{3/2} & \text{(Gibson and Ashby)} \\ C_b(\rho_f/\rho_b)^{3/2} & \text{(Hodge et al.)} \end{cases} \quad (29.1)$$

subscripts f and b denote foam and bulk properties, respectively. The $\rho_f = (V_{\text{total}} - V_{\text{void}})/V_{\text{total}}$. Substituting the $\sigma_b = \sigma_0(1 + AK^{-0.5})$ in the HPR for the σ_b in the modified scaling relation with a given porosity, Hodge et al. [45] derived the size dependence of ligament strength in Au foams, which follow the HPR relation with $C_b = 0.3$ as a factor of correction as shown in Fig. 29.9b.

The porosity-depressed Young's modulus of Pd and Cu specimens [58] was expressed in many mechanical simulations [59–61]:

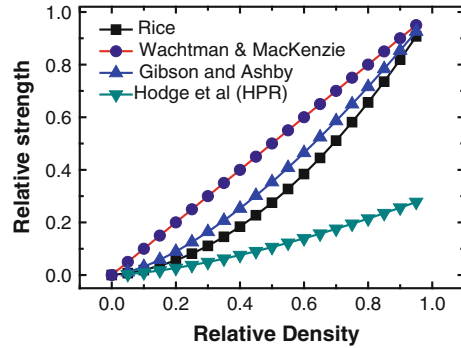
$$Y = Y_0 \times \begin{cases} 1 - 1.9p + 0.9p^2 & \text{(Wachtman and MacKenzie)} \\ (1 - p/p_0)^n & \text{(Rice)} \end{cases} \quad (29.2)$$

with p the porosity being defined as $p = V_{\text{void}}/V_{\text{total}}$. The density relates to the porosity as $\rho_p = 1 - p$. The decrease in Young's modulus and flow stress with density at larger pore sizes corresponds to the existing pores that provide sites for initiating failures. Rice [61] proposed a normalized porosity dependence of the Young's modulus in the form, where p_0 is the value of p for which the porosity-dependent properties go to zero. The index n and p_0 are adjustable parameters. This model fits with $n = 1$ linearly to the measured Y of various pores. Figure 29.5 compares the model predictions of density dependence of mechanical strength of metallic foams.

The theory of linear elasticity describes the deformation behavior of multiphase materials of larger pore sizes. The strength of foam materials always decreases with increasing porosity. The mechanical properties of foams are related to the porosity or the relative density of the material as the dominating parameter, and neither the effect of sizes of pores nor the effect of bond nature of the matrix are involved. In fact, nanomechanical measurements of nanoporous foams on a submicron scale [62, 63] revealed close resemblance of the nanosized ligaments in foams showing a dramatic increase in strength with decreasing sample size [44, 47]. Therefore, the effects of pore size, bond nature, and temperature must be considered in practice because the high proportion of the undercoordinated atoms become predominant in controlling the physical behavior of nanoporous foams.

Because the mechanical behavior of the surface is different from the bulk interior of the material, it would be an effective approach to consider the effective

Fig. 29.5 Density dependence of the mechanical strength of metallic foams (reprinted with permission from [9])



elastic constants of nanocomposites in terms of a three-phase structure, i.e., the bulk matrix, the voids, and the interfacial skins [64]. The effect of surface energy and surface stress has been considered in analyzing the deformation of microscale structures by many researchers. For examples, Sader [65] analyzed the effects of homogeneous surface stress on the deflection of cantilever plates used in AFM. Cammarata and Sieradzki [66] evaluated the effect of surface stress on the elastic modulus of thin films and superlattices. Yang and Li [67] discussed the effect of chemical stress on the bending of a single-layer and bilayer micromechanical beam. Sharma et al. [68] found that surface elasticity can significantly alter the stress state of materials at the length scale of nanometers. They suggested that the dependence of the stress state on the size of the embedded inhomogeneities could be significant in determining the effective elastic modulus of composites. Yang [69] proposed solutions to the effective shear modulus and bulk modulus, which turned out to be a function of the surface energy and the size of the nanocavity.

The dependence of the elastic response to size of the nanocavity in composite materials differs from the classic results obtained in the linear elasticity theory, suggesting the importance of the surface energy of the nanocavity in the deformation of nanometer-scaled structures. In order to apply the scaling relation to nanoporous metal foams, the yield strength should be considered as a variable of the ligament or void size. An atomistic analysis of the effective elastic modulus of the porous systems from the perspective of bond breaking and the associated nearby strain and trapping is necessary. Despite these exciting prospects, the understanding of the mechanical and thermal behavior of metal foams at the nanometer scale is still very much in its infancy [44, 70].

29.3 BOLS Formulation: Defect Mechanics

Strikingly, atomic vacancies, point defects, nanocavities, and nanoporous foams perform very much the same as nanostructures in the enhancement of stiffness (elastic strength) and toughness (plastic strength) and in the depression of thermal

Table 29.1 Functional dependence of mechanical and thermal properties of porous structures on the atomic CN, bond nature, and temperature of testing

| | |
|---|--|
| $\Delta Q(K)/Q(\infty) = \Delta_q = \sum_{i \leq 3} (\Delta q_i/q)$ | $q_i(z, m, d(T), E_b(T))$ |
| Melting point (T_{mi}) | $\propto z_i E_i(0)$ |
| Young's modulus (Y_i) | $\propto E_i(T) \times [d_i(T)]^{-3}$ |
| Extensibility (β_i) | $\propto d_i(T) \times [\eta_i(T_{mi}-T)]^{-1}$ |
| Yield strength (P_i , IHPR) | $\propto (1 + f \times K^{-0.5} \times \exp[T_m(K)/T]) \times [d_i(T)]^{-3} \times (T_{mi}-T)$ |

stability because of the large proportion of the undercoordinated atoms. Nanovoids increase the proportion of undercoordinated atoms at the negatively curved pore surfaces, whereas the nanodots or rods provide such undercoordinated atoms in the positively curved particle surfaces. These two kinds of nanostructures differ from one another mainly in the exact proportion of the lower coordinated atoms and the slight difference in the coordination environment, given the same surface chemical finishing conditions. For the negatively curved pores, the effective CN follows the same relation but the $K < 0$, $z_1 = 4(1-0.75/K)$.

Naturally, the T-BOLS correlation applies directly to the porous structures and allows prediction of the elasticity, thermal stability, and the yield strength in plastic deformation by repeating the practice in previous sections with the derived surface-to-volume ratio, $r_i(n, L, K)$ with the constraint of

$$2(L+1)(n+1/2) \leq K-2 \quad (29.3)$$

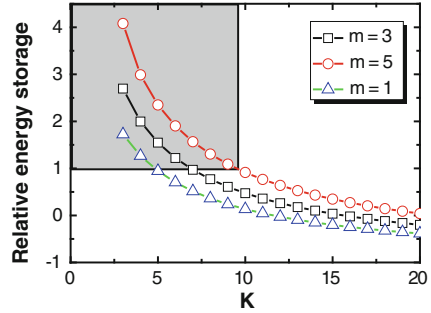
with n being the number of spherical voids of L radius aligned along the radius of a spherical dot of K size, for instance. With the known expressions for the size, bond nature, and temperature dependence of the melting point, elasticity, extensibility, and the yield strength in the IHPR premise, as given in Table 29.1, one is ready to predict the performance of a porous system.

29.4 Verification

29.4.1 Critical Size: Total Energy Storage

Assuming a hollow sphere of K exterior radius with a shell of $C_{1L} + C_{1K}$ thick, or three contracted atomic layers, the total energy stored in this hollow sphere at 0 K in comparison with that stored in an ideal solid sphere of the same size without surface effect being considered,

Fig. 29.6 Bond nature dependence of the critical size below which the total energy stored in the shell of the hollow sphere of three atomic layers is greater (shaded area) than the energy stored in an ideal bulk of the same size (reprinted with permission from [9])



$$\begin{aligned}
 \frac{\Delta E_{\text{shell}}}{E_{\text{sphere}}} &= \frac{C_{1L}^{-(m+3)} \int_{K-(C_{1L}+C_{1K})}^{K-C_{1K}} 4\pi R^2 dR + C_{1K}^{-(m+3)} \int_{K-C_{1K}}^K 4\pi R^2 dR}{\int_0^K 4\pi R^2 dR} - 1 \\
 &= C_{1L}^{-(m+3)} \left[(1 - C_{1K}/K)^3 - (1 - (C_{1L} + C_{1K})/K)^3 \right] \\
 &\quad + C_{1K}^{-(m+3)} \left[1 - (1 - C_{1K}/K)^3 \right] - 1
 \end{aligned} \tag{29.4}$$

Calculations based on the given C_i and the curvature-dependent z_i values derive the trends in Fig. 29.6. One can find the critical size below which the energy stored in the shell of the hollow sphere is greater than that stored in the ideal bulk of the same volume without considering the surface and temperature effects.

The estimation indicates that the critical size is bond nature dependent. The critical size is $K = 6, 8$ and 10 for $m = 1, 3$, and 5 , respectively. Similarly, for hollow tubes, the corresponding critical K values are estimated to be $7, 10$, and 14 . For the single-walled hollow structure, the integration crosses only the diameter of the wall atom.

The elasticity of the skin shell of the pore is always higher than the bulk interior because the elasticity is proportional to the energy density though the total energy stored in the shell may be lower than the entire sphere beyond the critical size. For plastic deformation, the hollow sphere could be tougher than the ideal bulk because of the long-distance effect in the indentation measurement. On the other hand, the thermal stability of the hollow sphere is always lower than the solid sphere [71].

29.4.2 Defect-Mediated Strength of Graphene

MD and DFT computations [72] revealed that the mechanical strength of a graphene is higher for high-angle grain boundaries (GB) even though they have a higher density of defects (5- and 7-membered rings forming the GB) than for low-angle grain boundaries, because of the particular ring bonds and their elongation dynamics. This finding and the associated mechanism may provide possible solution to the long-standing puzzle [2] of the defect-density modulated

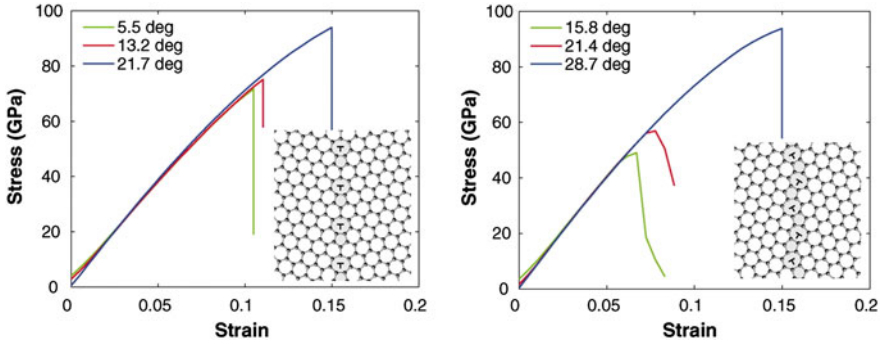


Fig. 29.7 Defect density (*grain boundary angle*) dependence of the stress–strain curves of (*left*) zigzag-oriented and (*right*) armchair-oriented graphene sheet pulled perpendicular to the grain boundaries. Insets show the defect consisting 5 and 7 atoms, of which the density determines the grain boundary angles (reprinted with permission from [72])

mechanical strength of a bulk as well. This kind of defects without atom missing provides not only centers initiating the mechanical failure but also sites for energy pinning as the mechanical strength is proportional to the binding energy density [9]. The strength of the C–C bond in the rings of 5- and 7-atoms is relatively stronger than those rings with ordinary 6 atoms on average [73] (Fig. 29.7).

29.4.3 Elasticity and Thermal Stability

With the derived $\gamma_i(n, L, K)$ relation and the given expressions for the $q(z_i, d_i(t))$, $E_i(t)$, one can readily predict the size, cavity density, and temperature dependence of the melting point, elasticity, and the flow stress of a system with large proportion of undercoordinated atoms without involving hypothetical parameters.

Calculations of the elasticity and melting point based on a fixed sphere radius $K = 600$ with different pore sizes and pore numbers revealed the correlation between them. Figure 29.8 shows the predicted porosity dependence of T_m and Young’s modulus of metal foams ($m = 1$) with different pore sizes. Porous structures demonstrate the following:

- (1) The T_m drops when the porosity is increased; at the same porosity, the specimen with smaller pore size is thermally less stable than the ones with larger pores.
- (2) The Young’s modulus increases with the porosity, and the Young’s modulus of the specimen with smaller pores increases faster.

The predicted trends of thermal stability and strength agree well with the experiment observations for the size-dependent mechanical properties of nanoporous Au [45]. It is important to note that there exists a limit of the porosity for

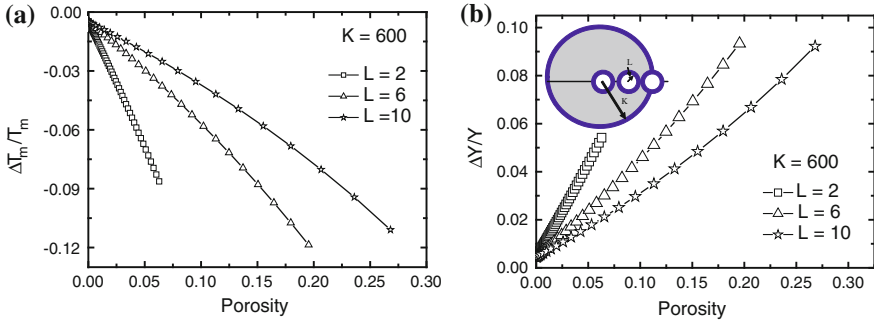


Fig. 29.8 Porosity dependence of **a** T_m and **b** Y of porous Au foams with different pore sizes of a $K = 600$ sphere [71]. Inset illustrates the K and the L and the three-phase structure (pore, skin, and matrix) in the porous sphere (reprinted with permission from [9])

the specimens with small pore sizes. This discussion applies to the small pores, but the conclusion may be subject to further verification for specimen of larger pores that are expected to drop in strength with pore size depending on the surface-to-volume ratio. For the T_m consideration, the surface-to-volume ratio should not include the volume of pores; for Y consideration, the pore volume contributes.

29.4.4 Plasticity and IHPR

To deal with the IHPR plastic deformation, one has to find the effective volume of the foam by excluding the pore volume in the specimen:

$$\frac{4\pi}{3}K'^3 = \frac{4\pi}{3} \left[K^3 - \frac{4\pi}{3}(n + 1/2)^3 L^3 \right] \tag{29.5}$$

$$x = K'^{-0.5}$$

Figure 29.9a shows the predicted IHPR as a function of L for $10 < K < 600$ specimens. Compared with the situation of single nanoparticle, the strongest size is significantly reduced for the foams. Figure 29.9b compares the predicted IHPR of Au with experimental results. The ligament size $x(K^{-1/2})$ is derived from Au foams with the modified scaling relation of Eq. (29.1). IHPR 2 and IHPR 1 are the IHPR with and without involving the intrinsic competition between energy density and atomic cohesive energy as discussed for the nanoparticles. The extremely high strength of ligaments smaller than 5 nm deviation from the expected IHPR is beyond the expectation of IHPR. One possibility for the extremely high strength of 5-nm ligands is the surface chemical conditions of the ligands because of the higher chemical reactivity of small particles. A combination of the present IHPR with the scaling relation of Eq. (29.1) may describe the observed trends at larger porosities.

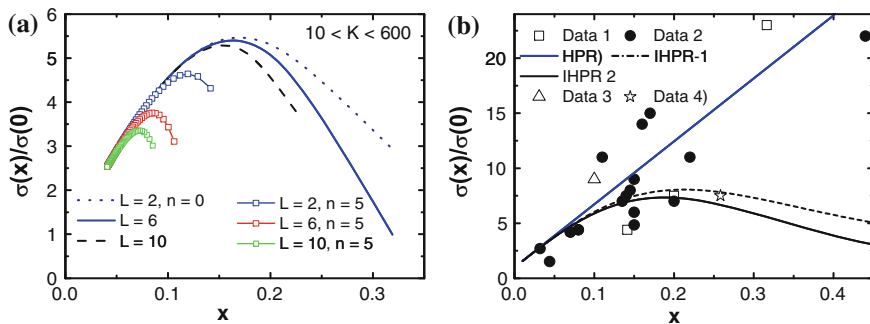


Fig. 29.9 Prediction of **a** the IHPR for nanoporous Au sphere with $10 < K < 600$ and different pore sizes L and pore numbers. **b** Comparison of the predicted IHPR with measurements of porous Au [40, 43, 44, 47]. The ligament size $x(K^{-1/2})$ is derived from Au foams with the modified scaling relation of Ashby (reprinted with permission from [9])

According to the current understanding, the magnitude of $T_m - T$ or the ratio T/T_m , plays a key role in determining the relative strength. The T_m of Al (933.5 K) is lower than that of Au (1,337 K), which explains why the relative strength of Al foam to Al bulk is lower than that of Au. Unfortunately, no immediate mechanism is apparent to explain the difference in vacancy-induced hardening between the IVb nitride and the Vb carbide compound. The excessive electron lone pair of a nitrogen atom and the shorter ionic radius of nitrogen (0.17 nm) compared to that of carbon (0.26 nm) [74] could be possible reasons for this difference. Increasing the number of N vacancies or reducing the number of the shorter ionic bonds of nitrides may lower the strength; this is open to further investigation.

29.5 Summary

The undercoordinated atoms in the negatively curved surfaces of atomic vacancies, point defects, nanocavities, and the syntactic foams are responsible for the strain hardening and thermal stability depression of the negatively curved systems, being the same in nature to those at the positively and zero-curved surfaces. Numerically, the negatively curved systems differ from the zero or the positively curved systems only by the fraction of the undercoordinated atoms and the coordination environment that determines the extent of the BOLS-induced property change. Therefore, all derivatives and conclusions for the flat surface and the positively curved surface apply to the negatively curved ones without needing any modifications. Nanopores play dual roles in mechanical strength enhancement. The shorter and stronger bonds near the pores act as pinning centers inhibiting motion of atomic dislocations because of the strain and the trapping; the pores provide sites for initiating structure failure under plastic deformation.

References

1. A.M.A. Huq, K.L. Goh, Z.R. Zhou, K. Liao, On defect interactions in axially loaded single-walled carbon nanotubes. *J. Appl. Phys.* **103**(5), 054306 (2008)
2. C. Kittel, *Introduction to Solid State Physics*, 8th edn. (Wiley, New York, 2005)
3. Y.A. Chang, L.M. Pike, C.T. Liu, A.R. Bilbrey, D.S. Stone, Correlation of the hardness and vacancy concentration in FeAl. *Intermetallics* **1**(2), 107–115 (1993)
4. M.S. Miao, W.R.L. Lambrecht, Effects of vacancies and impurities on the relative stability of rocksalt and zincblende structures for MnN. *Phys. Rev. B* **76**(19), 195209 (2007)
5. J.M. Yan, X.F. Ma, W. Zhao, H.G. Tang, C.J. Zhu, S.G. Cai, Crystal structure and carbon vacancy hardening of (W_{0.5}Al_{0.5}) C_{1-x} prepared by a solid-state reaction. *Chem. Phys. Chem.* **6**(10), 2099–2103 (2005)
6. I. Kaplan-Ashiri, S.R. Cohen, K. Gartsman, V. Ivanovskaya, T. Heine, G. Seifert, I. Wiesel, H.D. Wagner, R. Tenne, On the mechanical behavior of WS₂ nanotubes under axial tension and compression. *Proc. Natl. Acad. Sci. U.S.A.* **103**(3), 523–528 (2006)
7. M. Salmakorpi, A. Krasheninnikov, A. Kuronen, K. Nordlund, K. Kaski, Mechanical properties of carbon nanotubes with vacancies and related defects. *Phys. Rev. B* **70**(24), 245416 (2004)
8. N.M. Pugno, R.S. Ruoff, Quantized fracture mechanics. *Phil. Mag.* **84**(27), 2829–2845 (2004)
9. C.Q. Sun, Thermo-mechanical behavior of low-dimensional systems: The local bond average approach. *Prog. Mater. Sci.* **54**(2), 179–307 (2009)
10. S.H. Jhi, S.G. Louie, M.L. Cohen, J. Ihm, Vacancy hardening and softening in transition metal carbides and nitrides. *Phys. Rev. Lett.* **86**(15), 3348–3351 (2001)
11. H. Holleck, Material selection for hard coatings. *J. Vac. Sci. Technol. A: Vac. Surf. Films* **4**(6), 2661–2669 (1986)
12. X. Jiang, M. Wang, K. Schmidt, E. Dunlop, J. Haupt, W. Gissler, Elastic-constants and hardness of ion-beam-sputtered TiN_x films measured by Brillouin-scattering and depth-sensing indentation. *J. Appl. Phys.* **69**(5), 3053–3057 (1991)
13. L.E. Toth, *Transition Metal Carbides and Nitrides* (Academic Press, New York, 1971)
14. R. Sahara, T. Shishido, A. Nomura, K. Kudou, S. Okada, V. Kumar, K. Nakajima, Y. Kawazoe, Mechanism of the increase in bulk modulus of perovskite ScRh₃B_x by vacancies. *Phys. Rev. B* **73**(18), 184102 (2006)
15. C.S. Shin, D. Gall, N. Hellgren, J. Patscheider, I. Petrov, J.E. Greene, Vacancy hardening in single-crystal TiN_x(001) layers. *J. Appl. Phys.* **93**(10), 6025–6028 (2003)
16. V.K. Luk, M.J. Forrestal, D.E. Amos, Dynamic spherical cavity expansion of strain-hardening materials. *J. Appl. Mech.-Trans. ASME* **58**(1), 1–6 (1991)
17. G.H. Lu, Q. Wang, F. Liu, The role of vacancy on trapping interstitial O in heavily As-doped Si. *Appl. Phys. Lett.* **92**(21), 211906 (2008)
18. J.A. Knapp, D.M. Follstaedt, S.M. Myers, Hardening by bubbles in He-implanted Ni. *J. Appl. Phys.* **103**(1), 013518–013519 (2008)
19. C.H.P. Poa, R.G. Lacerda, D.C. Cox, F.C. Marques, S.R.P. Silva, Effects of stress on electron emission from nanostructured carbon materials. *J. Vac. Sci. Technol., B* **21**(4), 1710–1714 (2003)
20. R.G. Lacerda, M.C. dos Santos, L.R. Tessler, P. Hammer, F. Alvarez, F.C. Marques, Pressure-induced physical changes of noble gases implanted in highly stressed amorphous carbon films. *Phys. Rev. B* **68**(5), 054104 (2003)
21. C.H. Poa, R.G. Lacerda, D.C. Cox, S.R.P. Silva, F.C. Marques, Stress-induced electron emission from nanocomposite amorphous carbon thin films. *Appl. Phys. Lett.* **81**(5), 853–855 (2002)
22. B.J. Waclawski, J.W. Gadzuk, J.F. Herbst, UV photoemission for rare-gases implanted in Ge. *Phys. Rev. Lett.* **41**(8), 583–586 (1978)
23. C. Biswas, A.K. Shukla, S. Banik, S.R. Barman, A. Chakrabarti, Argon nanobubbles in Al(111): A photoemission study. *Phys. Rev. Lett.* **92**(11), 115506 (2004)

24. P.H. Citrin, D.R. Hamann, Measurement and calculation of polarization and potential-energy effects on core-electron binding-energies in solids: X-ray photoemission of rare-gases implanted in noble-metals. *Phys. Rev. B* **10**(12), 4948–4963 (1974)
25. R.E. Watson, J.F. Herbst, J.W. Wilkins, Core level shifts of rare-gas atoms implanted in noble-metals. *Phys. Rev. B* **14**(1), 18–25 (1976)
26. G. Kaindl, T.C. Chiang, D.E. Eastman, F.J. Himpsel, Distance-dependent relaxation shifts of photoemission and auger energies for Xe on Pd(001). *Phys. Rev. Lett.* **45**(22), 1808–1811 (1980)
27. R.G. Lacerda, L.R. Tessler, M.C. dos Santos, P. Hammer, F. Alvarez, F.C. Marques, EXAFS study of noble gases implanted in highly stressed amorphous carbon films. *J. Non-Cryst. Solids* **299**, 805–809 (2002)
28. J.H. Kim, S.M. Seo, H.H. Lee, Nanovoid nature and compression effects in organic light emitting diode. *Appl. Phys. Lett.* **90**(14), 143521 (2007)
29. R.W. Lynch, H.G. Drickame, Effect of high pressure on lattice parameters of diamond graphite and hexagonal boron nitride. *J. Chem. Phys.* **44**(1), 181–184 (1966)
30. S. Bhattacharyya, S.V. Subramanyam, Metallic conductivity of amorphous carbon films under high pressure. *Appl. Phys. Lett.* **71**(5), 632–634 (1997)
31. K. Umemoto, S. Saito, S. Berber, D. Tomanek, Carbon foam: Spanning the phase space between graphite and diamond. *Phys. Rev. B* **64**(19), 193409 (2001)
32. S. Mirabella, E. Bruno, F. Priolo, F. Giannazzo, C. Bongiorno, V. Raineri, E. Napolitani, A. Carnera, Role of surface nanovoids on interstitial trapping in He implanted crystalline Si. *Appl. Phys. Lett.* **88**(19), 191910 (2006)
33. R.G. Lacerda, P. Hammer, F. Alvarez, F.C. Marques, Influence of stress on the electron core level energies of noble gases implanted in hard amorphous carbon films. *Diam. Relat. Mater.* **10**(3–7), 956–959 (2001)
34. C.S. Dai, D.L. Wang, F. Ding, X.G. Hu, Z.H. Jiang, Review of metal foam electrode material. *Rare Metal Mater. Eng.* **33**(6), 1–5 (2004)
35. D.C. Dunand, Processing of titanium foams. *Adv. Eng. Mater.* **6**(6), 369–376 (2004)
36. C. Korner, R.F. Singer, Processing of metal foams: Challenges and opportunities. *Adv. Eng. Mater.* **2**(4), 159–165 (2000)
37. K.M. Hurysz, J.L. Clark, A.R. Nagel, C.U. Hardwicke, K.J. Lee, J.K. Cochran, T.H. Sanders, Steel and titanium hollow sphere foams, in *Porous and Cellular Materials for Structure Applications*, ed. by D.S. Schwartz, et al. (Materials Research Society, Warrendale, 1998), pp. 191–203
38. <http://en.wikipedia.org/wiki/Porosity>
39. J. Erlebacher, M.J. Aziz, A. Karma, N. Dimitrov, K. Sieradzki, Evolution of nanoporosity in dealloying. *Nature* **410**(6827), 450–453 (2001)
40. A.M. Hodge, J. Biener, J.R. Hayes, P.M. Bythrow, C.A. Volkert, A.V. Hamza, Scaling equation for yield strength of nanoporous open-cell foams. *Acta Mater.* **55**(4), 1343–1349 (2007)
41. A. Mathur, J. Erlebacher, Size dependence of effective Young's modulus of nanoporous gold. *Appl. Phys. Lett.* **90**(6), 061910 (2007)
42. J.N. Armstrong, S.Z. Hua, H.D. Chopra, Strength of metals at the Fermi length scale. *Phys. Status Solidi* **9**, 99–101 (2012)
43. J. Biener, A.M. Hodge, J.R. Hayes, C.A. Volkert, L.A. Zepeda-Ruiz, A.V. Hamza, F.F. Abraham, Size effects on the mechanical behavior of nanoporous Au. *Nano Lett.* **6**(10), 2379–2382 (2006)
44. J. Biener, A.M. Hodge, A.V. Hamza, L.M. Hsiung, J.H. Satcher, Nanoporous Au: A high yield strength material. *J. Appl. Phys.* **97**(2), 024301 (2005)
45. A.M. Hodge, J. Biener, L.L. Hsiung, Y.M. Wang, A.V. Hamza, J.H. Satcher, Monolithic nanocrystalline Au fabricated by the compaction of nanoscale foam. *J. Mater. Res.* **20**(3), 554–557 (2005)
46. M. Hakamada, M. Mabuchi, Mechanical strength of nanoporous gold fabricated by dealloying. *Scr. Mater.* **56**(11), 1003–1006 (2007)

47. C.A. Volkert, E.T. Lilleodden, D. Kramer, J. Weissmuller, Approaching the theoretical strength in nanoporous Au. *Appl. Phys. Lett.* **89**(6), 061920 (2006)
48. D. Lehmhus, J. Banhart, Properties of heat-treated aluminium foams. *Mater. Sci. Eng. A: Struct. Mater. Prop. Microstruct. Process.* **349**(1–2), 98–110 (2003)
49. O. Kraft, D. Saxa, M. Haag, A. Wanner, The effect of temperature and strain rate on the hardness of Al and Al-based foams as measured by nanoindentation. *Z. Metallk.* **92**(9), 1068–1073 (2001)
50. B. Jiang, Z.J. Wang, N.Q. Zhao, Effect of pore size and relative density on the mechanical properties of open cell aluminum foams. *Scr. Mater.* **56**(2), 169–172 (2007)
51. S. Ko, D. Lee, S. Jee, H. Park, K. Lee, W. Hwang, Mechanical properties and residual stress in porous anodic alumina structures. *Thin Solid Films* **515**(4), 1932–1937 (2006)
52. J.F. de Deus, A.C. Tavares, C.M. Lepienski, L. Akcelrud, Nanomechanical properties of poly(methyl methacrylate-co-9-anthryl methyl methacrylate). *Surf. Coat. Technol.* **201**(6), 3615–3620 (2006)
53. X.M. Bai, M. Li, Nucleation and melting from nanovoids. *Nano Lett.* **6**(10), 2284–2289 (2006)
54. S.H. Jhi, J. Ihm, S.G. Louie, M.L. Cohen, Electronic mechanism of hardness enhancement in transition-metal carbonitrides. *Nature* **399**(6732), 132–134 (1999)
55. Z.P. Wang, Q. Jiang, A yield criterion for porous ductile media at high strain rate. *J. Appl. Mech.-Trans. ASME* **64**(3), 503–509 (1997)
56. I. Lubomirsky, Mechanical properties and defect chemistry. *Solid State Ion.* **177**(19–25), 1639–1642 (2006)
57. L.J. Gibson, M.F. Ashby, *Cellular Solids: Structure and Properties*, 2nd edn. (Cambridge University Press, Cambridge, 1997)
58. P.G. Sanders, J.A. Eastman, J.R. Weertman, Elastic and tensile behavior of nanocrystalline copper and palladium. *Acta Mater.* **45**(10), 4019–4025 (1997)
59. J.B. Wachtman (ed.), *Mechanical and Thermal Properties of Ceramics* (NBS Special Publication, Washington, 1963), p. 139
60. J.K. Mackenzie, The elastic constants of a solid containing spherical holes. *Proc. Phys. Soc. London Sect. B* **63**(361), 2–11 (1950)
61. R.W. Rice, Use of normalized porosity in models for the porosity dependence of mechanical properties. *J. Mater. Sci.* **40**(4), 983–989 (2005)
62. B. Wu, A. Heidelberg, J.J. Boland, Mechanical properties of ultrahigh-strength gold nanowires. *Nat. Mater.* **4**(7), 525–529 (2005)
63. M.D. Uchic, D.M. Dimiduk, J.N. Florando, W.D. Nix, Sample dimensions influence strength and crystal plasticity. *Science* **305**(5686), 986–989 (2004)
64. L.K. Pan, C.Q. Sun, C.M. Li, Estimating the extent of surface oxidation by measuring the porosity dependent dielectrics of oxygenated porous silicon. *Appl. Surf. Sci.* **240**(1–4), 19–23 (2005)
65. J.E. Sader, Surface stress induced deflections of cantilever plates with applications to the atomic force microscope: V-shaped plates. *J. Appl. Phys.* **91**(11), 9354–9361 (2002)
66. R.C. Cammarata, K. Sieradzki, Effects of surface stress on the elastic-moduli of thin-films and superlattices. *Phys. Rev. Lett.* **62**(17), 2005–2008 (1989)
67. F.Q. Yang, J.C.M. Li, Diffusion-induced beam bending in hydrogen sensors. *J. Appl. Phys.* **93**(11), 9304–9309 (2003)
68. P. Sharma, S. Ganti, N. Bhate, Effect of surfaces on the size-dependent elastic state of nano-inhomogeneities. *Appl. Phys. Lett.* **82**(4), 535–537 (2003)
69. F.Q. Yang, Size-dependent effective modulus of elastic composite materials: Spherical nanocavities at dilute concentrations. *J. Appl. Phys.* **95**(7), 3516–3520 (2004)
70. J. Biener, A.M. Hodge, A.V. Hamza, Microscopic failure behavior of nanoporous gold. *Appl. Phys. Lett.* **87**(12), 121908 (2005)
71. Y. Ding, C.Q. Sun, Y.C. Zhou, Nanocavity strengthening: Impact of the broken bonds at the negatively curved surfaces. *J. Appl. Phys.* **103**(8), 084317 (2008)

72. R. Grantab, V.B. Shenoy, R.S. Ruoff, Anomalous strength characteristics of Tilt Grain boundaries in graphene. *Science* **330**(6006), 946–948 (2010)
73. Y.J. Wei, J.T. Wu, H.Q. Yin, X.H. Shi, R.G. Yang, M. Dresselhaus, The nature of strength enhancement and weakening by pentagon-heptagon defects in graphene. *Nat. Mater.* **11**(9), 759–763 (2012)
74. C.Q. Sun, Size dependence of nanostructures: Impact of bond order deficiency. *Prog. Solid State Chem.* **35**(1), 1–159 (2007)

Chapter 30

Compounds and Nanocomposites: Hetero-Coordination

- *Additional trap or barrier forms at the interface, which changes the interface energy density and atomic cohesive energy.*
- *Excessive energy due to bond contraction and bond nature alteration reinforces a compacted interface, which is applicable to multi-layers, alloys, compounds, and impurities.*
- *A dissociated interface is identical to a free surface with potential barrier in the gap between GB skins, followed by a potential trap in the skin.*
- *The filler, interface, or the surface of the matrix reinforces the mechanical strength of a nanocomposite, depending on the intermixing conditions and the strength of the filler.*

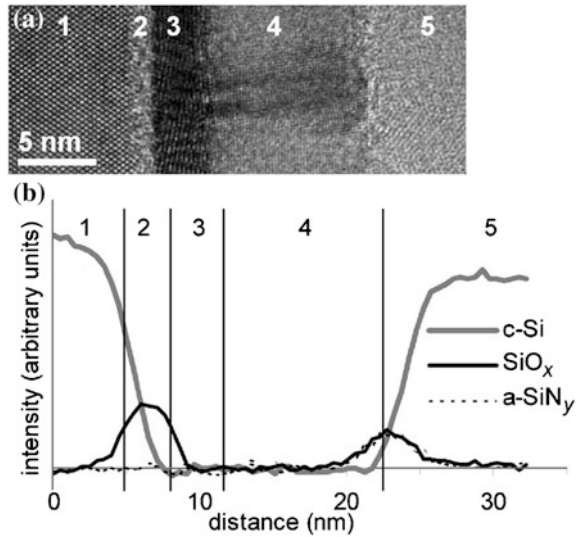
30.1 Known Facts

30.1.1 Hetero-Junction Interfaces

Hetero-juncture interface enhances the mechanical strength of the layered structures. The significance of an interface between two compositional specimens is the interface mixing, as shown in Fig. 30.1. At the boundaries between different chemical compositions, atoms diffuse from one part to another. The interface mixing sometimes causes detrimental effect to the MOS device with dielectric failure or forms barrier to prevent interdiffusion [1, 2]. The excessive energy in the diffused interface will enlarge the bandgap and hence reduce the dielectric constant locally [3]. Formation of potential barrier or trap also modifies the interface energy that determines the interface strength [4].

Multi-layered structures such as nc-TiN/a-Si₃N₄, nc-TiN/a-Si₃N₄/ and nc-TiSi₂, nc-(Ti_{1-x}Al_x)N/a-Si₃N₄, nc-TiN/TiB₂, nc-TiN/BN [6, 7], TiN/CrN [8], CrN/AlN, TiN/AlN [9], Cu/Au [10], and Ni [11] manifest enhanced mechanical strength and thermal stability, because of the interfacial bond strengthening. The microhardness of multi-layer nitride films increased with the number of layers, except if the two

Fig. 30.1 **a** High-resolution TEM image of the stack showing the (1) Si, (2) SiO₂, (3) HfO₂, (4) TiN, and (5) poly-Si and **b** the corresponding EELS elemental profiles across the stack normalized to the same maximum height interface mixing (reprinted with permission from [5])



layers mutually dissolved. A microhardness of 78 GPa was achieved in a 180-layer TiN/NbN film [12]. The nanocrystalline or amorphous composites show hardness approaching that of diamond [7], yet oxygen interface impurities cause a significant reduction in the interface strength [13].

Figure 30.2 shows the microhardness of TiN/ZrN, TiN/NbN, and TiN/CrN multi-layer films as a function of the layer number for films with a similar total thickness of nearly 2 nm. For TiN/NbN and TiN/ZrN films with ~ 180 layers (with monolayer thickness of ~ 10 nm), the hardness is about 70–80 GPa, i.e., approximately that of diamond. The different behavior of TiN/CrN is connected with (Ti, Cr)N solution formation for more than 100 layers, as XRD analysis revealed. This observation indicates the significance of interlayer mixing to the mechanical strength that is proportional to the local energy density and therefore the presence of interface strain and trapping.

30.1.2 Intergrain Twin Boundaries

Intergrain twin boundaries break the IHPR. Tian et al. [15] synthesized cubic cBN polycrystalline of twin domains of average thickness ~ 3.8 nm from specially prepared BN precursor nanoparticles possessing onion-like nested structures and examined the mechanical strength as a function of the applied load and the twin size (see Fig. 30.3). The resulting nanotwinned cBN bulk samples are optically transparent with a striking combination of physical properties: an extremely high Vickers hardness (exceeding 100 GPa, the optimal hardness of synthetic diamond), a high oxidization temperature ($\sim 1,294$ °C), and a large fracture toughness (>12 MPa m^{1/2}, well beyond the toughness of commercial cemented tungsten

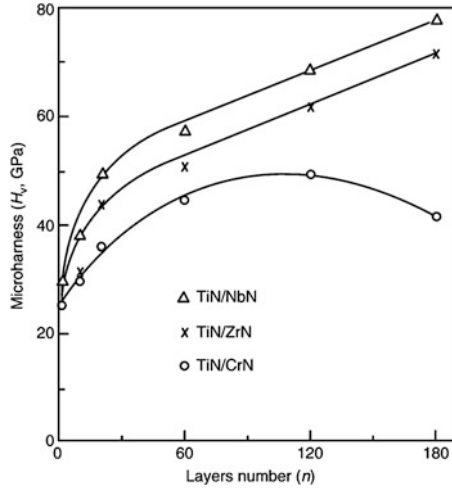


Fig. 30.2 The layer number dependence of the microhardness of nitride films [12] indicates the significance of interlayer mixing of the mechanical strength that is proportional to the local energy density that depends on the interface strain and quantum entrapment (reprinted with permission from [14])

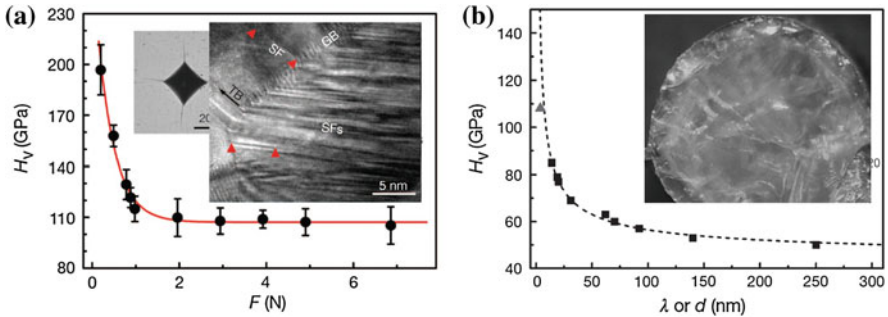


Fig. 30.3 Vickers hardness (H_V) as a function of **a** the applied load and **b** the average grain size (d) or the twin thickness (λ) for cBN polycrystals. Inset TEM image shows the grain boundaries (GB), stacking faults (SFs), and twin boundaries (TBs). The specimen is colorless and totally transparent (reprinted with permission from [15])

carbide, $\sim 10 \text{ MPa m}^{1/2}$). Most strikingly, the hardening of cBN remains as the twin thickness down to the smallest sizes surpassing the strongest size in the IHPR, $\sim 10\text{--}15 \text{ nm}$ for metals and alloys.

The original idea is that [15] the boundaries between grains can arrest internal motion and help resist deformation, like a series of tiny walls within a larger structure. The essence of the strategy is to reduce the scale of the microstructures within the material by generating features called ‘ultrafine nanotwins.’ A nanotwin is a crystalline segment that mirrors the orientation of atoms on the other side of an

interface within a material. As such, a polycrystal made of nanotwin domains is a bit like a slab of plywood where the wood grain reverses direction in each successive layer. The onion-like precursors contain numerous defects where crystals can nucleate under high temperature and pressure but resist rapid crystal growth, yielding numerous discrete pockets of crystalline order within a larger, somewhat disordered polycrystalline structure.

The principle and the success of the cBN clarify the physical organ for the mechanical enhancement of pure Cu [16–18], Au [19], and Al [20] by introducing high-density twins. The stacking fault pinning prevents atoms from gliding dislocations, which enhances the local energy density by lattice distortion. The role of the densely packed twin boundaries is more significant than the usual grain boundaries in the mechanical enhancement: the former destroys the IHPR that grained materials often follow.

30.1.3 Filler–Matrix Interaction in Nanocomposites

The filler–matrix interaction dominates the mechanical strength of nanocomposites. Polymer nanocomposite foams filled with hard fillers have received increasing attention in both scientific and industrial sectors. The combination of functional nanoparticles such as SiC, CNT, clay, glass fibers, rubbers, and supercritical fluid foaming technology has a high potential to generate a new class of materials that are lightweight, high strength, and multi-functional [21–28]. For a 60 % clay nanocomposite example, its elastic modulus increases up to 21.4 GPa, which is five times higher than that of the agarose matrix [29].

A small amount of well-dispersed nanoparticles in the polymer domain may serve as the nucleation sites to facilitate the bubble nucleation process. Under compressive loadings, the continuous nanotube polymer composites with continuous nanotube composites improve more than an order of magnitude the longitudinal modulus (up to 3,300 %) as well as damping capability (up to 2,100 %) (see Fig. 30.4). Composites with a random distribution of nanotubes of the same length and similar filler fraction provide, however, three times less effective reinforcement in composites [30]. The nanoscaled particles are suitable for micrometer-scaled reinforcement because of the large surface area for interface chemical bonding between the filler and the matrix, thus achieving the macroscopic mechanical enhancement.

Haraguchi et al. [31] used gel formation in an aqueous medium to create a composite of hydrophobic poly(2-methoxyethyl acrylate) and hydrophilic hectrite clay. During the polymerization, the clay platelets are excluded from the polymer particles. Once dried, the clay shells comprised a three-dimensional network. A surprising feature of the composites was the ability to undergo huge elongations when being subject to a stress. After an initial irreversible necking deformation, subsequently applied large strains were shown to be reversible, with good shape recovery observed on release. The remarkable mechanical properties

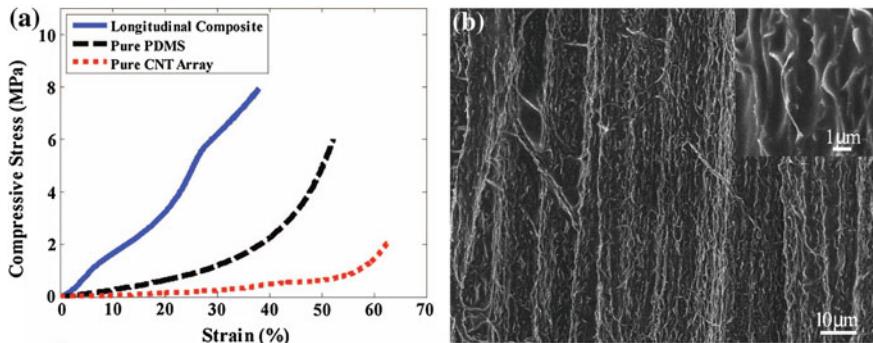


Fig. 30.4 **a** The stress–strain behavior of the composite and its constituent CNT and PDMS polymer and **b** the SEM image of the continuously reinforced carbon nanotubes PDMS composite (reprinted with permission from [30])

of nanocomposite coatings, such as superhardness, high elastic modulus, high elastic recovery, excellent resistance against cracking, low wear rate, and high thermal stability, are due to their unique structures and deformation mechanisms at the nanometer scale.

30.1.4 High-Entropy Alloys

Blending different types of atoms in a solid could enhance the hardness of the solid preferably in an amorphous state, as so-called high-entropy materials [32]. In addition to the high-entropy superhard materials, intermetallic superalloys, such as NiAl, FeAl, and TiAl systems, form another kind of important materials of tougher than ever the individual constituent elemental solid. In these alloys, raising the ductility is an important goal when metals are added into the alloy [33]. The significant characteristic of the superalloys is the mixture of at least two kinds of elements with different bulk melting points. The mixture as such may make the alloy both ductile and thermally stable.

30.2 Known Mechanisms

30.2.1 Interface Interaction

Hardness is the ability of one material to resist being scratched or dented by another. This property is not so easily defined at the atomic scale, and there is no fundamental theory that could tell material scientists how to arrange atoms to

make a hard structure. Theoretical progress in understanding the role of interface in the nanocomposite is still limited. Jiang et al. [34] investigated the cohesive interfaces between the CNT fillers and the polymer epoxy that are not well bonded with the van der Waals force in terms of the tensile cohesive strength and the interface cohesive energy. The area density of CNT and the volume density of polymer as well as the parameters in the van der Waals force describe the interaction. For a CNT in an infinite polymer, the shear cohesive stress vanishes and the tensile cohesive stress dominates, depending only on the opening displacement. However, for a CNT in a finite polymer matrix, the tensile cohesive stress remains unchanged, but the shear cohesive stress depends on both opening and sliding displacements, i.e., the tension/shear coupling. Analytical expressions of the cohesive behavior have been used to study the CNT-reinforced composites to give an improved understanding of the interfacial effect.

30.2.2 Ionicity, Bond Length, and Bandgap Dominance

A number of models for the mechanical strength have been developed based on the concept of ionicity to predict the hardness of several compounds [35–38]. It is anticipated that covalent bonds take the responsibility for increasing the hardness. The hardness, or the activation energy required for plastic gliding, was related to the bandgap E_G , which is proportional to the inverse bond length in a d^{-n} fashion with the power index n varying from 2.5 to 5.0.

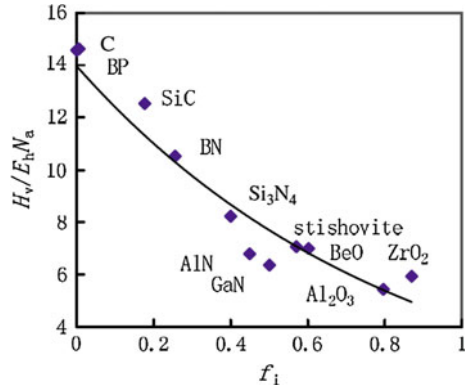
Ionicity is related to the strength of atomic bonds. In a so-called covalent material, such as diamond, germanium, or silicon, each pair of atoms shares a pair of electrons equally to form a bond. In polar covalent materials, there is some asymmetry, and one atom or the other has greater control over any shared electrons. In the extreme case—an ionic material—one atom takes over its neighbor's electron entirely, and the two are held together by their newly acquired opposing charges. This electrostatic attraction, called an ionic bond, is much weaker than a covalent bond of shared electrons.

Tian and Gao [35] proposed a formula based on the concept of ionicity bond length and the number of electrons to predict the hardness of multiple compounds. They started by assuming that hardness measures the combined resistance of chemical bonds to indentation—the more the bonds in a region of the surface, the harder the material. Shorter and denser chemical bonds should then favor hardness. Hard materials should also have low ionicity, the team reasoned, in agreement with other researchers, because covalent bonds are stronger than ionic bonds. The hardness, or the activation energy required for plastic gliding, was related to the bandgap E_G . The hardness of a covalent solid is described as follows: $H_V(GPa) =$

$$556 \frac{N_a e^{-1.191f_i}}{d_0^{2.5}} f_i = 1 - (E_h/E_G)^2$$

where N_a is the number of covalent bonds per unit volume. The E_G for a binary polar covalent system can be separated into both covalent or homopolar gap

Fig. 30.5 Ionicity (f_i), bandgap, and bond length dependence of the reduced hardness of covalent crystals, $H_v/E_h N_a$ (reprinted with permission from [35])



$E_h = 39.74 d_0^{-2.5} E_h (= 39.74 d_0^{-2.5})$ [36] and ionic or hetero-polar gap C . The d_0 is the covalent bond length in angstrom. This formulation successfully predicts the hardness for multiple materials (see Fig. 30.5).

30.2.3 Bond Length and Charge Transfer Dominance

Philips [37] and Liu and Cohen [39] have proposed another relationship for the bulk modulus B of a compound solid,

$$B = N_c/4 \times (19.71 - 2.20f_i)d_0^{-3.5}(\text{Mbar})$$

where N_c is the nearest atomic CN. The parameter f_i accounts for the reduction in B arising from increased charge transfer. The value of $f_i = 0, 1$, and 2 for group IV, III–V, and II–VI solids in the periodic table. For a tetrahedral system, $N_c = 4$; otherwise, the N_c is an average of atomic CN. For diamond, $f_i = 0$, $d = 1.54 \text{ \AA}$, and hence, $B = 4.35 \text{ Mbar}$, compared with an average experimental value of 4.43 Mbar . This relationship was applied to BN and β - Si_3N_4 with corresponding prediction of $B = 3.69$ and 2.68 Mbar . Litovchenko [38] also derived that the $E_G \propto d^{-2}$, and then, the elastic modulus follows the relation of $B \propto d^{-5}$. This prediction has stimulated tremendous interest in the experimental search for the superhard carbon–nitride phase worldwide [40–43], as the diameter of an N atom is 0.14 – 0.148 nm shorter than that of carbon in the C–C bond in a diamond.

All the expressions indicate that shorter and denser chemical bonds as well as smaller ionicity should favor hardness. In order to obtain a compound with large bulk modulus, one must find such a covalent compound that has both shorter bond length and smaller ionicity, and high compactness in atomic arrangement inside. Thus, the atomic CN-imperfection-induced bond contraction should contribute directly to the hardness at the surface or sites surrounding defects. Therefore, a nanometer-sized diamond is expected to be $100\% (0.88^{-5.56} - 1)$ harder than the

bulk natural diamond, but the hardness should be subject to the IHPR [44]. The diamond tip with high curvature is expected harder than the flat surface of the diamond. According to the predicted IHPR, the strongest size of diamond is 20 nm (Table 28.1).

30.3 BOLS: Hetero-Coordination Entrapment or Polarization

Compared with the surface strengthening of nanosolids and nanocavities, the mechanical strengthening of twin GBs, multi-layers, and blending composites arises from the strain and chemical effect due to atomic hetero-coordination. The coordination environment and the alteration of bond nature of the interatomic bonding upon compound or alloy formation should take the responsibility. The bond contracts at the interface because of the bond order (length and angle) distortion that also stores energy locally. Therefore, bond contraction and bond nature alteration occur at the interface, generating local strain and energy entrapment or polarization.

Currently available database allows for the interface quantum entrapment or polarization, as illustrated in Fig. 30.6 for the compact and dissociated interface, agreeing with the findings of Popovic and Satpathy in calculating oxide superlattices and microstructures [45]. They found the essentiality to introduce a wedge-shaped potential well for the monolayer structure sandwiched between the SrTiO₃ and LaTiO₃ superlattices. The potential well of trapping originates from the Coulomb potential of a two-dimensional charged La sheet, which in turn confines the electrons in the Airy-function-localized states. For the compact interface, there is a monotrap at the interface. Localization and densification of charge and energy occur at the interface. The energy levels of atoms in the interface region also shift positively unless interface dipoles are formed. For the dissociated interface, double potential traps will present associated with one barrier in between. The Z is the coordinate directing into the bulk. Cutting off at $Z = 0$, one side of the double well converges to the case of free surface or atomic vacancy defect—a barrier followed by an immediate trap in the surface skin.

30.4 Verification

30.4.1 Interface Bond Contraction

Evidence in Sect. 12.2 shows that bond contraction takes place at sites surrounding impurities and at the interfaces. For instances, a substitutional As dopant impurity has induced an 8 % bond contraction around the impurity (acceptor dopant As) at

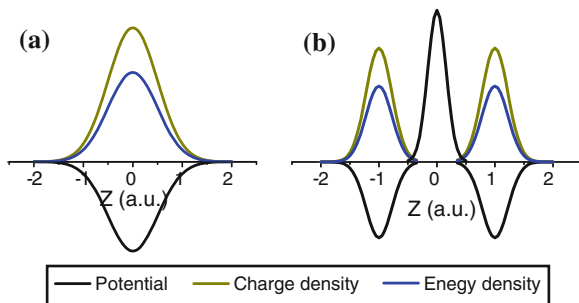


Fig. 30.6 Models for the atomic coordination imperfection induced surface and interface quantum trapping and the associated charge and energy density gain in the **a** compacted and the **b** dissociated interfaces. One addition barrier is located at the dissociated interface. Z is the coordination directing into one medium. For defect edge or a free surface, $Z > 0$ in **b** applies (reprinted with permission from [14])

the Te sublattice in CdTe, as observed using EXAFS and XANES [46]. A 3 % Ti–N bond contraction occurs at the TiN/Si₃N₄ interface [47], being responsible for the hardening of the crystalline/amorphous TiN/Si₃N₄ multi-layer films. EXAFS investigation [48] has revealed size-dependent interatomic distance contraction in thiol-capped gold nanoparticles. A slight nearest-neighbor distance reduction was observed as a function of particle diameter (2–4 nm range), but for all samples, it was less than 1 %. This value is smaller compared with the larger effect expected and found in other systems, especially for the smallest particles (2 nm).

The Au–Au bond of Au nanocrystals embedded in SiO₂ was found to contract by 0.04–0.03 nm [49]. The Sb–In bond in the first shell of the SbIn embedded in a SiO₂ matrix contracted slightly by about 0.002 nm compared with that of the bulk SbIn [50]. Mn ion implantation onto a heated Si substrate to form clusters with 6–8 atoms located in the first coordination sphere in three subshells [51]. The first subshell has one atom at a distance of 2.31 Å, the second subshell has three atoms at 2.40 Å, the third subshell has three atoms at 2.54 Å, and finally the fourth subshell contains six Mn atoms at a distance of 2.80 Å. The finding of dopant-induced bond contraction and the interface bond contraction could provide an atomic scale understanding of the bond in a junction interface.

According to Veprek and Veprek-Heijman [52] on the a-XN interface monolayer strengthening of nc-MN/a-XN nanocomposites (M = Ti, W, V, (TiAl), X = Si, B), the enhanced mechanical strength of the one-monolayer interface is a general nature that can be understood in terms of an extension of the BOLS correlation with the effect of monolayer interface mixing. The bond contraction and bond nature evolution upon interface formation do cause local strain and the associated quantum trapping and pinning, which should be responsible for the monolayer strengthening as observed.

Theoretical calculations, confirmed by electron microscopy measurement [53], revealed that homojunction dislocations in aluminum have either compact or

dissociated core interlayers. The calculated minimum stress (σ_P) required for moving an edge dislocation is approximately 20 times higher for the compact dislocations than for the equivalent dissociated dislocations. As compared with the theoretical tensile strength in the direction [001] or [111] of an Al single crystal, the Al-GB is still strong due to the interface reconstruction, which indicates the special strength of the reconstructed and undercoordinated GB bonds [54].

Encouragingly, a GIXR study revealed that the interface of SiO₂/Si has a higher electron density than the Si and SiO₂ constituents in separate forms. The higher density persists disregarding the thickness of the layered films [55]. The charge density in the Pt/BaTiO₃ interface dead layer region is about 10 % higher than the bulk because of the lattice strain [56]. A dead layer of 3 nm thick has also been found in the Ba_{0.7}Sr_{0.3}TiO₃/SrRuO₃ interface [57]. The dead layer formation could lower the dielectric permittivity and hence modulate the microcapacitance [58] and magnetocapacitance as well [59]. These observations provide robust evidence for the expectation for compact interfaces having deeper trapping potential wells and higher bond strength, resulting in the localization and densification of charge and energy in the surface/interface skins, which makes the interface region an insulating dead layer with lower dielectric constant because of the strain and quantum entrapment.

30.4.2 Bond Nature Alteration

An atom performs differently at a free surface compared to an atom at the interface. Although the coordination ratio at the interfaces undergoes little change ($z_{ib} \sim 1$), formation of an interfacial compound or alloy alters the nature of the interatomic bond that is either stronger or weaker. Energy storage due to bond geometry distortion also contributes to the bond energy. Overheating occurs in substances covered by relatively higher T_m substances, or stronger binding systems, as the T_m relates directly to the atomic cohesive energy [60].

At the mixed interface, the z_i may not change substantially, so we can introduce the interfacial bond energy as $E_{int} = \gamma E_b$ and the interfacial atomic cohesive energy as $E_{C,int} = \gamma z E_b$, and then, all the equations for the surface effect are adoptable to the interface properties. A numerical fit of the size dependence of overheating for In/Al [61], Ag/Ni [62], and Pb/Al and Pb/Zn [63] core-shell nanostructures, presented in Fig. 14.3(i) has led to a γ value of 1.8, indicating that an interfacial bond is 80 % stronger than a bond in the bulk of the core material [64]. If one took the bond contraction to be 0.90–0.92 as determined from the As- and Bi-doped CdTe compound [46] into consideration, the m value is around 5.5–7.0.

The high m value indicates that the bond nature indeed evolves when a compound is formed. The m value increases from 1 for the initially metallic to 4 or higher for the interfacial compound, which indicates the covalent interfacial bond nature. The electroaffinity and the interfacial DOS are expected to shift positively by 80 % of the corresponding bulk $\Delta E_C(\infty)$ value. Therefore, the deformed and

shortened interfacial bond is much stronger, meaning that electrons at an interface are deeply entrapped, giving rise to the observable interfacial local DOS. From this perspective, twins of nanograins [18] and the interfaces of multi-layered structures [65] should be stronger and thermally more stable because of the interfacial strain and quantum entrapment.

Experiments also show that the interfacial fcc-SiN can strengthen the TiN/SiN hetero-coordinated structures only when its thickness is about 1–2 ML [66]. A work [67] on the size-dependent melting points of the silica-embedded crystalline Ge nanowires with mean diameters ranging from 2.2 to 8.5 nm revealed strong interactions at the interface between the nanowire and the matrix. The bond enthalpy between Ge–O and Ge–Ge is significantly larger, i.e., 385 kJ mol^{-1} compared to 188 kJ mol^{-1} , leading to the observed superheating by some 60 K compared to the bulk Ge (1,200 K) [68].

In order to obtain a compound with large bulk modulus, one must find such a covalent compound that has both a shorter bond and smaller ionicity, and high compactness in internal atomic arrangement [35].

The detrimental effect of oxygen in the interface may arise from the introduction of non-bonding lone pairs and the lone-pair-induced dipoles, according to the understanding of O-induced stress [69]. The excessive lone pair of nitrogen should weaken the local non-bond strength and the strength of the entire sample. However, the measured strength depends on the sum of binding energy per unit volume. If the energy density of nitride in the interface region is higher than that of a diamond, the nitride interface will then be stronger. In contrast, oxygen involvement doubles the number of lone pairs and lowers the local binding energy density. This understanding may explain why the nitride interface is stronger and why oxygen addition could lower the strength.

Nitriding multi-layers show the high strength compatible with diamond, while the stronger carbide multi-layers are seldom reported. The current understanding suggests that carbon-induced compressive stress may prevent interlayer mixing, as being in the case of diamond/Ti poor adhesion [70]. Neutralizing the interfacial stress by introducing the graded metallic carbon–nitride buffer layers such as TiCN could have overcome the difficulty in nitride/carbide multi-layer formation.

30.4.3 Tian Series: Covalency and Bond Length

Tian and co-workers [71–73] developed an atomistic model to connect the bulk modulus of various crystals to the parameters of bond order, length, and polarity, which has reproduced the measured bulk moduli of a series of polar covalent crystals. Although conceptually similar to the BOLS correlation, they presented more appreciably with much details to various situations to form the series.

They calibrated the bond strength in covalent and ionic crystals by using the effectively bonded valence electron (EVBE) number, n_{AB} , of a chemical bond, which can be used as a parameter to characterize the bond type

$$n_{AB} = \frac{n_A n_B}{\sqrt{n_A^2 + n_B^2}} \quad (30.1)$$

where $n_A = Z_A/N_A$ and $n_B = Z_B/N_B$ are the nominal valence electrons contributed to A–B bond. The EBVE numbers of diamond (0.707) and NaCl (0.163) are in good agreement with the Mulliken overlap population from first-principles calculations.

For single-bond crystals, the normalized bond volume, $v = n_b d^3 / \Omega$, can be used as a measure of crystal geometry, where n_b , d , and Ω are the bond number in the unit cell, bond length, and unit cell volume, respectively [74]. Both the EVBE number and the coordination number product can easily be calculated for a designated crystal, which also applies to multi-bond crystals.

Three main parameters affecting the bulk modulus, i.e., the bond length (d), EVBE number (n_{AB}), and coordination number product ($p = n_A n_B$), are determined. The empirical expression for bulk modulus is deduced for simple $A^N B^{8-N}$ type covalent crystals with one coordination number. The generalization to covalent crystals with diverse coordination numbers and ionic crystals are presented sequentially, followed by generalization to multi-bond crystals.

1. **Monocovalent $A^N B^{8-N}$ crystals.** The single-bond $A^N B^{8-N}$ type covalent crystals with zinc blende, wurtzite, and rocksalt structures contain only one type of chemical bond and one coordination number. For this kind of materials, the bond length and valence electron dependence of the bulk modulus can be quantified as

$$B(\text{GPa}) = Cp^l d^m \exp(kn_{AB}) \quad (30.2)$$

where C , l , m , and k are the fitting constants and can be extrapolated from the experimental bulk modulus data for these covalent crystals using the Levenberg–Marquardt method [75, 76],

$$B(\text{GPa}) = 54.7p^{0.914} d^{-3.46} \exp(1.485n_{AB}) \quad (30.3)$$

Table A3-1 features the measured and calculated bulk moduli for $A^N B^{8-N}$ covalent crystals and related parameters [71, 77–86].

2. **$A_n B_m$ ($n \neq m$) type covalent crystals.** For the $A_n B_m$ crystals, $N_{\max} = \max[N_A, N_B]$ and $N_{\min} = \min[N_A, N_B]$ apply. Using N_A and N_B individually as input parameters, with the power law indexes determined by fitting the experimental data or introducing an asymmetry parameter, $\Lambda = N_{\max}/N_{\min}$, for two bonded atoms with different coordination numbers. The power law indexes can be determined by fitting the experimental data. The bulk modulus formulae are $B(\text{GPa}) = CN_{\max}^s N_{\min}^t d^m \exp(kn_{AB})$ and $B(\text{GPa}) = Cp^l A^t d^m \exp(kn_{AB})$, respectively. The power law indexes to N_{\max} , N_{\min} , and Λ are adjusted during data fitting and determined to be 1.201, 0.672, and 0.370, respectively. These two schemes give similar results ($B_{\text{cal},1}$ and $B_{\text{cal},2}$ in Table A3-2). The second scheme follows

$$B(\text{GPa}) = 54.7p^{0.914}A^{0.37}d^{-3.46}\exp(1.485n_{\text{AB}}) \quad (30.4)$$

which formulates the bulk modulus of both $A^N B^{8-N}$ and $A_n B_m$ type covalent crystals. Table A3-2 lists the measured and calculated bulk moduli for $A_n B_m$ covalent crystals and related parameters [71, 87–91].

3. **Ionic crystals.** For the bulk moduli of I–VII rocksalt ionic crystals, a different pre-factor and power law index is expected [92], and the bulk modulus for rocksalt-structured ionic crystals follows

$$B(\text{GPa}) = 25.4p^{0.914}d^{-3.15}\exp(1.485n_{\text{AB}}) \quad (30.5)$$

Table A3-3 shows the consistency in predicating and the measurements of the cesium halides (with NaCl and CsCl structures) and produces bulk moduli in good agreement with experimental ones [71, 87, 93, 94].

4. **Multi-bond crystals.** The bulk modulus of a multi-component material results from the superposition of that of the individual component. From the definition of bulk modulus, Tian et al. derived

$$\frac{1}{B} = -\frac{dV}{VdP} = -\frac{\sum_{\mu} dV_{\mu}}{VdP} = \frac{\sum_{\mu} V_{\mu}(-dV_{\mu}/V_{\mu}dP)}{V} = \frac{\sum_{\mu} V_{\mu}/B_{\mu}}{V} = \sum_{\mu} v_{\mu}/B_{\mu} \quad (30.6)$$

where B_{μ} and $v_{\mu} = V_{\mu}/V$ are the bulk modulus and volume fraction of the μ component, respectively. For a multi-bond crystal, B_{μ} can be determined by using previous equations, and the volume fraction of distinct chemical bond can be calculated as $v_{\mu} = N_{\mu}d_{\mu}^3 / \sum_{\mu} N_{\mu}d_{\mu}^3$, where d_{μ} and N_{μ} are the bond length and bond multiplicity of the μ -type bond in the unit cell, respectively. Table A3-4 shows the outcome in comparison with measurements for multi-bond covalent crystals [87, 89, 95–98].

5. **Tensile strength versus bond energy.** Tian and co-workers [72] correlated the tensile strength of various crystals with the length d_{ij} and the EBVE number of a chemical bond: $\sigma_{\text{hkl}}^{\text{theor}}(\text{Pa}) = 6.6 \times 10^{-10} S_{\text{hkl}} d_{ij}^{-1.32} \exp(3.7n_{ij})$. The bond strength depends exclusively on two microscopic parameters: bond length and EBVE number. This model allows determination of the bond strength for a variety of crystals and accounts for the observation that a low coordination number of binding atoms has a tendency to higher bond strength.

Figure 30.7 shows the consistency between calculations and measurements of a number of crystals.

6. **Harder than diamond?** One may wonder that if one can make materials that are harder than the nature diamond—the hardest ever known. If it can be made, can its hardness be reliably measured? The answers to these questions are yes.

Firstly, synthesis based on the multilayer structure with hetero-junction interface mixing [99] and nanotwinning [15, 100] can realized thus. Bond nature alteration

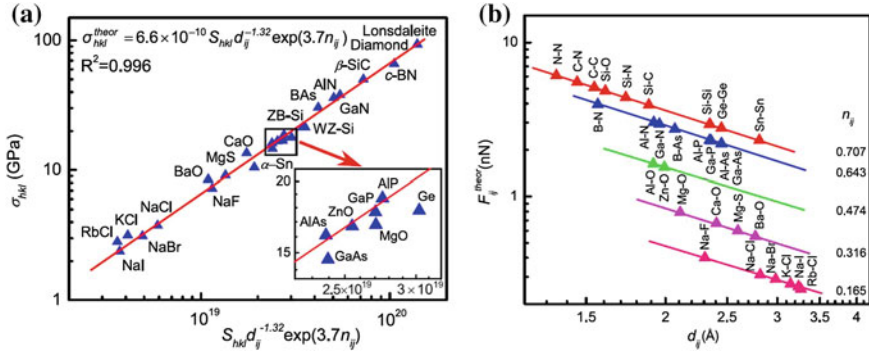


Fig. 30.7 **a** Ideal tensile strength σ_{hkl} of a crystal along the weakest $\langle E_{hkl} \rangle$ direction as a function of $\sigma_{hkl}^{theor}(\text{Pa}) = 6.6 \times 10^{-10} S_{hkl} d_{ij}^{-1.32} \exp(3.7n_{ij})$. S_{hkl} is the number of the broken bonds per unit area on the (hkl) plane, d_{ij} the bond length in angstrom, and n_{ij} the number of EVBEs. $F_{ij} = d_{ij}^{-1.32} \exp(3.7n_{ij})$ scales the maximal tensile force unbonding the i-j bond [72]. **b** Bond strength $F_{hkl}^{theor}(N) = \sigma_{hkl}^{theor}(\text{Pa})/S_{hkl}$ versus bond length d_{ij} in crystals with various numbers of the EVBEs, n_{ij} (reprinted with permission from [72])

from low indicator (m , see Sect. 14.2) to higher and bond length contraction [60], leading to local densification of bond energy and pinning of dislocations at boundaries of the twined grains and at the interface region.

Secondly, indentation hardness is determined by load divided by the projected area of a permanently formed indentation. In measurement, stress states in the indenter tip are different from that of the tested zone: the tip of the diamond indenter is subjected to a compressive stress field, and the sample undergoes plastic shear deformation around the indenter [100]. The compressive strengths of diamond are within the range of 223 and 470 GPa, depending on crystal orientation, whereas the shear strengths of diamond is 93 GPa and that for cBN is 65 GPa. Indentation hardness can be measured reliably as long as the shear strength of the sample is lower than the compressive strength of the indenter diamond. Diamond can measure the hardness of any material with an upper-limit of shear stress of 470 GPa.

Thirdly, according to the IHPR estimation, diamond reaches its strongest size at 20 nanometer (Table 28.1) [101], which corresponds to the curvature of the indentation tip or around. At the strongest size, the hardness is at least 3 times higher than the bulk value (Fig. 28.3) [14].

Therefore, materials harder than diamond can be synthesized by bond engineering through twinning and interfacing and the curved diamond indentation tip can measure sample of harder than nature diamond because of the IHPR effect and the stress state difference between the tip and the testing sample.

30.5 Interface Energy Determination: XPS

In order to determine the bond energy associated with the heterogeneous interfaces using XPS, one needs to find firstly the energy levels of an isolated atom and their bulk shifts of the constituent elements for reference. As introduced in [Chap. 16](#), XPS analysis of the elemental surfaces provides such information. One then measures the energy shifts of the specific energy levels upon interface alloy formation. Subtracting the referential spectrum from that collected from the alloy distills the interface effect on the binding energy. Calibrated based on the energy levels and bulk shifts derived from elemental surfaces, one can derive the bond energy, the energy density, the atomic cohesive energy, and the free energy at the interface region.

30.5.1 Atomistic Definition of Interface Energy

In fact, the performance of an interface is governed by its remnant energy in terms of the bond energy, atomic cohesive energy, or the local binding energy density, instead of the energy cost upon interface formation [[102](#), [103](#)]. In the interface region, the single-body Hamiltonian undergoes the perturbation due to the bond nature alteration with charge entrapment or polarization according to the tight-binding band theory [[60](#), [104](#)], which is expressed as follows:

$$\begin{aligned}
 H &= -\frac{\hbar^2 \nabla^2}{2m} + V_{\text{atom}}(r) + V_{\text{cryst}}(r, \text{I}) \\
 &= -\frac{\hbar^2 \nabla^2}{2m} + V_{\text{atom}}(r) + V_{\text{cryst}}(r, \text{B})(1 + \Delta_H)
 \end{aligned}
 \tag{30.7}$$

where the intra-atomic trapping potential, $V_{\text{atom}}(r)$, determines the specific v th energy level of an isolated atom $E_v(0)$, from which the binding energies (BE) start to shift upon the crystal potential $V_{\text{cryst}}(r)$ being involved. Δ_H is the perturbation due to bond nature alteration, entrapment, or polarization. The parameters B and I represent the bulk and the interface, respectively. Only the $V_{\text{cryst}}(r)$ can be perturbed because the intra-atomic potential $V_{\text{atom}}(r)$ is intrinsically unchangeable.

30.5.2 Interface Core-Level Shift

The XPS BE shift is uniquely proportional to the crystal potential at equilibrium, i.e., cohesive energy per bond. Any perturbation to the crystal potential by the quantum entrapment or polarization at the interface will lead to the core-level shift:

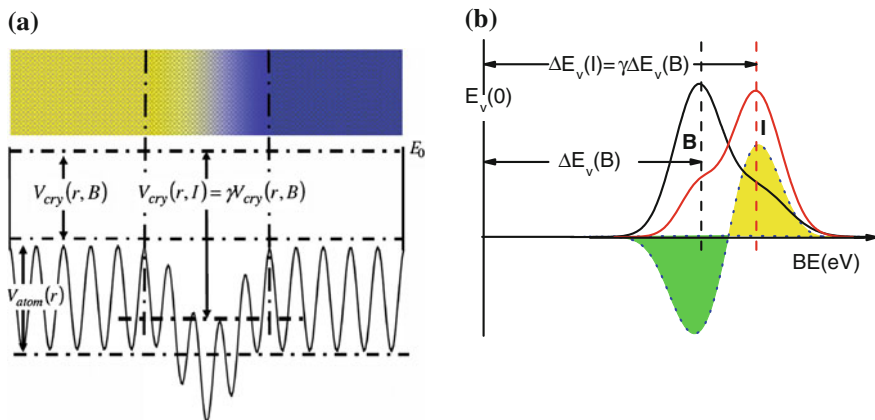


Fig. 30.8 Illustration of **a** the interfacial quantum entrapment and the associated **b** core-level shift. $V_{cry}(r, B)$ and $V_{cry}(r, I)$ are interatomic potentials in the bulk and in the interface region, respectively. $\gamma = \Delta E_v(I)/\Delta E_v(B)$ is the coefficient. $\gamma > 1$ represents the compact interface with dominance of quantum entrapment, and $\gamma < 1$ represents the dissociated interface or interface with dominance of polarization (reprinted with permission from [106])

$$\frac{\Delta E_v(I)}{\Delta E_v(B)} = \frac{V_{cryst}(r, I)}{V_{cryst}(r, B)} = 1 + \Delta_H = \gamma \begin{cases} > 1 & \text{(entrapment)} \\ < 1 & \text{(polarization)} \end{cases} \quad (30.8)$$

where $\Delta E_v(I)$ represents the shift of a particular v th level from the $E_v(0)$.

Figure 30.8a illustrates the interface quantum entrapment mechanism. There is a gradient of chemical composition due to the diffusion of the constituent atoms. $V_{cry}(r, B)$ represents the periodic interatomic potential experienced by electrons in the constituent bulk (B). Moving cross the interface region from one to the other constituent, the $V_{cry}(r, B)$ evolves into $V_{cry}(r, I)$ at the middle of the interface (I) because of valence charge intermixing or bond nature alteration. The coefficient γ represents the interface bond energy ratio to that of the constituent bulk. The $V_{cry}(r, I)$ may be deeper ($\gamma > 1$) or shallower ($\gamma < 1$) than the corresponding $V_{cry}(r, B)$ for a specific constituent. If dipole is produced in the interface region [105], then $\gamma < 1$; otherwise, $\gamma > 1$.

Figure 30.8b illustrates the evolution of the XPS profiles of a particular energy level upon interface formation. The peak $E_v(B)$ evolves into the $E_v(I)$ upon alloy formation by heating the heterogeneous layered film to a certain temperature. The $E_v(I)$ can move upward (polarization, $\gamma < 1$) or the otherwise. A subtraction of the $E_v(B)$ from the $E_v(I)$ upon structural area normalization results in the residual spectrum that is purely the interface effect—quantum entrapment or polarization dominance.

Figure 30.9 compares the XPS and the residual ZPS profiles for the valence and the core bands of Ag, Cu, and Pd in their parent metals and in the alloys. Figure 30.10 shows the evolution of the core band for Be and W upon alloy formation. Table 30.1 features quantitative information about the absolute values

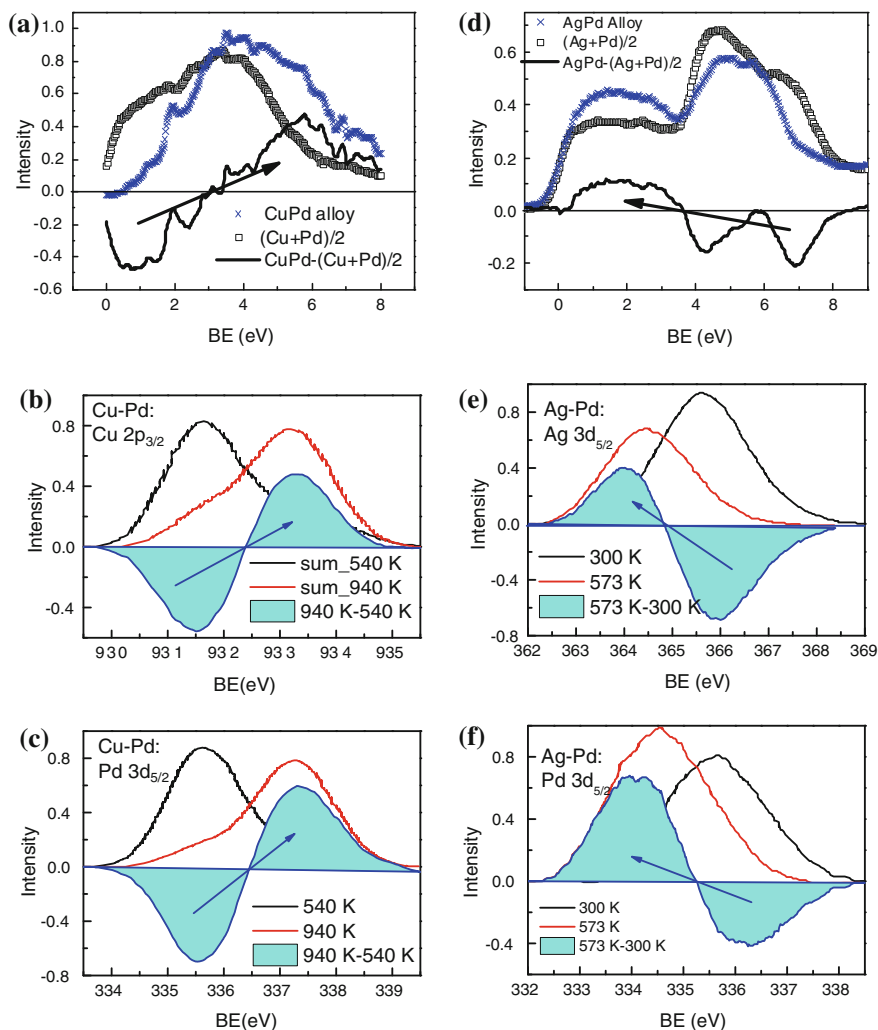


Fig. 30.9 XPS and the residual ZPS spectra of **a** the valence of CuPd, **b** Cu 2p_{3/2}, and **c** Pd 3d_{5/2} bands show the dominance of entrapment in CuPd alloying interface. **d** The valence of AgPd, **e** Ag 3d_{5/2}, and the **f** Pd 3d_{5/2} bands show the dominance of polarization in the AgPd interface [105]. Indicated are temperatures of annealing for alloy formation

of the binding energy, the bulk binding energy, the interface component binding energy, the bulk shift, and interface energy shift.

Results indicates that the binding energies experienced by electrons of Be, W, Ag, and Pd become weaker in the BeW and AgPd alloys, but the electronic binding energy becomes stronger in the CuPd alloy. The upward shift in the valence and core band binding energy indicates the interface polarization, and hence, the BeW and AgPd interfaces are mechanically weaker than these

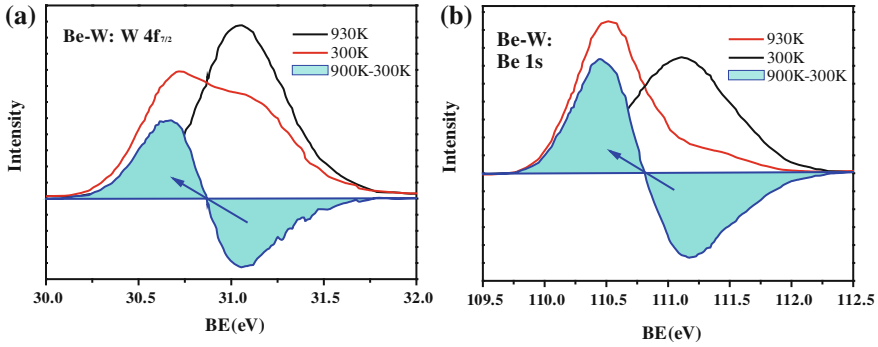


Fig. 30.10 XPS and the residual ZPS spectra of the **a** Be 1s and **b** W $4f_{7/2}$ components show the dominance of polarization in BeW alloying interface [107]. Indicated are temperatures of annealing for alloy formation

Table 30.1 Core-level energy of an isolated atom $E_v(0)$, bulk shift $\Delta E_v(B)$, interface shift ($\Delta E_v(I)$), and the ratio of $\Delta E_v(I)/\Delta E_v(B)$ (γ) for components in the BeW, CuPd, and AgPd alloy interfaces (in eV unit) [105, 107–111]

| Alloy | E levels | $E_v(0)$ | $E_v(B)$ | $E_v(I)$ | $\Delta E_v(B)$ | $\Delta E_v(I)$ | γ |
|-------|---------------|----------|----------|----------|-----------------|-----------------|----------|
| BeW | Be 1s | 106.42 | 111.11 | 110.48 | 4.69 | 4.06 | 0.87 |
| | W $4f_{7/2}$ | 28.91 | 31.08 | 30.66 | 2.17 | 1.75 | 0.81 |
| CuPd | Cu $2p_{3/2}$ | 931.00 | 932.70 | 934.28 | 1.70 | 3.28 | 1.93 |
| | Pd $3d_{5/2}$ | 330.34 | 334.32 | 335.87 | 3.98 | 5.53 | 1.39 |
| AgPd | | | | 333.1 | | 2.76 | 0.69 |
| | Ag $3d_{5/2}$ | 363.02 | 367.65 | 366.47 | 4.63 | 3.45 | 0.75 |

elemental solids stand alone. In contrast, CuPd alloy formation causes interface strengthening. Both the valence and the core bands shift positively, indicating the quantum entrapment dominance at the CuPd interface.

30.5.3 Interface Bond Energy

According to the BOLS correlation and the band theory, the energy value of $V_{\text{cryst}}(r)$ at equilibrium is proportional to the mean cohesive energy per bond, $\langle E_b \rangle$. That is, the interface BE shift is proportional to the local bond energy $\langle E_l \rangle$. Using Eq. (30.8), one can determine the bond energy of a constituent element at the interface as follows:

$$\frac{\langle E_l \rangle}{\langle E_b \rangle} = \frac{\Delta E_v(I)}{\Delta E_v(B)} = \gamma \quad (30.9)$$

Table 30.2 Bond energy and lattice constant of the constituent bulk reference E_b and l_b [114] and their values at the interface region $E_I(A-A$ or $B-B)$ and the exchange bond energy $E_I(A-B)$

| Alloy | Atom | E_b (eV) | $E_I(A-A)$ (eV) | $E_I(A-B)$ (eV) | $\langle E_{IS} \rangle$ (eV) | l_b (nm) | $\langle l_I \rangle$ (nm) |
|-------|------|------------|-----------------|-----------------|-------------------------------|------------|----------------------------|
| BeW | Be | 0.28 | 0.24 | 0.38 | 0.52 | 0.229 | 0.273 |
| | W | 0.74 | 0.60 | | | 0.316 | |
| CuPd | Cu | 0.29 | 0.56 | 0.50 | 0.63 | 0.360 | 0.375 |
| | Pd | 0.32 | 0.45 | | | 0.389 | |
| AgPd | Pd | 0.32 | 0.22 | 0.20 | 0.26 | 0.389 | 0.399 |
| | Ag | 0.25 | 0.19 | | | 0.409 | |

$\langle E_{IS} \rangle$ and $\langle l_I \rangle$ are the average

where $\langle E_I \rangle$ and $\langle E_B \rangle$ represent the mean bond energy of the particular element at the interface and in the bulk. This allows for the value of $\langle E_I \rangle$ with high precision. The value of $\Delta E_v(B)$ can be determined by decomposition of the surface BE spectrum [108, 110, 112, 113], and $\langle E_B \rangle$ is a given constant for a specific element in the bulk [114].

The interface bond energy $\langle E_{IS} \rangle$ and bond length $\langle d_{IS} \rangle$ consist of three parts: A–A, B–B, and A–B interactions. The following approach gives the mean $\langle E_{IS} \rangle$ [115, 116]:

$$\langle E_{IS} \rangle = xE_{IA} + (1-x)E_{IB} + x(1-x)\sqrt{E_{IA}E_{IB}} \quad (30.10)$$

The last term denotes the exchange interaction between atoms A and B. Vegard's notation derives the interface lattice constant $\langle l_{IS} \rangle$ [117],

$$\langle l_{IS} \rangle = xl_A + (1-x)l_B \quad (30.11)$$

With the derived $\langle l_{IS} \rangle$ and $\langle E_{IS} \rangle$, one is able to determine the binding energy density and atomic cohesive energy, and the interface free energy is given by

$$\left\{ \begin{array}{ll} E_C = z_I \langle E_{IS} \rangle & \text{atomic cohesive energy} \\ E_D = \frac{E_{\text{sum-cell}}}{V_{\text{cell}}} = \frac{N \cdot z_I \cdot \langle E_{IS} \rangle}{2l_{IS}^3} & \text{binding energy density} \\ \gamma_I = \frac{E_{\text{sum-cell}}}{A_{\text{sectional}}} = \frac{N \cdot z_I \cdot \langle E_{IS} \rangle}{2l_{IS}^2} & \text{interface free energy} \end{array} \right. \quad (30.12)$$

where z_I is the interface atomic coordination number and N is the number of atoms in a unit cell in the interface region. Hence, from the analysis of an XPS measurement, we are able to gain quantitative information of interface energetics.

From Eq. (30.10), we can determine the A–A and B–B bond energies of the constituents in the interface. For instance, the bond energy of Be and W in the BeW alloy is 0.24 and 0.60 eV, respectively. The bond energy of one element in different interfaces diverges. For example, in CuPd, the Pd–Pd bond energy is 0.45 eV, but it is 0.22 eV in AgPd. Then, using Eqs. (30.10) and (30.11), one can estimate the mean bond length, bond energy, and lattice constant in the interface of the three alloys, as listed in Table 30.2.

Table 30.3 Interfacial atomic cohesive energy E_{Coh} , binding energy density E_{Den} , and the free energy γ_I

| Alloy | E_c (eV) | E_D (10^{10} J/m ³) | γ_I (J/m ²) |
|-------|------------|--------------------------------------|--------------------------------|
| BeW | 6.24 | 9.85 | 26.85 |
| CuPd | 7.56 | 4.59 | 17.20 |
| AgPd | 2.76 | 1.57 | 6.28 |

30.5.4 Binding Energy Density and Atomic Cohesive Energy

It is meaningful to redefine the interface energy as the energy density per unit cell in the interface region, in place of the conventionally defined excessive energy per unit area. To be in line with the conventional definition, the interface free energy density will equal to the energy per unit cell divided by the cross-sectional area of the cell.

For simplicity, we assume that the interface alloys remain fcc structures. Then, there are four atoms in a unit cell. The atoms in the interface are in full coordination, $N = 4$, $z_b = 12$. In addition, with the derived mean bond energy $\langle E_{\text{IS}} \rangle$ and the mean lattice constants $\langle l_{\text{IS}} \rangle$, the interface free energies γ_I of BeW, CuPd, and AgPd can be estimated to be 26.85, 17.20, and 6.28 J/m² by using Eq. (30.12), respectively.

Table 30.3 features the interface atomic cohesive energy and energy density of these alloys. The interfacial energy density and the interfacial atomic cohesive energy may be different from that of the corresponding constituent because of interface effect. The energy density of the BeW interface is the largest among the three, which justifies that the BeW becomes an important medium for radiation protection in the International Thermonuclear Experimental Reactor devices due to its large energy density.

Therefore, the BOLS correlation theory and the XPS measurements enable determination of the interface energetics. The accuracy of estimation is strictly subject to the measurement. Other factors such as materials' purity, defect concentration, and testing techniques may lead to the accuracy of the derived $E_v(0)$ and $E_v(I)$ values. The developed approach could enhance the power of XPS for extracting more quantitative information regarding the interface properties. The concepts of quantum entrapment and polarization are essential for understanding the bonding and electronic behaviors of hetero-coordinated atoms at the interface region.

Note that the interface free energy equals the energy density multiplied by the length of interface region. Here, we make it to be the energy per cell dividing the cross-sectional area of cell. As the mechanical strength of concern, the higher energy density means high mechanical strength of the interface and the alloy as well.

30.6 Summary

Hetero-coordination enhances the local mechanical strength through binding energy density gain-increasing covalency, bond number density and shortening bond length. Bond nature alteration at the interface and in the twin grain boundary is another choice as the distortion pins dislocations and increases the local energy density. Harder than diamond could be realized and tested as the indentation tip suffers the compressive stress and the testing sample undergoes shear dislocation that is much lower than the compressive stress.

The hetero-coordination-induced bond strain and the energy quantum entrapment serve as centers of pinning in the interface region to inhibit motion of atomic dislocations and hence interfacial hardening. On the other hand, alloy or compound formation at the interface alters the originally metallic bonds of the components to be ionic or covalent, and hence, the bond nature indicator, m , evolves from the original value for each constituent element to the higher values. The bond nature alteration provides an additional mechanism of interfacial strengthening. As the mesoscopic mechanics depend functionally on atomic CN, bond length, bond energy, and the temperature of operation, the T-BOLS correlation can readily be extended to the interface by introducing a parameter, γ , to correlate the interfacial bond energy with the bulk standard, $E_{\text{int}}(T) = \gamma E_{\text{b}}(T)$, and then, the T-BOLS correlation mechanism applies to the cohesive interface, if the atomic CN changes insignificantly and the bond strain is not reliably determined. However, polarization due to interface formation may be detrimental to the strength of the interface.

References

1. K.L. Pey, R. Ranjan, C.H. Tung, L.J. Tang, V.L. Lo, K.S. Lim, T.A.L. Selvarajoo, D.S. Ang, Breakdowns in high-k gate stacks of nano-scale CMOS devices. *Microelectron. Eng.* **80**, 353–361 (2005)
2. C.H. Tung, K.L. Pey, L.J. Tang, M.K. Radhakrishnan, W.H. Lin, F. Palumbo, S. Lombardo, Percolation path and dielectric-breakdown-induced-epitaxy evolution during ultrathin gate dielectric breakdown transient. *Appl. Phys. Lett.* **83**(11), 2223–2225 (2003)
3. L.K. Pan, C.Q. Sun, T.P. Chen, S. Li, C.M. Li, B.K. Tay, Dielectric suppression of nanosolid silicon. *Nanotechnology* **15**(12), 1802–1806 (2004)
4. Y. He, W.F. Chen, W.B. Yu, G. Ouyang, G.W. Yang, Anomalous interface adhesion of graphene membranes. *Sci. Rep.* **3**, 2660 (2013)
5. M. MacKenzie, A.J. Craven, D.W. McComb, S. De Gendt, Interfacial reactions in a HfO₂/TiN/poly-Si gate stack. *Appl. Phys. Lett.* **88**(19), 192112 (2006)
6. S. Veprek, Electronic and mechanical properties of nanocrystalline composites when approaching molecular size. *Thin Solid Films* **297**(1–2), 145–153 (1997)
7. S. Veprek, S. Reiprich, A concept for the design of novel superhard coatings. *Thin Solid Films* **268**(1–2), 64–71 (1995)
8. X.T. Zeng, S. Zhang, C.Q. Sun, Y.C. Liu, Nanometric-layered CrN/TiN thin films: mechanical strength and thermal stability. *Thin Solid Films* **424**(1), 99–102 (2003)

9. S.K. Tien, J.G. Duh, Comparison of microstructure and phase transformation for nanolayered CrN/AlN and TiN/AlN coatings at elevated temperatures in air environment. *Thin Solid Films* **515**(3), 1097–1101 (2006)
10. Y.P. Li, G.P. Zhang, W. Wang, J. Tan, S.J. Zhu, On interface strengthening ability in metallic multilayers. *Scr. Mater.* **57**(2), 117–120 (2007)
11. C.D. Gu, J.S. Lian, Q. Jiang, Layered nanostructured Ni with modulated hardness fabricated by surfactant-assistant electrodeposition. *Scripta Mater.* **57**(3), 233–236 (2007)
12. R.A. Andrievski, Nanostructured superhard films as typical nanomaterials. *Surf. Coat. Technol.* **201**(13), 6112–6116 (2007)
13. S.Q. Hao, B. Delley, S. Veprek, C. Stampfl, Superhard nitride-based nanocomposites: Role of interfaces and effect of impurities. *Phys. Rev. Lett.* **97**(8), 086102 (2006)
14. C.Q. Sun, Thermo-mechanical behavior of low-dimensional systems: The local bond average approach. *Prog. Mater. Sci.* **54**(2), 179–307 (2009)
15. Y.J. Tian, B. Xu, D.L. Yu, Y.M. Ma, Y.B. Wang, Y.B. Jiang, W.T. Hu, C.C. Tang, Y.F. Gao, K. Luo, Z.S. Zhao, L.M. Wang, B. Wen, J.L. He, Z.Y. Liu, Ultrahard nanotwinned cubic boron nitride. *Nature* **493**(7432), 385–388 (2013)
16. E. Ma, Y.M. Wang, Q.H. Lu, M.L. Sui, L. Lu, K. Lu, Strain hardening and large tensile elongation in ultrahigh-strength nano-twinned copper. *Appl. Phys. Lett.* **85**(21), 4932–4934 (2004)
17. M. Dao, L. Lu, Y.F. Shen, S. Suresh, Strength, strain-rate sensitivity and ductility of copper with nanoscale twins. *Acta Mater.* **54**(20), 5421–5432 (2006)
18. L. Lu, R. Schwaiger, Z.W. Shan, M. Dao, K. Lu, S. Suresh, Nano-sized twins induce high rate sensitivity of flow stress in pure copper. *Acta Mater.* **53**(7), 2169–2179 (2005)
19. K.A. Afanasyev, F. Sansoz, Strengthening in gold nanopillars with nanoscale twins. *Nano Lett.* **7**(7), 2056–2062 (2007)
20. A. Froseth, H. Van Swygenhoven, P.M. Derlet, The influence of twins on the mechanical properties of nc-Al. *Acta Mater.* **52**(8), 2259–2268 (2004)
21. S.Y. Fu, B. Lauke, R.K.Y. Li, Y.W. Mai, Effects of PA6,6/PP ratio on the mechanical properties of short glass fiber reinforced and rubber-toughened polyamide 6,6/polypropylene blends. *Compos. Pt. B-Eng.* **37**(2–3), 182–190 (2006)
22. S.Y. Fu, Q.Y. Pan, C.J. Huang, G. Yang, X.H. Liu, L. Ye, Y.W. Mai, A preliminary study on cryogenic mechanical properties of epoxy blend matrices and SiO₂/epoxy nanocomposites, in *Fracture of Materials: Moving Forwards*, ed. by H.Y. Liu, X. Hu, M. Hoffman (Trans Tech Publications Ltd, Zurich-Uetikon, 2006), pp. 211–216
23. Z.D. Wang, J.J. Lu, Y. Li, S.Y. Fu, S.Q. Jiang, X.X. Zhao, Studies on thermal and mechanical properties of PI/SiO₂ nanocomposite films at low temperature. *Compos. Pt. A- Appl. Sci. Manuf.* **37**(1), 74–79 (2006)
24. P. Sharma, S. Ganti, Size-dependent Eshelby's tensor for embedded nano-inclusions incorporating surface/interface energies. *J. Appl. Mech.-Trans. ASME* **71**(5), 663–671 (2004)
25. M. Lu, K.T. Lau, W.Y. Tam, K. Liao, Enhancement of Vickers hardness of nanoclay-supported nanotube reinforced novel polymer composites. *Carbon* **44**(2), 383–386 (2006)
26. H. Liu, K. Liao, Tensile behavior and morphology studies of glass-fiber-reinforced polymeric in situ hybrid composites. *J. Appl. Polym. Sci.* **94**(1), 211–221 (2004)
27. X.J. Xu, M.M. Thwe, C. Shearwood, K. Liao, Mechanical properties and interfacial characteristics of carbon-nanotube-reinforced epoxy thin films. *Appl. Phys. Lett.* **81**(15), 2833–2835 (2002)
28. K. Liao, S. Li, Interfacial characteristics of a carbon nanotube-polystyrene composite system. *Appl. Phys. Lett.* **79**(25), 4225–4227 (2001)
29. X.D. Li, H.S. Gao, W.A. Scrivens, D.L. Fei, V. Thakur, M.A. Sutton, A.P. Reynolds, M.L. Myrick, Structural and mechanical characterization of nanoclay-reinforced agarose nanocomposites. *Nanotechnology* **16**(10), 2020–2029 (2005)
30. L. Ci, J. Suhr, V. Pushparaj, X. Zhang, P.M. Ajayan, Continuous carbon nanotube reinforced composites. *Nano Lett.* **8**(9), 2762–2766 (2008)

31. K. Haraguchi, M. Ebato, T. Takehisa, Polymer-clay nanocomposites exhibiting abnormal necking phenomena accompanied by extremely large reversible elongations and excellent transparency. *Adv. Mater.* **18**(17), 2250 (2006)
32. B. Cantor, I.T.H. Chang, P. Knight, A.J.B. Vincent, Microstructural development in equiatomic multicomponent alloys. *Mater. Sci. Eng.-Struct. Mater. Prop. Microstruct. Process.* **375**, 213–218 (2004)
33. W. Liu, J.C. Li, W.T. Zheng, Q. Jiang, NiAl(110)/Cr(110) interface: A density functional theory study. *Phys. Rev. B* **73**(20), 205421 (2006)
34. L.Y. Jiang, Y. Huang, H. Jiang, G. Ravichandran, H. Gao, K.C. Hwang, B. Liu, A cohesive law for carbon nanotube/polymer interfaces based on the van der Waals force. *J. Mech. Phys. Solids* **54**(11), 2436–2452 (2006)
35. F.M. Gao, J.L. He, E.D. Wu, S.M. Liu, D.L. Yu, D.C. Li, S.Y. Zhang, Y.J. Tian, Hardness of covalent crystals. *Phys. Rev. Lett.* **91**(1), 015502 (2003)
36. M.L. Cohen, T.K. Bergstre, Band structures and pseudopotential form factors for 14 semiconductors of diamond and zinc-blende structures. *Phys. Rev.* **141**(2), 789 (1966)
37. J.C. Philips, *Covalent Bonding in Crystals, Molecules and Polymers* (Chicago University Press, Chicago, 1969)
38. V. Litovchenko, Analysis of the band structure of tetrahedral diamondlike crystals with valence bonds: Prediction of materials with superhigh hardness and negative electron affinity. *Phys. Rev. B* **65**(15), 153108 (2002)
39. A.Y. Liu, M.L. Cohen, Prediction of new low compressibility solids. *Science* **245**(4920), 841–842 (1989)
40. E.G. Wang, Research on carbon nitrides. *Prog. Mater. Sci.* **41**(5), 241–298 (1997)
41. E.G. Wang, A new development in covalently bonded carbon nitride and related materials. *Adv. Mater.* **11**(13), 1129 (1999)
42. W.T. Zheng, H. Sjostrom, I. Ivanov, K.Z. Xing, E. Broitman, W.R. Salaneck, J.E. Greene, J.E. Sundgren, Reactive magnetron sputter deposited CN_x: effects of N-2 pressure and growth temperature on film composition, bonding, and microstructure. *J. Vacuum Sci. Technol.-Vacuum Surf. Films* **14**(5), 2696–2701 (1996)
43. S. Veprek, Conventional and new approaches towards the design of novel superhard materials. *Surf. Coat. Technol.* **97**(1–3), 15–22 (1997)
44. H. Van Swygenhoven, P.M. Derlet, A. Hasnaoui, Atomic mechanism for dislocation emission from nanosized grain boundaries. *Phys. Rev. B* **66**(2), 024101 (2002)
45. Z.S. Popovic, S. Satpathy, Wedge-shaped potential and Airy-function electron localization in oxide superlattices. *Phys. Rev. Lett.* **94**(17), 176805 (2005)
46. H.E. Mahnke, H. Haas, E. Holub-Krappe, V. Koteski, N. Novakovic, P. Fochuk, O. Panchuk, Lattice distortion around impurity atoms as dopants in CdTe. *Thin Solid Films* **480**, 279–282 (2005)
47. Z.Y. Pan, Z.H. Sun, Z. Xie, J.H. Xu, I. Kojima, S.Q. Wei, Interfacial intermixing of TiN/Si₃N₄ super-hard multilayer films studied by fluorescence x-ray absorption fine structure. *J. Phys. D-Appl. Phys.* **39**(13), 2796–2802 (2006)
48. D. Zanchet, H. Tolentino, M.C.M. Alves, O.L. Alves, D. Ugarte, Inter-atomic distance contraction in thiol-passivated gold nanoparticles. *Chem. Phys. Lett.* **323**(1–2), 167–172 (2000)
49. P. Kluth, B. Johannessen, V. Giraud, A. Cheung, C.J. Glover, G.D. Azevedo, G.J. Foran, M.C. Ridgway, Bond length contraction in Au nanocrystals formed by ion implantation into thin SiO₂. *Appl. Phys. Lett.* **85**(16), 3561–3563 (2004)
50. D.L. Chen, C.S. Li, Z.G. Zhu, J.W. Fan, S.Q. Wei, Interface effect of InSb quantum dots embedded in SiO₂ matrix. *Phys. Rev. B* **72**(7), 075341 (2005)
51. A. Wolska, K. Lawniczak-Jablonska, M. Klepka, M.S. Walczak, A. Misiuk, Local structure around Mn atoms in Si crystals implanted with Mn+studied using x-ray absorption spectroscopy techniques. *Phys. Rev. B* **75**(11), 113201 (2007)
52. S. Veprek, M.G.J. Veprek-Heijman, The formation and role of interfaces in superhard nc-MenN/a-Si₃N₄ nanocomposites. *Surf. Coat. Technol.* **201**(13), 6064–6070 (2007)

53. S.G. Srinivasan, X.Z. Liao, M.I. Baskes, R.J. McCabe, Y.H. Zhao, Y.T. Zhu, Compact and dissociated dislocations in aluminum: Implications for deformation. *Phys. Rev. Lett.* **94**(12), 125502 (2005)
54. G.H. Lu, S.H. Deng, T.M. Wang, M. Kohyama, R. Yamamoto, Theoretical tensile strength of an Al grain boundary. *Phys. Rev. B* **69**(13), 134106 (2004)
55. S. Banerjee, S. Ferrari, R. Piagge, S. Spadoni, Electron density profile at the interface of SiO₂/Si(001). *Appl. Surf. Sci.* **253**(1), 17–20 (2006)
56. X.L. Li, B. Chen, H.Y. Jing, H.B. Lu, B.R. Zhao, Z.H. Mai, Q.J. Jia, Experimental evidence of the “dead layer” at Pt/BaTiO₃ interface. *Appl. Phys. Lett.* **87**(22), 222905 (2005)
57. J.Q. He, E. Vasco, C.L. Jia, R.H. Wang, Direct observation of a fully strained dead layer at Ba_{0.7}Sr_{0.3}TiO₃/SrRuO₃ interface. *Appl. Phys. Lett.* **87**(6), 062901 (2005)
58. M. Stengel, N.A. Spaldin, Origin of the dielectric dead layer in nanoscale capacitors. *Nature* **443**(7112), 679–682 (2006)
59. M. Maglione, Interface-driven magnetocapacitance in a broad range of materials. *J. Phys.-Condens. Matter* **20**(32), 322202 (2008)
60. C.Q. Sun, Y. Shi, C.M. Li, S. Li, T.C.A. Yeung, Size-induced undercooling and overheating in phase transitions in bare and embedded clusters. *Phys. Rev. B* **73**(7), 075408 (2006)
61. V.P. Skripov, V.P. Koverda, V.N. Skokov, Size effect on melting of small particle. *Phys. Status Solidi A-Appl. Res.* **66**(1), 109–118 (1981)
62. J. Zhong, L.H. Zhang, Z.H. Jin, M.L. Sui, K. Lu, Superheating of Ag nanoparticles embedded in Ni matrix. *Acta Mater.* **49**(15), 2897–2904 (2001)
63. H.W. Sheng, G. Ren, L.M. Peng, Z.Q. Hu, K. Lu, Superheating and melting-point depression of Pb nanoparticles embedded in Al matrices. *Philos. Mag. Lett.* **73**(4), 179–186 (1996)
64. C.Q. Chen, Y. Shi, Y.S. Zhang, J. Zhu, Y.J. Yan, Size dependence of Young’s modulus in ZnO nanowires. *Phys. Rev. Lett.* **96**(7), 075505 (2006)
65. S. Veprek, M.G.J. Veprek-Heijman, P. Karvankova, J. Prochazka, Different approaches to superhard coatings and nanocomposites. *Thin Solid Films* **476**(1), 1–29 (2005)
66. R.F. Zhang, S.H. Sheng, S. Veprek, Mechanical strengths of silicon nitrides studied by ab initio calculations. *Appl. Phys. Lett.* **90**(19), 191903 (2007)
67. G. Audoit, J.S. Kulkarni, M.A. Morris, J.D. Holmes, Size dependent thermal properties of embedded crystalline germanium nanowires. *J. Mater. Chem.* **17**(16), 1608–1613 (2007)
68. L.H. Liang, J.C. Li, Q. Jiang, Superheating thermodynamics of nanocrystals based on the interface effect. *Phys. B-Condens. Matter* **322**(1–2), 188–192 (2002)
69. C.Q. Sun, Oxidation electronics: bond-band-barrier correlation and its applications. *Prog. Mater Sci.* **48**(6), 521–685 (2003)
70. C.Q. Sun, Y.Q. Fu, B.B. Yan, J.H. Hsieh, S.P. Lau, X.W. Sun, B.K. Tay, Improving diamond-metal adhesion with graded TiCN interlayers. *J. Appl. Phys.* **91**(4), 2051–2054 (2002)
71. B. Xu, Q. Wang, Y. Tian, Bulk modulus for polar covalent crystals. *Sci. Rep.* **3**, 3068 (2013)
72. X. Guo, L.M. Wang, B. Xu, Z. Liu, D. Yu, J. He, H.T. Wang, Y. Tian, Unbinding force of chemical bonds and tensile strength in strong crystals. *J. Phys.: Condens. Matter* **21**(48), 485405 (2009)
73. B. Xu, X. Guo, Y. Tian, Universal quantification of chemical bond strength and its application to low dimensional materials, in *Graphene Simulation*, ed. by J. Gong (InTech, Rijeka, 2011), pp. 211–226
74. B.F. Levine, Bond susceptibilities and ionicities in complex crystal-structures. *J. Chem. Phys.* **59**(3), 1463–1486 (1973)
75. K. Levenberg, A method for the solution of certain non-linear problems in least squares. *Q. Appl. Math.* **2**, 164–168 (1944)
76. D.W. Marquardt, An algorithm for least-squares estimation of nonlinear parameters. *SIAM J. Appl. Math.* **11**(2), 431–441 (1963)
77. S. Kamran, K. Chen, L. Chen, Semiempirical formulae for elastic moduli and brittleness of diamondlike and zinc-blende covalent crystals. *Phys. Rev. B* **77**(9), 094109 (2008)

78. H. Kamioka, Temperature variations of elastic moduli up to eutectic temperature in tin-bismuth alloys. *Jpn. J. Appl. Phys.* **22**(12), 1805–1809 (1983)
79. G.G. Bentle, Elastic constants of single-crystal BeO at room temperature. *J. Am. Ceram. Soc.* **49**(3), 125–128 (1966)
80. K. Li, Z. Ding, D. Xue, Electronegativity-related bulk moduli of crystal materials. *Phys. Status Solidi B* **248**(5), 1227–1236 (2011)
81. S.V. Sinogeikin, J.D. Bass, Single-crystal elasticity of MgO at high pressure. *Phys. Rev. B* **59**(22), R14141–R14144 (1999)
82. P.E. Van Camp, V.E. Van Doren, J.L. Martins, High pressure properties of the alkaline-earth sulphides. *Phys. Status Solidi B* **190**(1), 193–197 (1995)
83. R.A. Bartels, V.H. Vetter, The temperature dependence of the elastic constants of CaO and SrO. *J. Phys. Chem. Solids* **33**(10), 1991–1992 (1972)
84. S. Ves, U. Schwarz, N.E. Christensen, K. Syassen, M. Cardona, Cubic ZnS under pressure: Optical-absorption edge, phase transition, and calculated equation of state. *Phys. Rev. B* **42**(14), 9113 (1990)
85. D.B. Sirdeshmukh, K.G. Subhadra, Bulk modulus-volume relationship for some crystals with a rock salt structure. *J. Appl. Phys.* **59**, 276 (1986)
86. R.M. Hazen, L.W. Finger, Bulk modulus-volume relationship for cation-anion polyhedra. *J. Geophys. Res.* **84**(NB12), 6723–6728 (1979)
87. A. Otero-de-la-Roza, V. Luaña, Topological partition of the elastic constants of crystals. *J. Phys. Chem. A* **115**(45), 12953–12961 (2011)
88. F. Namavar, G. Wang, C.L. Cheung, R.F. Sabirianov, X.C. Zeng, W.N. Mei, J. Bai, J.R. Brewer, H. Haider, K.L. Garvin, Thermal stability of nanostructurally stabilized zirconium oxide. *Nanotechnology* **18**(41), 415702 (2007)
89. D.L. Anderson, O.L. Anderson, Bulk modulus-volume relationship for oxides. *J. Geophys. Res.* **75**(17), 3494–4000 (1970)
90. J. Haines, J.M. Leger, X-ray diffraction study of the phase transitions and structural evolution of tin dioxide at high pressure: Relationships between structure types and implications for other rutile-type dioxides. *Phys. Rev. B* **55**(17), 11144 (1997)
91. R.M. Hazen, L.W. Finger, Bulk moduli and high-pressure crystal-structures of rutile-type compounds. *J. Phys. Chem. Solids* **42**(3), 143–151 (1981)
92. M.L. Cohen, Calculation of bulk moduli of diamond and zinblende solids. *Phys. Rev. B* **32**(12), 7988–7991 (1985)
93. G.K. White, Thermal expansion at low temperatures of the alkaline earth fluorides and PbF₂. *J. Phys. C: Solid State Phys.* **13**(26), 4905 (1980)
94. S. Narain, Analysis of the Debye temperature for ANB₈–N type ionic and partially covalent crystals. *Phys. Status Solidi B* **182**(2), 273–278 (1994)
95. A. Zerr, G. Miehe, G. Serghiou, M. Schwarz, E. Kroke, R. Riedel, H. Fuess, P. Kroll, R. Boehler, Synthesis of cubic silicone nitride. *Nature* **400**(6742), 340–342 (1999)
96. D.M. Teter, R.J. Hemley, Low-compressibility carbon nitrides. *Science* **271**(5245), 53–55 (1996)
97. X.-F. Zhou, J. Sun, Y.-X. Fan, J. Chen, H.-T. Wang, X. Guo, J. He, Y. Tian, Most likely phase of superhard BC₂N by ab initio calculations. *Phys. Rev. B* **76**(10), 100101 (2007)
98. N.L. Ross, J. Shu, R.M. Hazen, High-pressure crystal chemistry of stishovite. *Am. Mineral.* **75**(7–8), 739–747 (1990)
99. S. Veprek, A.S. Argon, Towards the understanding of mechanical properties of super- and ultrahard nanocomposites. *J. Vac. Sci. Technol., B* **20**(2), 650–664 (2002)
100. X. Zhang, Y. Huang, Z. Ma, C.Q. Sun, Mpemba paradox revisited: numerical reinforcement. <http://www.arxiv.org/abs/1312.1014>
101. C.Q. Sun, S. Li, C.M. Li, Impact of bond order loss on surface and nanosolid mechanics. *J. Phys. Chem. B* **109**(1), 415–423 (2005)
102. M. Zhao, W.T. Zheng, J.C. Li, Z. Wen, M.X. Gu, C.Q. Sun, Atomistic origin, temperature dependence, and responsibilities of surface energetics: An extended broken-bond rule. *Phys. Rev. B* **75**(8), 085427 (2007)

103. Z.S. Ma, Z.F. Zhou, Y.L. Huang, Y.C. Zhou, C.Q. Sun, Mesoscopic superelasticity, superplasticity, and superrigidity. *Sci. China G: Phys. Mech. Astron.* **55**(6), 963–979 (2012)
104. M.A. Omar, *Elementary Solid State Physics: Principles and Applications* (Addison-Wesley, New York, 1993)
105. C.Q. Sun, Y. Wang, Y.G. Nie, B.R. Mehta, M. Khanuja, S.M. Shivaprasad, Y. Sun, J.S. Pan, L.K. Pan, Z. Sun, Interface charge polarization and quantum trapping in AgPd and CuPd bimetallic alloy catalysts. *PCCP* **12**, 3131–3135 (2010)
106. Y. Nie, Y. Wang, Y. Sun, J.S. Pan, B.R. Mehta, M. Khanuja, S.M. Shivaprasad, C.Q. Sun, CuPd interface charge and energy quantum entrapment: a tight-binding and XPS investigation. *Appl. Surf. Sci.* **257**(3), 727–730 (2010)
107. Y. Wang, Y.G. Nie, L.K. Pan, Z. Sun, C.Q. Sun, Potential barrier generation at the BeW interface blocking thermonuclear radiation. *Appl. Surf. Sci.* **257**(8), 3603–3606 (2011)
108. Y. Wang, Y.G. Nie, J.S. Pan, L.K. Pan, Z. Sun, L.L. Wang, C.Q. Sun, Orientation-resolved 3d(5/2) binding energy shift of Rh and Pd surfaces: anisotropy of the skin-depth lattice strain and quantum trapping. *PCCP* **12**(9), 2177–2182 (2010)
109. Z.S. Ma, Y. Wang, Y.L. Huang, Z.F. Zhou, Y.C. Zhou, W.T. Zheng, C.Q. Sun, XPS quantification of the hetero-junction interface energy. *Appl. Surf. Sci.* **265**, 71–77 (2013)
110. Y. Wang, Y.G. Nie, J.S. Pan, L.K. Pan, Z. Sun, C.Q. Sun, Layer and orientation resolved bond relaxation and quantum entrapment of charge and energy at Be surfaces. *PCCP* **12**(39), 12753–12759 (2010)
111. Y.G. Nie, X. Zhang, S.Z. Ma, Y. Wang, J.S. Pan, C.Q. Sun, XPS revelation of tungsten edges as a potential donor-type catalyst. *PCCP* **13**(27), 12640–12645 (2011)
112. H.J. Bian, X.F. Chen, J.S. Pan, W. Zhu, C.Q. Sun, Effects of sputtering pressure on the field emission properties of N-doped SrTiO₃ thin films coated on Si tip arrays. *Appl. Surf. Sci.* **255**(9), 4867–4872 (2009)
113. Y. Sun, Y. Wang, J.S. Pan, L.L. Wang, C.Q. Sun, Elucidating the 4f Binding Energy of an Isolated Pt Atom and Its Bulk Shift from the Measured Surface- and Size-Induced Pt 4f Core Level Shift. *J. Chem. Phys. C* **113**(33), 14696–14701 (2009)
114. C. Kittel, *Introduction to Solid State Physics*, 8th edn. (Wiley, New York, 2005)
115. Y. Wang, G. Ouyang, L.L. Wang, L.M. Tang, D.S. Tang, C.Q. Sun, Size- and composition-induced band-gap change of nanostructured compound of II-VI semiconductors. *Chem. Phys. Lett.* **463**(4–6), 383–386 (2008)
116. Y.F. Zhu, X.Y. Lang, Q. Jiang, The effect of alloying on the bandgap energy of nanoscaled semiconductor alloys. *Adv. Funct. Mater.* **18**(9), 1422–1429 (2008)
117. L. Vegard, H. Schjelderup, The constitution of mixed crystals. *Phys. Z.* **18**, 93–96 (1917)

Chapter 31

Concluding Remarks

- *Broken-bond-induced local strain and the associated quantum entrapment and non-bonding electron polarization dictate skin and defect mechanics.*
- *The LBA could be an effective way of complementing the continuum and the quantum approaches in atomistic understanding of the solid mechanics at the atomic scale with involvement of pressure and temperature as the key elements.*
- *New approaches result in quantitative information about the cohesive energy and the bonding identities of specimens varying from atomic chains, graphene, nanowires, grains, cavities, and the interfaces.*
- *Interface bond nature alteration and the associated entrapment or polarization dictates the mechanical behavior of alloys, compounds, and interfaces.*
- *Competition between the atomic cohesive energy and the energy density dictates the deformation intrinsically, and the competition between the activation and the prohibition of atomic glide dislocations determines the plastic deformation and yield strength extrinsically.*

31.1 Attainment

A set of analytical expressions has been developed from the perspective of LBA for the elasticity, extensibility, and mechanical strength of low-dimensional systems in terms of bond order, bond length, bond strength, and their response to the coordination environment, temperature, and stress field. The effect of a broken bond on the identities of the remaining bonds between the undercoordinated atoms dominates the mechanical performance and thermal stability of the mesoscopic systems. The presented approaches connect the macroscopic properties to the atomistic factors by developing the functional dependence of the measurable quantities on the bonding identities and the response of the bonding identities to external stimulus, which complement the classical theories of continuum medium mechanics and statistic thermodynamics that have demonstrated the limitation to mesoscopic systems. The developed approaches also provide predictive

observation from the perspective of bond formation, dissociation, relaxation, and vibration.

The following facts have been taken into consideration as physical constraints in developing the atomistic solutions:

1. For a given specimen, the nature and the total number of bonds do not change under external stimulus unless phase transition occurs, whereas the length and strength of all the bonds involved, or their representative, will response to the stimulus. This fact enables one to implementing the LBA approach to focus on the behavior of the representative bond for the mechanical behavior of the entire specimen.
2. The mechanical strength and elastic modulus of a substance are proportional to the sum of binding energy per unit volume. Atomic cohesive energy determines the thermal stability. Mechanical strength of a substance couples with its thermal stability closely.
3. Heating lengthens and weakens the bond through the increase in internal energy in Debye approximation. Therefore, the joint effect of bond breaking and the associated local strain and quantum entrapment as well as the bond vibrating under thermal stimulus represented by the T-BOLS correlation is of key importance to the mesoscopic mechanics.
4. Compression shortens and strengthens the bond and hence increases the mechanical strength of a specimen. Bond stretching and compressing will release energy that heat up the specimen to a certain extent.
5. The molten phase is extremely soft and highly extensible, following Born's criterion, yet the intrinsic elastic modulus remains nonzero at T_m or above because of the detectable sound velocity in liquid and gaseous phases.

The LBA and the TP-BOLS approach result in the following progresses and understandings:

1. Concepts of the energy density gain in the surface/interface skin and the residual cohesive energy for the undercoordinated surface atoms are essential and more effective to describe the behavior of atoms and processes occurring at a surface and an interface. The deepened potential well at sites of the undercoordinated atoms provides a mechanism for the defect pinning as observed in mechanical deformation tests because of the locally densified and lowered energy states though the broken bonds provide sites initiating structure failure.
2. A solid skin is harder and more elastic at temperatures far below the T_m , but the skin melts more easily compared to the bulk interior. The elastic sheet of a liquid surface skin tends to solidify more easily than the liquid interior, which may provide a mechanism for liquid drop and bubble formation.
3. The HPR-IHPR transition arises from the intrinsic competition between the atomic residual cohesive energy of the undercoordinated atoms and energy density gain near the grain boundaries and the extrinsic competition between the activation and prohibition of atomic dislocation motion. The undercoordinated atoms in the skin dominate such transition, yet atoms in the grain interior

retain their bulk nature. For thin film samples, the hardness shows no IHPR, and the hardness and elastic modulus correlate linearly. Therefore, the HPR and IHPR effects in nanograins are activated by the extrinsic competition between dislocation activation and dislocation inhibition in detection.

4. The mechanical strengthening and thermal weakening induced by vacancies, cavities, and pores arise from the increased proportion of the undercoordinated atoms at the negatively curved surfaces, which is naturally the same as those atoms at the flat surfaces or the positively curved surfaces of nanograins. Metallic foams should be stiffer with smaller pore sizes and lower porosities, whereas it would be tougher but thermally less stable with higher porosities and larger pores, being similar to the IHPR effect.
5. Interfacial bond contraction and the associated bond strengthening, and the bond nature alteration upon alloy and compound formation at the junction interfaces are responsible for the hardening and overheating of twin grains interfaces, and nanocomposites.
6. The Debye temperature, θ_D , depends on $(T_m - T)^{1/2}/d$. The specific heat capacity generally decreases when the solid size is reduced. The reduction in the specific heat capacity is more pronounced for larger m values at lower temperatures.

Reproduction of experimental observations reveals the following:

1. Surface relaxation and reconstruction of an elemental solid arise from the effect of bond breaking, which originates the surface energetics. The surface stress results from the surface strain rather than the otherwise, as one often believes. The surface and size induced hardening arises from bond breaking and the associated nearby strain and quantum entrapment and the thermally induced mechanical softening results from bond expanding and vibrating upon being heated.
2. The adsorbate-induced surface stress arises from charge repopulation and polarization upon adsorbate bond making, which is very complicated and varies from situation to situation. Knowing the bonding kinetics and dynamics is crucial to understanding the adsorbate-induced surface stress and the process of reconstruction.
3. The equilibrium bond length, strength, thermal stability, and the strain limit of monatomic chains can be quantified without needing involvement of charge or atomic mediation. Without external stimuli, the metallic bond in a MC contracts by $\sim 30\%$, associated with $\sim 43\%$ magnitude rise of the bond energy compared with the bulk standard cases. A metallic MC melts at 0.24-fold of the bulk T_m . The strain limit of a bond in a metallic MC under tension does not vary apparently with mechanical stress or strain rate, but apparently does with temperature difference $T_{mi} - T$. It is anticipated that extendable MCs of other elements could be made at an appropriate range of temperatures of operation.
4. The developed approach has allowed for determination of the actual values of the Young's modulus and the wall (C-C bond) thickness to advance a

consistent understanding of the mechanical strength and the chemical and thermal stability of CNTs. The C–C bond in the SWCNT contracts by $\sim 18.5\%$ with an energy rise by $\sim 68\%$. The effective thickness of the C–C bond is ~ 0.142 nm, which is the diameter of an isolated C atom. The melting point of the tube wall is slightly (~ 12 K) higher than that of the open edge of the tube end. The documented values of the tip-end T_m and the product of Yt essentially represent the true situations of a SWCNT in which the Young's modulus is 2.5 times and the T_m is 0.42 times that of bulk graphite. Predictions of the wall thickness dependence agree well with the insofar-observed trends in T_m suppression and Y enhancement of the multi-walled hollow tubes and nanowires. It is anticipated that at temperature far below the surface T_m , a nanosolid should be fragile with lower extensibility, whereas when T approaches the surface T_m or higher, the nanosolid should be ductile.

5. The Young's modulus of a nanosolid may be depressed, increased, or remain unchanged when the solid size is decreased, depending on the nature of the bond involved, temperature of operation, surface passivation, and experimental techniques. This understanding clarifies why the Y values for some materials are elevated and why those of others are not upon size reduction. It is not surprising to observe the elastic modulus change in different trends of different materials measured under different conditions, or even one material measured under different conditions.
6. Reproduction of the temperature dependence of surface tension, Young's modulus and Raman shift has led to quantitative information regarding the mean bond energy of a specimen in the bulk at 0 K though the accuracy is subject to the involvement of artifacts in measurement.
7. Mechanism for the superplasticity of nanograins becomes clear. The bond unfolding and atomic sliding dislocations of the undercoordinated atoms at grain boundaries dominate the superplasticity, as the detectable maximal bond strain at a temperature close to the melting point is limited to within 140%. On the other hand, the self-heating during bond unfolding and breaking should raise the actual temperature of the small samples, which softens the substance. A metallic nanosolid at $T \ll T_m$ is in quasi-molten state as the critical temperature for the solid-to-quasi-molten transition is much lower than the temperature of melting.
8. The undercoordinated atoms in the negatively curved surfaces of atomic vacancies, point defects, nanocavities, and the syntactic foams are responsible for the strain hardening and thermal instability of the negatively curved systems, being the same by nature to the atoms at the positively curved and flat surfaces. The shorter and stronger bonds near the pores act as pinning centers inhibiting motion of atomic dislocations because of the strain and the quantum trapping; the pores provide however sites for initiating structure failure under plastic deformation.
9. The IHPR originates intrinsically from the competition between the bond order loss and the associated bond strength gain of atoms in the GBs. The IHPR is

activated by the contacting measurement. As the solid size shrinks, a transition from dominance of energy density gain to dominance of cohesive energy loss occurs at the IHPR critical size because of the increased fraction of lower coordinated atoms. During the transition, both bond order loss and bond strength gain contribute competitively.

10. The IHPR critical size is predictable. The critical size is dominated intrinsically by bond nature, the T/T_m ratio, and extrinsically by experimental conditions or other factors such as size distribution and impurities. The IHPR at larger solid size converges to the normal HPR that maintains its conventional meaning of the accumulation of atomic dislocations that resist further atomic displacements in plastic deformation. The slope in the traditional HPR is proportional to $\exp(T_m/T)$, which represents the relationship between the hardness and the activation energy for atomic dislocations.

31.2 Limitations

One may wonder that there is often competition between various factors for a specific phenomenon to occur. However, the broken bond affects almost all the intrinsic aspects of concern, and therefore, the atomic CN imperfection should dominate the performance of a nanosolid through the competing factors. In the nanoindentation test, errors may arise because of the shapes and sizes of the indentation tips, such as in the cases described in Ref. [1]. In practice, the stress-strain profiles of a nanosolid are not symmetrical when comparing the situation under tension to the situation under compression. The flow stress is dependent of the strain rate, loading mode and time, and materials compactness, self-heating, as well as particle size distribution. Fortunately, the effect of tip shape and loading mode never affects the origin and the hardness peaking at the surface in detection. By taking the relative change of the measured quantity into account, the present approach of seeking for the change relative to the bulk values can minimize contributions from such artefacts. On the other hand, the extrinsic factors could be modeled by changing the pre-factor in the IHPR modeling procedure. The relative change of intensity, the peak position, and the trend of change could reflect the intrinsic physical characteristics.

Furthermore, the thermal energy released from bond breaking and bond unfolding should raise the actual temperature of the system. The fluctuation in grain size distribution and surface passivation also affects the actual melting point of the individual atoms at boundaries of grains of different sizes. These factors make the measurements deviate from the predicted results. Nevertheless, one could not expect to cover fluctuations due to mechanical (strain rate, stress direction, loading mode and time, etc.), thermal (self-heating during process), crystal structure orientation, impurity density, or grain size distribution effects in a

theoretical model, as these fluctuations are extrinsic, ad hoc, and hardly controllable [2, 3].

In dealing with the effect of temperature, the Debye specific heat for constant volume may not be accurate. In fact, most of the measurements were conducted under constant pressure. The specific heat for constant pressure should be preferable. However, for solid state, the ratio of $(C_p - C_v)/C_p$ is 3 % or less [4]. Therefore, assuming the specific heat to follow the Debye approximation is reasonably acceptable.

The internal stress signature of nano- and microstructures plays a critical role in determining the appropriate rate-limiting process. When dislocations mediate the plasticity, the defect structure (over many length scales) through the internal stress plays a critical role in determining the final macroscopic plasticity. The strength of a material is therefore a function of many temporal and spatial length scales. Plastic deformation follows the rule of the atomic movements of a long scale for strain accumulation, accompanied with the atomic interaction among many atoms. On the other hand, in non-crystalline regions, the local stress at an atomic site arises from all the bonds that the atom is involved. However, the average of local bonds over the measured size could represent the measurement collecting statistic information from the given volume. The disordered structures or system with large amount of defects will result in the deviation of the derived bond energy from the true value in ideal case. The long-range interaction can be folded into the representative bonds, which has proven effective.

For compounds, different kinds of bonds are involved and each kind of bond is suitably described using one kind of interatomic potential, the description using a representative bond herewith seems inappropriate. However, the average of the local bond is substantially the same as the approach used in the DFT or MD calculations solving the Schrödinger equation or the Newton motion of equations with the average interatomic potential as a key factor. The long-range atomic dislocation and the effect of pressure-induced strengthening would be the focus for future study. Nevertheless, one should focus more on the nature and trend of the unusual behavior in mechanics, as accurate detection of the absolute values remains problematic.

As the LBA approach and the T-BOLS correlation deals with only the joint effects of pressure, temperature, and bond order imperfection, none of the particularities of the elements, crystal or phase structures, or the exact form of pair potential is involved. What one needs to consider are the nature of the bond and the equilibrium atomic distance with and without external stimulus, which could be one of the advantages of the reported approach. It is impractical for one theory to model all the factors simultaneously in particular those extrinsic, kinetic, and random factors that contribute little to the nature.

31.3 Prospects

Further extension of the LBA approach and the T-BOLS premise should stimulate new ways of thinking and activities about the under- and hetero-coordinated systems from the perspective of a bond breaking and remaking that seems not to contribute directly to the physical properties of the systems. Consistent understanding and consistency in the numerical match are expected to give evidence of the validity of the approaches that may represent the true situation of the under-coordinated systems. More attention is going to be paid to the following continuing challenges:

1. Miniaturization of dimensionality not only allows us to tune the physical properties of a solid but also provides us with opportunity to elucidate information including the energy levels of an isolated atom, the vibration frequency of an isolated dimer, and the specific heat per bond, as well as discriminating the contribution of bond order loss from the effect of chemical passivation to the detectable quantities. Further exploitation in these areas may provide profound information that is beyond the scope of conventional approaches.
2. Extension of the LBA and T-BOLS correlation to domains such as external electric field could lead to new knowledge that would be even more fascinating and useful. For instance, the bending strength of PZT-841 ceramics was measured to decrease by 25 % when the temperature was increased from 300 K to the Curie point T_c (543 K) with a valley at temperatures around 498 K. A positive or negative electric field larger than 3 kV/cm reduces the bending strength of the specimen significantly [5], indicating a combined effect of Joule heat and electric field. Under an applied electric field, the transverse and axial Young's moduli of a nanowire are different from those of a nanowire in the absence of the field [6]. The effect of the electric field on Young's modulus is related to the intensity of the field, the size of the wire, and the direction of the wire. The mesoscopic systems also show unusual performance under an external stress field in terms of the critical temperature for phase transition, spectroscopic features of lattice vibration, and photoluminescence.
3. Transport dynamics in thermal and electrical conductivity play an important role in the performance of nanostructured devices. Introduction of the quantum trapping near the defects would be a topic that leads to new knowledge and in addition to the known mechanism of surface scattering, the surface/interface quantum trapping may play a dominant role in determining the intrinsic transport dynamics of nanometer-sized electronic and photonic devices. Employing the BOLS-induced barrier and trap in the crystal potential for a nanosolid and for an assembly of nanosolids could improve the understanding on the kinetic and dynamic performance of a nanosolid under external stimuli.
4. The effect of bond order loss may correlate the nanostructures and amorphous states in their physical behavior. The bond order loss occurs orderly at the skins of nanostructures, yet it presents randomly in the bulk amorphous. One can imagine that for a solid contains n different elements, there will be a

combination of $(n, 2) = n!/((n-2)!2!) = n(n-1)/2$ pairing potentials. The convolution of these potential may be responsible for the disorder effect. Exploration of the similarities and differences between the nanostructured and the amorphous state from the perspective of the joint hetero- and undercoordination effect would be rewarding.

5. The new degree of the freedom of size, and its combination with temperature, pressure, chemical, and other factors could amplify the parameter space for functional materials design. For example, a comparative study of thermomechanical properties of nanopolycrystalline nickel (nano-Ni) and micrometer-polycrystalline nickel (micron-Ni) by in situ high-pressure-temperature (P - T) diffraction experiments [7] revealed that the yield strength of 2.35 GPa for the nano-Ni measured under high-pressure triaxial compression is more than three times that of the micron-Ni. The nano-Ni in high-pressure plastic deformation stage demonstrates significant work hardening, whereas the micron-Ni experiences minor high-pressure work-softening and considerable energy dissipation into heat. The significantly reduced energy dissipation for the nano-Ni during the loading-unloading cycle indicates that the nanostructured materials can endure much greater mechanical fatigue in cyclic loadings. The nano-Ni exhibits steady grain growth during bulk plastic deformation at high-pressure loading, and drastic stress reduction and grain growth occur during the high P - T cycle.
6. It is interesting as noted in a nonlinear constitutive modeling [8] and first-principle calculation [9] that in the indentation test the pressure enhancement of both elastic modulus and yield strength is significant. A comparison with classical linear elasticity, which uses constant, zero-pressure, values of the modulus, and constant yield strength, shows that the enhancement of the elastic modulus and of the yield strength due to extreme high pressures that develop in material under the indenter has a significant effect in hard and superhard materials. This enhancement has to be accounted for if accurate modeling of the mechanical response of such materials with extreme properties is to be achieved. The pressure effect on the elasticity enhancement could be described by the extension of the BOLS to pressure domain that causes bond deformation associated with storage of the deformation energy.
7. Incorporating the BOLS correlation, pressure and temperature dependence to the established computation methodologies could not only refine the parameters used in practice, but also expand the capability of computation tools to reveal true situation and minimize the gap between measurement and calculation.
8. Harnessing the local bond and electrons at sites surrounding edges, defects, impurities, and interfaces and making them of use in designing new functional devices would also be very interesting. Integrating the broken bonds and the non-bonding states and the associated approaches developed would amplify the surface and interface sciences tremendously.

These topics would form challenging branches of further study toward profound knowledge and practical applications. The progresses may evidence the validity of

the LBA approach and the BOLS correlation, which has enabled us to touch the skin of the vast field of low-dimensional physics and chemistry.

References

1. R.A. Mirshams, P. Parakala, Nanoindentation of nanocrystalline Ni with geometrically different indenters. *Mater. Sci. Eng. Struct. Mater. Prop. Microstruct. Process.* **372**(1–2), 252–260 (2004)
2. D.M. Dimiduk, C. Woodward, R. LeSar, M.D. Uchic, Scale-free intermittent flow in crystal plasticity. *Science* **312**(5777), 1188–1190 (2006)
3. S. Ogata, J. Li, S. Yip, Ideal pure shear strength of aluminum and copper. *Science* **298**(5594), 807–811 (2002)
4. M.J. Sinnott (ed.), *The Solid State for Engineers* (Wiley, New York, 1963)
5. R. Fu, T.Y. Zhang, Influences of temperature and electric field on the bending strength of lead zirconate titanate ceramics. *Acta Mater.* **48**(8), 1729–1740 (2000)
6. X.J. Zheng, L.L. Zhu, Theoretical analysis of electric field effect on Young's modulus of nanowires. *Appl. Phys. Lett.* **89**(15), 153110 (2006)
7. Y.S. Zhao, J.Z. Zhang, B. Clausen, T.D. Shen, G.T. Gray, L.P. Wang, Thermomechanics of nanocrystalline nickel under high pressure-temperature conditions. *Nano Lett.* **7**(2), 426–432 (2007)
8. R.G. Veprek, D.M. Parks, A.S. Argon, S. Veprek, Non-linear finite element constitutive modeling of mechanical properties of hard and superhard materials studied by indentation. *Mater. Sci. Eng. Struct. Mater. Prop. Microstruct. Process.* **422**(1–2), 205–217 (2006)
9. W.M. Mook, J.D. Nowak, C.R. Perrey, C.B. Carter, R. Mukherjee, S.L. Girshick, P.H. McMurry, W.W. Gerberich, Compressive stress effects on nanoparticle modulus and fracture. *Phys. Rev. B* **75**(21), 214112 (2007)

Part III

Atomistic Solid Mechanics

A.1 Highlights

- Atomic chains, defects, skins, hollow tubes, nanocavities, foams, nanograins, and nanostructures share the same attributes of atomic undercoordination and its consequences.
- Impurities, interfaces, twin grains, alloys, compounds, and composites share the same nature of atomic hetero-coordination and its consequences.
- Binding energy density determines the mechanical strength and elasticity and the atomic cohesive energy determines the thermal stability of a substance.
- Intrinsic competition between the cohesive energy and energy density originates and the extrinsic competition between activation and accumulation of atomic dislocation activates the IHPR.
- Solid skin dictates the multifield coupling at the nanometer scale, creating mechanical and thermal fascinations.
- Elastic modulus correlates to the Raman shift by $[\omega^2] \propto [Yd]$. Reproduction of temperature dependence turns out the atomic cohesive energy, Debye temperature, reproduction of pressure dependence results in the energy density and compressibility.
- ZPS provides an efficient means to determine the interface energetics (bond length, energy, energy density, atomic cohesive energy) of conducting or semiconducting specimens.

Part IV

Water Myths

Abstract Hydrogen bonds form a pair of asymmetric, coupled, H-bridged oscillators with ultra short-range interactions, whose asymmetric relaxation and the associated binding electron entrapment and nonbonding electron polarization discriminate water and ice from other usual materials in the structure order and the physical anomalies.

Part IV deals with the geometric structure, local potential, and physical anomalies demonstrated by water ice upon being cooled, compressed, and reduced number of neighbors. A “master-slave segmented H-bond” forms a pair of asymmetric, coupled oscillators whose asymmetric relaxation in length and energy and the associated binding electron entrapment and nonbonding electron polarization dictate the unusual performance of water ice. This O:H–O bond notation allows specification of the short-range interactions and forces driving its asymmetric and cooperative relaxation. It has been revealed that: (i) Compression shortens-and-stiffens the softer “O:H” bond and lengthens-and-softens the stiffer “H–O” covalent bond via the inter electron-pair repulsion, yielding the low compressibility, O:H and H–O length symmetry, phase-transition temperature (T_c) depression, softer phonon ($< 300 \text{ cm}^{-1}$) stiffening and stiffer phonon ($> 3000 \text{ cm}^{-1}$) softening; (ii) Molecular-undercoordination effects oppositely to compression due to the spontaneous contraction of the H–O covalent bond. This process results in a supersolid phase that undergoes molecular volume expansion, melting point (viscosity) elevation, binding energy entrapment, bonding charge densification, nonbonding lone electron polarization, stiffer phonon stiffening, and softer phonon softening. The supersolidity of molecule clusters, surface skins, and ultrathin films of water makes them perform like ice and hydrophobic at the ambient temperature; (iii) The disparity of the segmental specific heat discriminates the O:H from H–O in responding to cooling, which shortens alternatively the segments in liquid, liquid–solid transition, solid, and at $T < 80 \text{ K}$, resulting in density and phonon-stiffness oscillation. The basic rule of sp^3 -orbital hybridization of oxygen, detectable density, and the segmental length cooperativity have enabled solution to the discrepancies on

the size, separation, structural order, and mass density of molecules packing in water and ice. Reconciling observations of O:H and H-O length symmetry under compression, O-O separation change at a surface and at cooling, solution clarifies: (i) the preference of the fluctuated tetragonal structure of water, (ii) the essence of interelectron-pair repulsion, and (iii) the presence of the supersolid phase at regions consisting molecules with fewer than four neighbors. A combination of the Lagrangian mechanics of oscillator's vibration, molecular dynamics decomposition of volume evolution, and Raman spectroscopy of phonon relaxation has enabled probing of the asymmetric, local, short-range potentials pertaining to the H-bond. Numerical solution to the Fourier equation for the fluid thermodynamics with the skin supersolidity clarified the Mpemba paradox that arises intrinsically from O:H-O bond relaxation and happens only in the non-adiabatic ambient. O:H-O bond relaxation not only determines the manner of heat emission but also heat conduction. Heat emission proceeds at a rate depending on the initial energy storage and the skin supersolidity creates the gradients of density, specific heat, and thermal conductivity.

Chapter 32

Introduction

- *Most abundant, least known, water and ice are too strange, too anomalous, and too challenge.*
- *As the origin and part of all lives, water and ice has attracted much attention because of its anomalies pertaining to issues from galaxy to geology, astrophysics, biology, climate, and to our daily lives.*
- *Correlation, clarification, formulation, and quantification of all properties using one model could be possible if the systems are properly sampled.*
- *Cooperative relaxation of the H-bond (O:H-O) in the angle, length, and energy and the associated core electron entrapment and nonbonding electron polarization could be the starting point.*
- *It would be more reliably revealing to focus on the statistic mean of all the cooperative parameters simultaneously than on the instantaneous accuracy of any single parameter at a time for the strongly correlated and fluctuating system.*

32.1 Scope

This part starts with a brief overview in this section on the significance and current understandings of the structure and anomalies of water ice, which drives the efforts based on knowledge and approach described in previous parts of this book. [Chapter 33](#) discusses the basic rules that govern the performance of the H-bond (O:H-O, H-bond) and the structure order of water ice. The short-range interactions and the involvement of Coulomb repulsion between electron pairs on adjacent oxygen atoms form the key to discriminating water and ice from other usual materials in performance. The disparity of the two segments within the H-bond, O:H and H-O makes the H-bond a pair of asymmetric, coupled oscillators whose relaxation in length and energy dictate the property change in water and ice. An extension of the Ice Rule [1] results in the statistically expected water structure that correlates the mass density to O-O distance. [Chapter 34](#) is focused on the

anomalies of compressed ice. The described H-bond reconciled the anomalies of proton symmetrization, phase transition temperature depression, low compressibility, and bandgap expansion demonstrated by ice under compression. [Chapter 35](#) deals with the anomalies demonstrated by molecules with fewer than four neighbors presented in the clusters, hydration shells, skins, and ultrathin films. Supersolid phase forms at these places, which is elastic, polarized, thermally stable, hydrophobic, and ice like. [Chapter 36](#) deals with the oscillation of mass density and phonon stiffness of water ice over the full temperature range. Specific heat disparity between the O:H and the H–O bond forms the origin yet the cooling contraction, and Coulomb repulsion provides the force driving the oscillations. [Chapter 37](#) describes the approaches and outcome of mapping the asymmetric local potentials of the H-bond. Lagrangian mechanics could be insofar the most efficient way that turns out the segmental force constant, bidding energy at each quasi-equilibrium state with the measured segmental lengths and phonon frequencies as input. [Chapter 38](#) determines the size, separation, structure order, and mass density of molecules packing in water ice. Water and ice prefer the fluctuated, tetrahedrally coordinated structure with supersolidity at edges despite fluctuations in the O:H length and the O:H–O angles. No frustration of the proton between two oxygen atoms happens. [Chapter 39](#) discusses the coupling effect of cluster size, pressure, and temperature on the phonon stiffness and O 1s binding energy, which further evidence the consistency of the proposed H-bond notations. The skin supersolidity slipperizes ice and enhances the surface tension of water. The main body of this work ends with a solution to the Mpemba paradox that involves almost all the knowledge described. The solution evidences that the hydrogen bond has memory effect to emit energy at a rate depending on the initial storage. The skin supersolidity creating gradient of thermal diffusion ensures eddy current flowing outwardly of the liquid. [Chapter 40](#) addresses some open questions on anomalies associated with salinity, sugar, and heating effect on the phonon stiffness. Perspectives are also presented on the Hofmeister series, dielectric relaxation of water and ice, electro-, magneto-, mechano-stimulated freezing, and water–protein and water–cancer tissue interactions. [Chapter 41](#) features the understandings. Furnished with current understating, further efforts on unveiling the anomalies of water ice and their functionality in other areas would be even more fascinating, promising, and rewarding.

32.2 Overview

32.2.1 Significance

Water is the source and the important part of all lives. Life can only evolve or continue with the presence of liquid water. As the key component of water and other biomolecules, H-bonds are ubiquitous—and universally important. They

give water its unique properties, speed or slow reactions, and hold together the three-dimensional shapes of DNA, proteins, and other supramolecular structures [2–4]. Given its paramount importance in nature [5–15] and geochemical sciences [16, 17] and its role in DNA and protein folding [2, 18–20], gene delivering [21–23], cell culturing [24], drug target binding [25], ion channel activating and deactivating [26], etc., H₂O, and the H-bond as well, has been extensively studied since the dawn of civilization with considerable advancement in recent decades. Active areas include the following: (1) crystal structure optimization, phase formation, and transition [27, 28]; (2) reaction dynamics with other ingredients [29, 30]; (3) H-bond weak interactions [31, 32]; (4) determination of binding energy [33–39]; and (5) characterization of phonon relaxation dynamics under various conditions [9, 30, 40–42].

Authoritative reviews have been documented in the literature on the understanding of water structures [43–45], phonon relaxation [17, 46], surface polarization [47], water clusters [48–51], water adsorption to metals or other inorganic surfaces [52–56], ion effects on water structure [57], water surface charging [58], ice surface melting [59], slippery and friction of ice [60], surface photoelectron emission [61, 62], and water under positive [63, 64] and negative pressure [48, 65], etc., from various perspectives. Techniques have been developed for water surface and interface studies such as the sum frequency generation (SFG) [47, 66], microjet photoelectron emission [67], glancing angle Raman spectroscopy [68, 69], etc. However, water ice is too strange, too anomalous, and too challenge [5, 70, 71]. Tremendous mysteries pertaining to the structure, local potentials, and the physical anomalies, as summarized in the respective sections, remain puzzling.

32.2.2 *Known Mechanisms*

Numerous models have been developed for the structure of water ice. The elegantly used models include the rigid and non-polarizable TIPnP (n varies from 1 to 5) series [45, 72] and the polarizable models [73]. In all TIPnQ models, for instance, the V-shaped gas-phase geometry is used for the water molecule, with a bond length of $r_{\text{OH}} = 0.9572 \text{ \AA}$ and a bond angle of $\theta_{\text{HOH}} = 104.52^\circ$.

H-bond potentials are often assumed symmetric, paired, and identical, which are located between the adjacent oxygen atoms. These pairing potentials make H proton to be ‘frustration’ in location [74]. Teixeira [75] suggested that as the oxygen atoms are forced together, the potential energy changes from a symmetric double to a single well, forcing the ‘fluctuated H proton’ [74] to be certain in the middle of two oxygen ions. Wernet et al. [76] proposed an asymmetric H-bonding model which Soper [77] investigated further by assuming different charges on the hydrogen ions in order to create an asymmetry and investigate whether that could be supported by diffraction data. Similar attempts have been carried out by Wikfeldt et al. [78] and Leetmaa et al. [79]. However, this assumption could not be

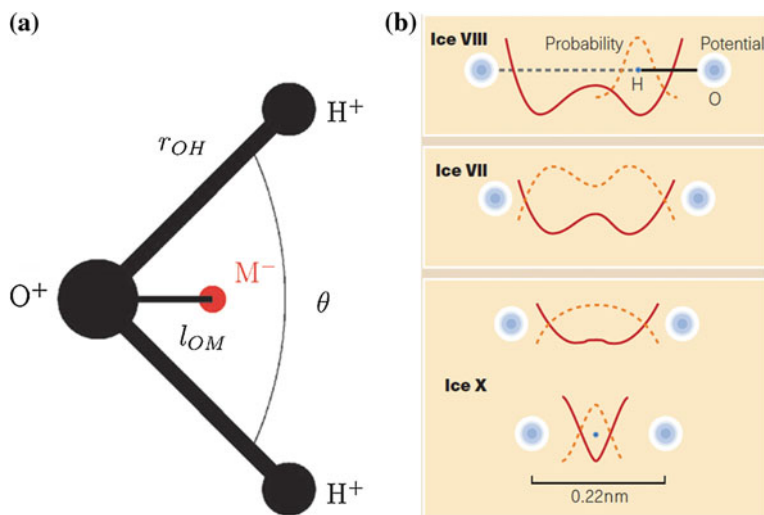


Fig. 32.1 **a** The rigid non-polarizable TIP4Q/2005 model has a positive point charge q_O on the oxygen, a positive point charge q_H on each hydrogen atom, and a negative point charge q_M on a site M located at a distance l_{OM} from the oxygen atom along the bisector of the $\angle HOH$ -bond angle. The molecule is electrically neutral; thus, $q_M = -(2q_H + q_O)$. q_H , q_O , l_{OM} , σ_{OO} , and ϵ_{OO} are independent parameters to be determined. σ_{OO} and ϵ_{OO} are the Leonard-Jones parameters for O–O interaction. (Reprint with permission from [80]). **b** The ‘double symmetric potential well’ model indicates that the H proton frustrates in the two identical sites between the adjacent oxygen atoms. Under compression, oxygen atoms are forced together, and the potential energy changes from a symmetric double to a single well, forcing the ‘fluctuated H proton’ to be certain in the middle of two oxygen ions [74] (Reprint with permission from [75])

certain at that point of time as X-ray/neutron diffraction and IR/Raman are neither direct nor sensitive to the interatomic potentials.

Figure 32.1 illustrates the models of TIP4Q/2005 structure [80] for water molecule and the symmetric local potentials for the H-bond. The success of the existing models is that they have contributed significantly to the crystal structural optimization and entropy calculations. More than 17 phases for water ice have been derived and experimentally confirmed insofar. The ‘double symmetric potential well’ model describes the H proton position between the adjacent oxygen atoms [74]. Oxygen atoms are forced together, and the potential energy changes from a symmetric double to a single well, forcing the ‘fluctuated H proton’ to be certain in the middle of two oxygen ions.

Microscopic imaging of the hydrogen bond in water is infrequent. However, Zhang et al. [81] could characterize hydrogen-bonding contacts formed between 8-hydroxyquinoline molecules adsorbed on the Cu(111) surface under cryogenic conditions using a decoration of atomic force microscope tips with terminal CO molecules.

32.3 Challenges and Objectives

Unlocking the structure order of water ice, the local potentials of H-bond, and the mysteries demonstrated by water ice remains as historical challenge. For instance, the rigid and non-polarizable models [80, 82, 83] exclude the essentiality of O:H–O bond angle and length relaxation and charge polarization. H-bond relaxation in length and energy and the associated bonding charge entrapment and non-bonding electron polarization drive the property change of a substance including water and ice [84]. The length, energy, and charge distribution of a substance must respond, without any exception, to the applied stimuli including cooling, compressing, clustering, and electric and magnetic fields, etc. Ultrashort-range interactions and the segmental disparity of the H-bond should dominate the property change. Modeling hypotheses and expectations, numerical calculations, and experimental measurements should be correlated and consistent in addressing the property change of the highly correlated and fluctuating system.

Examination of the *statistic* mean of the complete set of the correlated quantities with certain rules could be more realistic and meaningful than focusing on the *instantaneous* detail of an individual quantity at a point of time of the correlated and fluctuating system. This work will be focused on the correlation and the mechanism underneath the anomalies demonstrated by water ice under stimuli of compression, coordination reduction, and cooling excitation as well as determining the structure order and local potentials. An extension of the 3B and BOLS premises described in the previous parts to water and ice has led to a model of the master–slave-segmented O:H–O bond with identification of the ultrashort-range interactions and forces acting on each oxygen atom. A combination of DFT and MD calculations, Lagrangian mechanics, Raman and IR spectroscopy, XPS measurements has enabled clarification, correlation, formulation, and quantification of multiple puzzles demonstrated by water and ice and thus verified hypothesis and expectations of this practitioner.

References

1. J.D. Bernal, R.H. Fowler, A Theory of water and ionic solution, with particular reference to hydrogen and hydroxyl ions. *J. Chem. Phys.* **1**(8), 515–548 (1933)
2. G.H. Zuo, J. Hu, H.P. Fang, Effect of the ordered water on protein folding: an off-lattice Go\$\$(\$\$) over-bar-like model study. *Phys. Rev. E* **79**(3), 031925 (2009)
3. J.L. Kulp, D.L. Pompliano, F. Guarnieri, Diverse fragment clustering and water exclusion identify protein hot spots. *J. Am. Chem. Soc.* **133**(28), 10740–10743 (2011)
4. A. Twomey, R. Less, K. Kurata, H. Takamatsu, A. Aksan, In situ spectroscopic quantification of protein-ice interactions. *J. Phys. Chem. B* **117**(26), 7889–7897 (2013)
5. P. Ball, Water: water—an enduring mystery. *Nature* **452**(7185), 291–292 (2008)
6. I.V. Stiopkin, C. Weeraman, P.A. Pieniazek, F.Y. Shalhout, J.L. Skinner, A.V. Benderskii, Hydrogen bonding at the water surface revealed by isotopic dilution spectroscopy. *Nature* **474**(7350), 192–195 (2011)

7. D. Marx, M.E. Tuckerman, J. Hutter, M. Parrinello, The nature of the hydrated excess proton in water. *Nature* **397**(6720), 601–604 (1999)
8. Y. Yoshimura, S.T. Stewart, M. Somayazulu, H. Mao, R.J. Hemley, High-pressure X-ray diffraction and Raman spectroscopy of ice VIII. *J. Chem. Phys.* **124**(2), 024502 (2006)
9. D. Kang, J. Dai, Y. Hou, J. Yuan, Structure and vibrational spectra of small water clusters from first principles simulations. *J. Chem. Phys.* **133**(1), 014302 (2010)
10. J.W.M. Frenken, T.H. Oosterkamp, Microscopy when mica and water meet. *Nature* **464**(7285), 38–39 (2010)
11. J.M. Headrick, E.G. Diken, R.S. Walters, N.I. Hammer, R.A. Christie, J. Cui, E.M. Myshakin, M.A. Duncan, M.A. Johnson, K.D. Jordan, Spectral signatures of hydrated proton vibrations in water clusters. *Science* **308**(5729), 1765–1769 (2005)
12. J.K. Gregory, D.C. Clary, K. Liu, M.G. Brown, R.J. Saykally, The water dipole moment in water clusters. *Science* **275**(5301), 814–817 (1997)
13. N. Bjerrum, Structure and properties of ice. *Science* **115**(2989), 385–390 (1952)
14. A.K. Soper, J. Teixeira, T. Head-Gordon, Is ambient water inhomogeneous on the nanometer-length scale? *PNAS* **107**(12), E44 (2010)
15. C.S. Zha, R.J. Hemley, S.A. Gramsch, H.K. Mao, W.A. Bassett, Optical study of H₂O ice to 120 GPa: dielectric function, molecular polarizability, and equation of state. *J. Chem. Phys.* **126**(7), 074506 (2007)
16. R.J. Bakker, M. Baumgartner, Unexpected phase assemblages in inclusions with ternary H₂O-salt fluids at low temperatures. *Central European J. Geosci.* **4**(2), 225–237 (2012)
17. R.J. Bakker, Raman spectra of fluid and crystal mixtures in the systems H₂O, H₂O–NaCl and H₂O–MgCl₂ at low temperatures: applications to fluid-inclusion research. *Can. Mineral.* **42**, 1283–1314 (2004)
18. M. Smyth, J. Kohanoff, Excess electron localization in solvated DNA bases. *Phys. Rev. Lett.* **106**(23), 238108 (2011)
19. P. Baaske, S. Duhr, D. Braun, Melting curve analysis in a snapshot. *Appl. Phys. Lett.* **91**(13), 133901 (2007)
20. A. Kuffel, J. Zielkiewicz, Why the solvation water around proteins is more dense than bulk water. *J. Phys. Chem. B* **116**(40), 12113–12124 (2012)
21. C. Castellano, J. Generosi, A. Congiu, R. Cantelli, Glass transition temperature of water confined in lipid membranes as determined by anelastic spectroscopy. *Appl. Phys. Lett.* **89**(23), 233905 (2006)
22. J.H. Park, N.R. Aluru, Water film thickness-dependent conformation and diffusion of single-strand DNA on poly (ethylene glycol)-silane surface. *Appl. Phys. Lett.* **96**(12), 123703 (2010)
23. F. Garczarek, K. Gerwert, Functional waters in intraprotein proton transfer monitored by FTIR difference spectroscopy. *Nature* **439**(7072), 109–112 (2006)
24. P. Ball, Water as an active constituent in cell biology. *Chem. Rev.* **108**(1), 74–108 (2008)
25. Y.B. Shan, E.T. Kim, M.P. Eastwood, R.O. Dror, M.A. Seeliger, D.E. Shaw, How does a drug molecule find its target binding site? *J. Am. Chem. Soc.* **133**(24), 9181–9183 (2011)
26. J. Ostmeyer, S. Chakrapani, A.C. Pan, E. Perozo, B. Roux, Recovery from slow inactivation in K channels is controlled by water molecules. *Nature* **501**(7465), 121–124 (2013)
27. H.M. Lee, S.B. Suh, J.Y. Lee, P. Tarakeshwar, K.S. Kim, Structures, energies, vibrational spectra, and electronic properties of water monomer to decamer. *J. Chem. Phys.* **112**(22), 9759 (2000)
28. H.G. Lu, Y.K. Wang, Y.B. Wu, P. Yang, L.M. Li, S.D. Li, Hydrogen-bond network and local structure of liquid water: an atoms-in-molecules perspective. *J. Chem. Phys.* **129**(12), 124512 (2008)
29. C.K. Lin, C.C. Wu, Y.S. Wang, Y.T. Lee, H.C. Chang, J.L. Kuo, M.L. Klein, Vibrational predissociation spectra and hydrogen-bond topologies of H + (H₂O) (9–11). *PCCP* **7**(5), 938–944 (2005)
30. A. Lenz, L. Ojamae, A theoretical study of water equilibria: the cluster distribution versus temperature and pressure for (H₂O) (n), n = 1–60, and ice. *J. Chem. Phys.* **131**(13), 134302 (2009)

31. S.O.N. Lill, Application of dispersion-corrected density functional theory. *J. Phys. Chem. A* **113**(38), 10321–10326 (2009)
32. S.N. Steinmann, C. Corminboeuf, Comprehensive bench marking of a density-dependent dispersion correction. *J. Chem. Theo. Comput.* **7**(11), 3567–3577 (2011)
33. K. Kobayashi, M. Koshino, K. Suenaga, Atomically resolved images of I(h) ice single crystals in the solid phase. *Phys. Rev. Lett.* **106**(20), 206101 (2011)
34. A. Hermann, P. Schwerdtfeger, Blueshifting the onset of optical UV absorption for water under pressure. *Phys. Rev. Lett.* **106**(18), 187403 (2011)
35. W. Chen, X.F. Wu, R. Car, X-ray absorption signatures of the molecular environment in water and ice. *Phys. Rev. Lett.* **105**(1), 017802 (2010)
36. Y. Wang, H. Liu, J. Lv, L. Zhu, H. Wang, Y. Ma, High pressure partially ionic phase of water ice. *Nat. Commun.* **2**, 563 (2011)
37. M. Abu-Samaha, K.J. Borve, Surface relaxation in water clusters: evidence from theoretical analysis of the oxygen 1s photoelectron spectrum. *J. Chem. Phys.* **128**(15), 154710 (2008)
38. O. Bjornholm, F. Federmann, S. Kakar, T. Moller, Between vapor and ice: free water clusters studied by core level spectroscopy. *J. Chem. Phys.* **111**(2), 546–550 (1999)
39. G. Ohrwall, R.F. Fink, M. Tchapyguine, L. Ojamae, M. Lundwall, R.R.T. Marinho, A.N. de Brito, S.L. Sorensen, M. Gisselbrecht, R. Feifel, T. Rander, A. Lindblad, J. Schulz, L.J. Saethre, N. Martensson, S. Svensson, O. Bjornholm, The electronic structure of free water clusters probed by Auger electron spectroscopy. *J. Chem. Phys.* **123**(5), 054310 (2005)
40. S. Hirabayashi, K.M.T. Yamada, Infrared spectra and structure of water clusters trapped in argon and krypton matrices. *J. Mol. Struct.* **795**(1–3), 78–83 (2006)
41. P. Andersson, C. Steinbach, U. Buck, Vibrational spectroscopy of large water clusters of known size. *Eu. Phys. J. D.* **24**(1–3), 53–56 (2003)
42. S. Maheshwary, N. Patel, N. Sathyamurthy, A.D. Kulkarni, S.R. Gadre, Structure and Stability of Water Clusters (H₂O)_n, n) 8–20: An Ab Initio Investigation. *J. Phys. Chem. A* **105**, 10525–10537 (2001)
43. A. Nilsson, L.G.M. Pettersson, Perspective on the structure of liquid water. *Chem. Phys.* **389**(1–3), 1–34 (2011)
44. G.N.I. Clark, C.D. Cappa, J.D. Smith, R.J. Saykally, T. Head-Gordon, The structure of ambient water. *Mol. Phys.* **108**(11), 1415–1433 (2010)
45. C. Vega, J.L.F. Abascal, M.M. Conde, J.L. Aragones, What ice can teach us about water interactions: a critical comparison of the performance of different water models. *Faraday Discuss.* **141**, 251–276 (2009)
46. J.L. Skinner, P.A. Pieniazek, S.M. Gruenbaum, Vibrational Spectroscopy of water at interfaces. *Acc. Chem. Res.* **45**(1), 93–100 (2012)
47. Y.R. Shen, V. Ostroverkhov, Sum-frequency vibrational spectroscopy on water interfaces: polar orientation of water molecules at interfaces. *Chem. Rev.* **106**(4), 1140–1154 (2006)
48. R. Ludwig, The importance of tetrahedrally coordinated molecules for the explanation of liquid water properties. *Chem. Phys. Chem.* **8**(6), 938–943 (2007)
49. B. Santra, A. Michaelides, M. Fuchs, A. Tkatchenko, C. Filippi, M. Scheffler, On the accuracy of density-functional theory exchange-correlation functionals for H bonds in small water clusters. II. The water hexamer and Van der Waals interactions. *J. Chem. Phys.* **129**(19), 194111 (2008)
50. K. Liu, J.D. Cruzan, R.J. Saykally, Water clusters. *Science* **271**(5251), 929–933 (1996)
51. V. Buch, S. Bauerecker, J.P. Devlin, U. Buck, J.K. Kazimirski, Solid water clusters in the size range of tens-thousands of H₂O: a combined computational/spectroscopic outlook. *Int. Rev. Phys. Chem.* **23**(3), 375–433 (2004)
52. C.H. Sun, L.M. Liu, A. Selloni, G.Q. Lu, S.C. Smith, Titania-water interactions: a review of theoretical studies. *J. Mater. Chem.* **20**(46), 10319–10334 (2010)
53. M.A. Henderson, The interaction of water with solid surfaces: fundamental aspects revisited. *Surf. Sci. Rep.* **46**(1–8), 5–308 (2002)
54. A. Hodgson, S. Haq, Water adsorption and the wetting of metal surfaces. *Surf. Sci. Rep.* **64**(9), 381–451 (2009)

55. A. Verdaguier, G.M. Sacha, H. Bluhm, M. Salmeron, Molecular structure of water at interfaces: wetting at the nanometer scale. *Chem. Rev.* **106**(4), 1478–1510 (2006)
56. J. Carrasco, A. Hodgson, A. Michaelides, A molecular perspective of water at metal interfaces. *Nat. Mater.* **11**(8), 667–674 (2012)
57. Y. Marcus, Effect of Ions on the structure of water: structure making and breaking. *Chem. Rev.* **109**(3), 1346–1370 (2009)
58. M. Chaplin, Theory vs experiment: what is the surface charge of water?. *Water* 1(1–28) (2009)
59. Y. Li, G.A. Somorjai, Surface premelting of ice. *J. Chem. Phys. C* **111**(27), 9631–9637 (2007)
60. A.-M. Kietzig, S.G. Hatzikiriakos, P. Englezos, Physics of ice friction. *J. Appl. Phys.* **107**(8), 081101–081115 (2010)
61. M. Faubel, K.R. Siefermann, Y. Liu, B. Abel, Ultrafast soft X-ray photoelectron spectroscopy at liquid water microjets. *Acc. Chem. Res.* **45**(1), 120–130 (2011)
62. A. Morita, T. Ishiyama, Recent progress in theoretical analysis of vibrational sum frequency generation spectroscopy. *PCCP* **10**(38), 5801–5816 (2008)
63. S.K. Sikka, S.M. Sharma, The hydrogen bond under pressure. *Phase Trans.* **81**(10), 907–934 (2008)
64. P. Pruzan, J.C. Chervin, E. Wolanin, B. Canny, M. Gauthier, M. Hanfland, Phase diagram of ice in the VII–VIII–X domain. Vibrational and structural data for strongly compressed ice VIII. *J. Raman Spec.* **34**(7–8), 591–610 (2003)
65. K. Davitt, E. Rolley, F. Caupin, A. Arvengas, S. Balibar, Equation of state of water under negative pressure. *J. Chem. Phys.* **133**(17), 174507 (2010)
66. Y.R. Shen, Basic theory of surface sum-frequency generation. *J. Phys. Chem. C* **116**, 15505–15509 (2012)
67. K.R. Wilson, B.S. Rude, T. Catalano, R.D. Schaller, J.G. Tobin, D.T. Co, R.J. Saykally, X-ray spectroscopy of liquid water microjets. *J. Phys. Chem. B* **105**(17), 3346–3349 (2001)
68. S.N. Wren, D.J. Donaldson, Glancing-angle Raman spectroscopic probe for reaction kinetics at water surfaces. *Phys. Chem. Chem. Phys.* **12**(11), 2648–2654 (2010)
69. T.F. Kahan, J.P. Reid, D.J. Donaldson, Spectroscopic probes of the quasi-liquid layer on ice. *J. Phys. Chem. A* **111**(43), 11006–11012 (2007)
70. M. Chaplin, Water structure and science (2011). <http://www.lsbu.ac.uk/water/>
71. So Much More to Know ... *Science*, **309**(5731), 78–102 (2005)
72. V. Molinero, E.B. Moore, Water modeled as an intermediate element between carbon and silicon. *J. Phys. Chem. B* **113**(13), 4008–4016 (2009)
73. P.T. Kiss, A. Baranyai, Density maximum and polarizable models of water. *J. Chem. Phys.* **137**(8), 084506–084508 (2012)
74. L. Pauling, The structure and entropy of ice and of other crystals with some randomness of atomic arrangement. *J. Am. Chem. Soc.* **57**, 2680–2684 (1935)
75. J. Teixeira, High-pressure physics—the double identity of ice X. *Nature* **392**(6673), 232–233 (1998)
76. P. Wernet, D. Nordlund, U. Bergmann, M. Cavalleri, M. Odelius, H. Ogasawara, L.A. Naslund, T.K. Hirsch, L. Ojamae, P. Glatzel, L.G.M. Pettersson, A. Nilsson, The structure of the first coordination shell in liquid water. *Science* **304**(5673), 995–999 (2004)
77. A.K. Soper, An asymmetric model for water structure. *J. Phys. Condens. Matter* **17**(45), S3273–S3282 (2005)
78. K.T. Wikfeldt, M. Leetmaa, M.P. Ljungberg, A. Nilsson, L.G.M. Pettersson, On the range of water structure models compatible with X-ray and neutron diffraction data. *J. Phys. Chem. B* **113**(18), 6246–6255 (2009)
79. M. Leetmaa, K.T. Wikfeldt, M.P. Ljungberg, M. Odelius, J. Swenson, A. Nilsson, L.G.M. Pettersson, Diffraction and IR/Raman data do not prove tetrahedral water. *J. Chem. Phys.* **129**(8), 084502 (2008)

80. J. Alejandre, G.A. Chapela, H. Saint-Martin, N. Mendoza, A non-polarizable model of water that yields the dielectric constant and the density anomalies of the liquid: TIP4Q. *PCCP* **13**, 19728–19740 (2011)
81. J. Zhang, P. Chen, B. Yuan, W. Ji, Z. Cheng, X. Qiu, Real-space identification of intermolecular bonding with atomic force microscopy. *Science* **342**(6158), 611–614 (2013)
82. C. Vega, J.L.F. Abascal, P.G. Debenedetti, Physics and chemistry of water and ice. *PCCP* **13**(44), 19660–19662 (2011)
83. C. Vega, J.L.F. Abascal, Simulating water with rigid non-polarizable models: a general perspective. *PCCP* **13**(44), 19663–19688 (2011)
84. C.Q. Sun, Dominance of broken bonds and nonbonding electrons at the nanoscale. *Nanoscale* **2**(10), 1930–1961 (2010)

Chapter 33

Theory: Hydrogen Bond Cooperativity

- *An extension of the Ice Rule results in the building block of an ideal tetrahedron consisting two H₂O molecules and four identical O:H–O bonds.*
- *The O:H–O bond performs as a pair of asymmetric, coupled, H-bridged oscillators.*
- *Under external stimulus, one part of the O:H–O bond serves as the ‘master’ and the other as a ‘slave.’ Coulomb repulsion between electron pairs on oxygen dislocates the O atoms in the same direction under excitation along the O:H–O bond but by different amounts. The softer O:H bond relaxes always more than the stiffer H–O bond does.*
- *Relaxation of the H–O bond energy determines the amount of the O 1s energy shift, the high-frequency phonon relaxation, and the critical temperature change for phase transition. Relaxation of the O:H bond energy shifts the frequency of the low-frequency phonon.*
- *Cooperative relaxation of the H-bond in length and energy and the associated binding electron entrapment and non-bonding electron polarization determine the anomalies.*

33.1 H-Bond: Asymmetric, Coupled, H-Bridged Oscillators

33.1.1 Extended Ice Rule

The sp^3 -orbital hybridization is the unique choice of oxygen upon reacting with atoms of relatively lower electronegativity, irrespective of the structural phase [1, 2]. As shown in Fig. 33.1a, an oxygen atom ($2s^2 2p^4$) catches two electrons from neighboring partners such as hydrogen (H) and metals and then hybridizes its 2sp orbits with tetrahedrally directional orbits. In the case of H₂O, one O forms two intramolecular H–O bonds with shared electron pairs and ~ 4.0 eV binding energy [3] and fills up the rest two orbits with its non-bonding electron lone pairs ‘:’ to

form the intermolecular O:H non-covalent bonds of <0.1 eV binding energy [4]. The inhomogeneous distribution of charge and energy around the central oxygen atom entitles a H_2O molecule only C_{v2} group symmetry except for the rotation and vibration of the molecule. Therefore, an oxygen atom always tends to find four neighbors to form a stable tetrahedron, but the non-equivalent bond angles ($\angle\text{H-O-H} \leq 104.5^\circ$ and $\angle\text{H:O:H} \geq 109.5^\circ$) and the repulsion between electron pairs on oxygen [3, 5] refrain the steady tetrahedron from being formed in the liquid phase. The strong fluctuation proceeds more like the motion of a complex pendulum surrounded by four non-bond interactions, because of the O:H bond switching on and off restlessly in a period of subpicosecond [6–9]. Therefore, it would be more realistic and meaningful to consider the statistic expectation of the coordination number, the structure order, and the molecular separation in all phases at question for a long time span rather than the instantaneous value of a certain independent quantity by taking the snapshot at a quick flash [7].

The packing order of H_2O molecules follows the Ice Rule [10, 11] in all phases except for water under extremely high temperature and high pressure [12]. Despite thermal fluctuation in the O:H non-covalent bond lengths and the $\angle\text{O:H-O}$ bond angles, the average separation and the size of molecules will change when the H_2O transits from the strongly ordered solid phase, to the weakly ordered liquid phase, and to the disordered amorphous or vapor phase, as the Ice Rule retains. An extension of the Ice Rule results in an ideal tetrahedron, shown in Fig. 33.1b, with higher C_3 group symmetry. This tetrahedron containing two equivalent H_2O molecules and four identical O:H–O bonds at different orientations forms the basic block building up the bulk water and ice.

Figure 33.1 shows the sampling procedure for extending the Ice Rule to the H-bond and the ideal structure of ice and water [5]. The central tetrahedron in Fig. 33.1b illustrates the Ice Rule [10, 11]. In the hexagonal or cubic ice phase, the oxygen ions form each a tetrahedron with an O–O bond length 0.276 nm, while the H–O bond length measures only 0.096 nm. Every oxygen ion is surrounded by four hydrogen ions, and each hydrogen ion is connected to two oxygen ions. Maintaining the internal H_2O molecule structure, the minimum energy position of a proton is not halfway between two adjacent oxygen ions. There are two equivalent positions that a hydrogen ion may occupy on the line of the O–O bond, a far and a near position. Thus, a rule leads to the ‘frustration’ of positions of the proton for a ground state configuration: For each oxygen ion, two of the neighboring protons must reside in the far position and two of them in the near, so-called two-in two-out frustration. The open tetrahedral structure of ice affords many equivalent states including spin glasses that satisfy the Ice Rule.

33.1.2 Hydrogen Bond Segmentation

The building block in Fig. 33.1b results in two entities. One is the geometric structure in Fig. 33.1c that water and ice prefers statistically and the other is

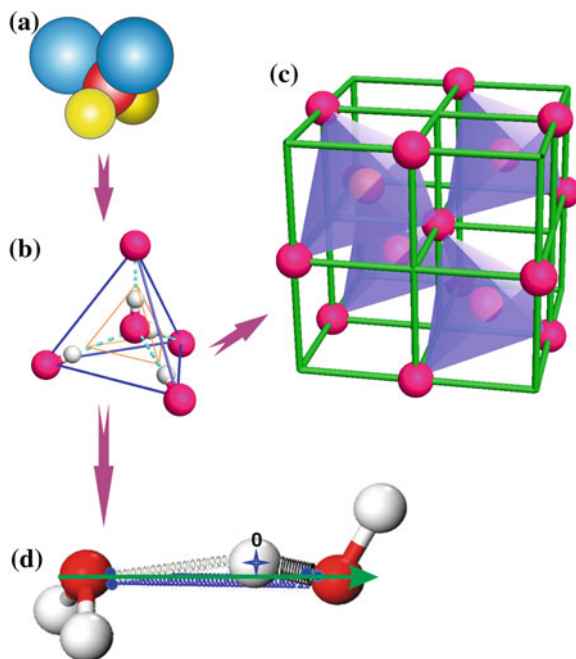


Fig. 33.1 **a** Sampling procedure for extending the Ice Rule [10, 11]. The sp^3 -hybridized oxygen with two lone pairs (*green*) and two bonding (*yellow*) orbitals forms a quasi-tetrahedron of C_{2v} group symmetry [2]. An extension of this quasi-tetrahedron yields **b** an ideal tetrahedron of C_{3v} that contains two H_2O molecules and four identical O:H–O bonds. A collection of the basic C_{3v} blocks in a sp^3 order yields **c** a diamond structure that correlates the size, separation, and mass density of molecules packing in water and ice [13]. **d** The H-bond forms a pair of asymmetric, coupled, H-bridged oscillators whose relaxation in length and energy mystifies water and ice (Reprinted with permission from [5])

H-bond oscillators in Fig. 33.1d with asymmetric and ultrashort-range interactions. The H atom at the coordinate origin donates its electron to the O shown on the right, to form the intramolecular H–O polar covalent bond, whereas the electron lone pair ‘:’ of the O shown on the left polarizes the shared electron pair ‘–’ to form an intermolecular O:H non-bond without sharing any charge but polarization. The H-bond is thus segmented into a shorter, stronger, and stiffer H–O covalent bond with stronger exchange interaction and a longer, weaker, and softer O:H non-bond with weak vdW interaction [3, 5]. The H proton must stay always closer to the O in the right without any frustration being allowed because of the disparity in interaction. Table 33.1 specifies the H-bond in comparison with the C–C bond identities in a diamond.

The H-bond forms the basic structural unit for O–O interaction in solid and liquid H_2O phases irrespective of phase structures [13], except for phases created under extreme conditions. For instance, H_2O turns to be partially ionic $2H_2O \rightarrow H_3O + HO$ at extremely high pressure (2 TPa) and temperature

Table 33.1 Comparison of the length (nm), strength (energy in eV), and stiffness (vibration frequency) of the O:H and the H–O bond with those of the C–C bond in diamond

| | Length d_x (nm) | Energy E_x (eV) | Phonons ω_x (cm^{-1}) | Θ_D (K) | T_m (K) | Interaction type |
|--------|----------------------|----------------------|--|-------------------|-----------|----------------------|
| H–O(H) | ~0.10 | ~3.97 | >3,000 | >2,000 | ~5,000 | Exchange |
| O:H(L) | ~0.17 | ~0.05–0.10 | <300 | 198 | 273 | vdW |
| O–O | – | – | – | – | – | Coulomb repulsion |
| C–C | 0.15 | 1.84 | 1,331 | 2,230 | 3,800 | Exchange |

Subscript $x = L$ and H represent for the O:H low- and H–O high-frequency vibration bond, respectively (Reprinted with permission from [14])

(2,000 K) based on computation [12]. Proton symmetrization under 60 GPa compression makes the charge distribute symmetrically around the center of O:H–O in Ice X phase [15–17] but hardly dehybridizes the sp orbitals of oxygen.

33.1.3 Asymmetric Short-Range Interactions

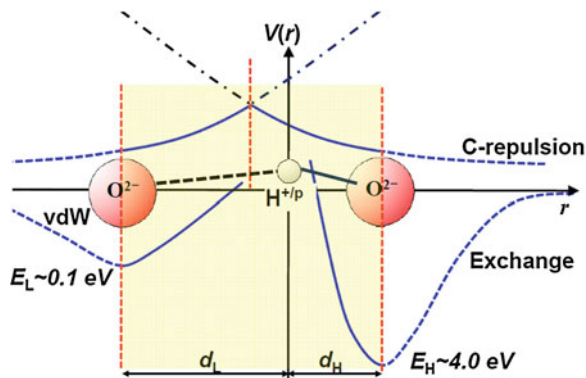
The short-range interactions include the vdW force limited to the O:H bond [18], the exchange interaction to the H–O polar covalent bond [19], and the Coulomb repulsion between the lone and the shared electron pairs attached to the adjacent oxygen ions, represented by the following potentials:

$$\left\{ \begin{array}{l} V_L(r_L) = V_{L0} \left[\left(\frac{d_{L0}}{r_L} \right)^{12} - 2 \left(\frac{d_{L0}}{r_L} \right)^6 \right] \quad (\text{L--J potential}(V_{L0}, d_{L0})) \\ V_H(r_H) = V_{H0} \left[e^{-2\alpha(r_H - d_{H0})} - 2e^{-\alpha(r_H - d_{H0})} \right] \quad (\text{Morse potential}(\alpha, V_{H0}, d_{H0})) \\ V_C(r_C) = \frac{q_L q_H}{4\pi\epsilon_r \epsilon_0 r_C} \quad (\text{Coulomb potential}(q_L, q_H, \epsilon_r)) \end{array} \right. \quad (33.1)$$

where V_{L0} and V_{H0} , commonly denoted E_{L0} and E_{H0} , are the potential well depths of the respective bonds. r_x and d_{x0} ($x = L, H$, and C) denote the interionic distances (corresponding to the lengths of springs). The α parameter determines the width of the potential well. $\epsilon_r = 3.2$ is the relative dielectric constant of ice, which is subject to change with experimental conditions and the location of water molecules. $\epsilon_0 = 8.85 \times 10^{-12}$ F/m is the vacuum dielectric constant. The q_L and q_H denote the lone and the shared electron pairs on oxygen ions.

With least number of adjustable parameters, the Morse potential for the exchange interaction suffices. One can hardly tell which potential is better than the other as we are concentrated about the equilibrium coordinates of bond length and bond energy, disregarding shapes of the potential curves. Because of the short-range nature of the interactions, the solid lines are only effective in the shaded area

Fig. 33.2 Asymmetric, local, short-range potentials for the segmented H-bond. Interactions include the short-range vdW (*left hand side*) and the exchange (*right hand side*) interactions and the Coulomb repulsion between electron pairs on adjacent oxygen atoms (Reprinted with permission from [13])



for the basic O:H–O unit in Fig. 33.2a. One must switch off a particular potential and on the other immediately when one moves to the boundary of the region. No spatial decay of any potential is allowed in the irrespective regime, which may add difficulty in quantum calculations.

33.1.4 Forces Driving Asymmetric Relaxation

The segmented H-bond allows for the specification of forces acting on the electron pairs of O atoms, as illustrated in Fig. 33.3. If one average the surrounding interactions by other H₂O molecules or protons as the background and ignore the nucleus quantum effect on fluctuations [20], there are three forces acting on the electron pairs of an oxygen atom:

1. Coulomb repulsion between the unevenly bound electron pairs, $f_q = -\partial u_q(r)/\partial r$. Replacing one O²⁻ with a charged ion of salt, sugar, protein, cell, or a biomolecule should modulate the f_q and hence the dissociation energy, local density, and the functionalities of H-bond and water molecules.
2. The force of deformation recovery $f_{rx} = -k_x \Delta x = -\partial u_x(r)/\partial r$. The force constant k_x approximates the second-order differential of the respective $u_x(r)$ at equilibrium, and the f_{rx} points always against the direction of deformation.
3. The force driving relaxation of the respective segment, f_{dx} ($x = L$ and H for the low and the high frequency of vibration), points toward/outward the H coordinate. The f_{dx} drives the intrinsic response to the applied stimulus such as coordination conditions, pressure, temperature, etc.

Figure 33.3 derives the following relations that define the master segment and hence the O–O length relaxation under stimulus of cooling, compressing, and molecular CN reduction.

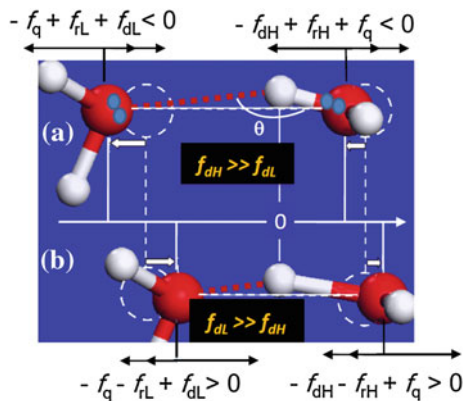


Fig. 33.3 Forces and relaxation dynamics of the segmented O:H–O bond. Asymmetric and coupling relaxation dynamics of the master–slave-segmented O:H–O bond in water ice under applied stimulus. Short-range interactions of intramolecular H–O bond exchange interaction, intermolecular O:H non-bond vdW interaction (*broken red lines*), interelectron-pair Coulomb repulsion (*broken white lines*), forces of Coulomb repulsion f_q , deformation recovery f_{rx} , and the force driving relaxation f_{dx} acting on the electron pairs (*small dots*). H atom is the coordinate origin. Because of the strength disparity, $|\Delta d_L| > |\Delta d_H|$; the Coulomb repulsion makes the Δd_H and the Δd_L shift in the same direction by different amounts (Reprinted with permission from [14])

$$\begin{array}{ll}
 \text{(a)}(\text{freezing, molecular CN reduction}) & \text{(b)}(\text{compression, liquid and solid cooling}) \\
 \left\{ \begin{array}{l} -f_q + f_{rL} + f_{dL} < 0 \\ -f_{dH} + f_{rH} + f_q < 0 \end{array} \right. & \left\{ \begin{array}{l} -f_q - f_{rL} + f_{dL} > 0 \\ -f_{dH} - f_{rH} + f_q > 0 \end{array} \right. \\
 \text{or,} & \text{or,} \\
 f_{rL} + f_{dL} - f_{dH} + f_{rH} < 0 & -f_{rL} + f_{dL} - f_{dH} - f_{rH} > 0 \\
 \text{or,} & \text{or,} \\
 f_{dH} - (f_{rL} + f_{dL} + f_{rH}) > 0 & f_{dL} - (f_{rL} + f_{dL} + f_{rH}) > 0 \\
 \left. \begin{array}{l} f_{dH} > (f_{dL} + f_{rL} + f_{rH}) \\ f_{dL} > (f_{dH} + f_{rL} + f_{rH}) \\ f_{dH} = f_{dL} \end{array} \right\} \Rightarrow \Delta d_{O-O} \left\{ \begin{array}{l} > \\ < \\ = \end{array} \right\} 0
 \end{array}
 \quad (33.2)$$

Each segment of the H-bond follows a certain rule of contraction/elongation cooperatively through the Coulomb repulsion. One dominates the contraction/elongation under a certain condition and the other follows—lengthens/contracts. The segment that drives relaxation is assigned to be the ‘master,’ whereas the other behaves as a ‘slave.’ Under stimulus such as squeezing, cooling, or clustering, the master segment will contract and push, through inter electron-pair Coulomb repulsion, the electron pair of the slave away from the H origin, the slave segment expands. Meanwhile, the repulsion widens the angle θ and polarizes the electron pairs during relaxation.

If $f_{dH} \gg f_{dL}$, the master H–O bond (H) contracts slightly and elongates the slave O:H non-bond considerably, resulting in a net O–O length gain and an accompanying volume expansion. If $f_{dL} \gg f_{dH}$, the master and the slave swap roles, a net O–O contraction and thus a gain in density will result. At $f_{dH} = f_{dL}$, there is a transition between O–O expansion and contraction, corresponding to the density extremes.

Most importantly, Coulomb repulsion between the electron pairs plays a role of dominance, not only in H₂O but also in the dynamics of oxygen chemisorption to metal surfaces. STM/VLEED study of oxygen chemisorption on Cu(001) surface [2] (Chap. 7) revealed that the O–Cu bond and the O:Cu bond relax oppositely in lengths. The O^{2–}–Cu⁺ contracts to 0.163 nm, while the O:Cu expands to 0.195 nm in the Cu:O–Cu configuration with creation of Cu^p dipoles and missing Cu vacancies.

Three variables of the O:H–O bond angle θ , the segmental lengths d_x ($x = L$ and H for the O:H and the H–O bond, respectively) describe the H-bond relaxation dynamics. Response of these variables, the change in stiffness of each segment, the entrapment of the bonding charge, and the polarization of the electron pairs under excitation are basic concerns, as these primary quantities dominate the physical and chemical performance of water ice such as phonon relaxation, binding energy entrapment, T_C change, elasticity, chemical reactivity, etc.

Because of the high strength of the H–O, the V-shaped H₂O motif is expected intact, while the θ and the d_L are subject to thermal fluctuations depending on environment and stimulus applied. The H proton tends always to approach the O ions in the O:H interaction, but this process is subject to interelectron-pair repulsion. Therefore, the V-shaped H₂O motifs act like ‘pendulum’ motion in liquid phase (see movie in A4-1). The O:H attraction and the O–O repulsion make the H₂O motifs move restlessly. The segmented, flexible, polarizable, and fluctuating H-bond represents the average of all O–O interactions in the solid and liquid phases of H₂O, even in the ring- or chain-like H-bond networks [6, 21–33].

33.1.5 Segmental Asymmetric Relaxation

At the equilibrium, $f_{dH} = f_{dL}$, see Fig. 33.3; one can derive the rules for the segmental cooperative asymmetric relaxation. Letting k_H and k_L be the respective force constants and δd_H and δd_L the corresponding displacements, the f_{ix} , k_x , and δd_x satisfy the relation

$$f_{rH} + f_{rL} = k_H \delta d_H + k_L \delta d_L = 0,$$

which yields,

$$k_L/k_H = -\frac{\delta d_H/\delta t}{\delta d_L/\delta t} = -\frac{\delta^2 d_H/\delta t^2}{\delta^2 d_L/\delta t^2} \quad (33.3)$$

as constraints for the H-bond segmental cooperative relaxation. The variable t can be any stimulus of T , P , or N for (H₂O)_N clusters, or beyond. This relation

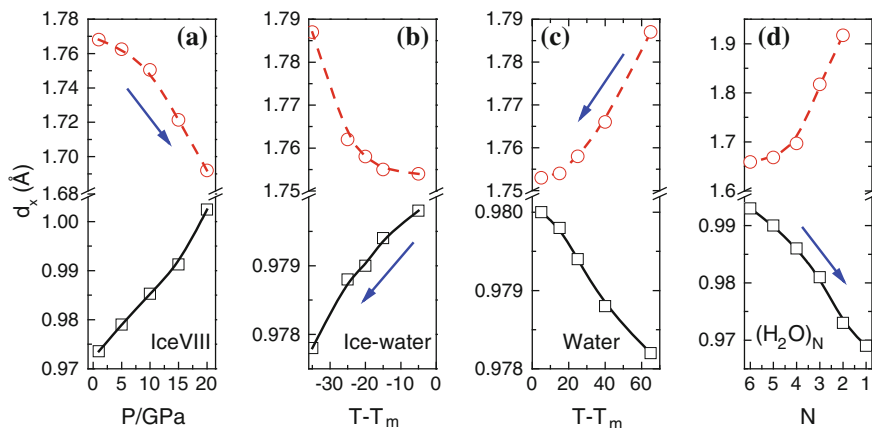


Fig. 33.4 MD-derived cooperative O:H and H-O relaxation dynamics of the segmented H-bond **a** under compression, **b** cooling below, **c** cooling above the melting point (T_m), and **d** cluster size reduction. *Arrows* indicate the master segments and their relaxation directions. Either the O:H or the H-O shrinks and the other one expands, disregarding the stimuli applied or the structural phases because of the interelectron-pair Coulomb repulsion

correlates and constrains the relaxation curves for the H-bond segments—the slopes and the curvatures of the segmental relaxations must be inversely and negatively correlated.

Figure 33.4 shows MD-derived relaxation trends under various stimuli. The slopes and the curvatures of the $d_x - t(P, T, N)$ curves are indeed cooperative. If one segment contracts, the other is lengthened; the two curves in one panel change in a way either ‘face to face’ or ‘back to back’ when the segments are relaxed. Outcome indicates that the O:H serves as the master under (a) compression and (c) cooling or heating in liquid and solid phase and the H-O a slave. The H-O bond serves as the master in (b) the transition phase at $T < T_m$ and (d) upon molecular CN reduction. In solid phase, the O:H dominates the thermally driven O-O relaxation [14].

33.1.6 Electron Pair Localization and Polarization

Figure 33.5 shows the DFT trajectory of the strongly localized and polarized electron pairs (red) in the cross-sectional plane of a unit cell. Gridlines are used as references. As expected, both the bonding and non-bonding electron pairs are strongly polarized and localized at sites closing to oxygen ions. Because of the mechanical strength and length disparity within the O:H-O bond, the bulk ice is formed by the solid H_2O monomers with their tightly bound electron pairs located on the nodes of an extremely weak ‘spring coiled’ ‘:’ networks.

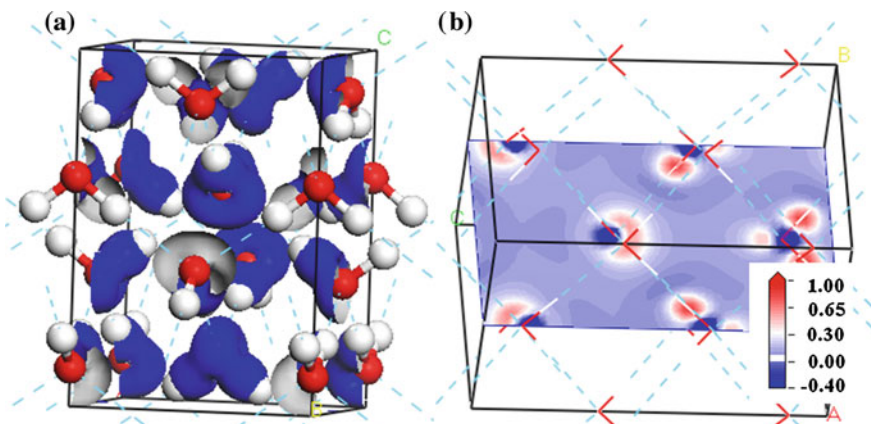


Fig. 33.5 **a** DFT-derived residual charge density of ice-VIII unit cell with isosurface 0.1 electron/Å³. Residual density is the difference between the charge of H₂O in ice-VIII and that of an isolated O atom. **b** The positive regions (*red*) correspond to the gain of electrons and the negative regions (*blue*) to the electron loss. The strong localization of the residual charges provides foundation for the presence of Coulomb repulsion between electron pairs. A piece of bulk ice is a collection of the stiff H₂O motifs located at nodes of the three-dimensional sponge-like ‘spring coil’ networks

33.1.7 Vibrational Features and Orbital Image

33.1.7.1 Bond Vibration

The frequency shift of lattice vibration, probed using FTIR or Raman spectroscopy, is proportional to the square root of bond stiffness and approximates directly the length and strength change in the bond during relaxation. This is valid for a usual material that approximates the bond representing all bonds in the specimen, from the perspective of Fourier transformation. Comparing the energy of a vibration system to the Taylor series of the interatomic potential energy, $u_x(r)$, yields the dimensionality of the vibration (phonon) frequencies for an uncoupled system [3]:

$$\Delta\omega_x \propto \left(\frac{\partial^2 u_x(r)}{m_x \partial r^2} \Big|_{r=d_x} \right)^{1/2} \propto \sqrt{E_x/m_x}/d_x \propto \sqrt{Y_x d_x}. \quad (33.4)$$

The stiffness is the product of the Young’s modulus ($Y_x \propto E_x/d_x^3$) and the length of the segment in question [5]. The m_x is the reduced mass of the vibrating dimer. Therefore, the frequency shift measures directly the segmental stiffness based on the dimensionality analysis. The Coulomb coupling in water ice revises this relation to be $\Delta\omega_x \propto ((k_x + k_c)/m_x)^{1/2}$ for the x segment of the H-bond with k_c being the force constant of Coulomb repulsion, as will be addressed shortly [34].

Figure 33.6 shows the typical spectra of FTIR absorption, Raman reflection, and neutron diffraction from water at the ambient. There are four features

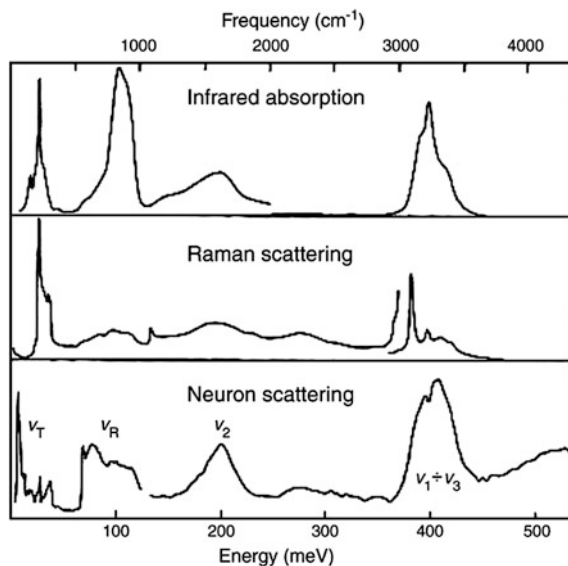


Fig. 33.6 Typical vibrational spectra as measured using IR absorption, Raman reflection, and inelastic neutron scattering [35] from water at the ambient. Peaks correspond to: O:H stretching mode: $\omega_L < 300 \text{ cm}^{-1}$, $\angle\text{O:H-O}$ bending mode: $\omega \sim 500 \text{ cm}^{-1}$, $\angle\text{H-O-H}$ bending liberation mode: $1,500 < \omega < 1,800 \text{ cm}^{-1}$. H-O stretching mode in bulk water: $\omega_H \sim 3,200 \text{ cm}^{-1}$, H-O stretching mode in the liquid skin: $\omega_H \sim 3,450 \text{ cm}^{-1}$. The liberation mode is insensitive to the external stimulus. See Appendix A4-1 for the vibration mode frequency correspondence

corresponding to, from high to low frequencies (see appendix A4-1), (1) the H-O stretching phonons in the skin ($\omega_H \sim 3,450 \text{ cm}^{-1}$) and in the bulk ($\sim 3,200 \text{ cm}^{-1}$); (2) the liberation mode of $\angle\text{H-O-H}$ bending at $\omega_{B1} 1,600 \sim 1,750 \text{ cm}^{-1}$; (3) the $\angle\text{O:H-O}$ bending mode at $\omega_{B2} \sim 500 \text{ cm}^{-1}$; and (4) the O:H stretching mode at $\omega_L \sim 200 \text{ cm}^{-1}$. The liberation mode is insensitive to the experimental conditions. The intensity of the peaks below 500 cm^{-1} is rather weak but very sensitive. Monitoring both the high-frequency ω_H and the low-frequency ω_L cooperative relaxation would be more comprehensive for examining the stiffness of the respective H-bond segment.

33.1.7.2 Images of H₂O molecular orbitals

Gao et al. [36] has firstly acquired reproducible images and dI/dV spectra of H₂O monomer and H₂O tetramer deposited on NaCl(001) surface using an STM at 5 K temperature, see Fig. 33.7. The HOMO orbital of the monomer appears as a double-lobe structure with a nodal plane in between, while the LUMO corresponds to an egg-shaped lobe developing between the two HOMO lobes. The STS spectra

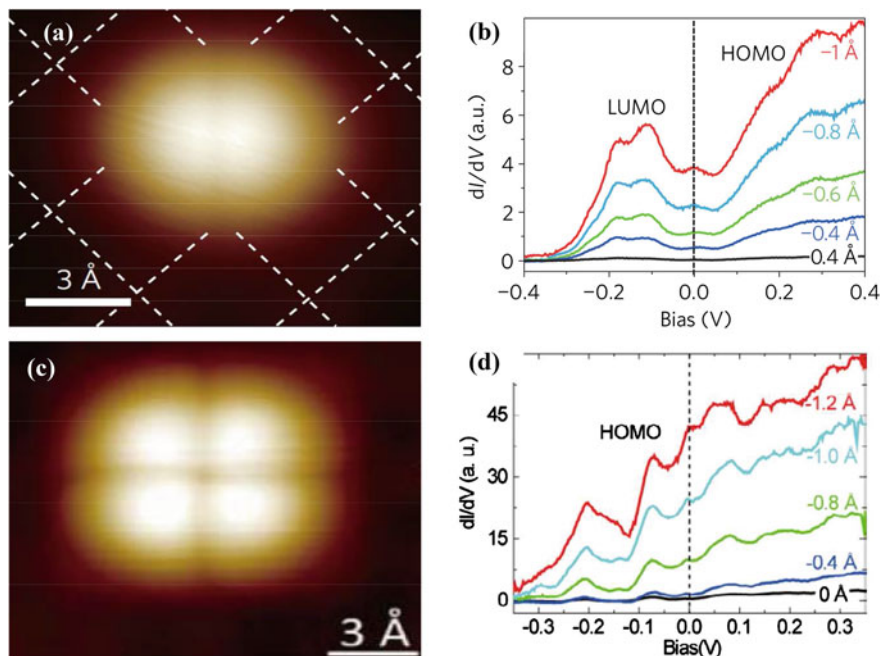


Fig. 33.7 Disparity of the Θ_{DX} and the η_X (R is the gas constant) of the segmented H-bond gives rise to the complex specific heat curve exhibiting four temperature regions. The number of regions coincides with that demonstrated by the $\rho(T)$ profiles [25, 41, 42]. Because of the difference in their Debye temperatures (Table 33.1), the specific heat η_L of the O:H rises faster toward the asymptotic maximum value than the η_H . The four regions correspond, respectively, to the phases of liquid (I), solid (III, IV), and liquid–solid transition (II) with different specific heat ratios. At extremely low temperatures (IV), $\eta_L \approx \eta_H \approx 0$. (The η_L in the solid phase differs from the η_L in the liquid, which does not influence the validity of the hypothesis.) The crossing points correspond to the density extremes (Reprinted with permission from [14])

at different heights discriminate the tetramer from the monomer in the density of states crossing Fermi energy.

Discoveries evidence the sp-orbit hybridization of oxygen in H_2O monomer and clarify the intermolecular interaction involved in $(H_2O)_4$. According to the 3B notation discussed in Part I, the LUOM corresponds the electron lone pair of oxygen upon its sp-orbit being hybridized and the HOMO to the empty antibonding states that to be occupied by electrons of dipoles [37]. The image of the monomer showing the directional lone pairs suggests that the lone pairs point to the direction way of the surface due to the $Cl^- - H^+$ Coulomb interaction as H^+ can only share its unpaired electron with oxygen. Bond switching from H-O to H-Cl might happen under thermal excitation. The spectral difference between the tetramer and the monomer could be indicative of the intermolecular interaction, particularly, the repulsion between electron pairs on adjacent oxygen atoms [38]. These findings are stimulating to the understanding of the electronic and geometric details.

33.2 Segmental Disparity

33.2.1 Mechanical Disparity

Letting the compression force $f_{dx} \sim P/s_x$, with s_x being the cross-sectional area of the x segment and P the pressure, one can derive the geometrical and mechanical disparity of the H-bond. At quasi-equilibrium (P drives O:H contraction),

$$\begin{aligned} f_{dL} - f_{dH} &= P(1/s_L - 1/s_H) = (f_{rL} + f_{rH}) > 0 \\ \text{or} & \\ s_H - s_L &> s_L s_H > 0. \end{aligned} \tag{33.5}$$

As the constraint for the P -induced H-bond relaxation, this relationship indicates that the effective cross-sectional area of the O:H non-bond is smaller than that of the H–O bond, which explains why the O:H non-bond ‘masters’ the relaxation dynamics of water ice upon being compressed and why the O:H relaxes more than the H–O bond does in the relaxation [5].

33.2.2 Thermodynamic Disparity

Generally, the specific heat is regarded as a macroscopic quantity integrated over all bonds of the specimen and is the amount of energy required to raise the temperature of the substance by 1 K. However, in dealing with the representative of all bonds of the entire specimen, one has to consider the specific heat per bond that is obtained by dividing the bulk specific heat by the total number of bonds involved [39].

For other usual materials, the specimen can be approximated using one representative bond for all bonds involved, and therefore, the thermal response of all the bonds are the same, without discriminating one bond from another in cooling contraction [40]. However, for water ice, the representative O:H–O bond is composed of two segments with strong disparity in the Debye temperature, Θ_{Dx} , and the specific heat, η_x , because of the different binding energies. The superposition of the two η_x curves makes the heat capacity of water ice to be different from that of other usual materials. The specific heat disparity makes these two segments to respond to thermal stimulus differently in different temperature ranges.

The Debye temperature Θ_{Dx} determines the slope of the specific heat curve, while the cohesive energy per bond E_x determines the integral of the specific heat curve from 0 K to the melting point T_{mx} [39]. The specific heat curve of the segment with a relatively lower Θ_{Dx} value will rise to saturation faster than the other segment does. The Θ_{Dx} , which is lower than the T_{mx} , is proportional to the characteristic frequency of the vibration (ω_x) of the segment. Thus, (see data in Table 33.1),

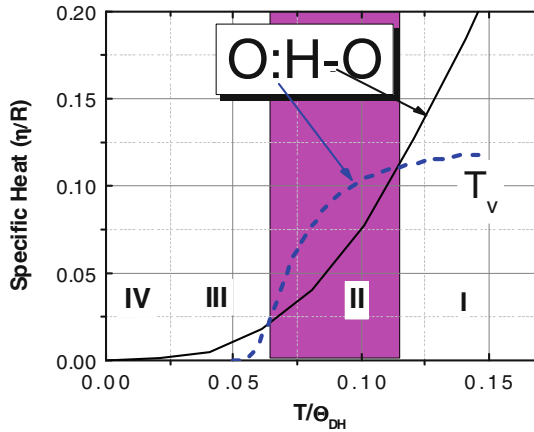


Fig. 33.8 Disparity of the and the $\Theta_{DX}\eta_x$ (R is the gas constant) of the segmented H-bond gives rise to the complex specific heat curve exhibiting four temperature regions. The number of regions coincides with that demonstrated by the $\rho(T)$ profiles [25, 41, 42]. Because of the difference in their Debye temperatures (Table 33.1), the specific heat η_L of the O:H rises faster toward the asymptotic maximum value than the η_H . The four regions correspond, respectively, to the phases of liquid (I), solid (III, IV), and liquid–solid transition (II) with different specific heat ratios. At extremely low temperatures (IV), $\eta_L \approx \eta_H \approx 0$. (The η_L in the solid phase differs from the η_L in the liquid, which does not influence the validity of the hypothesis.) The crossing points correspond to the density extremes (Reprinted with permission from [14])

$$\begin{cases} \Theta_{DL}/\Theta_{DH} \approx 198/\Theta_{DH} \approx \omega_L/\omega_H \approx 200/3000 \sim 1/15 \\ \left(\int_0^{T_{mH}} \eta_H dt \right) / \left(\int_0^{T_{mL}} \eta_L dt \right) \approx E_H/E_L \approx 4.0/0.1 \sim 40 \end{cases} \quad (33.6)$$

The Θ_{DL} has been determined to be $198 < 273$ K (T_m) and the molecular cohesive energy to be 0.38 eV/molecule from analyzing the temperature dependence of water surface tension [4]. Hence, $\Theta_{DH} \approx 10 \times \Theta_{DL} \approx 2,000$ K. The η_L should terminate at melting, 373 K, and the η_H ends at a temperature well above 2,000 K. Based on these constraints, the relative specific heat maxima of the segments is estimated as $\eta_H/\eta_L \approx 8$. Such a specific heat disparity between the O:H and the H–O segments yields four temperature regions with different η_L/η_H ratios and two crossing points, which should correspond to the phases of liquid (I), solid (III, IV), and liquid–solid transition (II). The crossing points correspond to the density extremes [14]. At extremely low temperatures (IV), $\eta_L \approx \eta_H \approx 0$ (Fig. 33.8).

The profiling consistency in the mass density [28, 41, 42] and the proposed specific heat for water ice suggests that the segment of lower specific heat serves as the master whose thermal expansion or cooling contraction drives the asymmetric relaxation, while the other one serves as the slave. The length response of a segment to the thermal stimulus is determined by its specific heat (η_x). The segment of lower η_x is more active than the one with higher η_x value when they are thermally provoked under the same condition. According to the specification, the

O:H non-covalent bond serves as the master to contract in the liquid (I) and solid (III) phases, and the slave H–O covalent bond expands slightly, leading to the seemingly normal process of cooling densification. In the transition phase II, the master–slave role swaps, and hence, water volume expands. The crossing points correspond to the density maximum at 4 °C and minimum below the freezing point [25, 43]. At extremely low temperatures, the resultant η approaches zero, which means cooling contraction happens to neither of the segments.

The thermodynamic disparity of the H-bond indicates that H–O dominates the extremely high heat capacity of water instead of the weaker non-bond ‘springs’ (lone pair or the H-bond network) because of the high $\eta_{\text{H}}/\eta_{\text{L}}$ ratio [44]. According to the current notation, the four-region density and phonon stiffness oscillation of water ice follows the following relations:

$$\left. \begin{array}{ll} \text{II} & (\eta_{\text{H}} < \eta_{\text{L}}) : f_{\text{dH}} > (f_{\text{dL}} + f_{\text{rL}} + f_{\text{rH}}) \\ \text{I, III} & (\eta_{\text{L}} < \eta_{\text{H}}) : f_{\text{dL}} > (f_{\text{dH}} + f_{\text{rL}} + f_{\text{rH}}) \\ \text{IV} & (\eta_{\text{L}} \cong \eta_{\text{H}} \cong 0) : \Delta\theta > 0; \Delta d_{\text{x}} = 0 \\ \text{Cross} & (\eta_{\text{L}} = \eta_{\text{H}}) : f_{\text{dH}} = f_{\text{dL}} \end{array} \right\} \Rightarrow \Delta d_{\text{O-O}} \left\{ \begin{array}{l} > \\ < \\ = \\ = \end{array} \right\} 0. \quad (33.7)$$

33.2.3 Molecular Undercoordination: Extended BOLS

According to the BOLS notation [45–48], bond order loss shortens and strengthens the remnant bonds of undercoordinated atoms with an association of local densification and quantum entrapment of the binding energy and the bonding and core electrons, irrespective of the nature of the bond or the structure phase of the specimen. On the other hand, the locally and densely entrapped bonding charge in turn polarizes the non-bonding electrons [45], which are responsible for the emerging anomalies of nanostructures such as the catalytic enhancement, dilute magnetism of noble metals [49] and ZnO [49], and the creation of Dirac-Fermi polarons at graphene zigzag edges and graphite point defects [51].

The encapsulated and the free-standing $(\text{H}_2\text{O})_{\text{N}}$ molecular clusters, surface skins, or ultrathin films of water should share the same entity of bond order deficiency to follow the BOLS premise without exception. However, the involvement of the weak lone pair interaction and the interelectron-pair repulsion prevents the two segments of the H-bond from following the BOLS mechanism simultaneously. The binding energy difference between the O:H and H–O and the presence of the interelectron-pair repulsion define the H–O covalent bond to be the ‘master’ that contracts by a smaller degree than which the BOLS notation predicts. The contraction of the H–O bond lengthens and softens the ‘slave’ O:H bond by repulsion.

The process of covalent bond contraction results in dual process of polarization of the non-bonding lone pairs. Firstly, the densely entrapped bonding and core electrons of an oxygen atom polarize the lone pairs of its own. The polarized lone

pairs on the adjacent oxygen atoms will polarize and repel one another, resulting in the dual process of polarization, which explains why the surface of water ice is so strongly polarized, and why they are hydrophobic and slippery.

33.3 Correlation of Detectable Quantities

33.3.1 *Non-Bonding Electron Polarization*

The non-bonding lone pairs are associated with reaction process of tetrahedral coordinated bond formation of O, N, or F atoms [2, 52]. Replacing O^{2-} with N^{3-} or F^- and replacing H^{+p} with any element M^{+p} of lower electronegativity, H-bond-like bond forms [2, 52]. The strength of the non-bonding lone pair also varies with the local environment [53] and breaks at the boiling point of water (373 K) [54]. The O:Cu non-bond breaks at about 450 K, as detected using VLEED at annealing [55].

Because of its rather weak interaction, the O:H binding energy contributes insignificantly to the Hamiltonian or to the atomic cohesive energy and the associated properties [45]. These electrons add, however, impurity states in the vicinity of Fermi energy, which neither follow the regular dispersion relations nor occupy the allowed states of the valence band and below. They are located right in the energy scope of STM/S surrounding E_F . The lone pair and dipole interactions not only act as the most important function groups in the biologic and organic molecules but also play an important role in the inorganic compounds such as high- T_C superconductors and topologic insulators. Under UV irradiation or thermal excitation, the hybrid sp^3 orbit can be dehybridized and the lone pairs and dipoles are annihilated accordingly, altering their functionalities.

In addition to the weak interactions with energies of ~ 50 meV, as detected using Raman and EELS [2], these lone pairs polarize the neighboring atoms instead causing change to dipoles. The relaxation of the O:H bond contributes to the volume change, polarization, molecular dissociation, low-load elasticity, friction reduction, and the associated ω_L phonon relaxation dynamics. If one wants to get rid of one molecule from the bulk, one has to break four O:H bonds of the molecule simultaneously.

33.3.2 *Binding Energy Entrapment*

According to the energy band theory [56], the energy shift ΔE_{1s} of a specific (O 1s) core band from that of an isolated atom $E_{1s}(0)$ is proportional to the cohesive energy per bond E_H [57]. Any perturbation to the crystal potential will shift the specific energy band away from the bulk reference. The energy shift can be

positive or negative depending on the sources of perturbation, including bond relaxation [58, 59], bond nature alteration [60], charge polarization [59], etc. The OIs energy shift in water ice follows the relation, with z , P , and T as the stimulus of coordination number, pressure, and temperature:

$$\frac{\Delta E_{1s}(z, T, P)}{\Delta E_{1s}(z_b, T_0, P_0)} = \frac{E_{1s}(z, T, P) - E_{1s}(0, T_0, P_0)}{E_{1s}(z_b, T_0, P_0) - E_{1s}(0, T_0, P_0)} = \frac{E_H(z, T, P)}{E_H(z_b, T_0, P_0)}. \quad (33.8)$$

33.3.3 Elastic Modulus and Transition Temperature

By definition, the Young's modulus is proportional to the second-order differentiation, or the curvature, of the pairing potential $u(r)$ with respect to volume V at equilibrium [61]. The elastic modulus, and the surface tension as well, is proportional, by dimension, to the bonding energy density of the corresponding segments at different loading scales [4]. At relatively low load, the L segment dominates [62], the polarization contributes.

For other usual materials, the critical temperature for phase transition is proportional to the atomic cohesive energy, $T_C \propto zE_z$, with z being the effective atomic CN and E_z the bond energy of the z -coordinated atom [48]. For water molecules, T_C is proportional to the cohesive energy of the covalent bond E_z because of the 'isolation' of the H₂O molecule by its surrounding four lone pairs.

33.3.4 Phonon Frequency and Segmental Stiffness

The Raman or the spectroscopy is one of the powerful techniques that could resolve the vibrations of the intermolecular O:H non-covalent bond and the intramolecular H–O bond according to their stiffness based on Fourier transformation. Any perturbation even sunlight irradiation can change the spectra feature of liquid water [63].

From the dimensional point of view, the second-order derivative of the $u_x(r)$ at equilibrium is proportional to the bind energy E_x divided by the square of bond length in the form of d_x^2 . The $E_x^{1/2}/d_x \cong \sqrt{Y_x d_x}$ with $Y_x \approx E_x/d_x^3$ is right the square root of the stiffness being the product of the Young's modulus and the bond length [14, 64]. In practice, polarization effect on the elasticity needs to be included.

It is universally true that if one segment becomes shorter, it will be stiffer; on expansion, it becomes softer [5]. Therefore, the phonon frequency shift tells directly the variation in length, strength, and stiffness of the respective segment under applied stimulus. Because of the Coulomb repulsion mediation, the ω_L and ω_H shift in such a way that if one becomes stiffer, the other becomes softer, and vice versa.

Therefore, all detectable quantities (q) of the specimen depend functionally on the order, length, and energy of the representative segment of the H-bond. The relaxation of the O:H bond contributes to the volume expansion, polarization, and molecular dissociation energy. The stiffening of the H–O bond increases the O1s core-level shift, ΔE_{1s} , elevates the critical temperature T_C for phase transition (superheating), and increases the H–O phonon frequency ω_H according to the following relations [57, 65, 66]:

$$\left. \begin{array}{l} T_C \\ \Delta E_{1s} \\ \Delta\omega_x \end{array} \right\} \propto \left\{ \begin{array}{l} E_H \\ E_H \\ \sqrt{E_x}/d_x = \sqrt{Y_x d_x} \end{array} \right. \quad (33.9)$$

E_x is the cohesive energy of the respective bond. Theoretical reproduction of the critical temperature T_C for ice VII–VIII phase transition under compression confirmed that the H–O bond energy determines the T_C [14].

33.4 Summary

O:H–O bond forms a pair of asymmetric, coupled, and H-bridged oscillators with short-range interactions, whose cooperative relaxation in length and energy and the associated entrapment and polarization discriminate water and ice from other usual materials. All detectable properties depend functionally on the performance of either the H–O or the O:H bond. The involvement of the Coulomb repulsion forms the key to the anomalies of water and ice.

References

1. P.W. Atkins, *Physical Chemistry*, 4th edn. (Oxford University Press, 1990)
2. C.Q. Sun, Oxidation electronics: bond-band-barrier correlation and its applications. *Prog. Mater. Sci.* **48**(6), 521–685 (2003)
3. C.Q. Sun, X. Zhang, J. Zhou, Y. Huang, Y. Zhou, W. Zheng, Density, Elasticity, and Stability Anomalies of Water Molecules with Fewer than Four Neighbors. *J. Phys. Chem. Lett.* **4**, 2565–2570 (2013)
4. M. Zhao, W.T. Zheng, J.C. Li, Z. Wen, M.X. Gu, C.Q. Sun, Atomistic origin, temperature dependence, and responsibilities of surface energetics: an extended broken-bond rule. *Phys. Rev. B* **75**(8), 085427 (2007)
5. C.Q. Sun, X. Zhang, W.T. Zheng, Hidden force opposing ice compression. *Chem. Sci.* **3**, 1455–1460 (2012)
6. P. Wernet, D. Nordlund, U. Bergmann, M. Cavalleri, M. Odelius, H. Ogasawara, L.A. Naslund, T.K. Hirsch, L. Ojamae, P. Glatzel, L.G.M. Pettersson, A. Nilsson, The structure of the first coordination shell in liquid water. *Science* **304**(5673), 995–999 (2004)
7. T.D. Kuhne, R.Z. Khaliullin, Electronic signature of the instantaneous asymmetry in the first coordination shell of liquid water. *Nat. Commun.* **4**, 1450 (2013)

8. V. Petkov, Y. Ren, M. Suchomel, Molecular arrangement in water: random but not quite. *J. Phys.: Condens. Matter* **24**(15), 155102 (2012)
9. A. Nilsson, C. Huang, L.G.M. Pettersson, Fluctuations in ambient water. *J. Mol. Liq.* **176**, 2–16 (2012)
10. J.D. Bernal, R.H. Fowler, A theory of water and ionic solution, with particular reference to hydrogen and hydroxyl ions. *J. Chem. Phys.* **1**(8), 515–548 (1933)
11. L. Pauling, The structure and entropy of ice and of other crystals with some randomness of atomic arrangement. *J. Am. Chem. Soc.* **57**, 2680–2684 (1935)
12. Y. Wang, H. Liu, J. Lv, L. Zhu, H. Wang, Y. Ma, High pressure partially ionic phase of water ice. *Nat. Commun.* **2**, 563 (2011)
13. Y. Huang, X. Zhang, Z. Ma, Y. Zhou, J. Zhou, W. Zheng, C.Q. Sun, Size, separation, structure order, and mass density of molecules packing in water and ice. *Sci. Rep.* **3**, 3005 (2013)
14. C.Q. Sun, X. Zhang, X. Fu, W. Zheng, J.-L. Kuo, Y. Zhou, Z. Shen, J. Zhou, Density and phonon-stiffness anomalies of water and ice in the full temperature range. *J. Phys. Chem. Lett.* **4**, 3238–3244 (2013)
15. E. Katoh, H. Yamawaki, H. Fujihisa, M. Sakashita, K. Aoki, Raman study of phase transition and hydrogen bond symmetrization in solid DCl at high pressure. *Phys. Rev. B* **61**(1), 119 (2000)
16. P. Loubeyre, R. LeToullec, E. Wolanin, M. Hanfland, D. Husermann, Modulated phases and proton centring in ice observed by X-ray diffraction up to 170 GPa. *Nature* **397**(6719), 503–506 (1999)
17. M. Benoit, D. Marx, M. Parrinello, Tunnelling and zero-point motion in high-pressure ice. *Nature* **392**(6673), 258–261 (1998)
18. R.F. McGuire, F.A. Momany, H.A. Scheraga, Energy parameters in polypeptides. V. An empirical hydrogen bond potential function based on molecular orbital calculations. *J. Phys. Chem.* **76**, 375–393 (1972)
19. N. Kumagai, K. Kawamura, T. Yokokawa, An interatomic potential model for H₂O: applications to water and ice polymorphs. *Mol. Simulat.* **12**, 177–186 (1994)
20. X.Z. Li, B. Walker, A. Michaelides, Quantum nature of the hydrogen bond. *Proc. Natl. Acad. Sci. U.S.A.* **108**(16), 6369–6373 (2011)
21. I.V. Stiopkin, C. Weeraman, P.A. Pieniazek, F.Y. Shalhout, J.L. Skinner, A.V. Benderskii, Hydrogen bonding at the water surface revealed by isotopic dilution spectroscopy. *Nature* **474**(7350), 192–195 (2011)
22. N. Bjerrum, Structure and properties of ice. *Science* **115**(2989), 385–390 (1952)
23. A.K. Soper, J. Teixeira, T. Head-Gordon, Is ambient water inhomogeneous on the nanometer-length scale? *Proc. Natl. Acad. Sci. U.S.A.* **107**(12), E44 (2010)
24. C. Huang, K.T. Wikfeldt, T. Tokushima, D. Nordlund, Y. Harada, U. Bergmann, M. Niebuhr, T.M. Weiss, Y. Horikawa, M. Leetmaa, M.P. Ljungberg, O. Takahashi, A. Lenz, L. Ojamäe, A.P. Lyubartsev, S. Shin, L.G.M. Pettersson, A. Nilsson, The inhomogeneous structure of water at ambient conditions. *Proc. Natl. Acad. Sci. U.S.A.* **106**(36), 15214–15218 (2009)
25. F. Mallamace, C. Branca, M. Broccio, C. Corsaro, C.Y. Mou, S.H. Chen, The anomalous behavior of the density of water in the range 30 K < T < 373 K. *Proc. Natl. Acad. Sci. U.S.A.* **104**(47), 18387–18391 (2007)
26. F. Mallamace, M. Broccio, C. Corsaro, A. Faraone, D. Majolino, V. Venuti, L. Liu, C.Y. Mou, S.H. Chen, Evidence of the existence of the low-density liquid phase in supercooled, confined water. *Proc. Natl. Acad. Sci. U.S.A.* **104**(2), 424–428 (2007)
27. P.H. Poole, F. Sciortino, U. Essmann, H.E. Stanley, Phase-behavior of metastable water. *Nature* **360**(6402), 324–328 (1992)
28. L.M. Xu, P. Kumar, S.V. Buldyrev, S.H. Chen, P.H. Poole, F. Sciortino, H.E. Stanley, Relation between the Widom line and the dynamic crossover in systems with a liquid–liquid phase transition. *Proc. Natl. Acad. Sci. U.S.A.* **102**(46), 16558–16562 (2005)
29. O. Mishima, H.E. Stanley, The relationship between liquid, supercooled and glassy water. *Nature* **396**(6709), 329–335 (1998)

30. N.J. English, J.S. Tse, Density fluctuations in liquid water. *Phys. Rev. Lett.* **106**(3), 037801 (2011)
31. S. Woutersen, U. Emmerichs, H.J. Bakker, Femtosecond mid-IR pump-probe spectroscopy of liquid water: evidence for a two-component structure. *Science* **278**(5338), 658–660 (1997)
32. N. Agmon, Liquid water: from symmetry distortions to diffusive motion. *Acc. Chem. Res.* **45**(1), 63–73 (2012)
33. T. Head-Gordon, M.E. Johnson, Tetrahedral structure or chains for liquid water. *Proc. Natl. Acad. Sci. U.S.A.* **103**(21), 7973–7977 (2006)
34. Y. Huang, X. Zhang, Z. Ma, Y. Zhou, G. Zhou, C.Q. Sun, Hydrogen-bond asymmetric local potentials in compressed ice. *J. Phys. Chem. B* **117**(43), 13639–13645 (2013)
35. R. Aswani, J.C. Li, A new approach to pairwise potentials for water–water interactions. *J. Mol. Liq.* **134**(1–3), 120–128 (2007)
36. J. Guo, X. Meng, J. Chen, J. Peng, J. Sheng, X.-Z. Li, L. Xu, J.-R. Shi, E. Wang, and Y. Jiang, Real-space imaging of interfacial water with submolecular resolution. *Nat Mater*, 2014. doi: [10.1038/nmat3848](https://doi.org/10.1038/nmat3848)
37. C.Q. Sun, *Oxidation electronics: bond-band-barrier correlation and its applications*. Progress in Materials Science, 2003. **48**(6):521–685
38. C.Q. Sun, X. Zhang, J. Zhou, Y. Huang, Y. Zhou, and W. Zheng, *Density, Elasticity, and Stability Anomalies of Water Molecules with Fewer than Four Neighbors*. The Journal of Physical Chemistry Letters, 2013. 4:2565–2570.
39. C.Q. Sun, Thermo-mechanical behavior of low-dimensional systems: the local bond average approach. *Prog. Mater. Sci.* **54**(2), 179–307 (2009)
40. M.X. Gu, Y.C. Zhou, C.Q. Sun, Local bond average for the thermally induced lattice expansion. *J. Phys. Chem. B* **112**(27), 7992–7995 (2008)
41. M. Erko, D. Wallacher, A. Hoell, T. Hauss, I. Zizak, O. Paris, Density minimum of confined water at low temperatures: a combined study by small-angle scattering of X-rays and neutrons. *PCCP* **14**(11), 3852–3858 (2012)
42. K. Rottger, A. Endriss, J. Ihringer, S. Doyle, W.F. Kuhs, Lattice-constants and thermal-expansion of H₂O and D₂O Ice Ih between 10 and 265 K. *Acta Crystallogr. B* **50**, 644–648 (1994)
43. E.B. Moore, V. Molinero, Structural transformation in supercooled water controls the crystallization rate of ice. *Nature* **479**(7374), 506–508 (2011)
44. S.V. Lishchuk, N.P. Malomuzh, P.V. Makhlaichuk, Contribution of H-bond vibrations to heat capacity of water. *Phys. Lett. A* **375**(27), 2656–2660 (2011)
45. C.Q. Sun, Dominance of broken bonds and nonbonding electrons at the nanoscale. *Nanoscale* **2**(10), 1930–1961 (2010)
46. L. Pauling, Atomic radii and interatomic distances in metals. *J. Am. Chem. Soc.* **69**(3), 542–553 (1947)
47. V.M. Goldschmidt, Crystal structure and chemical correlation. *Ber. Dtsch. Chem. Ges.* **60**, 1263–1296 (1927)
48. C.Q. Sun, Size dependence of nanostructures: impact of bond order deficiency. *Prog. Solid State Chem.* **35**(1), 1–159 (2007)
49. E. Roduner, Size matters: why nanomaterials are different. *Chem. Soc. Rev.* **35**(7), 583–592 (2006)
50. J.W. Li, S.Z. Ma, X.J. Liu, Z.F. Zhou, C.Q. Sun, ZnO meso-mechano-thermo physical chemistry. *Chem. Rev.* **112**(5), 2833–2852 (2012)
51. W.T. Zheng, C.Q. Sun, Underneath the fascinations of carbon nanotubes and graphene nanoribbons. *Energ. Environ. Sci.* **4**(3), 627–655 (2011)
52. W.T. Zheng, C.Q. Sun, Electronic process of nitriding: mechanism and applications. *Prog. Solid State Chem.* **34**(1), 1–20 (2006)
53. M. Hus, T. Urbic, Strength of hydrogen bonds of water depends on local environment. *J. Chem. Phys.* **136**(14), 144305 (2012)
54. P.C. Cross, J. Burnham, P.A. Leighton, The Raman spectrum and the structure of water. *J. Am. Chem. Soc.* **59**, 1134–1147 (1937)

55. C.Q. Sun, Time-resolved VLEED from the O-Cu(001): Atomic processes of oxidation. *Vacuum* **48**(6), 525–530 (1997)
56. M.A. Omar, *Elementary Solid State Physics: Principles and Applications* (Addison-Wesley, New York, 1993)
57. C.Q. Sun, Surface and nanosolid core-level shift: impact of atomic coordination-number imperfection. *Phys. Rev. B* **69**(4), 045105 (2004)
58. C.Q. Sun, Y. Nie, J. Pan, X. Zhang, S.Z. Ma, Y. Wang, W. Zheng, Zone-selective photoelectronic measurements of the local bonding and electronic dynamics associated with the monolayer skin and point defects of graphite. *RSC Adv.* **2**(6), 2377–2383 (2012)
59. C.Q. Sun, Y. Wang, Y.G. Nie, Y. Sun, J.S. Pan, L.K. Pan, Z. Sun, Adatoms-induced local bond contraction, quantum trap depression, and charge polarization at Pt and Rh surfaces. *J. Phys. Chem. C* **113**(52), 21889–21894 (2009)
60. C.Q. Sun, Y. Wang, Y.G. Nie, B.R. Mehta, M. Khanuja, S.M. Shivaprasad, Y. Sun, J.S. Pan, L.K. Pan, Z. Sun, Interface charge polarization and quantum trapping in AgPd and CuPd bimetallic alloy catalysts. *PCCP* **12**, 3131–3135 (2010)
61. X.J. Liu, J.W. Li, Z.F. Zhou, L.W. Yang, Z.S. Ma, G.F. Xie, Y. Pan, C.Q. Sun, Size-induced elastic stiffening of ZnO nanostructures: skin-depth energy pinning. *Appl. Phys. Lett.* **94**, 131902 (2009)
62. C.Q. Sun, B.K. Tay, S.P. Lau, X.W. Sun, X.T. Zeng, S. Li, H.L. Bai, H. Liu, Z.H. Liu, E.Y. Jiang, Bond contraction and lone pair interaction at nitride surfaces. *J. Appl. Phys.* **90**(5), 2615–2617 (2001)
63. T. Yokono, S. Shimokawa, M. Yokono, H. Hattori, Infra-red spectroscopic study of structural change of liquid water induced by sunlight irradiation. *Water* **1**, 29–34 (2009)
64. G. Ouyang, G.W. Yang, C.Q. Sun, W.G. Zhu, Nanoporous structures: smaller is stronger. *Small* **4**(9), 1359–1362 (2008)
65. C.Q. Sun, L.K. Pan, C.M. Li, S. Li, Size-induced acoustic hardening and optic softening of phonons in InP, CeO₂, SnO₂, CdS, Ag, and Si nanostructures. *Phys. Rev. B* **72**(13), 134301 (2005)
66. C.Q. Sun, Y. Shi, C.M. Li, S. Li, T.C.A. Yeung, Size-induced undercooling and overheating in phase transitions in bare and embedded clusters. *Phys. Rev. B* **73**(7), 075408 (2006)

Chapter 34

Compressed Ice: Inter Electron-Pair Repulsion

- *Coulomb repulsion and mechanical disparity within the H-bond differentiate ice from other materials in response to compression.*
- *Compression shortens and strengthens the O:H bond and meanwhile lengthens and softens H–O bond through repulsion toward O:H and H–O length symmetry.*
- *Compression also stiffens the O:H stretching phonons ($<400\text{ cm}^{-1}$) and softens the H–O stretching phonons ($>3,000\text{ cm}^{-1}$).*
- *Cohesive energy loss of the H–O bond lowers the T_C for the VIII–VII phase transition, which derives the $E_H = 3.97\text{ eV}$ for ice.*
- *Entrapment of the bonding electrons and polarization of the lone electron pairs widen the bandgap.*

34.1 Observations

It is usual for other materials that the critical temperature (T_C) for liquid–solid or disordered–ordered phase transition increases under compression [1–3]; however, the T_C for ice transferring from ice-VIII to the proton-disordered ice-VII phase drops from 280 to 150 K when the P is increased from 1 to 50 GPa [4–6]. Compression shortens the O–O distance but lengthens the H–O bond, yielding the low compressibility [7] of ice with respect to other usual materials. The liquid phase is more readily compressed than the solid phase.

Length symmetrization of the O:H–O bond in ice happens under ~ 60 GPa compression [8–10]. In 1972, Holzappel [11] predicted that, under compression, an H-bond might be transformed from the highly asymmetric O:H–O configuration to a symmetric state in which the H proton lies midway between the two O ions, leading to a non-molecular symmetric phase of ice-X. This prediction was experimentally confirmed in 1998 by Goncharov et al. [12] using an in situ high-pressure Raman spectroscopy. Proton symmetrization of ice-VIII happens at 60 GPa and 100 K, as no further phonon relaxation happens with the increase in

pressure. Proton symmetrization also happens to ice-VIII at about 59 GPa with 0.20 nm O–O distance [9] and happens to liquid H₂O at 60 GPa and to D₂O at 70 GPa at 85 and 300 K [13].

This phenomenon was attributed to the ‘translational proton quantum tunneling under compression’ [10, 14, 15] or the extraordinary behavior of the inter- and intramolecular bonds [16]. Teixeira [8] suggested that as the oxygen atoms are forced together, the potential energy changes from a symmetric double to a single well, making the ‘fluctuated H proton’ [17] to be certain in a position right between the O ions.

Generally, the applied pressure stiffens all the Raman phonons of other materials such as carbon allotropes [18], ZnO [19], group IV [20], group III–V [21], and group II–VI [22] compounds without exception, because compression shortens and stiffens all chemical bonds simultaneously; however, for water ice, the applied pressure stiffens only the softer phonons ($\omega_L < 300 \text{ cm}^{-1}$) but softens the stiffer phonons ($\omega_H > 3,000 \text{ cm}^{-1}$) of ice [4, 6, 23, 24] and water [25] as well. Figure 34.1 shows the pressure-induced ω_H and ω_L cooperative relaxation of ice-VIII at 80 K [26, 27]. The ω_H softening also happens to water at 23 °C under (0.05, 0.386) GPa pressures [25], which shall be accompanied with ω_L stiffening, because of the corporative interaction between the H-bond segments.

The phase formation, phase transition resolved in the Raman and IR spectra, the low compressibility, T_C depression, proton symmetrization, softer phonon stiffening, and stiffer phonon softening are correlated. These correlations remain open for exploitation.

34.2 Density Profile Decomposition

Table 34.1 lists the MD- and DFT-derived segmental relaxation dynamics and the density and bandgap change as a function of pressure. As shown in Fig. 34.2a, compression shortens the O:H from 0.1767 to 0.1692 nm and meanwhile lengthens the H–O from 0.0974 to 0.1003 nm when the pressure is increased from 1 to 20 GPa. The calculated H–O and O:H distances agree well with the trends reported in [28–30]. The relaxation of each segment, denoted with subscript x , follows the polynomial form, $d_x = d_{x0}[1 + \alpha_x(P - P_0) + \beta_x(P - P_0)^2]$ with $P_0 = 1 \text{ GPa}$:

$$\begin{pmatrix} d_H/0.975 \\ d_L/1.768 \\ V/1.060 \end{pmatrix} = \begin{pmatrix} 1 & +9.510 \times 10^{-4} & +2.893 \times 10^{-5} \\ 1 & -3.477 \times 10^{-4} & -10.280 \times 10^{-5} \\ 1 & -2.380 \times 10^{-2} & +4.700 \times 10^{-4} \end{pmatrix} \begin{pmatrix} P^0 \\ P^1 \\ P^2 \end{pmatrix}. \quad (34.1)$$

Yoshimura et al. [23] measured the V – P curve of ice firstly using the in situ high-pressure and low-temperature synchrotron X-ray diffraction and Raman spectroscopy. Numerical match of calculations to measurements of ice-VIII V – P curves [23] in Fig. 34.2b gives rise to the equation of state $V/V_0 - P$ with $V_0 = 1.06 \text{ cm}^3/\text{kg}$. Numerical simultaneous reproduction of both the $V/V_0 - P$ and the $d_x/d_{x0} - P$ profiles means that the latter decomposes the former with high reliability [31].

Fig. 34.1 Pressure dependence of the frequency of **a** the H–O and **b** the O:H stretching vibrational modes with solid lines as being fitted by a least squares method (reprinted with permission from [23, 24])

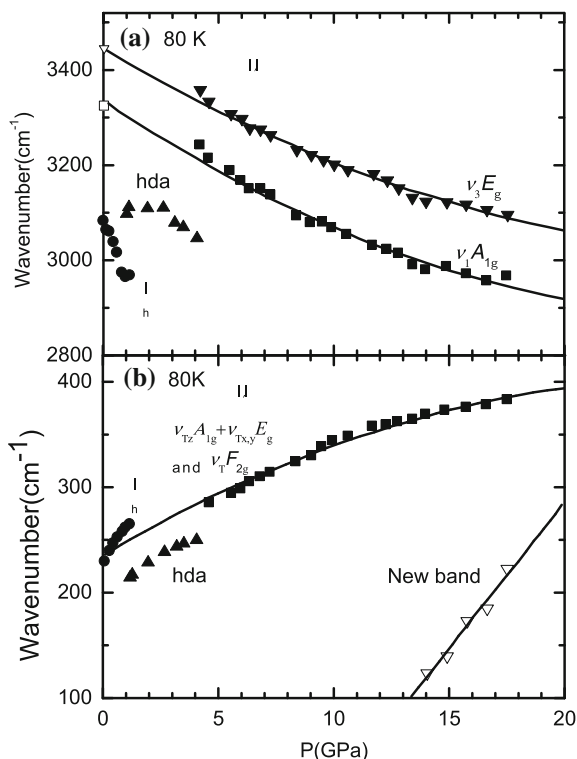


Table 34.1 DFT- and MD-derived segmental lengths (Å), O–O distance (Å), mass density, and the bandgap (eV) of ice as a function of $P = (P' - 1)$ (GPa) with derivative of the equations of states

| P | DFT | | | | MD | | |
|-----|-----------------------------|-------|-------|-------|-------|-------|-----------|
| | ρ (g/cm ³) | d_H | d_L | E_G | d_H | d_L | d_{O-O} |
| 1 | 1.659 | 0.966 | 1.897 | 4.531 | 0.974 | 1.767 | 2.741 |
| 5 | 1.886 | 0.972 | 1.768 | 4.819 | 0.979 | 1.763 | 2.742 |
| 10 | 2.080 | 0.978 | 1.676 | 5.097 | 0.985 | 1.750 | 2.736 |
| 15 | 2.231 | 0.984 | 1.610 | 5.353 | 0.991 | 1.721 | 2.713 |
| 20 | 2.360 | 0.990 | 1.556 | 5.572 | 1.003 | 1.692 | 2.694 |
| 25 | 2.479 | 0.996 | 1.507 | 5.778 | – | – | – |
| 30 | 2.596 | 1.005 | 1.460 | 5.981 | | | |
| 35 | 2.699 | 1.014 | 1.419 | 6.157 | | | |
| 40 | 2.801 | 1.026 | 1.377 | 6.276 | | | |
| 45 | 2.900 | 1.041 | 1.334 | 6.375 | | | |
| 50 | 2.995 | 1.061 | 1.289 | 6.459 | | | |
| 55 | 3.084 | 1.090 | 1.237 | 6.524 | | | |
| 60 | 3.158 | 1.144 | 1.164 | 6.590 | | | |

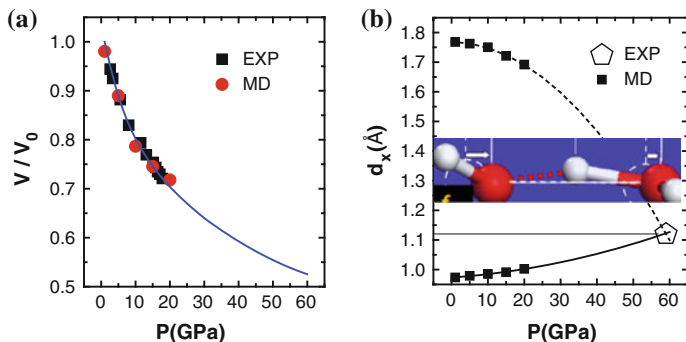


Fig. 34.2 **a** MD reproduction of the measured V - P profiles [23] yields. **b** The asymmetric relaxation of O:H and H-O, which matches the proton centralization occurring under 59 GPa and 0.22 nm [10, 12] (reprinted with permission from [31])

MD results show the general trend of pressure-induced O:H shortening and H-O lengthening. An extrapolation of the MD-derived polynomial expressions leads to the proton symmetrization occurring at 58.6 GPa with the O-O distance of 0.221 nm, which is in good accordance with measurements of 59 GPa and 0.220 nm [10]. Therefore, it is confirmed that the proton symmetrization arises from the pressure-induced asymmetric segmental relaxation.

34.3 Phonon Stiffness Relaxation Dynamics

Figure 34.3 shows that MD-derived phonon relaxation trends agree with Raman and IR measurements of ice-VIII at 80 K [4, 6, 23]. As P increases, the calculated ω_H is softened from 3,520 to 3,320 cm^{-1} and the ω_L is stiffened from 120 to 336 cm^{-1} , disregarding the possible phase change and other supplementary peaks nearby. The pressure-derived cooperative relaxation of the ω_L and the ω_H in both water [25] and ice [4-6] confirms the expectations that the longer and softer O:H becomes shorter and stiffer, while the H-O does the otherwise.

This outcome is consistent with the finding of first principle and quantum Monte Carlo calculations [32] that the contribution to the lattice energy from the vdW intermolecular interaction increases and that from the intramolecular H-bonding decreases with the increase in pressure.

34.4 T_C Depression and H-O Bond Energy E_H

The change in the phase transition temperature, T_C , is proportional to the bond energy (E_x) [1], which follows

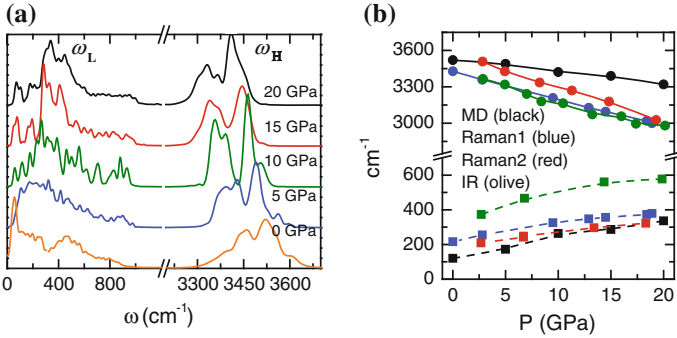
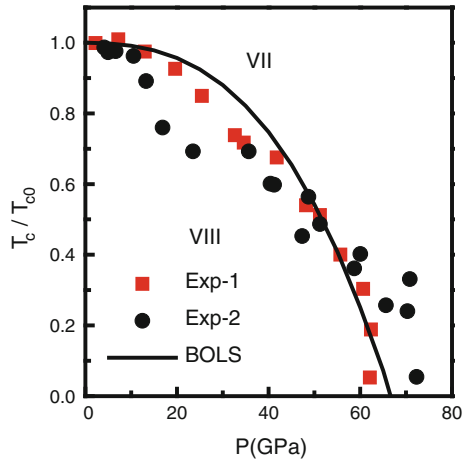


Fig. 34.3 **a** MD-derived ω_H and ω_L relaxation and **b** the P -trend agreement with the Raman and IR measurements for ice-VIII at 80 K [4, 6, 23] as a function of pressure

Fig. 34.4 Equation (34.2) reproduction of the measured (Exp-1, Exp-2) T_C - P data [4–6] confirmed that the H–O bond energy dictates the T_C with derivative of $E_H = 3.97$ eV for ice (reprinted with permission from [31])



$$\frac{\Delta T_C(P)}{T_C(P_0)} = \frac{\Delta E_x(P)}{E_{x0}} = \frac{-\int_{V_0}^V p dv}{E_{H0}} = \frac{-s_0 \int_{P_0}^P p \frac{dd_H}{dp} dp}{E_{H0}} < 0 \tag{34.2}$$

$$\frac{dd_x}{dp} = d_{x0}[\alpha_x + 2\beta_x(P - P_0)]$$

Reproduction of the measured P -dependent T_C for the VII–VIII phase transition [4–6] in Fig. 34.4 justifies that the change in T_C is dominated by the binding energy of the H–O bond, as given in Eq. (34.1), only the H–O bond possesses the positive slope. The binding energy of the lone pair in the 10^{-2} eV level is too low to contribute. The matching leads to an estimation of the real-bond energy of E_H (at 1 GPa) = 3.97 eV by assuming the H–O bond diameter as that of the H atom [33], 0.106 nm.

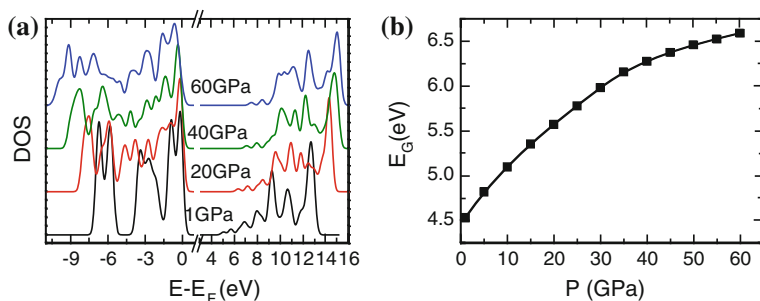


Fig. 34.5 **a** Bandgap expansion of ice-VIII under compression. Compression induced (a) valence DOS entrapment, and conduction DOS polarization results in **b** E_G expansion (reprinted with permission from [31])

34.5 Bandgap Expansion

Compression enlarges the bandgap due to bonding electron entrapment and non-bonding electron polarization. Figure 34.5 shows the DFT-derived evolution of the DOS of ice-VIII with pressure varying from 1 to 60 GPa. The energy shift of the DOS above Fermi level results from polarization by the lone pair and the entrapped core charge, and the energy shift of the valence DOS below E_F arises from the entrapment of the bonding states of oxygen [34, 35]. The bottom edge of the valence band shifts down from -6.7 eV at 1 GPa to -9.2 eV at 60 GPa, while the conduction band shifts up from 5.0 – 12.7 eV at 1 GPa to 7.4 – 15.0 eV at 60 GPa. This E_G enlargement arises from the polarization of the lone pair and entrapment of the valence DOS by compression. The E_G expands further at higher pressure from 4.5 to 6.6 eV, as shown in Fig. 34.5b when the P is increased from 1 to 60 GPa. This fact is consistent with what observed in [36] using first principle calculations and many-body optical absorption spectroscopy. Hermann and Schwerdtfeger [36] showed that the optical UV absorption onset of solid water is blueshifted with increasing pressure almost linearly, making ice more transparent. They attribute this unusual effect to an increase in the Stark shift caused by water's electrostatic environment at smaller volumes.

34.6 Summary

Consistency between MD-derived and measured proton symmetrization [10, 12], low compressibility [23], and phonon relaxation dynamics [4–6] of water ice verified the hypothesis that the weaker O:H bond is highly compressive, yet the stronger H–O bond is elongated because of the resultant force of the compression, the repulsion, and the mechanical disparity within the H-bond. One may conclude

1. Coulomb repulsion between the electron pairs and the mechanical disparity of the segments to compression form the key to the physical anomalies of ice upon compression.
2. The resultant forces of compression, Coulomb repulsion, and the recovery of dislocation of the electron pairs in the respective segment of the H-bond dominate the *P*-derived proton symmetrization, vibration, volume compression, and phase transitional anomalies of ice under compression.
3. The initially longer and softer non-bond becomes shorter and stiffer, but the initially shorter and stronger real bond becomes the otherwise under compression, which is in line with the findings of energy contribution of different segments to the lattice energy [32].
4. Compression stiffens the softer phonons and softens the stiffer phonons as a consequence of the asymmetric relaxation of the bond segments.
5. The pressure-enhanced bandgap expansion evidences the entrapment of the bonding electrons and the polarization of the lone pair electrons upon compression.

References

1. C.Q. Sun, Thermo-mechanical behavior of low-dimensional systems: the local bond average approach. *Prog. Mater. Sci.* **54**(2), 179–307 (2009)
2. D. Errandonea, B. Schwager, R. Ditz, C. Gessmann, R. Boehler, M. Ross, Systematics of transition-metal melting. *Phys. Rev. B* **63**(13), 132104 (2001)
3. Z.W. Chen, C.Q. Sun, Y.C. Zhou, O.Y. Gang, Size dependence of the pressure-induced phase transition in nanocrystals. *J. Phys. Chem. C* **112**(7), 2423–2427 (2008)
4. P. Pruzan, J.C. Chervin, E. Wolanin, B. Canny, M. Gauthier, M. Hanfland, Phase diagram of ice in the VII-VIII-X domain. Vibrational and structural data for strongly compressed ice VIII. *J. Raman. Spec.* **34**(7–8), 591–610 (2003)
5. K. Aoki, H. Yamawaki, M. Sakashita, Observation of Fano interference in high-pressure ice VII. *Phys. Rev. Lett.* **76**(5), 784–786 (1996)
6. M. Song, H. Yamawaki, H. Fujihisa, M. Sakashita, K. Aoki, Infrared absorption study of Fermi resonance and hydrogen-bond symmetrization of ice up to 141 GPa. *Phys. Rev. B* **60**(18), 12644 (1999)
7. G.M. Marion, S.D. Jakubowski, The compressibility of ice to 2.0 kbar. *Cold Reg. Sci. Technol.* **38**(2–3), 211–218 (2004)
8. J. Teixeira, High-pressure physics: the double identity of ice X. *Nature* **392**(6673), 232–233 (1998)
9. P. Loubeyre, R. LeToullec, E. Wolanin, M. Hanfland, D. Husermann, Modulated phases and proton centring in ice observed by X-ray diffraction up to 170 GPa. *Nature* **397**(6719), 503–506 (1999)
10. M. Benoit, D. Marx, M. Parrinello, Tunnelling and zero-point motion in high-pressure ice. *Nature* **392**(6673), 258–261 (1998)
11. W. Holzappel, On the symmetry of the hydrogen bonds in ice VII. *J. Chem. Phys.* **56**(2), 712 (1972)

12. A.F. Goncharov, V.V. Struzhkin, H.-K. Mao, R.J. Hemley, Raman spectroscopy of dense H₂O and the transition to symmetric hydrogen bonds. *Phys. Rev. Lett.* **83**(10), 1998–2001 (1999)
13. A.F. Goncharov, V.V. Struzhkin, M.S. Somayazulu, R.J. Hemley, H.K. Mao, Compression of ice to 210 gigapascals: infrared evidence for a symmetric hydrogen-bonded phase. *Science* **273**(5272), 218–220 (1996)
14. I.A. Ryzhkin, “Symmetrical” phase and collective excitations in the proton system of ice. *J. Exp. Theor. Phys.* **88**(6), 1208–1211 (1999)
15. F.H. Stillinger, K.S. Schweizer, Ice under compression-transition to symmetrical hydrogen-bonds. *J. Phys. Chem.* **87**(21), 4281–4288 (1983)
16. L.N. Tian, A.I. Kolesnikov, J.C. Li, Ab initio simulation of hydrogen bonding in ices under ultra-high pressure. *J. Chem. Phys.* **137**(20) (2012)
17. L. Pauling, The structure and entropy of ice and of other crystals with some randomness of atomic arrangement. *J. Am. Chem. Soc.* **57**, 2680–2684 (1935)
18. W.T. Zheng, C.Q. Sun, Underneath the fascinations of carbon nanotubes and graphene nanoribbons. *Energ. Environ. Sci.* **4**(3), 627–655 (2011)
19. J.W. Li, S.Z. Ma, X.J. Liu, Z.F. Zhou, C.Q. Sun, ZnO meso-mechano-thermo physical chemistry. *Chem. Rev.* **112**(5), 2833–2852 (2012)
20. M.X. Gu, Y.C. Zhou, L.K. Pan, Z. Sun, S.Z. Wang, C.Q. Sun, Temperature dependence of the elastic and vibronic behavior of Si, Ge, and diamond crystals. *J. Appl. Phys.* **102**(8), 083524 (2007)
21. M.X. Gu, L.K. Pan, T.C.A. Yeung, B.K. Tay, C.Q. Sun, Atomistic origin of the thermally driven softening of Raman optical phonons in group III nitrides. *J. Phys. Chem. C* **111**(36), 13606–13610 (2007)
22. C. Yang, Z.F. Zhou, J.W. Li, X.X. Yang, W. Qin, R. Jiang, N.G. Guo, Y. Wang, C.Q. Sun, Correlation between the band gap, elastic modulus, Raman shift and melting point of CdS, ZnS, and CdSe semiconductors and their size dependency. *Nanoscale* **4**, 1304–1307 (2012)
23. Y. Yoshimura, S.T. Stewart, M. Somayazulu, H. Mao, R.J. Hemley, High-pressure x-ray diffraction and Raman spectroscopy of ice VIII. *J. Chem. Phys.* **124**(2), 024502 (2006)
24. Y. Yoshimura, S.T. Stewart, M. Somayazulu, H.K. Mao, R.J. Hemley, Convergent Raman features in high density amorphous ice, ice VII, and ice VIII under pressure. *J. Phys. Chem. B* **115**(14), 3756–3760 (2011)
25. T. Okada, K. Komatsu, T. Kawamoto, T. Yamanaka, H. Kagi, Pressure response of Raman spectra of water and its implication to the change in hydrogen bond interaction. *Spectrochimica Acta A* **61**(10), 2423–2427 (2005)
26. I.V. Stiopkin, C. Weeraman, P.A. Pieniazek, F.Y. Shalhout, J.L. Skinner, A.V. Benderskii, Hydrogen bonding at the water surface revealed by isotopic dilution spectroscopy. *Nature* **474**(7350), 192–195 (2011)
27. F. Mallamace, M. Broccio, C. Corsaro, A. Faraone, D. Majolino, V. Venuti, L. Liu, C.Y. Mou, S.H. Chen, Evidence of the existence of the low-density liquid phase in supercooled, confined water. *Proc. Natl. Acad. Sci. U.S.A.* **104**(2), 424–428 (2007)
28. D. Kang, J. Dai, Y. Hou, J. Yuan, Structure and vibrational spectra of small water clusters from first principles simulations. *J. Chem. Phys.* **133**(1), 014302 (2010)
29. K. Liu, J.D. Cruzan, R.J. Saykally, Water clusters. *Science* **271**(5251), 929–933 (1996)
30. R. Ludwig, Water: from clusters to the bulk. *Angew. Chem. Int. Ed.* **40**(10), 1808–1827 (2001)
31. C.Q. Sun, X. Zhang, W.T. Zheng, Hidden force opposing ice compression. *Chem. Sci.* **3**, 1455–1460 (2012)
32. B. Santra, J. Klimeš, D. Alfè, A. Tkatchenko, B. Slater, A. Michaelides, R. Car, M. Scheffler, Hydrogen bonds and Van der Waals forces in ice at ambient and high pressures. *Phys. Rev. Lett.* **107**(18), 185701 (2011)

33. C.Q. Sun, H.L. Bai, B.K. Tay, S. Li, E.Y. Jiang, Dimension, strength, and chemical and thermal stability of a single C–C bond in carbon nanotubes. *J. Phys. Chem. B* **107**(31), 7544–7546 (2003)
34. C.Q. Sun, Dominance of broken bonds and nonbonding electrons at the nanoscale. *Nanoscale* **2**(10), 1930–1961 (2010)
35. C.Q. Sun, Oxidation electronics: bond-band-barrier correlation and its applications. *Prog. Mater. Sci.* **48**(6), 521–685 (2003)
36. A. Hermann, P. Schwerdtfeger, Blueshifting the onset of optical UV absorption for water under pressure. *Phys. Rev. Lett.* **106**(18), 187403 (2011)

Chapter 35

Molecular Clusters, Skins, and Ultrathin Films

- *Molecular under-coordination effects oppositely to compression.*
- *Spontaneous H–O contraction elongates and polarizes the O:H bond significantly via inter electron-pair repulsion.*
- *Under-coordinated H₂O molecules shrink in size but enlarge their separation.*
- *The shortening of the H–O bond entraps bonding electrons and raises the local density, which in turn polarizes the lone pairs of electrons on oxygen.*
- *The stiffening of the shortened H–O bond increases the magnitude of the O 1s shift, causes the blueshift of the H–O phonon frequencies, and elevates the T_m of molecular clusters and ultrathin films of water, which gives rise to their supersolid phase of elastic, hydrophobic, ice-like, polarized with ultra-low-density.*

35.1 Observations

Under-coordinated water molecules refer to those with fewer than the ideal four neighbors as in the bulk of water [1–4]. They occur in terminated H-bonded networks, in the skin of a large volume of water, in the hydration shell, and in the gaseous state. Such under-coordinated water molecules exhibit even more fascinating behavior than those fully coordinated ones [1, 5–12]. For instances, water droplets encapsulated in hydrophobic nanopores [13, 14] and ultrathin water films on graphite, silica, and selected metals [7, 15–22], behave like ice at room temperature, i.e., they melt at a temperature higher than the T_m (273 K) of water in bulk (monolayer ice melts at 325 K) [23]. Encapsulated in hydrophilic nanopores [24, 25] or wetting with hydrophilic topologic configurations [26], water molecules perform oppositely. (Empirically, the T_m is the temperature at which the vibration amplitude of an atom is increased abruptly to more than 3 % of its diameter irrespective of cluster size) [27, 28].

Figure 35.1a shows that molecular under-coordination enlarges the O 1s shift. The O 1s level is 536.6 eV in the bulk of water [29], 538.1 eV in the skin of water,

and 539.8 eV in gaseous molecules that do not have O:H bond at all [30, 31]. The energy for dissociating an $(\text{H}_2\text{O})_N$ cluster into $(\text{H}_2\text{O})_N + \text{H}_2\text{O}$ (Fig. 35.1b) [32] also increases upon the cluster size being reduced to a trimer.

On the other hand, an ultrafast liquid-jet UPS [33], shown in Fig. 35.2, resolved the bound (vertical binding as an equivalent of work function) energies of 1.6 and 3.3 eV for solvated electrons at the water skin and in the bulk solution, respectively. The bound energy decreases with the number of water molecules, indicating the size-induced strong polarization [34].

The CN loss of water molecules shifts the H–O phonon frequency (ω_{H}) of bulk water toward higher frequencies. The ω_{H} phonon frequency has a peak centered at $3,200\text{ cm}^{-1}$ for the bulk of water, $3,450\text{ cm}^{-1}$ for the skins of water and ice [35], and $3,650\text{ cm}^{-1}$ for gaseous molecules [36–38]. The ω_{H} shifts from $3,200$ to $3,650\text{ cm}^{-1}$ when the N of the $(\text{H}_2\text{O})_N$ drops from 6 to 1 (Fig. 35.3) [38, 39]. The ω_{H} increases from $3,420$ to $3,650\text{ cm}^{-1}$ when the surface water molecules turn to be gaseous molecules [40]. IR measurements [38, 41] revealed that the ω_{H} shifts from $3,225$, $3,350$, $3,380$ to $3,525\text{ cm}^{-1}$ when N drops from 6, 5, 4 to 3 of $(\text{H}_2\text{O})_N$ encapsulated in inert matrices. The frequencies change slightly by $5\text{--}10\text{ cm}^{-1}$ when the clusters are capsuled in Ke and Ar matrices [41]. Figure 35.3b also shows that the size stiffening of ω_{H} happens to large clusters [37]. When the N is reduced from 475 to 85, the ω_{H} transits from the $3,200\text{ cm}^{-1}$ component dominance to the $3,450\text{ cm}^{-1}$ component dominance [42]. The high frequency at $\sim 3,700\text{ cm}^{-1}$ arises from the dangling H–O bonds with charge transportation [12] at skins of water and ice [43].

Cluster size-reduction-induced O1s energy entrapment, valance charge polarization, cohesive energy enhancement, and ω_{H} stiffening, as discussed above, are associated with molecular volume expansion [5, 46–49], charge entrapment [8, 50–52], charge densification [9, 10, 33, 51, 53, 54], etc. The intermolecular O–O distance expands by 5.9 % at the liquid water surface, in contrast to liquid methanol for which there is a 4.6 % contraction [49]. In addition, the volume of water molecules confined to 5.1 and 2.8 nm TiO_2 pores increases by 4 and 7.5 %, respectively, with respect to that in the bulk [55]. More interestingly, a monolayer film of water at room temperature manifests ‘quasi-solid’ and hydrophobic nature that prevents the monolayer water from being wetted by a water droplet [21, 56].

The rate of the pressure-driven water flow through carbon nanotubes is high orders in magnitude, faster than would be predicted from conventional fluid-flow theory [57]. The thinner of the channel diameter is, the faster the flow rate of the fluid will be [58, 59]. An air gap of 0.5–1.0 nm thick exists between the water droplet and the hydrophobic substrates [60]. The gap increases with the contact angle of the droplet. Such abnormal super-hydrophobicity, lubricity, fluidity, and solidity at contacting interfaces has been shown to arise from the Coulomb repulsion between the ‘dipoles locked in the elastic solid skins or the solid-like covering sheets of liquid droplets’ [61]. According to the BOLS notation, the local energy densification stiffens the skin and the densely and tightly entrapped bonding charges polarize nonbonding electrons to form anchored skin dipoles.

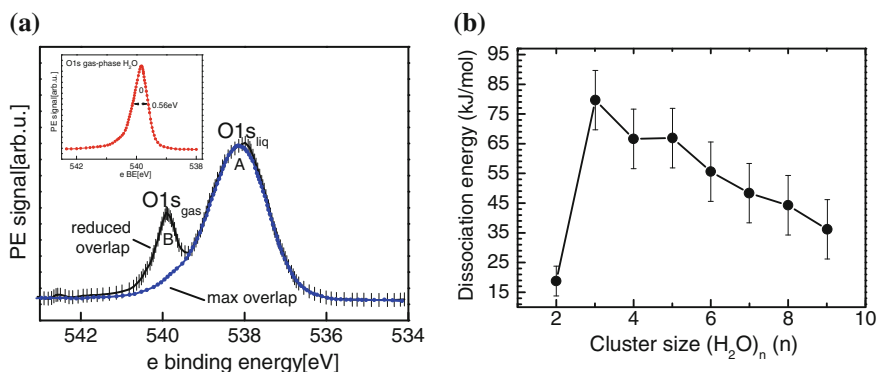


Fig. 35.1 XPS O 1s spectra of (a, left) liquid water contain emission from the liquid phase (peak A at 538.1 eV) and gas phase (peak B and inset at 539.9 eV) (Reprinted with permission from [29]). (b, right) Energy required for dissociating $(\text{H}_2\text{O})_N \rightarrow (\text{H}_2\text{O})_{N-1} + \text{H}_2\text{O}$ (1 kJ/mol = 0.02 eV/molecule) (Reprinted with permission from [32])

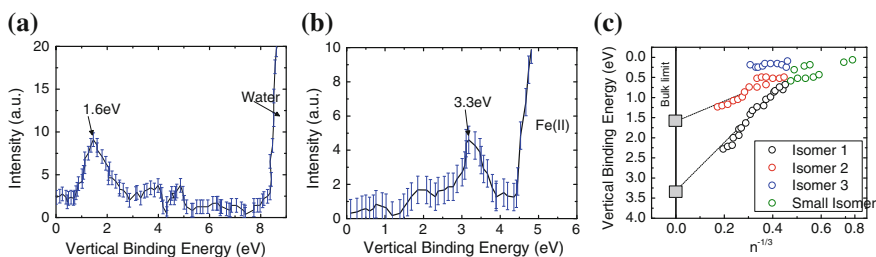


Fig. 35.2 Under-coordination-induced molecular polarization (Reprint with permission from [33]). Vertical binding energy (work function) for solvated electrons (as probe) was measured as a 1.6 eV at surface and b 3.3 eV in the bulk of liquid water. c The binding energy reduces further with the number of molecules in water clusters

35.2 O:H and H-O Length Cooperativity

The slight shortening of the H-O covalent bond and the significant lengthening of the O:H interaction result in the O:H-O bond lengthening and molecular volume expansion. Further polarization and an increase in the elasticity and viscosity of the molecules take place. For a molecular cluster of a given size, the BOLS-NEP effect becomes more significant as one moves away from the center. The smaller the molecular cluster, the stronger the BOLS-NEP effect will be, because of the higher fraction of under-coordinated molecules. Therefore, molecular clusters, ultrathin films, hydration shells, and the skin of the bulk of water could form an ice-like, low-density phase that is stiffer, hydrophobic, and thermally more stable compared with the bulk liquid.

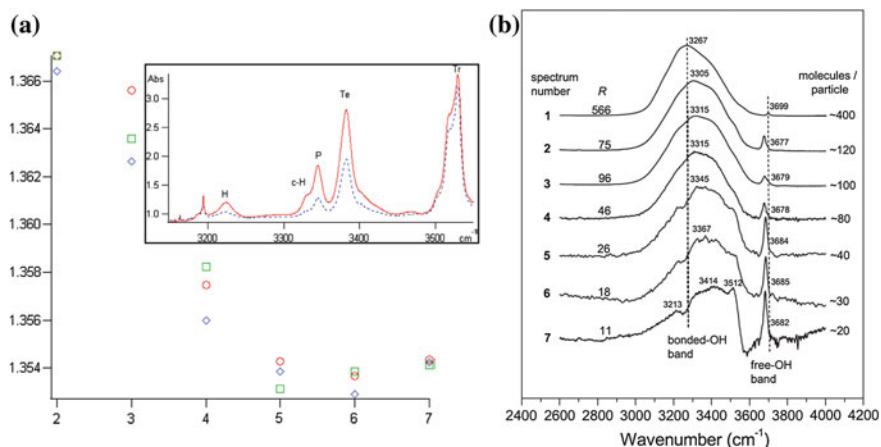


Fig. 35.3 Cluster size dependence of the ω_H of **a** (in the frequency ratio of OH/OD), and **b** large clusters (Reprinted with permission from [37]). Indicated (2) corresponds to dimer [44], (3, Tr) to trimer [45], (4, Te) to tetramer, (5, P) to pentamer, (6, c-H) to cyclic hexamer, (7, H) to cage hexamer, (red circles) to He matrix, (green squares) to Ar matrix, (blue diamonds) to p-H₂ measured at 2.8 K (Reprinted with permission from [38]). Inset denotes the absolute sharp shifts. Size-reduction stiffens the H–O bonds with little disturbance of the free H–O bonds at 3,700 cm⁻¹ that corresponded to arising from surface pre-melting

Figure 35.4 and Table 35.1 compare the segment lengths of the O:H–O bond as a function of (H₂O)_{*N*} cluster size (*N*) optimized using the PW [62] and the OBS [63] algorithms in DFT computations [34]. OBS considered dispersion correction with inclusion of the vdW or H-bond interactions. Results are in accordance with those reported in refs [1, 4]. Comparison of results derived from different methods confirms that: (1) molecular CN-reduction shortens the H–O bond and lengthens the O:H, and (2) the shortening (lengthening) of the H–O bond is always coupled with the lengthening (shortening) of the O:H, which is independent of the algorithm used.

As the *N* is reduced from 24 (an approximation of the number of molecules in bulk water) to two (a dimer), the H–O bond contracts by 4 % from 0.101 to 0.097 nm and the O:H bond expands by 17 % from 0.158 to 0.185 nm, according to the OBS derivatives. This cooperative relaxation gives a 13 % expansion of O–O distance, which is a significant amount for the dimer. The O:H–O bond angle-length profiles over the size range of concern are nonmonotonic because of different effective CNs in different structure configurations. The monotonic O:H and H–O relaxation profiles for $N \leq 6$ will be discussed in the subsequent sections without influencing the generality of conclusions.

Fig. 35.4 Cluster size dependence of the segmental lengths in the $(\text{H}_2\text{O})_N$ clusters optimized using the PW [62] and the OBS [63] methods. $N = 6$ gives the three ‘cage,’ ‘book,’ and ‘prism’ hexamer structures, all with nearly identical binding energy (Reprinted with permission from [11]). See appendix A4-2 for the optimal $(\text{H}_2\text{O})_N$ configurations

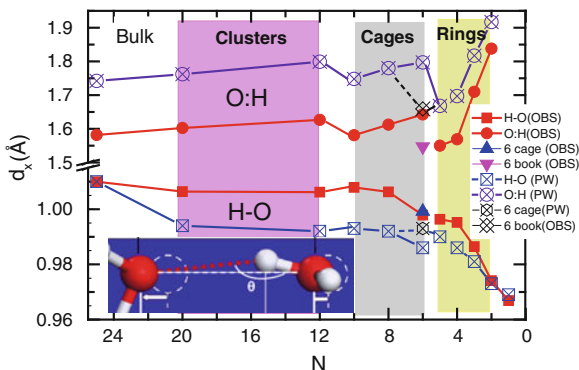


Table 35.1 DFT-derived segmental length, d_H , d_L , and respective contraction/elongation coefficient, C_H , C_L , total electronic binding energy, E_{Bind} ($-\text{eV}$), and the segmental bond energy, E_H and E_L , of $(\text{H}_2\text{O})_N$ clusters*

| | N | d_H | C_H | d_L | C_L | θ | $L_{\text{O-O}}$ | E_{Bind} | E_H | E_L |
|----------|-----|-------|-------|-------|-------|----------|------------------|-------------------|--------|--------|
| Monomer | 1 | 0.969 | 0.959 | | | | | 10.4504 | 5.2252 | – |
| Dimer | 2 | 0.973 | 0.963 | 1.917 | 1.100 | 163.6 | 2.864 | 21.0654 | 5.2250 | 0.1652 |
| Trimer | 3 | 0.981 | 0.971 | 1.817 | 1.043 | 153.4 | 2.730 | 31.8514 | 5.2238 | 0.1696 |
| Tetramer | 4 | 0.986 | 0.976 | 1.697 | 0.974 | 169.3 | 2.672 | 42.4766 | 5.2223 | 0.1745 |
| Pentamer | 5 | 0.987 | 0.977 | 1.668 | 0.958 | 177.3 | 2.654 | 53.1431 | 5.2208 | 0.1870 |
| Book | 6 | 0.993 | 0.983 | 1.659 | 0.952 | 168.6 | 2.640 | 63.8453 | 5.2194 | 0.2020 |
| Cages | 6 | 0.988 | 0.978 | 1.797 | 1.032 | 160.4 | 2.748 | – | – | – |
| | 8 | 0.992 | 0.982 | 1.780 | 1.022 | 163.6 | 2.746 | – | – | – |
| | 10 | 0.993 | 0.983 | 1.748 | 1.003 | 167.0 | 2.725 | – | – | – |
| Clusters | 12 | 0.992 | 0.982 | 1.799 | 1.033 | 161.7 | 2.758 | – | – | – |
| | 20 | 0.994 | 0.984 | 1.762 | 1.011 | 165.4 | 2.735 | – | – | – |
| Bulk | Ih | 1.010 | 1.000 | 1.742 | 1.000 | | | | | |

* While the total energy of a cluster is in principle the total energy required to excite all the electrons to vacuum level; the binding energy E_{Bind} is the energy to combine atoms together to make a cluster: $E_{\text{Bind}} = E_{\text{cluster}} - \sum E_{\text{atom}} = \sum E_{\text{bond}}$. For $N = 1$, there are two H–O bonds and no O:H bond to contribute to the binding energy. Thus, the H–O bond energy is a half of E_{Bind} : $E_H(1) = E_{\text{Bind}}(1)/2$. For $N = 2-6$, H–O bond energy can be described as: $E_H(N) = E_H(1) - \alpha(L_H(N) - L_H(1))^2$, where α is the elastic constant, 10

35.3 Phonon Cooperative Relaxation

Figure 35.5a shows the cluster size dependence of the vibration spectra of $(\text{H}_2\text{O})_N$ with respect to that of ice Ih phase. As expected, N reduction stiffens the ω_H and meanwhile softens the softer ω_L from 250 to 170 as the water turns to be dimers. The $\angle\text{O:H-O}$ bending mode ω_{B1} ($400-1,000 \text{ cm}^{-1}$) shifts slightly, but the $\angle\text{H-O-H}$ bending mode ω_{B2} ($\sim 1,600 \text{ cm}^{-1}$) remains silent [64].

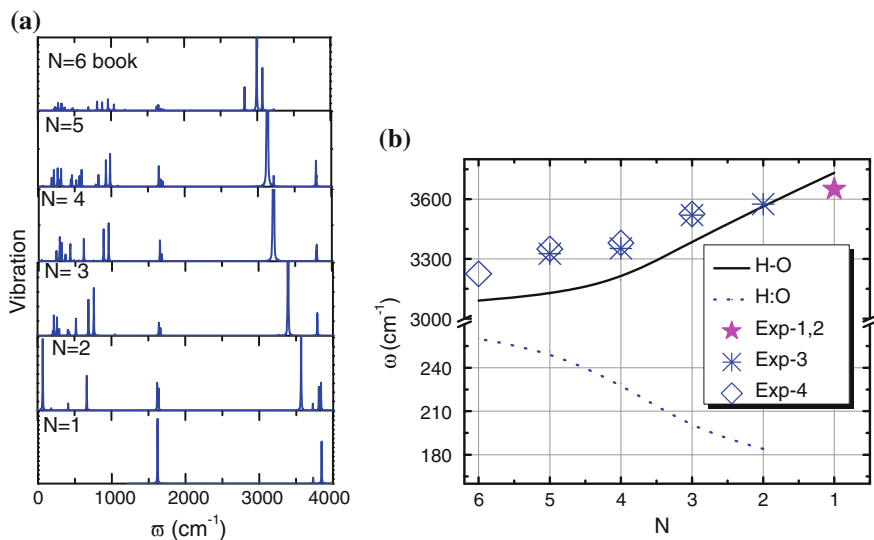


Fig. 35.5 Size dependence of $(\text{H}_2\text{O})_N$ clusters ($N \leq 6$) **a** phonon relaxation (Reprinted with permission from [34]). **b** The calculated (solid line) ω_{H} blueshift has a similar trend as the measured frequencies (scattered data) of the H–O phonons of $(\text{H}_2\text{O})_N$, shown as Exp-1 [40], Exp-2 [39], Exp-3 [38], and Exp-4 [41]. Measurements of the ω_{L} redshift are not presently available due to experimental sensitivity limitations

The trend of ω_{H} stiffening in Fig. 35.5b is consistent with experimental measurements (Fig. 35.3). For instances, the ω_{H} is stiffened from 3,200 to 3,650 cm^{-1} when water cluster $(\text{H}_2\text{O})_N$ drops from $N = 6$ to 1 [39] and from 3,420 to 3,650 cm^{-1} when the water (surface) becomes gaseous molecules [40]. IR measurements [38, 41] revealed that the ω_{H} shifts from 3,225, 3,350, 3,380 to 3,525 cm^{-1} when N drops from 6, 5, 4 to 3 of $(\text{H}_2\text{O})_N$ encapsulated in inert matrices. When the ice cluster reduces from 475 to 85 molecules, the ω_{H} transits from 3,200 dominance to 3,500 cm^{-1} [42], suggesting the shortening the real bond and stiffening the ω_{H} phonons when the cluster size is reduced. Coordination-reduction also stiffens the ω_{H} for $\text{H}^+(\text{H}_2\text{O})_N$ ($n = 20 - 200$) [65].

35.4 Volume Expansion and Viscosity Elevation

Figure 35.6a plots the N -dependence of the O–O distance derived from Fig. 35.4. The O–O distance expands by 8 %, when the N is reduced from 20 to 3, which is compatible to the value of 5.9 % measured in the water surface at 25 °C [49]. Polarization enhancement of the under-coordinated water molecules [1, 66] is related to the O–O distance because of the charge conservation of the molecules. As it has been discovered [33], the dissociation energy for an electron in solution

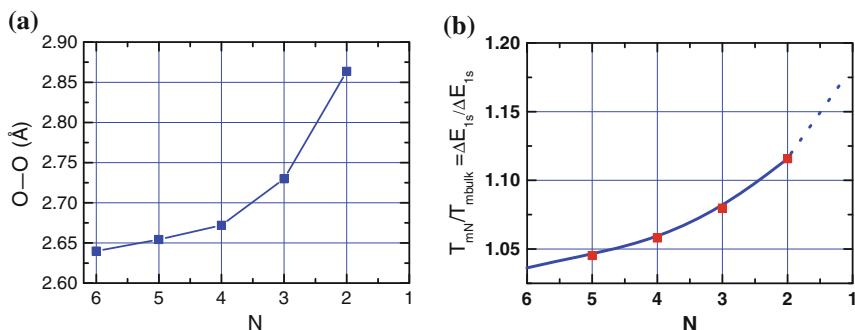


Fig. 35.6 N -dependence of **a** the O–O distance, **b** the melting point, T_{mN} , (to $N = 2$ for dimers) and the O 1s core-level shift (to $N = 1$ for gas monomers) of $(\text{H}_2\text{O})_N$ clusters based on DFT derived d_{HN}/d_{HB} values in table (Reprinted with permission from [34])

changes from a bulk value of 3.3 to 1.6 eV at the water surface. The dissociation energy, as a proxy of work function and surface polarization, decreases further with molecule cluster size. These findings verify BOLS-NEP predictions on the under-coordination-induced volume expansion and polarization of water molecules.

The polarization of molecules caused by both under-coordination and inter-electron-pair repulsion enhances the elasticity and the viscosity of the skin of water, which is generally proportional to the curvature of the interatomic potentials. The high elasticity and the high density of surface dipoles form the essential conditions for the hydrophobicity of a contacting interface [67]. It is now clear why the monolayer film of water is hydrophobic [21].

Figure 35.6b shows the anticipated T_{mN} elevation and ΔE_{1sN} enhancement, which are correlated by: $T_{mN}/T_{mBulk} = \Delta E_{1sN}/\Delta E_{1sBulk} = (d_{HN}/d_{HBulk})^{-m} = C_H^{-4}$ ($m = 4$ for the real bond in H_2O [68]). Table 35.1 indicates that when the N is reduced from infinitely large to 5 and 2, the T_m will increase by 4.4 % to 285 ($N = 5$) and 12 % to 305 K ($N = 2$). This trend explains why the molecular clusters, surface skins, and ultrathin films of water are glue- or ice-like at the ambient. Water manifests high-viscosity or ‘quasi-solid’ nature when it is cooled approaching T_m . Generally, the viscosity of water reaches its maximum at $T \sim T_m$ [69]. Agreement in the predictions and observations suggests that a liquid layer could hardly form on ice surfaces. Surfaces [70] and point defects [71] also raise the melting point of ice.

35.5 Entrapment and Polarization

The strengthening of the H–O bond is associated with the interatomic potential well depression, which shifts the E_{1sN} from that of an isolated O atom $E_{1s}(0)$ in the form of [68]:

$$E_{1sN} = E_{1s(0)} + (E_{1sBulk} - E_{1s(0)})C_H^{-4}.$$

The bind energy is expected to be entrapped by further 20 % or more if the bulk water turns to be monomers. Measurements revealed that the O 1s binding energy shifts from 538.1 to 539.7 eV when water turns to be a collection of monomers (Fig. 35.1a) [30, 31]. Such a binding energy entrapment is associated with increase in the $(H_2O)_N \rightarrow (H_2O)_N + H_2O$ dissociation energy (Fig. 35.1b) [32] upon the cluster size being reduced. The E_{1s} shifts from 538.2 to 538.6 eV when the water cluster size is reduced from $N = 200 - 40$ and up to 539.8 eV for the free water molecules [30, 72]. The E_{1s} of water skin is dominated by a main peak centered at 538.1 eV with an ice bulk satellite at 536.6 eV with respect to the peak at 539.9 eV for gaseous phase [29]. The densely and locally entrapped core electrons will polarize the nonbonding electrons, and hence, the molecular clusters, surface skins, and ultrathin films will demonstrate the strong polarization nature.

35.6 Summary

Thus, a hybridization of the H–O bond contraction [68, 73, 74], local entrapment and polarization [75, 76], and the segmented H-bond relaxation [77] clarify the anomalous behavior of water molecules with fewer than four neighbors. This exercise also reconciled the anomalies of O–O expansion, O 1s electron densification and entrapment, surface electron polarization, high-frequency phonon stiffening, and the ice-like and hydrophobic nature of such under-coordinated water molecules. Agreement between numerical calculations and experimental observations validated the following hypothesis and predictions:

1. Under-coordination-induced H–O bond contraction and interelectron-pair repulsion-driven O:H elongation dictate the unusual behavior of water molecules in the nanoscale O:H–O networks and in the skin of water.
2. The shortening of the H–O bond raises the density of the core and bonding electrons in the under-coordinated molecules, which in turn polarizes the nonbonding electron lone pairs on oxygen.
3. The stiffening of the H–O bond increases the O 1s core-level shift, causes the blueshift of the H–O phonon frequency, and elevates the melting point of water molecular clusters, surface skins, and ultrathin films of water.
4. Under-coordinated water molecules could form an ice-like, low-density phase that is hydrophobic, stiffer, and thermally more stable than the bulk water [5, 6].

References

1. J.K. Gregory, D.C. Clary, K. Liu, M.G. Brown, R.J. Saykally, The water dipole moment in water clusters. *Science* **275**(5301), 814–817 (1997)
2. T.D. Kuhne, R.Z. Khaliullin, Electronic signature of the instantaneous asymmetry in the first coordination shell of liquid water. *Nat. commun.* **4**, 1450 (2013)
3. V. Petkov, Y. Ren, M. Suhomel, Molecular arrangement in water: random but not quite. *J. Phys. Condens. Matter* **24**(15), 155102 (2012)
4. F.N. Keutsch, R.J. Saykally, Water clusters: untangling the mysteries of the liquid, one molecule at a time. *PNAS* **98**(19), 10533–10540 (2001)
5. K. Liu, J.D. Cruzan, R.J. Saykally, Water clusters. *Science* **271**(5251), 929–933 (1996)
6. R. Ludwig, Water: from clusters to the bulk. *Angew. Chem. Int. Ed.* **40**(10), 1808–1827 (2001)
7. A. Michaelides, K. Morgenstern, Ice nanoclusters at hydrophobic metal surfaces. *Nat. Mater.* **6**(8), 597–601 (2007)
8. L. Turi, W.S. Sheu, P.J. Rossky, Characterization of excess electrons in water-cluster anions by quantum simulations. *Science* **309**(5736), 914–917 (2005)
9. J.R.R. Verlet, A.E. Bragg, A. Kammrath, O. Cheshnovsky, D.M. Neumark, Observation of large water-cluster anions with surface-bound excess electrons. *Science* **307**(5706), 93–96 (2005)
10. N.I. Hammer, J.W. Shin, J.M. Headrick, E.G. Diken, J.R. Roscioli, G.H. Weddle, M.A. Johnson, How do small water clusters bind an excess electron? *Science* **306**(5696), 675–679 (2004)
11. C. Perez, M.T. Muckle, D.P. Zaleski, N.A. Seifert, B. Temelso, G.C. Shields, Z. Kisiel, B.H. Pate, Structures of cage, prism, and book isomers of water hexamer from broadband rotational spectroscopy. *Science* **336**(6083), 897–901 (2012)
12. T. Ishiyama, H. Takahashi, A. Morita, Origin of vibrational spectroscopic response at ice surface. *J. Phys. Chem. Lett.* **3**, 3001–3006 (2012)
13. M.L. Lakhnani, B.R. Puri, Boiling point of capillary-condensed water. *Nature* **172**(4385), 917–917 (1953)
14. L. Li, Y. Kazoe, K. Mawatari, Y. Sugii, T. Kitamori, Viscosity and wetting property of water confined in extended nanospace simultaneously measured from highly-pressurized meniscus motion. *J. Phys. Chem. Lett.* **3**(17), 2447–2452 (2012)
15. A. Hodgson, S. Haq, Water adsorption and the wetting of metal surfaces. *Surf. Sci. Rep.* **64**(9), 381–451 (2009)
16. K. Xu, P.G. Cao, J.R. Heath, Graphene visualizes the first water adlayers on mica at ambient conditions. *Science* **329**(5996), 1188–1191 (2010)
17. D. Xu, K.M. Liechti, K. Ravi-Chandar, Mechanical probing of icelike water monolayers. *Langmuir* **25**(22), 12870–12873 (2009)
18. P.B. Miranda, L. Xu, Y.R. Shen, M. Salmeron, Icelike water monolayer adsorbed on mica at room temperature. *Phys. Rev. Lett.* **81**(26), 5876–5879 (1998)
19. F. McBride, G.R. Darling, K. Pussi, A. Hodgson, Tailoring the structure of water at a metal surface: a structural analysis of the water bilayer formed on an alloy template. *Phys. Rev. Lett.* **106**(22), 226101 (2011)
20. S. Meng, E.G. Wang, S.W. Gao, Water adsorption on metal surfaces: a general picture from density functional theory studies. *Phys. Rev. B* **69**(19), 195404 (2004)
21. C. Wang, H. Lu, Z. Wang, P. Xiu, B. Zhou, G. Zuo, R. Wan, J. Hu, H. Fang, Stable liquid water droplet on a water monolayer formed at room temperature on ionic model substrates. *Phys. Rev. Lett.* **103**(13), 137801–137804 (2009)
22. J.C. Johnston, N. Kastelowitz, V. Molinero, Liquid to quasicrystal transition in bilayer water. *J. Chem. Phys.* **133**(15) (2010)
23. H. Qiu, W. Guo, Electromelting of confined monolayer ice. *Phys. Rev. Lett.* **110**(19), 195701 (2013)

24. F.G. Alabarse, J. Haines, O. Cambon, C. Levelut, D. Bourgoigne, A. Haidoux, D. Granier, B. Coasne, Freezing of water confined at the nanoscale. *Phys. Rev. Lett.* **109**(3), 035701 (2012)
25. E.B. Moore, E. de la Llave, K. Welke, D.A. Scherlis, V. Molinero, Freezing, melting and structure of ice in a hydrophilic nanopore. *PCCP* **12**(16), 4124–4134 (2010)
26. Q. Yuan, Y.P. Zhao, Topology-dominated dynamic wetting of the precursor chain in a hydrophilic interior corner. *Proc. Roy. Soc. A: Math. Phys. Eng. Sci.* **468**(2138), 310–322 (2011)
27. M.A. Omar, *Elementary Solid State Physics: Principles and Applications* (Addison-Wesley, New York, 1993)
28. F.A. Lindemann, The calculation of molecular natural frequencies. *Physikalische Zeitschrift* **11**, 609–612 (1910)
29. B. Winter, E.F. Aziz, U. Hergenahn, M. Faubel, I.V. Hertel, Hydrogen bonds in liquid water studied by photoelectron spectroscopy. *J. Chem. Phys.* **126**(12), 124504 (2007)
30. M. Abu-Samaha, K.J. Borve, M. Winkler, J. Harnes, L.J. Saethre, A. Lindblad, H. Bergersen, G. Ohrwall, O. Bjornholm, S. Svensson, The local structure of small water clusters: imprints on the core-level photoelectron spectrum. *J. Phys. B* **42**(5), 055201 (2009)
31. K. Nishizawa, N. Kurahashi, K. Sekiguchi, T. Mizuno, Y. Ogi, T. Horio, M. Oura, N. Kosugi, T. Suzuki, High-resolution soft X-ray photoelectron spectroscopy of liquid water. *PCCP* **13**, 413–417 (2011)
32. L. Belau, K.R. Wilson, S.R. Leone, M. Ahmed, Vacuum ultraviolet (VUV) photoionization of small water clusters. *J. Phys. Chem. A* **111**(40), 10075–10083 (2007)
33. K.R. Siefermann, Y. Liu, E. Lugovoy, O. Link, M. Faubel, U. Buck, B. Winter, B. Abel, Binding energies, lifetimes and implications of bulk and interface solvated electrons in water. *Nat. Chem.* **2**, 274–279 (2010)
34. C.Q. Sun, X. Zhang, J. Zhou, Y. Huang, Y. Zhou, W. Zheng, Density, elasticity, and stability anomalies of water molecules with fewer than four neighbors. *J. Phys. Chem. Lett.* **4**, 2565–2570 (2013)
35. T.F. Kahan, J.P. Reid, D.J. Donaldson, Spectroscopic probes of the quasi-liquid layer on ice. *J. Phys. Chem. A* **111**(43), 11006–11012 (2007)
36. Y.R. Shen, V. Ostroverkhov, Sum-frequency vibrational spectroscopy on water interfaces: polar orientation of water molecules at interfaces. *Chem. Rev.* **106**(4), 1140–1154 (2006)
37. V. Buch, S. Bauerecker, J.P. Devlin, U. Buck, J.K. Kazimirski, Solid water clusters in the size range of tens-thousands of H₂O: a combined computational/spectroscopic outlook. *Int. Rev. Phys. Chem.* **23**(3), 375–433 (2004)
38. J. Ceponkus, P. Uvdal, B. Nelander, Water tetramer, pentamer, and hexamer in inert matrices. *J. Phys. Chem. A* **116**(20), 4842–4850 (2012)
39. Q. Sun, The Raman OH stretching bands of liquid water. *Vib. Spectrosc.* **51**(2), 213–217 (2009)
40. P.C. Cross, J. Burnham, P.A. Leighton, The Raman spectrum and the structure of water. *J. Am. Chem. Soc.* **59**, 1134–1147 (1937)
41. S. Hirabayashi, K.M.T. Yamada, Infrared spectra and structure of water clusters trapped in argon and krypton matrices. *J. Mol. Struct.* **795**(1–3), 78–83 (2006)
42. C.C. Pradzynski, R.M. Forck, T. Zeuch, P. Slavicek, U. Buck, A fully size-resolved perspective on the crystallization of water clusters. *Science* **337**(6101), 1529–1532 (2012)
43. X. Wei, P. Miranda, Y. Shen, Surface vibrational spectroscopic study of surface melting of ice. *Phys. Rev. Lett.* **86**(8), 1554–1557 (2001)
44. J. Ceponkus, P. Uvdal, B. Nelander, Intermolecular vibrations of different isotopologs of the water dimer: experiments and density functional theory calculations. *J. Chem. Phys.* **129**(19), 194306 (2008)
45. J. Ceponkus, P. Uvdal, B. Nelander, On the structure of the matrix isolated water trimer. *J. Chem. Phys.* **134**(6), 064309 (2011)
46. A. Lenz, L. Ojamae, A theoretical study of water equilibria: the cluster distribution versus temperature and pressure for (H₂O)(n), n = 1–60, and ice. *J. Chem. Phys.* **131**(13), 134302 (2009)

47. M. Abu-Samaha, K.J. Borve, Surface relaxation in water clusters: evidence from theoretical analysis of the oxygen 1 s photoelectron spectrum. *J. Chem. Phys.* **128**(15), 154710 (2008)
48. K.R. Wilson, B.S. Rude, T. Catalano, R.D. Schaller, J.G. Tobin, D.T. Co, R.J. Saykally, X-ray spectroscopy of liquid water microjets. *J. Phys. Chem. B* **105**(17), 3346–3349 (2001)
49. K.R. Wilson, R.D. Schaller, D.T. Co, R.J. Saykally, B.S. Rude, T. Catalano, J.D. Bozek, Surface relaxation in liquid water and methanol studied by x-ray absorption spectroscopy. *J. Chem. Phys.* **117**(16), 7738–7744 (2002)
50. R. Vacha, O. Marsalek, A.P. Willard, D.J. Bonthuis, R.R. Netz, P. Jungwirth, Charge transfer between water molecules as the possible origin of the observed charging at the surface of pure water. *J. Phys. Chem. Lett.* **3**(1), 107–111 (2012)
51. O. Marsalek, F. Uhlig, T. Frigato, B. Schmidt, P. Jungwirth, Dynamics of electron localization in warm versus cold water clusters. *Phys. Rev. Lett.* **105**(4), 043002 (2010)
52. F. Baletto, C. Cavazzoni, S. Scandolo, Surface trapped excess electrons on ice. *Phys. Rev. Lett.* **95**(17), 176801 (2005)
53. S. Liu, J. Luo, G. Xie, D. Guo, Effect of surface charge on water film nanoconfined between hydrophilic solid surfaces. *J. Appl. Phys.* **105**(12), 124301–124304 (2009)
54. D.H. Paik, I.R. Lee, D.S. Yang, J.S. Baskin, A.H. Zewail, Electrons in finite-sized water cavities: hydration dynamics observed in real time. *Science* **306**(5696), 672–675 (2004)
55. E.G. Solveyra, E. de la Llave, V. Molinero, G. Soler-Illia, D.A. Scherlis, Structure, dynamics, and phase behavior of water in TiO₂ nanopores. *J. Chem. Phys. C* **117**(7), 3330–3342 (2013)
56. M. James, T.A. Darwish, S. Ciampi, S.O. Sylvester, Z.M. Zhang, A. Ng, J.J. Gooding, T.L. Hanley, Nanoscale condensation of water on self-assembled monolayers. *Soft Matter* **7**(11), 5309–5318 (2011)
57. J.A. Thomas, A.J.H. McGaughey, Reassessing fast water transport through carbon nanotubes. *Nano Lett.* **8**(9), 2788–2793 (2008)
58. M. Whitby, L. Cagnon, M. Thanou, N. Quirke, Enhanced fluid flow through nanoscale carbon pipes. *Nano Lett.* **8**(9), 2632–2637 (2008)
59. X.C. Qin, Q.Z. Yuan, Y.P. Zhao, S.B. Xie, Z.F. Liu, Measurement of the rate of water translocation through carbon nanotubes. *Nano Lett.* **11**(5), 2173–2177 (2011)
60. A. Uysal, M. Chu, B. Stripe, A. Timalisina, S. Chattopadhyay, C.M. Schlepütz, T.J. Marks, P. Dutta, What x rays can tell us about the interfacial profile of water near hydrophobic surfaces. *Phys. Rev. B* **88**(3), 035431 (2013)
61. C.Q. Sun, Y. Sun, Y.G. Ni, X. Zhang, J.S. Pan, X.H. Wang, J. Zhou, L.T. Li, W.T. Zheng, S.S. Yu, L.K. Pan, Z. Sun, Coulomb repulsion at the nanometer-sized contact: a force driving superhydrophobicity, superfluidity, superlubricity, and supersolidity. *J. Chem. Phys. C* **113**(46), 20009–20019 (2009)
62. J.P. Perdew, Y. Wang, Accurate and simple analytic representation of the electron-gas correlation-energy. *Phys. Rev. B* **45**(23), 13244–13249 (1992)
63. F. Ortmann, F. Bechstedt, W.G. Schmidt, Semiempirical van der Waals correction to the density functional description of solids and molecular structures. *Phys. Rev. B* **73**(20) (2006)
64. S.A. Deshmukh, S.K. Sankaranarayanan, D.C. Mancini, Vibrational spectra of proximal water in a thermo-sensitive polymer undergoing conformational transition across the lower critical solution temperature. *J. Phys. Chem. B* **116**(18), 5501–5515 (2012)
65. K. Mizuse, N. Mikami, A. Fujii, Infrared spectra and hydrogen-bonded network structures of large protonated water clusters H⁺ + (H₂O)_n (n = 20–200). *Angew. Chem.* **49**(52), 10119–10122 (2010)
66. F. Yang, X. Wang, M. Yang, A. Krishtal, C. van Alsenoy, P. Delarue, P. Senet, Effect of hydrogen bonds on polarizability of a water molecule in (H₂O)_N (N = 6, 10, 20) isomers. *Phys. Chem. Chem. Phys.* **12**(32), 9239–9248 (2010)
67. J. Li, Y.X. Li, X. Yu, W.J. Ye, C.Q. Sun, Local bond average for the thermally driven elastic softening of solid specimens. *J. Phys. D-Appl. Phys.* **42**(4), 045406 (2009)
68. C.Q. Sun, Size dependence of nanostructures: impact of bond order deficiency. *Prog. Solid State Chem.* **35**(1), 1–159 (2007)

69. M.J. Holmes, N.G. Parker, M.J.W. Povey, Temperature dependence of bulk viscosity in water using acoustic spectroscopy. *J. Phys: Conf. Ser.* **269**, 012011 (2011)
70. L. Vrbka, P. Jungwirth, Homogeneous freezing of water starts in the subsurface. *J. Phys. Chem. B* **110**(37), 18126–18129 (2006)
71. D. Donadio, P. Raiteri, M. Parrinello, Topological defects and bulk melting of hexagonal ice. *J. Phys. Chem. B* **109**(12), 5421–5424 (2005)
72. O. Bjorneholm, F. Federmann, S. Kakar, T. Moller, Between vapor and ice: free water clusters studied by core level spectroscopy. *J. Chem. Phys.* **111**(2), 546–550 (1999)
73. L. Pauling, Atomic radii and interatomic distances in metals. *J. Am. Chem. Soc.* **69**(3), 542–553 (1947)
74. V.M. Goldschmidt, Crystal structure and chemical correlation. *Ber. Deut. Chem. Ges.* **60**, 1263–1296 (1927)
75. C.Q. Sun, Dominance of broken bonds and nonbonding electrons at the nanoscale. *Nanoscale* **2**(10), 1930–1961 (2010)
76. E. Abrahams, P.W. Anderson, D.C. Licciardello, T.V. Ramakrishnan, Scaling theory of localization: absence of quantum diffusion in two dimensions. *Phys. Rev. Lett.* **42**(10), 673–676 (1979)
77. C.Q. Sun, X. Zhang, X. Fu, W. Zheng, J.-L. Kuo, Y. Zhou, Z. Shen, J. Zhou, Density and phonon-stiffness anomalies of water and ice in the full temperature range. *J. Phys. Chem. Lett.* **4**, 3238–3244 (2013)

Chapter 36

Thermally Driven Density and Phonon-Stiffness Oscillation

- *The density and phonon-stiffness of water ice oscillates over the full temperature range, transiting at 277, 258, and 80 K.*
- *The segment of relatively lower specific heat contracts at cooling, which forces the other part of the H-bond to elongate via Coulomb repulsion.*
- *In the liquid and solid phases, O:H bond contracts more than the H-O elongates; hence, an O:H–O cooling contraction and the seemingly ‘regular’ process of cooling densification take place.*
- *During freezing, the H–O contracts less than the O:H elongates, leading to an O:H–O elongation and volume expansion. At $T < 80$ K, the length and energy of both segments conserve but the O:H–O angle stretches, resulting in slight volume expansion.*
- *In ice, the O–O distance is longer than it is in water, resulting in a lower density, so that ice floats.*
- *Length contraction/elongation of the specific segment is associated with phonon-stiffening/softening.*

36.1 Observations: Why Does Ice Float?

H₂O density anomalies, particularly, floating of ice, continues puzzling the community despite decades-long research in this specific field [1–15]. When water freezes at 0 °C, its volume increases by up to 9 % under atmospheric pressure compared with liquid argon that shrinks by 12 % on freezing [16]. The density–temperature profiles for 1.4 nm [6] and 4.4 nm [17] sized droplets in Fig. 36.1 show that in the liquid (I) and solid (III) phases, H₂O exhibits the seemingly normal process of cooling densification at different rate; at the transition phase (II), freezing expansion happens; at temperature below 80 K(IV), ice volume increases slightly [18]. The lower temperature for density transition is strongly droplet size dependence, varying from 205 to 244 K. Numerical calculations [19] could hardly reproduce the entire density profile.

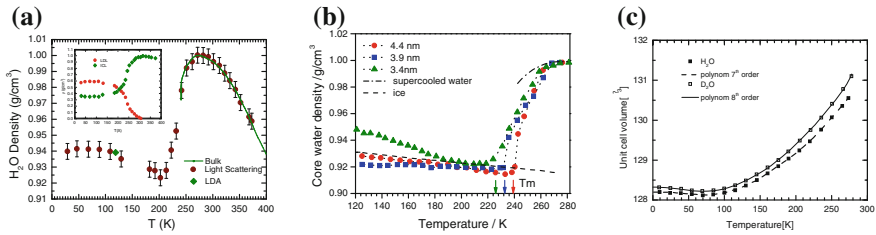


Fig. 36.1 Density $\rho(T)$ profiles of water droplets measured using (a) Raman and FTIR (1.4 nm) (Reprinted with permission from [6]) and (b) small-angle scattering of X-rays (SAXS) (Reprinted with permission from [17]) showing cooling densification in the liquid (I: $T > 273$ K), freezing expansion (II: $273 > T > 205(244)$ K), cooling densification in the solid (III: $205(244)$ K $> T > 80$ K, which varies with droplet size) and (c) slight volume expansion of H₂O and D₂O at very low temperatures. (IV: $T < 80$ K) (Reprinted with permission from [18])

The vibration frequencies of phonons of other materials shift to lower frequencies at heating because of the thermal lengthening and softening of the involved bonds [20–27]. However, heating stiffens the stiffer ω_H phonons (Fig. 36.2) and softens the softer ω_L phonons in the liquid [28] and in the solid phases at $T > 80$ K [29–32] as well. The anomalous phonon relaxation dynamics has been observed from water above the T_m [32–35], at 27 and 75 °C [36], from 10 to 90 °C [37], and from -34.6 to 90.0 °C for undercooled free-standing water droplet [38]. This trend remains in solid phases [30, 39] under a given pressure. Thermal annealing of the low-density amorphous ice from 80 to 155 K results in the red shift of the H–O phonons [40] from 3,120 to 3,180 cm^{-1} , which is opposite to the trend in ice-VIII phase. Using attenuated total reflectance (ATR) infrared spectroscopy, Marechal [41] revealed that thermal ω_H stiffening and ω_L softening happen not only to liquid H₂O but also to liquid D₂O with considerable offsets of the characteristic peaks. However, the ω_H transition at 0 °C from thermal-stiffening to cooling-stiffening, as shown in Fig. 36.2b [32] received little attention.

At $T < 80$ K, both the ω_H and the ω_L conserve [43, 44]. Using IR spectroscopy, Medcraft et al. [44] measured the size and temperature dependence of the low-frequency O:H ($\omega_L \sim 200 \text{ cm}^{-1}$) phonons in the temperature range of 4–190 K and observed that heating softens the ω_L at $T > 80$ K, but the ω_L changes insignificantly at $T < 80$ K see Fig. 36.3. Earlier Raman spectroscopy [46] of bulk ice revealed that the ω_L drops monotonically within the temperature range of 25 and 272 K in addition to the resolvable fluctuations in frequency at temperatures close to 272 K [47].

Heating also deepens the O 1s core level. Soft X-ray emission spectroscopy studies [48–50] revealed two components of O 1s binding energy that shift deeper toward that of gaseous molecules when the specimen is being heated. The thermal entrapment of the O 1s components was assigned to be a consequence of the mixed-phase configuration, i.e., tetrahedral and strongly distorted H-bonded species [51, 52].

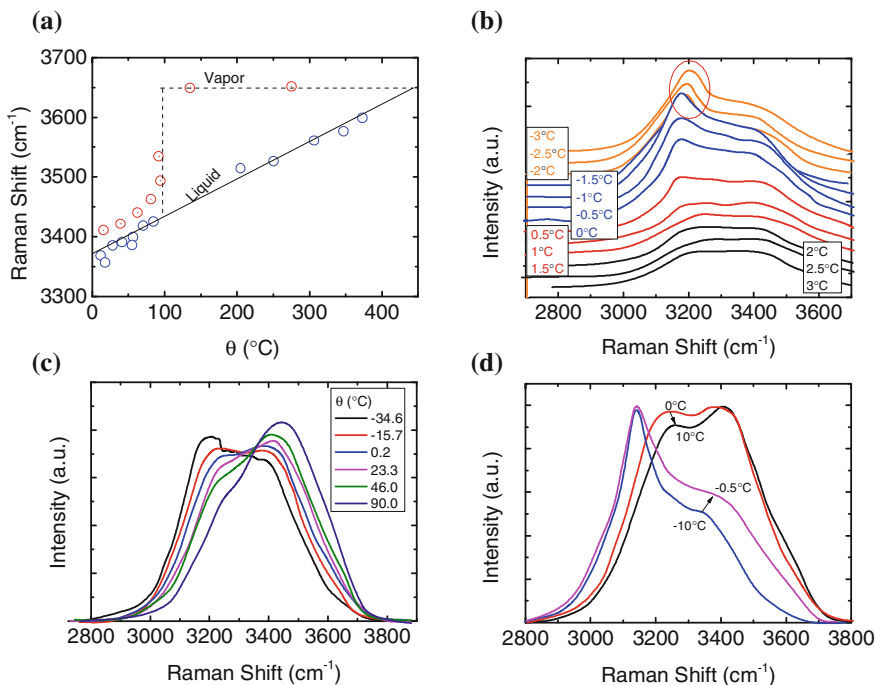


Fig. 36.2 a IR absorption profiles of the anomalous ω_H thermal-stiffening of water from 0 to 300 °C (Reprinted with permission from [28]). The ω_H keeps silent in vapor phase (half-filled circle) at 3,650 cm⁻¹; empty circle shows linear dependence of the ω_H on T in the superheating liquid phase. b Raman spectra in the temperature range of -3 to 3 °C (Reprinted with permission from [32]) show a ω_H transition at 0 °C from thermal-stiffening to cooling-stiffening, as circled. Components centered at 3,400 and 3,200 cm⁻¹ are attributed to the skin and the bulk components of water, respectively. c ω_H heating stiffening (-34.6 to 90 °C) at the ambient pressure of optically levitated supercooled water droplet (Reprinted with permission from [38]). d Raman spectra ω_H evolution with change in temperature with characteristic ω_H peak for ice at 3,150 cm⁻¹ (Reprinted with permission from [42])

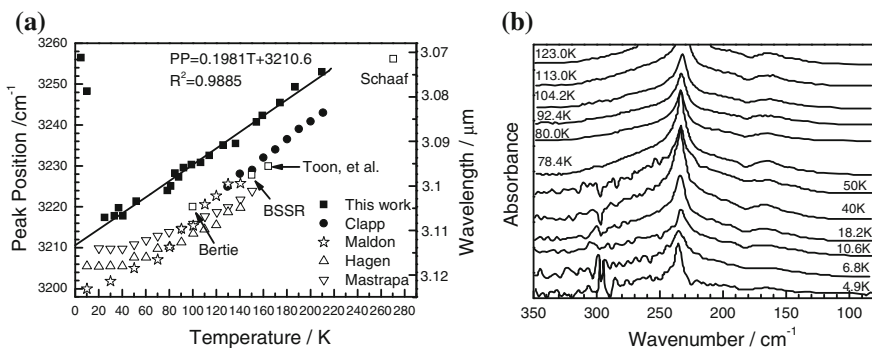


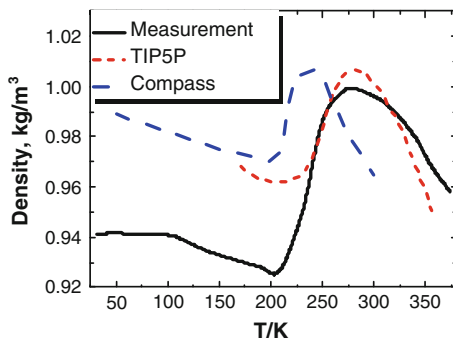
Fig. 36.3 Conservation of the ω_H at $T < 55$ K and the ω_L at $T < 73$ K (Reprinted with permission from [43, 44]) indicates the dominance of \angle O:H-O angle stretching in volume change as the length and energy of the O:H and the H-O bonds keep constant due to $\eta_L \cong \eta_H \cong 0$ [45]

Vibration and energetic spectroscopic, and structural diffraction studies up to date were focused mainly on the structural-phase composition and phase transition under various pressures and temperatures [29, 30, 53, 54]. Mechanism for the thermal-stiffening and pressure-softening of the stiffer ω_H , and the cooperative ω_L relaxation dynamics in liquid and solid phases remain as virgin for discussion [28, 32, 34–38]. Particularly, cooling-stiffening of ω_H at transition phase has been overlooked. It is also unclear why the thermal entrapment happens to the O 1s binding energy.

Theoretical studies on density anomalies of water ice have mainly focused on the density change of the freezing temperatures with supercooling water to mimic the freezing process. This process was discussed in the following mechanisms:

1. The mixed-phase model [3, 5–8, 11, 14, 15] suggests that the competition between the ring- or chain-like low-density liquid (LDL) and ‘ice-like’ nano-scaled fragments with the tetrahedral high-density liquid (HDL) fragments dictates the volume expansion of the supercooled water that mimic freezing expansion [5, 52]. The many-body electronic structure effects and the non-local vdW interactions could be important to this respect [55]. A SAXS measurements of water structure at three different temperatures (7, 25 and 66 °C) under normal pressure resolved shell structure out to ~ 0.12 nm in comparison to the TIP4P/2005 force-field calculations that produced 0.04–0.12 nm thick [56]. The same set of SAXS data could be numerically fitted using both homo- [1, 13] and hetero-generous [5] topologic configurations.
2. The mono-phase model [1, 2, 4, 10, 13] suggests that water contains homogeneous, three-dimensional, tetrahedrally coordinated structures with thermal fluctuations that are random but not quite [4, 9]. Unlike the mix-phase model, this mono-phase model explains the freezing expansion at transition as a consequence of the relaxation on the length and angle, in a certain yet unclear manner.
3. Linear correlation model [57] suggests that the local density changes with H-bond length, angle, and network topology. Liquid water expands quite homogeneously when it cools to approach its form of low density. H-bond elongation is responsible for thermal expansion, and angular distortion in the network is responsible for thermal contraction. Therefore, the competition between the angle and the length relaxation determines the density anomalies of water ice. Supercooling of liquid water involves structural heterogeneity, i.e., mix-phase configurations.
4. Two kinds of H-bond model [58, 59] of different strengths. The strong and weak H-bonds are in the ratio of about 2:1 are randomly distributed throughout the network of ice, which reproduce the neutron diffraction spectra. By introducing these two types of H-bond—strong and weak, Tu and Fang [59] reproduced a number of anomalies of water, particularly the thermodynamic properties at supercooled state. They found that the exchange of strong and weak H-bond enhances the competition between the open and collapsed structures of liquid water, which might be the key to the anomalies of supercooled water.

Fig. 36.4 Deviation between the calculated and measured [60] H₂O densities, indicating the generally computational limitations [3], including the ultrashort-ranged interactions and the presence of the low-density skin topologies of H-bond networks [1, 5–10] that further lower the density and elevate the critical temperature, according to BOLS premise



In fact, the density and phonon frequency oscillate over the full temperature range, which is far beyond the description of available models. Little attention has been paid to the mechanism for the seemingly regular process of cooling densification in both the liquid and the solid phases or to the mechanism for the slight drop in density at extremely low temperatures. Correlation between the density and phonon relaxation could be more comprehensive [45].

Figure 36.4 compares the measured [60] density–temperature profile with those derived from calculations using the MD force fields Compass 27 and the rigid, non-polarizable TIP5P model. The deviations from measurements in the highest-density–temperature ($T_{\max} = 277$ K) and in the lowest density (at $T_{\min} \sim 200$ K) suggest two possibilities causing disagreement. One is the limitations of the currently available computation methods [3] or models to include the ultrashort-range interactions; the other is the possible presence of the low-density fragments or the H-bond networks in water [1, 5–10]. Because of the limitations in computations, one cannot expect to reproduce the measurements seamlessly by any means at this moment.

According to the BOLS premise [61–64], reducing the molecular CN will shorten and strengthen the H–O covalent bond, and hence, raising the T_{\max} , which, in turn, will lengthen and weaken the O:H non-bond and thereby cause further O–O expansion and density drop [47]. Therefore, an introduction of the low-density phase or the ring- or chain-like topologies will further elevate the T_{\max} and lower the density, which could compensate to a certain extent for the deviation between calculations and measurements.

36.2 Bond Angle-Length and Density Oscillation

Figure 36.5 shows the MD-derived relaxation of (a) the segmental lengths, (b) the O:H–O bond angle θ , (c) the snapshots of the MD trajectory, and (d) the O–O distance as a function of temperature. As shown in Fig. 36.5a, the shortening of the master segments (denoted with arrows) is always coupled with a lengthening of the

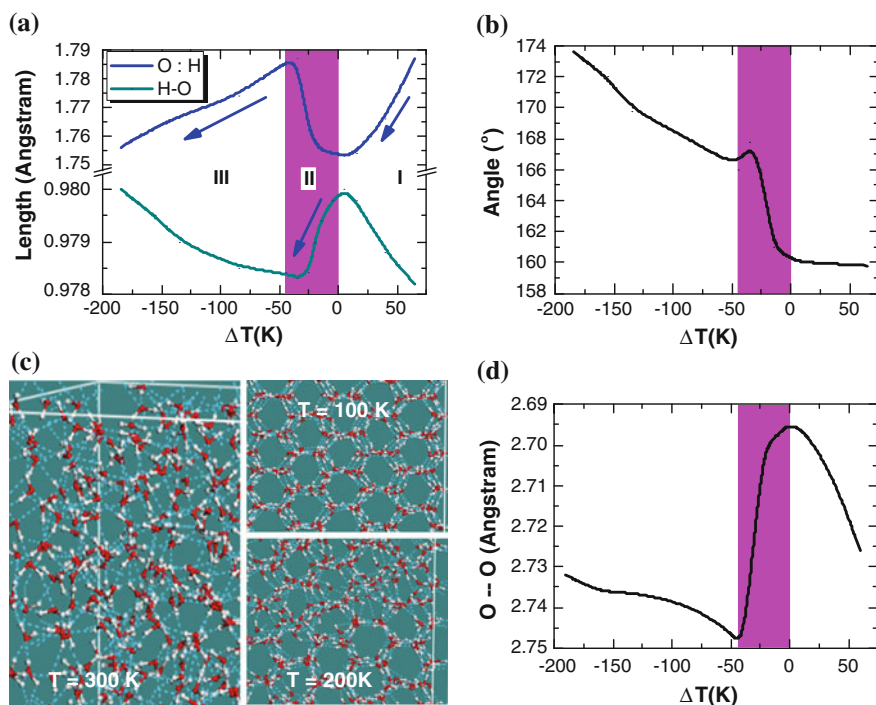


Fig. 36.5 MD-derived H-bond length and angle relaxation dynamics (Reprinted with permission from [45]). **a** Cooperative relaxation dynamics of the master–slave segments; *arrow* indicates the master segment that contracts associated with expansion of the slave at different regions. $\Delta T = T - T_{\max}$ with $T_{\max} = 277$ K is the maximal density–temperature. **b** Cooling-driven O:H–O angle widening. **c** The snapshots of MD trajectory show that the V-shaped H₂O motifs remain intact at 300 K because of the stronger H–O covalent bond (3.97 eV/bond), albeit high quantum fluctuations in the angle and the d_L of the O:H non-bond in liquid phase. Therefore, the molecules in water are slightly random [4]. **d** The calculated O–O distance changes are in good agreement with the measured density of water ice (Fig. 36.4) [6]

slaves during cooling. The temperature range of interest consists of three regions: in the liquid region I and the solid region III, the O:H bond contracts significantly more than the H–O bond elongates, resulting in a net loss of the O–O length. Thus, cooling-driven densification of H₂O happens in both the liquid and the solid phases. This mechanism differs completely from the mechanism conventionally adopted for the standard cooling densification of other regular materials in which only one kind of chemical bond is involved [65]. In contrast, in the transition phase II [6, 8, 11], the master and the slave swap roles. The O:H bond elongates more than the H–O bond shortens so that a net gain in the O–O length occurs.

As seen in Fig. 36.5b, the θ angle widening contributes to the volume change. In the liquid phase I, the mean θ valued at 160° remains almost constant. However, the snapshots of the MD trajectory in Fig. 36.5c and the MD movie [45] (Appendix A4-1) show that the V-shaped H–H–O molecules remain intact at

300 K over the entire duration recorded. This configuration is accompanied by high fluctuations in the θ and the d_L in this regime, which indicates the dominance of tetrahedrally coordinated water molecules [66]. In region II, cooling widens the θ from 160° to 167° , which contributes a maximum of $+1.75\%$ to the O:H–O bond elongation and $\sim 5.25\%$ to volume expansion. In phase III, the θ increases from 167° to 174° and this trend results in a maximal value of -2.76% to the volume contraction. An extrapolation of the θ enlargement in Fig. 36.5b results in the O–O distance lengthening, which explains the slight drop in density and the steady ω_L (d_L and E_L) observed at extremely low temperatures [44, 46].

The calculated evolution of the O–O distance shown in Fig. 36.5d agrees well in trend with the measured density in the concerned temperature range [6]. In ice, the O–O distance is always longer than that in water, and hence, ice floats. The O–O length relaxation dominates the density evolution at transition while the mixed-phase configuration plays a complementary role.

The calculated temperature dependence of the O–O distance shown in Fig. 36.5d matches satisfactorily with that of the measured density profile [6, 17]. Importantly, the O–O distance is longer in ice than it is in water, and therefore, ice floats.

The MD-movie (Appendix A4-3) shows that in the liquid phase, the H and the O attract each other between the O:H, but the O–O repulsion prevents this occurrence. The intact O–H–O motifs are moving restlessly because of the high fluctuation and frequent switching of the O:H interactions. Furthermore, the cooperative ω_L and ω_H shifts provide further evidence for the persistence of the Coulomb repulsion between the bonding and the non-bonding electron pairs in liquid. Therefore, the H₂O in the bulk form of liquid could possess the tetrahedrally coordinated structures with thermal fluctuation [4].

One phenomenon needs to note is the density transition that varies from 205, 242, to 258 K when the water droplet increases from 1.4 [6] to 4.4 [17] and to the bulk [45], see Figs. 36.1a, b and 36.6. As discussed in Chap. 4, droplet size reduction increases the curvature and the fraction of under-coordinated molecules, which stiffens the H–O bond and softens the O:H bond in terms of statistic mean. This happening raises the T_m of the H–O bond and lowers the T_m of the O:H bond, enlarging the separation between the extreme points in the specific heat curve, or results in depression/elevation of the temperatures corresponding to the density extremes. Thus, the temperature of the least density drops with droplet size. However, if the droplet is encapsulated in hydrophilic pores, situation reverses.

36.3 Cooperative Phonon Relaxation

The measured Raman spectra in Fig. 36.6 show three regions: $T > 273$ K(I), $273 \geq T \geq 258$ K(II), and $T < 258$ K(III), which are in accordance with predictions [45]:

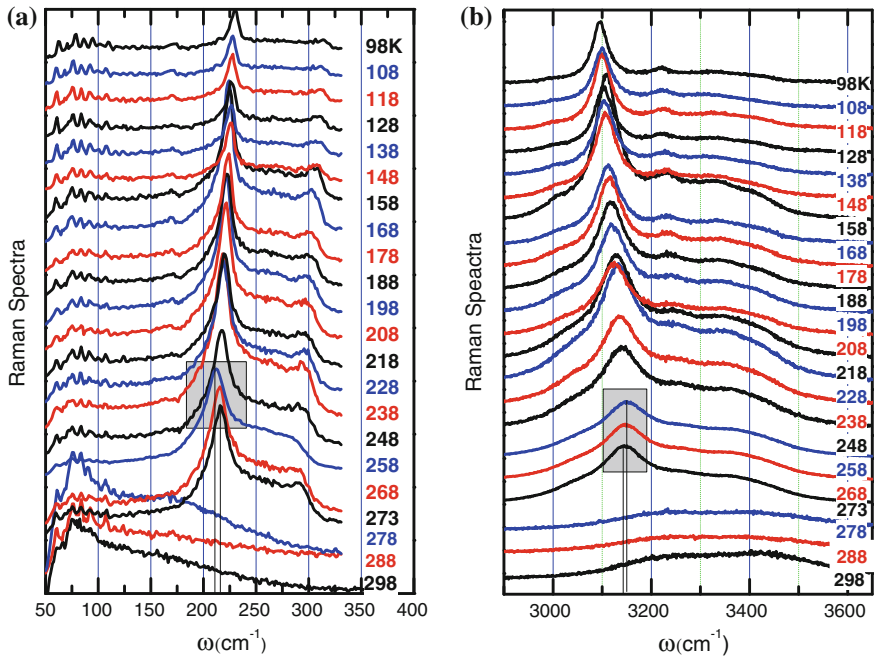


Fig. 36.6 Temperature-dependent Raman shifts of, (a) $\omega_L < 300 \text{ cm}^{-1}$, (b) $\omega_H > 3,000 \text{ cm}^{-1}$ in the regions of $T > 273 \text{ K}$, $273 \geq T \geq 258 \text{ K}$, and $T < 258 \text{ K}$, showing cooperative phonon-stiffness relaxation (Reprinted with permission from [45])

1. At $T > 273 \text{ K}$ (I), the abrupt shifts at cooling of the ω_L from 75 to 220 cm^{-1} and the ω_H from 3,200 to 3,140 cm^{-1} indicate ice formation. The cooperative ω_L blueshift and ω_H redshift indicate that cooling shortens and stiffens the O:H bond but lengthens and softens the H–O bond in the liquid phase, which confirms the predicted master role of the O:H bond in liquid water.
2. At $T < 258 \text{ K}$ (III), the trend of phonon relaxation remains as it is in the region of $T > 273 \text{ K}$ despite a change in the relaxation rates. Cooling from 258 K stiffens the ω_L from 215 to 230 cm^{-1} and softens the ω_H from 3,150 to 3,100 cm^{-1} . Other supplementary peaks at ~ 300 and $\sim 3,400 \text{ cm}^{-1}$ (skin mode) change insignificantly. The cooling softening of the ω_H mode agrees with that measured using IR spectroscopy [43] of ice clusters of 8–150 nm sizes. When the temperature drops from 209 to 30 K the ω_H shift from 3,253 to 3,218 cm^{-1} . For clusters of 5 nm size or smaller, the ω_H is stiffened by an addition of 40 cm^{-1} .
3. At 273–258 K(II), situation reverses. Cooling shifts the ω_H from 3,140 to 3,150 cm^{-1} and the ω_L from 220 to 215 cm^{-1} , see the shaded areas. Agreeing with the Raman ω_H shift measured in the temperature range around 273 K [31, 42], the cooperative shift of the ω_H and the ω_L confirms the exchange in the master and slave role of the O:H and the H–O bond during freezing.

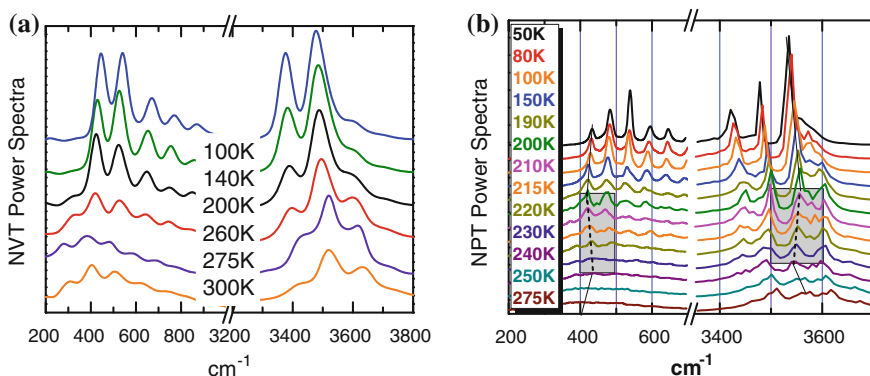


Fig. 36.7 MD-derived T -dependent power spectra of H₂O. **a** Splitting of the NVT high-frequency peaks at 260 K indicates the transition from water to ice at 200–260 K. **b** NPT -derived three temperature regions show the same phonon-stiffening (softening) trend to the Raman measurements in Fig. 36.6

- Figure 36.3 shows that both the ω_H and the ω_L remain almost constant at $T < 75$ K, which indicates that neither the length nor the energy of the two segments change with temperature because of their extremely low specific heat.
- The H–O phonon redshift [40] indicates densification of the amorphous ice upon annealing. Existence of molecules with fewer than four neighbors in the amorphous phase stiffens the H–O phonon, while structure ordering improves the quality of ice by removing the defects.

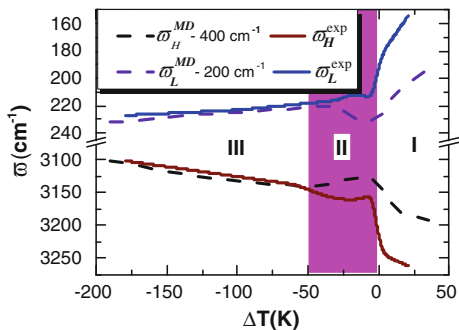
Figure 36.7 shows the T -dependent power spectra of H₂O derived from MD calculations. The splitting of the NVT high-frequency peaks at 260 K indicates the transition from water to ice taking place at 200–260 K. The NPT -derived spectra show three temperature regions, which follows the same phonon-stiffening (softening) trend to the measurements in Fig. 36.6.

Figure 36.8 compares the measured and the calculated temperature dependence of phonon relaxation dynamics. As expected, the non-bond stretching mode ω_L (~ 300 cm⁻¹) stiffening (softening) is always coupled with ω_H ($\sim 3,000$ cm⁻¹) softening (stiffening). Offsets of the calculated ω_L by -200 cm⁻¹ and ω_H by -400 cm⁻¹ with respect to the measurements suggest that the MD algorithm exaggerates the ultrashort-range interactions and hence underestimates the respective segment length and overestimates the phonon and segment stiffness.

36.4 Phonon Relaxation of Light and Heavy Water

It is clear now why cooling softens the ω_H and stiffens the ω_L of liquid H₂O (region I in Fig. 36.2) [28, 32, 34–38] other than the otherwise as happened in other usual materials. The cooling shortening and stiffening of the master O:H bond is

Fig. 36.8 Comparison of the measured and calculated phonon relaxation dynamics. The calculated ω_L and ω_H are offset by -200 and -400 cm^{-1} , respectively, with respect to the measurements



accompanied by lengthening and softening of the slave H–O bond, as a consequence of the interelectron-pair repulsion. Nevertheless, the abnormal cooperative $\omega_H(\omega_L)$ relaxation evidences the persistence of the O:H–O basic units and the Coulomb interactions in liquid H_2O [1, 10, 13, 67, 68] albeit thermal fluctuation.

Using an attenuated total reflection (ATR) IR spectroscopy, Marechal [41] measured the phonon spectra of ordinary (H_2O) and heavy (D_2O) water, as shown in Fig. 36.9. The isotope has two effects. One is the intensity attenuation of the absorption peaks and the other is the softening of the frequencies of all the detectable vibration modes of H_2O [41].

The phonon-frequency shift is proportional to the $(E_x/\mu_x)^{1/2}/d_x$. The isotope contributes only to reducing the effective mass, $\mu(m_1, m_2) = m_1 m_2 / (m_1 + m_2)$. Therefore, the relative shift is as follows:

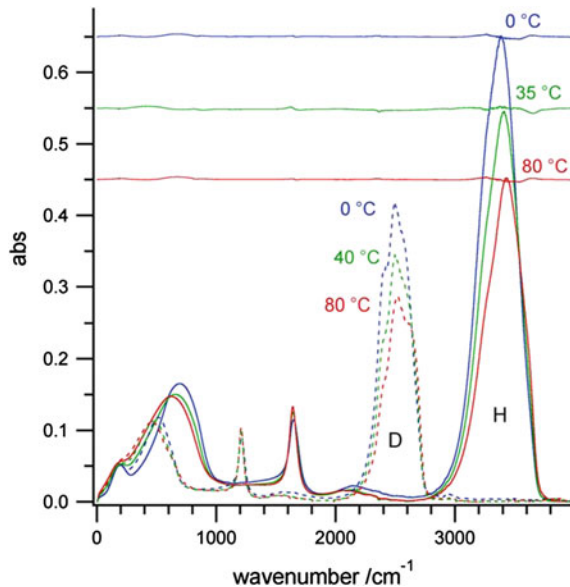
$$\frac{\Delta\omega_{xH}}{\Delta\omega_{xD}} \cong \left(\frac{\mu_D}{\mu_H}\right)^{1/2} = \begin{cases} \left[\frac{\mu_D(2, 16)}{\mu_H(1, 16)}\right]^{1/2} = (17/9)^{1/2} = 1.374 & (\omega_H) \\ \left[\frac{\mu_D(20, 20)}{\mu_H(16, 16)}\right]^{1/2} = (5/4)^{1/2} = 1.180 & (\omega_L) \end{cases} \quad (36.1)$$

For intramolecular vibration, m_1 is the mass of H or D (2 atomic unit), m_2 is the mass of O (16 unit); for intermolecular vibration, $m_1 = m_2$ is the mass of 2H + O (18 unit) or 2D + O (20 unit). Based on the derived ratios and the measurements, one can find

$$\frac{\Delta\omega_{xH}}{\Delta\omega_{xD}} \approx \begin{cases} 3400/2500 = 1.36 & (\omega_H) \\ 1620/1200 = 1.35 & (\omega_B) \\ 750/500 = 1.50 & (\omega_L) \end{cases}$$

Devotion of ω_x arising from the Coulomb coupling will play a certain role, but it is different from other effects, such as quantum fluctuation and polarization, are negligible. It is thus justified that the first-order approximation is sufficient to describe the isotopic effect on the phonon relaxation dynamics of ω_H and ω_B . The large deviation of the ω_L arises from the polarization and Coulomb repulsion. Therefore, the addition of isotope softens all the phonons by mediation of the effective mass of the dimer. Isotope also lowers the peak intensities because of the enhanced scattering by the low-frequency vibrations.

Fig. 36.9 IR spectra of 1 μm thick ordinary water 'H' and heavy water 'D' show the isotopic effect on ω_H thermal-stiffening and ω_L softening, in addition to the intensity attenuation in addition to the thermal relaxation (Reprinted with permission from [41])



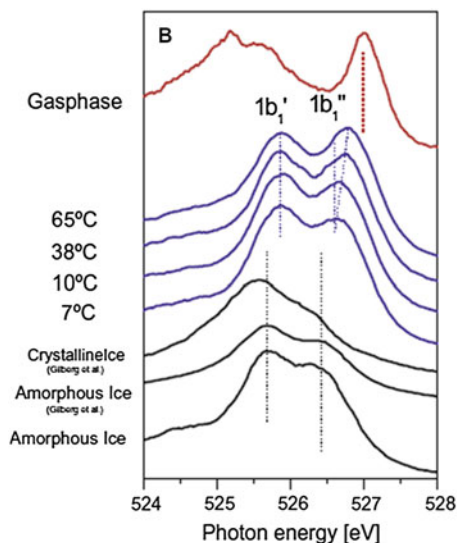
36.5 Binding Energy Entrapment

Figure 36.10 shows the O 1s level of water shift toward that of gaseous molecules. Based on comparison with ice- and gas-phase spectra, Tokushima et al. [49] assigned the lone-pair derived peaks ($1b_1'$ and $1b_1''$), respectively, to tetrahedral and strongly distorted H-bonded species.

As mentioned above, the binding energy entrapment is proportional to the H–O bond energy E_H . The O 1s features arise from the skin ($1b_1''$) and the bulk ($1b_1'$) and the H–O thermal-stiffening effect, corresponding to (Fig. 35.3) the bulk component ω_H at 3,200 and skin component at 3,450 cm^{-1} . The O 1s shows two peaks, but Raman spectrum shows only one for gaseous molecules. Polarization of the O:H non-bonding electron pairs by the entrapped H–O bond charge contributes, which split and screen the local crystal field and hence create two peaks [69]. The polarization modifies the ω_H peak value but does not split it.

Such assignments are consistent to expectations that the H–O bond become stronger upon the sample is being heated, and meanwhile, the densely entrapped bonding charge polarizes the non-bonding electrons. On the other hand, X-ray emission spectroscopy collects information composing the bulk and the skin competitively, because of the limited penetration depth. It is, therefore, anticipated that the structure of liquid water is dominated by the fluctuating tetrahedron with a skin supersolid phase that is subject to H–O bond contraction, non-bonding electron polarization. Therefore, both the mono-phase and mixed-phase models are correct from certain perspectives.

Fig. 36.10 O 1s soft X-ray emission spectra of amorphous ice (Reprinted with permission from [48]), gases, and liquid water at different temperatures, showing the thermal entrapment and splitting of the O 1s binding energy (Reprinted with permission from [49]) toward that of gaseous molecules



36.6 Summary

The four-region profiling consistency of density evolution, segmental length and phonon-stiffness relaxation, XPS O 1s energy shift, and the expected specific heat evidence consistently the coupled H-bond oscillator model that describes essentially the true situations of water-ice under cooling.

The proposed mechanisms for the thermally driven density and phonon-stiffness oscillation of water ice have thus been justified. Agreement between calculations and the measured mass-density, O 1s energy shift, and phonon-frequency relaxation dynamics in the full temperature range verified the following hypotheses and predictions:

1. Interelectron-pair Coulomb repulsion and the segmental specific heat disparity of the O:H-O bond determine the change in its angle, length, and stiffness and the density and the phonon-frequency anomalies of water ice.
2. The segment with a relatively lower specific heat contracts and drives the O:H-O bond cooling relaxation. The softer O:H bond always relaxes more in length than the stiffer H-O bond does in the same direction. The cooling widening of the O:H-O angle contributes positively to the volume expansion at freezing.
3. In the liquid and the solid phases, the O:H bond contracts more than the H-O bond elongates, resulting in the cooling densification of water and ice, which is completely different from the process experienced by other regular materials.
4. In the freezing transition phase, the H-O bond contracts less than the O:H bond lengthens, resulting in volume expansion during freezing. O:H-O bond angle stretching and the length and energy conservation of the d_x lower the density slightly at $T < 80$ K.

5. The O–O distance is larger in ice than it is in water, and therefore, ice floats.
6. The segment increases in stiffness and phonon frequency as it shortens, while the opposite occurs as it elongates.

References

1. A.K. Soper, J. Teixeira, T. Head-Gordon, Is ambient water inhomogeneous on the nanometer-length scale? *Proc. Natl. Acad. Sci. USA* **107**(12), E44–E44 (2010)
2. G.N.I. Clark, C.D. Cappa, J.D. Smith, R.J. Saykally, T. Head-Gordon, The structure of ambient water. *Mol. Phys.* **108**(11), 1415–1433 (2010)
3. V. Molinero, E.B. Moore, Water modeled as an intermediate element between Carbon and Silicon. *J. Phys. Chem. B* **113**(13), 4008–4016 (2009)
4. V. Petkov, Y. Ren, M. Suichomel, Molecular arrangement in water: Random but not quite. *J. Phys.: Condens. Matter* **24**(15), 155102 (2012)
5. C. Huang, K.T. Wikfeldt, T. Tokushima, D. Nordlund, Y. Harada, U. Bergmann, M. Niebuhr, T.M. Weiss, Y. Horikawa, M. Leetmaa, M.P. Ljungberg, O. Takahashi, A. Lenz, L. Ojamäe, A.P. Lyubartsev, S. Shin, L.G.M. Pettersson, A. Nilsson, The inhomogeneous structure of water at ambient conditions. *Proc. Natl. Acad. Sci. USA* **106**(36), 15214–15218 (2009)
6. F. Mallamace, C. Branca, M. Broccio, C. Corsaro, C.Y. Mou, S.H. Chen, The anomalous behavior of the density of water in the range $30\text{ K} < T < 373\text{ K}$. *Proc. Natl. Acad. Sci. USA* **104**(47), 18387–18391 (2007)
7. F. Mallamace, M. Broccio, C. Corsaro, A. Faraone, D. Majolino, V. Venuti, L. Liu, C.Y. Mou, S.H. Chen, Evidence of the existence of the low-density liquid phase in supercooled, confined water. *Proc. Natl. Acad. Sci. USA* **104**(2), 424–428 (2007)
8. O. Mishima, H.E. Stanley, The relationship between liquid, supercooled and glassy water. *Nature* **396**(6709), 329–335 (1998)
9. N.J. English, J.S. Tse, Density fluctuations in liquid water. *Phys. Rev. Lett.* **106**(3), 037801 (2011)
10. T. Head-Gordon, M.E. Johnson, Tetrahedral structure or chains for liquid water. *Proc. Natl. Acad. Sci. USA* **103**(21), 7973–7977 (2006)
11. E.B. Moore, V. Molinero, Structural transformation in supercooled water controls the crystallization rate of ice. *Nature* **479**(7374), 506–508 (2011)
12. C. Wang, H. Lu, Z. Wang, P. Xiu, B. Zhou, G. Zuo, R. Wan, J. Hu, H. Fang, Stable liquid water droplet on a water monolayer formed at room temperature on ionic model substrates. *Phys. Rev. Lett.* **103**(13), 137801–137804 (2009)
13. G.N. Clark, G.L. Hura, J. Teixeira, A.K. Soper, T. Head-Gordon, Small-angle scattering and the structure of ambient liquid water. *Proc. Natl. Acad. Sci. USA* **107**(32), 14003–14007 (2010)
14. A.J. Stone, Water from first principles. *Science* **315**(5816), 1228–1229 (2007)
15. K. Stokely, M.G. Mazza, H.E. Stanley, G. Franzese, Effect of hydrogen bond cooperativity on the behavior of water. *Proc. Natl. Acad. Sci. USA* **107**(4), 1301–1306 (2010)
16. G.M. Marion, S.D. Jakubowski, The compressibility of ice to 2.0 kbar. *Cold Reg. Sci. Technol.* **38**(2–3), 211–218 (2004)
17. M. Erko, D. Wallacher, A. Hoell, T. Hauss, I. Zizak, O. Paris, Density minimum of confined water at low temperatures: a combined study by small-angle scattering of X-rays and neutrons. *Phys. Chem. Chem. Phys.* **14**(11), 3852–3858 (2012)
18. K. Rottger, A. Endriss, J. Ihringer, S. Doyle, W.F. Kuhs, Lattice-constants and thermal-expansion of H_2O and D_2O Ice *ih* between 10 and 265 K. *Acta Crystallographica B* **50**, 644–648 (1994)

19. P.T. Kiss, A. Baranyai, Density maximum and polarizable models of water. *J. Chem. Phys.* **137**(8), 084506–084508 (2012)
20. M.X. Gu, Y.C. Zhou, L.K. Pan, Z. Sun, S.Z. Wang, C.Q. Sun, Temperature dependence of the elastic and vibronic behavior of Si, Ge, and diamond crystals. *J. Appl. Phys.* **102**(8), 083524 (2007)
21. M.X. Gu, L.K. Pan, T.C.A. Yeung, B.K. Tay, C.Q. Sun, Atomistic origin of the thermally driven softening of Raman optical phonons in group III nitrides. *J. Chem. Phys. C* **111**(36), 13606–13610 (2007)
22. I. Calizo, A.A. Balandin, W. Bao, F. Miao, C.N. Lau, Temperature dependence of the Raman spectra of Graphene and Graphene multilayers. *Nano Lett.* **7**(9), 2645–2649 (2007)
23. X.X. Yang, J.W. Li, Z.F. Zhou, Y. Wang, L.W. Yang, W.T. Zheng, C.Q. Sun, Raman spectroscopic determination of the length, strength, compressibility, Debye temperature, elasticity, and force constant of the C–C bond in graphene. *Nanoscale* **4**(2), 502–510 (2012)
24. H.Q. Zhou, C.Y. Qiu, H.C. Yang, F. Yu, M.J. Chen, L.J. Hu, Y.J. Guo, L.F. Sun, Raman spectra and temperature-dependent Raman scattering of carbon nanoscrolls. *Chem. Phys. Lett.* **501**(4–6), 475–479 (2011)
25. X.X. Yang, J.W. Li, Z.F. Zhou, Y. Wang, W.T. Zheng, C.Q. Sun, Frequency response of Graphene phonons to heating and compression. *Appl. Phys. Lett.* **99**(13), 133108 (2011)
26. J.W. Li, L.W. Yang, Z.F. Zhou, X.J. Liu, G.F. Xie, Y. Pan, C.Q. Sun, Mechanically stiffened and thermally softened Raman modes of ZnO crystal. *J. Phys. Chem. B* **114**(4), 1648–1651 (2010)
27. M.X. Gu, L.K. Pan, B.K. Tay, C.Q. Sun, Atomistic origin and temperature dependence of Raman optical redshift in nanostructures: A broken bond rule. *J. Raman Spec.* **38**(6), 780–788 (2007)
28. P.C. Cross, J. Burnham, P.A. Leighton, The Raman spectrum and the structure of water. *J. Am. Chem. Soc.* **59**, 1134–1147 (1937)
29. Y. Yoshimura, S.T. Stewart, M. Somayazulu, H.K. Mao, R.J. Hemley, Convergent Raman features in high density amorphous ice, Ice VII, and Ice VIII under pressure. *J. Phys. Chem. B* **115**(14), 3756–3760 (2011)
30. Y. Yoshimura, S.T. Stewart, H.K. Mao, R.J. Hemley, In situ Raman spectroscopy of low-temperature/high-pressure transformations of H₂O. *J. Chem. Phys.* **126**(17), 174505 (2007)
31. I. Durickovic, R. Claverie, P. Bourson, M. Marchetti, J.M. Chassot, M.D. Fontana, Water-ice phase transition probed by Raman spectroscopy. *J. Raman Spec.* **42**(6), 1408–1412 (2011)
32. M. Paolantoni, N.F. Lago, M. Albertí, A. Laganà, Tetrahedral Ordering in water: Raman profiles and their temperature dependence†. *J. Phys. Chem. A* **113**(52), 15100–15105 (2009)
33. M. Smyth, J. Kohanoff, Excess electron localization in solvated DNA bases. *Phys. Rev. Lett.* **106**(23), 238108 (2011)
34. J.D. Smith, C.D. Cappa, K.R. Wilson, R.C. Cohen, P.L. Geissler, R.J. Saykally, Unified description of temperature-dependent hydrogen-bond rearrangements in liquid water. *Proc. Natl. Acad. Sci. USA* **102**(40), 14171–14174 (2005)
35. F. Paesani, Temperature-dependent infrared spectroscopy of water from a first-principles approach. *J. Phys. Chem. A* **115**(25), 6861–6871 (2011)
36. Y. Marechal, Infrared-spectra of water. I. Effect of temperature and of H/D isotopic dilution. *J. Chem. Phys.* **95**(8), 5565–5573 (1991)
37. G.E. Walrafen, Raman spectral studies of the effects of temperature on water structure. *J. Chem. Phys.* **47**(1), 114–126 (1967)
38. H. Suzuki, Y. Matsuzaki, A. Muraoka, M. Tachikawa, Raman spectroscopy of optically levitated supercooled water droplet. *J. Chem. Phys.* **136**(23), 234508 (2012)
39. K. Furic, V. Volovsek, Water ice at low temperatures and pressures: New Raman results. *J. Mol. Struct.* **976**(1–3), 174–180 (2010)
40. J.J. Shephard, J.S.O. Evans, C.G. Salzmann, structural relaxation of low-density amorphous ice upon thermal annealing. *J. Phys. Chem. Lett.* 3672–3676 (2013)

41. Y. Marechal, The molecular structure of liquid water delivered by absorption spectroscopy in the whole IR region completed with thermodynamics data. *J. Mol. Struct.* **1004**(1–3), 146–155 (2011)
42. X. Xue, Z.-Z. He, J. Liu, Detection of water-ice phase transition based on Raman spectrum. *J. Raman Spec.* **44**(7), 1045–1048 (2013)
43. C. Medcraft, D. McNaughton, C.D. Thompson, D.R.T. Appadoo, S. Bauerecker, E.G. Robertson, Water ice nanoparticles: size and temperature effects on the mid-infrared spectrum. *Phys. Chem. Chem. Phys.* **15**(10), 3630–3639 (2013)
44. C. Medcraft, D. McNaughton, C.D. Thompson, D. Appadoo, S. Bauerecker, E.G. Robertson, Size and temperature dependence in the Far-IR spectra of water ice particles. *Astrophys. J.* **758**(1), 17 (2012)
45. C.Q. Sun, X. Zhang, X. Fu, W. Zheng, J.-L. Kuo, Y. Zhou, Z. Shen, J. Zhou, Density and phonon-stiffness anomalies of water and ice in the full temperature range. *J. Phys. Chem. Lett.* **4**, 3238–3244 (2013)
46. G.P. Johari, H.A.M. Chew, T.C. Sivakumar, Effect of temperature and pressure on translational lattice vibrations and permittivity of ice. *J. Chem. Phys.* **80**(10), 5163 (1984)
47. C.Q. Sun, X. Zhang, W.T. Zheng, Hidden force opposing ice compression. *Chem. Sci.* **3**, 1455–1460 (2012)
48. E. Gilberg, M.J. Hanus, B. Foltz, Investigation of the electronic-structure of ice by high-resolution x-ray spectroscopy. *J. Chem. Phys.* **76**(10), 5093–5097 (1982)
49. T. Tokushima, Y. Harada, O. Takahashi, Y. Senba, H. Ohashi, L.G.M. Pettersson, A. Nilsson, S. Shin, High resolution X-ray emission spectroscopy of liquid water: The observation of two structural motifs. *Chem. Phys. Lett.* **460**(4–6), 387–400 (2008)
50. J.H. Guo, Y. Luo, A. Augustsson, J.E. Rubensson, C. S  the, H.   gren, H. Siegbahn, J. Nordgren, X-Ray emission spectroscopy of hydrogen bonding and electronic structure of liquid water. *Phys. Rev. Lett.* **89**(13), 137402 (2002)
51. A. Nilsson, L.G.M. Pettersson, Perspective on the structure of liquid water. *Chem. Phys.* **389**(1–3), 1–34 (2011)
52. P. Wernet, D. Nordlund, U. Bergmann, M. Cavalleri, M. Odelius, H. Ogasawara, L.A. Naslund, T.K. Hirsch, L. Ojamae, P. Glatzel, L.G.M. Pettersson, A. Nilsson, The structure of the first coordination shell in liquid water. *Science* **304**(5673), 995–999 (2004)
53. Y. Yoshimura, S.T. Stewart, M. Somayazulu, H. Mao, R.J. Hemley, High-pressure x-ray diffraction and Raman spectroscopy of ice VIII. *J. Chem. Phys.* **124**(2), 024502 (2006)
54. M. Song, H. Yamawaki, H. Fujihisa, M. Sakashita, K. Aoki, Infrared investigation on ice VIII and the phase diagram of dense ices. *Phys. Rev. B* **68**(1), 014106 (2003)
55. A. Nilsson, C. Huang, L.G.M. Pettersson, Fluctuations in ambient water. *J. Mol. Liq.* **176**, 2–16 (2012)
56. C. Huang, K.T. Wikfeldt, D. Nordlund, U. Bergmann, T. McQueen, J. Sellberg, L.G.M. Pettersson, A. Nilsson, Wide-angle X-ray diffraction and molecular dynamics study of medium-range order in ambient and hot water. *Phys. Chem. Chem. Phys.* **13**(44), 19997–20007 (2011)
57. M. Matsumoto, Why does water expand when it cools? *Phys. Rev. Lett.* **103**(1), 017801 (2009)
58. J.C. Li, A.I. Kolesnikov, Neutron spectroscopic investigation of dynamics of water ice. *J. Mol. Liq.* **100**(1), 1–39 (2002)
59. Y.S. Tu, H.P. Fang, Anomalies of liquid water at low temperature due to two types of hydrogen bonds. *Phys. Rev. E* **79**(1), 016707 (2009)
60. J.L. Kulp, D.L. Pompliano, F. Guarnieri, Diverse fragment clustering and water exclusion identify protein hot spots. *J. Am. Chem. Soc.* **133**(28), 10740–10743 (2011)
61. C.Q. Sun, Thermo-mechanical behavior of low-dimensional systems: The local bond average approach. *Prog. Mater. Sci.* **54**(2), 179–307 (2009)
62. L. Pauling, Atomic radii and interatomic distances in metals. *J. Am. Chem. Soc.* **69**(3), 542–553 (1947)

63. V.M. Goldschmidt, Crystal structure and chemical correlation. *Ber. Deut. Chem. Ges.* **60**, 1263–1296 (1927)
64. C.Q. Sun, Size dependence of nanostructures: Impact of bond order deficiency. *Prog. Solid State Chem.* **35**(1), 1–159 (2007)
65. M.X. Gu, Y.C. Zhou, C.Q. Sun, Local bond average for the thermally induced lattice expansion. *J. Phys. Chem. B* **112**(27), 7992–7995 (2008)
66. T.D. Kuhne, R.Z. Khaliullin, Electronic signature of the instantaneous asymmetry in the first coordination shell of liquid water. *Nat. Commun.* **4**, 1450 (2013)
67. J.D. Smith, C.D. Cappa, B.M. Messer, W.S. Drisdell, R.C. Cohen, R.J. Saykally, Probing the local structure of liquid water by x-ray absorption spectroscopy. *J. Phys. Chem. B* **110**(40), 20038–20045 (2006)
68. A. Hermann, W.G. Schmidt, P. Schwerdtfeger, Resolving the optical spectrum of water: Coordination and electrostatic effects. *Phys. Rev. Lett.* **100**(20), 207403 (2008)
69. C.Q. Sun, Y. Nie, J. Pan, X. Zhang, S.Z. Ma, Y. Wang, W. Zheng, Zone-selective photoelectronic measurements of the local bonding and electronic dynamics associated with the monolayer skin and point defects of graphite. *RSC Adv.* **2**(6), 2377–2383 (2012)

Chapter 37

H-Bond Asymmetric Local Potentials

- *Lagrangian solution to the coupled oscillators enables mapping of the asymmetric, short-range potentials pertaining to the O:H–O bond.*
- *Both oxygen atoms in the O:H–O bond shift initially from their equilibrium (without coulomb coupling) outwardly with respect to the coordination origin (H), lengthening the O–O distance by Coulomb repulsion.*
- *Both oxygen atoms then move toward right along the O:H–O bond by different amounts upon being compressed and cooled, toward length symmetrization.*
- *The vdW potential $V_L(r)$ for the O:H non-covalent bond reaches a valley at -0.25 eV and the lowest exchange $V_H(r)$ for the H–O polar covalent bond values at -3.97 eV under compression.*

37.1 Lagrangian Mechanics

37.1.1 Asymmetric Short-Range Interactions

Because the \angle O:H–O angle in ice is valued at 170° and above [1], a linear approximation applies to the H-bond. By averaging the surrounding background long-range interactions of H_2O molecules, protons, and the nuclear quantum effect on fluctuations [2, 3], only the short-range interactions in a O:H–O bond dominate the relaxation [4]. The short-range interactions include the vdW force limited to the O:H bond [5], the exchange interaction in the H–O polar covalent bond [6], and the Coulomb repulsion between the lone and the shared electron pairs attached to the adjacent oxygen ions, as given in Eq. (37.1) and illustrated in Fig. 37.1.

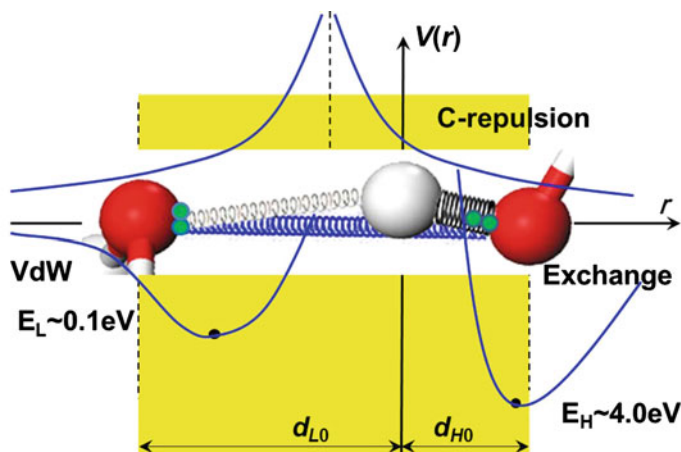


Fig. 37.1 Short-range interactions of the O:H–O bond oscillators with H atom being the coordination origin. The intramolecular exchange interaction is limited to the H–O bond (H, *right-hand side*). The intermolecular vdW force is limited to the O: (L, *left-hand side*). The interelectron-pair Coulomb repulsion (Repulsion) force is limited to region between adjacent O–O (C). The larger *red spheres* denote oxygen ions, and the smaller *gray sphere* denotes H proton. The pair of dots on oxygen in the *left* denotes the electron lone pair, and the pair of dots on the *right* denotes the bonding pair. The Coulomb repulsion pushes both O ions away from their ideal equilibrium positions and up slightly in energy (Reprinted with permission from [7])

37.1.2 Lagrangian Oscillator Dynamics

The segmented O:H–O bond is taken as a pair of asymmetric oscillators coupled by the Coulomb interaction and bridged by the H atom at the coordination origin. The reduced mass of the H₂O:H₂O oscillator is $m_L = 18 \times 18 / (18 + 18) m_0 = 9m_0$ and that of the H–O oscillator is $m_H = 1 \times 16 / (1 + 16) m_0 = 16/17m_0$ with m_0 being the unit mass of 1.66×10^{-27} kg. The motion of the coupled O:H–O oscillators follows the Lagrangian equation [8]:

$$\frac{d}{dt} \left(\frac{\partial L}{\partial (dq_x/dt)} \right) - \frac{\partial L}{\partial q_x} = Q_x. \quad (37.1)$$

The Lagrangian $L = T - V$ consists of the total kinetic energy T and the total potential energy V . Q_x denotes the generalized non-conservative forces. Here, it is the compression force f_p . The time-dependent $q_x(t)$, here, it is u_L and u_H , represents the generalized variables, denoting the displacements of O atoms from their

equilibrium positions in the springs L and H. The kinetic energy T consists of two terms

$$T = \frac{1}{2} \left[m_L \left(\frac{du_L}{dt} \right)^2 + m_H \left(\frac{du_H}{dt} \right)^2 \right]. \quad (37.2)$$

The potential energy V is composed of three terms:

$$\begin{cases} V_L(r_L) &= V_L(d_{L0} - u_L) && \text{(vdW)} \\ V_H(r_H) &= V_H(d_{H0} + u_H) && \text{(Exchange)} \\ V_C(r_C) &= V_C(d_{C0} - u_L + u_H) = V_C(d_C - u_C) && \text{(Coulomb-repulsion)} \end{cases}, \quad (37.3)$$

Here, $d_{C0} = d_{L0} + d_{H0}$ is the distance between the adjacent oxygen ions at equilibrium without contribution of Coulomb repulsion. The $d_C = d_L + d_H$ denotes the distance at quasi-equilibrium with involvement of the repulsion. The displacement of $u_C = u_L + \Delta_L - u_H + \Delta_H$ is the change in distance between the adjacent oxygen ions at quasi-equilibrium. Δ_x is the dislocation caused by repulsion. The u_L and u_H take opposite signs because of the O:H, and H-O dislocates in the same direction [9]. A harmonic approximation of the potentials at each quasi-equilibrium site by omitting the higher-order terms in their Taylor's series yields

$$\begin{aligned} V &= V_L(r_L) + V_H(r_H) + V_C(r_C) \\ &= \sum_n \left\{ \frac{d^n V_L}{n! dr_L^n} \Big|_{d_{L0}} (-u_L)^n + \frac{d^n V_H}{n! dr_H^n} \Big|_{d_{H0}} (u_H)^n + \frac{d^n V_C}{n! dr_C^n} \Big|_{d_C} (-u_C)^n \right\} \\ &\approx [V_L(d_{L0}) + V_H(d_{H0}) + V_C(d_C)] - V'_C u_C + \frac{1}{2} [k_L u_L^2 + k_H u_H^2 + k_C u_C^2] \end{aligned} \quad (37.4)$$

where $V_x(d_{x0})$, commonly denoted E_{x0} , is the potential well depths ($n = 0$ terms) of the respective bond. Noting that the Coulomb potential never has equilibrium and that the repulsion force is always greater than zero, one can then expand these potentials at their quasi-equilibrium points based on harmonic approximation. As will be shown shortly, this on-site harmonic approximation ensures sufficient accuracy of the potential paths.

In the Taylor series, the $n = 1$ term in the potentials equals zero for the L and the H segment at ideal equilibrium. At quasi-equilibrium, the criterion of $V'_x(d_x) + V'_C(d_C) = 0$, or $V''_x \cdot u_x + V''_C \cdot u_C = 0$, must meet. Here, V'_C denotes the first-order derivative at the quasi-equilibrium position, i.e., $dV_C/dr_C|_{d_C}$. Terms of $n = 2$, or the curvatures of the respective potentials, denote the force constants, i.e., $k_x = V'' = d^2 V_x/dr_x^2|_{d_{x0}}$ for harmonic oscillators. Terms of $n \geq 3$ are insignificant and omitted.

Substituting Eqs. (37.2) and (37.4) into (37.1) yields the Lagrangian equations for the O:H-O coupled oscillators,

$$\begin{cases} m_L \frac{d^2 u_L}{dt^2} + (k_L + k_C)u_L - k_C u_H + k_C(\Delta_L - \Delta_H) - V'_C - f_P = 0 \\ m_H \frac{d^2 u_H}{dt^2} + (k_H + k_C)u_H - k_C u_L - k_C(\Delta_L - \Delta_H) + V'_C + f_P = 0 \end{cases} \quad (37.5)$$

37.2 General Solutions

A Laplace transformation of the Lagrangian equation turns out the following general solutions (Appendix A4-4),

$$\begin{cases} u_L = \frac{A_L}{\gamma_L} \sin \gamma_L t + \frac{B_L}{\gamma_H} \sin \gamma_H t \\ u_H = \frac{A_H}{\gamma_L} \sin \gamma_L t + \frac{B_H}{\gamma_H} \sin \gamma_H t \end{cases} \quad (37.6)$$

The respective coefficient denotes the vibrational amplitude. γ_L and γ_H are the vibration angular frequencies of the respective segment, which depend on the force constants and the reduced masses of the oscillators. This set of general solutions indicates that the O:H and the H:O segments share the same form of eigenvalues of stretching vibration. The force constants k_x and the frequencies ω_x are correlated as follows

$$k_{H,L} = 2\pi^2 m_{H,L} c^2 (\omega_L^2 + \omega_H^2) - k_C \pm \sqrt{[2\pi^2 m_{H,L} c^2 (\omega_L^2 - \omega_H^2)]^2 - m_{H,L} k_C^2 / m_{L,H}} \quad (37.7)$$

where c is the velocity of light traveling in vacuum. Omitting the Coulomb repulsion will degenerate the coupled oscillators into the uncoupled H₂O:H₂O and the H:O oscillators with respective vibration frequencies of $\sqrt{k_L/m_L}$ and $\sqrt{k_H/m_H}$.

37.3 Specific Solutions

37.3.1 Short-Range Interactions

With the known Coulomb potential and the measured segmental length d_x (or density [10]) and phonon stiffness ω_x [9], parameters in the L-J (E_{L0} , d_{L0}) and in the Morse (E_{H0} , α) potentials can be mathematized. Table 37.1 lists the zeroth, first, second, and third derivatives of the respective Taylor series. Table 37.2 gives the corresponding evolution values (energies) of the items as a function of

Table 37.1 Derivatives of the L–J and the Morse potentials

| Derivatives | L–J potential | Morse potential | Results |
|-------------------|-------------------------|------------------------|----------------------|
| $V_{x0}(E_{x0})$ | E_{L0} | E_{H0} (3.97 eV) [4] | E_{x0} |
| $V'_x = 0$ | 0 | | d_{x0} |
| $V'_x + V'_c = 0$ | 0 | | $d_x = d_{x0} + u_x$ |
| $V''_x = k_x$ | $72E_{L0}/d_{L0}^2$ | $2\alpha^2 E_{H0}$ | α |
| V'''_x | $-1,512E_{L0}/d_{L0}^3$ | $-6\alpha^3 E_{H0}$ | |

Note With the measured frequency ω_x and calculated k_c , Eq. (37.8) gives the k_x . E_x is obtainable by the given parameters and the ω_x and d_x at each quasi-equilibrium sites

Table 37.2 Values for the first four items of the Taylor series of the L–J and the Morse potentials

| P (GPa) | L–J potential | | | | Morse potential | | | |
|-----------|---------------|-----|-----------------------------|-----------------------------|-----------------|-----|-----------------------------|-----------------------------|
| | 0th | 1st | 2nd ($\times 10^{-3}$) | 3rd ($\times 10^{-3}$) | 0th | 1st | 2nd ($\times 10^{-3}$) | 3rd ($\times 10^{-3}$) |
| 0 | 0.0625 | 0 | 16.8102 | 10.1750 | 3.9700 | 0 | 0.7465 | 0.0102 |
| 5 | 0.1063 | | 8.2883 | 2.7002 | 3.6447 | | 0.6387 | 0.0085 |
| 10 | 0.1458 | | 4.7185 | 0.9904 | 3.3859 | | 0.5300 | 0.0066 |
| 15 | 0.1755 | | 2.9185 | 0.4391 | 3.1875 | | 0.4247 | 0.0049 |
| 20 | 0.1919 | | 1.9033 | 0.2212 | 3.0450 | | 0.3271 | 0.0034 |
| 30 | 0.2477 | | 0.6599 | 0.0397 | 2.6290 | | 0.1880 | 0.0016 |
| 40 | 0.2498 | | 0.2432 | 0.0089 | 2.1285 | | 0.1022 | 0.0007 |
| 50 | 0.2165 | | 0.0967 | 0.0024 | 1.6465 | | 0.0581 | 0.0003 |
| 60 | 0.1605 | | 0.0697 | 0.0017 | 1.1595 | | 0.0626 | 0.0005 |

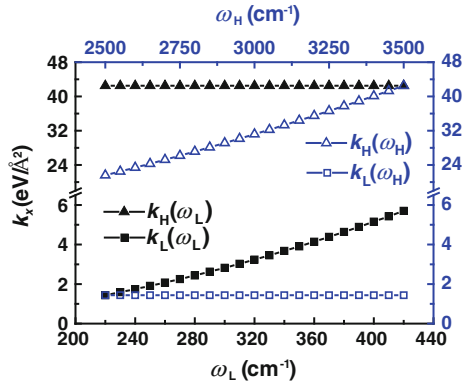
Nonlinear contribution of the third term is negligibly small (Reprinted with permission from [7])

pressure. The harmonic approximation is valid because the third derivative is much smaller than the second. The compression and Coulomb repulsion dislocate both O ions outwardly by Δ_x from their respective ideal equilibrium positions. d_{x0} is the interatomic distance at equilibrium without the involvement of Coulomb repulsion. $d_x = d_{x0} + \Delta_x$ is the quasi-equilibrium bond length with the Coulomb repulsion being involved. The Coulomb repulsion raises the cohesive energies of the O:H and the H–O from E_{x0} to E_x by the same amount.

37.3.2 Force Constants and Vibration Frequencies

If the ω_L , the ω_H , and the k_C are given, one can obtain the force constants k_x , the potential well depths E_{x0} , and the cohesive energy E_x , at each quasi-equilibrium state of the two parts of the O:H–O bond. The force constant due to Coulomb repulsion is $k_C = q_H q_L / (2\pi\epsilon_r \epsilon_0 d_C^3)$ at quasi-equilibrium. Here, $\epsilon_r = 3.2$ is the relative dielectric constant of bulk ice. $\epsilon_0 = 8.85 \times 10^{-12}$ F/m is the vacuum

Fig. 37.2 Functional dependence of the force constants k_x on the vibration frequencies of ω_x with $k_C = 0.17 \text{ eV/\AA}^2$. The $k_L(\omega_L)$ and the $k_H(\omega_H)$ are much more sensitive to their respective frequency than the across terms, $k_L(\omega_H)$ and the $k_H(\omega_L)$, that remain almost constant (Reprinted with permission from [7])



dielectric constant. The $q_L = 2e$ for the electron lone pair, and $q_H = 0.2e$, is the effective charge based on DFT optimization [7]. In this situation, the k_C equals to 0.17 eV/\AA^2 at 0 GPa.

Figure 37.2 shows the functional dependence of the k_x on the ω_x . The k_L increases from 1.44 to 5.70 eV/\AA^2 , while the k_H increases from 21.60 to 42.51 eV/\AA^2 with their respective frequency shifts. The cross terms of $k_L(\omega_H)$ and the $k_H(\omega_L)$ remains, however, almost constant. Therefore, Eq. (37.7) can be simplified as

$$\begin{aligned}
 k_x &= 4\pi^2 c^2 m_x \omega_x^2 - k_C \\
 &\text{or,} \\
 \omega_x &= (2\pi c)^{-1} \sqrt{\frac{k_x + k_C}{m_x}}
 \end{aligned} \tag{37.8}$$

With the measured $\omega_L = 237.42 \text{ cm}^{-1}$ and $\omega_H = 3326.14 \text{ cm}^{-1}$ for the ice-VIII phase under the atmospheric pressure [11–13], Eq. (37.7) yields $k_L = 1.70 \text{ eV/\AA}^2$ and $k_H = 38.22 \text{ eV/\AA}^2$. With the known $d_L = 0.1768 \text{ nm}$ and $d_H = 0.0975 \text{ nm}$ under Coulomb repulsion [9], one can obtain the free O:H length d_{L0} of 0.1628 nm and the d_{H0} of 0.0969 nm without involvement of the Coulomb repulsion. Coulomb repulsion lengthens the O–O distance from 0.2597 to 0.2733 nm by 0.0136 nm .

With the derived values of $k_L = 1.70 \text{ eV/\AA}^2$, $k_H = 38.22 \text{ eV/\AA}^2$, and $E_{H0} = 3.97 \text{ eV}$, one can determine all the parameters in the potentials and the force fields of the O:H–O bond at the ambient pressure

$$\begin{cases}
 k_L = 72E_{L0}/d_{L0}^2 = 1.70 \text{ eV/\AA}^2 \\
 k_H = 2\alpha^2 E_{H0} = 38.22 \text{ eV/\AA}^2
 \end{cases}
 \text{or}
 \begin{cases}
 E_{L0} = 1.70 \times 1.628^2/72 = 0.062 \text{ eV} \\
 \alpha = (38.22/3.97/2)^{1/2} = 2.19 \text{ \AA}^{-1}
 \end{cases} \tag{37.9}$$

37.3.3 Pressure-Dependent d_x , ω_x , k_x , and E_x

The $d_H(P)$ and the $d_L(P)$ curves (Figure 34.2a) [9] decomposed from the measured $V(P)$ profile of compressed ice [14] and the measured phonon relaxation dynamics $\omega_x(P)$ (Fig. 37.3a) [11–14] provide the input for solving the Lagrangian equation:

$$\begin{pmatrix} d_H/0.9754 \\ d_L/1.7687 \\ \omega_H/3326.140 \\ \omega_L/237.422 \end{pmatrix} = \begin{pmatrix} 1 & 9.510 \times 10^{-2} & 0.2893 \\ 1 & -3.477 \times 10^{-2} & -1.0280 \\ 1 & -0.905 & 1.438 \\ 1 & 5.288 & -9.672 \end{pmatrix} \begin{pmatrix} P^0 \\ 10^{-2}P^1 \\ 10^{-4}P^2 \end{pmatrix}. \quad (37.10)$$

Contribution of the Coulomb interaction proceeds by offsetting the intrinsic force constant of the oscillators. The measured d_x and the k_x that is available based on the known m_x , k_c , and the measured ω_x determine the other parameters involved in the respective potentials. The force constants and the cohesive energies can also be formulated as functional dependent on the pressure (Fig. 37.3b, c):

$$\begin{pmatrix} k_H/38.223 \\ k_L/1.697 \\ E_H/3.970 \\ E_L/0.046 \end{pmatrix} = \begin{pmatrix} 1 & -1.784 & 3.113 \\ 1 & 13.045 & -15.258 \\ 1 & -1.784 & 3.124 \\ 1 & 25.789 & -49.206 \end{pmatrix} \begin{pmatrix} P^0 \\ 10^{-2}P^1 \\ 10^{-4}P^2 \end{pmatrix}. \quad (37.11)$$

Results shown in Fig. 37.3b indicate that the k_C (curvature of the Coulomb potential) keeps almost constant under compression if the q_L , q_H , and the ε_r conserve. The k_L increases more rapidly than the k_H reduces because of the coupling of the compression, the repulsion, and the potential disparity of the two segments. Figure 37.3c indicates that increasing the pressure from 0 to 20 GPa strengthens the O:H bond from 0.046 to 0.190 eV and softens the H–O bond from 3.97 to 3.04 eV, as a result of repulsion. As given in Table 37.3, when the pressure is increased to 60 GPa, the $k_L = 10.03 \text{ eV}/\text{\AA}^2$, $k_H = 11.16 \text{ eV}/\text{\AA}^2$, and the E_L recover slightly.

37.3.4 Potential Paths for H-Bond Length Symmetrization

Table 37.3 also shows that compression shortens and stiffens the softer O:H bond, which lengthens and softens the H–O bond through Coulomb repulsion, which results in the contraction of the O–O distance toward O:H and H–O length symmetrization [9, 11–16]. As the d_L shortens by 4.3 % from 0.1768 to 0.1692 nm, the d_H lengthens by 2.8 % from 0.0975 to 0.1003 nm when the pressure is increased from 0 to 20 GPa [9]. When the pressure goes up to 60 GPa, the O:H bond equals to the H–O bond in length of about 0.11 nm, forming a symmetric O:H–O bond and ice X phase. Results indicate that the nature of the interaction within the

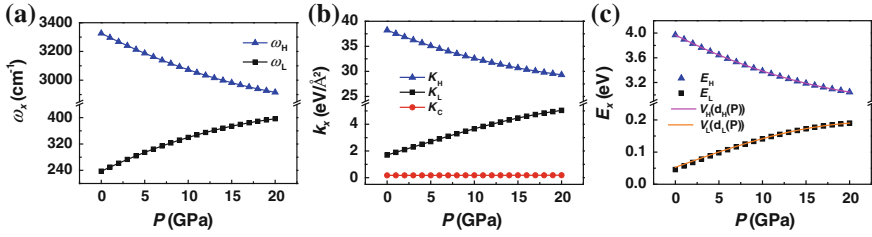


Fig. 37.3 Pressure dependence of **a** $\omega_x(P)$ [11–14], and the derived **b** force constant $k_x(P)$, and **c** cohesive energy $E_x(P)$ of the respective segment of the H-bond of ice under compression. The k_C remains almost constant, making insignificant contribution to the P dependence of k_x . Agreement between the scattered data of harmonic approximation at each quasi-equilibrium point and the continuum functions $V_x(d_x)$ in **c** verifies the validity of the on-site harmonic approximation for the inharmonic system (Reprinted with permission from [7])

Table 37.3 Pressure dependence of the O:H–O segmental cohesive energy (E_x), force constant (k_x), and the deviated displacement (Δ_x) from the equilibrium position

| P (GPa) | E_L (eV) | E_H (eV) | k_L (eV/Å ²) | k_H (eV/Å ²) | Δ_L (10 ⁻² nm) | Δ_H (10 ⁻⁴ nm) |
|-----------|------------|------------|----------------------------|----------------------------|----------------------------------|----------------------------------|
| 0 | 0.046 | 3.97 | 1.70 | 38.22 | 1.41 | 6.25 |
| 5 | 0.098 | 3.64 | 2.70 | 35.09 | 0.78 | 6.03 |
| 10 | 0.141 | 3.39 | 3.66 | 32.60 | 0.51 | 5.70 |
| 15 | 0.173 | 3.19 | 4.47 | 30.69 | 0.36 | 5.26 |
| 20 | 0.190 | 3.04 | 5.04 | 29.32 | 0.27 | 4.72 |
| 30 | 0.247 | 2.63 | 7.21 | 25.31 | 0.14 | 3.85 |
| 40 | 0.250 | 2.13 | 8.61 | 20.49 | 0.08 | 3.16 |
| 50 | 0.216 | 1.65 | 9.54 | 15.85 | 0.05 | 2.71 |
| 60 | 0.160 | 1.16 | 10.03 | 11.16 | 0.04 | 3.35 |

Subscript x denotes L and H. The measured $d_x(P)$ and $\omega_x(P)$ [9, 11–14] are used as input in calculations [7] (Reprinted with permission from [7])

segment remains though the length and force constant approaches to equality, which means that the sp^3 -hybridized oxygen could hardly be dehybridized by compression in the ice X phase at 60 GPa or below.

The asymmetric, local, short-range potentials pertaining to the O:H–O bond have thus been resolved and clarified. Figure 37.4 shows the $V_x(r)$ paths for the O:H–O bond in compressed and cooled ice. Reference [1] provides the input of $d_x(T)$ and $\omega(T)$ for the $V_x(r)$ paths at cooling. Both oxygen ions moves firstly outward from their ideal equilibrium because of Coulomb repulsion. Upon being compressed or cooled, both O ions in ice move to the right along the O:H–O with respect to the H coordination origin. The intrinsic equilibrium position of oxygen in the H–O bond almost superposes on its quasi-equilibrium position, with a displacement of only 6.25×10^{-4} nm at first. However, for the O:H, the displacement is 1.41×10^{-2} nm, evidencing that the O:H bond is much softer than the H–O bond. The cohesive energies of both segments relax along the respective contours as a result of the Coulomb repulsion and external stimulus.

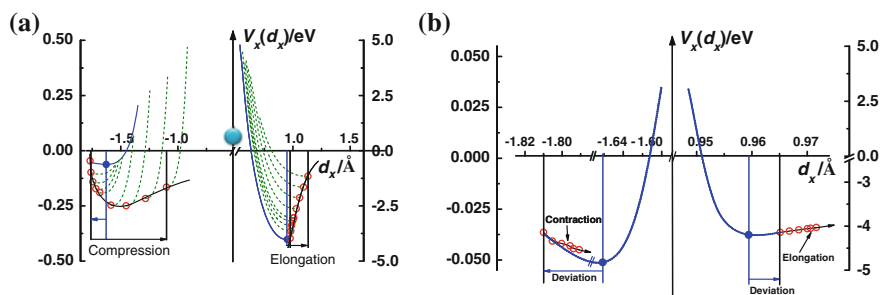


Fig. 37.4 The asymmetric, local, short-range potentials $V_x(r)$ of the O:H-O bond in **a** Compressed ice (from left to right, $P = 0, 5, 10, 15, 20, 30, 40, 50, 60$ GPa) and **b** Cooling ice [1]. *Small solid circles in blue* represent the intrinsic equilibrium coordinates (length and energy) of the oxygen ions without the Coulomb repulsion ($V'_x = 0, V_C = 0, P = 0$), and the *small open circles in red* denote the quasi-equilibrium coordinates caused by both the Coulomb repulsion and the pressure/temperature (*left ends* $V'_x + V'_C = 0, P = 0$; else: $V'_x + V'_C + f_{P,T} = 0$, with $f_{P,T}$ being the driving force of the applied stimuli). The broken curves show the potentials at quasi-equilibrium, while the thick solid lines passing all the open circles are the $V_x(r)$ paths of ice under compression/cooling. Note the vertical scale difference between the two segments (Reprinted with permission from [7])

Table 37.4 N dependence of the force constant and binding energy of the O:H-O bond in $(\text{H}_2\text{O})_N$

| N | E_L (meV) | E_H (eV) | k_L (eV/Å ²) | k_H (eV/Å ²) | Δ_L (10^{-1} Å) | Δ_H (10^{-3} Å) |
|-----|-------------|------------|----------------------------|----------------------------|---------------------------|---------------------------|
| 6 | 76.53 | 3.763 | 2.222 | 35.92 | 1.074 | 6.641 |
| 5 | 51.31 | 3.974 | 1.646 | 38.22 | 1.441 | 6.207 |
| 4 | 44.92 | 4.033 | 1.503 | 38.85 | 1.576 | 6.099 |
| 3 | 11.38 | 4.411 | 0.733 | 42.83 | 3.214 | 5.499 |
| 2 | 4.30 | 4.542 | 0.525 | 44.19 | 4.477 | 5.324 |

Dielectric constant change should modify the E_L and E_H values

37.3.5 Potential Paths for Undercoordinated H-Bond

Using the MD derivative of the d_x and the ω_x as input, Lagrangian solution has derived the force constant and bond energy for $(\text{H}_2\text{O})_N$ clusters of different sizes. Table 37.4 and Fig. 37.5 show the outcome. Numerically, the O:H bond energy at smaller N values seemed not so reasonable because the MD artifacts that take longer-range interaction and estimate the interaction improperly. Nevertheless, the trend and origin are within expectation.

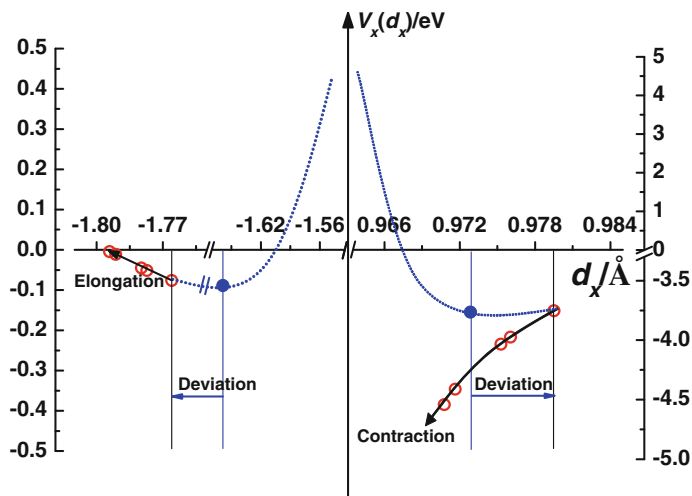


Fig. 37.5 Potential evolution of O:H–O bond (O:H in the left and H–O in the right) between undercoordinated water molecules ($N = 6, 5, 4, 3, 2$ from right to left)

37.4 Summary

A combination of the Lagrangian–Laplace mechanics of the coupled oscillators, molecular dynamics decomposition of volume evolution, and Raman spectroscopy of phonon relaxation has enabled probing of the local $V_x(r)$ potential paths for H-bond in compressed and cooled ice. This solution has enabled determination of the cohesive energy, force constant, potential field of each segment, and their pressure and temperature dependence. Results evidence consistently the persistence and significance of the asymmetric short-range interactions in the flexible, polarizable H-bond, which could be useful to other situations containing bonding and non-bonding short-range interactions. The immediacy of the off and on of the short-range potentials at the boundary is critical and essential, while the long-range interactions serve as the background.

References

1. C.Q. Sun, X. Zhang, X. Fu, W. Zheng, J.-L. Kuo, Y. Zhou, Z. Shen, J. Zhou, Density and phonon-stiffness anomalies of water and ice in the full temperature range. *J. Phys. Chem. Lett.* **4**, 3238–3244 (2013)
2. X.Z. Li, B. Walker, A. Michaelides, Quantum nature of the hydrogen bond. *PNAS* **108**(16), 6369–6373 (2011)
3. Y. Liu, J. Wu, Communication: long-range angular correlations in liquid water. *J. Chem. Phys.* **139**(4), 041103 (2013)

4. C.Q. Sun, X. Zhang, J. Zhou, Y. Huang, Y. Zhou, W. Zheng, Density, elasticity, and stability anomalies of water molecules with fewer than four neighbors. *J. Phys. Chem. Lett.* **4**, 2565–2570 (2013)
5. R.F. McGuire, F.A. Momany, H.A. Scheraga, Energy parameters in polypeptides. V. An empirical hydrogen bond potential function based on molecular orbital calculations. *J. Phys. Chem.* **76**, 375–393 (1972)
6. N. Kumagai, K. Kawamura, T. Yokokawa, An interatomic potential model for H₂O: applications to water and ice polymorphs. *Mol. Simulat.* **12**, 177–186 (1994)
7. Y. Huang, X. Zhang, Z. Ma, Y. Zhou, G. Zhou, C.Q. Sun, Hydrogen-bond asymmetric local potentials in compressed ice. *J. Phys. Chem. B* **117**(43), 13639–13645 (2013)
8. L.N. Hand, J.D. Finch, *Analytical Mechanics* (Cambridge University Press, Cambridge, 2008)
9. C.Q. Sun, X. Zhang, W.T. Zheng, Hidden force opposing ice compression. *Chem. Sci.* **3**, 1455–1460 (2012)
10. Y. Huang, X. Zhang, Z. Ma, Y. Zhou, J. Zhou, W. Zheng, C.Q. Sun, Size, separation, structure order, and mass density of molecules packing in water and ice. *Sci. Rep.* **3**, 3005 (2013)
11. P. Pruzan, J.C. Chervin, E. Wolanin, B. Canny, M. Gauthier, M. Hanfland, Phase diagram of ice in the VII–VIII–X domain. Vibrational and structural data for strongly compressed ice VIII. *J. Raman Spec.* **34**(7–8), 591–610 (2003)
12. M. Song, H. Yamawaki, H. Fujihisa, M. Sakashita, K. Aoki, Infrared absorption study of Fermi resonance and hydrogen-bond symmetrization of ice up to 141 GPa. *Phys. Rev. B* **60**(18), 12644 (1999)
13. Y. Yoshimura, S.T. Stewart, M. Somayazulu, H.K. Mao, R.J. Hemley, Convergent Raman features in high density amorphous ice, ice VII, and Ice VIII under pressure. *J. Phys. Chem. B* **115**(14), 3756–3760 (2011)
14. Y. Yoshimura, S.T. Stewart, M. Somayazulu, H. Mao, R.J. Hemley, High-pressure x-ray diffraction and Raman spectroscopy of ice VIII. *J. Chem. Phys.* **124**(2), 024502 (2006)
15. P. Loubeyre, R. LeToullec, E. Wolanin, M. Hanfland, D. Husermann, Modulated phases and proton centring in ice observed by X-ray diffraction up to 170 GPa. *Nature* **397**(6719), 503–506 (1999)
16. M. Benoit, D. Marx, M. Parrinello, Tunnelling and zero-point motion in high-pressure ice. *Nature* **392**(6673), 258–261 (1998)

Chapter 38

Molecular Size, Separation, Packing Order, and Density

- *The basic rule of sp -orbital hybridization of oxygen, the d_x cooperativity, and the known density enabled solution to the size, separation, structure order, symmetry, and mass density discrepancies simultaneously with neither assumption nor approximation.*
- *Solution reconciles the $O:H-O$ length symmetrization under compression, $O-O$ separation change at skins and at cooling.*
- *Water prefers the monophasic of the fluctuated, tetrahedrally coordinated structure with supersolid skin that consists of molecules with fewer than four neighbors.*
- *Coulomb repulsion between adjacent oxygen atoms dictates the relaxation of the $O:H-O$ bond, which is responsible for the anomalies of water and ice.*

38.1 Geometric Uncertainties

The structure and dimension of molecules packing in water and ice remain uncertain despite decades-long intensive investigation. Traditionally, one often seeks for the instantaneous accuracy of one of the strongly correlated parameters independently, resulting in endless argumentation. For instances, the separation between adjacent oxygen atoms (d_{OO}) was measured to vary from 2.70 to 3.00 Å [1–13] and the molecular size (d_H or the H–O bond length) changes from 0.970 to 1.001 Å [14]. The coordination number of a H₂O molecule varies instantaneously from two [15] to four or even greater [16]. The geometric structure of the weakly ordered H₂O liquid was under debate mainly between the monophasic of tetrahedrally coordinated configuration with thermal fluctuation [17–20] and the mixed-phase of low- and high-density fragments with thermally modulated fragmental ratios [15, 21, 22].

Scientific laws indicate that focusing on the statistic mean of the complete set of all the correlated parameters could be more realistic than on one of them alone at a time in coping with such a strongly correlated and fluctuating system. One may

note that the uncertainty of these seemingly independent issues determines intrinsically the density of water and ice, which constrains the solution to the uniqueness of structure order and length scale of liquid water. Based on the essential rule of sp-orbit hybridization of oxygen [23, 24] and the O:H–O bond segmental length cooperativity [17, 25, 26], one should be able to derive definitive conclusion toward these issues without needing any assumption or approximation.

38.2 Bond Length Cooperativity

An extension of the Ice Rule [23, 27] has resulted in the statistic structure of water as shown in Fig. 33.1c. Four of the eight cubes are occupied by the basic 2-H₂O block tetrahedrally and the rest four cubes are empty. This structure defines that each cube of a^3 volume accommodates only one H₂O molecule on average. With the known mass of a H₂O molecule consisting 8 neutrons, 10 protons, and 10 electrons, $M = (10 \times 1.672621 + 8 \times 1.674927 + 10 \times 9.11 \times 10^{-4}) \times 10^{-27}$ kg and the known density $\rho = M/a^3 = 1$ (g cm⁻³) at 4 °C under the atmospheric pressure, this structural order defines immediately and unambiguously the density-dependent molecular separation, d_{OO} . On the other hand, plotting the $d_L(P)$ against the $d_H(P)$, see Eq. (34.1), yields immediately the length cooperativity that is free from probing conditions or methods, d_H and d_L (unit in Å),

$$\begin{cases} d_{OO} = 2.6950\rho^{-1/3} & \text{(Molecular separation)} \\ d_L = \frac{2d_{H0}}{1+\exp[(d_H-d_{H0})/0.2428]}; & (d_{H0} = 1.0004, d_{L0} = 1.6946) \end{cases} \quad (38.1)$$

With any known density change, one is thus able to scale the size d_H and the separation d_{OO} of H₂O molecules with the given packing order in Fig. 33.1c with a known density. If the d_{OO} or the d_H matches the one of direct measurement, then the structure order in Fig. 33.1c, and the solution (38.1) is justified true and unique.

Figure 38.1a shows the conversion of the measured density $\rho(T)$ into the d_{OO} for water droplets of different sizes [28, 29]. The d_{OO} values of 2.70 Å measured at 25 °C and 2.71 Å at -16.8 °C [6] match exactly the conversion, which justifies that both Eq. (38.1) and the packing order in Fig. 33.1c, which describes the true structure order and the density dependence of molecular separation in water and ice, in terms of statistic mean. Furthermore, the data reported in Ref. [6] is essentially accurate and correct.

38.3 Solution Uniqueness

The non-covalent bond length d_L , molecular size d_H , molecular separation d_{OO} , and the mass density ρ can be obtained by solving the equation with any one of these parameters as a known input [30],

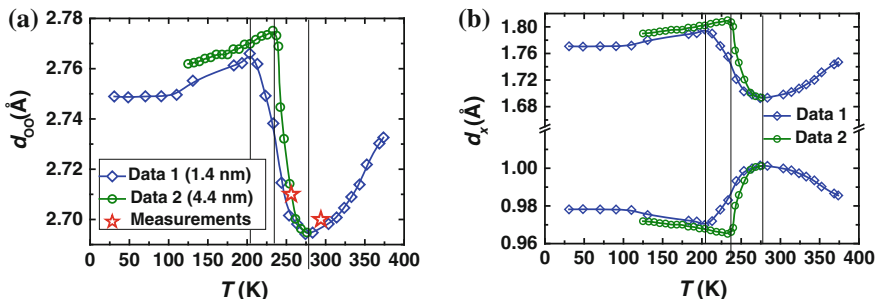


Fig. 38.1 **a** Validation of the $d_{OO} \sim \rho(T)$ relation [Eq. (38.1)] based on the measured $\rho(T)$ of water droplets [28, 29] and the d_{OO} values measured at 25 and -16.8 °C [6]. **b** Decomposing the d_{OO} into the d_H and the d_L based on MD derivative [25] of the measured $V(P)$ profile of ice [30]

$$d_L - 2.5621 \times [1 - 0.0055 \times \exp((d_{OO} - d_L)/0.2428)] = 0.$$

Figure 38.1b shows the decomposition of the d_{OO} into the d_x of water and ice at cooling [28, 29]. The $d_x(T)$ profiles follow the rules of O:H–O bond relaxation [17, 25, 26]: (1) both oxygen atoms dislocate in the same direction along the O:H–O bond by different amounts with respect to the H atom; (2) the longer-and-softer O:H part always relaxes more than the shorter-and-stiffer H–O part does. The cooperativity of the d_x relaxation confirms further that [26]: (1) cooling contraction happens only to the O:H bond in the liquid phase ($T > 277$ K) and in the solid phase ($T < 205$ K (Data 1) or 241 K (Data 2)), which lengthens the H–O bond slightly by interelectron-pair repulsion, resulting volume contraction; (2) in the freezing transition phase, the process of length relaxation reverses, leading to the O–O length gain and volume expansion at freezing. The $d_x(\theta = T - 273)$ curves about 273 K are formulated as,

$$\begin{cases} d_H(\theta) = 1.0042 \text{ \AA} / (1 + \exp(\theta - 312)/53) \\ d_L(\theta) = 1.6862 \text{ \AA} \times (1 + \exp(\theta - 257)/47.6438) \end{cases}$$

Figure 38.2 shows the solution consistency to the measured molecular size d_H , molecular separation d_L (or d_{OO}), mass density ρ , and structural order of: (1) compressed ice [30], (2) cooling water and ice [28, 29], and (3) water surface and molecular dimer [3, 6]. Currently derived d_H of 1.0004 Å at unity density is within the measured values ranging from 0.970 to 1.001 Å [14]. The d_{OO} values greater than the ideal value of 2.6950 Å at $\rho = 1$ (g cm^{-3}) correspond to the supersolid phase (low density, LDP) that exists indeed [15, 21, 22] but only in the skins of water ice composed of molecules with fewer than four neighbors (Fig. 38.2b) [17].

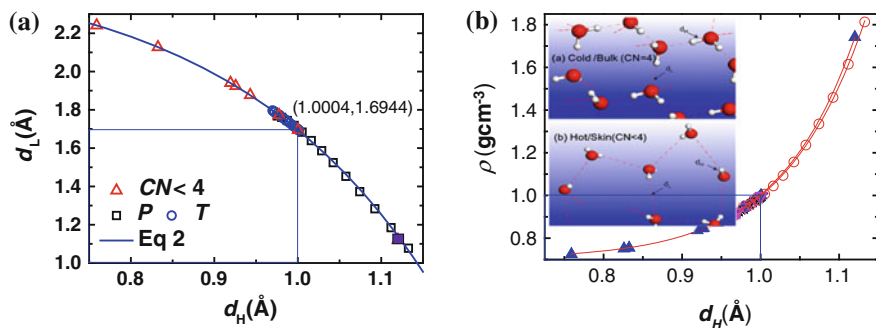


Fig. 38.2 Accordance of **a** molecular size d_H , molecular separation d_L (or $d_{OO} = d_H + d_L$), **b** mass density ρ , and packing order of H_2O molecules in the situations: (1) ice under compression ($d_H > 1.00 \text{ \AA}$) [30], (2) water ice at cooling ($0.96 < d_H < 1.00 \text{ \AA}$) [28, 29], and (3) liquid surface and dimer ($d_H < 1.00 \text{ \AA}$) [2, 4–6, 10–13]. The derived $d_H = 1.0004 \text{ \AA}$ at $\rho = 1$ is within the measurements ranging from 0.970 to 1.001 \AA [14]. The d_H shorter than 0.96 \AA corresponds to the supersolid phase (also LDP) in regions of molecules having fewer than four neighbors [1, 3, 17]. In such regions, a H_2O molecule shrinks in size and expands in separation because of interelectron-pair repulsion [17]

38.4 Summary

The straightforward yet simple solution has thus resolved the seemingly independent geometry and dimension uncertainties of water and ice with the following conclusions:

1. Focusing on the statistic mean of the complete set of all the factors and their cooperativity involved is reliably more revealing than on the instantaneous accuracy of the individual parameter once at a point of time for the strongly correlated and fluctuating water system.
2. The size, separation, structural order, and mass density of molecules packing in water and ice are correlated, which is independent of the structural phases of water and ice or the probing conditions.
3. Constrained by the Ice Rule, the d_H and d_L cooperativity, the solution has reconciled measurements of H-bond length symmetrization of ice under compression, d_{OO} relaxation of water and ice at cooling, and d_{OO} expansion of a water dimer and molecules at water surface.
4. With any one of the molecular separation, mass density, O:H bond length, and H–O distance as a known input, one can determine using this solution unambiguously the rest three parameters and their change with external conditions such as pressure, temperature, and coordination environment.
5. The tetrahedrally coordinated structure could be the unique choice of water and ice despite fluctuations in the d_L and the $\angle O:H-O$ angle.
6. The structure of water is composed of two parts. One is the bulk body of fluctuating tetrahedrally coordinated structures and the other is the supersolid

skin of two molecular layers. The skin is stiffer, ice-like, expanded, polarized, and elastic as the real bond of the skin molecules are subject to the BOLS correlation.

7. The supersolid (low density) phase indeed exists but only in regions consisting water molecules with fewer than four neighbors. The supersolidity phase forms because of the H–O bond contraction due to molecular undercoordination and the interelectron-pair repulsion pertaining to O:H–O bond.

References

1. K. Liu, J.D. Cruzan, R.J. Saykally, Water clusters. *Science* **271**(5251), 929–933 (1996)
2. K.R. Wilson, B.S. Rude, T. Catalano, R.D. Schaller, J.G. Tobin, D.T. Co, R.J. Saykally, X-ray spectroscopy of liquid water microjets. *J. Phys. Chem. B* **105**(17), 3346–3349 (2001)
3. K.R. Wilson, R.D. Schaller, D.T. Co, R.J. Saykally, B.S. Rude, T. Catalano, J.D. Bozek, Surface relaxation in liquid water and methanol studied by x-ray absorption spectroscopy. *J. Chem. Phys.* **117**(16), 7738–7744 (2002)
4. L.B. Skinner, C. Huang, D. Schlesinger, L.G. Pettersson, A. Nilsson, C.J. Benmore, Benchmark oxygen–oxygen pair-distribution function of ambient water from X-ray diffraction measurements with a wide Q-range. *J. Chem. Phys.* **138**(7), 074506 (2013)
5. K.T. Wikfeldt, M. Leetmaa, A. Mace, A. Nilsson, L.G.M. Pettersson, Oxygen-oxygen correlations in liquid water: addressing the discrepancy between diffraction and extended x-ray absorption fine-structure using a novel multiple-data set fitting technique. *J. Chem. Phys.* **132**(10), 104513 (2010)
6. U. Bergmann, A. Di Cicco, P. Wernet, E. Principi, P. Glatzel, A. Nilsson, Nearest-neighbor oxygen distances in liquid water and ice observed by x-ray Raman based extended x-ray absorption fine structure. *J. Chem. Phys.* **127**(17), 174504 (2007)
7. J. Morgan, B.E. Warren, X-ray analysis of the structure of water. *J. Chem. Phys.* **6**(11), 666–673 (1938)
8. L.A. Naslund, D.C. Edwards, P. Wernet, U. Bergmann, H. Ogasawara, L.G.M. Pettersson, S. Myneni, A. Nilsson, X-ray absorption spectroscopy study of the hydrogen bond network in the bulk water of aqueous solutions. *J. Phys. Chem. A* **109**(27), 5995–6002 (2005)
9. L. Orgel, The hydrogen bond. *Rev. Mod. Phys.* **31**(1), 100–102 (1959)
10. A.H. Narten, W.E. Thiessen, L. Blum, Atom pair distribution functions of liquid water at 25 °C from neutron diffraction. *Science* **217**(4564), 1033–1034 (1982)
11. L. Fu, A. Bienenstock, S. Brennan, X-ray study of the structure of liquid water. *J. Chem. Phys.* **131**(23), 234702 (2009)
12. J.L. Kuo, M.L. Klein, W.F. Kuhs, The effect of proton disorder on the structure of ice-Ih: a theoretical study. *J Chem Phys* **123**(13), 134505 (2005)
13. A.K. Soper, Joint structure refinement of X-ray and neutron diffraction data on disordered materials: application to liquid water. *J. Phys.: Condens. Matter* **19**, 335206 (2007)
14. M. Hakala, K. Nygård, S. Manninen, L.G.M. Pettersson, K. Hämäläinen, Intra- and intermolecular effects in the Compton profile of water. *Phys. Rev. B* **73**(3), 035432 (2006)
15. P. Wernet, D. Nordlund, U. Bergmann, M. Cavalleri, M. Odelius, H. Ogasawara, L.A. Naslund, T.K. Hirsch, L. Ojamae, P. Glatzel, L.G.M. Pettersson, A. Nilsson, The structure of the first coordination shell in liquid water. *Science* **304**(5673), 995–999 (2004)
16. A.K. Soper, Recent water myths. *Pure Appl. Chem.* **82**(10), 1855–1867 (2010)
17. C.Q. Sun, X. Zhang, J. Zhou, Y. Huang, Y. Zhou, W. Zheng, Density, elasticity, and stability anomalies of water molecules with fewer than four neighbors. *J. Phys. Chem. Lett.* **4**, 2565–2570 (2013)

18. T.D. Kuhne, R.Z. Khaliullin, Electronic signature of the instantaneous asymmetry in the first coordination shell of liquid water. *Nat. commun.* **4**, 1450 (2013)
19. V. Petkov, Y. Ren, M. Suchomel, Molecular arrangement in water: random but not quite. *J. Phys.: Condens. Matter* **24**(15), 155102 (2012)
20. T. Head-Gordon, M.E. Johnson, Tetrahedral structure or chains for liquid water. *PNAS* **103**(21), 7973–7977 (2006)
21. A. Nilsson, C. Huang, L.G.M. Pettersson, Fluctuations in ambient water. *J. Mol. Liq.* **176**, 2–16 (2012)
22. C. Huang, K.T. Wikfeldt, T. Tokushima, D. Nordlund, Y. Harada, U. Bergmann, M. Niebuhr, T.M. Weiss, Y. Horikawa, M. Leetmaa, M.P. Ljungberg, O. Takahashi, A. Lenz, L. Ojamäe, A.P. Lyubartsev, S. Shin, L.G.M. Pettersson, A. Nilsson, The inhomogeneous structure of water at ambient conditions. *PNAS* **106**(36), 15214–15218 (2009)
23. L. Pauling, The structure and entropy of ice and of other crystals with some randomness of atomic arrangement. *J. Am. Chem. Soc.* **57**, 2680–2684 (1935)
24. C.Q. Sun, Oxidation electronics: bond-band-barrier correlation and its applications. *Prog. Mater. Sci.* **48**(6), 521–685 (2003)
25. C.Q. Sun, X. Zhang, W.T. Zheng, Hidden force opposing ice compression. *Chem. Sci.* **3**, 1455–1460 (2012)
26. C.Q. Sun, X. Zhang, X. Fu, W. Zheng, J.-L. Kuo, Y. Zhou, Z. Shen, J. Zhou, Density and phonon-stiffness anomalies of water and ice in the full temperature range. *J. Phys. Chem. Lett.* **4**, 3238–3244 (2013)
27. J.D. Bernal, R.H. Fowler, A theory of water and ionic solution, with particular reference to hydrogen and hydroxyl ions. *J. Chem. Phys.* **1**(8), 515–548 (1933)
28. F. Mallamace, C. Branca, M. Broccio, C. Corsaro, C.Y. Mou, S.H. Chen, The anomalous behavior of the density of water in the range $30\text{ K} < T < 373\text{ K}$. *PNAS* **104**(47), 18387–18391 (2007)
29. M. Erko, D. Wallacher, A. Hoell, T. Hauss, I. Zizak, O. Paris, Density minimum of confined water at low temperatures: a combined study by small-angle scattering of X-rays and neutrons. *PCCP* **14**(11), 3852–3858 (2012)
30. Y. Huang, X. Zhang, Z. Ma, Y. Zhou, J. Zhou, W. Zheng, and C.Q. Sun, Size, separation, structure order, and mass density of molecules packing in water and ice. *Scientific Reports*, **3**, 3005 (2013)

Chapter 39

Skin Supersolidity of Water and Ice

- *The skins of water ice share the same nature of supersolidity, which is elastic, hydrophobic, polarized, highly thermal stable, slippery.*
- *The skin density reaches 0.75 g cm^{-3} , lower than that for ice 0.92 g cm^{-3} or liquid $\leq 1.0 \text{ g cm}^{-3}$; the ω_H is $3,450 \text{ cm}^{-1}$, higher than the value of $3,200 \text{ cm}^{-1}$ for the bulk water or the value of $3,150 \text{ cm}^{-1}$ for bulk ice.*
- *H–O bond contraction and the associated bonding electron entrapment and the dual processes of polarization create the supersolidity.*

39.1 Ultra-Low Density Yet High Elasticity

The term of supersolidity is adopted from the superfluidity of ^4He at mK temperatures in supersolid phase [1]. The ^4He fragments are highly elastic, repulsive, and frictionless in motion. Surface polarization and the enhanced elasticity of the surface covering sheet has been identified as the essential drivers for the hydrophobicity and lubricity of the surface, and therefore, it is not surprising that the ultrathin water films are hardly wetted by a water droplet [2]. The skin of water and ice, consisting molecules with fewer than four neighbours, forms such an amazing supersolid phase that possesses the attributes of elastic [3], hydrophobic [2, 4], polarized [5, 6], dielectrically instable [7], thermally stable [8] with densely entrapped bonding electrons [9–12] and ultra-low-density [13]. A video clip in Appendix A4-5 shows that water droplet dances at water surface, which evidence the high elasticity or surface tension and hydrophobicity of liquid surface.

Molecular volume expands at sites of molecular with fewer than four neighbors. If one considers the shortest distance of 2.70 \AA [14] and the longest 2.965 \AA [13] of measurements, the surface d_{OO} expands by up to 10 %. Furthermore, the volume of water molecules confined in 5.1 and 2.8 nm TiO_2 pores increase by 4 and 7.5 %, respectively, with respect to that in the bulk [15]. A $5\text{--}10 \text{ \AA}$ thick air gap between water molecules and the hydrophobic surface [16] make water molecules at the interface like free to exhibit skin vibration attributes [17] of $3,450 \text{ cm}^{-1}$

compared to that of $3,200 \text{ cm}^{-1}$ for the bulk water. The separation $d_{\text{OO}} = 2.980 \text{ \AA}$ for a dimer is even greater.

Stiopkin et al. [18] found that the strength of interactions of surface water molecules is distinctly different in structure from the rest of the liquid, and that the water surface has the thickness of just one layer of molecules, which is about 0.3 nm. The surface does not have a long-range impact on water. The timescale for H-bond switching dynamics at the surface is about three times slower than that in the bulk [19] because of the strong polarization induced viscosity. Vibrational sum frequency spectroscopy (VSFS) and MD simulations [20] suggested that the upper most two layers of water molecules are ordered ‘ice like’ with specific frequency of $3,217 \text{ cm}^{-1}$ at the air/water interface. The density of water molecules is higher in the second layer than the first.

The density of supersolid phase is indeed lower. In these supersolid regions, molecular under-coordination shortens the d_{H} and lengthens the d_{L} , resulting in d_{OO} expansion and polarization because of the inter electron-pair repulsion [21]. The least density of ice is 0.92, which corresponds to $d_{\text{OO}} = 2.695(0.92)^{-1/3} = 2.7710 \text{ \AA}$. However, the density of the supersolid phase is $\rho = (2.695/2.965)^3 = 0.7509 \text{ g cm}^{-3}$, which is far below the least density of the bulk ice or the maximal density of water (0.75/0.92/1.0).

The supersolid skin contains molecules upto two layers. A comparative study using x-ray and neutron scattering, sum-frequency vibrational spectroscopy and calorimetric measurements of the interaction between water and hydrophobic surface, as well as molecular-statistical calculations of the state of water molecules in the skin prove that the boundary water layer in the vicinity of hydrophobic surface consists of a thin ($\sim 0.5 \text{ nm}$) depletion layer. The density is as low as 0.4 g/cm^3 (correspond to $d_{\text{OO}} = 3.66 \text{ \AA}$) and a considerable amount (25–30 %) of water molecules with free OH groups, which is characterized by a more ordered network of H-bonds compared to liquid water [22, 23].

39.2 Charge Polarization and Entrapment

H–O bond contraction, Coulomb repulsion, and dual-process polarization drive the supersolidity with multiple features. The molecular separation $d_{\text{OO}} = d_{\text{L}} + d_{\text{H}}$ grows and molecular size d_{H} shrinks simultaneously at the skins because of the molecular under-coordination [21]. The H–O bond contraction follows the rule of BOLS correlation; the d_{OO} expansion results from the Coulomb repulsion between electron pairs on adjacent oxygen atoms [21, 24]. The polarization of water molecules in the molecular clusters [25, 26], surface skins, or ultrathin films of water is related to the molecule volume expansion because of the molecular charge conservation. The undercoordination-induced polarization lowers the work function of the bound electrons [6].

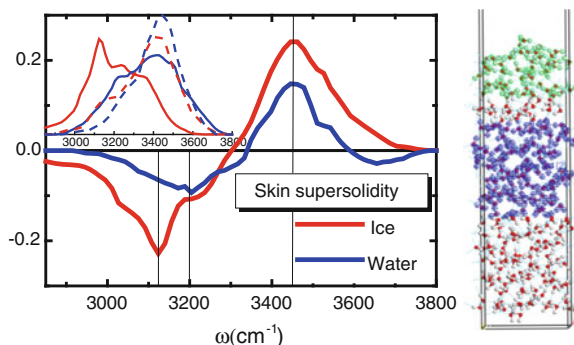


Fig. 39.1 Residual Raman spectra of the H–O stretching modes of bulk water at room-temperature (*solid blue trace*), the air–water interface (*dashed blue trace*), bulk ice at $-20\text{ }^{\circ}\text{C}$ (*dotted red trace*), and the air–ice interface at $-15\text{ }^{\circ}\text{C}$ (*dashed red trace*) detected using glancing angle Raman spectroscopy with insets being the raw data of measurements. The residual Raman spectra were obtained by subtracting the spectrum collected at larger angles (between the surface normal and the reflection beam) from the one collected at small angles (Reprinted with permission from [3]) upon the spectral area being normalized. The side panel shows the skin structure of water

In measurements using photoelectron emission, compatible amount of information from surface and the bulk contribute to the resultant spectral features [27] because of the limited depth of penetration. Therefore, low-density (supersolid) skin phase and the high-density bulk phase are compatible in spectral features. From DFT optimizations, the chain-or ring-like topologies could hardly form independently in liquid water [28].

From the current understanding, models of the monomial tetrahedral structure, the mixed LDP (supersolid skin or defects) and HDP phase structure, and the two different kinds of H-bond are true provided with the proper specification of component localions with consideration of penetration depth in optical reflection measurements. The weightage of the two phases or the two kinds of H-bond could be compatible if the penetration depth is limited to only a few molecular layers.

39.3 Skin Phonon

Figure 39.1 compares the residual Raman spectra of the ω_H of water with that of ice. The raw data were collected by Donaldson and co-workers [3] from water at room temperature and from ice (larger angle at $-20\text{ }^{\circ}\text{C}$ and smaller angle at $-15\text{ }^{\circ}\text{C}$) at different glancing angles between the surface normal and the reflected laser beam. Subtracting the spectrum collected from larger angle from the one collected at smaller angle upon spectral area normalization gives rise to the residual Raman spectrum. The skins of water and ice share the identical peak of $3,450\text{ cm}^{-1}$ for the H–O stretching mode. This finding reveals that the skins of

Table 39.1 Skin supersolidity (ω_x , d_x , E_x , ρ) of water and ice derived from the measurements (indicated with refs) and methods described in [29, 30]

| | Water (298 K) | | Ice (ρ_{\min}) | Ice (80 K) | Vapor |
|---|-------------------|---------------------------------|-----------------------|-------------------|-------------------|
| | bulk | skin | bulk | bulk | dimer |
| $\omega_H(\text{cm}^{-1})$ | 3,200 [3] | 3,450 [3] | 3,125 [3] | 3,090 [28] | 3,650 [31] |
| ω_L [28] | 220 | \sim 180 [21] | 210 | 235 | 0 |
| $d_{\text{OO}}(\text{\AA})$ | 2.700 [14] | 2.965 [13] | 2.771 | 2.751 | 2.980 [13] |
| $d_H(\text{\AA})$ | 0.9981 | 0.8406 | 0.9676 | 0.9771 | 0.8030 |
| $d_L(\text{\AA})$ | 1.6969 | 2.1126 | 1.8034 | 1.7739 | \geq 2.177 |
| $\rho(\text{g cm}^{-3})$ | 0.9945 | 0.7509 | 0.92 [32] | 0.94 [32] | \leq 0.7396 |
| $E_L(\text{meV}) \propto (\omega_x \times d_x)^2$ | 91.6 | 95 [33] | 94.2 | 114.2 | 0 |
| $*E_L(\text{meV}) (q_H = 0.20 \text{ e})$ | 24.6 | 24.4 | 26.2 | 44.3 | 0 |
| $E_L (q_H = 0.17 \text{ e})$ | 33.4 | 33.8 | 35.1 | 52.0 | 0 |
| $E_L (q_H = 0.10 \text{ e})$ | 49.9 | Increase with the drop of q_H | | | |
| $E_L (q_H = 0.05 \text{ e})$ | 58.3 | | | | |
| $*E_H(\text{eV}) (q_H = 0.20 \text{ e})$ | 3.6201 | 7.1967 | 4.0987 | 3.9416 | 8.6429 |
| $E_H (q_H = 0.17 \text{ e})$ | 3.6203 | 7.1968 | 4.0990 | 3.9418 | 8.6429 |
| $E_H (q_H = 0.10 \text{ e})$ | 3.6207 | Insensitive to q_H | | | |
| $E_H (q_H = 0.05 \text{ e})$ | 3.6209 | | | | |

water and ice share the same identity of much stronger H–O bond, neither liquid nor solid or quasi-states.

Surface pre-melting is therefore ruled out. Table 39.1 shows that the $\omega_H = 3,200 \text{ cm}^{-1}$ for the bulk water and $\omega_H = 3,125 \text{ cm}^{-1}$ for the bulk ice. In contrast, $\omega_H = 3,650 \text{ cm}^{-1}$ for gases in vapor composed of dimers. Reiteration of [29, 30], yields the ρ , d_{OO} , d_x and E_x of each phase, see Table 39.1. According to the current notation, the T_m is proportional to the E_H , the surface skin is thermally more stable than water or ice in the bulk.

39.4 Thermal Stability

Defects mediate the temperature of ice melting. MD simulations [34] show that freezing preferentially starts in the subsurface of water instead of the top layer that remains disordered during freezing. The subsurface accommodates better than the bulk the increase of volume connected with freezing. Furthermore, the bulk melting was found to be mediated by the formation of topological defects which preserve the coordination of the tetrahedral network. Such defect clusters form a defective region involving about 50 molecules with a surprisingly long lifetime [35]. Using microscopic, electrical potential, and UV–Vis absorption-spectra, infrared imaging, and NMR imaging, Zheng et al. [36] found that the solute-free zone is a physically distinct and less mobile phase of water that can co-exist indefinitely with the contiguous solute-containing phase in the hydrophilic

interface. These findings evidence the BOLS expectations that the undercoordinated water molecules are indeed hard to melt, which is opposite to the usual materials of which surfaces and defects facilitate pre-melting [37, 38]. No pre-melting happens at the skin as the T_m increases with the E_H .

Hydration shells manifest supersolidity. Direct interfacial force microscopy measurements at 24 °C of the normal force interactions between a mica-tungsten contact pair at various humidity levels revealed the presence of repulsive forces at about 0.5 nm before intimate contact [39]. Such repulsive interactions begin to appear above 20 % relative humidity (RH) and are fully developed in the range of 38–45 % RH. Using the Derjaguin-Muller-Toporov model of contact, elastic modulus of approximately 6.7 GPa was extracted from these repulsive interactions, providing direct evidence for the presence of ice-like water on mica at room temperature. Monolayer ice formation between tungsten and graphite at room temperature at 25 % RH is also ice like [40, 41].

39.5 Slippery of Ice

Ice surface is most slipper of known [42, 43]. The slippery was commonly perceived as a result of friction-heating or pressure-melting. However, neither of them can explain why ice can be so slippery even while one is standing still on it. Faraday [44] postulated in 1850s that a thin film of liquid water covers the surface even at temperature below freezing to serve as lubricant. Continued efforts suggested that ice surface pre-melting happens as the vibration amplitudes of the surface atoms were measured folds greater than the bulk [43]. However, an interfacial force microscopy and a spherical glass probe investigation revealed the opposite [43]. The surface layer is viscoelastic at temperatures over the ranging from -10 to -30 °C, resulting from the absence of the liquid layer at very low temperatures. Therefore, the concept of surface pre-melting seems in conflicting with the ice-like nature of ultrathin films of water, as afore-discussed.

Skin supersolidity slipperizes ice. The H–O contraction, core electron entrapment and dual polarization yield the high-elasticity, self-lubrication, and low-friction of ice and the hydrophobicity of water surface as well, of which the mechanism is the same to that of metal nitride [45, 46] and oxide [47] surfaces. Nanoindentation measurements revealed that the elastic recovery coefficient of TiCrN, GaAlN, and α -Al₂O₃ surfaces could reach 100 % under a critical indentation load of friction (<1.0 mN) at which the lone pair breaks with a friction coefficient being the same order to ice (0.1) [42], see Fig. 39.2. Albeit the pressure and the nature of loading pin materials, both show the comparatively low friction coefficients. The involvement of lone pairs makes the nitride and oxide surfaces more elastic and slippery under the critical load. This understanding supplements mechanism for the slippery of ice surface and the hydrophobicity of ultrathin water films as well.

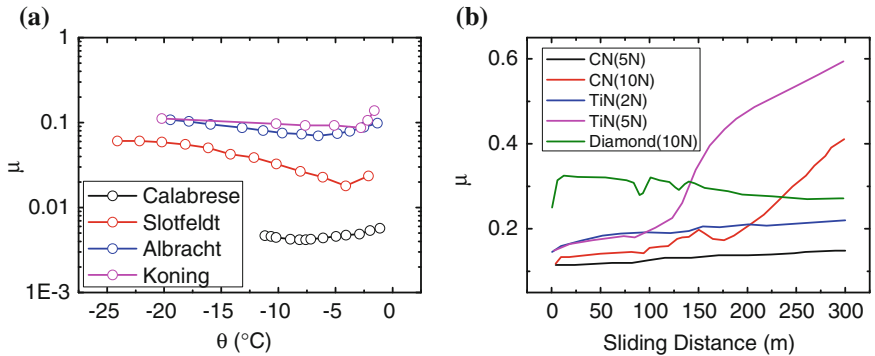


Fig. 39.2 Friction coefficients of ice at different temperatures (Reprinted with permission from [42] and refs therein) and nitrides at different loads (Reprinted with permission from [46])

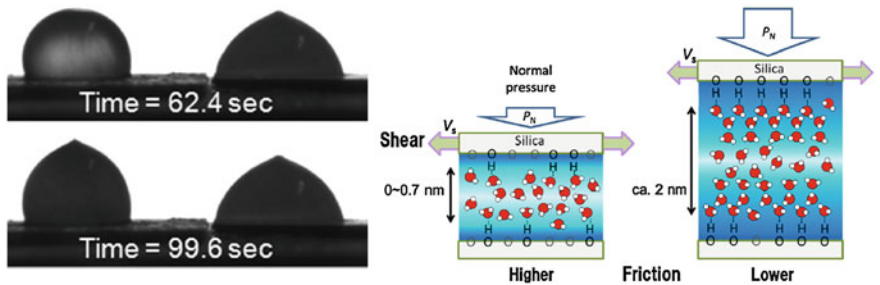


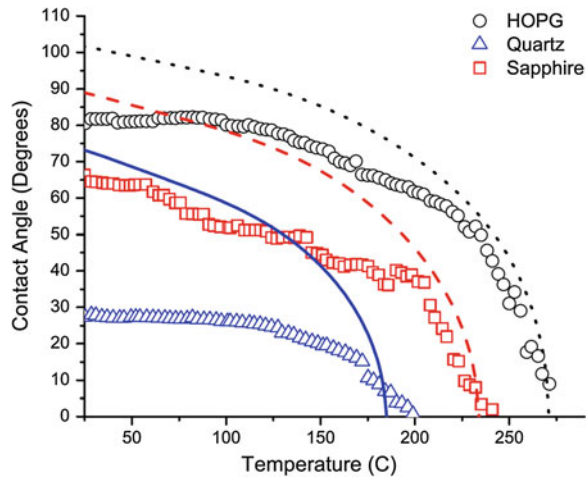
Fig. 39.3 Delayed freezing of high-contact-angle water droplet on hydrophobic (*left*) and less-hydrophobic Ag surfaces at -4 °C (Reprinted with permission from [49]) and the H₂O/SiO₂ interface viscosity enhancement by plasma sputtering of the SiO₂ plates (Reprinted with permission from [17])

On the other hand, transition of the contact angle between water and surfaces happens at different temperatures [54]. As shown in Fig. 39.3, the critical temperatures for transiting the contact angle to zero for quartz, sapphire, and graphite at 185, 234, and 271 °C, respectively. This finding discriminates the water-substrate potential and interface sharpness effect.

39.6 Further Evidence

The following important observations are in accordance with current understanding, see Fig. 39.4. Firstly, water droplet dances at solid surfaces disregarding the temperatures and materials of the substrate (CO₂ at -79 °C; hydrophobic surface at 22 °C and Al at 100 °C) [48], which indicates that the skin of the droplet is highly elastic and thermally stable.

Fig. 39.4 Contact angle of water on quartz, sapphire, and graphite as a function of temperature with solidlines are modelling results (Reprinted with permission from)



Secondly, water droplet on roughened Ag surface (with nanocolumnar structures) having a greater contact angle and higher curvature melts 62 s later than that on the smooth Ag surface at $-4\text{ }^{\circ}\text{C}$ [49], which indicates that water molecules at the highly curved skin are thermally even more stable.

Thirdly, the vibration frequency of the H–O bond for water molecules confined in the plasma-treated silica surfaces is around $3,200\text{ cm}^{-1}$ (bulk feature) and that confined in the untreated silica is around $3,400\text{ cm}^{-1}$ (skin feature with higher T_m) [17], which indicates that hydrophilic interface produces no surface effect. The air gap between the water and the hydrophobic substrate [16] makes the contacting skin more like free. However, water confined in hydrophilic nanopores [50, 51] or wetting with hydrophilic topologic configurations [52] exhibits supercooling effect, or melts at lower temperature than usual because of the lacking of broken bonds.

These discoveries further evidence for the elastic, solid-like, polarized, and hydrophobic attributes of the skin of ice and water or the topological defects. The fewer the molecular neighbors is, the smaller the water molecule size (d_H), the greater the molecular separation (d_{OO}), and the greater extents of the supersolidity attributes will be.

39.7 Summary

The slippery or low-friction of ice results from the lone pair weak yet elastic interaction and the high density of surface charge instead of the liquid lubrication. Because of the cohesive energy gain of the two intramolecular H–O bonds, a monolayer of water performs solid like with high elasticity and charge density as the increase of E_H raises the T_m . This expectation coincides with higher surface

charge density measured using thin film interferometry [53]. The strong surface field induced by the surface charge establishes a more ordered H-bonding network that promotes the forming of thicker water lubrication film between hydrophilic solid surfaces.

References

1. J. Day, J. Beamish, Low-temperature shear modulus changes in solid He-4 and connection to supersolidity. *Nature* **450**(7171), 853–856 (2007)
2. C. Wang, H. Lu, Z. Wang, P. Xiu, B. Zhou, G. Zuo, R. Wan, J. Hu, H. Fang, Stable liquid water droplet on a water monolayer formed at room temperature on ionic model substrates. *Phys. Rev. Lett.* **103**(13), 137801–137804 (2009)
3. T.F. Kahan, J.P. Reid, D.J. Donaldson, Spectroscopic probes of the quasi-liquid layer on ice. *J. Phys. Chem. A* **111**(43), 11006–11012 (2007)
4. M. James, T.A. Darwish, S. Ciampi, S.O. Sylvester, Z.M. Zhang, A. Ng, J.J. Gooding, T.L. Hanley, Nanoscale condensation of water on self-assembled monolayers. *Soft Matter* **7**(11), 5309–5318 (2011)
5. T. Ishiyama, H. Takahashi, A. Morita, Origin of vibrational spectroscopic response at ice surface. *J. Phys. Chem. Lett.* **3**, 3001–3006 (2012)
6. K.R. Siefertmann, Y. Liu, E. Lugovoy, O. Link, M. Faubel, U. Buck, B. Winter, B. Abel, Binding energies, lifetimes and implications of bulk and interface solvated electrons in water. *Nat. Chem.* **2**, 274–279 (2010)
7. C. Zhang, F. Gygi, G. Galli, Strongly anisotropic dielectric relaxation of water at the nanoscale. *J. Phys. Chem. Lett.* **4**, 2477–2481 (2013)
8. H. Qiu, W. Guo, Electromelting of confined monolayer ice. *Phys. Rev. Lett.* **110**(19), 195701 (2013)
9. B. Winter, E.F. Aziz, U. Hergenahm, M. Faubel, I.V. Hertel, Hydrogen bonds in liquid water studied by photoelectron spectroscopy. *J. Chem. Phys.* **126**(12), 124504 (2007)
10. M. Abu-Samha, K.J. Borve, M. Winkler, J. Harnes, L.J. Saethre, A. Lindblad, H. Bergersen, G. Ohrwall, O. Bjornholm, S. Svensson, The local structure of small water clusters: imprints on the core-level photoelectron spectrum. *J. Phys B-At. Mol. Opt. Phys.* **42**(5), 055201 (2009)
11. K. Nishizawa, N. Kurahashi, K. Sekiguchi, T. Mizuno, Y. Ogi, T. Horio, M. Oura, N. Kosugi, T. Suzuki, High-resolution soft X-ray photoelectron spectroscopy of liquid water. *Phys. Chem. Chem. Phys.* **13**, 413–417 (2011)
12. R. Vacha, O. Marsalek, A.P. Willard, D.J. Bonthuis, R.R. Netz, P. Jungwirth, Charge transfer between water molecules as the possible origin of the observed charging at the surface of pure water. *J. Phys. Chem. Lett.* **3**(1), 107–111 (2012)
13. K.R. Wilson, R.D. Schaller, D.T. Co, R.J. Saykally, B.S. Rude, T. Catalano, J.D. Bozek, Surface relaxation in liquid water and methanol studied by x-ray absorption spectroscopy. *J. Chem. Phys.* **117**(16), 7738–7744 (2002)
14. U. Bergmann, A. Di Cicco, P. Wernet, E. Principi, P. Glatzel, A. Nilsson, Nearest-neighbor oxygen distances in liquid water and ice observed by x-ray Raman based extended x-ray absorption fine structure. *J. Chem. Phys.* **127**(17), 174504 (2007)
15. E.G. Solveyra, E. de la Llave, V. Molinero, G. Soler-Illia, D.A. Scherlis, Structure, dynamics, and phase behavior of water in TiO₂ nanopores. *J. Chem. Phys. C.* **117**(7), 3330–3342 (2013)
16. A. Uysal, M. Chu, B. Stripe, A. Timalisina, S. Chattopadhyay, C.M. Schlepütz, T.J. Marks, P. Dutta, What x rays can tell us about the interfacial profile of water near hydrophobic surfaces. *Phys. Rev. B.* **88**(3), 035431 (2013)

17. M. Kasuya, M. Hino, H. Yamada, M. Mizukami, H. Mori, S. Kajita, T. Ohmori, A. Suzuki, K. Kurihara, Characterization of water confined between silica surfaces using the resonance shear measurement. *J. Phys. Chem. C*. **117**(26), 13540–13546 (2013)
18. I.V. Stiopkin, C. Weeraman, P.A. Pieniazek, F.Y. Shalhout, J.L. Skinner, A.V. Benderskii, Hydrogen bonding at the water surface revealed by isotopic dilution spectroscopy. *Nature* **474**(7350), 192–195 (2011)
19. Y. Ni, S.M. Gruenbaum, J.L. Skinner, Slow hydrogen-bond switching dynamics at the water surface revealed by theoretical two-dimensional sum-frequency spectroscopy. *Proc. Nat. Academy. Sci. USA*. **110**(6), 1992–1998 (2013)
20. Y.B. Fan, X. Chen, L.J. Yang, P.S. Cremer, Y.Q. Gao, On the structure of water at the aqueous/air interface. *J. Phys. Chem. B*. **113**(34), 11672–11679 (2009)
21. C.Q. Sun, X. Zhang, J. Zhou, Y. Huang, Y. Zhou, W. Zheng, Density, elasticity, and stability anomalies of water molecules with fewer than four neighbors. *J. Phys. Chem. Lett.* **4**, 2565–2570 (2013)
22. Y.I. Tarasevich, State and structure of water in vicinity of hydrophobic surfaces. *Colloid. J.* **73**(2), 257–266 (2011)
23. B.H. Chai, H. Yoo, G.H. Pollack, Effect of radiant energy on near-surface water. *J. Phys. Chem. B*. **113**(42), 13953–13958 (2009)
24. C.Q. Sun, X. Zhang, W.T. Zheng, Hidden force opposing ice compression. *Chem. Sci.* **3**, 1455–1460 (2012)
25. J.K. Gregory, D.C. Clary, K. Liu, M.G. Brown, R.J. Saykally, The water dipole moment in water clusters. *Science* **275**(5301), 814–817 (1997)
26. F. Yang, X. Wang, M. Yang, A. Krishtal, C. van Alsenoy, P. Delarue, P. Senet, Effect of hydrogen bonds on polarizability of a water molecule in (H₂O)(N) (N = 6, 10, 20) isomers. *Phys. Chem. Chem. Phys.* **12**(32), 9239–9248 (2010)
27. C.Q. Sun, Y. Nie, J. Pan, X. Zhang, S.Z. Ma, Y. Wang, W. Zheng, Zone-selective photoelectronic measurements of the local bonding and electronic dynamics associated with the monolayer skin and point defects of graphite. *RSC Adv.* **2**(6), 2377–2383 (2012)
28. C.Q. Sun, X. Zhang, X. Fu, W. Zheng, J.-L. Kuo, Y. Zhou, Z. Shen, J. Zhou, Density and phonon-stiffness anomalies of water and ice in the full temperature range. *J. Phys. Chem. Lett.* **4**, 3238–3244 (2013)
29. Y. Huang, X. Zhang, Z. Ma, Y. Zhou, J. Zhou, W. Zheng, C.Q. Sun, Size, separation, structure order, and mass density of molecules packing in water and ice. *Sci. Rep.* **3**, 3005 (2013)
30. Y. Huang, X. Zhang, Z. Ma, Y. Zhou, G. Zhou, C.Q. Sun, Hydrogen-bond asymmetric local potentials in compressed ice. *J. Phys. Chem. B*. **117**(43), 13639–13645 (2013)
31. Y.R. Shen, V. Ostroverkhov, Sum-frequency vibrational spectroscopy on water interfaces: polar orientation of water molecules at interfaces. *Chem. Rev.* **106**(4), 1140–1154 (2006)
32. F. Mallamace, M. Broccio, C. Corsaro, A. Faraone, D. Majolino, V. Venuti, L. Liu, C.Y. Mou, S.H. Chen, Evidence of the existence of the low-density liquid phase in supercooled, confined water. *Proc. Nat. Academy. Sci. USA*. **104**(2), 424–428 (2007)
33. M.W. Zhao, R.Q. Zhang, Y.Y. Xia, C. Song, S.T. Lee, Faceted silicon nanotubes: structure, energetic, and passivation effects. *J. Chem. Phys. C*. **111**(3), 1234–1238 (2007)
34. L. Vrbka, P. Jungwirth, Homogeneous freezing of water starts in the subsurface. *J. Phys. Chem. B*. **110**(37), 18126–18129 (2006)
35. D. Donadio, P. Raiteri, M. Parrinello, Topological defects and bulk melting of hexagonal ice. *J. Phys. Chem. B*. **109**(12), 5421–5424 (2005)
36. J.M. Zheng, W.C. Chin, E. Khijniak, G.H. Pollack, Surfaces and interfacial water: Evidence that hydrophilic surfaces have long-range impact. *Adv. Colloid Interface Sci.* **127**(1), 19–27 (2006)
37. C.Q. Sun, Y. Wang, B.K. Tay, S. Li, H. Huang, Y.B. Zhang, Correlation between the melting point of a nanosolid and the cohesive energy of a surface atom. *J. Phys. Chem. B*. **106**(41), 10701–10705 (2002)

38. Z. Zhang, M. Zhao, Q. Jiang, Melting temperatures of semiconductor nanocrystals in the mesoscopic size range. *Semicond. Sci. Technol.* **16**(6), L33–L35 (2001)
39. D. Xu, K.M. Liechti, K. Ravi-Chandar, Mechanical probing of icelike water monolayers. *Langmuir* **25**(22), 12870–12873 (2009)
40. K.B. Jinesh, J.W.M. Frenken, Experimental evidence for ice formation at room temperature. *Phys. Rev. Lett.* **101**(3), 036101 (2008)
41. K.B. Jinesh, J.W.M. Frenken, Capillary condensation in atomic scale friction: how water acts like a glue. *Phys. Rev. Lett.* **96**(16), 166103 (2006)
42. A.-M. Kietzig, S.G. Hatzikiriakos, P. Englezos, Physics of ice friction. *J. Appl. Phys.* **107**(8), 081101–081115 (2010)
43. R. Rosenberg, Why ice is slippery? *Phys. Today* **12**, 50–55 (2005)
44. M. Faraday, *Experimental researches in chemical and physics*, London: Taylor and Francis 372 (1859)
45. C.Q. Sun, Thermo-mechanical behavior of low-dimensional systems: the local bond average approach. *Prog. Mater. Sci.* **54**(2), 179–307 (2009)
46. C.Q. Sun, B.K. Tay, S.P. Lau, X.W. Sun, X.T. Zeng, S. Li, H.L. Bai, H. Liu, Z.H. Liu, E.Y. Jiang, Bond contraction and lone pair interaction at nitride surfaces. *J. Appl. Phys.* **90**(5), 2615–2617 (2001)
47. C. Lu, Y.W. Mai, P.L. Tam, Y.G. Shen, Nanoindentation-induced elastic-plastic transition and size effect in α -Al₂O₃(0001). *Philos. Mag. Lett.* **87**(6), 409–415 (2007)
48. C. Antonini, I. Bernagozzi, S. Jung, D. Poulikakos, M. Marengo, Water drops dancing on ice: how sublimation leads to drop rebound. *Phys. Rev. Lett.* **111**(1), 014501 (2013)
49. D.P. Singh, J.P. Singh, Delayed freezing of water droplet on silver nanocolumnar thin film. *Appl. Phys. Lett.* **102**(24), 243112 (2013)
50. F.G. Alabarse, J. Haines, O. Cambon, C. Levelut, D. Bourgogne, A. Haidoux, D. Granier, B. Coasne, Freezing of water confined at the nanoscale. *Phys. Rev. Lett.* **109**(3), 035701 (2012)
51. E.B. Moore, E. de la Llave, K. Welke, D.A. Scherlis, V. Molinero, Freezing, melting and structure of ice in a hydrophilic nanopore. *PCCP* **12**(16), 4124–4134 (2010)
52. Q.Z. Yuan, Y.P. Zhao, Topology-dominated dynamic wetting of the precursor chain in a hydrophilic interior corner. *Proc. R. Soc. A-Math. Phys. Eng. Sci.* **468**(2138), 310–322 (2012)
53. S. Liu, J. Luo, G. Xie, D. Guo, Effect of surface charge on water film nanoconfined between hydrophilic solid surfaces. *J. Appl. Phys.* **105**(12), 124301–124304 (2009)
- S.R. Friedman, M. Khalil, P. Taborek, Wetting transition in water. *Phys. Rev. Lett.* **111**(22) (2013)

Chapter 40

P, *T*, and *z* Coupling Effect

- *Pressure, temperature, and molecular undercoordination relax the bond in their own manner.*
- *Molecular CN reduction effects oppositely to that of compression on the H-bond length-stiffness relaxation and the associated properties of water ice.*
- *Cooling in liquid and solid effects the same to compression, resulting in O:H contraction and H–O elongation, with the same trends of property change.*
- *Freezing effects the same to molecular CN reduction causing volume expansion, H–O phonon stiffening and OIs energy entrapment, and non-bonding electron polarization.*
- *Mpemba paradox arises intrinsically from heating and undercoordination induced O:H–O bond relaxation. Heat emission proceeds at a rate depending on the initial energy storage, and the skin supersolidity creates the gradients of density, specific heat, and thermal conductivity for heat conduction in Fourier’s equation of fluid thermodynamics.*

40.1 Size and T Effect on Phonon Frequencies

Medcraft et al. [1] examined the size and temperature effect on the vibration frequencies of ice nanoparticles (3–150 nm diameter) over a wide range of temperatures (5–209 K). They found that a blueshift of the H–O stretching mode by 40 cm^{-1} for particles smaller than 5 nm, indicating the stiffening of the H–O bond. In the size regime of 8–200 nm, the size effect is insignificant because of the lower skin/volume ratio for larger particles. The ω_{H} peak shifting from $3,218\text{ cm}^{-1}$ at 30 K to $3,253\text{ cm}^{-1}$ at 209 K, evidence that heating stiffens the H–O bond and softens the other O:H bond. The liberation mode softens a little from 870 to 860 cm^{-1} in the temperature regime. MD simulations [2] suggested that cluster size reduction enhances the thermal stiffening of the stiffer ω_{H} , see Fig. 40.1. The ω_{H} of water at the polymer proxy undergoes a further 35 cm^{-1} blueshift at 310 K compared with the bulk at the same temperature; the ω_{L} of bulk water undergoes a

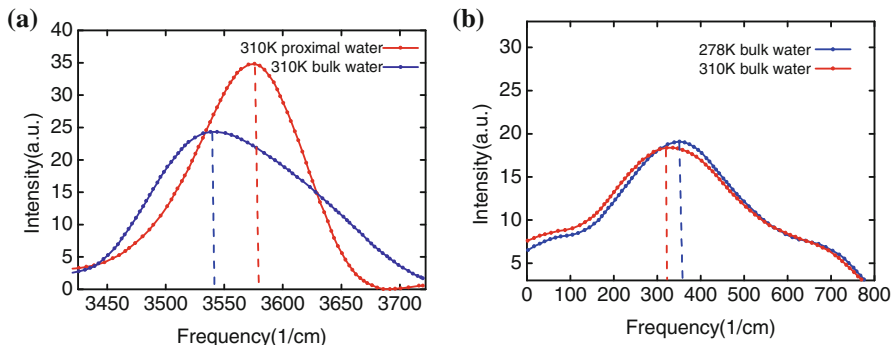


Fig. 40.1 **a** Cluster size reduction (proximal) stiffens the ω_H and **b** heating softens the ω_L of water (Reprinted with permission from [2]) because both molecular CN reduction and heating shortens and stiffens the H–O bond and lengthens softens the O:H bond

redshift upon being heated, instead. According to these observations, size reduction and heating have the same effect on ω_H stiffening. However, at $T < 80$ K, the ω_x keeps almost constant [1, 3], but the volume increases slightly [4] if the particle size remains unchanged. As mentioned in Chap. 41, the O:H–O angle stretching dominates the relaxation in this region.

The size and temperature coupling effect on the ω_H and ω_L of the proximal water droplet [2] is apparent. Size reduction shortens the H–O bond and stiffens the ω_H and meanwhile lengthens the O:H bond and softens the ω_L ; heating enhances this size trend. Therefore, heating and size reduction enhance each other in solid phase, leading to the MD-derived trends in Fig. 40.1.

40.2 Size and Pressure Effect on O1s Energy

Figure 40.2 shows that cluster size growth enhances the pressure effect on the redshift of the O1s-binding energy for free water clusters [5]. Except for the O1s peak at 539.7 eV for molecules, cluster size growth and pressure increase shift the binding energy from 539.7 to 538.2 eV toward the 538.1 eV component [6, 7].

The pressure and size coupling effect on the O1s-level shift follows the currently proposed mechanism. Molecular coordination reduction and pressure increase have the opposite effect on the H–O bond length and energy that determines the core-level shift. Therefore, coordination reduction effects the same to heating, growing size enhances the effect of pressure, on the phonon relaxation dynamics and binding energy entrapment.

Systematic studies [8, 9] also revealed that cooling enhances the effect of compression on the structure phase transition and dipole moment of ice.

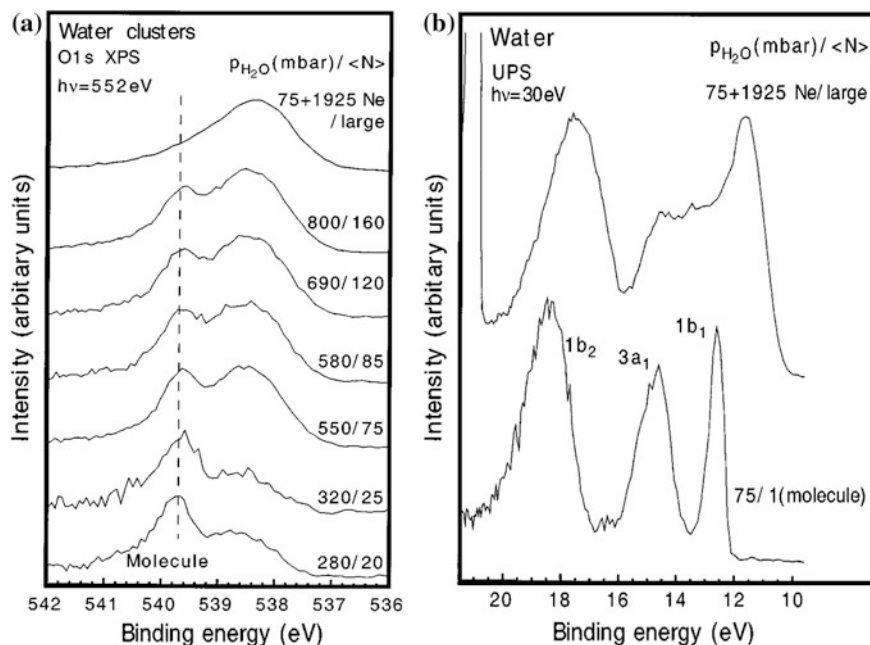


Fig. 40.2 Pressure and size joint effect on **a** the O1s and **b** valence band entrapment of water clusters. The valence peaks of water molecules are labeled according to the corresponding orbitals. The vertical hatched line denotes the O1s energy of the molecule. Both compression and size growth lengthens and softens the H–O bond and weakens the binding energy (Reprinted with permission from [5])

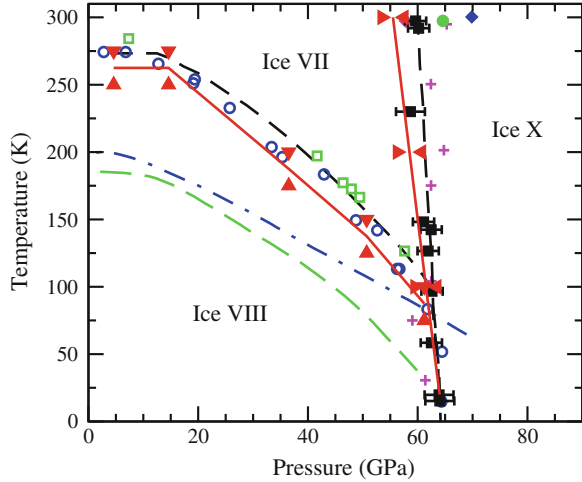
40.3 P and T Effect on Phase Stability

Systematic studies [8, 9] revealed that heating compensates for the effect of compression on the structure phase transition and dipole moment of ice. Compression lengthens the H–O bond, but heating shortens it. The dipole moment increases from 2.4 at 2,800 K to 3.0 Debye at 300 K and increases with density. Figure 40.3 shows the joint effect of pressure and temperature on the stability of ice VII, VIII, and X phases. The path integral MD calculations [9] agree well with measurements using infrared and Raman spectroscopy.

40.4 Water Surface Tension and O:H Bond Energy

Surface tension of liquid water is very important to our daily life. Small insects such as the water strider can walk and glide on water because their weight is not enough to penetrate the surface skin. If carefully placed on the surface, a small

Fig. 40.3 Comparison of calculated [9] and measured [10–14] phase diagram for ice VII, VIII, and X below 300 K (Reprinted with permission from [9]). The green-dashed and the blue dot-dashed lines are calculated by [15]



needle floats on the surface of water even though its density is times higher than water. If the surface is agitated to break up the surface tension, then the needle will quickly sink. The surface tension of water is 72 dynes/cm at 25 °C [16]. It would take a force of 72 dynes to break a surface film of water 1 cm long. The surface tension of water decreases significantly with temperature as shown in Fig. 40.4.

The temperature dependence of surface energy density, γ_{di} , follows the temperature dependence of surface tension and Young's modulus [17, 18]:

$$\gamma_{di}(T) \propto \frac{E_i(T)}{d_i^3(T)} = \frac{E_i(0) - \int_0^T \eta_{li}(t) dt}{d_i^3 \left(1 + \int_0^T \alpha_i(t) dt\right)^3}$$

where η_{li} is the specific heat of Debye approximation, and α_i the coefficient of thermal expansion. The proportional form is thus used because one is concerned about the relative change of these quantities to those of the bulk counterpart.

The relative changes of the surface energetics in the surface molecular layer to the bulk values at 0 K (γ_d and γ_f) measured at T can be derived as follows:

$$\frac{\gamma_{ds}(T)}{\gamma_d(0)} \cong \left(1 + \int_0^T \alpha_s(t) dt\right)^{-3} \times \begin{cases} 1 - \frac{\int_0^T \eta_s(t/\theta_D) dt}{E_s(0)}, & (T \leq \theta_D) \\ 1 - \frac{\eta_s T}{E_s(0)}, & (T > \theta_D) \end{cases} \quad (40.1)$$

where $E_s(0)$ is the surface molecular cohesive energy. Reproduction of the measured temperature dependence of surface energy, surface tension, and Young's modulus results in the molecular cohesive energy $E_s(0) = 0.38$ eV/mol and the Debye temperature $\theta_D = 198$ K [17]. For water skin with the known $\alpha = 0.162$ mJ/m²K, the derived Θ_D is compatible to that 185 ± 10 K derived from Helium scattering from ice surface at 150–191 K [19]. Figure 40.4 shows matching to the temperature dependence of the surface tension of liquid water [16, 17].

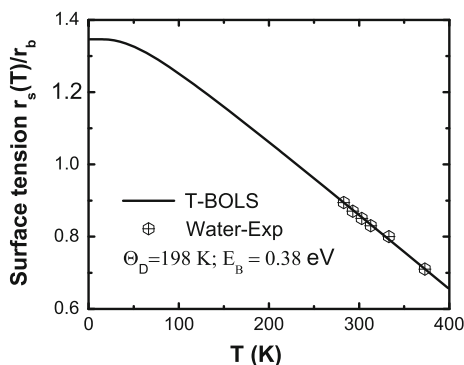


Fig. 40.4 Reproduction of the temperature-dependent surface tension of liquid H₂O results in an estimation of the Debye temperature $\theta_D = 198$ K and molecular cohesive energy $E_b(0) = 0.38$ eV [17], which gives rise to the $E_L = E_b(0)/4 = 0.095$ eV/non-bond (Reprinted with permission from [17])

It is understood now why hot water is a better cleaning agent. The thermal softening of the O:H bond decreases the surface tension and makes it a better ‘wetting agent’ to get into pores and fissures rather than bridging them with surface tension. Soaps and detergents may further weaken the O:H non-bond and hence help the cleaning of clothes by lowering the surface tension and strengthening the H–O bond of the water so that it more readily soaks into pores and soiled areas.

40.5 Summary

Hydrogen bond relaxes under the coupling of multiple fields and responds independently. Cooling in liquid and solid phase effect the same to water under compression to shortens the O:H nonbond and lengthens the H–O bond. Molecular undercoordination effects the same to the cooling transition from water to ice, which shortens the H–O bond and lengthens the O:H nonbond.

References

1. C. Medcraft, D. McNaughton, C.D. Thompson, D.R.T. Appadoo, S. Bauerecker, E.G. Robertson, Water ice nanoparticles: size and temperature effects on the mid-infrared spectrum. *Phys. Chem. Chem. Phys.* **15**(10), 3630–3639 (2013)
2. S.A. Deshmukh, S.K. Sankaranarayanan, D.C. Mancini, Vibrational spectra of proximal water in a thermo-sensitive polymer undergoing conformational transition across the lower critical solution temperature. *J. Phys. Chem. B* **116**(18), 5501–5515 (2012)

3. C. Medcraft, D. McNaughton, C.D. Thompson, D. Appadoo, S. Bauerecker, E.G. Robertson, Size and temperature dependence in the far-*Ir* spectra of water ice particles. *Astrophys. J.* **758**(1), 17 (2012)
4. K. Rottger, A. Endriss, J. Ihringer, S. Doyle, W.F. Kuhs, Lattice-constants and thermal-expansion of H₂O and D₂O Ice *ih* between 10 and 265 K. *Acta Crystallographica B* **50**, 644–648 (1994)
5. O. Bjorneholm, F. Federmann, S. Kakar, T. Moller, Between vapor and ice: free water clusters studied by core level spectroscopy. *J. Chem. Phys.* **111**(2), 546–550 (1999)
6. M. Abu-Samha, K.J. Borve, M. Winkler, J. Harnes, L.J. Saethre, A. Lindblad, H. Bergersen, G. Ohrwall, O. Bjorneholm, S. Svensson, The local structure of small water clusters: imprints on the core-level photoelectron Spectrum. *J. Phys. B: At. Mol. Opt. Phys.* **42**(5), 055201 (2009)
7. K. Nishizawa, N. Kurahashi, K. Sekiguchi, T. Mizuno, Y. Ogi, T. Horio, M. Oura, N. Kosugi, T. Suzuki, High-resolution soft X-ray photoelectron spectroscopy of liquid water. *Phys. Chem. Chem. Phys.* **13**, 413–417 (2011)
8. D.D. Kang, J.Y. Dai, J.M. Yuan, Changes of structure and dipole moment of water with temperature and pressure: a first principles study. *J. Chem. Phys.* **135**(2), 024505 (2011)
9. D.D. Kang, J. Dai, H. Sun, Y. Hou, J. Yuan, Quantum simulation of thermally driven phase transition and O *k*-edge absorption of high-pressure ice. *Sci. rep.* **3**, 3272 (2013)
10. A.F. Goncharov, V.V. Struzhkin, H.-K. Mao, R.J. Hemley, Raman spectroscopy of dense H₂O and the transition to symmetric hydrogen bonds. *Phys. Rev. Lett.* **83**(10), 1998–2001 (1999)
11. M. Song, H. Yamawaki, H. Fujihisa, M. Sakashita, K. Aoki, Infrared investigation on ice VIII and the phase diagram of dense ices. *Phys. Rev. B* **68**(1), 014106 (2003)
12. P. Pruzan, J.C. Chervin, B. Canny, Stability domain of the ice-VIII proton-ordered phase at very high-pressure and low-temperature. *J. Chem. Phys.* **99**(12), 9842–9846 (1993)
13. K. Aoki, H. Yamawaki, M. Sakashita, H. Fujihisa, Infrared absorption study of the hydrogen-bond symmetrization in ice to 110 GPa. *Phys. Rev. Lett. B* **54**(22), 15673–15677 (1996)
14. V.V. Struzhkin, A.F. Goncharov, R.J. Hemley, H.K. Mao, Cascading fermi resonances and the soft mode in dense ice. *Phys. Rev. Lett.* **78**(23), 4446–4449 (1997)
15. K. Umemoto, R.M. Wentzcovitch, S. de Gironcoli, S. Baroni, Order-disorder phase boundary between ice VII and VIII obtained by first principles. *Chem. Phys. Lett.* **499**(4–6), 236–240 (2010)
16. Temperature dependence of water surface tension. <http://hyperphysics.phy-astr.gsu.edu/hbase/surten.html#c3>
17. M. Zhao, W.T. Zheng, J.C. Li, Z. Wen, M.X. Gu, C.Q. Sun, Atomistic origin, temperature dependence, and responsibilities of surface energetics: an extended broken-bond rule. *Phys. Rev. B* **75**(8), 085427 (2007)
18. M.W. Zhao, R.Q. Zhang, Y.Y. Xia, C. Song, S.T. Lee, Faceted silicon nanotubes: Structure, energetic, and passivation effects. *J. Chem. Phys. C* **111**(3), 1234–1238 (2007)
19. M.T. Suter, P.U. Andersson, J.B. Pettersson, Surface properties of water ice at 150–191 K studied by elastic helium scattering. *J. Chem. Phys.* **125**(17), 174704 (2006)

Chapter 41

Mpemba Paradox: H-Bond Memory and Skin Supersolidity

- *Heating stores energy into water by stretching the O:H non-bond and shortening the H–O bond via a Coulomb coupling*
- *Heating and supersolid skin elevate jointly gradients of mass density, specific heat, and thermal conductivity in the liquid, favoring heat flowing outwardly in liquid*
- *Cooling does oppositely, like releasing a highly deformed bungee, to emit heat at a rate depending on initial storage*
- *Convection alone raises the skin temperature without the presence of Mpemba effect*
- *Being sensitive to the liquid volume and the temperature of the drain, Mpemba effect proceeds only in the strictly non-adiabatic source–drain interface ambient with a characteristic relaxation time that drops exponentially with the rise of the initial temperature of the source.*

41.1 Hotter Water Freezes Faster

Mpemba effect [1] is the assertion that warmer water freezes quicker than colder water does, even though it must pass the lower temperature on the way to freezing. This puzzle has baffled thinkers such as Francis Bacon and René Descartes [2], dating back to Aristotle who firstly noted that [3]: ‘The fact that the water has previously been warmed contributes to its freezing quickly: for so it cools sooner.’ Hence many people, when they want to cool water quickly, begin by putting it in the sun.

Although there is anecdotal support for this paradox [4], there is no agreement on exactly what the effect is and under what circumstances it occurs [5, 6]. This phenomenon remains a paradox in thermodynamics albeit so many possible explanations in terms of evaporation [7], frost [8], solutes [9], convection [10, 11], supercooling [8], etc [12]. According to the winner [13] of a competition held in 2012 by the Royal Society of Chemistry calling for papers offering explanations to the Mpemba paradox, the effect of convection enhances the probability of warmer

water freezing. It was best explained that [13] the flow in the first stage of cooling from θ_h (for hot) to θ_c (for cool) continues throughout the rest cooling process, accelerating cooling of the initially hotter water even after it reaches θ_c .

Despite claims often made by one source or another, there is no well-agreed explanation for how this phenomenon occurs. Actually, up to now explanations have just been guesswork about what is happening during the Mpemba effect with focusing mainly on extrinsic factors. Little attention [14, 15] has yet been paid to the nature of the heat source or mechanism behind the entire ‘source-path-drain’ cycling system. A combination of formulization of measurements and a solution to the one-dimensional, nonlinear Fourier’s initial and boundary condition problem using the finite element method with examination of all possible parameters enabled the solution to this mystery.

41.2 O:H–O Bond Relaxation

Generally, heating raises the energy of a substance by lengthening and softening all bonds involved; cooling does oppositely with volume contraction and heat emission. However, in water, heating stores energy to the liquid by lengthening and softening the O:H bond with energy at the 10^{-2} eV level and shortening and stiffening the H–O bond with energy around 4.0 eV because of the Coulomb coupling mechanism [16].

The heating–cooling cycling process reverses oxygen coordinates along the potential curves of Fig. 41.1a. The red spheres correspond to oxygen atoms in the hot state, and the blue ones in the cold state. At cooling, the shorter and stiffer H–O bond will be kicked up in the potential curve by O:H contraction, which releases energy to the drain. This process is like suddenly releasing a compressed bungee from different extents of deformation with the kicking by O:H contraction as an additional force propelling the energy emission. The rate of energy release is proportional to its initial energy storage.

In the process of molecular undercoordination, H–O contraction dominates because of the BOLS correlation [17]. Measurements given in Fig. 41.1b and c show that heating and molecular under-coordination (insets) share the same attribute of H–O contraction and O:H elongation and the associated blueshift of the H–O bond energy and vibration frequency. For example, heating from 0 to 90 °C raises the H–O vibration frequency from 3,190 to 3,260 cm^{-1} [18] and the O1s binding energy by 0.15 eV [19]. The H–O phonon frequency increases from 3,200 to 3,450 cm^{-1} [20] and the O1s energy increases by 1.5 eV [21–23] if one moves from the liquid bulk to the skin. The O–O distance increases by some 6–10 % from the bulk value of 2.695 [24] or 2.700 Å [25] to 2.960 Å [26] in the skin.

The joint effect of heating and molecular undercoordination is essential to the Mpemba effect [16, 17]. As the O:H contributes only $\sim 2\%$ to the system energy, one may focus on the H–O bond relaxation dynamics though this iteration applies to the H:O non-bond. The following relationship couples the thermal and

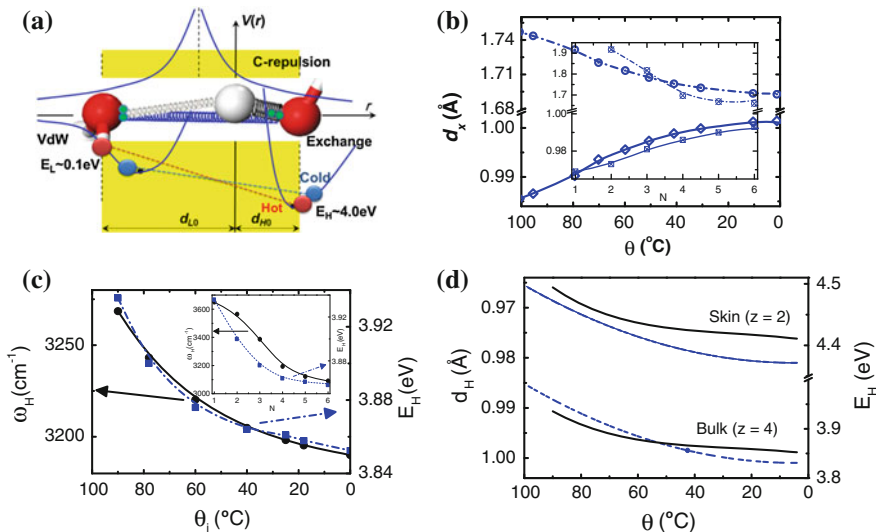


Fig. 41.1 O:H-O bond cooperative relaxation. **a** Interelectron-pair (small green pairing dots on oxygen) Coulomb repulsion couples the two parts to relax in the same direction but by different amounts as demonstrated by the length profiles of **(b)** the thermal (measurements [24, 27]) and inset molecular under-coordination (DFT calculations [17]) effects. **c** The corresponding variation in the H-O bond energy obtained from solving Lagrangian equation with the known vibration frequency at heating [18] and under-coordination [17, 18, 28–30] and the H-O bond length as input. **d** Heating and molecular under-coordination enhance each other in the H-O bond length and energy [31] that follows Eq. (41.1)

the under-coordination effect on bond length and energy [32], with the known skin $d_{OO} = 2.96 \text{ \AA}$ [26] (or $d_H = 0.84 \text{ \AA}$ [24]),

$$\begin{cases} d_H(z, \theta) = d_H(4, \theta) \times d_H(2, 0)/d_H(4, 0) \approx 0.84 d_H(4, \theta) \\ E_H(z, \theta) = E_H(4, \theta) + \Delta E_H(2, 0) = 0.18 + E_H(4, \theta) \end{cases} \quad (41.1)$$

$\Delta E_H(z, 0) = 0.18 \text{ eV}$ is the H-O bond energy gain when the molecular coordination number reduces from the bulk value to the value of the skin. Figure 41.1d compares the $d_H(z, \theta)$ and the $E_H(z, \theta)$ profiles for the bulk ($z = 4$) and the skin ($z \cong 2, N \cong 3$). Solving the Lagrangian equation [33] obtained the H-O bond energy $E_H(z, 0)$.

Water molecules with fewer than four neighbors form a supersolid phase that is elastic [20], polarized [34–36], hydrophobic [37, 38], viscous [39], thermally stable [40] with density being lower than that of ice (0.92 g cm^{-3}) [17]. The integral of the specific heat of the H-O bond, η_H , over the full temperature range is proportional to the cohesive energy E_H of the H-O bond [16], so the η_H varies with the thermal slope of the E_H . The thermal conductivity $\kappa \approx \eta_H v l \approx \eta_H (C_p)$ correlates with the specific heat η_H or its equivalence at constant pressure with v and l being the velocity and the mean free path of phonons, respectively. Therefore,

variation in the $dE_H/d\theta$ and the ρ [24] in the skin region redefine the local diffusion coefficient $\alpha = \kappa/(\rho C_p)$ in the Fourier equation, which heat conduction in the liquid follows. The addition of the supersolid skin creates the thermal conductivity gradient, which ensures thermal eddy current to flow outwardly toward the skin.

41.3 Numerical Solution: Skin Supersolidity

To verify the prediction on the presence of thermal conductivity gradient due to the joint effect of heating and skin supersolidity, one needs to solve the one-dimensional nonlinear Fourier equation [41] numerically by introducing the supersolid skin [17] in a tube container. Considering a one-dimensional approach, water in a cylindrical tube can be divided into the bulk (B) and the skin (S) region along the x-axial direction and put the tube into a drain of constant temperature 0 °C. The other end is open to the drain without the skin. The heat transfer in the partitioned fluid follows this transport equation and the associated initial and boundary conditions

$$\frac{\partial \theta}{\partial t} = \nabla \cdot (\alpha(\theta, x) \nabla \theta) - \mathbf{v} \cdot \nabla \theta \quad \left(\begin{array}{l} \alpha(\theta, x) = \frac{\kappa(\theta)}{\rho(\theta) C_p(\theta)} \begin{cases} 1 & (bulk) \\ \geq \rho_B \cdot \rho_S (= 4/3) & (skin) \end{cases} \\ \mathbf{v} = 10^{-4} \begin{cases} 1 & (bulk) \\ 10^{\pm 1} & (skin) \end{cases} \end{array} \right) \quad (41.2)$$

The first term describes diffusion and the second convection. The known temperature dependence of the thermal conductivity $\kappa_B(\theta)$, mass density $\rho_B(\theta)$, and specific heat under constant pressure $C_{pB}(\theta)$ see Appendix A4-6 determines the diffusion coefficient α_B . For simplicity, one can take the α_S in the skin ($z = 2$) as an adjustable for optimization. The following initial and boundary conditions apply:

$$\left\{ \begin{array}{ll} \theta = \theta_i & (t = 0) \\ \theta - \frac{\partial(\alpha_1 \theta_x)}{\partial x} + v_1 \theta_x = 0 & (t > 0; -l_1 < x < 0) \\ \theta - \frac{\partial(\alpha_2 \theta_x)}{\partial x} + v_2 \theta_x = 0 & (t > 0; 0 < x < l_2) \\ \theta(0^-) = \theta(0^+); \theta_x(0^-) = \theta_x(0^+) & (x = 0) \\ \theta + \frac{h_1}{\alpha_s} \theta_x = \theta_f & (x = -l_1) \\ \theta - \frac{h_2}{\alpha_s} \theta_x = \theta_f & (x = -l_2) \end{array} \right.$$

The heat transfer coefficient h of the cooling ends remains at 30 w/(m²K) and $\mathbf{v} = 10^{-4}$ m/s is the heat flow convection velocity in bulk water [42].

This equation can be solved using finite element analytical method. In numerical calculations, computer reads in the digitized documented data of $\rho(\theta)$, $\kappa(\theta)$, and $C_p(\theta)$ for the $\alpha_B(\theta)$. The skin $\alpha_S(\theta)$ is obtained by multiplying $\alpha_B(\theta)$ with a coefficient that is 4/3 that is the inverse of skin mass density. Figures 41.2 and 41.3 compare the examination results of the following parameters.

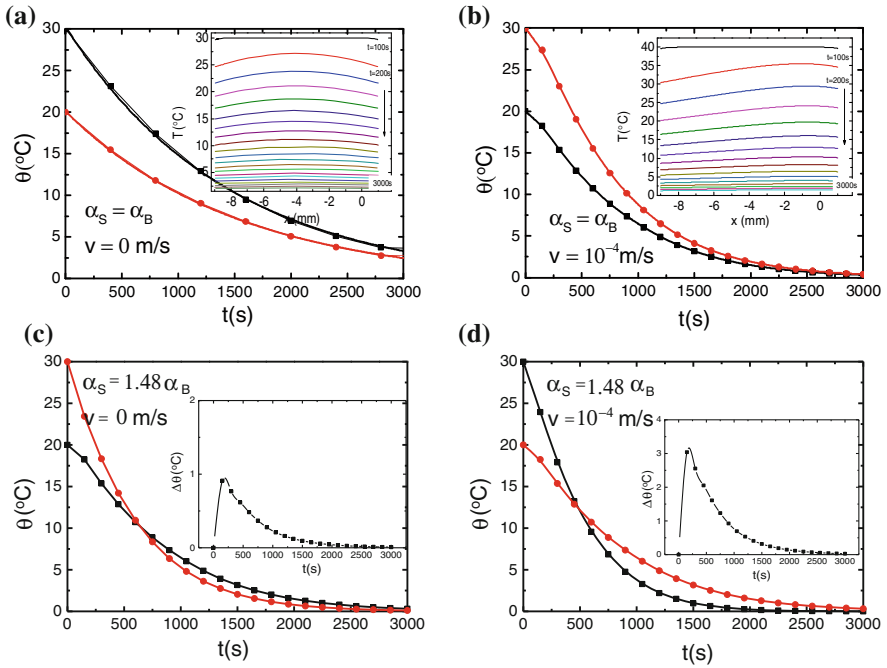


Fig. 41.2 $\theta(t)$ profiles for $\theta_i = 20$ and 30 °C with the given (v and α_S/α_B ratio) conditions with insets the $\theta(x, t)$ profiles for $\theta_i = 30$ °C in (a) and (b) and the $\Delta\theta(t)$ profile for $\theta_i = 20$ and 30 °C in (c) and (d). Convection ($v \neq 0$) raises only the skin temperature of $\Delta\theta(t) = 4$ °C without Mpemba effect. Skin supersolidity ($\alpha_S/\alpha_B = 1.48$) creates Mpemba effect with negligible skin temperature elevation. (d) Convection supplements the skin supersolidity to create Mpemba effect with noticeable skin temperature elevation maximal $\Delta\theta(t) = 3$ °C

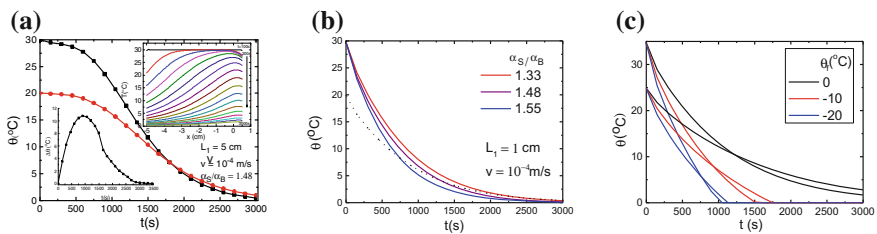


Fig. 41.3 Sensitivity to (a) tube size and (b) α_S/α_B ratio. **a** Volume inflation prolongs the time to reach the crossing temperature but raises the skin temperature in the present one-dimensional system. Continuing liquid volume inflation may annihilate the Mpemba effect because of the transitioning from the non-adiabatic to adiabatic ambient, which may extend to three-dimensional system. **b** The critical corresponds $\alpha_S/\alpha_B \geq 4/3$ to the ratio of $\rho_B/\rho_S = 1/0.75$. An increase in the α_S/α_B ratio shortens the time to the curves crossing. **c** The drain temperature (θ_i) determines the crossing temperature and relaxation time

| Parameters | | Observations | |
|-----------------------------------|---|---------------|----------------------------|
| Convection flow rate v (m/s) | Thermal diffusion coefficient α_S/α_B | Mpemba effect | Skin bottom $\Delta\theta$ |
| 0 | 1 | No | No |
| 10^{-4} | | | Yes |
| 0 | 1.48 | Yes | Tiny |
| 10^{-4} | | | Match measurements |

Numerical search based on the known temperature dependence of the thermal diffusion coefficient $\alpha(\theta)$ and the skin effect revealed the following: (1) the skin supersolidity enables the Mpemba effect; (2) heat convection alone only raises the skin temperature; (3) the critical ratio of the thermal diffusion coefficient $\alpha_S/\alpha_B \geq \rho_B/\rho_S = 4/3$ [24]; and (4) the crossing temperature is sensitive to the volume of the liquid and the temperature of the drain.

The optimal results in Fig. 41.4 match what Bregović, Mpemba, and Osborne have observed [1, 13]: (1) Hotter water freezes faster than colder water under the same conditions; (2) the temperature θ drops exponentially with cooling time (t) for transiting water into ice; (3) the skin is warmer than sites near the bottom in a beaker of water being cooled; and (4) the skin of hotter water is even warmer throughout the course of cooling [1], which indicates that the heat convection and diffusion rate increase with temperature.

41.4 Experimental Verification: O:H-O Bond Memory

The O:H–O bond possesses memory whose relaxation rate depends on initial energy storage. The following formulates the $\theta(t)$ decay profiles in Fig. 41.4a,

$$\begin{cases} d\theta = -\tau_i^{-1}\theta dt & \text{(decay function)} \\ \tau_i^{-1} = \sum_j \tau_{ji}^{-1} & \text{(relaxation time)} \end{cases} \quad (41.3)$$

The τ_i is the sum of τ_{ji} over all the possible j th processes of heat loss during cooling. Conducting experiments under identical conditions is necessary to minimize artifacts arising from processes such as radiation, source/drain volume ratio, exposure area, and container material. For instance, cooling one drop of 1 mL water needs shorter time than cooling one cup of 200 mL water at the same θ_i under the same conditions.

The measured $\theta(t)$ curves [1, 13] in Fig. 41.4 provide the $d\theta/dt = -\tau_i^{-1}\theta$. Converting the density $\rho(\theta)$ profile into the $d_H(\theta) = 1.0042 - 2.7912 \times 10^{-5} \exp[(\theta + 273)/57.2887]$ (Å) formulates the temperature dependence of the H–O bond length [24]. The $E_H = 0.5 k_H(\Delta d_H)^2$ approximates the energy stored in

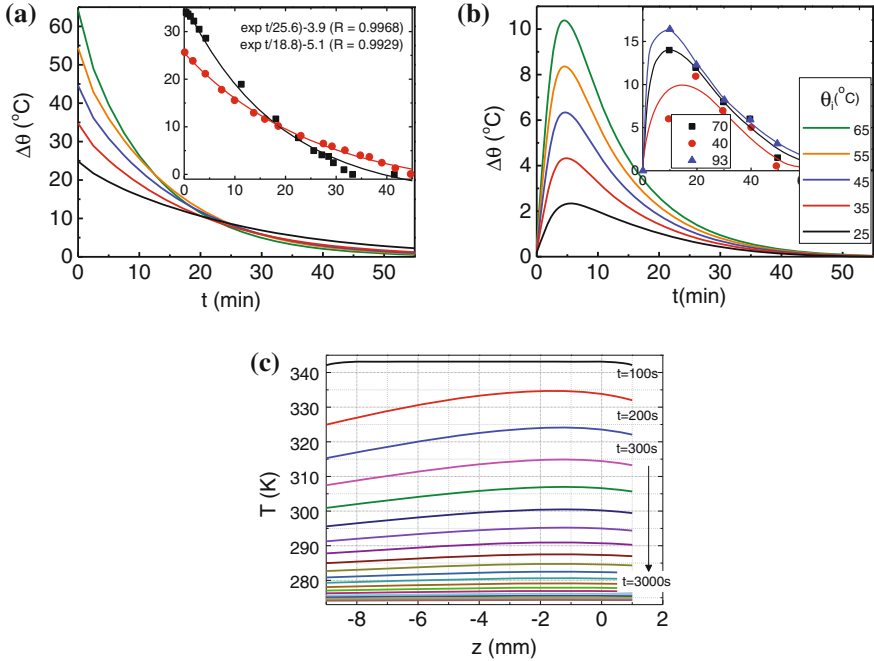


Fig. 41.4 Theoretical reproduction of (a) the $\theta(t)$ and (b) the skin bottom $\Delta\theta(t)$ curves for water cooling from different θ_i as recorded by Bregović, Mpemba, and Osborne (insets) [1, 13], (c) the $\theta(t, z)$ profiles under the optimal conditions of $\alpha_S = 1.48 \alpha_B$ (tube length 10 mm, skin thickness 2 nm). Formulating the experimental curves shows the θ_i dependent of the relaxation time τ

the H–O bond. Thus, one can determine the instantaneous velocity of the H–O bond length and energy:

$$\begin{cases} \frac{d(d_H(\theta))}{dt} = \frac{\partial(d_H(\theta))}{\partial\theta} \frac{d\theta}{dt} = -\tau_i^{-1}\theta \frac{\Delta d_H(\theta)}{57.2887}; \\ \frac{d(E_H(\theta))}{dt} = \frac{\partial(E_H(\theta))}{\partial(d_H(\theta))} \frac{d(d_H(\theta))}{dt} = -\tau_i^{-1}\theta \frac{k_H[\Delta d_H(\theta)]^2}{57.2887}. \end{cases} \quad (41.4)$$

Obtained from the Lagrangian solution [33], the force constant k_H increases from 32 to 35 eV/Å² when the ω_H shifts from 3,190 to 3,260 cm⁻¹ at heating from 0 to 90 °C. Figure 41.5 shows that the O:H–O bond possessing memory effect, which relaxes with momenta that depend on initial energy storage. Although passing the same temperature on the way to freezing, the H–O bond at initially higher temperature remains highly active in contrast to the otherwise when they meet. The enlargement of the Δd_H by under-coordination enhances the relaxation momenta of the H–O bond in the skin.

Solving the decay function (3), yields the $\tau_i(t_i, \theta_i, \theta_f)$,

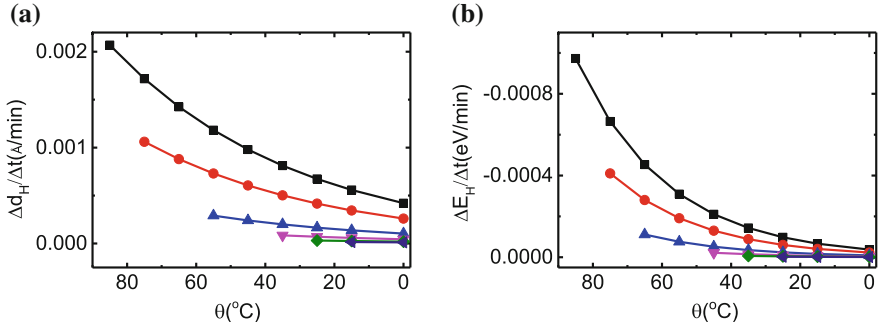


Fig. 41.5 Memory effect of the H–O bond. The relaxation rates in (a) length and (b) energy of the H–O bond are higher for the one cooling from initially higher temperature than the otherwise when they meet at the same temperature on the way of freezing

$$\tau_i = -t_i \left[\text{Ln} \left(\frac{\theta_f + b_i}{\theta_i + b_i} \right) \right]^{-1}$$

An offset of the $\theta_f (= 0)$ and the θ_i by a constant b_i assures $\theta_f + b_i \geq 0$, which constrains the drain temperature θ_f in calculations ($b_i = 5$ was taken with respect to the fitting in Fig. 41.2a).

Matching the solution of Eq. (41.3) to the $\theta(t)$ profiles in Fig. 41.2a inset, and then the experimental data of $t(\theta_i)$ in Fig. 41.6a yields the respective τ_i that drops exponentially indeed with the increase in the initial temperature θ_i , or with the increase in the initial energy storage and vibration frequency in Fig. 41.6b, as we expected.

It is emphasized that the Mpemba effect happens only under the circumstance that the temperature drops abruptly from θ_i to the constant θ_f at the source–drain interface. Fourier solution indicates that the Mpemba crossing temperature is sensitive to the volume of the liquid (Fig. 41.4a). If the liquid volume is too large, this effect may be prevented by slower heat dissipation. As experimentally confirmed by Brownridge [8], any spatial temperature decay between the source and the drain by tube sealing, oil film covering, source–drain vacuum isolating, muffin-tin like containers connecting, or even multiple sources putting into the limited volume of a refrigerator could prevent Mpemba effect from being happened.

H–O bond energy determines the critical temperature for phase transition [43]. Generally, superheating is associated with H–O bond contraction pertained to water molecules with fewer than four neighbors such as those formed the skin, monolayer film, or droplet on a hydrophobic surface with 5–10 Å air spacing between the drop and the surface presented [44]. Supercooling is associated with H–O bond elongation associated with water molecules in contact with hydrophilic surface [45] or being compressed [43]. The supercooling of the colder water in the Mpemba process [8] evidences that the initially longer H–O bond of cold water is lazier than those in the warmer water to relax at icing because of the lower momenta of relaxation.

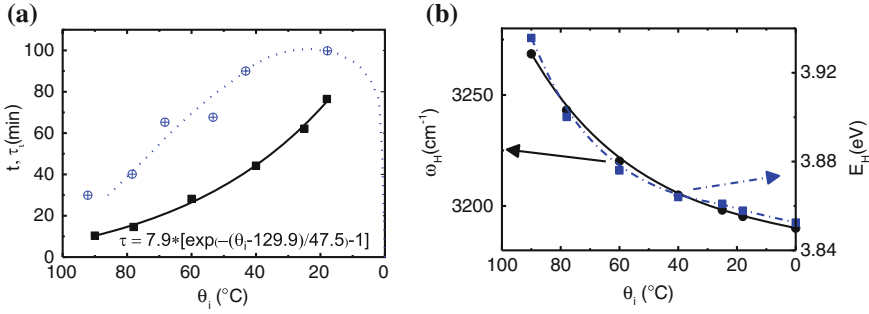


Fig. 41.6 Initial temperature θ_i dependence of **a** the freezing time (*dotted line*) (t) and the corresponding relaxation time (*solid line*) (τ), **b** in contrast to the measurements of the **c** initial $E_H(\theta_i)$ and $\omega_H(\theta_i)$ [18]. The $E_H(\theta_i)$ was derived from solving Lagrangian equation [33] based on the known $\omega_H(\theta)$ and $d_H(\theta)$ [24]

The involvement of ionic solutes or impurities [46, 47] mediates the Coulomb coupling and the H–O bond energy because of the alternation of charge quantities and ions volumes. Salting shares the same effect of heating on the H–O phonon blueshift [48, 49], which is expected to enhance the velocity of heat ejection at cooling. Mass loss due to evaporation at the temporarily higher temperatures [4] affects no rate of O:H–O bond relaxation albeit the negligible amount of water to be cooled.

41.5 Summary

Experimental derivatives and numerical reproduction of observations revealed the following pertaining to Mpemba paradox:

1. O:H–O bond possesses memory effect, whose thermal relaxation defines intrinsically the rate of energy ejection. Heating stores energy to water by O:H–O bond deformation. Cooling does oppositely to emit energy with a thermal momentum that is history dependent.
2. Heating and skin supersolidity create gradients of thermal diffusion with a critical coefficient ratio of $\alpha_S/\alpha_B \geq \rho_B/\rho_S = 4/3$ in the liquid for heat conduction. Convection alone raises only the skin temperature.
3. Highly non-adiabatic ambient with step temperature change is necessary to ensure the immediate energy dissipation. The Mpemba crossing temperature is sensitive to not only the volume of the water being cooled but also the drain temperature. This effect will not be observable if the liquid volume is too large.
4. Mpemba effect takes place with a characteristic relaxation time that drops exponentially with the increase in the initial temperature or the initial energy storage of the liquid.

References

1. E.B. Mpemba, D.G. Osborne, Cool? Phys. Educ. **14**, 410–413 (1979)
2. http://en.wikipedia.org/wiki/Mpemba_effect#cite_note-2
3. Aristotle, *Meteorology* 350 B.C.E: <http://classics.mit.edu/Aristotle/meteorology.1.i.html>
4. D. Auerbach, Supercooling and the Mpemba effect: when hot-water freezes quicker than cold. Am. J. Phys. **63**(10), 882–885 (1995)
5. M. Jeng, The Mpemba effect: when can hot water freeze faster than cold? Am. J. Phys. **74**(6), 514 (2006)
6. C.A. Knight, The Mpemba effect: the freezing times of hot and cold water. Am. J. Phys. **64**(5), 524 (1996)
7. M. Vynnycky, S.L. Mitchell, Evaporative cooling and the Mpemba effect. Heat Mass Transf. **46**(8–9), 881–890 (2010)
8. J.D. Brownridge, When does hot water freeze faster than cold water? A search for the Mpemba effect. Am. J. Phys. **79**(1), 78 (2011)
9. J.I. Katz, When hot water freezes before cold. Am. J. Phys. **77**(1), 27–29 (2009)
10. H. Heffner, *The Mpemba effect*: <http://www.mtaonline.net/~hheffner/Mpemba.pdf> (2001)
11. M. Vynnycky, N. Maeno, Axisymmetric natural convection-driven evaporation of hot water and the Mpemba effect. Int. J. Heat Mass Transf. **55**(23–24), 7297–7311 (2012)
12. P. Ball, Does hot water freeze first. Phys. World **19**(4), 19–21 (2006)
13. N. Bregović, *Mpemba effect from a viewpoint of an experimental physical chemist*. http://www.rsc.org/images/nikola-bregovic-entry_tcm18-225169.pdf (2012)
14. L.B. Kier, C.K. Cheng, Effect of initial temperature on water aggregation at a cold surface. Chem. Biodivers. **10**(1), 138–143 (2013)
15. X. Zhang, Y. Huang, Z. Ma, C.Q. Sun, *O:H-O bond anomalous relaxation resolving Mpemba paradox*. <http://arxiv.org/abs/1310.6514>
16. C.Q. Sun, X. Zhang, X. Fu, W. Zheng, J.-L. Kuo, Y. Zhou, Z. Shen, J. Zhou, Density and phonon-stiffness anomalies of water and ice in the full temperature range. J. Phys. Chem. Lett. **4**, 3238–3244 (2013)
17. C.Q. Sun, X. Zhang, J. Zhou, Y. Huang, Y. Zhou, W. Zheng, Density, elasticity, and stability anomalies of water molecules with fewer than four neighbors. J. Phys. Chem. Lett. **4**, 2565–2570 (2013)
18. P.C. Cross, J. Burnham, P.A. Leighton, The Raman spectrum and the structure of water. J. Am. Chem. Soc. **59**, 1134–1147 (1937)
19. T. Tokushima, Y. Harada, O. Takahashi, Y. Senba, H. Ohashi, L.G.M. Pettersson, A. Nilsson, S. Shin, High resolution X-ray emission spectroscopy of liquid water: the observation of two structural motifs. Chem. Phys. Lett. **460**(4–6), 387–400 (2008)
20. T.F. Kahan, J.P. Reid, D.J. Donaldson, Spectroscopic probes of the quasi-liquid layer on ice. J. Phys. Chem. A **111**(43), 11006–11012 (2007)
21. B. Winter, E.F. Aziz, U. Hergenbahn, M. Faubel, I.V. Hertel, Hydrogen bonds in liquid water studied by photoelectron spectroscopy. J. Chem. Phys. **126**(12), 124504 (2007)
22. M. Abu-Samaha, K.J. Borve, M. Winkler, J. Harnes, L.J. Saethre, A. Lindblad, H. Bergersen, G. Ohrwall, O. Bjornholm, S. Svensson, The local structure of small water clusters: imprints on the core-level photoelectron spectrum. J. Phys. B-At. Mol. Opt. Phys. **42**(5), 055201 (2009)
23. K. Nishizawa, N. Kurahashi, K. Sekiguchi, T. Mizuno, Y. Ogi, T. Horio, M. Oura, N. Kosugi, T. Suzuki, High-resolution soft X-ray photoelectron spectroscopy of liquid water. Phys. Chem. Chem. Phys. **13**, 413–417 (2011)
24. Y. Huang, X. Zhang, Z. Ma, Y. Zhou, J. Zhou, W. Zheng, C.Q. Sun, Size, separation, structure order, and mass density of molecules packing in water and ice. Sci. Rep. **3**, 3005 (2013)

25. U. Bergmann, A. Di Cicco, P. Wernet, E. Principi, P. Glatzel, A. Nilsson, Nearest-neighbor oxygen distances in liquid water and ice observed by x-ray Raman based extended x-ray absorption fine structure. *J. Chem. Phys.* **127**(17), 174504 (2007)
26. K.R. Wilson, R.D. Schaller, D.T. Co, R.J. Saykally, B.S. Rude, T. Catalano, J.D. Bozek, Surface relaxation in liquid water and methanol studied by x-ray absorption spectroscopy. *Chin. J. Chem. Phys.* **117**(16), 7738–7744 (2002)
27. F. Mallamace, C. Branca, M. Broccio, C. Corsaro, C.Y. Mou, S.H. Chen, The anomalous behavior of the density of water in the range $30\text{ K} < T < 373\text{ K}$. *Proc. Natl. Acad. Sci. U.S.A.* **104**(47), 18387–18391 (2007)
28. Q. Sun, The Raman OH stretching bands of liquid water. *Vib. Spectrosc.* **51**(2), 213–217 (2009)
29. J. Ceponkus, P. Uvdal, B. Nelander, Water tetramer, pentamer, and hexamer in inert matrices. *J. Phys. Chem. A* **116**(20), 4842–4850 (2012)
30. S. Hirabayashi, K.M.T. Yamada, Infrared spectra and structure of water clusters trapped in argon and krypton matrices. *J. Mol. Struct.* **795**(1–3), 78–83 (2006)
31. C.Q. Sun, *Relaxation of the Chemical Bond*. Springer Series in Chemical Physics, vol 108 (Springer, Berlin, 2014). ISBN: 978-981-4585-20-0. 550
32. X.X. Yang, J.W. Li, Z.F. Zhou, Y. Wang, L.W. Yang, W.T. Zheng, C.Q. Sun, Raman spectroscopic determination of the length, strength, compressibility, Debye temperature, elasticity, and force constant of the C–C bond in graphene. *Nanoscale* **4**(2), 502–510 (2012)
33. Y. Huang, X. Zhang, Z. Ma, Y. Zhou, G. Zhou, C.Q. Sun, Hydrogen-bond asymmetric local potentials in compressed ice. *J. Phys. Chem. B* **117**(43), 13639–13645 (2013)
34. J.K. Gregory, D.C. Clary, K. Liu, M.G. Brown, R.J. Saykally, The water dipole moment in water clusters. *Science* **275**(5301), 814–817 (1997)
35. K.R. Siefertmann, Y. Liu, E. Lugovoy, O. Link, M. Faubel, U. Buck, B. Winter, B. Abel, Binding energies, lifetimes and implications of bulk and interface solvated electrons in water. *Nat. Chem.* **2**, 274–279 (2010)
36. D.D. Kang, J.Y. Dai, J.M. Yuan, Changes of structure and dipole moment of water with temperature and pressure: a first principles study. *J. Chem. Phys.* **135**(2), 024505 (2011)
37. C. Wang, H. Lu, Z. Wang, P. Xiu, B. Zhou, G. Zuo, R. Wan, J. Hu, H. Fang, Stable liquid water Droplet on a water monolayer formed at room temperature on ionic model substrates. *Phys. Rev. Lett.* **103**(13), 137801–137804 (2009)
38. M. James, T.A. Darwish, S. Ciampi, S.O. Sylvester, Z.M. Zhang, A. Ng, J.J. Gooding, T.L. Hanley, Nanoscale condensation of water on self-assembled monolayers. *Soft Matter* **7**(11), 5309–5318 (2011)
39. Y. Ni, S.M. Gruenbaum, J.L. Skinner, Slow hydrogen-bond switching dynamics at the water surface revealed by theoretical two-dimensional sum-frequency spectroscopy. *Proc. Natl. Acad. Sci. U.S.A.* **110**(6), 1992–1998 (2013)
40. H. Qiu, W. Guo, Electromelting of confined monolayer ice. *Phys. Rev. Lett.* **110**(19), 195701 (2013)
41. J. Fourier, *The Analytical Theory of Heat* (Dover Publications, New York, 1955)
42. Water Thermal Properties—The Engineering Toolbox [Online]. Available: http://www.engineeringtoolbox.com/water-thermal-properties-d_162.html
43. C.Q. Sun, X. Zhang, W.T. Zheng, Hidden force opposing ice compression. *Chem. Sci.* **3**, 1455–1460 (2012)
44. A. Uysal, M. Chu, B. Stripe, A. Timalisina, S. Chattopadhyay, C.M. Schlepütz, T.J. Marks, P. Dutta, What x rays can tell us about the interfacial profile of water near hydrophobic surfaces. *Phys. Rev. B* **88**(3), 035431 (2013)
45. F.G. Alabarse, J. Haines, O. Cambon, C. Levelut, D. Bourgogne, A. Haidoux, D. Granier, B. Coasne, Freezing of water confined at the nanoscale. *Phys. Rev. Lett.* **109**(3), 035701 (2012)
46. M. Freeman, Cooler still. *Phys. Educ.* **14**, 417–421 (1979)
47. B. Wojciechowski, Freezing of aqueous solutions containing gases. *Cryst. Res. Technol.* **23**, 843–848 (1988)

48. Q. Sun, Raman spectroscopic study of the effects of dissolved NaCl on water structure. *Vib. Spectrosc.* **62**, 110–114 (2012)
49. S. Park, M.D. Fayer, Hydrogen bond dynamics in aqueous NaBr solutions. *Proc. Natl. Acad. Sci. U.S.A.* **104**(43), 16731–16738 (2007)

Chapter 42

Prospects

- *Understandings may apply to other areas containing short-range non-bonding interactions.*
- *Mechanism for water density oscillation applies to negative thermal expansion (NTE) as a consequence of specific heat disparity of the short-range interactions.*
- *Modulation of Coulomb repulsion could mediate intermolecular interaction that is responsible for electro- and magneto-melting, de- and anti-icing, etc.*
- *Coulomb mediation of H-bond interaction may mystify Hofmeister series for protein dissociation, activation and deactivation of ion channeling.*
- *Density, H–O bond energy, and polarization modulate dielectric performance of water ice.*

42.1 Negative Thermal Expansion and Spin Ices

The vast majority of materials have a positive coefficient of thermal expansion, and their volume increases on heating. There has been huge amount of materials, which display the unusual property of contracting in volume on heating [1–3], i.e., those with a NTE coefficient [4], following the discovery that cubic ZrW_2O_8 contracts over a temperature range in excess of 1,000 K [5, 6]. NTE also happens to diamond, silicon, and germanium at very low temperature (<100 K) [7] and glasses in the titania–silica family, Kevlar, carbon fibers, anisotropic Invar Fe–Ni alloys, and certain molecular networks, at room temperature. NTE materials can be combined with others demonstrating a positive thermal, expansion coefficient to fabricate composites exhibiting an overall zero thermal expansion (ZTE). ZTE materials are useful because they do not undergo thermal shock on rapid heating or cooling.

Various mechanisms explain the NTE in compounds. Models include transverse thermal vibrations of bridging oxygen in the M–O–M linkages [8] in ZrW_2O_8 , HfW_2O_8 , the $\text{SC}_2\text{W}_3\text{O}_{12}$, AlPO_4 , and faujasite SiO_2 [9]. The phonon modes (centered around 30 meV or equivalent $\sim 3,200 \text{ cm}^{-1}$) [10] can propagate without

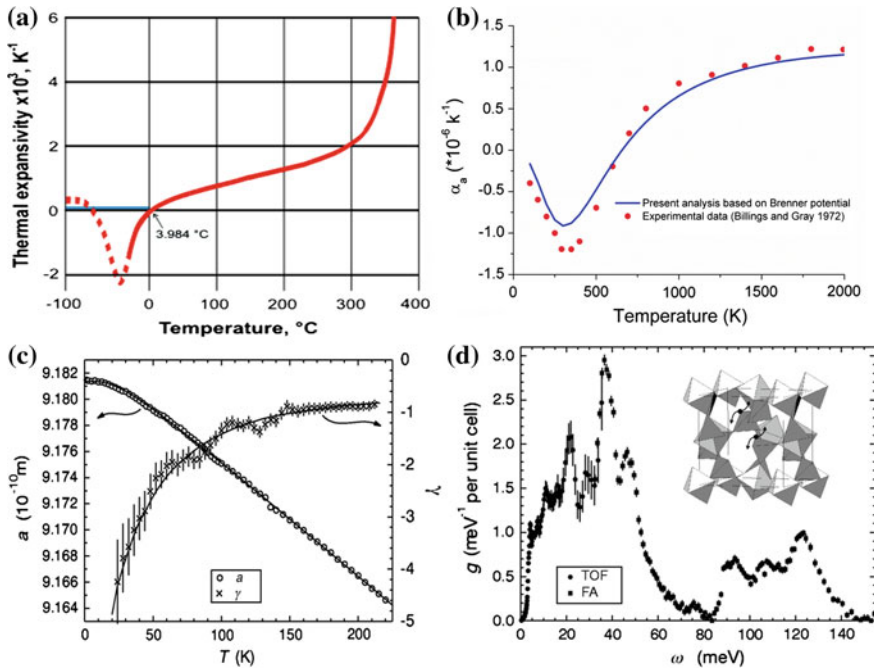


Fig. 42.1 The NTE of **a** H_2O (Reprinted with permission from [37]), **b** graphite (Reprinted with permission from [12]), and **c** ZrW_2O_8 (Reprinted with permission from [10]), with a (open circles) and Grüneisen parameter $\gamma = 3\alpha B/C_v$ (crosses). These NTEs share the same identity at different range of temperatures, which evidence the essentiality of two types of short-range interactions with specific-heat disparity. **d** ZrW_2O_8 phonon density of states measured at $T = 300$ K. Parameters α , B , and C_v correspond to thermal expansion coefficient, bulk modulus, and the specific heat at constant volume, respectively

distortions of the WO_4 tetrahedron and ZrO_6 octahedra, which is called ‘rigid unit mode.’ The rigid unit mode also accounts for the weak effect of the 430 K structural phase transition on the NTE [11].

The understanding of the NTE for water-ice may extend to the NTE in general. The NTE of graphite [12], graphene oxide paper [13], ZrWO_3 [5, 6] shares the same feature of water at freezing, see Fig. 42.1. Complementing the ‘rigid unit rotation mode’ mechanism [6], the understanding indicates that the NTE results from the involvement of at least two kinds of short-range interactions and the associated specific-heat disparity. For graphite instance, the (0001) intra-layer covalent bond and the interlayer van der Waals bond interactions may play the respective roles. O, N, and F create lone pair of electrons upon reaction, which add the short-range non-bonding interaction.

Spin ices are materials (such as $\text{Dy}_2\text{Ti}_2\text{O}_7$, $\text{Ho}_2\text{Ti}_2\text{O}_7$, $\text{Ho}_2\text{Sn}_2\text{O}_7$, and $\text{Dy}_2\text{Sn}_2\text{O}_7$) consisting of tetrahedron of ions, each of which has a nonzero spin, which satisfy some two-in, two-out rule analogous to water ice with H^+ proton ‘frustrating’ between two oxygen atoms. Spin ice materials therefore exhibit the

same residual entropy properties as water ice. While frustration is usually associated with triangular or tetrahedral arrangements of magnetic moments coupled via antiferromagnetic exchange interactions, spin ices are frustrated ferromagnets. It is the local nature of the strong crystal field forcing the magnetic moments to point either in or out of a tetrahedron that renders ferromagnetic interactions frustrated in spin ices.

The problem of the frustrated Ising antiferromagnet on a (pyrochlore) lattice of corner-shared tetrahedra has been related to the water ice problem [14]. Spin ice materials are characterized by disorder of magnetic ions even when said ions are at very low temperatures. AC magnetic susceptibility measurements find evidence for a dynamical freezing of the magnetic moments as the temperature is lowered somewhat below the temperature at which the specific heat displays a maximum.

It is the time dependence which distinguishes spin glasses from other magnetic systems, which is described by several models based on Ising premise [15–17]. Above the spin glass transition temperature, T_c , the spin glass exhibits typical magnetic behavior (such as paramagnetism). If a magnetic field is applied as the sample is cooled to the transition temperature, magnetization of the sample increases, which follows the Curie law. Upon reaching T_c , the sample becomes a spin glass, and further cooling results in little change in magnetization, undergoing the *field-cooled* magnetization. When the external magnetic field is removed, the magnetization of the spin glass falls rapidly to a lower value known as the *remnant* magnetization. Magnetization then decays slowly as it approaches zero. This slow decay is particular to spin glasses. Spin glasses differ from ferromagnetic materials by the fact that after the external magnetic field is removed from a ferromagnetic substance, the magnetization remains indefinitely at the remnant value.

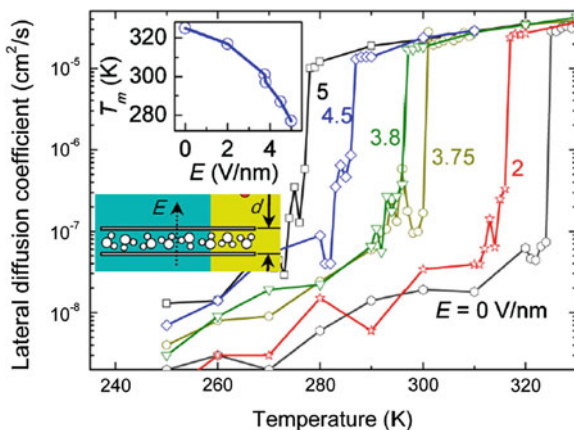
According to the current understanding, replacement of the H^+ proton with an ion of nonzero spin and the associated ion–ion and spin–spin interaction adding to the short-range interaction may discriminate spin ices from other magnetic materials. The short-range interactions and the repulsion between electron pairs on adjacent oxygen ions may also play the same roles as they do in water and ice.

42.2 Electro-, Mechano-, and Magneto-Freezing

External electric fields affect the freezing of water. For example, the rate of ice nucleation from vapor phase substantially increases from the normal growth rate in electric fields above 10^4 Vm^{-1} [18].

A surface charged with unlike charges has opposite effect on the freezing of water on it. Positively charged surfaces of pyroelectric LiTaO_3 crystals and SrTiO_3 thin films promote ice nucleation, whereas negatively charged surfaces of the same reduce the freezing temperature [19]. Accordingly, droplets of water cooled down on a negatively charged LiTaO_3 surface and remaining liquid at -11°C freeze immediately when this surface is heated to -8°C , as a result of the replacement of the negative surface charge by a positive one. Furthermore, the freezing on the

Fig. 42.2 Temperature dependence of the in-plane diffusion coefficient of the confined water at $d = 0.79$ nm under different external electric fields. Inset shows the T_m as a function of E (Reprinted with permission from [25])



positively charged surface starts at the solid/water interface, whereas on a negatively charged surface, ice nucleation starts at the air/water interface.

Freezing temperature of water is also altered by the electric fields within narrow cracks at the hydrophobic faces of α -amino acid single crystals [20]. Ice forms between the STM tip and the substrate [21], and water bridge forms between two beakers [22] under the field of 10^6 Vm^{-1} , though MD calculations [23, 24] predict that a strong electric fields strong ($>10^9 \text{ V m}^{-1}$) can align the water dipoles and crystallize liquid water into polar cubic ice. A MD calculation revealed that, see Fig. 42.2, the T_m of the monolayer ice decreases when the external electric field across increases to the level of 10^9 Vm^{-1} [25].

The floating water bridge is an interesting phenomenon first reported by Armstrong [26] in 1893 and by Fuchs et al. [27] in 2007. Two beakers filled with deionized water being subject to a DC [22] or AC (upto 1,000 Hz and 10 kV) [28] can form a bridge between them, which can last for hours and have a length exceeding 2 cm (see Fig. 42.3) [22, 29]. This experiment is stable, easy to reproduce, and leads to a special condition that the water in the bridge can be accessed and experimentally examined under high voltages and different atmospheric conditions [30]. The slight blueshift of the H–O mode from that of bulk water (see Fig. 42.3 (right) [28] is within the expectation of the enlarged skin supersolidity effect, according to the present understanding.

There are two different perspectives on the forces equilibrating the bridge. One is the tension along the bridge caused by the electric field within the dielectric material [31] and the other is the surface tension [32]. The latter indicates that the electric field only avoids the breakup of the bridge into small droplets and maintains stability.

The tension due to the electric field in a dielectric medium follows this relation [31]:

$$T_{\text{DE}} = \varepsilon_0(\varepsilon_r - 1)E^2A \quad (42.1)$$

where $A = \pi D^2/4$ is the cross-sectional area of the bridge, ε_r is the relative permittivity of water, and ε_0 is the vacuum permittivity. If a tension T is acting on a curved bridge with a curvature of ξ , the vertical force produced per unit length of the bridge is ξT , while the gravitational force per unit length is $\rho A g$. Thus, the ratio of the dielectric force and the gravitational force will be

$$R_{DE} = \frac{\varepsilon_0(\varepsilon_r - 1)E^2 \xi}{\rho g} \quad (42.2)$$

According to Aerov [32], the electric tension along the bridge is zero, and the tension holding the bridge is surface tension. The electric field causes stability of the bridge and avoids it breaking to droplets. The tension caused by surface tension is the sum of the tension on the sides (γP) and the repulsing tension caused by the pressure jump at the surface ($-\gamma P/2$):

$$T_{ST} = \frac{\gamma P}{2} \quad (42.3)$$

where $P = \pi D$ is the perimeter of the cross section of the bridge. According to this assumption, the ratio between the upward surface tension force and the gravitational force is

$$R_{ST} = \frac{2\gamma\xi}{\rho g D} \quad (42.4)$$

According to Namin et al. [22], both surface tension and electric tension contribute equally to holding the bridge. The Raman residual spectrum in Fig. 42.3 reveals, however, that the bridge formation changes little the H–O vibration frequency despite the small gain of the skin features at $3,450 \text{ cm}^{-1}$. Competition may exist between the skin supersolidity and the polarization of the dielectric bridge, which modulates the phonon frequency insignificantly. The skin supersolidity stiffens, while polarization screens potential and softens the H–O phonon.

MD calculations [33] revealed that under 10 T magnetic field and nanoscale hydrophobic confinement, liquid water freezes at 340 K and that the T_m is proportional to the magnetic field. Under $60 \times 10 \text{ T}$ DC magnetic field, the freezing point of the ambient water drops to $-7 \text{ }^\circ\text{C}$ [34]. $^1\text{H-NMR}$ measurements revealed that a 0.01–1.0 T magnetic field can decrease the surface tension and increase the viscosity of liquid water [35]. However, increasing the magnetic field up to 10 T , the surface tension of regular water at 298 K increases from 71.7 to 73.3 mN/m [36] and that of D_2O increases to 74.0 mN/m [36] in a B^2 manner.

Under compression, liquid water turns to be ice-VII at room temperature under 1 GPa [37]. Figure 42.4 shows the Raman spectra of 25 $^\circ\text{C}$ water as a function of pressure. During the phase transition, the pressure drops from 1.35 to 0.86 GPa, while the volume of the diamond cell change continually [38]. The sudden drop in pressure upon icing may indicate a new mechanism for the O:H and H–O energy transition (Fig. 42.4).

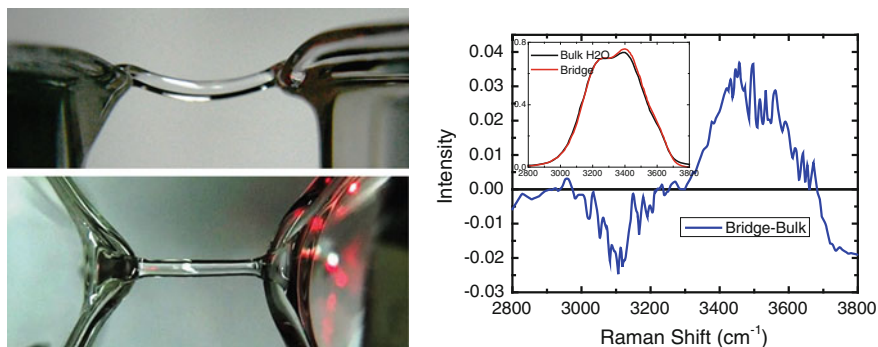


Fig. 42.3 (Left) Front and top views of floating water bridge (14 mm) formed between two beakers under a 10^6 Vm^{-1} electric field (Reprinted with permission from [22]). (Right) Residual Raman spectra of the bridge with respect to that of bulk water at 20 °C. Inset shows the respective normalized Raman spectrum (Reprinted with permission from [28])

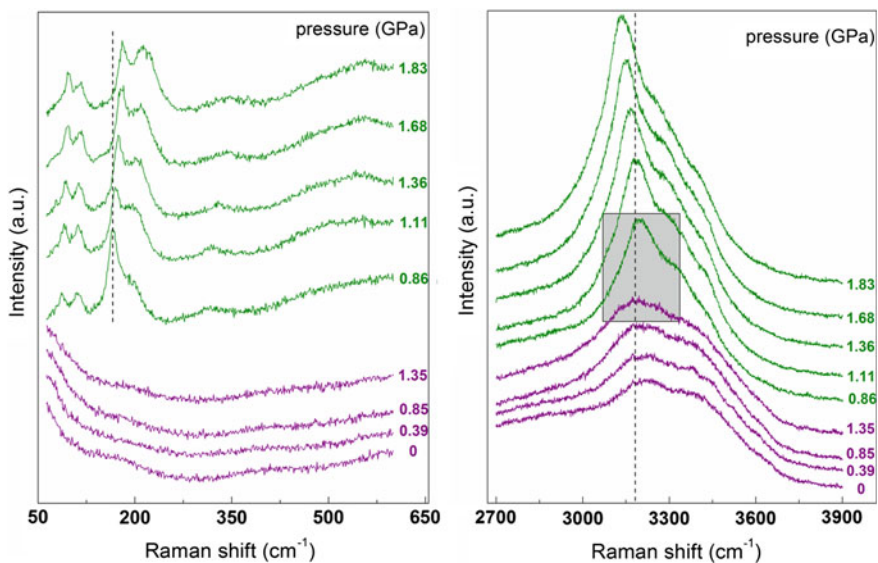


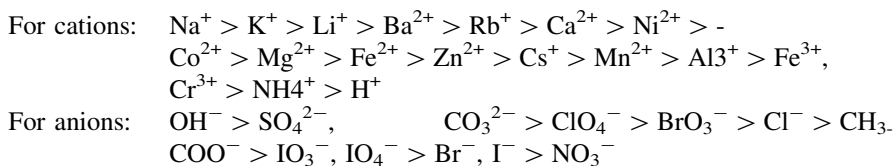
Fig. 42.4 Raman spectra of the mechano-freezing of water at room temperature, showing the pressure drop at freezing from 1.35 to 0.86 GPa [38]

The T_m is proportional to the H–O energy. How the electric, the magnetic, and the mechanical field mediate the H–O bond energy could be the key to these issues. The electric and magnetic field effects only on the electrons that may align in their own manner, and hence, the applied field modulates the H–O interaction. The electric [19, 21, 23–25, 39] and magnetic [33] fields can also modulate the Coulomb repulsion force.

42.3 Hofmeister Series, De-Icing, and Anti-Icing

The behavior of aqueous ions has profound effects on biological molecules such as proteins and deoxyribonucleic acid (DNA) and, thus, implications for health and disease [40]. The ions added in the form of salts or buffer reagents to the protein solution are crucial for maintaining protein stability. Different ions are better or worse at preventing aggregation and self-association. The core of the problem lies a phenomenon discovered in the late 1800s by the Czech chemist Franz Hofmeister see Fig. 42.5. He discovered that certain aqueous ions follow a peculiar order in their increasing or decreasing ability to precipitate egg whites in solution. Anions in particular, such as SO_4^{2-} , Cl^- , and SCN^- , follow a seemingly arbitrary sequence: In this order, they increasingly can denature and dissolve proteins and have increasing or decreasing effects on many other solution properties, such as surface tension [41].

Randall and Failey [42–44] realized that the efficiency of common cations and anions as salting-out agents follows the orders:



The effect of the addition of salts on solutions of nonelectrolytes is very complex, due to the different types of intermolecular interactions that involve the ions, the solvent, and the solute molecules [45].

There are two explanations of the mysterious Hofmeister series. One was that ions produced long-range effects on the structure of water, leading to changes in water's ability to let proteins fall out of, or stay dissolved in, a solution. That idea has largely been discarded. The currently popular view is that Hofmeister effects stem largely from the varying abilities of different salt ions to replace water at nonpolar molecular or macroscopic surfaces. But no theoretical framework can yet predict these actions [45].

Aqueous ionic solutions also lubricate the chemical machinery of the environment and life. Understanding the impact of ions on the properties of aqueous solutions and how these modified properties influence chemical and conformational dynamics remains an important and elusive objective of physical chemistry research. Sweet solutions can be obtained upon heating mixtures of simple carbohydrates, urea, and inorganic salts to moderate temperatures, to give new chiral media for organic reactions [46]. The solubility of sugar increases with temperature but drops with pressure [47]. Salt assists dissociating snow. Therefore, sugar and salt addition could lower the dissociation energy and hence anti-icing and de-icing take place.

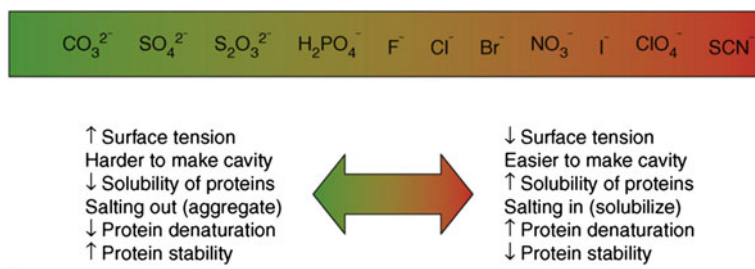


Fig. 42.5 Hofmeister series (Reprinted with permission from [85])

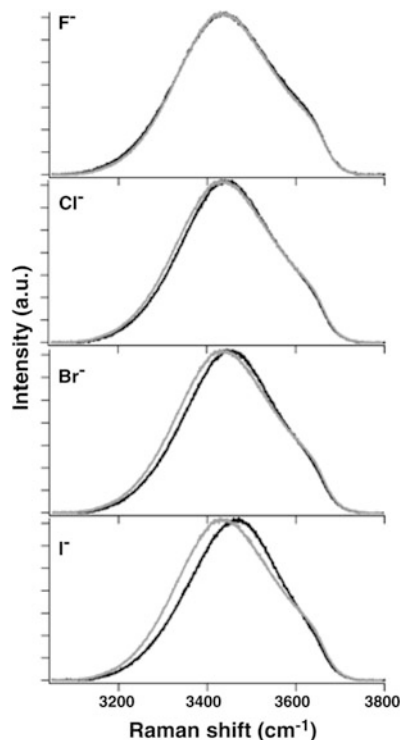
Using ultrafast (2-dimensional Infrared spectroscopy) vibrational spectroscopy and MD simulations, Park and Fayer [48] found that NaBr addition to 5% HOD in H_2O shifts the O–D stretching frequency from 2,509 to 2,539 cm^{-1} depending on the relative number (8, 16, 32) of H_2O molecules per Br^- ion. In aqueous NaBr solutions, the H-bond network of water is partially or completely disrupted depending on the concentration of NaBr salt. The HOD molecules are H-bonded to ions as $\text{HOD}-\text{Br}^-$, $\text{DOH}-\text{Br}^-$, and $\text{HDO}-\text{Na}^+$ in the hydration shells around the ions. Salt ions, such as NaCl [49], NaBe [48], LiCl [50], NaClO_4 and $\text{Mg}(\text{ClO}_4)_2$ [51–53], also induce blueshift of the hydroxyl group (–OH or –OD). Aqueous LiCl performs the same [50] to drop the supercooling temperature from 248 to 190 K by adding $\text{H}_2\text{O}/\text{LiCl}$ ratio from 100 to 6.7. The vibration frequency also changes with the pH value of organic liquid such as $\text{NH}_4\text{H}_2\text{PO}_4$ [54]. These features share the same attribute of the heating effect on the H–O stretching phonons [49, 55].

Figure 42.6 shows the residual FTIR ω_{B1} ($\sim 550 \text{ cm}^{-1}$ corresponding to the O:H–O being) and ω_H (3,200–3,450 cm^{-1}) spectra of water upon being heated and NaCl salted. The salted ω_H spectra are the same as reported in [49, 56]. Heating and salting effect the same on stiffening ω_H and softening the ω_L phonons, which indicates that heating and salting modulates the repulsion between electron pairs of oxygen atoms in a common mechanism.

The established understanding explains the salt stiffening of the high-frequency Raman phonons of liquid water. As demonstrated in [57], heating lengthens the d_{OO} , which weakens the Coulomb repulsion. Replacing an $\text{O}^{2\delta-}$ ion with the Cl^- and the Na^+ ion, the repulsion between the guested ions and the oxygen could be modulated—which could be the possible mechanism for the Hofmeister series [41, 45, 58]—cations and anions not only decrease the ability to augment water surface tension but also increase the ability to dissolve proteins.

Soaps, sugars, and detergents may functionalize the same as heating and salting in washing and cleaning. The replacement of $\text{O}^{2\delta-}$ ions with ions of salts, acids, or sugars and heating could weaken the Coulomb repulsion between the charged ions. According to the present understanding, reduction in repulsion restores the O in the H–O part to relax toward coordination origin and therefore shortens and stiffens the H–O bond [59], which stiffens the high-frequency phonons, as a probe.

Fig. 42.6 Comparison of the normalized H-O vibration spectra for 1 M KX ($X = F^-$, Cl^- , Br^- , and I^-) in HOD/D₂O (black lines) with that of pure HOD/D₂O (gray lines) (Reprinted with permission from ³⁷¹)



However, strengthening the repulsion will effect oppositely. Further investigation from the perspective ‘Coulomb mediation of H-bond interaction’ for these phenomena would be revealing.

42.4 Dielectric Relaxation

The relaxation of the static dielectric constant is related to the transition dynamics of electrons from the valence band to the conduction band. The dielectric constant relaxation depends functionally on E_G expansion, electron–phonon coupling, and lattice relaxation, showing the trend of interaction–enhancement resulted depression [60]. The dielectric permittivity ($\chi = \epsilon_r - 1$) of a semiconductor is approximately proportional to the inverse square of its bandgap, E_G [60–62], and the refractive index $n = \epsilon_r^{1/2} = (\chi + 1)^{1/2}$ will drop accordingly when the specimen is being compressed or cooled as E_G increases under such conditions [63–65]. However, the refractive index of water at room temperature increases with pressure in the same trend of density, see Fig. 42.7. The dielectric constant also increases at cooling. The joint effects of pressure and temperature on the dielectric behavior of water are opposite to those happened to usual materials.

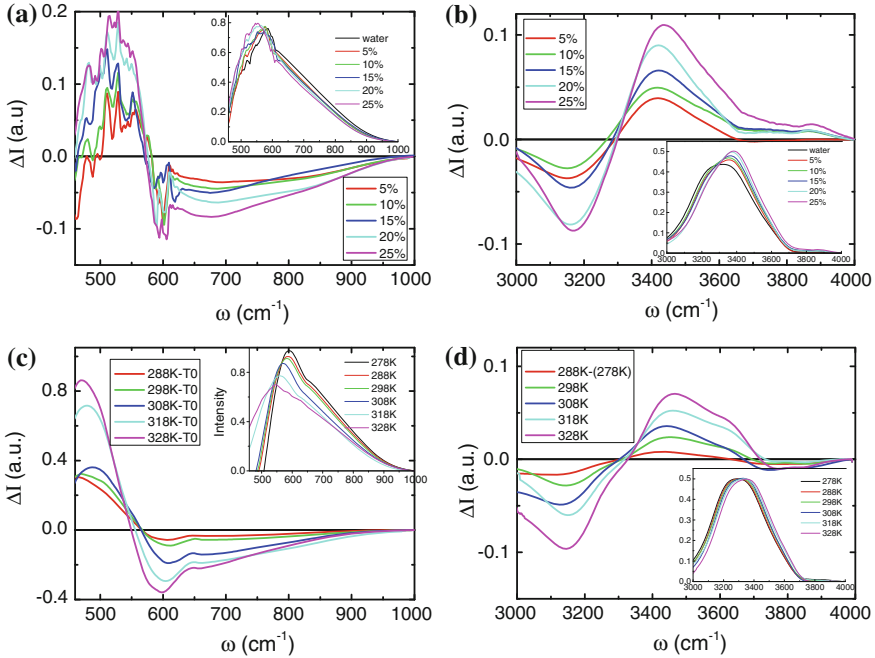


Fig. 42.7 FTIR residual spectra of water as a function of salinity (mass % NaCl) and heating with respect to the referential spectrum collected at 278 K without salting. *Insets* show the raw data [86]

On the framework developed, one may suggest the possible mechanism for the pressure- and cooling-enhanced dielectrics. Both compressing and cooling shorten the O:H bond and lengthen the H–O bond with density increase in water and ice. What is the factor among the following to dictate the dielectric enhancement or all the factors come into play?

$$\varepsilon_r \propto \begin{cases} \rho & \text{(Mass density)} \\ E_H & \text{(H–O energy)} \\ P & \text{(Polarization)} \end{cases}$$

This question is open for discussion. Furthermore, in the supersolid phase, how the dielectric constant changes with the molecular undercoordination? The dielectric constants of semiconductors drop with solid size, or under compression or under cooling. The dielectric constant is inversely proportional to the gradient of the bandgap [60]. All the bandgap, electron–phonon interaction, polarization, and bond length relaxation contribute, but unlikely the density, to the change in the dielectric constant.

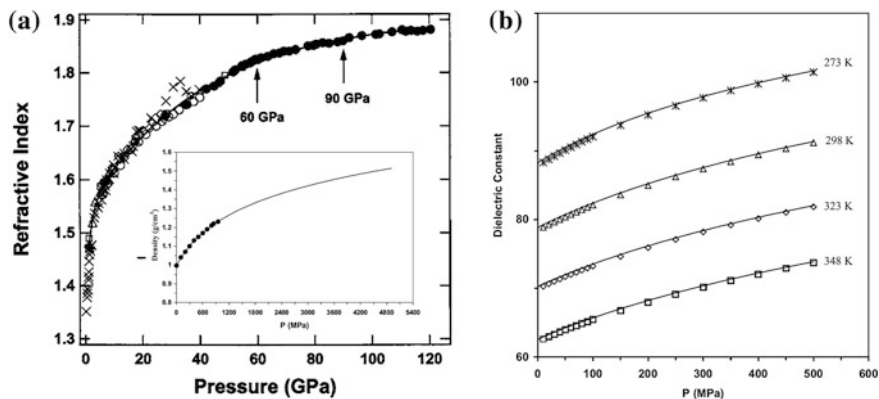


Fig. 42.8 **a** Pressure-enhanced refractive index (Reprinted with permission from [87]) and the water density (*inset*) measured at 298 K [88]. **b** Pressure and temperature dependence of the dielectric constant of water (Reprinted with permission from [88]). Both trends are opposite to that happened to other usual materials

42.5 H₂O-Cancer Cells and DNA Interaction

Interactions between water molecules and cells, membranes, proteins, etc., are areas that are fruitful for further investigation [66]. For instances, solvation water around proteins is denser than the bulk water [67]. Ice can absorb and entrap albumin (proteins) in solutions [68]. The geometry of the H-bond network within solvation layer differs from the one in bulk water to interact with protein surface. Unoccupied gap exists between the hydrophobic surface and neighboring solvation layer. The thickness of this gap depends on the local geometry of the water–protein interface, and it is a result of maintaining a balance between water–interface interactions and water–water interactions. Existence of this gap is one of the main factors that differentiate the hydrophobic hydration from hydration of the native form of kinesin [67].

Figure 42.8 compares the Raman spectra of the H–O mode in normal (non-cancerous) and cancerous breast tissues (infiltrating ductal cancer) compared with bulk neat water [69]. The spectra discriminate the H–O features of the cancerous tissue from that of the pure water and the healthy tissues. This spectral information shall reveal how the length and stiffness of the H–O bond changes once water interacts with cancerous tissues.

DNA is most important biomolecule because all the information regarding the structure and function of every living cell is stored in it. Like many other biomolecules, DNA's interaction with water determines to a large extent its structure and function. Much work has been done on the changes that DNA undergoes at different levels of hydration. However, the scattering from DNA and proteins in general is very weak and in a different energy-transfer range. One can observe the vibrations

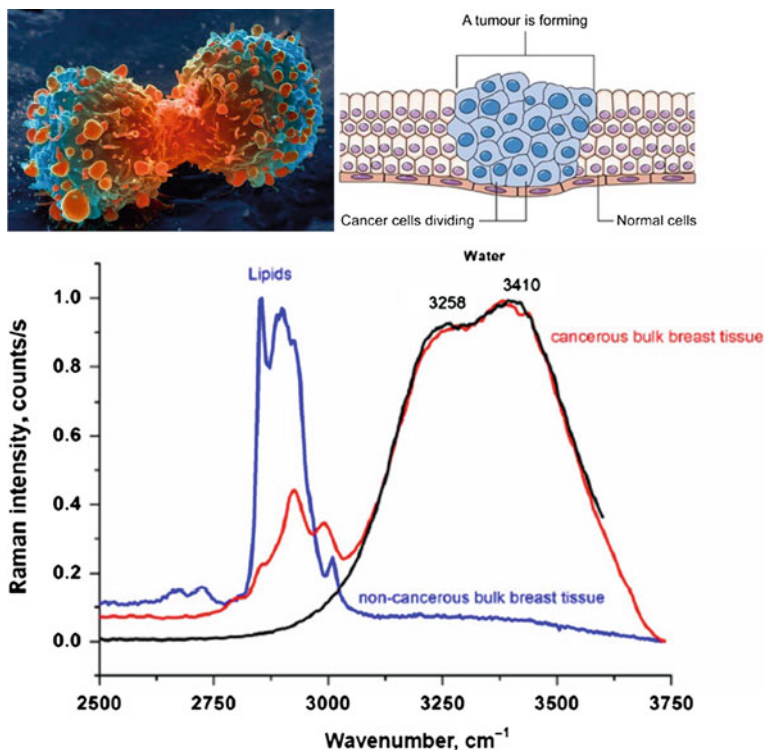


Fig. 42.9 Raman spectra of the H–O mode in normal (non-cancerous) and cancerous breast tissue illustrated (infiltrating ductal cancer) compared with bulk neat water (Reprinted with permission from [69])

largely due to water–water interactions perturbed by the biomolecules [70]. The neutron spectrum (predominated by H motion) in the low frequency region is mainly due to H-bonding between water and DNA, or between water molecules. Inelastic incoherent neutron scattering provides information in the same energy ranges as infrared and Raman spectroscopies. However, the intensity is directly proportional to the phonon density of states, which can be rigorously calculated using lattice or molecular dynamical methods based on a known potential function.

Figure 42.9 shows the neutron spectra of H₂O–DNA at 200 K. The OH stretching modes of water at about 400 meV shift to higher energy and the O:H stretching mode at about (below 5 meV, $\omega_x = \text{meV} \times 10^5 = \text{meV} \times 80.7 \text{ cm}^{-1}$) shift to lower energy at lower hydration level. Spectral peaks approach that of ice if the hydration level is sufficiently high. This effect is the same to that of heating and salting despite the inverse order of concentration.

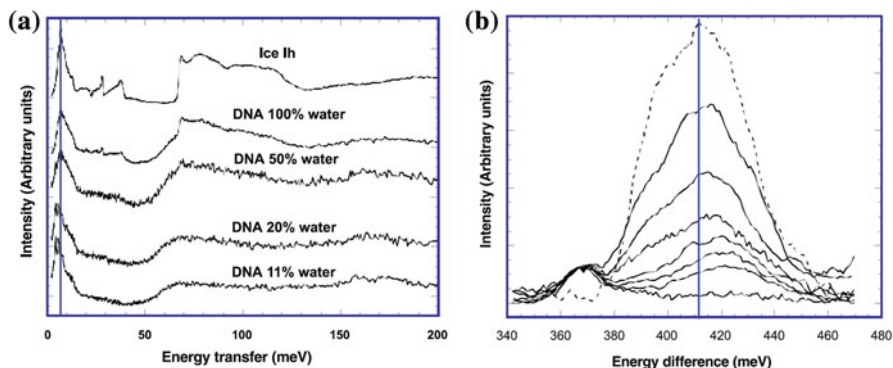


Fig. 42.10 Neutron vibration spectroscopy of H₂O–DNA at 20 K at different concentrations. **a** Number of percentage indicates grams of water per 100 g dry DNA. **b** Starting from *bottomcurve* is in order of lyophilized DNA, 25, 50, 75, 100, 150, 200 g of water per 100 g DNA (Reprinted with permission from [70])

42.6 H-Bond Likes in Organic Materials

The asymmetric, short-range H-bond potentials $V_x(r)$ could be intrinsic, which is independent of the applied stimuli. The short-range interactions and intermolecular repulsion could be applicable to inter- and intra-molecular interactions of other specimens containing F, O, and N. For instance, Raman spectral measurements [71] revealed the coupled ω_L (110–290 cm^{-1}) stiffening and ω_H ($\sim 3,000 \text{ cm}^{-1}$) softening of the N–O:H bonds in oxamide under compression [71]. The P-trends of the Raman shifts of melamine–boric acid adduct ($\text{C}_3\text{N}_6\text{H}_6 \cdot 2\text{H}_3\text{BO}_3$) supermolecules [72], as shown in Fig. 42.10, are the same to that of ice under compression [73]. Compression at pressure greater than 150 GPa also softens the phonons ($\sim 4,000 \text{ cm}^{-1}$) of hydrogen crystal at various temperatures [74]. Computations also revealed H–H bond length tends to symmetrization under compression [75]. These findings may be indicative that the short-range inter- and intra-molecular interactions and the interelectron repulsion exist in such crystals. Particularly, non-bonding electron lone pairs are associated not only with oxygen [76] but also with nitrogen and fluorine [77].

Therefore, H-bond exists in a versatile of specimens including H₂O, NH₃, HF, H₂, oxides, nitrides, and fluorides because of the presence of short-range inter- and intra-molecular interactions. N, O, and F create non-bonding lone pairs upon reacting with atoms of other less electronegative elements. Based on the currently established notations of hydrogen bond cooperativity, one can expect that the asymmetric relaxation in length and stiffness of the H-bond like dictates the functionality of species with the H-bond-like involvement, including biomolecules and organic materials.

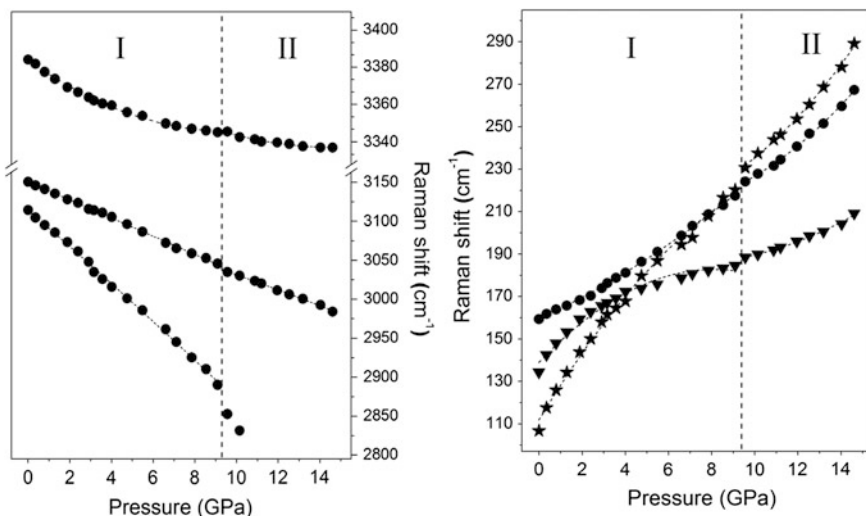


Fig. 42.11 Pressure-induced N–O:H ω_L stiffening and ω_H softening of oxamide (CONH_2)₂ molecular crystal in addition to the phase transition happened under 9.5 GPa (Reprinted with permission from [71])

42.7 Dynamic Wetting: Droplet Tap Dance and Leidenfrost Effect

Dynamic wetting of water droplet on either a hydrophobic or a hydrophilic surface of different roughness and at various temperatures is an issue of scientific interesting as it is related to liquid–solid interactions. Yuan and Zhao [78, 79] brought their insights into understanding the multiple-scale dynamics of moving contact line on lyophilic pillars and established the scaling relation: $R \sim t^x$ ($x = 1/3$ for a rough surface and $x = 1/7$ for a smooth surface) with R and t being the spreading radius and time, respectively. The spreading of a liquid drop on a hydrophilic, flexible pillared surface follows the same scaling relation. The flexible pillars accelerate the liquid when the liquid approaches and pin the liquid when the liquid passes. The liquid deforms the pillars, resulting energy dissipation at the moving contact line. The concerted effect of the surface topology, the intrinsic wettability, and the elasticity of a solid influences the flow pattern and the flow field of the droplet on the pillar-arrayed surface.

Yuan and Zhao first proposed and realized a concept of ‘electro-elasto-capillarity (EEC),’ controlling the wrapping and unwrapping of a soft membrane by applying an external electric field [80, 81]. During EEC, the precursor film competed with the soft substrate, causing capillary wave propagation [68]. Then, the substrate graphene was gradually delaminated. The dispersion relation showed

that the wave was controlled by the driving work difference of the precursor films that are solid-like and spreads in power law depending on the electric field.

Wang and Zhao [82, 83] reported a method of trapping tiny drops of salty water using a dynamic electric field to drive them moving to the beat on a hydrophobic surface. They combined effects of surface tension, elastic force, and Coulomb force to manipulate the flexible thin film to encapsulate and release a tiny droplet in a controllable and reversible manner. An AC electric field is applied to actuate the droplet and film to vibrate in a doubled frequency of input signal, as if they are dancing to a melody. During the dance, the droplet lies flat on the surface when the voltage reaches its peak, allowing it to be unwrapped in a controllable and reversible way.

The alternatively charging of the encapsulated salty droplet may alternate the repulsion and the attraction between the droplet and the hydrophobic surface that is highly elastic and polarized. This charge induction and the interface interaction might contribute to the tap dance of the droplet.

The skittering of water when it hits a hot pan is the Leidenfrost effect. When a liquid hits something really hot—about twice as hot as the liquid's boiling point—it never comes directly in contact with its surface. The effect is also responsible for the ability of liquid nitrogen to skitter across floors. The liquid drop produces an insulating vapor layer keeping that liquid from boiling rapidly. The vapor acts as a barrier to levitate the droplet. Water droplets can be made to climb up a steep incline—the sharper the teeth of the surface, the steeper incline they were able to climb [84]. The direction of the droplets' movement can be controlled by changing the temperature of the ratcheted surface.

This is because at temperatures above the Leidenfrost point, and the bottom part of the water droplet vaporizes immediately in contact with the hot plate. The resulting gas suspends the rest of the water droplet just above it, preventing any further direct contact between the liquid water and the hot plate. As steam has much poorer thermal conductivity, and further heat transfer between the pan and the droplet is slowed down dramatically. This also results in the drop being able to skid around the pan on the layer of gas just under it.

Liquid–vapor phase transition at the contacting point will eject molecules with momentum, which applies an impulse to the droplet. The direction of the impulse is subject to contacting conditions. The parallel component of the impulse will push the droplet upward the incline, and the perpendicular component will separate the pan and the droplet. Theoretical formulation of the Leidenfrost effect, particularly the upward movement of the droplet, from the perspective of momentum and impulse could be interesting.

Water evaporates more easily at higher temperatures under the less saturated vapour pressure than the otherwise because both heating and less-saturated vapour pressure lengthens and softens the O:H bond. The O:H bond energy determines the dissociation energy for molecular evaporation.

42.8 Summary

Coulomb mediation of interelectron pair interaction and additional polarization modulate the O:H and H-O bond strength and therefor the anomalous behavior of water and ice. Developed knowledge could apply to other systems involving electron lone pairs interactions. Analytical methods including XPS, Raman/FTIR in combination of MD and DFT could be revealing techniques for understanding the physics behind these systems.

References

1. S. Iikubo, K. Kodama, K. Takenaka, H. Takagi, M. Takigawa, S. Shamoto, Local lattice distortion in the giant negative thermal expansion material $\text{Mn}_3\text{Cu}_{1-x}\text{Ge}_x\text{N}$. *Phys. Rev. Lett.* **101**(20), 205901 (2008)
2. A.L. Goodwin, M. Calleja, M.J. Conterio, M.T. Dove, J.S.O. Evans, D.A. Keen, L. Peters, M.G. Tucker, Colossal positive and negative thermal expansion in the framework material $\text{Ag}_3\text{Co}(\text{CN})_6$. *Science* **319**(5864), 794–797 (2008)
3. A.C. McLaughlin, F. Sher, J.P. Attfield, Negative lattice expansion from the superconductivity-antiferromagnetism crossover in ruthenium copper oxides. *Nature* **436**(7052), 829–832 (2005)
4. J.S.O. Evans, Negative thermal expansion materials. *J. Chem. Soc.-Dalton Trans.* **19**, 3317–3326 (1999)
5. C. Martinek, F.A. Hummel, Linear thermal expansion of 3 tungstates. *J. Am. Ceram. Soc.* **51**(4), 227 (1968)
6. T.A. Mary, J.S.O. Evans, T. Vogt, A.W. Sleight, Negative thermal expansion from 0.3 to 1050 Kelvin in ZrW_2O_8 . *Science* **272**(5258), 90–92 (1996)
7. S. Stoupin, Y.V. Shvyd'ko, Thermal expansion of diamond at low temperatures. *Phys. Rev. Lett.* **104**(8), 085901 (2010)
8. A.W. Sleight, Compounds that contract on heating. *Inorg. Chem.* **37**(12), 2854–2860 (1998)
9. J.S.O. Evans, T.A. Mary, T. Vogt, M.A. Subramanian, A.W. Sleight, Negative thermal expansion in ZrW_2O_8 and HfW_2O_8 . *Chem. Mater.* **8**(12), 2809–2823 (1996)
10. G. Ernst, C. Broholm, G.R. Kowach, A.P. Ramirez, Phonon density of states and negative thermal expansion in ZrW_2O_8 . *Nature* **396**(6707), 147–149 (1998)
11. A.K.A. Pryde, K.D. Hammonds, M.T. Dove, V. Heine, J.D. Gale, M.C. Warren, Origin of the negative thermal expansion in ZrW_2O_8 and ZrV_2O_7 . *J. Phys.-Condens. Matter* **8**(50), 10973–10982 (1996)
12. Q.H. Tang, T.C. Wang, B.S. Shang, F. Liu, Thermodynamic properties and constitutive relations of crystals at finite temperature. *Sci. Chin.-Phys. Mech. Astron.* **G55**, 933 (2012)
13. Y.J. Su, H. Wei, R.G. Gao, Z. Yang, J. Zhang, Z.H. Zhong, Y.F. Zhang, Exceptional negative thermal expansion and viscoelastic properties of graphene oxide paper. *Carbon* **50**(8), 2804–2809 (2012)
14. P.W. Anderson, Ordering and antiferromagnetism in ferrites. *Phys. Rev.* **102**(4), 1008–1013 (1956)
15. D. Sherrington, S. Kirkpatrick, Solvable model of a spin-glass. *Phys. Rev. Lett.* **35**(26), 1792–1796 (1975)
16. K. Binder, A.P. Young, Spin glasses: experimental facts, theoretical concepts, and open questions. *Rev. Mod. Phys.* **58**(4), 801–976 (1986)

17. J.D. Bryngelson, P.G. Wolynes, Spin glasses and the statistical mechanics of protein folding. *Proc. Natl. Acad. Sci.* **84**(21), 7524–7528 (1987)
18. J.T. Bartlett, A.P. Vandenneuvel, B.J. Mason, Growth of ice crystals in an electric field. *Zeitschrift Fur Angewandte Mathematik Und Physik* **14**(5), 599 (1963)
19. D. Ehre, E. Lavert, M. Lahav, I. Lubomirsky, Water freezes differently on positively and negatively charged surfaces of pyroelectric materials. *Science* **327**(5966), 672–675 (2010)
20. M. Gavish, J.L. Wang, M. Eisenstein, M. Lahav, L. Leiserowitz, The role of crystal polarity in alpha-amino-acid crystals for induced nucleation of ice. *Science* **256**(5058), 815–818 (1992)
21. E.-M. Choi, Y.-H. Yoon, S. Lee, H. Kang, Freezing transition of interfacial water at room temperature under electric fields. *Phys. Rev. Lett.* **95**(8), 085701 (2005)
22. R.M. Namin, S.A. Lindi, A. Amjadi, N. Jafari, P. Irajizad, Experimental investigation of the stability of the floating water bridge. *Phys. Rev. E* **88**(3), 033019 (2013)
23. I.M. Svishchev, P.G. Kusalik, Electrofreezing of liquid water: a microscopic perspective. *J. Am. Chem. Soc.* **118**(3), 649–654 (1996)
24. R. Zangi, A.E. Mark, Electrofreezing of confined water. *J. Chem. Phys.* **120**(15), 7123–7130 (2004)
25. H. Qiu, W. Guo, Electromelting of confined monolayer ice. *Phys. Rev. Lett.* **110**(19), 195701 (2013)
26. W. Armstrong, Electrical phenomena The newcastle literary and philosophical society. *Electr. Eng.* **10**, 153 (1893)
27. E.C. Fuchs, J. Woisetschlager, K. Gatterer, E. Maier, R. Pecnik, G. Holler, H. Eisenkolbl, The floating water bridge. *J. Phys. D-Appl. Phys.* **40**(19), 6112–6114 (2007)
28. R.C. Ponterio, M. Pochylski, F. Aliotta, C. Vasi, M.E. Fontanella, F. Saija, Raman scattering measurements on a floating water bridge. *J. Phys. D-Appl. Phys.* **43**(17), 175405 (2010)
29. J. Woisetschlager, K. Gatterer, E.C. Fuchs, Experiments in a floating water bridge. *Exp. Fluids* **48**(1), 121–131 (2010)
30. E.C. Fuchs, Can a century old experiment reveal hidden properties of water? *Water* **2**(3), 381–410 (2010)
31. A. Widom, J. Swain, J. Silverberg, S. Sivasubramanian, Y.N. Srivastava, Theory of the Maxwell pressure tensor and the tension in a water bridge. *Phys. Rev. E* **80**(1), 016301 (2009)
32. A.A. Aerov, Why the water bridge does not collapse. *Phys. Rev. E* **84**(3), 036314 (2011)
33. G. Zhang, W. Zhang, H. Dong, Magnetic freezing of confined water. *J. Chem. Phys.* **133**(13), 134703 (2010)
34. Z. Zhou, H. Zhao, J. Han, Supercooling and crystallization of water under DC magnetic fields. *CIESC J.* **63**(5), 1408–1410 (2012)
35. R. Cai, H. Yang, J. He, W. Zhu, The effects of magnetic fields on water molecular hydrogen bonds. *J. Mol. Struct.* **938**(1–3), 15–19 (2009)
36. Y. Fujimura, M. Iino, The surface tension of water under high magnetic fields. *J. Appl. Phys.* **103**(12), 2940128 (2008)
37. M. Chaplin. Water structure and science. <http://www.lsbu.ac.uk/water/>
38. X. Zhang, T. Yan, B. Zou, C.Q. Sun, Mechano-freezing of the ambient water. <http://arxiv.org/abs/1310.1441>
39. D. Rzesanke, J. Nadolny, D. Duft, R. Muller, A. Kiselev, T. Leisner, On the role of surface charges for homogeneous freezing of supercooled water microdroplets. *Phys. Chem. Chem. Phys.* **14**(26), 9359–9363 (2012)
40. W.J. Xie, Y.Q. Gao, A simple theory for the Hofmeister series. *J. Phys. Chem. Lett.* **4**(24), 4247–4252 (2013)
41. E.K. Wilson, Hofmeister still mystifies. *Chem. Eng. News Arch.* **90**(29), 42–43 (2012)
42. M. Randall, C.F. Failey, The activity coefficient of gases in aqueous salt solutions. *Chem. Rev.* **4**(3), 271–284 (1927)
43. M. Randall, C.F. Failey, The activity coefficient of non-electrolytes in aqueous salt solutions from solubility measurements. The salting-out order of the ions. *Chem. Rev.* **4**(3), 285–290 (1927)

44. M. Randall, C.F. Failey, The activity coefficient of the undissociated part of weak electrolytes. *Chem. Rev.* **4**(3), 291–318 (1927)
45. P. Lo Nostro, B.W. Ninham, Hofmeister phenomena: an update on ion specificity in biology. *Chem. Rev.* **112**(4), 2286–2322 (2012)
46. G. Imperato, E. Eibler, J. Niedermaier, B. König, Low-melting sugar-urea-salt mixtures as solvents for Diels-Alder reactions. *Chem. Commun.* **9**, 1170–1172 (2005)
47. M.D.A. Saldaña, V.H. Alvarez, A. Haldar, Solubility and physical properties of sugars in pressurized water. *J. Chem. Thermodyn.* **55**, 115–123 (2012)
48. S. Park, M.D. Fayer, Hydrogen bond dynamics in aqueous NaBr solutions. *Proc. Natl. Acad. Sci. U.S.A.* **104**(43), 16731–16738 (2007)
49. Q. Sun, Raman spectroscopic study of the effects of dissolved NaCl on water structure. *Vib. Spectrosc.* **62**, 110–114 (2012)
50. F. Aliotta, M. Pochylski, R. Ponterio, F. Saija, G. Salvato, C. Vasi, Structure of bulk water from Raman measurements of supercooled pure liquid and LiCl solutions. *Phys. Rev. B* **86**(13), 134301 (2012)
51. S. Park, M.B. Ji, K.J. Gaffney, Ligand exchange dynamics in aqueous solution studied with 2DIR spectroscopy. *J. Phys. Chem. B* **114**(19), 6693–6702 (2010)
52. S. Park, M. Odellius, K.J. Gaffney, Ultrafast dynamics of hydrogen bond exchange in aqueous ionic solutions. *J. Phys. Chem. B* **113**(22), 7825–7835 (2009)
53. K.J. Gaffney, M. Ji, M. Odellius, S. Park, Z. Sun, H-bond switching and ligand exchange dynamics in aqueous ionic solution. *Chem. Phys. Lett.* **504**(1–3), 1–6 (2011)
54. C. Sun, D. Xu, D. Xue, Direct in situ ATR-IR spectroscopy of structural dynamics of NH₄H₂PO₄ in aqueous solution. *CrystEngComm* **15**(38), 7783–7791 (2013)
55. P.C. Cross, J. Burnham, P.A. Leighton, The Raman spectrum and the structure of water. *J. Am. Chem. Soc.* **59**, 1134–1147 (1937)
56. M. Baumgartner, R.J. Bakker, Raman spectroscopy of pure H₂O and NaCl-H₂O containing synthetic fluid inclusions in quartz—a study of polarization effects. *Mineral. Petrol.* **95**(1–2), 1–15 (2008)
57. C.Q. Sun, X. Zhang, X. Fu, W. Zheng, J.-L. Kuo, Y. Zhou, Z. Shen, J. Zhou, Density and phonon-stiffness anomalies of water and ice in the full temperature range. *J. Phys. Chem. Lett.* **4**, 3238–3244 (2013)
58. Y. Zhang, P. Cremer, Interactions between macromolecules and ions: the Hofmeister series. *Curr. Opin. Chem. Biol.* **10**(6), 658–663 (2006)
59. Y. Huang, X. Zhang, Z. Ma, Y. Zhou, G. Zhou, C.Q. Sun, Hydrogen-bond asymmetric local potentials in compressed ice. *J. Phys. Chem. B* **117**(43), 13639–13645 (2013)
60. L.K. Pan, C.Q. Sun, T.P. Chen, S. Li, C.M. Li, B.K. Tay, Dielectric suppression of nanosolid silicon. *Nanotechnology* **15**(12), 1802–1806 (2004)
61. L.K. Pan, H.T. Huang, C.Q. Sun, Dielectric relaxation and transition of porous silicon. *J. Appl. Phys.* **94**(4), 2695–2700 (2003)
62. R. Tsu, D. Babic, Doping of a quantum-dot. *Appl. Phys. Lett.* **64**(14), 1806–1808 (1994)
63. J.W. Li, L.W. Yang, Z.F. Zhou, P.K. Chu, X.H. Wang, J. Zhou, L.T. Li, C.Q. Sun, Bandgap modulation in ZnO by size, pressure, and temperature. *J. Phys. Chem. C* **114**(31), 13370–13374 (2010)
64. L.K. Pan, Y.K. Ee, C.Q. Sun, G.Q. Yu, Q.Y. Zhang, B.K. Tay, Band-gap expansion, core-level shift, and dielectric suppression of porous silicon passivated by plasma fluorination. *J. Vac. Sci. Technol. B* **22**(2), 583–587 (2004)
65. G. Ouyang, C.Q. Sun, W.G. Zhu, Atomistic origin and pressure dependence of band gap variation in semiconductor nanocrystals. *J. Phys. Chem. C* **113**(22), 9516–9519 (2009)
66. G.H. Zuo, J. Hu, H.P. Fang, Effect of the ordered water on protein folding: an off-lattice Go $\overline{\text{S}}\overline{\text{S}}$ -like model study. *Phys. Rev. E* **79**(3), 031925 (2009)
67. A. Kuffel, J. Zielkiewicz, Why the solvation water around proteins is more dense than bulk water. *J. Phys. Chem. B* **116**(40), 12113–12124 (2012)
68. A. Twomey, R. Less, K. Kurata, H. Takamatsu, A. Aksan, In Situ spectroscopic quantification of protein-ice interactions. *J. Phys. Chem. B* **117**(26), 7889–7897 (2013)

69. I.V. Stiopkin, C. Weeraman, P.A. Pieniazek, F.Y. Shalhout, J.L. Skinner, A.V. Benderskii, Hydrogen bonding at the water surface revealed by isotopic dilution spectroscopy. *Nature* **474**(7350), 192–195 (2011)
70. I. Michalarias, I. Beta, R. Ford, S. Ruffle, J.C. Li, Inelastic neutron scattering studies of water in DNA. *Appl. Phys. A Mater. Sci. Process.* **74**, s1242–s1244 (2002)
71. T. Yan, S. Li, K. Wang, X. Tan, Z. Jiang, K. Yang, B. Liu, G. Zou, B. Zou, Pressure-induced phase transition in N–H...O hydrogen-bonded molecular crystal oxamide. *J. Phys. Chem. B* **116**(32), 9796–9802 (2012)
72. K. Wang, D. Duan, R. Wang, A. Lin, Q. Cui, B. Liu, T. Cui, B. Zou, X. Zhang, J. Hu, G. Zou, H.K. Mao, Stability of hydrogen-bonded supramolecular architecture under high pressure conditions: pressure-induced amorphization in melamine-boric acid adduct. *Langmuir* **25**(8), 4787–4791 (2009)
73. Y. Yoshimura, S.T. Stewart, H.K. Mao, R.J. Hemley, In situ Raman spectroscopy of low-temperature/high-pressure transformations of H₂O. *J. Chem. Phys.* **126**(17), 174505 (2007)
74. C.-S. Zha, Z. Liu, R. Hemley, Synchrotron infrared measurements of dense hydrogen to 360 GPa. *Phys. Rev. Lett.* **108**(14), 146402 (2012)
75. H. Liu, H. Wang, Y. Ma, Quasi-molecular and atomic phases of dense solid hydrogen. *J. Phys. Chem. C* **116**(16), 9221–9226 (2012)
76. C.Q. Sun, Oxidation electronics: bond-band-barrier correlation and its applications. *Prog. Mater. Sci.* **48**(6), 521–685 (2003)
77. C.Q. Sun, Dominance of broken bonds and nonbonding electrons at the nanoscale. *Nanoscale* **2**(10), 1930–1961 (2010)
78. Q. Yuan, Y.-P. Zhao, Multiscale dynamic wetting of a droplet on a lyophilic pillar-arrayed surface. *J. Fluid Mech.* **716**, 171–188 (2013)
79. Q.Z. Yuan, Y.P. Zhao, Wetting on flexible hydrophilic pillar-arrays. *Sci. Rep.* **3**, 1944 (2013)
80. X.Y. Zhu, Q.Z. Yuan, Y.P. Zhao, Capillary wave propagation during the delamination of graphene by the precursor films in electro-elasto-capillarity. *Sci. Rep.* **2**, 927 (2012)
81. Q.Z. Yuan, Y.P. Zhao, Precursor film in dynamic wetting, electrowetting, and electro-elasto-capillarity. *Phys. Rev. Lett.* **104**(24), 246101 (2010)
82. Z. Wang, F.C. Wang, Y.P. Zhao, Tap dance of a water droplet. *Proc. R. Soc. A: Math. Phys. Eng. Sci.* **468**(2145), 2485–2495 (2012)
83. Y.P. Zhao, Droplet tap dance. <http://www.newscientist.com/blogs/nstv/2012/04/zapped-droplets-tap-dance-to-the-beat.html>
84. Leidenfrost effect. <http://www.dailymail.co.uk/sciencetech/article-2442638/Leidenfrost-Effect-makes-high-temperature-water-travel-uphill.html>
85. <http://tinyurl.com/ed5gj>
86. X. Zhang, C.Q. Sun, Coulomb mediation of hydrogen-bond short-range interactions by programmable heating and salting. <http://arxiv.org/abs/1310.0893> (2013)
87. C.S. Zha, R.J. Hemley, S.A. Gramsch, H.K. Mao, W.A. Bassett, Optical study of H₂O ice to 120 GPa: dielectric function, molecular polarizability, and equation of state. *J. Chem. Phys.* **126**(7), 074506 (2007)
88. W.B. Floriano, M.A.C. Nascimento, Dielectric constant and density of water as a function of pressure at constant temperature. *Braz. J. Phys.* **34**(1), 38–41 (2004)

Chapter 43

Conclusion

Consistency among the MD-DFT calculations, Lagrangian mechanics, Fourier fluid thermodynamics, and electron and phonon spectroscopy observations has verified the hypotheses and expectations on the anomalies of water ice under compressing, cooling, and clustering and their joint effect. Developed knowledge could be applicable to substances and interactions with electron lone pairs involvement. The following features the understandings:

1. It is essential to segment the O:H–O bond into the stronger H–O bond and the weaker O:H non-bond. Such a master–slave-segmented, flexible, polarizable, and fluctuating H-bond represents all O–O interactions in solid and liquid phases irrespective of topologic configurations or phase structures.
2. Ultrashort-range interactions of inter-electron-pair Coulomb repulsion, intermolecular van der Waals force, and intramolecular exchange form the key to the unusually asymmetric relaxation in length and stiffness of the O:H–O bond and therefore anomalies of water ice in response to cooling, clustering, and squeezing.
3. Compression shortens and stiffens the softer O:H bond, and meanwhile, lengthens and softens the stiffer H–O bond, through Coulomb repulsion, leading to the low compressibility, O:H–O proton symmetrization, phase-transition temperature (T_c) depression, bandgap expansion, softer phonon ($<300\text{ cm}^{-1}$) stiffening and stiffer phonon ($>3,000\text{ cm}^{-1}$) softening.
4. Molecular undercoordination of $(\text{H}_2\text{O})_N$ clusters functions oppositely to compression, resulting in molecular volume expansion, melting point (viscosity) elevation, binding energy entrapment, bonding charge densification and nonbonding charge polarization, stiffer phonon stiffening and softer phonon softening of molecular clusters, surface skins, and ultrathin films of water that manifest ice-like and hydrophobic nature at the ambient, without pre-melting.
5. The H–O bond contraction causes charge densification and further shifts the OIs energy, charge entrapment and densification, and elevation of the melting point of molecular clusters, surface skins, and ultrathin films of water.

6. The strong polarization results in the volume expansion, elasticity enhancement, self-lubricity, hydrophobicity, and viscosity of ultrathin films and surface skins of water.
7. The lacking of broken bonds for hydrophilically encapsulated water makes the water perform oppositely to that encapsulated in hydrophobic pores to demonstrate overcooling and easy wetting.
8. The superposition of the segmental specific heats of the H-bond shortens alternatively the segments below 373 K. In the liquid and the solid phases, the O:H bond serves as the master that contracts largely and meanwhile forces the stiffer real-bond as slave into Coulomb-repulsion-driven slight elongation, causing the O–O contraction and the seemingly normal cooling densification of water and ice; at the transition phase, the master–slave swap roles, turning the O–O into freezing elongation and volume expansion.
9. The extraordinarily high heat capacity of liquid water arises from the stronger H–O bond (3.97 eV) instead of the O:H lone pair networks (≤ 0.1 eV).
10. Thermal stiffening of the ω_H phonons in liquid water evidences the persistence of the fluctuating H-bond and the intermolecular repulsion.
11. The O–O distance is longer in ice than in water, and hence, ice floats.
12. Both the T_C and the O1s energy are proportional to the H–O bond energy, and they change accordingly upon being stimulated.
13. Cluster size growth enhances the pressure effect on the binding energy entrapment; size reduction enhances the thermal stiffening of the ω_H .
14. Water structure is composed of the fluctuating tetrahedrally configured bulk and of a supersolid skin that is stiffer, expanded, elastic, polarized, charge and energy entrapped. Both the monomial tetrahedral and the mixed-phase models are correct from considerable perspectives.
15. Skins of water and ice share the same H–O bond strength, which slipperizes ice and enhances the tension of water surface.
16. The O:H and H–O cooperative relaxation in length and stiffness shall be modulated by tuning the repulsive forces through replacing $O^{2\delta-}$ with other species such as biomolecules or inorganic salts.
17. Mpemba paradox arises intrinsically from heating and undercoordination-induced relaxation of the O:H–O bond that exhibits memory effect and forms eddy current inside the liquid. Heat emission proceeds at a rate depending on the initial energy storage, and the skin supersolidity creates the gradients of density, specific heat, and thermal conductivity for heat conduction in Fourier's equation of fluid thermodynamics.
18. One should focus more on the statistic mean of the complete set of cooperative parameters than on the instantaneous accuracy of one parameter at a pint of time in dealing with such a strongly correlated and fluctuating system.
19. Understandings can be extended to other physical anomalies of water such as Hofmeister series, Leidenfrost effect, and interaction with cells and proteins.
20. The concept of hydrogen bond cooperative relaxation also applicable to systems involving electron lone pairs.

Part IV

Water Myths

A.1 Highlights

- An extension of Ice Rule of Bernal–Fowler results in an ideal tetrahedron containing two H₂O molecules and four H-bonds, which forms the basic building block of H₂O and defines the density dependence of the molecular separation, $d_{OO} = 2.6950\rho^{-1/3}$ and H–O and O:H length cooperativity: $d_L = 2.5621 \times [1 - 0.0055 \times \exp(d_H/0.2428)]$.
- The flexible, polarizable, and segmented O:H–O H-bond forms a pair of asymmetric, Coulomb repulsion coupled, H-bridged oscillators, whose relaxation in length and energy and the associated electron entrapment and polarization determines the anomalies of water ice.
- The energy of the H–O polar-covalent bond dominates the T_C, the O_{1s} binding energy, and the high-frequency phonon ω_H shift; the O:H stiffness dominates the low-frequency ω_L shift and water dissolubility.
- Compression shortens and stiffens the softer O:H bond, meanwhile, lengthens and softens the H–O bond through repulsion between electron pairs on adjacent O atoms, which results in the O:H–O length symmetrization, low compressibility, T_C depression, phonon cooperative relaxation.
- At cooling, the density and phonon stiffness oscillates in four regions. O:H bond shortens more than the H–O bond lengthens in the liquid and solid phase; at freezing, the process inverts, because of the specific heat disparity of the two segments. At T < 80 K, O:H and H–O lengths remain because of identical specific heat ($\eta_L \approx \omega_H \approx 0$) but <O:H–O angle stretches, dropping density slightly. The d_{OO} in ice is longer than it is in water.
- With known bond lengths (or density) and vibration frequencies, Lagrangian mechanics maps H-bond asymmetric, local, short-range potentials
- Water and ice prefer statistically the fluctuated, tetrahedrally coordinated structure with supersolid skin despite the fluctuations in O:H length and <O:H–O angle

- Mpemba paradox arises intrinsically from O:H–O bond relaxation that not only determines the manner of heat emission but also heat conduction. Heat emission proceeds at a rate depending on the initial energy storage and the skin super-solidity creates the gradients of density, specific heat, and thermal conductivity.
- Focusing on the statistic mean of all cooperative parameters would be more reliably revealing than on the instantaneous accuracy of one parameter at a time for this strongly correlated and fluctuating system.

Appendices

Four-Stage Cu_3O_2 Bonding Kinetics

Video clip of STM/S optimized four-stage Cu_3O_2 bonding kinetics (see Electronic Supplementary Material)

Illustration: VLEED and STM quantification (Sec 3.2.4 and Fig 3.6) revealed the quantum stage from CuO_2 to Cu_3O_2 forming kinetics:

1. One O_2 molecule dissociates and bonds to one surface Cu in the $\text{Cu}(001)$ - $(222)\text{R}45$ unit cell to form a CuO_2 molecule with one Cu^{2+} and two O^- production, which polarizes the rest atoms in the top layer of the unit cell. This process leads to the “check-board” $c(22)$ - O^- STM image with protrusion being the interlocked dipoles (Fig 3.1a)
2. Each O^- rotates oppositely to get another electron from the nearest Cu in the second layer to form the Cu_3O_2 molecule. Further bond length and angle relaxation isolates and evaporates the Cu atom in the other row along the $2 \times 2 \text{R}45 \langle 11 \rangle$ direction—causing every fourth row of Cu atom missing
3. The sp^3 -orbit hybridization takes place with two lone pairs that polarize Cu atoms in the nearest row - the dipoles are coupled oppositely up to form bridge crossing over the missing row
4. Further relaxation adjusts the Cup-Cup distance, giving rise to the $(222)\text{R}45$ - 2O^{2-} “dumbbell” like STM image with protrusions being the oppositely coupled dipoles (Fig 3.1 and 3.13)

Atomic CN-Radius Correlation

Table of atomic-CN resolved bond length (see Electronic Supplementary Material)

Table 1 Appendix A2. Electronegativity (η), metallic (ionic) valency and metallic (ionic) radius of the elements

| η | Li(1.0) | Be(1.6) | H(2.2) | B(2.0) | C(2.5) | N(3.0) | O(3.5) | F(4.0) | | | | | | | | | |
|----------|---------|---------|---------|---------|----------|-------------|-----------|-----------|---------|---------|---------|---------|-------------|----------|----------|----------|---------|
| R(v) | 0.78(+) | 0.34(2) | 1.27(-) | - | 2.60(-4) | 1.71(-3) | 1.32(-2) | 1.33(-) | | | | | | | | | |
| R(CN=12) | 1.549 | 1.123 | - | 0.98 | 0.914 | 0.88,0.92 | - | - | | | | | | | | | |
| R(1) | 1.225 | 0.889 | 0.529 | 0.8 | 0.771 | 0.70,0.74 | 0.66,0.74 | 0.64,0.72 | | | | | | | | | |
| η | Na(0.9) | Mg(1.3) | | Al(1.5) | Si(1.9) | P(2.1) | S(2.5) | Cl(3.0) | | | | | | | | | |
| R(v) | 0.98(+) | 0.78(2) | | 0.57(3) | 0.41(4) | - | 1.72(-2) | 1.81(-) | | | | | | | | | |
| R(CN=12) | 1.896 | 1.598 | | 1.429 | 1.316 | 1.28 | 1.27 | - | | | | | | | | | |
| R(1) | 1.572 | 1.364 | | 1.248 | 1.173 | 1.1 | 1.04 | 0.994 | | | | | | | | | |
| η | K(0.8) | Ca(1.0) | Se(1.4) | Ti(1.5) | V(1.6) | Mn(1.6) | Fe(1.8) | Co(1.9) | Ni(1.9) | Cu(1.9) | Zn(1.7) | Ga(1.6) | Ge(2.0) | As(2.0) | Se(2.4) | Br(2.8) | |
| R(v) | 1.33(+) | 1.06(2) | 0.83(3) | 0.68(4) | -5 | (2.90,5.87) | 0.83(2) | 0.82(2) | 0.78(2) | 0.53(1) | 0.83(2) | 0.63(3) | 0.53(4) | - | 1.91(02) | 1.96(-) | |
| R(CN=12) | 2.349 | 1.97 | 1.62 | 1.467 | 1.338 | 1.357,1.267 | 1.26 | 1.252 | 1.244 | 1.276 | 1.379 | 1.408 | 1.366 | 1.39 | 1.4 | - | |
| R(1) | 2.025 | 1.736 | 1.439 | 1.324 | 1.224 | 1.168 | 1.165 | 1.157 | 1.149 | 1.173 | 1.249 | 1.245 | 1.223 | 1.21 | 1.17 | 1.142 | |
| η | Rb(0.8) | Sr(1.0) | Y(1.2) | Zr(1.3) | Nb(1.6) | Mo(2.2) | Ta(1.9) | Ru(2.2) | Rh(2.3) | Pd(2.2) | Ag(1.9) | Cd(1.7) | In(1.7) | Sn(2.0) | Sb(1.9) | Te(2.1) | I(2.5) |
| R(v) | 1.49(+) | 1.27(2) | - | 0.79(4) | - | -6 | -5.78 | -5.78 | -5.78 | -5.78 | 1.00(1) | 1.03(2) | -3.44 | (2.44,4) | - | 2.03(-2) | 2.20(-) |
| R(CN=12) | 2.48 | 2.148 | 1.797 | 1.597 | 1.456 | 1.386 | 1.336 | 1.342 | 1.373 | 1.442 | 1.543 | 1.66 | 1.620,1.542 | 1.59 | 1.6 | - | - |
| R(1) | 2.16 | 1.914 | 1.616 | 1.454 | 1.342 | 1.291 | 1.241 | 1.252 | 1.283 | 1.339 | 1.413 | 1.497 | 1.412,1.399 | 1.41 | 1.37 | 1.334 | - |
| η | Cs(0.8) | Ba(0.9) | La(1.1) | Hf(1.3) | Ta(1.5) | W(2.2) | Re(1.9) | Os(2.2) | Ir(2.2) | Pt(2.3) | Au(2.5) | Hg(2.0) | Tl(1.8) | Pb(2.3) | Po(2.0) | At(2.0) | |
| R(v) | 1.65(+) | 1.43(2) | - | - | - | -5.78 | -5.78 | -5.78 | -5.78 | -5.78 | -5.44 | 1.12(2) | 1.05(3) | -2.44 | - | - | - |
| R(CN=12) | 2.67 | 2.215 | 1.871 | 1.585 | 1.457 | 1.394 | 1.373 | 1.35 | 1.355 | 1.385 | 1.439 | 1.57 | 1.712 | 1.746 | - | - | - |
| R(1) | 2.35 | 1.981 | 1.69 | 1.442 | 1.343 | 1.299 | 1.278 | 1.255 | 1.26 | 1.29 | 1.336 | 1.44 | 1.549 | 1.538 | 1.52 | 1.53 | - |
| η | Fa(0.7) | Ra(0.9) | Ae | Th | Pa | U | Np | Pu | Am | Cm | | | | | | | |
| R(v) | - | - | 89.94 | - | - | -5.78 | - | - | - | - | - | - | - | - | - | - | - |
| R(CN=12) | (1.1- | | (1.1- | | | 1.4) | 1.795 | 1.516 | | | | | | | | | |
| r(1) | | | 1.652 | | | 1.421 | | | | | | | | | | | |
| η | | | Ce | Pr | Nd | Pm | Sm | Eu | Gd | Tb | Dy | Ho | Er | Tm | Yb | Lu | |
| R(v) | | | -3.2 | -3.1 | -3.1 | -2.8 | -2 | -3 | -3 | -3 | -3 | -3 | -3 | -3 | -2 | -3 | |
| R(CN=12) | | | 1.818 | 1.824 | 1.818 | 1.85 | 2.084 | 1.795 | 1.773 | 1.77 | 1.761 | 1.748 | 1.748 | 1.743 | 1.933 | 1.738 | |
| R(1) | | | 1.646 | 1.648 | 1.642 | 1.66 | 1.85 | 1.614 | 1.592 | 1.589 | 1.58 | 1.567 | 1.567 | 1.562 | 1.699 | 1.557 | |

R(v) is the ionic radius and v the valence value. R(CN=12) and R(1) is the corresponding bond radius

[From Pauling L., *J. Am. Chem. Soc.* **69**, 542 (1947), and Goldshmidt V. M., *Ber. Deut. Chem. Ges.* **60**, 1270 (1927)]

Solid Mechanics

Table A.3.1 Bulk moduli for $A^N B^{8-N}$ covalent crystals [1–11]

| Crystal | Structure | d | n_{ij} | P | B_{Exp} | $B_{Cal,1}$ | $B_{Cal,2}$ | $B_{Cal,3}$ |
|---------|-----------|------|----------|-----|-----------|-------------|-------------|-------------|
| C | A4 | 1.55 | 0.707 | 16 | 442 | 433 | 418.2 | 442.1 |
| Si | A4 | 2.35 | 0.707 | 16 | 100 | 103 | 97.4 | 95.6 |
| Ge | A4 | 2.45 | 0.707 | 16 | 78 | 89 | 84.2 | 81.3 |
| Sn | A4 | 2.81 | 0.707 | 16 | 55 | 55 | 52.1 | 52.6 |
| SiC | B3 | 2.81 | 0.707 | 16 | 211 | 222 | 202.9 | 203.6 |
| BN | B3 | 1.57 | 0.643 | 16 | 369 | 377 | 373 | 398.9 |
| BP | B3 | 1.97 | 0.643 | 16 | 173 | 172 | 180.4 | 170.8 |
| AlN | B4 | 1.9 | 0.643 | 16 | 201 | 195 | 180.9 | 196.6 |
| AlP | B3 | 2.36 | 0.643 | 16 | 86 | 92 | 88.3 | 89.9 |
| AlAs | B3 | 2.43 | 0.643 | 16 | 77 | 83 | 80.5 | 79.1 |
| AlSb | B3 | 2.66 | 0.643 | 16 | 59 | 61 | 56.1 | 61.3 |
| GaN | B4 | 1.97 | 0.643 | 16 | 190 | 172 | 164 | 193.8 |
| GaP | B3 | 2.36 | 0.643 | 16 | 89 | 92 | 86.6 | 88.8 |
| GaAs | B3 | 2.45 | 0.643 | 16 | 76 | 81 | 77.4 | 78.6 |
| GaSb | B3 | 2.65 | 0.643 | 16 | 57 | 62 | 59.6 | 62.1 |
| InN | B4 | 2.16 | 0.643 | 16 | 137 | 125 | 111.1 | 129.4 |
| InP | B3 | 2.54 | 0.643 | 16 | 73 | 71 | 66.1 | 69.3 |
| InAs | B3 | 2.61 | 0.643 | 16 | 60 | 65 | 61.2 | 62.8 |
| InSb | B3 | 2.81 | 0.643 | 16 | 47 | 50 | 47.7 | 51.4 |
| BeO | B4 | 1.64 | 0.474 | 16 | 244 | 252 | | |
| BeS | B3 | 2.1 | 0.474 | 16 | 105 | 107 | 132.7 | 112.9 |
| BeSe | B3 | 2.2 | 0.474 | 16 | 92 | 91 | 113.2 | 95.1 |
| BeTe | B3 | 2.4 | 0.474 | 16 | 67 | 68 | 86.5 | 72.2 |
| MgO | B1 | 2.1 | 0.316 | 36 | 163 | 178 | | 154.8 |
| MgS | B1 | 2.6 | 0.316 | 36 | 80 | 85 | 72.2 | 76.6 |
| CaO | B1 | 2.4 | 0.316 | 36 | 114 | 112 | | 98.8 |
| SrO | B1 | 2.58 | 0.316 | 36 | 88 | 87 | | 78.7 |
| BaO | B1 | 2.77 | 0.316 | 36 | 69 | 68 | | 62.5 |
| ZnO | B4 | 1.97 | 0.474 | 16 | 139 | 134 | | 141 |
| ZnS | B3 | 2.34 | 0.474 | 16 | 75 | 74 | 82.8 | 76.6 |
| ZnSe | B3 | 2.45 | 0.474 | 16 | 62 | 63 | 69.3 | 66.0 |
| ZnTe | B3 | 2.64 | 0.474 | 16 | 51 | 49 | 55.6 | 53.4 |
| CdS | B4 | 2.52 | 0.474 | 16 | 62 | 57 | 62.6 | 60.7 |
| CdSe | B4 | 2.62 | 0.474 | 16 | 56 | 50 | 54.4 | 53.7 |
| CdTe | B3 | 2.81 | 0.474 | 16 | 42 | 39 | 42.9 | 44.0 |
| HeSe | B3 | 2.63 | 0.474 | 16 | 49 | 49 | 55.1 | 53.0 |
| HgTe | B3 | 2.78 | 0.474 | 16 | 44 | 41 | 46.1 | 44.6 |
| MnO | B1 | 2.22 | 0.316 | 36 | 147 | 147 | | |
| FeO | B1 | 2.17 | 0.316 | 36 | 174 | 159 | | |

Table A.3.2 Bulk moduli for A_nB_m covalent crystals [1, 12–16]

| Crystal | Structure | d | n_{ij} | P | Λ | B_{Exp} | $B_{Cal,1}$ | $B_{Cal,2}$ |
|--------------------------------|-----------------|-------|----------|-----|-----------|-----------|-------------|-------------|
| Ag ₂ O | C3 | 2.044 | 0.474 | 8 | 2 | 84 | 79 | 81 |
| Cu ₂ O | C3 | 1.85 | 0.474 | 8 | 2 | 112 | 111 | 114 |
| ZrO ₂ | C1 | 2.195 | 0.474 | 32 | 2 | 235 | 223 | 222 |
| TiO ₂ | C4 | 1.96 | 0.596 | 18 | 2 | 224 | 233 | 235 |
| SnO ₂ | C4 | 2.05 | 0.596 | 18 | 2 | 205 | 200 | 201 |
| GeO ₂ | C4 | 1.878 | 0.596 | 18 | 2 | 258 | 269 | 271 |
| Al ₂ O ₃ | D5 ₁ | 1.915 | 0.474 | 24 | 1.5 | 252 | 253 | 246 |
| Fe ₂ O ₃ | D5 ₁ | 2.025 | 0.474 | 24 | 1.5 | 207 | 209 | 203 |

Table A.3.3 Bulk moduli for ionic crystals [1, 12, 17, 18]

| Crystal | Structure | d | n_{ij} | P | B_{Exp} | B_{Cal} |
|-------------------|-----------|-------|----------|-----|-----------|-----------|
| LiF | B1 | 2.01 | 0.165 | 36 | 76.4 | 76.7 |
| LiCl | B1 | 2.57 | 0.165 | 36 | 32.9 | 32.8 |
| LiBr | B1 | 2.75 | 0.165 | 36 | 26.0 | 25.9 |
| LiI | B1 | 3.01 | 0.165 | 36 | 19.3 | 19.0 |
| NaF | B1 | 2.31 | 0.165 | 36 | 47.1 | 47.4 |
| NaCl | B1 | 2.82 | 0.165 | 36 | 23.9 | 23.8 |
| NaBr | B1 | 2.99 | 0.165 | 36 | 19.6 | 19.4 |
| NaI | B1 | 3.24 | 0.165 | 36 | 14.9 | 14.7 |
| KF | B1 | 2.67 | 0.165 | 36 | 28.7 | 28.7 |
| KCl | B1 | 3.15 | 0.165 | 36 | 16.5 | 16.2 |
| KBr | B1 | 3.3 | 0.165 | 36 | 13.9 | 13.8 |
| KI | B1 | 3.53 | 0.165 | 36 | 11.1 | 10.9 |
| RbF | B1 | 2.83 | 0.165 | 36 | 24.1 | 23.5 |
| RbCl | B1 | 3.29 | 0.165 | 36 | 14.0 | 13.9 |
| RbBr | B1 | 3.44 | 0.165 | 36 | 12.0 | 12.0 |
| RbI | B1 | 3.67 | 0.165 | 36 | 9.6 | 9.6 |
| CsF | B1 | 3.00 | 0.165 | 36 | 19.3 | 19.2 |
| CsCl | B2 | 3.57 | 0.123 | 64 | 17.6 | 16.7 |
| CsBr | B2 | 3.72 | 0.123 | 64 | 15.4 | 14.5 |
| CsI | B2 | 3.96 | 0.123 | 64 | 12.5 | 11.7 |
| Li ₂ O | C1 | 2.01 | 0.237 | 32 | 88 | 100 |
| CaF ₂ | C1 | 2.365 | 0.247 | 32 | 84.0 | 85.6 |
| SrF ₂ | C1 | 2.5 | 0.247 | 32 | 71.3 | 70.7 |
| BaF ₂ | C1 | 2.683 | 0.247 | 32 | 55.5 | 55.3 |

Table A.3.4 Bulk moduli for multi-bond covalent crystals [1, 12, 14, 19–21]

| Crystal | Bond | N_μ | d | n_{ij} | P | Λ | B_μ | B_{Cal} | B_{Exp} |
|---|------|---------|-------|----------|-----|-----------|---------|------------------|------------------|
| Fe ₃ O ₄ | Fe–O | 4 | 1.927 | 0.474 | 16 | 1 | 144 | 178 | 187 |
| | Fe–O | 12 | 2.073 | 0.474 | 24 | 1.5 | 188 | | |
| SrTiO ₃ | Ti–O | 6 | 1.95 | 0.555 | 36 | 1 | 327 | 147 | 174 |
| | Sr–O | 12 | 2.76 | 0.165 | 72 | 2 | 134 | | |
| MgAl ₂ O ₄ | Mg–O | 4 | 1.88 | 0.474 | 16 | 1 | 157 | 210 | 202 |
| | Al–O | 12 | 1.95 | 0.474 | 24 | 1.5 | 233 | | |
| β -Si ₃ N ₄ | Si–N | 6 | 1.73 | 0.707 | 12 | 1.333 | 252.9 | 251 | 250 |
| | Si–N | 6 | 1.728 | 0.707 | 12 | 1.333 | 253.9 | | |
| | Si–N | 6 | 1.704 | 0.707 | 12 | 1.333 | 266.5 | | |
| | Si–N | 6 | 1.767 | 0.707 | 12 | 1.333 | 235 | | |
| c-Si ₃ N ₄ | Si–N | 1 | 1.78 | 0.781 | 16 | 1 | 298 | 308 | 300 |
| | Si–N | 3 | 1.88 | 0.588 | 24 | 1.5 | 311 | | |
| β -C ₃ N ₄ | C–N | 6 | 1.457 | 0.707 | 12 | 1.333 | 458 | 466 | 451 |
| | C–N | 6 | 1.447 | 0.707 | 12 | 1.333 | 469 | | |
| | C–N | 6 | 1.449 | 0.707 | 12 | 1.333 | 467 | | |
| | C–N | 6 | 1.447 | 0.707 | 12 | 1.333 | 469 | | |
| z-BC ₂ N | B–C | 4 | 1.559 | 0.6 | 16 | 1 | 361 | 411 | 403 |
| | C–C | 4 | 1.527 | 0.707 | 16 | 1 | 456 | | |
| | C–C | 8 | 1.537 | 0.707 | 16 | 1 | 445 | | |
| | B–N | 8 | 1.546 | 0.643 | 16 | 1 | 397 | | |
| | B–N | 4 | 1.579 | 0.643 | 16 | 1 | 369 | | |
| | C–N | 4 | 1.542 | 0.781 | 16 | 1 | 491 | | |
| SiO ₂ | Si–O | 4 | 1.76 | 0.596 | 18 | 2 | 340 | 329 | 314 |
| | Si–O | 2 | 1.808 | 0.596 | 18 | 2 | 310 | | |

Water and Ice

Video Clips of Different Modes and Frequencies (cm⁻¹) of (H₂O)_N Clusters (see Electronic Supplementary Material)

| | Dimer | Trimer | Tetramer | Penamer |
|----------------|-------|--------|----------|---------|
| O:H stretching | 184 | 251 | 229 | 198 |
| ∠O:H–O bending | 414 | 409 | 431 | 447 |
| ∠O–H–O bending | 1638 | 1644 | 1654 | 1646 |
| H–O stretching | 3565 | 3387 | 3194 | 3122 |

* 10^{-12} s = 1 THz = 33 cm⁻¹. ∠O:H–O bending is also called liberation mode.

(H₂O)_N Cluster Structures

Optimal configurations of (H₂O)_N clusters .

H₂O Structure at Different Temperatures

MD video clips of H₂O structure at different temperatures with ∠O:H–O and O:H length fluctuation. The dynamic structure changes from well-ordered to less-ordered because the thermal fluctuation with the rise of temperature. However, one can see the V-shaped O-H-O motifs remain intact in the less-ordered structure (see Electronic Supplementary Material)

300 K

200 K

100 K

Lagrangian-Laplace approach

Lagrangian mechanics of the O:H–O oscillators.

Water Skin Supersolidity of Water

Video clips: droplet dance on water surface evidence the hydrophobivity and elasticity of water skin (See Electronic Supplementary Material)

Temperature Dependence of Specific Heat, Density, and Thermal Conductivity of Water

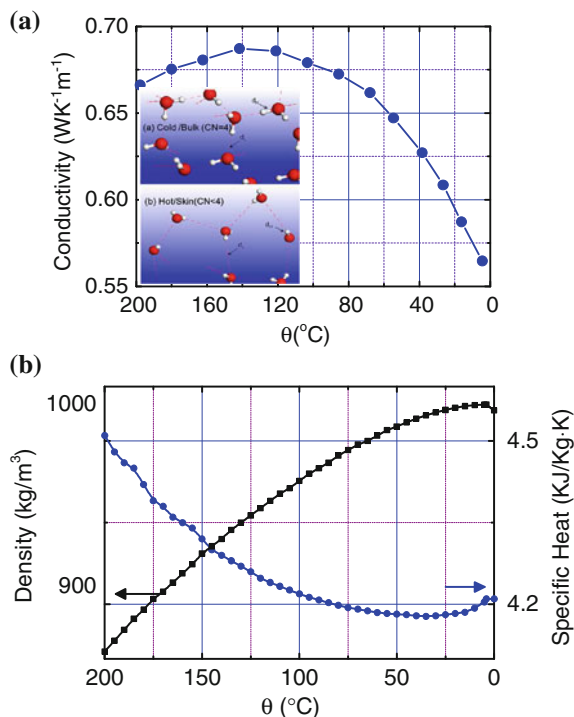


Fig. 1 Temperature dependence of (a) the thermal conductivity, mass density, and specific heat of H_2O [23]

References

1. J.M.D. Coey, Dilute magnetic oxides. *Curr. Opin. Solid State Mater. Sci.* **10**(2), 83–92 (2006)
2. S. Dahl, A. Logadottir, R.C. Egeberg, J.H. Larsen, I. Chorkendorff, E. Tornqvist, J.K. Nørskov, Role of steps in N_2 activation on $\text{Ru}(0001)$. *Phys. Rev. Lett.* **83**(9), 1814–1817 (1999)
3. B. Hammer, Bond activation at monatomic steps: NO dissociation at corrugated $\text{Ru}(0001)$. *Phys. Rev. Lett.* **83**(18), 3681 (1999)
4. T. Zambelli, J. Wintterlin, J. Trost, G. Ertl, Identification of the “active sites” of a surface-catalyzed reaction. *Science* **273**(5282), 1688–1690 (1996)
5. P. Kratzer, E. Pehlke, M. Scheffler, M.B. Raschke, U. Hofer, Highly site-specific H_2 adsorption on vicinal $\text{Si}(001)$ surfaces. *Phys. Rev. Lett.* **81**(25), 5596–5599 (1998)
6. G. Fratesi, S. de Gironcoli, Analysis of methane-to-methanol conversion on clean and defective Rh surfaces. *J. Chem. Phys.* **125**(4), 044701 (2006)
7. A. Kokalj, N. Bonini, C. Sbraccia, S. de Gironcoli, S. Baroni, Engineering the reactivity of metal catalysts: a model study of methane dehydrogenation on $\text{Rh}(111)$. *J. Am. Chem. Soc.* **126**(51), 16732–16733 (2004)
8. S. Abbet, A. Sanchez, U. Heiz, W.D. Schneider, A.M. Ferrari, G. Pacchioni, N. Rosch, Acetylene cyclotrimerization on supported size-selected Pd_n clusters ($1 \leq n \leq 30$): one atom is enough! *J. Am. Chem. Soc.* **122**(14), 3453–3457 (2000)
9. S. Abbet, U. Heiz, H. Hakkinen, U. Landman, CO oxidation on a single Pd atom supported on magnesia. *Phys. Rev. Lett.* **86**(26), 5950–5953 (2001)

10. C.J. Zhang, P. Hu, The possibility of single C–H bond activation in CH₄ on a MoO₃-supported Pt catalyst: a density functional theory study. *J. Chem. Phys.* **116**(10), 4281–4285 (2002)
11. F. Esch, A. Baraldi, C. Comelli, S. Lizzit, M. Kiskinova, P.D. Cobden, B.E. Nieuwenhuys, Atomic nitrogen on steps: a fast x-ray photoelectron spectroscopy study of the NO uptake on Rh(533), Rh(311), and Rh(111). *J. Chem. Phys.* **110**(8), 4013–4019 (1999)
12. S.W. Lee, S. Chen, J. Suntivich, K. Sasaki, R.R. Adzic, and Y. Shao-Horn, Role of surface steps of Pt nanoparticles on the electrochemical activity for oxygen reduction. *J. Phys. Chem. Lett.* 1316–1320 (2010)
13. P. Jakob, M. Gsell, D. Menzel, Interactions of adsorbates with locally strained substrate lattices. *J. Chem. Phys.* **114**(22), 10075–10085 (2001)
14. M. Gsell, P. Jakob, D. Menzel, Effect of substrate strain on adsorption. *Science* **280**(5364), 717–720 (1998)
15. J. Wintterlin, T. Zambelli, J. Trost, J. Greeley, M. Mavrikakis, Atomic-scale evidence for an enhanced catalytic reactivity of stretched surfaces. *Angew. Chem. Int. Ed.* **42**(25), 2850–2853 (2003)
16. B. Richter, H. Kuhlenbeck, H.J. Freund, P.S. Bagus, Cluster core-level binding-energy shifts: the role of lattice strain. *Phys. Rev. Lett.* **93**(2), 026805 (2004)
17. C.Q. Sun, Y. Wang, Y.G. Nie, B.R. Mehta, M. Khanuja, S.M. Shivaprasad, Y. Sun, J.S. Pan, L.K. Pan, Z. Sun, Interface charge polarization and quantum trapping in AgPd and CuPd bimetallic alloy catalysts. *PCCP* **12**, 3131–3135 (2010)
18. W. Li, A. Amirfazli, Superhydrophobic surfaces: adhesive strongly to water? *Adv. Mater.* **19**(21), 3421–3422 (2007)
19. X.M. Li, D. Reinhoudt, M. Crego-Calama, What do we need for a superhydrophobic surface? A review on the recent progress in the preparation of superhydrophobic surfaces. *Chem. Soc. Rev.* **36**(8), 1350–1368 (2007)
20. A.B.D. Cassie, S. Baxter, *Trans. Faraday Soc.* **40**, 546 (1944)
21. C. Lee, C.H. Choi, and C.J. Kim, Structured surfaces for a giant liquid slip. *Phys. Rev. Lett.* **101**(6), 064501 (2008)
22. G.P. Fang, W. Li, X.F. Wang, G.J. Qiao, Droplet motion on designed microtextured superhydrophobic surfaces with tunable wettability. *Langmuir* **24**(20), 11651–11660 (2008)
23. R.F. Service, Semiconductor clusters, nanoparticles, and quantum dots. *Science* (271), (1996)

Author Biography



Dr Chang Q Sun received a BSc in 1982 from Wuhan University of Science and Technology and an MSc in 1987 from Tianjin University, China and served there as a faculty till 1992. He completed his PhD in 1997 at Murdoch University, Australia, and then joined Nanyang Technological University in 1997 as a faculty member.

He has been working on the theme of coordination bond and electronic engineering, which include (1) bond-band-barrier (3B) correlation for C, N, O chemisorption 3B dynamics; (2) hydrogen-bond asymmetric relaxation and H₂O anomalies; (3) bond-order-length-strength (BOLS) correlation for the physical chemistry of defect, surface, and nanosolid; (4) nonbonding electron polarization (NEP) at under and hetero-coordinated sites; (5) local-bond-average approach for solid meso-mechano-thermo dynamics; (6) BOLS-TB algorithm for edge states discrimination; (7) coordination-resolved electron spectroscopy for local binding energy (ZPS); (8) Raman quantification of the length, energy, compressibility, Debye temperature, force constant and relaxation dynamics of bonds; (9) STM/S/VLEED quantification of four-stage Cu₃O₂ bonding kinetics; and (10) functional materials devise, etc.

Dr Sun has published over 250 principally-authored journal articles, 4 book chapters, 4 patents, and 12 themed reports in *Surface Science Reports*, *Chemical Reviews*, *Progress in Materials Science*, and *Progress in Solid State Chemistry*. etc.

He was conferred the First Laureate of the 25th Khwarizmi International Science Award in 2012, the Inaugural Nanyang Award of Research in 2005, and finalisted twice (2003 and 2012) for the Natinal/Presidential Science Award of Singapore. He was elected as Fellow of the Royal Society of Chemistry (FRSC, 2006) and the Institute of Physics (FInstP, 2007). He is currently on the Editorial Advisory Board for 8 journals and has received honorary/visiting appointments at China Jiliang University, City University Hong Kong, East China Normal University, Jilin University, King's College London, Tianjin University, Tokyo Institute of Technology, University of Texas at Dallas, Xiangtan University, etc.